

AD 701545



*Fundamental
Aspects of
Solid Propellant
Rockets*

F.A. WILLIAMS, M. BARRERE and N.C. HUANG

Reproduced by the
CLEARINGHOUSE
for Federal Scientific & Technical
Information Springfield Va. 22151

AGARD

The Advisory group for Aerospace Research and Development (AGARD) initiated in 1951 is part of the North Atlantic Treaty Organization and consists of a number of permanent specialist scientific panels and committees from NATO countries. These panels are responsible for sponsoring technical meetings and symposia and the publication of technical papers.

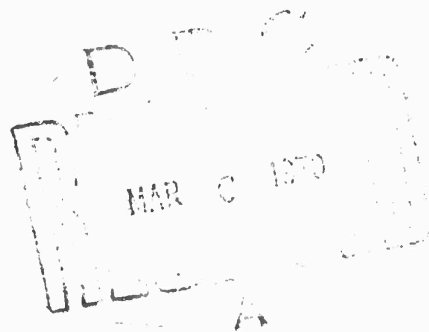
Part of the AGARD publishing programme takes the form of good quality letterpress or litho, hard cover volumes of symposia proceedings or monographs on significant areas of astronautical and aeronautical research and development.

AGARDograph Number
One Hundred and Sixteen

Fundamental Aspects of Solid Propellant Rockets



The Advisory Group for
Aerospace Research and
Development. NATO



Authors

F. A. WILLIAMS
M. BARRÈRE
N. C. HUANG

Published and printed by



Technivision Services
Slough, England

A Division of Engelhard Hanovia International Ltd.

Copyright



October 1989
The Advisory Group for Aerospace
Research and Development. NATO

Library of Congress Catalog Card No. 68-31381

Standard Book Number 85102.016.X

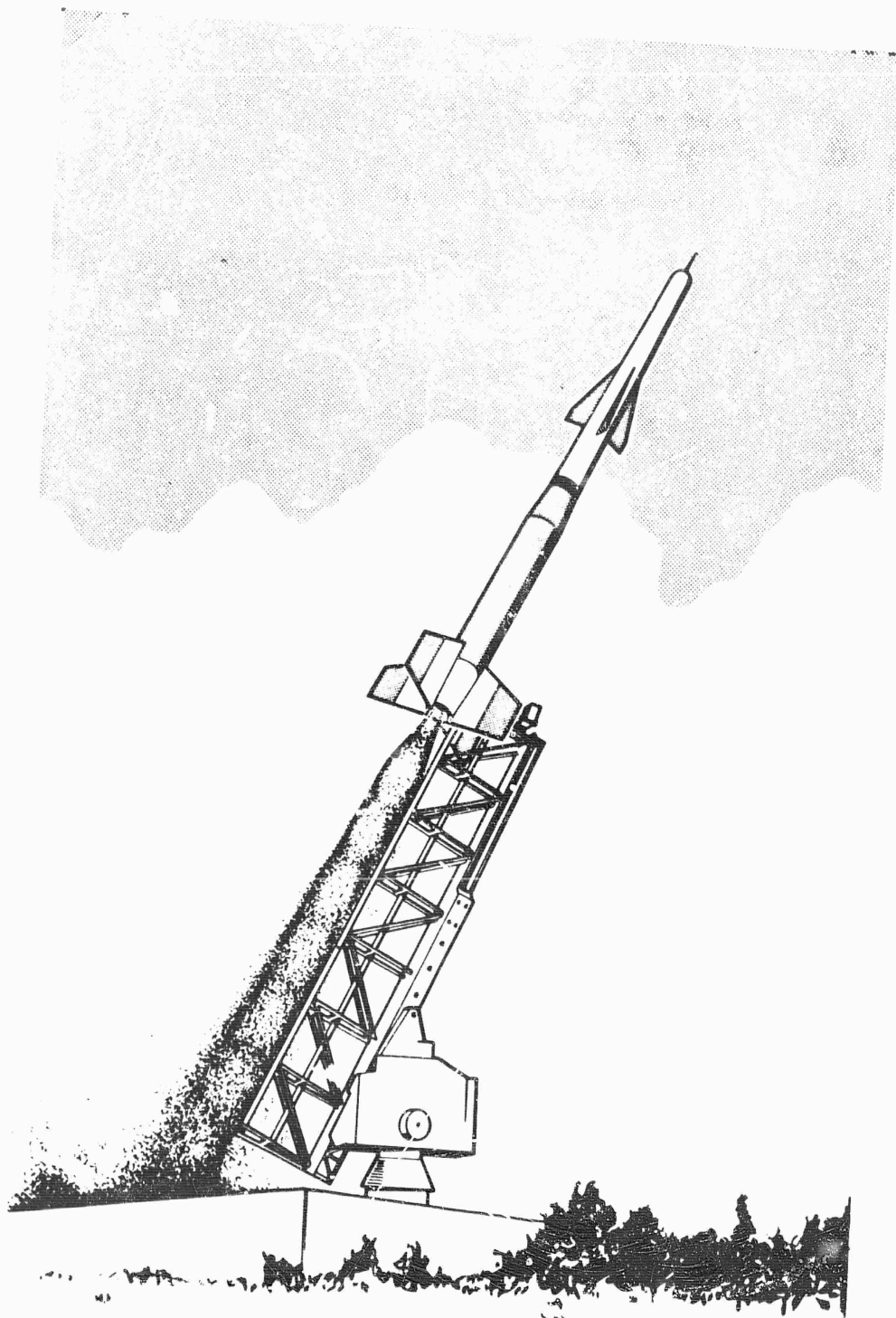


Plate 1. A solid propellant booster motor launches the experimental missile STATALTEX on a high-altitude, hypersonic ($> \text{Mach. } 5$) test flight, courtesy of ONERA.

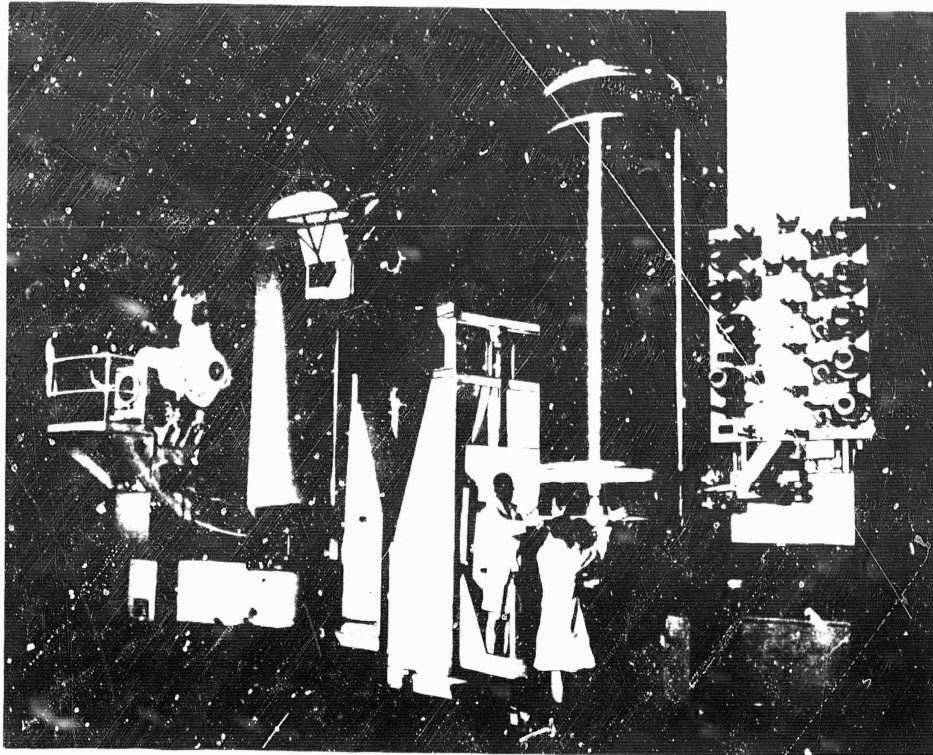


Plate 2. The manufacture of two first stage rocket motor chambers for the submarine-launched Polaris A-3 ballistic missile. The whirling arm of the machine in the rear is applying circumferential wraps of glass filaments over the mandrel while the machine in the foreground is applying the final hoop wraps. Following wrapping, the chamber is placed in an oven where the resin impregnated filaments become a homogeneous structure. The mandrel is then withdrawn prior to casting the chamber with propellant; courtesy Aerojet General Corporation.

Contents

Preface

xxi

Chapter 1

1

An Introduction to Solid Propellant Rocket Motors - Generalities

- 1 Introduction
- 2 Description and Brief History
 - 2.1 Description of Current Solid Propellant Rockets
 - 2.2 History
- 3 Classification
 - 3.1 Rocket Motors for Lower Stages (Boosters)
 - 3.2 Rocket Motors for Upper Stages and for Space Vehicles
 - 3.3 Satellite Launchers
 - 3.4 Sounding Rockets
 - 3.5 Auxiliary Rocket Motors to perform Guidance and Control Functions
 - 3.6 Assisted Take-off Rocket Motors for Aircraft
 - 3.7 Military Applications
 - 3.8 Diverse Applications
- 4 Interest in Solid Propulsion
- 5 Outline of the Presentation

Chapter 2

37

Nozzle Flow and Characteristic Parameters

- 1 Quasi-One-Dimensional Theory - Isentropic Expansion
 - 1.1 Introduction
 - 1.2 Derivation of Quasi-One-Dimensional Equations
 - 1.2.1 Mass Conservation
 - 1.2.2 Momentum Conservation
 - 1.2.3 Energy Conservation
 - 1.3 Isentropic Flow
 - 1.3.1 Simplified Conservation Equations
 - 1.3.2 One-component Ideal Gases with Constant Heat Capacities
 - 1.4 Nozzle Flow
 - 1.4.1 Choking in Isentropic Flow
 - 1.4.2 Flow in deLaval Nozzles
 - 1.4.3 Shock Waves
 - 1.4.4 Non-one-dimensional Flows in Nozzles
 - 1.4.5 Nozzle Flow Formulas
 - 1.5 Thrust and Rocket Performance Parameters
 - 1.5.1 Derivation of Thrust Formula
 - 1.5.2 Theoretical Thrust Formula; Maximum Thrust
 - 1.5.3 Thrust Coefficient
 - 1.5.4 Characteristic Velocity
 - 1.5.5 Specific Impulse
 - 1.5.6 Other Performance and Design Parameters
- 2 Effects of Multicomponent, Reacting Gas Flow
 - 2.1 Introduction
 - 2.2 Frozen or Equilibrium Isentropic Flow
 - 2.2.1 Frozen Flow
 - 2.2.2 Equilibrium Flow

- 2.2.3 Comparison of Performance with Equilibrium and Frozen Nozzle Flow
- 2.3 Relaxing Flows
- 3 Two-Phase Flow Effects
 - 3.1 Introduction
 - 3.2 Theories; Effects on Performance
 - 3.2.1 Two-Phase Flow Without Particle Lag
 - 3.2.2 Equations of Two-Phase Flow with Particle Lags
 - 3.2.3 Dimensionless Lag Parameter τ
 - 3.2.4 Large Lag Limit $\tau \gg 1$
 - 3.2.5 Small Lag Limit $\tau \ll 1$
 - 3.2.6 Numerical Calculations for Intermediate Values of τ
 - 3.2.7 Influence of Phenomena Neglected in the Theory of Section 3.2.2
 - 3.3 Effects on Nozzle Design
 - 3.4 Experimental Results
- 4 Nozzle Heat Transfer
 - 4.1 Introduction
 - 4.2 Unsteady Heat Conduction in Uncooled Nozzle Walls
 - 4.3 Steady-State, Turbulent Heat Transfer Through the Boundary Layer
 - 4.4 Additional Heat Transfer Considerations
- 5 Discussions of Other Deviations from Ideality
 - 5.1 Influence of Non-One-Dimensional Flow on Nozzle Performance and Design
 - 5.2 Boundary Layer Growth
 - 5.3 Jet Detachment
 - 5.4 Interaction of the External Exhaust Jet with its Surroundings
- 6 Thrust Vector Control
 - 6.1 Introduction
 - 6.2 Mechanical Control Surfaces
 - 6.3 Fluid Injection
 - 6.3.1 Description of the Phenomenon
 - 6.3.2 Theoretical Analyses
 - 6.3.3 Comparison with Experimental Results
 - 6.3.4 Choice of Injectant Fluid
 - 6.3.5 Hot Gas Valves
 - 6.4 Comparison of Mechanical and Fluid Injection Thrust Vector Control
- 7 Compatibility of Solid-Propellant Motors with New Nozzle Design Concepts

Chapter 3 Performance of Solid Propellants

107

- 1 Introduction
 - 1.1 Definition of Mixture Ratio
 - 1.2 Composition of Propellants and of Products of Combustion
 - 1.2.1 Propellants - Homogeneous Propellants
Heterogeneous Propellants
 - (a) Oxidizers
 - (b) Fuels
 - (c) Hybrid binders
 - 1.2.2 Combustion Products
- 2 Theoretical Performance Calculations
 - 2.1 Equilibrium Composition Equations
 - 2.1.1 Definition of Basis
 - 2.1.2 Governing Equations
 - Atom Conservation Equations
 - Chemical Equilibrium Equations

- 2.2 Simolified Calculations of Equilibrium Compositions
 - 2.2.1 Gaseous Combustion Products
 - 2.2.2 Combustion Products Containing a Condensed Material
- 2.3 General Methods for Calculating Equilibrium Compositions
 - 2.3.1 Huff Method
 - 2.3.2 White Method
 - 2.3.3 Brinkley Method
- 2.4 Examples of Applications to Propellants Containing H, Li, Be, B, C, Al, N, Cl, O and F
- 2.5 Evaluation of Propellant Performance
 - 2.5.1 Thermodynamics of Equilibrium Mixtures
 - 2.5.2 Calculation of Performance - Adiabatic Flame Temperature
 - General Aspects of Performance Calculation
 - Performance for Frozen Nozzle Flow
 - Performance for Equilibrium Nozzle Flow
 - Influence Coefficients
 - Performance of some Propellants
- 2.6 Research on Solid Propellant Constituents Conducive to Maximal Performance
 - 2.6.1 Studies of Energetic Fuel Additives
 - 2.6.2 Studies of Binders
 - 2.6.3 Studies of Oxidizers
 - 2.6.4 Studies of Liquid Injection
 - 2.6.5 General Remarks
- 3 Experimental Determination of Performance
 - 3.1 Laboratory Methods
 - 3.1.1 Method Based on Pressure Measurement
 - 3.1.2 Method Based on Velocity Measurement
 - 3.2 Rocket Motor Tests
 - 3.2.1 Conventional Test Stands
 - 3.2.2 Measurement of the Gas Velocity in the Motor
- 4 Comparison of Theory and Experiment

Chapter 4

185

Motor Operation

- 1 Introduction
- 2 Burning Rate Laws
 - 2.1 Laws Proposed for the Burning Rate (Influence of Certain Parameters)
 - 2.2 Techniques for Burning Rate Measurements
- 3 Motor Operating Characteristics (Time Evolution of the Pressure and of the Web Thickness)
 - 3.1 End Burning Grain
 - 3.2 Grains with Central Perforation
 - 3.3 Propellant Grain Geometry
 - a) General Case
 - b) Star and Wagon-Wheel Cross-Section Grains
 - c) Segmented Grains
 - d) Slotted Grains
 - e) Grains with Nonuniform Axial Profiles and Composite Configuration
 - f) Helical Grains
 - 3.4 Spherical Grains
 - 3.5 Dual-Composition Solid Propellant
 - 3.6 Remarks on the Pressure-Time Curve obtained during a Motor Firing
- 4 Optimization of the Motor Geometry in Particular Cases
- 5 Solid Sublimation Motors
- 6 Conclusions

Chapter 5 Experimental Aspects of Steady-State Combustion Phenomena

253

- 1 Introduction
- 2 Combustion of Double-Base, Homogeneous Propellants
 - 2.1 Experimental Techniques for Studying Homogeneous Solid Propellants
 - 2.2 Experimental Results
- 3 Determination of the Physico-Chemical Characteristics of the Propellant Components of Heterogeneous Propellants
 - 3.1 Linear Pyrolysis Rates
 - 3.1.1 Measurement Devices
 - 3.1.2 Results
 - 3.1.2.1 Fuels
 - 3.1.2.2 Oxidizers
 - 3.1.3 Importance of Pyrolysis Measurements
 - 3.2 Deflagration Rates of Certain Oxidizers
- 4 Proposed Model Experiments for the Analysis of the Mechanism of Heterogeneous Solid Propellant Combustion
 - 4.1 Combustion of Oxidizer Spheres in a Gaseous Fuel Stream
 - 4.2 Porous-Core Burner
 - 4.3 Reaction Kinetics in the Gas Phase
 - 4.4 Pressed Solid Propellant Strands
 - 4.5 Combustion of Metals
- 5 Studies of Combustion Mechanisms with Heterogeneous Propellants
 - 5.1 Direct Methods
 - 5.2 Indirect Methods
 - 5.2.1 Low Pressure Domain
 - 5.2.2 Moderate Pressure Domain (5 to 50 atm)
 - 5.2.3 Plateau Domain
 - 5.2.4 High Pressure Domain ($p > 100$ atm)
 - 5.3 Summary of Combustion Domains

Chapter 6 Theories of Steady-State Solid Propellant Combustion

333

- 1 Basic Equations of Aerothermochemistry
 - 1.1 Introduction
 - 1.2 Origin of the Equations
 - 1.3 Integral Form of the Governing Equations
 - 1.4 Differential Form of the Governing Equations
 - 1.5 Transport Phenomena; Reaction Rates
 - 1.6 Thermodynamic Relations; Counting of Variables
 - 1.7 Observation Conditions at an Interface
- 2 Theories of Homogeneous Solid Propellant Combustion
 - 2.1 Adiabatic Theories
 - 2.1.1 History
 - 2.1.2 Theories of Rice and Ginell and of Parr and Crawford
 - 2.1.3 Theories of Johnson and Nachbar and of Spalding
 - 2.1.3.1 Definition of the Johnson-Nachbar Model
 - 2.1.3.2 Basic Equations Governing the Gas-Phase Problem
 - 2.1.3.3 Boundary Conditions for the Gas-Phase Problem
 - 2.1.3.4 Dimensionless Mathematical Formulation of the Gas-Phase Problem
 - 2.1.3.5 Bounds for the Solution to the Gas-Phase Problem
 - 2.1.3.6 Iterative Solution of the Gas-Phase Problem
 - 2.1.3.7 The Surface Gasification Process
 - 2.1.3.8 Derivation of the Unopposed Surface Gasification Rate Law

- 2.1.3.9 The Surface Equilibrium Boundary Condition
- 2.1.3.10 Intermediate Surface Boundary Conditions
- 2.1.3.11 The Pressure Dependence of the Burning Rate for Unopposed Surface Gasification Process
- 2.1.3.12 The Johnson-Nachbar Results for the Adiabatic Burning Rate of Ammonium Perchlorate
- 2.1.3.13 The Pressure Dependence of the Burning Rate for Surface Equilibrium
- 2.1.3.14 Structure of Gas-Phase Reaction Zone
- 2.2 Nonadiabatic Theories
 - 2.2.1 The Role of Heat Losses
 - 2.2.2 Types of Heat Losses
 - 2.2.3 Energy Conservation Equations, Including Heat Losses
 - 2.2.4 The Origin of the Influence of Heat Loss on the Burning Rate
 - 2.2.5 Dependence of Heat Loss on Surface Temperature
 - 2.2.6 The Modifications Produced in the Burning Rate Analysis by Nonadiabaticity
 - 2.2.7 Nonadiabatic Analysis with Unopposed Surface Rate Process
 - 2.2.8 Interpretation of Double Eigenvalue Solution
 - 2.2.9 Comparison of the Nonadiabatic Theory of Johnson and Nachbar with Experiment
 - 2.2.10 Nonadiabatic Analysis with Surface Equilibrium
- 3 Theories of the Decomposition of Selected Constituents of Composite Propellants
 - 3.1 Introduction
 - 3.2 Theories of Hot-Plate Pyrolysis
 - 3.2.1 Porous Plate
 - 3.2.2 Impermeable Plate
 - 3.3 Pyrolysis of Propellant Constituents
 - 3.3.1 Fuel Constituents
 - 3.3.2 Ammonium Nitrate
 - 3.3.3 Ammonium Perchlorate
- 4 Theories of Heterogeneous Solid Propellant Combustion
 - 4.1 Introduction
 - 4.2 Two-Temperature Concept
 - 4.3 Ideas Concerning the Interplay of Diffusion Flames and Premixed Flames
 - 4.4 Sandwich Burner Models
- 5 Theories of Combustion of Metal Particles
 - 5.1 Introduction
 - 5.2 Description and Classification of Behavior of Various Burning Metals
 - 5.3 Theories of the Combustion of Spheres of Metals with Nonvolatile, Insoluble Oxides
 - 5.3.1 Dilute Heterogeneous Diffusion Flame
 - 5.3.2 Metal Sphere Combustion
 - 5.3.3 Remarks Concerning Assumptions for an Improved Theoretical Treatment of Aluminium-Sphere Combustion

Chapter 7 Erosive Burning

395

- 1 Introduction
- 2 Experimental Aspect
 - 2.1 Laboratory Methods for Determining the Erosion Function
 - a. Method of Marklund and Lake
 - b. Zucrow's method

- c. Nadaud's method
 - d. General remarks on the Laboratory Methods
 - 2.2 Direct Measurement of Erosive Burning Velocity in Rocket Motors
 - a. Burn Interruption Technique
 - b. Radiographic and Cineradiographic Techniques
 - c. Probe Techniques
 - 2.3 Indirect Methods on Rocket Motors
 - 2.4 Experimental Results
 - 2.4.1 General Description
 - 2.4.2 Influence of the Various Parameters
 - a. Influence of the Gas-flow
 - b. Influence of the Nature of the Propellant and of Grain Geometry
 - c. Influence of the Operating Conditions
 - d. Summary
 - 2.4.3 Proposed Experimental Laws
- 3 Theoretical Aspects
 - 3.1 Semi-Empirical Theories
 - a. Lenoir and Robillard's Theory
 - b. Theory of Vandenkherckhove
 - c. Theories Based upon the Flame Structure
 - 3.2 Aerothermochemical Approach to the Problem of Erosive Burning
- 4 Effect of Erosion Phenomena on the Geometry of the Central Port

Chapter 8

Ignition and Extinction of Solid Propellants

457

- 1 Ignition
 - 1.1 Introduction
 - 1.2 Experimental Methods in Ignition Studies
 - 1.3 Experimental Results
 - 1.4 Theoretical Analyses of Ignition
 - 1.4.1 Introduction
 - 1.4.2 Ignition by Means of a Stagnant Hot Gas
 - 1.4.3 Ignition by Means of a Flowing Hot Gas
 - Analysis
 - Discussion
 - Relationship to Stagnant Hot Gas Analysis
 - 1.4.4 Ignition Processes Involving Heterogeneous Reactions and Radiant Energy Transfer
 - Introduction
 - Derivation of Governing Integral Equation
 - Solution for Small Values of t
 - Numerical Solution for Hypergolic Ignition without Radiant Flux
 - Discussion of Results for Hypergolic Ignition without Radiant Flux
 - Diffusion-Controlled and Rate-Controlled Limits
 - Solution and Results for Radiant Ignition without Surface Reactions
 - Discussion of Results with Combined Incident Radiation and Hypergolicity
 - Generalizations
 - 1.4.5 Ignition by Means of Condensed Materials
 - 1.4.6 Critical Comparison of Existing Theoretical Studies

- 1.5 Motor Ignition
 - Introduction
 - Ignition Devices
 - Analyses of the Various Processes
 - Scale Effects
- 2 Extinction
 - 2.1 Extinction by Depressurization
 - Extinction of Samples by Depressurization
 - Motor Extinction by Depressurization
 - 2.2 Extinction by Injection of Inhibiting Substances
 - Extinction by Water Injection
 - Extinction by Powder Injection (Explosive Canister Technique)
- 3 Conclusions

Chapter 9

555

Experimental Aspects of Combustion Instability

- 1 History; Suppression Techniques
- 2 Classification of Instabilities
- 3 Experimental Methods for Analyzing Combustion Instabilities
 - 3.1 Instantaneous Pressure Measurements
 - 3.2 Vibrations of the Case
 - 3.3 Methods of Data Analysis
 - 3.4 Optical Methods for Combustion Instability Analysis
 - 3.5 Other Techniques
- 4 Experimental Studies of Linear Acoustic Instabilities (Fundamental Viewpoint)
 - 4.1 Basis for Fundamental Laboratory Studies
 - 4.2 Qualitative Experiments Employing Acoustic Generators
 - 4.3 Shock Tube Techniques
 - 4.4 Experiments with Small End-Burning Motors
 - 4.5 Experiments with Double Motors
 - 4.6 Experiments with T-Motors and T-Burners
 - 4.6.1 Definition
 - 4.6.2 Principles for Measurement of Acoustic Admittance
 - 4.6.3 Specific Configurations
 - 4.6.4 Experimental Strategies
 - 4.6.5 Experimental Results
- 5 Experimental Studies of Acoustic Instabilities in Motors
- 6 Experimental Studies of Nonacoustic and Nonlinear Combustion Instabilities
 - 6.1 Introduction
 - 6.2 Shock-Induced Oscillations
 - 6.3 Vortex Development
 - 6.4 Nonacoustic Oscillatory Instabilities at Low Pressure
 - 6.4.1 Introduction
 - 6.4.2 Motor Observations; Practical Consequences
 - 6.4.3 Explanations in Terms of Intrinsic Combustion Characteristics; Strand Observations
 - 6.4.4 Explanations in Terms of Combustion Response - Residence Time Interaction; L^* Instability
 - 6.4.5 Interaction of Acoustic and Nonacoustic Phenomena

Chapter 10

605

Theoretical Analyses of Combustion Instability

- 1 Introduction

- 2 Acoustic Vibrational Modes
 - 2.1 Derivation of Wave Equation
 - 2.2 Modes in Cavities
 - 2.3 Acoustic Energy in a Sound Field
- 3 Acoustic Amplification
 - 3.1 The Acoustic Admittance
 - 3.2 Relationship Between Admittance and Energy Growth Rate for Monochromatic Waves in Cavities
 - 3.3 Alternatives and Generalizations
- 4 Acoustic Damping Mechanisms
 - 4.1 Introduction
 - 4.2 Nozzle Damping
 - 4.2.1 End-Vented Chambers
 - 4.2.1.1 Literature
 - 4.2.1.2 Formulation
 - Solution for Linear Velocity Profiles
 - Discussion of Results
 - Non-One-Dimensional Oscillations
 - Comparison of Theory and Experiment
 - 4.2.2 Side-Vented Chambers
 - Sonic Nozzles
 - Literature on Subsonic Orifices
 - 4.3 Other Boundary Damping Processes
 - 4.3.1 Wall Friction
 - Introduction
 - Formulation
 - Solution and Results
 - Accurate Formulas for Dissipation due to Wall Friction
 - 4.3.2 Wall Heat Transfer
 - 4.3.3 Complex Wall Loss Phenomena
 - 4.4 Homogeneous Damping
 - 4.4.1 Viscous and Heat Conduction Losses
 - 4.4.2 Chemical and Molecular Relaxation Losses
 - 4.4.3 Other Homogeneous Damping Processes
 - 4.5 Particle Damping
 - 4.5.1 Overview and Literature
 - 4.5.2 Analysis for Very Small Particles
 - 4.5.3 Interpretation of Results
 - 4.5.4 Accurate Formulas
 - 4.5.5 Experimental Verification
 - 4.6 Viscoelastic Damping in the Solid
 - 4.6.1 General Aspects of Solid-Phase Losses
 - 4.6.2 Vibrations of Gas-Solid Systems
 - 4.6.3 Implications Concerning Attenuation
 - 4.6.4 Results of Calculations
 - 4.7 Summary
- 5 Theories of Acoustic Amplification Mechanisms
 - 5.1 Introduction
 - 5.2 General Properties of Interfacial Acoustic Admittance
 - 5.2.1 Relationship between Admittance and Perturbation of Mass Flow Rate
 - 5.2.2 Qualitative Properties of Admittance
 - 5.3 Time Lag Theories
 - 5.3.1 Simplified Time Lag Concept
 - 5.3.2 Improved Time Lag Theories
 - 5.3.3 Results and Critique of Time Lag Theories

- 5.4 Mechanistic Models
 - 5.4.1 Basic Model
 - 5.4.2 Extensions
- 5.5 Aerothermochemical Approaches
 - 5.5.1 Low-Frequency Response
 - 5.5.2 Response at Arbitrary Frequencies
- 5.6 Models for Heterogeneous Propellants
- 5.7 Small-Amplitude Erosive Effects
 - 5.7.1 Introduction
 - 5.7.2 Acoustic Response with Steady-State Erosion
 - 5.7.3 Acoustic Erosion without Steady-State Erosion
 - 5.7.4 Combined Steady-State and Acoustic Erosion
- 6 Theories of Nonlinear and Nonacoustic Instabilities
 - 6.1 Introduction
 - 6.2 Changes in Mean Burning Rate
 - 6.3 Inherent Instability
 - 6.4 Low-Frequency Instability and Chuffing
 - 6.5 Nonsinusoidal Wave Forms
- 7 Comparison of Theory with Experiment

Chapter 11

675

Mechanical Properties and Stress Analysis of Solid Propellant Grains

- 1 Introduction
 - 1.1 Overview
 - 1.2 Viscoelasticity
- 2 Mechanical Properties of Viscoelastic Solids
 - 2.1 Differential Operator Representation
 - 2.2 Integral Operator Representation
 - 2.3 Complex Modulus and Complex Compliance Representations
 - 2.4 Temperature Effects
 - 2.5 Representation Based on Irreversible Thermodynamics
 - 2.6 Nonlinear Stress-Strain Relations
- 3 Stress Analysis in Linear Viscoelasticity
 - 3.1 Stress Analysis in Linear Viscoelasticity
 - 3.2 Stresses in an Encased Viscoelastic Cylinder
 - 3.3 Stresses in an Encased Viscoelastic Spinning Cylinder with Ablating Cavity Surface
 - 3.4 Stress Analysis for Nonisothermal Viscoelastic Cylinders
 - 3.5 Grain Slump due to Axial Acceleration
 - 3.6 Viscoelastic Cylinder Reinforced by Elastic Wires
- 4 Failure and Failure Criteria for Solid Propellant Rockets
 - 4.1 Preliminary Remarks
 - 4.2 Formation and Propagation of Cracks
 - 4.3 Definition of Failure Criteria
 - 4.4 Conclusion

Chapter 12

751

The Future of Solid Propellant Rocketry

- 1 Introduction
- 2 Future of Propellants
 - (a) Energetic qualities
 - (b) Kinetic qualities
 - (c) Utilization qualities
- 3 Fundamental Research on the Combustion of New Propellants

xx

- 4 New Ideas on Unsteady Combustion**
- 5 Technological Development - Improvement of Flexibility and Thrust Control Capabilities**
- 6 New Uses for Solid Propellant Rockets**

Addendum	765
Names Index	771
Subject Index	779

Preface

For ten years there has been an acute need for a textbook in the English language on solid propellant rockets. Books have been published on propulsion in general and on rocket propulsion specifically, but these sometimes tend to de-emphasize propulsion by means of solid propellants, in order to devote more space to topics such as liquid-propellant or nuclear propulsion, which have occasionally been deemed more exciting or more exotic in some respects. The most recent book in English which is devoted exclusively to solid propellant rockets is the short monograph by Wimpers, entitled 'Internal Ballistics of Solid Propellant Rockets' and published in 1950. There are two recently published books in Russian on solid propellant rockets, one by Kurov and Doljanski (1961) and one by Zeldovich and Rivin (1963), but these have not been translated into English yet. The need for an English-language text on solid propellant rockets provided the underlying motivation for writing the present volume.

The objective of this book is twofold, first to present basic material on solid propellant rockets which can be used for classroom instruction and second to carry the reader to the frontiers of research in a number of specific areas of solid propellant rocketry. Although there is some material (e.g., Chapters 1, 2 and 12) which might appropriately be used in undergraduate courses, the instructional value of the book lies primarily at the graduate level. An attempt has been made to enhance the educational utility of the monograph by presenting the more elementary aspects of the subject first (Chapters 1 to 4), before proceeding to detailed and more advanced treatment of specific areas of research (Chapters 5 to 11). An attempt has also been made to present the research topics in a pedagogic manner, to aid the graduate student or the practising engineer who is not familiar with the subject material.

Research workers in the field of solid propellant rocketry should find this presentation useful, both as a reference to previous research endeavors and as a guide to desirable avenues for future research. The book delves more deeply into a number of areas of research than any previous volumes on the subject have done. Indeed, progress in the field has been continuing so rapidly that it has not been possible for earlier books to attain the depth of the present monograph in the specific areas of research chosen for emphasis herein.

It seems appropriate to record here the parts of the book for which each author assumed primary responsibility. Huang wrote all of Chapter 11, except for Section 4 on Failure Analysis which was prepared by Barrère and Section 1.1 which was prepared by Williams. The rest of the book was written jointly by Barrère and Williams, with Barrère preparing the first drafts for Chapters 3, 4, 5, 7 and for most of Chapter 8, and with Williams preparing the first drafts for Chapters 2, 6, 9 and 10. Chapters 1 and 12 were written jointly by Barrère and Williams, who also jointly revised successive versions of the entire monograph in an effort to make it into a coherent work. Williams is responsible for the final English-language editing of the manuscript.

We wish to thank many of our colleagues, especially those at the University of California, San Diego, at the Office National d'Etudes et de Recherches Aérospatiales and at the Direction des Poudres for numerous stimulating discussions relating to many aspects of this work. The list of names of those to whom we are indebted is too long to be presented here. However, we must explicitly thank Professor S.S. Penner for his interest and for his aid in initiating this work, Dr. W.R. Maxwell for his constructive review of the monograph and Mr. E.W. Price for his welcomed review of Chapter 9. The many hours spent by Simone Barrère and especially by Paulette Thompson in proofreading and typing successive

versions of the manuscript were essential to the successful completion of the book. One of us, F.A. Williams, wishes to thank the Propulsion Division of the Air Force Office of Scientific Research for continued support of research (Grant No. AF-AFOSR-927-67 and also Project THEMIS) on related subjects during the writing of this material. Another author, M. Barrere thanks the Direction des Poudres for granting permission to publish some results which were obtained under contract. We also extend our thanks to AGARD for supporting this writing under a contract supervised helpfully by Colonel Ch. Lupold.

M. Barrère Paris, France

N.C. Huang La Jolla, California

F.A. Williams

Chapter 1

An Introduction to Solid Propellant Rocket Motors- Generalities

Nomenclature

A	constant (see Eq. 1-5)
a_o	initial vehicle acceleration
F	thrust
\bar{g}	average acceleration of gravity experienced by vehicle over its flight path
g_o	gravitational conversion factor
I_{sp}	specific impulse
K_D	constant of proportionality between Δv_D and area
K_t	constant of proportionality, dependent on technology
K_v	constant of proportionality, dependent on technology
M_L	payload weight
M_p	propellant weight
M_s	structure weight
M_{sf}	structure weight proportional to thrust
M_{sv}	structure weight proportional to initial propellant volume
M_0	launch weight
R	mass ratio of rocket vehicle
t_b	burning time
u	$\equiv M_L / M_0$ ratio of payload mass to launch mass
v	$\equiv \rho M_L / M_p$, ratio of payload mass to propellant volume
α	constant (see Eq. 1-5)
Δv	velocity change imparted to a given payload
Δv_D	loss in velocity increment due to drag
ρ	propellant density
ψ	cosine of angle between vehicle trajectory and vertical

An Introduction to Solid Propellant Rocket Motors - Generalities

1. Introduction

In general a vehicle is propelled by forces, termed thrusts, which provide a desired component of acceleration. These forces can be produced in a variety of ways. Solid propellant rockets are examples of a pure reaction system in which the propulsive forces are produced by the ejection of mass (propellants) initially contained in the system. Self-contained systems of this type are called rocket motors and can operate in space as well as in atmospheres, since they do not require an external propulsive fluid.

Four categories of rocket motors may be defined, according to the physical state of the propellant materials carried within the rocket. These are solid propellant motors, liquid propellant motors, gaseous propellant motors and hybrid motors (which contain propellants stored in at least two of the three physical states of matter). The solid and liquid propellant motors and the hybrid motors employing solid-liquid combinations are of greatest practical interest because of the heavy tanks needed to store large masses of gas. This book is concerned only with the first of the four categories, solid propellant rocket motors. Additionally, attention is restricted to chemical propulsion, for which energy that is necessary for producing large thrusts is stored in the form of chemical energy of the propellants.

A solid propellant rocket is the simplest form of chemical propulsion. The fuel and oxidizer are both incorporated in a single solid, called the propellant grain, located inside a container called the combustion chamber. This chamber is large in comparison with the combustion chamber of a liquid propellant rocket motor. A schematic illustration of this type of motor is shown in Fig. 1-1(a). The grain shown here is tubular with a star-shaped cross section. A device called an igniter, which is designed to initiate the burning, is placed inside the central cavity of the combustion chamber. After ignition the hot gases, which are produced when the solid burns, flow through the central cavity and are accelerated to a high velocity by means of a nozzle. It will be seen in Chapter 2 that the resulting ejection of gases at high velocity greatly enhances the production of a propulsive thrust on the motor.

During combustion, gases evolve from the solid propellant grain only at its surface. Thus, the surface of the solid regresses normal to itself during burning, at the "linear regression rate" of the propellant grain. The combustion gases come into contact with the outer shell or case of the chamber only at the end of a firing. The purpose of the case is to contain the propellant and to withstand the high chamber pressures that are produced during combustion. Figure 1-1(a) emphasises the simplicity that arises from storing the propellant inside the chamber.

It is apparent from Fig. 1-1(a) that the principal parts of a solid propellant rocket motor are the grain, the case, the nozzle and the igniter. For comparison, schematic diagrams of liquid and hybrid rocket motors are shown in Fig. 1-1(b)

and 1-1(c). In a typical liquid propellant motor, fuel and oxidizer are stored in separate tanks. They are conveyed to the combustion chamber by means of a feed system, and are injected into the chamber and partially mixed by means of an injection system. The principal parts of the liquid propellant motor are thus the tanks, the feed (and control) system, the combustion chamber and the nozzle. The hybrid motor illustrated in Fig. 1-1(c) contains a solid fuel and a liquid oxidizer. Its main components are an oxidizer tank, a feed (and control) system, an injection system, a combustion chamber, a solid fuel grain and a nozzle.

It will be seen in Chapters 2 and 3 that the propulsion systems illustrated in Fig. 1-1 rely on exothermic chemical reactions for their effectiveness. There are numerous applications (such as space propulsion) for which these chemical rockets are currently the most important propulsive "work horses". The role and current standing of solid propellant rockets among these work horses will be discussed on page 19 after we have described solid propellant rockets in somewhat greater detail (page 4) and classified them according to their use (page 8). A brief history of solid propellant rocketry is given on page 4 and an outline of the development of the rest of this AGARDograph is presented on page 31. Additional material relevant to solid propellant rockets may be found in the bibliography listed as Ref. 1-16.

2 Description and Brief History

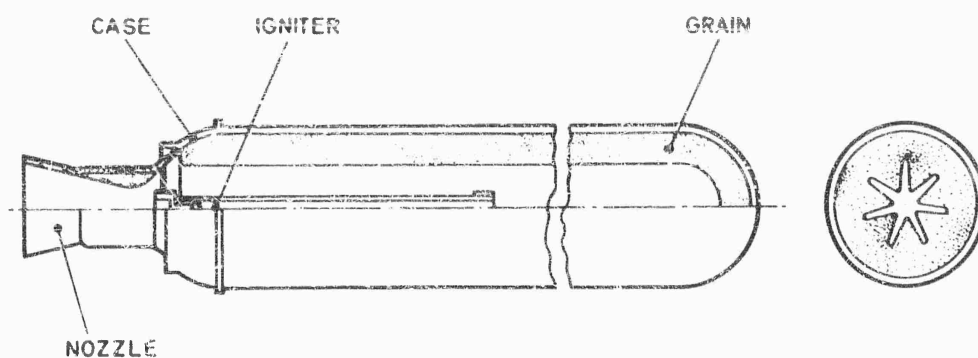
2.1. Description of Current Solid Propellant Rockets

We shall now discuss the solid propellant rocket system more deeply in order to accustom the reader to some specific terms used in solid rocket technology. The system is composed of four basic parts:

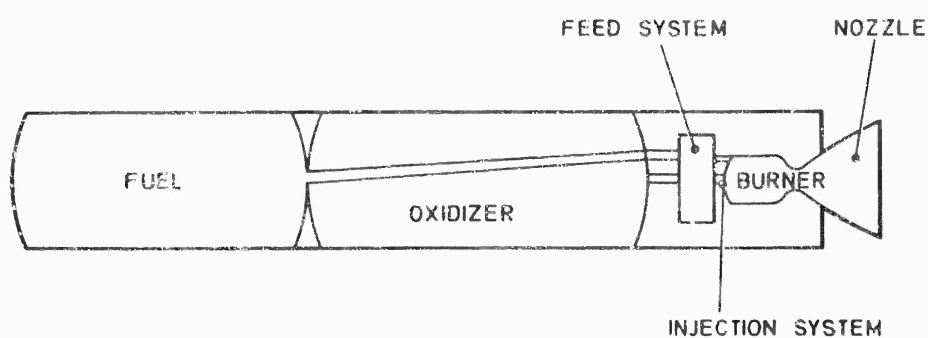
- the propellant grain
- the case
- the nozzle
- the igniter

The propellant generally consists of an oxidizer and a fuel, and the most common type today consists of crystalline ammonium perchlorate dispersed in a plastic fuel binder. The performance of this propellant is increased by the addition of finely ground light metals, such as aluminum. The basic propellant defined here is an example of a composite propellant, and the addition of metals is referred to as metalization. The mean size of the ammonium perchlorate crystals is of the order of 50μ , and that of aluminum powder is typically 5 to 30μ . The utilisation of a plastic binder enables one to construct large-size grains with good mechanical properties. These grains may be fabricated outside the casing or poured into it. In addition to composite propellants, double-base solid propellants are also used; these were the principal solid propellants twenty years ago. They consist of a mixture of nitrocellulose and nitroglycerin, each of which possesses both fuel and oxidizer characteristics. The performance of this double-base propellant is lower than that of the composite propellants just described.

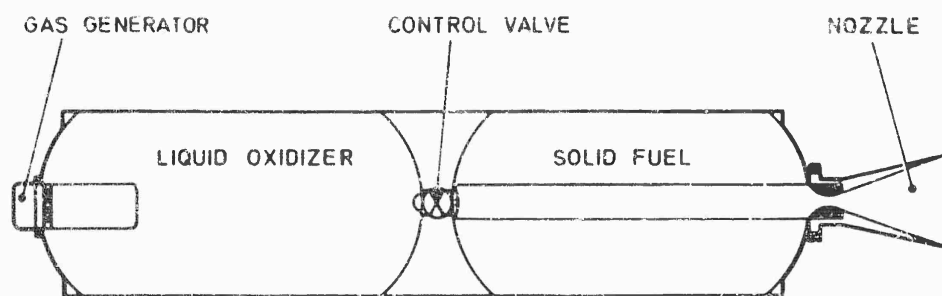
The grain geometry provides a basis for a preliminary classification of solid rocket propulsion systems. The grain configuration will essentially depend upon the mission, i. e. upon the thrust and burning time, or more precisely upon the thrust-time history. Once the grain is ignited, burning generally progresses until the propellant is completely consumed. The burning surface geometry and its time evolution will then impose the thrust-time history. The grain is called neutral if the thrust remains constant during the entire burning history. This occurs when the total burning surface area does not vary with time. There also exist progressive grains for which the thrust increases with time and regressive grains which the thrust decreases with time. Internally burning cylinders or tubes are progressive, while rod-shaped grains are regressive. The most common



(a) Schematic diagram of a solid propellant rocket motor



(b) Schematic diagram of a liquid propellant rocket motor



(c) Schematic diagram of a hybrid rocket motor

Fig. 1-1 Diagrams of solid, liquid and hybrid motors

current configurations are star-shaped cylindrical grains which provide a relatively large propellant surface area for burnt gas emission while maintaining approximately neutral burning. The motor burning time depends upon the propellant thickness and generally increases with increasing rocket size.

The star-shaped cross-section is not the only grain geometry used; more complex cross-sectional shapes are also employed. Complex geometries correspond to special applications, e.g. a high gas flow rate may be obtained by increasing the surface area of the propellant. These different configurations will be studied in detail in Chapter 4. However, we note here that neutral burning is also achievable with coaxial cylinders, although this geometry poses problems associated with the necessity of exposing grain supports to the hot gaseous combustion products. The simplest grain configuration is a cylinder burning at its end (cigarette burning), but this configuration has a low ratio of burning area to nozzle throat area, and is applicable only for long burning times and low values of the thrust per unit cross-sectional area of the rocket. Besides cylindrical grains, spherical grains are useful for some applications. Grain neutrality is difficult to obtain in spherical configurations, but it can be produced by employing grains with two compositions having different burning rates. Grain configuration controls the thrust-time program of solid rockets and has to be adapted to each mission.

The geometry of the motor case is related to that of the grain. Case design also depends on the application. Two principal types of casing materials are currently employed, metallic materials and glassy materials. Engineering problems arise in connection with the selection of case materials, case manufacturing processes and the tradeoff between conflicting requirements of light weight and reliability. Three important elements must be considered in motor case design:-

- a) the mechanical load (during motor operation the case is subjected to high pressure, several tens of atmospheres);
- b) the thermal load (some parts of the case which are in contact with burnt gases must be thermally protected);
- c) the auxiliary means of thrust-vector control (devices for controlling the direction of the force vector acting on the rocket are structurally supported by the case).

Many metallic materials, such as steel, are useful for motor cases because they tend to have a high modulus of elasticity and a high yield strength, and also because the associated dynamic problems (vibration of the structure) are less difficult to solve. Expansion of the propellant grain is a less severe problem with metallic cases than with glassy cases. Of the many glassy composite materials that have recently been considered for motor cases, the one that currently is adopted most often consists of wrapped fiberglass filaments impregnated with gelled epoxy resin. Many machines have been developed for fiberglass case winding. A machine designed by Aerojet-General Corporation for manufacturing Polaris rocket motors is shown in Plate 2; more than one and a half million miles of glass filament go into each chamber measuring more than 14 feet long and $4\frac{1}{2}$ feet in diameter. The advantage of glassy cases is that they often provide lighter-weight structures than metallic cases.

The propellant grain-case bonding must be accomplished with care. A plastic liner is generally inserted between grain and case. The liner has a manifold purpose: it acts as a combustion inhibitor, it prevents the burnt gases from coming into contact with the case, it protects the wall thermally when the burning surface reaches it and it acts as a mechanical bonding between grain and casing. A careful choice of liner is important because its weight and volume are not

negligible compared with that of the empty rocket. Thermal protection of the forward and rearward portions of the case that are exposed to hot gases during the entire firing is achieved by using high-temperature, often silica-reinforced plastics.

The nozzle attached to the downstream end of the rocket motor consists of a convergent section, a narrow-diameter throat and a divergent section. It will be seen in Chapter 2 that these three elements are needed in order to accelerate the hot combustion gases to the high velocities required for efficient production of thrust. Since solid propellant rocket nozzles are generally uncooled, it is necessary to use nozzle materials capable of withstanding a high thermal load. The manner of thermal protection of the convergent section will depend upon the aft-end geometry (single or multiple nozzles). Thermal protection of the throat is the greatest nozzle problem because the maximum heat transfer occurs there. The throat must generally be constructed from layers of different materials. The layer that sees the hot gas is composed of a high-temperature, refractory or metal material that exhibits a good resistance to erosion (e.g. tungsten, or graphite covered with tungsten); for large rockets it is sometimes possible to permit some erosion of the throat, so that uncoated graphite throat inserts can be employed. A material with a higher specific heat and a lower thermal conductivity is usually placed underneath the throat insert in order to absorb the heat load and to prevent it from being transmitted to the rest of the structure. Finally, a material having good mechanical properties is placed outside in order to resist the transmitted pressures. The divergent section is often composed of an ablative material (such as reinforced plastic).

Rapid thrust termination is required in certain applications, e.g. at staging times for satellite launchers. This is often achieved by means of openings located at the head end of the motor (the opposite end from the nozzle) and initially blocked by diaphragms. These diaphragms burst on command, thereby exposing the chamber to the ambient atmosphere. Most of the chamber gases then begin to exhaust through the head end, causing first thrust direction reversal and then extinction due to the rapid gas expansion. The presence of such openings in the case raises some structural problems, especially for fiberglass cases; it would be necessary either to cut some of the glass filaments or to wind the fibers around the holes during fabrication.

Solid propellant rocket motor igniters often consist of electrically initiated, conventional pyrotechnic compositions. The combustion of an auxiliary propellant contained in the igniter generates hot gases which come into contact with the grain surface and induce ignition of the grain. These pyrotechnic compositions generally consist of oxidizer-metal mixtures (e.g. potassium perchlorate-aluminum). The igniter combustion often produces hot condensed particles (e.g. solid or liquid alumina) which impinge on the grain surface, causing high local heat transport and local ignition of part of the surface area, followed by propagation of the flame to the rest of the grain. Mechanical properties of pyrotechnic compositions are usually such that for safety they must be shaped into pellets, which are placed inside a perforated enclosure, positioned so that the burnt gases will come into contact with the grain surface. For long rocket motors, sometimes small auxiliary rocket engines are used as igniters in order to provide more nearly simultaneous ignition of the entire grain surface than could be achieved with conventional techniques that rely on flame spread.

2.2 History

Although the origin of rocketry is obscure, undoubtedly the first rockets used solid propellants. Rockets are believed to have originated either in China or in Greece. The idea of employing rockets as weapons reached Europe in about 1250; their invention is mentioned by Arabic scientists in a book called "Liber Ignium" (Book of

From this date onward, many solid propellant rocket weapons have been developed and used in battles. Around 1800, rockets varying in weight from 8 to 100 lbs were constructed in England (William Congreve) (Fig. 1-2) and the stabilization of the projectile was improved by William Hale. That such weapons were put to use is demonstrated, for example, by the fact that the British attacked Copenhagen in 1807 with some 30,000 rockets. From the military point of view, rocket weapons have continually progressed to their current state of sophistication.

It is curious to note that astronautics pioneers like Ziolkowsky in Russia, Oberth in Germany, Goddard in the United States and Esnault Pelterie in France, whose studies were carried out between 1900 and 1930, considered only liquid propellants for space missions because they believed that liquids were essential for providing sufficient energy for such operations. This opinion rested on the fact that until 1900 black powder, consisting of charcoal, sulphur and saltpeter, was the material used as a solid propellant. Even in 1932, after changes in the propellant composition that resulted in smokeless powder (double-base composition) no grounds existed for forecasting performance improvements that could lead to the possibility of using solid propellants for space flights. Later, double-base solid propellants were considered for such applications because of their improved mechanical properties and higher performance. The mechanical properties of double-base propellants enabled one to envisage grain geometrics with large combustion areas and consequently high thrusts.

But the most important step in the progress of solid propellant rocketry was taken in 1944 by the Jet Propulsion Laboratory research workers, who developed the GALCIT propellant, consisting of approximately 75% potassium perchlorate and 25% asphalt-oil mixture. The development of this composite solid propellant was to open a vast field of research on high-energy solid propellants. This GALCIT propellant had some defects such as poor temperature sensitivity which led to bad behavior at low temperatures. However, hundreds of thousands of JATO-type rocket engines for assisting aircraft take-offs were constructed using this propellant and the working safety of solid propellant rockets was thus demonstrated.

Solid propellant rocket techniques have been widely improved since 1955, principally in two directions:

- a) development of propellants with higher performance (specific impulse and volumetric specific impulse - see page 19 for preliminary definitions of these two terms) and with better mechanical and combustion properties;
- b) development of light-weight structures for cases and for other motor components.

These improvements have led to the construction of high performance engines that can compete well with liquid or hybrid systems. One end result is the use of large solid-propellant motors as powerful boosters, such as in the "zero stage" of the TITAN III C, which achieves a total thrust of 2.4 million pounds from two large solid-propellant, segmented motors strapped on either side of a first-stage, liquid-propellant, core motor (parallel staging). Another result is the completely successful static test firing of a 260 in. diameter solid-propellant rocket motor containing 1,673,000 lb. of propellant and producing more than 3 million lb. thrust. A third consequence is the use of very light solid-propellant engines for upper stages of satellite launchers, having a ratio of propellant weight to total weight exceeding 90%.

3. Classification

There are several possible bases for categorizing current types of rocket propulsion systems. For solid propellant rockets, we use here a very elementary

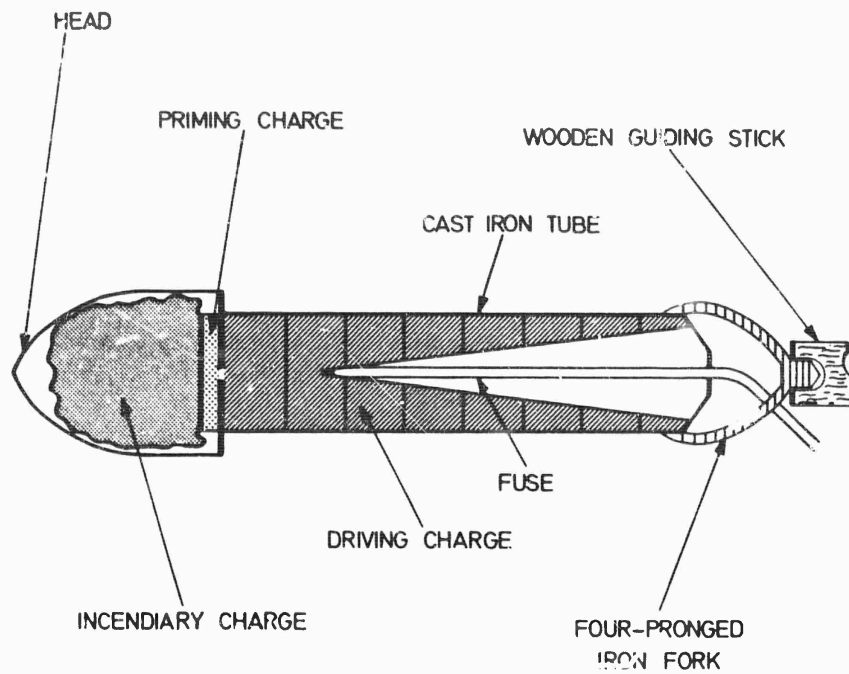


Fig. 1-2 Early 19th century solid propellant rocket.

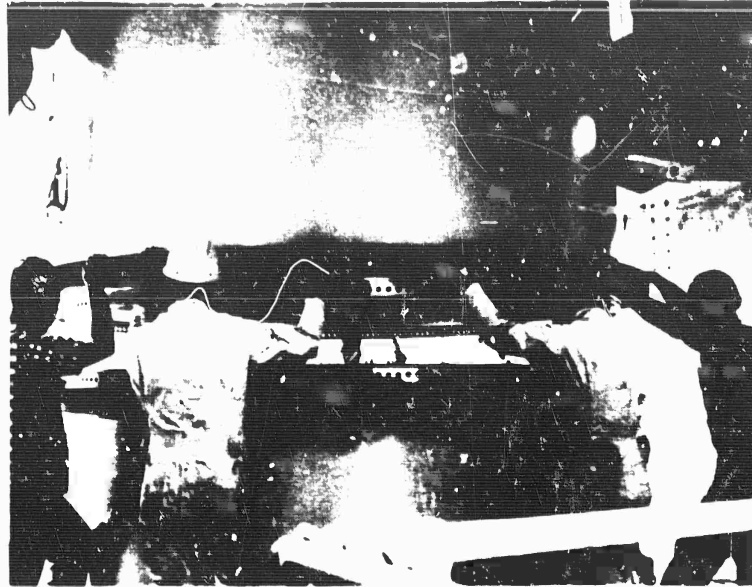


Fig. 1-3 Joining technique for segments of 120 inch solid-propellant motor. A crane lowers the 50 ton segment. Photo, courtesy of United Technology Center

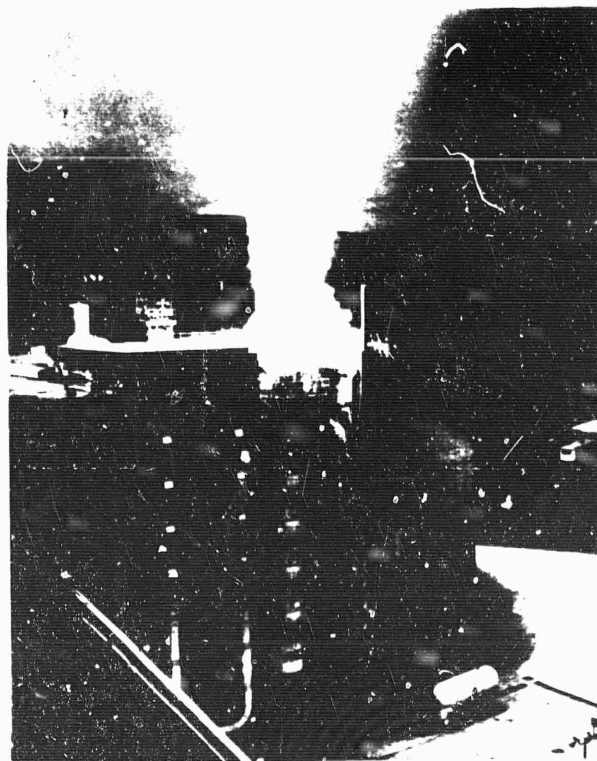


Fig. 1-4 Static test firing of 120 inch diameter segmented rocket motor. Photo, courtesy of United Technology Center.

classification scheme based on the field of application. The principal applications of solid propellant rocket systems can be listed under the following headings:

- Rocket motors for lower stages (boosters)
- Rocket motors for upper stages of ballistic missiles and for space vehicles
- Satellite launchers (complete vehicles)
- Sounding rockets
- Auxiliary rocket motors designed to perform specialized functions in the guidance and control of vehicles
- Assisted take-off rocket motors for aircraft
- Military applications, e.g. guided weapons, unguided bombardment and air-to-air rockets
- Diverse applications

3.1 Rocket Motors for Lower Stages (Boosters) - Solid propellant systems are of interest for use as boosters because their high propellant density leads to improved overall performance which in some instances exceeds that of competitive liquid propellant systems (see page 19). After the February 23 1966 successful test of a 260 in. diameter rocket motor, it is now possible to consider very powerful first stages using solid propellants. The era of solid propellant boosters is in its infancy; in some such applications they are already beginning to replace liquid propellants.

The 260 in. motor provides one example of a large solid propellant booster rocket. It employs a composite propellant consisting of polybutadiene, ammonium perchlorate and aluminum. Some data that we have not already mentioned is that the pressure measured in the chamber during the full-scale test was very close to the calculated one; it reached its maximum value of 601 psia after 40.5 seconds. The effective burning time was 114 seconds and the peak thrust was 3.51 million pounds. The ignition period lasted 335 milliseconds. The nozzle throat ablated at a rate of 4.8×10^{-3} in. per second.

Another example of a large solid-propellant booster rocket is the strap-on motor developed by United Technology Corporation for the TITAN III C, which is an improved version of the TITAN II missile. This application illustrates the "zero-stage" concept for improving capabilities of existing boosters; viz., an operational launch vehicle can effectively be launched from a high altitude by providing the entire vehicle with a (zero-stage) booster. Often this approach affords a less expensive solution to the problem of achieving higher weights in orbit than is afforded by the development of a new launch vehicle. The TITAN III C strap-on zero-stage motors are each 120 in. in diameter and develop more than one million pounds thrust each. The complete vehicle was successfully fired on December 21, 1965.

Each strap-on motor for the TITAN III C consists of 5 segments, weighs about 250 tons and burns for about 120 seconds. The direction of the thrust vector is controlled by injecting nitrogen tetroxide through the wall of the divergent section of the nozzle. In so large a rocket motor, the thicknesses of the walls and of the liner are small in comparison with the grain thickness, and the question of wall thermal protection can be solved relatively easily by using a protective coating about 1 inch thick. Three 6 mm-thick layers of liner are attached to the case by centrifugal coating, the last layer being put in just before loading. The case is made of LADISH D6AC steel. The propellant grain is attached to each segment. The central core through which burnt gases flow is a circular cylinder, the lateral faces of which are not inhibited from burning. Adjacent segments are held together by Clevis pin joints. The segment-joining technique is shown in Fig. 1-3, and Fig. 1-4 presents a view of the rocket motor during firing. The operating balance of a matched pair of motors is studied carefully for the TITAN III C application.

Another example of the use of solid propellant boosters is to accelerate a ramjet to its operating speed. The experimental missile STATALTEX, intended for studying high-altitude, high-speed ramjet propulsion (flight Mach number greater than 5) is shown on Plate 1. This ramjet is launched by a solid propellant booster.

There are, of course, a variety of other large scale and small-scale booster applications of solid propellant rockets.

3.2. Rocket Motors for Upper Stages and for Space Vehicles - Solid propellant rockets are also used as injection stages for satellites and as slow-down stages to initiate atmospheric re-entry. The change in vehicle speed (Δv) required in these applications is obtained most easily by using very light rocket motors rather than propellants with high specific impulse. Reinforced plastic cases can lead to propellant mass fractions (ratios of propellant mass to total vehicle mass) higher than 0.9. An example of a solid propellant rocket used in such space applications is shown in Fig. 1-5; this motor has been developed by Hercules Powder Company for orbiting a spacecraft whose purpose is to detect high-altitude nuclear explosions.

The third stage of SEREB Diamant launcher is shown on Fig. 1-6; its characteristics are as follows :

Length	2.06 m
Diameter	0.35 m
Case	wound fiberglass (impregnated with phenolic resin)
Empty weight without igniter	67.9 kg
Propellant	Isolane (polyurethane composite), weight 641 kg
Burning time	45 seconds
Thrust	varying between 2,700 and 5,300 kg
Nozzle throat diameter	9.6 cm
Divergent nozzle section material	orthostrasyl (ablativ plastic)

Solid propellant systems are ill-adapted to the propulsion of space vehicles that require rocket motors with long burning times and low thrusts. However, certain space missions are well-suited to solid rocket propulsion, particularly when the trajectory or orbit of the vehicle is to be modified impulsively (large thrust for short duration). Solid propellant motors are often used as the primary means of transmitting a specified Δv to a space vehicle. Guidance gas rockets are also needed in such systems to provide fine orbit adjustments after the solid rocket firings.

Many orbiting communications satellites, (for example the SYNCOM telecommunications satellites) use solid propellant apogee rockets that are usually spherical in shape and that place the satellite in a desired position with respect to the earth, in order for the satellite to be able to receive and emit signals in correct directions. The mission of these apogee injection motors is to increase the payload speed.

Slow-down solid propellant rocket motors of similar design are present on the GEMINI capsules and also on soft-landing lunar vehicles of the SURVEYOR type.

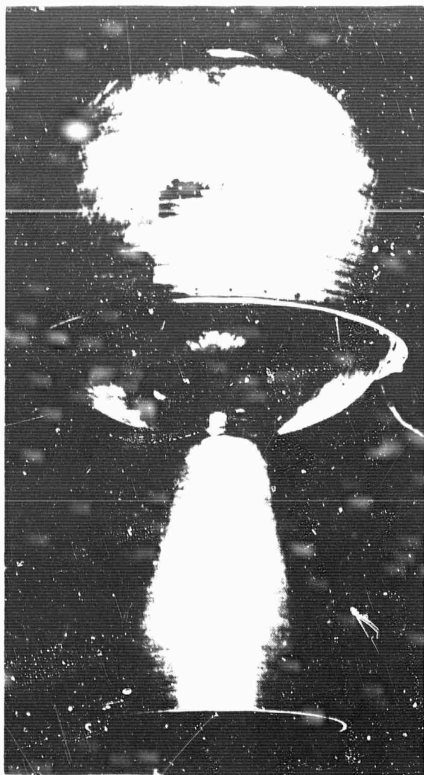


Fig. 1-5 Solid propellant motor, about 1ft. in diameter, used to inject satellite from orbiting vehicle into higher-altitude orbit, courtesy of Hercules Powder Company.

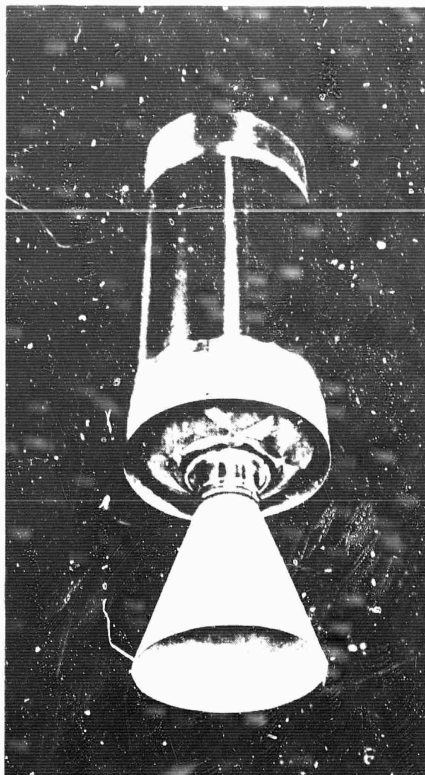


Fig. 1-6 Motor for upper stage of Diamant launcher, courtesy of ONERA

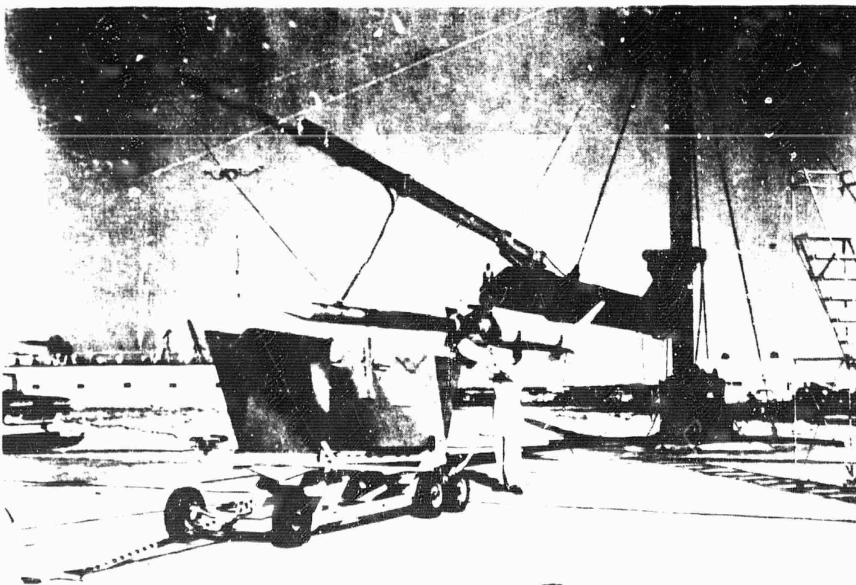


Fig. 1-7 Nike-Cajun rocket, courtesy of NASA

3.3 Satellite Launchers - Since solid propellant systems are attractive as boosters because of their high propellant density, and since they have become competitive as injection motors because of the achievement of light structures, they possess most of the qualities that are necessary for a complete satellite launcher. Advantages of such systems stem from their low manufacturing costs and from their reliability.

One of the earliest examples of a vehicle propelled solely by solid propellants and capable of orbiting a satellite is the SCOUT, which contains four solid propellant stages. The characteristics of the system are the following :

Total length	:	70.98 ft		
Initial weight	:	36240 lb		
First stage (ALGOL)			Second stage (CASTOR)	
Length	:	30.83 ft	Length	: 20.70 ft
Diameter	:	40 in	Diameter	: 31 in
Total weight	:	23524 lb	Total weight	: 9 475 lb
Empty weight	:	9 600 lb	Empty weight	: 2 700 lb
Thrust	:	203 000 lb	Thrust	: 62 000 lb
Specific impulse	:	214 seconds	Specific impulse	: 224 seconds
Burning time	:	40 seconds	Burning time	: 27 seconds
Third stage (ANTARES X 254)			Fourth stage (ALTAIR X 248)	
Length	:	11.17 ft	Length	: 8.28 ft
Diameter	:	31 in	Diameter	: 20 in
Total weight	:	2 592 lb	Total weight	: 649 lb
Empty weight	:	525 lb	Thrust	: 2 800 lb
Thrust	:	13 600 lb	Specific impulse	: 255 seconds
Specific impulse	:	255 seconds	Burning time	: 38 seconds
Burning time	:	39 seconds		

With this vehicle it is possible to place 300 lb in a (low) 300 n.mi. orbit. The principal purpose of the SCOUT is to orbit scientific payloads for international uses.

3.4 Sounding Rockets - Sounding rockets are used for the exploration of the upper atmosphere and space in order to gather scientific data. There exist many types of such vehicles, not less than 60 in the United States alone. They are characterized by their payload and by the maximum altitude that they can reach. One of the earliest meteorological rockets is the one-stage ARCAS rocket which weighs 65 lb and lifts a 12-lb payload to an altitude of 40 mi. The two-stage ARCAS rocket weighs 100 lb and can lift 12 lb to an altitude of 50 mi. As an example of a larger sounding rocket, we describe the NIKE-CAJUN used by NASA. The characteristics of this rocket, which is shown in Fig. 1-7, are the following :

Length	:	26 ft
Diameter	:	16.5 in
Initial weight	:	1 550 lb
Payload	:	50 to 100 lb
Altitude	:	100 mi
Speed	:	4 200 mi/h

The vehicle consists of two solid propellant stages, the first (HERCULES) having a thrust of 48 700 lb and the second having a thrust of 9 620 lb. The second stage weighs 257 lb.

3.5. Auxiliary Rocket Motors to perform Guidance and Control Functions - Few solid propellant rocket motors are specifically designed for the purpose of controlling the thrust vector of a main engine or of otherwise providing the attitude control forces needed for steering a vehicle under thrust. In one exception, forces for the control of attitude and hence the direction of main engine thrust are obtained by means of four small solid rocket motors located at the aft end of the vehicle. Their nozzles are set at an adjustable angle with respect to the axis of the main rocket motor. Torques to change attitude, and hence thrust direction modifications, are achieved by varying the orientations of the nozzles of these rocket motors. This kind of vehicle attitude control is employed in the four-stage solid propellant rocket BERENICE, which is designed for studying in flight the kinetic heating of hypersonic vehicles during atmospheric re-entry. In the photograph of the BERENICE that is shown in Fig. 1-8, one can see the four control rocket motors at the aft end of the vehicle. The burning time of these control motors is of the same order of magnitude as that of the first stage. The propellant grain geometry of each is cylindrical with cigarette burning. The burning rate is increased by placing silver wires in the propellant perpendicular to the burning surface.

Solid propellant rocket motors are rarely used to supply the attitude control forces for satellite guidance because of their short burning times. Compressed gases or subliming solid substances can perform this function better.

Solid propellant impulse rockets have been constructed for spinning up certain missile stages (PET rocket) and also for accomplishing stage separation.

3.6. Assisted Take-off Rocket Motors for Aircraft - Few rockets are now used for increasing the take-off power of aircraft because of improvements in the peak power output of turbojets. The most famous take-off rocket is the Aerojet JATO, the propellant of which is an extruded composite. The JATO motor has the following characteristics:

Thrust	:	450 kg
Burning time	:	16 seconds
Chamber pressure	:	70 kg cm ⁻²
Propellant weight	:	45 kg
Rocket motor weight	:	72.5 kg

3.7. Military Applications - The most important weapons composing the arsenals of armies nowadays use solid propellant systems as a propulsion mode. Such systems have indisputable superiorities: permanent readiness of the engine, good reliability, low maintenance, easy preparation of a firing. Military rockets are distinguished according to their mission, i.e. surface-to-surface, surface-to-air, air-to-surface, air-to-air and anti-submarine.

For surface-to-surface missions, three types of missiles are distinguished.

a) There are intercontinental ballistic missiles (ICBM), such as the MINUTEMAN which consists of three solid propellant stages. The missile range is about 6 000 to 7 000 n.mi. The MINUTEMAN can be prepared for firing in about 32 seconds and requires about 10 seconds for the selection of an objective. The overall length of the three stages for different missiles in this series is A - 53.17 ft, B - 55.9 ft, F - 59.3 ft. The missile is about 55 000 lb.

A MINUTEMAN is shown in flight in Fig. 1-9. The principal contractors for MINUTEMAN propulsion are: THIokol for the first stage; AEROJET for the second and HERCULES for the third. The first stage has a diameter of 1.65 m and a propellant weight of about 20 tons. The case is made of LADISH D6AC steel. Four nozzles with axes aligned with the vehicle are used for the first stage; their divergent sections employ phenolic refrasil for heat protection. It has been difficult to solve problems associated with the thermal protection of the interior chamber walls. The single-composition, solid propellant

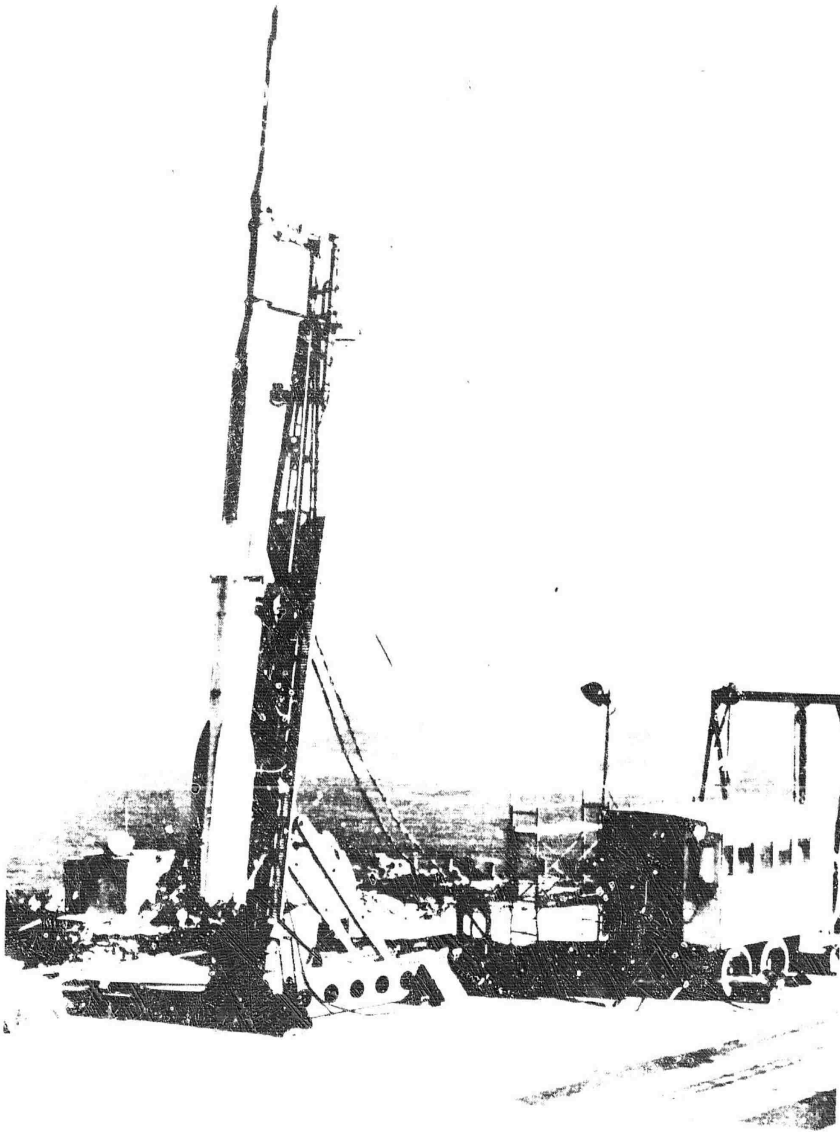


Fig. 1-8 Four-stage, BERL NICE, solid-propellant rocket vehicle, for testing re-entry vehicles at Mach 12, courtesy of ONERA.

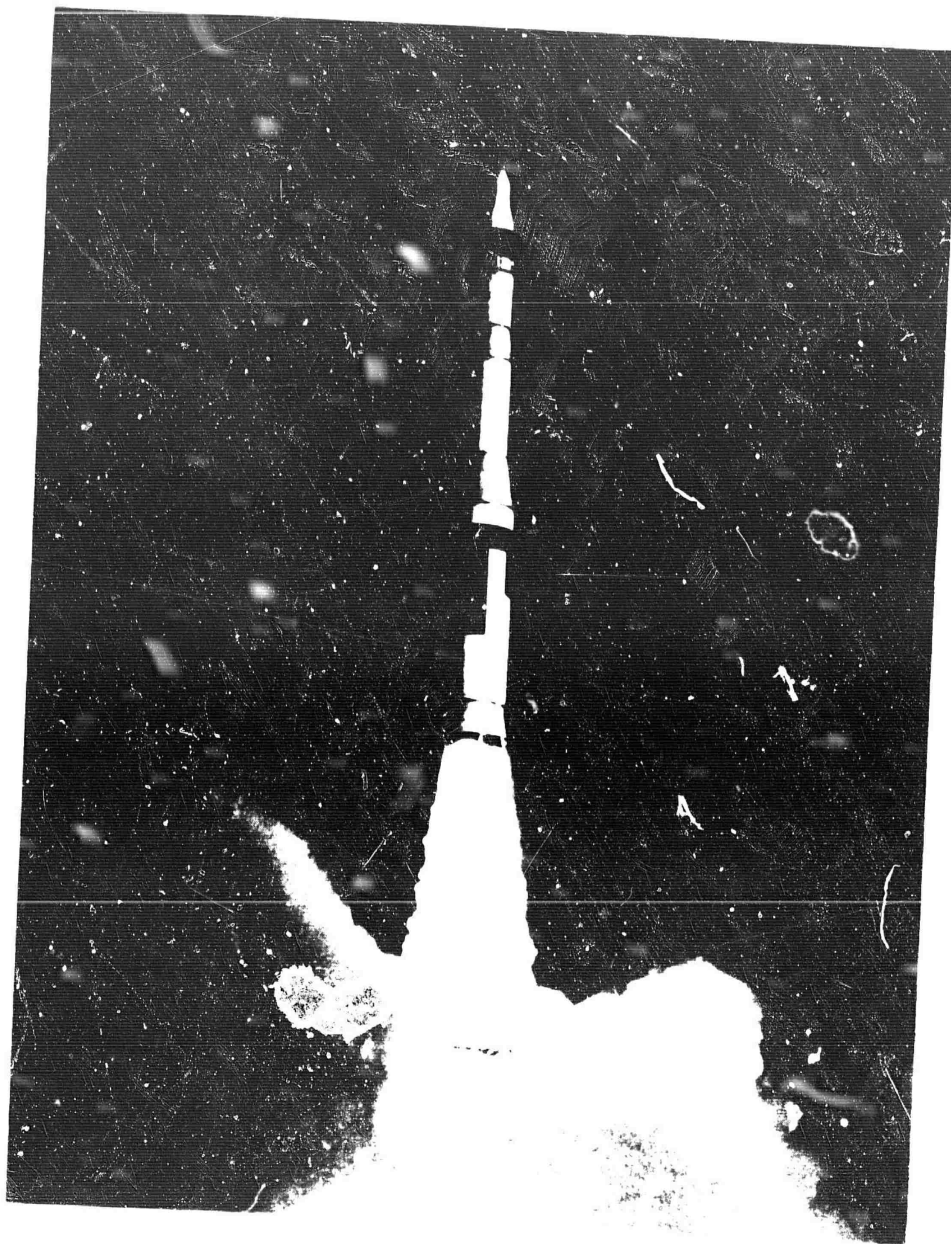


Fig. 1-9 MINUTEMAN in flight (Thiokol Chemical Corp).

grain has a star-shaped configuration (6 arms). The propellant consists of PBAA (polybutadiene acrylic acid) and ammonium perchlorate. A pressure peak observed at the beginning of a firing has been decreased by a partial inhibition of the grain.

b) There are surface-to-surface missiles of intermediate range (IREM) such as the POLARIS series of strategic missiles which are fired from submerged submarines. The three variations A_1 , A_2 , A_3 each consist of two solid propellant stages. These engines have the following characteristics:

A_1	Length	:	28 ft
	Diameter	:	4.5 ft
	Weight	:	28 000 lb
A_2, A_3	Length	:	30.5 ft
	Diameter	:	4.5 ft
	Weight	:	30 000 lb

The range of the A_1 type is about 1 200 n.mi., that of the A_2 is 1 500 n.mi. and that of the A_3 is 2 500 n.mi.

c) There are short-range missiles, such as the PERSHING rocket (range from 100 to 400 n.mi.) with two solid propellant stages, or the SERGENT (range 25 to 75 n.mi.) consisting of only one solid propellant stage. The smaller HONEST JOHN (range 12 n.mi.), consisting of one solid propellant stage, also falls into this category; it has the following characteristics:

Length	:	24.8 ft
Diameter	:	30 in
Weight	:	4 500 lb

One of the smallest surface-to-surface rockets is the antitank ENTAC rocket which has the following characteristics: weight 27 lb, range of 6 600 ft, guidance by a wire.

The spectrum of surface-to-surface missiles, from MINUTEMAN to ENTAC, is impressive. This wide variety also exists for each of the other military mission categories. It would take too much space for us to present a comprehensive discussion, therefore we shall give only a few examples for each category.

Surface-to-air HAWK rocket : It has two propulsion regimes, a boost regime and a cruising flight regime. Its length is 16.9 ft., diameter 14 in., weight 1275 lb and can engage targets at heights between 1 000 and 45 000 ft.

Surface-to-air NIKE HERCULES rocket : This ground-launched antimissile missile has a length of 41 ft, diameter 31.5 in., weight 10 000 lb. The rocket is composed of two solid propellant stages. Ceiling: 100 000 ft, speed: Mach 3. The newer and larger NIKE ZEUS rocket has an initial weight of 22 800 lb.

Surface-to-air SPRINT A rocket : This antimissile rocket is used for protection against ICBM/SLBM. It has a conical rocket motor, employs two stages and develops a very high initial acceleration.

Air-to-air FALCON rocket : This is a one-stage rocket motor with thrust of 6 000 lb; length 6.5 ft, diameter 0.54 ft, weight 100 lb and range 5 n.mi.

Air-to-surface rocket, anti-tank missile SS11 : This missile has a length of 46 in., diameter 3 in., weight 63 lb.

Anti-submarine SUBROC rocket : This missile for submarine attack has a length of 21 ft, diameter 21 in., weight 4 000 lb.

These few examples show the important place taken by solid propellant propulsion in the field of modern weapons. The essential quality that dictates the choice of this propulsion system is readiness.

3.8. Diverse Applications - Solid propellant rocket motors are useful in many specialized applications that do not fit well into any of the preceding categories. One such application is to generate gases that are needed to drive the feed systems of liquid propellant rockets. Gas generator rockets can pressurize a high-pressure feed system or can drive the turbine of a turbopump feed system.

Another specialized type of application arises in the propulsion unit required for safety systems in some missions. For example, in the Apollo manned lunar flight, if the astronauts have to evacuate the launch vehicle during liftoff, then a solid propellant rocket motor on a tower atop the command module is fired in order to propel the three astronauts to a safe distance from the primary vehicle. This separation rocket motor, which is to be mounted tail-down on the tower, is shown undergoing a test firing in Fig. 1-10. Four nozzles, canted outboard, split the exhaust of the solid rocket motor into four equal tails to prevent it from impinging on the command module.

Solid-propellant rocket motors are also often used to propel target vehicles during weapons tests. Another application is as the propulsion unit for high-speed test sleds or carriages. Numerous other special uses can be cited.

4. Interest in Solid Propulsion

In an introductory chapter, it is necessary to ask what place solid propellant rockets occupy in relationship to other types of rocket propulsion and to attempt to define as precisely as possible the boundaries of the field of application of solid propellant rockets. Having discussed current applications of solid propellant rocket motors, we are now in a position to begin to make the necessary comparisons. In these comparisons, we shall consider only chemical propellants and principally only solid and liquid systems. Before proceeding with specific qualitative comparisons, it is necessary for us to discuss quantitative aspects of mission performance evaluation at somewhat greater depth.

A mission may be defined approximately by stating the value of the velocity change Δv that must be imparted to a given payload. The ability of a propulsion system to deliver a Δv depends not only on its chemical energy content but also on the physical and mechanical properties of the propellant, such as its density, which influence the ratio of the burnout to liftoff weights of the propulsion unit. It is true that valid comparisons of propulsion systems must be based on precisely defined missions and that it is not possible to find rules of comparison that are both general and correct. However, we shall try by means of a highly simplified development to expose certain advantages and disadvantages of solid propellant rocket systems.

The launch weight M_L of a solid or liquid propellant rocket stage is the sum of many parts, each representing a different element of the system. We shall use the formula:

$$M_L = M_L + M_p + M_s$$



Fig. 1-10 Test firing of the APOLLO launch escape motor, (Lockheed Propulsion Co).

where M_p is the weight of the payload, M_p is the weight of the propellant and M_s is the weight of the structure.

We shall further break up the structural weight into two parts,

$$M_s = M_{sf} + M_{sv},$$

where M_{sf} is assumed to be proportional to the thrust and independent of the initial volume of the propellant, while M_{sv} is assumed to be proportional to the initial volume of the propellant and independent of the thrust. Thus,

$$M_{sf} = K_f F = K_f a_o M_o,$$

where F is thrust, a_o is the initial vehicle acceleration and K_f is a constant of proportionality. Similarly,

$$M_{sv} = K_v M_p / \rho,$$

where ρ is the density of the propellant and K_v is another constant of proportionality. The values of K_f and K_v will depend on a multitude of technological aspects of the design of the vehicle and of its propulsion system. The only important point for our present purposes is that these quantities are constants whose values are independent of the choice of propellants. Although it is clearly a gross oversimplification to break up the structural weight as we have done, nevertheless it is true that some structural items (e.g. propellant tanks) tend to increase in weight as the propellant volume increases, while others (e.g. the nozzle) tend to increase in weight as the thrust increases. This breakup could further be justified (approximately) by examining statistics on existing rockets.

Two different criteria of excellence can be defined for a propulsion system. One which might be called an engineering criterion, is the ratio of the payload mass to the launch mass,

$$u \equiv M_L / M_o.$$

The other which might be called a financial criterion, is the ratio of the payload mass to the propellant volume,

$$v \equiv \rho M_L / M_p.$$

A maximum u is desirable, for a specific payload, if the minimum take-off weight is required and roughly, a maximum v is a desirable for minimum vehicle cost. This follows from a comparison of existing rocket systems which shows that vehicle cost is approximately proportional to the total volume of the propellants with predominantly liquid or solid systems having approximately the same constant of proportionality. The conclusion is true for liquid propellant motors because the structure is the principal contributor to the cost and size of the structure is approximately proportional to propellant volume; it is true for solid propellant motors because the propellant is the principal contributor to the cost and the amount of propellant is of course proportional to the propellant volume. Nevertheless the conclusion is only approximate and might well change with time.

The mass ratio of a rocket vehicle, the ratio of its launch weight to its weight at burnout, is :

$$R = M_o / (M_o - M_p).$$

By making use of preceding definitions, we find that :

$$b \cdot \quad R = (1 + K_v / \rho) (u + K_f / a_o) \quad (\text{Eq. 1-1})$$

and that :

$$R = (1 + K_v/\rho + v/\rho) / (v/\rho + K_v/\rho + K_f a_0). \quad (\text{Eq. 1-2})$$

These formulas express R in terms of the parameters of interest. The quantity R is of importance because it is directly related to the velocity increment Δv imparted to the system; for rectilinear flight of a rocket vehicle, in the absence of gravity and of atmospheric drag, and with a constant ratio of thrust to time rate of ejection of propellant mass during the entire burning duration, one can easily show from mechanics that :

$$\Delta v = I_{sp} g_0 \ln R, \quad (\text{Eq. 1-3})$$

where g_0 is the gravitational conversion factor and I_{sp} is the specific impulse of the rocket motor. The quantity $I_{sp} g_0$ is the effective exhaust velocity of the propellant gases with respect to the rocket vehicle; it is also the ratio of the thrust to the rate (mass per second) at which propellant is ejected, and its value, which is generally larger for liquid propellant rockets than for solid propellant rockets, depends primarily on what propellants are used in the motor (see Chapters 2 and 3). Values of Δv , K_v , K_f , a_0 , and either u or v are all specified, then by using either Eq. 1-1 or Eq. 1-2 in Eq. 1-3, it is clear that a relationship between I_{sp} and ρ is obtained. This relationship defines a locus of propellant systems (in the $I_{sp} - \rho$ plane) with the same figure of merit (u or v), that can achieve the specified mission Δv , with specified technological coefficients K_v and K_f and a specified initial acceleration a_0 . Such curves of specific impulse versus propellant density are useful for comparing the relative excellence of various chemical rocket propulsion systems.

The approach that we have just described is, of course, quite approximate, and is subject to improvement in many ways. For example, the effects of gravity and drag can be included in an approximate way; under a suitable set of restrictive assumptions, one can show that Eq. 1-3 is replaced by :

$$\Delta v = I_{sp} g_0 \ln R - \psi \bar{g} t_b - \Delta v_D$$

where ψ is the cosine of the angle between the vehicle trajectory and the vertical direction, \bar{g} is an average acceleration of gravity experienced by the vehicle over its flight path, t_b is the burning time and Δv_D is the loss in velocity increment caused by atmospheric drag. We note that t_b is expressible in terms of the specific impulse, the initial acceleration and the mass ratio,

$$t_b = (g_0 I_{sp} a_0) (R-1)/R.$$

The quantity Δv_D can be assigned the approximate propellant-density dependence:

$$\Delta v_D = K_D \rho^{-2/3}$$

($K_D = \text{constant}$), since the atmospheric drag on the vehicle is roughly proportional to the $2/3$ power of its volume (which, in turn, is roughly inversely proportional to propellant density). The improved formula for the approximate dependence of I_{sp} on propellant density, obtained by substituting these last two formulas into the generalized Δv equation and then solving for I_{sp} , is:

$$I_{sp}(\rho) = \{\Delta v + \Delta v_D(\rho)\} / \{g_0 \ln R(\rho) - (\psi \bar{g} g_0 / a_0) [R(\rho) - 1] / R(\rho)\} \quad (\text{Eq. 1-4})$$

If Δv , ψ , \bar{g} , a_0 , K_v , K_f , K_D and either u or v are all given, then this relationship (along with Eq. 1-1 or 1-2 and the formula for Δv_D) determines a curve of I_{sp} as a function of ρ .

In addition to improvements of this type, the equations that we have given can form the basis of an optimization analysis; i.e., a criterion of excellence is chosen, the corresponding quantity (u or v) is maximized for a given Δv subject to variation of a parameter such as a_0 , and a relationship between R and a_0 for the optimum systems is derived. This relationship removes the necessity of specifying a_0 in drawing the $I_{sp}(\rho)$ curves and therefore may be used as a basis for comparing the optimized (with respect to launch acceleration) performance of various propellant systems. It turns out that results of comparisons based on this optimization technique are approximately the same as results of comparisons based on constant a_0 and therefore we shall not pursue the optimization discussion further.

Some curves of specific impulse vs. propellant density, obtained from Eq. 1-4, are shown in Fig. 1-11 for the values $u = 0.2$ and $v = 0.2$, for two accelerations ($a_0 = 2g_0$ and $a_0 = 10g_0$), and for $\Delta v = 1500$ m/sec and 2500 m/sec. One can see, for example, that for a mission with $\Delta v = 2500$ m/sec and $a_0 = 2g_0$, a rocket with $\rho = 1.5 \text{ gm/cm}^3$ and $I_{sp} = 240$ sec. has the same financial excellence ($v = 0.2$) as a rocket with $\rho = 0.5 \text{ gm/cm}^3$ and $I_{sp} = 500$ sec. It is for this reason that solid propellants, which typically have low I_{sp} but high ρ , can compete favorably with liquid propellants, which typically have high I_{sp} and low ρ .

The values of specific impulse and propellant density for some solid propellants are shown in Fig. 1-12 on an $I_{sp} - \rho$ diagram. One sees that generally speaking, the specific impulse tends to decrease as the propellant density increases. If Fig. 1-12 is superposed on a graph like Fig. 1-11 that has been constructed for a particular application, then it becomes easy to see which of the various possible propellant combinations would be likely to perform the mission with the highest figure of merit. Because of the general shapes of the curves in Fig. 1-11, there are many applications for which various solid propellant combinations shown in Fig. 1-12 are better suited than, for example, the hydrogen-oxygen liquid system, which has $I_{sp} = 390$ sec. and $\rho \approx 0.3 \text{ gm/cm}^3$.

The shapes of the curves shown in Fig. 1-11 can all be approximated by the formula:

$$I_{sp} \rho^\alpha = A, \quad (\text{Eq. 1-5})$$

where α and A are constants, and α generally lies between 0 and 1. The value of α , which determines the sensitivity of overall performance to density, depends on the mission, the technological coefficients K_v and K_b , the choice of criterion of excellence, and the initial acceleration (or the burning time).

The product $I_{sp} \rho$, which emerges in the limit $\alpha = 1$ of relatively strong propellant-density dependence, is called the volumetric specific impulse; whether the specific impulse or the volumetric specific impulse is a better measure of the overall performance produced by a particular propellant system, depends on the mission, the criterion of excellence, etc. If we choose the engineering criterion u , then we find that for booster type of applications with $\Delta v \approx 2000$ m/sec, α is of the order of 0.8, and the volumetric specific impulse would be the better indicator, while for the larger values of Δv that correspond to upper stages, α is about 0.2, and the specific impulse is the better measure of excellence. The value of α increases as K_v increases, and it is usually smaller when the engineering (u) criterion of excellence is used than when the financial (v) criterion is employed.

The value of the exponent α can be discussed with some assumptions; for instance we have

$$\Delta v + \Delta v_D = I_{sp} g_0 \left[\ln R - \frac{\psi g}{a_0} - \frac{k-1}{R} \right].$$

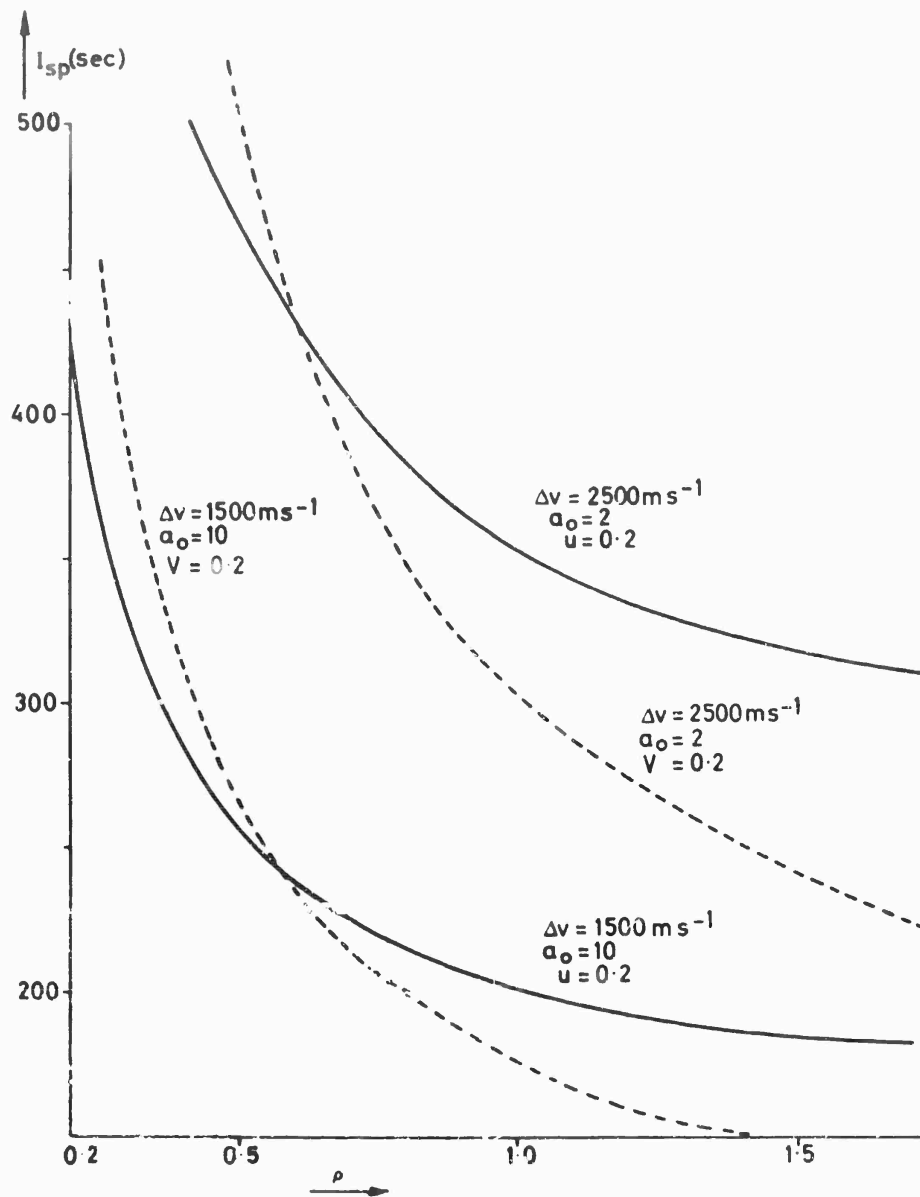


Fig. 1-11 Specific impulse versus density ρ for various values of velocity increase Δv , initial acceleration a_0 and overall performance criterion u or V .

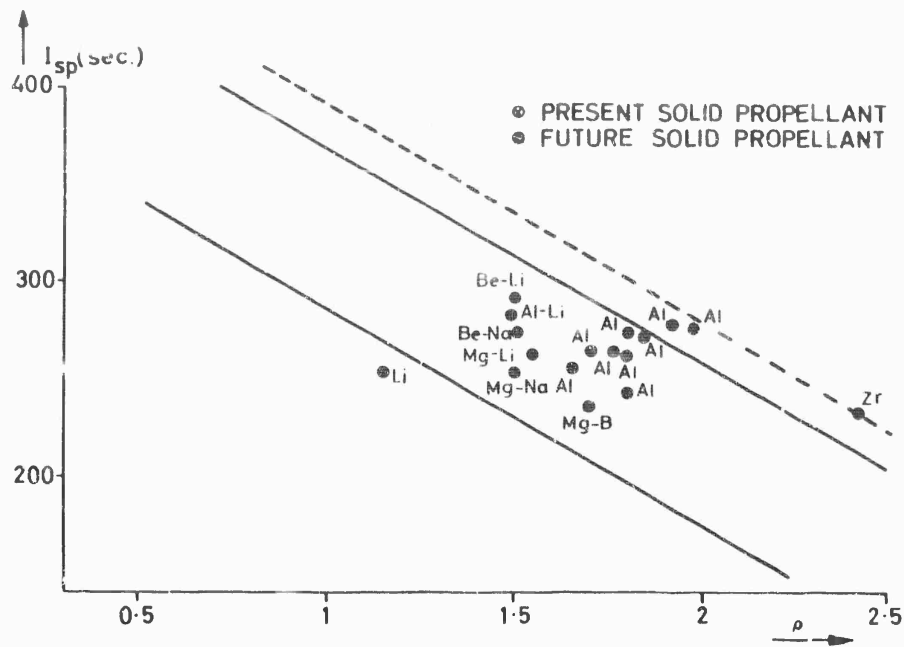


Fig. 1-12 Specific impulse versus propellant density for various propellants.

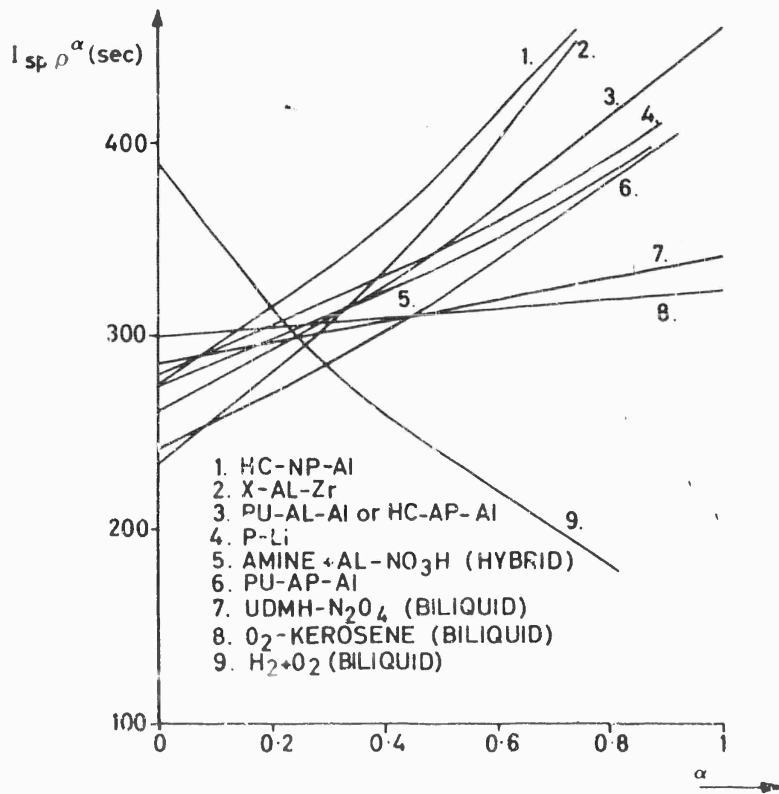


Fig. 1-13 Performance of some solid propellants. Specific impulse times density to the power of α versus exponent α .

and if we assume a constant missile volume for a single stage with $d(\Delta v + \Delta v_D) = 0$, we get

$$\frac{d I_{sp}}{I_{sp}} + \frac{dR}{R} \left[\frac{1 - \frac{\psi \bar{g}}{a_0} \frac{1}{R}}{\ln R - \frac{\psi \bar{g}}{a_0} \frac{R-1}{R}} \right] = 0,$$

and $\frac{dR}{R} = \frac{R-1}{R} \frac{d\rho}{\rho}$, in this case the exponent $\alpha = \alpha_v$ is equal to

$$\alpha_v = \frac{R-1}{R} \left[\frac{1 - \frac{\psi \bar{g}}{a_0} \frac{1}{R}}{\ln R - \frac{\psi \bar{g}}{a_0} \frac{R-1}{R}} \right].$$

It will be seen that, with mass ratio R high as in a long range ballistic missile ($R \approx 10$) and $\psi = 0$, α_v is small ($\alpha_v = 0.39$) and when R is small ($R \approx 1.5$), α_v is close to one ($\alpha_v = 0.83$).

If we assume a constant missile weight, we get

$$\frac{dR}{R} = \frac{K_v}{\rho} \frac{R-1}{\frac{K_v}{\rho} + 1} \frac{d\rho}{\rho} = \frac{K_v}{K_v + \rho} (R-1) \frac{d\rho}{\rho},$$

and the exponent $\alpha = \alpha_M$ is equal to :

$$\alpha_M = \frac{K_v (R-1)}{K_v + \rho} \left[\frac{1 - \frac{\psi \bar{g}}{a_0} \frac{1}{R}}{\ln R - \frac{\psi \bar{g}}{a_0} \frac{R-1}{R}} \right].$$

When $\psi = 0$

$$\alpha_M = \alpha_v \left(\frac{K_v}{K_v + \rho} \cdot \frac{R-1}{R} \right) \approx \alpha_v \frac{K_v}{\rho} \frac{R-1}{R}.$$

K_v is a function of the technology; the range of K_v is (6 - 600 kg m⁻³) and the range of ρ (200 - 2000 kg m⁻³).

It is concluded that in a ballistic missile where R is high an improvement in propellant specific impulse is much more valuable than a similar improvement in density. When R is small an improvement in propellant density is almost as valuable as a similar improvement in propellant specific impulse.

A useful way of obtaining a more detailed comparison of propellant systems than can be achieved by using only specific impulse and volumetric specific impulse is to plot $I_{sp} \rho^\alpha$ versus α for the propellant systems under consideration. When such curves are available, one need only obtain the value of α that corresponds to a particular application in order to see what propellants are likely to perform the application best. A plot of $I_{sp} \rho^\alpha$ versus α for a few solid and liquid propellant combinations is shown in Fig. 1-13. Representative solid propellant curves refer to a polyurethane-ammonium perchlorate-aluminum mixture (PU-AP-Al) and a plastic hydrocarbon-nitronium perchlorate-aluminum mixture (HC-NP-Al). Some liquid systems shown are the nonstorable hydrogen-oxygen (H₂-O₂) system and the storable unsymmetrical dimethyl hydrazine-nitrogen tetroxide (UDMH-N₂O₄).

system. We see in general that if the exponent α exceeds 0.6, then the solid propellant systems have a sizeable advantage, while if α becomes less than 0.2, then the liquid propellant systems shown become superior. Generally, solids tend to become the most attractive propellants when α exceeds about 0.3 or 0.4. This condition is usually satisfied for booster applications, and also for upper stages when the financial criterion of excellence is used. We must emphasize that specific engineering design tradeoff studies would not use the foregoing techniques. In specific engineering studies much more detailed calculations would be made for a number of definite systems that appear to be promising for the mission. The best potential system would be selected on the basis of these calculations and many small variations in the design of components of the system would be studied in an effort to arrive at an optimum system for the particular mission.

As a further comparison of solid and liquid propulsion systems, in Table 1-1 we give properties of a pair of solid and liquid systems having the same launch weight, the same payload and the same rocket engine weight. Although the specific impulse of the liquid system is higher, it is seen that the solid system imparts considerably greater energy to the payload in this example. The solid propellant system (here and also in general) has a smaller volume and a high initial acceleration a_0 .

Let us next consider qualitative advantages and disadvantages of solid propellant rockets. We shall first discuss advantages and then disadvantages. An advantage that we have already discussed in the introduction is the simplicity of the solid propellant system. Another advantage is the ease with which large motors can be constructed, due to the development of segmented solids. The segmentation technique described on page 11 facilitates fabrication, transport, mission operation, safety in use and ease in casting. There is a weight penalty of perhaps 4% due to segmentation, and the best chamber pressures for segmented motors are somewhat lower than those of unsegmented design. Nevertheless, in a practical sense segmentation makes it possible to envisage very large solid propellant boosters.

It is well known that small solid propellant rockets are generally less expensive than liquid propellant systems of comparable thrust. Although large solid propellant boosters are currently more expensive than comparable liquid propellant systems, there are prospects for reducing solid booster costs to make them financially more competitive (17). To elaborate on this point, let us examine representative weight and cost breakdowns for the 260-in. diameter engine, which has an optimal chamber pressure of about 550 lb/in². This motor weighs (in millions of pounds) :

Miscellaneous	0.05	1.6%
Nozzle	0.02	0.65%
Heat Protection	0.015	0.5%
Structure	0.13	4.25%
Propellant	2.83	93.0%
<hr/>		
Total	3.045	

and costs (in millions of dollars) :

Miscellaneous	1	21.7%
Nozzle	0.4	8.7%
Heat Protection	0.1	2.2%
Structures	0.4	8.7%
Propellant	2.7	58.7%
<hr/>		
Total	4.6	

The costs shown here, particularly in structures, can be reduced appreciably by using high-strength, (higher-priced) propellant materials to effect a large reduction

	Solid	Liquid
Thrust (10 ⁶ lb)	3.7	1.6
Burning time (sec)	45	125
Total impulse (10 ⁶ lb sec)	168	200
I _{sp}	249	266
Attitude at burnout (deg)	40	40
Velocity at burnout (ft sec ⁻¹)	6500	5320
Altitude at burnout (10 ³ ft)	111	166
a ₀	3.13 g ₀	1.31 g ₀
Burnout acceleration	7.87 g ₀	4.02 g ₀
Payload energy (10 ⁹ ft lb)	228	180

Table 1-1 Comparison of Solid and Liquid Propellant Systems

From L. Buchanan (18)

in inert structural weight. For very large booster applications, solid propellant motors with increased chamber pressures (made possible by higher strength materials) are considerably smaller than liquid propellant motors (which are inherently restricted to low chamber pressures and low propellant densities). On-site fabrication and loading of solid propellant boosters therefore affords the possibility of constructing larger boosters than are feasible with liquid propellant systems.

Another price advantage of solid propellant systems is their general tendency to require much lower development costs than comparable liquid propellant systems. One of many factors contributing to this is the ease with which accurate calculations of thrust-time histories can be made in the preliminary design phase. Experience has shown that calculated thrust-time curves are very close to those measured in tests, and therefore the amount of developmental testing that is required is greatly reduced.

The reliability of solid propellant rocket motors is generally higher than that for liquids when one takes sufficient care in propellant fabrication, in thermal protection, and in motor construction. This advantage arises from simplicity; solid propellant systems have fewer elements in series and are therefore less susceptible to aborts caused by failure of a minor element. Furthermore, many solid propellant problems associated with reliability are alleviated in the larger motors; for example, thermal protection is a delicate problem for small motors (say, propellant weights of the order of a ton) when performance tolerances are narrow, but for large motors (containing, say 100 or 1000 tons of propellant), the weight of the protection material is a very small percentage of the total weight, and much wider margins of safety can then be used.

Unlike many liquid propellants, solid propellants are inherently storable. Solid propellants have been stored for many years without appreciable deterioration or changes in performance. Questions about storability may, however, arise for the newer, higher energy solid propellants, and limits on the storage time may have to be established.

Much research effort has been spent in improving the safety of solid propellants. The greatest safety hazards arise in various solid propellant manufacturing processes; solid propellant fabrication is more dangerous than liquid propellant fabrication. However, after the propellant has been fabricated, subsequent processes such as casting and firing are generally less dangerous than comparable liquid propellant operations.

Solid propellant motors can be spin-stabilized much more easily than liquid propellant motors. Spin often interferes with the internal operation of liquid rockets. The capability of spin stabilization alleviates guidance problems in some applications.

The major disadvantage of solid propellant rockets is their relatively low specific impulse. Although their volumetric specific impulse is high, liquids and hybrids have a much higher mass-based specific impulse. The necessity of including both fuel and oxidizer in the same matrix prevents one from using the high-energy, highly reactive propellants that can be used in liquid and hybrid systems. The necessity of achieving good mechanical properties of the grain sets additional restrictions on solid propellant compositions and often prevents one from using fuel-oxidizer mixture ratios that would produce optimum performance. It seems safe to say that solid propellants will be limited to values of the specific impulse below 300 sec., which is nearly a factor of 2 below the maximum specific impulse that can be envisaged for other chemical propulsion systems.

Another disadvantage of solid propellant motors in many applications, such as space vehicle propulsion, is their short firing time. In some other applications, short

firing time is, of course, an advantage. In applications requiring a low chamber pressure (e.g., again, many space applications) solid propellants are at a disadvantage, because they generally operate poorly (and with low efficiency of combustion in small motors) for chamber pressures below, very roughly, 15 atmospheres.

Small solid propellant motors experience problems in thermal protection, as we have already emphasised. Thermal protection difficulties arise in the nozzle as well as in the chamber. Liquid propellants are well-suited to liquid cooling techniques for solving thermal protection problems, but solids are not. These difficulties can limit the use of high-energy solid propellants that produce high chamber temperatures. In fact, the chamber temperature is an important propellant parameter (which we have not yet discussed) that affects the choice of solid propellants for use in many applications. Thermal protection problems have been partially circumvented by the development of new ablative materials.

Solid propellant engine systems are basically less flexible in operation than liquid or hybrid propellant systems. In early solid propellant systems, after the motor was ignited no changes in its thrust-time history could be made. However, great advances in our ability to control solid motor operation have now been made. Venting or water injection produces controlled thrust termination; thrust vector control has been achieved by fluid injection into the nozzle as well as by other techniques; thrust modulation is achievable by liquid injection or by complex chamber designs; restart capabilities have been provided, e.g. by injection of a hypergolic liquid, etc. Thus, present-day solid propellant motors are practically as flexible as other systems. However, all of these improvements are obtained at the expense of greater complexity of the engine system. It is true in general that the system complications entailed in achieving control of the operation of solid propellant engines are much greater than those needed to provide comparable control of liquid or hybrid engines.

Mechanical properties of solid propellant grains sometimes produce problems in large motors and under operating conditions of high acceleration. Effort is required to eliminate grain deformation without increasing structural weight, in order to improve the suitability of solid propellants in these applications for which they are already superior to liquid systems.

Combustion instabilities sometimes appear in both liquid and solid propellant motors. These instabilities manifest themselves in irregular combustion and in pressure oscillations. Instabilities must be eliminated during motor development and therefore they increase development time. It is difficult to say whether instabilities pose greater problems in solid or liquid propellant motors, but we note here that more research is currently devoted to liquid propellant instabilities and that the large, segmented solid propellant motors did not experience instabilities during development.

In view of these advantages of solid propellant rocket systems, it is understandable why they are employed in the many applications discussed on page 8. The practical value of solid propellant rockets can nevertheless be enhanced by improvements in the following areas:

- a) augmentation of specific impulse,
- b) simplification of steps in propellant manufacturing and casting,
- c) reduction in structural weight of the case and nozzle,
- d) increasing the flexibility of the motor during operation,

- e) reduction in cost of the overall system,
- f) developing greater understanding of mechanisms of solid propellant combustion.

5. Outline of the Presentation

This book is divided into 12 chapters which probe various problems that are posed by current attempts to enhance the progress of solid propellant rocket propulsion. The problems considered lie in the fields of fluid flow in nozzles, of performance, of steady-state motor operation, of solid propellant combustion fundamentals (experiments and theory), of special erosive effects (due to flow of gases along tubular grains), of unsteady phenomena such as ignition, extinction and instability, and finally of mechanical properties of propellant grains. Except for the last of these topics, the problems listed here fall in the domain which is commonly referred to as internal ballistics. Thus, although they are important, we shall not discuss processes for manufacturing propellant grains, some problems associated with the manufacturing of nozzles, cases and other structures, topics in guidance and control, staging and its optimization, overall vehicle design and construction, and mission analysis. In spite of these and other omissions, it is hoped that the fundamental importance of internal ballistics to solid propellant rocketry will enable this book to serve as a textbook on solid propellant rockets. It is with this aim in mind that space is allotted to the development (from first principles) of the material that is covered and that a pedagogic view of presenting first the simpler material (e.g. Chapter 3) and then the more complex material (e.g. Chapter 6 or 10) is adopted. In these respects, the present work differs from most other *AGARD*-ographs. In the present section, we wish to highlight some of the special topics that are treated later.

We analyze performance first from the viewpoint of flow in the nozzle, where the thermal energy liberated by combustion is transformed into ordered kinetic energy. The study of this flow permits us to define characteristic parameters of rocket performance. The analysis is first made on the basis of an idealized model and then is extended to include various real effects. Although the basic analysis will be applicable to all propulsion systems in which gas is accelerated in a nozzle, the specific problems of solid propellant rocket systems will be emphasized in our approach.

Since current solid propellants generally contain aluminum, condensed aluminum oxide particles are often present in the gaseous combustion products. The consequent two-phase nozzle flow affects motor operation and performance. In particular, the specific impulse depends on particle size and on nozzle geometry. Special attention is paid to this problem in Chapter 2. Another special problem area of solid propellant rockets which is considered in some detail here is thrust vector control. While the magnitude and direction of the thrust vector of liquid rockets can be controlled relatively easily, solid propellant systems possess inherent control difficulties which are often best solved by externally injecting a fluid into the diverging section of the nozzle.

Specific impulse gains of a few seconds are appreciable for solid propellants because the maximum achievable specific impulse is relatively low for solids. Therefore it is important to carry out solid propellant performance calculations accurately. For this reason, we discuss in Chapter 3 the techniques by which these careful calculations can be made when the number and properties of the chemical species composing the propellant are known. Theoretical performance results are given, thus illustrating the effect of the nature of the propellant on the specific impulse. The choice of propellant compositions is limited by many factors, such as the ease with which the chemical heat release can be made to occur, the stability

of the propellant, the chemical and physical changes that occur during nozzle flow and special mission requirements. The results given here are intended to indicate possible ways of improving propellant performance, consistent with these limitations. The experimental determination of performance by measurements on small samples is discussed and comparisons of these results with those obtained in motor firing are given.

Motor operation is governed by the surface regression rate of the propellant, the geometry of the grain, and the relationship between chamber conditions and the mass flow rate through the nozzle. The surface regression rate is itself affected by various chamber operating conditions, such as chamber pressure, grain temperature, and the gas velocity parallel to the burning surface. It is necessary to develop methods for determining propellant regression rates of samples in constant-pressure bombs, and it is particularly important to compare these results with measurements obtained from motor firings. Such comparisons demonstrate that the flow fields inside motors affect the burning rate. Regression rate curves obtained in bomb experiments often have the same shape as motor-firing curves but are displaced in magnitude.

Grain geometries will differ according to whether the internal motor geometry is cylindrical, spherical, etc. By suitably shaping the grain and by suitably positioning propellants with differing burning rates, it is possible to design motors so that burnout occurs simultaneously over the entire internal surface, thereby eliminating undesirably long thrust tailoff times at the end of motor operation. Grain and motor geometries depend strongly on the mission and should be optimized for each application. We shall elaborate on these points in Chapter 4.

Combustion processes of solid propellants are complex and depend strongly on the nature of the solid propellant. In Chapters 5 and 6, we classify solid propellants into two principal categories, homogeneous and heterogeneous. For homogeneous propellants, we briefly examine the experimental techniques used in studying the combustion process, and we give the principal experimental results concerning flame structure. The experimental analysis of heterogeneous propellants is covered in much greater detail. An entire section is devoted to the decomposition and pyrolysis of the oxidizer ammonium perchlorate. The combustion of ammonium perchlorate propellants is also discussed. These experiments have resulted in a classification of possible mechanisms of combustion of heterogeneous propellants under various conditions of propellant formulation and motor operation.

Microcinematographic techniques reveal fine details of the combustion zones of heterogeneous propellants. They also shed light on the complex formation and combustion mechanisms of small liquid aluminum spheres which issue from the surface of aluminized propellants. Results of these photographic studies are discussed. The pyrolysis of plastic binder materials is also studied.

Theories of homogeneous and heterogeneous propellant combustion are discussed on the basis of the fundamental conservation equations of aerothermochemistry. Theories of homogeneous combustion are considered first in an attempt to discover the important stages which accompany the transformation of the solid to a gas. Particular attention is paid to the various types of reactions that may occur at the solid-gas interface. Since bomb experiments often involve nonadiabatic conditions, the nonadiabatic theory with radiative and convective heat losses is examined. Flammability limits for solids are also discussed.

Combustion mechanisms of heterogeneous solid propellants are so much more complex that there are no satisfactory theories giving the burning mechanism or the burning rate. A few models have been proposed on the basis of some experimental observations, but their theoretical foundations are questionable. Therefore we treat theories of heterogeneous propellant combustion more briefly than theories of

homogeneous propellant combustion. We consider the decomposition of some oxidizers (ammonium nitrate and ammonium perchlorate) that are used in composite propellants. The sandwich model of composite propellant combustion and the models of Summerfield and of Penner are described. Theories of the combustion of metal particles in oxidizing atmospheres are also reviewed briefly; the formation of condensed products complicates the combustion mechanism, and the theories emphasize the importance of diffusion phenomena.

Current propellant grains usually burn laterally and therefore experience erosive gas velocities, parallel to the grain, which increase in magnitude from zero at the head end of the motor to a maximum value at the nozzle end of the port. This erosive velocity modifies the burning rate and thereby affects the time development of the grain geometry. In the first part of Chapter 7 we discuss the experimental techniques which permit one to observe the effect of gas mass flow rate on the propellant regression rate. Novel techniques such as ionization probes, which can be used to measure erosive phenomena during motor firings, are also described. Existing experimental results on erosive burning are reviewed.

Satisfactory theoretical analyses of erosive burning phenomena are difficult to develop because of the complexity of the fluid dynamical and combustion processes. Part of the difficulty arises from the fact that the boundary layer approximation is usually valid over part but not all of the grain because the Reynolds number of the gas flow in the central cavity varies from 0 to 10^5 . Essentials of the approximate, semi-empirical theories that currently exist will be described, and possibilities of developing more basic theories will be discussed.

Unsteady regimes of ignition, extinction and combustion instability are as important as steady regimes in motor operation. Conditions for propellant ignition generally are first ascertained in the laboratory by studying samples of the propellant. Radiative heating, convective heating and contact with reactive fluids have been employed in these studies. The experimental methods will be discussed and compared (Chapter 8). These techniques enable one to determine necessary conditions for ignition and the time required for the development of a flame.

The various theories of ignition postulate the occurrence of a chemical ignition reaction in the solid, at the solid-gas interface, or in the gas phase. The site of the ignition reaction therefore affords a convenient means of categorizing ignition theories. Various possible ignition theories are discussed and existing detailed theories are compared. It appears that each of the three basic types of theories should be applicable for the right propellant under appropriate ignition stimuli.

In laboratory ignition experiments and in ignition theories, conditions are approximately uniform over the propellant surface. But with practical motor ignition devices, often a small portion of the propellant surface is first ignited, and then the flame propagates along the surface to the rest of the propellant. The flame propagation during motor ignition and the buildup of chamber pressure due to gas evolution by the solid during ignition will be discussed. Practical ignition devices (electrical, explosive charge, hypergolic liquid) are also reviewed.

The basic simplicity of solid propellant motors is offset by severe complexities in achieving thrust modulation, command extinction and reignition, for applications in which control of these processes is required. We have already stated that through a considerable amount of effort, practical realizations of all of these operations have been attained. Two methods of achieving extinction are by venting the chamber or by injecting water into it. The mechanisms of these two extinguishing techniques are discussed in Chapter 8. Conditions for which the intermittent extinction phenomenon of chuffing occurs are discussed in Chapters 9 and 10.

Experimental observations of undesirable periodic variations in combustion chamber pressure and in thrust date back to the early days of solid propellant rocketry. Much effort has been spent in attempts to eliminate these motor oscillations and many empirical "fixes" were discovered before the nature of the phenomenon was understood. The prevalent use of aluminum in propellants has alleviated these instability problems somewhat, because aluminum tends to suppress some types of combustion instability. Experimental aspects of combustion instabilities are discussed in Chapter 9 where the classifications into acoustic and nonacoustic instabilities, and linear and nonlinear instabilities are employed in an effort to clarify this complex subject. Laboratory experiments on instabilities under controlled conditions and observations of instabilities in motor firings, are both described. Of the many measurement techniques that we discuss, instantaneous chamber pressure measurements with fast-response transducers have proven to be most useful and most universally applicable, particularly for studies of acoustic instabilities. Pressure transducer measurements in T-burners (small, cylindrical, laboratory burners vented on the side instead of at the end) have now provided much experimental data on the acoustic admittance of burning solid propellants; these admittances are the most important parameters for determining whether linear acoustic instability will occur in a motor. Relatively recent observations of the occurrence of vortices in motors and of the amplification of shock-induced oscillations in otherwise stably burning motors demonstrate clearly that nonacoustic and nonlinear instabilities can also be of importance. We briefly discuss the experimental studies of these more complex phenomena, studies which are in their infancy.

A thorough theoretical understanding of the nature of combustion instability phenomena exists today only for linear, acoustic instabilities. Most of Chapter 10 is devoted to a presentation of the theory of linear, acoustic instability and to a review of the existing theoretical work in this field. Since these instabilities always involve acoustic oscillations of the gas in the chamber of the motor, we first develop the theory of acoustics and derive conditions for amplification and damping of acoustic waves. Acoustic oscillations can occur only if the amplification rate is greater than or equal to the damping rate. We discuss in detail first acoustic damping mechanisms and then theories of acoustic amplification mechanisms. There are numerous damping mechanisms; some of them are (roughly in the probable order of decreasing importance) damping of waves by reflection from the choked nozzle, damping of waves by small solid or liquid particles in the gas, viscous damping of waves at the boundaries of the chamber cavity, homogeneous gas-phase damping by chemical relaxation effects and viscoelastic damping in the solid. There is only one primary amplification mechanism, the acoustic response of the combustion zone at the surface of the burning solid. It is much more difficult to carry out accurate theoretical analyses of this amplification mechanism than to analyse the damping mechanisms mentioned above. We review the early time-lag theories of combustion zone amplification, later mechanistic models, attempts based on the full equations of aerothermochemistry, and models designed particularly to account for the heterogeneities of composite propellants. Predictions of many of these models are in qualitative agreement with trends observed experimentally.

Only a few theoretical concepts exist concerning possible mechanisms for nonlinear or nonacoustic instabilities. We review the ideas that have been advanced for explaining observed changes in mean burning rates of propellants during combustion instability, for ascertaining conditions of inherent instability of the combustion processes of solid propellants, for explaining nonacoustic instabilities which are observed to occur at low chamber pressures (and particularly for aluminized propellants), and for describing modes of instability that involve shock-like wave disturbances in the motor. The practical significance of these concepts of nonlinear and nonacoustic instability phenomena is unknown.

The bases for describing mechanical properties of viscoelastic solids are presented in Chapter 11. Methods for stress analysis of solid propellant grains are covered, and peculiar mechanical effects that may occur in solid propellants are described. Solid propellant materials present the solid mechanician with truly complicated problems because of their complex structure and time-dependent properties. Consequently, only limited progress toward obtaining a satisfactory description of the mechanical properties of solid propellants has been made. We present the various techniques that are useful for linear viscoelastic systems and formulate the complicated underlying theory from which future valid and useful approaches to the analysis of nonlinear viscoelasticity must emerge.

Failure analyses of solid propellant motors provide *a posteriori* information on mechanical properties that is useful for improving design. Techniques and results of failure analyses are discussed in Chapter 11.

Finally, in Chapter 12 we speculate on the future of solid propellant rocketry.

References

- (1) Wimpress R. N. Internal Ballistics of Solid Fuel Rockets. McGraw-Hill, 1950.
- (2) Shafer J. I. 'Solid Rocket Propulsion'. Space Technology edited by H. S. Seifert Chap 16. John Wiley and Sons, 1959.
- (3) Huggett C. 'The Combustion of Solid Propellants'. Combustion Processes Vol. II Princeton Series, p 514, 1956.
- (4) Geckler R. D. 'The Mechanism of Combustion of Solid Propellants.' Selected Combustion Problems I. AGARDograph Butterworth's London.
- (5) Barrère M., Jaumotte A., Fraeijs de Veubeke B. and Vandekerckhove J. Rocket Propulsion. Elsevier, 1960.
- (6) Sutton G. P. Rocket Propulsion Elements. John Wiley and Sons, 1949.
- (7) Carton D. S., Maxwell W. R. and Hurden D. Rocket Propulsion Technology, Vol. I Plenum, New York, 1961.
- (8) Zeldovich Y. B. et Rivin M. A. Fusées à Propergol Solide, Moscow 1963.
- (9) Kurov V. D. et Doljanski J. M. Roquettes à propergol solide, Moscow 1961.
- (10) Summerfield M. Solid Propellant Rocket Research. Academic, New York, London, 1960.
- (11) Barrère M. 'Les Recherches dans le Domaine de la Propulsion Chimique'. Semaine d'Etude sur la Propulsion Chimique, Paris 4 - 6 Mai 1964, Service de Documentation Scientifique et Technique de l'Armement.
- (12) Attali C. 'Structure des Propulseurs à Poudre à Structure Métallique'. Semaine d'Etude sur la Propulsion Chimique, Paris 4-6 Mai 1964, Service de Documentation Scientifique et Technique de l'Armement.
- (13) Jube G. 'Le Plastique armé Structure de l'avenir pour les Propulseurs à

Poudre'. Semaine d'Etude sur la Propulsion Chimique, Paris 4-6 Mai 1964, Service de Documentation Scientifique et Technique de l'Armement.

- (14) **Boisson J. et Betin P.** 'Etude de la Balistique Interieure des Fusées à Poudre'. Semaine d'Etude sur la Propulsion Chimique, Paris 4-6 Mai 1964, Service de Documentation Scientifique et Technique de l'Armement.
- (15) **Koelle H. H.** Handbook of Astronautical Engineering - McGraw-Hill, 1961.
- (16) 'Missiles and Rocket' - Ninth Annual World Missile/Space Encyclopedia. 26 July 1965.
- (17) **Alexander R. V. and Fournier C. A.** 'Cost and Performance Considerations in the Selection of Structural Materials for Ultra-Large Size Booster', J. Spacecraft and Rockets Vol. No. 1, p. 62, Jan - Feb 1964.
- (18) **McNabb J.** 'Design and Application of Large Solid Propellant Propulsion Systems', Advances in Astronautical Propulsion, edited by C. Casci, pp. 47 - 62. Pergamon Press 1962.

Chapter 2

Nozzle Flow and Characteristic Parameters

Nomenclature

A	cross-sectional area of duct or channel
a	velocity of sound
A_e	nozzle exit area
A_j	port exit area
A_w	wall area
A_t	throat area
c^*	characteristic velocity
C_D	drag coefficient
C_F	thrust coefficient
C_F^o	optimum thrust coefficient
c_p	specific heat at constant pressure
C_{pi}	$\equiv dH_i/dT$, the molar heat capacity of i species
c_s	specific heat of wall material or of condensed particles
D	characteristic length; local diameter
\hat{D}	total drag force exerted on fluid
D_o	value of D at nozzle entrance
F	axial thrust
f	friction factor; also a representative flow variable
F^o	thrust at design exit pressure
F_s	side force, (Eq. 2-94)
h	enthalpy per unit mass
\hat{h}	heat transfer coefficient
h_e	enthalpy at nozzle exit
H_i	molar enthalpy of pure i species
h_{so}	total stagnation enthalpy per unit mass
I	total impulse
I_{sp}	specific impulse
I_{sp}^o	optimum specific impulse

k	average wall roughness
K_{pk}	equilibrium constant for partial pressures, for k-th reaction
L	characteristic length of nozzle
M	Mach number
\dot{m}	total mass flow rate (mas/sec)
\dot{m}_j	mass injection rate
n	reciprocal of the average molecular weight of mixture $\equiv \sum_{i=1}^N n_i$
\vec{n}	unit vector normal to surface
n_i	number of moles of i species per unit mass of mixture
n_j	number of condensed particles per unit volume
Nu	Nusselt number
P	duct perimeter
p	pressure; average free stream static pressure
p_a	ambient pressure
p_c	chamber pressure
p_e	pressure just inside exit plane
p_j	injection pressure
Pr	Prandtl number, $\mu c_p / \lambda$
p_{so}	stagnation pressure
q	heat flux from gas to wall
\dot{q}	total heat added per second
R	gas constant per unit mass
r	particle radius; radial coordinate
R°	universal gas constant
Re	Reynolds number based on pipe diameter, $\rho vD / \mu$
R_e	nozzle exit radius
r_1	throat radius

r_g	radius of curvature of the nozzle at throat
s	entropy per unit mass
S_c	Schmidt number
S_i^o	molar entropy of pure i species at 1 atm pressure
T	absolute temperature
t	time
\bar{T}	mean temperature in boundary layer
t_b	burning time
T_c	chamber temperature
T_j	jet temperature
T_s	surface temperature
T_{so}	stagnation (total) temperature
u	internal energy per unit mass
v	velocity
v_e	axial component of velocity at exit plane; exhaust velocity
v_{ge}	gas velocity at nozzle exit
v_j	velocity of injectant normal to wall at port exit
$v_{j\infty}$	asymptotic flow velocity of injectant
v_a	condensed-phase velocity at nozzle exit
\dot{w}	total work done per second
x	axial position
X_i	mole fraction of i species
α_e	expansion cone half angle of nozzle divergent section
β	dimensionless proportionality factor between side force and momentum flow rate (Eq. 2-94)
γ	ratio of specific heats, c_p/c_v
Δh	heat transfer potential
∇	gradient operator (vector)
$\nabla \cdot$	divergence
δ	displacement thickness

δ_i	thickness of insulating material
ϵ	mass flow fraction of condensed phase
ϵ_s	surface emissivity
θ	divergence angle
λ	thermal conductivity of gas
λ_s	thermal conductivity of wall material
μ	viscosity coefficient of gas
μ_i	chemical potential of species i
ν_{ik}	stoichiometric coefficient for species i appearing as a reactant in reaction k
ν_{ik}	stoichiometric coefficient for species i appearing as a product in reaction k
ν_i^k	number of atoms of kind k in molecule of type i
ρ	density
ρ_s	specific gravity of wall material or of condensed particles
ρ_{so}	stagnation density
σ	Stefan-Boltzmann constant
τ	dimensionless lag parameter (Eq. 2-78)
τ_w	shear stress per unit area on wall
φ	shock angle
χ	flow deflection angle

Script Letters

\mathcal{C}	symbol for a chemical compound
ℓ	combustion chamber length
m	molecular weight of reaction products

Subscripts

c	chamber condition
e	exit condition; also chemical equilibrium
g	gas property; free stream conditions

- o stagnation conditions
- s condensed-phase property
- t throat conditions
- w conditions of gas at wall

Nozzle Flow and Characteristic Parameters

1 Quasi-One-Dimensional Theory - Isentropic Expansion

1.1. Introduction

The quasi-one-dimensional theory of compressible fluid flow provides the basis for evaluating and comparing the performance of rocket motors of all kinds. Application of the theory to the process of conversion of heat to ordered kinetic energy of the propulsive fluid, which occurs in the rocket nozzle, produces relationships between motor performance and properties of the propellants and of the motor design. These relationships are conveniently expressed in terms of formulas for a number of characteristic parameters that rocket engineers traditionally use in the selection and design of rocket systems. The formulas for the characteristic parameters are derived in this section.

To understand the finer details of the following development, the reader must have knowledge of thermodynamics and of some of the elements of fluid mechanics, (1), (2), (3), (4). However, a thorough knowledge of the material contained in these references is not an essential prerequisite for gleaning the principal points of the following discussion.

The quasi-one-dimensional theory is an idealization of the full equations of aerothermochemistry. The idealization is useful in that it provides a sufficient basis for an approximate discussion of rocket motor performance. For more accurate and more detailed analyses of rocket and nozzle performance, it is necessary to consider phenomena that cannot be described within the framework of the idealized theory. The non-ideal phenomena that are important in the nozzle flow for solid-propellant rockets are considered in the later sections of this chapter. The full equations of aerothermochemistry, that are needed for accurate analyses of the combustion and flow processes in solid-propellant rockets, are developed in Chapter 5.

The quasi-one-dimensional theory describes flow in a duct or channel and is based on the assumptions that the flow is steady in time and that flow properties are uniform across every cross section of the duct. Neither of these basic assumptions is exactly true; for example, viscous phenomena force the flow velocity to approach zero at the solid wall of a duct, regardless of how large the velocity in the center of the duct is. Therefore, at best the quasi-one-dimensional theory is applicable only to average flow variables, space averages (over a cross section) in all cases and time averages as well if the flow is unsteady or turbulent. Exactly how these averages are to be computed from local, instantaneous flow variables is a subject that has received a considerable amount of study but has not been resolved completely. An approach to one aspect of this problem may be found in Ref. (3), pp. 87-89 and pp. 157-159; a different approach to another aspect of the problem is given in Ref.

(5). In spite of these imprecisions associated with the basis of the quasi-one-dimensional conservation equations, the equations are often quite useful in practical problems and even in basic problems in fluid dynamics, yielding reasonably good agreement with experiment and reproducing most of the essential results of much more sophisticated analyses that are based on considerably more complex equations. Furthermore, the equations can often be improved by introducing correction factors to account in an approximate way for non-quasi-one-dimensionality. We proceed now to develop and use the quasi-one-dimensional flow equation.

1.2. Derivation of Quasi-One-Dimensional Equations

It is convenient to adopt the control volume illustrated in Fig. 2-1. At the axial position x , the cross-sectional area of the duct or channel is A , the density is ρ , the pressure is p , the velocity is v , the internal energy per unit mass is u , and the enthalpy per unit mass is h . At position $x + dx$, these quantities will have changed to $A + dA$, $\rho + d\rho$, $p + dp$, $v + dv$, $u + du$ and $h + dh$. All quantities represent averages. Body forces, radiative transport, and axial components of transport vectors are neglected in the development.

1.2.1. Mass Conservation - The mass of fluid per second flowing into the element shown in Fig. 2-1, across the surface located at position x , is $\rho v A$. The mass of fluid per second flowing out of the element, across the surface located at $x + dx$, is $(\rho + d\rho)(v + dv)(A + dA)$. In steady flow, these two quantities must be equal since no mass can accumulate inside the control volume. Expanding to first order in the differential quantities, we therefore find that :

$$d(\rho v A) = 0,$$

the integral of which is :

$$\rho v A \equiv \dot{m} = \text{constant}, \quad (\text{Eq. 2-1})$$

where \dot{m} is the total mass flow rate (mass/sec), which is independent of x . Equation 2-1 is a statement of the law of conservation of mass.

1.2.2. Momentum Conservation - The law of conservation of momentum states that the time rate of increase of the x component of momentum of the fluid within the control volume equals the x component of the sum of the forces acting on the fluid in the control volume.

When fluid can flow across the surface of the control volume, the "time rate of change" of a quantity is composed of two parts, the change of the quantity at points within the control volume and the change due to the fact that material possessing different values of the quantity may be transported into and out of the control volume. In steady flow, the change of the quantity at points within the control volume is zero. Therefore, in the present development, by time rate of change of a quantity within the control volume, we mean the change incidental to the fact that material is transported across the surface of the control volume. This time rate of change equals the mass flow rate multiplied by the difference between the value of the quantity per unit mass of fluid at $x + dx$ and the value of the quantity per unit mass of fluid at x , in Fig. 2-1.

The x component of momentum of the fluid entering at x in time dt is $\dot{m} v dt$, while the x component of momentum of the fluid leaving at $x + dx$ in time dt is $\dot{m}(v + dv)dt$. Hence, in a steady state the time rate of increase of the x component of momentum of the fluid within the control volume is :

$$\dot{m} dv.$$

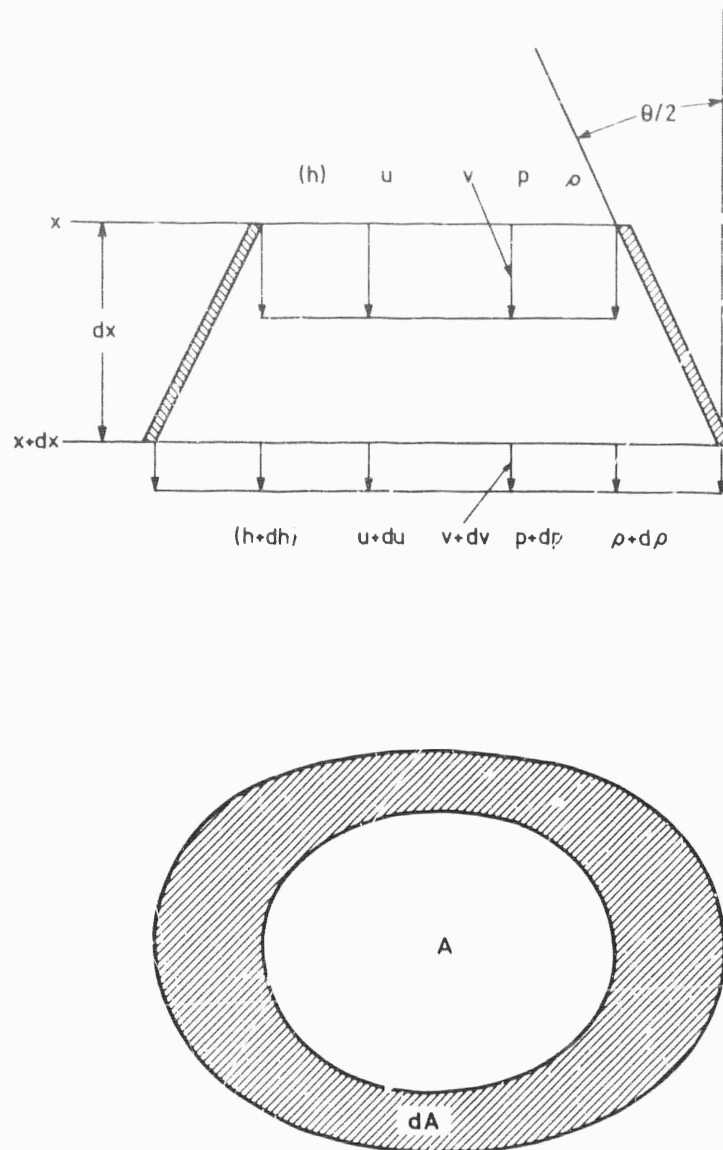


Fig. 2-1 Schematic diagram of control volume for deriving quasi-one-dimensional conservation equations.

The forces that we shall consider are pressure forces, drag forces of objects located within the control volume and friction forces on the wall.

The x component of the pressure force on the surface located at position x is pA . The x component of the pressure force on the surface at $x + dx$ is $-(p + dp)(A + dA)$. The x component of the pressure force on the wall is pdA , to first order in differential quantities. Hence, to first order in differential quantities, the total pressure force on the fluid within the control volume is :

$$- A dp .$$

We denote the x component of the total drag force exerted on the fluid within the control volume by objects such as orifices, screens, vanes, corners, etc., by :

$$- d\hat{D} .$$

These drags, which are a consequence of separation and skin friction effects, are difficult to calculate and therefore are generally measured empirically. The conventional formula for the integral of $d\hat{D}$ for an object is :

$$\hat{D} = 1/2 \rho v^2 A C_D , \quad (\text{Eq. 2-2})$$

where ρ , v and A refer to conditions upstream from the object, and C_D is a dimensionless drag coefficient. For many objects, values of C_D are tabulated in handbooks (6), (7).

The x component of the frictional force on the wall is $-\tau_w dA_w \cos(\theta/2)$ where τ_w is the shear stress per unit area on the wall, dA_w is the wall area of the control volume and $\theta/2$ is the divergence angle, illustrated in Fig. 2-1. A dimensionless friction factor f is usually defined in such a way that :

$$\tau_w = \rho v^2 f / 8 , \quad (\text{Eq. 2-3})$$

and a hydraulic diameter is defined as :

$$D = 4A/P ,$$

where P is the perimeter of the duct. (Note that the hydraulic diameter reduces to the true diameter for a duct of circular cross section.) Then, $dA_w \cos(\theta/2) = P dx = (4A/D) dx$, and the x component of the wall friction becomes :

$$-(1/2) \rho v^2 f A dx/D .$$

The friction factor which appears in this formula has been studied both theoretically and experimentally. For fully-developed laminar Poiseuille flow in a circular pipe, $f = 64 / \text{Re}$, where $\text{Re} \equiv \rho v D / \mu$ is the Reynolds number based on the diameter of the pipe (μ is coefficient of viscosity); friction factors applicable to other conditions have been tabulated in handbooks and textbooks, (6), (7), see also Section 5.2.

Collecting the pressure, drag and friction forces and equating them to the rate of increase of momentum, we find that the equation for conservation of momentum becomes :

$$\dot{m} \frac{dv}{dx} + A \frac{dp}{dx} + \frac{d\hat{D}}{dx} + (1/2) \rho v^2 f A/D = 0 . \quad (\text{Eq. 2-4})$$

Unlike the equation for conservation of mass, Eq. 2-4 is a differential equation for

which the integral cannot be written down immediately.

1.2.3. Energy Conservation - The equation for conservation of energy is a statement of the first law of thermodynamics; the heat added to the fluid in the control volume is the sum of the increase in the energy of the fluid in the control volume and the work done by the fluid in the control volume.

In time dt , the internal energy $\dot{m} u dt$ enters the control volume across the surface located at position x in Fig. 2-1, while the internal energy $\dot{m} (u + du) dt$ leaves the control volume across the surface located at position $x + dx$. This contributes a term :

$$\dot{m} du$$

to the time rate of increase of energy. Similarly, in time dt the kinetic energy $\dot{m} (v^2/2) dt$ enters at x , and the kinetic energy $\dot{m} [(v + dv)^2/2] dt \approx \dot{m} (v^2/2) dt + \dot{m} v dv dt$ leaves at $x + dx$, thereby contributing :

$$\dot{m} v dv$$

to the time rate of increase of energy. The sum of these two terms appears as the time rate of increase of total energy in the statement of the first law of thermodynamics for a steady-state, open system.

The main contribution to the work done by the fluid in the control volume is the so-called "displacement work". In time dt , particles at the upstream edge of the control volume move a distance $v dt$ against the pressure force pA , thus doing an amount of work $pA v dt$ on the element. In the same time interval, particles at the downstream edge of the control volume move a distance $(v + dv) dt$ while experiencing the force $(p + dp)(A + dA)$, thereby receiving the work $(p + dp)(A + dA)(v + dv) dt \approx pA v dt + d(pA v) dt$ from the element. The displacement work done per unit time by the fluid in the control volume is therefore :

$$d(pAv) .$$

The fluid in the control volume may also do external work (e.g., driving a turbine); we let :

$$d\dot{w}$$

denote the external work done by the fluid in the control volume per unit time.

We also let :

$$d\dot{q}$$

denote the heat added to the fluid in the control volume per unit time (e.g., by heat conduction across the walls of the duct).

Then the equation for conservation of energy becomes :

$$d\dot{q} = \dot{m} du + \dot{m} v dv + d(pAv) + d\dot{w} ,$$

the integral of which is :

$$\dot{q} + \text{constant} = \dot{m} u + \dot{m} v^2/2 + pAv + \dot{w} \quad (\text{Eq. 2-5})$$

since $v dv = d(v^2/2)$. Here \dot{q} and \dot{w} denote the total heat added per second and the

total work done per second between some definite upstream reference station and the local station along the duct.

It is convenient to introduce the enthalpy per unit mass,

$$h = u + p/\rho, \quad (\text{Eq. 2-6})$$

in order to combine the displacement work term and the internal energy term; it can be seen from Eq. 2-1 that:

$$\dot{m}u + pAv = \dot{m}h.$$

Thus, Eq. 2-5 can be written as:

$$h + v^2/2 = h_{s0} + (\dot{q} - \dot{w})/\dot{m}, \quad (\text{Eq. 2-7})$$

where h_{s0} is a constant, equal to the stagnation enthalpy $(h + v^2/2)$ at the upstream reference station. The last term in Eq. 2-7 obviously represents the heat added to the fluid per unit mass, less the external work done by the fluid per unit mass, during its history of migration from the upstream reference station to the local station (x). In the absence of heat transfer and external work, Eq. 2-7 reduces to the statement that the stagnation enthalpy is a constant of the motion.

1.3. Isentropic Flow

1.3.1. Simplified Conservation Equations - In order to obtain an idealized theory for nozzle flow, we may assume that no external work is done by the system ($\dot{w} = 0$), that the system is adiabatic ($\dot{q} = 0$) and that the system is reversible in a thermodynamic sense. The assumption of reversibility implies that the last two terms in Eq. 2-4 vanish, since the viscous phenomena leading to drag and skin friction are necessarily irreversible. The conservation equations (Eqs. 2-1, 2-4 and 2-7) then become:

$$\rho vA = \dot{m} = \text{constant}, \quad (\text{Eq. 2-8})$$

$$\rho v \frac{dv}{dx} + \frac{dp}{dx} = 0, \quad (\text{Eq. 2-9})$$

$$h + \frac{v^2}{2} = h_{s0} = \text{constant}. \quad (\text{Eq. 2-10})$$

It is known from thermodynamics that the assumptions of adiabaticity and reversibility together imply that the flow is isentropic. Equations 2-8, 2-9 and 2-10 must therefore imply that entropy is constant. Indeed, by employing the general thermodynamic relationship:

$$Tds = du + pd(1/\rho) = dh - 1/\rho dp \quad (\text{Eq. 2-11})$$

(T = absolute temperature, s = entropy per unit mass) along with Eq. 2-9 and the differential form of Eq. 2-10, one can show that $ds = 0$, i.e.,

$$s = \text{constant}. \quad (\text{Eq. 2-12})$$

[Equation 2-11, which is a familiar result for one-component systems, rests on the hypothesis that the flow is either chemically frozen or in chemical equilibrium when it is applied to multicomponent, reacting gases; see Section 2.2]. Equations 2-8, 2-10 and 2-12 constitute a set of algebraic conservation equations governing isentropic flow.

Now, it should be emphasized that if the thermodynamic properties of the fluid are known, then Eqs. 2-8, 2-10 and 2-12 are sufficient for determining all flow variables as functions of x , provided that the area variation $A(x)$ is given. This conclusion is a consequence of the fact that thermodynamic relationships (including the equation of state and the caloric equation of state) enable one to express all thermodynamic properties in terms of two independent thermodynamic properties. Equations 2-8, 2-10 and 2-12 thus constitute three independent relationships among two independent thermodynamic variables and the dynamical variable v . It is possible to discuss isentropic flows on the basis of Eqs. 2-8, 2-10 and 2-12 without invoking any further assumptions concerning the thermodynamic properties of the fluid. However, because it often provides a reasonably good approximation to the true flow, we shall first introduce the additional assumptions that the fluid is a one-component ideal gas with constant heat capacities.

1.3.2. One-Component Ideal Gases with Constant Heat Capacities - An ideal gas obeys the equation of state :

$$p = \rho RT, \quad (\text{Eq. 2-13})$$

where R is the gas constant per unit mass (the universal gas constant divided by the molecular weight). For a one-component ideal gas, it can be shown from Eq. 2-13 by thermodynamical reasoning that the enthalpy h is a function of temperature alone. If, further, the specific heat at constant pressure, $c_p \equiv (\partial h / \partial T)_p$, is assumed to be constant, then :

$$h = c_p T + \text{constant}. \quad (\text{Eq. 2-14})$$

We assume that the notation of thermodynamics concerning partial differentiation is known to the reader (2).

From Eqs. 2-11, 2-13 and 2-14, it can be shown that the entropy is given by :

$$\begin{aligned} s &= R \left\{ \left[\gamma / (\gamma - 1) \right] \ln T - \ln p \right\} + \text{constant} \\ &= R \left\{ \left[1 / (\gamma - 1) \right] \ln T - \ln \rho \right\} + \text{constant} \\ &= R \left\{ \left[1 / (\gamma - 1) \right] \ln p - \left[\gamma / (\gamma - 1) \right] \ln \rho \right\} + \text{constant}, \end{aligned} \quad (\text{Eq. 2-15})$$

where $\gamma \equiv c_p / c_v$ is the ratio of specific heats. [The specific heat at constant volume is defined as $c_v \equiv (\partial u / \partial T)_\rho = c_p - R$, in which the last equality is a consequence of Eqs. 2-6, 2-13 and 2-14.]

The equations for quasi-one-dimensional, isentropic flow of a one-component, ideal gas with constant heat capacities are conveniently studied by employing the Mach number as a parameter. The Mach number is defined as :

$$M = v/a,$$

where a is the velocity of sound. The velocity of sound is the speed at which a small-amplitude, longitudinal wave propagates in the fluid; it can be shown to be given by $a = [(\partial p / \partial \rho)_s]^{1/2}$, which is a thermodynamic property of the system. From Eqs. 2-13 and 2-15 it can be seen that :

$$a = \sqrt{\gamma RT} \quad (\text{Eq. 2-16})$$

for a one-component, ideal gas with constant heat capacities. Equations 2-8, 2-10 and 2-13, 2-16 can be used to express flow variables in terms of Mach number.

By using Eq. 2-16 Eq. 2-10 can be written as :

$$h + (\gamma/2) RT M^2 = h_{s0} .$$

As a convention, we may set the constant in Eq. 2-14 equal to zero. Then, from Eq. 2-14 and the preceding relationship, we obtain :

$$c_p T (1 + \frac{\gamma}{2} \frac{R}{c_p} M^2) = h_{s0} ,$$

which, in view of the definition of γ , can be written as :

$$T = T_{s0} (1 + \frac{\gamma-1}{2} M^2)^{-1} , \quad (\text{Eq. 2-17})$$

where $T_{s0} \equiv h_{s0}/c_p$ is the stagnation or total temperature, which is constant in adiabatic flow.

Equations 2-12 and 2-15 imply that :

$$p/T^\gamma/(\gamma-1) = \text{constant}$$

and that :

$$p/\rho^\gamma = \text{constant} ,$$

which are well-known relationships for isentropic processes. In view of Eq. 2-17 the first of these expressions implies that :

$$p = p_{s0} (1 + \frac{\gamma-1}{2} M^2)^{-\gamma/(\gamma-1)} , \quad (\text{Eq. 2-18})$$

Finally, a relationship between the Mach number and the cross-sectional area can be obtained from Eq. 2-8 by employing Eqs. 2-19 and 2-20. Thus, we find :

$$\rho = \rho_{s0} (1 + \frac{\gamma-1}{2} M^2)^{-1/(\gamma-1)} . \quad (\text{Eq. 2-19})$$

In Eq. 2-18, the symbol p_{s0} has been introduced for the constant obtained in the derivation; from Eq. 2-18 it is obvious that p_{s0} is the pressure at a point where $M = 0$ (stagnation conditions) in the isentropic flow, and therefore p_{s0} represents the stagnation pressure, which is constant for isentropic flow. Similarly, the constant $\rho_{s0} = p_{s0}/RT_{s0}$, which appears in Eq. 2-19, is the stagnation density. [An expansion of Eq. 2-18 for small values of M shows that $p_{s0} = p + (\rho v^2/2) \{ 1 + M^2/4 + O(M^4) \}$, thus implying that at low Mach numbers the stagnation pressure approaches $p + \rho v^2/2$, which is a familiar formula for incompressible flow.]

The velocity can be expressed in terms of the Mach number by using Eqs. 2-16 and 2-17. The result is :

$$v = \sqrt{\gamma RT_{s0}} M (1 + \frac{\gamma-1}{2} M^2)^{-\frac{1}{2}} . \quad (\text{Eq. 2-20})$$

Finally, a relationship between the Mach number and the area can be obtained from Eq. 2-8 by employing Eqs. 2-19 and 2-20. Thus, we find :

$$A = \left(\frac{\dot{m}}{p_{s0} \sqrt{\gamma / RT_{s0}}} \right) M^{-1} \left(1 + \frac{\gamma-1}{2} M^2 \right)^{(\gamma+1)/(2(\gamma-1))} \quad (\text{Eq. 2-21})$$

Since the leading coefficient on the right-hand side is a constant in each of the Eqs. 2-17 to 2-21 each equation relates a property to the Mach number, at every point in the flow, provided that this property is known at any one value of the Mach number. For graphs or tabulations, it is therefore convenient to select a reference Mach number and to plot or list the ratio of the local value of the property to the value of the property at the reference Mach number, as a function of the local Mach number, for various values of the one remaining parameter γ . For T , p and ρ , the reference Mach number is chosen to be zero. However, according to Eqs. 2-20 and 2-21, v vanishes and A approaches infinity as M goes to zero. Therefore $M = 0$ is not an acceptable reference condition for velocity or area. For reasons that will appear below (Section 1.4.1), the value $M = 1$ is chosen as the reference condition for velocity and area, and values of properties at $M = 1$ are identified by the subscript t . Equations 2-17 - 2-21 thus enable us to plot or list T/T_{s0} , p/p_{s0} , ρ/ρ_{s0} , v/v_t and A/A_t as functions of M for various values of γ . One such graph, for $\gamma = 1.4$, is shown in Fig. 2-2. Tables which cover values of γ ranging from 1.0 to 1.67 and which are useful in performing accurate calculations for isentropic flow problems, may be found in Ref. (8) as well as in a number of other sources.

1.4. Nozzle Flow

1.4.1. Choking in Isentropic Flow - From Fig. 2-2 it is seen that the area ratio A/A_t decreases with increasing M for $M < 1$, passes through a minimum at $M = 1$, and increases with increasing M for $M > 1$. Since the velocity is seen to be a monotonically increasing function of M in Fig. 2-2, we may conclude that in order to accelerate the flow, one must cause A to decrease if $M < 1$ and to increase if $M > 1$. The purpose of a nozzle is to accelerate the flow. Therefore, in order to construct an isentropic nozzle in which the Mach number passes from an upstream value less than unity to a downstream value greater than unity, it is necessary to contour the nozzle so that the flow converges for $M < 1$ and diverges for $M > 1$. Such a convergent-divergent nozzle is called a deLaval nozzle. The Mach number is unity at the minimum area, or throat, of a deLaval nozzle. Thus, the subscript t in Fig. 2-2 identifies conditions at the nozzle throat. Figure 2-2 also shows that the temperature, pressure and density decrease monotonically as M increases in a deLaval nozzle. As M approaches infinity, A must approach infinity, and T , p and ρ approach zero, but v approaches a finite non-zero limiting value {equal to $[2\gamma RT_{s0}/(\gamma-1)]^{1/2}$, according to Eq. 2-20} which represents the maximum velocity that can be achieved in an isentropic expansion.

Although Fig. 2-2 is valid only for a one-component, ideal gas with constant heat capacities (and, moreover, only for $\gamma = 1.4$), nevertheless all of the results that we have just stated (except, of course, the formula for v in the limit of infinite M) remain valid for an arbitrary working fluid. They can be derived from Eqs. 2-8 - 2-12 and the result $a^2 = (\partial p / \partial \rho)_s$ alone. Thus, for example, the differential form of Eq. 2-8 can be written as :

$$\frac{dv}{v} + \frac{d\rho}{\rho} + \frac{dA}{A} = 0 ,$$

which can be expressed as :

$$\frac{dv}{v} + \frac{dp}{\rho a^2} + \frac{dA}{A} = 0 ,$$

in view of Eq. 2-12. Substituting Eq. 2-9 for dp into this expression yields :

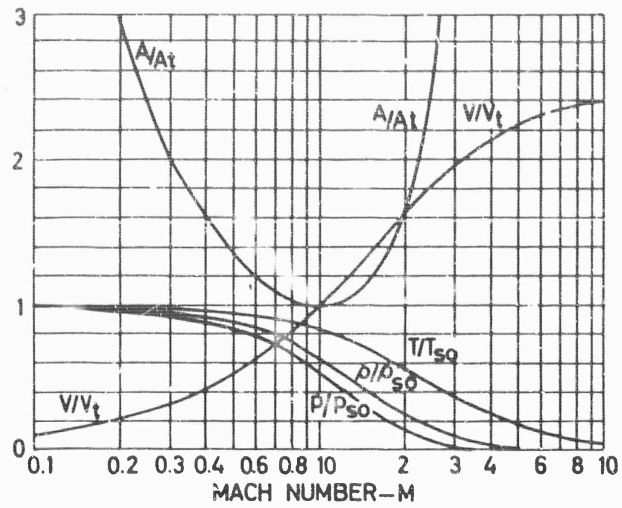


Fig. 2-2 Isentropic flow functions for a one-component, ideal gas with $\gamma = 1.4$.

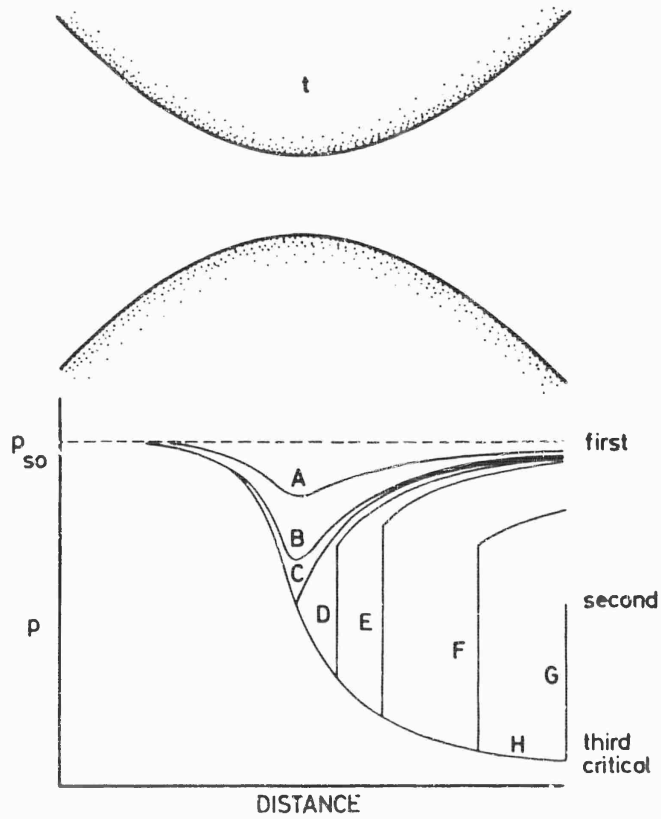


Fig. 2-3 Flow development in a deLaval nozzle.

$$\frac{dv}{v} (1 - M^2) + \frac{dA}{A} = 0, \quad (\text{Eq. 2-22})$$

which proves quite generally the assertion that was made in the second sentence of the preceding paragraph. Similar arguments may be employed to derive the other results.

'Choking' is said to occur in an isentropic deLaval nozzle, whenever the Mach number at the throat is unity. Since small disturbances propagate at the sonic velocity ($M = 1$), a small disturbance generated downstream from a sonic throat cannot propagate upstream past the throat in the fluid to inform the oncoming flow of its presence. Therefore changes in downstream conditions will not affect the upstream stagnation conditions, the upstream property profiles or the mass flow rate. This is one reason for the terminology choked flow. We might also remark that if one adds an additional contraction section onto the downstream end of a convergent nozzle in which the exit Mach number is unity, then the upstream conditions must necessarily change for a steady-flow solution to exist.

1.4.2. Flow in deLaval Nozzles - It is instructive to consider what happens in a deLaval nozzle of fixed geometry and fixed upstream stagnation conditions as the exit pressure of the nozzle is gradually decreased. The resulting pressure profiles, on the basis of quasi-one-dimensional theory, are illustrated in Fig. 2-3. Initially, with the exit pressure equal to the stagnation pressure, the pressure is uniform and there is no flow. As the exit pressure is decreased, flow begins and velocities remain subsonic throughout the nozzle. Eventually, at the first critical exit pressure (curve C in Fig. 2-3), the velocity becomes sonic at the throat. As argued above and illustrated in Fig. 2-3, at all lower exit pressures the flow in the upstream portion of the nozzle remains unchanged. However, on the basis of our isentropic flow equations, there is no flow solution for exit pressures below the first critical value, except for the solution in which the flow is entirely supersonic in the downstream portion of the nozzle, which occurs at the third critical exit pressure (curve H of Fig. 2-3). The third critical exit pressure is the 'design' exit pressure of a deLaval nozzle. Supersonic nozzles with exit pressures above the third critical value are termed 'overexpanded', those with exit pressures below the third critical value are termed 'underexpanded'. At exit pressures between the first and third critical values and also below the third critical value, our isentropic quasi-one-dimensional theory yields no solution. The nature of the nozzle flow under these conditions requires further consideration. We now proceed to introduce the concepts that are required.

1.4.3. Shock Waves - As the exit pressure is reduced from the first critical pressure to a value slightly below this pressure, sound signals can move upstream only as far as the nozzle throat. This results in acceleration of the fluid just downstream from the throat. The flow just downstream from the throat therefore becomes supersonic, while the flow in most of the downstream part of the nozzle is subsonic. Supersonic flow cannot become subsonic isentropically in a diverging section. However, if we permit a nonisentropic discontinuity to occur in flow properties (e.g., curve D in Fig. 2-3) then we can match the supersonic and subsonic flows. Such a discontinuity, which is called a normal shock wave, must of course satisfy the conservation equations even though the requirement of isentropic flow is removed. The equations relating properties on the upstream and downstream sides of a shock wave are developed below.

Since a normal shock is assumed to occur at a plane normal to the flow direction, there is no change in area in passing through the shock wave. When $A = \text{constant}$, the conservation equations are simplified. Equation 2-1 becomes :

$$d \cdot \rho v = \dot{m}/A = \text{constant} . \quad (\text{Eq. 2-23})$$

Momentum conservation, Eq. 2-4, may be integrated formally to yield :

$$\rho v^2 + p + \hat{D}/A + \int \frac{1}{2} \rho v^2 dx/D = \text{constant} . \quad (\text{Eq. 2-24})$$

Energy conservation, in adiabatic systems with $\dot{w} = 0$, again reduces to Eq. 2-10.

According to Eq. 2-23, properties on the upstream (subscript 1) and downstream (subscript 2) sides of a normal shock wave must obey the condition :

$$\rho_1 v_1 = \rho_2 v_2 . \quad (\text{Eq. 2-25})$$

Now, since the flow is isentropic upstream and downstream of the shock wave, \hat{D} is zero at stations 1 and 2 (even though it differs from zero in the interior of the wave). Also, since the shock wave has negligible thickness, the integral of the wall friction term is negligible. Therefore Eq. 2-24 yields :

$$\rho_1 v_1^2 + p_1 = \rho_2 v_2^2 + p_2 . \quad (\text{Eq. 2-26})$$

Finally, Eq. 2-10 provides the condition :

$$h_1 + v_1^2/2 = h_2 + v_2^2/2 . \quad (\text{Eq. 2-27})$$

Equations 2-25, 2-26 and 2-27, together with thermodynamic properties of the system, will determine properties on one side of a normal shock wave from the properties on the other side.

For a one-component ideal gas with constant heat capacities, one can show from Eq. 2-25, 2-26 and 2-27 that :

$$M_2^2 = [2 + (\gamma - 1) M_1^2] / [2\gamma M_1^2 - (\gamma - 1)] \quad (\text{Eq. 2-28})$$

$$T_2/T_1 = [2\gamma M_1^2 - (\gamma - 1)][(\gamma - 1)M_1^2 + 2]/(\gamma + 1)^2 M_1^2 \quad (\text{Eq. 2-29})$$

$$p_2/p_1 = [2\gamma M_1^2 - (\gamma - 1)] / (\gamma + 1) , \quad (\text{Eq. 2-30})$$

$$\text{and } \rho_2/\rho_1 = v_1/v_2 = (\gamma + 1) M_1^2 / [(\gamma - 1) M_1^2 + 2] . \quad (\text{Eq. 2-31})$$

Stagnation properties (other than T_{s0}) also change across a normal shock; appropriate expressions for the changes can be obtained by substituting Eqs. 2-18 and 2-19 into Eqs. 2-30 and 2-31. As an aid in computation, the preceding quantities are tabulated as functions of M_1 for various values of γ in Ref. (8) and elsewhere.

We might mention that in constant-area flow, the equation :

$$h + \frac{1}{2} (\dot{m}/A)^2 / \rho^2 = \text{constant} \quad (\text{Eq. 2-32})$$

defines a curve in the $h - \rho$ plane when (\dot{m}/A) is specified. Thermodynamic relationships may be used to transform this curve into a curve in a plane whose coordinates are given by any pair of thermodynamic properties (provided that restrictions such as chemical equilibrium or chemically frozen flow are employed to reduce the total number of thermodynamic variables to two). When transformed to the $h-s$ plane, Eq. 2-32 is useful for studying constant-area, adiabatic flow with friction (and with no external work). The curve in the $h-s$ plane represented by Eq. 2-32 is called the Fanno line. In a similar manner, the relationship between thermodynamic properties defined by the equation :

$$p + (\dot{m}/A)^2 / \rho = \text{constant} , \quad (\text{Eq. 2-33})$$

when (\dot{m}/A) is specified, is termed the Rayleigh line and is useful for studying con-

stant-area, frictionless flows with heat addition. By comparing Eqs. 2-32 and 2-33 with Eqs. 2-26 and 2-27, it can be seen that conditions on the upstream and downstream sides of a normal shock wave are represented by the intersection of the Rayleigh line with the Fanno line. This is illustrated schematically in Fig. 2-4.

Of course, the discontinuity represented by the normal shock wave cannot be of exactly zero thickness. The viscous terms in the momentum equation become large as dv/dx increases and approach infinity as $dv/dx \rightarrow \infty$. The interior structure of a shock wave can be calculated from the full equations of fluid dynamics describing steady-state, constant-area, one-dimensional flows in which all properties become uniform at $x = \pm \infty$. The solutions to these equations show that shock wave thicknesses are of the order of a few molecular mean free paths, a result which has been borne out experimentally. Therefore shock thicknesses are indeed negligible compared with characteristic dimensions of practical nozzles. However, the flow in real nozzles is not exactly quasi-one-dimensional and inviscid outside of the shock wave, and therefore a somewhat more gradual increase in pressure is observed experimentally in a real nozzle instead of the sharp increase illustrated in Fig. 2-3.

Equation 2-28 shows that if the Mach number on one side of a normal shock wave is subsonic, then the Mach number on the other side is supersonic, and vice versa. Solutions to the full equations of fluid dynamics for the structure of a shock wave show that the Mach number upstream is always supersonic and the Mach number downstream is always subsonic (as implied by the notation on Fig. 2-4). Thermodynamical arguments alone imply that this must be so, since Eqs. 2-25 - 2-27 can be employed to show that were it not so then the entropy upstream would exceed the entropy downstream, a condition which the adept thermodynamicist could readily exploit to construct a machine that would violate the second law of thermodynamics. Supersonic upstream conditions and subsonic downstream conditions are consistent with the requirements of the nozzle flow problem (Fig. 2-3).

Shock waves are so thin that the equations of fluid dynamics are of questionable validity in the interior of a shock wave. Analyses of shock structure based on the kinetic theory of gases have been completed. They indicate that fluid dynamics provide an accurate description of shock structure only for weak shocks (shocks involving a small pressure jump). However, the results that we have just cited concerning the order of magnitude of the shock thickness and the entropy and Mach number changes across the shock are supported by the kinetic theory studies.

Returning now to Fig. 2-3, we remark that when the exit pressure is assigned a value slightly below the first critical pressure, then the isentropic flow equations and shock wave equations yield a unique solution for the location of the normal shock and for the property profiles. For exit pressures near the first critical pressure, the normal shock is weak and is located near the throat. As the exit pressure is decreased more, the shock becomes stronger and moves farther downstream (curves E and F of Fig. 2-3). Eventually, at a second critical exit pressure, the normal shock sits right at the exit of the nozzle. Thus, introducing normal shocks enables us to construct flow fields for all exit pressures except those lying between the second and third critical pressures and below the third critical pressure. Non-one-dimensional phenomena must be considered in discussing nozzle flows in the two remaining regimes of exit pressure.

1.4.4. Non-one-dimensional Flows in Nozzles - Knowledge of oblique shock waves and of Prandtl-Meyer expansion fans is needed for understanding exit flows in the

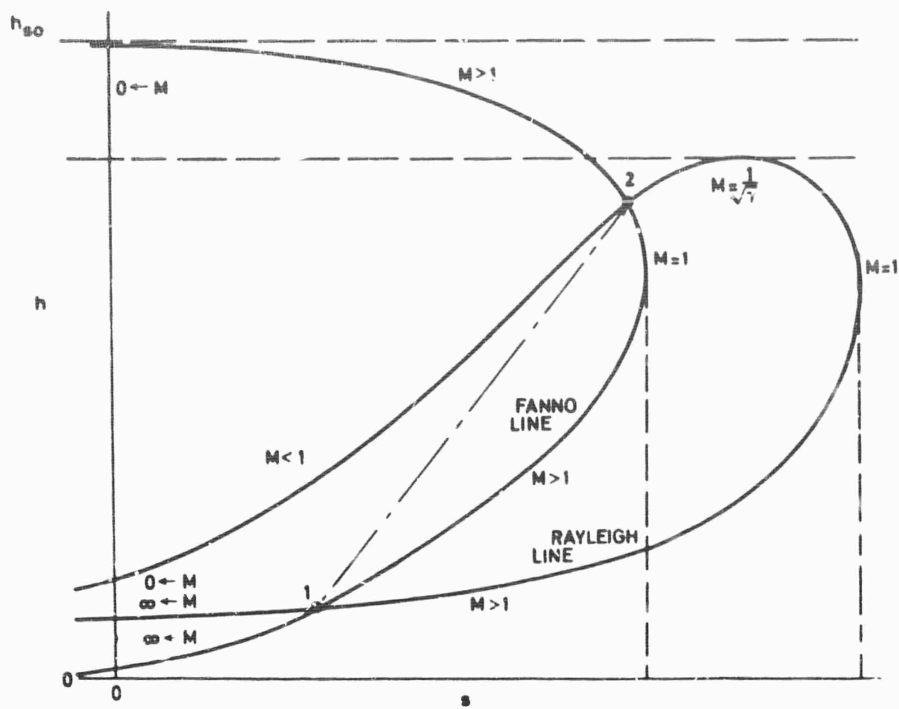


Fig. 2-4 Schematic diagram of Fanno and Rayleigh lines, showing normal shock wave as intersections.

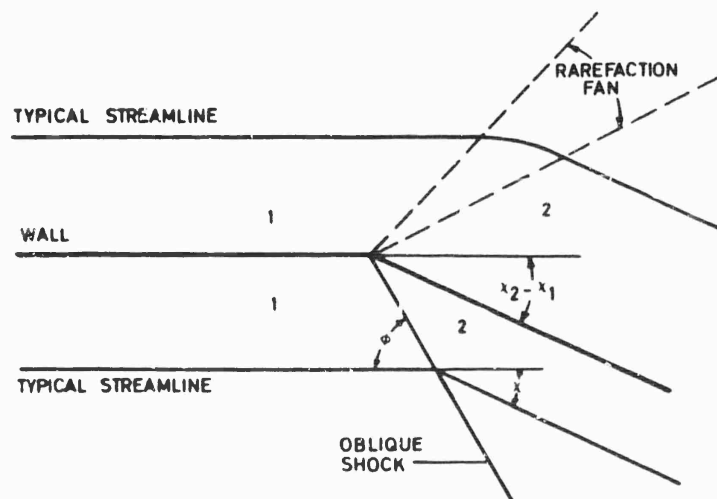


Fig. 2-5 Schematic diagram of oblique shock wave and of Prandtl-Meyer expansion fan.

two remaining regimes of exit pressure.

A shock wave may sit at any angle φ relative to the velocity vector of a uniform stream (see lower part of Fig. 2-5). Across any such 'oblique' shock wave, the equation for mass conservation and the equation for conservation of the component of momentum normal to the shock wave imply that Eqs. 2-25 and 2-26 remain valid provided that each velocity appearing therein is replaced by the corresponding normal component of velocity. On the other hand, stagnation enthalpy conservation applies along a streamline, and therefore the magnitude of the velocity appears in Eq. 2-27. In addition to these equations, momentum tangential to the shock wave must also be conserved; this condition implies that the tangential component of velocity is continuous across the shock wave. The normal component of velocity on the downstream side of the wave is less than that on the upstream side and therefore the flow turns toward the oblique shock in passing through the wave. Formulas analogous to Eqs. 2-28 - 2-31, can be derived; in particular, one finds that :

$$M_2^2 = \frac{2 + (\gamma - 1) M_1^2}{2\gamma M_1^2 \sin^2 \varphi - (\gamma - 1)} + \frac{2M_1^2 \cos^2 \varphi}{2 + (\gamma - 1) M_1^2 \sin^2 \varphi}, \quad (\text{Eq. 2-34})$$

$$p_2/p_1 = [2\gamma M_1^2 \sin^2 \varphi - (\gamma - 1)] / (\gamma + 1), \quad (\text{Eq. 2-35})$$

and :

$$\cot \chi = \tan \varphi \left[\frac{(\gamma + 1) M_1^2}{2(M_1^2 \sin^2 \varphi - 1)} - 1 \right], \quad (\text{Eq. 2-36})$$

where φ is the shock angle and χ is the deflection angle of the flow. The velocity upstream from an oblique shock is always supersonic, while the velocity downstream may be either subsonic or supersonic, depending on the values of M_1 and φ . Velocities downstream from oblique shocks are often supersonic. The downstream pressure always exceeds the upstream pressure, and the entropy of the fluid increases in passing through the wave.

Expansions through which the pressure decreases occur continuously instead of at discontinuities in steady non-one-dimensional flows. These rarefactions can be isentropic. A particular example of a steady, two-dimensional, isentropic rarefaction is the Prandtl-Meyer expansion of a supersonic flow about a sharp corner, illustrated in the upper part of Fig. 2-5. For a one-component ideal gas with constant heat capacities, the Prandtl-Meyer expansion is described by the equation :

$$\chi = \sqrt{\frac{\gamma+1}{\gamma-1}} \tan^{-1} \left[\sqrt{\frac{\gamma-1}{\gamma+1}} (M^2 - 1) \right] - \tan^{-1} \sqrt{M^2 - 1} + \text{constant}, \quad (\text{Eq. 2-37})$$

where χ is the local flow deflection angle and M is the local Mach number. Other flow variables are related to M by the isentropic conditions (Eqs. 2-17 - 2-20). Given M_1 , one can use Eq. 2-37 to calculate M_2 for a given deflection angle ($\chi_2 - \chi_1$), and then the isentropic equations can be used to calculate the other flow variables at station 2. (Tables are available to facilitate the use of Eq. 2-37 and also of Eqs. 2-34 - 2-36.) The value of M must exceed unity everywhere in the Prandtl-Meyer expansion, and M and v always increase while p , T and ρ decrease as χ increases. There is a maximum turning angle χ (the value of which depends on γ) at which p goes to zero, M goes to infinity, and Mach lines become parallel to streamlines.

For exit pressures lying between the second and third critical values, the flow at the exit must be compressed to a pressure greater than the design pressure but less than the pressure behind a normal shock wave. Equation 2-35 implies that this can be accomplished non-one-dimensionally by means of an oblique shock wave with an angle $\varphi < 90^\circ$ determined by the value of the exit pressure. After calculating φ from Eq. 2-35, one can compute the flow deflection angle from Eq. 2-36. The resulting exit flow pattern, which can be mapped out by considering equations governing oblique shock waves, two-dimensional, isentropic expansions and compressions and their interactions, is illustrated in Fig. 2-6a.

For exit pressures lying below the third critical value, the flow at the exit can expand non-one-dimensionally through an isentropic rarefaction fan until it reaches the prescribed exit pressure. (Thus, whenever the exit pressure is below its second critical value, the pressure at the exit plane in the nozzle equals the design exit pressure.) In an ideal-gas, two-dimensional flow approximation, the Mach number after the external expansion can be calculated from Eq. 2-18 (with p equal to the exit pressure), and then the deflection angle is given by Eq. 2-37. The complete exit flow pattern is illustrated in Fig. 2-6b. A photograph of the beautiful pattern is shown in Fig. 2-7; the compressions heat the flow and cause it to become luminous. Thus, solutions for the flow through a deLaval nozzle (Fig. 2-3) have been obtained for all values of the exit pressure.

More detailed descriptions and more accurate calculation procedures for idealized non-one-dimensional flows in supersonic nozzles can be based on the theory of characteristics of axially symmetrical flows [see, for example, Chapter 17 of Ref. (4)]. Some results derived from this view will be discussed later (Section 5.1). However, the greatest drawback to the preceding discussion is that non-ideal phenomena, such as flow separation in overexpanded nozzles, are not considered. These real effects, which modify some of our statements concerning the qualitative nature of the flow, also will be covered in Section 5.

1.4.5. Nozzle Flow Formulas - Since the upstream flow profiles in a nozzle are independent of the exit pressure so long as the Mach number at the throat is unity, it is convenient to calculate the mass flow rate through a nozzle with sonic throat conditions by using the throat area. For a one-component ideal gas with constant heat capacities, the appropriate expression for the mass flow rate can be obtained by setting $M = 1$ and $A = A_t$ in Eq. 2-21 and then solving for \dot{m} . The result is :

$$\dot{m} = A_t p_{s0} \sqrt{\gamma/RT_{s0}} [(2/(\gamma + 1))^{(\gamma + 1)/(2(\gamma - 1))}] \quad (\text{Eq. 2-38})$$

Equation 2-38 gives the mass flow rate in terms of the throat area and stagnation conditions. If the fluid is not an ideal gas, then Eqs. 2-8, 2-10 and 2-12 must be employed in obtaining the mass flow rate from the throat area and stagnation conditions.

A general formula for the exhaust velocity of a nozzle in terms of the stagnation enthalpy and the enthalpy at the exit of the nozzle follows from Eq. 2-10. It is :

$$v_e = \sqrt{2(h_{s0} - h_e)} \quad (\text{Eq. 2-39})$$

If the nozzle flow is isentropic, then the value of h_e appearing in Eq. 2-39 can be related to the pressure at the exit station of the nozzle and to stagnation conditions through Eqs. 2-8, 2-10 and 2-12. It is desirable to express v_e in terms of exit pressure because this is one of the experimentally adjustable parameters. For

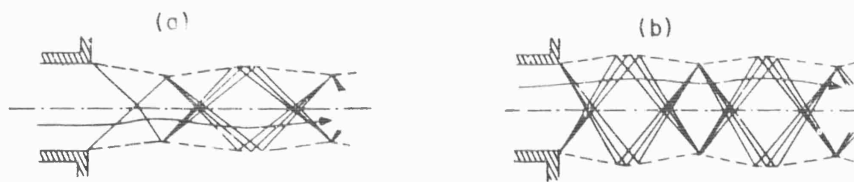


Fig. 2-6 Schematic diagram of exit flow when the value of the exit pressure lies between the second and third critical pressures overexpanded, diagram (a) and when the value of the exit pressure lies below the third critical (design) exit pressure underexpanded, diagram (b). Single lines are oblique shocks, multiple lines are expansion or compression fans, dashed lines are jet boundaries and arrows are flow streamlines.

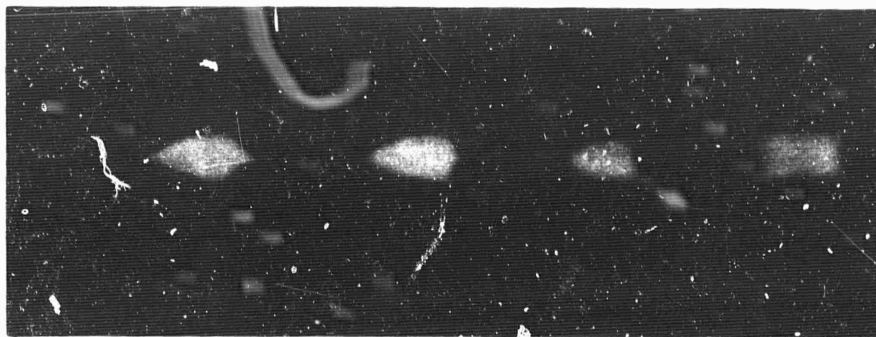


Fig. 2-7 Photograph of an underexpanded jet; the succession of wedge-shaped expansions and contractions is clearly shown.

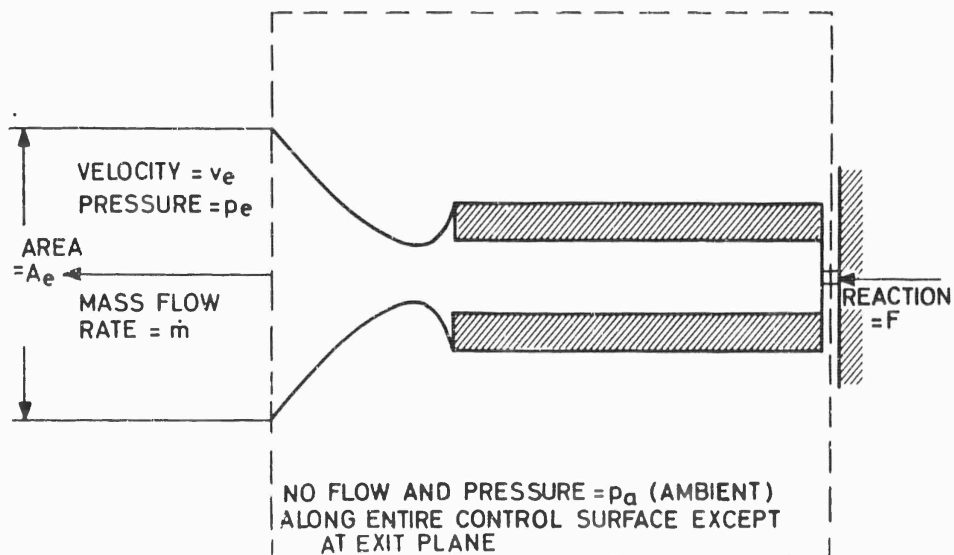


Fig. 2-8 Schematic diagram of measurement of thrust of a solid-propellant rocket on a test stand.

isentropic flow of a one-component ideal gas with constant heat capacities, we find from Eq. 2-39 [using $h = RT\gamma/(\gamma - 1)$ and $p/T\gamma/(\gamma - 1) = \text{constant}$] :

$$v_e = \left\{ \frac{2\gamma}{\gamma - 1} RT_{s0} \left[1 - \left(\frac{p_e}{p_{s0}} \right)^{(\gamma - 1)/\gamma} \right] \right\}^{1/2}, \quad (\text{Eq. 2-40})$$

which is useful for calculating the exit velocity at design conditions.

The exit to throat area ratio at design conditions for isentropic flow of a one-component ideal gas with constant heat capacities can be shown from Eqs. 2-18 and 2-21 to be expressible as :

$$\frac{A_e}{A_t} = \sqrt{\frac{\gamma - 1}{2}} \left(\frac{2}{\gamma + 1} \right)^{(\gamma + 1)/[2(\gamma - 1)]} \left(\frac{p_e}{p_{s0}} \right)^{-1/\gamma} \left[1 - \left(\frac{p_e}{p_{s0}} \right)^{(\gamma - 1)/\gamma} \right]^{-1/2} \quad (\text{Eq. 2-41})$$

For convenient use, functions appearing in this section are plotted versus p_{s0}/p_e for various values of γ in textbooks, e.g., pp. 60-69 of Ref. (9).

1.5. Thrust and Rocket Performance Parameters

1.5.1. Derivation of Thrust Formula - The thrust of a solid-propellant rocket is the total force exerted on the motor case by the propellant gases. Static thrust can be measured by firing the rocket on a test stand equipped with instrumentation for recording the reaction force required to keep the rocket stationary, as shown schematically in Fig. 2-8. Thrust can be calculated from flow variables by integrating pressure and shear forces over the interior of the motor case. However, a simpler method for calculating the static thrust is to employ a force balance for the control volume illustrated in Fig. 2-8.

According to Newton's law, the axial component of the force acting on the control volume must equal the time rate of change of the axial component of momentum. The force is composed of pressure forces and the reaction force, while the momentum change is associated only with the flow of propellant gases across the exit plane (since the velocity of the motor, solid propellant and other equipment is identically zero and the flow inside the rocket motor is assumed to be steady). Hence,

$$F + p_a A_e = \dot{m} v_e + p_e A_e, \quad (\text{Eq. 2-42})$$

where F is the axial thrust, \dot{m} is the total mass flow rate across the exit plane, v_e is the axial component of the velocity at the exit plane averaged over the exit area, p_e is the pressure just inside the exit plane, also averaged over the exit area, p_a is the ambient pressure, and A_e is the exit area of the nozzle. The area A_e appears on the left-hand side of Eq. 2-42 because pressure forces over the rest of the area of the control volume cancel.

Although it was derived for static systems, clearly Eq. 2-42 can be used also under dynamical conditions. For example if at some instant of time the system is at rest but the thrust bearing support in Fig. 2-8 is removed, then at that instant F equals the time rate of change of momentum of the rocket system (everything contained in the control volume of Fig. 2-8), which again is what we would call the thrust of the rocket motor. Alternatively, if the rocket is in steady flight at a constant altitude, then the acceleration is zero and F equals the sum of the aerodynamic drag forces on the rocket vehicle (including those arising from the interaction of the external exhaust jet with the external flow field). In accelerating flight at nonzero velocity, F is the sum of the axial drag forces and the time rate of change of axial momentum

of the vehicle. In all cases, F is obviously to be interpreted as the axial thrust of the rocket motor.

1.5.2. Theoretical Thrust Formula; Maximum Thrust - By assuming that the nozzle flow is isentropic and quasi-one-dimensional, that properties are uniform across the exit plane and that the exit velocity vector lies in the axial direction, we can write down a formula for the thrust F in terms of motor and flow conditions, provided that the working fluid is a one-component ideal gas with constant heat capacities. Thus, by substituting Eqs. 2-38 and 2-40 into Eq. 2-42, we obtain :

$$F = p_{s0} A_t \left\{ \left(\frac{2\gamma^2}{\gamma-1} \right)^{\frac{1}{2}} \left(\frac{2}{\gamma+1} \right)^{\frac{\gamma+1}{2(\gamma-1)}} \left[1 - \left(\frac{p_e}{p_{s0}} \right)^{\frac{\gamma-1}{\gamma}} \right]^{\frac{1}{2}} + \frac{A_e}{A_t} \left(\frac{p_e}{p_{s0}} - \frac{p_a}{p_{s0}} \right) \right\} \quad (\text{Eq. 2-43})$$

If the ratio of chamber area to throat area is sufficiently large, then chamber conditions are approximately equal to the stagnation conditions at the throat, and p_{s0} can be replaced by the chamber pressure p_c in Eq. 2-43.

At the design exit pressure, $p_e = p_a$; only the first term in Eq. 2-43 contributes to F . The second term in Eq. 2-43 produces a positive contribution to F for over-expanded nozzles and a negative contribution for underexpanded nozzles.

Equation 2-41 may be substituted for the ratio A_e/A_t in Eq. 2-43. The result is :

$$f = [1 - x^{(\gamma-1)/\gamma}]^{\frac{1}{2}} \{ 1 + [\gamma-1]/2\gamma \} x^{-1/\gamma} [1 - x^{(\gamma-1)/\gamma}]^{-1} (x-a) \quad , \quad (\text{Eq. 2-44})$$

where $f \equiv (F/p_{s0} A_t) \{ (\gamma-1)/2\gamma^2 \}^{\frac{1}{2}} \{ (\gamma+1)/2 \} (\gamma+1)/[2(\gamma-1)]$, $x \equiv p_e/p_{s0}$ and $a \equiv p_a/p_{s0}$. Differentiating Eq. 2-44 twice with respect to x shows that $df/dx = 0$ and $d^2f/dx^2 < 0$ at $x = a$. This indicates that, for given stagnation conditions and a given throat area (implying also a given \dot{m} , see Eq. 2-38), the thrust is maximum when the value of the exit area is such that $p_e = p_a$, i.e., at design conditions. The same result applies for isentropic flow with an arbitrary working fluid, since differentiating Eq. 2-42 and employing Eqs. 2-8 and 2-9 shows that $dF = \dot{m} dv_e + A_e dp_e + (p_e - p_a) dA_e = (p_e - p_a) dA_e \rightarrow 0$ at $p_e = p_a$ and that $d^2F = (p_e - p_a) d^2A_e + dp_e dA_e \rightarrow dp_e dA_e = -(\dot{m}/v_e)(dv_e)^2/(M_e^2 - 1) < 0$ at $p_e = p_a$.

1.5.3. Thrust Coefficient - The thrust coefficient is a dimensionless measure of the thrust of a rocket motor. It is defined as :

$$C_F \equiv F/p_c A_t \quad , \quad (\text{Eq. 2-45})$$

where F is thrust, A_t is throat area, and p_c is chamber pressure. A test-stand measurement of F , combined with a pressure-gage measurement of p_c and a geometrical measurement of A_t yields a value of C_F directly from experiments.

Equation 2-43 implies that C_F depends largely on the nature of the expansion process that occurs in the nozzle. Subject to the restrictions imposed in obtaining Eq. 2-43 and also to the restriction that $p_{s0} = p_c$, Eq. 2-43 obviously provides an explicit formula for C_F which we need not reproduce here. For convenience of use, curves of C_F vs. A_e/A_t for various values of p_a/p_c , as obtained from Eq. 2-43 under the above restrictions, are given in textbooks, (9), (10). One such curve is given in Fig. 2-9a. It can be seen from these graphs or from the formulas that the thrust coefficient and the thrust achieve their largest values as p_e/p_c and p_a/p_c approach zero.

Clearly, the thrust coefficient achieves a maximum value under the same conditions that the thrust achieves a maximum value (design conditions). The maximum value

of the thrust coefficient is termed the optimum thrust coefficient and is denoted by C_F^o . If Eq. 2-43 is valid with $p_{s0} = p_c$, then C_F^o is given by the first term in the brackets in Eq. 2-43. The optimum thrust coefficient determined in this manner is plotted as a function of p_c/p_a for various values of γ in Fig. 2-9b, (9), (10).

Effects of losses and of nonideal behavior on C_F are considered later.

1.5.4. Characteristic Velocity - The characteristic velocity is related to the rate at which mass flows through the nozzle. It is defined as :

$$c^* \equiv p_c A_t / \dot{m} , \quad (\text{Eq. 2-46})$$

where p_c is chamber pressure, A_t is throat area and \dot{m} is mass flow rate. It can be seen from Eq. 2-46 that the units of c^* are always those of a velocity. As with C_F , c^* can be measured experimentally; in order to obtain c^* one must measure the mass of the propellant and the burning time in addition to p_c and A_t .

The value of c^* is independent of processes occurring downstream from the throat of the nozzle. Primarily, it is characteristic of conditions in the combustion chamber. If we assume that the stagnation pressure and temperature at the throat equal the chamber pressure and the chamber temperature, and that the flow from the chamber to the throat corresponds to an isentropic process in a one-component ideal gas with constant specific heats, then we may use Eq. 2-38 to obtain an explicit expression for c^* in terms of the chamber temperature. The result is :

$$c^* = \sqrt{RT_c/\gamma} [(\gamma+1)/2]^{(\gamma+1)/[2(\gamma-1)]} , \quad (\text{Eq. 2-47})$$

where T_c is the chamber temperature and where it should be remembered that the gas constant per unit mass, R , is inversely proportional to the molecular weight of the gas that flows from the chamber to the throat.

From Eq. 2-47, it can be seen that the value of c^* depends on the amount of heat released in the combustion chamber and on the molecular weight of the product gas. Large values of c^* are desirable (see discussion of specific impulse), and thus large heat release and low molecular weight are desirable. Typical values of c^* for solid-propellant rockets range from 4000 to 6000 ft/sec.

In the design of solid-propellant rockets, often the reciprocal of c^* is used instead of c^* . The reciprocal is termed the mass flow factor. It is given either in units of a reciprocal velocity or, through multiplication by a gravitational-constant conversion factor, in units of reciprocal seconds. We shall use c^* instead of the mass flow factor.

1.5.5. Specific Impulse - The performance parameter that is used most of all is the specific impulse. It is defined as the ratio of the thrust to the mass flow rate,

$$I_{sp} \equiv F/\dot{m} . \quad (\text{Eq. 2-48})$$

However, a gravitational conversion factor is always included in the definition (the mass flow rate is expressed as weight per second), so that the units of I_{sp} are seconds. We consistently omit all conversion factors from our formulas, it being understood that conventional units are used. Obviously, I_{sp} can be measured on a test stand.

The terminology 'specific impulse' can be justified as follows. The total impulse delivered by the rocket motor is :

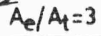
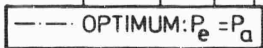


Fig. 2-9(b) The optimum thrust coefficient as a function of the chamber to ambient pressure ratio for various values of the ratio of specific heats.

$$I = \int_0^t F dt,$$

where t_b is the burning time. If F is constant over the burning time, then $I = Ft_b$. If the mass flow rate of propellant is constant over the burning time, then the total mass of propellant consumed is $m = \dot{m}t_b$. Therefore the ratio of the impulse to the mass of propellant is $I/m = F/\dot{m} = I_{sp}$. Thus, with constant thrust and constant mass flow rate, the specific impulse is the impulse per unit mass. By our definition (Eq. 2-48), I_{sp} is an instantaneous quantity that can differ from I/m for nonzero burning times if F and/or \dot{m} vary during a firing. Particularly for solid propellant rockets, it is I/m rather than I_{sp} that is generally measured on a test stand. Nevertheless, we prefer to define I_{sp} as an instantaneous quantity because it then has greater relevance to nozzle flow and also to vehicle performance [e.g., the I_{sp} that appears in generalizations of Eq. 1-3 of Chapter 1 is a weighted time average of the present I_{sp} and differs in general from I/m], and because fewer details of motor design need to be specified in discussing the value that I_{sp} assumes at one instant of time. Since a solid-propellant rocket carries all of its propellant in the chamber, the impulse itself, as well as the specific impulse, is of importance in chamber design.

It should be clear from this discussion that large values of the specific impulse are desirable. Since the purpose of a rocket motor is to deliver an impulse (in order to increase altitude of a vehicle, accelerate a missile, change orbit of a spacecraft, etc.), the maximum value of I is desired. However, if a large propellant mass m is required to produce this I , then much of the impulse is wasted in accelerating the propellants. The efficiency with which a rocket motor can deliver an impulse to a vehicle (or 'payload') is therefore I/m . Detailed mission calculations usually show that for optimum performance of the mission, this ratio, which equals the average I_{sp} , should be a maximum (see Chapter 1).

A formula can be written for I_{sp} which is valid if the nozzle flow is isentropic and quasi-one-dimensional, if properties are uniform across the exit plane, if the exit velocity vector is parallel to the axis of the motor, if the working fluid is a one-component ideal gas with constant heat capacities and if chamber conditions are the same as stagnation conditions in the nozzle. The formula is the ratio of Eq. 2-43 to Eq. 2-38. Of greatest interest is the form taken by this formula at design conditions,

$$I_{sp}^o = \left\{ \frac{2\gamma}{\gamma-1} \frac{R^o}{m} T_c \left[1 - \left(\frac{p_e}{p_c} \right)^{(\gamma-1)/\gamma} \right] \right\}^{1/2}, \quad (\text{Eq. 2-49})$$

where the dependence of R on the molecular weight has been exhibited explicitly ($R = R^o/m$, $R^o =$ universal gas constant).

Equation 2-49 implies that I_{sp}^o increases as p_e/p_c decreases, at first rapidly but then more slowly, approaching a finite maximum value as $p_e/p_c \rightarrow 0$. It is seen that this maximum value of I_{sp}^o is independent of nozzle design in that it depends only on properties of the propellant gases. Its dependence on T_c and m can be seen to be the same as that of c^* . (Compare Eq. 2-47.) This limiting value, the ideal specific impulse for design expansion to zero pressure, is often quoted as a figure of merit of propellant combinations. It is seen from Eq. 2-49 that this limiting value is proportional to $\sqrt{\gamma/(\gamma-1)}$, proportional to $\sqrt{T_c}$ and proportional to $1/\sqrt{m}$. Although the first of these proportionalities implies that a low value of γ is desirable and that in fact the limiting value of $I_{sp}^o \rightarrow \infty$ as $\gamma \rightarrow 1$, nevertheless in the actual I_{sp}^o this tendency is counteracted and often reversed at reasonable

pressure ratios by the pressure-dependent factor in Eq. 2-49. The value of γ for most propellant gases lies between 1.2 and 1.3 so that changes in γ do not have a very large influence on I_{sp}^0 . Propellants are chosen to produce a high chamber temperature T_c (a high heat release) and a low molecular weight m of reaction products in order to obtain the highest specific impulse. (Increasing the chamber pressure p_c reduces dissociation thereby increasing T_c and m , but usually the effect on T_c is greater so that T_c/m increases and I_{sp}^0 is improved to a somewhat greater extent than the explicit dependence in Eq. 2-49 would indicate.) For solid propellant rockets, specific impulses (theoretical and measured) generally lie between 170 and 320 sec.

Effects of nonideality on I_{sp} will be considered later.

A performance parameter that is entirely equivalent to the specific impulse is the effective exhaust velocity, which is defined in the same way as the specific impulse but without the gravitational conversion constant, so that its units are those of a velocity. Since Eq. 2-42 shows that $F/\dot{m} = v_e$ when $p_e = p_a$, it follows that the effective exhaust velocity equals the actual exhaust velocity at design conditions. Hence, the entire preceding discussion about I_{sp}^0 is really a discussion of the exhaust velocity v_e . Furthermore, if chamber conditions are known then isentropic flow tables may be used to obtain ideal values of v_e and therefore of I_{sp}^0 . The importance of Eqs. 2-39 and 2-40 follows principally from their close connection with the specific impulse.

Occasionally the reciprocal of the specific impulse, which is termed the specific fuel consumption, will be mentioned in rocket design. Another parameter that is sometimes considered is the volumetric specific impulse, which is defined as the product of the specific impulse and the propellant density. One reason for the importance of this parameter in solid-propellant rocket design is that the propellant is carried inside the chamber, so that a lower propellant density (or a lower volumetric specific impulse) would necessitate a larger high-pressure chamber and therefore a heavier motor case. Increasing volumetric specific impulse can significantly decrease the chamber weight penalty.

1.5.6. Other Performance and Design Parameters - Many other parameters are used in design and performance calculations for solid-propellant rocket vehicles. For example, mass fractions involving the ratio of the propellant mass to the total vehicle mass, will appear. The L^* of a motor is often discussed; this is the ratio of the chamber volume to the throat area and is a measure of the residence time of the propellant gases in the chamber. The ratio of port area to throat area for cylindrical grains often arises. All of these additional parameters will be introduced later as they are needed.

2. Effects of Multicomponent, Reacting Gas Flow

2.1. Introduction

We now begin to discuss various ways in which real solid-propellant rocket systems deviate from the ideal behavior analyzed above. Effects of the fact that the propellant gases contain more than one chemical species and can react chemically are considered here. Other effects are treated in subsequent sections.

2.2. Frozen or Equilibrium Isentropic Flow

A general result of thermodynamics for an N-component, homogeneous system (2), (5) is :

$$Tds = dh - dp/\rho - \sum_{i=1}^N \mu_i dn_i \quad (\text{Eq. 2-50})$$

where n_i represents the number of moles of species i per unit mass of the mixture, μ_i denotes the chemical potential of species i , and all other symbols have been defined previously. This implies that the derivation of Eq. 2-12 is valid only if :

$$\sum_{i=1}^N \mu_i dn_i = 0 \quad . \quad (\text{Eq. 2-51})$$

There are two ways in which Eq. 2-51 can be satisfied. If the composition of the system is fixed, then $dn_i = 0$ for all species i ; under these conditions the flow is said to be chemically frozen. On the other hand, the general requirement for

chemical equilibrium in a multicomponent mixture (2), (5) is $\sum_{i=1}^N \mu_i dn_i = 0$,

which implies that Eq. 2-51 is also satisfied for flows in chemical equilibrium. If chemical processes occur at finite, nonzero rates in the flow, then Eq. 2-51 is not satisfied and Eq. 2-12 is invalid. In this section we consider the two limiting cases of frozen and equilibrium flow.

Our ultimate objective is to develop methods for calculating the exhaust velocity v_e , since this is directly related to the specific impulse. However, the velocity and temperature at the nozzle throat are also of interest. The maximum wall heat transfer rates generally occur at the throat, and therefore throat conditions influence the proper design of the throat and the selection of throat wall materials. We have also seen that throat conditions determine the mass flow rate, which is an additional design parameter that must be computed.

We restrict our attention to multicomponent, reacting mixtures of ideal gases. At the high temperatures representative of rocket exhausts, it is a very accurate approximation to assume that all gases behave ideally. (However, especially for metalized solid propellants, some liquid or solid reaction products are often present; these require special consideration, see Section 3).

For ideal gas mixtures, the entropy per unit mass can be shown to be given (2), (5), (9) by:

$$s = n \left\{ \sum_{i=1}^N X_i (S_i^\circ - R^\circ \ln X_i) - R^\circ \ln p \right\} , \quad (\text{Eq. 2-52})$$

where $n \equiv \sum_{i=1}^N n_i$ equals the reciprocal of the average molecular weight of the mixture, X_i is the mole fraction of species i , S_i° is the molar entropy of pure species i at the standard pressure of 1 atm (and is therefore a function of temperature alone, see Eq. 2-15), R° is the universal gas constant, and the units of the pressure p must be atmospheres. The term involving $\ln X_i$ in Eq. 2-52 is the so-called entropy of mixing. The enthalpy of an ideal gas mixture (2), (5), (9) is simply:

$$h = n \sum_{i=1}^N X_i H_i , \quad (\text{Eq. 2-53})$$

where H_i is the molar enthalpy of pure species i and therefore depends only on T . Each molar enthalpy appearing in Eq. 2-53 must include the enthalpy of formation

of the species. The equation of state of an ideal gas mixture can be written as:

$$\rho = p/nR^\circ T. \quad (\text{Eq. 2-54})$$

2.2.1. Frozen Flow - Let us consider first the case of frozen composition. For frozen flow, n and X_i take on known constant values corresponding to chamber conditions. When the thermodynamic properties of the species are known, S_i° and H_i are known functions of the temperature, and therefore the only unknowns appearing in Eqs. 2-52, 2-54 are T and p . These three equations may therefore be substituted into Eqs. 2-8, 2-10 and 2-12, yielding three equations in three unknowns, provided that chamber conditions and \dot{m} are known. In rocket nozzle flow calculations, generally \dot{m} is not known in advance; instead, the throat area A_t is specified. To relate \dot{m} to A_t and chamber conditions, we may proceed as follows.

Since we have shown that $M = 1$ at the throat (see Eq. 2-22), it follows that $v_t = [(\partial p / \partial \rho)_s]_t^{1/2}$. The partial derivative appearing here can be evaluated by observing that under the present conditions, Eqs. 2-50 and 2-53 imply that:

$$dp/\rho = dh = n \sum_{i=1}^N X_i C_{pi} dT,$$

where $C_{pi} \equiv dH_i/dT$ is the molar heat capacity of species i at temperature T , while Eq. 2-54 implies that:

$$dT/T = dp/p - d\rho/\rho.$$

Eliminating dT from these two formulas and employing Eq. 2-54 yields:

$$(\partial p / \partial \rho)_s = n R^\circ T \sum_{i=1}^N X_i C_{pi} / \left(\sum_{i=1}^N X_i C_{pi} - R^\circ \right),$$

and therefore the velocity at the throat is:

$$v_t = \left\{ n R^\circ T_t \sum_{i=1}^N X_i C_{pi}(T_t) / \left[\sum_{i=1}^N X_i C_{pi}(T_t) - R^\circ \right] \right\}^{1/2} \quad (\text{Eq. 2-55})$$

The unknown constant \dot{m} is then expressed in terms of the temperature and pressure at the throat, according to the formula:

$$\dot{m} = (p_t A_t / n R^\circ T_t) v_t, \quad (\text{Eq. 2-56})$$

where use has been made of Eqs. 2-8 and 2-54 and v_t is given by Eq. 2-55.

Equation 2-56 relates \dot{m} to A_t and throat conditions. In order to relate throat conditions explicitly to chamber conditions, we may note that Eqs. 2-12 and 2-52 imply:

$$\sum_{i=1}^N X_i [S_i^\circ(T_c) - S_i^\circ(T)] = R_0 \ln(p_c/p) \quad (\text{Eq. 2-57})$$

and that Eqs. 2-10 and 2-53 imply :

$$v = \left\{ 2n \sum_{i=1}^N X_i [H_i(T_c) - H_i(T)] + v_c^2 \right\}^{1/2} \quad (\text{Eq. 2-58})$$

It should be recognized here that heat capacity data alone are sufficient for evaluating the entropy and enthalpy functions appearing in Eqs. 2-57 and 2-58, since

$$S_i^\circ(T_c) - S_i^\circ(T) = \int_T^{T_c} (C_{pi}/T) dT \text{ and } H_i(T_c) - H_i(T) = \int_T^{T_c} C_{pi} dT. \text{ Evaluating}$$

Eq. 2-58 at the throat and equating the result to Eq. 2-55 produces an equation in which the only unknown is T_t . The first step in calculating the frozen nozzle flow is to obtain T_t (by trial and error) from this equation. Then v_t may be computed from Eq. 2-55, p_t may be computed from Eq. 2-57, and \dot{m} may be computed from Eq. 2-56.

After \dot{m} has been computed, conditions at other points in the nozzle are most easily calculated by assuming a value for the local temperature, calculating p from Eq. 2-57, v from Eq. 2-58 and A from the formula $A = \dot{m} R^\circ T / v p$, implied by Eqs. 2-8 and 2-54. In particular, the exit velocity v_e may be obtained for various exit pressures p_e in this manner. Thus, after calculating the throat temperature by trial and error, all required nozzle flow parameters can be computed directly from straightforward algebraic formulas for chemically frozen nozzle flow.

If thermodynamic data concerning the temperature dependence of C_{pi} are not available for the reaction products, then for frozen flow a constant average specific heat

$$\bar{c}_p = n \sum_{i=1}^N X_i \bar{C}_{pi} \quad \text{may be introduced, and all of the simplified (one-component,}$$

ideal-gas, constant-property) formulas for the preceding section become valid. Indeed, the restriction to constant composition renders the ideal gas mixture equivalent to a one-component ideal gas, and effectively the only innovation that we have introduced here is to permit the specific heat at constant pressure to be a function of temperature. Additional complications arise for systems that maintain equilibrium composition.

2.2.2. Equilibrium Flow - When chemical equilibrium is maintained in the mixture, then it can be shown from Eq. 2-51 that some number M of independent chemical equilibrium equations must be satisfied. For ideal gas mixtures, these equations (2), (5), (9) take the form :

$$\prod_{i=1}^N X_i^{\nu'_{ik} - \nu_{ik}} = K_{pk} p^{-\sum_{i=1}^N (\nu'_{ik} - \nu_{ik})}, \quad k = 1, \dots, M, \quad (\text{Eq. 2-59})$$

where K_{pk} , which is the equilibrium constant for partial pressures for the k 'th reaction, is a function only of temperature. The exponents ν_{ik} and ν'_{ik} in Eq. 2-59

represent stoichiometric coefficients for species i appearing as a reactant and as a product, respectively, in the k 'th reaction, which can be written symbolically as :

$$\sum_{i=1}^N \nu_{ik} \mathcal{S}_i \rightleftharpoons \sum_{i=1}^N \nu'_{ik} \mathcal{S}_i, \quad k = 1, \dots, M. \quad (\text{Eq. 2-60})$$

In addition to Eq. 2-59, a certain number L of atom conservation equations must be satisfied; these are linear and can be written as :

$$n \sum_{i=1}^N \nu_i^k X_i = A_k, \quad k = 1, \dots, L \quad (\text{Eq. 2-61})$$

where ν_i^k are constants representing the number of atoms of type k in chemical species i and A_k are constants of integration determined by the chemical composition of the reaction products in the combustion chamber. Space does not permit us to derive and discuss the origin of these equations or to give specific illustrations of their meaning; the reader is referred to standard texts for this background material, (2), (5), (9), (11). It suffices to state that there are always exactly the correct number of independent relationships of the type given in Eqs. 2-59 and 2-61 to relate each of the mole fractions X_i to p and T . In general, Eqs. 2-59 and 2-61 are difficult to solve for X_i . Methods of solution are discussed in detail in Chapter 3 and also in Refs. (9) and (11); the calculations are usually done by iteration and employ electronic computers.

After Eqs. 2-59 and 2-61 are solved for X_i as functions of p and T , Eqs. 2-52 - 2-54 may be used to obtain s , h and ρ as functions of p and T . In the computation, it must be remembered that n is also a variable now; it is given by :

$$n = \left(\sum_{i=1}^N X_i m_i \right)^{-1}, \quad (\text{Eq. 2-62})$$

where m_i denotes the molecular weight of species i . A solution procedure utilizing Eqs. 2-8, 2-10 and 2-12 in a manner analogous to that described in the preceding section can be established after the functions $X_i(p, T)$ and $n(p, T)$ are obtained (9). For the reason indicated below, equilibrium nozzle flow calculations are not as important for solid-propellant rockets as they are for liquid-propellant rockets.

2.2.3. Comparison of Performance with Equilibrium and Frozen Nozzle Flow - The temperature of the gases entering the nozzle is usually high enough to cause a certain amount of dissociation. If the gases remain dissociated in the nozzle flow (frozen composition), then no additional thermal energy is released in the expansion. However, if recombination can occur as the temperature drops in the expansion process (equilibrium composition), then additional thermal energy is released in the nozzle and is available for conversion into ordered kinetic energy. This effect generally outweighs the derogatory influence of recombination arising from the associated increase in the average molecular weight, so that the performance (e.g., I_{sp}°) is greater for equilibrium nozzle flow than for frozen nozzle flow.

For solid-propellant rockets, values computed for I_{sp}° with frozen and equilibrium nozzle flow usually differ little (i.e., not by more than a few sec.). For example, e* for a composite propellant employing ammonium perchlorate as an oxidizer and

containing metallic aluminum, the difference between the frozen and equilibrium I_{sp} lies between 3 and 4% for conditions under which $I_{sp} \approx 250$ sec. (12). (In contrast, high-performance liquid-propellant systems can exhibit differences exceeding 10%.) Most of the 3 to 4% difference can be traced to effects of the recombination of gaseous aluminum, aluminum oxides and oxygen to form solid or liquid Al_2O_3 and thus is related to the two-phase flow phenomena that will be considered in Section 3. Purely gas-phase recombination processes in solid-propellant rocket nozzles produce very little difference between the frozen and equilibrium I_{sp} , and therefore the difference is usually negligible for nonmetalized propellants. A consequence of this observation is that the choice of whether to assume frozen or equilibrium nozzle flow in motor design and performance calculations is often based on the availability of suitable computer calculation programs.

2.3. Relaxing Flows

In general, the nozzle flow is neither chemically frozen nor in chemical equilibrium. Under these intermediate conditions, the derivation of Eq. 2-12 is invalid, see Eq. 2-50, s is not constant, and rigorous calculation of nozzle flow variables entails solving at least one differential equation. Fortunately, these calculations generally are unnecessary for solid-propellant rockets because the equilibrium and frozen flow results lie so close together. However, we shall discuss the subject briefly because it has experienced a number of advances in recent years.

First, we remark that when thermal energy is released in the nozzle, e.g., by recombination, then throat conditions no longer correspond exactly to a Mach number of unity with the Mach number based on the frozen sound speed $a_f = [(\partial p / \partial \rho)_s]^{1/2}$, $x_i = 1, \dots, N$. Our previous analysis in fact implies that this "frozen Mach number" is not unity at the throat for equilibrium flow either. For equilibrium flow the derivation of Eq. 2-22 involves the equilibrium sound speed $a_e = [(\partial p / \partial \rho)_s]^{1/2}$, $x_i = x_{ie}(p, \rho)$, $i = 1, \dots, N$, implying that the Mach number based on a_e is unity at the throat, and it can be proven from thermodynamics that $a_e \leq a_f$ (5). If heat release occurs at a finite rate in the nozzle (e.g., due to finite recombination rates), then no simple Mach number criterion can be employed to define throat conditions. The Mach number based on a_f is found to pass through unity at a point determined by the relative rates of heat release and of area change. The geometrical nozzle throat position lies upstream from the plane at which the M based on a_f is unity. A qualitative picture of the effect of finite heat release rates in nozzle flow can be obtained by studying a one-component, constant-heat-capacity, ideal gas that is subjected to a specified rate of heat addition (4). For very high rates of heat addition (such as those which might occur in the nozzle of a motor whose chamber is too short for the combustion reactions to reach equilibrium) the condition $M_f = 1$ can be attained in a constant-area duct (thermal choking) or in a nozzle whose converging section is removed (a diverging reactor). The first of these flows (constant-area, diabatic flow) can be studied by utilizing the Rayleigh line (Fig. 2-4) and has been discussed in rocket texts, e.g., pp. 83-86 of Ref. (9). Thermal choking and diverging reactors can be produced experimentally with liquid-propellant rocket motors, but the effects of heat release in the nozzle are generally negligible for solid-propellant systems.

Even if conditions at the plane $M_f = 1$ are known, difficulties are encountered in attempting to calculate the flow of a relaxing gas in the supersonic portion of the nozzle. One might guess that a stepwise forward numerical integration of the governing differential equations would be straightforward even though laborious. However, mathematical difficulties make ordinary integration techniques inapplicable. The problem stems from the fact that as a reaction approaches chemical equilibrium its forward rate becomes equal to its backward rate. In integration procedures the difference between the forward and backward rates must be computed, and the accuracy of conventional electronic computers is too low to obtain a meaningful

number for the difference. Through a great deal of effort, this problem has been solved recently by linearization techniques. Therefore, numerical calculations of relaxing supersonic nozzle flows can now be performed. Pertinent literature is cited in Ref. (13) - (24).

For most purposes, the accurate numerical calculations are not needed. The earliest studies of relaxing flows aimed only at developing criteria for equilibrium or frozen flow. One or the other limiting flow calculations would then be selected, depending on which criterion was most nearly satisfied. The first studies were rather heuristic, while later ones were somewhat more rigorous (5) (25-36).

Later, it was noticed from numerical solutions of relaxing nozzle flow problems that often the upstream flow was nearly in equilibrium, there was a short region of transition from equilibrium to frozen flow in the nozzle, and the downstream flow was nearly frozen. This effect is produced by the density dependence of the rates of reactions. Its discovery engendered the "sudden freezing" approximation for relaxing nozzle flows, in which it is assumed that equilibrium conditions exist upstream from a transition plane and frozen conditions exist downstream from this plane. The location of the sudden freezing plane in the nozzle is estimated in terms of the forward and backward reaction rates (16), (19), (37). Although the sudden freezing approximation provides an improvement over the approximations of entirely equilibrium or entirely frozen flow, it does not permit any increase in entropy in the flow and therefore may be amenable to further improvement. However, even the refinement represented by sudden freezing is unnecessary in most solid-propellant rocket nozzle flow calculations.

3. Two-Phase Flow Effects

3.1. Introduction

Unlike relaxing flow effects, the influence of two-phase flow on solid-propellant rocket motor performance is often appreciable. Two-phase flow will occur in the nozzle if the products of combustion contain liquid or solid materials at nozzle conditions of temperature and pressure. Propellants whose constituents are composed only of molecules constructed from the elements C, H, O, N, F and Cl usually have purely gaseous combustion products, although fuel-rich solid propellants sometimes produce solid carbon. However, if appreciable amounts of Li, Be, B, Na, Mg, Al, Si, or K, etc., are contained in the propellant, then combustion products in condensed phases usually appear. The most common examples of solid propellants producing two-phase nozzle flow are metalized systems for which the solid or liquid metal oxide is an important product of combustion.

One of the principal reasons for adding metals to solid propellants is to improve their performance by increasing the total amount of chemical heat release. Much more energy per unit mass is liberated when typical metals combine with oxygen to form metal oxides than when the most energetic nonmetalized solid propellants burn. However, the heats of vaporization of the metal oxides are so high that increased energy release and improved performance are achievable only if the metal oxides in the exhaust gases exist predominantly in a condensed phase. Therefore, two-phase nozzle flow must occur with metalized solid propellant systems for the associated improvement in performance to be realized.

In the following section we present simplified theories of two-phase nozzle flow and then discuss the more complex theories. The effects of two-phase flow on nozzle design and the few available experimental results are considered subsequently.

3.2. Theories; Effects on Performance

3.2.1. Two-Phase Flow Without Particle Lag - As the first step toward gaining

an understanding of two-phase nozzle flow, let us treat a one-component ideal gas with constant heat capacities containing solid or liquid particles (also with constant heat capacities) that flow at the same velocity as the gas (no velocity lag), maintain the same temperature as the gas (no temperature lag), and do not exchange mass with the gas (no condensation or vaporization). Our objective is to generalize the quasi-one-dimensional, isentropic flow theory of Section 1.3.2 and to develop formulas for the performance parameters.

In neglecting condensation we are treating frozen flow, an approximation the validity of which depends on the chemical composition of the system. Lags in the temperature and velocity histories of the condensed phase behind the temperature and velocity histories of the gas are negligible provided that the condensed particles are small enough. However, we shall also neglect any contribution of the Brownian motion of the particles to the pressure of the system, thereby requiring that the particles be sufficiently large. Typically, condensed particle diameters lie in the .1 to 10-micron range, so that both of these conditions are reasonably well satisfied as a first approximation.

Overall mass, momentum and energy balances for the system are given by Eqs. 2-8, 2-9 and 2-10, where ρ must now denote the total mass per unit volume of the gas-particle mixture and h is the total enthalpy per unit mass of the mixture. Therefore, the results of Section 1 that do not depend on the use of an equation of state or on the specification of thermodynamic properties remain valid in the two-phase system. However, in Eq. 2-13 the gas density alone must appear instead of ρ .

We shall let the subscript g identify properties of the gas and the subscript s identify properties of the condensed phase and we shall denote the mass flow fraction of the condensed phase by ϵ , so that the mass flow fraction of the gas is $(1 - \epsilon)$. Since ϵ is a constant in the flow,

$$h = (1 - \epsilon) c_p T + \epsilon c_s T + \text{constant} \quad (\text{Eq. 2-63})$$

In writing the appropriate form of Eq. 2-13, it must be realized that in multiphase flow each component excludes the other components from the volume it occupies, and therefore there is a difference between the mass of a component per unit total volume of space and the mass of a component per unit volume of space available to the component. Here we assign the subscripts g and s to the latter definition of density, obtaining :

$$\epsilon / \rho_s + (1 - \epsilon) / \rho_g = 1 / \rho ,$$

with ρ_s representing simply the specific gravity of the condensed material. The equation of state for the gas, Eq. 2-13, then becomes :

$$p = \rho_g R_g T = \rho (1 - \epsilon) R_g T (1 - \epsilon \rho / \rho_s)^{-1} , \quad (\text{Eq. 2-64})$$

in which the last factor is the ratio of the total volume to the volume occupied by the gas. Since the value of ϵ seldom exceeds 0.3 in rocket nozzles and ρ_s / ρ_g is typically of the order of 10^3 , the last factor in Eq. 2-64 seldom differs from unity by more than 0.03% and therefore can be set equal to unity with excellent accuracy.

It will be noted from Eqs. 2-63 and 2-64, with the last factor omitted, that if we define an average specific heat at constant pressure and gas constant per unit mass for the mixture by :

$$\bar{c}_p \equiv (1 - \epsilon) c_p + \epsilon c_s \quad (\text{Eq. 2-65})$$

and :

$$\bar{R} = (1 - \epsilon) R_g, \quad (\text{Eq. 2-66})$$

then we retrieve entirely the equations governing isentropic flow of a one-component ideal gas with constant heat capacities (Eqs. 2-8 - 2-10, 2-13 and 2-14). Therefore the mixture behaves in exactly the same manner as an ideal gas with the properties \bar{c}_p and \bar{R} instead of c_p and R . All of the preceding results for ideal gases therefore remain applicable, with this change in notation. In formulas involving the specific heat ratio, the quantity :

$$\begin{aligned} \bar{\gamma} &= [(1 - \epsilon)c_p + \epsilon c_s] / \{ [(1 - \epsilon)c_p + \epsilon c_s] - (1 - \epsilon) R_g \} \\ &= [(1 - \epsilon)c_p + \epsilon c_s] / [(1 - \epsilon)c_v + \epsilon c_s] \end{aligned} \quad (\text{Eq. 2-67})$$

will appear for the mixture. Obviously, $\bar{\gamma}$ is less than the value of γ for the gaseous constituent; as ϵ increases, the nozzle flow tends to become more nearly isothermal.

We need not rewrite the formulas for the performance parameters. It is sufficient to note that in Eqs. 2-47 and 2-49 γ is to be replaced by $\bar{\gamma}$ and R and R°/m are to be replaced by \bar{R} . The \bar{R} replacement merely introduces a factor $\sqrt{1 - \epsilon}$ in c^* and I_{sp}° . The $\bar{\gamma}$ replacement introduces more complicated changes, but the overall effect is qualitatively the same as the effect of the \bar{R} replacement for all conditions of practical interest. Thus, c^* and I_{sp}° decrease as ϵ increases at constant T_c . This implies, for example, that adding a metal to a solid propellant will increase its performance only if the associated additional heat release can produce an increase in T_c that more than offsets the decrease in I_{sp}° due to the necessary increase in ϵ . What we have shown in this section is that the mere presence of condensed materials in the exhaust tends to reduce performance. (In certain cases, addition of suitable metals also increases the propellant density and decreases the molecular weight of the gaseous products, thereby offering a few advantages in addition to the increase in T_c . However, adding metals also increases the ionization level in the external exhaust, which is generally undesirable.)

Another implication of the isentropic flow equations is that for $\epsilon > 0$ the velocity at the nozzle throat is slightly below the velocity of sound of the gaseous constituent. The magnitude of this effect and also of the performance decrease are not excessively large; at a constant chamber temperature and pressure ratio, I_{sp}° , c^* and the throat velocity decrease by roughly 8% as ϵ increases from 0 to 0.2.

Analyses of the type given in this section may be found in Refs. (9) and (38-42).

3.2.2. Equations of Two-Phase Flow with Particle Lags - Let us now generalize the preceding analysis only to the extent that lags in the temperature and velocity of the particles are allowed to occur. We retain the approximation that the condensed phase occupies a negligible fraction of the total volume and focus our attention first on the conservation equations for the gas phase.

According to Eq. 2-1, mass conservation for the gas phase can be expressed under the present assumptions as :

$$\rho_g v_g A = \dot{m}_g = (1 - \epsilon) \dot{m} = \text{constant}, \quad (\text{Eq. 2-68})$$

where the mass flux fraction ϵ now differs from the mass fraction, so that formulas such as the last equality in Eq. 2-64 of the previous section are no longer valid.

Equation 2-4 must now be used for momentum conservation of the gas since a non-zero drag term $d\hat{D}/dx$ will be produced by the drag forces that the solid particles

exert on the gas. The presence of this term causes the flow to be nonisentropic. The value of dD/dx can be estimated by approximating the condensed phase as a collection of solid spheres, each of radius r , for which Stokes' law of drag of a sphere, $6\pi r\mu(v_g - v_s)$, is applicable. We assume further that each condensed particle has the same velocity and temperature. These approximations are reasonable for obtaining rough estimates of performance penalties and may be improved at the expense of complicating the algebra. Clearly, the quantity of dD is the product of the Stokes force per particle, the number of particles per unit volume n_s and the volume element of the flow $A dx$. Hence, Eq. 2-4 for the gas phase is :

$$\dot{m}_g \frac{dv_g}{dx} + A \frac{dp}{dx} + A n_s 6\pi r\mu (v_g - v_s) = 0 \quad (\text{Eq. 2-69})$$

The equation for energy conservation of the gas can be obtained from the differential form of Eq. 2-5. The rate at which the gas does work on the particles in the element dx is :

$$d\dot{w} = [(A dx) n_s] [6\pi r\mu (v_g - v_s)] (v_s) ,$$

which is the product of the number of particles in the element, the force per particle, and the distance per second over which this force acts. The rate at which heat is added to the gas, by heat conduction from the particles, in the element dx is :

$$d\dot{q} = [(A dx) n_s] [4\pi r^2 \lambda (T_s - T_g)/r] ,$$

where λ is the thermal conductivity of the gas. For brevity of development, the second factor in this equation, which is the formula for the rate of heat flow from a sphere in an infinite stagnant atmosphere, does not contain a correction for velocity of the gas relative to the particle. In view of the expressions for $d\dot{w}$ and $d\dot{q}$, the differential form of Eq. 2-5 becomes :

$$\dot{m}_g \left[c_v \frac{dT_g}{dx} + \frac{d}{dx} \left(\frac{v_g^2}{2} \right) \right] + \frac{d}{dx} (pA v_g) + A n_s 6\pi r\mu (v_g - v_s) v_s - A n_s 4\pi r \lambda (T_s - T_g) = 0 \quad (\text{Eq. 2-70})$$

In the present notation and under the present assumptions, the equation of state of the gas is :

$$p = \rho_g R_g T_g \quad (\text{Eq. 2-71})$$

Turning now to the condensed phase, we see that its momentum and energy conservation equations can be written as :

$$6\pi r\mu (v_g - v_s) = \left(\frac{4}{3} \pi r^3 \rho_s \right) (v_s \frac{dv_s}{dx}) \quad (\text{Eq. 2-72})$$

and:

$$4\pi r \lambda (T_s - T_g) = \left(\frac{4}{3} \pi r^3 \rho_s \right) c_s \left(-v_s \frac{dT_s}{dx} \right) \quad (\text{Eq. 2-73})$$

where ρ_s is the specific gravity of the condensed material (so that $\frac{4}{3} \pi r^3 \rho_s$ is the mass of a particle) and c_s is its heat capacity per unit mass. Equations 2-72 and 2-73 are merely momentum and energy balances for a single particle, as can be seen by noting that $d/dt = v_s \cdot d/dx$ for a particle. The equation for conservation of mass of the condensed phase is :

$$\left[n_s \left(\frac{4}{3} \pi r^3 \rho_s \right) \right] v_s A = \dot{m}_s = \epsilon \dot{m} = \text{constant}, \quad (\text{Eq. 2-74})$$

since the quantity in square brackets obviously equals the mass of the condensed phase per unit volume of the flow field.

Equations 2-68 - 2-74 comprise seven equations for the seven unknowns T_g , T_s , v_g , v_s , ρ_g , n_s and either p or A . For a given nozzle shape, $A(x)$ is specified and $p(x)$ is unknown, but analyses can often be simplified while yielding the required information by treating $A(x)$ as an unknown and specifying $p(x)$.

Equations 2-72 - 2-74 can be substituted into Eq. 2-70 in order to obtain an overall energy conservation equation that can be expressed in an integrated form, viz.,

$$\dot{m}_g (c_p T_g + v_g^2 / 2) + \dot{m}_s (c_s T_s + v_s^2 / 2) = \text{constant} \quad (\text{Eq. 2-75})$$

This integrated energy equation would have been obtained directly had we chosen to derive conservation equations for the two-phase mixture instead of for the gas. Thus there are essentially three first-order ordinary differential equations and four algebraic equations in the governing set. In general, numerical integration of the three differential equations is necessary in obtaining solutions, but for the limits of either small or large lags most of the analysis can be done analytically. Criteria for small particle lags and large particle lags are discussed next. Theories for large lag and small lag limits are then considered and finally, calculations for intermediate values of τ are reviewed.

3.2.3. Dimensionless Lag Parameter τ - It can be seen from Eq. 2-72, for example, that the characteristic time required for velocity equilibration is approximately :

$$t_{vel} \equiv \frac{4}{3} \pi r^3 \rho_s / (6 \pi r \mu). \quad (\text{Eq. 2-76})$$

In order to estimate the extent of the velocity lag, this time can be compared with a representative residence time of a particle in the nozzle,

$$t_{res} \equiv L/a, \quad (\text{Eq. 2-77})$$

where L is a characteristic length of the nozzle and the representative speed has been set equal to the sound velocity a for the gas (Eq. 2-16). As a rough approximation, L might be set equal to the nozzle length; a better approximation would be $L = A/dA/dx$, since it is the rate of change of conditions in the nozzle that produces the lag. The dimensionless lag parameter :

$$\tau \equiv t_{vel}/t_{res} = 2r^2 \rho_s a / 9 \mu L \quad (\text{Eq. 2-78})$$

provides an indication of the magnitude of the velocity lag in the nozzle. If $\tau \ll 1$, the lag will be small, $(v_g - v_s)/v_s \ll 1$. If $\tau \gg 1$, the lag will be large, $(v_g - v_s)/v_s \gg 1$.

An analogous lag parameter for temperature can be defined by introducing a characteristic time for temperature equilibration, obtained from Eq. 2-73 in the same manner that Eq. 2-76 is obtained from Eq. 2-72. With the heat transfer formula that we have employed, the only change in Eq. 2-78 is that μ is replaced by $2\lambda/3c_s$. Since the ratio $3c_s \mu / 2\lambda$ is generally of the order of unity, we may conclude that the parameter τ defined in Eq. 2-78 provides a reasonable indication of the magnitude of both velocity $[(v_g - v_s)/v_s]$ and temperature $[(T_s - T_g)/T_g]$ lags.

In many respects, the small lag and large lag limits are analogous to near-equilibrium and near-frozen flows of a chemically reacting gas. For example, we saw in Section 3.2.1 that when lags are negligible the flow is isentropic. Occasionally we shall refer to the small-lag and large-lag limits as 'equilibrium' and 'frozen' conditions, respectively.

The manner in which the lag is influenced by properties of the particles and the gas may be inferred from Eq. 2-78. Thus, it is apparent that a small particle radius r , low specific gravity ρ_s of the condensed material, a high ratio of the coefficient of viscosity to the sound speed (μ/a) for the gas, and a large characteristic nozzle dimension L , all favor small lags. The condition $\tau = 1$ may be taken as a very rough indication of where lag effects begin to become significant. With the representative values $\rho_s = 1 \text{ gm/cm}^3$ and $4.5\mu/a = 10^{-8} \text{ gm/cm}^2$, we obtain $r^2 = L \times 10^{-8} \text{ cm}$ as the critical condition, which at the typical length $L = 1 \text{ ft}$, yields $r = 6 \times 10^{-4} \text{ cm}$ as the critical particle radius. Thus, lags are expected to be large if r exceeds about 10 microns and small if r is less than about 1 micron.

3.2.4. Large Lag Limit $\tau \gg 1$ - The first approximation to the solution of the flow equations in the small lag limit, $\tau \ll 1$, was given in Section 3.2.1. The corresponding approximation for the large lag limit may be obtained by assuming that v_g and T_s are both known constants throughout the nozzle.

We may first note that the substitution of Eqs. 2-72 and 2-74 into Eq. 2-69 yields :

$$\dot{m}_g \frac{dv_g}{dx} + A \frac{dp}{dx} + \dot{m}_s \frac{dv_s}{dx} = 0 \quad (\text{Eq. 2-79})$$

as a general result. It then follows from Eqs. 2-68, 2-71, 2-75 and 2-79 that when v_g and T_s are constants, the gas obeys a set of equations which are identical to those that describe isentropic nozzle flow of an ideal gas with constant heat capacities. Well-known algebraic equations may therefore be used to calculate the x dependence of gas properties in this extreme case. In particular, the velocity of the gas at the nozzle exit, v_{ge} , is given directly by Eq. 2-40 {with $(\gamma/\gamma-1)R T_{so} = [\text{constant} - \dot{m}_s (c_s T_s + v_s^2/2)]/\dot{m}_g$, in which the constant is the same one that appears in Eq. 2-75}.

The specific impulse with two-phase flow for expansion to the design exit pressure is given in general by the formula :

$$I_{sp}^o = (1 - \epsilon) v_{ge} + \epsilon v_{se}, \quad (\text{Eq. 2-80})$$

where v_{ge} and v_{se} are the gas and condensed-phase velocities at the nozzle exit. Equation 2-80 is obtained from an obvious generalization of the development of Section 1.5. In the limiting case currently under discussion ($v_g = \text{constant}$), the value of v_{se} is the same as the value of the particle velocity at the nozzle entrance, and therefore $v_{se} \leq v_{ge}$. It follows that $I_{sp}^o \approx (1 - \epsilon) v_{ge}$ in this case. Since we have found that under present conditions v_{ge} is the exhaust velocity for isentropic nozzle flow of a purely gaseous working fluid, we may conclude that the presence of condensed materials causes I_{sp}^o to decrease approximately in proportion to $(1 - \epsilon)$ in the large lag limit. This performance penalty is appreciably greater than the penalty ($\sim \sqrt{1 - \epsilon}$) that is paid in the absence of lag phenomena (e.g., there is now a 20% reduction in I_{sp}^o for $\epsilon = 0.2$). Propellant combinations producing two-phase nozzle flow are therefore unlikely to lead to improved performance unless the particle sizes of the condensed phases in the exhaust gases can be kept below about 10 microns.

Analyses permitting large temperature lag but no velocity lag, and vice versa, show that the degradation in performance is due primarily to the velocity lag. If $T_s = T_g$ but $v_s = \text{constant}$, then I_{sp}^o is still approximately proportional to $(1 - \epsilon)$, while on

the other hand if $T_s = \text{constant}$ but $v_s = v_g$, then I_{sp}^0 is approximately proportional to $\sqrt{1-\epsilon}$, which is a relatively small penalty. We shall not give details of the reasoning by which these conclusions are drawn, because for realistic values of the physical parameters temperature and velocity lags are generally of the same order of magnitude.

Techniques can be devised for perturbing about the limit in which $v_s = \text{constant}$ and $T_s = \text{constant}$. One approach is to substitute the large lag limiting results [identified by superscript (0)] into the left-hand sides of Eqs. 2-72 and 2-73, to calculate improved [superscript (1)] approximations for v_s and T_s by integrating these two equations, i.e.,

$$v_s^{(1)}(x) = v_s^{(0)} + \int_0^x \left\{ a [v_g^{(0)}(x) - v_s^{(0)}] / \tau v_s^{(0)} \right\} dx/L \quad (\text{Eq. 2-81})$$

and :

$$T_s^{(1)}(x) = T_s^{(0)} + \int_0^x \left\{ a [T_s^{(0)}(x) - T_s^{(0)}] / \tau v_s^{(0)} \right\} (2\lambda / 3\mu c_s) dx/L \quad (\text{Eq. 2-82})$$

and then to use these results in Eqs. 2-68, 2-71, 2-75 and 2-79 for calculating improved approximations for gas flow variables such as $v_g^{(1)}(x)$. Other approaches can also be used. Results of the perturbations often show that the value of I_{sp}^0 is smaller for "near-frozen" conditions than it is in the limit of frozen flow, because the decrease of v_{se} produced by particle drag outweighs the corresponding increase of v_{se} in Eq. 2-80. We shall not discuss these perturbation techniques further because performance in the near-frozen limit is too poor for the analyses to be of much practical importance.

3.2.5. Small Lag Limit $\tau \ll 1$ - Since the two-phase nozzle flows of practical utility must always lie near the small τ limit, it is of interest to attempt to expand the equations about the equilibrium solution of Section 3.2.1. Such an expansion can be made formally by expressing each variable as a power series in τ . If f denotes any flow variable, we would write $f = f^{(0)} + f^{(1)}\tau + \dots$, where $f^{(0)}$ is the solution given in Section 3.2.1. This type of expansion, through the term $f^{(1)}$, has been carried out by Rannie (43) and Marble (44), (45). Treating $p(x)$ as a specified function and τ as constant throughout the nozzle, these authors have derived a formula for I_{sp}^0 that requires only the evaluation of an integral from nozzle entrance to exit conditions of a function of $p(x)$ and its first derivative (dp/dx). The development is a little too lengthy to present here; the final formula is :

$$\frac{I_{sp}^{(0)} - I_{sp}^0}{I_{sp}^0} = \frac{\epsilon \tau \sqrt{(1-\epsilon)\bar{\gamma}}/\bar{\gamma}}{\bar{\gamma}^2 M_c^{(0)2}} \int_{p_c}^{p_e} \left[1 + \frac{3\mu c_s^2}{2\lambda \bar{c}_p} (\bar{\gamma} - 1) M^{(0)2} \right] \left[\frac{dp/d(x/L)}{M^{(0)2} p^2} \right] dp, \quad (\text{Eq. 2-83})$$

where L is the length of the nozzle,

$$M^{(0)} = \left\{ \frac{2}{\bar{\gamma} - 1} \left[\left(\frac{p_e}{p} \right)^{(\bar{\gamma}-1)/\bar{\gamma}} - 1 \right] \right\}^{-1/2}$$

is the Mach number in equilibrium flow (Section 2.3.2.1), $I_{sp}^{(0)}$ is the value of I_{sp}^0 as obtained for equilibrium flow, and \bar{c}_p , $\bar{\gamma}$ and τ are defined in Eqs. 2-65, 2-67 and 2-78 respectively. The subscripts e and c refer to exit and chamber conditions, the latter assumed to be a stagnation state. Equation 2-83 gives a correction factor for I_{sp}^0 that is proportional to the product $\epsilon \tau$.

3.2.6. Numerical Calculations for Intermediate Values of τ - The two-phase flow equations for arbitrary values of τ have been programmed for electronic computer solution by authors who report their work in Refs. (46-51), (102). Numerical difficulties arise in the vicinity of the throat when $A(x)$ is specified instead of $p(x)$; each group of authors developed their own procedures for circumventing the difficulties. Typical results show substantial performance losses for particle diameters above 2 microns, as illustrated in Fig. 2-10, (52).

We note here that the results of many numerical calculations can be correlated by the formula :

$$I_{sp}^0 = v_{gc}^0 (0) \left\{ 1 - \epsilon a_1 / [1 + a_2 (r_1 r_2)^{1/4} / r] \right\},$$

where r_1 is the throat radius, r_2 is the radius of curvature of the nozzle at the throat, r is again the particle radius, and a_1 and a_2 are constants whose values are independent of the values of r , r_1 , r_2 and ϵ . Previously unmentioned dependences emphasized by this formula are that I_{sp}^0 increases when either r_1 or r_2 is decreased. The dimensional group $r/(r_1 r_2)^{1/4}$ appears here and is related to the result that for many nozzle geometries most of the loss is determined by conditions in the vicinity of the throat.

3.2.7. Influence of Phenomena neglected in the Theory of Section 3.2.2. - If the differential equations are to be solved numerically, then little additional work is involved in permitting the properties of the gas and condensed phase to depend on temperature. Some of the computer programs referenced above do permit temperature-dependent properties and also variable gas composition to a limited extent. No new general trends are uncovered in this manner. To be accurate, a distribution in particle sizes should also be included. The formalism for this is also easy to incorporate in computer programs (48), but seldom is size distribution data available. Equations that include losses by heat transfer and viscous dissipation in the gas and buoyancy forces on the particles have also been presented (53).

Two-dimensional flow effects may be of importance in gas-particle systems because particles can slip across the gas streamlines. Calculation of these effects is difficult. Characteristic methods have been developed for two-dimensional supersonic gas-particle flows, but starting data downstream from the sonic plane are difficult to obtain and introduce uncertainties in the results (48). Particle trajectories can be calculated in prescribed two-dimensional gas flows, but this entails neglecting the effects of the particles on the gas flow (51). This last study indicates that particles often tend to accumulate near the axis of the nozzle.

Some particles may impinge on the wall of the nozzle. The effects of impingement are largely a topic of speculation. Impingement may cause nozzle erosion or may cause deposits to form on the nozzle. A substantial amount of deposition is usually observed with aluminized solid propellants. The consequent changes in geometry modify nozzle performance, and properties of deposited materials as well as the impingement process itself influence the wall friction and wall heat transfer losses, usually increasing both (52), see Section 4.4.

The presence of particles in the flow may also introduce significant radiative heat transfer effects (52).

The assumption of no particle growth by condensation or agglomeration in the nozzle is open to some question. Apparently, two-phase nozzle flow theories accounting for these phenomena have not been developed. To account for condensation on particles formed in the combustion chamber would be relatively straightforward, but the basic physical understanding necessary in accounting for nucleation and agglomeration is not available yet (54). The difference between equilibrium and frozen

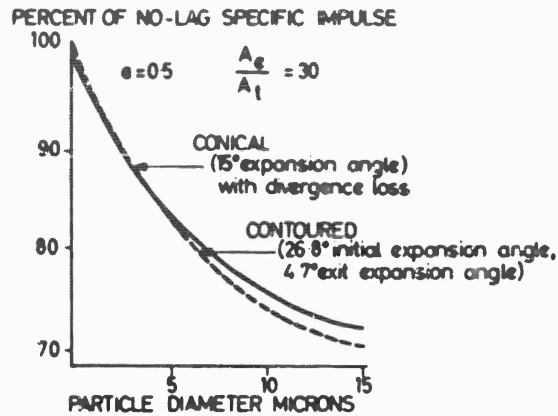


Fig. 2-10 Effect of particle lag on specific impulse, from Ref. (52).

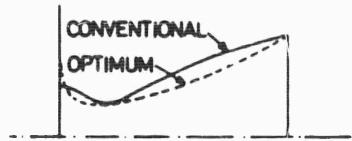


Fig. 2-11 Comparison of optimum nozzle contour with that of conventional nozzle⁴⁵ ($p_c/p_e = 59.6$).

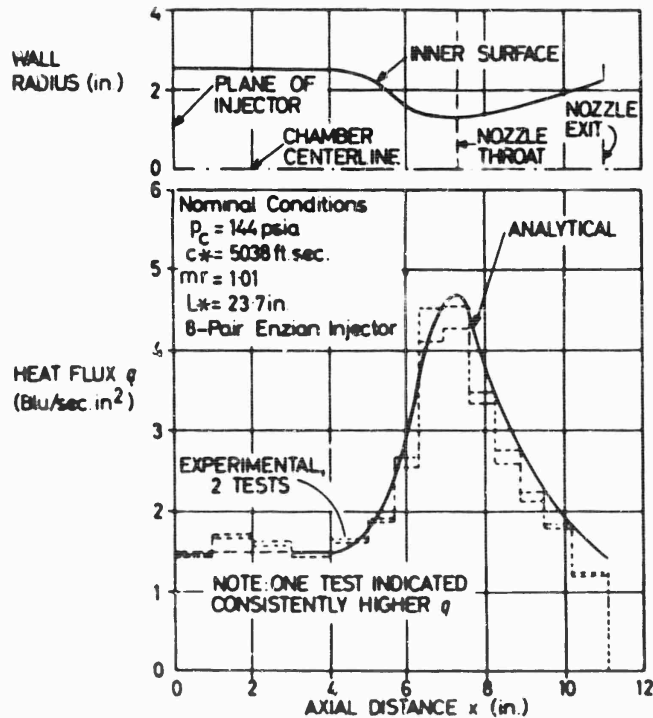


Fig. 2-12 Comparison of predicted values with experimental heat-flux measurements made with 4-to-1 contraction-area-ratio nozzle at low chamber pressure [Ref. (74)].

gas-condensed phase reactions in nozzle flow typically amounts to 3 to 4% in I_{sp}^0 for metalized propellants (12), so estimates of conditions under which each limiting chemical behavior prevails are worth obtaining. The interactions of these phenomena with the loss mechanisms analyzed in Sections 3.2.1 to 3.2.6 may be negligibly small.

Collisions between particles in the gas may conceivably introduce additional effects on I_{sp}^0 by giving rise to interparticle heat and momentum transfer and perhaps by producing agglomeration. These effects are expected to be significant at relatively high particle concentrations. Recent work has increased our understanding of the dynamics of particle-particle collisions in gases (55-64). It does not appear that this work has been applied to two-phase nozzle flow performance calculations.

3.3. Effects on Nozzle Design

Since impingement of particles on nozzle walls often degrades performance, the designer of nozzles for two-phase flow is motivated to attempt to minimize the amount of impingement. This dictates that curvature of the walls toward the axis should be avoided. It also implies that large curvatures away from the axis should be avoided, because such curvatures can give the particles radial velocities that enable them to reach the wall farther downstream. In general, wall curvature should be small except near the exit plane, where large curvatures away from the axis are permissible. These observations imply that conical nozzles are better adapted to small rates of deposition in two-phase flow than are the bell-shaped nozzles (see Section 5) contoured for optimum ideal-gas performance.

The theory of Section 3.2.5 has been extended to obtain predictions of optimum nozzle contours for minimum particle lag losses in nozzles of prescribed mass flow, length, and exit pressure or exit area (45). The optimum contours tend to have a very long throat and an outward flare at the exit, (see Fig. 2-11). Both of these characteristics are undesirable from the viewpoint of heat transfer and flow divergence losses. Furthermore, although the velocity and temperature lags in the throat region were reduced to about 1/3 of those for a conventional nozzle, the specific impulse loss due to particle lag for the optimum nozzle was only about 30% less than that of a conventional nozzle (45). Therefore, contouring nozzles to reduce particle lag losses does not appear to be appealing. Since the particle lag losses for conical nozzles do not differ much from those for bell-shaped nozzles (see Fig. 2-10), lag losses alone are not influenced significantly by reasonable variations in nozzle design. Deposition and erosion phenomena are the primary two-phase flow effects that should be considered in nozzle design.

It may be worthwhile to state here explicitly that lag losses as well as deposition and erosion depend appreciably on the shape of the subsonic, converging portion of the nozzle. It has also been implied by the preceding development that two-phase flow losses are more severe for small nozzles than for large nozzles.

3.4. Experimental Results

Relatively few experimental results have been published on two-phase nozzle flow.

Aluminum oxide particle sizes and some size distributions have been measured for various aluminized propellants (65) - (68). Most of the measurements, including a detailed study of the dependence of particle size on chamber pressure, (67), have been made on strand burners and presumably correspond to conditions existing in the combustion chamber. Some measurements of sizes of particles collected from rocket exhausts also have been reported, (65), (66), (68). There is some indication that particles in the exhaust are larger than in the chamber, (65), (68). Mean (number-weighted average) particle diameters appear to lie between 1 and 2 microns in

the chamber, (65), (67), and between 1 and 4 microns after passing through the nozzle, (65), (66), (68). There are some uncertainties and disagreements in the published data.

Experimental measurements of velocity and temperature lags are much more difficult to obtain. Velocity lags in rough agreement with theory were inferred from particle number density measurements by Carlson, (103). A framing camera was used to measure particle velocities in order to obtain velocity lags in Ref. (69). Spectroscopic techniques were employed in measuring particle and gas temperatures in Ref. (70); the sodium D line was used for the gas temperature and particle emission for the particle temperature. The experimental velocity and temperature lags obtained in Refs. (69) and (70) are in agreement with theoretical calculations, within experimental accuracy. The accuracies of both experiments were quite low. The temperature lag measurements are somewhat simpler to perform than direct velocity lag measurements. New photographic techniques for velocity lag measurements are under development; see Fulmer and Wirtz, (104), who obtained indications on the basis of streak photography that the hypothesis of a constant ratio of lag velocity to gas velocity overestimates the velocity lag.

Results of thrust measurements for many rocket firings are, of course, available. Effects of two-phase flow on performance can be extracted from some of these measurements by carefully accounting for all loss mechanisms. A number of results of this type are shown, for example, in Ref. (48), where theoretical and experimental specific impulses are found to agree, within experimental uncertainty. Also, examination of nozzles after firing yields information on the extent of deposition or erosion.

Finally, we note that the presence of particles in the gas modifies the structure of the external exhaust flow (considered in Section 5.4) downstream from the nozzle exit. Experimental measurements and theoretical correlations are available for those effects (71).

4. Nozzle Heat Transfer

4.1. Introduction

Since the temperature of the gases passing through the nozzle generally exceeds the melting point of the nozzle wall material, it is evident that heat must be transferred from the hot gases to the cooler walls. The nozzle walls therefore cause the flow to be nonadiabatic (as well as nonisentropic due to wall friction, see Section 5). The nonadiabaticity affects the nozzle performance, and the heat transfer profoundly influences nozzle design.

The way that performance is affected by heat transfer to the wall can be inferred from Eq. 2-7. If the total heat energy per second absorbed by the walls is \dot{q} , then Eq. 2-7 implies that the stagnation enthalpy per unit mass of the gas at the exit plane will be reduced by an amount \dot{q}/\dot{m} . Since the specific impulse I_{sp}^0 is proportional to v_e , which, in turn is the square root of twice the kinetic energy per unit mass at the exit plane, it follows that I_{sp}^0 is reduced approximately by the fractional amount:

$$(\Delta I_{sp})/I_{sp}^0 = 1 - (1 - 2\dot{q}/\dot{m}I_{sp}^0)^{1/2},$$

where I_{sp}^0 is the specific impulse in the absence of wall heat transfer. Typically, wall heat transfer reduces I_{sp}^0 by 2%, so the effect on performance is not large. However, the effect on nozzle design is important and is the principal topic that we shall consider in the rest of this section.

f The basis of heat transfer theory is covered in textbooks (72), (73), and introduct-

ions to its application to rocket nozzle design are presented in Refs. (9) and (10). A recent comprehensive review of heat transfer in rocket nozzles is presented in Ref. (74). In view of the existence of this wealth of material, we shall treat the subject only briefly and shall recommend Ref. (74) to the reader who is interested in a thorough development.

Most of the gas flowing past any given cross section of the nozzle has relatively uniform temperature and velocity. However, in a thin region adjacent to the wall, the gas temperature drops appreciably and its velocity also decreases, approaching zero at the wall. The processes occurring in this thin region, termed the boundary layer, govern the skin friction losses (see Section 5.2) and the rate of heat transfer to the wall. The velocity and temperature profiles in the boundary layer usually correspond to steady-state, turbulent motion, so that steady-state, turbulent boundary layer relations can be employed to calculate the skin friction and heat transfer rate. On the other hand, the heat conduction processes occurring in the wall of the nozzle of a solid-propellant rocket are almost always unsteady, because nozzles of solid-propellant rockets are generally uncooled. (Liquid-propellant rocket motors usually have a ready source of liquid coolant in one or both of the liquid propellants, so that the nozzle wall can be made relatively thin, conducive to establishing steady temperature profiles. But for solid rockets, coolants are seldom available, and the running times are usually short enough for nozzles to be made of uncooled heat-sink materials that are capable of maintaining their strength as their average temperature increases during the entire duration of a firing.) Unsteady heat conduction in the wall is discussed in the following section. Next, steady-state boundary-layer heat transfer in the gas is considered. Finally, a few special heat transfer phenomena and design concepts that are peculiar to solid-propellant rockets will be mentioned.

4.2. Unsteady Heat Conduction in Uncooled Nozzle Walls

The equation describing unsteady heat conduction in a solid is :

$$\rho_s c_s \partial T / \partial t = \nabla \cdot (\lambda_s \nabla T) \quad , \quad (\text{Eq. 2-84})$$

where ρ_s , c_s and λ_s are the specific gravity, specific heat and thermal conductivity, respectively, for the solid material, T is temperature, t is time, ∇ denotes the (vector) gradient operator and $\nabla \cdot$ is the divergence. Equation 2-84 is valid even if the properties λ_s and c_s are functions of temperature. Initial conditions and boundary conditions must be specified before one can attempt to obtain the solution to Eq. 2-84. The initial condition is $T = T_0 = \text{constant}$ at $t = 0$, where T_0 is the initial temperature of the nozzle material. The boundary condition at the internal surface of the wall is $-\lambda_s \mathbf{n} \cdot \nabla T = q$ for $t > 0$, where \mathbf{n} is a unit vector normal to the surface, pointing into the wall, and q is the heat flux from the gas to the wall (see Section 4.3 for formulas for q). A boundary condition must also be specified at the external surface of the nozzle wall material; this boundary condition depends on what is adjacent to the external surface. Sometimes the insulated wall condition $\mathbf{n} \cdot \nabla T = 0$ is applicable there, but frequently the firing time is short enough for the external surface to be heated to a negligible extent, so that the temperature distribution during firing is insensitive to the boundary condition at the external surface (and the nozzle wall can be approximated as a semi-infinite solid).

The three-dimensional form of Eq. 2-84 is difficult to solve. Usually symmetry about the axis of the nozzle enables us to conclude that the solution will be independent of the azimuthal coordinate in a cylindrical coordinate system, and Eq. 2-84 reduces to :

$$\rho_s c_s \partial T / \partial t = \partial / \partial x (\lambda_s \partial T / \partial x) + (1/r) \partial / \partial r (r \lambda_s \partial T / \partial r) \quad , \quad (\text{Eq. 2-85})$$

where x and r are the axial and radial coordinates, respectively. Trouble is even encountered in solving Eq. 2-85, but finite-difference approximations to the equations have been programmed for computer solution. Essentially, the nozzle wall can be thought of as being broken into a finite number of isothermal elements that transfer heat among each other at rates dependent upon the sizes and relative temperatures of adjacent elements. Nowadays, unsteady heat conduction calculations for real nozzles are practically always carried out by means of one-dimensional time-dependent or two-dimensional time-dependent computer programs. The basis of one such program is described Ref. (9). Accurate calculations of this type, for values of q and material properties corresponding to nozzle design, are important because they determine the weight of nozzle material needed for protection against nozzle failure. We might note that a short firing time, cool propellant gases, a high specific heat of the wall material, good high-temperature strength properties of the wall material, a low thermal conductivity of the nozzle material near the hot gas surface (to reduce the rate of heat influx), and a high thermal conductivity of the nozzle material elsewhere (to reduce thermal stresses and to distribute the heat through a larger volume, improving the overall capacity to absorb heat) all tend to reduce the weight of an uncooled nozzle.

4.3. Steady-State, Turbulent Heat Transfer Through the Boundary Layer

In the theory of convective heat transfer, the energy per unit wall area per second transferred to the wall is always expressed as :

$$q = \hat{h} \Delta h, \quad (\text{Eq. 2-86})$$

where \hat{h} is a heat transfer coefficient (or conductance) and Δh is a driving force or potential for heat transfer. For low-speed flow of a one-component ideal gas with constant heat capacities and thermal conductivity, Δh is set equal to the difference between the temperature of the gas outside the boundary layer (the "free-stream" static temperature) and the temperature of the surface of the wall. For high-speed flow of a one-component ideal gas with constant properties, Δh may be set equal to the difference between the free stream stagnation temperature and the wall temperature; however, as a refinement in this case, Δh is often set equal to the difference between the adiabatic wall temperature and the wall surface temperature, where the adiabatic wall temperature equals the free stream static temperature plus the product of a 'recovery factor' with the difference between the stagnation and static free stream temperatures. The recovery factor can be obtained experimentally by measuring the surface temperature of an adiabatic (insulated) wall, or it can be calculated by means of a fluid dynamical analysis of boundary-layer flow; its value is found to depend on the Prandtl number Pr ($Pr \equiv \mu c_p / \lambda$; μ = viscosity, λ = the thermal conductivity) of the gas. For one-component gases with variable properties there is some question as to the proper choice of Δh , and a number of additional questions arise for multicomponent, reacting gas mixtures with variable properties. It has been found that one reasonable definition of Δh in the latter case is the difference between the values of the total stagnation enthalpy per unit mass of the gas mixture (the sum of the thermal and chemical enthalpies per unit mass and the kinetic energy per unit mass) in the free stream and in the gas immediately adjacent to the surface of the wall. However, sometimes a recovery factor for kinetic energy and also a recovery factor for chemical enthalpy are inserted into the definition of Δh , but these factors have not been determined very well either experimentally or theoretically. As a relatively simple and convenient definition for general use, we recommend here :

$$\Delta h \equiv h_{s0g} - h_{s0w}, \quad (\text{Eq. 2-87})$$

where h_{s0} is the total (thermal plus chemical) stagnation enthalpy, the subscript g identifies free-stream conditions, and the subscript w identifies conditions of the

gas at the surface of the wall. Estimates indicate that for solid-propellant rocket nozzles, heat transfer rates computed on the basis of this definition will differ by less than 30% from those computed on the basis of more complex definitions.

Having chosen Δh we allow Eq. 2-86 to define the heat transfer coefficient \hat{h} , and we employ theoretical and experimental heat transfer results to calculate h from the equation. In nozzle design, one then employs these data for h in Eq. 2-86 in order to calculate the heat transfer rate. The data for h are conveniently represented in nondimensional form by introducing the Nusselt number, defined as :

$$Nu = \hat{h} c_p D / \lambda \quad (\text{Eq. 2-88})$$

where c_p and λ correspond to free-stream gas properties, and D is a characteristic length. The value of D is taken to be the local diameter of the nozzle, some other characteristic length of the nozzle, or a thickness of the boundary layer, depending on the geometry of the system. Theory and experiment yield expressions for the Nusselt number as a function of the Reynolds number, Mach number, Prandtl number, Schmidt numbers Sc (ratios of kinematic viscosity to diffusion coefficients) and other dimensionless parameters characterizing the thermochemical and transport properties of the gas. At present, the best expression to use for Nu in rocket nozzle heat transfer calculations for conventional nozzles appears to be, (74),

$$Nu = 0.0346 Re^{0.8} Pr^{7/15} (2l/D_0)^{-1/5} (D_0/D)^{-1/20} (\bar{T}/T)^{-0.6} \quad (\text{Eq. 2-89})$$

where the Nusselt number Nu and the Reynolds number Re are based on the local diameter D , the quantity D_0 is the value of D at the entrance to the nozzle, l is the length of the combustion chamber, and \bar{T} is a mean temperature in the boundary layer, which is usually taken to be the arithmetic mean of the free stream and wall temperatures, $\bar{T} = (T + T_w)/2$. The density, viscosity, specific heat and thermal conductivity that appear in Nu , Re and Pr are to be evaluated for a gas at the same pressure and chemical composition as the free stream but at the mean temperature \bar{T} . Equation 2-89 differs from earlier formulas in the presence of the terms involving l and D_0 , which are intended to account in an approximate way for the non-zero thickness of the boundary layer at the entrance to the nozzle. The local rate of heat transfer to the wall of a rocket nozzle is calculated by using first Eq. 2-89, then Eq. 2-88, next Eq. 2-87, and finally Eq. 2-86. The reader may infer from these equations the manner in which the heat transfer coefficient depends on various design parameters.

In order to carry out the calculation of q , values of the thermodynamic and transport properties of the gas must be found (9), (74).

Sometimes property data are difficult to evaluate, especially at the mean temperature \bar{T} . In such cases, the simplified formula :

$$Nu = 0.023 Re^{0.8} \quad (\text{Eq. 2-90})$$

is recommended in place of Eq. 2-89, where now the properties appearing in both Nu and Re are to be evaluated at local free stream conditions. Equation 2-90 is especially suitable for uncooled solid-propellant rocket nozzles since it represents a correlation of measurements made on such a solid-propellant system (75).

We should perhaps emphasize that the theoretical basis of Eq. 2-89 (and, of course, also Eq. 2-90) is tenuous. The boundary layer in a rocket nozzle is very difficult to understand theoretically. Some of the complicating factors are secondary flows and oscillations in the chamber, a variable-area duct, an accelerating free stream with a rapid axial rate of decrease of pressure, a chemically reacting boundary-layer flow that possibly attains neither chemical equilibrium nor frozen conditions

and instead is influenced by the rates of chemical reactions, diffusion of chemical species to the wall where additional exothermic chemical rate processes may occur, and, of course, turbulence. Equations 2-86 - 2-89 represent an attempt to account for all of these effects as well as possible. In view of the difficulties involved, the attempt has been rather successful, as judged from agreement between calculations and most experiments. At present, the primary justification for Eqs. 2-86 - 2-90 is empirical.

A comparison of theoretical calculations of the wall heat flux with experiment for a liquid-propellant rocket motor burning nitrogen tetroxide and hydrazine is shown in Fig. 2-12. The work was done by Welsh and Witte and the figure is taken from Ref. (74). Theory and experiment are best compared for liquid-propellant rockets because the experimental data available for liquid propellant systems are much more extensive than for solid-propellant rocket nozzles. The analytical curve shown was calculated on the basis of an older equation for Nu than Eq. 2-89, (although more complete than Eq. 2-90), but the differences in the values of Nu given by Eq. 2-89 and the older equation are quite small. Theory and experiment are seen to agree quite well in Fig. 2-12. However, the case shown represents about the closest agreement obtainable between predictions and measurements; discrepancies of the order of 50% in q are not uncommon.

Figure 2-12 shows that the wall heat flux attains a rather sharp maximum either at the throat or just upstream from the throat. This is a characteristic of all rocket nozzles. The boundary layer becomes very thin and the heat transfer coefficient becomes very high in the vicinity of the throat. A consequence is that the problem of nozzle wall material design for withstanding the heat load is crucial in the vicinity of the throat.

4.4. Additional Heat Transfer Considerations

A number of ideas have been used for solving the problem of heat protection of the converging and throat sections of the nozzle. One suggestion is to make the downstream end of the propellant grain out of a material that gasifies at a low temperature and can bathe the nozzle wall in a cool gas. Another is to make the nozzle wall itself of an ablative material, generally composed of glassy and organic substances (e.g., phenolic nylon), which gasifies and carries away the heat primarily in the gas phase instead of transferring it to the solid. This last method is useful upstream from the throat, but were it to be used at the throat it would cause the throat area to increase with time, leading to undesirable variations in performance. If either of these methods are employed, the problem of calculating the rate of heat transfer into the wall is modified, since the formulas given earlier will not be valid. Instead, the heat transfer rate is obtained from an ablation temperature, a heat of ablation, and an ablation rate which can be calculated by using a formalism resembling that for heat transfer (5).

An alternative to a gasifying material is an insulating liner for the nozzle wall. Ceramic throat inserts such as graphite, silicon carbide, silicon nitride, and refractory metal oxides (e.g., zirconia and magnesia) have been employed. Pyrolytic graphite, which has a high thermal conductivity in one direction but a very low thermal conductivity (an order of magnitude lower) normal to this direction, is an appealing material for distributing the heat load in an acceptable fashion. Refractory metals such as molybdenum and tungsten have also been used successfully in uncooled nozzle throats. If a thin insulating solid material is used on the inner surface of the nozzle wall, then the overall heat transfer coefficient h_T for transfer of heat from the gas to the main nozzle material, defined with a driving potential equal to the difference between the free-stream gas temperature and the surface temperature of the main nozzle material, is given approximately by :

f*

$$1/\hat{h}_T = 1/c_p \hat{h} + \delta_i / \lambda_i, \quad (\text{Eq. 2-91})$$

where δ_i is the thickness of the insulating material and λ_i is its thermal conductivity. Equation 2-91 can be used to calculate the reduction in heat transfer rate caused by a thin insulating liner. An example of a multilayer nozzle design is shown in Fig. 2-13.

Additional complications arise in heat transfer calculations for propellants (such as metalized systems) that produce condensed materials in their combustion products. At present, we do not know how to modify Eqs. 2-86 - 2-90 to account for two-phase flow, so the two-phase system is treated as a gas in calculating heat transfer coefficients. However, if deposition of the condensed material occurs on the nozzle surface, then it is essential that the presence of the deposits be considered in computing the heat transfer rate. If the thickness of the deposit layer and its thermal conductivity can be estimated, then Eq. 2-91 can be used to calculate the effective (overall) heat transfer coefficient. It has been shown experimentally that aluminized propellants can deposit a layer of liquid alumina on the entire surface of a nozzle wall, (75). The alumina acts as an insulator, substantially reducing the rate of heat transfer. Agreement between measured and calculated (using Eq. 2-90 for Nu) heat transfer rates was obtained only after Eq. 2-91 was used to account for the thermal resistance of the alumina. Incidentally, in the tests of Ref. (75), experimental heat transfer rates were much higher than theoretical rates for both aluminized and nonaluminized propellants in the converging section of the nozzle, but Eq. 2-91 still brought the experimental results for aluminized and nonaluminized systems into agreement with each other (but not with theory) in this section.

For two-phase nozzle flows in sufficiently large motors, heat transfer from the propellant gases to the nozzle wall by means of radiation may begin to become an important mechanism. Methods for calculating radiative heat transfer rates are available (9), (72), but the calculations are difficult to perform. For uncooled nozzles of large expansion ratios, radiative heat loss from the inner surface of the nozzle may become an important cooling mechanism. The rate of this type of radiative heat transfer is relatively easy to calculate; the energy loss per unit area per second is $f \epsilon_s \sigma T_s^4$, where f is a geometrical factor, ϵ_s is the surface emissivity, T_s is the surface temperature and σ is the Stefan-Boltzmann constant (0.57×10^{-11} watts/cm² °K⁴).

5. Discussions of Other Deviations from Ideality

5.1. Influence of Non-One-Dimensional Flow on Nozzle Performance and Design

Two-dimensional flow phenomena were considered in Section 1.4.4. We shall now discuss the effect of isentropic non-one-dimensional flow inside the nozzle on performance and design. If we exclude the possibility of some swirl at the nozzle entrance, then the steady, isentropic flow will be axially symmetrical, and the method of characteristics can be employed to calculate the supersonic flow field in a nozzle of specified geometry (4). The transonic flow field in the vicinity of the throat must, of course, be known in order to begin characteristics calculations. In addition to providing the supersonic starting conditions for the method of characteristics, axially symmetrical, transonic flow calculations give the shape of the sonic line and a non-one-dimensional flow correction (a decrease, generally of less than 1%) in the nozzle mass flow rate. We do not cover this material here. For a very recent presentation, the reader may consult (106). This reference thoroughly covers supersonic characteristics calculations as well as the transonic regime. It also treats two-phase flow and thrust-vector control at length. For conical nozzles with moderate or large expansion ratios, the calculations show that the streamlines at the exit diverge approximately radially as if they had originated at a point source in three dimensions. This divergence reduces the axial component of the thrust,

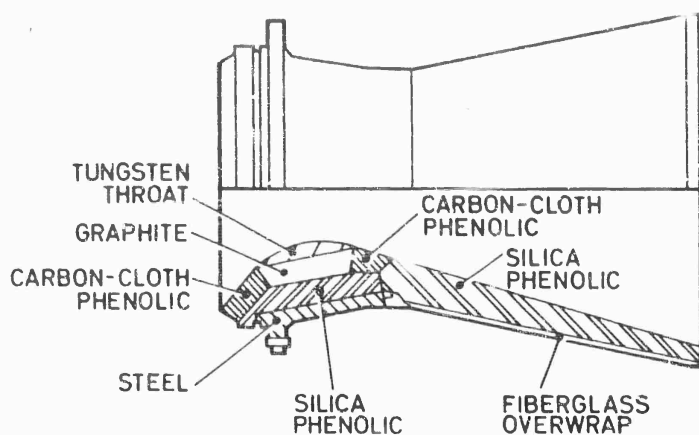


Fig. 2-13 Advanced nozzle design for solid-propellant motor employs heat-sink walls and complex throat insert, (105).

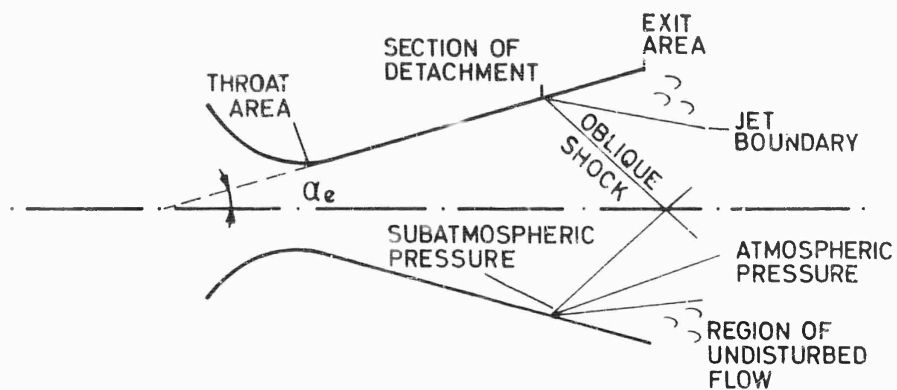


Fig. 2-14 Schematic illustration of detachment of overexpanded jet, from Ref. (10).

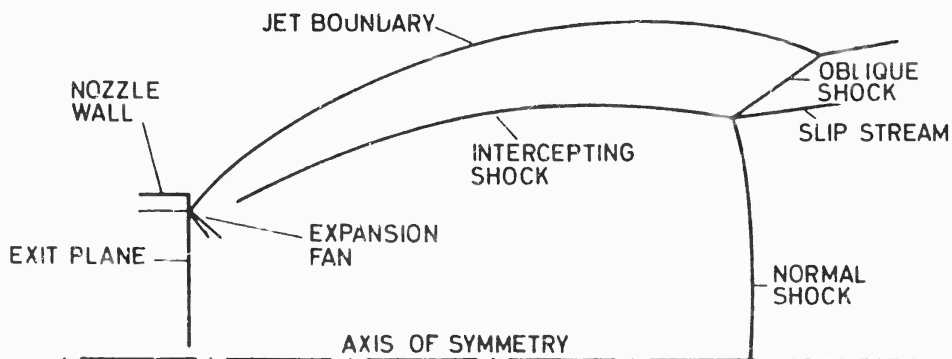


Fig. 2-15 Schematic diagram of exit flow pattern of highly under-expanded exhaust jet.

as we shall now demonstrate, (9), (10).

As a control surface, we adopt a segment of the surface of a sphere whose center is located at the effective origin of the point source. The radius of the sphere is chosen so that its surface intersects the expansion cone of the nozzle at the nozzle exit. The thrust F° for the design exit pressure can be calculated by integrating the axial component of the momentum flux over the segment of the spherical surface bounded by the circle proscribed by the exit of the nozzle cone. If α is the angle between the nozzle axis and a line from the center of the sphere to an arbitrary point on the surface of the sphere, then the mass flow rate through a ring about the axis of angular extent $d\alpha$ at angle α is :

$$d\dot{m} = \rho_e v_e (2\pi R_e \sin \alpha) (R_e d\alpha) ,$$

where R_e is the radius of the sphere. In terms of the half-angle of the expansion cone α_e , the total mass flow rate across the control surface is :

$$\dot{m} = 2\pi R_e^2 \rho_e v_e \int_0^{\alpha_e} \sin \alpha d\alpha ,$$

and the exit area of the nozzle (in a plane perpendicular to the nozzle axis) is $A_e = \pi R_e^2 \sin^2 \alpha_e$. The axial component of momentum flux through the ring at angle α is $(v_e \cos \alpha) d\dot{m}$, and therefore the axial thrust (the integral of the axial momentum flux over the control surface) is :

$$F^\circ = 2\pi R_e^2 \rho_e v_e^2 \int_0^{\alpha_e} \cos \alpha \sin \alpha d\alpha .$$

Evaluating the integrals appearing in the expressions for \dot{m} and F° , we find that :

$$F^\circ = \dot{m} v_e (1 + \cos \alpha_e)/2 . \quad (\text{Eq. 2-92})$$

Hence, the specific impulse I_{sp}° is reduced by a factor $(1 + \cos \alpha_e)/2$ because of the divergence of the nozzle expansion cone. For the representative expansion angle $\alpha_e = 15^\circ$, the correction factor is 0.983, which is near unity.

If a high expansion ratio (exit area over throat area) is required, a 15° conical nozzle becomes very long and excessively heavy. Increasing the nozzle cone angle would decrease the length and weight of the nozzle, but the divergence loss begins to become appreciable as α_e is increased above 15° . A solution to this dilemma is provided by contoured nozzles. A nozzle shaped like a bell, with a divergence half-angle that varies continuously from about 35° at the throat to perhaps 10° at the exit, can be designed by the method of characteristics to give very low divergence losses at the exit and also be shorter and lighter than a conical nozzle. In principle, contouring can eliminate divergence losses entirely, but this usually requires a long nozzle for which weight and wall friction (Section 5.2) losses are large.

It is possible to formulate variational problems for optimizing nozzle thrust, within the framework of the theory of characteristics. Rao developed such an analysis for determining the nozzle contour that produces maximum nozzle thrust, for prescribed values of the ambient pressure, the length of the nozzle divergent section, and the curvature of the nozzle at the throat, (76), (77). The optimum contour often leads to flows whose properties are quite nonuniform across the exit plane. However, an optimized nozzle can produce the same thrust as a conical nozzle 10% to 25% longer (9).

We might mention that contoured nozzles are more difficult to manufacture than simple conical nozzles. Representative simple nozzle designs employ a conical convergent section with a half-angle of 30° to 45° , a toroidal throat section with torous radius about twice the throat radius, and a conical divergent section with a half-angle of about 15° . Nozzle performance is not greatly sensitive to nozzle design, (9).

5.2. Boundary Layer Growth

In addition to controlling the heat transfer rate, the boundary layer on the wall of the nozzle affects performance directly by exerting a frictional drag on the flow. The effect of the wall drag on the flow can be included in the governing equations by introducing a friction factor f , as shown in the derivation of Eq. 2-4. Wall friction, *per se* does not affect the approximation of adiabaticity, but it does cause the flow to become nonisentropic. However, the effect is quite small for most nozzles (so long as detachment does not occur, see Section 5.3); it becomes important only for rockets requiring large area ratios (and therefore relatively long nozzles).

In accounting for frictional effects, local wall friction coefficients must be estimated. Since the boundary layer flow is generally turbulent, one might employ the empirical fully-developed turbulent pipe flow formula :

$$f = 5.5 \times 10^{-3} [1 + (2 \times 10^4 k/D + 10^6 / \text{Re})^{1/3}]$$

locally as a first rough approximation if data for a better estimate are not available. Here Re is based on the local diameter D and on free-stream gas properties, and k (which has the same units as D) is the average roughness (protrusion height) of the wall. If the displacement thickness δ of the boundary layer can be estimated, then it is better to use a flat-plate formula, such as :

$$f = 0.18 \text{Re}_\delta^{-1/4},$$

which is valid for a smooth wall, and in which the Reynolds number Re_δ is based on free stream properties and on the local thickness of the boundary layer. Improvements of this result (e.g., curves accounting for roughness) may be found in Ref. (78). In all of these results, effects of free stream Mach number and of the strong accelerating pressure gradient are neglected; too few experimental and theoretical results on turbulent boundary layers are available yet to enable one to account for these additional effects with a reasonable degree of assurance. In using a formula involving δ , one may be guided by the general observation that δ decreases in the contraction section, reaches a minimum in the vicinity of the throat, and then begins to increase in the divergent section (74).

One rough approximation for the downstream part of the nozzle is $\delta = 0.004$ times the axial distance to the throat. There is some indication that the thin throat boundary layer, combined with the favorable pressure gradient and the high cooling rate ($dp/dx < 0$ and heat transfer from the gas to the wall tend to delay transition from laminar to turbulent flow) may tend to "damp out" much of the turbulence in the vicinity of the throat, producing a small region where the boundary layer exhibits some features of a laminar boundary layer, (74). If so, the friction factor there may be smaller than predicted by the preceding formulas.

Refined designs of contoured nozzles involve calculating the displacement thickness of the boundary layer and adjusting the wall contour accordingly. The resulting correction for the nozzle throat area (and therefore for the nozzle mass flow rate) are usually negligibly small. The area correction is largest at the nozzle exit, where it may be of the order of 3%.

In order to calculate the effect of wall friction on nozzle performance parameters on the basis of quasi-one-dimensional theory we may note that friction produces an increase in entropy given by the formula :

$$\Delta s = \int_0^x (f v^2 / 2DT) dx ,$$

which can be derived from Eqs. 2-4, 2-8, 2-10 and 2-11. For a one-component, ideal gas with constant heat capacities, this change in entropy causes the stagnation pressure to decrease according to the formula :

$$p_s/p_{s0} = e^{-\Delta s/R} ,$$

but it does not affect the stagnation temperature. The derivations of Eqs. 2-43 and 2-45 indicate that the thrust coefficient for the design exit pressure will be decreased by roughly this same factor. The consequent penalty in C_F is typically of the order of 1%, increases with increasing area ratio, and seldom ever exceeds 5%.

5.3. Jet Detachment

When quasi-one-dimensional nozzle flow calculation implies that a normal shock should sit somewhere in the diverging section of the nozzle, the real nozzle flow seldom exhibits a single normal shock. The pressure rises very steeply through a shock wave, and this strong, unfavorable ($dp/dx > 0$) pressure gradient tends to destabilize the boundary-layer flow, causing it to separate from the wall of the nozzle. The ambient pressure can "leak up" the separated boundary layer, causing the pressure just downstream from the shock wave to be approximately ambient. This converts the normal shock wave into an oblique shock wave. The overall result is that the nozzle operates in almost the same way as a nozzle of a smaller area ratio, still slightly overexpanded but not overexpanded to the extent implied by the quasi-one-dimensional theory for the original nozzle. This jet-detachment phenomenon is illustrated in Fig. 2-14 and is also discussed (9), (79-82).

The location of the separation point in the nozzle can be estimated from the experimental observations that the ambient pressure is about 2.5 to 3.5 times the pressure on the wall just upstream from the origin of the oblique shock that triggers the separation. The presence of solid particles in the flow has been observed to reduce this pressure ratio to perhaps 1.7. For a nozzle of fixed geometry, as the ambient pressure increases the separation point moves farther upstream leaving more of the downstream part of the nozzle as useless excess weight. The location of the separation point is a smooth function of ambient pressure for conical nozzles of reasonable divergence angles, but for bell-shaped nozzles the separation point depends strongly on ambient pressure when conditions are such that separation occurs near the exit of the nozzle. This strong dependence has been observed to lead to oscillations in the location of the separation point, thus implying that a divergence half-angle exceeding about 10° is desirable for maintaining steady over-expanded flow patterns. The nature of the flow pattern that develops as the separation point approaches the throat of the nozzle is still in question.

Jet detachment influences the off-design performance of the nozzle and the rate of heat transfer to the nozzle wall. The modification in performance parameters is easily obtained by employing the appropriate formulas of Section 1.3 - 1.5 to calculate the performance parameters of the given nozzle, and then employing the appropriate formulas of the same sections to calculate the performance parameters of a truncated nozzle (truncated at a point where the pressure is roughly 1/3 of ambient pressure). The truncated nozzle is found to have a higher thrust, so jet detachment improves performance. Usually, it also causes the wall heat transfer

rate to decrease somewhat in the region downstream from the point of separation. In contoured nozzles, the onset of detachment is usually found to occur at higher ambient pressures than in conical nozzles, so that conical nozzles tend to exhibit better low-altitude, off-design performance than contoured nozzles.

The effects of jet detachment must be kept in mind in deciding whether to use a nozzle with a contour optimized for a particular altitude or a simple conical nozzle.

5.4. Interaction of the External Exhaust Jet with its Surroundings

A number of nonideal effects of the external exhaust jet flow deserve to be mentioned.

First, we note that flow of the ambient atmosphere around a moving vehicle may interact with the exhaust jet. This may influence both drag and thrust through separation effects. (Appreciably underexpanded exhaust jets tend to cause the boundary layer on the external surface of the vehicle to separate, thereby reducing skin friction drag.)

Secondly we note that when the jet becomes appreciably underexpanded (as all jets do at sufficiently high altitudes), the ideal jet pattern shown in Fig. 2-6b is no longer attained. Instead, the jet boundary blooms nearly radially outward from the lip of the nozzle exit (it can move forward on the exterior side of the nozzle at sufficiently low ambient pressures), an oblique shock wave develops inside the jet boundary, and some distance downstream this shock wave intersects an oblique shock that extends to the jet boundary and a nearly normal shock that crosses the jet axis at right angles. This pattern, which is illustrated schematically in Fig. 2-15, may be repeated (with some modifications) further downstream. Our present rather detailed knowledge of the character of this flow pattern was obtained in studies reported in Refs. (71), (83-88), although general features of the pattern were known much earlier (9).

The illustrated pattern is governed almost entirely by inviscid phenomena and is influenced somewhat by ambient flow past the jet (resulting from movement of the motor through the atmosphere). Theoretical calculations employing the method of characteristics have reproduced the pattern shown, and simple analytical approximations exist for gross parameters such as the axial distance from the exit plane to the normal shock. The fluid dynamics of single exhaust plumes are therefore reasonably well understood. On the other hand, for multi-engine vehicles, the fluid flow in the exhaust region is poorly understood, and even for single plumes the chemical kinetic processes that produce regions of luminosity, ionization, and appreciable radiant energy emission are not well understood.

Solid propellant rockets usually have highly luminous exhaust plumes that prevent one from observing the detailed wave patterns (such as those shown in Fig. 2-7). This is particularly true for metalized systems, which exhibit high rates of emission of radiant energy. Metalized solid propellants also produce greatly increased electron densities in the exhaust plume (because exhaust temperatures are higher and metals ionize easily). These special characteristics have practical consequences, see below.

One of the primary practical effects of the external exhaust flow is to produce heat transfer to the external surfaces of the rocket vehicle and to its surroundings. Convective, conductive and radiative heat transfer processes each play a role here. Which mechanism is dominant in transferring heat to the base of the vehicle and to other surfaces depends on base geometry, ambient pressure, and other conditions. It is therefore impractical to attempt to present general results for rates of heat transfer to external surfaces; each case must be considered individually.

External exhaust plume structure also determines where the combustion products

will be deposited. This information is of practical interest if any of the products of combustion are toxic.

Ionization in rocket exhausts can block radio communications with the vehicle by reflecting and absorbing electromagnetic waves. These interference phenomena can be calculated relatively easily if the spatial and temporal distributions of electron density in the plume, including the statistics of turbulent electron density fluctuations, are known. The aim of research on communications interference is therefore to obtain electron density distributions.

Finally, the ionization and spectral light emission characteristics of rocket plumes may enable an observer to identify properties of the rocket vehicle, propulsion system, or propellant composition. It is therefore of interest to attempt to reduce these observables.

6. Thrust Vector Control

6.1. Introduction

The term 'thrust vector control' refers to methods for varying the direction of the thrust vector of a rocket motor for purposes of controlling the flight path of a rocket-propelled vehicle. Three separate classes of methods (aside from the use of multiple rocket motors) are available for varying (primarily) the direction of the thrust vector of a rocket motor. These are mounting the motor on gimbals so that the motor as a whole can turn, employing mechanical control surfaces in the exhaust jet of the motor to deflect the jet exhaust, and injecting fluid into the wall of the exhaust nozzle in order to deflect the jet exhaust. Motor gimbaling may be practical for very small solid-propellant motors (e.g., vernier rockets) designed to control a larger vehicle, but it is usually impractical for moderate- or large-sized solid-propellant motors, or for any solid-propellant motor that serves as the primary propulsive device of a vehicle, because of the great weight of the motor (which must carry all of its propellant within it). Therefore we shall not discuss motor gimbaling here. The other two methods, mechanical control surfaces (including techniques for nozzle deflection) and fluid injection, are considered in the two following sections. The relative effects of these directional control devices on the magnitude of the thrust and the impulse will be covered very briefly in Section 6.4.

6.2. Mechanical Control Surfaces (9)

A variety of mechanical surfaces have been employed for deflecting the exhaust jets of solid-propellant rockets. Jet vane defectors, permanently located in the exhaust jet, are illustrated schematically in Fig. 2-16. The effect of the vanes on the exhaust jet can be calculated approximately from aero-dynamic theory of an airfoil in supersonic flow. To obtain accurate values of the side force (the component of thrust normal to the axis of the motor) as a function of the deflection angle of the vanes, theory must be supplemented by experimental measurements. Typically, a maximum side force about 20% as large as the axial thrust can be obtained reproducibly.

Disadvantages of locating vanes permanently in the exhaust include a permanent loss of thrust due to vane drag and severe problems in maintaining strength and integrity of the vanes under the high dynamic pressure and high heat flux conditions that they experience. For motors with sufficiently short burning times, graphite and molybdenum have been used successfully as vane materials; they are often supported internally by high-strength metals. Ablation heat shields, such as phenolic nylon or phenolic refrasil, usually provide a better degree of thermal protection for longer burning times.

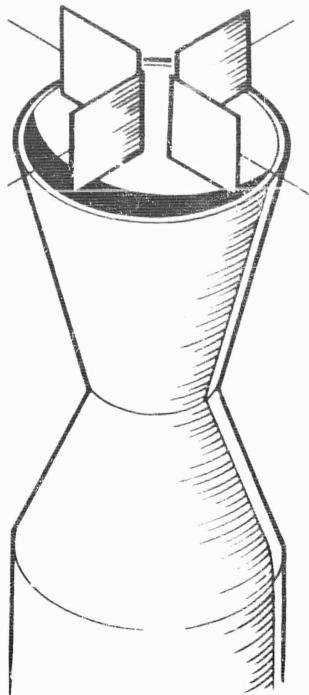


Fig. 2-16 Thrust vector control obtained by jet vane deflectors, from Ref. (9).

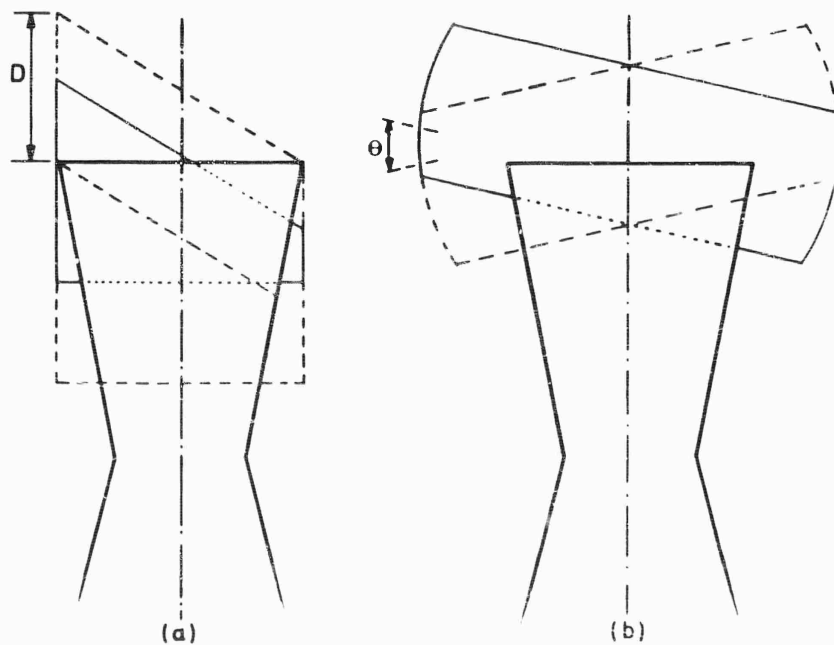


Fig. 2-17 Thrust vector control obtained by a bevelled extension (a) and by a jetavator (b) from Ref. (9).

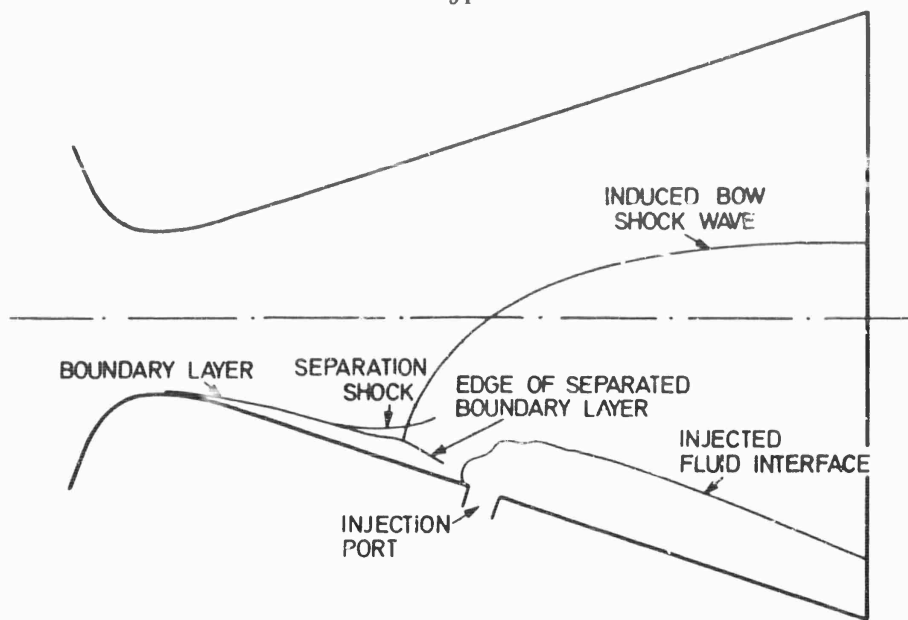


Fig. 2-18 Schematic diagram of nozzle flow induced by injecting a fluid through the wall of the divergent section.

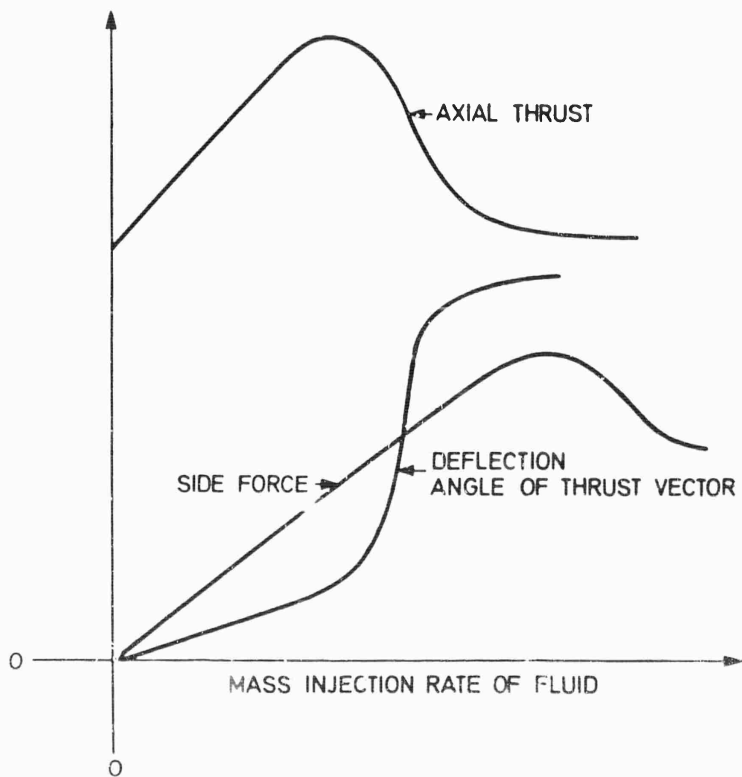


Fig. 2-19 Schematic illustration of dependence of axial thrust, side force and deflection angle of thrust vector on injection rate of TVC fluid.

Elimination of the loss in axial thrust under zero jet deflection conditions and some reduction in the severity of the heating problem are provided by sleeve designs such as those illustrated in Fig. 2-17. These devices interfere with the jet only when deflecting it. A related approach which in some respects can be considered to represent an extreme version of devices of the type illustrated in Fig. 2-17b, is to deflect the nozzle of the motor. For solid propellant motors, control of the thrust vector can be achieved by gimbaling the nozzle or by constructing the motor with a four-nozzle system that can be rotated.

6.3. Fluid Injection

6.3.1. Description of the Phenomenon - The thrust loss and heating problems are practically eliminated if the jet is deflected by injecting a fluid through the wall of the nozzle instead of employing solid surfaces. A schematic diagram of this method of thrust vector control is presented in Fig. 2-18. Fluid injection has received a considerable amount of attention recently, from the standpoints of theoretical and experimental research as well as practical application (89-101). It has now been demonstrated that fluid injection schemes can produce a sufficient side force to meet the requirements of many applications.

From Fig. 2-18 it can be seen that in addition to displacing a portion of the nozzle fluid, the injected fluid produces a shock wave in the nozzle that propagates through a significant fraction of the flow. The side force therefore results from two phenomena; the momentum flux (plus pressure forces) across the injection port of the injected material produces a side reaction force, and the modified pressure distribution on the wall of the nozzle gives rise to an additional side force. The added pressure effect increases the side force above that which would be obtained were the injectant to be exhausted directly into the ambient atmosphere (an increase by a factor of 2 or 3 is typical for gas injection (95)). It should be apparent from Fig. 2-18 that were the injection port to be moved closer to the throat of the nozzle, then a larger fraction of the primary nozzle flow would be influenced by the shock wave, and the side force would be increased. Similarly, increasing the mass flow rate of injectant affects a larger fraction of the primary flow and increases the side force. Injection also increases the axial component of the thrust; the shock wave usually tends to decrease the axial thrust, but this phenomenon is offset by the increase in axial mass flow rate due to injectant addition, and the thrust increase resulting from the increased flow rate is the dominant effect at low injection rates. At higher injection rates, the shock wave begins to intercept the opposite wall, affecting all of the primary nozzle flow, and the axial thrust begins to decrease. At still higher flow rates, interaction of the injected flow with the opposite wall causes the side force to begin to decrease. This behavior and its influence on the deflection angle of the thrust vector are illustrated schematically in Fig. 2-19. Deflection angles of 7° can now be obtained reliably with liquid injection, and angles exceeding 10° can be produced with gas injection.

6.3.2. Theoretical Analyses - Theoretical analyses of the flow field induced by fluid injection may be found in Refs. (93), (96), (99-101). The analyses are applicable only to the region at small values of the injection rate. Here we shall present a discussion of the qualitative dependence of the side force on injection and flow parameters, based on ideas developed (99). Our discussion will be applicable for the injection of either a gas or a nonvaporizing liquid.

Based on experimental observations, it is reasonable to approximate the shape of the boundary between the injected fluid and the primary nozzle fluid as half of a circular cylinder with a hemispherical nose cap. The pressure force parallel to the wall that the primary nozzle fluid exerts on this surface is proportional to $r^2 p$, where r is the radius of the cylinder, p is the average free stream static pressure, and the constant of proportionality depends on the free stream Mach number and

the specific heat ratio of the primary fluid. A force balance implies that this pressure force accelerates the injected fluid until its momentum flow rate parallel to the wall equals the pressure force. Here, any vaporization, mixing or viscous, forces acting at the boundary of the injected jet are neglected. We obtain :

$$\dot{m}_j v_{j\infty} \sim r^2 p, \quad (\text{Eq. 2-93})$$

where \dot{m}_j is the mass injection rate (assumed equal to the asymptotic mass flow rate of injectant parallel to the wall) and $v_{j\infty}$ is the asymptotic flow velocity of the injectant. It may be assumed that $v_{j\infty}$ is the velocity attained when the injected fluid expands isentropically from a stagnation pressure equal to the known injection pressure p_j at the injection port to the pressure p , and hence $v_{j\infty}$ may be treated as a known parameter which depends only on p_j , p and thermodynamic properties of the injectant. Equation 2-93 therefore determines the geometrical parameter r and shows that $r \sim \sqrt{\dot{m}_j v_{j\infty} / p}$.

The force normal to the wall is composed of the momentum flow rate of the injectant normal to the wall at the injection port, $\dot{m}_j v_j$ (where v_j is the velocity of injectant normal to the wall at the port exit), the difference between the pressure forces at the exit port with and without injection, (i.e., $(p_j - p)A_j$, where A_j is the exit area of the port), and the difference between the integral over the wall area of the wall pressure with and without injection. (When wall curvature is not negligible in the region affected by the shock wave, only the component of this pressure force that lies along the axis of the injected jet contributes to the net side force.) Computation of this wall pressure force is complicated, but the inviscid fluid flow equations of the primary nozzle fluid imply that the force will be proportional to $r^2 p$, with a proportionality constant depending on the free stream Mach number and the specific heat ratio of the primary nozzle fluid. Assuming that the wall divergence angle is sufficiently small for us to neglect contributions to the side force arising from forces other than the wall pressure force and the injectant momentum, we find that the side force can be written as,

$$F_s = [\dot{m}_j v_j + (p_j - p)A_j] \cos \alpha_c + \beta \dot{m}_j v_{j\infty}, \quad (\text{Eq. 2-94})$$

where α_c is the expansion half-angle of the divergent section of the nozzle and β is a dimensionless proportionality factor that depends on nozzle geometry, the location of the injection port, and the specific heat ratio of the nozzle fluid. Typical values of β are of the order of unity.

6.3.3. Comparison with Experimental Results - A comparison of some predictions of Eq. 2-94 with experiments may be obtained from Figs. 2-20 and 2-21. It will be noted that the prediction $F_s \sim \dot{m}_j$, valid when $(p_j - p)A_j$ is either negligible or proportional to \dot{m}_j , is borne out by all of the experiments. Furthermore, Fig. 2-20 shows that the slope of the curve of F_s vs. \dot{m}_j for gas injection depends on what gas is injected. This can be traced to the dependence $v_{j\infty} \sim \sqrt{RT_j} = \sqrt{R^0 T_j / m}$ for isentropic expansion of a gas from the jet temperature T_j and pressure p_j to pressure p , which implies that the constant of proportionality between F_s and \dot{m}_j depends on the molecular weight m . Numerical calculations (96) for gas injection based on a formula like Eq. 2-94, in which the molecular weight dependence is evaluated, are seen to agree well with experiment. The absence of a dependence of the slope of the curve of F_s vs. \dot{m}_j on the area A_j (see Eq. 2-94) for gas injection has also been verified experimentally (99). On the other hand for injection of a volatile liquid such as freon, the slope of the F_s vs. \dot{m}_j curve does depend on the port area A_j (see Fig. 2-21). This has been explained as arising from vaporization of the liquid, an effect that was neglected in the arguments that led to Eq. 2-94. A theory that accounts for vaporization of a volatile injected liquid is given in Ref. (93).

6.3.4. Choice of Injectant Fluid - Experiments have been performed with numer-

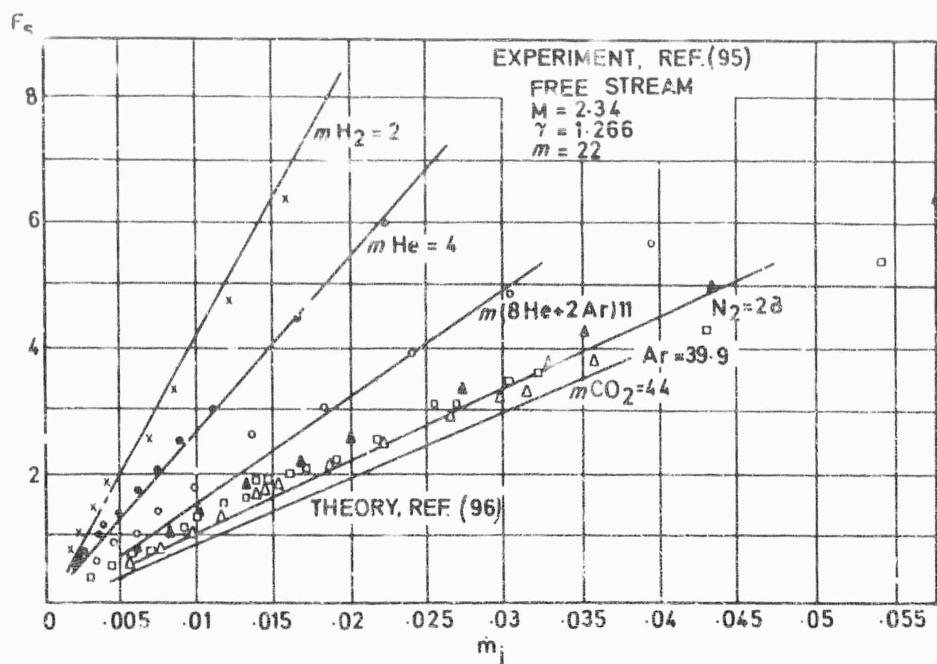


Fig. 2-20 Effect of molecular weight on curve of side force (in pounds) vs injectant mass flow (in pounds mass per second) for gas injection, from Ref. (96). Injector diameter = 0.0625 in., main axial thrust = 111.2 lb.; primary flow rate = 0.84 pounds mass per second.

SIDE FORCE:
 MAIN AXIAL THRUST

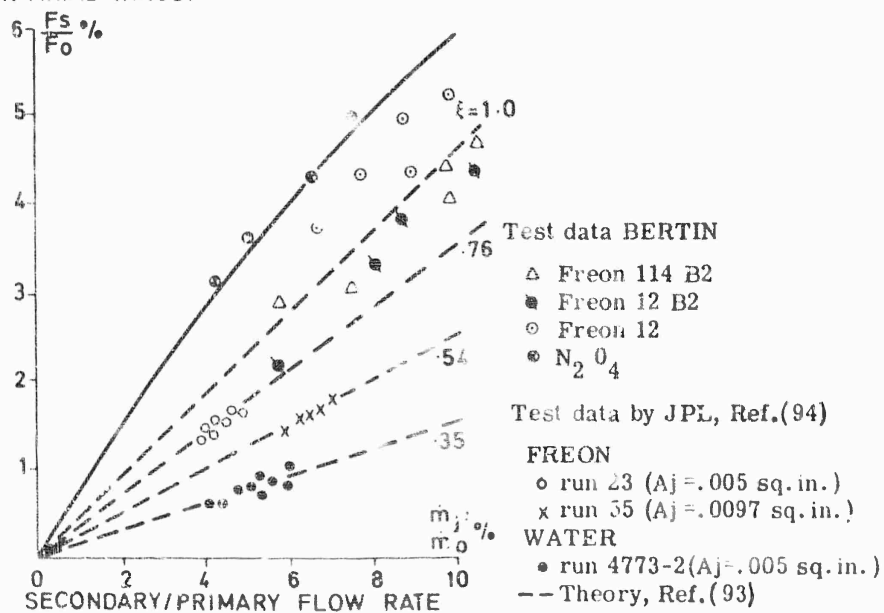


Fig. 2-21 Effect of fraction of fluid vaporized (ξ) and area of injector port (A_j) on curve of side force as a function of injected mass flow rate for liquid injection.

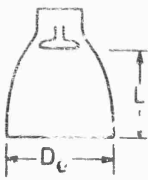
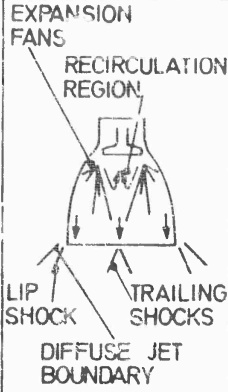
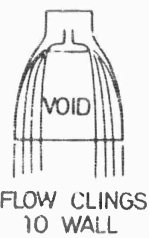

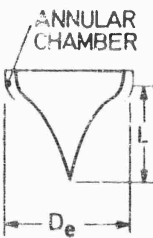
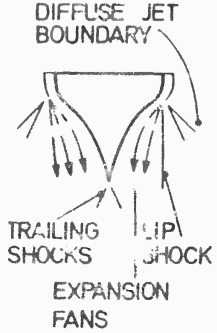
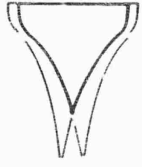
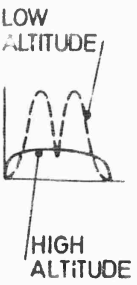
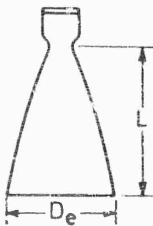
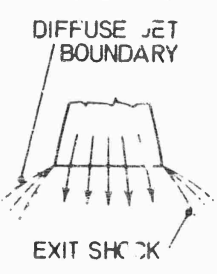


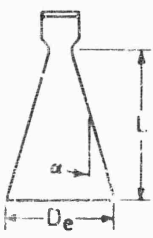
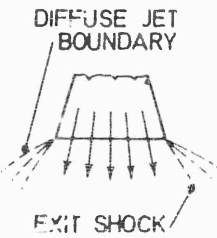
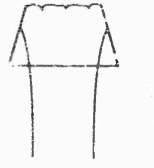
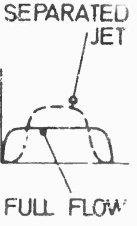
	SHAPE	FLOW WITH UNDEREXPANSION, ALTITUDE	FLOW WITH OVEREXPANSION, (SEA LEVEL)	MASS FLOW DISTRIBUTION, AT EXIT
EXPANSION-DEFLECTION				
PLUG				
CONToured OR BELL-SHAPED				
CONE				

Fig. 2-22 Properties of plug nozzles and expansion-deflection nozzles, and comparison with more conventional nozzles (from Ref. (10), courtesy John Wiley and Sons).

ous injectant fluids. In addition to those indicated in Fig. 2-20 and 2-21, studies have been made of liquid nitrogen (98). A number of injectants have been studied which are capable of reacting exothermically either alone or with the combustion products. Points for one such injectant, N_2O_4 , appear in Fig. 2-21.

Storage problems and mechanical problems of injection are less severe for liquids than for gases for given values of the total injectant mass and mass flow rate. However, the side force at a given injection rate is appreciably lower with liquid injection (compare Fig. 2-20 and 2-21). Liquids can provide sufficiently large side forces at acceptable injection rates only if they produce enough vapor. Freon is an example of such a liquid; at present, freon is a very promising injectant for a number of applications.

If the weight penalty for the storage and injection systems permits the use of gas injection, then it is desirable to inject a gas with a low molecular weight (see Fig. 2-20; recall that $v_{j\infty} \sim 1/\sqrt{m}$). It is also desirable to inject gas at a high temperature (recall that $v_{j\infty} \sim \sqrt{T_j}$). But here again, additional weight and design problems arise for hot gas injection.

Injection of a reacting gas can increase the side thrust by a mechanism somewhat analogous to that occurring with the injection of a hot gas, provided that the reacting gas can be made to liberate its heat inside the nozzle instead of in the external exhaust. The high velocities in the diverging portion of the nozzle impose the requirement of a very short chemical reaction time in order for a reacting gaseous injectant to be effective. Theoretical formulas for the increase in side force due to heat liberation by the injected fluid may be found (101).

6.3.5. Hot Gas Valves - The necessity of storing a fluid injectant can be eliminated if some propellant gases from the combustion chamber can be injected through the nozzle wall. Furthermore, much smaller injectant flow rates of propellant gases would be needed to produce a given side force, because the propellant gases have high temperatures and low molecular weights. All that is required is a valve for regulating a small mass flow of propellant gases from the chamber to a port in the nozzle wall.

To develop such a hot gas valve is a formidable problem. A considerable amount of effort has been spent on this problem, but it has not been solved yet. Nevertheless, with continued effort, one may expect to find hot gas valves controlling the thrust vectors of future solid-propellant rocket motors.

6.4. Comparison of Mechanical and Fluid Injection Thrust Vector Control

The relative weight penalties of mechanical- and fluid-injection devices for directing the thrust vector depend upon the specific application. However, it may be stated that use of mechanical devices always leads to a (small) decrease in the magnitude of the axial thrust and the total impulse, while fluid injection increases these performance parameters.

7. Compatibility of Solid-Propellant Motors with New Nozzle Design Concepts

In recent years, various new concepts of nozzle design have been proposed. Notable among them are the plug nozzle and the expansion-deflection (ED) nozzle. The properties of these nozzles are described and compared with those of more conventional nozzles in Fig. 2-22. We shall consider briefly the compatibility of these nozzles with solid-propellant motors.

First, we note that the plug and ED nozzles, and also the intermediate but less sophisticated double-cone nozzle (with a central pointed cone and an outer diverging cone, possibly of differing cone angles) are all essentially annular type nozzles. As such, they are particularly suitable for solid-propellant combustion chambers

with annular grains. The mechanical supports required for annular grains could be adapted relatively easily to serve as supports for the plug or deflector as well. The new nozzles lend themselves well to grain designs giving approximately neutral thrust-time curves. The ED nozzles may be best suited for slightly progressive burning, while the plug nozzle, with the larger central portion, may work best for slightly regressive burning. Exploitation of this compatibility in developing integrated chamber-nozzle designs for particular applications appears to be warranted, especially for large solid-propellant rocket boosters.

References

- (1) **Spalding D.B. and Cole E.H.**, Engineering Thermodynamics. Edward Arnold Ltd., London, 1958.
- (2) **Lee J.F. and Sears F.W.**, Thermodynamics. Addison-Wesley Publishing Co., Reading, Massachusetts, 2nd edition, 1963.
- (3) **Li W.H. and Lam S.H.**, Principles of Fluid Mechanics. Addison-Wesley Publishing Co., Reading, Massachusetts, 1964.
- (4) **Shapiro A.H.**, The Dynamics and Thermodynamics of Compressible Fluid Flow. The Ronald Press, New York, 1953.
- (5) **Williams F.A.**, Combustion Theory. Addison-Wesley Publishing Co., pp. 4-9, 61, 62, Reading, Massachusetts, 1965.
- (6) **Marks L.S.**, Mechanical Engineering Handbook. McGraw-Hill Book Co., New York, 6th edition, pp. 3-72, 3-73, 3-78, 11-79 to 11-87, 1958.
- (7) **Hall, N.A.**, Thermodynamics of Fluid Flow. Ice-Hall, Englewood Cliffs, N.J., pp. 26-35, 1951.
- (8) **Keenan J.H. and Kaye J.**, Gas Tables. John Wiley and Sons, New York, 1948.
- (9) **Barrère M., Jaumotte A., Fraeijs de Veubeke B., and Vandekerckhove J.**, Rocket Propulsion. Elsevier Publishing Co., New York, 1960.
- (10) **Sutton G.P.**, Rocket Propulsion Elements. John Wiley and Sons, New York, 3rd edition, 1963.
- (11) **Penner S.S.**, Chemistry Problems in Jet Propulsion. Pergamon Press, New York, 1958.
- (12) **Olson W.T.**, ARS Journal 32, 675, 1962.
- (13) **Krieger F.J.**, J. Am. Rocket Soc. 21, 179, 1951.
- (14) **Curtiss C.F., and Hirschfelder J.O.**, Proc. Natl. Acad. Sci. 38, 235 (1952).
- (15) **Heims S.P.**, NACA Tech. Note No. 4144, 1958.
- (16) **Bray K.N.C.**, J. Fluid Mech. 6, 1, 1959.

- (17) Emanuel G., and Vincenti W.G., Method of calculation of the one-dimensional nonequilibrium flow of a general gas mixture through a hypersonic nozzle. Arnold Engineering Development Center TDR-62-131, 1962.
- (18) Westenberg A.A., and Favin S., Ninth International Symposium on Combustion. Academic Press, New York, p. 785, 1963.
- (19) Bray, K.N.C., Ninth International Symposium on Combustion. Academic Press, New York, pp. 770-784, 1963.
- (20) Brainerd J.J., and Levinsky E.S., AIAA J. 1, 2474, 1963.
- (21) Gravalos F.G., The flow of a chemically reacting gas mixture. General Electric Document 63 SD 200, 1963.
- (22) Emanuel G., Problems underlying the numerical integration of the chemical and vibrational rate equations in a near-equilibrium flow. Arnold Engineering Development Center TDR-63-82, 1963.
- (23) Moretti G., AIAA J. 3, 223, 1965.
- (24) DeGroat J., and Abbett M., AIAA J. 3, 381, 1965.
- (25) Penner S.S., and Altman D., J. Franklin Inst. 245, 421, 1948.
- (26) Altman D., and Penner S.S., J. Chem. Phys. 17, 56, 1945.
- (27) Penner S.S., J. Am. Chem. Soc. 71, 788, 1949.
- (28) Penner S.S., J. Franklin Inst. 249, 441, 1950.
- (29) Penner S.S., J. Chem. Phys. 17, 841, 1949.
- (30) Penner S.S., Introduction to the Study of Chemical Reactions in Flow Systems. Butterworths Scientific Publications, London, Chapter 3, 1955.
- (31) Altman D., and Carter J.M., Expansion Processes, in Combustion Processes. Vol. II of High Speed Aerodynamics and Jet Propulsion, edited by B. Lewis, R.N. Pease, and H.S. Taylor, Princeton University Press, Princeton, N.J., pp. 26-63, 1956.
- (32) Rudin M., Phys. Fluids 1, 384, 1958.
- (33) Rudin M., and Aroeste H., Combustion and Flame 3, 273, 1959.
- (34) Leard M., Gas dynamics of chemically reacting gas mixtures near equilibrium. General Electric Co., Space Science Lab. Rept. No. R62 SD985, 1962.
- (35) Williams F.A., Phys. Fluids 7, 620, 1964.
- (36) Lenard M., Phys. Fluids 8, 550, 1965.
- (37) Stollery J.L., and Smith J.E., J. Fluid Mech. 13, 225, 1962.
- (38) Vandenkerckhove J., Généralisation de la théorie des tuyères à certains cas particuliers d'écoulements hétérogènes. Revue M. 4, No. 1, 1958.

- (39) **Amman D., and Carter J.M.,** Expansion Processes. in Combustion Processes, Vol. II of High Speed Aerodynamics and Jet Propulsion, edited by B. Lewis, R.N. Pease and H. S. Taylor, Princeton University Press, Princeton, N.J., Chapter B, 1956.
- (40) **Wilde K. A.,** Jet Propulsion 27, 668, 1957.
- (41) **Maxwell W.R., Dickenson W., and Caldin E. F.,** Aircraft Eng. 18, 350, 1946.
- (42) **Greene S.A. and Gordon L.J.,** Jet Propulsion 27, 667, 1957.
- (43) **Rannie W.D.,** A perturbation analysis of one-dimensional heterogeneous flow in rocket nozzles. Progress in Astronautics and Rocketry: Detonation and Two-Phase Flow, Vol. 6, edited by S.S. Penner and F.A. Williams, Academic Press, New York, pp.117-144, 1962.
- (44) **Marble F.E.,** Dynamics of a gas containing small solid particles. Proceedings of the Fifth AGARD Combustion and Propulsion Colloquium, Pergamon Press, New York, 1963
- (45) **Marble F.E.,** AIAA J. 1, 2793, 1963.
- (46) **Gilbert M., Davis D., and Altman D.,** Jet Propulsion 25, 26, 1955.
- (47) **Kliegel J.R.,** One dimensional flow of a gas particle system. Space Technology Labs. TR-59-0000-00746, 1959; IAS Paper 60-3, Jan. 1960.
- (48) **Kliegel J.R., and Nickerson G.R.,** Flow of gas-particle mixtures in axially symmetric nozzles. ARS Preprint 1713-61 (April 1961); Progress in Astronautics and Rocketry: Detonation and Two-Phase Flow, Vol. 6, edited by S.S. Penner and F.A. Williams, Academic Press, New York, pp.173-194, 1962.
- (49) **Morgenthaler J.H.,** Analysis of two-phase flow in supersonic exhausts. ARS Preprint 1715-61 (April 1961); Progress in Astronautics and Rocketry: Detonation and Two-Phase Flow, Vol. 6, edited by S.S. Penner and F.A. Williams, Academic Press, New York, pp.145-172, 1962.
- (50) **Glauz R.D.,** Combined subsonic-supersonic gas-particle flow. ARS Preprint 1717-61, April 1961.
- (51) **Bailey W.S., Nilson E.N., Serra R.A., and Zupnik T.F.,** ARS J. 31, 793, 1961.
- (52) **Hogland R. F.,** ARS J. 32, 662, 1962.
- (53) **Lype E. F.,** One dimensional analysis of non-entropic two-phase flow. ARS Preprint 1605-61, February 1961.
- (54) **Courtney W.G.,** ARS J. 31, 751, 1961.
- (55) **Langmuir I., and Blodgett K.B.,** General Electric Report RL-225 (1945); J. Meteor. 5, 175, 1948.
- (56) **Ranz W., and Wang J.,** Ind. Eng. Chem 44, 1371, 1952.

- (57) **Fuchs N.A.**, The Mechanics of Aerosols. The Macmillan Company, New York, pp.159, 181, 1964.
- (58) **Lindblad N.R.**, and **Semonin R.G.**, J. Geophys. Res. 68, 1051, 1963.
- (59) **Soo S.L.**, in Proceedings of Symposium on Interaction between Fluids and Particles, Institute of Chemical Engineers, London, p.50, 1962.
- (60) **Hinze J.O.**, Appl. Sci. Res. A11, 33, 1962.
- (61) **Soo S.L.**, Project SQUID Report ILL-18-P, 1964.
- (62) **Peskin R.L.**, in Proceedings of the Heat Transfer and Fluid Mechanics Institute. Stanford University Press, Stanford, Calif.. 1960.
- (63) **Marble F.E.**, Phys. Fluids 7, 1270, 1964.
- (64) **Culick F.E.C.**, Phys. Fluids 7, 1898, 1964.
- (65) **Brown B.**, and **McArty K.P.**, Particle size of condensed oxides from combustion of metalized solid propellants. Proceedings of the Eighth International Combustion Symposium, Williams and Wilkins Co., Baltimore, Md., p.814, 1962.
- (66) **Seghal R.**, An experimental investigation of a gas-particle system. Jet Propulsion Laboratory TR 32-238, 1962.
- (67) **Povinelli L.A.**, and **Rosenstein R.A.**, AIAA J. 2, 1754, 1964.
- (68) **Cheung H.**, and **Cohen N.S.**, AIAA J, 3, 250, 1965.
- (69) **Brown B.**, Particle velocity lag in metalized propellants. Progress in Astronautics and Rocketry: Detonation and Two-Phase Flow, Vol.6, edited by S.S. Penner and F.A. Williams, Academic Press, New York, pp.195-208, 1962.
- (70) **Carlson D.J.**, Static temperature measurements in hot gas-particle flows. Temperature, Its Measurement and Control in Science and Industry, Reinhold Publishing Corp., New York, 1962; ARSJ. 32. 1107, 1962.
- (71) **Bauer A.B.**, AIAA J. 3. 1187, 1965.
- (72) **McAdams W.H.**, Heat Transmission. McGraw-Hill, New York, 1954.
- (73) **Jacob M.**, Heat Transfer. Vols. I and II, John Wiley and Sons, New York, 1949, 1957.
- (74) **Bartz D.R.**, Survey of the relationship between theory and experiment for convective heat transfer from rocket combustion gases. Advances in Heat Transfer, Vol.II, edited by J. P. Hartnett and T. F. Irvine, Jr., Academic Press, New York, 1965.
- (75) **Colucci S.E.**, Experimental determination of solid rocket nozzle heat transfer coefficient. Ballistic Missile and Space Technology, Vol.II, edited by D. P. LeGalley, Academic Press, New York, pp.303-353. 1960.
- (76) **Rao G.V.R.**, Jet Propulsion 28, 337, 1958.

- (77) Rao G.V.R., ARS J. 31, 1488, 1961.
- (78) Schlichting H., Boundary Layer Theory. McGraw-Hill Book Co., New York, 4th edition, Chapters XXI and XXII, 1960.
- (79) Summerfield M., Foster C.R., and Swan W.C., Flow separation in over-expanded supersonic exhaust nozzles. Paper presented at Heat Transfer and Fluid Mechanics Institute, ASME, Los Angeles, Calif., 1948.
- (80) Scheller J.A., and Bierlein J.A., J. Am. Rocket Soc. 23, 28, 1953.
- (81) McKenney J.D., An Investigation of Flow Separation in Over-Expanded Supersonic Nozzles. Thesis, California Institute of Technology, Pasadena, Calif, 1949.
- (82) Green L., J. Am. Rocket Soc. 23, 34, 1953.
- (83) Adamson T.C. Jr., and Nicholls J.A., J. Aero. Sci., 26, 16, 1959.
- (84) Love E.S., Grigsby C.E., Lee L.P., and Woodling M.J., Experimental and theoretical studies of axisymmetric free jets. NASA TR R-6, 1959.
- (85) Adamson T.C. Jr., The structure of the rocket exhaust plume without reaction at various altitudes. The University of Michigan, Institute of Science and Technology Report No. 4613-45-T, June 1963.
- (86) Eastman D.W., and Radtke L.P., AIAA J. 1, 918, 1963.
- (87) Lewis C.H. Jr., and Carlson D.J., AIAA J. 2, 776, 1964.
- (88) D'Attorre L., and Harshbarger F., Experimental and theoretical studies of underexpanded jets near the mach disc. General Dynamics/Astronautics Rept. GDA-DBE 64-008, Feb. 1964.
- (89) Hausmann G.F., Thrust axis control of supersonic nozzles by airjet shock interference. United Aircraft Corp. Dept. Rept. R-63143-24, May 1952.
- (90) Bankston L.T., and Barnes G.G., Gas injection thrust vectoring. U.S. Naval Ordnance Test Station, NOTS Rept. IDP 662, China Lake California, July 1959.
- (91) Amick J.L., and Hays P.B., Interaction effects of side jets issuing from flat plates and cylinders aligned with a supersonic stream. Wright Air Development Division Technical Rept. 60-329, May 1960.
- (92) Green C.J., and McCullough F. Jr., Liquid injection thrust vector control. Naval Ordnance Test Station, NAVWEPS Rept. 7744, NOTS TD 2711, China Lake, Calif. (June 1961). AIAA J 1, 573, 1963.
- (93) Wu J.M., Chapkis R.L., and Mager A., ARS J. 31, 1677, 1961.
- (94) Newton J.F. Jr., and Spaid F.W., ARS J. 32, 1203, 1962.
- (95) Walker R.E., Stone A.R., and Shandor M., AIAA J. 1, 334, 1963.
- (96) Broadwell J.E., AIAA J. 1, 1911, 1963.

- (97) **Kallis J. M., and Adelberg M.,** Recent advances in the fluid dynamics of gas injection for thrust vector and trajectory control. Aerospace Corporation Rept. No. ATN-63(3305)-3, July 1963.
- (98) **Dowdy M. W., and Newton J. F. Jr.,** Investigation of liquid and gaseous secondary injection phenomena on a flat plate with $M = 2.01$ to $M = 4.54$. Jet Propulsion Laboratory Technical Rept. No. 32-542, Pasadena, Calif. Dec. 1963.
- (99) **Zukoski E. E., and Spaid F. W.,** AIAA J. 2, 1689, 1964.
- (100) **Hsia H. T-S., Seifert H. S., and Karamcheti K.,** Shocks induced by secondary fluid injection. AIAA Preprint 64-111, January 1964.
- (101) **Walker R. E., and Shandor M.,** Influence of injectant properties for fluid injection thrust vector control. AIAA Preprint 64-112, January 1964.
- (102) **Hoffman J. D., and Lorenc S. A.,** AIAA J. 3, 103 (1965); AIAA J. 4, 169, (1966).
- (103) **Carlson D. J.,** AIAA J. 3, 354, 1965.
- (104) **Fulmer R. D., and Wirtz D. P.,** AIAA J, 3, 1506, 1965.
- (105) **Sutton G. P., Wagner W. R., and Seader J. D.,** Advanced Cooling Techniques for Rocket Engines. Astronautics and Aeronautics, Vol. 4, No. 1, pp. 60-71, January 1966.
- (106) **Peters C. E.,** Short Course on Internal Aerodynamics of Rocket Engines. Course Note 58, von Kármán Institute for Fluid Dynamics, Rhode-Saint-Genese, Belgium, April 1966.

Chapter 3

Performance of Solid Propellants

Nomenclature

A	local cross-sectional area of stream tube
a	sound speed
B	nR^0T_c
c^*	characteristic velocity
C_F	thrust coefficient
c_p	specific heat at constant pressure
$C_{p,i}$	molar heat capacity at constant pressure for species i
c_v	specific heat at constant volume
D_p, D_T	thermodynamic coefficients defined in Eq. 3-97
F	thrust
F_i^0	standard molar free energy of species i
h	enthalpy per unit mass
H_i	molar enthalpy of species i
H_i^0	molar heat of formation of species i at standard temperature
I_{sp}	specific impulse
I_t	total impulse
K_p	equilibrium constant for partial pressures
m	total mass of propellant; number of gaseous compounds in the system
M_i	symbol defined in Eq. 3-40
m_j	mass of species j contained in the propellant
\dot{m}_p	propellant mass flow rate
MR	mixture ratio defined in Eq. 3-8
MR_s	stoichiometric mixture ratio
n	total number of compounds in the system; nitrogen percentage by mass; total number of moles of gas-phase species per unit mass of the system
N_i	number of atoms of type i in a molecule
n_i	number of moles of chemical species i in a unit mass of mixture

n_j^c	number of moles (per unit mass of system) of condensed species j
p	total pressure
p_i	partial pressure of species i in the gas
p_{max}	peak pressure
r	regression rate
R^o	universal gas constant
s	entropy per unit mass
S_1^o	standard molar entropy of species i
T	temperature
t_b	burning time
T_1	initial temperature of propellant
u	internal energy per unit mass
v	velocity
$v_{g\perp}$	gas velocity perpendicular to surface
V_I	valence of atom of type I
v_p	particle velocity
\underline{x}	state vector
X_i	mole fraction of gas-phase species i
X_j	mole fraction of species j
\bar{X}_j	symbol defined in Eq. 3-91
X_j^c	symbol defined in Eq. 3-87
Y_j	mass fraction of species j
Z_i	$\ell n X_i$
α_{ik}	number of atoms of the chemical element A^k contained in chemical compound e^i
$\hat{\alpha}_{kj}$	a nonsingular square submatrix of α_{ik}
$\beta_{i,j}$	number of molecules B^j required to construct compound e^i
$\Delta()$	generally denotes change in a quantity ()
Δh^o	standard heat released in a reaction per unit mass of reactant consumed
δ_{ij}	Kronecker delta

δ_j	symbol defined in Eq. 3-29
ξ_c^*, ξ_F, ξ_s	quality indices
λ_j	Lagrange multiplier
μ_i	chemical potential of species i
i	nitrogen index for homogeneous propellant
ν_i, ν_i'	stoichiometric coefficients for species i appearing as a reactant or product, respectively
ρ	gas density
σ	quantity defined in Eq. 3-109
Φ	molecule equivalence ratio defined in Eq. 3-6
φ	overall equivalence ratio for composite propellant defined in Eq. 3-10
\sum_j'	sum over gas-phase basis species

Script Letters

\mathcal{A}^k	symbol for a chemical element
\mathcal{B}^j	a basic constituent
\mathcal{C}^i	symbol for a chemical species
ℓ	number of elements in the system
m_j	gram molecular weight of chemical species j
\mathcal{N}_k	total number of atoms of type k in a unit mass of the chemical system, divided by Avogadro's number
$\hat{\mathcal{N}}_j$	total number of basic constituents of type j in a unit mass of the chemical system, divided by Avogadro's number
\mathcal{V}	volume of strand burner

Superscripts

(a)	approximate solution
c	condensed phase
o	standard
(0)	zeroth approximation
(1)	first approximation

Subscripts

c	chamber conditions
e	equilibrium; exit conditions
F	fuel
f	frozen
g	gas
j	molecule identification
O	oxidizer
p	identifies propellant properties
s	stoichiometric condition identification
t	throat conditions

Performance of Solid Propellants

1 Introduction

The determination of the performance of solid propellants is an important step in the development of the field. It is necessary to calculate somewhat more accurately in solid propellants than in other propellants because the specific impulse is limited to about 300 seconds. An increase of a few seconds in the specific impulse provides an appreciable gain which can affect the choice of propellant. In the present chapter we shall describe two aspects of this problem, first theoretical performance calculations by the various methods that are currently employed and then experimental techniques that are used to verify these results.

In general, exothermic combustion reactions require two reactants, an oxidizer and a fuel, which are distinguished by their positions in the periodic table (1) (2). Chemical elements which act as fuels are hydrogen, lithium, beryllium, boron, carbon, sodium, magnesium, aluminium, silicon, etc ..., while elements which acts as oxidizers are oxygen, fluorine, chlorine, etc.. nitrogen is a neutral element in this context. Thus, fuels generally fall in the chemical groups 1 through 4, oxidizers are in groups 6 and 7 and group 5 separates fuels from oxidizers. A solid propellant constituent which contains both fuel and oxidizer elements can be denoted by the general chemical formula :



The indices C, H, B, \dots, O, F indicate the number of atoms of each type contained in the molecule.

The gram molecular weight of the propellant constituent identified in Eq. 3-1 is :

$$m = C m_C + H m_H + B m_B + \dots + O m_O + F m_F \quad (\text{Eq. 3-2})$$

where m_C, m_H, \dots are the molecular weights of the elements. In describing propellant compositions, one often specifies $[6.06 \times 10^{23}]^{-1}$ times the number of atoms in a kilogram of the material instead of the number of atoms in a molecule of the material. The corresponding chemical formula would be :



where the lower case indices are defined by :

$$\frac{C}{c} = \frac{H}{h} = \frac{B}{b} = \dots = \frac{O}{o} = \frac{F}{f} = \frac{m}{10^3}$$

For example, nitroglycerin, which is a constituent of homogeneous solid propellants has the molecular formula $C_3H_5N_3O_9$, and the formula $C_{13.2}H_{22.0}N_{13.2}O_{39.7}$ based on gross-weight.

We note that the notation of Eq. 3-3 can also be used to describe the composition of multimolecular mixtures. If a system contains n different chemical species j , each present in a mole fraction X_j and each having lower-case indices c_j, h_j, \dots , then the values of the gross-weight indices c, h, \dots that appear in the form of Eq. 3-3 which describes the overall mixture are, (1), (3) :

$$c = \sum_{j=1}^n X_j c_j, \quad h = \sum_{j=1}^n X_j h_j, \dots \quad (\text{Eq. 3-4})$$

1.1 Definition of Mixture Ratio

Molecular constituents of solid propellants are often composed of both fuel and oxidizer elements which can combine chemically to produce gaseous reaction products. For any given molecular constituent, this chemical combination can occur in such a way that all of the elements (except nitrogen) from molecules with saturated chemical bonds i.e., stoichiometrically, provided that the total number of oxidizer valences equals the total number of fuel valences, i.e.

$$\left[\sum_i N_i V_i \right]_O = \left[\sum_i N_i V_i \right]_F \quad (\text{Eq. 3-5})$$

where N_i is the number of atoms of type i in the molecule, V_i is the valence of an atom of type i , and the subscripts O and F imply that the sums are to be carried over oxidizer and fuel elements, respectively (4). In general, we define the equivalence ratio of a molecule as :

$$\Phi = \frac{\left[\sum_i N_i V_i \right]_O}{\left[\sum_i N_i V_i \right]_F} \quad (\text{Eq. 3-6})$$

This quantity is unity for molecules of stoichiometric composition but in general it differs from unity. In the case of nitroglycerin, for example, $\Phi = 2 \times 9 / (3 \times 4 + 5) = 18 / 17$; thus this molecule contains an excess of oxidizer. We note that this definition of Φ can be generalized to multimolecular systems according to the formula :

$$\Phi = \sum_j X_j \left[\sum_i N_{ji} V_{ji} \right]_O / \sum_j X_j \left[\sum_i N_{ji} V_{ji} \right]_F$$

in which the subscript j identifies the different molecules. Although the molecular equivalence ratio Φ may be defined for any molecule, it is useful only for certain molecular constituents of propellants, as we now indicate.

One may define two classes of solid propellants : (a) homogeneous solid propellants are propellants that contain no nonhomogeneities of dimensions which are larger than the sizes of macromolecules. These propellants generally contain fuel and oxidizer elements in the same molecule. A pure substance of this type is called a propellant base. The most common propellant bases are nitroglycerin and nitrocellulose ($C_{24}H_{28}O_{44}N_{12}$). Single base propellants contain only one base (e.g., nitrocellulose). Most homogeneous propellants are double base and contain both nitrocellulose and nitroglycerin. (b) Heterogeneous solid propellants are propellants that contain nonhomogeneities of dimensions which are larger than the sizes of macromolecules. The heterogeneous propellants of

interest to us in this section are composite propellants which contain macroscopic oxidizer particles (e.g., ammonium perchlorate, NH_4ClO_4) in a plastic fuel matrix called the binder.

Molecular equivalence ratios are most useful in discussing bases of homogeneous propellants; they would take on the values 0 and ∞ for many fuel and oxidizer molecules that are used as constituents in heterogeneous propellants. For composite propellants, one speaks of the overall mixture ratio, which is defined in a manner similar to that of liquid bipropellants and which describes the overall propellant composition. The stoichiometric mixture ratio is :

$$\text{MR}_s = \left[m_F / m_O \right]_s \quad (\text{Eq. 3-7})$$

where the subscript s identifies stoichiometric conditions and m_F and m_O are the masses of fuel and oxidizer, respectively, contained in the propellant. In using Eq. 3-1 of course one first identifies the fuel molecules and the oxidizer molecules of the propellant. The mixture ratio of any given composite propellant formulation is simply :

$$\text{MR} = m_F / m_O \quad (\text{Eq. 3-8})$$

When the propellant contains only one type of molecule that acts as a fuel and only one type of molecule that acts as an oxidizer, it is clear that :

$$\text{MR}_s = \frac{m_F}{m_O} \frac{\left[\sum_i N_i V_i \right]_O}{\left[\sum_i N_i V_i \right]_F} \quad (\text{Eq. 3-9})$$

where the definitions of the sums differ from those appearing in Eq. 3-6 because the sums are now to be taken over all elements of the oxidizer (fuel) molecule, with the valences of oxidizer elements (fuel elements) taken to be positive and the valences of fuel elements (oxidizer elements) taken to be negative. For example, the oxidizer NH_4ClO_4 would have $\left[\sum_i N_i V_i \right]_O = 0 \times 1 - 4 \times 1 + 1 \times 1 + 4 \times 2 = 5$ here.

The reader may derive the generalizations of Eq. 3-9 which are applicable to systems with more than one fuel and oxidizer.

The overall equivalence ratio for a composite propellant is defined as the ratio of the mixture ratio to the stoichiometric mixture ratio :

$$\phi = \frac{\text{MR}}{\text{MR}_s} \quad (\text{Eq. 3-10})$$

which is unity for stoichiometric propellant formulations.

In technical analyses of solid propellants, one often uses the mass fraction of the molecular species j :

$$Y_j = m_j / m \quad (\text{Eq. 3-11})$$

where $m = \sum_j m_j$ is the total mass of the propellant. For example, with a propellant containing the three chemical components : ammonium perchlorate (AP), polyurethane (PU) and aluminum (Al), we have:

$$Y_{AP} = m_{AP} / m, \quad Y_{PU} = m_{PU} / m, \quad Y_{Al} = m_{Al} / m,$$

and the mixture ratio is :

$$MR = (Y_{AI} + Y_{PU}) / Y_{AP} \quad (\text{Eq. 3-12})$$

We note that occasionally other nomenclature (e.g. mixture ratios defined as the ratio of the oxidizer mass to fuel mass, or mixture ratios based on number of moles) may be found in the literature.

1.2 Composition of Propellants and of Products of Combustion

1.2.1 Propellants - Homogeneous Propellants

The most common homogeneous solid propellants are mixtures of nitroglycerin ($C_3H_5(ONO_2)_3$) with solid nitrate esters such as nitrocellulose. Typical chemical formulas of the second constituent can be expressed in the form :



for which the molecular weight is $m = 648 + 45\nu$ and the nitrogen percentage by mass is $n = 1400\nu / (648 + 45\nu)$. In the various applications, n generally lies between 11 and 14.

A representative propellant composition is that of JPN which is listed below.

Composition of JPN Propellant	percent
Nitrocellulose (13.25% nitrogen)	51.5
Nitroglycerin	43
Diethylphthalate	3.25
Potassium sulfate (flash-suppressor)	1.25
Ethyl centralite (asym-diethyldiphenylurea)	1.0
Carbon black	0.2
Wax	0.08
Density	1.62g/cm ³

We note that most homogeneous propellants contain a large percentage of nitrocellulose plasticized (made malleable) by a liquid nitric ester, so that the final propellant will have the consistency of a gel. They also contain stabilizers to prevent the chemical composition from changing (diphenylamine, ethyl centralite, diethylphenylurea); the slow degradation of nitroglycerin and nitrocellulose liberates compounds (oxides of nitrogen) which accelerate the decomposition, and the role of the stabilizers is to fix these compounds before appreciable acceleration of the decomposition process can occur. Carbon black is an opacifier which prevents radiant energy transmission to the interior of the propellant; such energy transmission can cause undesirable internal ignitions. Certain catalysts (potassium sulfate) are used to modify the burning rate of the propellant. Some other materials are added to facilitate extrusion and other manufacturing operations.

In Table 3-1 we give compositions of some homogeneous solid propellants used in France, Germany, Russia, the United Kingdom and the United States.

By comparing the values of Φ for nitroglycerin which has an excess of oxygen and for nitrocellulose ($\Phi = (40 + 4\nu) / (136 - \nu)$) which is deficient in oxygen, we see that in principle it is possible by mixing these two constituents to obtain an overall mixture ratio which is stoichiometric. However, this is not possible in practice, and we emphasize here that the practical specific impulse obtainable with mix-

Propellants	SD (F)	CORONITE (USSR)	JP (US)	M7 (US)	MRN (US)	R-61 (US)	BACA (US)
Constituents							
nitrocellulose	66	56.5	52.2	54.5	56.51	61.5	59.9
dinitrodiethylene glycol						35.0	
dinitrotriethylene glycol							
nitroglycerin	25	28	43	35.5	28.0		26.9
dinitrotoluene		11			11		
trinitrotoluene							
centralite	8	3.5		0.9	4.5		2.9
diethylphthalate			3.0				
diphenylamine			0.6				
diphenylurea						2.1	
ethylphenylurea						1.4	
stabilizer	1	1					
alphanitronaphthalene							6.1
dimethylphthalate							
KNO ₃			1.2				
K ₂ SO ₄					1.5		2.0
BaSO ₄ TiO							
MgO				1.0			
TiO ₂							0.9
Carbon black				1.2	0.5		
Wax					0.08		
CO ₃ Ca							
ClO ₄ K				7.8			
Propellants	JPN (US)	SC (UK)	HSC (UK)	105.5 (UK)	17H (G)	R 61 (G)	Z 167 (G)
Constituents							
nitrocellulose	51.5	49.5	49.5	60.0	63.7	67.8	55.8
dinitrodiethylene glycol				39.66	16.0	35.3	16.35
dinitrotriethylene glycol					16.0		16.35
nitroglycerin	43.0	41.5	47.0				
dinitrotoluene							9
trinitrotoluene							12.5
centralite	1.0	9.0	3.5		2.0		
diethylphthalate							
diphenylamine						0.8	
diphenylurea					1		
ethylphenylurea						1.1	
stabilizer				0.74		1.5	0.5
alphanitronaphthalene							
dimethylphthalate	3.25						
KNO ₃					0.6		
K ₂ SO ₄	1.25						
BaSO ₄ TiO					0.5		
MgO				0.4		0.25	
TiO ₂							
Carbon black	0.2			0.1	0.3		
Wax	0.08	0.07	0.07				
CO ₃ Ca		0.35	0.35				

h*

Table 3-1 Some Homogeneous Propellants

tures of nitroglycerin and nitrocellulose is relatively low (of the order of 200 to 220 seconds). For maximum performance (i. e. for nearly stoichiometric conditions) the ratio by mass of nitroglycerin to nitrocellulose should be about 6.8. However, at present it is not possible to obtain a storable propellant gel with nitroglycerin mass fractions greater than about 47 percent.

Although new compounds are being studied for improving homogeneous propellant performance, these propellants have largely been superseded by heterogeneous propellants which exhibit superior performance.

Heterogeneous Propellants - We distinguish two categories of heterogeneous propellants, (a) simple heterogeneous propellants (typified by the AP - PU composite system) in which the binder is not capable of sustaining combustion by itself and (b) hybrid heterogeneous propellants which employ energetic binders whose constituents can in themselves serve as basics for homogeneous propellants. We consider the oxidizer and fuel constituents of simple heterogeneous propellants first.

(a) **Oxidizers** - The oxidizers used in heterogeneous propellants are usually perchlorates and currently are most often ammonium perchlorate. The choice of oxidizer is based on its heat of formation, which should be as nearly positive as is consistent with stability, its density, which should be as high as possible and its oxygen content, which should of course be as large as possible. Table 3-2 gives some properties of various oxidizers; in Table 3-2 the percent oxygen available is 100 times the mass of oxygen that remains after all fuel valences in the oxidizer molecule are satisfied, divided by the molecular weight of the oxidizer molecule. The molecular weights and heats of formation of another selection of oxidizers are shown in Fig. 3-1; the lines through the origin indicate values of the heat of formation per unit mass. Nitronium perchlorate is a most interesting oxidizer in these selections (5), but it reacts violently with fuel binders and therefore is difficult to use safely. Its use may be made possible by protecting the oxidizer particles from the fuel binder by means of an oxidizing binder made from derivatives of fluorine, for example. Hydrazine perchlorate also presents some problems which are inherent in its tendency to decompose. Although the choice of possible oxidizers is restricted to molecules with relatively high bonding energies by the requirement that the oxidizer be a solid with sufficient stability, nevertheless current oxidizer might be improved by investigating compounds containing fluorine.

(b) **Fuels** (6) - Developments in the plastics industry have made it possible to utilize a wide variety of materials for fuel binders. Some of the available polymers are polysulfide polyester, epoxy, synthetic rubbers, polyurethane, polybutadiene, polyisobutylene, and phenolic or cellulosic resins. Polysulfide polymers that have been used as binders include ethylformalpolysulfide $(-CH_2CH_2OCH_2OCH_2CH_2SS-)_x$, butyletherpolysulfide $(-(CH_2)_4OCH_2O(CH_2)_4SS-)_x$, dodecamethylenepolysulfide $(-CH_2)_{12}SS-)_x$. A handicap of these plastics is that it is difficult to add a light metal to them because they retain water during curing reactions. An advantage is that they possess good mechanical properties.

Polyurethanes are useful in solid propellants because they are generally formed by the condensation of an isocyanate and a diol, for example diisocyanate and a glycol, which brings about the precipitation of the polymer without the necessity of eliminating water. A chemical reaction of a diisocyanate with a glycol can be written as:



A chemical formula based on gross weight for a polyurethane polymer is:

Oxidizer	Formula	Molecular Weight g/mole	Density	Percent Oxygen Available	Heat of Formation kcal/mole at 25° C
Ammonium perchlorate	NH_4ClO_4	117.49	1.95	34.04	-69.4
Ammonium nitrate	NH_4NO_3	80.05	1.725	20.0	-87.3
Hydrazine nitrate	$\text{N}_2\text{H}_5\text{NO}_3$	95.0	1.685	8.4	-59.0
Lithium nitrate	LiNO_3	68.95	2.38	58.015	-115.3
Lithium perchlorate	LiClO_4	106.40	2.429	60.15	-98.0
Nitronium perchlorate	NO_2ClO_4	145.46	2.22*	66	18.0*
Potassium perchlorate	KClO_4	138.55	2.524	46.19	-103.6
Hydrazine perchlorate	$\text{N}_2\text{H}_5\text{ClO}_4$	132.49	1.939**	24.2	-42.5**

* SIEGEL and SCHIELER, *Energetics of Propellant Chemistry*, Wiley p.175, 1964.

** LEVY, von ELBE, et. al. *Research on the Deflagration of High - Energy Oxidizers*, Atlantic Research Corp., Final Tech. Rept., Contract AF 49 (638)-1169, 1965.

Table 3-2 Properties of some Oxidizers

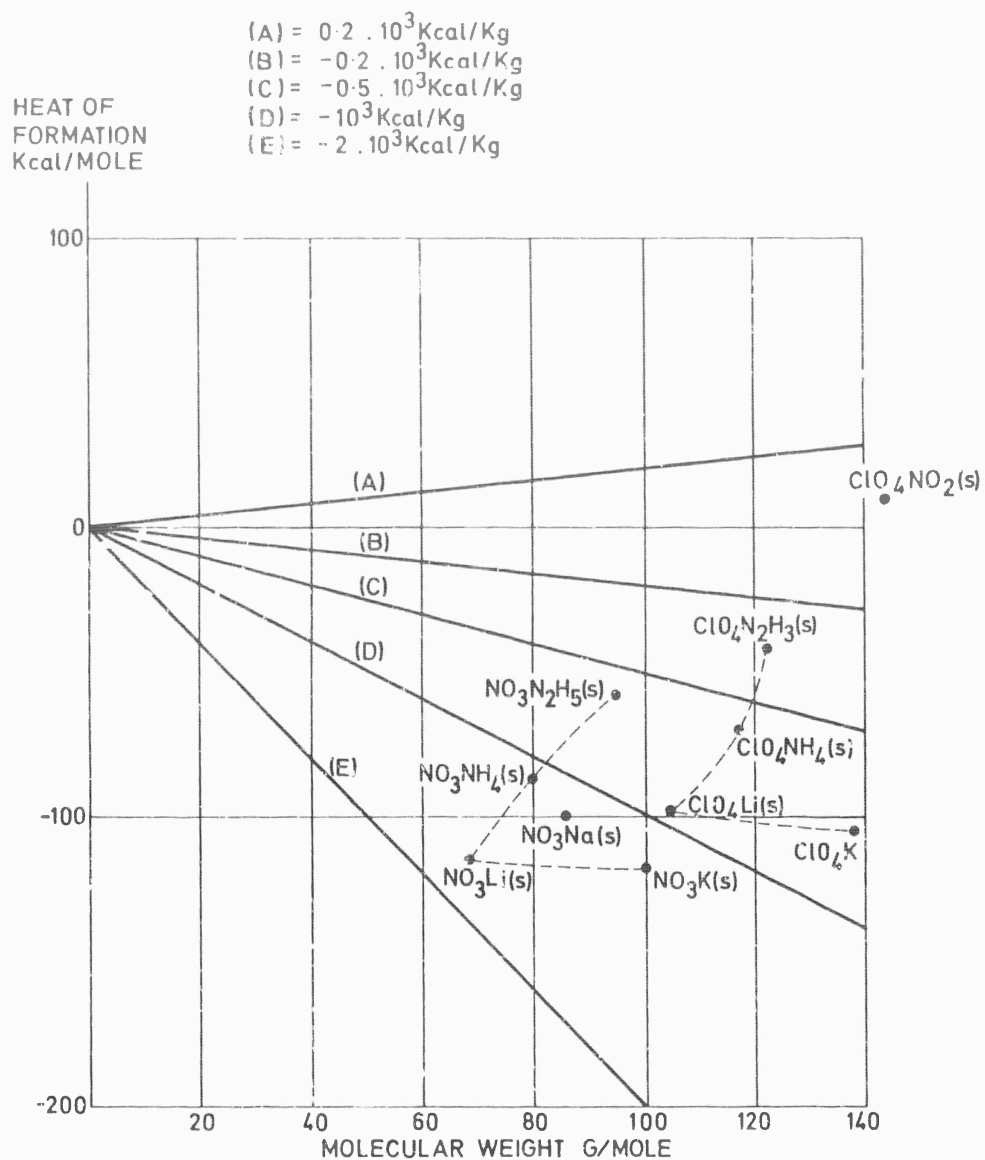


Fig. 3-1 Heats of formation of some solid oxidizers.



with a heat of formation of about -830 kcal/kg. Propellant binders based on these materials have excellent mechanical properties and good performance.

Polybutadiene - acrylic acid polymers (PBAA) have numerous industrial uses and are also applicable in propellant formulations because of their good mechanical properties. These copolymers are of the form:



and have a density of about 0.91 gm/cm³; A formula based on gross weight for a polymer of this type is:



with a heat of formation around - 90 kcal/kg.

Aluminum (Al) is the metal that is most often added to solid propellants to increase their performance, but boron (B), lithium (Li), beryllium (Be), Magnesium (Mg) and zirconium (Zr) are some of the other metals that can also be used.

The binder serves to hold together the oxidizer particles as well as the metal particles in metalized propellants. Consequently, problems may arise in the mechanical properties of the grain; in order to obtain a particular desired cohesiveness and elasticity of the grain it may be necessary to avoid using certain binder materials that are desirable from the viewpoint of performance.

To illustrate this point, we note that for polyethylene (CH₂)_x, the stoichiometric mixture ratio MR_s with ammonium perchlorate is about 0.1 giving a stoichiometric mass fraction of polyethylene of 0.09. At this low binder mass fraction, it would be very difficult to obtain acceptable mechanical properties of the grain.

The volume fractions more than the mass fractions of the various constituents in the propellant affect the mechanical properties. This is why constituent densities are important. Binders with lower densities usually have better mechanical properties but worse performance. Binders containing oxygen are useful in propellants because the corresponding stoichiometric binder mass fractions are relatively high, so that good mechanical properties can be obtained at the mixture ratios that yield maximum performance.

(c) Energetic binders - The earliest hybrid heterogeneous propellants were of the composite - double base type, in which oxidizer particles (e.g. ammonium perchlorate) were mixed in conventional, fuel-rich, double-base binders in order to increase performance. Later systems incorporated metals (such as aluminum) as well, along with additional amounts of oxidizer, in order to obtain still higher performance. Plasticizers other than nitroglycerin can be used. It is also attractive to use polyurethane nitroplastics which contain 3 to 40% oxygen. A variety of different nitropolymers have appeared in propellants. Polyurethane nitroplastics have increased the binder fraction by 20% while increasing the specific impulse by three seconds (244 sec to 247 sec).

1.2.2. Combustion Products - Performance is affected by the heat released during combustion, the chemical species produced in combustion, and the physical states of these reaction products in the chamber and also in the nozzle.

Representative stable reaction products are H₂O, HF, HCl, CO₂, CF₄, CCl₄, Al₂O₃, AlF₃, AlCl₃, ... at high temperatures, these materials dissociate into

OH, HCl, HF, H_2O , Al_2O_3 , Al_2O , AlO atomic species also appear at sufficiently high temperatures. Product gases may also contain H_2 , O_2 , N_2 . . .

The enthalpy of any species equals its standard heat of formation plus the enthalpy exchange in going from its standard state to the prevailing conditions of pressure and temperature. We take the standard state of a species to be the form of the species that is stable at atmospheric pressure and at 25 °C. The standard heat of formation of a species (denoted here by h_f° when referred to a unit mass) is then the energy required at atmospheric pressure and at a temperature of 25 °C to form the species in its standard state from its elements in their standard states. For example, the standard heat of formation of Al_2O_3 is the energy absorbed in the process:



at 1 atm and 25 °C; the heat of formation of Al_2O_3 is -399 kcal/mole. The standard heat released in a reaction, Reactants \longrightarrow Products, is then:

$$\Delta h^\circ = h_{\text{reactants}}^\circ - h_{\text{products}}^\circ \quad (\text{Eq. 3-13})$$

In an adiabatic system, this heat release serves to increase the chamber temperature. Since high chamber temperature leads to high performance (see Chapter 2), high standard heat of reaction are desirable for the combustion reactions. Therefore large positive values of Δh° are desirable. Equation 3-13 shows that this can be achieved by making $h_{\text{reactants}}^\circ$ as nearly positive as possible and by making $h_{\text{products}}^\circ$ large and negative. The heats of formation of some combustion products are shown in Fig. 3-2. Taking the heat of formation per unit mass as a criterion for performance, we see from this figure that the line connecting $\text{LiF}(\text{s})$, $\text{BeO}(\text{s})$, $\text{B}_2\text{O}_3(\text{s})$ and $\text{Al}_2\text{O}_3(\text{s})$ provides a locus of species which are the most desirable reaction products.

The physical states of reaction products in the chamber and in the nozzle may be inferred from Fig. 3-3 or 3-4 for system in which the oxidant is oxygen or fluorine, respectively. It is seen from Fig. 3-3 that the formation (excluding CO_2 and H_2O) generally tends to condense in the nozzle and sometimes in the chamber. As indicated in the Chapter 2, this condensation is usually essential for good performance, but it also leads to two-phase flow problems. It may be seen from Fig. 3-4 that in general fluorine compounds are less likely to condense than oxygen compounds.

2. Theoretical Performance Calculations

The first step in performance calculations is to determine equilibrium composition of the combustion products as a function of pressure and temperature, (7).

2.1. Equilibrium Composition Equations

2.1.1. Definition of Basis - Let us consider a general system containing n different chemical species, of which m are gaseous and $n - m$ are in condensed states. The formation of a chemical species \mathcal{S}^i from its constituent elements \mathcal{A}^k can be written symbolically as:

$$\mathcal{S}^i = \sum_{k=1}^l \alpha_{ik} \mathcal{A}^k \quad i=1, \dots, n, \quad (\text{Eq. 3-14})$$

in which α_{ik} denotes the number of atoms of the chemical element \mathcal{A}^k contained in chemical compound \mathcal{S}^i . The indices i are assigned in the following way:

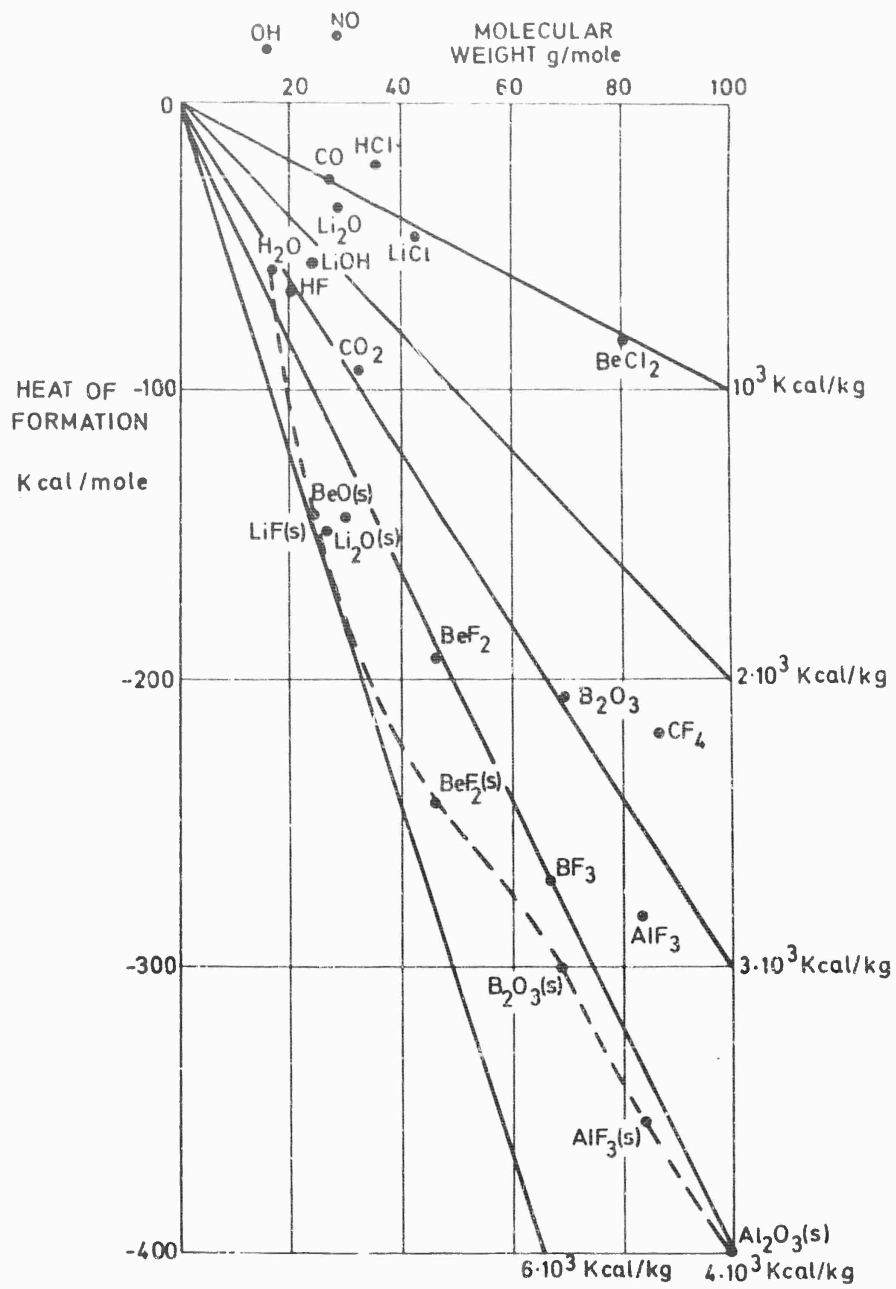


Fig. 3-2 Heats of formation of major species composing combustion products.

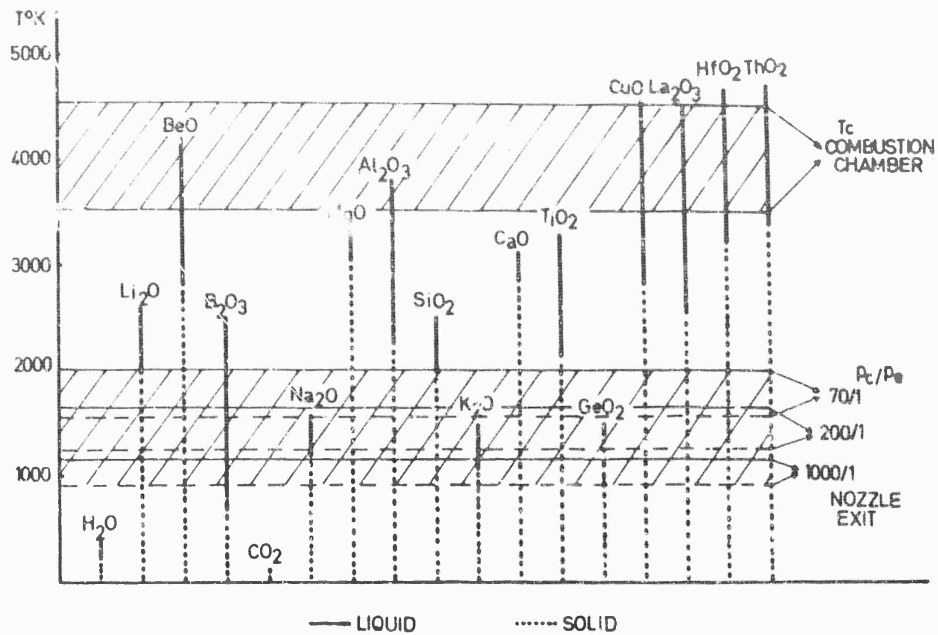


Fig. 3-3 Temperature domains of condensed phases in combustion gases. Oxidizer: oxygen.

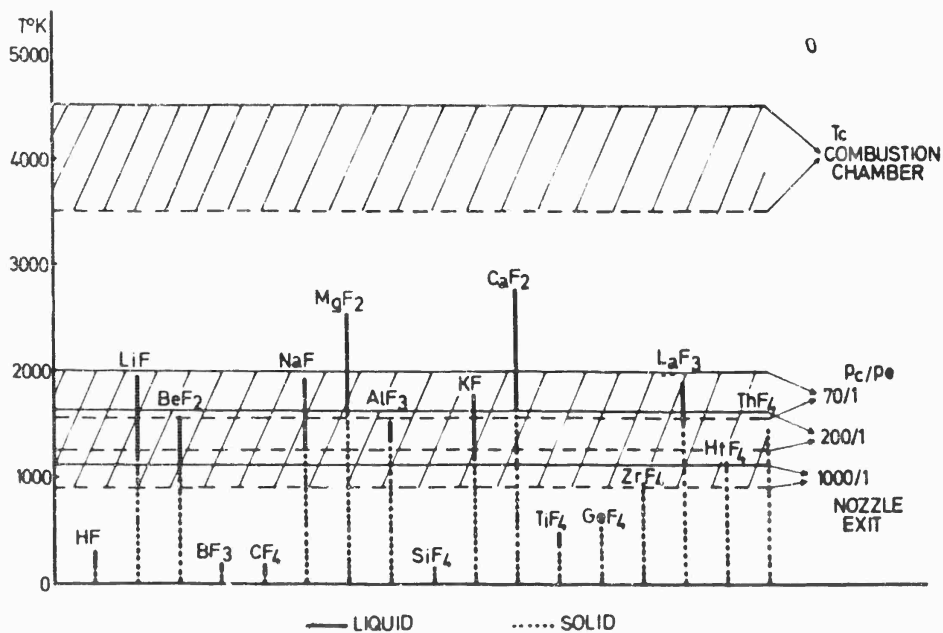


Fig. 3-4 Temperature domains of condensed phases in combustion gases. Oxidizer: fluorine.

$i = 1, \dots, \ell$	gaseous elements
$i = \ell + 1, \dots, m$	gaseous compounds
$i = m + 1, \dots, n$	condensed species

and the description of the chemical system is augmented if necessary so that all of the ℓ basic elements appear as chemical species. Identical compounds in different phases are treated as different chemical species, and condensed solutions as well as the simultaneous existence of more than one condensed phase of the same compound will later be ruled out. Thus each condensed phase will be treated as a pure substance, and relatively unimportant phase-transition regimes in which the number of independent thermodynamic variables other than compositions is reduced will not be discussed. We note here that for the elements ($i = 1, \dots, \ell$), $\alpha_{ik} = 1$ when $k = i$ and $\alpha_{ik} = 0$ when $k \neq i$. Therefore if the ℓ elements are the only species present, then the matrix α_{ik} is obviously of rank ℓ . These results, along with the observation that in general α_{ik} is an $\ell \times n$ matrix with $n \geq 1$, imply that α_{ik} is always a matrix of rank ℓ , (2) (7) (8) (9) (10).

Although in the formulation of Eq. 3-14 the element symbols \mathcal{E}^i were taken to represent atoms in order to facilitate understanding, we emphasize here that it is not necessary to choose atoms as the basic building blocks from which the chemical compounds are constructed. There are many possible choices for the independent set of ℓ basic constituents. In order to see this and to glean information about restrictions on the choice of these basic constituents, let us assume that each compound \mathcal{E}^i is broken into ℓ basic constituents \mathcal{G}^j , some of which differ from atoms but all of which are present in the system (i.e. are members of the set of all \mathcal{E}^i). The composition of \mathcal{E}^i is then written symbolically as:

$$\mathcal{E}^i = \sum_{j=1}^{\ell} \beta_{ij} \mathcal{G}^j \quad i = 1, \dots, n \quad (\text{Eq. 3-15})$$

where β_{ij} is the number of molecules \mathcal{G}^j required to construct compound \mathcal{E}^i (note that the elements of β_{ij} may be nonintegral or negative). Since \mathcal{G}^j are members of \mathcal{E}^i , Eq. 3-14 implies that:

$$\mathcal{G}^j = \sum_{k=1}^{\ell} \hat{\alpha}_{jk} \mathcal{A}^k \quad j = 1, \dots, \ell, \quad (\text{Eq. 3-16})$$

where $\hat{\alpha}_{jk}$ is a square submatrix of α_{ik} . If $\hat{\alpha}_{jk}$ possesses an inverse (denoted by $\hat{\alpha}_{kj}^{-1}$ here), then the formula implies that:

$$\mathcal{A}^k = \sum_{j=1}^{\ell} \hat{\alpha}_{kj}^{-1} \mathcal{G}^j \quad k = 1, \dots, \ell,$$

which upon substitution into Eq. 3-14 yields:

$$\mathcal{E}^i = \sum_{k=1}^{\ell} \sum_{j=1}^{\ell} \alpha_{ik} \hat{\alpha}_{kj}^{-1} \mathcal{G}^j \quad i = 1, \dots, n,$$

Comparison of this expression with Eq. 3-15 shows that:

$$\beta_{ij} = \sum_{k=1}^{\ell} \alpha_{ik} \hat{\alpha}_{kj}^{-1} \quad i = 1, \dots, n, \quad j = 1, \dots, \ell \quad (\text{Eq. 3-17})$$

which is a matrix-multiplication transformation rule for computing the coefficients β_{ij} from α_{ik} for any choice of basic constituents \mathcal{G}^j . The restriction on the derivation of Eq. 3-17 is obviously that the square submatrix $\hat{\alpha}_{jk}$ must be nonsingular (so that $\hat{\alpha}_{kj}^{-1}$ exists); this restriction can be expressed formally by the requirement that its determinant does not vanish:

$$\left| \hat{\alpha}_{jk} \right| \neq 0 \quad (\text{Eq. 3-18})$$

If one were to attempt to evaluate the coefficient β_{ij} , in a simple physical way from Eq. 3-15 by counting the number of molecules required to make the compound \mathcal{S}^i , one would find that some compounds \mathcal{S}^j could not be constructed from the set \mathcal{S}^j if $|\hat{\alpha}_{jk}|$ were equal to zero.

Any set of constituents \mathcal{S}^j , given by Eq. 3-16 and satisfying this Eq. 3-18, forms an acceptable set of basic constituents and may be termed a basis of the chemical system. In practical composition calculations, it is often convenient to choose a basis which differs from the set of all atomic species.

To illustrate the operation of basis transformation, let us consider the system constructed from the atoms H and O. Let the matrix α_{ik} be defined by the table:

		$\longrightarrow i$					
k		H_2O	HO	H_2	H	O_2	O
	H	2	1	2	1	0	0
	O	1	1	0	0	2	1

so that:

$$[\alpha_{ik}] = \begin{vmatrix} 2 & 1 & 2 & 1 & 0 & 0 \\ 1 & 1 & 0 & 0 & 2 & 1 \end{vmatrix} \quad (\text{Eq. 3-19})$$

Suppose we were to take H_2O and H_2 as a new basis. Then we should have:

		$\longrightarrow j$	
k		H_2O	H_2
	H	2	2
	O	1	0

so that the submatrix would be:

$$[\alpha_{jk}] = \begin{vmatrix} 2 & 2 \\ 1 & 0 \end{vmatrix}$$

We note that the determinant $\hat{\alpha}_{jk} = -2 \neq 0$ here, and therefore the new choice is an acceptable basis. Since the value of the matrix α_{jk} implies that:

$$[\hat{\alpha}_{kj}^{-1}] = \begin{vmatrix} 0 & 1 \\ \frac{1}{2} & -1 \end{vmatrix} \quad (\text{Eq. 3-20})$$

by means of a simple matrix calculation we then find from Eq. 3-17 and Eq. 3-19 that:

$$[\beta_{ij}] = \begin{vmatrix} 1 & 1 & 0 & 0 & 2 & 1 \\ 0 & -\frac{1}{2} & 1 & \frac{1}{2} & -2 & -1 \end{vmatrix} \quad (\text{Eq. 3-21})$$

An advantage in using a basis other than the atoms arises from the fact that sometimes the concentrations of various free atoms in the system are negligibly small. If one eliminates such atoms from the basis, then it is possible to neglect these free atomic species entirely in calculating chemical compositions, thereby reducing n and the number of columns in β_{ij} , so that the amount of necessary computational work is decreased.

In practical computations, it is therefore unnecessary to augment the description of the chemical system as was done at the beginning of this section. As a related point, we note that in eliminating certain atoms from consideration, we may actually reduce the rank of the matrix β_{ij} that is used in computations. A simple example of a system in which the rank of the matrix β_{ij} that is needed in composition calculations is less than the number of different kinds of atoms, is provided by the two-component system experiencing only the reaction $\text{N}_2\text{O}_4 \rightleftharpoons 2 \text{NO}_2$ and containing only the species NO_2 and N_2O_4 ; here NO_2 may be taken as the basis and the rank of β_{ij} then equals 1, even though the 2 atoms N and O are present in the molecules.

Modern computing machines are usually large enough to handle the complete augmented system of chemical species. However, even when such machines are available, there are advantages in using as a basis a set of molecules which differ from the atomic species. Chemical compositions must be found by iterative calculations and the molecules belonging to the basis usually assume a central role in the iterations. Most calculation schemes converge more rapidly if the basis is composed of molecules that are present in relatively high concentrations. In such schemes, it is therefore important to select principal reaction products for the basis, and atomic species usually are not principal reaction products of the combustion of solid propellants. An additional reason for choosing a basis composed of constituents other than free atoms in electronic computer calculations of compositions is that the calculations are often simplified by including all condensed species in the basis whenever condensation occurs (9) (10) (11) (12).

2.1.2. Governing Equations - Equilibrium compositions are determined by a system composed of two types of equations, namely equations of atom conservation and equations of chemical equilibrium. We shall discuss atom conservation equations first.

Atom Conservation Equations - We let \mathcal{N}_k ($k = 1, \dots, \ell$) denote $[6.06 \times 10^{23}]^{-1}$ times the total number of atoms of type k in a unit mass of the chemical system. In computing each \mathcal{N}_k one is to count all atoms of the type k , whether they be free or contained in chemical compounds. Thus, the ℓ numbers \mathcal{N}_k specify the overall atomic composition of the system. We note here that if the unit of mass is taken to be 1 kg, then \mathcal{N}_k for each atom is numerically equal to the corresponding subscript that appears in Eq. 3-3, the gross-weight chemical formula for the overall composition of the mixture. In other words, the formula in Eq. 3-3 then becomes:

$$\text{C } \mathcal{N}_\text{C} \text{ H } \mathcal{N}_\text{H} \text{ B } \mathcal{N}_\text{B} \dots \text{O } \mathcal{N}_\text{O} \text{ F } \mathcal{N}_\text{F} \quad (\text{Eq. 3-22})$$

By definition,

$$\sum_{k=1}^{\ell} \mathcal{N}_k m_k = 1 \quad (\text{Eq. 3-23})$$

where m_k is the atomic weight (in the units of mass adopted for \mathcal{N}_k) for a mole of k atoms. Calculations of equilibrium chemical compositions can be undertaken meaningfully when the pressure, temperature and all \mathcal{N}_k are specified for the system.

Since atoms are neither created nor destroyed in chemical reactions, there are ℓ separate atom conservation equations which, in view of Eq. 3-14, the definition of α_{ik} , can be written in the form:

$$\mathcal{N}_k = \sum_{i=1}^n \alpha_{ik} n_i \quad k = 1, \dots, \ell, \quad (\text{Eq. 3-24})$$

where n_i denotes the number of moles of chemical species i in a unit mass of mixture. Equation 3-24 applies equally well whether n_i refers to the initial propellant composition or to the equilibrium product composition. One may calculate the quantities \mathcal{N}_k either from Eq. 3-24 by inserting values of n_i and representing the initial propellant composition, or else directly from the gross weight chemical formula for the overall propellant composition, as indicated earlier. After the values of \mathcal{N}_k are known, Eq. 3-24 constitutes a number of independent equations that the values of n_i for the equilibrium product composition must satisfy. For the augmented chemical system, the relations for n_i appearing in Eq. 3-24 are linearly independent, and therefore Eq. 3-24 provides ℓ independent equations for the n unknowns n_i , $i = 1, \dots, n$.

When working with a basis containing species other than atoms, it is convenient to express the overall atomic composition of the system in terms of the constituent number $\hat{\mathcal{N}}_j$ of 'atoms' of each of the species \mathcal{A}^j which make up the basis. We define these quantities $\hat{\mathcal{N}}_j$ by the equation:

$$\mathcal{N}_k = \sum_{j=1}^{\ell} \hat{\alpha}_{jk} \hat{\mathcal{N}}_j \quad k = 1, \dots, \ell \quad (\text{Eq. 3-25})$$

where $\hat{\alpha}_{jk}$ is the submatrix defining the basis. The solution of Eq. 3-25 for $\hat{\mathcal{N}}_j$ enables us to calculate $\hat{\mathcal{N}}_j$ from prescribed values of \mathcal{N}_k and $\hat{\alpha}_{jk}$, viz,

$$\hat{\mathcal{N}}_j = \sum_{k=1}^{\ell} \hat{\alpha}_{kj}^{-1} \mathcal{N}_k \quad j = 1, \dots, \ell \quad (\text{Eq. 3-26})$$

By substituting the original set of atom conservation equation, Eq. 3-24 into Eq. 3-26 and using Eq. 3-17, we see that the set of atom conservation equations can be written as:

$$\hat{\mathcal{N}}_j = \sum_{i=1}^n \beta_{ij} n_i \quad j = 1, \dots, \ell \quad (\text{Eq. 3-27})$$

After the quantities $\hat{\mathcal{N}}_j$ have been calculated, Eq. 3-27 gives the restrictions on the equilibrium compositions n_i that are imposed by atom conservation. It is sometimes useful to break up the sum appearing Eq. 3-27 into separate sums over gaseous and condensed species. Recalling that we let $i = 1, \dots, m$ identify gaseous species, we may write Eq. 3-27 in the form:

$$\hat{\mathcal{N}}_j = \sum_{i=1}^m \beta_{ij} n_i + \sum_{i=m+1}^n \beta_{ij} n_i, \quad j = 1, \dots, \ell \quad (\text{Eq. 3-28})$$

where the last sum encompasses all condensed species. It is clear from the phase rule that $n - m = \ell$; therefore it is always possible to adopt the convention that every condensed species in the system is to be included in the basis, and it can be shown that for $i = m + 1, \dots, n$, $\beta_{ij} = 0$ unless the subscripts i and j both correspond to the same condensed species and $\beta_{ij} = 1$ when their correspondence occurs. It then becomes possible to write Eq. 3-28 in the form:

$$\hat{\mathcal{N}}_j = \delta_j n_j^c + \sum_{i=1}^m \beta_{ij} n_i, \quad j = 1, \dots, \ell \quad (\text{Eq. 3-29})$$

where $\delta_j = 0$ if the subscript j identifies a gaseous member of the basis, $\delta_j = 1$ if the subscript j identifies a condensed member of the basis and n_j^c is the number of moles, per unit mass of the system, of the condensed species which is identical to condensed member j of the basis. Equation 3-29 serves to assign a special role to condensed materials and to reduce the sum over the index i to a sum over gaseous species only.

We note quite generally by substituting Eq. 3-25 into Eq. 3-23 that:

$$\sum_{j=1}^{\ell} \hat{\mathcal{N}}_j \left[\sum_{k=1}^{\ell} \hat{\alpha}_{jk} m_k \right] = 1, \quad (\text{Eq. 3-30})$$

It is obvious from the definitions that the molecular weight of species j of the basis is:

$$m_j = \sum_{k=1}^{\ell} \hat{\alpha}_{jk} m_k \quad (\text{Eq. 3-31})$$

and therefore Eq. 3-30 is equivalent to:

$$\sum_{j=1}^{\ell} \hat{N}_j m_j = 1, \quad (\text{Eq. 3-32})$$

which is expected.

As an illustration of the transformation of atom conservation equations from N_k to \hat{N}_j notation, let us return to the H - O system that was discussed in Eq. 3-19 to 3-21. If we know N_H and N_O (from the overall gross-weight formula of the propellant, for example), then according to Eq. 3-26, we have from Eq. 3-20 that:

$$\hat{N}_{H_2O} = N_O \text{ and } \hat{N}_{H_2} = \frac{1}{2} N_H - N_O \quad (\text{Eq. 3-33})$$

This is, of course, consistent with Eq. 3-25, which states that:

$$N_H = 2 \hat{N}_{H_2O} + 2 \hat{N}_{H_2} \text{ and } N_O = \hat{N}_{H_2O} \quad (\text{Eq. 3-34})$$

in this case.

Chemical Equilibrium Equations - The relations in Eq. 3-15 give rise to chemical equilibrium equations for determining the species composition. If one selects at random the reactions for which chemical equilibrium equations are written down, then one cannot be sure that the resulting equilibrium equations will be independent or complete. A systematic procedure for selecting equilibrium equations is needed in order to assure independence and completeness in complex chemical systems with multiple reactions. One such procedure can be based on Eq. 3-15. Since the species \mathcal{S}^j ($j = 1, \dots, \ell$) are all members of the set of compounds \mathcal{S}^i ($i = 1, \dots, n$) by definition, it is clear that ℓ of the relations in Eq. 3-15 are merely chemical identities and no chemical equilibrium equations can be derived from them. On the other hand, $n - \ell$ of the relations in Eq. 3-15 correspond to chemical reactions in which a molecule \mathcal{S}^i not contained in the set of all \mathcal{S}^j , is formed from the molecules \mathcal{S}^j . Chemical equilibrium equations can be written down for these formation reactions. Obviously $n - \ell$ such equations can be obtained from Eq. 3-15. Since the compounds \mathcal{S}^i are all different, it is clear that the $n - \ell$ formation reactions are linearly independent, and it follows from this that when the resulting $n - \ell$ chemical equilibrium equations are combined with the ℓ independent atom conservation equations (Eq. 3-27), a set of n independent equations is obtained for the n unknown concentrations n_i ($i = 1, \dots, n$).

The effect of the choice of basis on the set of equilibrium equations that arise from Eq. 3-15 can be illustrated by reference to the H - O system that we have discussed before. Thus, for example, for the species OH (the second column in Eq. 3-19), if the atoms H and O are taken as the basis, then the corresponding chemical equilibrium equation refers to the reaction:



but if H_2O and H_2 are taken as the basis, then the chemical equilibrium equation refers to the reaction:

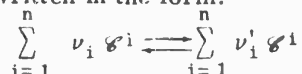


The coefficient on the right-hand side of Eq. 3-35 are the elements in the second column of Eq. 3-19 while the coefficients on the right-hand side of Eq. 3-36 are the elements in the second column of Eq. 3-21. The equilibrium constant for the reaction in Eq. 3-36 is likely to be of a reasonable size when the equilibrium constant for Eq. 3-35 is extremely small. This suggests how computational problems might arise in using H and O as the basis under conditions for which they do not arise in using H_2O and H_2 on a basis.

The general condition of chemical equilibrium, see Eq. 2-51 of Chapter 2, is:

$$\sum_{i=1}^n \mu_i \, d n_i = 0, \quad (\text{Eq. 3-37a})$$

where μ_i is the chemical potential of species i . For an arbitrary chemical reaction written in the form:



with ν_i and ν'_i representing stoichiometric coefficients, this formula implies that:

$$\sum_{i=1}^n (\nu'_i - \nu_i) \mu_i = 0 \quad (\text{Eq. 3-37})$$

at equilibrium. In order to obtain explicit equilibrium equations, it is therefore important to have formulas for the chemical potentials μ_i . For practical purposes, the chemical potentials of condensed species are functions only of the temperature:

$$\mu_i^c = \mu_i^c(T). \quad (\text{Eq. 3-38})$$

The temperature dependence of μ_i^c is best presented in tabular form, the tables being obtained from experimental results. For practical purposes, gases may be assumed to be ideal in computing their chemical potentials and the chemical potential of an ideal gas is expressible as:

$$\mu_i = \mu_i^c(T) + R^\circ T \ln p_i \quad (\text{Eq. 3-39})$$

where μ_i is a function only of T (and again is best obtained from tabulations based on experimental results), R° is the universal gas constant, and p_i is the partial pressure of species i in the gas, which can be related easily to the total pressure and the concentrations of species in the system.

Instead of working with μ_i^c and with μ_i° , it is sometimes convenient to work with the related quantity:

$$M_i \equiv \begin{cases} -\mu_i^c/R^\circ T & \text{for a condensed phase} \\ -\mu_i^\circ/R^\circ T & \text{for a gaseous species} \end{cases} \quad (\text{Eq. 3-40})$$

In the standard chemical notation, M_i , which is a function only of temperature, is given by:

$$M_i = -F_i^\circ/R^\circ T = S_i^\circ/R^\circ - H_i/R^\circ T \quad (\text{Eq. 3-40a})$$

where H_i is the molar enthalpy, S_i° is the standard molar entropy, and F_i° is the standard molar free energy. Tabulations of H_i and S_i° are prevalent in the chemical literature.

When Eq. 3-37 to 3-40 are applied to the formation reactions given in Eq. 3-15, one easily finds that:

$$\ln p_i - M_i = \sum_j' \beta_{ij} \ln p_j - \sum_{j=1}^{\ell} \beta_{ij} M_j, \quad i = 1, \dots, m$$

$$- M_i = \sum_j' \beta_{ij} \ln p_j - \sum_{j=1}^{\ell} \beta_{ij} M_j, \quad i = m+1, \dots, n$$
(Eq. 3-41)

where \sum_j' denotes a sum over only gas-phase basis species. Only $n - \ell$ of the n

equations given here are nontrivial. If we adopt the convention that every condensed species in the system is to be included in the basis, then Eq. 3-41 is satisfied trivially for $i = m+1, \dots, n$, and the remaining relations in Eq. 3-41 can, with the aid of the notation introduced in Eq. 3-29, be written in the form:

$$\ln p_i - \sum_{j=1}^{\ell} (1 - \delta_{ij}) \beta_{ij} \ln p_j = M_i - \sum_{j=1}^{\ell} \beta_{ij} M_j, \quad i = 1, \dots, m \quad (\text{Eq. 3-42})$$

Only $n - \ell$ of the m relations given in Eq. 3-42 are nontrivial. For ideal gases, partial pressures are related to the total pressure p and to the number of moles per unit mass according to Dalton's law,

$$p_i = p n_i / n, \quad i = 1, \dots, m \quad (\text{Eq. 3-43})$$

where:

$$n \equiv \sum_1' n_i = \sum_{i=1}^m n_i, \quad (\text{Eq. 3-44})$$

is the total number of moles of gas-phase species per unit mass of the system (since \sum_1' is defined to denote a sum over all gas-phase species).

By way of illustration, we note that for Eq. 3-35, Eq. 3-42 takes the form:

$$\ln p_{\text{OH}} - \ln p_{\text{H}} - \ln p_{\text{O}} = M_{\text{OH}} - M_{\text{H}} - M_{\text{O}}$$

and Eq. 3-43 is:

$$p_{\text{OH}}/n_{\text{OH}} = p_{\text{H}}/n_{\text{H}} = p_{\text{O}}/n_{\text{O}} = \dots = p / n$$

On the other hand, the chemical equilibrium expression (Eq. 3-42) corresponding to Eq. 3-36 is:

$$\ln p_{\text{OH}} - \ln p_{\text{H}_2\text{O}} + \frac{1}{2} \ln p_{\text{H}_2} = M_{\text{OH}} - M_{\text{H}_2\text{O}} + \frac{1}{2} M_{\text{H}_2}.$$

As an example of a system involving a condensed phase, we may point out that for the reaction:



the equilibrium equation takes the form:

$$2 \ln p_{\text{Al}} + 3 \ln p_{\text{O}} = 2 M_{\text{Al}} + 3 M_{\text{O}} - M_{\text{Al}_2\text{O}_3}(\text{c}).$$

2.2 Simplified Calculations of Equilibrium Compositions, (13) (14) (15)

Before proceeding to a discussion of general methods for solving the equations governing equilibrium compositions, let us consider simplified solutions for two special cases, one in which only gas-phase products appear and the other in which a condensed phase is also present.

2.2.1. Gaseous Combustion Products - The solid propellants of simplest composition are homogeneous propellants with gross weight formulas for the form:



The fact that practical systems of this type are generally somewhat fuel rich causes the water gas reaction to be most important. Recognition of this result enables us to simplify our calculations. We consider only those gas-phase reactions that are likely to be of importance in fuel-rich systems. We assume that the gas is composed of the species CO_2 , CO , H_2O , OH , H_2 , H , O_2 , O , N_2 , N and NO .

The atom conservation equations are:

$$\left. \begin{aligned} \mathcal{N}_C &= n_{\text{CO}_2} + n_{\text{CO}} \\ \mathcal{N}_H &= 2 n_{\text{H}_2\text{O}} + n_{\text{OH}} + 2 n_{\text{H}_2} + n_{\text{H}} \\ \mathcal{N}_O &= 2 n_{\text{CO}_2} + n_{\text{CO}} + n_{\text{H}_2\text{O}} + n_{\text{OH}} + 2 n_{\text{O}_2} + n_{\text{O}} + n_{\text{OH}} \\ \mathcal{N}_N &= 2 n_{\text{N}_2} + n_{\text{N}} + n_{\text{NO}} \end{aligned} \right\} \quad (\text{Eq. 3-45})$$

For an equilibrium reaction of the form:



the chemical equilibrium equation is:

$$\left. \begin{aligned} \ln p_{\text{CO}_2} + \ln p_{\text{H}_2} - \ln p_{\text{H}_2\text{O}} - \ln p_{\text{CO}} &= \\ \ln n_{\text{CO}_2} + \ln n_{\text{H}_2} - \ln n_{\text{H}_2\text{O}} - \ln n_{\text{CO}} &= \\ M_{\text{CO}_2} + M_{\text{H}_2} - M_{\text{H}_2\text{O}} - M_{\text{CO}} &\equiv \ln (K_p(T)) \end{aligned} \right\} \quad (\text{Eq. 3-47})$$

where K_p is the equilibrium constant (see Eq. 2-59 of Chapter 2).

Assuming that the concentrations of OH , H , O_2 , O , N and NO are small compared with the concentrations of CO_2 , CO , H_2O , H_2 and N_2 , Eq. 3-45 and 3-47 reduce approximately to:

$$\left. \begin{aligned} \mathcal{N}_C &= n_{\text{CO}_2} + n_{\text{CO}} \\ \mathcal{N}_H &= 2 n_{\text{H}_2\text{O}} + n_{\text{H}_2} \\ \mathcal{N}_O &= n_{\text{H}_2\text{O}} + 2 n_{\text{CO}_2} + n_{\text{CO}} \\ \mathcal{N}_N &= 2 n_{\text{N}_2} \\ K_p(T) &= n_{\text{CO}_2} n_{\text{H}_2} / n_{\text{H}_2\text{O}} n_{\text{CO}} \end{aligned} \right\} \quad (\text{Eq. 3-48})$$

which constitutes 5 equations in 5 unknowns. It is easy to reduce Eq. 3-48 to a simple quadratic equation for, say, n_{CO_2} , with the quantities \mathcal{N}_C , \mathcal{N}_H , \mathcal{N}_O , \mathcal{N}_N , and K_p appearing therein. Solving the quadratic equation and then calculating the remaining four unknowns readily yields a first approximation to the composition of the system, which we denote by $n_{\text{CO}_2}^0$, n_{CO}^0 , $n_{\text{H}_2}^0$, $n_{\text{H}_2\text{O}}^0$ and $n_{\text{N}_2}^0$.

One then calculates the concentrations of the remaining species from the equilibrium formulas corresponding to their reactions of formation from these five major constituents. Thus, for n_{H} consider $\text{H}_2 \rightleftharpoons 2\text{H}$, giving:

$$n_H^\circ = K_{p_H}(T) (n_{H_2}^\circ)^{\frac{1}{2}} (p/n^\circ)^{\frac{1}{2}}$$

$$\text{with } n^\circ = n_{CO_2}^\circ + n_{CO}^\circ + n_{H_2}^\circ + n_{H_2O}^\circ + n_{H_2}^\circ$$

$$\text{and with } \ln K_{p_H}(T) = M_H - \frac{1}{2} M_{H_2}$$
(Eq. 3-49)

Similarly, $H_2O \rightleftharpoons \frac{1}{2} H_2 + OH$

$$n_{OH}^\circ = K_{p_{OH}}(T) (n_{H_2O}^\circ / n_{H_2}^\circ)^{\frac{1}{2}} (p/n^\circ)^{-\frac{1}{2}}$$

$$\ln K_{p_{OH}}(T) = M_{OH} + \frac{1}{2} M_{H_2} - M_{H_2O}$$
(Eq. 3-50)

$H_2O + \frac{1}{2} N_2 \rightleftharpoons H_2 + NO$

$$n_{NO}^\circ = K_{p_{NO}}(T) n_{N_2}^{\frac{1}{2}} n_{H_2}^{-1} (p/n^\circ)^{-\frac{1}{2}}$$

$$\ln K_{p_{NO}}(T) = M_{NO} + M_{H_2} - M_{H_2O} - \frac{1}{2} M_{N_2}$$
(Eq. 3-51)

$N_2 \rightleftharpoons 2N$

$$n_N^\circ = K_{p_N}(T) (n_{N_2}^\circ)^{\frac{1}{2}} (p/n^\circ)^{-\frac{1}{2}}$$

$$\ln K_{p_N}(T) = M_N - \frac{1}{2} M_{N_2}$$
(Eq. 3-52)

$H_2O \rightleftharpoons H_2 + O$

$$n_O^\circ = K_{p_O}(T) (n_{H_2O}^\circ / n_{H_2}^\circ) (p/n^\circ)^{-1}$$

$$\ln K_{p_O}(T) = M_O + M_{H_2} - M_{H_2O}$$
(Eq. 3-53)

$O_2 \rightleftharpoons 2O$

$$n_{O_2}^\circ = K_{p_{O_2}}(T) (n_O^\circ)^2 (p/n^\circ)$$

$$\ln K_{p_{O_2}}(T) = M_{O_2} - 2 M_O$$
(Eq. 3-54)

Having thus obtained a complete set of first approximations n_i° , one calculates the quantities:

$$\left. \begin{aligned} \mathcal{N}_C' &= \mathcal{N}_C \\ \mathcal{N}_H' &= \mathcal{N}_H - n_{OH}^\circ - n_H^\circ \\ \mathcal{N}_O' &= \mathcal{N}_O - n_{OH}^\circ - 2 n_{O_2}^\circ - n_O^\circ - n_{NO}^\circ \\ \mathcal{N}_N' &= \mathcal{N}_N - n_N^\circ - n_{NO}^\circ \end{aligned} \right\} \quad \text{(Eq. 3-55)}$$

Equation 3-48 is then solved for the next approximations $n_{CO_2}^1$, n_{CO}^1 , $n_{H_2O}^1$, $n_{H_2}^1$ and $n_{N_2}^1$ using the new values \mathcal{N}_j' for \mathcal{N}_j . The next approximations for the other species are then obtained from Eq. 3-49 to 3-54, using for n° the total number of moles corresponding to the first approximation. This iterative procedure is then continued until convergence is obtained. Convergence is very rapid.

This method is most valuable for double-base propellants. Resulting concentrations as functions of temperature are shown in Fig. 3-5 for a representative double-base propellant at $p = 70$ atm. We note that the concentrations of the main species H_2O , CO , CO_2 , N_2 and H_2 vary little with temperature but the concentrations of the lesser species increase rapidly with increasing temperature. However, at the usual combustion temperature of these propellants, the concentrations of the lesser species remain small.

We have indicated that nitrocellulose contains varying amounts of nitrogen. One can easily show that as a function of the quantity n defined in Section 1.2.1 under 'Homogeneous Propellants', $N_C = 37.1 - 1.19 n$, $N_H = 61.72 - 2.70 n$, $N_O = 30.86 - 0.44 n$ and $N_N = 0.714 n$ when the unit of mass is taken as 1 kg. Figure 3-6 shows the dependence of the adiabatic flame temperature (defined later) as well as the compositions of the principal reaction products as functions of the nitrogen percentage n . The water gas reaction predicts that the temperature increases and the concentrations of H_2 and CO decrease as n increases.

For propellants containing the elements H, C, O, N as well as some Cl the simplified approach outlined here is quite accurate, as long as the water gas reaction governs the principal product concentrations.

2.2.2. Combustion Products Containing a Condensed Material - The technique which we now described is applicable to systems containing for example, the elements H, C, O, N, Cl, Al. A representative propellant based on these materials is the polyurethane, ammonium perchlorate, aluminum system.

The first approximation to the composition of the system is obtained from Eq. 3-48, modified by including n_{HCl}^0 in the equation for N_H and $n_{Al_2O_3(c)}^0$ in the equation for N_O . The first approximation for these two additional species is given by:

$$\left. \begin{aligned} n_{HCl}^0 &= N_{Cl} \\ n_{Al_2O_3(c)}^0 &= \frac{1}{2} N_{Al} \end{aligned} \right\} \quad (\text{Eq. 3-56})$$

Thus, no additional complications arise in obtaining $n_{H_2}^0$, $n_{CO_2}^0$, n_{CO}^0 , $n_{H_2O}^0$, $n_{N_2}^0$, n_{HCl}^0 and $n_{Al_2O_3(c)}^0$.

The first approximation to the concentrations of six secondary species are again calculated from Eq. 3-49 to 3-54, where now:

$$n^0 = n_{H_2}^0 + n_{CO_2}^0 + n_{CO}^0 + n_{H_2O}^0 + n_{N_2}^0 + n_{HCl}^0$$

Note that this sum refers to gaseous species and therefore does not contain $n_{Al_2O_3(c)}^0$. Additional secondary species appear in this system. The first approximation for their concentrations are calculated from the equations:

$$\left. \begin{aligned} \frac{1}{2} H_2 + Cl &\rightleftharpoons HCl \\ n_{HCl}^0 &= K_{Cl}(T) \frac{n_{HCl}^0}{(n_{H_2}^0)^{\frac{1}{2}}} \left(\frac{p}{n_g^0} \right)^{-\frac{1}{2}} \end{aligned} \right\} \quad (\text{Eq. 3-57})$$

$$\left. \begin{aligned} (Al_2O_3)_c + H_2 &\rightleftharpoons 2 AlO + H_2O \\ n_{AlO}^0 &= K_{AlO}(T) \frac{(n_{H_2}^0)^{\frac{1}{2}}}{(n_{H_2O}^0)^{\frac{1}{2}}} \cdot \left(\frac{p}{n_g^0} \right)^{-1} \end{aligned} \right\} \quad (\text{Eq. 3-58})$$

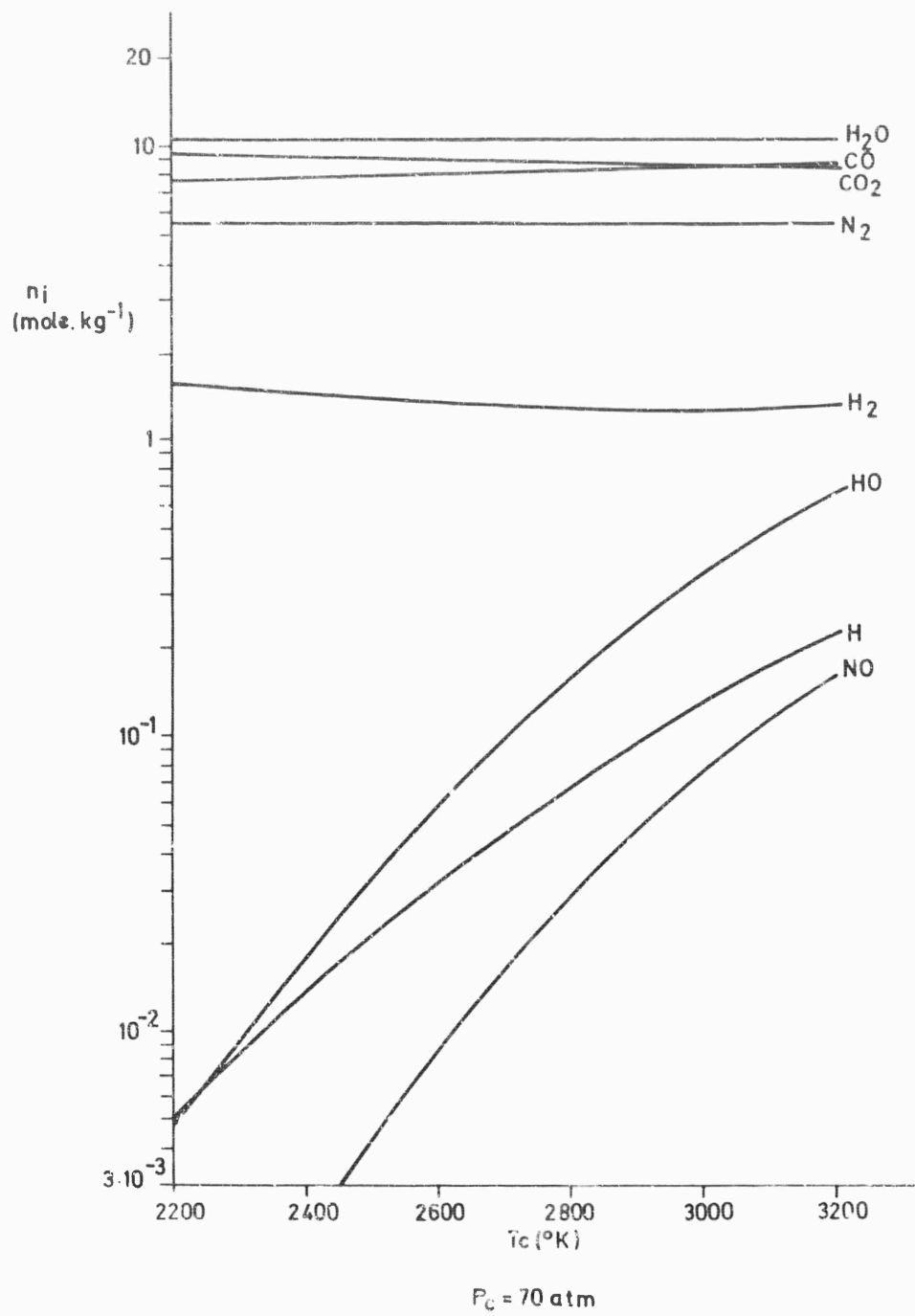


Fig. 3-5 Equilibrium composition in gaseous systems (H, O, C, N) as function of temperature.

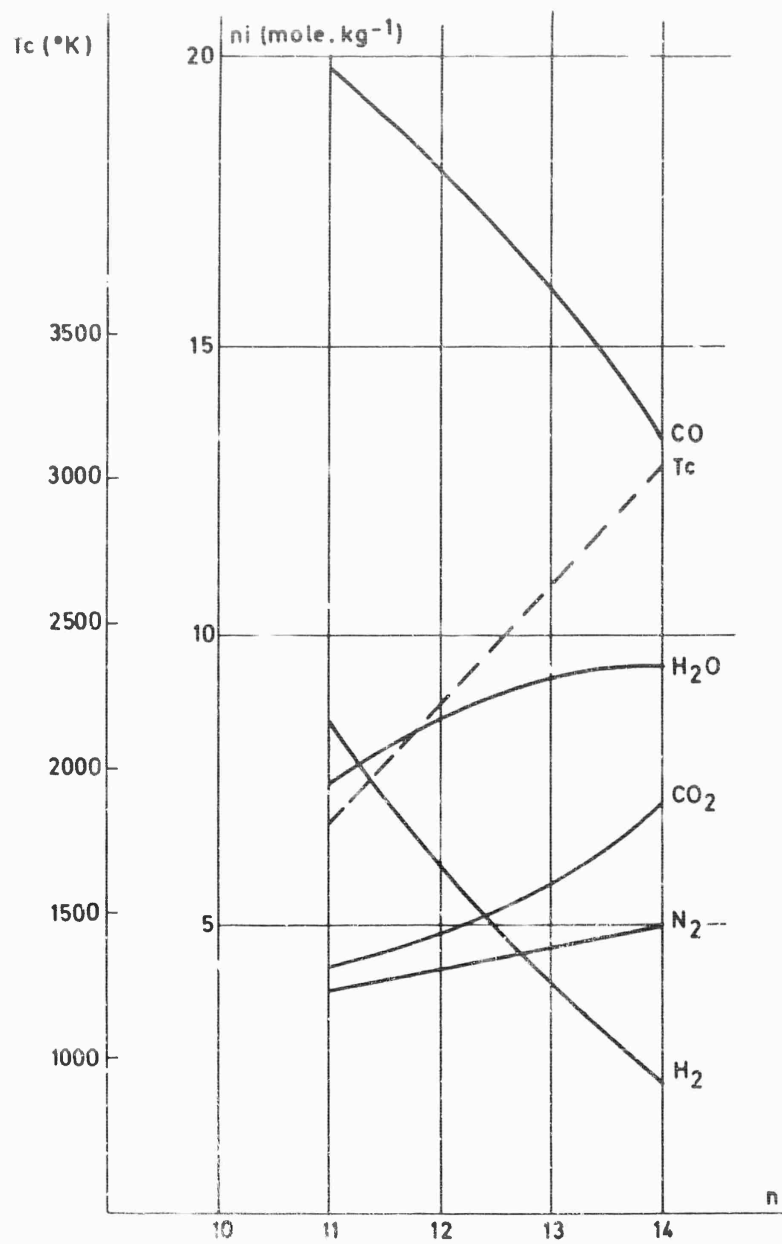


Fig. 3-6 Equilibrium composition in gaseous systems (H, O, C, N) versus n .

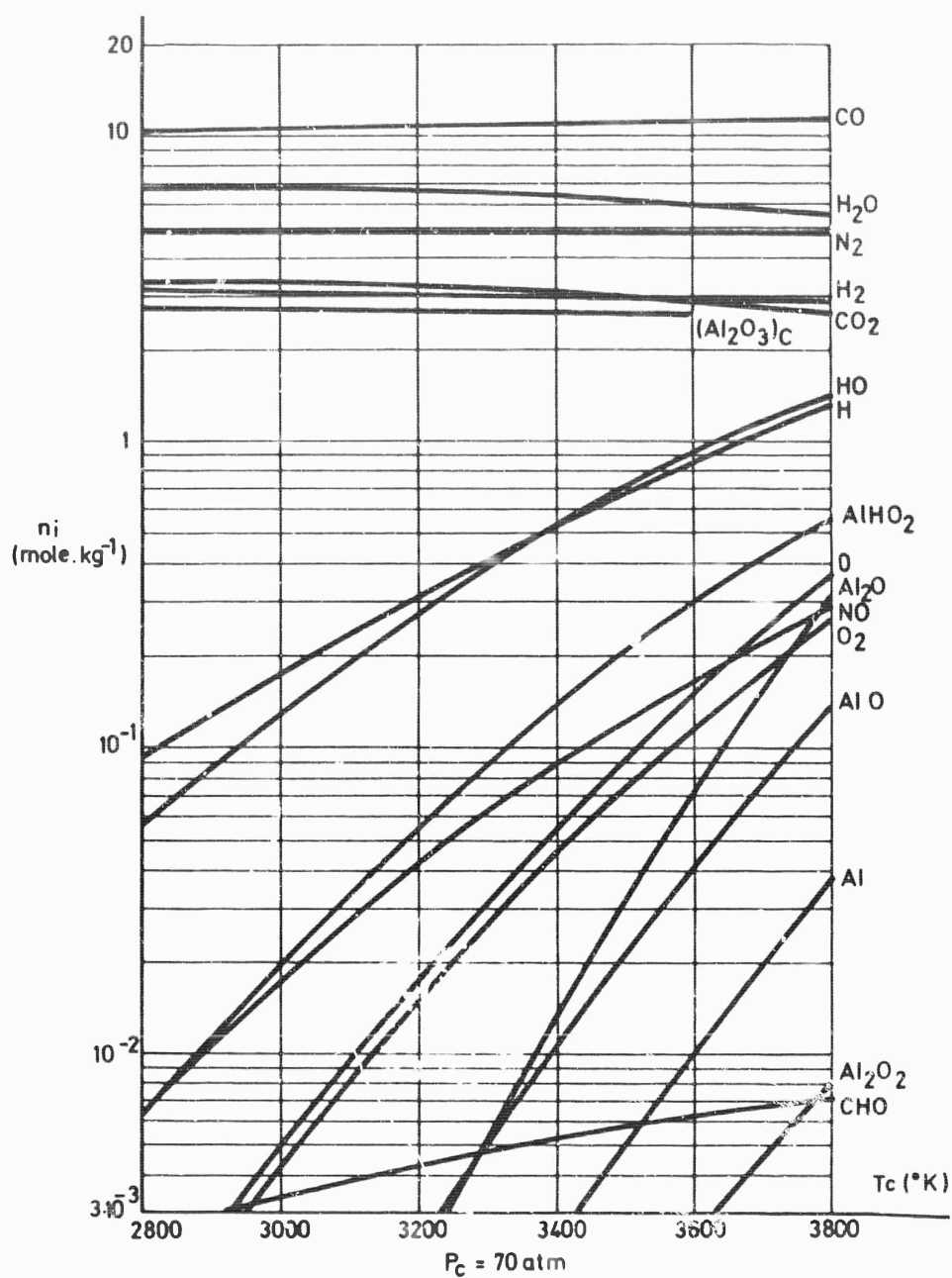
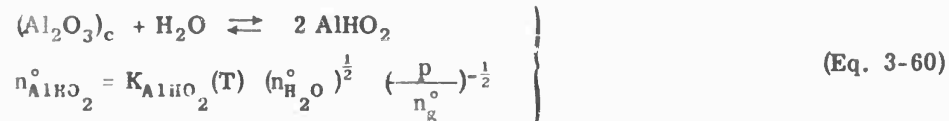
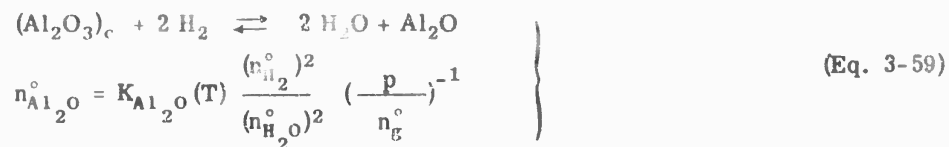


Fig. 3-7 Equilibrium composition in gaseous systems involving condensed phases (Al_2O_3) as a function of temperature



The quantities corresponding to Eq. 3-55 are calculated from:

$$\left. \begin{aligned} \mathcal{N}_C' &= \mathcal{N}_C \\ \mathcal{N}_H' &= \mathcal{N}_H - n_{\text{OH}}^\circ - n_{\text{H}}^\circ - n_{\text{AlHO}_2}^\circ \\ \mathcal{N}_{\text{Al}}' &= \mathcal{N}_{\text{Al}} - n_{\text{AlO}}^\circ - 2n_{\text{Al}_2\text{O}}^\circ - n_{\text{AlHO}_2}^\circ \\ \mathcal{N}_N' &= \mathcal{N}_N - n_{\text{N}}^\circ - n_{\text{NO}}^\circ \\ \mathcal{N}_O' &= \mathcal{N}_O - n_{\text{OH}}^\circ - 2n_{\text{O}_2}^\circ - n_{\text{O}}^\circ - n_{\text{NO}}^\circ - n_{\text{AlO}}^\circ - n_{\text{Al}_2\text{O}}^\circ - 2n_{\text{AlHO}_2}^\circ \\ \mathcal{N}_{\text{Cl}}' &= \mathcal{N}_{\text{Cl}} - n_{\text{Cl}}^\circ \end{aligned} \right\} \quad (\text{Eq. 3-61})$$

These new values are used in the modified form of Eq. 3-48 and in Eq. 3-56 to calculate improved estimates $n_{\text{CO}_2}^1$, n_{CO}^1 , $n_{\text{H}_2\text{O}}^1$, $n_{\text{H}_2}^1$, n_{HCl}^1 , $n_{\text{Al}_2\text{O}_3(c)}^1$ and $n_{\text{H}_2}^1$.

Equations 3-49 - 3-54 and 3-57 - 3-60 are then used for improved estimates of the remaining concentrations, now with $n^\circ = n_{\text{CO}_2}^\circ + n_{\text{CO}}^\circ + n_{\text{H}_2\text{O}}^\circ + n_{\text{H}_2}^\circ + n_{\text{HCl}}^\circ + n_{\text{N}_2}^\circ + n_{\text{H}}^\circ + n_{\text{OH}}^\circ + n_{\text{AlHO}_2}^\circ + n_{\text{AlO}}^\circ + n_{\text{Al}_2\text{O}}^\circ + n_{\text{N}}^\circ + n_{\text{NO}}^\circ + n_{\text{O}_2}^\circ + n_{\text{O}}^\circ + n_{\text{Cl}}^\circ$. The rest of the iterative procedure is entirely analogous with that of the preceding problem.

In the Fig. 3-7 we indicate how the resulting number of moles of the various species vary with temperature at a pressure of 70 atm., for an aluminized double-base propellant with representative properties. Concentrations of two trace species for which we have not given equations are also shown in Fig. 3-1; the reader shall have no difficulty in seeing how to compute these two additional concentrations. The concentrations of the principal products CO , H_2O , N_2 , CO_2 , H_2 and $\text{Al}_2\text{O}_3(c)$ exhibit the same lack of temperature dependence that was evident in Fig. 3-5.

2.3. General Methods for Calculating Equilibrium Compositions

There are numerous methods for calculating equilibrium compositions. We have selected three for presentation here, the methods of Huff, White and Brinkley. We shall spend most time on the method of Brinkley, which appears to be best adapted to problems related to the composition of combustion products of solid propellants.

2.3.1. Huff Method (2) - The iterative method of Huff is based on replacing the nonlinear equations by a set of linear equations for correcting an approximate solution. The linear equations are obtained from a first-order Taylor series expansion about the approximate solution. If the concentration is represented as a state vector $\mathbf{x} = (x_1, x_2, \dots, x_n)$, then the change in any function $U(\mathbf{x})$ in the neighborhood of $\mathbf{x} = \mathbf{x}^{(a)}$ is approximated by:

$$\Delta U \equiv U(\mathbf{x}) - U(\mathbf{x}^{(a)}) \approx \sum_{i=1}^n \left(\frac{\partial U}{\partial x_i} \right)^{(a)} (x_i - x_i^{(a)}), \quad (\text{Eq. 3-62})$$

which is linear in $\mathbf{x} - \mathbf{x}^{(a)}$.

Consistent with this linearization, the number of moles n_1 is set equal to $x_1^{(a)}(1 + \xi_1)$, so that:

$$\left. \begin{aligned} n_1 &= x_1^{(a)} (1 + \xi_1) \\ \ln n_1 &\approx \ln x_1^{(a)} + \xi_1 \end{aligned} \right\} \quad (\text{Eq. 3-63})$$

where $x_1^{(a)}$ is an approximate solution and $|\xi_1| \ll 1$. When use is made of Eq. 3-63, Eq. 3-27 becomes:

$$\sum_{i=1}^n \beta_{ij} x_i^{(a)} \xi_i = \hat{N}_j - \sum_{i=1}^n \beta_{ij} x_i^{(a)} \equiv \Delta \hat{N}_j \quad (\text{Eq. 3-64})$$

We remark that Huff develops his method for a general multiphase system but we consider here only the form for which the development of Eq. 3-42 is valid.

Setting:

$$M_1 - \sum_{i=1}^l \beta_{ij} M_j \equiv \ln K_1(T), \quad (\text{Eq. 3-65})$$

we obtain from Eq. 3-42 and 3-43:

$$\begin{aligned} \ln n_1 - \sum_{j=1}^l (1 - \delta_j) \beta_{1j} \ln n_j - \left[1 - \sum_{j=1}^l (1 - \delta_j) \beta_{1j} \right] \ln n \\ = \ln K_1(T) - \left[1 - \sum_{j=1}^l (1 - \delta_j) \beta_{1j} \right] \ln p. \end{aligned} \quad (\text{Eq. 3-66})$$

Substitution of Eq. 3-63 into this formula yields:

$$\begin{aligned} \xi_1 - \sum_{j=1}^l (1 - \delta_j) \beta_{1j} \xi_j - \left[1 - \sum_{j=1}^l (1 - \delta_j) \beta_{1j} \right] (\ln n - \ln n^{(a)}) \\ = \ln K_1(T) - \left[1 - \sum_{j=1}^l (1 - \delta_j) \beta_{1j} \right] \ln p + \ln x_1^{(a)} - \sum_{j=1}^l (1 - \delta_j) \beta_{1j} \ln x_j^{(a)} \\ + \left[1 - \sum_{j=1}^l (1 - \delta_j) \beta_{1j} \right] \ln n^{(a)} \equiv \ln (K_1 / K_1^{(a)}) \end{aligned} \quad (\text{Eq. 3-67})$$

where $n^{(a)}$ is given by Eq. 3-44 with n_1 replaced by $x_1^{(a)}$. Substitution of Eq. 3-63 into Eq. 3-44 gives:

$$\sum_{i=1}^n x_i^{(a)} \xi_i = n - n^{(a)} \equiv \Delta n \quad (\text{Eq. 3-68})$$

since the linearization implies that:

$$\ln n - \ln n^{(a)} = \ln (n/n^{(a)}) = \ln (1 + \Delta n/n^{(a)}) \approx \Delta n/n^{(a)}$$

Eq. 3-67 can be written in the form:

$$\xi_1 - \sum_{j=1}^l (1 - \delta_j) \beta_{1j} \xi_j - \left[1 - \sum_{j=1}^l (1 - \delta_j) \beta_{1j} \right] \frac{\sum_{j=1}^n x_j^{(a)} \xi_j}{\sum_{j=1}^n x_j^{(a)}} = \ln \left[\frac{K_1}{K_1^{(a)}} \right] \quad (\text{Eq. 3-69})$$

where use been made of Eq. 3-68 and of the definition of $n^{(a)}$.

Equations 3-64 and 3-69 constitute explicit linear relationships for $\Delta \hat{N}_i$ and $\ln (K_i / K_i^{(a)})$ in terms of the quantities ξ_i . From the development of Eq. 3-27 and 3-44, it is seen that n of these relationships are nontrivial and are linearly independent in the variables ξ_i . The independent relationships contained in Eq. 3-54 and 3-69 may therefore be expressed symbolically in the form:

$$\sum_{k=1}^n B_{ik} \xi_k = A_i \quad i = 1, \dots, n, \quad (\text{Eq. 3-70})$$

where the coefficient B_{ik} depend only on δ_j , β_{ij} and $x_j^{(a)}$, and the elements of A_i are $\Delta \hat{N}_i$ and $\ln (K_i / K_i^{(a)})$, which are defined in Eq. 3-64 and 3-67, respectively. The elements of A_i are seen to depend on δ_j , β_{ij} , $x_j^{(a)}$, \hat{N}_j , p and $K_j(T)$. If the chemical system is specified by giving δ_j , β_{ij} , \hat{N}_j , p and K_j , then for any set of approximate solutions $x_j^{(a)}$ the vector A_i and the matrix B_{ik} can be evaluated. Since B_{ik} is nonsingular, Eq. 3-70 can then be solved for the vector ξ_k by standard

techniques ($\xi_k = \sum_{i=1}^n B_{ki}^{-1} A_i$). The resulting values of ξ_k provide improved esti-

mates for n_i when substituted into Eq. 3-63. The improved estimate would constitute the correct solution if the linearization were precisely correct. Since the initial choices of $x_i^{(a)}$ are not likely to fall accurately within the range of validity of a linearization about the correct solution, the improved estimates will not coincide with the correct solution. Nevertheless, they are expected to lie closer to the correct solution than the $x_i^{(a)}$ do and they may therefore be taken as new, improved trial solutions $x_i^{(a)}$. The iterative process thus implied may be continued until some criterion for convergence is met.

The linearization technique that we have described is amenable to various generalizations. For example, in rocket motor analyses the temperature in the combustion chamber is determined by an energy conservation law which is equivalent to the statement that the enthalpy of the mixture of combustion products is a known constant. The determination of chamber temperature can be combined with the linearized calculation of product gas composition by introducing an additional element in the vector ξ , namely ξ_T , which is defined by $T = T^{(a)}(1 + \xi_T)$ where $T^{(a)}$ is an approximate estimate for the chamber temperature. The thermodynamic expression for the enthalpy of the system in terms of pressure, temperature and composition provides the additional independent equation that is needed in order to determine ξ_T from a set of expressions that is similar to Eq. 3-70. Of course, in this case all quantities $K_i(T)$ must be expanded linearly about $T^{(a)}$, and so the relationship analogous to Eq. 3-70 becomes considerably more complex. As another example for a generalization, we note that in ideal nozzle flow the process is both adiabatic and isentropic. It is possible to linearize the pressure (in addition to the temperature) about an approximate estimate of the thermodynamic state and to use the thermodynamic expression for the entropy as a function of pressure, temperature and composition (along with the enthalpy expression) in the isentropic and adiabatic equations in order to obtain $n + 2$ linear independent equations for ξ_i , ξ_T and ξ_p , that are similar in form to Eq. 3-70. The result would be an iterative procedure for calculating the specific impulse directly. In practice however, the complexity that is produced by these additional linearizations is usually so great that it is less laborious first to compute equilibrium compositions for a range of values of p and T , than to compute enthalpies and entropies of the mixture for various values of p and T from the equilibrium compositions and thermodynamic properties, and finally to note from these results what sequence of $p - T$ values gives isentropic and/or isenthalpic conditions.

The major inconvenience with the linearization method is that an error in the approximate concentration $x_1^{(a)}$ of any one of the species has an appreciable effect on the calculated value of ξ_1 and hence on the convergence of the iterative procedure.

High precision is therefore required in calculating all ξ_1 and this precision requirement reduces the number of species that can be handled with current computing machines. There is the related hazard that the linearization technique may lead to negative concentrations, $x_1^{(a)} (1+\xi_1)$ at some stage in the calculation, particularly for species that are present in very low concentrations, unless the initial estimates $x_1^{(a)}$ are known rather accurately. The method, of course, breaks down (equilibrium equations become inapplicable) if negative concentrations appear. This last difficulty can be circumvented by performing calculations first with a small number of species in order to obtain a fairly accurate estimate of the composition, and then repeating the calculations with a larger number of species, using information obtained in the first calculation to provide starting estimates $x_1^{(a)}$.

We note that since the pressure and the total number of gaseous species both appear in the governing equations only in the form p/n , the calculation procedure can be simplified somewhat if calculations are made for specified values of p/n instead of specified values of p . This change provides no real inconvenience when properties are being calculated for a range of values of p ; it merely means that the pressure for which each calculation applies is not known precisely in advance. The resulting simplification is that the last term on the left-hand side of Eq. 3-69 does not appear. Many other variations of Huff's method can be proposed for simplification, generalization or improvement in convergence and in precision.

2.3.2. White Method (11) - In White's technique, the equilibrium composition is determined by searching for an extremum in the Gibbs free energy of the system. The method is thus based in essence on a direct application of Eq. 3-57a to a closed system at fixed pressure and temperature and fixed total numbers of atoms.

The Gibbs free energy of the chemical system is simply:

$$F = \sum_{i=1}^n \mu_i n_i \quad (\text{Eq. 3-71})$$

in which the quantities μ_i are given by Eqs. 3-38 and 3-39 for condensed and gaseous species, respectively. At a stable point of chemical equilibrium, the function F is a minimum for all isothermal, isobaric property variations in a closed system. It is convenient to work with the function:

$$\Phi(n_i) \equiv \frac{F}{R^o T} = - \sum_{i=1}^n M_i n_i + \sum_{i=1}^n n_i \ln n_i + n \ln \left(\frac{p}{n} \right) \quad (\text{Eq. 3-72})$$

where use has been made of Eq. 3-38 to 3-40 and of Dalton's law (Eq. 3-43 and 3-44). The fact that F is a minimum at the equilibrium implies that Φ is also a minimum there.

The calculation is begun by selecting arbitrarily a set of values x_i for n_i (of course with an attempt to take these values as near to the equilibrium values as possible). It is hoped that the true equilibrium solution will lie within the range of validity of a second-order Taylor expansion of Φ about x_i .

A second order Taylor expansion of Φ about x_i yields:

$$\Phi(y_i) \approx \Phi(x_i) + \sum_{i=1}^n \frac{\delta \Phi}{\delta x_i} (y_i - x_i) + \frac{1}{2} \sum_{i=1}^n \sum_{j=1}^n \frac{\delta^2 \Phi}{\delta x_i \delta x_j} (y_i - x_i) (y_j - x_j), \quad (\text{Eq. 3-73})$$

in which Eqs. 3-72 and 3-44 imply that:

$$\frac{\delta \Phi}{\delta x_i} = \begin{cases} -M_i + \ln x_i + \ln(p/x), & i = 1, \dots, m \\ -M_i, & i = m+1, \dots, n \end{cases} \quad (\text{Eq. 3-74})$$

and:

$$\frac{\delta^2 \Phi}{\delta x_i \delta x_j} = \begin{cases} \delta_{ij}/x_i - 1/x & \text{if both } i \leq m \text{ and } j \leq m \\ 0 & \text{if either } i > m \text{ or } j > m \end{cases} \quad (\text{Eq. 3-75})$$

where δ_{ij} is Kronecker delta and $x \equiv \sum_{i=1}^m x_i$. The next step in the calculation is to attempt to choose values of y_i in Eq. 3-73 that are equal to the equilibrium values of n_i .

The equilibrium condition is the stationarity of Φ subject to the atom conservation constraints (Eq. 3-27). We can apply this condition to the point $n_i = y_i$ by defining the function:

$$\Lambda(y_i) = \Phi(y_i) + \sum_{j=1}^l \lambda_j (\hat{N}_j - \sum_{i=1}^n \beta_{ij} y_i), \quad (\text{Eq. 3-76})$$

where λ_j are Lagrange multipliers that enforce the validity of Eq. 3-27. Standard variational calculus then shows that the stationary (extremum) condition is given by:

$$\delta \Lambda / \delta y_i = \delta \Phi / \delta y_i - \sum_{j=1}^l \lambda_j \beta_{ij} = 0, \quad i = 1, \dots, m \quad (\text{Eq. 3-77})$$

Equation 3-77, along with Eq. 3-27, would define the exact equilibrium condition if the exact function $\Phi(y_i)$ were employed therein. Since the exact function contains troublesome nonlinearities, Eq. 3-73 is used as an approximation for $\Phi(y_i)$ in Eq. 3-77. The result will be an approximate equilibrium condition y , which can be improved by taking it to be the value x_i in a second calculation of y_i . An iterative procedure thus emerges.

In order to see explicitly how to calculate y_i from Eqs. 3-73 and 3-77, we note that differentiation of Eq. 3-73 and utilization of Eqs. 3-74 and 3-75 yields; upon substitution into Eq. 3-77,

$$-M_i + \ln x_i + \ln(p/x) + y_i/x_i - y/x - \sum_{j=1}^l \lambda_j \beta_{ij} = 0, \quad i = 1, \dots, m \quad (\text{Eq. 3-78})$$

and:

$$-M_i - \sum_{j=1}^l \lambda_j \beta_{ij} = 0 \quad i = m+1, \dots, n \quad (\text{Eq. 3-79})$$

where $y = \sum_{i=1}^m y_i$. Recalling that y_i must also satisfy Eq. 3-27, we have additionally:

$$\sum_{i=1}^n \beta_{ij} (y_i - x_i) = \hat{N}_j - \sum_{i=1}^n \beta_{ij} x_i \equiv \Delta \hat{N}_j \quad j = 1, \dots, \ell \quad (\text{Eq. 3-80})$$

from which it may be noted that the x_i are not required to satisfy Eq. 3-27 exactly. Equations 3-78 -3-80 constitute $n + \ell$ independent linear equations in the ℓ unknown constants λ_j and the n unknown approximate equilibrium concentrations y_i .

White reduced the dimensions of the matrix that must be inverted in order to solve this set of equations, by multiplying Eq. 3-78 by $\beta_{ik} x_i$, summing from $i = 1$ to m , and then subtracting Eq. 3-80 with subscript j replaced by k from the result.

One thus obtains:

$$\begin{aligned} & \sum_{j=1}^{\ell} \lambda_j \left[\sum_{i=1}^m \beta_{ik} \beta_{ij} x_i \right] + \sum_{i=m+1}^n \beta_{ik} \Delta x_i + \Delta x \sum_{i=1}^m \beta_{ik} \frac{x_i}{x} \\ & = \Delta \hat{N}_k + \sum_{i=1}^m \beta_{ik} x_i \left[-M_i + \ln x_i + \ln \left(\frac{p}{x} \right) \right] \quad k = 1, \dots, \ell \end{aligned} \quad (\text{Eq. 3-81})$$

where:

$$\Delta x_i \equiv y_i - x_i, \quad i = m+1, \dots, n \quad (\text{Eq. 3-82})$$

and:

$$\Delta x \equiv y - x \quad (\text{Eq. 3-83})$$

Multiplying Eq. 3-78 by x_i and summing from $i = 1$ to m yields:

$$\sum_{j=1}^{\ell} \lambda_j \left[\sum_{i=1}^m \beta_{ij} x_i \right] = \sum_{i=1}^m x_i \left[-M_i + \ln x_i + \ln \left(\frac{p}{x} \right) \right]. \quad (\text{Eq. 3-84})$$

Equations 3-79, 3-81 and 3-84 constitute $n - m + \ell + 1$ linear equations in the $n - m + \ell + 1$ unknowns:

$$\begin{aligned} & \Delta x_i, \quad i = m+1, \dots, n \\ & \lambda_j, \quad j = 1, \dots, \ell \\ & \Delta x. \end{aligned}$$

After the $n - m + \ell + 1$ dimensional matrix for this linear set is inverted to give $(\Delta x_i, \lambda_j, \Delta x)$, Eq. 3-78 gives the m remaining unknowns y_i ($i = 1, \dots, m$) directly.

As with method described in the preceeding section, it is possible that this calculation procedure will lead to negative values of some of the y_i 's. If this occurs, the differences $y_i - x_i$ are reduced proportionally to assure positive concentrations at the expense of not satisfying Eqs. 3-77 and 3-27 exactly. If the x_i satisfy the atom conservation equations so that $\Delta \hat{N}_j = 0$, then the proportional reduction preserves the satisfaction of Eq. 3-27.

The method encounters difficulties if one considers a condensed species which is not actually present at equilibrium. An incorrect solution is obtained when the concentration of a condensed species goes to zero. In this case, it is necessary to abandon the solution and to begin again with a system prescribed in such a way that the offending species is not included.

2.3.3. Brinkley Method (8) - Brinkley's method requires that all condensed species be included in the basis and therefore employs Eqs. 3-23 and 3-42 as a starting point. For gas-phase species, it also employs mole fractions as variables instead of the number of moles per unit mass. In order to express the governing equations in terms of mole fractions, we may first divide Eq. 3-29 by n , obtaining:

$$\frac{\hat{N}_j}{n} = \delta_j X_j^c + \sum_{i=1}^m \beta_{ij} X_i, \quad j = 1, \dots, m, \quad (\text{Eq. 3-85})$$

in which the mole fractions of gas-phase species are defined as:

$$X_i \equiv n_i/n \quad i = 1, \dots, m \quad (\text{Eq. 3-86})$$

and the symbols:

$$X_j^c \equiv n_j^c/n \quad (\text{set } j \text{ such that } 1 \leq j \leq \ell \text{ and } \delta_j = 1) \quad (\text{Eq. 3-87})$$

are dimensionless measures of the number of moles of each condensed species in the system. The quantity n is then eliminated from Eq. 3-85 by multiplying the equation by $(1 - \delta_j)$ and then summing over all j . Since $\delta_j (1 - \delta_j)$ is zero for all j by definition, we obtain:

$$\frac{1}{n} = \frac{\sum_{i=1}^m \beta_i X_i}{\sum_{j=1}^{\ell} (1 - \delta_j) \hat{N}_j} \quad (\text{Eq. 3-88})$$

where:

$$\beta_i \equiv \sum_{j=1}^{\ell} (1 - \delta_j) \beta_{ij} \quad i = 1, \dots, m \quad (\text{Eq. 3-89})$$

Substitution of Eq. 3-89 for $1/n$ into Eq. 3-85 finally yields the desired form of the atom conservation laws, viz.,

$$\bar{X}_j = \sum_{i=1}^m X_i [\beta_{ij} + (1 - \beta_i) \bar{X}_j] = \delta_j X_j^c, \quad j = 1, \dots, \ell \quad (\text{Eq. 3-90})$$

where nondimensional overall atomic composition has been defined as:

$$\bar{X}_j = \hat{N}_j / \sum_{k=1}^{\ell} (1 - \delta_k) \hat{N}_k, \quad j = 1, \dots, \ell \quad (\text{Eq. 3-91})$$

and where use has been made of the identity $\sum_{i=1}^m X_i = 1$ in order to express Eq. 3-90

in a form that is convenient for later developments. The mole-fraction form of the chemical equilibrium equations is obtained much more simply from Eq. 3-42; substitution of Eq. 3-43 and 3-86 into Eq. 3-42 readily yields:

$$\ln X_i = \sum_{j=1}^{\ell} (1 - \delta_j) \beta_{ij} \ln X_j + M_i - \sum_{j=1}^{\ell} \beta_{ij} M_j - (1 - \beta_i) \ln p, \quad i = 1, \dots, m \quad (\text{Eq. 3-92})$$

It should be recalled that only $n-\ell$ of these m relations are nontrivial.

One now sees that the concentrations of condensed species are essentially already eliminated from the nonlinear system of governing equations given in Eqs. 3-90 and 3-92. The quantities X_j do not appear at all in Eq. 3-92 and they appear in Eq. 3-90 only for values of j such that $\delta_j = 1$. The $n-m$ relations obtained from Eq. 3-90 with $\delta_j = 1$ give each of the $n-m$ quantities X_j in terms of X_i and specified constants; the remaining $\ell + m-n$ relations for which $\delta_j = 0$ in Eq. 3-90, when considered along with the $n-\ell$ nontrivial relations in Eq. 3-92, provide a total of m relations for the m unknown X_i 's. Our task now is to devise a method for solving these m nonlinear coupled equations. Once we have this solution, we may calculate all $n-m$ of the X_j values directly from the $\delta_j = 1$ equations of Eq. 3-90, and we may also calculate n directly from Eq. 3-88, thereby obtaining all concentrations (through Eqs. 3-86 and 3-87).

An iterative method is proposed for solving Eq. 3-92 along with the $\delta_j = 0$ equations of Eq. 3-90. In the iterative method, it is necessary to treat the gaseous species contained in the basis differently from the other gaseous species. We let:

$$Z_i \equiv \ln X_i \quad (1 \leq i \leq m, \text{ species } i \in \text{ basis}) \quad (\text{Eq. 3-93})$$

only for gaseous species contained in the basis. We may then write Eq. 3-92 in the form:

$$\ln X_i = \sum_{j=1}^{\ell} (1-\delta_j) \beta_{ij} Z_j + \Omega_i, \quad i = 1, \dots, m \quad (\text{Eq. 3-94})$$

where Ω_i stands for the last three terms in Eq. 3-92 (all of which are known constants). The $n-\ell$ nontrivial relations appearing here obviously correspond to the values of i for which we have not defined Z_i . If we choose trial values Z_i^0 of Z_i , e.g., by setting $Z_i^0 = \ln \bar{X}_i$, then the relations given here determine corresponding values for the remaining $n-\ell$ quantities $\ln X_i^0$ (viz those not contained in the basis) such that the equilibrium equations are all satisfied exactly. However, the atom conservation equations (including the condition $\sum_{i=1}^m X_i = 1$) in general will not be satisfied exactly. Equations 3-90 for $\delta_j = 0$ are obviously to be used to correct the trial values Z_i^0 in such a way that the atom conservation equations will be satisfied. These corrections are performed by expanding the atom conservation equations linearly about X_i^0 and choosing corrections ΔZ_i^0 (with $Z_i = Z_i^0 + \Delta Z_i^0$), so as to make these expanded equations satisfy atom conservation.

Thus explicitly the linear Taylor expansion of Eq. 3-90 about X_i^0 for $\delta_j = 0$ is:

$$\bar{X}_j - \sum_{i=1}^m X_i^0 [\beta_{ij} + (1-\beta_i) \bar{X}_j] - \sum_{i=1}^m X_i^0 [\beta_{ij} + (1-\beta_i) \bar{X}_j] \Delta \ln X_i^0 = 0$$

(set j such that $1 \leq j \leq \ell$ and $\delta_j = 0$).

The corresponding linear expansion of Eq. 3-94 is:

$$\Delta \ln X_i^0 = \sum_{k=1}^{\ell} (1-\delta_k) \beta_{ik} \Delta Z_k^0, \quad i = 1, \dots, m$$

(where we note that these equations can be used for all values of i because they are identities when species i is contained in the basis) and therefore by substitution we have:

$$\sum_{k=1}^{\ell} (1-\delta_k) \left\{ \sum_{i=1}^m \beta_{ik} X_i^{\circ} [\beta_{1i} + (1-\beta_1) \bar{X}_j] \right\} \Delta Z_k^{\circ} = \bar{X}_j - \sum_{i=1}^m X_i^{\circ} [\beta_{1j} + (1-\beta_1) \bar{X}_j] \quad (\text{Eq. 3-95})$$

(set j such that $1 \leq j \leq \ell$ and $\delta_j = 0$)

Equation 3-95 constitutes a set of $\ell + m - n$ linear, independent equations in the $\ell + m - n$ unknown ΔZ_k° . These equations, of the general form $\sum_k B_{jk} \Delta Z_k^{\circ} = A_j$,

are easily inverted by standard matrix inversion to give ΔZ_k° ($\Delta Z_k^{\circ} = \sum_j B_{kj}^{-1} A_j$).

The values of ΔZ_k° thus obtained are used to compute the improved estimates for Z_k , viz,

$$Z_k^1 = Z_k^{\circ} + \Delta Z_k^{\circ}$$

From Eq. 3-94 the improved estimates for the logarithm of the gas-phase mole fractions are therefore:

$$\ln X_i^1 = \sum_{j=1}^{\ell} (1-\delta_j) \beta_{1j} Z_j^1 + \Omega_i, \quad i = 1, \dots, m$$

The continuation of the iterative process thus implied should be evident. The general formulae for n 'th iteration are:

$$X_i^{(n)} = \exp \left[\sum_{j=1}^{\ell} (1-\delta_j) \beta_{1j} Z_j^{(n)} + \Omega_i \right] \quad i = 1, \dots, n$$

$$\sum_{j=1}^{\ell} (1-\delta_j) \left\{ \sum_{i=1}^m \beta_{ij} X_i^{(n)} [\beta_{1i} + (1-\beta_1) \bar{X}_k] \right\} \Delta Z_j^{(n)} = \bar{X}_k - \sum_{i=1}^m X_i^{(n)} [\beta_{1i} + (1-\beta_1) \bar{X}_k], \quad (\text{Eq. 3-96})$$

$$Z_j^{(n+1)} = Z_j^{(n)} + \Delta Z_j^{(n)}$$

in which the second relationship is to be solved for $\Delta Z_j^{(n)}$ by matrix inversion.

Unlike the other methods described earlier, the iteration procedure defined here can never lead to negative concentrations (essentially because the linearization is entirely in terms of $\ln X_i$). After the iteration has converged sufficiently, the values of X_j^c are computed from Eq. 3-90 with $\delta_j = 1$. If any of these values are found to be negative, one may conclude that the species with $X_j^c < 0$ are not present in the condensed phase when the system is in equilibrium. One then repeats the calculation, adopting a new chemical system from which these condensed species have been excluded. An answer for which all X_j^c are greater than zero is a correct answer for the equilibrium composition of the system.

Aside from this procedural advantage the Brinkley method achieves computational economy at the expense of some analytical intricacy. Thus, the minimum possible number of independent species enters into the iterative calculation, and the dimension ($\ell + m - n$) of the matrix that must be inverted is smaller than the dimensions of the matrices that must be inverted in other procedures. It is possible that if they do not encounter problems of negative concentrations, other methods (e.g., White's method) will converge in fewer iterative steps, but such advantages would largely be offset by the greater complexity of the calculation for each step.

We note additionally that to begin the Brinkley iterative calculation one need only guess $\ell + m - n$ concentrations, whereas a larger number (n) of concentrations is required by the other techniques. If the gaseous species contained in the basis are taken to be those species that are expected to be present in the highest gas-phase concentrations in the equilibrium product mixture, then rather accurate starting concentrations

can often be estimated, thereby decreasing the time required for convergence. It is much more difficult to make good guesses for the values of all n concentrations than to make good guesses for the values of the concentrations of $l + m + n$ principal gaseous constituents.

2.4 Examples of Applications to Propellants Containing H, Li, Be, B, C, Al, N, Cl, O and F.

The computational method of Brinkley has been programed for digital machines at ONERA in such a way that equilibrium compositions can be obtained for systems having a maximum of 20 elements, 20 condensed phases and 250 different chemical species present in equilibrium (9). The program utilizes the thermodynamic data compiled in the JANAF tables by Dow Chemical Co. (16) (17) and is based on the standard reference states used in National Bureau of Standards publications and defined in Section 1.2.2. The program has been used to calculate the performance of numerous propellants. An example of equilibrium compositions is given in Table 3-3 for a propellant composed of 50% ammonium perchlorate, 35% tetrafluoroethylene, 10% aluminum and 5% lithium, at a chamber pressure of 70 atm and at the adiabatic flame temperature. This propellant contains 8 elements and produces more than 80 chemical species in equilibrium. The concentrations of the species are variable and some of the concentrations are negligibly small.

We have given concentrations of H C O N and H C O N Al systems earlier (Section 2.2.) It is of interest to observe the isobaric temperature dependence of the equilibrium compositions of ammonium perchlorate -polyurethane propellants containing metals other than aluminum. Such curves are shown in Fig. 3-8 - 3-10.

We see from Fig. 3-8 that CO, H₂, Li, LiOH, H₂O, LiCl and N₂ are the predominant species when Li is present; H, OH, CO₂, LiH, LiO, LiN, Li₂O, HCl and NO are present in lesser concentrations. Fig. 3-9 refers the adiabatic chamber temperature and shows the effect of varying percentage of Be in an ammonium perchlorate propellant. The dominant species here are BeO(c), H₂, CO, HCl, N₂, H and BeOH; the concentration of H₂O decreases rapidly as the Be percentage increases. Polymers of BeO were not taken into account in the computation. Including boron in the propellant gives rise to many product species, as shown in Fig. 3-10. In addition to the usual principal products such as H₂, CO, H, HCl and N₂, one obtains significant concentrations of BOH, BO, BOC1, BO₂H and B₂O₂. The concentration of B₂O₃ decreases as the temperature increases; at high temperature B₂O₃ is not an important oxidation product.

Compositions of combustion products produced by more complex propellants containing, for example, mixtures of light metals or new fluorine-containing oxidants, can also be computed by the Brinkley method without any difficulties that are apparent *a priori*.

2.5. Evaluation of Propellant Performance.

Having obtained equilibrium product compositions as functions of pressure and temperature, we must next evaluate a number of thermodynamic properties of the system in order to complete the performance calculations.

2.5.1. Thermodynamics of Equilibrium Mixtures - Once the composition of a thermodynamic system is known as a function of pressure and temperature, standard thermodynamic formulas may be used to evaluate such basic thermodynamic properties as enthalpy and entropy for the system (as function of pressure and temperature) from tables of thermodynamic properties (such as enthalpies and entropies) of its constituents. However, in performance calculations various thermodynamic partial derivatives

Gross-weight elemental
composition indices
(moles/kg)

F : 13.987201 H : 17.021711
C : 4.2554278 L₁ : 7.2046109
O : 17.021711 C : 6.9986002
N : 4.2554278 Al : 3.7078235

Composition moles/kg	chamber	Exit pres- sure ratio (70/1)	Composition moles/kg	chamber	Exit pres- sure ratio (70/1)	Composition moles/kg	chamber	Exit pres- sure ratio (70/1)
F	0.0192817	0.0007868	C1	0.3020686	0.0817777	O	0.1943330	0.0016070
N	0.0001213	0.0000003	H	0.4140147	0.0675420	L ₁	0.0785821	0.0068460
Al	0.0010292	0.0000002	F ₂	0	0	C	0	0
O ₂	0.3130395	0.0016949	N ₂	2.0607058	2.1266243	C1 ₂	0.0002773	0.0000233
Li ₂	0.0000118	0	C ₂	0	0	H ₂	0.9657979	0.8646759
H ₂ O	4.1013839	2.3295018	CO	4.4881175	4.6399859	C ₃	0	0
CF ₄	0	0	HCl	1.0471652	1.4469794	HF	4.3251830	9.0700569
A1C1 ₃	0.0001968	0.0000044	OF	0.0000015	0	CC1 ₄	0	0
NO	0.1306202	0.0011429	FO	0.7185647	0.027199	OC1	0.0010793	0.0000041
AlO	0.0090399	0.0000010	Li ₂ O	0.0007069	0.0000033	LiO	0.01505495	0.0000738
Al ₂ O	0.0028056	0	Al ₂ O ₃	0.40847718	0.0000447	CO ₂	2.5099419	2.3586015
C1F ₃	0	0	NF	0	0	C1F	0.0000179	0.0000003
CNF	0.0000009	0	LiF	4.3947331	4.4630257	NOF	0.0000020	0
LiOF	0	0	CF	0	0	Li ₂ F ₂	0.0012002	0.0007054
CF ₃	0	0	C ₂ F ₂	0	0	CF ₂	0	0
AlF	0.2555879	0.0019428	AlF ₂	1.6611564	0.0774372	COF ₂	0.0000004	0
AlOF	0.0071010	0.0000078	LiC1	2.4270476	2.7112474	AlF ₃	0.3990417	0.0946291
LiOC1	0.0000002	0	CC1	0	0	Li ₂ C1 ₂	0.0003734	0.0002385
A1C1 ₂	0.0173492	0.0001517	A1OC1	0.0010867	0.0000005	A1C1	0.0222021	0.0000705
A1C1 ₂ F	0.0063772	0.0003112	A1C1F ₂	0.0621293	0.0070185	A1C1F	0.3428053	0.0068613
AlN	0.0000001	0	LiH	0.0019171	0.0000325	NOC1	0.0000033	0
CH ₂	0	0	CH ₃	0	0	CH	0	0
C ₂ H ₂	0	0	C ₂ H ₄	0	0	CH ₄	0	0
H ₂ N	0.0000078	0	H ₃ N	0.0000048	0.0000002	HN	0.0001096	0.0000005
LiHO	0.2795452	0.0214554	Li ₂ H ₂ O ₂	0.0000001	0	AlH	0.0000309	0
HOC1	0.0004779	0.0000059	A1HO ₂	0.0997208	0.0000708	HOF	0.0000085	0
LiN	0.0031467	0.0000360	CHO	0.0005347	0.0000134	OC1 ₂	0	0
CHOF	0.0000057	0.0000002	Al ₂ O ₂	0.0001813	0	CN	0.0000005	0
Al ₂ O ₃ (C)	0	1.7596139	LiF (C)	0	0	AlHO	0.0000416	0
LiC1 (C)	0	0				AlF ₃ (C)	0	0

Table 3-3 Composition of products of combustion of a propellant containing aluminum and lithium

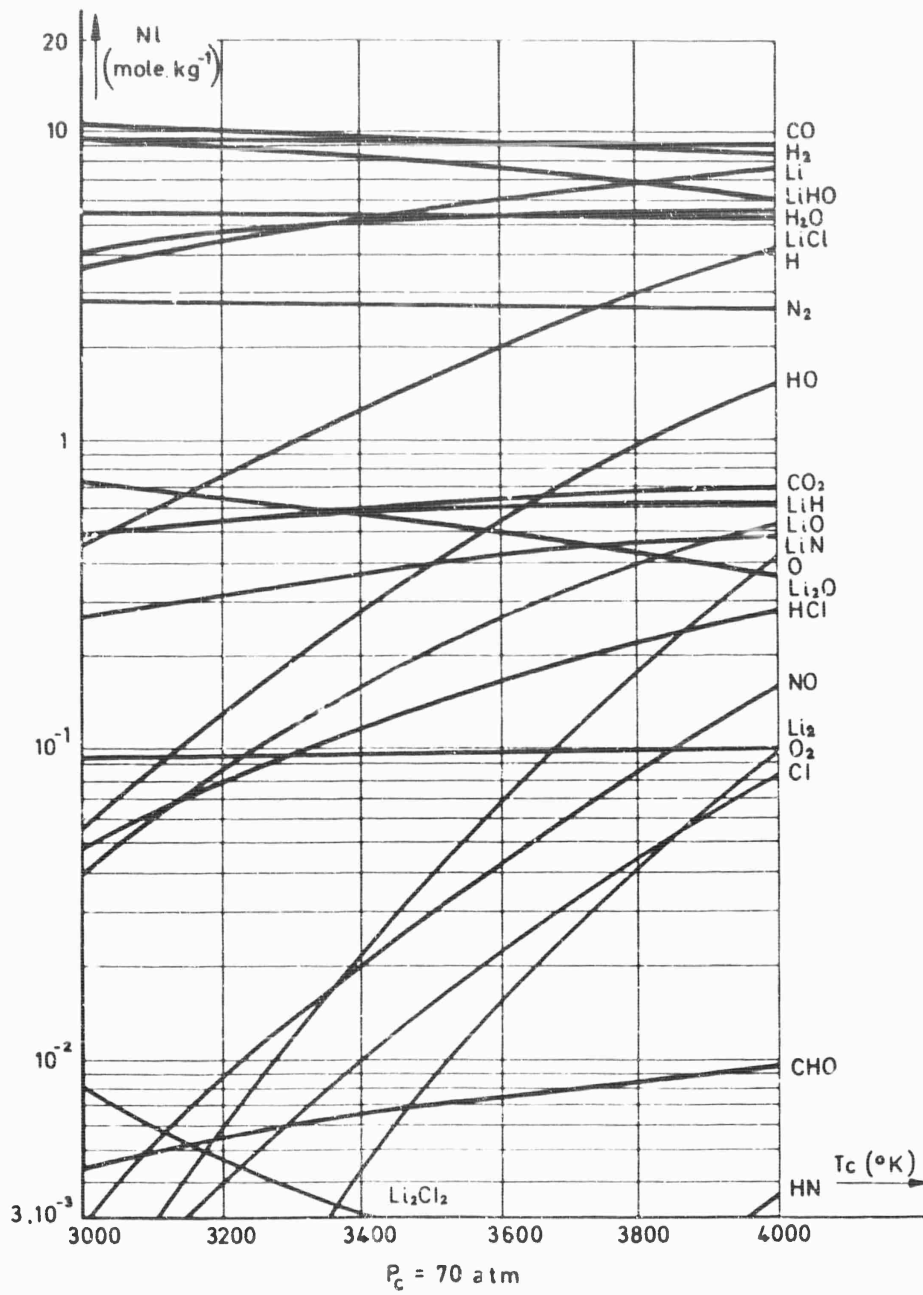


Fig. 3-8 Equilibrium composition in systems involving lithium

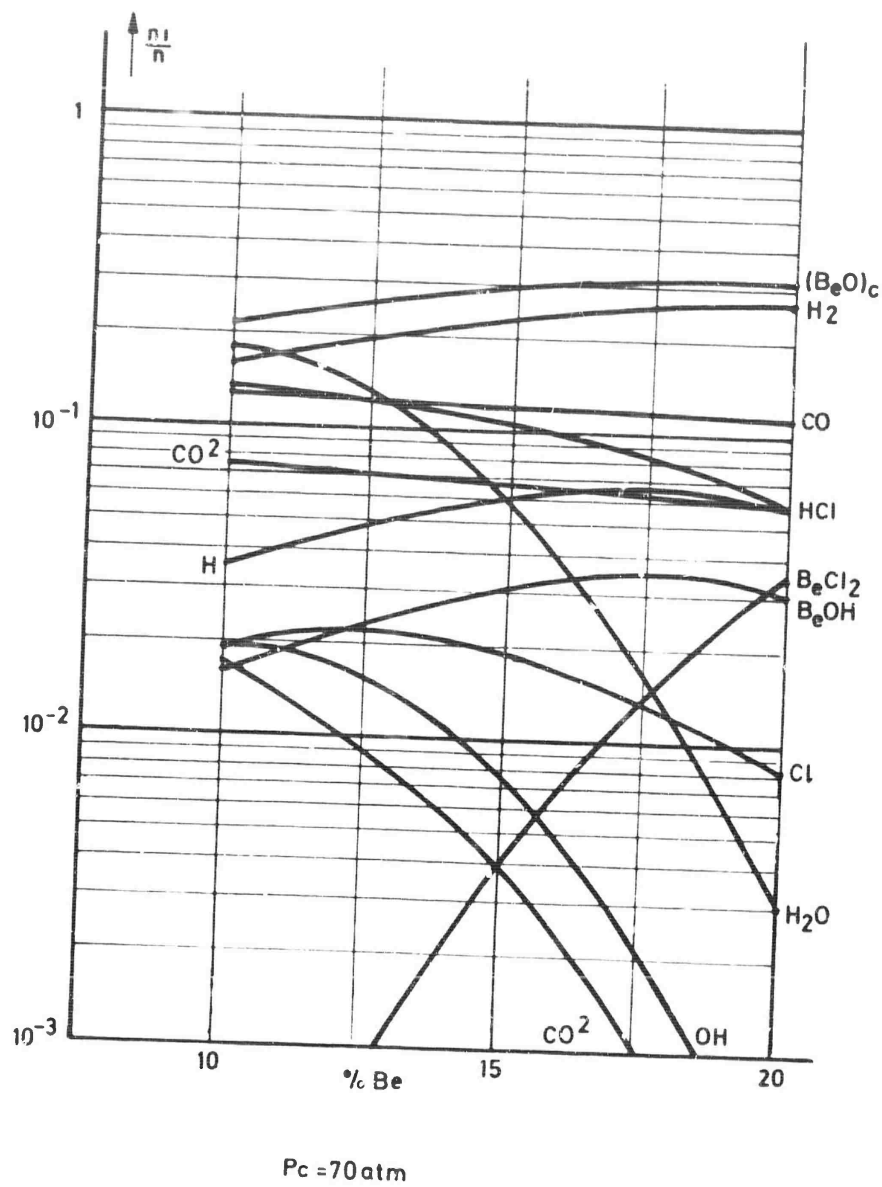


Fig. 3-9 Equilibrium composition in systems involving beryllium

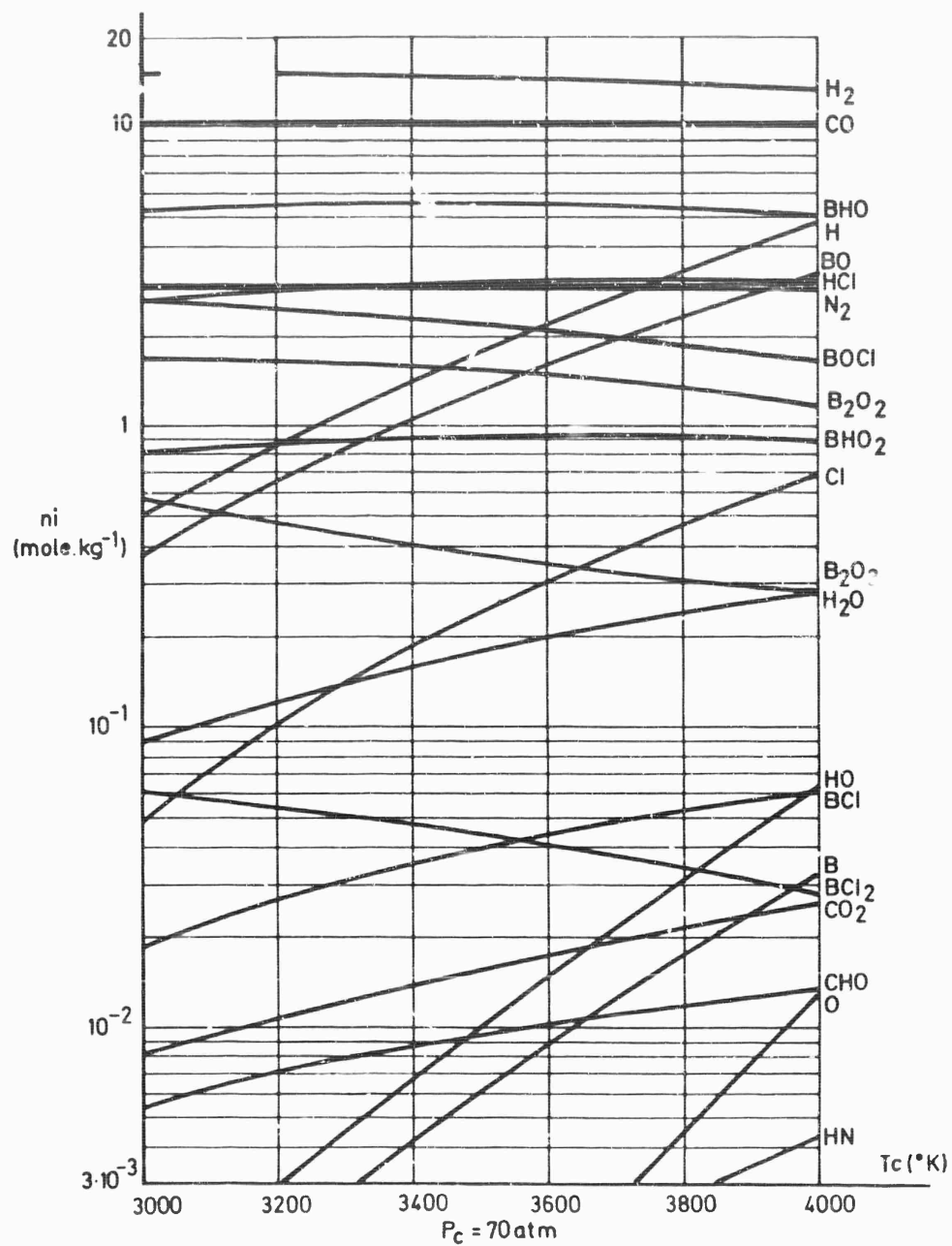


Fig. 3-10 Equilibrium composition in systems involving boron

are needed which are not easily evaluated from standard formulas and existing tables. Two kinds of thermodynamic derivatives are of particular interest, derivatives in which the composition is held fixed and derivatives in which the composition is maintained at equilibrium. No particular difficulties arise in evaluating derivatives at fixed composition; such quantities as the frozen specific heat at constant pressure $c_{pf} \equiv (\partial h / \partial T)_{pf}$, the frozen specific heat at constant volume, $c_{vf} \equiv (\partial u / \partial T)_{pf}$ (u , internal energy per unit mass), and the frozen ratio of specific heats $(\partial \ln p / \partial \ln \rho)_{sf} \equiv \gamma_f = c_{pf} / c_{vf} = c_{pf} / (c_{pf} - nR^\circ)$, which is related to the frozen sound speed a_f by means of the formula $a_f = \sqrt{\gamma_f p / \rho}$, are all easily evaluated from available properties of the constituents. Here the subscript f identifies conditions that are completely frozen chemically. Sufficient conditions for the applicability of these formulas to multiphase systems are the restrictions on condensed solutions and on the simultaneous existence of condensed phases that were stated at the beginning of Section 2.1.1., the hypothesis that the gaseous constituents are all ideal gases, and the assumptions that the specific heat at constant pressure equals the specific heat at constant volume and depends only on temperature for each condensed phase. All of these conditions are satisfied rather accurately for propellant products of practical interest.

However, the evaluation of derivatives at equilibrium composition presents some special problems which we now wish to resolve.

There are basically two independent partial derivatives that need to be considered; the other partial derivatives of interest (aside from those which arise in the evaluation of the heat capacity, which we discuss later) can all be related to these two. We chose as the two independent quantities:

$$D_p \equiv (\partial \ln n / \partial \ln p)_{T_e}, \quad D_T \equiv (\partial \ln n / \partial \ln T)_{p_e} \quad (\text{Eq. 3-97})$$

where n is defined in Eq. 3-44. The motivation for using the quantity n in Eq. 3-91 arises from the fact that a simple generalization of the analysis given in Chapter 2 Section 3.2.1. to multicomponent, multiphase systems with variable heat capacities (but subject to the restrictions emphasized at the top of this page) leads to the equation of state:

$$p = n \rho R^\circ T, \quad (\text{Eq. 3-98})$$

provided additionally that the total volume occupied by condensed phases is negligible compared with the total volume occupied by gas (an approximation which is generally accurate to within 0.1% for propellant products. We assume henceforth that Eq. 3-98 is valid and it follows that Eq. 3-97 refers to derivatives of $\ln(p/\rho T)$ which can be related to the partial derivatives of interest. By standard thermodynamic reasoning. It can be shown, in particular, that:

$$(\partial \ln T / \partial \ln p)_{s_e} = n_e (1 + D_T) / c_{pe}. \quad (\text{Eq. 3-99})$$

and that:

$$\gamma_e \equiv (\partial \ln p / \partial \ln \rho)_{s_e} = c_{pe} / [c_{pe} (1 - D_p) - n_e R^\circ (1 + D_T)^2] \quad (\text{Eq. 3-100})$$

with the equilibrium sound speed a_e related to γ_e through $a_e = [\gamma_e p / \rho]^{1/2}$. One should note that according to the present definitions, $c_{pe} / c_{ve} = (1 - D_p) \gamma_e \neq \gamma_e$. We now proceed to indicate how to calculate D_p and D_T from equilibrium compositions obtained by Brinkley's method. For brevity of notation, we omit the subscript e , it being understood that equilibrium is always to be maintained.

Consider first the calculation of D_T . By differentiating Eq. 3-92 and substituting the resulting values of $d \ln X_i$ into the differential form of Eq. 3-90 for $\delta_j = 0$, we obtain:

$$\begin{aligned} & \sum_{k=1}^l (1-\delta_k) \left\{ \sum_{i=1}^m \beta_{ik} X_i [\beta_{ij} + (1-\beta_i) \bar{X}_j] \right\} (\partial \ln X_k / \partial \ln T)_p \\ &= - \sum_{i=1}^m X_i [\beta_{ij} + (1-\beta_i) \bar{X}_j] \partial (M_i - \sum_{k=1}^l \beta_{ik} M_k) / \partial \ln T, \end{aligned} \quad (\text{Eq. 3-101})$$

a set of $l + m - n$ independent, linear equations for the derivatives $(\partial \ln X_k / \partial \ln T)_p$ for the $l + m - n$ gaseous species that are contained in the basis. After this set of equations is solved by matrix inversion, the corresponding derivatives for the gaseous species not contained in the basis can be calculated directly from the differential of Eq. 3-92. By differentiating Eq. 3-90 with $\delta_j = 1$, one then obtains explicit expressions for each of the $n - m$ quantities $(\partial \ln X_j^0 / \partial \ln T)_p$ in terms of these results. One may then calculate the desired derivative of n in terms of these results by using Eq. 3-88, viz:

$$D_T = -[n / \sum_{j=1}^l (1-\delta_j) \hat{N}_j] \sum_{i=1}^m \beta_i X_i (\partial \ln X_i / \partial \ln T)_p \quad (\text{Eq. 3-102})$$

One may also use this result along with the others just obtained to calculate the quantities:

$$D_{T1} \equiv (\partial \ln n_1 / \partial \ln T)_p \quad \text{and} \quad D_{Tj}^c \equiv (\partial \ln n_j^c / \partial \ln T)_p \quad (\text{Eq. 3-103})$$

which are also useful for other purposes (see Eq. 3-106).

The parameter D_p is obtained in an entirely analogous way, by considering changes at constant temperature instead of at a constant pressure; the only difference that arises is that the right-hand side of Eq. 3-101 is replaced by:

$$\sum_{i=1}^m X_i [\beta_{ij} + (1-\beta_i) \bar{X}_j] (1-\beta_i) \quad (\text{Eq. 3-104})$$

Secondary parameters D_{p1} and D_{pj}^c analogous to those appearing in Eq. 3-104, may also be defined.

In order to calculate the equilibrium specific heat at constant pressure, one may recall that:

$$h = \sum_{i=1}^n n_i H_i = \sum_{i=1}^m n_i H_i + \sum_{j=1}^l \delta_j n_j^c H_j^c, \quad (\text{Eq. 3-105})$$

where the molar enthalpy of any species i is:

$$H_i = H_i^\circ + \int_{T^\circ}^T C_{pi} dT,$$

H_i° being the standard molar heat of formation at the standard temperature T° . C_{pi} being the molar heat capacity at constant pressure. We consistently adopt convention that as well as chemical formula must be given to define a species. The equilibrium specific heat at constant pressure for the mixture is therefore:

$$\begin{aligned} c_p \equiv (\partial h / \partial T)_p &= \sum_{i=1}^m n_i C_{pi} + \sum_{j=1}^l \delta_j n_j^c C_{pj}^c \\ &+ T^{-1} \left[\sum_{i=1}^m n_i H_i D_{T1} + \sum_{j=1}^l \delta_j n_j^c H_j^c D_{Tj}^c \right] \end{aligned} \quad (\text{Eq. 3-106})$$

where D_{T1} and D_{Tj}^c are defined by Eq. 3-103.

The entropy of the mixture can be written in the present notation as:

$$s = \sum_{i=1}^m n_i S_i^\circ + \sum_{j=1}^J \delta_j n_j^c S_j^{\circ c} - n R^\circ \ln p - R^\circ \sum_{i=1}^m n_i \ln (n_i/n) \quad (\text{Eq. 3-10})$$

Other equilibrium thermodynamic properties, such as γ_0 and the equilibrium sound speed, can easily be evaluated from these results.

2.5.2. Calculation of Performance - Adiabatic Flame Temperature

The adiabatic flame temperature T_c is defined by the assumption of isobaric, adiabatic heat release during the combustion process in the chamber. For a propellant at an initial temperature T_i , the adiabatic condition is defined by the equation:

$$h_p \equiv h_p^\circ + \left(\int_{T_0}^{T_i} c_p dT \right)_p = \sum_{i=1}^m n_i [H_i^\circ + \int_{T_0}^{T_c} C_{p,i} dT] + \sum_{j=1}^J \delta_j n_j^c [H_j^{\circ c} + \int_{T_0}^{T_c} C_{p,j}^c dT] \equiv h(p_c, T_c), \quad (\text{Eq. 3-178})$$

in which the subscript p identifies propellant properties. Here the n_i and n_j^c functions are evaluated for equilibrium conditions at chamber pressure p_c and chamber temperature T_c . If thermodynamic properties of the solid propellant are known (see below), then the left-hand side of Eq. 3-108 is known, and for any prescribed p_c Eq. 3-108 along with the known equilibrium functions (p_c, T_c) , $n_i^c(p_c, T_c)$ determine the value of T_c . The simplest numerical scheme for calculating T_c is one of trial and error; select trial values for T_c , compute n_i , n_j^c and h for these trial values, and see whether Eq. 3-108 is satisfied. If the first trial value yields $h < h_p$, increase the estimate of T_c ; if it yields $h > h_p$ decrease the estimate of T_c . Linear interpolation or extrapolation in temperature after two guesses, can sometimes speed convergence of the trial-and-error procedure.

Heats of formation of solid propellants are usually estimated theoretically by using band-energy considerations and measured heats of reaction of various chemical processes, related to their formation. Attempts are often made to obtain direct experimental measurements of propellant heats of formation in calorimeters, but such measurements are difficult to perform accurately because of problems associated with determining the product composition. This is especially true when oxygen is the primary oxidizer, because condensed-phase products then appear and complicate the problem of determining product composition. Experimental values of propellant heats of formation may be obtained indirectly from the approaches described in Section 3.

Adiabatic flame temperatures usually lie between 2000°K and 2800°K for homogeneous propellants, between 2400°K and 3000°K for nonmetalized heterogeneous propellants and between 3000°K and 4000°K for metalized systems. These temperatures are given for some propellants in Table 3-4.

General Aspects of Performance Calculation - Nozzle flow must be considered in analyzing performance. One generally assumes either frozen or equilibrium chemical conditions in making nozzle flow calculations. This subject has been discussed in Chapter 2.

In performance calculations any condensed particles present are assumed to be finely divided and uniformly dispersed in the gas phase, so that particle lag effects can be neglected. Contribution of particles to the hydrostatic pressure because of their Brownian motion is also neglected; this requires that the number of particles smaller than about $10^{-2}\mu$ in diameter be negligible. The volume occupied by particles is assumed to be negligibly small compared with the volume occupied by gas; this approximation has been discussed earlier and has a negligible influence on

Composition	J P N	1662	CARDE	M. L. C. P. E.	S. P.	CARDE
Ammonium Perchlorate			56	75	65	62 70
Binder with 35% Explosive plastic						25
Binders					19	
Polyurethanes			25			
Polyethylenes				15		
Epoxy Polysulfide				25		
Aluminum			19	20	19	5
Nitrocellulose	(13.25N)	51.5 58(12.39N)				
Nitroglycerin	43	34				
Miscellaneous	5.5	8				
Theoretical specific impulse	230	238	226	207	265	259 254
Measured specific impulse	216				244	238
Combustion temperature (°K)	3125		2810	2550	3200	
Characteristic velocity m. sec ⁻¹		1500	1450	1320		1570
Standard thrust coefficient		1.597		1.57		1.62
Molar weight g. mole ⁻¹	26.4		28.92	25.0		
Specific heat ratio	1.215					
Density g. cm ⁻³	1.62	1.602	1.67	1.70	1.7	1.73

Table 3-4 Performances of Certain Propellants.

performance results. The weight fraction of particles in the system, on the other hand, is not negligible since 50% by mass of the reaction products may be in condensed phases in extreme cases. The conservation equations for nozzle flows have been given in Chapter 2. Ideal performance calculations are performed on the basis of isentropic nozzle flow.

Performance for Frozen Nozzle Flow - For frozen isentropic nozzle flow, the quantity:

$$\sigma(p, T) \equiv \sum_{i=1}^m n_i S_i^\circ + \sum_{j=1}^k \delta_j n_j^c S_j^{\circ c} - n R^\circ \ln p, \quad (\text{Eq. 3-109})$$

is constant throughout the nozzle [$\sigma(p, T) = \sigma(p_c, T_c)$] and the functions n_i , n_j^c and n appearing therein are also fixed constants (viz fixed at their chamber values). Equation 3-109 thus explicitly determines the pressure as a function of temperature for frozen-flow performance calculations. Since the fixed composition is also known, tables of thermodynamic properties permit one to calculate all thermodynamic properties as functions of the temperature for the nozzle flow. The energy conservation equation then gives the velocity as a function of temperature, and setting the throat velocity equal to sonic velocity determines the temperature at the throat. After this is known, the mass flow rate per unit throat area, the characteristic velocity c^* , the thrust coefficient C_F , the exit to throat area ratio A_e/A_t , the specific impulse I_s and any other ideal performance parameters that are desired can easily be calculated. The method is the same as that described in Chapter 2, Section 2.2.1 and therefore details will not be repeated here.

Performance for Equilibrium Nozzle Flow - Calculations of equilibrium nozzle flow are more complex, since the chemical composition varies in the nozzle. Isentropic nozzle flow is defined by keeping the quantity s , defined in Eq. 3-101 constant throughout the flow [$s(p, T) = s(p_c, T_c)$]. In Eq. 3-101, the quantities $n_i(p, T)$, $n_j^c(p, T)$ and $n(p, T)$ are now determined by the equilibrium composition solutions applied locally. Thus, Eq. 3-101 provides a complicated formula for determining the pressure as a function of temperature. The calculations are carried out by selecting a temperature, estimating the pressure, calculating equilibrium compositions at this pressure, then calculating $s(p, T)$ and checking to see if it equals $s(p_c, T_c)$. If the equality isn't satisfied sufficiently well, then a new pressure is chosen and the calculations are repeated etc. There are advantages in selecting a temperature close to the chamber temperature for the first calculation and then proceeding in relatively small temperature increments, because then Eq. 3-99 can be used to provide a rather accurate first estimate of the pressure, and Eq. 3-103 can be used to provide rather accurate first estimates of equilibrium compositions which are needed for beginning the composition calculation loop; the composition calculations, as well as any iteration of pressure, will therefore converge more rapidly. It should be noted that various new condensed species may appear as one marches down the nozzle, and therefore the equilibrium composition calculations may have to be changed (e.g. in the Brinkley method, it may be necessary to change the basis by replacing a gaseous component in the basis by the corresponding condensed species, at a point in the nozzle where the calculations show that the partial pressure of the gaseous component reaches the equilibrium vapor pressure).

After pressure and composition have thus been found as functions of temperature, the rest of the calculations proceed in the same way as for frozen flow. Application of the throat condition is slightly more complex in this case because the sound speed depends on pressure, temperature and composition. However, no important differences in principle arise. The primary problem with the equilibrium performance calculations is that they are so time-consuming.

Table 3-5 gives an example of equilibrium and frozen properties and performance for a particular solid propellant.

Influence Coefficients - Performance parameters are usually calculated for some values of the operating parameters and then performance for other operating parameters is estimated by interpolation or sometimes extrapolation. Influence coefficients are useful in such interpolations.

Suppose that the chamber enthalpy is changed from h_c to $h_c + \Delta h_c$ at constant chamber pressure. Then the exit velocity takes on a modified value v_{em} determined by (see Eq. 2-39 of Chapter 2)

$$v_{em}^2 = v_e^2 + 2 (\Delta h_c - \Delta h_e)$$

where Δh_e is the change in exit enthalpy produced by the change Δh_c . Since the geometry of the nozzle is fixed and p_c is fixed, it follows that p_e also remains constant. Therefore:

$$\frac{dh_e}{dh_c} = \frac{(\partial s / \partial h)_{p_c}}{(\partial s / \partial h)_{p_e}} = \frac{T_e}{T_c}$$

which gives by substitution:

$$v_{em}^2 = v_e^2 + 2 \Delta h_c \left(1 - \frac{T_e}{T_c}\right) \quad (\text{Eq. 3-110})$$

This result is useful for estimating changes in performance, since:

$$(v_{em} - v_e) / v_e = (I_{sp_m} - I_{sp}) / I_{sp} \approx (c_m^* - c^*) / c^*$$

(see Chapter 2 Section 5.1.5.) Equation 3-110 is equivalent to the specification of a dimensional influence coefficient $(\partial v_e^2 / \partial h_c)_{p_c}$.

Another type of useful influence coefficient refers to changes at constant h_c and at constant p_c / p_e , with variable p_c . If λ is an arbitrary parameter evaluated at p_c and λ' is the value of λ at the chamber pressure p'_c , then one may write (for p'_c near p_c):

$$\lambda' = \lambda (p'_c / p_c)^{\alpha_\lambda}$$

where:

$$\alpha_\lambda \equiv (\partial \ln \lambda / \partial \ln p_c)_{h_c, p_c/p}$$

is a general influence coefficient evaluated at a point in the nozzle where the pressure equals p . It is readily seen from Eq. 2-39 of Chapter 2 that for the velocity v at any position (where pressure = p) in the nozzle, the influence coefficient is:

$$\alpha_v = - \frac{h}{2(h_c - h_e)} \left(\frac{\partial \ln h}{\partial \ln p_c} \right)_{h_c, p_c/p}$$

A thermodynamic calculation then yields:

$$\alpha_v = R^\circ T [n_c - n] / v^2 \quad (\text{Eq. 3-111})$$

Properties	p	T	h	s	c _p
Units	Atm	°K	Kcal/kg	cal/kg °K	Kcal/kg °K
Chamber	20	3264.7	-876.29	2215.66	0.95596
equi- librium	11.6740	3113.2	-985.15	2215.64	1.46966
Throat					
frozen	11.2060	2927.8	-991.23	2215.66	
equi- librium	0.2857	2241.8	-1623.48	2215.65	0.55654
Exit					
frozen	0.2857	1433.1	-1483.96	2215.66	0.31473

Properties	γ	a	n	c *	I _{sp}
Units	-	msec ⁻¹	gas moles per kg	msec ⁻¹	sec
Chamber	1.13598	994.7	32.09154		
equi- librium	1.10893	954.3	31.72536	1474.2	
Throat					
frozen	1.23120	980.7	32.09154	1421.7	
equi- librium	1.12964	800.2	30.41144		255.0
Exit					
frozen			32.09154		229.9

Table 3-5 Thermodynamic Properties and Performance of a Solid Propellant
Containing Aluminum and Lithium

Other influence coefficients of this type (α_T which refers to the temperature at any position in the nozzle, α_{c*} which refers to the characteristic velocity, α_A which refers to the exit to throat area ratio, and α_{CF} which refers to the thrust coefficient) are given by:

$$\left. \begin{aligned} \alpha_T &= n R^\circ \frac{1 + D_T}{c_p} - n_c R^\circ \frac{1}{c_p} \\ \alpha_{c*} &= [D_p - \alpha_v + \alpha_T (1 + D_T)]_t \\ \alpha_A &= [D_p - \alpha_v + \alpha_T (1 + D_T)]_e - \alpha_{c*} \\ \alpha_{CF} &= \alpha_{v_e} - \alpha_{c*} \end{aligned} \right\} \quad (\text{Eq. 3-112})$$

where the subscripts c, t and e refer to chamber throat and exist conditions, and the subscript e should not be confused with earlier subscripts e which implies equilibrium. The corresponding influence coefficient for specific impulse is α_{v_e} , the influence coefficient for velocity evaluated at the exit.

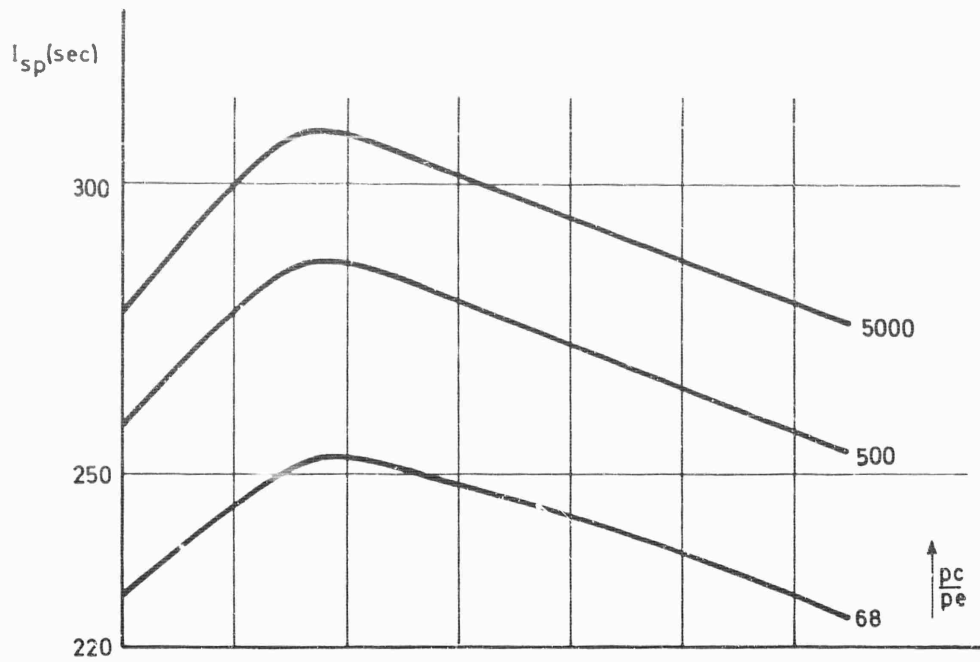
Performance of some Propellants (18), (19) - Performance of double-base propellants have been published in numerous works. We summarize some results in Table 3-4, which gives one a feeling for the order of magnitude of the adiabatic flame temperature, the average molecular weight, the specific heat ratio and the specific impulse. The specific impulse is of the order of 200 sec for the representative case of the JATC propellant, which has 25% nitroglycerin and 75% nitrocellulose, and produces an adiabatic flame temperature of about 1900°K. Here we shall discuss principally heterogeneous propellants, which are now used much more often.

The performance of propellants containing the currently common oxidizer ammonium perchlorate in a plastic binder such as polyethylene is shown in Figs. 3-11 and 3-12. It is seen in Fig. 3-11 that the maximum specific impulse is obtained at a binder mass fraction of 10%, which is too small to obtain good mechanical properties of a grain. For a pressure ratio of 68/1, the maximum specific impulse is 242 sec for frozen nozzle flow and 253 sec for equilibrium nozzle flow. The specific impulse of course increases with increasing pressure ratio; the 68/1 curves in Fig. 3-11 might correspond to a booster application, while the 500/1 curves would be for an upper stage. The maximum chamber temperature is of the order of 3000°K (Fig. 3-12) and the peak theoretical characteristic velocity is about 1520 m/sec. The molecular weight decreases as the percentage of fuel increases.

These performance results are rather sensitive to the choice of binder. Figure 3-13 gives corresponding curves for the same oxidizer in a polyurethane binder (here the mean molecular weight is 1000/n and the expansion ratio for the higher specific impulse curve is 70/0.14 = 500). With this binder, the maximum specific impulse is obtained at a fuel mass fraction of 17% the maximum characteristic velocity is in the neighborhood of 1500 m/sec, and the peak adiabatic flame temperature is about 2800°K.

Performance of these propellants can be increased by adding finely divided aluminum particles. Triangular composition diagrams, such as that shown in Fig. 3-14 are useful for easily seeing the effects of adding varying amounts of aluminum to the oxidizer-binder systems. On Fig. 3-14 the percentage of $(CH_2)_n$ is marked along the base of the triangle, the percentage aluminum along the left side and the percentage ammonium perchlorate along the right side. Curves of constant specific impulse are traced inside the triangle. The maximum specific impulse, which occurs at a composition of about 10% binder and 23% metal, is 267 sec. On diagrams of this type it is possible to draw lines which define composition limits based on considerations other than performance. Thus for example considerations of the mechanical strength of the grain, safety in manufacture, propellant burning

EQUILIBRIUM COMPOSITION



FROZEN COMPOSITION

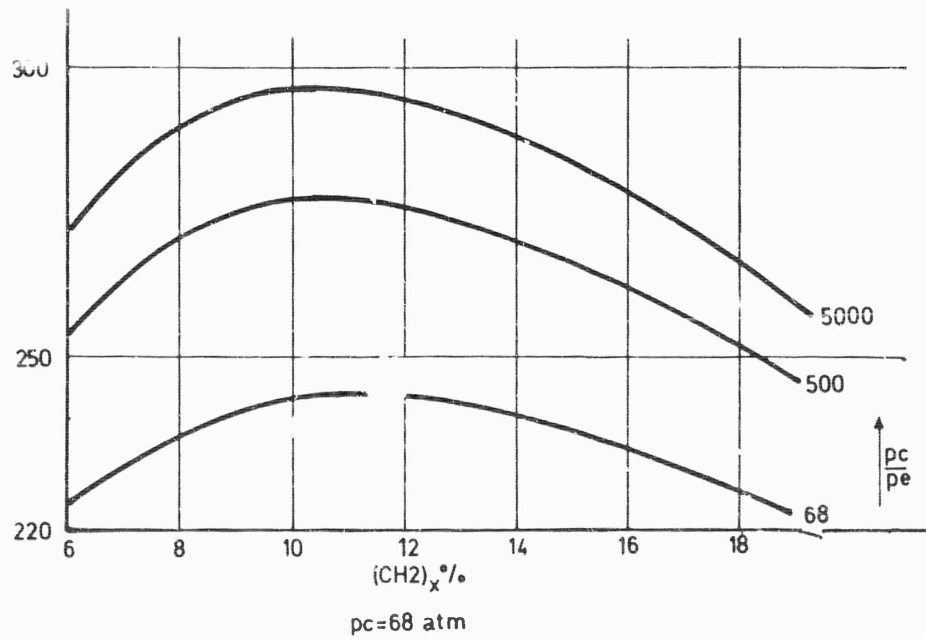


Fig. 3-11 Performance of $[NH_4ClO_4 - (CH_2)_x]$ propellant. Frozen and equilibrium composition.

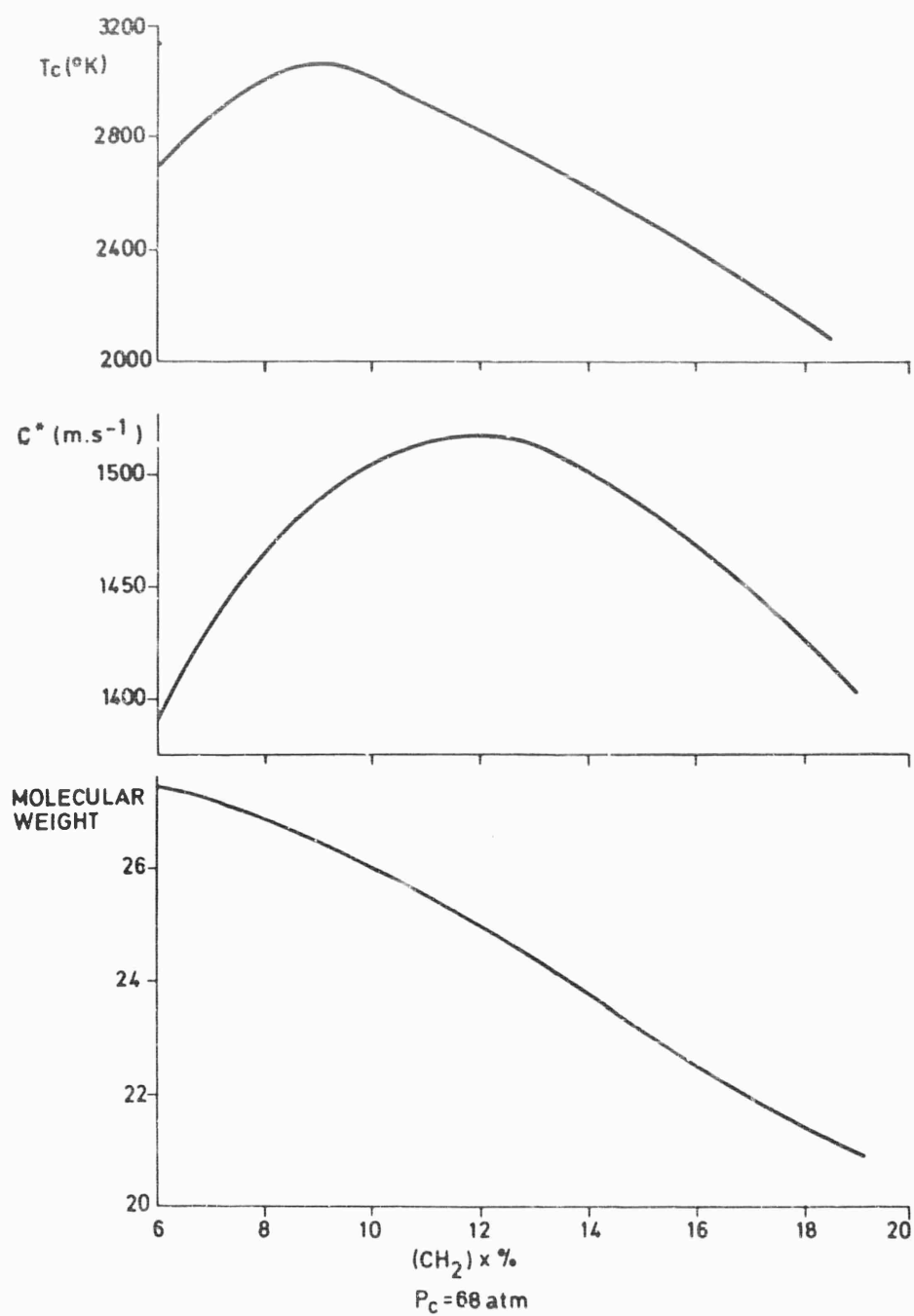


Fig. 3-12 Characteristic velocity, chamber temperature and gaseous molecular weight of $\text{NH}_4\text{ClO}_4 - (\text{CH}_2)_x$ propellant.

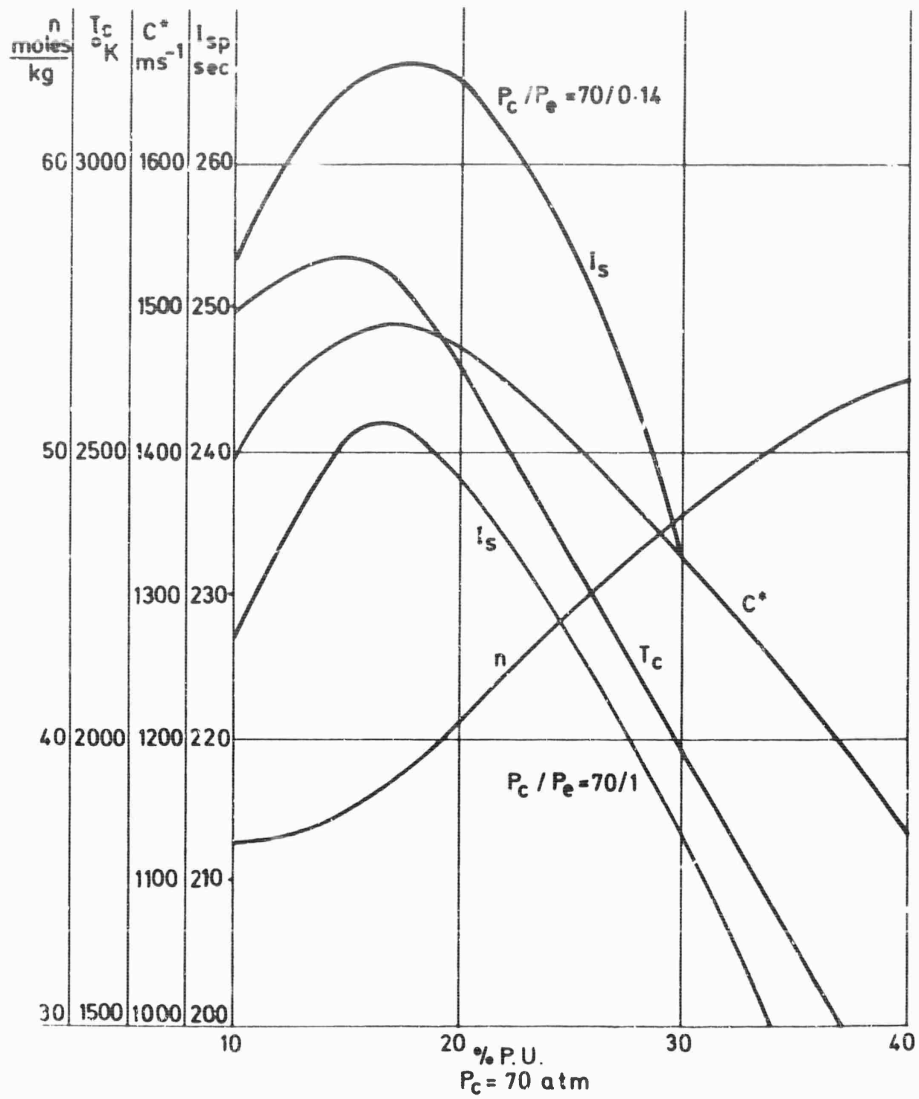


Fig. 3-13 P.U.-A.P. performance, frozen composition.

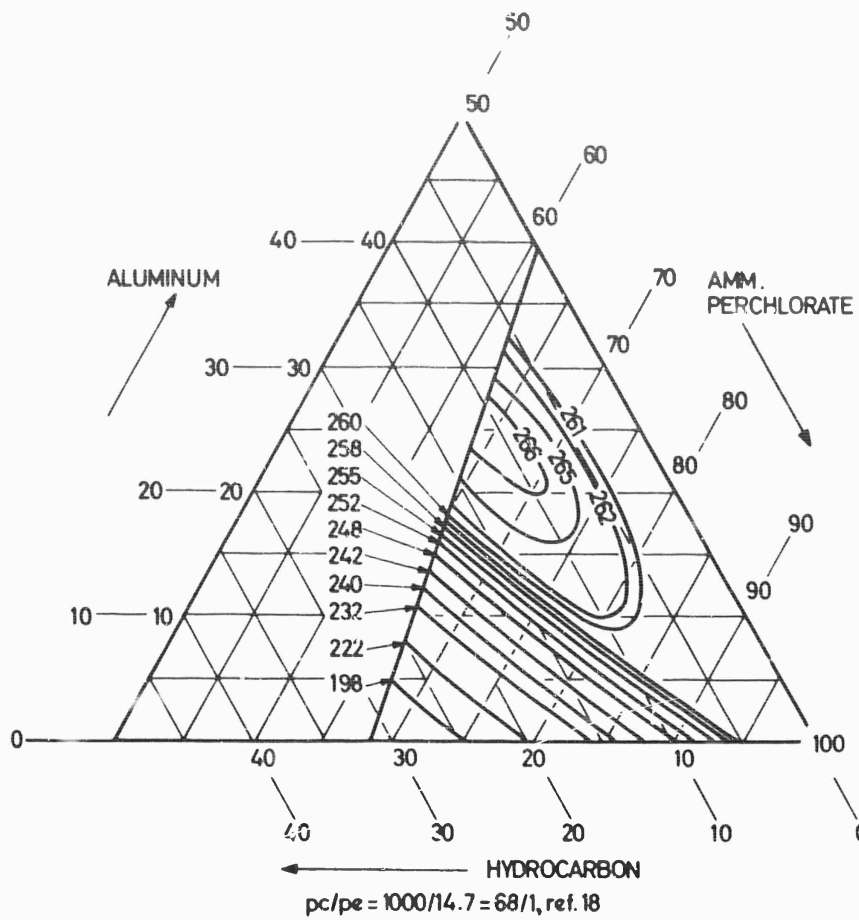


Fig. 3-14 Theoretical specific impulse for ammonium perchlorate - aluminum-hydrocarbon system.

rate or the effect of chamber temperature on nozzle strength, may rule out certain portions of the diagram.

Diagrams similar to Fig. 3-14 have been constructed for many other systems. For example, if the binder is changed to polyurethane, one finds from such a diagram that the maximum specific impulse is 264 sec; it occurs at a composition of 15% binder and 23% aluminum and corresponds to an adiabatic flame temperature of 3600 °K. Figure 3-15 shows effects on performance of adding percentages of aluminum to an ammonium perchlorate-polyurethane propellant at a fixed polyurethane mass fraction of 20%; the peak specific impulse is 260 sec at a pressure ratio of 70/1 and it occurs at about 19% aluminum mass fraction.

Varying the chamber pressure typically affects performance in the manner illustrated in Fig. 3-16. Because of effects of this type, it is necessary to specify both the chamber and exit pressures when quoting performance figures. The standard procedure (and the one that we shall follow) is to give ideal performance data for design expansion from a chamber pressure of either 70 atm or 1000 psi = 68 atm, to atmospheric exit pressure. Furthermore, unless otherwise stated, performance results that we show correspond to chemically frozen nozzle flow.

Curves such as those shown in Fig. 3-14, 3-15 and 3-16 aid one in choosing the best available propellant combinations for any given application.

Table 3-4 shows the performance of some classical propellants.

2.6. Research on Solid Propellant Constituents Conducive to Maximal Performance

In efforts to increase propellant performance, one may search for energetic fuel additives such as aluminum or light metals, one may attempt to modify the plastic binder or one may look for more energetic oxidizers. A further possibility is to inject a liquid fuel or oxidizer; this approaches hybrid systems.

2.6.1. Studies of Energetic Fuel Additives - The first possibility that suggests itself is to replace aluminum by a more energetic metallic additive; lithium, beryllium, boron and magnesium are attractive as possible substitutes. The best metal to use depends strongly on the nature of the oxidizer and the binder; with oxidizers containing fluorine, lithium is likely to have the best performance, while beryllium and boron have better performance with oxygen (20), (21). One might also ask whether some alloys would have better performance than pure metals. The results of an analysis aimed at answering this question are shown in Fig. 3-17 for a typical ammonium perchlorate - $(CH_2)_x$ propellant. Certain alloys are seen to be superior to others, the most remarkable being Li-Be, Li-Al and Li-Mg, in order of decreasing performance. The performance advantage of beryllium is offset somewhat by toxicity problems that arise during manufacturing and to a lesser extent during firing; BeO and especially pure Be metal are extremely toxic materials, in comparison to other propellant constituents. Toxicity problems in manufacturing and storage might be alleviated by coating beryllium with aluminum. Bimetal systems may provide a solution to practical problems associated with the use of beryllium in propellants.

Metallic hydrides are also interesting additives from the viewpoint of performance. Most metal hydrides (e.g. lithium hydride, beryllium hydride, magnesium hydride, aluminum hydride and borohydrides) exist as solids. As one example, we show in Fig. 3-18 the gain in performance produced by the addition of lithium aluminum hydride (AlH_4Li) to an ammonium perchlorate - polyurethane propellant. For the conditions shown, maximum performance occurs at an additive mass fraction

of 23%. The flame temperature decreases as the amount of additive is increased and it reaches 2600°K at the peak specific impulse. The maximum specific impulse is high, but unfortunately the corresponding propellant density is decreased (from about 1% to about 1.5%). If one assumes equilibrium rather than frozen nozzle flow, the peak specific impulse at a pressure ratio of 70/1 increases to 280 sec. A difficulty with the use of metallic hydrides is that they may react during manufacturing processes and during storage. A solution envisaged for this problem consists in coating the metal hydrides.

2.6.2. Studies of Binders - In attempting to modify binders, one is limited by the necessity of maintaining good mechanical properties and good coating properties. Attractive new binders are nitroplastics, nitropolymers, nitrals, materials containing amine groups and materials containing fluorine.

2.6.3. Studies of Oxidizers - As improvements for ammonium perchlorate, nitronium perchlorate (NO_2ClO_4), nitrosylperchlorate (NOClO_4), and perchlorates of hydrazine have been considered. The use of these energetic oxidizers presents serious problems because they decompose easily and react hypergolically with many binders. Grain handling is therefore delicate. As an illustration of the improvement in performance obtainable from energetic binders, we show in Fig. 3-19 the variation of the specific impulse of a nitronium perchlorate composite propellant as a function of the mass fraction of a $(\text{CH}_2)_x$ binder. We note that the two propellants shown here are hypergolic and that it would be necessary to protect the oxidizer by an inert layer. Comparison of Fig. 3-19 and 3-11 reveals a 10% increase in specific impulse with the energetic oxidizer.

2.6.4. Studies of Liquid Injection - To provide better flexibility of operation for solid propellant rockets, injection of liquids into the combustion chamber is currently under consideration. The choice of a liquid fuel or oxidizer is important in determining the extent of improvement in performance. Figure 3-20 shows as an example the performance gain that one can attain by injecting liquid hydrazine as a fuel. The specific impulse is increased by about 4% for hydrazine mass fractions in the vicinity of 20%. A most interesting fuel injectant is hydrogen, as one can see from Fig. 3-21 which shows gains exceeding 12%. Mechanical penalties are, of course, paid for liquid augmentation of solid propellant rockets.

2.6.5. General Remarks - In attempting to improve performance of solid propellants, one is always faced with contradictory requirements of high energy release and propellant stability. In general, one must consider the following items: choice of fuel elements and of oxidizer elements, choice of bonding elements (nitrogen-carbon), bonding energies of the elements, compatibility of the components selected and density of the mixture.

3. Experimental Determination of Performance

There are two categories of experimental methods for determining propellant performance, viz. laboratory testing with small samples of the grain and testing in an assembled motor.

3.1. Laboratory Methods

It is always desirable to determine the performance of a new propellant from a "sample analysis". This is often a delicate task and few applicable experimental methods have been developed although these techniques become very important, when only a small sample of the propellant material is available for analysis.

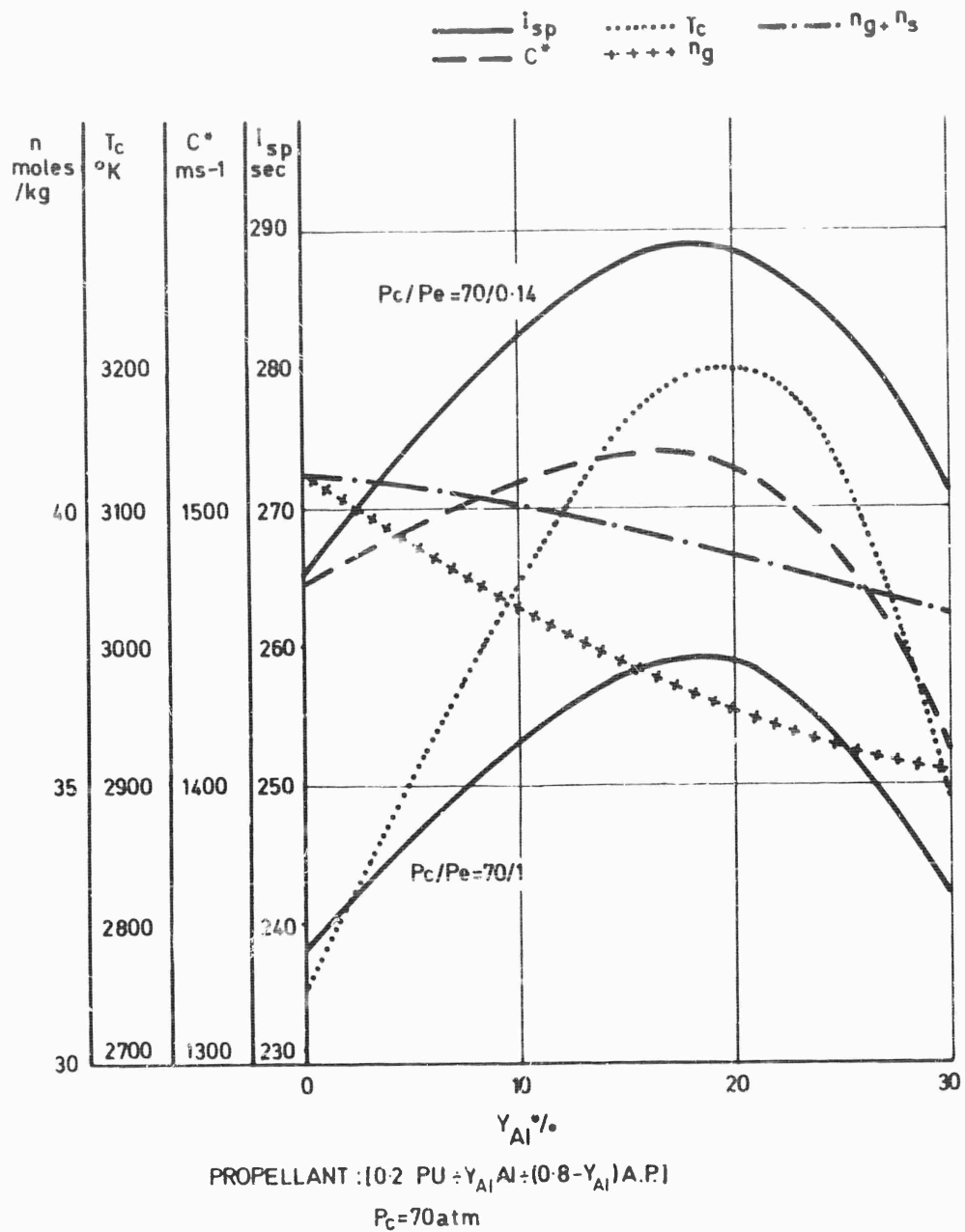


Fig. 3-15 Influence of metal mass fraction

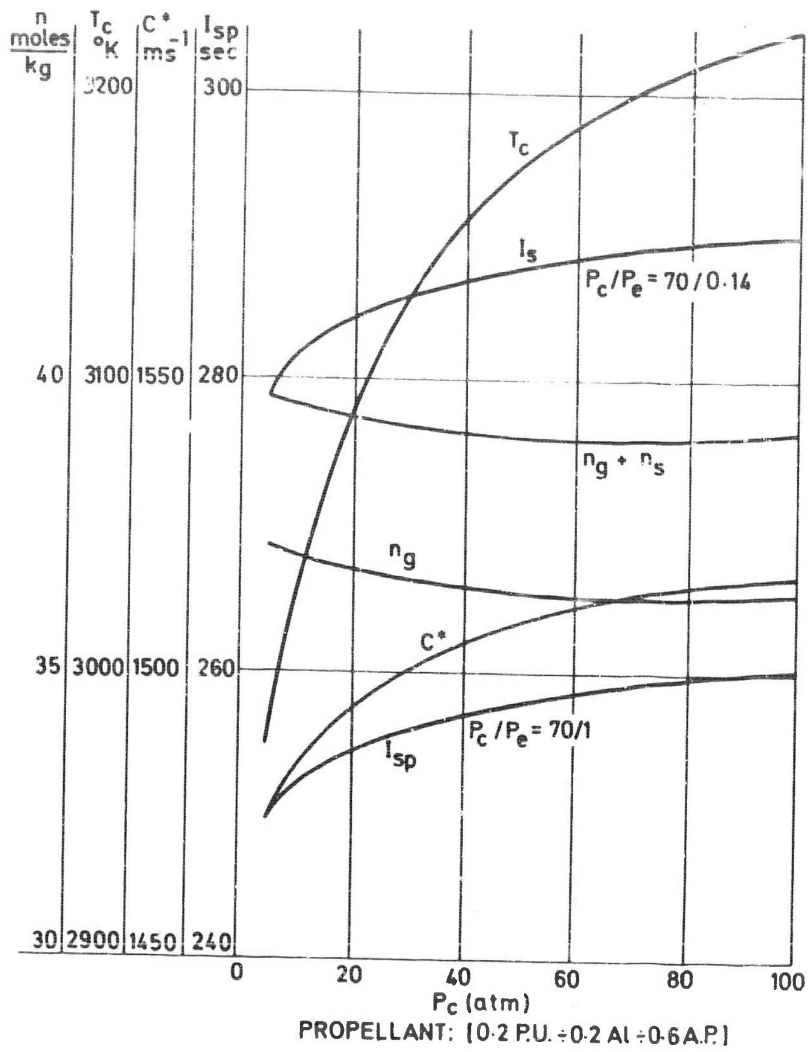


Fig. 3-18 Influence of chamber pressure.

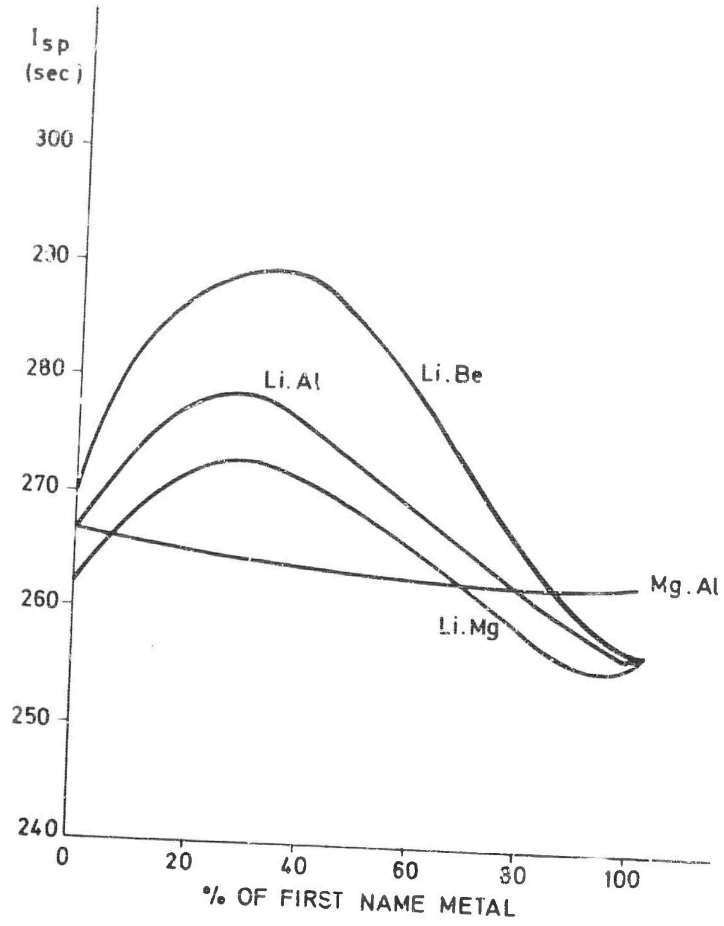
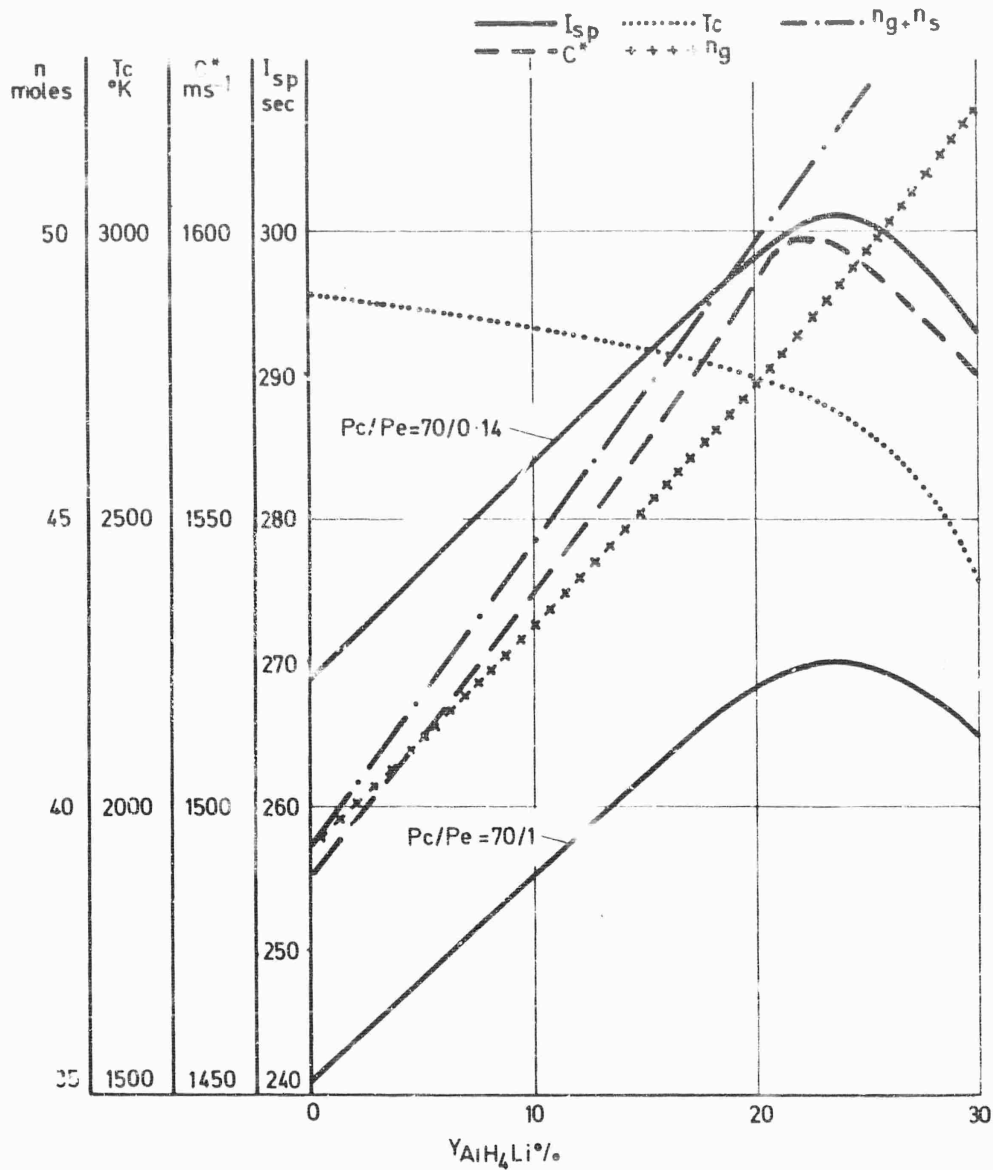


Fig. 3-17 Performance versus composition of bimetallic additives.

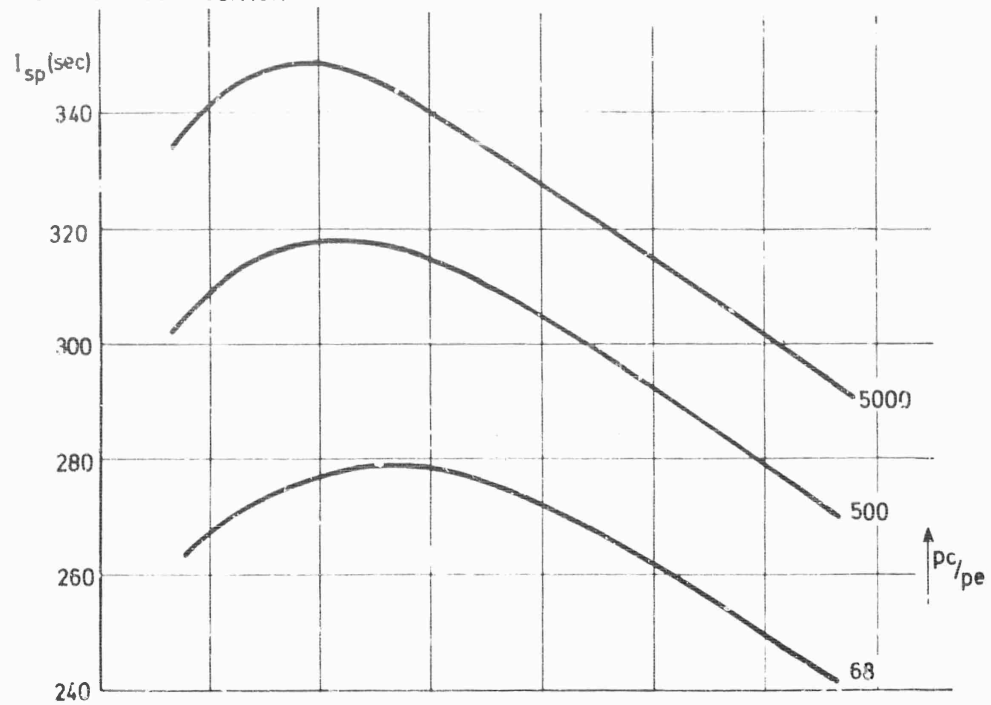


PROPELLANT: $[0.18PU + Y_{AlH_4Li}AlH_4Li + (0.82 - Y_{AlH_4Li})A.P.]$

$P_c = 70 \text{ atm}$

Fig. 3-18 Influence of lithium aluminum hydride mass fraction.

EQUILIBRIUM COMPOSITION



FROZEN COMPOSITION

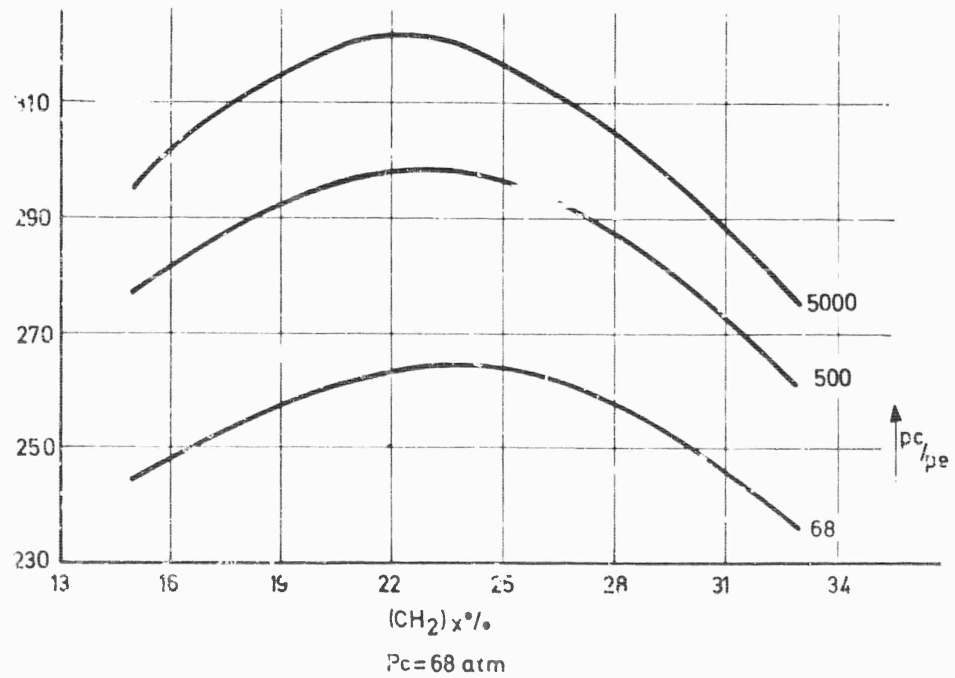
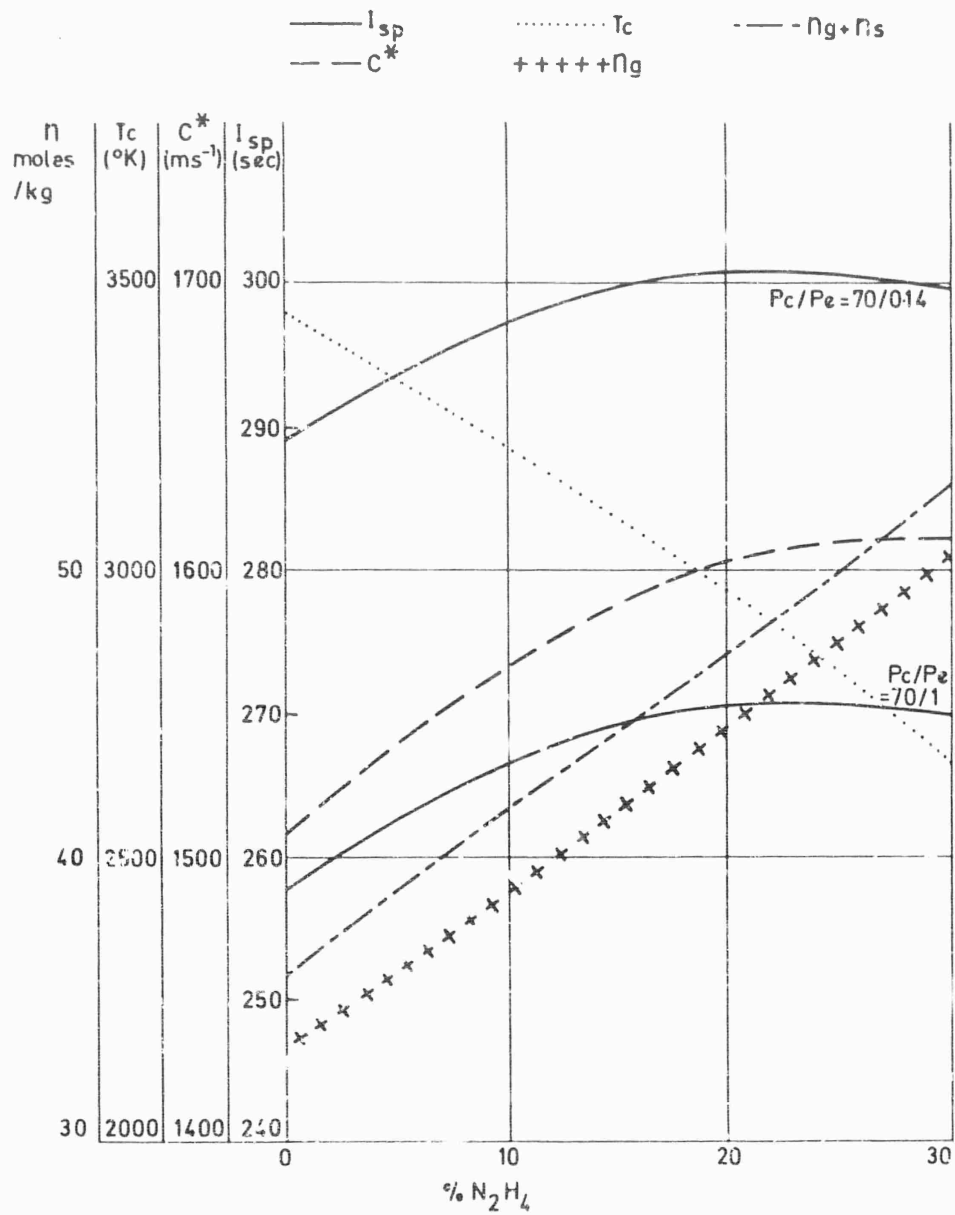


Fig. 3-19 Perform. with nitronum perchlorate oxidizer



PROPELLANT: [0.15 P.U. + 0.2 Al + 0.65 AP.]
 $P_c = 70 \text{ atm}$

Fig. 3-20 Influence of hydrazine mass fraction.

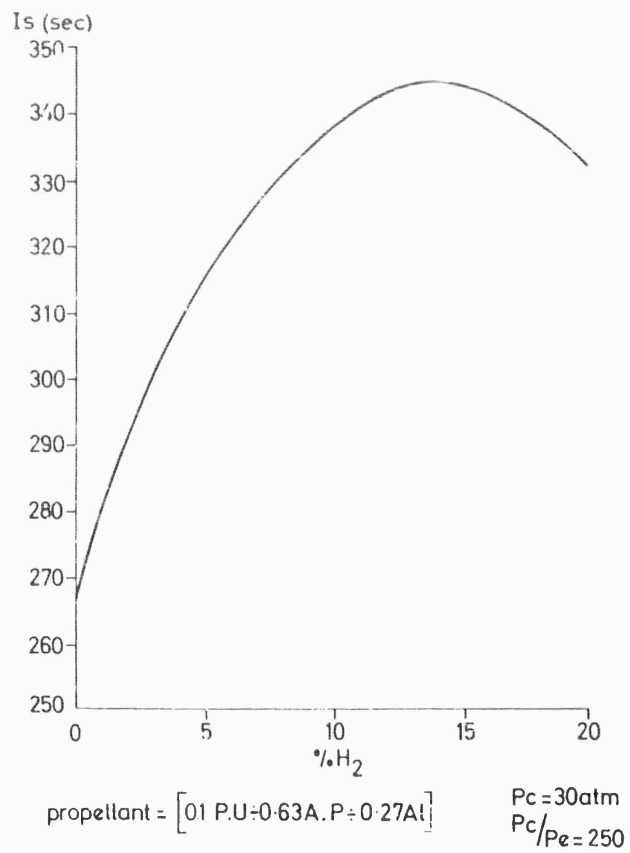


Fig. 3-21 Influence of Hydrogen mass fraction on the theoretical performance at frozen composition.

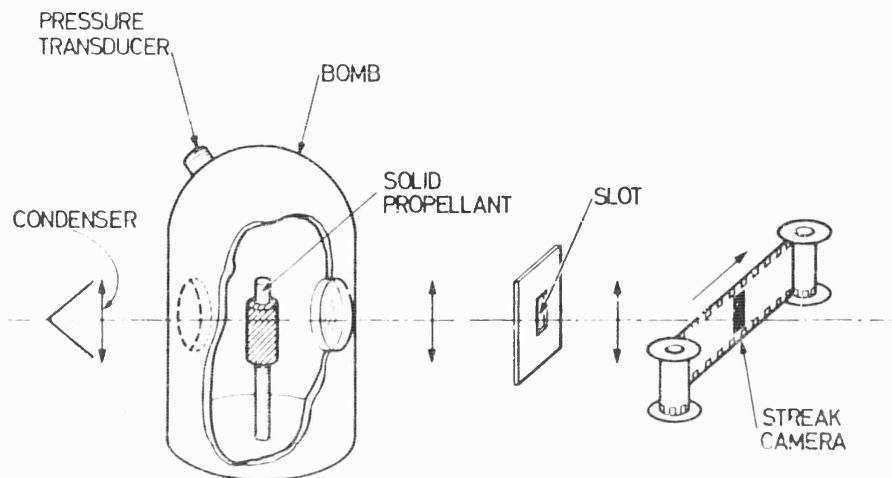


Fig. 3-22 Schematic diagram of experimental apparatus.

We shall discuss two such laboratory methods here. The first is based on a pressure measurement and the second primarily on a velocity measurement.

3.1.1. Method Based on Pressure Measurement (22) - A sample of mass m is burned in a strand burner of known volume V . During the combustion one measures the peak pressure attained (p_{\max}). The equation of state then leads to the determination of the performance-related quantity $B \equiv nR^\circ T_c$ where n represents the number of moles of gaseous product per unit mass of mixture, R° the universal gas constant and T_c the temperature at the end of combustion; viz:

$$B = nR^\circ T_c = \frac{p_{\max} V}{m}$$

Improved determination of B at high pressures, can be made by accounting for the co-volume b through the formula:

$$B = nR^\circ T_c = p_{\max} \left(\frac{V}{m} - b \right).$$

If several experiments are carried out with various masses of propellant, it is then possible to plot the straight line:

$$\frac{p_{\max} V}{m} = b p_{\max} - B,$$

with p_{\max} as the abscissa and $p_{\max} \frac{V}{m}$ as the ordinate. The ordinate of the curve at $p_{\max} = 0$ defines B . The quantity B appears in the equation for the characteristic velocity, since:

$$c^* = F(\gamma) \sqrt{B}$$

where $F(\gamma)$ can be inferred by comparison with Eq. 2-47 of Chapter 2. However the laboratory results cannot be used directly in this formula because combustion in the laboratory burner takes place at constant volume, while motor combustion occurs at constant pressure. We can take account of this difference by noticing that:

$$(T_c)_{p_{\text{const}}} = \gamma (T_c)_{p_{\text{const}}}$$

so that:

$$B_v = \gamma B_p$$

B_p being the value of B that must be used in the expression for the characteristic velocity.

The specific impulse is calculated from the relation:

$$I_{sp} = C_F F(\gamma) \sqrt{B_p}$$

One can improve this method by calibration of the apparatus with a propellant whose value of B is known.

3.1.2. Method Based on Velocity Measurement (23) - The apparatus used is illustrated in Fig. 3-22. The sample of propellant burns in a controlled atmosphere in a strand burner. An optical image of the sample is formed on a slit perpendicular to the regressing surface of the propellant. This image is then projected on the film of a streak camera. A source of light, placed on the opposite side of the strand

burner increases the contrast. Measurement of the angles made by the streaks on the film yields regression rate of the propellant and the velocity of the incandescent products during combustion. Representative streak photos are shown in Fig. 3-23. The method is applicable to both metalized and conventional solid propellants.

In order to relate the experimental results to performance, we note that the equation of continuity for a stream tube of cross section A_b (Fig. 3-24) in contact with the propellant can be written as:

$$\rho_p r A_b = \rho_g v_{g\perp} A_g \quad (\text{Eq. 3-113})$$

where $v_{g\perp}$ is the velocity of the gases perpendicular to the cross-section A_g of the stream tube and ρ_g is the density of the gases. By assuming that the velocity $v_{g\perp}$ is equal to the v_{reg} of the particles deduced from the traces of the fastest particles (greatest streak angle) and also that $A_b \approx A_g$ we obtain:

$$\rho_g = \frac{\rho_p r}{v_p}$$

From the equation of state, ρ_g is

$$\rho_g = \frac{p}{nR^\circ T_g}$$

so that:

$$B = nR^\circ T_c \approx nR^\circ T_g = \frac{p v_p}{\rho_p r} \quad (\text{Eq. 3-114})$$

Therefore the characteristic velocity is:

$$c^* = F(\gamma) \sqrt{\frac{p v_p}{\rho_p r}} \quad (\text{Eq. 3-115})$$

Thus the characteristic velocity is deduced from the measurement of the pressure p of the particles velocity v_p and of the regression rate r . With the experimental technique described above we obtain on the same recording v_p and r (which, incidentally, is itself a kinetic parameter of considerable interest); the value of p is obtained simply by measuring the pressure in the strand burner.

The measurement of c^* and of I_{sp} by this method is based on a number of hypotheses. However the values of c^* obtained are reasonably close to those found in motor tests. Furthermore, it is easy with just a few measurements to compare a number of properties of different solid propellants in the laboratory and also (by varying burner air or nitrogen pressure), to obtain propellant properties over the full range of operating conditions. The curves of Fig. 3-25 show the variation of the characteristic velocity with pressure for two propellants, one containing metal particles.

We remark that this technique is inapplicable in the plateau burning domain of ammonium perchlorate composite propellants. The plateau domain is defined as a pressure regime in which the regression rate is insensitive of pressure. In this domain, flames are observed to move about on the surface of the propellant in a manner that is too irregular for meaningful average gas velocities to be extracted from the streak measurements, due to the consequent inapplicability of Eq. 3-113.

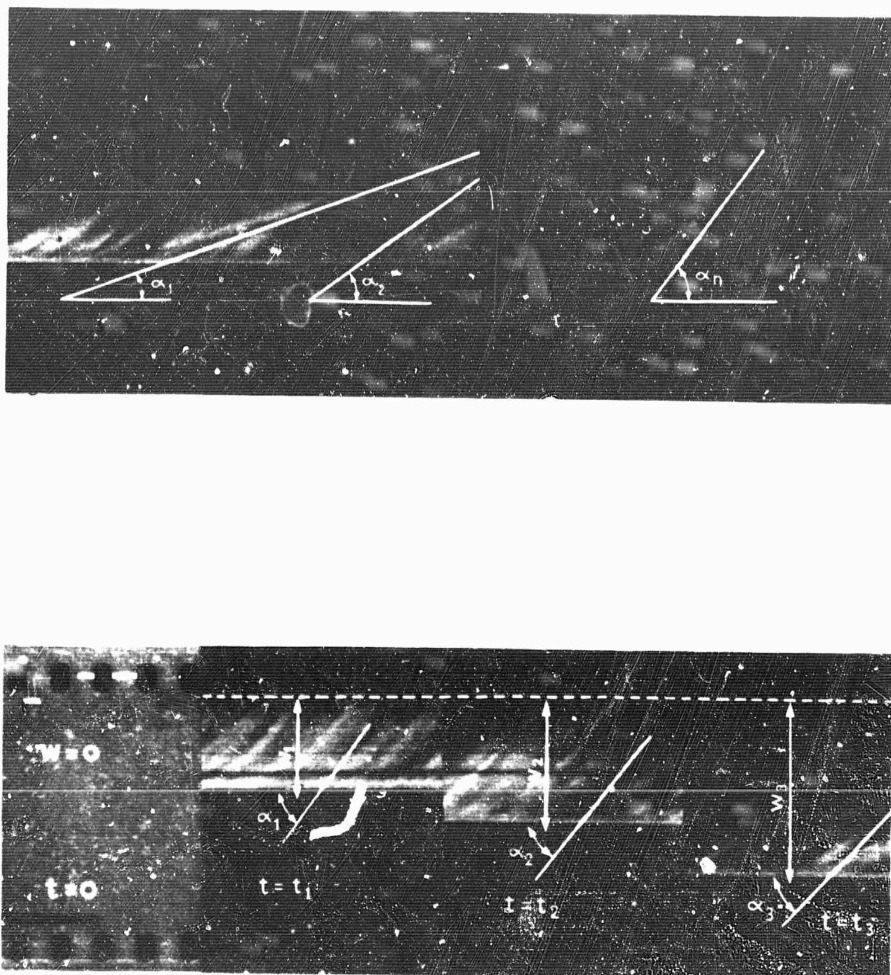


Fig. 3-23 Typical recordings.

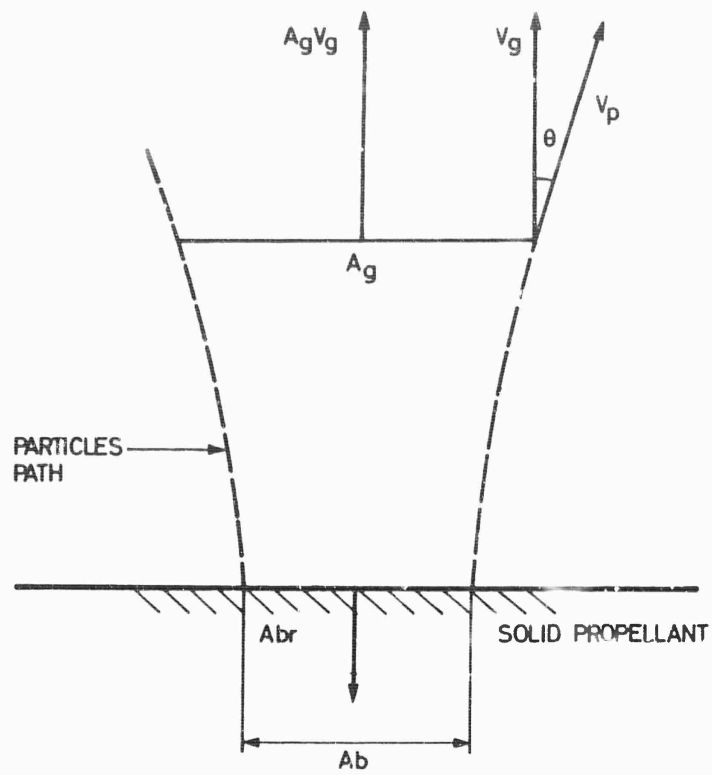


Fig. 3-24 Model for determining the characteristic velocity.

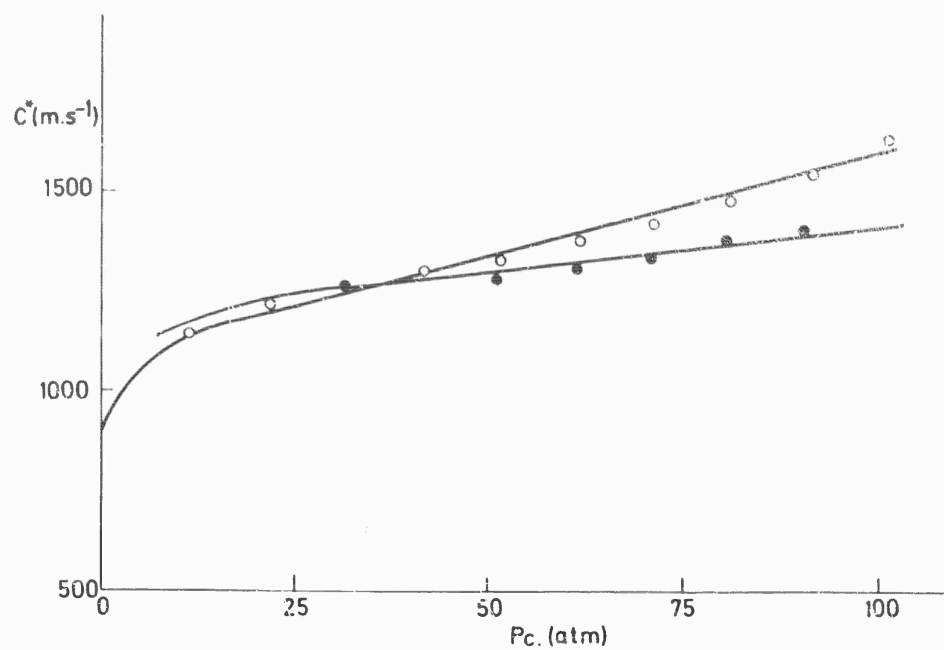


Fig. 3-25 Characteristic velocity versus chamber pressure.

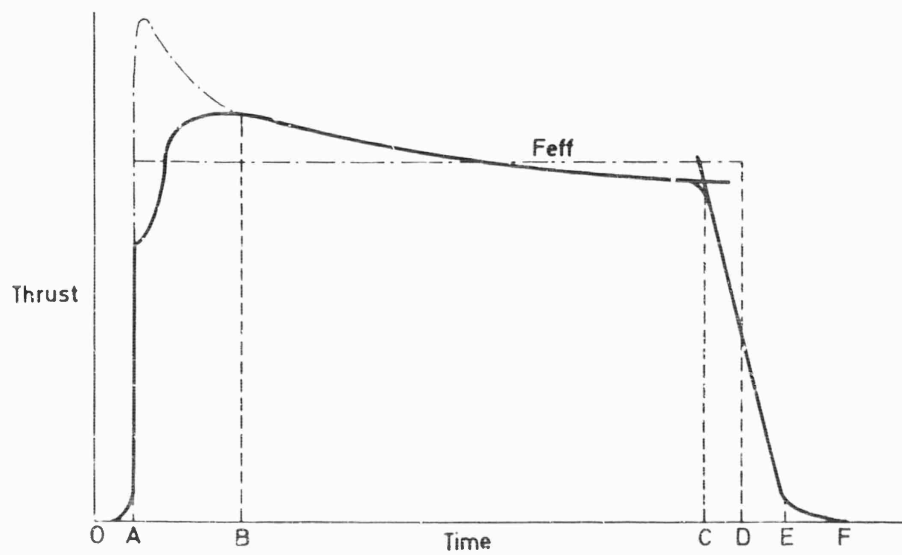


Fig. 3-26 Thrust history.

3.2. Rocket Motor Tests

3.2.1. Conventional Test Stands - The most common method of measuring propellant performance is by means of static rocket firing. Generally one employs standard motors to determine propellant performance; standard motors permit for different propellants direct comparison of test results.

Propellant-test firings are made during propellant development programs and also after manufacturing the complete full-scale rocket, particularly when the propellant must be poured and cured without the possibility of checking its characteristics in the motor after curing.

In the motor-test approach to propellant performance determination, a statistical analysis of test data acquired in many motor firings, is used to obtain best estimates of the propellant performance parameters. The raw test data consists of measured parameters and test recordings. Measured parameters are the mass m of propellant burned (obtained by subtracting the weight after the firing from the weight before) and the cross-sectional area A_t of the nozzle throat (which, in the case of ablating nozzles, varies with time). The test recordings contain the thrust $F(t)$ and the chamber pressure $p_c(t)$ (which we assume to be the stagnation pressure). Test recordings are similar to the curves shown in Fig. 3-26 where one sees pressure build-up with and without a maximum, an erosive effect (A.B), the steady part of the run which is either progressive, regressive or neutral (B.C) and finally the tailoff (C.F). Mean values can be derived rather accurately from these curves. For example the mean characteristic velocity is:

$$\bar{c}^* = \frac{\left[\int_0^{t_b} p(t) dt \right] A_t}{\bar{m}_p}$$

where $\int_0^{t_b} p(t) dt$ is the area under the pressure curve, \bar{m}_p is the difference in mass of the motor before and after the firing, A_t represents the mean cross-sectional area of the throat, and t_b denotes the burning time. A mean thrust coefficient can be written in a similar way:

$$\bar{C}_F = \frac{\int_0^{t_b} F(t) dt}{\left[\int_0^{t_b} p(t) dt \right] A_t}$$

and the corresponding mean specific impulse is:

$$\bar{I}_{sp} = \frac{\int_0^{t_b} F(t) dt}{\bar{m}_p} = \frac{I_t}{\bar{m}_p}$$

where I_t represents the total impulse.

These definitions are unambiguous and for each firing it is easy to determine \bar{c}^* , \bar{C}_F and \bar{I}_{sp} accurately and to compare their values with theory.

Instantaneous values of the performance are more difficult to obtain accurately from motor tests because of uncertainties in the length of the combustion time t_b . By

using the notion of useful thrust the burning time t_b is defined by the length of the segment AD on the recording. The propellant mass flow rate can then be assumed to be $\dot{m}_p = \bar{m}_p/t_b$ so that instantaneous performance parameter

$$c^*(t_1) = \frac{p_c(t_1) A_c(t_1)}{\dot{m}_p}$$

$$c_F(t_1) = \frac{F(t_1)}{p(t_1) A(t_1)}$$

$$I_{sp}(t_1) = \frac{F(t_1)}{\dot{m}_p}$$

and it is seen that the uncertainty in the instantaneous values of $c^*(t_1)$ and $I_{sp}(t_1)$ is directly proportional to the uncertainty in t_b . Experimental techniques have been developed whereby the nozzle (for instance) can be ejected rapidly, thereby causing combustion to cease rapidly (within a few tens of milliseconds) and permitting t_b to be defined more accurately.

Performing tests for a variety of different run durations also leads to a better definition of the instantaneous mass flow rate and therefore of the instantaneous characteristic velocity and specific impulse.

Comparison of theory with experimental may be made on the basis of the following quantities called quality indices:

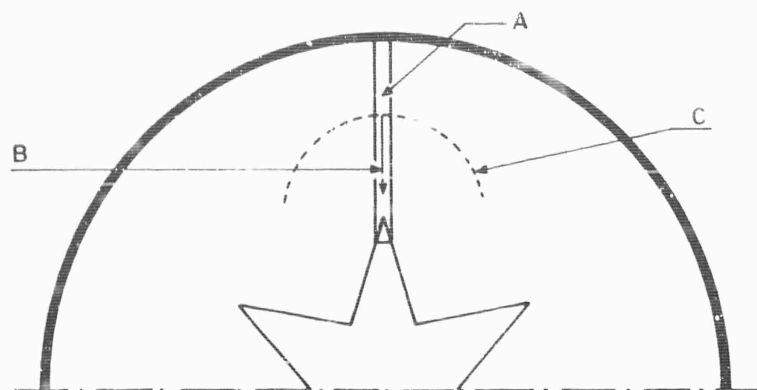
$$\xi_{c^*} = \frac{c_{\text{exp}}^*}{c_{\text{th}}^*}, \quad \xi_F = \frac{(C_F)_{\text{exp}}}{(C_F)_{\text{th}}}, \quad \xi_{sp} = \frac{(I_{sp})_{\text{exp}}}{(I_{sp})_{\text{th}}}$$

Experimental determination of propellant performance by means of conventional motor testing must be based on a large number of firings. Statistical analyses of the performance should be made by obtaining mean values and standard deviations for a large number of parameters such as pressure, thrust, characteristic velocity, mass flow rate coefficient and specific impulse.

3.2.2. Measurement of the Gas Velocity in the Motor (24) - The method described in Section 3.1.2. may be applied also to a propellant burning in a motor. Geometrical restrictions and propellant gas obscuration generally prevent one from observing downstream portions of the grain where erosive effects occur. However, careful experiments can yield streak pictures of the combustion at the head end of the grain. As a particular illustration, we describe the details of one such experiment.

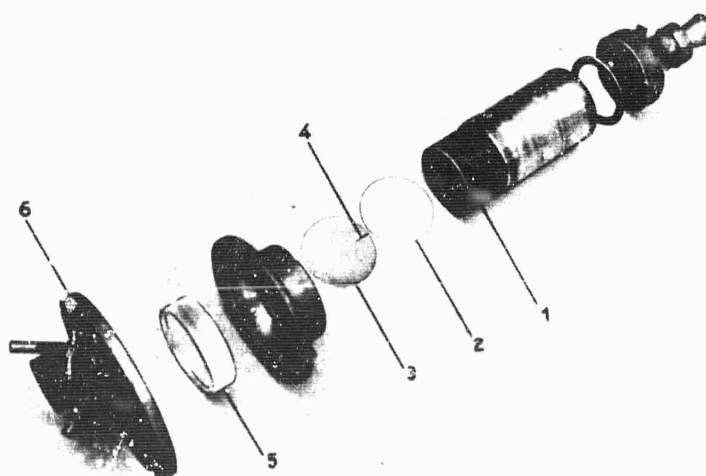
The method of performance analysis from the streaks camera traces is the same as described in Section 3.1.2. and will not be repeated here. However we should remark here that the technique is also applicable to plateau propellants because the constraints of the motor geometry, make Eq. 3-113 more nearly correct. Instead of describing the governing equation further we discuss the experimental method.

In a particular test on a star-shaped grain, illustrated in Fig. 3-27, a radial slit in an aluminum sheet extended along one of the star points of the grain facing the motor head.



- A: Slot
B: Particle path
C: Flame front

Fig. 3-27 Slot positioning



- | | |
|---------------------|-----------------------|
| 1: Propellant grain | 4: Slot |
| 2: Lucite plate | 5: Observation window |
| 3: Slotted plate | 6: Forward closure |

Fig. 3-28 Disassembled rocket motor

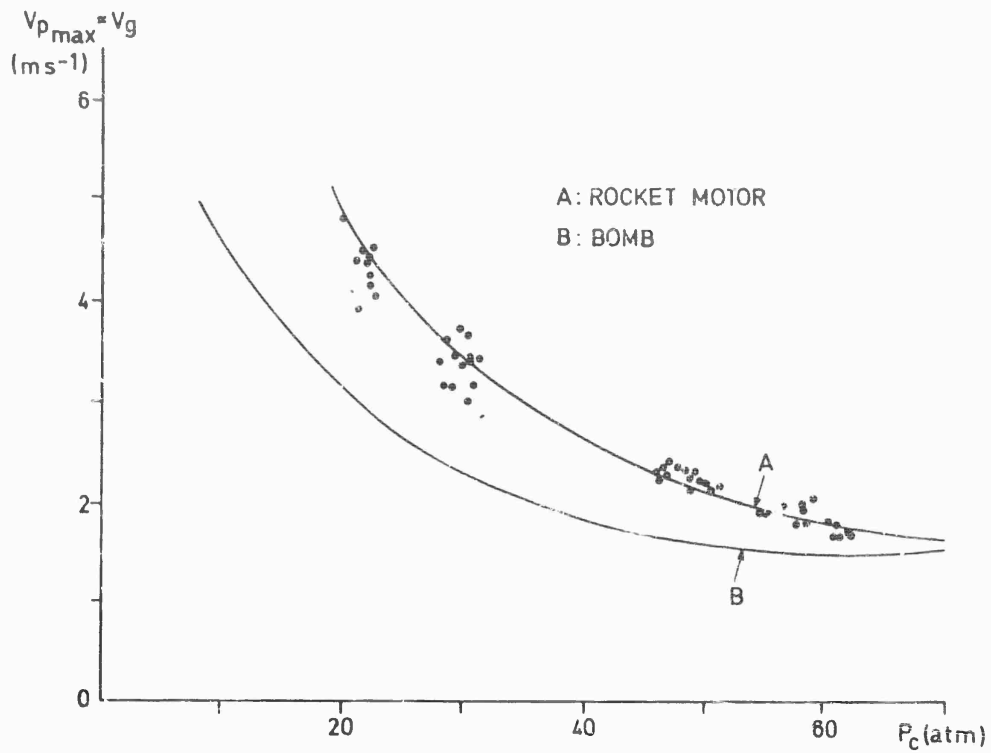
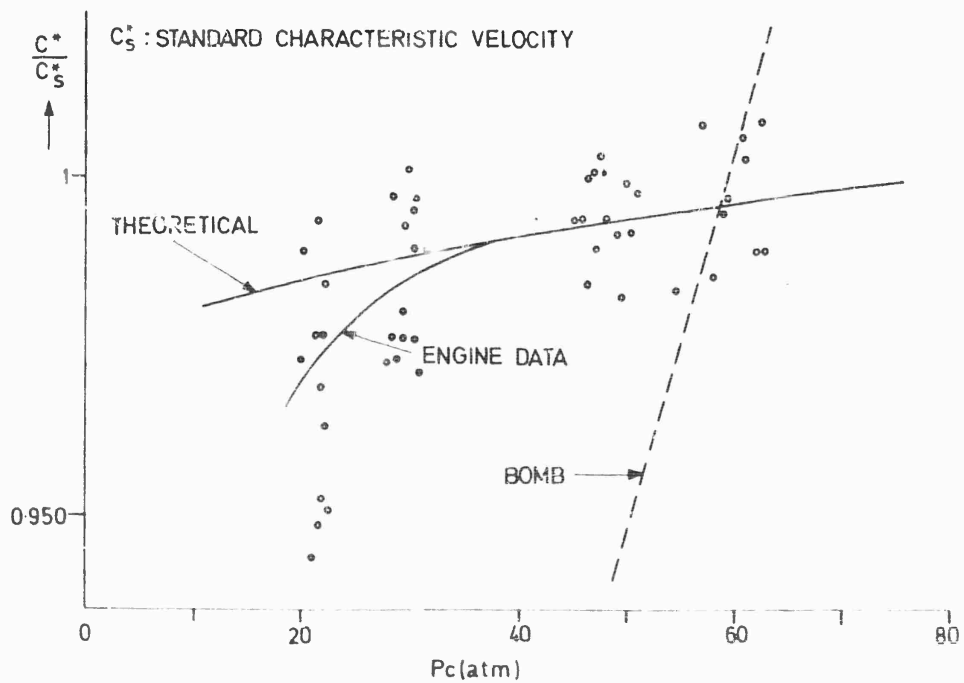
Fig. 3-29 $V_p \approx V_g$ versus pressure

Fig. 3-30 Characteristic velocity versus pressure

A flat lucite window of optical quality, serves as the motor head and permits flow observation. The aluminum foil containing the slit is 0.4 mm in thickness and is placed adjacent to the face of the grain that is to be observed.

A transparent coating of inhibitor prevents burning on the surface of the grain facing the head and also the eventual acceleration reduces the ratio of heat flow from the foil to the interior of the grain.

A disassembled rocket motor view is shown in Fig. 3-28. The head is a circular hole permitting observation through the slit and the camera objective lens is placed in this hole, where it is protected from gases and pressure. Two lateral optical system pass light through the slit before the test and aid in adjusting the position of the camera. The slit is usually slightly longer than the thickness of the web, so that the chamber wall can be observed before firing. A number of variations of the apparatus described here has been employed successfully.

The results obtained with a plateau propellant at chamber pressure between 30 and 70 atmospheres are shown in Figs. 3-29 and 3-30. It can be seen that the regression rate is greater when measured on a motor, than when measured in the strand burner; the same is true for the velocity of the gases (Fig. 3-29). The simultaneous knowledge of r and of $v_{p_{max}}$ leads to the determination of the characteristic velocity

c^* from the previously established relation. The pressure dependence of the ratio of this experimental c^* to the theoretical c^* calculated at 70 atmospheres by Brinkley's method is shown in Fig. 3-30. There is appreciable scatter at the low pressure levels; above 40 atmospheres the theoretical and experimental results are in good agreement. Below 40 atmospheres the experimental curve diverges from the theoretical curve because of a decrease in combustion efficiency with decreasing pressure p .

4. Comparison of Theory and Experiment

Specific comparisons based on quality indexes such as ξ_c^* , ξ_p or ξ_s are not very meaningful because the numerators and denominators in these ratios change as the techniques and theories for performance evaluation improve.

Typical current values of the quality index ξ_s lie between 0.90 and 0.95 when the theoretical calculation assumes equilibrium nozzle flow. Theoretical causes for differences between theory and experiment have been discussed in Chapter 2. However, we shall perhaps emphasize here that the available thermodynamic data on heats of formation of propellants and on thermodynamic properties of condensed phases that must be used in the theoretical calculations, is sometimes questionable.

There are many possible experimental causes of quality indices differing from unity. The most important one is measurement error; the determination of the parameters such as the characteristic velocity, the thrust coefficient or the specific impulse is based on the measurement of several quantities and the accumulated errors produce uncertainties of at least a few percent.

Scale effects produce experimental errors due to heat losses and especially due to combustion efficiency in metalized propellants. Additional experimental errors arise if proper care is not taken to account for mass loss effects, caused by liner pyrolysis and gasification of the other protective materials.

There is an advantage in separating as much as possible the losses related to combustion phenomena from the losses due to the flow expansion in the nozzle. A first approximation to this aspect of the problem is given by the determination of the quality index ξ_c^* , linked to combustion phenomena and to the presence of condensed particles, and of the quality index ξ_p which is mainly affected by the losses in the nozzle. Usually ξ_c^* losses are more important than ξ_p losses; typically ξ_c^* is of the order of 0.93 to 0.95 and ξ_p varies from 0.97 to 0.98. The distinctions between those losses characterised by the values of ξ_c^* and ξ_p are less evident for very energetic propellants.

References

- (1) Penner S.S. Chemistry Problems in Jet Propulsion, Pergamon Press, London, 1957.
- (2) Huff V.N., Gordon S. and Morell V.E. General Method and Thermodynamic Tables for Computation of Equilibrium Composition and Temperature of Chemical Reaction. N.A.C.A. rep. 1037, 1951.
- (3) Williams F.A. Combustion Theory. Addison Wesley Publishing Co. Inc.
- (4) Barrere M., Jaumotte A., Fraeijs De Veubeke B. and Vanderkerckhove J. Rocket Propulsion. Elsevier, 1960.
- (5) Lawrence Wilkins R. Theoretical Evaluation of Chemical Propellants. Prentice Hall, Technology Series, 1963.
- (6) Siegel B. and Schieler L. Energetics of Propellant Chemistry. John Wiley, New York, 1964.
- (7) Bahn G.S. and Zukoski E.E. Kinetics Equilibria and Performance of High Temperature Systems. Butterworths, 1959.
- (8) Brinkley S.R. Combustion Processes. Princeton University Press, 1956.
- (9) Crampel B., Barrere S., Lemaitre P. et Jaubert J. Méthode Programmée de Calcul des Equilibres Chimiques avec Phases Condensées. Notes Techniques ONERA n° 90-91-92, 1967.
- (10) Crampel B. Méthode de Calcul des Performances de Propergols dans le Cas de Systèmes Chimiques Hétérogènes Complexes. Entropie. N°9, Mai/Juin, 1966.
- (11) White W.B., Johnson S.M. and Dantzig G.B. Chemical Equilibrium in Complex Mixtures. Rand Corporation Report, P. 1059, 8 Oct. 1957.
- (12) Altman D. and Carter J.M. Combustion Processes Vol II. Princeton University Press, 1956.
- (13) Napoly C., Boisson J. et Quentin D. Evaluation des Performances Théoriques des Propergols. XXX III ème Congrès International de Chimie Industrielle, 1961.
- (14) Lampens G. et Vandekerckhove J. Performances des Propergols Solides. Rapport des Poudreries Réunies de Belgique, 1958.

- (15) Le Grives E. et Barrere S. Méthodes algébriques de Calcul de la Composition à l'Equilibre des Produits de Réactions Hautement Energétiques. La Recherche Aéronautique, N°68 pp. 31-39, Janv. Févr. 1959.
- (16) JANAF Thermochemical Data. The Dow Chemical Company Midland, Michigan.
- (17) Mayer J.E. and Mayer M.G. Statistical Mechanics. John Wiley and Sons, New York 1954.
- (18) Koelle H.H. Handbook of Astronautical Engineering, (See Solid Propellant Rocket Engines). R.D. Geckler, K. Klager (19), Mc Graw Hill Book Company 1961.
- (19) Penner S.S. and Ducarme J. The Chemistry of Propellants. AGARD Meeting 1959, Pergamon Press, 1960.
- (20) Gordon L.J. and Lee J.B. Metal as fuels in Multicomponent Systems. ARS J, April 1962.
- (21) Blackman A.W. and Kuehl D.K. Use of Binary Light Metal Mixtures and Alloys as Additives for Solid Propellants. ARS Journal, vol 31, N°9, Sept. 1961.
- (22) Griffin D.N., Turner C.F. and Campbell G.T. A Ballistic Bomb Method for Determining the Experimental Performance of Rocket Propellants. ARS Journal, Vol 29, No. 1, Jan. 1959.
- (23) Nadaud L. La Combustion des Propérgols Solides Métallisés. La Recherche Aéronautique N°85, Nov., Dec, 1961.
- (24) Larue P. Méthode Expérimentale de Qualification des Poudres à Plateau. La Recherche Aérospatiale. N° 99, Mars, Avril, 1964.

Chapter 4

Motor Operation

Nomenclature

A	cross-sectional area
a	sound speed; burning rate constant defined in Eq. 4-6
a'	burning rate constant defined in Eq. 4-7
A_b	burning surface area
a_0	initial acceleration of rocket
A_p	cross-sectional area of port
A_s	propellant surface area for sublimation rocket
b	burning rate constant defined in Eq. 4-6
b'	burning rate constant defined in Eq. 4-7
c^*	characteristic velocity
C_F	thrust coefficient
C_m	average curvature of initial surface
C_t	total curvature of initial surface
D	grain diameter
D_t	nozzle throat diameter
F	thrust
G	mass flow rate per unit cross-sectional area in central port
g	dimensionless variable G/G^* ; also gravitational acceleration
g_0	gravitational acceleration at sea level
h	enthalpy per unit mass
h_0	stagnation enthalpy
h_r	reference enthalpy at 0°K
J	ratio of nozzle throat area to cross-sectional area of port
K	ratio of burning surface area to nozzle throat area
Kn	Knudsen number
L	length of grain
M	Mach number
\dot{m}	mass flow rate

m_i	initial mass of vehicle
m_c	combustion chamber mass
\dot{m}_b	mass burning rate
m_n	nozzle mass
m_p	propellant mass
\dot{m}_s	mass flow rate of propellant for sublimation rocket
\dot{m}_t	mass flow rate through nozzle
m_v	$m_D - m_p$ mass of empty vehicle
N	parameter defined in Eq. 4-56
n	number of moles per unit mass for gas; number of singular recesses and spikes; burning rate constant defined in Eq. 4-6
P	port perimeter
p	pressure
p_s	stagnation pressure
p_v	equilibrium vapor pressure
R	mass ratio of vehicle
r	linear regression rate
\bar{r}	average regression rate, defined in Eq. 4-59
R°	universal gas constant
R_1, R_2	principal radii of curvature
T	temperature
t	time
t_b	burning time
T_f	flame temperature ($^\circ K$)
T_o	reference temperature for propellant; also stagnation temperature for gas
u	average gas velocity; also burning rate constant defined in Eq. 4-11
v_e	effective exhaust velocity
w	web thickness
w_b	burned web thickness

y	$\bar{r}t$
α	burning rate constant defined in Eq. 4-10; evaporation coefficient; angle defining surface geometry at a singularity
β	dA_p/dA_b
Γ	function of γ defined in Eq. 2-47 of Chapter 2
γ	ratio of specific heats
Δv	velocity increase of vehicle
ϵ_e	nozzle area ratio, A_e/A_t
ϵ_I	design parameter defined in Eq. 4-83
ϵ_{II}	design parameter defined in Eq. 4-84
θ	angle defining surface geometry at a singularity
Λ	slenderness ratio L/D ; also parameter defined in Eq. 4-55
λ	molecular mean free path
ξ	structural index = m_v/m_p
Π_T	coefficient of temperature sensitivity for burning rate
$(\Pi_T)_K$	coefficient defined in Eq. 4-22
ρ	gas density
ρ_m	density of structural material
ρ_p	propellant density
σ_a	maximum allowable stress
$(\sigma_T)_K$	coefficient defined in Eq. 4-23
φ	angle between tangent to cross-sectional contour and a reference direction; also $\sqrt{1 - g^2}$
Ψ	function defined in Eq. 4-47

Script Letters

\mathcal{A}_b	effective burning surface area
m	molecular weight of gas
\mathcal{V}	volume

Superscripts

o	condition at $t = 0$
-----	----------------------

* identifies sonic conditions

Subscripts

- b burning surface
- c chamber
- e nozzle exit
- o upstream end of grain
- s stagnation
- t nozzle throat
- 1 conditions at port exit

Motor Operation

1 Introduction (1)(2)(3)

Steady-state motor operation is influenced by the mass flow rate of gases issuing from the burning grain surface. According to the continuity equation this mass flow rate is a function of the propellant density ρ_p , of the burning surface area A_b , and of the burning rate r , as expressed by the formula:

$$\dot{m}_b = \rho_p A_b r \quad (\text{Eq. 4-1})$$

Since most propellant densities lie between 1.6 and 1.7 g.cm⁻³, the choice of the density is limited and only two variable parameters, A_b and r , are available to the designer for controlling the flow rate.

The gaseous combustion products flow through a nozzle at a mass flow rate \dot{m}_t . Both flow rates \dot{m}_b and \dot{m}_t are functions of the chamber pressure. A steady operating condition can be achieved only if two conditions are fulfilled; on one hand both mass flow rates must be equal to a high degree of approximation, viz:

$$\dot{m}_b(p_c) = \dot{m}_t(p_c) \quad (\text{Eq. 4-2})$$

which determines the pressure p_c ; on the other hand the operation must be stable so that any pressure increase causes a more rapid augmentation in the flow rate through the nozzle, than in the rate of production of gases at the surface of the grain, viz:

$$\left. \frac{d\dot{m}_t}{dp} \right|_{p_c} > \left. \frac{d\dot{m}_b}{dp} \right|_{p_c} \quad (\text{Eq. 4-3})$$

Since the mass flow rate through the nozzle is approximately proportional to the pressure, the condition expressed by Eq. 4-3 can be written in the form:

$$\left. \frac{d \ln r}{d \ln p} \right|_{p_c} < 1 \quad (\text{Eq. 4-4})$$

where use has been made of the fact that the only pressure dependent parameter in the expression, for the mass flow rate from the surface of the grain, is the burning rate.

The burning velocity thus plays a very important role in the operation of a motor and the first section of the present chapter will be devoted to a discussion of burning velocity laws. In the second section we shall study the operation of different motors with various grain shapes such as end-burning grains, cylindrical grains with central perforation and with radial combustion, and spherical grains.

We shall also consider dual composition grains which allow, in certain cases, improvement in the neutrality of burning of the grain or suppression of the pressure tail-off. As another topic, we shall study the time evolution of the pressure and shall indicate parameters that influence this evolution. In Section 4 the influence of the operating parameters on motor optimization is analyzed and in Section 5 the operation of small sublimation motors is studied.

2 Burning Rate Laws

Combustion of solid propellants can occur in two regimes which are characterized by widely different propagation velocities for the flame, namely detonation and deflagration. In the first regime the propagation velocity is of the order of several thousands of meters per second and in the second a few centimeters per second. The deflagration regime is used in propulsion. The operating pressure in the motor varies from a few tens to a few hundreds of atmospheres, depending on the application. Since the burning rate (deflagration velocity) depends appreciably on pressure, it can vary considerably. In order to define the burning rate one assumes that the combustion takes place in parallel layers so that a velocity vector, perpendicular to the surface and of equal magnitude everywhere on the surface, can be identified, viz:

$$r = \frac{dw}{dt} \quad (\text{Eq. 4-5})$$

where w is the web thickness. Equation 4-5 defines the regression rate of the solid.

The hypothesis of combustion in parallel layers was first proposed by Piobert in 1839. It remains valid if the heterogeneity of the propellant is of sufficiently small scale and if average propellant and gas-phase properties vary little from one point to another.

In Section 2.1 we shall give various burning rate laws and we shall discuss effects of the most important parameters. In Section 2.2 we shall review measurement techniques briefly.

2.1 Laws Proposed for the Burning Rate (Influence of Certain Parameters)

Since the most important parameter is the pressure, investigators have endeavored to develop a law relating r to p . A general form of such a law is:

$$r = a + bp^n \quad (\text{Eq. 4-6})$$

where the values of a , b and n depend upon the nature of the propellant and the pressure range.

For most propellants at low pressures (of the order of one atmosphere), $a = 0$ and $n = 1$. At moderate pressures (of the order of ten atmospheres) Saint-Robert's law ($a = 0$) has been verified; the exponent n is then usually of the order of 0.7 for homogeneous propellants and of the order of 0.4 for heterogeneous propellants.

At very high pressures (> 200 atm), Muraour's law ($n = 1$) is often used. In this case 'a' is often independent of the composition and, for homogeneous propellants, is of the order of 10 mm sec^{-1} . However 'b' is a function of the heat released during combustion and can be obtained from the equation:

$$\log (1000 b) = 1.214 + 0.308 T_f/1000,$$

where T_f is the flame temperature ($^{\circ}\text{K}$) and where the units of 'b' are $(\text{min sec}^{-1} \text{atm}^{-1})$. In a formula of this type, the quantity T_f can be related to the heat combustion.

For composite propellants at moderate pressures ($20 < p < 80 \text{ atm}$) one can also use Summerfield's law (4):

$$\frac{\bar{p}}{r} = a' + b' p^{2/3} \quad (\text{Eq. 4-7})$$

This relation has also been verified experimentally.

Burning rate laws for several homogeneous and heterogeneous propellants are given in Chapter 5. As an indication of orders of magnitudes, we give in Fig. 4-1 the burning rates of classical propellants which follow closely the p^n type laws:

$$r = b p^n \quad (\text{Eq. 4-8})$$

Figure 4-1 shows that the burning rate is sensitive to the propellant temperature T as well as to pressure; temperature sensitivity is expressed by a law of the general form:

$$r = r_0(p) \cdot f(T) \quad (\text{Eq. 4-9})$$

Typical $f(T)$ functions are:

$$f(T) = \frac{\alpha}{\alpha - (T - T_0)} \quad (\text{Eq. 4-10})$$

and:

$$f(T) = e^{u(T - T_0)} \quad (\text{Eq. 4-11})$$

where T_0 is a reference temperature corresponding to $r = r_0$ and where α and u are constants. The temperature sensitivity of the propellant burning rate is characterized by the coefficient:

$$(R_T)_p = \left(\frac{\partial \ln r}{\partial T} \right)_p \quad (\text{Eq. 4-12})$$

An expansion in series shows that:

$$e^{u(T - T_0)} = 1 + u(T - T_0) + \dots \approx \frac{1}{1 - u(T - T_0)}$$

whence:

$$(R_T)_p = u \approx \frac{1}{\alpha}$$

For numerous propellants over normal grain temperature ranges, u is of the order of $0.004 (^{\circ}\text{C})^{-1}$. However, u is not constant over extended temperature ranges; it generally increases when T increases.

Gas flow parallel to the burning surface influences the regression rate r . This erosive combustion effect is an important phenomenon which will be studied at length in Chapter 7. In each application, we shall indicate the form of the erosion law considered whenever erosion affects the operation of the motor.

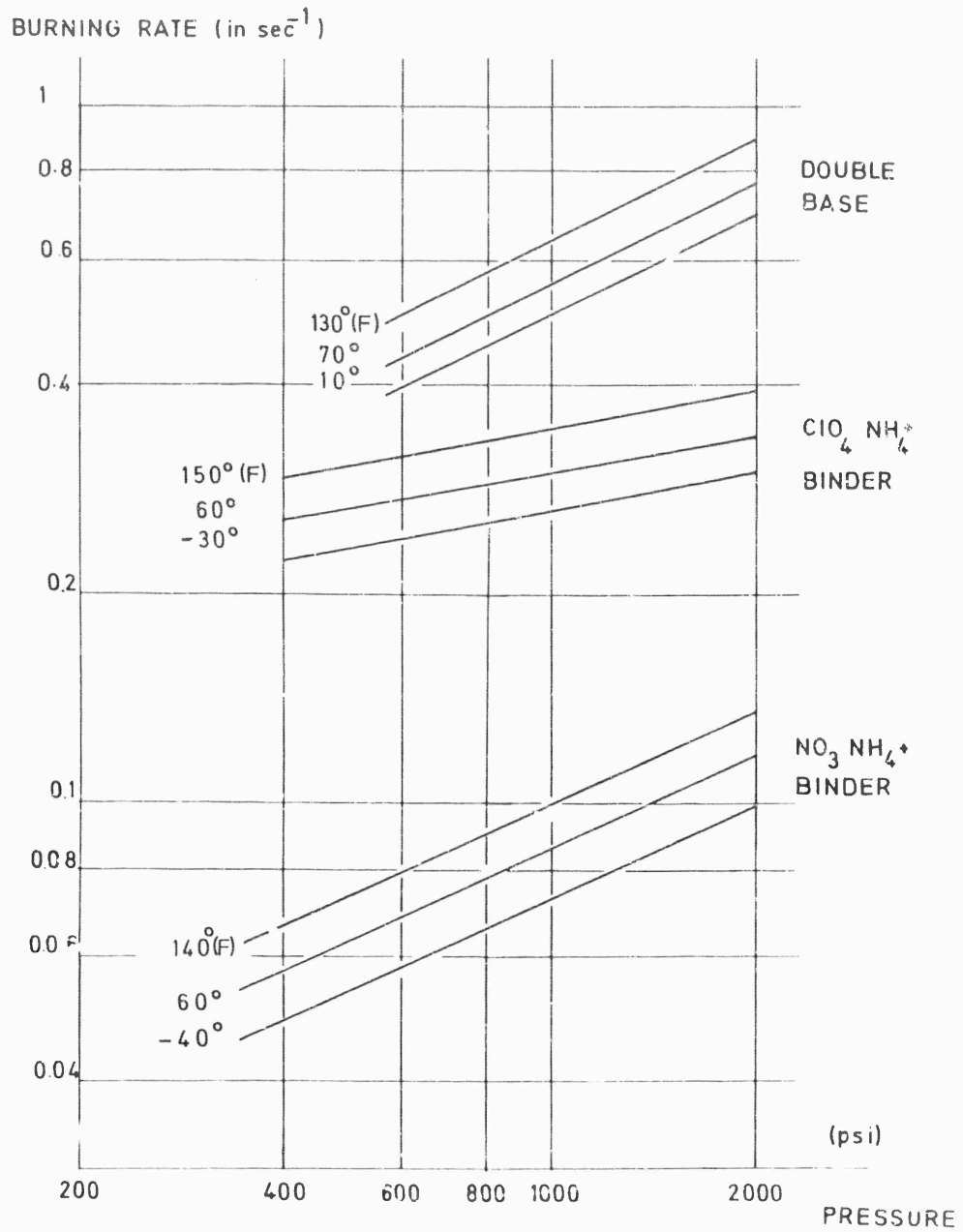


Fig. 4-1 Burning rates of different propellants.

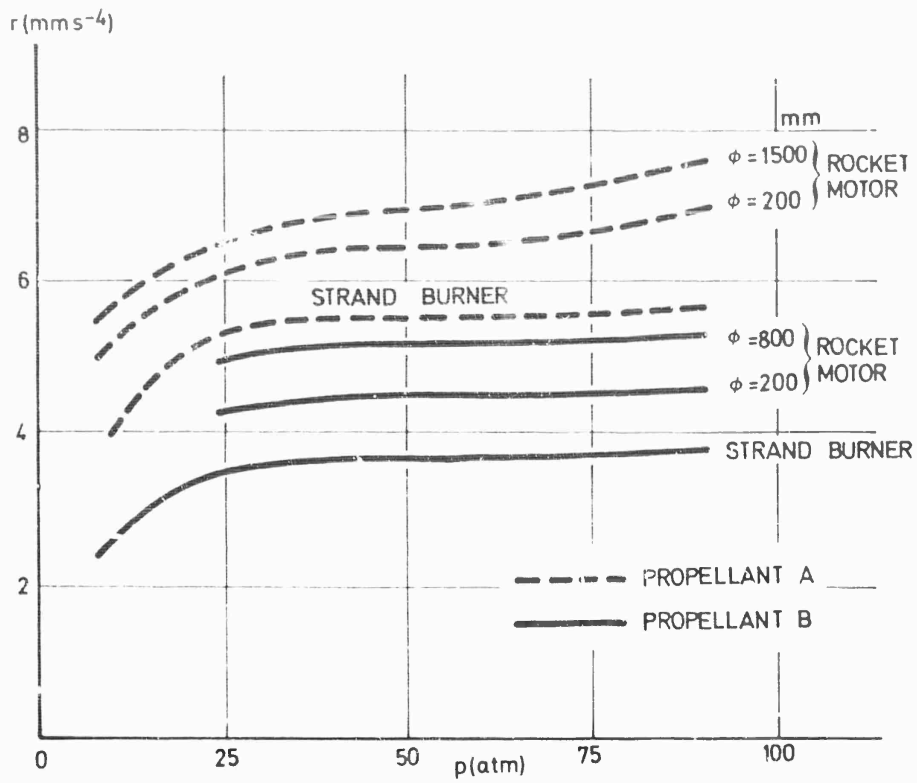


Fig. 4-2 Burning rate obtained by different methods (8).

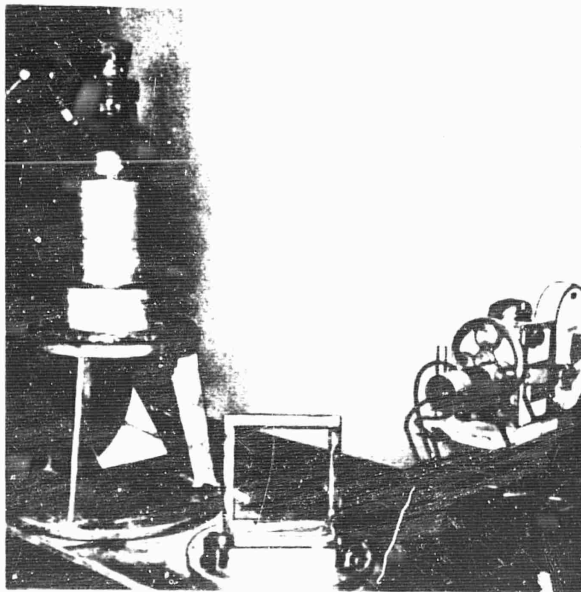


Fig. 4-3 Rocket motor with transparent wall.

The burning rate also depends upon the nature of the propellant; for any given propellant there exist catalysts which can be used for the control of the burning rate. Lithium fluoride, for example, decreases the burning rate by a factor proportional to the lithium fluoride concentration. Copper chromite and silica increase both the burning rate and the pressure exponent. Introducing aluminum into the propellant usually does not change the burning rate curve. With certain catalysts and for a given granule size of ammonium perchlorate, burning rates independent of the pressure can be obtained; this corresponds to the 'plateau' domain (see Fig. 4-2).

In addition to chemical means there exist physical means for controlling the burning rate. In particular it is possible to include in the grain heat conducting substances that affect the oxidizer and fuel decomposition rates. The most widely used technique consists of introducing metal wires into the grain during the casting process. Silver threads a few hundredths of a micron in diameter are the most efficient. The effect of the shape of the metallic additives is given in the following table (5):

Hollow spheres	burning rate increase of	50 - 100 %
Hollow tubes	" " "	10 - 200 %
Threads	" " "	50 - 400 %
Foil	" " "	50 - 450 %

With threads the velocity increases from 0.5 in. sec.⁻¹ to 2.65 in. sec.⁻¹ (silver)
 2.32 " " (copper)
 1.82 " " (tungsten)
 1.16 " " (aluminum)

Addition of suitably shaped heat conducting materials to the propellant is usually the most effective way to obtain an increased burning rate that is needed for achieving a specified regression rate or burning area history. One can also exploit erosive phenomena by designing the grain with slits, through which the hot gases flow in patterns that increase the erosive effect. The burning rates required for a few applications are given in the following table:

Application	r (in. sec. ⁻¹)
Booster	1 - 10
Sustainer-motor	0.2 - 1.0
Separation	1 - 10
Spin-motor	1 - 10
Space applications	0.05 - 5.0
Gas generator	0.01 - 0.2

2.2 Techniques for Burning Rate Measurements

Two types of measurement techniques are used, depending on the grain size. Small samples are burned in a strand burner and large grains in a motor.

a) Strand Burner Techniques for Burning Rate Measurements (6) - The samples are shaped like cylinders a few centimeters long with a circular or square cross-section. Lateral surfaces are protected by an inhibitor. The measurements are made in a bomb, in which the adjustable pressure ranges from one to a few hundred atmospheres. The pressurizing gas is usually nitrogen. Ignition of the sample is achieved electrically. The burning rate is obtained either by measuring the

time required for the flame front to pass between two electrical sensors (e.g. thin wires which melt) or by recording optically the continuous movement of the flame front (see Section 3 of Chapter 3).

Table 4-1 compares these two techniques; the photographic method is superior.

Techniques using small samples can lead to erroneous results because of small burning areas, the presence of an inhibitor, the presence of cold gases in the vicinity of the combustion zone and dilution of combustion products by ambient gases. However, strand burners are very convenient tools in developing new formulations, in monitoring a manufacturing process or in studying propellant combustion.

b) Burning Rate Measurements on a Motor (7), (8) - Burning rate measurements on a motor are preferable to those in a strand burner, but the number of motor runs is limited, since motor tests are costly.

In motor experiments the regression rate of the grain can be determined by direct methods, which include techniques based on interruption of burning, techniques utilizing probes embedded in the propellant and optical techniques which require the motor to be provided with a window.

Figure 4-3 shows apparatus for burning rate measurements in a transparent motor. The motor is mounted vertically and the window is located at the fore end of the combustion chamber. Two motion picture cameras are placed in a horizontal plane. One camera operates at a standard framing rate and the other operates at high speed. A totally reflecting mirror and a semi-transparent mirror are used in transmitting the image of the fore end of the motor to each camera.

Photographs of the combustion zone at different times during burning are shown in Fig. 4-4. It can be seen from the outermost bright zone that the surface of the grain regresses normal to itself during combustion. The burned web thickness w_b can be obtained as a function of time from the photographs and Fig. 4-5 shows that the resulting curves differ at different points on the burning surface. This lack of uniformity is believed to be caused by ignition phenomena, in the particular example shown here. The slopes of the curves in Fig. 4-5 give the instantaneous burning rate.

Indirect methods for measuring the burning rate can also be used. These methods employ accurate pressure measurements obtained during the run. Through the mass flow conservation equation, it is possible to relate directly $r A_b$ to the pressure:

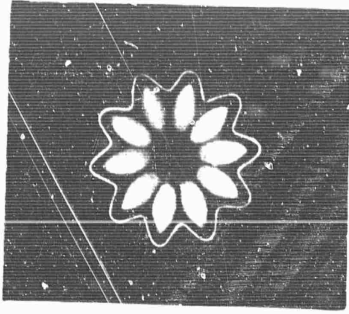
$$r \cdot A_b = f(p(t)) \quad (\text{Eq. 4-13})$$

By assuming a value for the burning surface area at time t , one can calculate the burning rate r from Eq. 4-13. Such an assumption is unnecessary if one uses a neutral configuration, for which the burning surface area A_b remains constant during the entire run. The operating conditions and the accuracies of motor methods are summarized in Table 4-1.

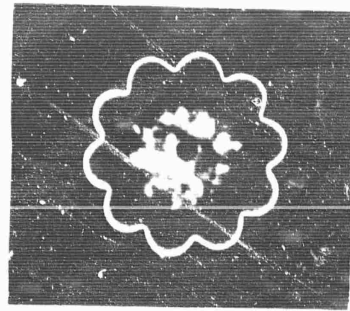
Discrepancies between the results obtained by the different methods often occur. These discrepancies arise principally from the differing burning conditions in each type of experiment. Figure 4-2 shows, for two composite plateau propellants, results obtained in the strand burner and in firings of two motors with different diameters. These results indicate that the burning rates measured in a strand burner are lower than those measured on a motor. The difference may be caused by the larger convective heat losses in a bomb than in a motor. Radiation effects

Techniques	Operating Conditions	Accuracy	Remarks
Strand Burner Sample Methods Wire Technique	Semi-realistic	Poor	Average burning rates
Photographic	Semi-realistic	Fair	Instantaneous burning rates Visualization of anomalies
Motor Firing Methods			
Interrupted burning	Realistic	Fair	Average burning rates
Probes	Realistic	Fair	Average burning rates
Photographic	Realistic	Good	Instantaneous burning rates Rocket motor with transparent window
Analysis of the pressure time recording	Realistic	Poor	Instantaneous

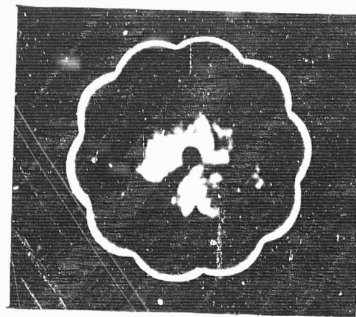
Table 4-1 Comparison of Experimental Techniques



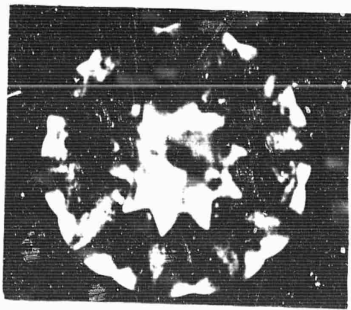
A



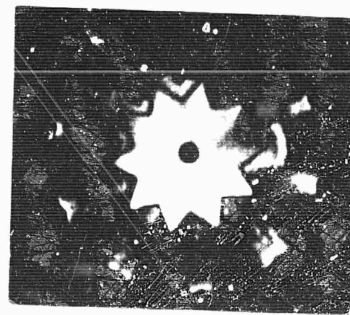
B



C



D



E

Fig. 4-4 Evolution of the geometry during combustion.

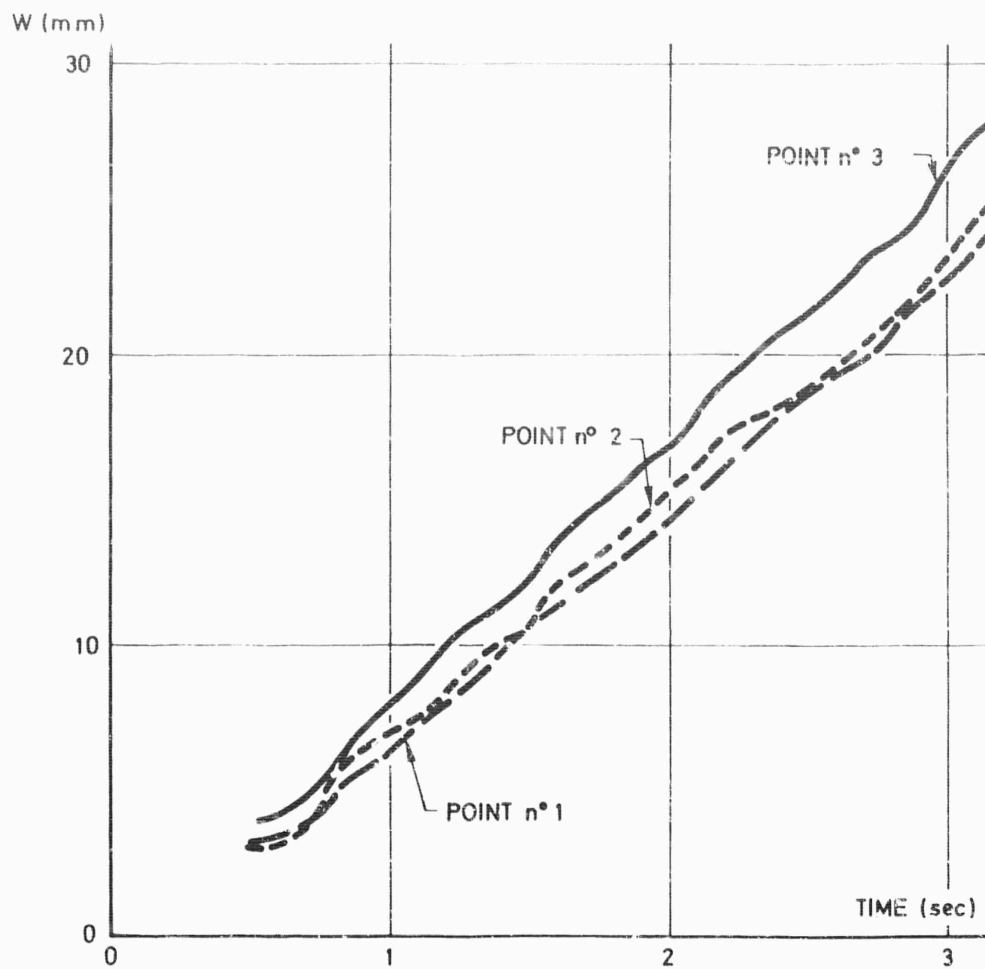


Fig. 4-5 Web evolution versus time.

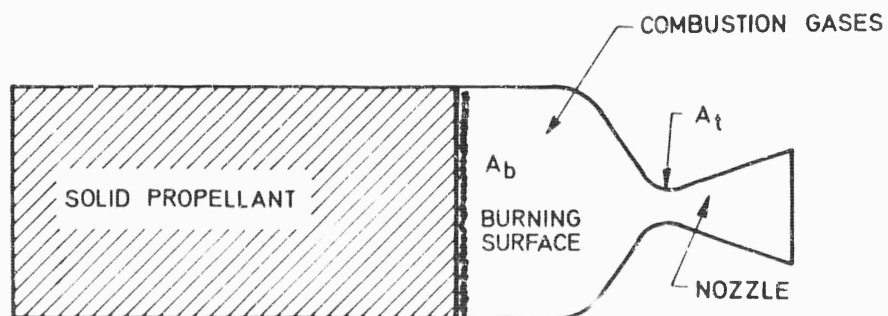


Fig. 4-6 End-burning solid propellant grain.

may also be significant. It is also seen that the burning rate increases with the motor diameter, although the general shape of the curve remains the same.

3 Motor Operating Characteristics (Time Evolution of the Pressure and of the Web Thickness)

3.1. End Burning Grain

The particularly simple, end-burning, cylindrical grain configuration is illustrated schematically in Fig. 4-6. The burning surface area remains constant during the entire firing. The mass conservation equation states that the mass flow rate from the surface of the propellant is equal to the sum of the mass flow through the nozzle and the time rate of increase of the gaseous mass contained in the combustion chamber:

$$\rho_p A_b r = \frac{d(\rho_c \gamma_c)}{dt} + \frac{p_c A_t}{c^*} \quad (\text{Eq. 4-14})$$

where $\rho_c \gamma_c$ is the mass of gaseous combustion products in the combustion chamber.

Since $\rho_c \frac{d\gamma_c}{dt} = \rho_c A_b r$, $c^* \Gamma^2 = n R T_c$ and $p_c = \rho_c n R T_c$,

where $\Gamma \equiv \sqrt{\gamma} \left(\frac{2}{\gamma+1} \right)^{(\gamma+1)/2}$, see Eq. 2-47 of Chapter 2, the mass conservation equation becomes:

$$\frac{\gamma_c}{A_t} \frac{1}{K} \frac{dp_c}{dt} + \frac{p_c \Gamma^2 c^*}{K} = (\rho_p n R T_c - p_c) r, \quad (\text{Eq. 4-15})$$

where K denotes the first geometric similitude parameter, the ratio of the burning surface area to the nozzle throat area, which is called the restriction ratio.

Let us first study the case where $\rho_p n R T_c$ is much larger than p_c , which is valid for most applications. During steady-state operation of a neutral grain, $\frac{dp_c}{dt} = 0$, so that:

$$p_c / K c^* = \rho_p r \quad (\text{Eq. 4-16})$$

The left-hand side of Eq. 4-16 represents the mass flow rate through the nozzle per unit burning surface area and the right-hand side is the mass rate of production of gaseous combustion products, also per unit burning surface area. Equation 4-16 yields the operating pressure of the motor. The stability condition becomes:

$$\frac{d}{dp_c} \left(\frac{p_c}{K c^*} \right) > \rho_p \frac{dr}{dp_c} \quad (\text{Eq. 4-17})$$

With a burning rate law of the form:

$$r = b p^n,$$

the operating pressure is given by the formula:

$$\rho_p c^* b K = p_c^{(1-n)} \quad (\text{Eq. 4-18})$$

We shall assume that, in this case, the characteristic velocity c^* is not very sensitive to the pressure. It is then quite clear from Eq. 4-18 that for specified propellant properties, the ratio K is an important motor design parameter which de-

termines the operating pressure of the motor. The stability condition becomes:

$$\frac{d \ln r}{d \ln p_c} < 1 \quad (\text{Eq. 4-19})$$

or:

$$n < 1 \quad (\text{Eq. 4-20})$$

The motor will operate stably only if this last condition is satisfied. We have defined the coefficient:

$$(\Pi_T)_p = \left(\frac{\partial \ln r}{\partial T} \right)_p \quad (\text{Eq. 4-21})$$

which expresses the sensitivity of the burning rate to the temperature. During steady-state operation two other parameters are of practical interest:

$$(\Pi_T)_K = \left(\frac{\partial \ln r}{\partial T} \right)_K \quad (\text{Eq. 4-22})$$

and

$$(\sigma_T)_K = \left(\frac{\partial \ln p}{\partial T} \right)_K \quad (\text{Eq. 4-23})$$

The first of these two coefficients expresses the sensitivity of the burning rate to the temperature for a motor with a constant area ratio, the second expresses the sensitivity of the chamber pressure to variations in the grain temperature at a constant value of K.

Since $r = b_0 e^{u(T - T_0)} p^n$, the following relations are obtained:

$$\frac{\partial \ln r}{\partial T}_K \equiv (\Pi_T)_K = u + n \left(\frac{\partial \ln p}{\partial T} \right)_K = u + n (\sigma_T)_K \quad (\text{Eq. 4-24})$$

and

$$(\sigma_T)_K = \frac{u}{1-n} = (\Pi_T)_K \quad (\text{Eq. 4-25})$$

An increase in the pressure exponent n increases the temperature sensitivity for operation at constant K.

With other burning rate laws, similar expressions are obtained. For instance with Summerfield's law the operating pressure is given by the relation:

$$b' p_c^{2/3} = \rho_p K c^* - a' \quad (\text{Eq. 4-26})$$

and with Muraour's law:

$$p_c (1 - \rho_p c^* K b) = \rho_p c^* K a \quad (\text{Eq. 4-27})$$

For Summerfield's law, the stability condition becomes:

$$\frac{1}{r} > \frac{a'}{p_c} + \frac{b'}{3p_c^{1/3}} \quad (\text{Eq. 4-28})$$

which is always satisfied if a' and b' are positive.

For Murauour's law, the stability condition is:

$$\rho_p c^* K b < 1 \quad (\text{Eq. 4-29})$$

and the constant 'a' is always positive.

If $\rho_p n R T_c$ is not assumed to be negligible in comparison with p_c and ρ_p is not negligible compared with ρ_c , then the equilibrium pressure is given by the formula:

$$\frac{p_o \Gamma^2 c^*}{K} = (p^* - p_c) r \quad (\text{Eq. 4-30})$$

with

$$p^* = \rho_p n R T_c$$

A burning rate law of the p^n type leads to the following stability condition:

$$n < \frac{p^*}{p^* - p_c} \quad (\text{Eq. 4-31})$$

The motor operation can then be stable for values of n larger than unity, but since p^* is typically of the order of 14,000 atm., realistic values of p_c permit 'n' to exceed unity only by a very small amount. The minimum value of p_c for stability is:

$$(p_c)_{\text{stable}} = \frac{n-1}{n} p^* \quad (\text{Eq. 4-32})$$

3.2. Grains with Central Perforations (9)

For grains with central perforations the problem of calculating grain shape evolution is complicated because of the presence of a flow in the central port and the presence of axial variations of grain shape. Figure 4-7 shows a schematic illustration of a motor with a perforated grain. The central port may be cylindrical or tapered. The mass flow rate at time t through a cross section at abscissa x , is given by:

$$\dot{m}(x) = \rho_p \int_0^x p_b(x) r(x) dx = \rho_p \int_0^{A_b} r. dA_b \quad (\text{Eq. 4-33})$$

where $\gamma(x)$ is the internal perimeter of the grain at axial position x . The mass flow rate at position x is also given by the formula:

$$\dot{m}(x) = \rho(x). A_p(x). u(x) \quad (\text{Eq. 4-34})$$

where $\rho(x)$ and $u(x)$ denote the average gas-phase density and velocity at position x . Quantities such as $u(x)$ affect the local burning rate. At the exit section ($x = L$), the mass flow rate is equal to the flow rate through the nozzle:

$$\rho_1 A_{p1} u_1 = \frac{p_c A_t}{c^*} \quad (\text{Eq. 4-35})$$

A second geometrical similitude parameter therefore arises, namely, $J_1 = A_t/A_{p1}$, the ratio of the nozzle throat area to the port exit cross-sectional area. This parameter J_1 , determines the Mach number in the exit cross-section of the port. Typically J_1 is of the order of 1/2 at the beginning of a firing. The value of J_1 determines the severity of erosion in the central port.

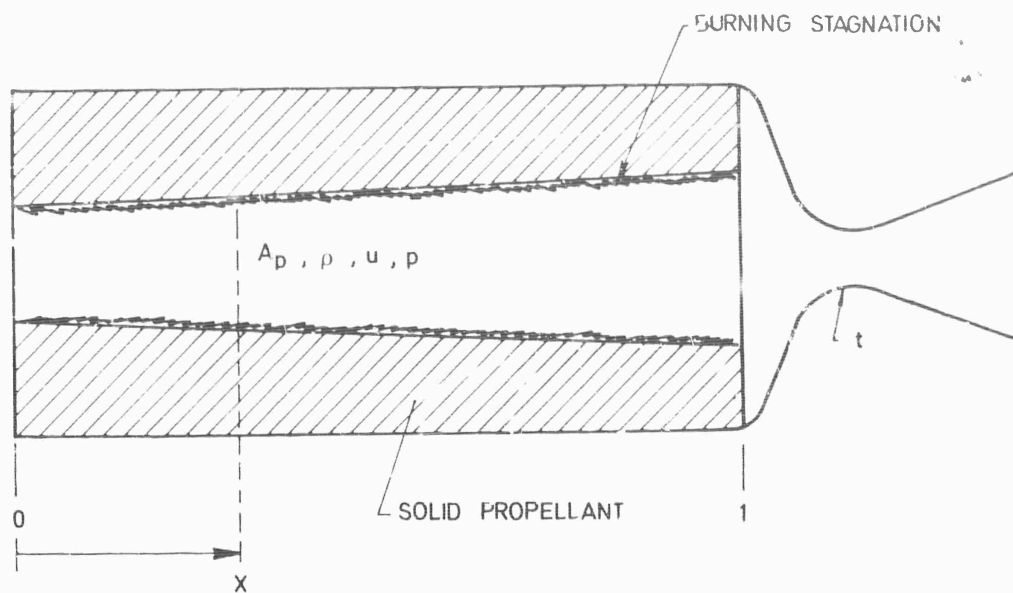


Fig. 4-7 Tapered port rocket motor.

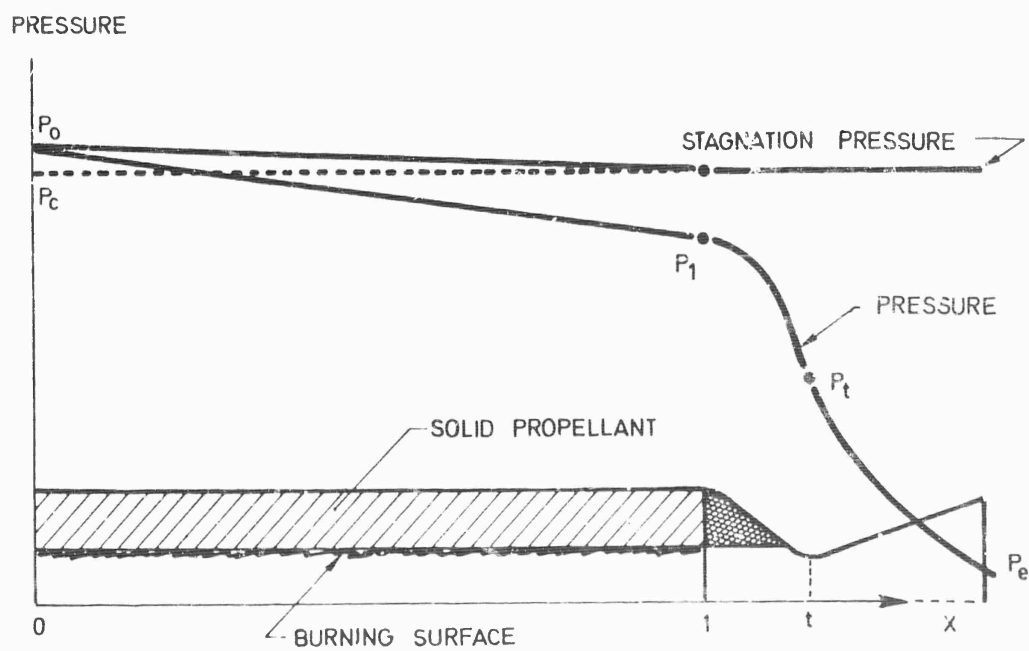


Fig. 4-8 Pressure evolution along the grain.

Let us consider axial pressure profiles in the central port (Fig. 4-8). Due to the low flow velocity at section 0, the stagnation pressure is practically equal to the static pressure there. The stagnation pressure decreases as x increases because of mass and energy addition by combustion. At the exit of the port, the discontinuity in cross-sectional areas can cause a sudden variation in total pressure. We shall assume here that this discontinuity is small and furthermore that no chemical reactions take place in the nozzle; the stagnation pressure is needed for computing the mass flow rate through the nozzle because the stagnation pressure at the throat appears in the formula for the mass flow rate. Since the mass flow rate increases as x increases, the flow velocity in the central port increases and the static pressure decreases continuously.

For steady-state, adiabatic flow, the conservation equations are:

$$\text{conservation of mass : } \dot{m} = \rho u A_p \quad (\text{Eq. 4-36})$$

$$\text{conservation of momentum : } d(\dot{m} u) + A_p dp = 0 \quad (\text{Eq. 4-37})$$

$$\text{conservation of energy : } h_o = h + \frac{u^2}{2} \quad (\text{Eq. 4-38})$$

the subscript o corresponds to the upstream end of the grain where $u_o \approx 0$. In the energy conservation equation, we shall assume that all the mass introduced into the system has the same stagnation enthalpy h_o and the same stagnation temperature $T_s = T_o$. The gases are also assumed to obey the perfect gas law,

$$p = \rho n RT \quad (\text{Eq. 4-39})$$

and the enthalpy assumed to be given by the formula:

$$h = h_r + c_p T \quad (\text{Eq. 4-40})$$

where h_r is the reference enthalpy at 0°K . We have thus five equations 4-36 to 4-40 relating the seven variables: ρ , u , p , T , h , \dot{m} , A_p from which we shall choose two independent variables, \dot{m} and A_p .

In this problem \dot{m} and A_p appear in relations such as :

$$g = \frac{G}{G^*} \quad (\text{Eq. 4-41})$$

where G is the specific mass flow rate in the central port and G^* the specific mass flow corresponding to sonic conditions. Thus,

$$G = \frac{\dot{m}}{A_p} = \rho u \quad (\text{Eq. 4-42})$$

and

$$G^* = \rho^* u^* = \frac{\gamma p_o}{\sqrt{2\gamma(\gamma+1)nRT_o}} = \frac{p_o}{2} \left(\frac{\gamma+1}{2} \right)^{-\frac{1}{\gamma-1}} \frac{1}{c^*} \quad (\text{Eq. 4-43})$$

Equation 4-36 to 4-40 can be transformed into differential equations of the form:

$$\begin{aligned} & -d(p/p_o) + \gamma d \left\{ (p/p_o)^2 + \left(\frac{\gamma-1}{\gamma+1} \right) g^2 \right\}^{1/2} \\ & + \gamma \left\{ -(p/p_o) + \sqrt{\left(\frac{p}{p_o} \right)^2 + \left(\frac{\gamma-1}{\gamma+1} \right) g^2} \right\} d \ln A_p = 0 \end{aligned} \quad (\text{Eq. 4-44})$$

In the particular case for which $dA_p = 0$, the following equations give the dependent variables as functions of the independent variable $\varphi = \sqrt{1-g^2}$

$$\left\{ \begin{array}{l} \frac{T}{T_o} = \frac{2}{\gamma+1} \cdot \frac{1+\gamma\varphi}{1+\varphi} \\ \frac{p_s}{p_o} = \frac{1+\gamma\varphi}{1+\gamma} \left(\frac{\gamma+1}{2} \cdot \frac{1+\varphi}{1+\gamma\varphi} \right)^{\frac{\gamma}{\gamma-1}} \\ \frac{p}{p_o} = \frac{1+\gamma\varphi}{1+\gamma} \\ \frac{\rho}{\rho_o} = \frac{1+\varphi}{2} \\ \frac{u}{u^*} = \frac{1-\varphi}{\sqrt{1-\varphi^2}} \\ \frac{u}{a_o} = \frac{2}{\gamma+1} \left(\frac{1-\varphi}{1+\varphi} \right)^{\frac{1}{2}} \\ \frac{h}{h_o} = 1 - \frac{u^{*2}}{2h_o} \cdot \frac{1-\varphi}{\sqrt{1-\varphi^2}} \\ J_x = \frac{A^*(x)}{A_p} = \sqrt{1-\varphi^2} \frac{(1+\gamma\varphi)^{(1/\gamma-1)}}{(1+\varphi)^{(\gamma/\gamma-1)}} \end{array} \right. \quad (\text{Eq. 4-45})$$

Here u^* is the value of u for $g = 1$ and $A^*(x)$ is the cross-sectional area of the throat of a fictitious sonic nozzle, that discharges the same mass flow rate as the flow rate through the port section $A_p(x)$ at position x . The quantity g and the Mach number M are related by the equation:

$$g = \frac{M \sqrt{2(\gamma+1) \left\{ 1 + \frac{\gamma-1}{2} M^2 \right\}}}{1 + \gamma M^2} \quad (\text{Eq. 4-46})$$

In general, $dA_p \neq 0$ and two independent variables are needed in expressing the solutions. The dimensionless variables g and $\frac{p}{p_o}$ are useful replacements for the dimensional independent variables A_p and \dot{m} .

In order to simplify the expressions let:

$$\Psi = \sqrt{\frac{\gamma-1}{\gamma+1}} \cdot \frac{p_o}{p} \cdot g \quad (\text{Eq. 4-47})$$

The resolution of the system of equation yields T , ρ , h , u , M and p_s :

$$\left\{ \begin{array}{l} \frac{T}{T_o} = \frac{2}{\Psi^2} \left[\sqrt{1 + \Psi^2} - 1 \right] \\ \frac{\rho}{\rho_o} = \frac{p}{p_o} \frac{\Psi^2}{2 (\sqrt{1 + \Psi^2} - 1)} \\ \frac{p_s}{p_o} = \frac{p}{p_o} \left[\frac{1 + \sqrt{1 + \Psi^2}}{2} \right]^{\frac{\gamma}{\gamma - 1}} \\ \frac{u}{u^*} = \sqrt{\frac{\gamma + 1}{\gamma - 1}} \left[\frac{\sqrt{1 + \Psi^2} - 1}{\Psi} \right] \\ \frac{h}{h_o} = 1 - \frac{u^{*2}}{2 h_o} \frac{\gamma + 1}{\gamma - 1} \left\{ \frac{\Psi^2 + 2(1 - \sqrt{1 + \Psi^2})}{\Psi^2} \right\} \\ M = \left\{ \frac{\sqrt{1 + \Psi^2} - 1}{\gamma - 1} \right\}^{\frac{1}{2}} \\ J = \frac{\Psi}{\sqrt{\gamma^2 - 1}} \left[\frac{1 + \sqrt{\gamma^2 + 1}}{\gamma + 1} \right] - \frac{\gamma}{\gamma - 1} \end{array} \right. \quad (\text{Eq. 4-48})$$

The value of p/p_o is determined from equation 4-44. To equation 4-44, 4-46 and 4-48 we must add an expression for the mass flow rate at the port exit:

$$\dot{m}_1 = \dot{m}_t = \frac{A_t p_{s1}}{c^*} = \frac{A_t p_{c1}}{c^*} \quad (\text{Eq. 4-49})$$

Equation 4-49 rests on the assumption that the stagnation pressure in Section 1, p_{s1} , is equal to the stagnation pressure at the nozzle throat. In particular at the exit section g_1 is given by:

$$g_1 = \frac{\dot{m}_1}{A_{p1}} \cdot \frac{1}{G^*} = J_1 \frac{p_{s1}}{p_o} 2 \left(\frac{2}{\gamma + 1} \right)^{\frac{1}{\gamma - 1}} \quad (\text{Eq. 4-50})$$

Introducing into the definition of g the expression for the flow rate of combustion products, we obtain the formula:

$$g = \frac{\dot{m}}{A_p} \cdot \frac{1}{G^*} = \frac{\rho_p}{A_p} \cdot \frac{1}{G^*} \int_0^{A_b} r \left(\frac{p}{p_o}, g \right) dA_b \quad (\text{Eq. 4-51})$$

The functional dependence of the burning surface area on the local port cross sectional area must also be given:

$$A_b = a(A_p) \quad (\text{Eq. 4-52})$$

The system formed by equations 4-44, 4-48, 4-50, 4-51 and 4-52 allows solution of some problems related to the operation of a motor.

As an illustrative example, consider a profile defined by $\beta = \frac{dA_p}{dA_b} = \text{constant}$ and a burning law of the form $r = b p^n (1 + k u^*)$. Equation 4-51 $\frac{dA_p}{dA_b}$ becomes then:

$$g = \frac{\rho_p b p_o^n}{\beta G^*} \left(\frac{1}{\left(\frac{\beta A_b}{A_{p_o}} + 1 \right)} \int_0^{\beta A_b/A_{p_o}} \left(\frac{p}{p_o} \right)^{\frac{1}{\gamma}} (1 + k \frac{u}{u^*}) d \frac{\beta A_b}{A_{p_o}} \right) \quad (\text{Eq. 4-53})$$

For reasons of convenience Price introduced two parameters which appear in the preceding expression. First he defined an area ratio $K_o = A_b/A_t$. Neglecting the effect of the mass flow through the motor, one can write an approximate expression for K_o , which treats the motor as an isobaric system operating at pressure p_o viz.,

$$K_o = \frac{p_o}{\rho_p b p_o^n c^*} \quad (\text{Eq. 4-54})$$

Price then defined:

$$\Lambda = \frac{\beta G^*}{\rho_p b p_o^n} = \frac{\beta G^* K_o c^*}{p_o} \quad (\text{Eq. 4-55})$$

and introduced the notation:

$$N = \frac{A_b}{A_p} \frac{1}{K_o} = \frac{L}{K_o} = \frac{1}{\beta K_o} \frac{\beta A_b}{A_{p_o}} \left(\frac{1}{1 + \frac{\beta A_p}{A_{p_o}}} \right), \quad (\text{Eq. 4-56})$$

whence

$$\frac{\beta A_b}{A_{p_o}} = \frac{\beta N K_o}{1 - \beta N K_o},$$

so that the parameters Λ and N appear in the expression for g (N is expressed as a function of $\frac{\beta A_b}{A_{p_o}}$).

Figures 4-9 and 4-10 give the variation of p/p_o with N (Fig. 4-9) and with g (Fig. 4-10) for several values of J and Λ . In these examples we have taken a plateau-type propellant ($n = 0$) and an erosion factor k equal to 2; the ratio of the specific heats, γ , is 1.22. The limit of isentropic flow corresponds to an idealised system in which the mass is introduced at zero velocity at a pressure p_o and is accelerated isentropically. In this case:

$$K = K_o, \quad N = J \frac{K}{K_o} = J,$$

and the variable g is given by:

$$g = \frac{J p_o}{G^* c^*} \quad (\text{Eq. 4-57})$$

Two additional parameters can also be introduced. We define an average burning rate \bar{r} by the equation:

$$\frac{\bar{r}}{r_o} = \frac{g}{J} \frac{G^*}{p_o} c^*, \quad (\text{Eq. 4-58})$$

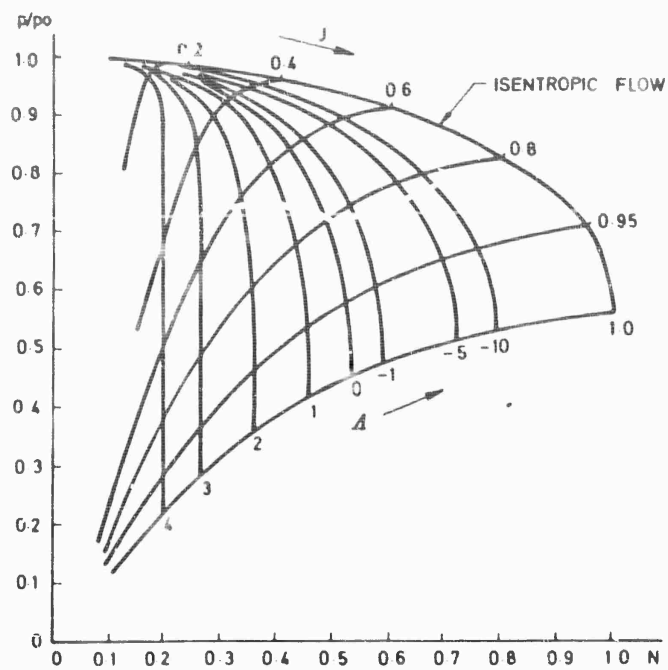


Fig. 4-9 Variation of pressure versus N in constant β channels ($n = 0$, $k = 2.0$) (9).

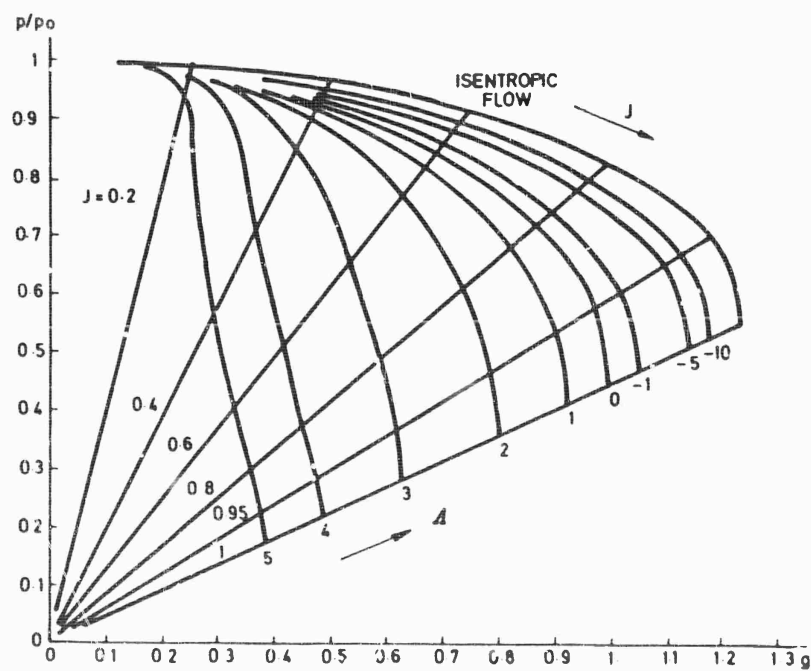


Fig. 4-10 Variation of pressure vs. g in constant β channels ($n = 0$, $k = 2.0$) (9).

so that:

$$\bar{r} = \frac{\dot{m}}{\rho_p A_b} \quad (\text{Eq. 4-59})$$

In particular, the average burning rate for the entire grain is:

$$\bar{r} = \frac{\dot{m}_1}{\rho_p A_b} \quad (\text{Eq. 4-60})$$

The thrust F is related to an effective exhaust velocity v_e by the formula:

$$F = \dot{m}_1 v_e \quad (\text{Eq. 4-61})$$

and can be written in the form:

$$\frac{F}{p_o A_{p1}} = \frac{1}{c^*} \frac{A_t}{A_{p1}} \cdot \frac{p_{s1}}{p_o} v_e = \frac{1}{c^*} J \frac{p_{s1}}{p_o} v_e = \frac{g_1 G^*}{p_o} v_e \quad (\text{Eq. 4-62})$$

The graphical representation is convenient for solving certain problems related to motor operation. Let us consider one application; other examples of this type are also given in reference (9).

Consider a propellant with the following characteristics:

$b = 8 \text{ mm sec}^{-1}$, $n = 0$, $k = 2.0$, $\gamma = 1.22$, $\rho_p = 1.7 \text{ g.cm}^{-3}$, $c^* = 1500 \text{ m sec}^{-1}$, $v_e = 2500 \text{ m.s}^{-1}$. We shall calculate the motor size required for generating a thrust of $F = 10 \text{ T}$, at an operating pressure $p_o = 50 \text{ atm}$ and a pressure ratio $p_1/p_o = 0.80$. The central port will be tapered with $\beta = 3 \cdot 10^{-3}$. The grain geometry is defined by specifying the values of A_{p1} , A_t , J , A_t , A_b and K . We shall also wish to calculate the value of the average burning rate \bar{r} .

In order to use the graphs of Figs. 4-9 and 4-10, we must compute Λ :

$$\Lambda = \frac{\beta G^*}{\rho_p b} = \frac{\beta}{\rho_p} \cdot \frac{p_o}{b} \cdot \frac{1}{2} \left(\frac{\gamma + 1}{2} \right)^{1/\gamma - 1} \cdot \frac{1}{c^*} = 0.599$$

From Fig. 4-10 we find $J_1 = 0.66$, $N = 0.419$ and from Fig. 4-9, $g_1 = 0.725$. The remaining computations are:

$$A_{p1} = \frac{F}{g_1 G^* v_e} = 199 \text{ cm}^2$$

$$A_t = J_1 A_{p1} = 131 \text{ cm}^2$$

$$K_o = \frac{p_o \Lambda}{G^* \beta c^*} = 249$$

$$L = NK_o = 104.3 = J_1 K$$

$$K = 158$$

$$A_b = KA_t = 20700 \text{ cm}^2$$

$$A_{p_0} = A_{p_1} - \beta A_b = 136.9 \text{ cm}^2$$

$$\frac{r}{r_0} = \frac{E_1}{J_1} \frac{G^*}{p_0} \quad c^* = 0.881$$

This one-dimensional analysis could be improved by considering either a stratified flow or a two-dimensional flow. However, its accuracy would be limited by our knowledge of burning rates and of the laws which control them, so that a more complex theory is not justified. This analysis can also be extended to more complex port geometries.

3.3. Propellant Grain Geometry

a) General Case - In an end burning grain the area of the burning surface is independent of time and therefore the pressure also remains constant; the grain is neutral. In a grain with a central perforation the pressure remains constant only if the quantity $\bar{r} A_b$ does not vary during the firing, \bar{r} being the instantaneous area-average burning rate. The grain will be neutral if $\bar{r} A_b$ is constant, progressive if $\bar{r} A_b$ increases with time and regressive if $\bar{r} A_b$ decreases. In Section 3.2 we focused our attention on the effect of the flow on the operation of the motor and we did not discuss details of the choice of the burning rate or of the grain geometry. We shall now begin to consider these topics and shall start by assuming that the burning velocity is the same at each point on the propellant surface. Consider (Fig. 4-11) a burning surface $A_b(0)$ at time $t = 0$; the new surface at time t later is defined as the envelope of the spheres centered on surface $A_b(0)$ and of radius equal to the burned web thickness $y = \bar{r} t$. The surface $A_b(t)$ thus defined is parallel to the first one. An analogy exists between the definition of a burning surface and Huygens' principle of wave-front propagation in optics. Our present problem is equivalent to that of wave propagation in an isotropic medium.

Let E_0 be a point contained in an area element da^0 of the surface $A_b(0) = A_b^0$. The two principal radii of curvature of the surface at point E_0 are R_1^0 and R_2^0 . To the point E_0 of surface A_b^0 corresponds at time t a point E of surface A_b such that the distance $E_0 E = y$ (y is chosen sufficiently small so that the principal centers of curvature are located neither on surface A_b nor between A_b^0 and A_b). To the area element da^0 corresponds an area element da on surface A_b and the principal radii of curvature at point E , are $R_1 = R_1^0 - y$ and $R_2 = R_2^0 - y$. Since the solid angle $d\omega = da / R_1 R_2$ is conserved in wave-front propagation, it follows that:

$$\frac{da^0}{R_1^0 R_2^0} = \frac{da}{R_1 R_2} \quad (\text{Eq. 4-63})$$

The area A_b is given by the integral:

$$A_b = \int_{A_b} da = \int_{A_b^0} \frac{(R_1^0 - y)(R_2^0 - y)}{R_1^0 R_2^0} da^0, \quad (\text{Eq. 4-64})$$

which can be expressed in terms of the average (C_m) and total (C_t) curvatures of the initial surface,

$$C_m = \frac{1}{2} \left(\frac{1}{R_1^0} + \frac{1}{R_2^0} \right), \quad C_t = \frac{1}{R_1^0 R_2^0}, \quad (\text{Eq. 4-65})$$

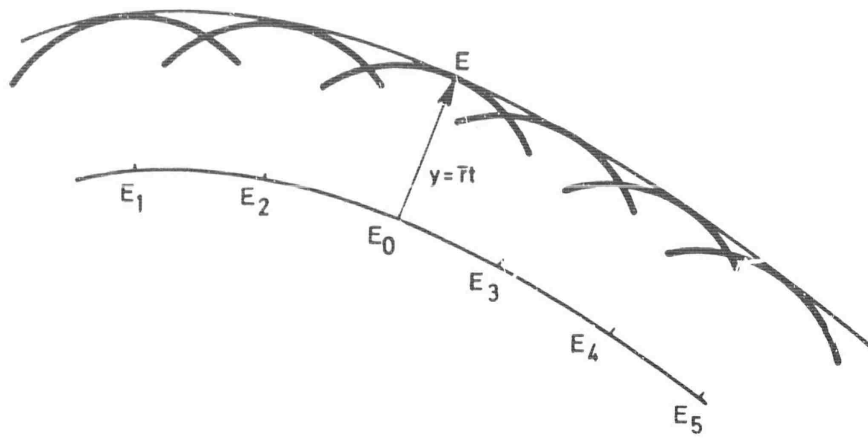


Fig. 4-11 Burning surface evolution.

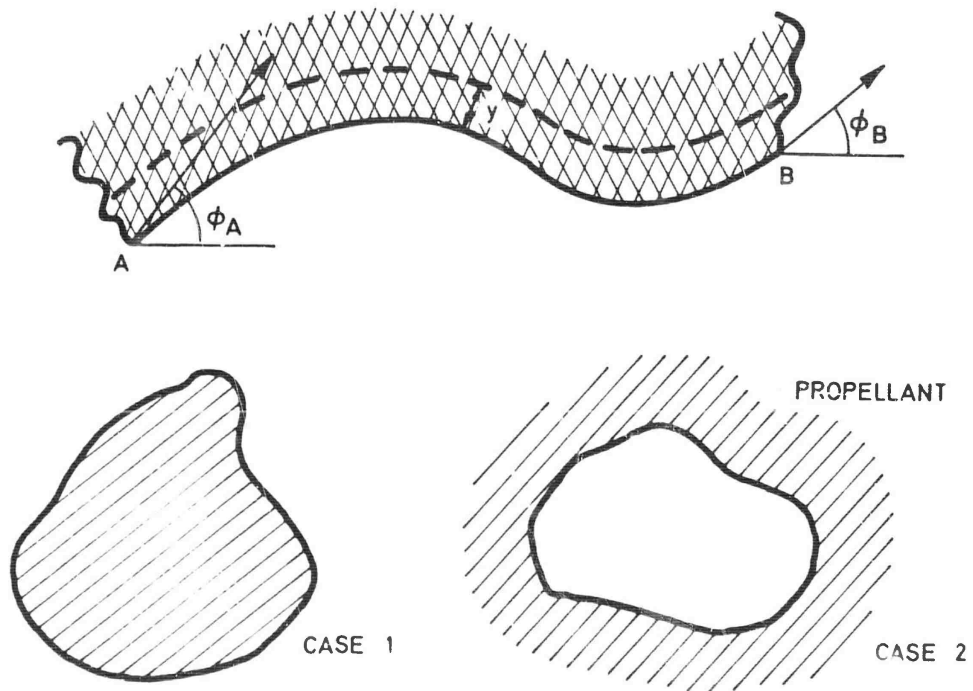


Fig. 4-12 Burning surface evolution without singularity.

$$\begin{aligned}
 A_b &= \int_{A_b^0} (1 - 2yC_m + y^2C_t) da_o \\
 &= A_b^0 - 2y \int_{A_b^0} C_m da_o + y^2 \int_{A_b^0} C_t da_o, \quad (\text{Eq. 4-66})
 \end{aligned}$$

Developing A_b in a Mac-Laurin series leads to the relation:

$$A_b = A_b^0 + \frac{dA_b^0}{dy} y + \frac{1}{2!} \frac{d^2A_b^0}{dy^2} y^2 + \frac{1}{3!} \frac{d^3A_b^0}{dy^3} y^3 + \dots$$

Equating the last two expressions for A_b shows that only the first and second derivatives have nonzero values; the higher order derivatives are identically equal to zero. We see that:

$$\frac{dA_b^0}{dy} = -2 \int_{A_b^0} C_m da_o, \quad \frac{d^2A_b^0}{dy^2} = \int_{A_b^0} C_t da_o \quad (\text{Eq. 4-67})$$

which lead to the following conclusions:

1) Knowledge of the derivatives $\frac{dA_b^0}{dy}$ and $\frac{d^2A_b^0}{dy^2}$ is sufficient to define the

surface at any later time t and to determine the entire burning history of the surface.

2) The grain will be neutral if $\frac{dA_b}{dy} = 0$, i.e., as a first approximation, if the average curvature of the surface is zero ($C_m = 0$).

3) In the particular case of a cylindrical surface the burning surface area is equal to the product of the port perimeter P and the length L of the grain:

$$A_b = LP$$

In this case the radius of curvature R_2^0 is infinite whence $d^2A_b^0/dy^2 = 0$ and $R_1^0 = R^0$ so that:

$$\frac{dA_b^0}{dy} = L \frac{dP^0}{dy} = -L \int_A^B \frac{dP^0}{R^0} = -L \int_{\varphi_A}^{\varphi_B} d\varphi$$

where φ is the angle between the tangent to the cross-sectional contour and a reference direction ($dP^0 = R^0 d\varphi$). The burning surface area A_b at instant t is then simply:

$$A_b = A_b^0 - Ly(\varphi_B - \varphi_A) \quad (\text{Eq. 4-68})$$

If a closed contour contains the propellant (Fig. 4-12, case 1), then we have:

$$\varphi_B = \varphi_A + 2\pi$$

and

$$A_b = A_b^0 - Ly2\pi \quad (\text{Eq. 4-69})$$

and the grain is then regressive regardless of the profile that is chosen. If the contour is closed with the propellant on the outside (Fig. 4-12, case 2), then

$$\varphi_A = \varphi_E + 2\pi$$

and

$$A_b = A_b^0 + Ly2\pi \quad (\text{Eq. 4-70})$$

and the grain is progressive. Neutrality of a single cylindrical grain can therefore be achieved, only if there are singularities on its surface.

Consider first a grain with a recess-type singularity (Fig. 4-13); let (Γ) be the locus of this singularity and let E be a point on the curve, (Γ) . The vector (\overrightarrow{ET}) is the tangent to this curve at point E and (Π) is a plane perpendicular to this tangent at point E. The intersection of the propellant surface with the plane (Π) is formed by curve segments DE and EF, their tangents at E being $(\overrightarrow{ET_D})$ and $(\overrightarrow{ET_F})$. In the plane (Π) we draw the normals $(\overrightarrow{EN_F})$ to $(\overrightarrow{ET_F})$ and $(\overrightarrow{EN_D})$ to $(\overrightarrow{ET_D})$ at E and also the vector (\overrightarrow{EN}) containing the radius of curvature R of (Γ) . Let θ' and θ'' be the angles that the vector (\overrightarrow{EN}) makes with $(\overrightarrow{EN_D})$ and with $(\overrightarrow{EN_F})$ and let ds be an element of arc of the curve (Γ) . The propellant surface A at time t is defined by the contour (G B I C H) and the initial surface A_b^0 is given by D E F. During the time interval t, the area increases by the arc B I C, whence (30):

$$A_b = A_b^0 + y \int_{(\Gamma)} (\theta'' - \theta') ds + y^2 \int_{(\Gamma)} \frac{\sin \theta'' - \sin \theta'}{R} ds \quad (\text{Eq. 4-71})$$

Only the first derivative of this expression is of interest for the neutrality condition. We find:

$$\frac{dA_b^0}{dy} = -2C_m + \int_{(\Gamma)} (\theta'' - \theta') ds = -2[C_m - \int_{(\Gamma)} \theta] ds \quad (\text{Eq. 4-72})$$

where

$$\theta'' - \theta' \equiv 2\theta$$

The case of a spike-type singularity is shown in Fig. 4-14, where the notation is the same as in Fig. 4-13. For the sake of clarity, we show only the plane (Π) . At time t, point E becomes point I and contour D E F becomes G I H. The angle between the two normals is 2θ and the angle between the tangents is $2\alpha = \pi - 2\theta$. The burning surface area decreases by an amount corresponding to the arcs B E and E C, so that:

$$A_b = A_b^0 - \int_{(\Gamma)} (B E + E C) ds \quad (\text{Eq. 4-73})$$

A first order approximation for the integral is:

$$\int_{(\Gamma)} 2y \operatorname{tg} \theta ds \quad (\text{Eq. 4-74})$$

The first derivative is thus:

$$\frac{dA_b}{dy} = -2[C_m + \int_{(\Gamma)} \operatorname{tg} \theta ds] \quad (\text{Eq. 4-75})$$



STAR



WAGON-WHEEL



FORKED WAGON-WHEEL

Fig. 4-15 Grain configurations.

For a cylindrical grain with a cross section containing n singular recesses and spikes, with an angle θ between the normals, the first derivative of A_b is:

$$\frac{dA_b}{dy} = -L [\varphi_B - \varphi_A + 2n (\operatorname{tg} \theta - \theta)] \quad (\text{Eq. 4-76})$$

Equation 4-76 is applicable to various star-shaped grains, for example. In most applications, internally burning grains are employed, so that:

$$\varphi_B - \varphi_A = 2\pi$$

and Equation 4-76 becomes:

$$\frac{dA_b}{dy} = -2L [-\pi + n (\operatorname{tg} \theta - \theta)] \quad (\text{Eq. 4-77})$$

The neutrality condition ($\frac{dA_b}{dy} = 0$) then becomes:

$$\operatorname{tg} \theta - \theta = \frac{\pi}{n}.$$

If the spikes are characterized by the angle α between the propellant surface tangents, such that $\theta = \frac{\pi}{2} - \alpha$, then this result becomes:

$$\cotg \alpha + \alpha = \frac{\pi}{2} + \frac{\pi}{n} \quad (\text{Eq. 4-78})$$

The following table gives the values of α for integral values of n between 1 and 10.

Table of α

n	α (°)
1	12° 32'.80
2	19° 39'.86
3	24° 32'.79
4	28° 12'.96
5	31° 07'.71
6	33° 31'.70
7	35° 33'.40
8	37° 18'.40
9	38° 50'.38
10	40° 12'.00

We have assumed here that the singularities exist on the initial surface A_b^0 ; they can also appear in the course of the combustion, provided that the grain has an appropriate geometry. The basic aspects of the preceding method are sufficiently general to be applicable to any surface.

In practical applications the grains are generally cylindrical and often have a star-shaped cross section; we shall study this type of grain in greater detail.

b) Star and Wagon-Wheel Cross Section Grains - Typical star and wagon-wheel configurations are shown in Fig. 4-15. For these geometries, it is possible to compute the time evolution of the pressure. Let us first study the classical star

shaped configuration illustrated in Fig. 4-16. For the sake of simplicity, we shall discuss only cases for which $R_1 = 0$, $R_2 = f$ and $\alpha_2 \pi/n = \pi/n$, in the notation of Fig. 4-16.

During the first phase of combustion, when $\frac{y+f}{\ell} < \frac{\sin(\pi/n)}{\cos \alpha}$, the burning surface area per unit grain length, A_b/L , is:

$$\frac{A_b(t)}{L} = 2n \left[\ell \frac{\sin(\pi/n)}{\sin \alpha} + (y + \ell) \left(\frac{\pi}{n} + \frac{\pi}{2} - \alpha - \cotg \alpha \right) \right], \quad (\text{Eq. 4-79})$$

where y is the burned web thickness, perpendicular to the surface, and n the number of star points.

The neutrality condition is very simply expressed by requiring that $A_b(t)$ in Equation 4-79 be independent of y , viz.,

$$\frac{\pi}{n} + \frac{\pi}{2} - \alpha - \cotg \alpha = 0$$

which has previously been shown to be of more general validity.

During the second phase of combustion, when $\frac{y+f}{\ell} \geq \frac{\sin(\pi/n)}{\cos \alpha}$ the burning surface area becomes:

$$\frac{A_b}{L} = 2n \left\{ (y + \ell) \left[\frac{\pi}{n} + \sin^{-1} \left(\frac{\ell}{y+f} \sin \frac{\pi}{n} \right) \right] \right\}. \quad (\text{Eq. 4-80})$$

The grain is then progressive and A_b increases linearly with $y = r t$.

When the flame front reaches the case ($y = w$), the grain becomes regressive, producing thrust decay.

The initial port cross-sectional area is:

$$A_p = 2n\ell \left\{ \frac{\ell}{2} \sin \frac{\pi}{n} \left(\cos \frac{\pi}{n} - \sin \frac{\pi}{n} \cotg \alpha \right) + f\ell \frac{\sin(\pi/n)}{\sin \alpha} + f^2 \left(\frac{\pi}{2} + \frac{\pi}{n} - \alpha - \cot \alpha \right) \right\}. \quad (\text{Eq. 4-81})$$

With more complex shapes, such as the one in Fig. 4-17, similar but more complex relations are obtained. In Fig. 4-17, the number of geometrical parameters is nineteen. By appropriately choosing these parameters it is possible to achieve almost any desired time evolution of the burning surface area and, consequently, of the pressure. In order to determine the importance of each parameter and its influence on the burning surface area, it is desirable to know the partial derivatives $\frac{\partial A_b}{\partial \alpha_j}$ with respect to each parameter α_j (10). For small changes in the parameters α_j :

$$\Delta A_b = \sum_{j=1}^{j=n} \frac{\partial A_b}{\partial \alpha_j} \Delta \alpha_j \quad (\text{Eq. 4-82})$$

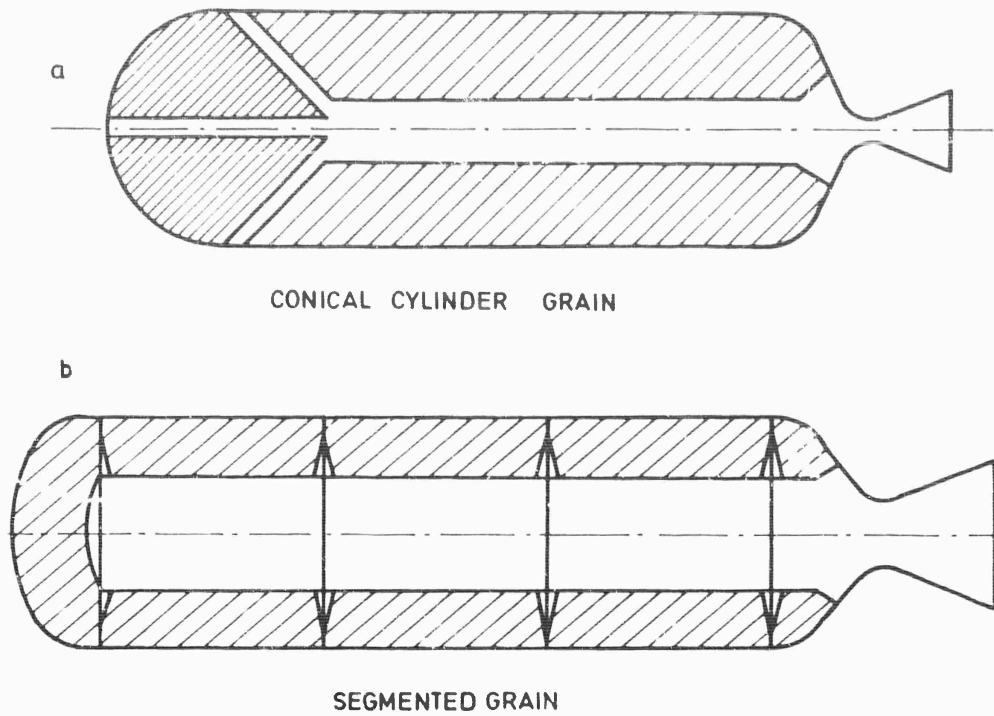


Fig. 4-18 Multibloc configuration.

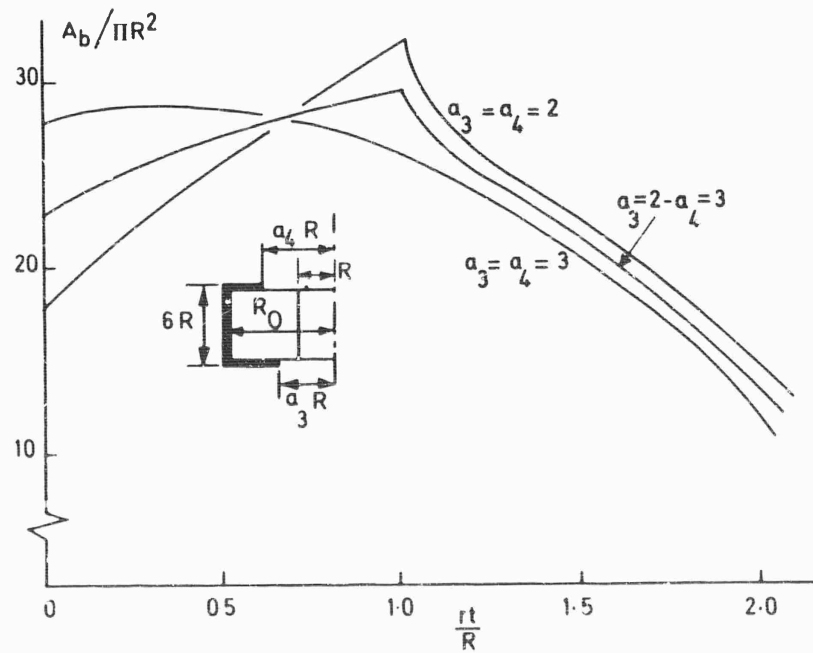


Fig. 4-19 Burning surface time evolution in a segmented grain.

In spite of the multiplicity of the parameters, it is possible to analyse the grain configuration shown in Fig. 4-17 in a short time, by using electronic computers.

It is also of importance to calculate the evolution of the geometry of the propellant in the fore and aft closures of the motor.

For different grain designs that produce a specified chamber pressure history, two additional parameters affect the designer's choice of grain configuration. One is the loading fraction ϵ_I which is defined as the ratio of the propellant volume to the motor volume (nozzle excluded),

$$\epsilon_I = \frac{\text{Propellant volume}}{\text{Motor volume}} \quad (\text{Eq. 4-83})$$

The other is the thrust decay loss, or 'sliver' loss parameter ϵ_{II} , which is defined as the ratio of the propellant volume that remains when $y = w$, to the total initial propellant volume.

$$\epsilon_{II} = \frac{\gamma_w}{\gamma_p} = \frac{\text{Sliver volume}}{\text{Propellant volume}} \quad (\text{Eq. 4-84})$$

Grain configurations are chosen so that ϵ_I is as close to unity as possible and ϵ_{II} is as close to zero as possible; the loading fraction should thus be maximal and the thrust decay losses minimal.

c) Segmented Grains (11)- Grains are sometimes built in segments, either for stress relief, or as the best means of achieving the required thrust time curve. They are constructed by combining cones and cylinders, as shown in Fig. 4-18a, or circular cylindrical grains (Fig. 4-18b). It is necessary to have adequate thermal protection at the junctions between grains. The time evolution of the burning surface area is determined very simply in the case of a circular port (stage 0 grains for the Titan III-C).

Let us take as an example, a tubular grain of initial radius R and of external (wall) radius $a_1 R$; the grain length is $a_2 R$ and the fore and aft end faces of the grain are coated with a restrictor from the wall to radius $a_3 R$ and $a_4 R$, respectively (see Fig. 4-19). During the earliest stage of combustion, the burning surface area A_b at time t is:

$$\frac{A_b(t)}{\pi R^2} = \frac{A_b(0)}{\pi R^2} + \frac{2}{R} \left[a_2 - 4 + \frac{\pi}{2} (a_3 + a_4) \right] rt - \frac{2}{R^2} (rt)^2 \quad (\text{Eq. 4-85})$$

By appropriate choices of a_1 , a_2 , a_3 and a_4 it is possible to approximate neutrality; the area A_b is a parabolic function of time.

Figure 4-19 shows how the fraction of the lateral areas covered with restrictor affects the burning area history. During the earliest stage of combustion, the grain is progressive if $a_3 = a_4 = 2$ and becomes regressive at larger values of a_3 and a_4 . Solutions close to neutrality are obtained for $a_4 = 3$ and $2 < a_3 < 3$. It should be emphasized that the approach discussed here is useful principally for large motors.

Ignition and erosion effects in segmented grains can present problems when there are sudden variations in the cross-sectional area of the central port along the grain.

d) Slotted Grains - Ordinary slotted grain configuration are tubular with slots of the type illustrated in Fig. 4-20 located at its ends. The number of slots and their lengths vary with the design. Slots facilitate manufacturing and improve mechanical properties of the grain. They enable the designer to select small port diameters and thereby to achieve better loading fractions. Their major drawback arises from the need to protect the motor case from the hot gases in the slots; this may degrade the structural index somewhat. Slot configurations have several burning regimes, depending on the values of the web thickness w and of the other parameters that are indicated on Fig. 4-20. At a critical web thickness $y = y^*$, the internal circle disappears and the burning surfaces become parallel to the faces G B and B F in Fig. 4-20. The value of y^* can be calculated by setting $\overline{BA} = \overline{BE}$. We shall let z denote the length BF parallel to the slot and m the length CD perpendicular to BF. The grain shape changes when y becomes equal to y^* , m or the axial slot length ℓ . The possible combinations are:

- | | | | |
|----|--------------|---------------|---------------|
| a) | $y < y^*$ | $y \leq \ell$ | |
| b) | $y < y^*$ | $y \leq m$ | $y > \ell$ |
| c) | $y \geq y^*$ | $y \leq m$ | $y \leq \ell$ |
| d) | $y \geq y^*$ | $y \leq m$ | $y > \ell$ |
| e) | $y > y^*$ | $y > m$ | |

We note that $y^* = (d \sin \alpha - 2e) / 2 (1 - \sin \alpha)$ and that $m = \frac{D}{2} \sin \alpha - e$.

The intersection of the central cylinder with the cylinder of diameter $2e$ at the bottom of the slot, leads to elliptic integrals of the form:

$$B(k^2) = \int_0^{\pi/2} \frac{\cos^2 \varphi \, d\varphi}{\sqrt{1 - k^2 \sin^2 \varphi}}$$

in formulas for the burning area. In particular, in case a) the burning surface area A_b ($y = rt$) at time t is given by:

$$\begin{aligned} A_b(t) = & \pi u (L - y) + \frac{\pi}{4} (D^2 - u^2) - 2\pi v^2 B(k^2) \\ & + \frac{n}{4} u (d + 6y - 4\ell) \arcsin \frac{2v}{u} + n (\ell + 1.0708e + 0.0708y)z \\ & - \frac{nD^2}{4} \arcsin 2 \frac{(e + w)}{D} \end{aligned} \quad (\text{Eq. 4-86})$$

where n is the number of slots and where

$$u = d + 2y$$

$$v = e + y$$

$$z = \sqrt{D^2 - 4v^2} - \sqrt{u^2 - 4v^2}$$

$$k = \frac{2v}{u} < 1$$

Experiments reported by Stone (12) have shown that this configuration can be made to approximate neutrality well.

e) Grains with Nonuniform Axial Profiles and Composite Configuration - In certain applications, such as when a very high initial acceleration of the rocket is required, or when it is desirable to assure uniform gas flow in the central port, axially dependent grain profiles can be used. For example, a star shape may be designed to undergo a progressive deformation from the upstream end of the grain to the downstream end. Sometimes the cross-sectional area is made to increase in the flow direction, in order to maintain an approximately constant gas velocity

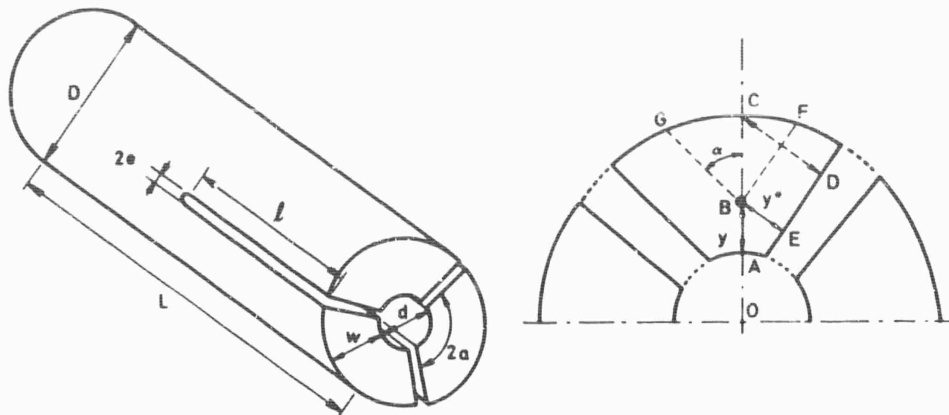


Fig. 4-20 Slotted grain.

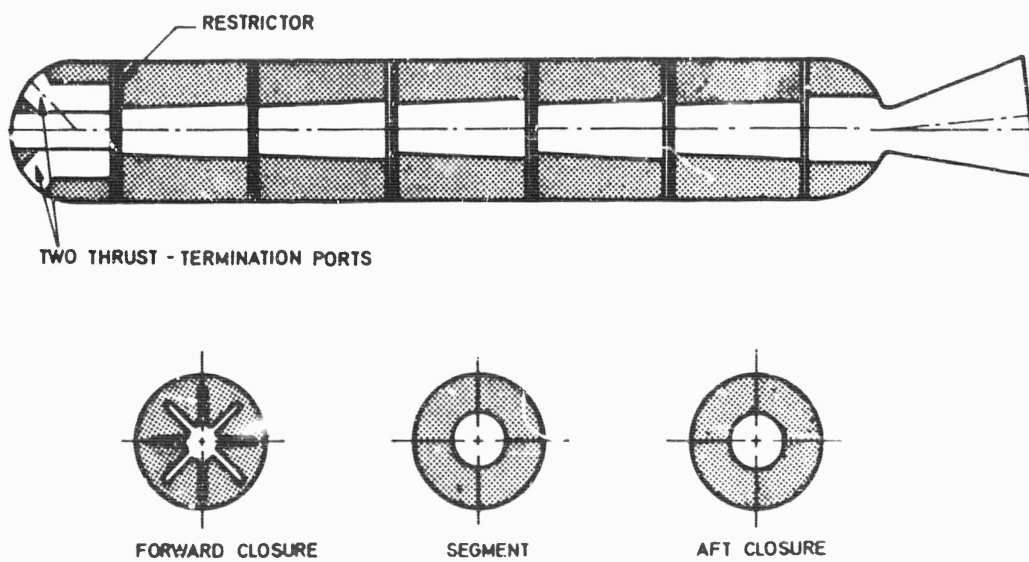


Fig. 4-21 120-inch motor grain design (11).

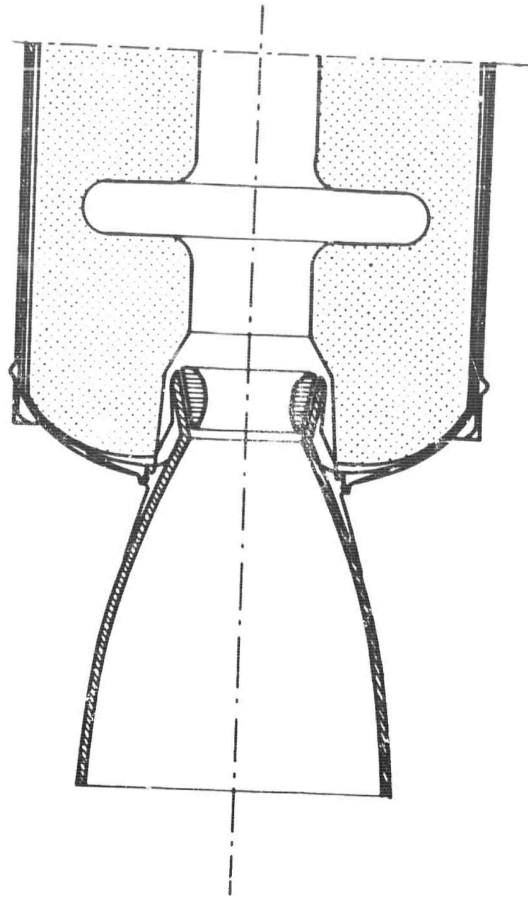


Fig. 4-22 Slotted tube rocket motor

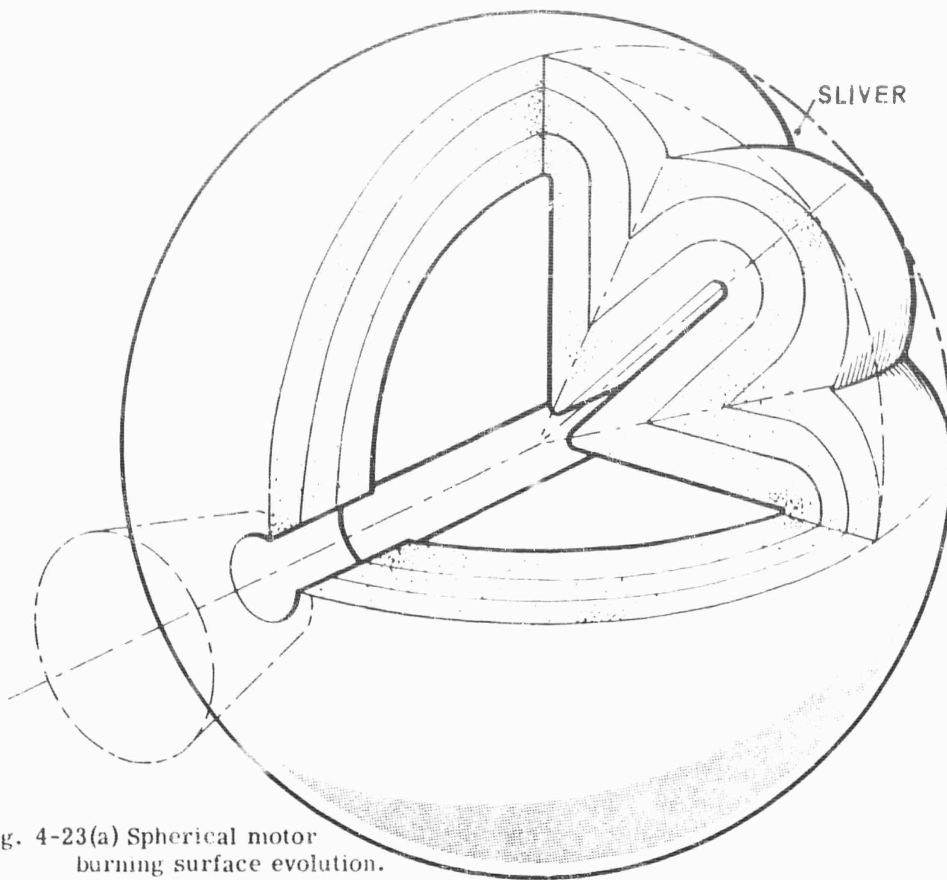


Fig. 4-23(a) Spherical motor
burning surface evolution.

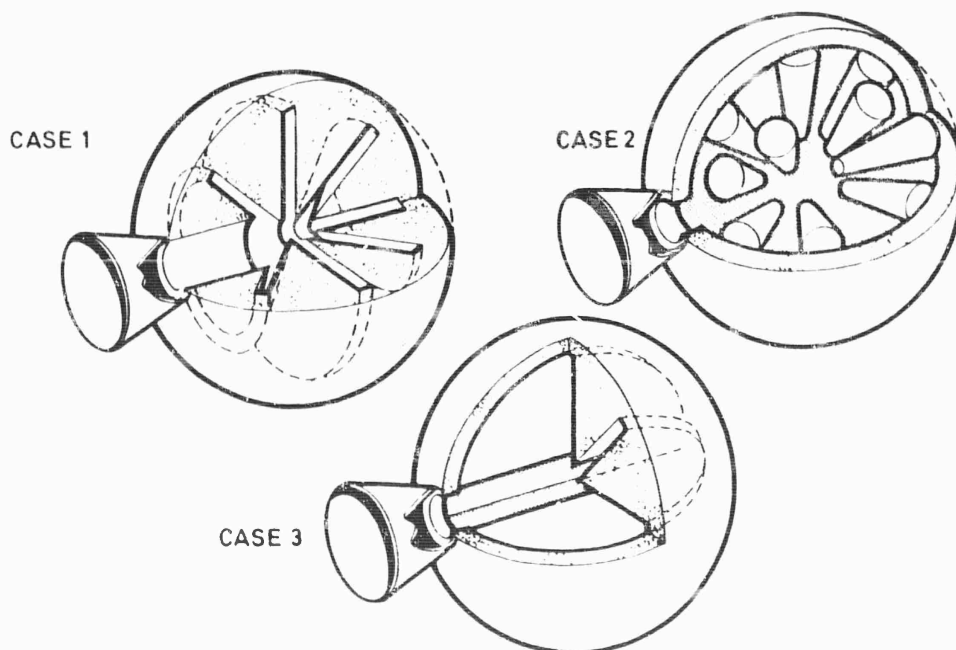


Fig. 4-23(b) Three spherical internal configurations considered
in analysis (14).

along the central channel.

For convenience, designers sometimes use greatly different cross-sectional geometries on the same grain. Figure 4-21 shows an example of a star-shaped section followed by a circular section in a segmented motor.

f) Helical Grains - It is possible to design grains with axial (cross section) profiles such as that shown in Fig. 4-22. These profiles can be constructed by assembling circular plates with different sized central holes. Another design consists in manufacturing a grain with a helical groove along the central channel. The shape of such a grain resembles that of a mechanical nut. This geometry causes the gaseous mass flowing in the central port to rotate.

3.4 Spherical Grains

Optimizing a thruster for orbit injection of a satellite, for slowing down a spacecraft, for changing orbits, or generally, for any mission requiring a large velocity increase in an environment where gravity forces are small and atmospheric drag is negligible, leads to thrusters with small slenderness ratio. The motor shape is then nearly spherical, since the cylindrical part of the grain is short. Spherical design also leads to small structural indices and is of interest for the application mentioned above. We should emphasize that the optimization process must take into account the fact that attachment systems can sometimes be heavier for a spherical motor than for a cylindrical one. The attachment problem, is, however, less crucial in some applications, such as an apogee motor or a retro-rocket.

Within the framework of the spherical motor concept, many types of new grain configurations have been proposed. Just as in the case of cylindrical motors, design criteria include requirements for constant burning surface area for high volumetric loading and for low sliver losses. In the version studied by NASA (14) for instance, the following conditions were imposed:

loading density		95%
neutrality	±	10%
sliver loss		7%

Figures 4-23 a and b show several possible spherical grain configurations. In one popular design, termed 'melon slices', the internal surface is generated by rotating a star-shaped section around an axis contained in the plane of the star. Manufacturing spherical grains presents some problems. One can use a mandrel similar to the type employed in casting cylindrical grains, but consisting of a hemispherical cap which produces only half a sphere, prolonged by a short star-shaped cylinder which extends the star branches up to the 'melon slices' and facilitates the removal of the mandrel after casting (Fig. 4-24). Alternatively, one can use a metal mandrel which has a melting point below the ignition temperature of the solid propellant and above the casting temperature of the propellant. This limited temperature range severely restricts the choice of mandrel material; Thibodaux (14) used a mandrel made of 'Cerrobend', an alloy of lead, tin, bismuth and cadmium, which melts at 158° F. After the mandrel is melted, a thin layer of alloy remains on the propellant surface and can be dissolved by mercury. Grain bonding techniques can also be used in spherical grain construction, provided that either two hemispheres of a metal motor case can be united or the case be made by filament winding around the bonded grain.

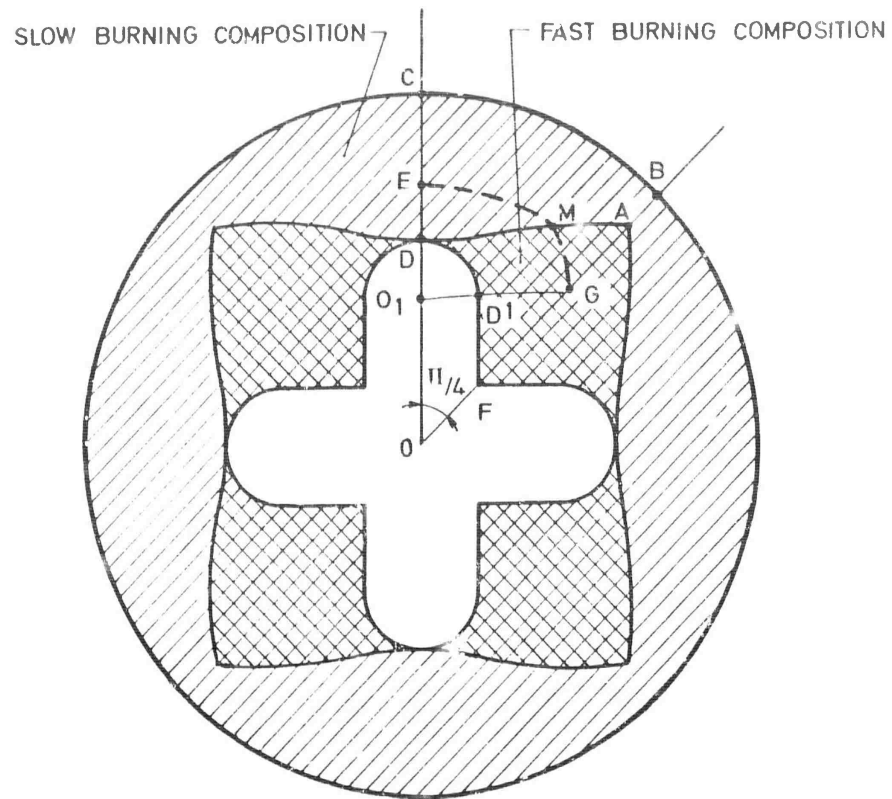


Fig. 4-26 Configuration with dual burning rate propellant.

Exact computation of the burning surface area is lengthy and use is almost always made of approximate methods, such as the one developed by Thibodaux (14) or Segal (15). We shall not present these methods, which resemble those described in connection with cylindrical grains. The dependence of burning area on burned web thickness for one such geometry is given in Fig. 4-25. Neutrality is achieved only within $\pm 10\%$ in this example. The losses due to pressure tail-off are also rather large.

At the present time, there are many space missions for which spherical motors of this type are used.

3.5 Dual-Composition Solid Propellant

We have seen that a number of inconveniences arise from the use of solid propellants with only one burning rate; neutrality is difficult to achieve (spherical rocket motors), thrust decay losses are appreciable, the geometry is sometimes complex. Improvements in grain design can be obtained by using propellants with two different burning rates in the same grain. The ratio k of these burning rates constitutes an additional parameter, which introduces more flexibility into the choice of a grain configuration that is best adapted to neutrality or to any other specified characteristic. It is usually possible to design grains of dual composition that eliminate thrust tail-off.

Let us consider a cylindrical grain with star-shaped port. Symmetry implies that the entire grain can be reconstructed from a sector such as COB (Fig. 4-26). Let r be the burning rate of the slow-burning composition and kr that of the fast-burning composition ($k > 1$); at time t the burning surface in sector COB is represented by the contour GME, such that $\overline{DE} = rt$ and $\overline{HL} = krt$, where DE and HL are normals to the burning surface in each composition, as illustrated in Fig. 4-27. Two families of parallel surfaces are thus defined; they intersect along the boundary DMA.

The problems to be solved are (a) to find a boundary curve DMA that eliminates sliver losses and (b) to choose the various design parameters in order to obtain progressive, regressive or neutral burning.

In order to obtain a grain without sliver losses, the trace of the burning surface in the slow-burning composition must always be on a circle centered at O and of radius $R + rt$. In the fast-burning composition, due to the initial ENF profile, the trace of the burning surface at time t is composed of the circular arc ML centered at O_1 and of radius $a + krt$, plus the rectilinear segment LG parallel to HF. From the shape of the initial star, two types of grains can be distinguished, depending on whether the straight line OH intersects segment OA or the outer boundary. In the first case there are always two combustion periods and transition, from the first to the second, occurs when the burning surface coincides with the line $E^*M^*G^*$, where point G^* is located at the intersection of OH and OA. In the first period the burning perimeter is formed by two circular arcs, EM and ML, and the straight line LG; in the second period the straight line has disappeared. The dimension w_1 is the web thickness of the slow-burning composition burned during the first period and w_2 the slow-burning web thickness in the second period, Fig. 4-27.

In both cases the parameters at the designer's disposal are the length of segment $OD = R$, the length of segment $O_1D = a$, the angle θ between HF and OA (which need not have the value π/n shown in Fig. 4-26), the number n of star points and the ratio k of the burning velocities.

The boundary DMA can easily be constructed geometrically by drawing two families of circles, one centered at O and of radius $R + rt$, the other centered at O_1 and of radius $a + krt$. The points of intersection M of these two families represent the boundary curve. In the optical analogy, OM and O_1M are rays of two cylindrical light waves, one generated at O and propagating in the first medium with a velocity r and the other generated at O_1 and propagating in the second medium with a velocity kr . The slow-burning composition can be thought of as an isotropic medium of index k and the fast-burning composition an isotropic medium of index unity (Fig. 4-28)

The equation of the boundary curve in polar coordinates (Fig. 4-29a) can be written as:

$$\begin{aligned} \rho &= R + e \\ \cos \lambda &= \frac{(R + e)^2 + (R - a)^2 - (a + ke)^2}{2(R - a)(R + e)} \end{aligned} \quad (\text{Eq. 4-87})$$

with $e = rt$.

The mass flow of combustion products is then:

$$\dot{m}_b = \rho_p r A_b + \rho_p kr A'_b = \rho_p r (A_b + kA'_b) = \rho_p r \mathcal{A}'_b \quad (\text{Eq. 4-88})$$

where A_b and A'_b are the burning surface areas in the slow-burning and in the fast-burning compositions respectively. The densities of the two compositions have been assumed to be equal ($\rho_p = \rho'_p$), which is an excellent approximation in most applications since the increase in burning velocity is obtained by adding small amounts of catalysts to the propellant.

In the first combustion period the values of A_{b1} and A'_{b1} for a cylindrical grain of length L are given by the equation:

$$\begin{aligned} A_{b1} &= (R + e_1) \lambda_1 \quad 2nL \\ A'_{b1} &= \left\{ (a + ke_1) \beta_1 + [(R - a) \operatorname{tg} \frac{\pi}{n} - (a + ke_1)] \cot \frac{\pi}{n} \right\} 2nL \end{aligned} \quad (\text{Eq. 4-89})$$

where:

$$\cos \beta_1 = \frac{(R + e_1) \sin \lambda}{a + ke_1}.$$

The quantities λ_1 and β_1 are defined in Fig. 4-29b.

In the second combustion period:

$$\begin{aligned} A_{b2} &= (R + c_2) \lambda_2 \quad 2nL \\ A'_{b2} &= (a + ke_2) (\beta_2 - \delta_2) 2nL, \end{aligned} \quad (\text{Eq. 4-90})$$

where:

$$\delta_2 = \frac{\pi}{2} - \left(\frac{\pi}{n} + \gamma \right)$$

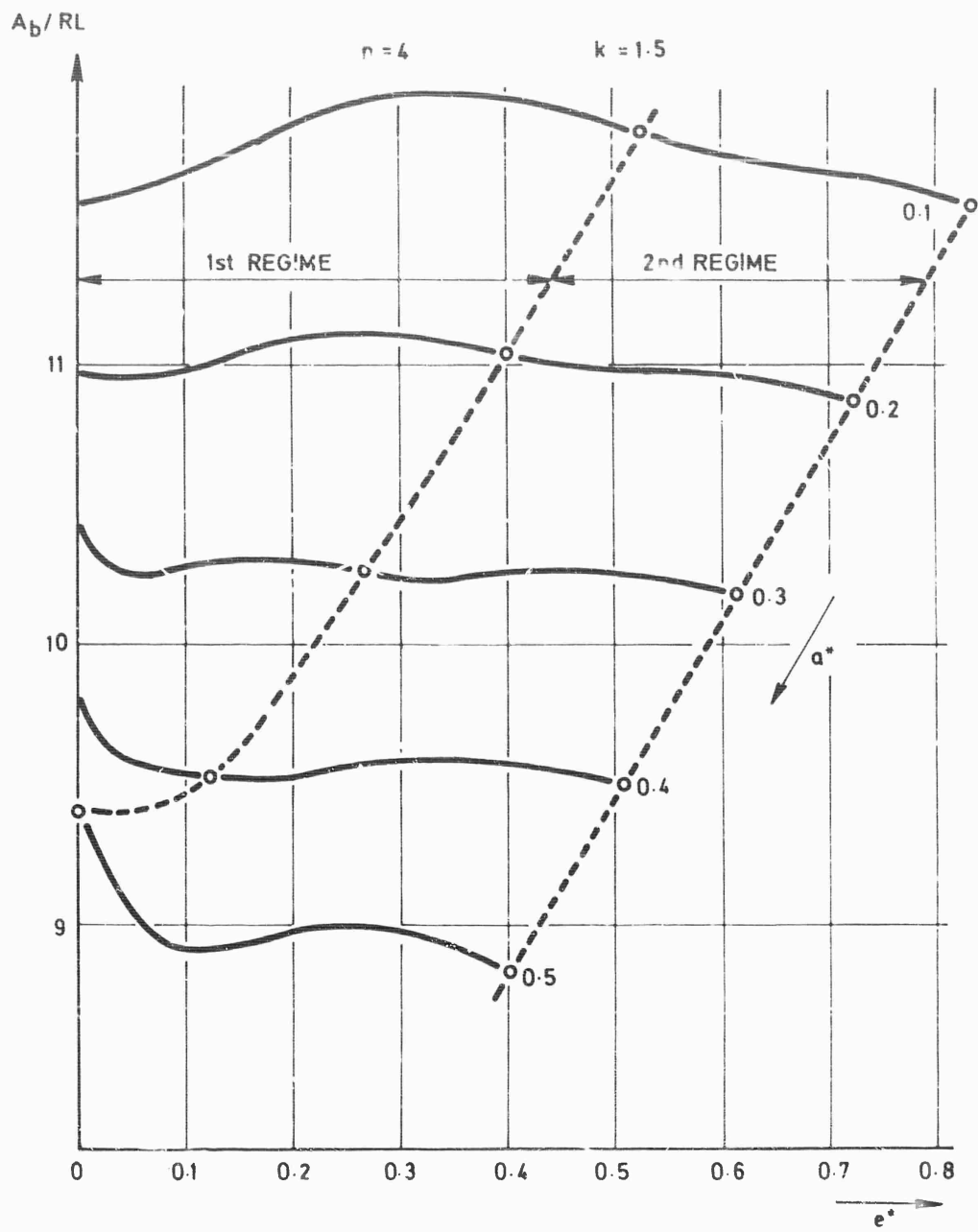


Fig. 4-30 Burning area vs. web thickness.

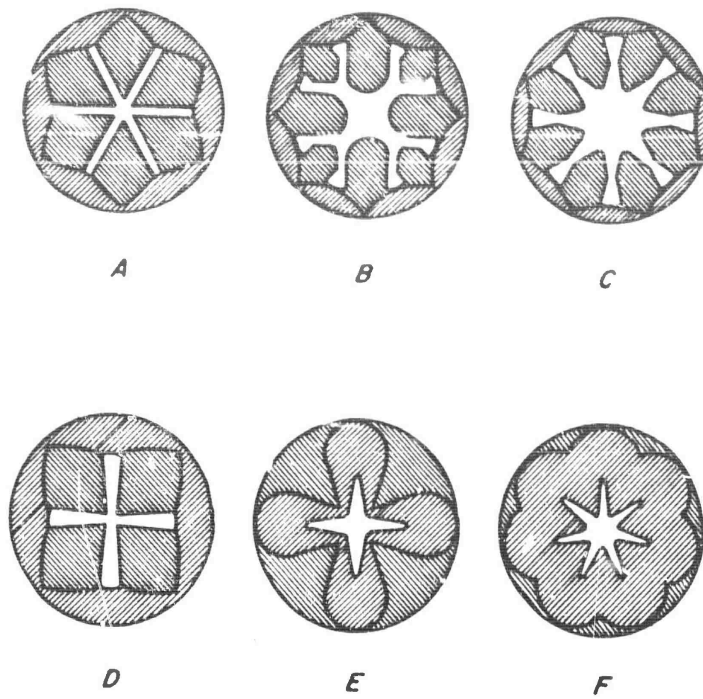


Fig. 4-31 Solid propellant charges (19).

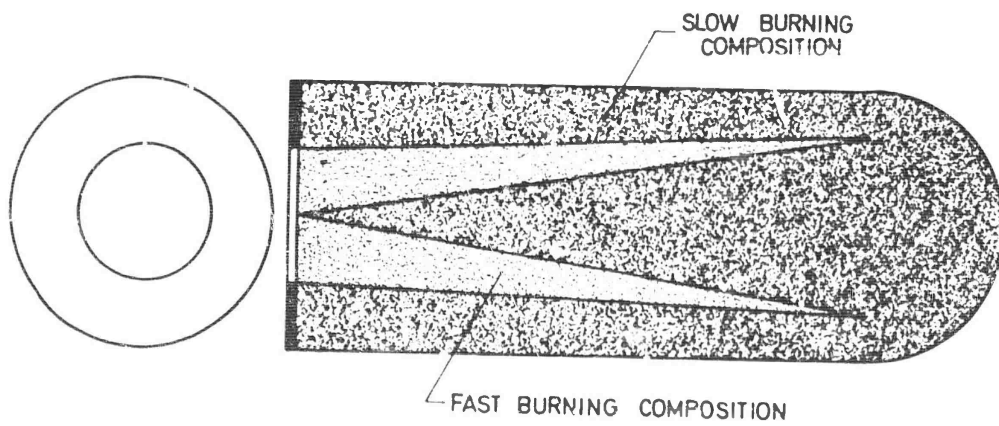


Fig. 4-32 Multiple propellant grain (20)

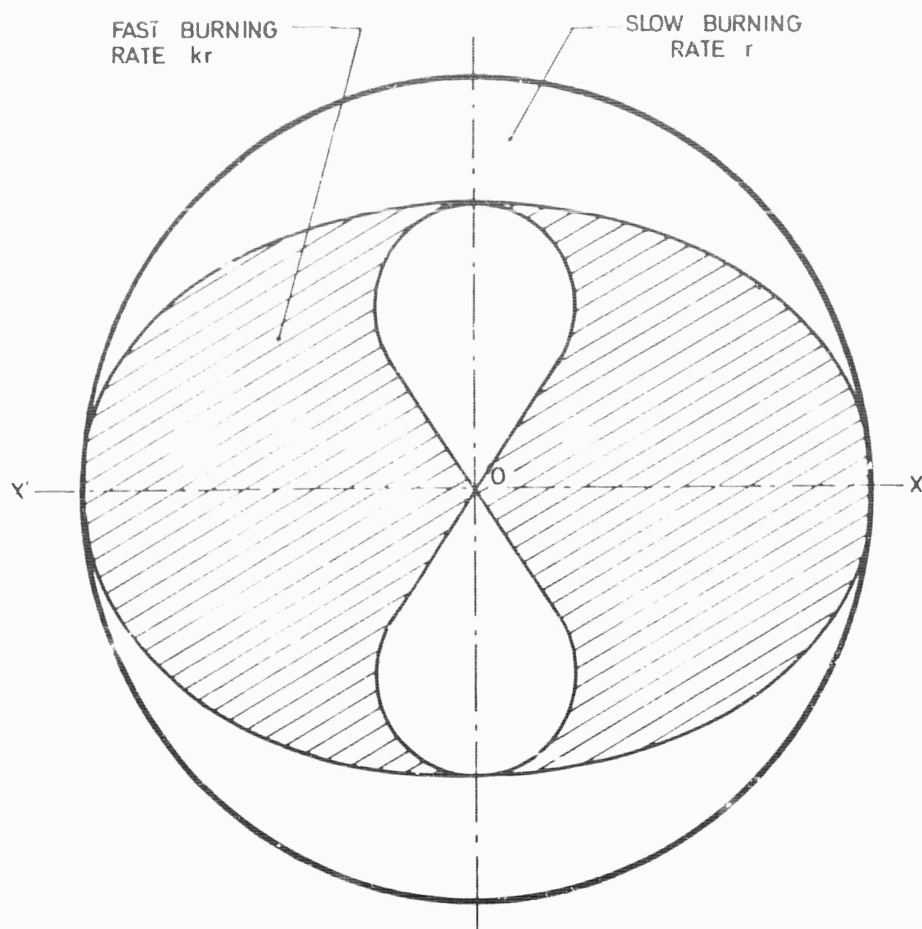


Fig. 4-33 Spherical rocket motor with dual composition solid propellant.

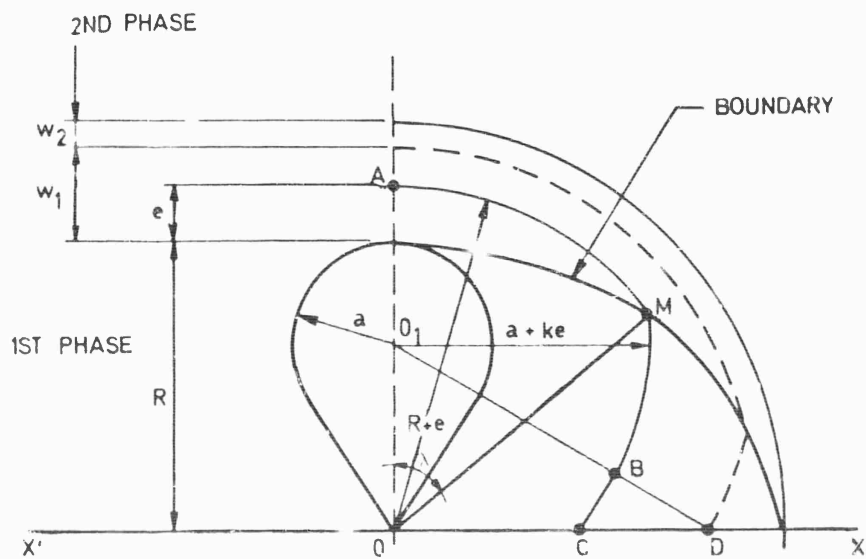


Fig. 4-34 Geometry definition.

and:

$$\sin \gamma = \frac{R - a}{a + ke_2} \sin \frac{\pi}{n}.$$

The angles λ_2 , δ_2 , β_2 and γ are defined in Fig. 4-29c.

The burning time is given by:

$$t_b = \frac{w}{r}, \quad (\text{Eq. 4-91})$$

and the burned web thicknesses are:

$$\begin{cases} w_1 = [(R - a) \operatorname{tg} \frac{\pi}{n} - R] \frac{1}{k} \\ w_2 = w - w_1 \end{cases} \quad (\text{Eq. 4-92})$$

With this configuration it is of interest to investigate conditions which achieve the best neutrality or the best loading fraction. Theoretically, there are not sliver losses because the burning surface reaches the motor casing at the same instant at each point.

Let us first study the neutrality condition. In dimensionless notation, for a given value of n the burning area depends on the parameters $a^* = a/R$, k and $e^* = e/R$. The quantity A_b/RL is shown as a function of e^* for several values of $a^* = a/R$ in Fig. 4-30 for the case $n = 4$, $k = 1.5$. It is seen that rather good neutrality is achieved. Generally speaking, the degree of neutrality depends strongly upon the values of n and k and for optimal neutrality (in our case $n = 4$, $k = 1.48$) the grain is neutral within $\pm 1\%$. For other values however, e.g. for $n = 6$ and $k = 1.21$, neutrality will be achieved only to within $\pm 10\%$. The loading fraction generally decreases when a^* increases.

Figure 4-31 shows a few dual composition grain geometries given by Schluter (19). It is possible, for example, to design an ordinary neutral star, in which the combustion of the slow-burning composition begins only when neutrality, due to the star shape, disappears. The grain can thereby be kept neutral over the entire burning time and sliver losses can be eliminated. Dual composition or multi-composition design concepts can be applied to noncylindrical grains as illustrated in Fig. 4-32. The fast-burning composition is located at the center, so that a rapid increase in port cross section takes place initially, thereby allowing the combustion gases to flow through the motor, Braun (20) has designed several grains of this type.

Dual composition spherical motors can also be designed. The added flexibility has been used to improve neutrality and to decrease sliver losses.

Let us consider a grain with the cross section illustrated in Fig. 4-33. The grain is generated by rotation around axis XX' . The internal profile which generates the central toroidal cavity, is composed of an arc of circle and two straight lines which converge at the center. The outer propellant is a slow-burning composition of regression rate r and the inner propellant is a fast-burning composition of regression rate kr . To a burned web thickness e in the slow-burning composition corresponds a thickness ke in the fast-burning composition. The common point M on the boundary curve is defined (Fig. 4-34) by the intersection of a circle of radius $R + e$ centered at O , with a circle of radius $a + ke$ centered at O_1 . The boundary curve can be constructed by the same technique that was described for a cylindrical grain. Two periods of combustion occur. In the first, the burning

surface is composed of the arc AM centered at O in the slow-burning composition, the arc MB centered at O_1 in the fast-burning composition and the straight line \overline{BC} . In the second period the straight line has disappeared.

The effective burning surface area A_b is given by:

$$\frac{A_b}{R^2} = \frac{A_{b1}}{R^2} + k \frac{A_{b2}}{R^2}, \quad (\text{Eq. 4-93})$$

where index 1 refers to the slow-burning composition and index 2 to the fast-burning composition.

The relevant areas can be calculated easily because they are portions of a sphere, a torus or a cone. It is to be noted, however, that bounds exist for certain parameters. For example, the value of k is limited by the requirement that the web thickness w_1 be smaller than w and the quantity w must satisfy a quadratic equation, which possesses a positive solution only for combinations of values of k and a/R which obey a particular inequality. At the limit of this inequality, $k_1 = \infty$ when $a = 0.35 R$, $k_1 = 2.802$ when $a = 0.3 R$ and $k_1 = 1.43$ when $a = 0.2 R$. The complete computation for this configuration shows that for acceptable neutrality the values of a/R and k can not deviate very much from the conditions $a = 0.35 R$ and $k = 2.85$. The curve representing A_b/R^2 as a function of e/R is shown in Fig. 4-35, the departure from neutrality being of the order of $\pm 3\%$. The dual-composition, spherical-motor concept has led to the design shown in Fig. 4-36.

3.6 Remarks on the Pressure-Time Curve Obtained During a Motor Firing

The results given in the preceding paragraphs can be summarized as follows. In studying the time evolution of the pressure and thrust one must consider equations for the regression of the propellant surface and equations for the dependence of the burning rate on the gas flow in the chamber. Equations of the first type relate the burning surface area at time $t + \Delta t$ to the burning surface area at time t . In the time interval Δt , the surface of the propellant at a given point M regresses normal to itself through a distance:

$$\Delta e(M) = \Delta t \cdot r(M)$$

where $r(M)$ is the burning rate at point M . The total area of the burning surface at time $t + \Delta t$, is then given by the formula:

$$A_b(t + \Delta t) = A_b(t) - 2 \Delta e \int_{A_b} C_m dA_b + (\Delta e)^2 \int_{A_b} C_t dA_b, \quad (\text{Eq. 4-94})$$

where C_m and C_t are the average and total curvatures of the surface. In practice, $A_b(t + \Delta t)$ is calculated by approximate methods which assume that the surface is generated by a combination of straight lines and circles or ellipses; the equation of a straight line is of the form:

$$y = m x + b + f(\Delta e), \quad (\text{Eq. 4-95})$$

where m and b are constants and where the only variable is $f(\Delta e)$ which is a function of the burned web thickness, while the equation for a circle is:

$$(x - p)^2 + (y - q)^2 = (R + \Delta e)^2, \quad (\text{Eq. 4-96})$$

where Δe can be positive or negative.

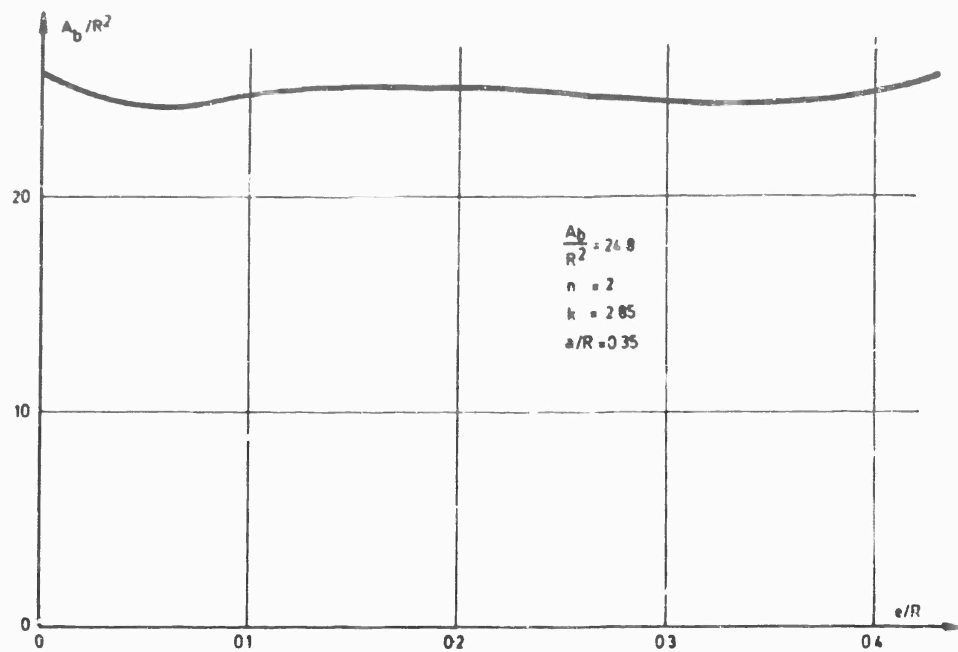
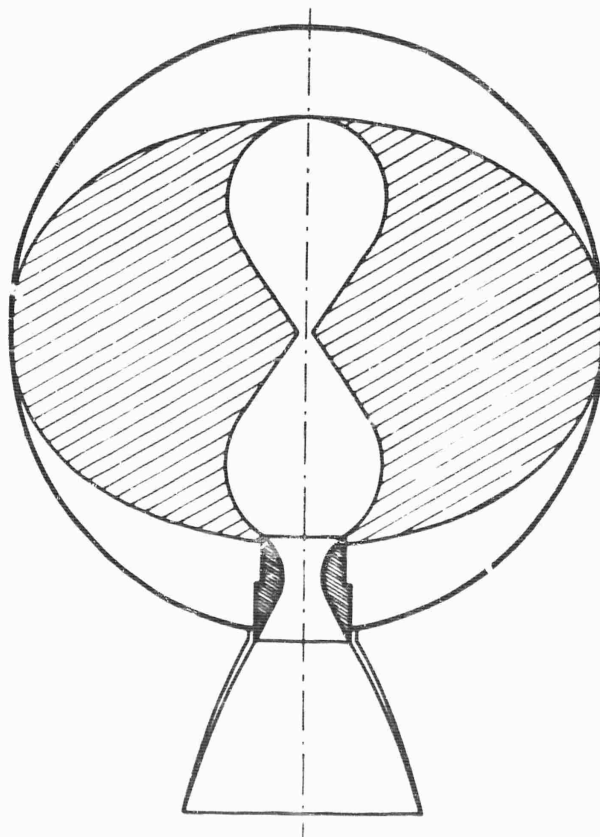
Fig. 4-35 Curve of A_b/R^2 vs. e/R 

Fig. 4-36 Spherical - motor design

Equations of the second type determine the burning rate at the point M as a function of the static pressure at point M, the density at point M and the gas velocity at point M:

$$r(M) = r[p(M), \rho(M), u(M)] \quad (\text{Eq. 4-97})$$

The values of p , ρ and u are determined by the mass, momentum and energy conservation equations for a flow field contained in boundaries which move with time. The mass conservation equation must take into account the mass injection from the burning propellant into the central cavity. This complex problem will be studied in Chapter 7. Since pressures need not be known to an accuracy better than 1%, motion of the boundaries can be neglected in calculating a quasisteady flow field in the central cavity and the flow conditions at point M can then be evaluated at any time t by a method analogous to that described in Section 3.2 but generalized, if necessary, by accounting for time variations of pressure through the use of the equation:

$$\frac{p_c A_t}{c^*} = \int_{A_b} (\rho_p - \rho) r dA_b - \int \frac{d\rho}{dt} d\gamma \quad (\text{Eq. 4-98})$$

in place of equation 4-35. It may also be necessary to use the equation for the time rate of increase of chamber volume:

$$\frac{d\gamma}{dt} = \int_{A_b} r dA_b \quad (\text{Eq. 4-99})$$

A step-by-step integration of the conservation equations determines the total and static pressures at each point on the surface of the grain. The accuracy of these calculations can be tested experimentally by measuring the pressure p_b at the upstream end of the grain and the pressure $p_{s1} \approx p_c$ at the downstream end (Fig. 4-8)

Under some environmental conditions, the grain temperature will not be uniform (25) and equation 4-97 must be replaced by the more general relationship:

$$r = r[p(M), \rho(M), u(M), T_1(M)] \quad (\text{Eq. 4-100})$$

the use of which entails a calculation of the temperature distribution in the grain at the time of firing.

At the present time, it seems to be possible to predict with a good accuracy the time evolution of the total pressures p_o and p_c . Comparisons between theory and experiment may be found in refs. (10), (22) and (23).

Methods for determining the time evolution of the chamber pressure can be coupled with motor performance determinations in computer programs. One can thus optimize the design of the motor for a given mission. Representative input values are the average pressure and the burning time or else a curve giving the desired thrust program as a function of time (the integral of which equals the total impulse). The motor diameter or, sometimes, the admissible motor length is also given. Optimizing a motor within these requirements necessitates the knowledge of additional information concerning the physical and ballistic properties of the propellant, the ambient environment and the type of geometry. The performances of various designs are computed in order to obtain optimal values for the rocket velocity at the end of combustion, the loading fraction, the operating pressure, the ratio of the total impulse to motor weight, the structural index, etc.

The determination of the time evolution of the thrust or of the pressure, the computation of the motor performance and the establishment of a preliminary design rely upon the knowledge of a certain number of ballistic parameters. The accuracy to which these parameters are known should be given in each case. Uncertainties in values of ballistic parameters sometimes justify making simplifying assumptions in theories. Observed departures from the predicted results can be attributed to unavoidable variations in local and overall compositions, since slightly different performance is achieved with each batch of propellant. To indicate typical reproducibility, statistical deviations in various ballistic parameters are listed in the following table, which is based on data obtained in 100 motor firings.

Variation of ballistic parameters (24)

Parameter	Maximum fluctuation from average	Standard deviation
Density	$\pm 0.331\%$	0.111×10^{-2}
Mass flow coefficient $C_w = \frac{g}{c^*}$	$\pm 5.23\%$	1.57×10^{-2}
Burning rate constant a	$\pm 5.7\%$	1.12×10^{-2}
Throat area A_t	$\pm 0.188\%$	1.83×10^{-4}

The poorest reproducibility occurs in the burning velocity and in the mass flow coefficient. Local variations in the burning rate are likely to exceed those indicated in the table (see Fig. 4-5).

4 Optimization of the Motor Geometry in Particular Cases

We have seen in Chapter 1 that motor optimization can be performed in a rational way, only if the mission is specified. One way to characterize a mission is to specify that a given velocity increment Δv be imparted to a payload of given mass m_u . Within the framework of a given mission, various optimization criteria can be considered, such as a maximum ratio of payload mass to total launch mass $u = m_u/m_0$ (engineer's criterion) or a maximum ratio of the payload mass to the overall cost of the operation $v = m_u/C$ (economist's criterion). The optimal systems differ according to the criterion chosen.

In such extremum calculations use must be made of equations expressing the motion of the rocket (the ballistic equations), the distribution of masses and the overall cost. The computation is a step-by-step procedure. For a given technology which determines the weight of the structural parts and for a given propellant with known performance (although supporting studies can be made with different propellants,) one can obtain a ballistic equation of the form:

$$F(V, \gamma, z, m(t), v_e, g, A, q_{air}, \dots) = 0 \quad (\text{Eq. 4-101})$$

which relates the velocity, the acceleration, the position and the mass of the rocket at time t , to the exhaust velocity of the gases, the acceleration of the gravity, the reference area, the dynamic pressure of the air, etc...

For flight in the absence of atmospheric drag at an angle α with respect to the horizontal direction ($\varphi \equiv \sin \alpha$), the velocity increase of the rocket is:

$$\Delta V = v_e \ln \frac{m_0}{m_v} - \varphi \bar{g} t_b \quad (\text{Eq. 4-102})$$

or

$$\Delta V = v_e \left[\ln R - \varphi \frac{\bar{g}}{g_0} \frac{1}{a_0} \frac{R-1}{R} \right] \quad (\text{Eq. 4-103})$$

where the mass ratio is $R \equiv m_0/m_v$, the velocity increase is ΔV , the exhaust velocity is v_e , the average acceleration due to gravity is \bar{g} , the gravitational acceleration at sea level is g_0 and the initial acceleration of the rocket is a_0 . We have:

$$a_0 = \frac{F}{g_0 m_0} = \frac{m_p}{m_0} \frac{v_e}{g_0 t_b} \quad (\text{Eq. 4-104})$$

where m_p is the propellant mass. Equation 4-104 is valid only for a constant rate of propellant consumption m_p/t_b .

In a similar way the initial mass of the rocket can be written under the following simplified form:

$$m_0 = m_u + m_p + k_v \frac{m_p}{\rho_p} + k_F a_0 m_0$$

or

$$u = 1 - \frac{R-1}{R} \left(1 + \frac{k_v}{\rho_p} \right) - k_F a_0 \quad (\text{Eq. 4-105})$$

where the structural index k_v identifies the part of the structural mass that is proportional to the propellant volume and the structural index k_F identifies the part of that mass that is proportional to the thrust. Optimization with respect to the parameter $u = m_u/m_0$ leads to the relation:

$$k_F R a_0^2 - \frac{\varphi \bar{g}}{g_0} k_F a_0 - \frac{\varphi \bar{g}}{g_0} \left(1 + \frac{k_v}{\rho_p} \right) \frac{R-1}{R} = 0 \quad (\text{Eq. 4-106})$$

Equation 4-106 constitutes an additional relation between a_0 and R , which can be used in conjunction with equation 4-103, where ΔV is known to calculate values of R and a_0 . Equation 4-105 then yields the optimal value of $u = m_u/m_0$, thereby determining m_0 since m_u is known. This elementary computation yields:

$$F = a_0 g_0 m_0, \quad t_b = \frac{R-1}{R} \frac{v_e}{g_0 a_0} \quad (\text{Eq. 4-107})$$

It is possible to carry out more refined and more complete mission optimization calculations or to use other criteria, but our purpose has been to present a simple example that illustrates how a first estimate can be made.

After the thrust F , burning time t_b and total impulse $F t_b$, have been obtained from the mission optimization analysis, it is possible to fill in more details of a motor design. For a given propellant, the grain geometry best adapted to the application can be selected on the basis of the known thrust-time history $F(t)$, which dictates whether it is preferable to choose an end-burning or radial-burning grain and a single-composition or dual composition propellant. If a radial-burning grain is chosen, then one may next carry out a preliminary study to define

the internal channel geometry which maximizes loading fraction ϵ_1 (while maintaining a suitable value for the area ratio $J = A_t/A_p$) and minimizes the sliver losses which are characterized by the quality index ϵ_{11} (ϵ_1 and ϵ_{11} have been defined in Section 3.3). As a basis for continuing our discussion of the design procedure, let us assume that at this point the designer has decided that an internally burning cylindrical grain with a star shaped cross section appears to be best suited to the particular application. The star geometry must then be defined. The designer may first choose the number of star points arbitrarily and then compute the various parameters represented on Fig. 4-16. The parameter α_1 of the angle $\alpha_1 \pi/n$ is related to the sliver-loss parameter ϵ_{11} . The radius of curvature $R_2 = f$ is determined by the practical necessity of removing the mandrel and by the mechanical stresses imposed upon the grain during the ignition phase. Too small a value for the radius R_1 must be avoided to prevent cracks. The angle α is determined by the neutrality condition, the thickness w by the burning time and burning rate and the parameter ℓ is determined by the ratio $J = A_t/A_p$. A quadratic equation for ℓ is obtained since, with neutral grains and for $\alpha_1 = 1$:

$$A_p(0) = \frac{A_t}{J} = 2n \left\{ \frac{f^2}{2} \sin \frac{\pi}{n} \left[\cos \frac{\pi}{n} - \sin \frac{\pi}{n} \cot \alpha \right] + \ell f \frac{\sin(\pi/n)}{\sin \alpha} \right\} \quad (\text{Eq. 4-108})$$

The internal port geometry is thereby determined. The parameters remaining to be studied in the optimization problem are the number of star points, the chamber pressure p_c and the burning rate r . In any design it is necessary to study the influence of parameters such as 'a' and 'n' in the burning rate law $r = ap_c^n$. Although it is not possible to modify the exponent n very much, we have seen that, for a given propellant, one can significantly change the value of a . For a given application, it must be decided whether fast-burning or slow-burning grains are to be preferred.

The optimum number of star points is generally found to be about 6 or 7. One can draw curves of chamber pressure versus grain diameter for different numbers of star points. The grain diameter decreases as the pressure increases and the curves move toward lower pressures, when the number of star points is increased. For a given pressure range and a given diameter range, these curves determine the number of points.

The two remaining important parameters are now p_c and a .

The characteristic velocity is not very sensitive to p_c and obeys an equation of the form:

$$c^* = K_1 p_c^{\beta_1} \quad (\text{Eq. 4-109})$$

with $\beta_1 \approx 0.001$. The thrust coefficient C_F depends chiefly upon the expansion ratio p_c/p_e , where p_e is the pressure at the exit of the nozzle. For a given mission, p_e is related to C_F by an equation of the approximate form:

$$C_F = K_1 \left(\frac{p_c}{p_e} \right)^{\beta_2} \quad (\text{Eq. 4-110})$$

with $\beta_2 \approx 0.1$ and $K_2 \approx 1$. The throat area is determined, for each pressure, by the thrust equation.

The evaluation of the time evolution of the motor mass and the complete definition of the grain geometry are sometimes accomplished by assuming that the web thickness w is proportional to the grain diameter D :

$$w = C D$$

For a star shaped configuration:

$$C = \frac{w}{2[w + f + \ell \left(\frac{A_t}{J}, f, n \right)]} \quad , \quad (\text{Eq. 4-111})$$

which yields:

$$C \approx 0.25$$

since $w + f \approx e$. The parameter C depends on the combustion constant c . With a high burning rate and small burning durations, C can drop to 0.1 and for small burning rates and long burning duration, C rises to 0.3.

The calculation of the masses of each element is conveniently performed as a function of the slenderness ratio $\Lambda = L/D$ of the grain. The propellant mass m_p is given by:

$$\frac{m_p}{\rho_p D^3} = \left[\frac{\pi}{4} (\Lambda + C_1) - \frac{A_p}{D^2} (\Lambda + C_2) \right] \quad , \quad (\text{Eq. 4-112})$$

where C_1 and C_2 are constants defined by the geometry of the ends of the grains. The port cross-sectional area is given by:

$$\frac{A_p}{D^2} = \frac{1}{J} \frac{m_p}{D^3} \frac{c^* a p_c^n}{C p_c} \quad , \quad (\text{Eq. 4-113})$$

which yields the nondimensional result:

$$\frac{m_p}{\rho_p D^3} = \frac{\frac{\pi}{4} (\Lambda + C_1) J C p_c}{J C p_c + \rho_p c^* a p_c^n (\Lambda + C_2)} \quad . \quad (\text{Eq. 4-114})$$

The mass of the combustion chamber is:

$$\frac{m_f}{\rho_m D^3} = \frac{\pi}{2} \frac{p_c}{\sigma_a} C_3 \left\{ \Lambda + C_4 - C_5 \left(\frac{\Lambda + C_1}{\Lambda + C_2} \right) \left(1 - \frac{C p_c J}{C p_c J + \rho_p a p_c^n c^* (\Lambda + C_2)} \right) \right\} \quad (\text{Eq. 4-115})$$

where σ_a is the maximum allowable stress, ρ_m is the density of the structural material and C_3 , C_4 and C_5 are constants. The reduced inhibitor mass is $\frac{m_i}{\rho_i D^3}$. The nozzle mass m_n is proportional to the total impulse $F \cdot t_b$:

$$m_n = C_7 F \cdot t_b \quad , \quad (\text{Eq. 4-116})$$

where the constant C_7 depends upon the burning duration, the pressure p_c and the nozzle area ratio $\epsilon_e = A_e/A_t$.

From the preceding formulas one can calculate the ratio of the combustion chamber mass m_c to the propellant mass m_p and the structural index $\xi = m_c/m_p$ (the ratio of the mass of the empty motor to the propellant mass) for various slenderness ratios λ , various pressures p_c and burning rates. Representative resulting curves of m_c/m_p are shown in Fig. 4-37, where the symbols M_1 and M_2 identify two different metal case designs and the symbols P_1 and P_2 identify two different filament-wound cases. In this particular example, the propellant with the slow-burning rate requires a lighter chamber, especially at large values of the slenderness ratio. Figure 4-38 shows the variation of ξ with pressure for a filament-wound case. An optimum chamber pressure ($p_c \sim 50$ atm) exists for the propellant with the high burning rate.

These various results can be introduced into the ballistic equation and the equation for $u = m_u/m_p$, in order to check whether the design departs from the optimized solution. By successive modifications, the geometry of the optimal motor can thus be obtained.

5 Solid Sublimation Motors (27) (28) (29)

For certain space applications, it is necessary to generate very small thrusts (between 10^8 and 1 lb) which are difficult to obtain with classical solid propellants.

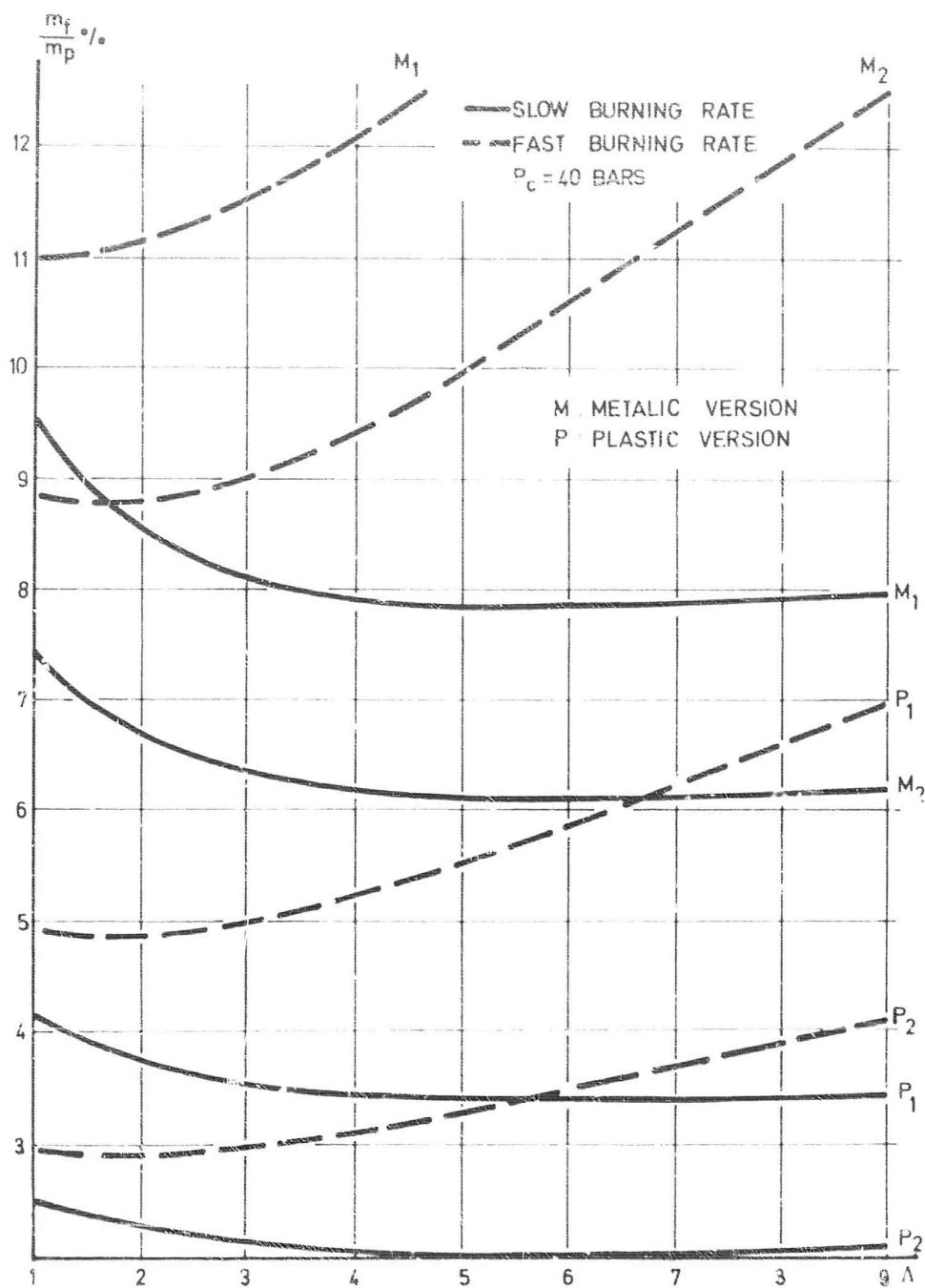
These low thrust motors are needed in the following applications:

Change of orbit	$F : 10^{-2}$ to 10 lb
Reorientation	$F : 10^{-3}$ to 1 lb
Spin motor	$F : 10^{-3}$ to 1 lb
Compensation of external perturbations (aerodynamic, magnetic, gravity, solar perturbations)	$F : 10^{-8}$ to 10^{-4} lb
Compensation of propellant venting effects	$F : 10^{-4}$ to 10^{-1} lb

Subliming solid systems are well adapted for most of these missions (see Fig. 4-39). These motors consist of a propellant container, a heating device to sublime the solid propellant, a valve to control the gas flow and a nozzle through which the gas is expanded. The propellants used are simple subliming materials and do not release heat when they are gasified. However, just as for solid propellants, it is necessary to obtain high specific impulses from sublimation motors. Since the chamber temperature is approximately the same for all propellants, the choice of the subliming substance should depend primarily on its molecular weight. Table 4-2 gives properties of various propellant substances chosen by Hardt (27). Substances generating gases with molecular weights between 25 and 30 g/mole are of interest for this type of propulsion. The operation of such a motor is simple. The mass flow rate of propellant \dot{m}_s is given by Knudsen's relation:

$$\dot{m}_s = \alpha A_s \left(\frac{gm}{2\pi RT} \right)^{1/2} (p_v(T) - p_c) \quad (\text{Eq. 4-117})$$

where α is the evaporation coefficient, A_s is the propellant surface area, m is the molecular weight of the gas, p_v is the equilibrium vapor pressure at the surface temperature T and p_c is the chamber pressure. Since the mass flow rate through the nozzle is:

Fig. 4-37 Case weight fraction versus Λ

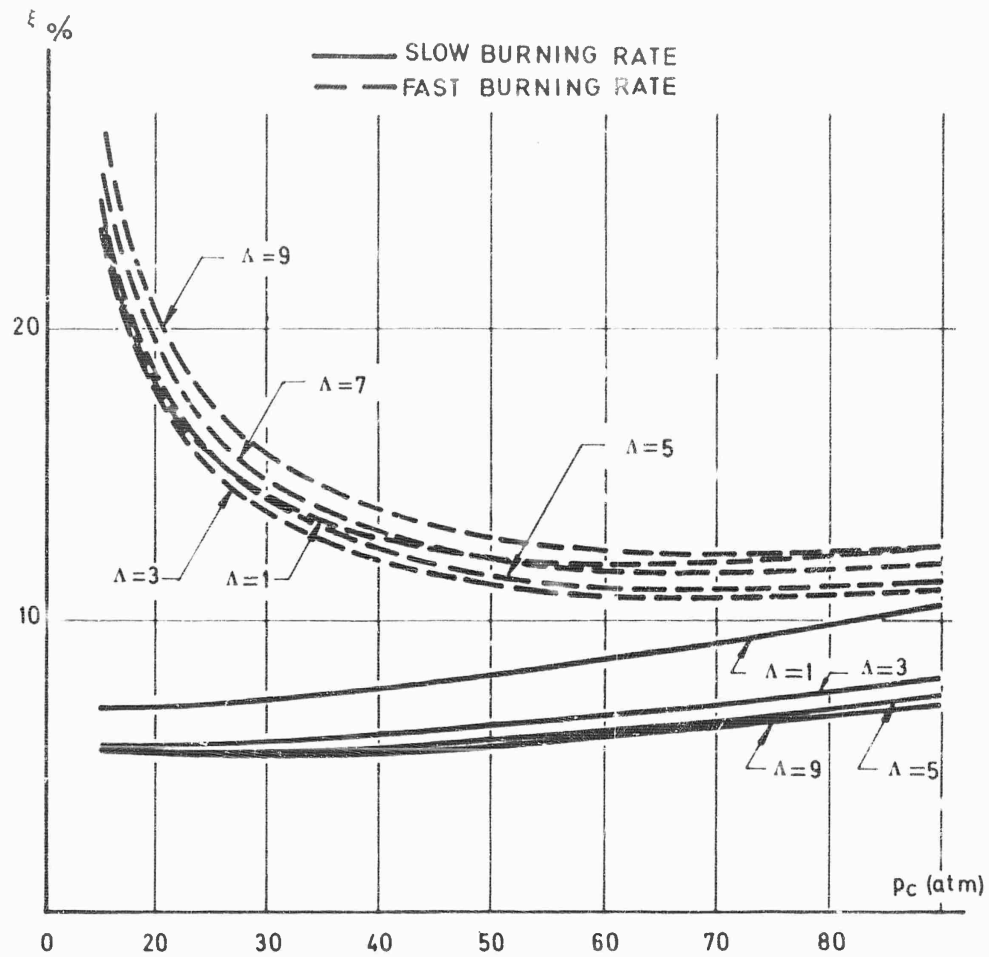


Fig. 4-38 Structural index vs. chamber pressure.

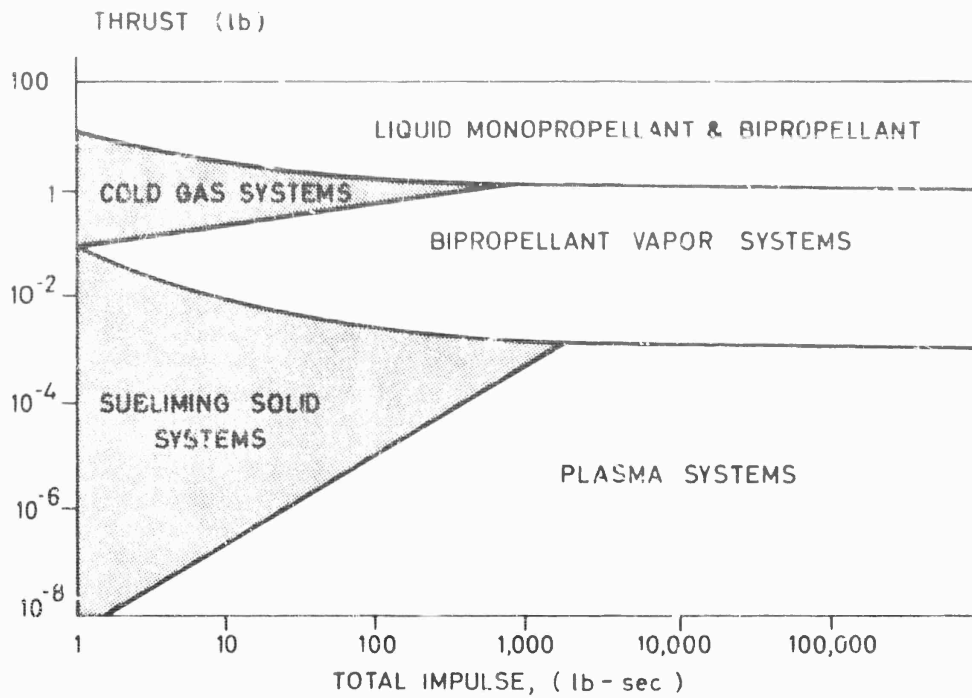


Fig. 4-39 Reaction control systems (39)

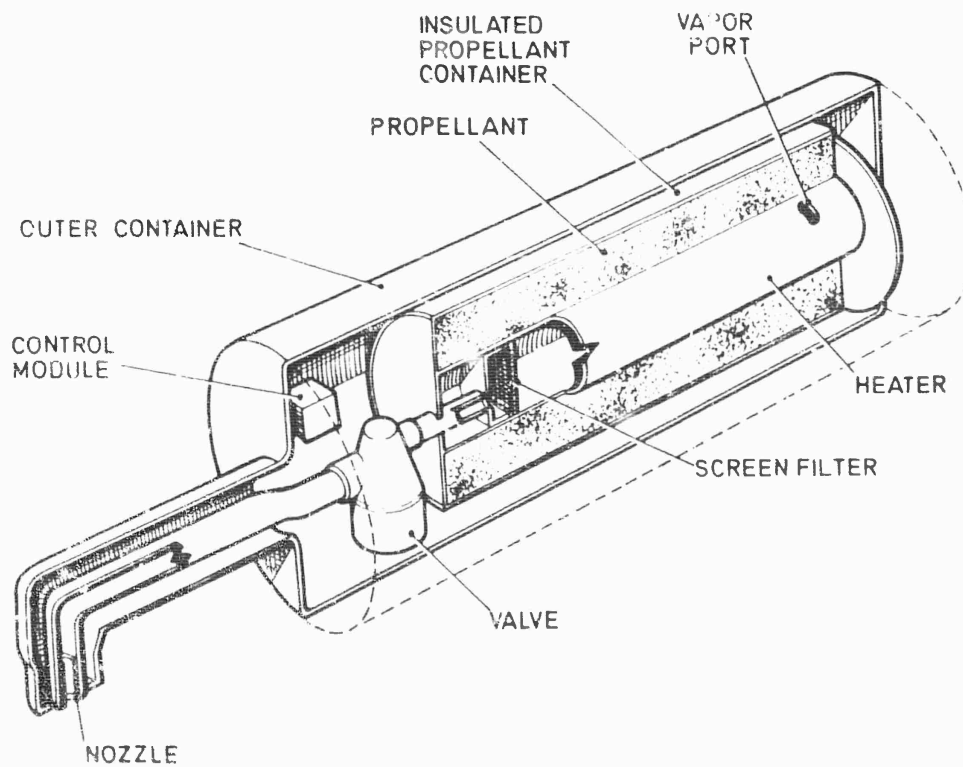


Fig. 4-40 Schematic of subliming solid engine (27)

$$\dot{m}_t = \frac{P_c A_t}{c^*} \quad (\text{Eq. 4-118})$$

the operating pressure is given by the equation:

$$P_c = \frac{P_v(T)}{1 + \frac{A_t}{A_s} \frac{1}{\alpha c^*} \sqrt{\frac{2\pi RT}{gm}}} \quad (\text{Eq. 4-119})$$

Usual values of A_s/A_t are much larger than unity. For sufficiently large values of α the second term of the denominator is small compared with unity. The chamber pressure then depends only upon the temperature and is insensitive to A_s . On the other hand, if α is small, the chamber pressure will be proportional to the area A_s .

Table 4-2 gives values of the evaporation coefficient α and of the specific heat ratio γ for various sublimation propellants. The evaporation coefficient is a function of temperature and experimental data on temperature dependence of α are quite scarce.

The energy required for sustained sublimation is obtained electrically. A representative heater consists of a thin titanium film on an aluminum oxide substratum. The energy required is of the order of 0.015 watt per micro-pound of thrust. A schematic diagram of a motor of this type is given on Fig. 4-40. The principal elements shown are the heater, the propellant, the mass flow regulation valve and the nozzle. The exhaust velocity is given by:

$$v_e = C_F c^* \quad (\text{Eq. 4-120})$$

The value of the thrust coefficient C_F depends upon the nature of the flow in the nozzle. The throat diameters for these small thrusts are of the order of a few tenths of a millimeter. The flow regime depends upon the Knudsen number $Kn = \lambda/D_t$, where λ is the molecular mean free path and D_t is the nozzle throat diameter. In the present application:

$$Kn = B \frac{T^{1,1}}{P_c D_t} = C \frac{D_t T^{1,1}}{F} \quad (\text{Eq. 4-121})$$

where the temperature T , the throat diameter D_t and the thrust F appear. For example, with a throat diameter of 0.25 mm, conditions correspond to continuum flow for a thrust greater than or equal to 10^{-4} lb and slip flow for a thrust of 10^{-5} lb. For $F = 10^{-6}$ lb conditions correspond to the transition zone between slip flow and free molecular flow. When evaluating the thrust coefficient and the specific impulse, the nature of the flow must be taken into account.

6 Conclusions

The steady-state regime of motor operation can at present be predicted with good accuracy by the theory presented in this chapter. Improvements can be brought about by studying more closely the heterogeneous and generally stratified flow in the central channel and nozzle, but, considering the scatter obtained in the experimental values of the burning rates, it seems to us that refinement of these theories is at the present time somewhat academic. The study of motor operation allows preliminary designs to be made and the optimal rocket for a given application to be defined.

Compound	Composition	Mean Mol. Wt. of gas g/mole	Vapor Pressure 25° C mm Hg	Evaporation Coefficient α	γ
Ammonium Bisulfide	NH_4HS	25.5	380		
Monomethylamine Bisulfide	$\text{CH}_3\text{NH}_3\text{HS}$	32.5	86		
Ammonium Carbamate	$\text{NH}_4\text{CO}_2\text{NH}_2$	26.0	63	2.0×10^{-5}	1.31
Ammonium Bicarbonate	NH_4HCO_3	26.3	50	1.0×10^{-6}	
Ammonium Carbonate	$(\text{NH}_4)_2\text{CO}_3 \cdot \text{H}_2\text{O}$	25.8	40	6.2×10^{-6}	
Monomethylamine Carbamate	$\text{CH}_3\text{NH}_3\text{CO}_2\text{NHCH}_3$	35.3	15	2.0×10^{-5}	
Paraformaldehyde	$\text{HO}(\text{CH}_2\text{O})_n\text{H}$	29.3	1.5	4.8×10^{-7}	
Ammonium Azide	NH_4H_3	30.0	0.65		
Ammonium Acetate	$\text{NH}_4\text{CH}_3\text{COOH}$	38.5	0.47	2.25×10^{-3}	
Ammonium Formate	NH_4COOH	31.0	0.03	2.7×10^{-3}	
Ammonium Chloride	NH_4Cl	26.8	10^{-4}	1.0×10^{-2}	1.36

Table 4-2 Physical Properties of Dissociating Solids (27)

References

- (1) Huggett C., Bartley C.E. and Mills M.M. Solid Propellant Rockets No. 2, Princeton University Press.
- (2) Barrère M., Jaumotte A., Fraeijs de Veubeke B. and Vandekerckhove J. Rocket Propulsion, Elsevier Publishing Company, 1960.
- (3) Geckler R.D. and Klager K. Solid Propellant Rocket Engines. Handbook of Astronautical Engineering, McGraw-Hill.
- (4) Summerfield M., Sutherland G.S., Webb M.J., Tabak M.J. and Hall K.P. Burning Mechanism of Ammonium Perchlorate Propellants, Vol. 1 of ARS Series, Progress in Astronautics and Rocketry, pp. 141-182, Academic Press, New York, 1960.
- (5) Golub G. Need for a Variable Burning Rate Solid Propellant, J. of Spacecraft AIAA, Vol. 2, No. 4, July-August 1965.
- (6) Crawford B.L., Huggett C., Daniels F. and Wilfong R.E. Direct Determination of Burning Rates of Propellant Powders, Anal. Chem. 19, No. 9, Sept. 1947.
- (7) Larue P. Visualisation de la Combustion d'un Propergol Solide à l'Intérieur d'un Propulseur, La Recherche Aéronautique No. 91, pp. 23-31, Nov. - Dec. 1962.
- (8) Boisson J. et Betin P. Etude de la Balistique Intérieure des Fusées à Poudre, Semaine d'Etude sur la Propulsion Chimique, CNES, Paris SDSTA pp.69-82, 4-6 May, 1964.
- (9) Dehority G.L., Bradley H.H. and Price E.W. Flow of Gas in Tapered Channel with Mass Addition, U.S. Naval Ordnance Test Station, NOTS T. P. 3626, NAVWEPS Report 8606.
- (10) Bryce Wilhite V.H. Systematic Design of Solid Propellant Configurations to Permit Predetermined Thrust-Time Delivery, AGARD Symposium on Propellant Chemistry, Dec. 1960.
- (11) Zimmerman C.A. A Review of the Status of the Large Solid Rocket Motor Program, XVII Congress of IAF, Oct. 1966.
- (12) Stone M.W. Slotted Tube Grain Design, J.A.R.S. Vol. 31 No. 2, pp. 223-228, Feb. 1961.
- (13) Dorléac B., Poggi J.C. et Lauroua J. Mise à Poste d'un Satellite Géostationnaire Européen par le Lanceur ELDO A, XVII Congress of IAF, Oct. 1966.
- (14) Thibodaux J.G., Swain R.L. and Wright G. Analytical and Experimental Studies of Spherical Solid-Propellant Rocket Motor, NASA, R.M. L57 G 12 a, 16 Aug. 1957.
- (15) Segal P.M. Rapid Evaluation and Design of Spherical Motors, Solid Propellant Rocket Conference. ARS, Preprint 1617-61.

- (16) **Rogers K. H.** Mathematical Design of a Sliverless Rocket Engine, ARS Paper 1616-61, New York, Feb 1961.
- (17) **Ternier, Vacelet and Pontvianne.** Etude de Blocs à Deux Compositions sans Résiduel Théorique, Mémoires des Poudres, 1961.
- (18) **Barrière M. et Larue P.** Fusées à Propergol Solide Utilisant Deux Poudres Ayant des Vitesses de Combustion Différentes, La Recherche Aérospatiale No. 91, Nov.-Dec. 1962.
- (19) **Schluter P. M.** Solid Propellant Charge for Rocket Motors, Patent 3, 260, 208, 12 July 1966.
- (20) **Braun J. V.** Multiple Propellant Grain for Rocket Motors, Patent 3, 217, 651, 16 Nov. 1965.
- (21) **Larue P.** Propulseur Sphérique à Propergol Solide bi-composition, La Recherche Aérospatiale No. 109, pp. 21-22, Nov.-Dec. 1965.
- (22) **Vellacott R. J. and Caveny L. M.** A Computer Program for Solid - Propellant Rocket Motor Design and Ballistic Analysis, Solid Propellant Rocket Conference, ARS, Paper 2315-62, 1962.
- (23) **Gorny L. S.** A Generalized Approach to Rapid Evaluation of Solid Propellant Grain Geometries, Solid Propellant Rocket Conference, ARS, Paper 2316-62, 1962.
- (24) **Majerus J. N., Briar H. P. and Wiegand J. H.** Behaviour and Variability of Solid Propellants and Criteria for Failure and for Rejection, J. of Spacecraft, AIAA Vol. 2, No. 6 pp. 833-846, Nov.-Dec. 1965.
- (25) **Phillips B. R. and Tanger G. E.** A Study of the Effects of Non-Uniform Grain Temperature on Solid Propellant Rocket Motor Ballistic Parameters. Solid Propellant Rocket Conference, ARS, Paper 2309-62, 1962.
- (26) **Thackwell H. L.** Generalized Study of Solid Propellant Rockets for Upper Stages of Multistage Rocket Vehicles, CGR Report AC-12, 1960.
- (27) **Hardt A. P., Foley W. M. and Brandon R. L.** The Chemistry of Subliming Solids for Micro Thrust Engines, Astronautica Acta Vol. 11, No. 5 Sept.-Oct. 1965.
- (28) **Jonath A. D.** Gasdynamic Problems in Low Pressure Microthrust Engine, Astronautica Acta Vol. 11, No. 5, Sept.-Oct. 1965.
- (29) **Zimmerman C. A.** Low Thrust Reaction Control Systems, XVII Congress IAF, Madrid, 9-15 Oct. 1966.
- (30) **Arribat I. G.** Quelques Propriétés Géométriques de la Combustion des Poudres Homogènes par Couches Parallèles. Mémoires de L'Artillerie Française, tome 40, 1er Fascicule, pp. 167-203, 1966.

Chapter 5

**Experimental Aspects of Steady-State
Combustion Phenomena**

Nomenclature

a	constant in burning rate formula
a'	constant in burning rate formula
B	frequency factor
b	constant in burning rate formula
b'	constant in burning rate formula
c	constant in burning rate formula
c_p	specific heat at constant pressure
d	sphere diameter of AP particle
E	activation energy
\dot{m}	propellant mass flow rate per unit area
n	constant in burning rate formula
p	pressure
λ	linear regression rate
R°	universal gas constant
Re	Reynolds number
r_p	pyrolysis rate
T	temperature
t	time
T_o	initial grain temperature
T_s	surface temperature
v	flame speed (in gas phase)
x	distance normal to propellant surface
Δh	amount of energy liberated per unit mass by the chemical reaction
Δl	energy required to bring the solid into a gaseous state
λ	thermal conductivity
μ	gas mean viscosity
ρ_o	oxidizer density
ρ_p	propellant density

φ	equivalence ratio
ϕ	particle size
Subscripts	
g	gas
m	motor
s	solid; also strand burner

Experimental Aspects of Steady-State Combustion Phenomena

1. Introduction

The preceding chapters were concerned with practical aspects of solid propellant rocket propulsion. We now begin to discuss topics that are farther removed from applications and are related more intimately to details of the combustion processes, that occur inside the motor. The material in Chapters 5-10 probes various aspects of motor combustion as deeply as the current state of scientific research in the field will permit. Although these basic studies uncover more problems than they solve, nevertheless they are of practical value in providing the rocket designer with new ideas and new ways of thinking.

As in most of the areas of research that will be considered in this book, the experimental studies that have been performed on steady solid propellant combustion are too numerous for us to present an exhaustive list. Therefore, we restrict our attention here to some recent work related to the analysis of steady-state solid propellant combustion mechanisms and we refer the reader to reviews, such as that of Schultz, Green and Penner (1), for more thorough discussions of earlier studies.

The propellant classifications defined earlier are of paramount importance in distinguishing types of experimental studies of steady-state propellant combustion. Therefore, we restate the definitions here. A heterogeneous propellant is one in which the mean dimension of its elements exceeds typical dimensions of macromolecules and colloids. Under this definition fall all composite propellants (possibly metalized), the plastic binders of which may or may not include oxidizing elements such as oxygen and fluorine. Metalized double-base propellants also fall in this category but conventional double-base propellants do not. Conventional double-base propellants are homogeneous. A homogeneous propellant is one in which the mean dimension of its elements is less than typical dimensions of macromolecules and colloids.

A microphotographic examination of a heterogeneous propellant (Fig. 5-1) reveals its degree of heterogeneity. For heterogeneous propellants, the thickness of the combustion zone is usually comparable with or smaller than typical heterogeneity dimensions.

The experimental methods contributing to an analysis of the combustion mechanisms of homogeneous and heterogeneous propellants may be divided into the three categories identified below :

(a) Experiments in the first category are designed to determine physico-chemical characteristics of each of the propellant constituents. Measurement of the linear pyrolysis rate is an example of such a determination; another example is the measurement of the decomposition velocity of appropriately prepared oxidizing constituents. Data obtained in these experiments can be used in combustion models (such as the two-temperature model defined later).

(b) Methods falling within the second category consist of inventing and constructing combustion models that resemble reality as closely as possible but are easier to analyze. One such method is the study of the combustion of oxidizer spheres in gaseous streams. Another is the preparation of hybrid propellants in which one constituent is a solid and the other a gas. Studies of gas-phase combustion between materials composing solid propellants have enabled investigators to ascertain whether the gas-phase process is important. Study of the combustion of metal particles in gaseous oxidizing streams has facilitated analysis of metal combustion phenomena and has yielded characteristic metal combustion times, thereby contributing to our understanding of the combustion of metallized propellants. These simplified experimental models throw light on the fundamental combustion processes and emphasize the effect of the flame configuration on the regression rate of the solid. The interaction between the flame and the surface is an important part of the mechanism of heterogeneous propellant combustion.

(c) The third category of experimental methods contains the studies of combustion of real solid propellants. The procedures are based on direct or indirect observation and measurements. The direct methods consist of examining the combustion zone and the regressing surface by microcinematographic techniques, in order to observe in detail the evolution of the flame geometry and of the apparent contour of the solid. Subsidiary nonphotographic measurements are also involved here. The indirect methods, on the other hand, use as a basis of comparison a measurable parameter linked to the combustion phenomena, such as the propellant regression rate. The dependence of this parameter on others enables one to draw certain conclusions concerning the combustion mechanism.

In this Chapter, experimental studies of heterogeneous propellant combustion will be described under the three headings (a), (b) and (c) given above; the main results will be presented as well as difficulties of interpretation. However, before considering heterogeneous propellants, we shall briefly discuss experiments with homogeneous propellants. Although results from a number of methods (e.g. differential thermal analysis) falling in category (a) are available for homogeneous propellant constituents, these results are not very directly applicable to homogeneous propellant combustion, because the intimate mixing that leads to homogeneity generally modifies the kinetic mechanisms of the constituents. Methods falling in category (b) are difficult to devise for homogeneous propellants. Therefore the homogeneous propellant techniques that we shall consider here all belong to the third category (c). Our emphasis on experiments with heterogeneous rather than homogeneous propellants is partially justified by the current widespread use of heterogeneous propellants.

2. Combustion of Double-Base, Homogeneous Propellants

The compositions of double-base propellants have been described in Chapter 3, where it is pointed out that most of them use nitroglycerin and nitrocellulose.

The flame structure of double-base propellants is relatively simple compared with that of composite propellants. Three zones are distinguishable (Fig. 5-2): a fizz or foam reaction zone lies close to the surface and contains suspended particles. A dark zone in the gas, where chemical reactions occur slowly, is adjacent to the fizz zone. The chemical reactions go to completion in a luminous flame or explosion zone adjacent to the dark zone. Before studying the structures of these zones in which different combustion steps occur, we shall review a few experimental techniques used in studying double-base propellants. Some of these techniques are generally applicable to all solid propellants.

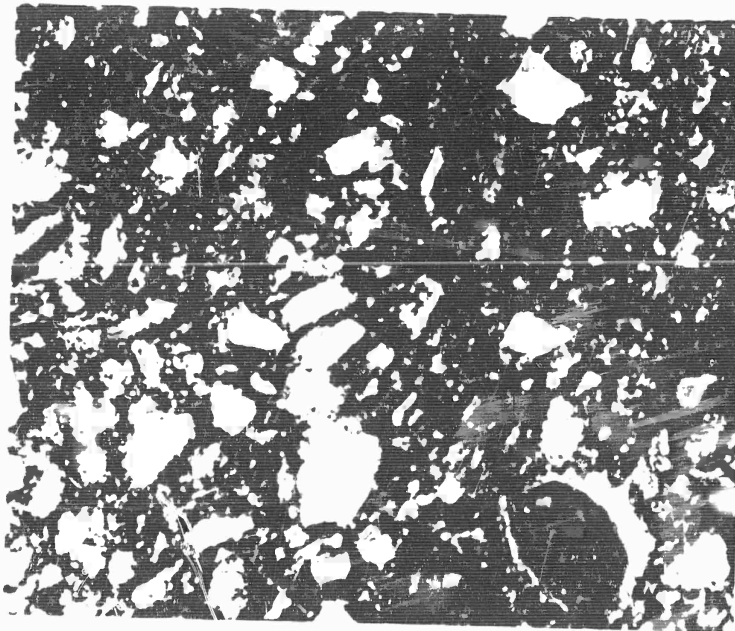
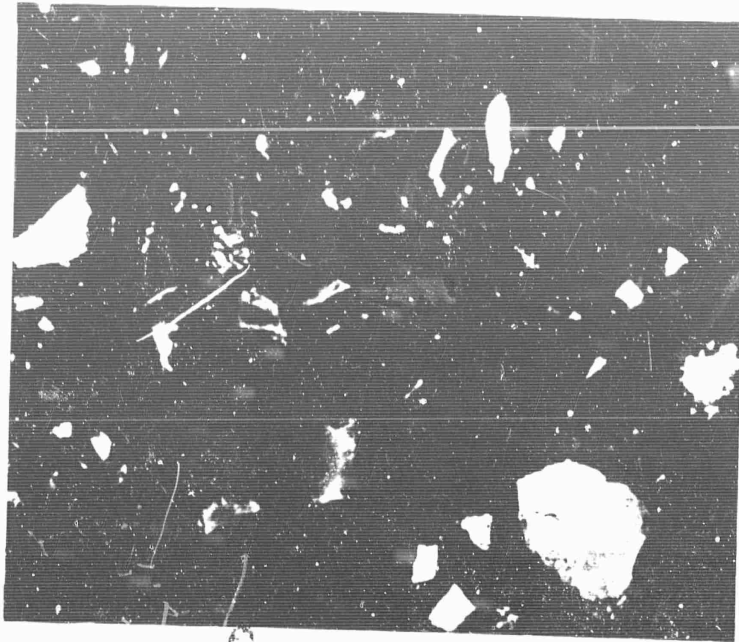


Fig. 5-1 Microphotograph of the surface of a composite propellant

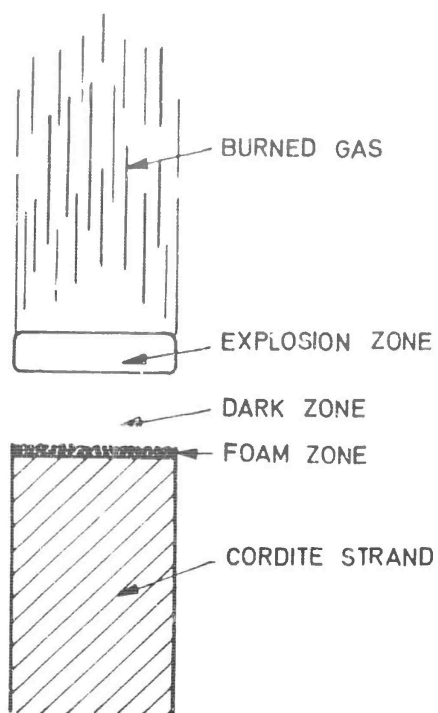


Fig. 5-2 Zone structure of a cordite flame

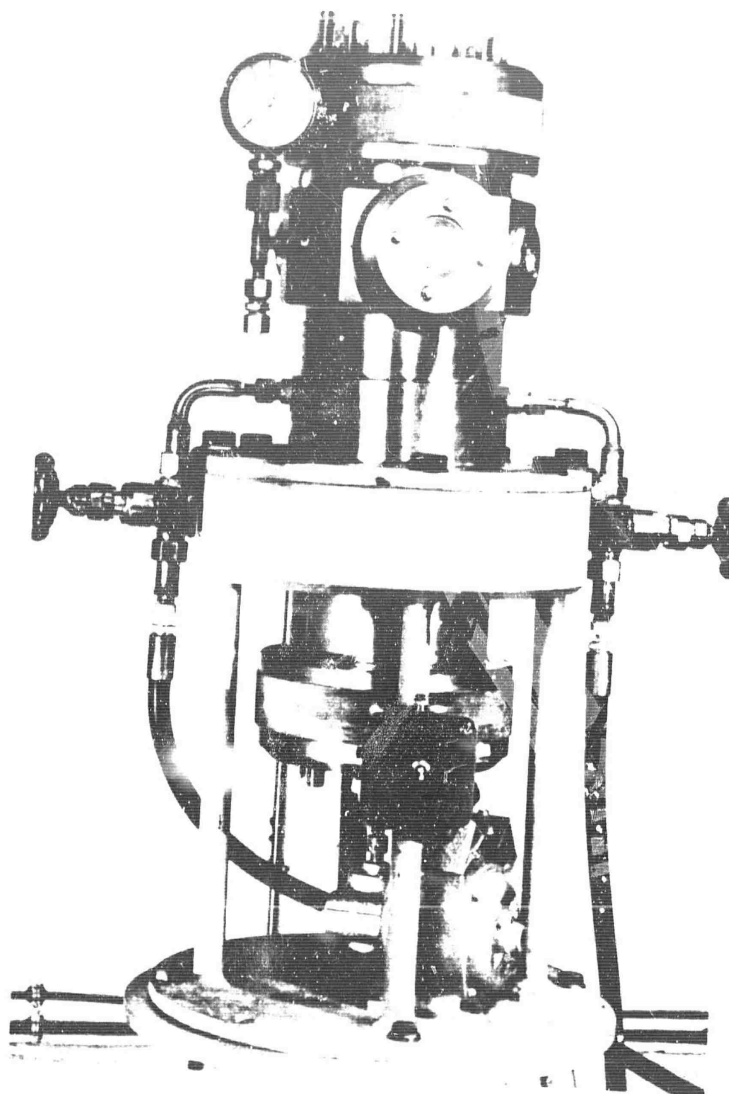
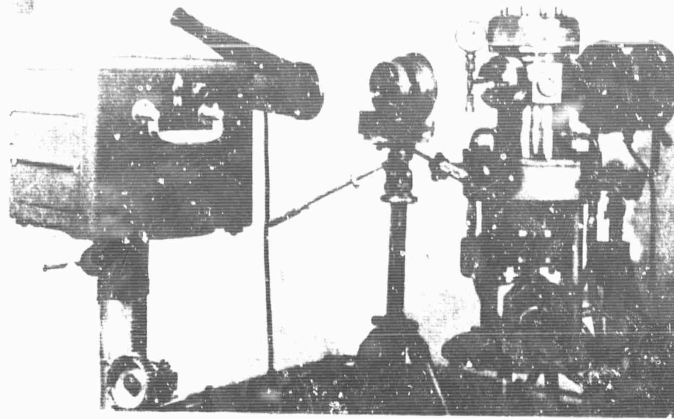
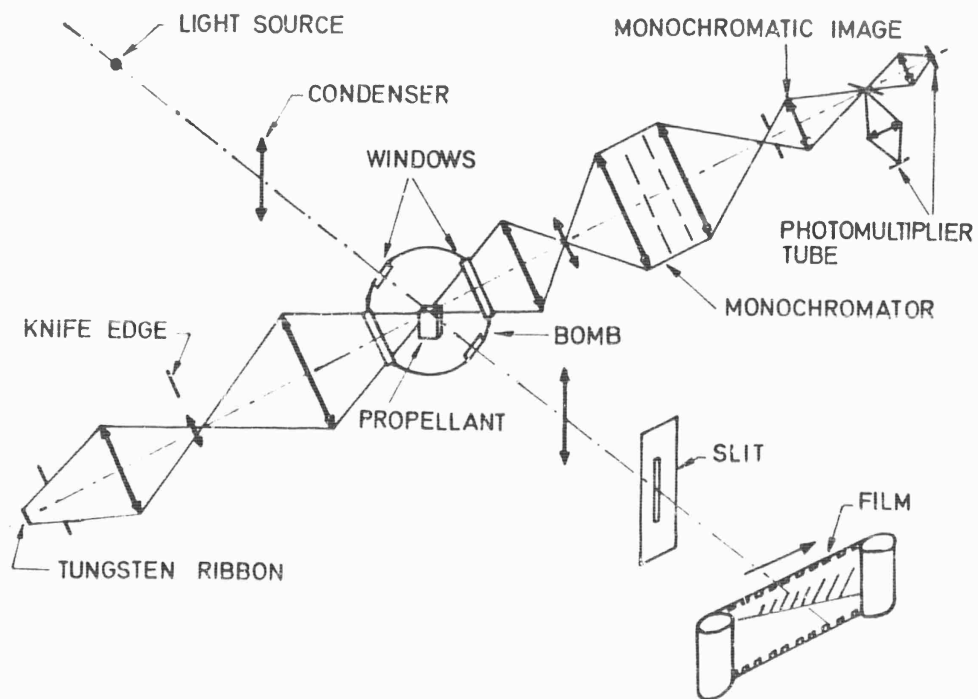


Fig. 5-3 BR. 14 bomb

q*



VIEW OF APPARATUS

Fig. 5-4 Schematic of measurement apparatus for r , c^* and T_g

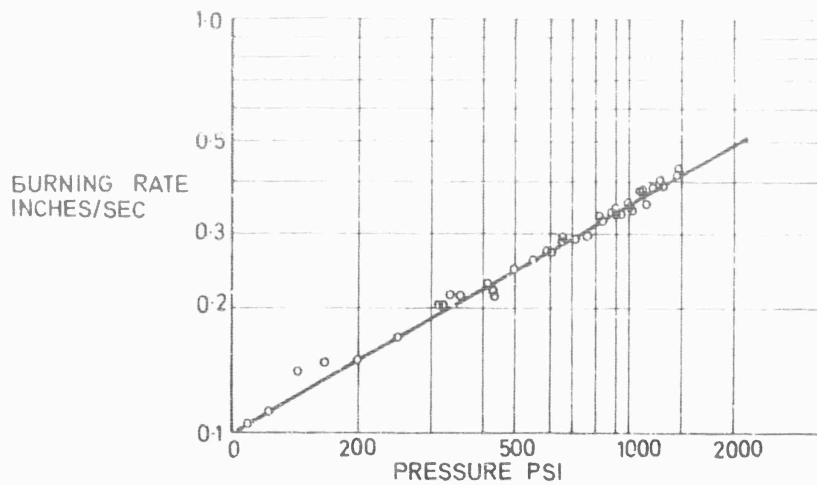


Fig. 5-5a Variation of burning rate with pressure (2)

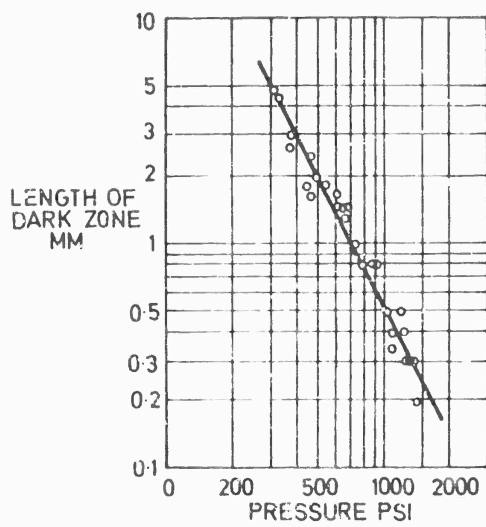


Fig. 5-5b Variation of dark zone length with pressure (2)

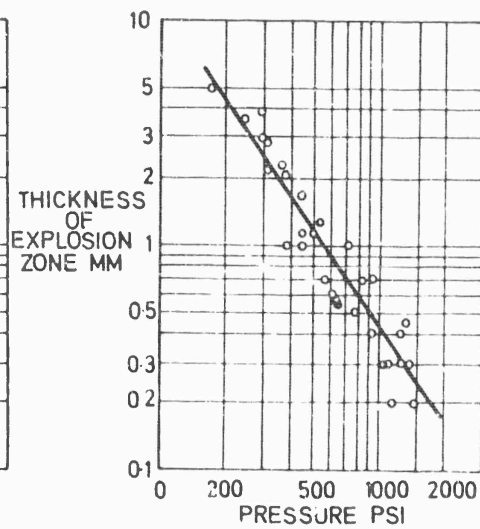


Fig. 5-5c Variation of explosion zone thickness with pressure (2)

2.1. Experimental Techniques for Studying Homogeneous Solid Propellants

The burning velocity is the basic quantity which must be measured as a function of pressure for all propellants.

The combustion of a sample takes place in a bomb which is kept at a constant pressure during the experiment by means of pressure regulators. Such a bomb is shown in Fig. 5-3. This bomb can be disassembled rapidly since it is mounted with interrupted threads; quarter turn locks the lid. The design eliminates the task of tightening many bolts. Two visual observation lines allow one to perform several simultaneous experiments. The sample can also be moved upward at a predetermined rate so that the burning zone can be kept at a fixed location in order to facilitate optical analysis. The lids are interchangeable for purposes of varying the internal volume of the bomb, or including a smoke exhaust or a pressure regulating device. Two viewing windows are equipped with a quick-attachment device, and several electric jacks are provided for electric leads. The bomb can be pressurized rapidly.

The burning velocity of a propellant sample is generally determined by measuring the lapse of time between the flame-rupture of two or several wires, positioned at known spacings.

Optical methods are also used; they are more complex to apply but allow one to observe the state of the combustion process at each moment. Burning velocities are determined from motion pictures taken during the combustion. Many measurements are thus available and anomalous phenomena occurring during the combustion are easily detected.

Another useful technique is to focus the image of the sample on a slit and to record this image with a drum camera. By recording the flame-front luminosity, the film produces a diagram representing the burnt propellant thickness versus time. The tangent to the curve yields the burning velocity of the propellant. This method is depicted schematically in Fig. 5-4.

Figure 5-5a shows the burning velocity of a homogeneous solid propellant (SU/K cordite) (2).

The burning law is of the form :

$$r = a p^n$$

where n is approximately 0.56.

This slit technique has also been described in Chapter 3, in the discussion of the characteristic velocity.

The burning rate measurement can be completed by an optical study of the combustion temperature. Figure 5-4 depicts schematically the experimental set-up, which is described more extensively in Ref. (3). It uses the line reversal technique usually of sodium, this substance being included in small quantities in the propellant. This technique involves comparison of the energy radiated by the flame with the energy emitted by a luminous source seen through the flame plus that emitted by the flame. The comparison of these two energies with that of the luminous filament determine the point of line reversal and the flame temperature. The results obtained with double base propellants are accurate and agree well with the theoretical values.

A spectroscopic study of the combustion zone can complement the preceding results.

Photographic, cinephotographic and cinemicrographic techniques allow one to observe and study in detail the structure of the combustion zone and in particular to evaluate the relative thicknesses of the flame zone and of the dark zone.

A burning surface can also be examined by the optical techniques, at least at low pressures.

Aside from optical techniques, temperature measurements in the solid and in the dark zone have been carried out with very thin thermocouples (7.5μ). The sample is cut in half pieces and the thermocouples are glued to one cut face, in the shape of the letter V with the point toward the burning surface (4).

During combustion the evolution of temperature can be studied as the flame front moves. A typical temperature profile is given in Fig. 5-6.

To investigate the significance of the profile, let T_0 be the initial grain temperature. The temperature in a medium with heat production by chemical reaction is then given by :

$$\frac{d}{dx} \left[\ln (T - T_0) \right] = \frac{\dot{m} c_p}{\lambda} - \frac{1}{\lambda(T - T_0)} \int_{-\infty}^{+\infty} \dot{W}_x \Delta h \, dx ,$$

where \dot{W}_x is the mass production rate of the species contributing to the chemical reaction, Δh is the amount of energy liberated per unit mass by the chemical reaction and \dot{m} is the mass flow rate. When there is no chemical reaction ($\dot{W}_x \approx 0$) the temperature profile is a straight line in a semi-logarithmic plot (Fig. 5-6). The slope of this line yields $\dot{m} c_p / \lambda_s$, and hence λ_s , the thermal conductivity in the solid. From Fig. 5-6, λ_s is approximately 7.8×10^{-4} cal/cm sec $^{\circ}\text{C}$, and the surface temperature lies in the vicinity of 330°C .

The difference of temperature gradients at the surface determines the amount of energy $\Delta \ell$ required to gasify the solid, possibly under the influence of contribution from surface reactions:

$$\dot{m} \Delta \ell = \left(\lambda \frac{dT}{dx} \right)_s - \left(\lambda \frac{dT}{dx} \right)_g$$

2.2. Experimental Results

Photographs of the combustion zone of homogeneous solid propellants show in the surface small black spheres corresponding to a charring of the surface, and light points which appear then disappear. The diameter of these points or these spheres is of the order of 10μ . The light points correspond to a local intense combustion; streaks extend from them into the dark zone.

It is generally supposed that a break-up of O - NO₂ bonds occurs first in the nitro-cellulose and nitroglycerine molecules. The thickness of the foam zone in which this process occurs is of the order of 10μ , and the surface temperature is about 600°K .

In the dark zone the decomposition products of the propellant, such as nitrogen dioxide and organic fragments, react and give NO, N₂, CO, H₂, These reactions are not luminous. The temperature in this zone varies between 600° and 1600°K . The zone thickness is very sensitive to pressure as shown in Fig. 5-5b. It varies according to a relationship of the form :

$$\epsilon_D p^m = \text{const.}$$

The exponent m is of the order of 1.6 for cordite and it depends strongly upon the nature of the propellant.

This zone corresponds also to an induction period for reacting species before they reach the luminous combustion zone and its exothermic reactions.

The thickness of the luminous zone where the main combustion occurs, decreases when the pressure increases as indicated on Fig. 5-5c. A law similar to that for the dark zone is obtained but the exponent m is smaller.

The measurement of the final combustion temperatures has produced values close to the theoretical ones obtained by taking into account the losses by radiation. Using a black body hypothesis Heath (2) found the following values :

Pressure	atm	51
Burning rate	cm. sec ⁻¹	0.76
\dot{m}	g. sec ⁻¹ cm ⁻²	1.22
Heat loss by radiation from upper surface	cal. sec ⁻¹	13.2
Heat loss from periphery	cal. sec ⁻¹	5.4
Total	cal. sec ⁻¹	18.6
Theoretical temperature	°K	2440
Theoretical temperature corrected for losses	°K	2327
Measured temperature	°K	2360

These results indicate that the losses by radiation are smaller than the theory predicts. Flame temperature measurements can be used as a guide in discussing energetics of a homogeneous propellant.

Burning velocities for this type of propellant are given by laws of the form :

$$r = a + b p^n$$

where the exponent n varies between 0.5 and 1. A few typical burning velocity laws are given below :

S P Propellant

	T°C	r cm. sec ⁻¹
$p^*_{\min} < p < 150 \text{ atm}$	-20	$0.0683 p^{0.71}$
	20	$0.0832 p^{0.71}$
	60	$1.011 p^{0.71}$
$150 \text{ atm} < p < 300 \text{ atm}$	20	$0.32 + 0.0049 p$

SPN Propellant

	T°C	r cm.sec ⁻¹
$p_{\min}^* < p < 150 \text{ atm}$	-20	$0.0762 p^{0.69}$
	20	$0.0879 p^{0.69}$
	60	$0.1016 p^{0.69}$
$150 \text{ atm} < p < 300 \text{ atm}$	20	$0.51 + 0.0043 p$

I7 H Propellant

	T°C	r cm.sec ⁻¹
$p_{\min}^* < p < 150 \text{ atm}$	-20	$0.0233 p^{0.72}$
	20	$0.0270 p^{0.72}$
	60	$0.0315 p^{0.72}$

Here the symbol p_{\min}^* denotes the low-pressure limit of flammability. The value of the exponent n , which is close to 0.7, suggests the importance of chemical phenomena in the combustion of this type of propellant.

3. Determination of the Physico-Chemical Characteristics of the Components of Heterogeneous Propellants

Since the high-temperature combustion zone causes the various components of the propellant to gasify, it is of interest to investigate the regression rate laws of propellant constituents when they are subjected to heat fluxes that are comparable with the flux from the combustion zone. Techniques for achieving heat fluxes of this magnitude include the use of heated plates and of other devices for producing pyrolysis of the constituent and (for constituents that are capable of decomposing exothermically) studies of deflagration of the isolated constituent. In the present section we discuss pyrolysis and deflagration results obtained on separate propellant constituents.

3.1. Linear Pyrolysis Rates

Before discussing the importance of linear pyrolysis measurements, we shall describe the most recent devices used to determine pyrolysis rates.

3.1.1. Measurement Devices - Schultz and Dekker developed the first linear pyrolysis apparatus leading to useable results (see discussion and literature cited in Ref. (1)). The solid whose pyrolysis rate we wish to determine, is placed against an electrically heated plate which is kept at a constant temperature. The measured velocity at which the solid regresses is assumed to represent the pyrolysis rate at the temperature of the heated plate; a thermocouple embedded in the thin nichrome plate measures this temperature. The force applied to the sample is adjustable and depends upon the nature of the solid and upon the pyrolysis rate; with most propellant constituents, there is a range of applied force over which the regression rate remains constant.

This device has two disadvantages : (a) The solid surface temperature differs from the plate temperature because of the gas layer separating the solid from the

plate. (b) The gas flows parallel to the surface and thereby may change the value of the pyrolysis rate. To overcome these disadvantages, Nachbar and Williams (5) suggested replacing the solid heating plate by a porous plate. With this modified device, the decomposition gases pass through the porous wall thus providing nearly a one-dimensional flow pattern above the sample. An experimental technique based on this principle has been developed at ONERA. Three types of electrically heated plates have been used by Guinet at ONERA (Fig. 5-7) :

- (a) A solid plate similar to that of Schultz.
- (b) A porous plate larger than the sample, with a gas stream surrounding the sample.
- (c) A porous plate of the same size as the sample.

In the porous-plate experiments of Guinet, the temperature is measured on the axis of the sample on the downstream side of the plate (temperature T_2). A calibration procedure provides the means of calculating the upstream temperature (T_1) of the surface of contact between the plate and the sample from the downstream temperature (T_2). The relationship between T_2 and T_1 is measured as a function of the mass-flow rate (produced by suction) and of the nature of the gas, in the absence of a solid sample. The difference between T_2 and T_1 increases with increasing mass flow rate. The calibration obtained in this manner is used for interpreting results of measurements with solid samples.

In testing propellant constituents, the temperature T_2 and the velocity of the sample relative to the plate are recorded as functions of time. From these results it is possible to determine the pyrolysis rate as a function of the temperature T_1 , which is considered to be the temperature at the surface of the solid.

A photograph of the apparatus is given in Fig. 5-7b.

Later ONERA experiments by Lieberherr eliminated the temperature calibration procedure by employing a thermocouple imbedded in the surface of the porous plate.

Coates (8) also made measurements with a porous plate limited in size to the dimensions of the sample. Coates heated the plate by radiation from an arc instead of electrically. Figure 5-11 shows details of how the sample and the porous plate are supported. The arc-source used by Coates delivered $30 \text{ cal cm}^{-2} \text{ sec}^{-1}$ on an area of approximately 5 cm^2 and the plate temperature was varied by moving the plate, with respect to the focal point of the reflector that concentrated the arc output.

An application of these techniques to the pyrolysis of ammonium perchlorate (AP) has shown important differences between solid plate and porous plate experiments.

For a given pyrolysis rate, the temperature at the surface of the sample decreases with increasing pressure when a solid plate is used but does not vary when a porous plate is used (Fig. 5-8). This experimental result implies that for the solid plate, the thickness of the gaseous layer varies with pressure, thereby producing a modification of the regression velocity. Andersen indicates (6) that to overcome this difficulty, it is necessary to change the applied force as the pyrolysis velocity varies. At high velocities, large forces are necessary for obtaining a pyrolysis rate that is independent of the force, and it seems that the gas flow parallel to the surface of the sample has an appreciable velocity which may affect the pyrolysis rate. This phenomenon has been analyzed theoretically for a restricted range of parameters in a paper by Cantrell (7).

Experiments with the porous plate exhibit somewhat less scatter in the results.

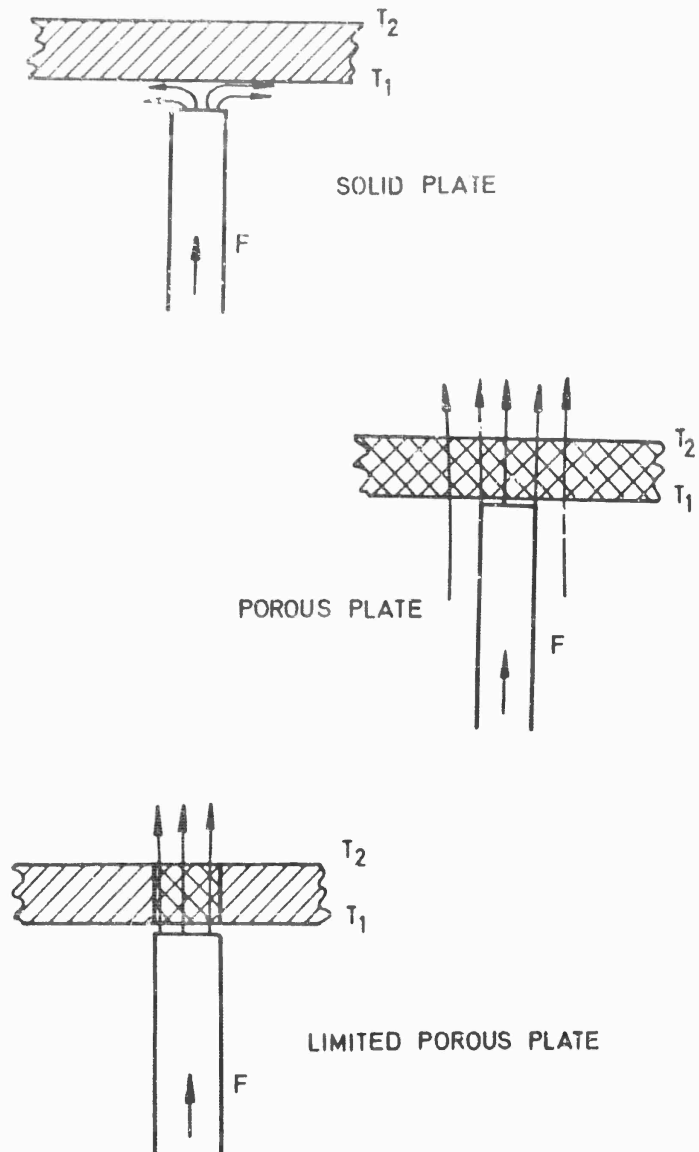


Fig. 5-7a Schematic setups for the measurement of pyrolysis rates

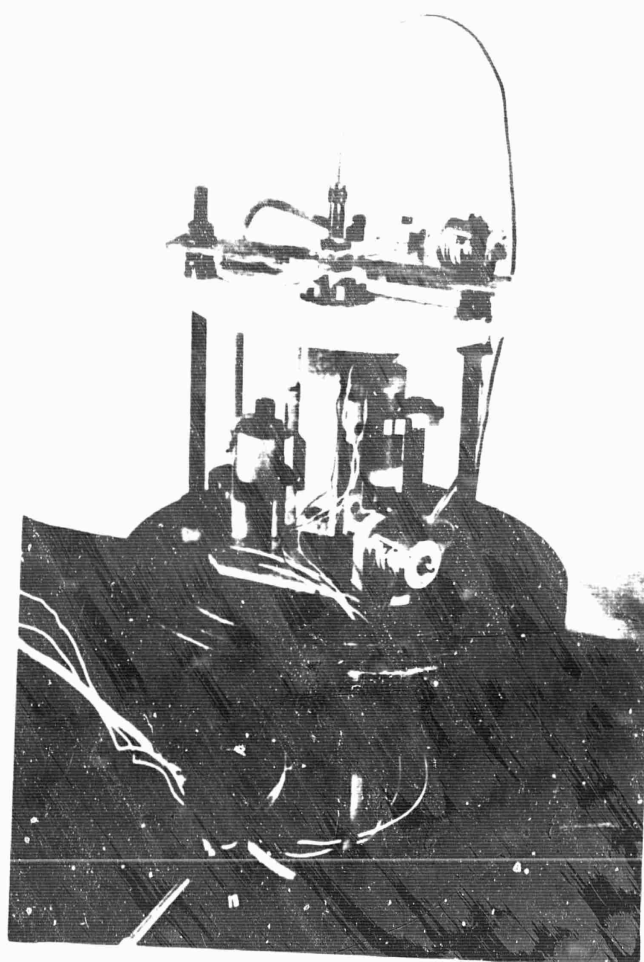


Fig. 5-7b Inside view of linear pyrolysis apparatus

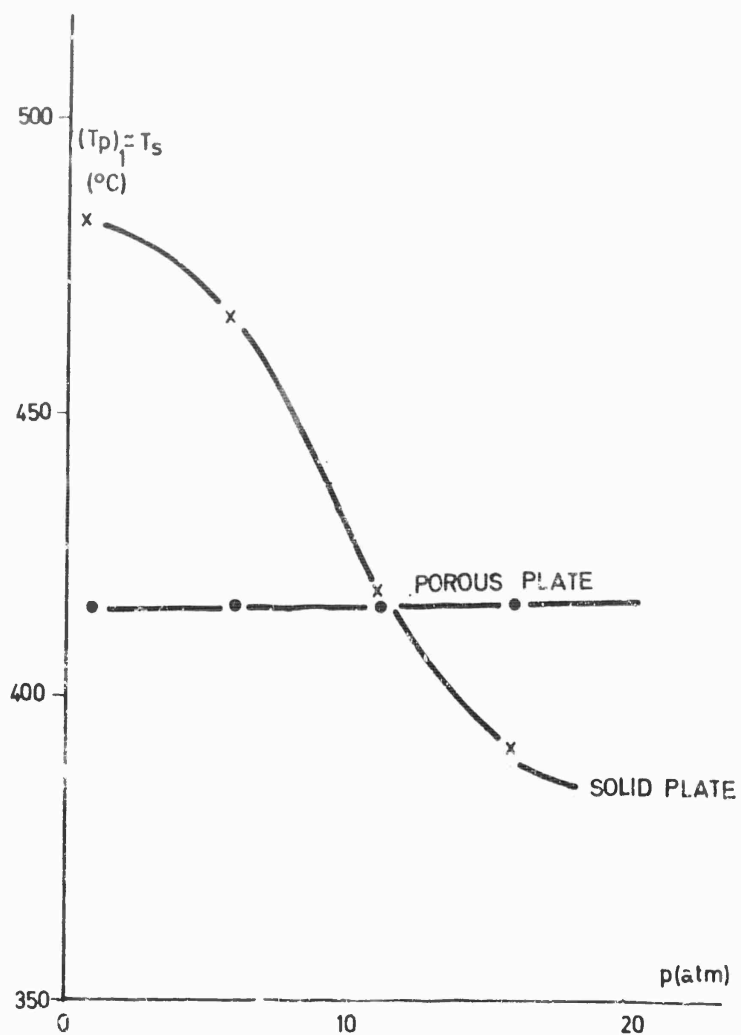
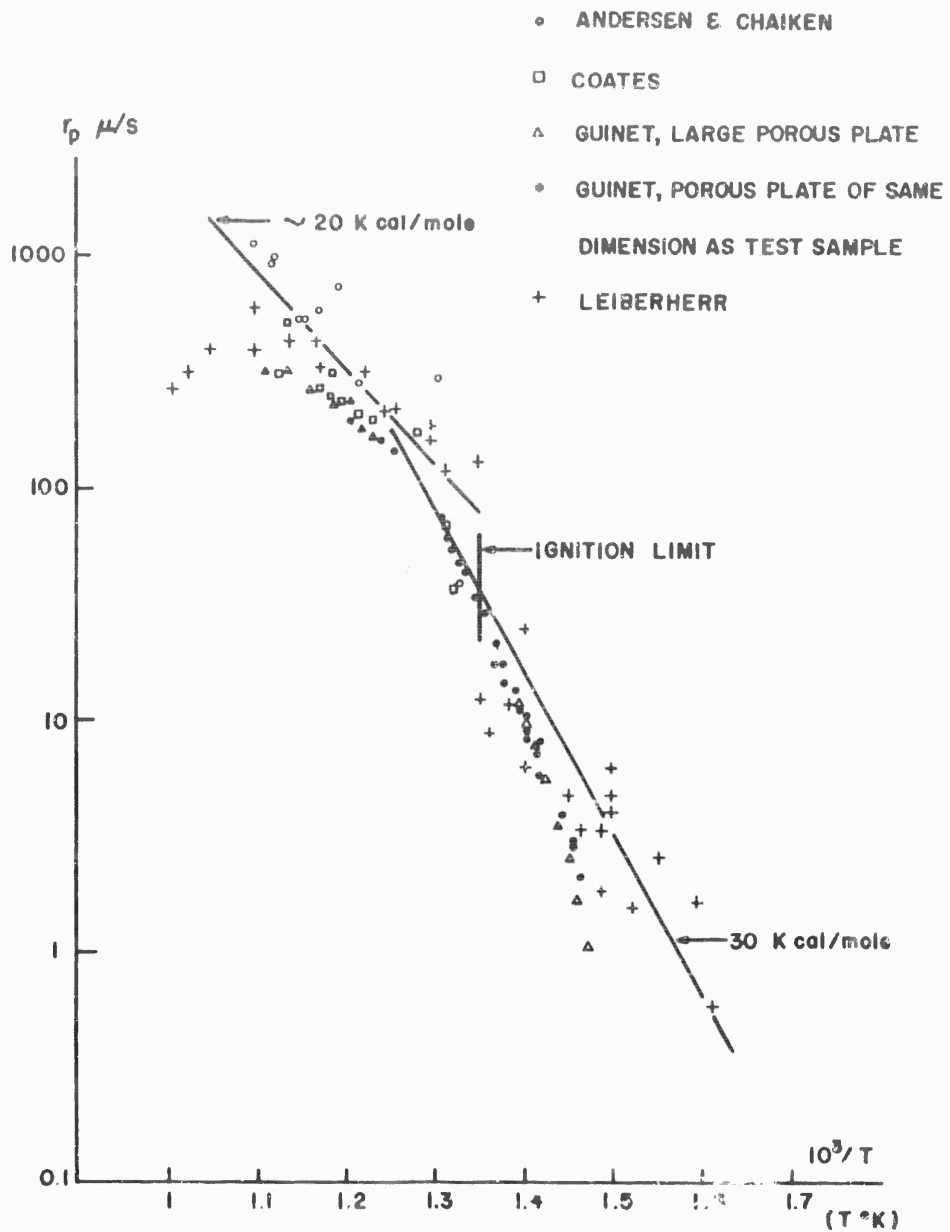


Fig. 5-8 Temperature versus pressure for a given pyrolysis rate

Fig. 5-9 Pyrolysis rate versus $1/T$

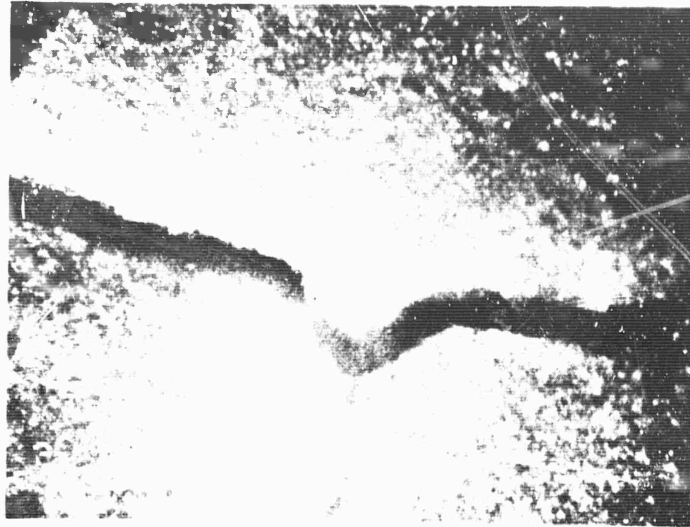


Fig. 5-10 Crack in A P sample after measurement of pyrolysis rate with a solid plate

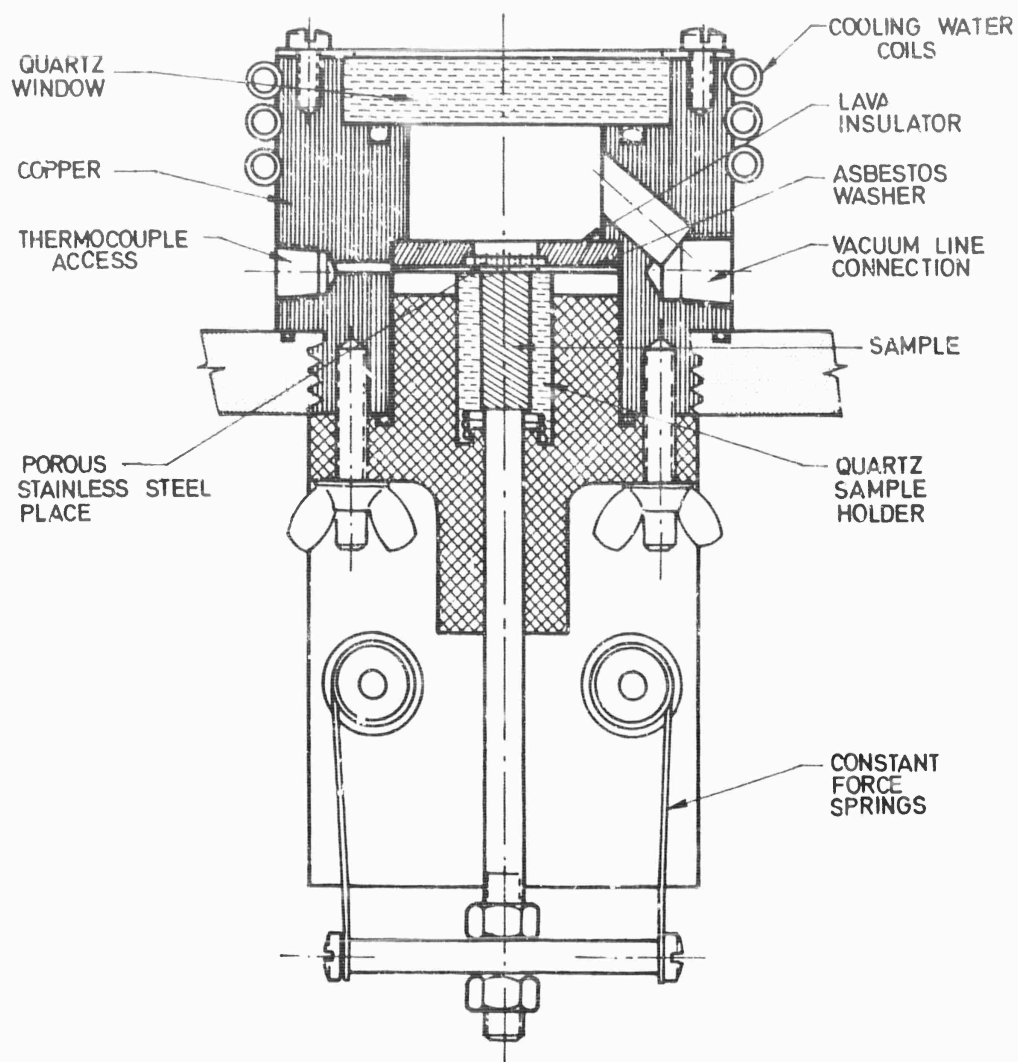


Fig. 5-11 Assembly drawing of porous plate holder and sample positioning mechanism (Coates)

Data obtained by Andersen with the solid plate and those obtained with porous plates are shown in Fig. 5-9, from which it can be seen that the porous plate produces the least scatter when the technique of temperature calibration is used. The porous plate limited in dimensions to those of the sample, is preferable to the large porous plate with a gas flow along the sample. In the determination of A.P. pyrolysis rates with the solid plate, instabilities have been observed at temperatures between 750°K and 800°K. These instabilities disappear when the porous plate technique of Guinet is used (see Section 3.1.2). When a solid plate is used, one also observes cracks in the A.P. sample which may modify the pyrolysis velocity to some extent (Fig. 5-10).

These few remarks indicate that there are advantages in using porous plate devices and also in developing accurate methods for determining the surface temperature.

A second technique has been developed by McAlevy and Hansel (9), who studied the pyrolysis velocity of a material in contact with hot gases; the apparatus is sketched in Fig. 5-12. Either solid or porous samples may be used; with porous samples it is possible to inject an inert gas or a gas contributing to the surface reaction. The surface temperature is determined by an optical method. This device has been used for the study of the pyrolysis of plastic materials such as polystyrene; the results are shown in Fig. 5-13. With a compact polystyrene material, McAlevy obtained curve No. 1 which is fairly close to Chaiken's curve No. 3 on polystyrene obtained by using a heated solid plate. The agreement is best for high temperatures. These results do however, differ considerably from those published by Chaiken in Ref. (10) (curve No. 4 of Fig. 5-13). McAlevy notes that his polystyrene was of a different age than Chaiken's and was obtained from a different supplier; he suggests that it would be useful to have a standard specimen available to each investigator.

Using porous polystyrene and injecting a neutral gas such as nitrogen displaces curve No. 1 to the right (curve No. 2). Although the curve profile is about the same, it is possible to obtain the same pyrolysis velocity for much lower temperatures. This difference may originate in the surface geometry, the heat transfer for a solid plate being different from that for a surface formed by the juxtaposition of small diameter spheres.

3.1.2. Results - The linear pyrolysis rate has been determined for many solid propellant constituents.

3.1.2.1. Fuels : The pyrolysis of fuels which do not lead to the formation of a carbon layer may be studied by this technique. Experimental results on such materials have been reported in Refs. (1), (11), (12) and (13). Two points of particular interest should be noted :

(a) In general, adding inert materials to the plastic fuel does not greatly affect the pyrolysis rate; at a given surface temperature, inerts decrease the pyrolysis rate slightly. As an example, the pyrolysis rate of stratyl containing an increasing percentage of aluminum powder (to levels commonly employed in metalized solid propellants) is shown in Fig. 5-14. A decrease in the pyrolysis rate is noticeable principally at high temperatures. The decrease occurs in such a way that in the Arrhenius expression for the pyrolysis rate, the activation energy is practically unchanged. Only the frequency factor is affected by the inert additive.

(b) The regression velocity of laminates of two plastic materials that have different pyrolysis rates, is very nearly that corresponding to the material with the lowest pyrolysis rate. The difference in height between the surfaces of the two materials decreases linearly as the temperature of the plate is increased.

3.1.2.2. Oxidizers : Until 1958, ammonium nitrate was the oxidizer whose pyroly-

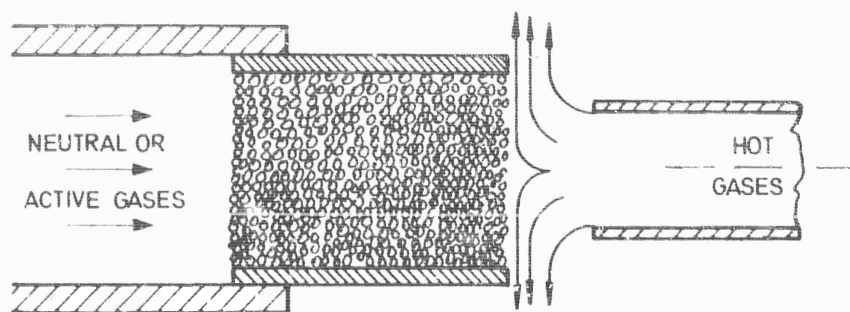


Fig. 5-12 McAlevy-Hansel hot gas-jet technique for pyrolysis studies

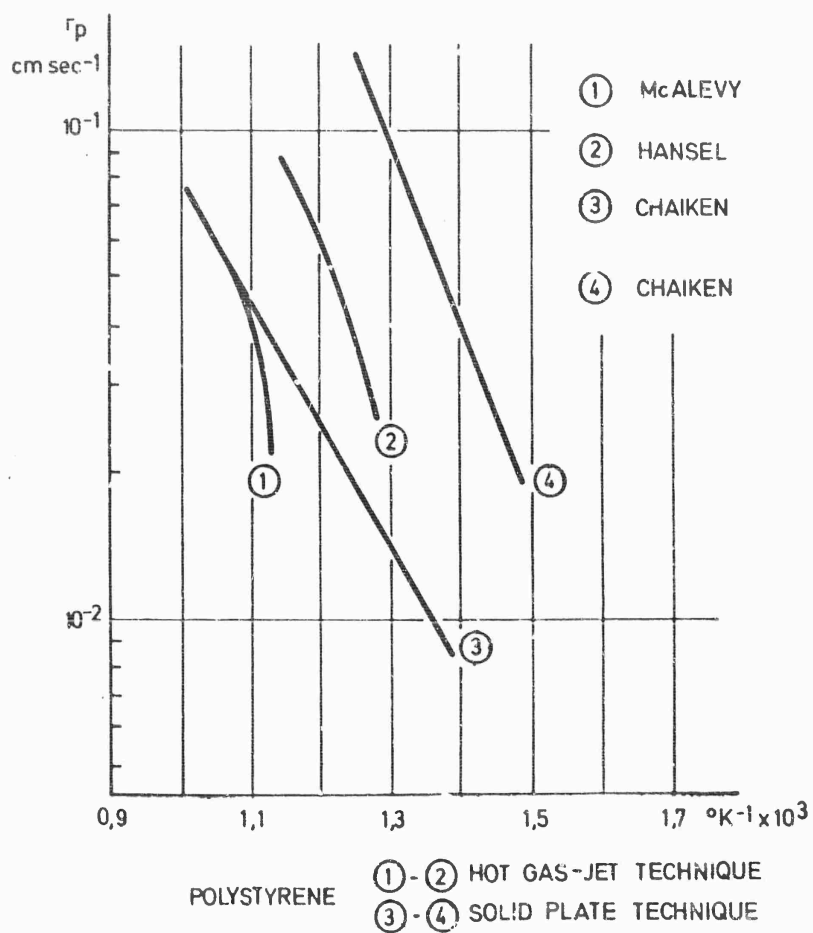


Fig. 5-13 Comparison of linear pyrolysis rates of polystyrene

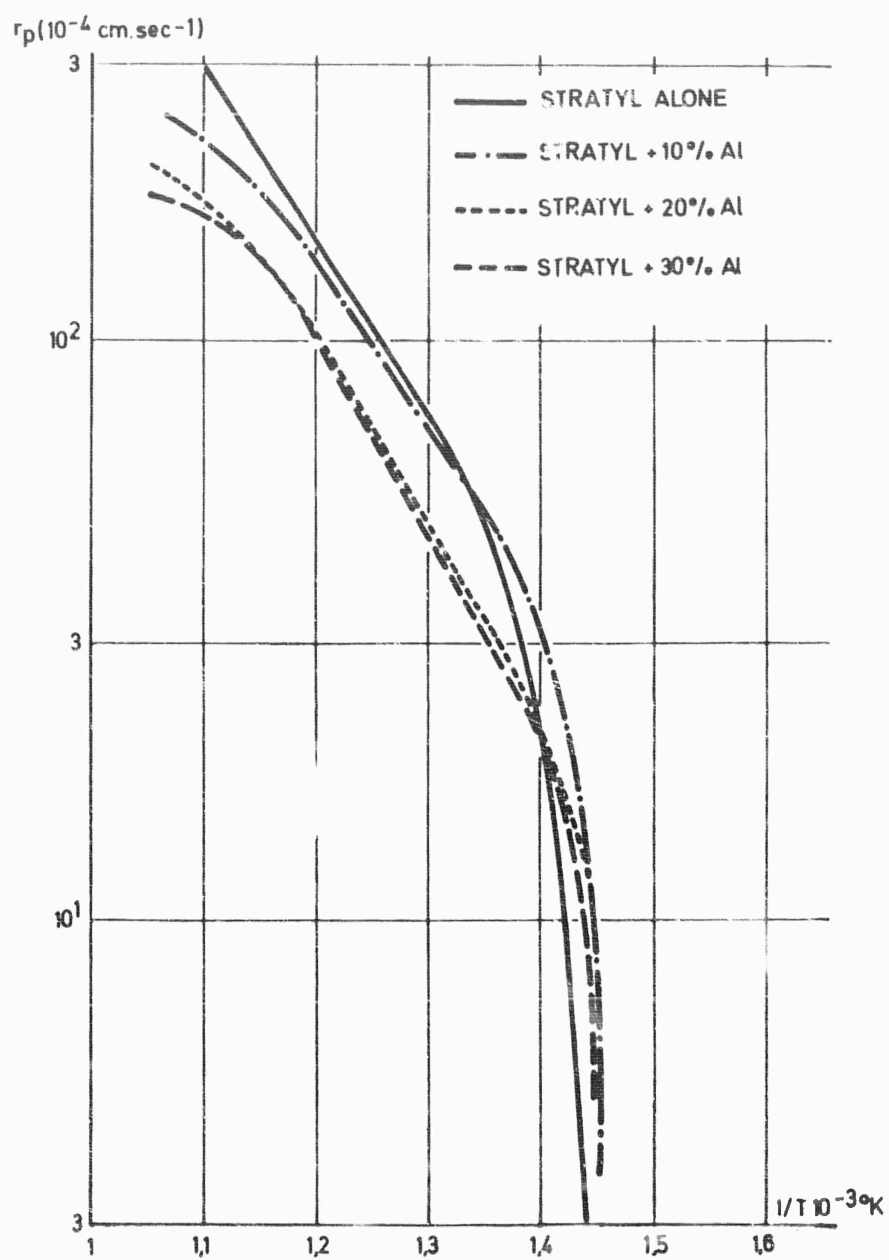


Fig. 5-14 Pyrolysis rates of Stratyl with several aluminum concentrations

sis rate received a great amount of study. More recently, many investigators have studied the pyrolysis of AP. The study of this substance is important because at present it is the most commonly employed oxidizer.

These recent studies indicate that there may be two pyrolysis domains. When $690^{\circ}\text{K} < T < 750^{\circ}\text{K}$, the pyrolysis rate measured experimentally by Guinet is :

$$r_p = 1.9 \times 10^{12} \exp(-50,000/R^{\circ}T_p)(\text{cm sec}^{-1}) ,$$

while that of Lieberherr exhibits an activation energy closer to 30,000 cal/mole. Although Guinet's results exhibit much less scatter than those of Lieberherr in this low-temperature regime, there may be a systematic error in the calibration technique by which the surface temperature was computed from the measured temperature on the downstream side of the plate. Lieberherr's activation energy of 30,000 cal/mole is consistent with the recent work of Jacobs and Russell-Jones who, on the basis of improved thermogravimetric results, developed an interpretation for the kinetics of the sublimation process :



which yielded this same activation energy. Lieberherr's experimental data extends to a sufficiently low temperature to provide a small range of overlap between the hot-plate measurements and the more classical (low temperature) thermal decomposition studies. Evidence is growing to the effect that at all temperatures below 750°K , the activation energy for gasification of pure AP is 30,000 cal/mole.

There appears to be a transition at a temperature of about 750°K . For higher temperatures, $750^{\circ}\text{K} < T < 900^{\circ}\text{K}$, the pyrolysis rate measured by Guinet is of the form :

$$\dot{r}_p = 3250 \exp(-20,000/R^{\circ}T) .$$

This formula yields lower rates than those published by Andersen [$r_p = 4600 \exp(-20,000/R^{\circ}T)$ or $r_p = 5.88 T \exp(-20,000/R^{\circ}T)$]. The results of Coates and of Lieberherr in the high-temperature regime generally lie between those of Guinet and those of Andersen. One of Andersen's latest reports gives 22,000 cal/mole for the activation energy (6); the correction is intended to account for the difference between the plate temperature and the surface temperature of the sample, which is not negligible in the high-temperature domain. An estimate given in Ref. (5) for this correction raised the activation energy to 30,000 cal/mole. Thus, it is conceivable that the underlying surface gasification process exhibits the same activation energy and possesses the same rate-determining step in both the high-temperature and low-temperature regimes. An exothermic gas-phase reaction, observed experimentally in the high-temperature domain (beyond the "ignition limit" identified in Fig. 5-9), may also have a bearing on the apparent low activation energy at high temperatures.

When the solid plate was used, instabilities appeared at temperatures between 750°K and 800°K . These instabilities involved fluctuating emission of gases at the plate and produced variations of the plate temperature and irregularities of the surface geometry, which led to widely scattered experimental results for the pyrolysis rate. This phenomenon may be similar to that observed by Cantrell (7) for solid CO , but alternatively it may be associated with intermittent ignition phenomena. The solid-plate technique of increasing the applied force to bring the surface temperature of the sample near the temperature of the plate does not eliminate the instabilities; increasing the applied force decreases the thickness of the gaseous film, producing an increase in the lateral velocity of the gases which may be a source of experimental error. The instabilities disappeared for the porous plate used by Guinet.

In addition to AP other oxidizers are of interest, such as nitronium perchlorate NO_2ClO_4 , hydrazine perchlorate $\text{N}_2\text{H}_4\text{HClO}_4$ (14) or hydrazine diperchlorate $\text{N}_2\text{H}_6(\text{ClO}_4)_2$. Although the decomposition of these substances is being studied in several laboratories, few results have been published. Publications of this material are just beginning to appear (15). We might mention here that these substances break down into components at temperatures below that of AP. For instance, hydrazine perchlorate decomposes between 180°C and 240°C , exhibiting an activation energy for thermal decomposition of the order of 23,000 cal/mole. Above 250°C , hydrazine perchlorate decomposes rapidly and explodes. Catalysts such as MnO_2 and Cu_2Cl_2 lower the temperature of explosive decomposition.

3.1.3. Importance of Pyrolysis Measurements - Wilfong, Penner and Daniels have introduced the idea that the regression rates of solid propellants are determined by the thermal decomposition of their components. It is possible to assume that each propellant constituent has a regression rate measurable by experiments of the type discussed above. Then, if we consider for example a two-component propellant, we are led to the conclusion that the surface temperature T_{s1} and T_{s2} of each component must be different, in order for a steady state to be established in which each constituent regresses at the same rate :

$$r_b = B_1 \exp(-E_1/R^\circ T_{s1}) = B_2 \exp(-E_2/R^\circ T_{s2}) .$$

The preceding 'two-temperature' hypothesis might be acceptable if the flame were in a plane parallel to the propellant surface; experimentally, it applies very well to studies of laminate pyrolysis. Unfortunately, the model is violated by the flame geometry, in heterogeneous solid propellants. Therefore, in the combustion model one should not assume flames parallel to the surface. The geometries of flames are determined by the heterogeneity of the propellant.

Although the two-temperature hypothesis is not always acceptable, measurements of the pyrolysis rates of the propellant components are of great interest because these results may yield the frequency factor and the activation energy of the gasification reactions, and also in some cases permit further details of the reaction process in the zone adjacent to the surface to be ascertained.

3.2. Deflagration Rates of Certain Oxidizers

Certain components of heterogeneous solid propellants behave as monopropellants, exhibiting self-sustained surface regression under appropriate conditions. For these components, exothermic reactions in the gas phase transfer enough energy back to the surface to cause gasification. Studies of these deflagrations have been made principally with AP; the deflagration velocity was determined for various pressures and temperatures. Figure 5-15 shows the deflagration velocities, as functions of pressure, obtained by various investigators (16-19). The various results agree fairly well, in view of differences in the sizes of the AP elements used for the fabrication of the samples and in view of the differing experimental conditions.

Adams and Irvin each correlated their results by an equation of the form $r_d = c p^n$. Irvin found two combustion regimes with a transition at a pressure of 300 atm. Above 300 atm, the observed exponent of p was of the order of 1.75. This rapid increase of the deflagration velocity was attributed to cracks in the grain, which may arise from either the pressure level or the heat flux.

Shannon has made a detailed study of the effect of AP grain size and temperature on the deflagration rate. His results are shown in Fig. 5-16. The mean diameter of the AP grains has a measurable effect on the deflagration velocity; the law obtained is of the form :

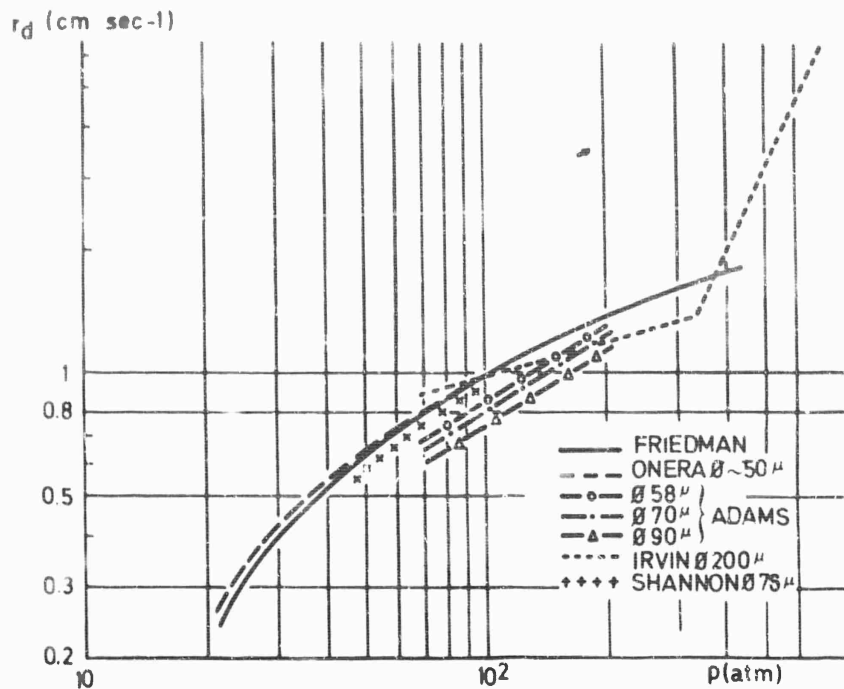


Fig. 5-15 Comparison of results on deflagration velocities of AP, as a function of pressure

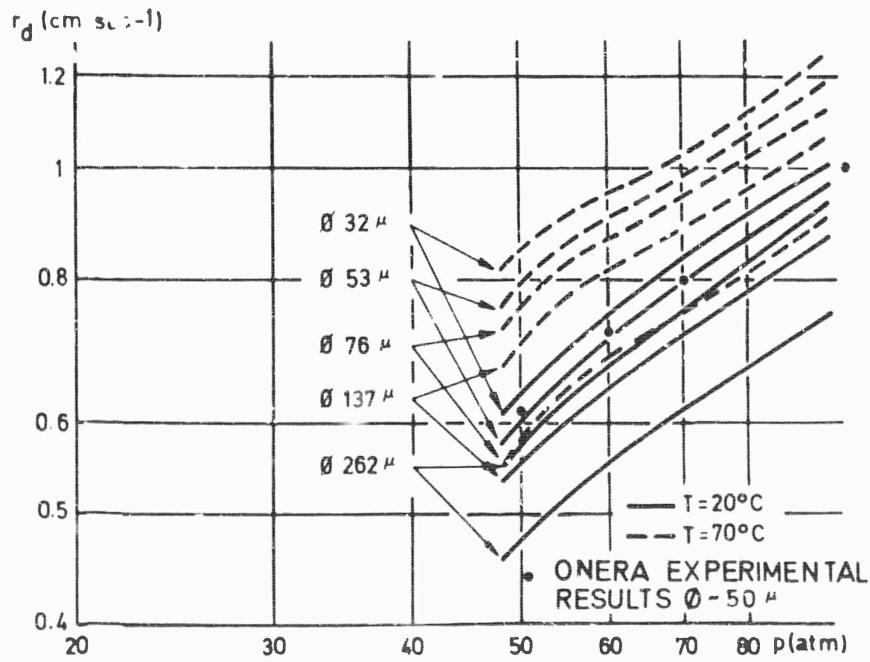


Fig. 5-16 Deflagration velocity of AP (Shannon)

$$1/r_d = K_1 d + K_2,$$

where d is the sphere diameter employed in manufacturing the AP strands. The initial temperature of the AP affects the deflagration velocity appreciably.

In order to explain his empirical results, Shannon postulates that the spherical AP crystals regress linearly and equates the total combustion time of a crystal of diameter d to the sum of the ignition time and the propagation time for the deflagration. The combustion of compressed AP spheres is complex, however, and the linear regression which is characteristic of strand experiments is not observed. We illustrate in Fig. 5-17a the variation with time of the geometry of a sphere ignited from the top. One observes a fast propagation of the deflagration toward the center of the sphere because the outer surface is cooler and therefore its decomposition is slower. The surface decomposition geometry of a cylinder is shown in Fig. 5-17b.

The effect of catalysts on the AP deflagration rate has been studied by Scurlock and Friedman (16), (20) (see Fig. 5-18). The results obtained from such investigations depend on whether the AP is pure or is embedded in a fuel binder. To show the effect of composition of adjacent materials, small strands of double composition have been developed at ONERA (Fig. 5-19). The upper part is made of pure AP and the lower part of AP containing a catalyst, which is copper chromite in the particular microphotograph shown in Fig. 5-19. With these samples it is possible to obtain in one experimental run the deflagration velocity of AP alone and of AP incorporating a catalyst. In particular, for concentrations where it produces an acceleration effect on the combustion velocity, the copper chromite exerts the opposite effect with AP alone; we observe extinction when the deflagration reaches the catalyst-containing oxidizer. Copper chromite is an effective catalyst only if the surface temperature is sufficiently high. This same technique has been employed to study AP containing aluminium; in this case too, extinction of the deflagration occurs when transition is reached. For this reason the catalyst must be studied under conditions that approximate as closely as possible the conditions expected in application. The study of AP deflagration rates is of importance because for certain pressure levels, the combustion velocity of the solid propellant appears to be controlled by the AP deflagration velocity.

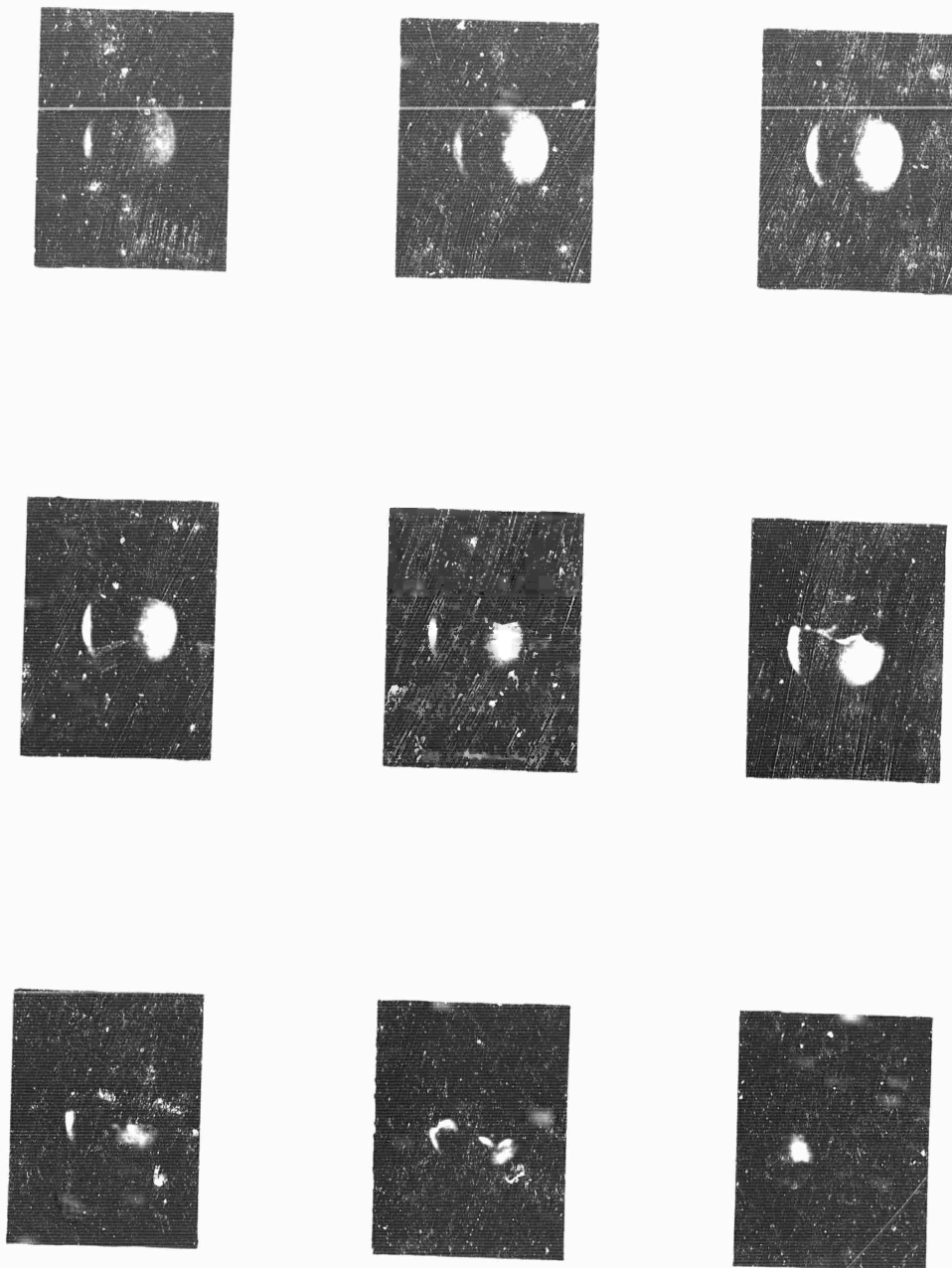
4. Proposed Model Experiments for the Analysis of the Mechanism of Heterogeneous Solid Propellant Combustion

As we have pointed out, the study of propellant components alone provides physico-chemical data, but it does not provide information on the mechanism of the fuel-oxidizer combustion processes in heterogeneous propellants.

4.1. Combustion of Oxidizer Spheres in a Gaseous Fuel Stream

In order to study the combustion of the oxidizer under conditions approximating those found at the surface of the solid grain, measurements have been made of the regression rate of oxidizer spheres placed in a flowing gaseous fuel. The crystals of the oxidizer within the propellant can be treated as spheres progressively emerging at the surface as a result of the pyrolysis of the plastic binder.

The experimental set up (21) consists of placing a stationary sphere of oxidizer in a flowing gaseous fuel. Several supports for the spheres have been tested. The best results were obtained by allowing the sphere to rest on a platinum wire gauze. The sphere was ignited at the top by means of an electrically heated wire. The combustion was photographed with a motion picture camera to obtain the time evolution of the shape of the sphere. By this procedure, the combustion of the oxidizer spheres can be analyzed as a function of the (a) nature of the oxidizer, (b) nature



TIME INTERVAL: 0.1sec-/P=40atm

Fig. 5-17a Combustion of an AP sphere in nitrogen



Fig. 5-17b Combustion of an AP parallelepiped in nitrogen
 $P=40\text{ atm}$

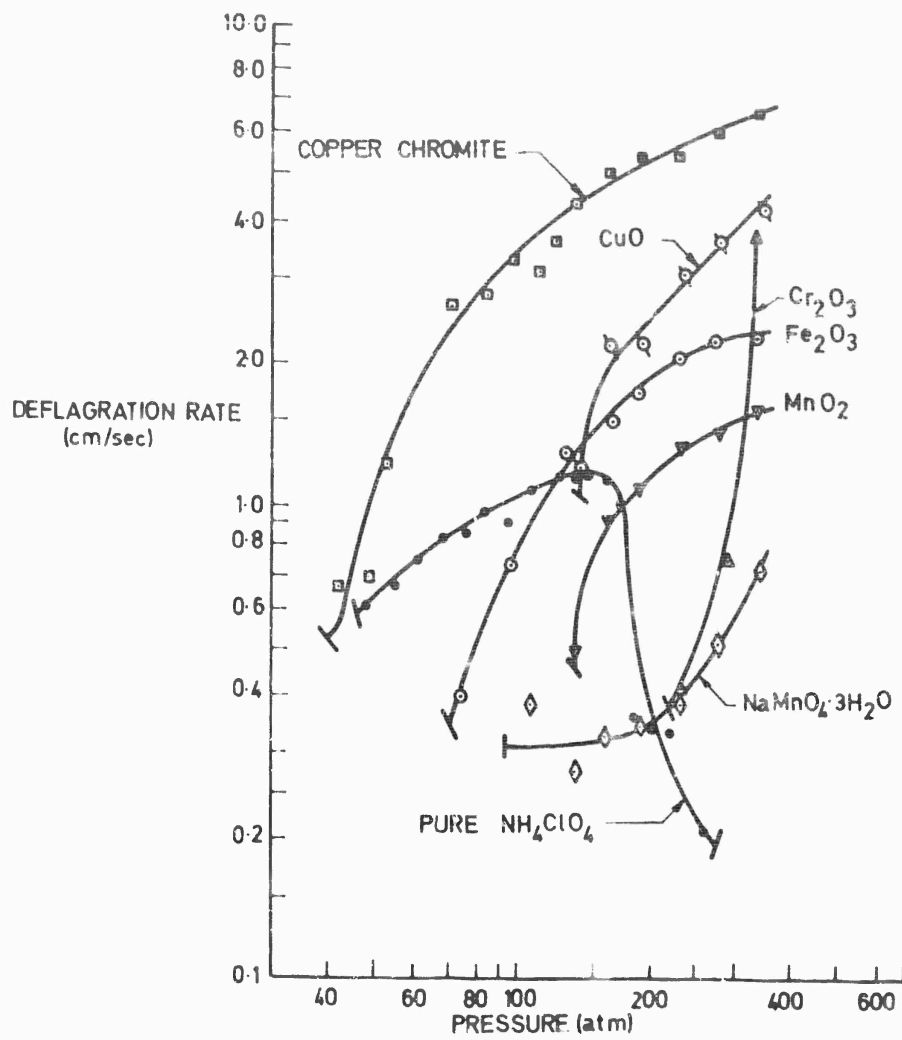
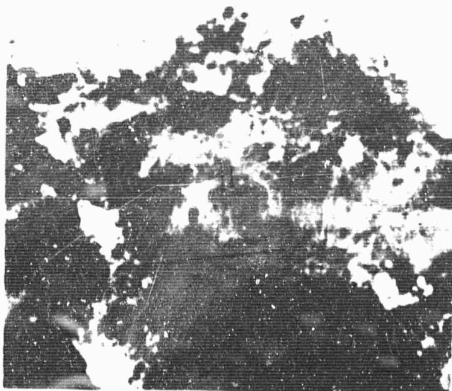


Fig. 5-18 Rate of deflagration of "as received" ammonium perchlorate with three percent additions of various catalysts (16)

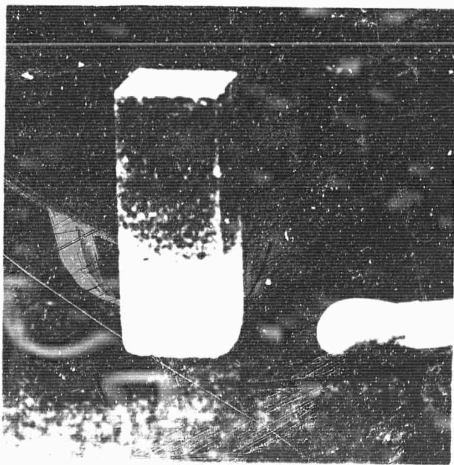


AP + Cu CHROMITE



AP + Al

TRANSITION AREA
A P AT TOP



TRANSITION AREA
A P AT TOP

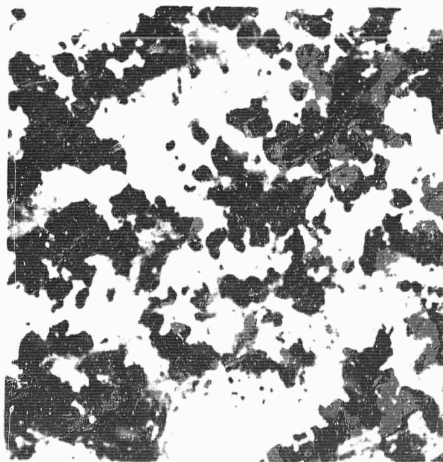


Fig. 5-19 Microphotographs of a two-component rod

of the fuel, (c) geometry of the oxidizer, (d) temperature of the solid and of the gas, (e) gas velocity, (f) pressure.

In addition to AP spheres of other oxidizing materials, such as potassium perchlorate, ammonium nitrate and potassium nitrate, have been studied at ONERA. The most reproducible results were obtained with AP. With potassium perchlorate for instance, combustion starts normally but stops after some time because the surface of the sphere becomes covered with a layer of potassium chloride. We shall describe only the results obtained with AP.

The spheres are fabricated by compression. To facilitate the removal of the spheres from their molds, the surface of each mold is polished to optical specifications. Spheres of various diameters have been constructed by this technique.

The nature of the fuel gas affects the flame flashback; ignition takes place at the top of the sphere and the resulting flame progresses at constant velocity towards the base of the sphere. This flame flashback may be thought of as approximating the pyrolysis of the plastic binder in a real solid propellant grain. The flashback velocity is high, reaching a few cm sec^{-1} , when the gaseous fuel is hydrogen. With propane or ammonia, the flashback velocity is about 0.6 cm sec^{-1} .

The structure of the flame varies greatly with the nature of the gas as can be seen in the photographs of Fig.5-20. With propane, we observe a decomposition flame and two diffusion flames, while a diffusion flame alone appears with ammonia. In hydrogen there is a thicker and more homogeneous diffusion flame.

We can use the maximum horizontal diameter d to characterize the time evolution of the shape of the sphere. For propane and ammonia, the dependence of d on time can be written in the form :

$$d^2 = d_0^2 - K_2 t$$

(the square of the diameter is proportional to time). This dependence is illustrated by the curves of Fig.5-21a. The constant K_2 increases as the flow velocity of the fuel gas increases.

For hydrogen and hydrogen-nitrogen mixtures, the time dependence of d is given by:

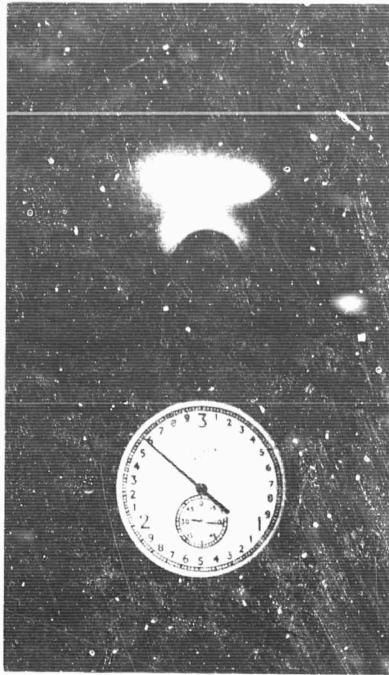
$$d^3 = d_0^3 - K_3 t ,$$

(the cube of the diameter is proportional to time, Fig.5-21b). The constant K_3 again increases as the gas velocity is increased. The constants K_2 and K_3 depend on the initial diameter of the sphere (Fig.5-21c), especially K_3 which is proportional to the diameter, thus implying that the complete law for hydrogen is of the form :

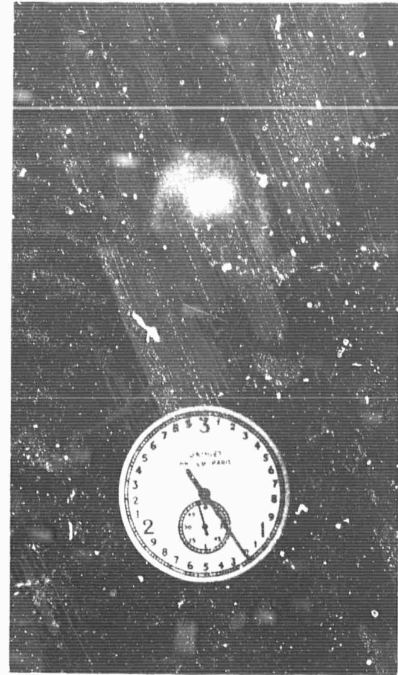
$$d^3 = d_0^3 - K'_3 d_0 t .$$

The combustion constants K_2 and K_3 depend on pressure. The experimental results are correlated by a pressure exponent of 0.57 for propane and 0.64 for hydrogen (Fig.5-21d). These exponents are very close to those obtained in pure AP deflagration tests. The exponent seems somewhat high for diffusion phenomena. The maximum pressure during testing was 16 atm. It would be interesting to obtain the numerical value of this exponent in the operational domain of solid propellants (pressures above 20 atm).

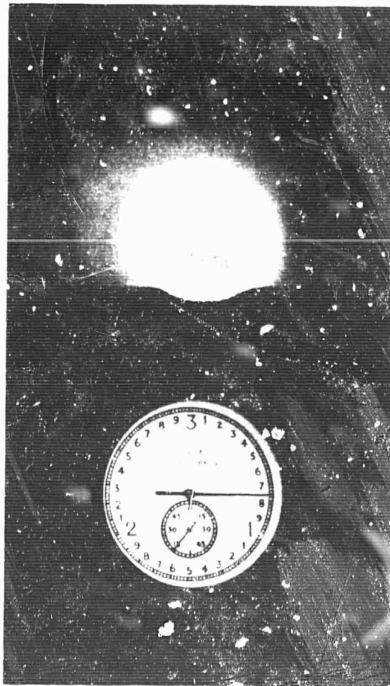
The constants K_2 and K_3 are also sensitive to the temperatures of the solid and of the gas. When the gas is at the same temperature as the solid, we observe for



PROPANE



AMMONIA



HYDROGEN

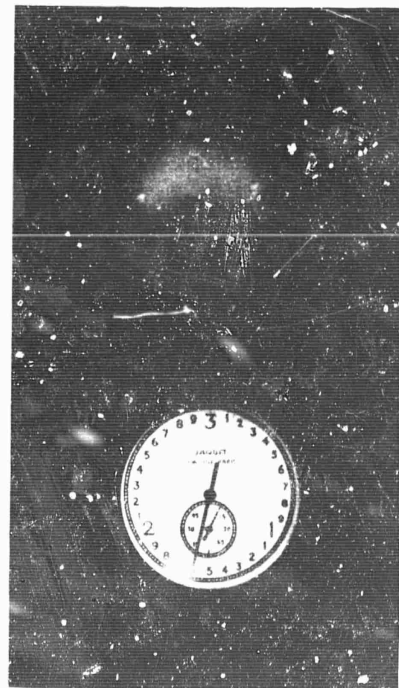
HYDROGEN + NITROGEN ($y_{H_2} = 0.066$)

Fig. 5-20 Combustion of AP spheres in various fuels

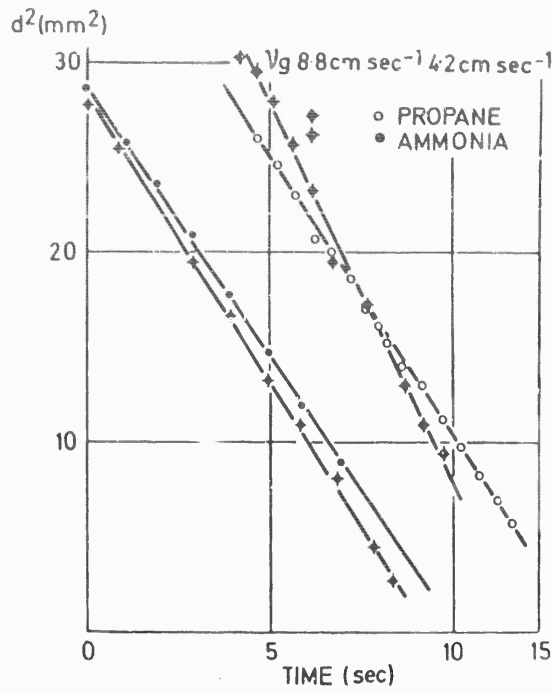


Fig. 5-21a Variation of square of sphere diameter versus time

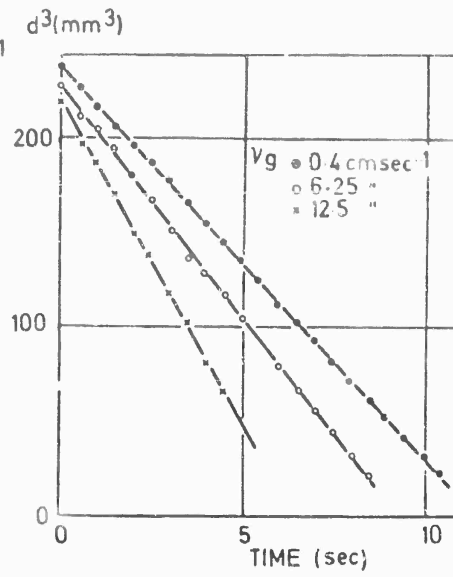


Fig. 5-21b Variation of third power of diameter versus time (hydrogen)

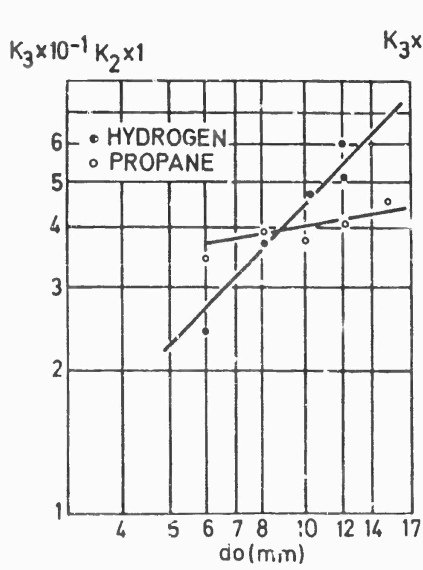


Fig. 5-21c Influence of initial diameter

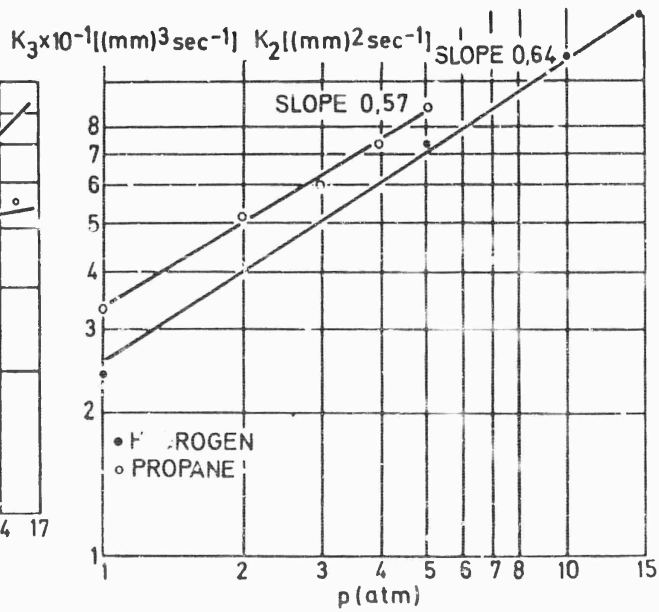


Fig. 5-21d Influence of pressure on combustion constants

propane a gradual increase of the combustion constant as the temperature is increased from -35°C to 20°C , and then no appreciable change in the constant for temperatures up to 100°C .

Catalysts modify the combustion constant. For example, K_2 goes from $3.5 \text{ mm}^2 \text{ sec}^{-1}$ to $5 \text{ mm}^2 \text{ sec}^{-1}$ when 1 per cent of copper chromite is added to AP. On the other hand, aluminum has little effect on the value of the combustion constant; aluminum burns adjacent to the oxidizer surface (Fig. 5-22) and also in the diffusion flame surrounding the sphere.

The conclusions which can be drawn from these tests are:

a) In determining the AP regression rate, it is not possible to neglect the effect of the diffusion flame and to consider only the decomposition zone of AP near the surface. With some fuels, the decomposition zone disappears completely as a result of the diffusion phenomena, the fuel being able to reach locations very near the surface. The importance of diffusion phenomena is indicated by the form of the combustion laws obtained with the AP spheres. Moreover, if the decomposition phenomena were dominant, there would be no effect of the composition of the gaseous atmosphere on the regression rate of the solid.

b) If one adopts combustion laws of the general form :

$$d^{\alpha} = d_0^{\alpha} - K d_0^{\beta} p^n t$$

for a set of perchlorate spheres, then the total mass per second flowing out of a sphere is given by a formula of the form :

$$\dot{m} = \varphi \rho_0 d^{\beta - \alpha + 3} p^n$$

in which φ is a constant including a form factor and ρ_0 is the density of the oxidizer. From the experimental results, $\beta - \alpha + 3 \approx +1$.

c) So far as possible, the gaseous fuel velocities have been chosen to exhibit the same Reynolds number during testing as in the actual combustion of AP crystals in solid propellant grains. With hydrogen, the Reynolds numbers are of the order of 10, while they reach 100 with propane. The value of about 0.6 for exponent n may be a consequence of the value of the Reynolds number used in these tests.

d) The above experiments have been carried out at moderate pressures not exceeding the pressure limit of deflagration of AP ($p_{\text{limit}} \approx 20 \text{ atm}$). Ignition of

the top of the sphere at higher pressures leads to a combustion in parallel planes, as indicated in Fig. 5-23. A decomposition of the perchlorate occurs first, then a combustion of the oxidizing gases generated by the decomposition with the fuel gases. These high pressure experiments show the importance of the decomposition process. It must be noted however that the regression rate of the sphere is larger than the rate obtained during decomposition in a nitrogen atmosphere.

e) The combustion of AP parallelepipeds in a fuel atmosphere is similar to the process which occurs with spheres. As an example Fig. 5-24 shows the burning rate of AP strands in methane at various pressure. The flame propagates along the strand at a velocity which decreases as the pressure increases. Above a certain pressure, combustion in planes parallel to the surface takes place.

4.2. Porous-Core Burner

The combustion of an AP sphere in a gaseous fuel stream represents one of the

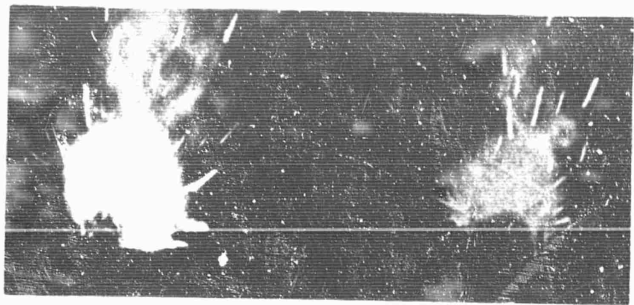


Fig. 5-22 Combustion of an AP sphere containing aluminum in a gaseous fuel atmosphere

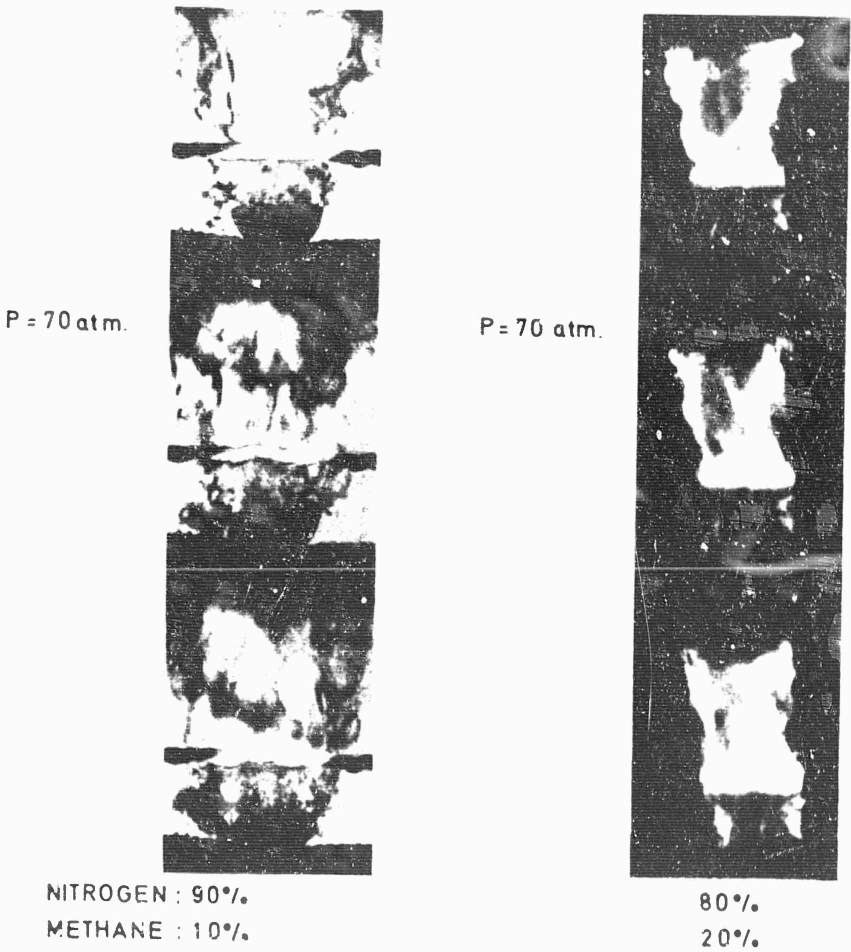


Fig. 5-23 Combustion of AP sphere at high pressure

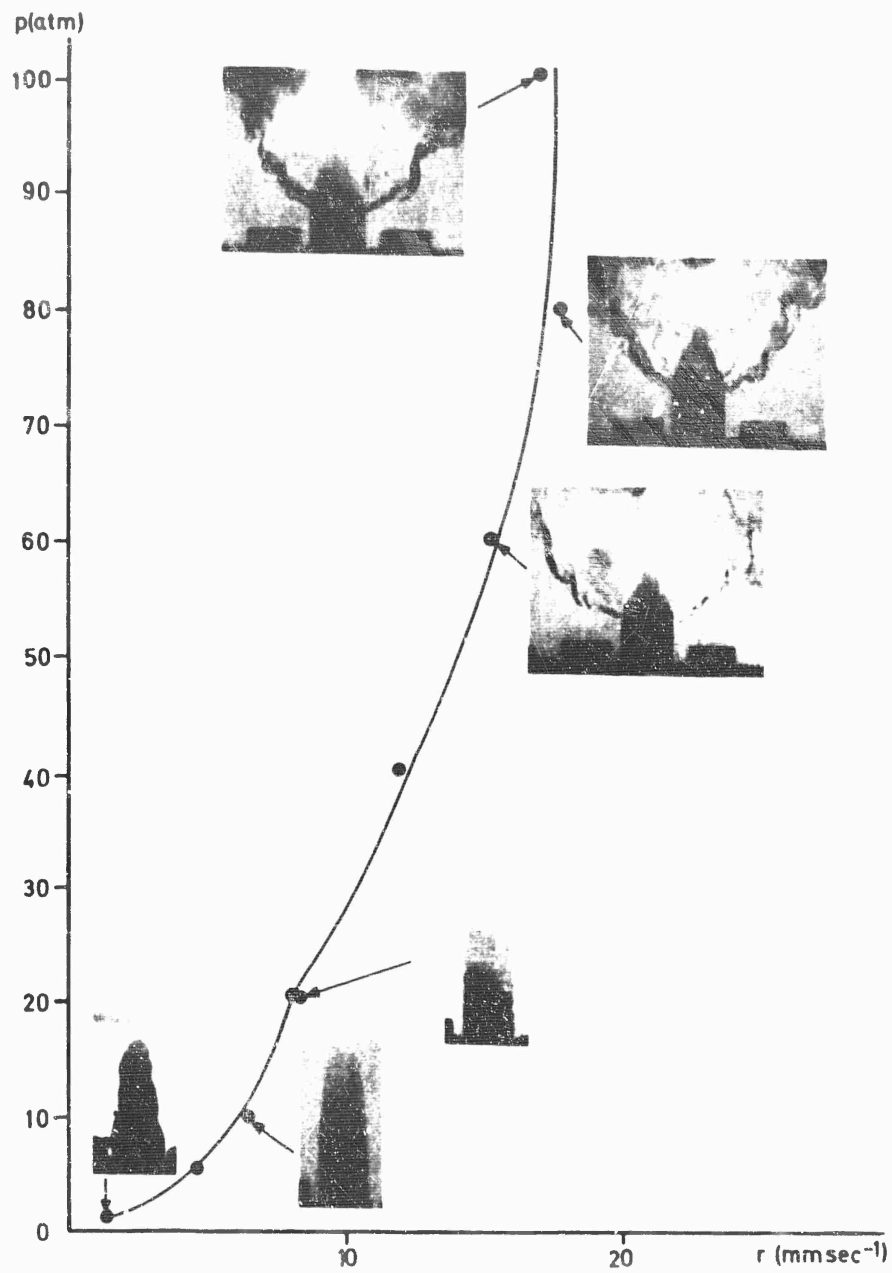


Fig. 5-24 r versus pressure --AP strands in pure methane

simplest models we can imagine for solid-propellant combustion. For this reason some investigators have tried to work with more elaborate models in an effort to approximate the real conditions more closely.

A hybrid burner, containing only one of the propellant components (either oxidizer or fuel) in the solid phase, represents an attempt to develop such a model. The dimensions of the solid granules are intended to be comparable with the heterogeneity scale of the composite propellant. The burner used is a metal or quartz tube packed with a fine powder of oxidizer or fuel. The powder grains are agglomerated to produce a porous mass through which a gas can be passed. After ignition at the top of this burner, combustion propagates inside at a rate which depends on parameters such as the composition and mass flow rate of the gas, the composition and geometry of the solid, pressure, etc. . . . In this simplified experimental model, only one solid component is present, thereby reducing the number of parameters (22) (23). It is also possible to vary the mixture ratio by adjusting the gas mass-flow rate.

Burger and Van Tiggelen (22) have studied the combustion of polymethacrylate grains of dimensions between 0.25 and 0.54 mm in oxygen and nitrogen streams. The maximum regression rate occurs at stoichiometric conditions. Hydrogen added to the gaseous oxidizer increases the regression rate, while carbon oxide acts as an inhibitor.

The results of greatest interest were obtained with porous solid AP oxidizer and fuel gases. We note first of all, that the maximum AP regression rate occurs at the stoichiometric mixture ratio (Fig. 5-25). The value of the maximum regression rate depends on what fuel gas is used; the mass-flow rate per unit area ($\dot{m} = \rho v$) is 0.11 g.cm⁻² sec⁻¹ with propane and 0.315 g.cm⁻² sec⁻¹ with hydrogen. The mass-flow rate per unit of area is therefore three times higher with hydrogen than with propane. This effect also exists for AP spheres but it is less pronounced. The mass-flow rate values quoted above correspond to tests carried out at atmospheric pressure, under which conditions the theoretical mixing height is of the order of the AP grain diameter. Therefore, the flame is partially heterogeneous even though the pressure is low (25). Burger and Van Tiggelen believe that it is not possible to represent these heterogeneous phenomena by a diffusion flame model following the macroscopic diffusion flame laws. Therefore, they sought a relationship between the oxidizer regression rate and the propagation velocity v_o of a premixed flame by treating the hydrochloric acid as a diluent or as an inhibitor. The maximum mass-flow rate per unit area \dot{m}_M of AP has therefore been corre-

lated with a parameter $W = \frac{v_{OM} n_i/n_f}{\sqrt{X_{HCl}}}$ in which v_{OM} is the maximum flame

speed of a premixed combustible gas, X_{HCl} is the molar concentration of hydrochloric acid, and n_i and n_f are the numbers of moles at the beginning and at the end of combustion. A good correlation between \dot{m}_M and W was obtained for various fuels (Fig. 5-26). Although this correlation may be applicable at low pressures, where chemical phenomena are predominant for heterogeneous propellants, nevertheless at high pressure, the flame speed depends only weakly on pressure ($v_o \propto p^{\alpha/2-1}$, α being the reaction order) so that the relationship between $\dot{m}_M(p)$ and $v_o(p)$ might change considerably when the pressure increases.

The influence of pressure on burners of this type has been studied by McAlevy and Kiczek (23), (24). When the fuel flow rate is small ($\phi \sim 0.5$), the pressure exponent is close to 0.9, while for mixture ratios near stoichiometric ($\phi = 1$), the exponent is of the order of 0.5, which is the same as that obtained with single AP spheres (Fig. 5-27).

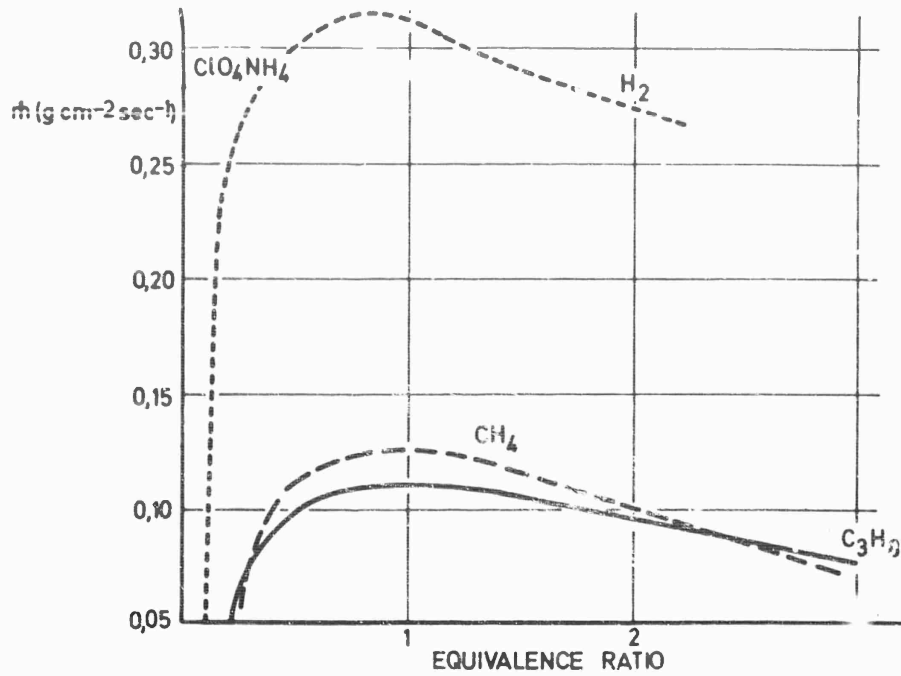


Fig. 5-25 Variation of AP mass flow rate versus equivalence ratio [d_{AP} 250 to 540 μ]

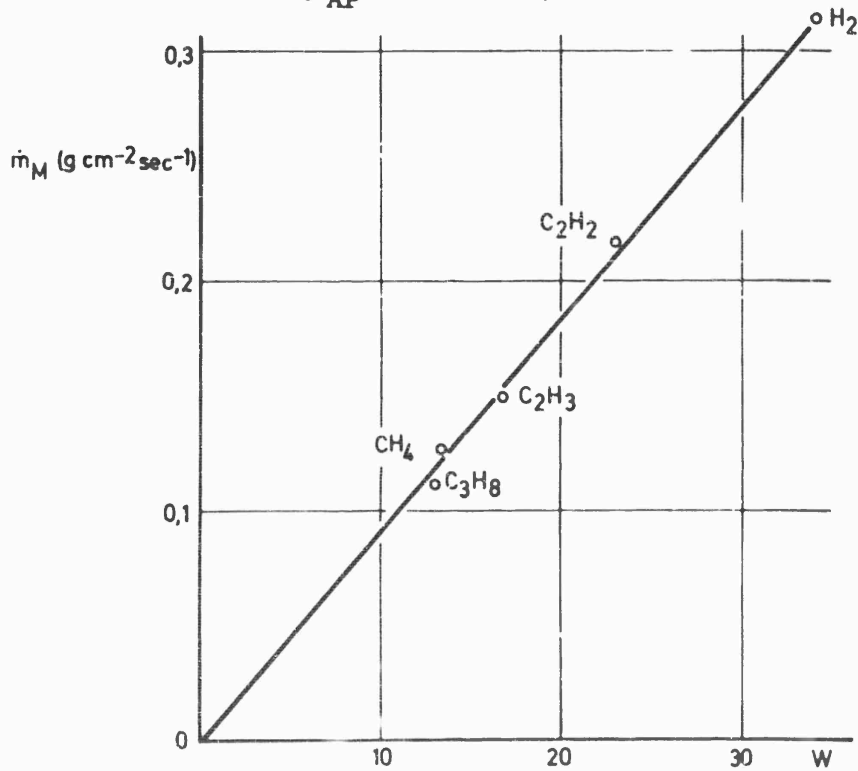


Fig. 5-26 Variation of mass flow rate versus W , with an equivalence ratio = 1, for several gaseous fuels

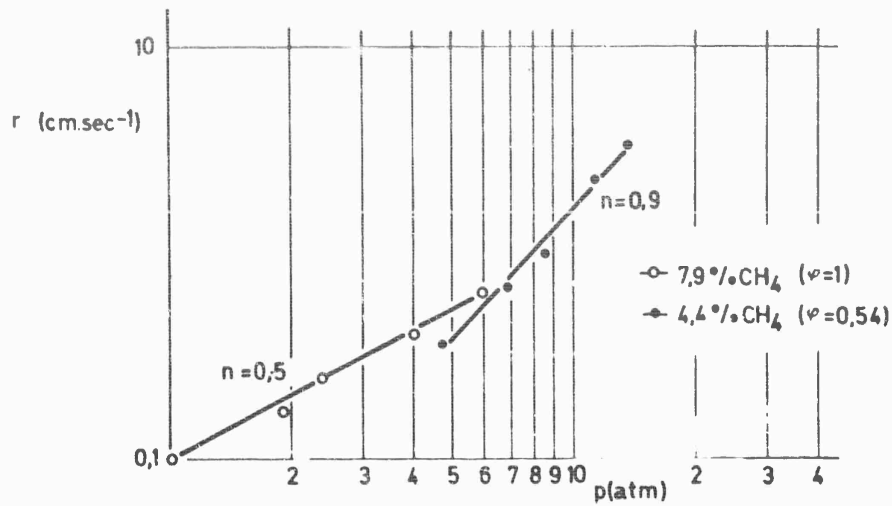


Fig. 5-27 Deflagration velocity of AP versus pressure at two fuel flow rates

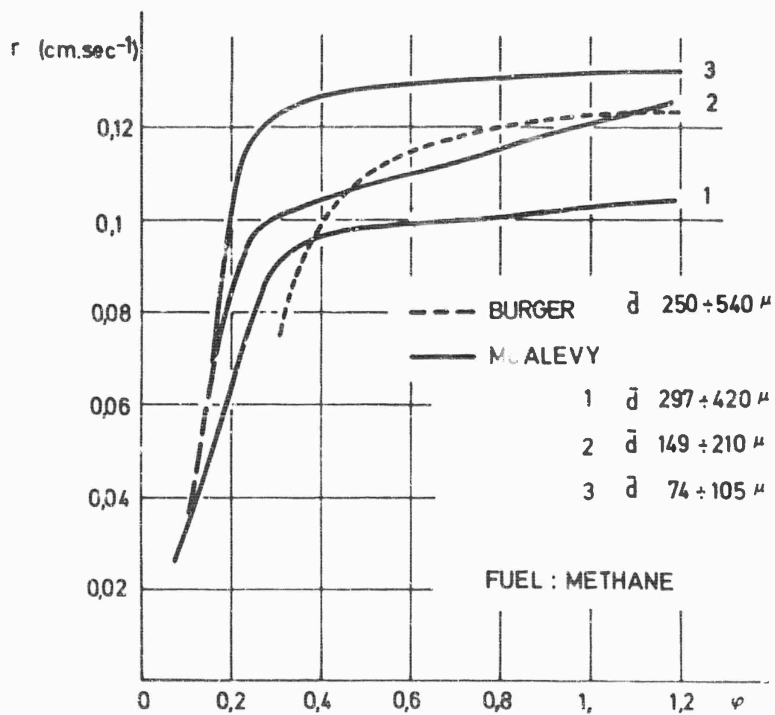


Fig. 5-28 Influence of AP granulometry on regression rate ($p = 1 \text{ atm}$)

Many fuels have been studied in liquid or gas phases (26) at atmospheric pressure. The effect of the AP grain size has received little attention. Fig. 5-28 shows the regression rates obtained for three different grain sizes (27); as with solid propellants, the velocity increases when the mean diameter of the crystals decreases.

This porous burner technique seems interesting and more elaborate tests should be carried out to study the influence of pressure more accurately. In particular pressure ranges corresponding to solid propellant applications should be investigated. The effect of the AP grain size also merits further study.

4.3. Reaction Kinetics in the Gas Phase

We have noted in the preceding paragraphs that the nature of the fuel has an important effect on the AP regression rate. For this reason some investigators believe that the important processes in solid propellant combustion take place in the gas phase, as might be implied by the correlation (indicated in Section 4.2) between the solid regression rate and the flame propagation velocity. Following this reasoning, Cumming and Hall have studied the premixed flame of gaseous fuels with vaporized perchloric acid as the oxidizer (28) (29).

These authors first showed that the decomposition flame of perchloric acid alone obeys the Zeldovich flame speed law, with an activation energy of about 45 kcal/mole. Adding hydrogen increases the propagation velocity but decreases the activation energy to a value of about 15 kcal/mole. The structure of the flame depends greatly on the nature of the fuel. At low pressures two-stage combustion is observed. The acid and its decomposition products react much more energetically than diluted oxygen. The flame speed is very high (Fig. 5-29), reaching 375 cm sec⁻¹, which is three times the value for oxygen-nitrogen-methane mixtures. The maximum propagation velocity occurs for a fuel-rich mixture ($\phi \approx 1.5$). The flame temperature measured by means of the OH line reversal method is close to that calculated by assuming chemical equilibrium.

Since the results for perchloric acid-fuel flames differ so from those for oxygen-fuel mixtures, it appears to be unreasonable if the hypothesis of perchloric acid formation is valid, to compare the results obtained with AP with those deduced from the oxygen-fuel flame studies, as did Burger.

The flame speed of ammonia-perchloric acid systems also differs greatly from results obtained with ammonia-oxygen and chlorine-oxygen-ammonia systems at the same final temperature. In experimental models of the combustion of solid propellants containing AP, it is therefore necessary to use AP itself rather than its constituents.

4.4. Pressed Solid Propellant Strands

In order to elucidate the combustion mechanism of solid heterogeneous propellants and to obtain interpretable results, it is of interest to use well-defined geometries. The easiest procedure consists in placing strands of fuel and oxidizer side by side, as indicated in Fig. 5-30a. This technique allows one to observe the influence on the regression rate of the nature of the propellant components and of certain parameters such as the pressure.

For pressures below the deflagration limit of perchlorate the highest solid regression rate is found to occur at the junction between ammonium perchlorate and the plastic fuel. This maximum depth of penetration is well marked as Fig. 5-30a shows for a test at atmospheric pressure. One cannot say however, after analyzing the maximum penetration zone, that the flame tends to penetrate into the oxidizer.

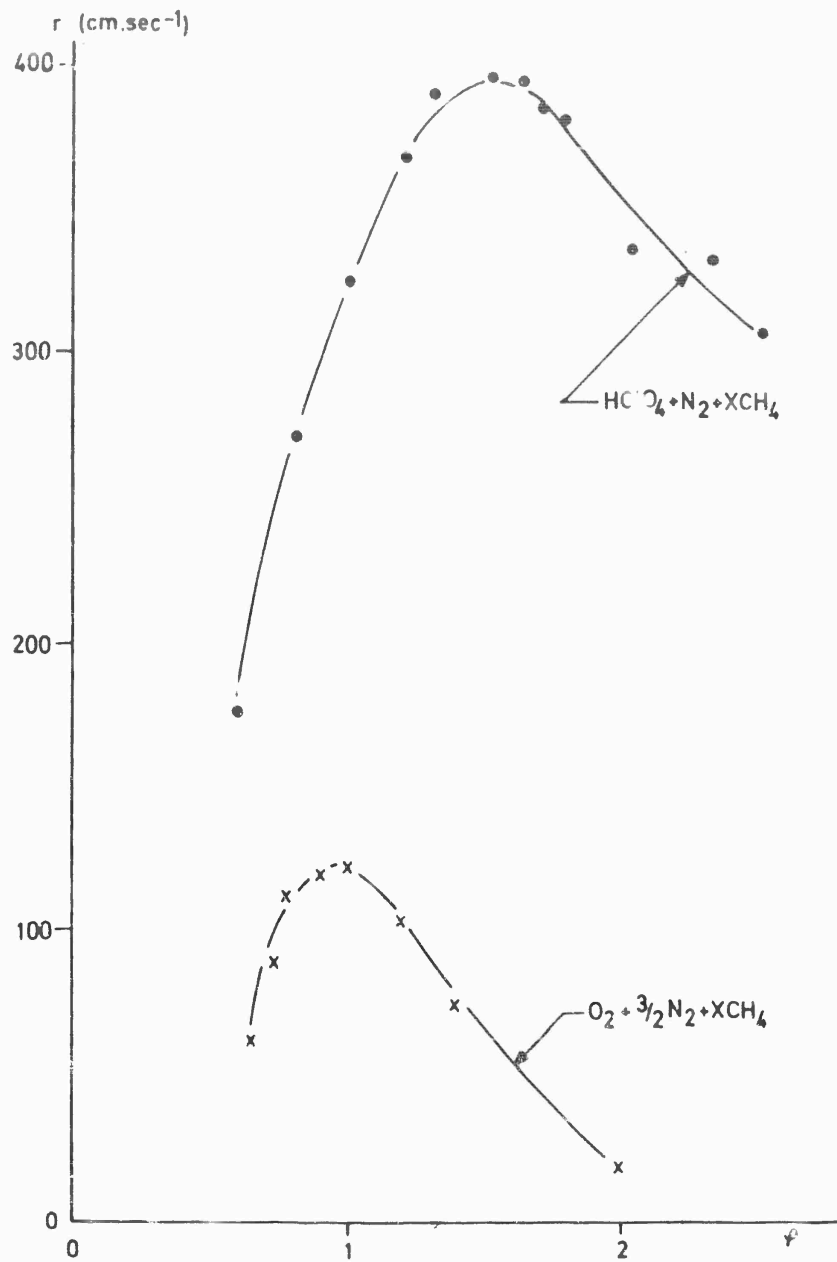


Fig. 5-29 Deflagration velocity of an HClO_4 , N_2 , CH_4 mixture and an N_2 , O_2 , CH_4 mixture ($p = 1 \text{ atm}$)

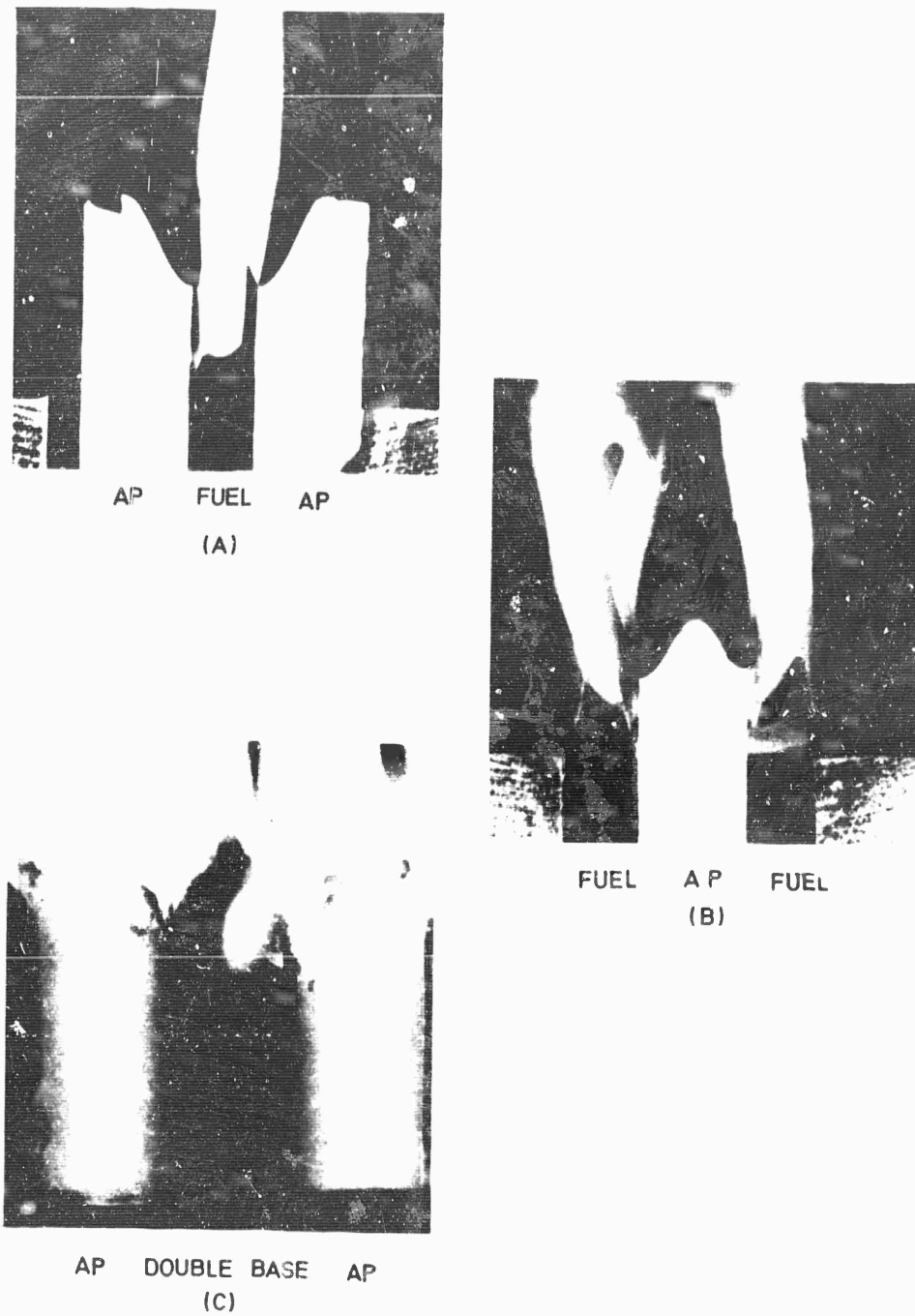


Fig. 5-30a Aspect of the surface and combustion zone in a heterogeneous system

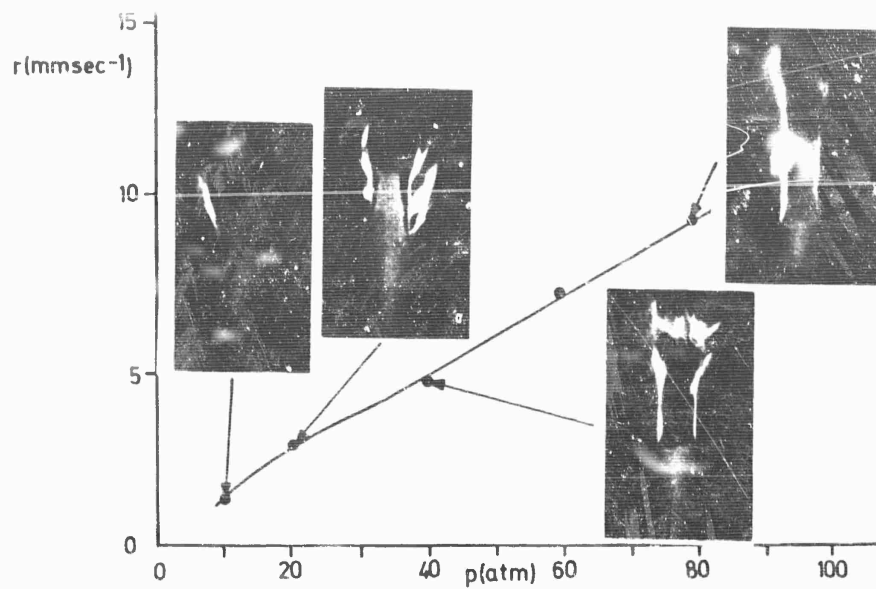


Fig. 5-30b r versus pressure, AP between two polyurethane strands in nitrogen atmosphere

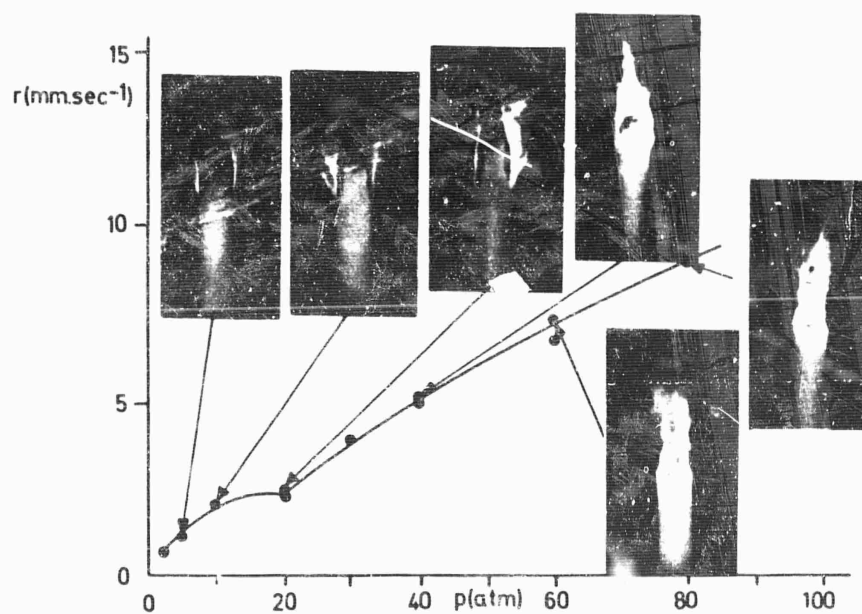


Fig. 5-30c r versus pressure, AP between polybutadiene strands in nitrogen atmosphere

zer fuel interface. There is nothing resembling propagation into a crack, one can only see that the curvature of the AP surface is more pronounced than the curvature of the fuel.

The surface profile changes completely when the pressure increases (Fig. 5-30b). The perchlorate decomposition is then the important phenomenon which controls the regression rate.

The measured regression rate is close to the rate for AP alone and the observed difference is due to the physical nature of the binder and to the pyrolysis conditions (Fig. 5-30b and Fig. 5-30c).

According to Powling, the pyrolysis of certain binders can produce liquids which inhibit the penetration of the flame. This liquid can flow over the AP surface. Certain neutral additives such as extremely fine ground silica powder can hold up the liquid, thus causing the regression rate to increase.

In order to obtain a model with three-dimensional transfer processes (as exhibited by heterogeneous solid propellants), Adams and his coworkers (30) studied pressed solid propellants, which are easier to manufacture than the usual propellants and facilitate study of the effect of oxidizer and fuel grain sizes of the mixture ratio, and (with AP) of the nature of the fuel. The pressed samples were made from a pulverized mixture of oxidizer and fuel, compressed into a square-base parallelepiped; the compression pressure was about 1,000 atm. Important results have been obtained by Adams (30) and Powling (31), (32) using this technique.

The solid regression rate is observed to be very sensitive to the mixture ratio. In Fig. 5-31, the variation of the regression velocity with fuel percentage is shown; the AP grain size is between 76 and 104 μ . The strong influence of the mixture ratio, which was observed for all propellants tested, is an important property of combustion processes in heterogeneous media.

Also of interest is the dependence of regression rate upon pressure. Four conclusions can be drawn:

a) At subatmospheric pressures, the burning rate law can be written in the form :

$$r = b p + a$$

where a is equal to zero in many cases.

This law closely resembles that obtained with conventional propellants. The flame is sufficiently far from the surface for gas-phase mixing of fuel and oxidizer to occur before combustion; the chemical processes then become important and the overall behavior resembles that of a homogeneous propellant. The thickness of the combustion zone is greater than the mean size of the oxidizer and fuel particles.

b) At low fuel concentrations, the law obtained is identical to the one in paragraph (a); this result is similar to that already found with gaseous fuels. The value of the pressure exponent ($n \approx 1$) confirms the importance of the chemical processes in fuel-lean mixtures. The AP decomposition reaction would therefore be modified if a small amount of fuel were to diffuse into the decomposition zone. The exponent decreases when the fuel mass fraction increases (Fig. 5-32).

c) In the pressure range from 1 to 200 atm, there appears to be a change in the combustion regime (Fig. 5-32), which occurs in the neighborhood of 70 atm. When the pressure is below this value, the experimental burning rate law of the form

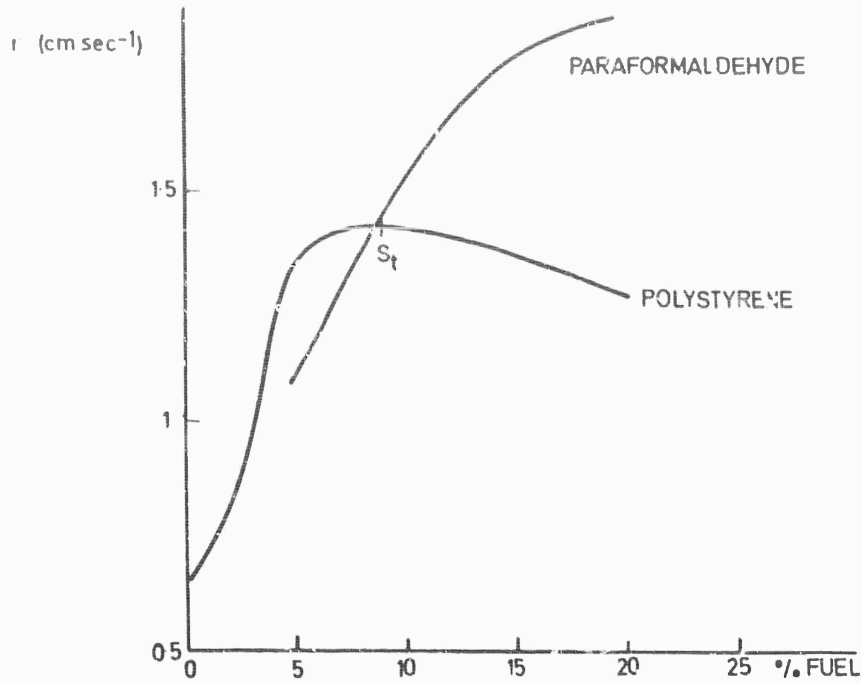


Fig. 5-31 Burning velocity versus mixture ratio for pressed propellant ($p = 68$ atm)

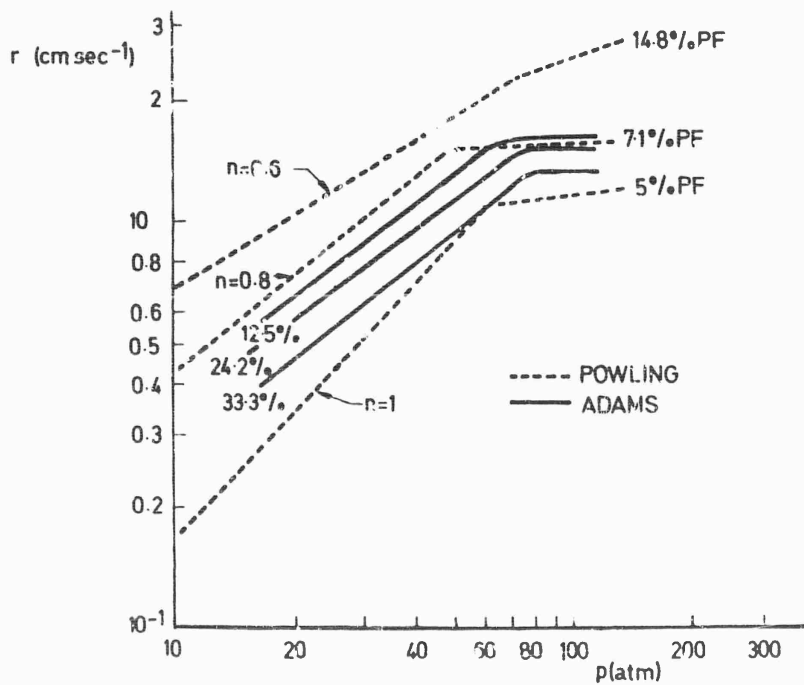


Fig. 5-32 Burning velocity versus pressure for several mixture ratios: Paraformaldehyde/AP

$r = a p^n$; this is the domain of normal combustion which will be considered in greater detail later. For higher pressures, we observe a phenomenon similar to the plateau effect; the regression velocity varies little with pressure and in some cases it may even decrease when the pressure increases. This plateau effect depends upon the nature of the fuel (Fig. 5-33) and may be more or less pronounced depending on the values of the mixture ratio and the oxidizer grain size. The burning rate in this domain is controlled by a mechanism which is not very sensitive to pressure and which might be caused by a local variation of the mixture ratio, which may be due to very different regression rates of the fuel and the oxidizer. Carbon does not exhibit a plateau (Fig. 5-33), perhaps because of a catalytic phenomenon.

d) The nature of the fuel also influences the stability of combustion. With the fuels which are easily gasified, the flame temperature may be correlated with the combustion velocity. The same observation applies to gaseous fuels (propane, ammonia, formaldehyde, polystyrene) but fluctuations in the temperature measurements occur when the fuels are less volatile (carbon, benzoic acid or stearic acid).

The grain size also influences the deflagration velocity, smaller sizes producing higher velocities.

A very interesting study has been reported by Powling; the temperature at the AP surface was determined as a function of the deflagration velocity at atmospheric pressure for systems with various fuels added in small amounts. The surface temperature T_s is not easily obtained from indirect measurements since it is relatively independent of the deflagration velocity (it is of the order of 730°K); however the flame temperature increases when the deflagration velocity increases. Measuring the surface temperature for different pressures between 1/20 and 5 atm, led to a heat of decomposition on the surface of 57 kcal/mole which corresponds to AP dissociation into ammonia and perchloric acid, the samples used for this measurement were a mixture of AP and formaldehyde (32). Powling recently found that at these low pressures, the surface temperature depends on mixture ratio, thus casting doubt on the hypothesis of equilibrium sublimation to dissociation products.

For a very volatile fuel, Powling proposed the combustion model illustrated in Fig. 5-34, which can be valid for gaseous and easily gasified fuels.

We have seen that a single AP sphere ignited at the top in a flowing gaseous fuel exhibits a flame flashback. This flashback may occur with pressed propellants if the fuel gasifies rapidly; we can therefore assume that the flame moves upstream along the AP crystals and gasifies the fuel. The AP grains then burn in a diffusion flame in a gaseous medium of nonhomogeneous composition. Two partially overlapping zones may thus be distinguished, a fuel gasification zone and an AP combustion zone. The combustion process involves sequentially (a) ignition of the crystal, (b) flame propagation along the crystal and (c) AP combustion.

Since fuel gasifies when the flame approaches, the gas has an effect only if chemical transformations or phase changes modify the surface geometry, thereby affecting the local fuel flow rate and thus influencing the flame flashback. It should be noted that flame flashback is significant at low pressures only.

Therefore we might use the AP sphere test results to deduce the burning behavior of a set of spheres, if we assume that combustion is the slowest of the three processes. The regression rate of the solid would then be of the form :

$$r = \frac{K p^{0.6}}{d}$$

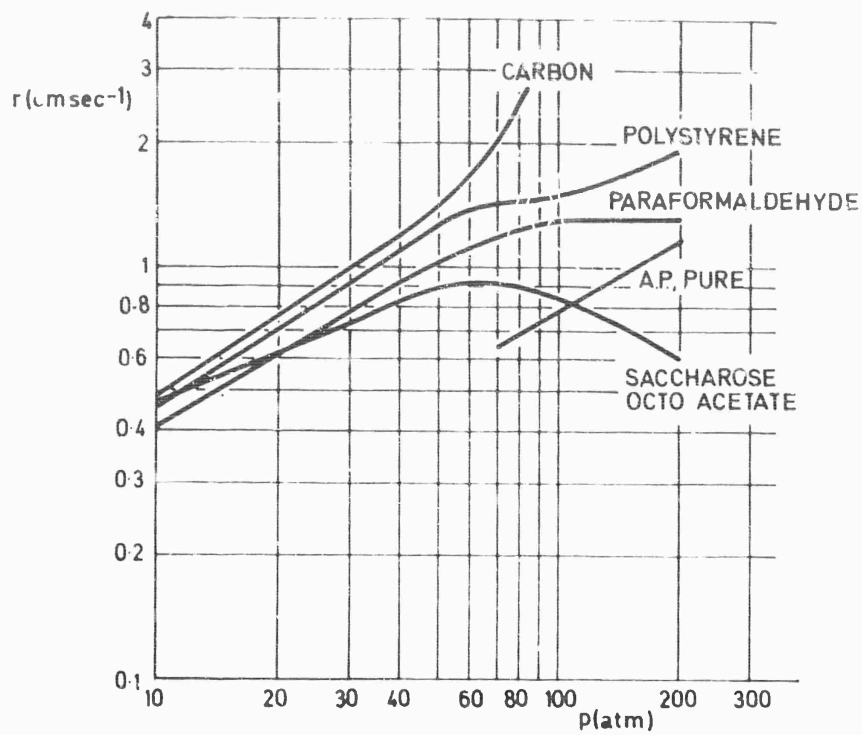


Fig. 5-33 Influence of the nature of the fuel on burning velocity

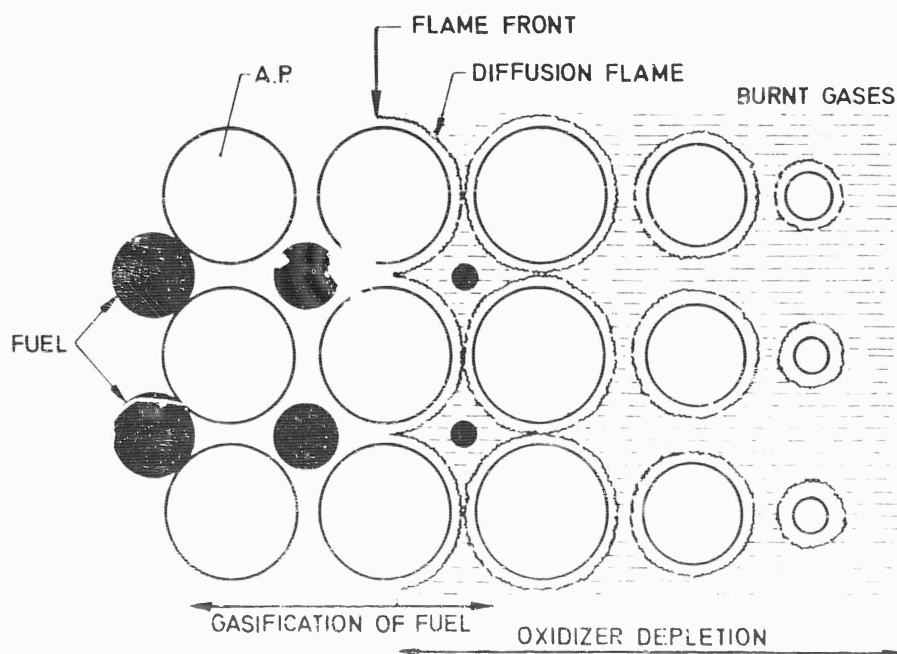


Fig. 5-34 Schematic combustion process of AP and polyformaldehyde according to Powling

The experimental results yield instead :

$$r = \left(a + \frac{b}{p}\right) p^{0.6}$$

at least in the normal combustion domain ($p < 70$ atm).

4.5. Combustion of Metals

Most modern solid propellants contain metal to improve their performance. The combustion of these metals (included in the propellant as powder grains) generally takes place rather far from the surface, so that they modify neither the combustion process nor therefore, the regression rate (50). The study of their combustion can thus be made outside of the propellant.

The conventional method (33) (34) consists in using a burner which produces a hot stream of oxidizer (for instance, a burner fed with a propane-oxygen-nitrogen mixture) with a means for varying the flow temperature and the oxygen percentage. Since aluminum is the most commonly used metal, we shall give results concerning this metal. At atmospheric pressure, the stream temperature must exceed the melting point of alumina ($\approx 2300^\circ\text{K}$) if the aluminum particles are to ignite. The ignition temperature decreases slightly when the oxygen concentration increases. Under conditions permitting ignition to occur, the ignition time lag, (which is equal to 4 millisecon for a particle diameter of 35μ) is proportional to the square of the particle diameter. Different combustion processes may occur, depending on the oxygen percentage in the burnt gases; as a first approximation, we can identify two mechanisms: (a) At high oxygen concentrations, one notices that the sphere of aluminum around the particle bursts during combustion, (b) At a lower concentration, normal (nonbursting) combustion of the aluminum sphere occurs; combustion takes place in the vapor phase at the surface of the hollow alumina sphere surrounding the particle; the combustion duration is then proportional to the diameter of the particle raised to the power 1.8, which is similar to results for combustion of hydrocarbon droplets. This shows the importance of the diffusion phenomena (34) (35).

In another experimental technique, aluminum wires are burned in an oxidizing atmosphere; the wires are heated by an electric current until ignition occurs (35). It is again possible to distinguish various combustion domains depending mainly upon the oxygen concentration (argon being the dilution agent). These various domains are represented in a diagram of molar concentration versus pressure (Fig. 5-35). In regions 1 and 2 liquid aluminum spheres are formed at the ends of the ruptured wire. These spheres burn as they regress towards the electrodes. In region 3, the aluminum wire burns with a vapor phase flame reminiscent of the combustion of liquid fuel droplets. In region 4, one notices the formation of a large drop with a bright flame moving around on its surface. In region 5, combustion is difficult to achieve.

Some propellants contain beryllium powder to increase the specific impulse; the grain diameters employed are of the order of 30 to 40μ . The combustion of this metal is similar to that of aluminum, but in order to obtain ignition one must use propellants whose final combustion temperature exceeds the melting point of the oxide (2800°K).

5. Studies of Combustion Mechanisms with Heterogeneous Propellants

5.1. Direct Methods

At present, direct methods generally employ optical procedures, particularly microcinematography. The combustion zone is magnified by means of a microscope that permits filming of the regressing combustion surface, with a camera synchronized

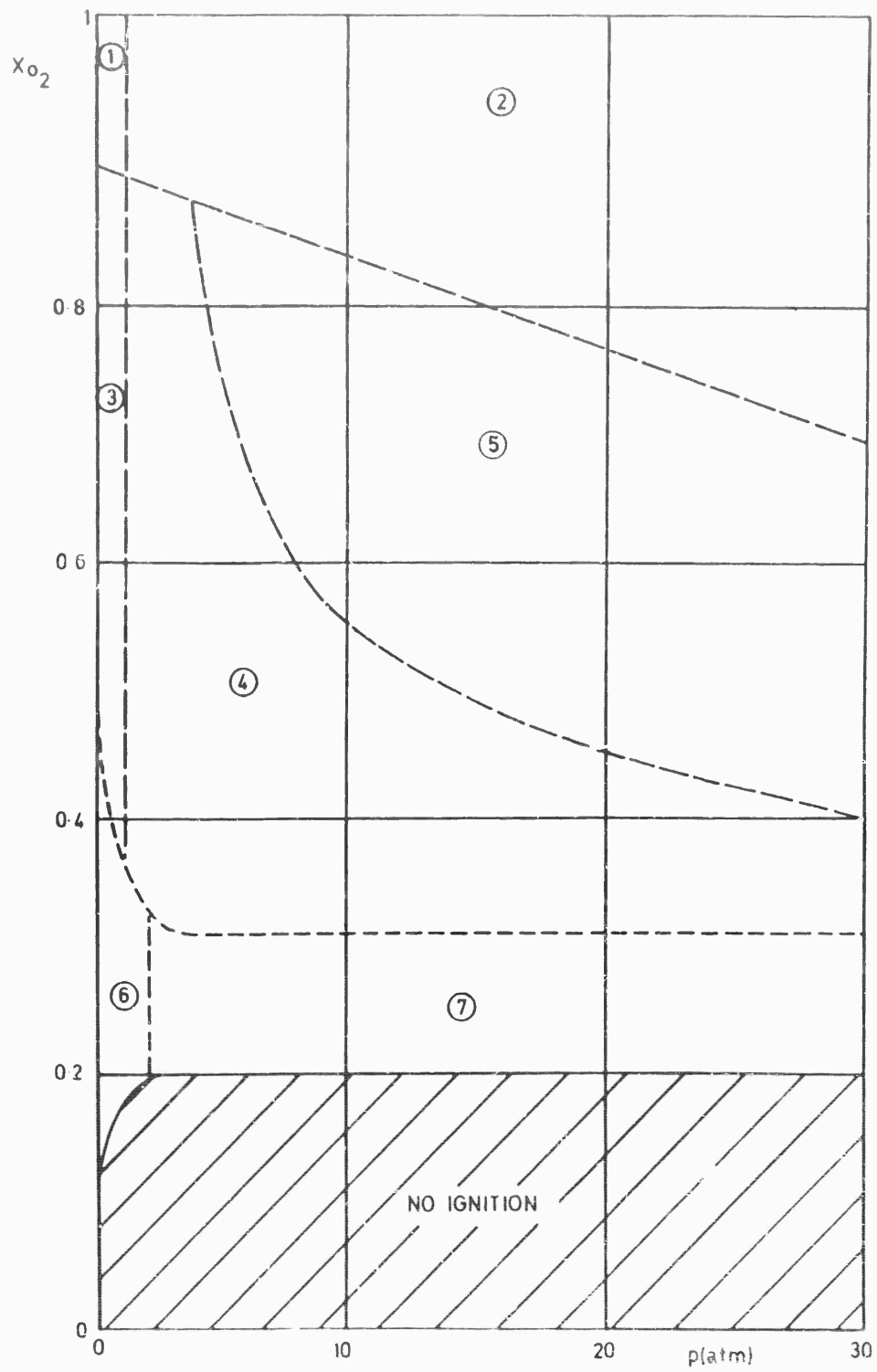


Fig. 5-35 Combustion domain of aluminum

with a flash tube (36) (Fig. 5-36).

This technique yields a local combustion velocity but there is considerable scatter in the results because of the non-homogeneity of the medium. Microcinematography also sheds light on the combustion mechanism. With sharp contrast, it is possible to observe a dark band indicating a modification of the binder along the solid-gas interface. The sharp edges of the AP crystals disappear as soon as the flame approaches. The flame structure depends on the propellant composition. One observes a series of individual flames starting on the surface instead of a continuous flame front (Fig. 5-31). In the pressure range from 1 to 60 atm, flame heights increase and bright combustion cores appear near the surface.

From microphotographic examination, it is possible to distinguish two simultaneous modes of combustion in the immediate vicinity of the AP crystals. Small flames apparently correspond to premixed combustion. Brighter diffusion flames also develop from the AP crystals (Fig. 5-31).

Interesting results on the mechanism of metal combustion in solid propellants have been obtained with this technique (37). The initial dimensions of the aluminum powder particles in the propellant (typically of the order of a few microns) are of no significance in the metal combustion process. At the surface of the propellant, the binder gasifies rapidly, producing a lace pattern of agglomerated aluminum grains. Upon reaching the hot combustion zone, the aluminum agglomerates melt and coalesce into large aluminum drops which are driven off by the combustion gases. Since we have seen that the ignition lag is proportional to the square of the diameter of the metal drop, it is clear that the coalescence process is important. Propellants having high temperatures and high temperature gradients near the surface, produce small metal drops; thus the temperature profile in the gas zone near the surface governs the ultimate metal grain size. This fact is illustrated in Fig. 5-38. The sequence on the left, which corresponds to a propellant with fine AP grains and therefore with high temperature gradients, exhibits smaller aluminum drops than that on the right, which corresponds to a propellant with large AP grains.

Microphotographic techniques yield the size of the aluminum drops before combustion (Fig. 5-39) and reveal conditions producing small-diameter drops. As indicated above, grain sizes shown in Fig. 5-39 (mean diameter in the order of 100 to 200 μ) differ from those of the aluminum introduced into the propellant (mean diameter of the order of 5 to 10 μ).

Aluminized composite propellants with energetic binders, such as nitrocellulose, produce smaller metal drops than conventional metalized composite systems because of the high temperature gradients.

With microcinematographic techniques it is also possible to follow droplet combustion, observing the evolution of the shape of the drop and of the diameter of the flame surrounding it (Fig. 5-40). Information on the motion of the burning metal can also be obtained. An overall view of the metal combustion process is thereby developed. This combustion process is in Fig. 5-41a and Fig. 5-41b. The liquid aluminum drop is almost spherical. Combustion produces an alumina cap touching the aluminum sphere. The alumina cap rotates, either because it moves on the surface of the drop or because the drop itself rotates (Fig. 5-41a). A second combustion zone is located at a surface that is nearly spherical and surrounds the drop. This 'skin' is composed of liquid alumina and is open at one end. The existence of these two combustion zones, one close to the surface, the other farther away from the surface, can be explained by the non homogeneity of the gases at the propellant surface; neighbouring fuel rich and oxidizer rich zones exist there. As indicated in the discussion of Fig. 5-35, when metal combustion takes place in an oxidizer-poor medium, the burning zone is loc-

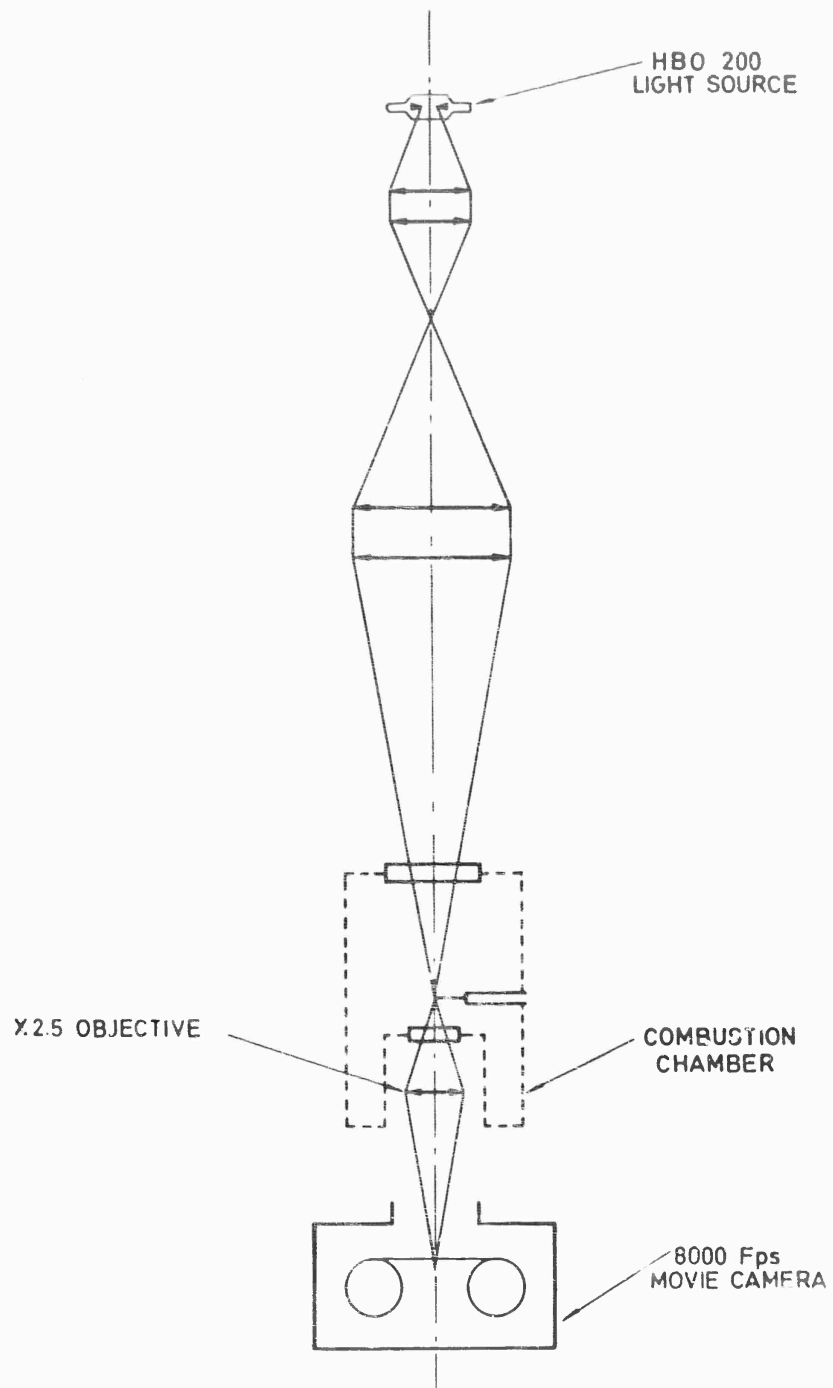
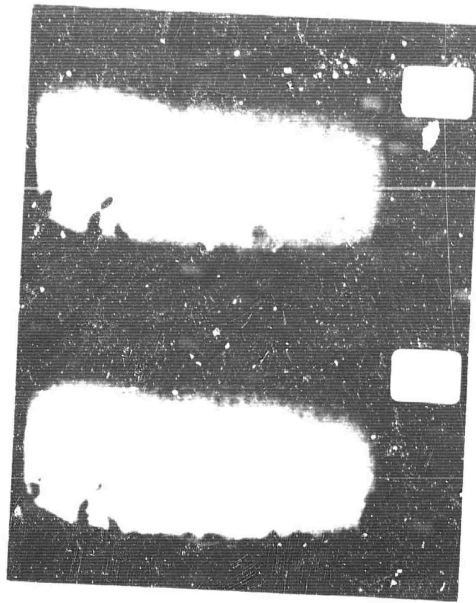
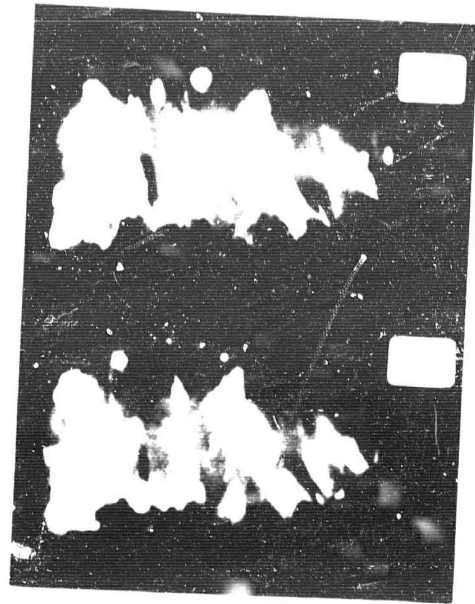


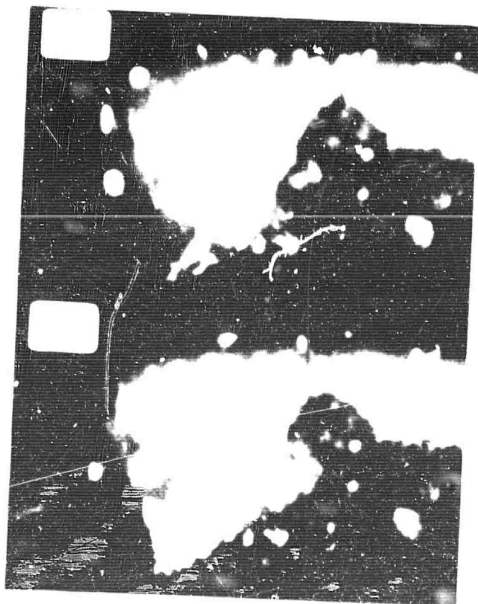
Fig. 5-36 Schematic of cinematographic apparatus



$P = 1 \text{ atm}$



$P = 35 \text{ atm}$



$P = 70 \text{ atm}$

Fig. 5-27 $r \approx 20$ metalized composite propellant

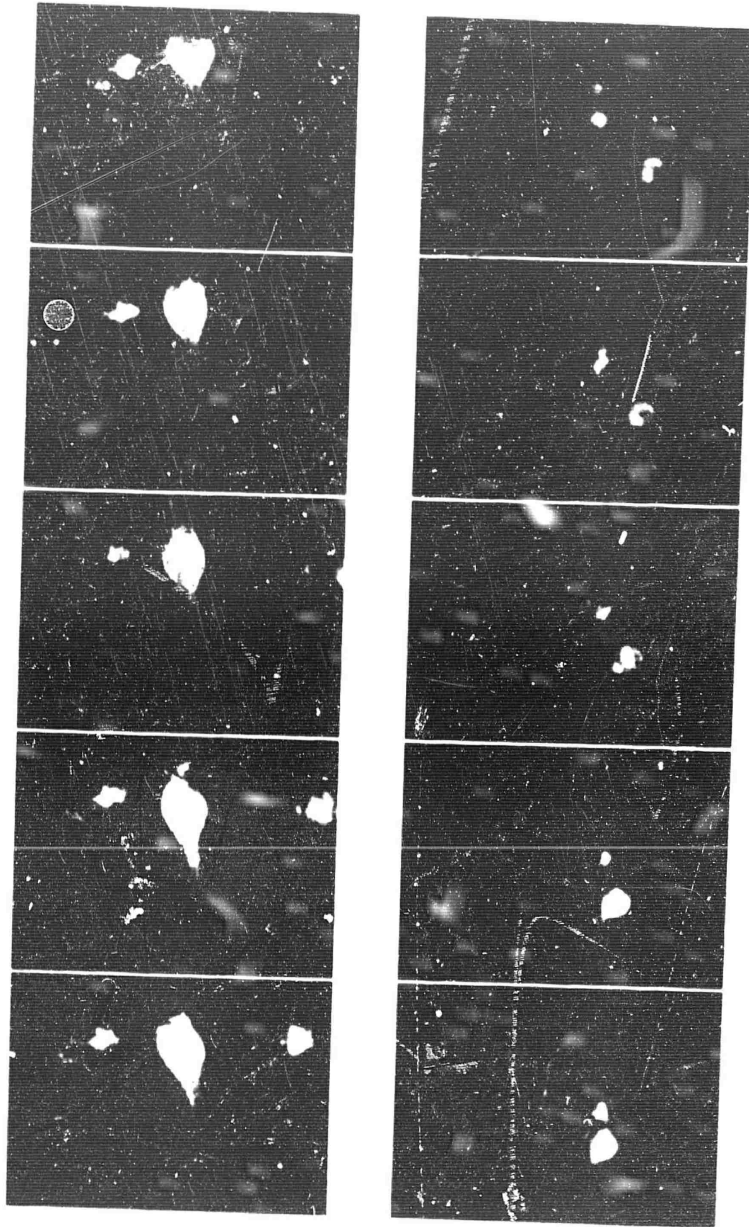


Fig. 5-38 Formation of aluminum droplets

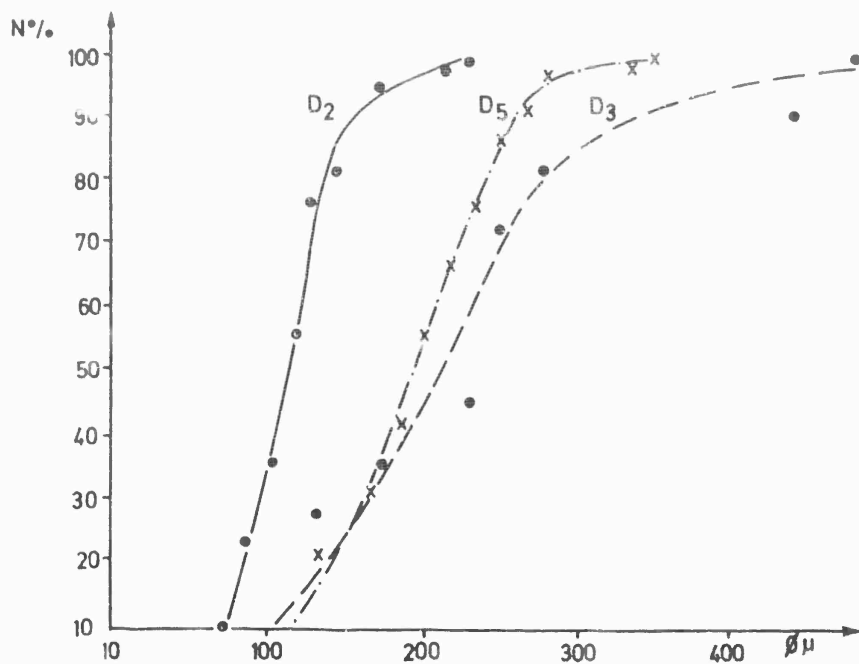


Fig. 5-39 Cumulative frequencies of aluminum droplet diameters, $p = 1$ bar

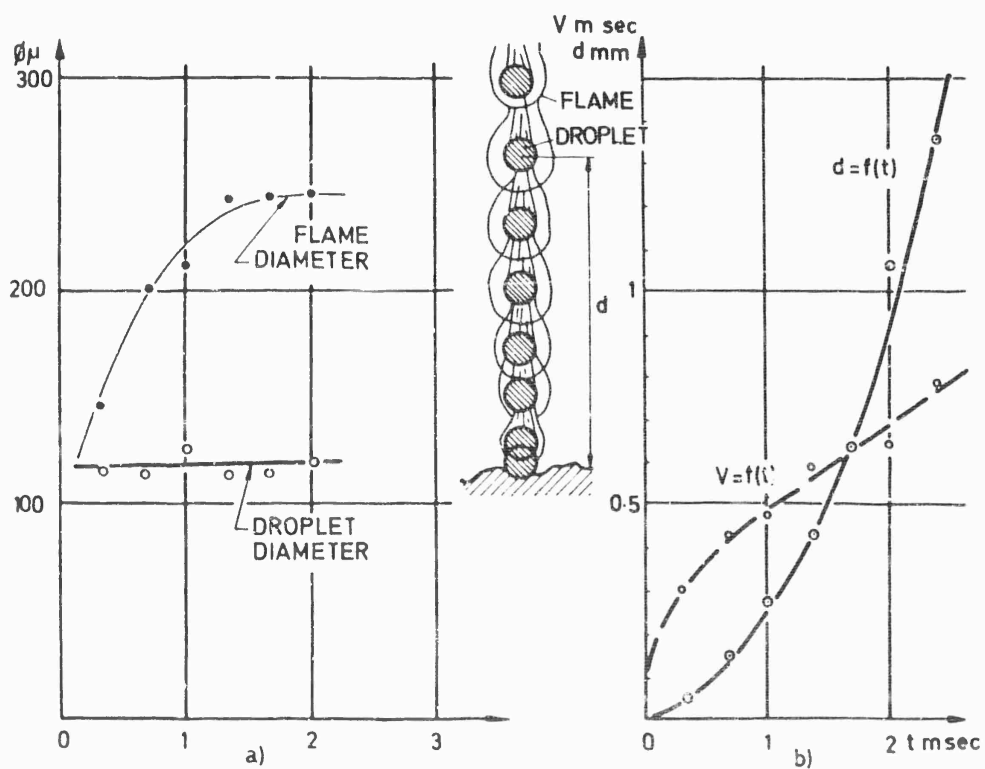


Fig. 5-40 Combustion history of aluminum droplet

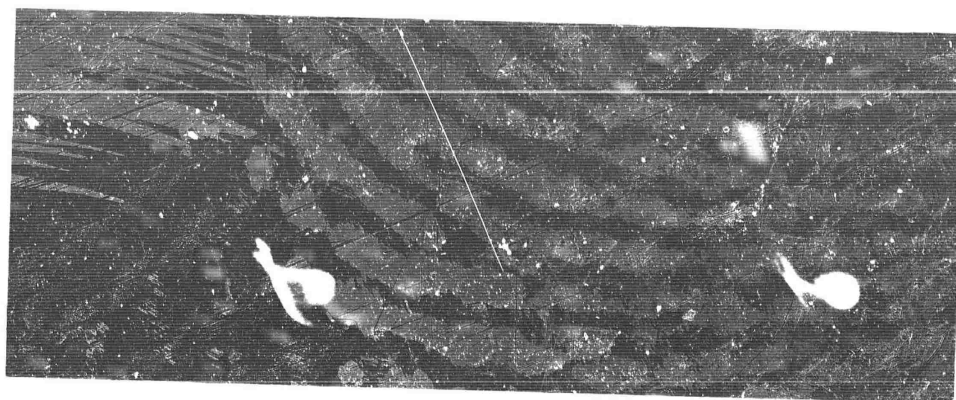


Fig. 5-41a Combustion of aluminum

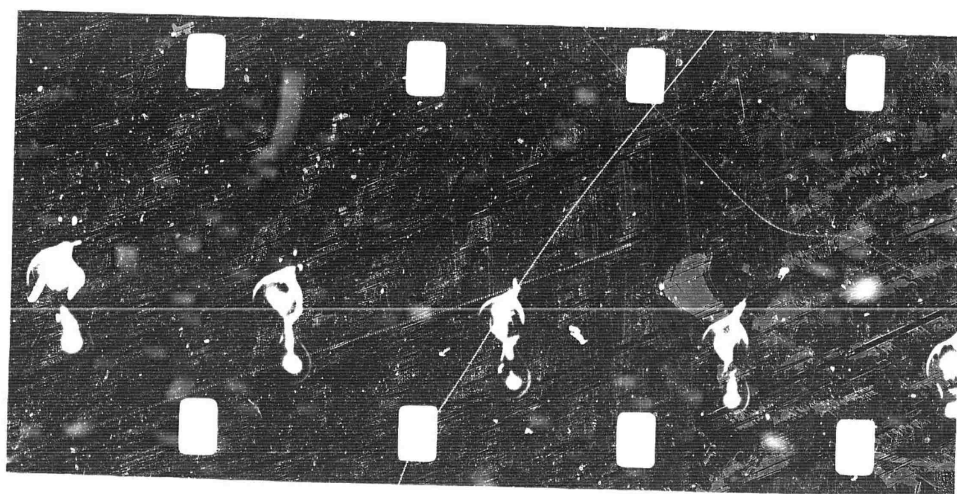


Fig. 5-41b Combustion of aluminum

ated close to the surface; whereas when the oxidizer mass fraction is large enough, a diffusion flame with condensed phases is established at a certain distance from the liquid surface. It is then possible to assume that because of the possible variation of the mixture ratio at the surface, both types of flames can coexist.

Surface burning can start as soon as the aluminum droplet is formed. When formation occurs one observes the presence, on the liquid surface, of alumina, which is most likely due to slow oxidation of the metal.

The formation of hollow alumina spheres may also be observed by collecting the combustion products on a cold plate; a microscopic examination of the products shows an aluminum drop inside an alumina envelope (Fig. 5-42). During combustion in atmospheres enriched in oxygen, most of the drops and most of the alumina envelopes burst. The shape of the alumina envelopes at the time of bursting is shown in Fig. 5-43a, which is taken from films that reveal the time evolution of the apparent contour of the hollow sphere (Fig. 5-43b). Bursting is preceded by a rapid increase of the apparent diameter of the alumina sphere.

The motion of droplets during combustion, can be attributed to an unsymmetrical evolution of the droplet. The presence of hot alumina on one side of the droplet creates a sizeable local temperature gradient which may lead to bursting of the droplet.

Under the direction of Professor Summerfield, many optical methods for studying the combustion zone and the surface have been developed at Princeton, all methods aimed toward setting up a possible model for the combustion of solid heterogeneous propellants (38). In particular the temperature profile in the solid, in the fuel zone and in the gas has been determined using thermocouples. This technique is described in Section 2.1. Typical temperature profiles for composite propellants are given in Fig. 5-6; the measured surface temperatures are of the order of 600°C. A critical analysis of this method has been presented by Powling (42), showing the influence of thermocouple dimensions. Nevertheless it remains that Sabadell's (4) work has determined the thermal conductivity of the propellant, which for composite propellants varies from 5 to $30 \times 10^{-4} \text{ cal cm}^{-2} \text{ sec}^{-1} \text{ }^{\circ}\text{K}^{-1}$ and depends on pressure, and indicated the amount of energy liberated on the surface. Such experiments are very useful to determine the decomposition process of AP for instance, which occurs very close to the surface.

Microphotographs of the surface after sudden extinction, assuming that the geometry of this surface is frozen in the state it was in during combustion, show an important change of aspect according to pressure. For low pressures, below 30 atm, the AP crystals seem to stand out, the binder pyrolyzing more rapidly than the oxidizer (39).

The inverse situation occurs at high pressures, above 30 atm. In fact the distinction is not as sharp as Fig. 5-44 seems to indicate since the crystals stand out as well as the craters, the latter indicating a disappearance of the crystals. The sudden depressurization of the chamber to achieve extinction, can have a mechanical effect on the burning surface. The Princeton group and in particular Cole, have therefore attempted to develop a technique for taking microphotographs of the surface during combustion (40). The examination of the photographs shows an important heterogeneity of the surface: large AP crystals appear in the surface, surrounded by a haze; large craters also appear with luminous centers in some of them. At low pressures a few luminous points are noted close to the large AP crystals. A smaller scale heterogeneity appears between the craters.

It follows from these observations that the regression rate of the AP crystals and the binder, is not the same all over the propellant surface.

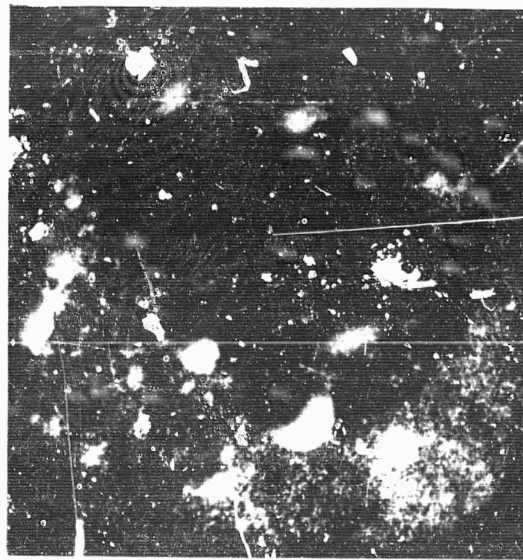


Fig. 5-42 Microphotographs of combustion products of an aluminum loaded propellant

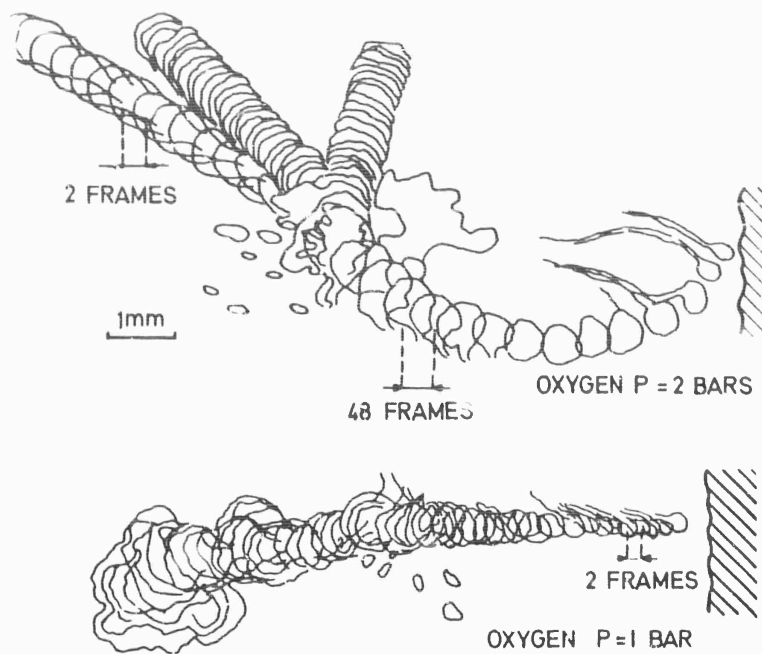


Fig. 5-43a Evolution of the apparent shape of a sphere when exploding

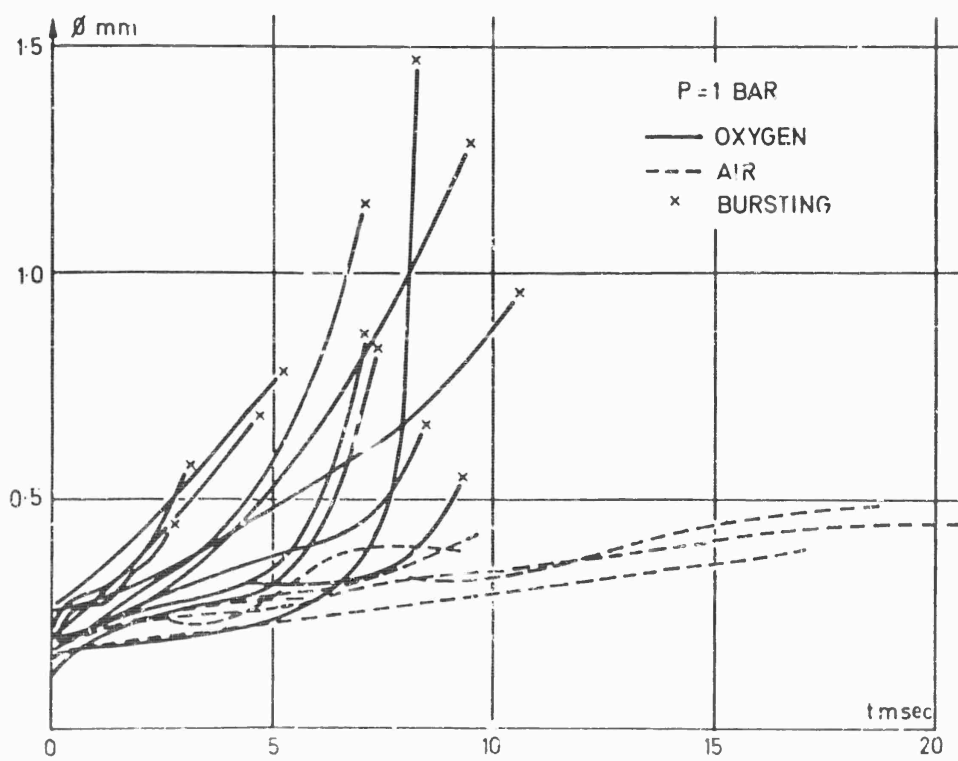
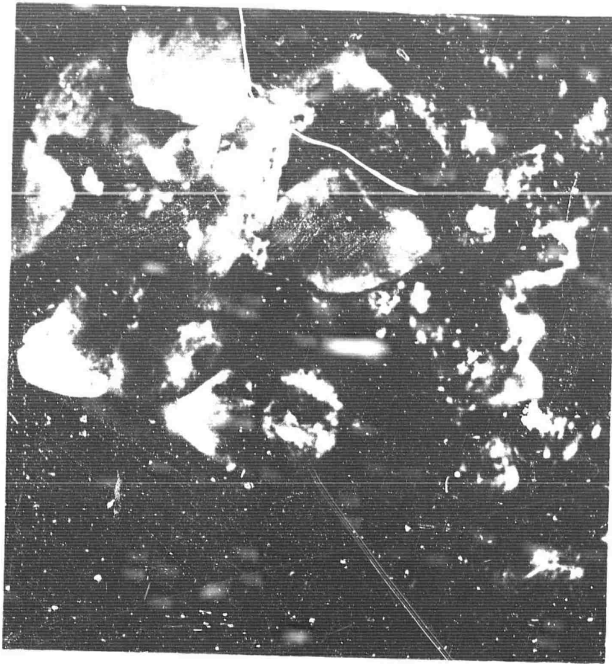


Fig. 5-43b Evolution of the apparent diameter of the alumina sphere



- non metalized propellant -
P = 65 bars



- metalized propellant -
P = 16 bars

Fig. 5-44 Cinematographic aspect after extinction by sudden expansion

The propellant regression rate has been determined at low pressures in the absence of a flame, by submitting the surface to an intense radiant flux, the pressure being below the limiting combustion pressure. This technique allows the study of phenomena which take place in the solid phase (41).

Optical methods have been developed in the U.K. by Powling and Smith (31) (32) (42), who have determined the surface temperature of propellants from the measurement of infra-red radiation at specific wavelengths. The first difficulty was to distinguish the emission of the surface itself from that of the hot gases. The second problem was to determine the emissivity of a thin surface layer, from measurements on the heated zone of the propellant grain. To avoid the first difficulty, a wavelength was chosen, for which the hot gas radiation was low in relation to that from the surface, and the products were rapidly sucked away from the burning surface. Furthermore an accurate choice of the wavelength facilitated the measurement of the emissivity of a thin surface layer. The apparatus is illustrated in Fig. 5-45.

The measurements were performed on ammonium perchlorate composite propellants and nitric ester propellants (double-base).

According to the results, the surface temperature of perchlorate propellants is not sensitive to the burning velocity; a temperature of about 490°C is observed for different mixtures at atmospheric pressure. At pressures between 25 and 760 mm Hg, an Arrhenius relation was obtained between pressure and surface temperature (Fig. 5-45), with an activation energy of 57 kcal/mole, which can be explained by assuming that perchlorate sublimates simply (enthalpy change of 30 kcal/mole) or by introducing the hypothesis of a reversible dissociation into $\text{NH}_3 + \text{HClO}_4$ (enthalpy change of 56 kcal/mole). The experiments at a pressure higher than atmospheric are less conclusive because the gradients are so steep that the heated zone becomes too thin for an accurate determination of the temperature, with the infra-red emission technique (42). Furthermore recent observations introduce interpretive difficulties concerning the measurements which supported the reversible dissociation hypothesis.

For various formulations of nitric ester-based propellants, an appreciable increase of the surface temperature, with burning rate at atmospheric pressure, was observed (31).

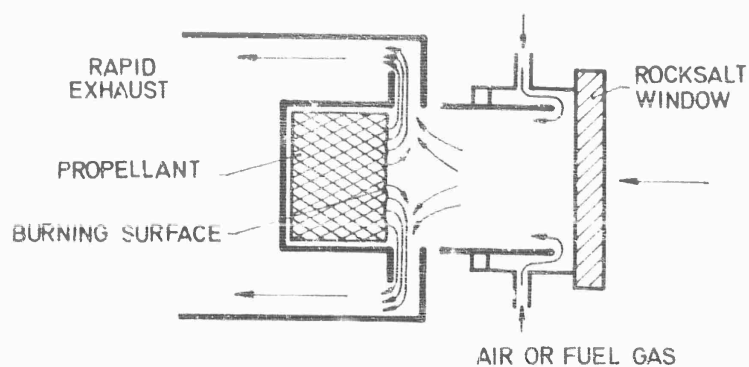
Spectrographic techniques have also been used to determine the structure of the combustion zone; a recent study by Povinelli, on the emission of the C - N radical at 3883°A , showed that the emission of C - N for a (PBAA - AP) propellant burning at atmospheric pressure started at 70 microns from the surface. The maximum intensity is reached at 235 microns and this radical emits until 2×10^3 microns from the surface (43).

5.2. Indirect Methods

Indirect methods are based on the measurement of a parameter related to the combustion mechanism. The easiest parameter to measure is the linear regression rate, which is also of practical importance in rocket motor operation.

The parameters affecting the regression rate are pressure, initial solid grain temperature, gas velocity, fuel-oxidizer ratio, composition of the propellant (including oxidizer, binder and additives) and the particle size of each component.

To investigate burning rate laws systematically, we may select initially two parameters to vary and hold all other parameters constant. We choose pressure which affects the combustion process and the mean diameter of the oxidizer crystals which is related to the heterogeneity, thus defining combustion domain in the pressure versus diameter diagram. Later it will be possible to investigate how these



DETAILS OF THE APPARATUS - BURNER

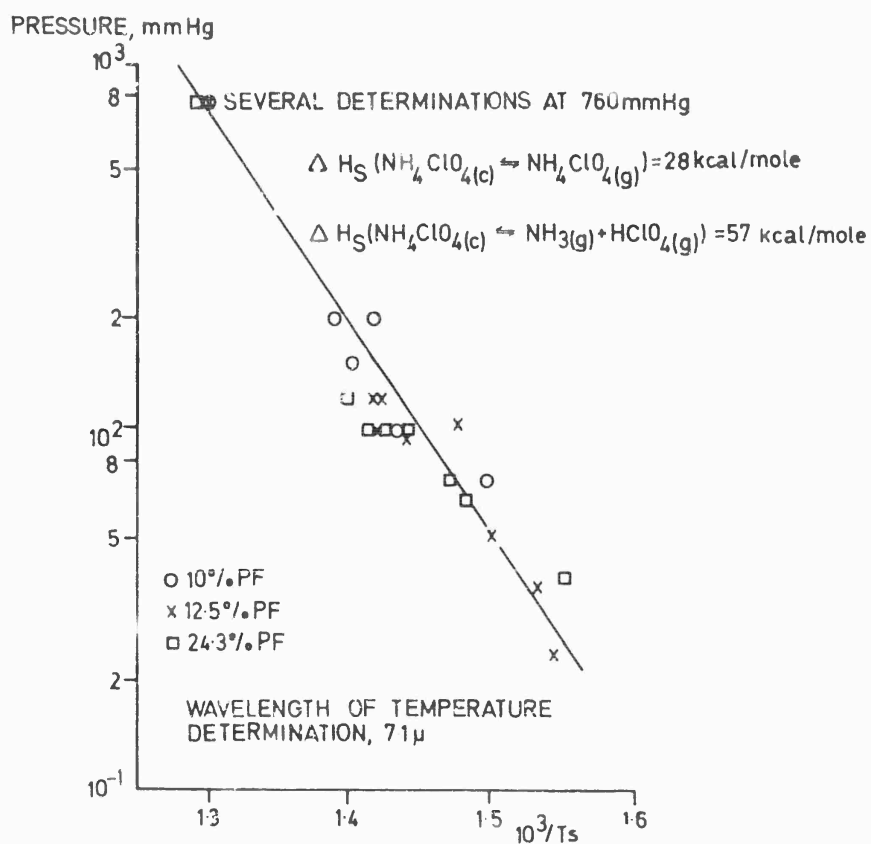


Fig. 5-45 Surface temperature/pressure relationship for burning ammonium perchlorate mixtures (PF = paraformaldehyde) (42)

domains are deformed when other parameters, such as the mixture ratio and the nature of the components, are varied (38) (39) (44) (46).

5.2.1. Low Pressure Domain - At subatmospheric pressures, the combustion zone thickness is large compared to the oxidizer crystal mean diameter, so that the oxidizer and the fuel have time to mix in the gas phase before combustion. A premixed flame process therefore occurs and chemical phenomena govern the solid regression rate. This model is confirmed by the law obtained for the burning rate, which is of the form $r = b p$ or $r = b p + a$, (44) (45). The exponent of the pressure term is unity, thus supporting the importance of the chemical reactions. The characteristics of the combustion zone are the same as for homogeneous grains (see Fig. 5-37). The combustion zone is transparent and in some cases at low pressures, it is possible to see a dark zone near the surface a few tenths of a millimeter thick, where mixing of gaseous fuel and oxidizer may be occurring.

Since the regression rate depends mainly on gas-phase chemical reactions, one might expect it to be independent of heterogeneity parameters such as the oxidizer grain size. Such a supposition would not be entirely correct. As a model, we may consider the propellant surface to be formed by small tubes whose diameters are of the same order of magnitude as the AP particle diameter. We may assume that gaseous oxidizer is injected into these tubes and that gaseous fuel passes through the spaces between the tubes. The smaller the size of diameter of the tubes, the faster the mixing rate of fuel and oxidizer. It therefore appears that for a real propellant, the overall combustion time will decrease as the AP grain diameter decreases; thereby decreasing the height of the combustion zone and consequently increasing the solid regression rate.

The fuel and oxidizer mass flow is not the same at low pressures and at moderate pressures; the oxidizer mass flow decreases in certain cases more rapidly than the fuel mass flow. This variation of the local mixture ratio is also affected by the granulometry of the AP and by the mass flow in each oxidizer tube. This representation is, of course, only schematic and below a certain grain size one reaches practically the limit, which is a homogeneous premixed flame with a finite flame height. Chemical surface reactions which depend on the grain size, can also take place in this low pressure domain.

Although the premixed flame combustion process may be important, as Powling and Burger and Van Tiggelen indicate, it remains that this mechanism cannot explain all experimental results in the low pressure domain, particularly the influence of the perchlorate granulometry.

In the law $r = a + b p$, a and b are functions of the AP grain diameter and increase when the diameter decreases.

This influence of the AP granulometry on the burning velocity has been confirmed by Cole's experiments (40).

As the pressure is decreased, a limiting pressure is reached, below which combustion is no longer possible. But extinction does not occur simultaneously over the entire surface. Near the low-pressure flammability limit, flame spots move about the surface, as if looking for zones where combustion would still be possible. A microphotographic examination after extinction, shows partially sublimed AP crystals protruding above the fuel and dark carbon pyrolysis residues deposited on the binder. It thus appears that the oxidizer gasification ceases first.

Decreasing the pressure exerts a twofold effect: (a) At low pressures, the flame front moves farther from the surface until, at a critical distance, the heat transfer from the combustion zone is no longer sufficient to gasify the solid. (b) An asym-

metry arises in the mass flow rates of fuel and oxidizer which produces a richer mixture ratio that eventually leads to extinction.

The low pressure flammability limit is not strongly dependent on oxidizer grain size, although we have observed a slightly lower limiting pressure with large AP grains than with smaller ones. The oxidizer, fuel and catalysts affect the flammability limit in a manner that is best investigated by observing combustion at progressively decreasing pressures.

The determination of the pressure flammability limit is an important point in the study of heterogeneous propellants. Unfortunately few results have been published on the subject.

5.2.2. Moderate Pressure Domain (5 to 50 atm) - As the pressure is increased, the flame passes from a homogeneous to a heterogeneous structure. Luminous streaks, indicating local variations of the mixture ratio, appear with an intensity that increases rapidly at a critical transition pressure. Experimental observation of the transition process is therefore straightforward.

The heterogeneous combustion domain that we shall now discuss is important because it occurs in most practical applications. The burning rate law is generally of the form $r = c p^n$, where n varies from 0.2 to 0.6 according to the nature of the propellant. Summerfield suggested a law of the form :

$$\frac{p}{r} = a + b p^{2/3}$$

and Penner proposed :

$$\left(\frac{p}{r}\right)^2 = a' + b' p^{4/3}$$

These formulas agree well with the experimental results in the domain under discussion. In the first formula, 'a' characterizes a chemical process and 'b' a diffusion process. Measurements on an actual rocket engine and on strand burners conform to this law. In most studies, the pressure range is narrow enough for the earlier (p^n) law to agree closely with Summerfield's law.

Figure 5-46 shows the variation of $\frac{p}{r}$ with $p^{2/3}$ for a rocket engine. The burning rate was measured at the star points and star recesses. Straight lines are obtained, indicating good agreement with Summerfield's law. In the present case, the ordinate at the origin is close to zero, implying a small contribution from the chemical process. At any given pressure, the burning rate is higher at the star points than at the star recesses.

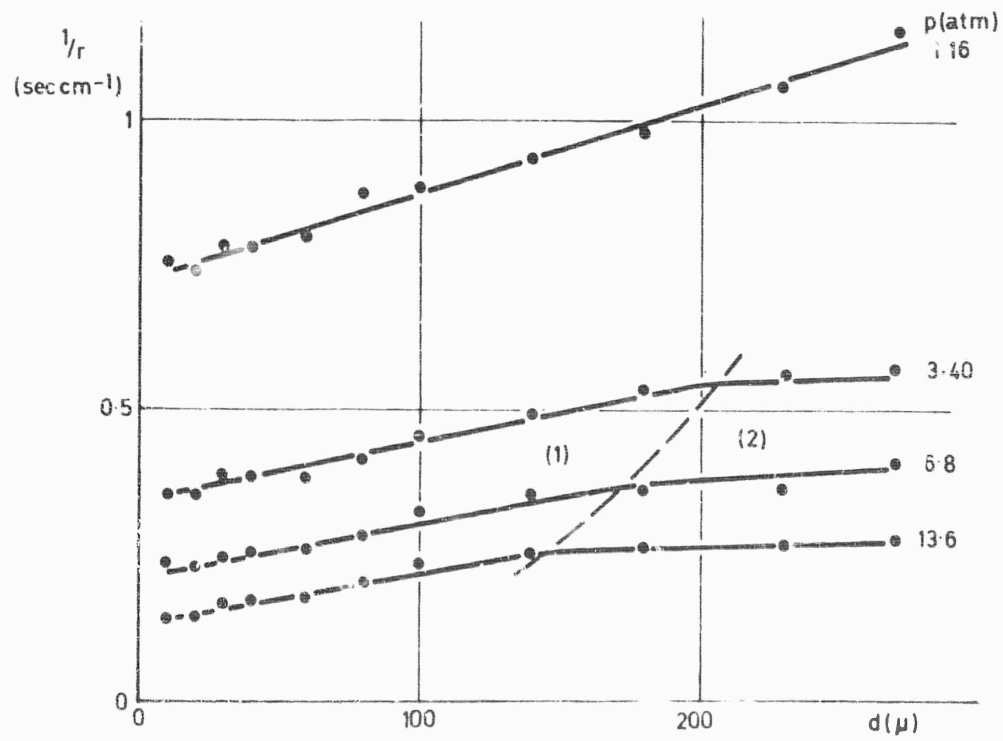
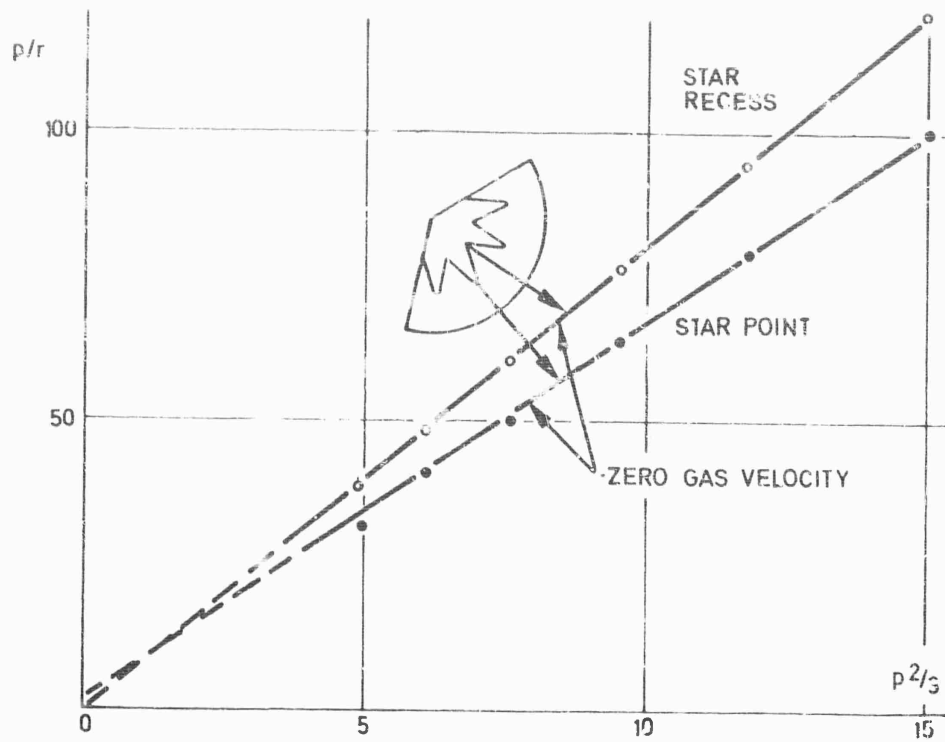
The chemical process is similar to that described in the paragraph on low pressures. Therefore 'a' is not completely independent of the mean diameter 'd' of the AP grains. On the other hand, 'b', which characterizes the diffusion process, varies linearly with 'd' (Fig. 5-47).

The work of Bastress represents the first systematic investigation of particle size effects in heterogeneous propellant combustion (39).

Two subdomains of the moderate pressure domain can be distinguished. At low pressure levels and small mean diameters, the empirical law is of the form:

$$\frac{p}{r} = a + b' d p^{2/3}$$

For higher pressures and larger diameters the relationship becomes:



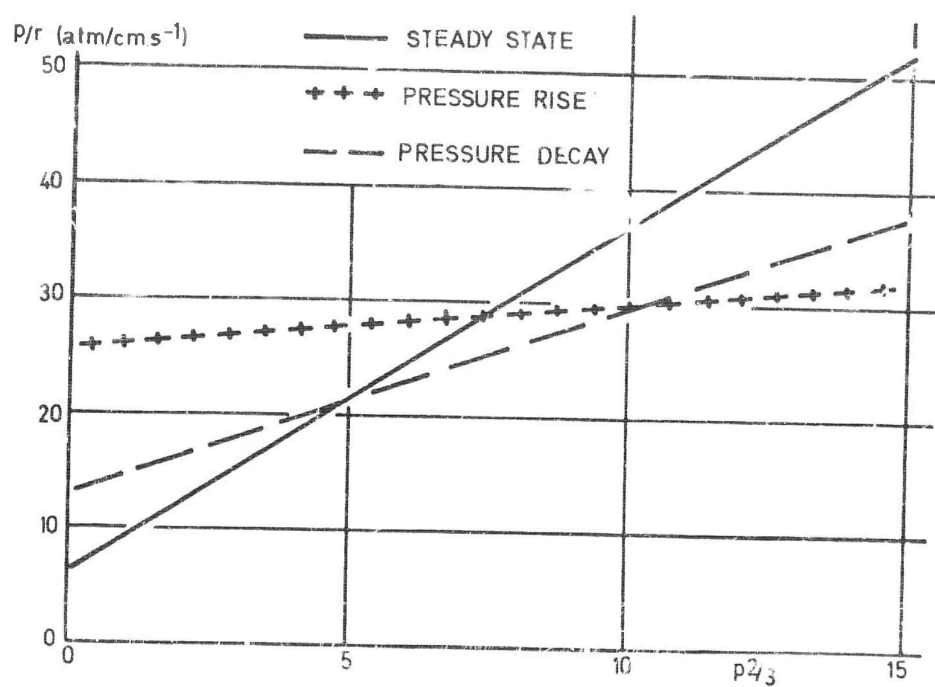


Fig. 5-48 Variation of burning velocity during unsteady motor operation

$$\frac{p}{r} = a + b' d^\alpha p^{2/3}$$

where the exponent α is smaller than unity.

An explanation of the existence of two subdomains can be offered in terms of the

Reynolds number $Re = \rho_p r d / \mu$, where ρ_p is the density of the propellant and

μ the mean viscosity of the gas. By increasing the pressure or the diameter of the AP grains, the Reynolds number is increased and the diffusion process may undergo a transition, from laminar to turbulent transport.

We have seen that on an actual rocket and in strand burner tests, Summerfield's law is fairly well satisfied. If we write for the rocket :

$$\left(\frac{p}{r}\right)_m = a_m + b_m p^{2/3}$$

and for the strand burner :

$$\left(\frac{p}{r}\right)_s = a_s + b_s p^{2/3},$$

then we find :

$$\frac{p}{(r)_m} = \frac{b_m}{b_s} \frac{p}{(r)_s} + a_m - a_s \frac{b_m}{b_s}.$$

This correlation is fairly well satisfied. It is observed that $b_m > b_s$ and that $a_m < a_s$ (47).

The Summerfield correlation has also been employed for transient regimes in actual rockets (Fig. 5-48). During pressure buildup, when the combustion chamber is vented or when the nozzle throat area is changed during combustion (48), one observes that the value of 'a' is larger than its steady-state value and the value of 'b' is smaller. This observation seems to imply that during transient regimes, the chemical process became relatively pronounced in comparison with the diffusion phenomena. Perhaps mixing is intensified during transients. The effect is more noticeable during pressure buildup than during pressure decay.

Gas flow parallel to the surface, may modify the flame structure and thereby change the burning rate law (erosive burning); this problem will be studied in Chapter 7.

For large diameter oxidizer grains, diffusion phenomena predominate. This suggests that the experimental model of oxidizer spheres in gaseous fuel streams, may be applicable. The burning rate is of the form :

$$r = c p^n d^{-\alpha}$$

where n is about 0.5 and α is between 0.1 and 0.5. We can hypothesize a series of processes, such that the total propagation time t for an element composed of a layer of fuel and a layer of oxidizer, is equal to the sum of three terms :

$$t = t_o + t_h + t_f,$$

where t_o corresponds to the combustion time of the oxidizer by a diffusion process, t_h corresponds to the combustion time of the fuel by the same process and t_f is the

transition time required to pass from a solid oxidizer-gaseous fuel system to a solid fuel-gaseous oxidizer system. In the preceding relationship for large diameter crystals, we have assumed that t_h and t_t can be neglected in comparison to t_o .

In the moderate pressure domain, we finally reach the following conclusions:

With propellants, for which the binder pyrolysis rate is high compared with that of the oxidizer, one may assume that the burning rate is governed by the surface distribution of premixed flames (parallel to the surface) and of diffusion flames (perpendicular to the surface). In terms of the burning velocities r_c and r_d for each of the processes, the propellant burning rate may then be expressed as :

$$\frac{1}{r} = \frac{a_1}{r_c} + \frac{b_1}{r_d}$$

where a_1 and b_1 depend on the proportion of pre-mixed and diffusion flames.

When the AP grains are large compared with the thickness of the combustion zone, the diffusion processes are the most important.

5.2.3. Plateau Domain - Under appropriate conditions, the burning rate is independent of pressure and the propellant is said to burn in the plateau domain.

Generally, we observe that when the AP grain diameter decreases, the extent of the plateau zone increases. At a critical minimum grain diameter, the flame is extinguished. When the concentration of the oxidizer is decreased, we also observe zones in which the combustion velocity is independent of pressure.

This plateau effect has been studied cinematographically. An irregular, pulsating type of combustion with partial extinction is observed. The sequence in Fig. 5-49a illustrates this random combustion. A microphotographic examination of the surface after combustion provides an explanation for this behavior; Fig. 5-49b shows that the AP crystals have disappeared from the propellant surface, leaving craters behind. One can therefore conclude that the decomposition velocity of AP greatly exceeds the binder pyrolysis velocity under these conditions and that, as demonstrated by the brown deposit on the surface, the fuel lacks sufficient oxidizer to burn.

An explanation for the plateau effect may therefore be as follows:

Consider a cylinder of propellant whose combustion surface is perpendicular to the cylinder generatrix. Because of the AP crystal disposition and of the different regression rates of the binder and of the oxidizer, combustion will not be steady. Instead, depending on the pressure, normal combustion will occur over a certain distance along the cylinder, progressing at a normal velocity which, depending on the pressure domain, corresponds to one of the relationships given previously. Then suddenly combustion ceases because of the change in structure. In the non-burning interval, the combustion zone surrounding the cylinder modifies the structure of the surface (through pyrolysis of the plastic binder), permitting combustion start again. Therefore, we observe a succession of combustion and extinction periods. The mean burning rate is an average over the combustion and extinction intervals.

Propellant combustion in the plateau zone would then occur through a discontinuous mechanism distributed randomly in space and time. This is an extreme case; generally complete extinction does not occur. Instead, there is a local modification of the mixture ratio which affects the solid regression rate.

This mechanism is outlined in Fig. 5-50, where the burning rate is plotted as a

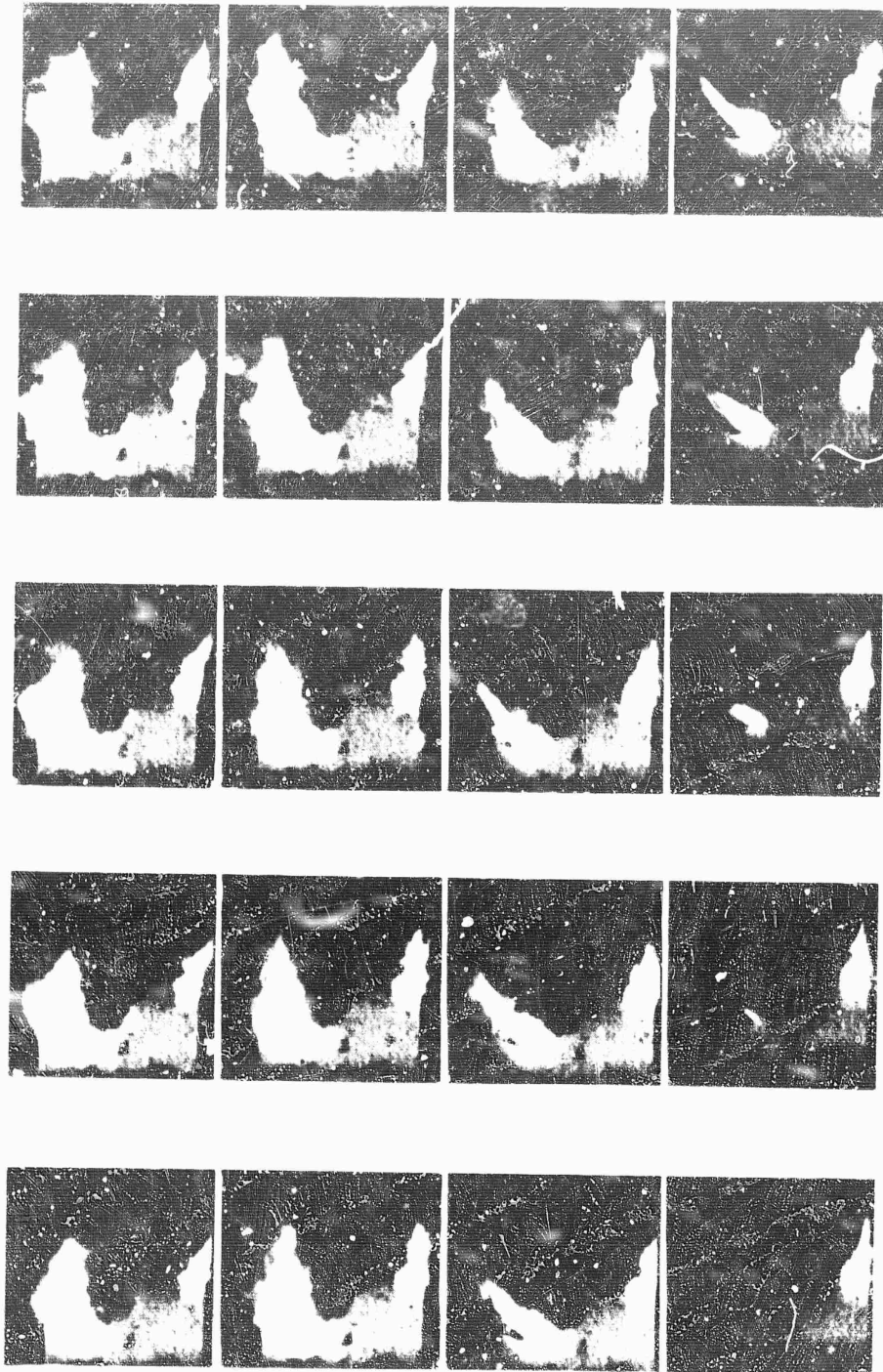


Fig. 5-49a Local extinction (plateau domain) $p = 70$ atm



Fig. 5-49b Microphotograph of surface after extinction
(plateau domain)

u*

BURNING VELOCITY

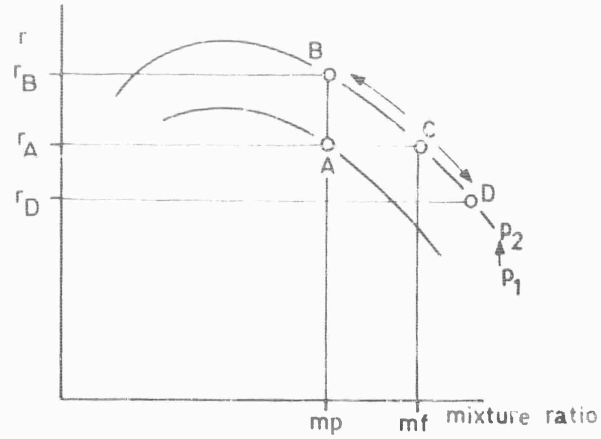


Fig. 5-50 Diagram of combustion in the plateau domain

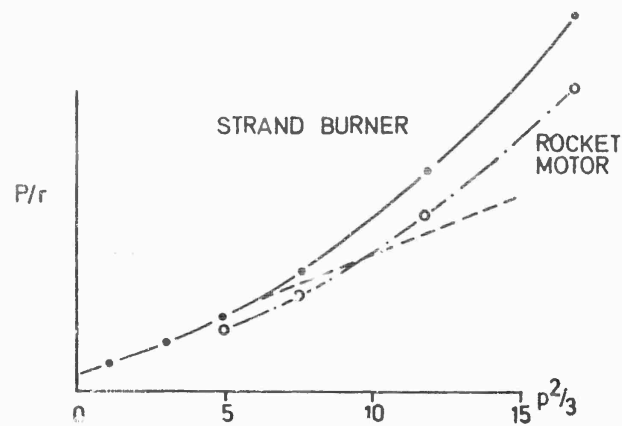


Fig. 5-51 Burning velocities as determined in strand burner and in rocket engine, for a plateau-grain

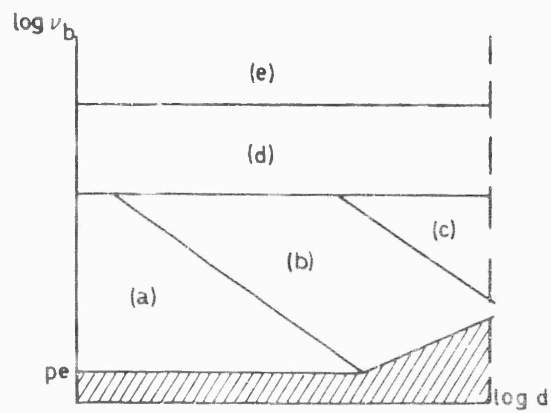


Fig. 5-52 Combustion domains of solid propellants containing AP

function of the mixture ratio m_p , for two pressures p_1 and p_2 . Points A and B identify the burning velocities at pressures p_1 and p_2 , respectively, for the original propellant mixture ratio m_p . If, because of the distribution of the oxidizer and of the fuel, part of the propellant has its normal burning velocity r_B and the other (richer) part has the modified burning velocity r_D , then the mean burning velocity will be the average between r_D and r_B , which is smaller than r_B . This mean burning velocity can be the same as the normal burning velocity r_A of the propellant at a lower pressure p_1 , thereby producing the plateau effect. We note that this same mechanism might cause the burning rate to increase, decrease or remain constant as the pressure is increased. Burning effectively occurs at a mixture ratio m_1 that varies with pressure.

One might guess that in an actual rocket, this type of plateau effect would disappear because of the effect of the flow on the flame structure. However, experience shows that burning rates determined from rocket and strand burner tests are comparable (Fig. 5-51).

5.2.4. High Pressure Domain ($p > 100$ atm) - At high pressures and for large AP grain diameter, the burning rate with some fuels is very close to the AP decomposition rate. We might assume that since the regression rate of AP is higher than that of the fuel, the AP grains become embedded in the fuel and cannot receive much heat or mass from fuel gases. Then the decomposition zone at the crystal surface controls the burning rate. The decomposition gases burn with the fuel gases much further away and, according to Friedman, do not contribute to the linear regression velocity.

For other fuels however, the difference between the burning velocity and the regression rate of AP is more marked at high pressure than at low pressure, as Fig. 5-33 indicates. Powling suggested that in certain cases the decomposition rate of AP is high and decomposition can proceed independently of the oxidation process of the fuel, but that with certain fuels the regression rate of AP can be increased or decreased by adding fuel. He believes that the flame temperature, hence the global burning rate can be modified at the interface between fuel and oxidizer (diffusion flame). The flame propagation velocity from one crystal to the next can also be inhibited by liquified fuel; the thermal stability of the fuel plays an important part and one can, as a first approximation, classify the burning rates in the same order as the pyrolysis rates. Low volatile fuels, such as carbon or aluminum, have a larger effect at high pressure than at low pressure since they do not hinder the flame propagation.

5.3. Summary of Combustion Domains

The various combustion domains that we have identified are grouped schematically in Fig. 5-52.

- a) Premixed flame domain: The mechanism controlling the burning rate is very close to that observed with homogeneous solid propellants, the dominant processes being of chemical origin.
- b) Mixed flame domain: The combustion zone is composed of a juxtaposition of premixed and diffusion flames; the chemical and diffusion processes interfere in this domain.
- c) Diffusion flame domain: For large diameter oxidizer grains, the premixed flames disappear and only diffusion flames remain.
- d) Plateau domain: For a given grain size, in a certain pressure interval, the burning rate is independent of pressure; this is attributed to random local varia-

tions of the mixture ratio.

- e) High pressure domain: At high pressure, the AP decomposition process controls the burning rate of the solid propellant.

The description of these domains implies that it is not possible to present a single mechanism for the combustion of heterogeneous solid propellants. We have attempted to discover the important phenomena, but our description evidently remains a very simplified view of the combustion of heterogeneous solid propellants. However, it permits a preliminary investigation of this very complex problem.

References

- (1) Schultz R.B., Green L. and Penner S.S., Combustion and Propulsion, Pergamon Press, New York, pp. 367 - 420, 1958.
- (2) Heath G.A. and Hirst R., Some Characteristics of the High Pressure Combustion of Double-Base Propellant, Eighth Symposium (International) on Combustion. The Williams and Wilkins Company, Baltimore, 1962.
- (3) Moutet A. et Nadaud L., Températures rapidement variables. Techniques de L'ingénieur R. 2760, 1, Paris.
- (4) Sabadell A.J., Wergrat J. and Summerfield M., The Measurement of Temperature Profiles through Solid Propellant Flames. AIAA Solid Propellant Conference, Preprint No. 64-106, January 1964.
- (5) Nachbar W. and Williams F.A., On the Analysis of Linear Pyrolysis Experiments. IX Symposium (International) on Combustion, Academic Press, New York, pp. 345-357, 1963.
- (6) Andersen W.H., Comments on Gas Film Effects in the Linear Pyrolysis of Solids. AIAA Journal, Vol. 2, pp. 404-405, 1964.
- (7) Cantrell R.H., Gas Film Effects in the Linear Pyrolysis of Solids. AIAA Journal, Vol. 1, pp. 1544-1555, 1963.
- (8) Coates R.L., Linear Pyrolysis Rate Measurements of Propellant Constituents. AIAA Preprint No. 65-55, January 1965.
- (9) Hansel J.M., Lee S.Y. and McAlevy III R., Experimental Study of the Composite Solid Propellant-Deflagration Process on a Fundamental Level. Stevens Institute of Technology, Hoboken N.J., Contract Nonr 263(48), 1964.
- (10) Chaiken R.F. and Andersen W.H., The Role of Binder in Composite Propellant Combustion Solid Propellant Rocket Research. Progress in Astronautics and Rocketry, Vol. 1, pp. 227-249, 1960.
- (11) Chaiken R.F. et al., Kinetics of the Surface Degradation of Polymethylacrylate, J. Chem. Phys., Vol. 32, pp. 141-146, 1960.
- (12) Blatz P.J. and Andersen W.H., Fundamental Problems Relating to the Fabrication of Plastics for High Temperature Application. Fifth AGARD Combustion and Propulsion Colloquium, Pergamon Press, New York, 1963.
- (13) Guinet M., La vitesse de pyrolyse de matériaux composites. La Recherche Aéronautique, Vol. 80, p. 33, 1961.

- (14) Chidlovsky A. A., Décomposition Thermique et Combustion du Perchlorate d'hydrazine, J. Chimie Appliquée, Tome 35, pp. 756-759, 1962.
- (15) Levy J. B., von Elbe G. et al., Research on the Deflagration of High-Energy Solid Oxidizers, Atlantic Research Corp., Alexandria, Va., Final Technical Rept., Contract No. AF 49 (638)-1169, November 1965.
- (16) Levy J. B. and Friedman R., Further Studies of Pure A F Deflagration. 8th Symposium (International) on Combustion, Williams and Wilkins, Baltimore, pp. 663-672, 1962.
- (17) Adams G. K. et al., The Combustion of Propellants based upon A P. 8th Symposium (International) on Combustion, Williams and Wilkins, Baltimore, pp. 593-705, 1962.
- (18) Irvin O. R. et al., Deflagration Characteristics of A. P. at High Pressure. 9th Symposium (International) on Combustion, Academic Press, New York, pp. 358-365, 1963.
- (19) Shannon L. J. and Petersen E. E., Deflagration Characteristics of A P Strands. AIAA Journal, Vol. 2, pp. 168-169, 1964.
- (20) Friedman R. et al., Deflagration of A. P. 6th Symposium (International) on Combustion, Reinhold Publishing Corp., New York, pp. 612-618, 1956.
- (21) Barrère M. and Nadaud L., Combustion of Ammonium Perchlorate Spheres in a Flowing Gaseous Fuel. 10th Symposium (International) on Combustion, The Combustion Institute, Pittsburgh, Pa., 1381-94, 1965.
- (22) Burger J. and Van Tiggelen A., Contribution à l'étude de la combustion des poudres composites. Memoires Academie Royale De Belgique, Tome XXXIV, fac. 3.
- (23) McAlevy III R. F., Experimental Study of the Composite Solid Propellant Deflagration Process on a Fundamental Level. Stevens Institute of Technology, 10th Quarterly Progress Report, Hoboken, N. J. Contract Nonr. 263(48), March, 1964.
- (24) Kiczek C. R., Lee S. Y. and McAlevy III R. F., Experimental Study of the Composite Solid Propellant Deflagration Process on a Fundamental Level. Stevens Institute of Technology, Hoboken, N. J., 11th Quarterly Progress Report, Contract Nonr. 263(48), April-June 1964.
- (25) Burger J., Application de la notion de coincement a la combustion des propergols solides composites. C. R. Ac. Sc., Paris, t 258, pp. 2821-2824, 9 March 1964.
- (26) Burger J. and Van Tiggelen A., Etude de la combustion de propergols hybrides composites. Bulletin de la Société Chimique de France, p. 3122, 1964.
- (27) McAlevy III R. F. and Lee S. Y., A Porous Plug Burner Technique for the Study of Composite Solid Propellant Deflagration. Heterogeneous Combustion, Vol. 15 of AIAA Series Progress in Astronautics and Rocketry, Academic Press, New York, pp. 583-608, 1964.
- (28) Cummings G. A. McD. and Pearson G. S., Perchloric Acid Decomposition Flame. Combustion and Flame, Vol. 8, pp. 199-202, 1964.

- (29) Cummings G.A. McD. and Hall A.R., Perchloric Acid Flames. I. Pre-mixed Flames with Methane and Other Fuels. 10th Symposium (International) on Combustion, The Combustion Institute, Pittsburgh, Pa., 1365-1372, 1965.
- (30) Adams G.K., Newman B.M. and Robins A.B., The Combustion of Propellants based upon A.P. 8th Symposium (International) on Combustion, Williams and Wilkins Co., Baltimore, pp.693-705, 1962.
- (31) Arden E.A., Powling J. and Smith W.A., Observations on the Burning of A.P. Combustion and Flame, Vol. 6, pp. 21-33, 1962.
- (32) Powling J. and Smith W.A., Measurement of the Burning Surface Temperatures of Propellant Compositions by Infrared Emission. Combustion and Flame, Vol. 7, pp. 269-275, 1963.
- (33) Friedman R. and Macek A., Ignition and Combustion of Aluminum Particles. Combustion and Flame, Vol. 6, pp. 9-19, 1962.
- (34) Glassman I., Metal Combustion Process. American Rocket Society Paper No. 938-59, 1959.
- (35) Brzustowski T.A. and Glassman I., Vapor-Phase Diffusion Flames in the Combustion of Magnesium and Aluminum. Heterogeneous Combustion, Vol. 15 of AIAA Series Progression Astronautics and Rocketry, Academic Press, New York, pp. 75-158, 1964.
- (36) Kling R. and Brulard J., Etude de la combustion des poudres composites par la microphotographie ultra-rapide. La Recherche Aéronautique, No. 80, pp. 2-11, 1961.
- (37) McCarty K.P., Techniques for Studying the Combustion of Aluminum in Solid Propellants. Pyrodynamics, Vol. 1, pp. 71-89, 1964.
- (38) Summerfield M., Burning Mechanism of A.P. Propellants. Solid Propellant Rocket Research — Progress in Astronautics, Vol. 1, Academic Press, New York, 1960.
- (39) Bastress E.K., Hall K.P. and Summerfield M., Modification of the Burning Rate of Solid Propellant by Oxidizer Particle Size Control. Solid Propellant Conference, American Rocket Society, 1961.
- (40) Cole R.B., Wenograd J. and Summerfield M., Solid Propellant Combustion Mechanism Studies. Aerospace and Mechanical Sciences Report No. 446-0, Princeton University, 17 June 1965.
- (41) Ohlemiller T.J., Wenograd J. and Summerfield M., Solid Propellant Combustion Mechanism Studies. Aerospace and Mechanical Sciences Report No. 446 r, Princeton University.
- (42) Powling J. and Smith W.A., The Surface Temperature of Ammonium Perchlorate Burning at Elevated Pressures. Tenth Symposium (International) on Combustion, The Combustion Institute, Pittsburgh, Pennsylvania, pp. 1373-1380, 1965.
- (43) Povinelli L.A., Study of Composite Solid Propellant Flame Structure Using a Spectral Radiation Shadowgraph Technique. AIAA Preprint No. 65-60, 1965.

- (44) **Barrère M. and Nadaud L.**, Les Domaines de Combustion des Poudres Composites. *La Recherche Aéronautique*, No. 98, pp. 15-31, 1964.
- (45) **Silla M.**, Burning Rate of Composite Solid Propellants at Subatmospheric Pressure. *ARS Journal* Vol. 31, 1961.
- (46) **Selzer H.**, Über Den Verbrennungsmechanismus von Composite Treibstoffen, *Raketentechnik und Raumfahrt Forschung*, Heft 2/63, pp. 41-46.
- (47) **Merrington L.E.**, Correlation of Motor and Strand Composite Propellant Burning Rate. *AIAA Journal*, Vol. 2, pp. 1671-1673, 1964.
- (48) **Dubrow B., Guth E.D. and Wong M.W.**, Ballistics of Solid Propellants during Thrust Modulation. Solid Propellant Rocket Conference, Palo Alto, Preprint No. 64-130, 1964.
- (49) **Davis A.**, The Combustion of Particles of Metal Ingredients. *Combustion and Flame*, Vol. 7, 1963.
- (50) **Watermeier L.A., Aungust W.P. and Pfaff S.P.**, An Experimental Study of the Aluminum Additive Role in Unstable Combustion of Solid Rocket Propellants. Ninth Symposium (International) on Combustion, Academic Press, New York, 316-326, 1963.
- (51) **Jacobs P.W.M. and Russell-Jones A.**, *AIAA J.*, 5, 829, 1967.

Chapter 6

**Theories of Steady-State Solid Propellant
Combustion**

Nomenclature

B_k	temperature-independent coefficient of the frequency factor for the k-th reaction
c_i	concentration of species i in the gas phase
c_p	isobaric specific heat
c_s	actual number of moles of condensed material per unit surface area
c_s^{\neq}	number of moles of activated complex per unit surface area
d	diameter of oxidizer crystal
E	gas-phase activation energy
E_k	activation energy for k-th reaction
E_s	activation energy for gasification process
\tilde{f}_i	body force on species i per unit mass of species i
g	$\equiv d\tau/d\xi$
h	enthalpy per unit mass of fluid; Planck's constant; average flame height
h_c	enthalpy per unit mass for the condensed material
h_i	enthalpy per unit mass for chemical species i
h_i^o	enthalpy of formation of species i at reference temperature T^o
k	Boltzmann's constant
K_s^{\neq}	equilibrium constant for activation process
L	enthalpy of gasification per unit mass
m	temperature exponent of product of thermal conductivity and reaction rate
\dot{m}	mass burning rate per unit area
n	overall order of the gas-phase reaction
P	permeability of porous plate
p	hydrostatic pressure
\mathbf{p}	total pressure tensor
p_e	equilibrium vapor pressure
p_{∞}	pressure on downstream side of plate

q	energy released per gram of product formed in a reaction
\vec{q}	energy flux vector
q_C	total energy per unit surface area per second lost from condensed phase
\vec{q}_R	radiant heat flux vector
$q_{R,t}$	heat loss (per unit area per sec) by radiation from the surface
q_s	partition function of the unexcited surface molecules
q_s^{\ddagger}	partition function of the complex (with translation in the reaction coordinate and ground-state energy factors removed)
q_v	vibrational partition function
r	linear regression rate
R^0	universal gas constant
T	temperature
τ	shear stress tensor
T^0	reference temperature
T_f	flame temperature
T_{fa}	adiabatic flame temperature
T_i	initial temperature of solid
T_p	plate temperature
T_s	surface temperature
U	unit tensor
\vec{v}	fluid mass-average velocity
\vec{V}_i	diffusion velocity of species i
w	mass rate of production of products per unit volume
w_i	mass rate of production of species i per unit volume by chemical reactions
w_i'	surface mass rate of production species i per unit area
\vec{x}	velocity of control surface
X_i	mole fraction of chemical species i
X_j	mole fraction of chemical species j
Y_i	mass fraction of chemical species i

Y_1^*	dimensionless quantity defined in Eq. 6-23
α	surface accommodation ("sticking") coefficient for species 1
α_k	exponent determining the temperature dependence of the frequency factor for the k-th reaction
δ	flame height; distance in the reaction coordinate at the col over which the complex is assumed to exist
ϵ_i	mass flux fraction of species i in the gas
κ	coefficient of bulk viscosity
Λ	dimensionless (constant) burning rate eigenvalue (see Eq. 6-39)
λ	thermal conductivity
μ	coefficient of (shear) viscosity
$\nu_{1,k}, \nu'_{1,k}$	stoichiometric coefficient for species i appearing as a reactant and a product, respectively, in reaction k
ξ	dimensionless independent variable defined in Eq. 6-34
ρ	fluid density
ρ'	mass per unit surface area
ρ_c	density of condensed phase
τ	dimensionless dependent temperature variable defined in Eq. 6-33; average time for a complex to decay to gas-phase products.
ω	dimensionless reaction rate function (see Eq. 6-40)

Script Letters

a	surface
\mathcal{C}^i	symbol for chemical species i
\mathcal{D}_{ij}	binary diffusion coefficient for the species pair i and j
$\mathcal{D}_{T,i}$	thermal diffusion coefficient for species i in multicomponent gas mixture
m	molecular weight of the gasifying species
\overline{m}	average molecular weight
m_i	molecular weight of chemical species i
\mathcal{V}	volume
∇	gradient operator

Superscripts

T transpose of tensor

Subscripts

c conditions in the condensed phase

f conditions at $x = \infty$

g conditions in the gas phase

i a chemical species

j a chemical species

k a chemical reaction

s conditions at $x = 0+$

l reactant that vanishes when the reaction goes to completion

Theories of Steady-State Solid Propellant Combustion

1. Basic Equations of Aerothermochemistry

1.1. Introduction

The most accurate theories of the steady-state combustion of solid propellants are based on the full equations of aerothermochemistry. At this point, it is therefore necessary for us to introduce these basic equations. Time dependences in the equations are not needed in the present chapter. However, unsteady phenomena are considered in later chapters and the unsteady terms introduce little additional complexity into the full equations. Therefore the time-dependent equations will be developed here.

In Section 2, after discussing some of the early models for combustion of double base propellants, the equations of aerothermochemistry are applied to the analysis of steady-state combustion of homogeneous solid propellants. Adiabatic combustion is analyzed first and then the effects of heat losses are considered. Theories of the decomposition of ammonium nitrate and ammonium perchlorate are treated in Section 3. Various mechanisms for combustion of composite solids are reviewed in Section 4 and metal combustion is considered in the final section. In all of these studies, truly acceptable theories must recognize and satisfy the equations of aerothermochemistry.

1.2. Origin of the Equations

Equations governing the conservation of mass for each of the chemical species, momentum and energy are required. The viewpoint either of continuum mechanics or of kinetic theory may be adopted in deriving these equations. Some references to the development of the continuum viewpoint for multicomponent gases may be found in Ref. (1); the kinetic viewpoint was developed through the work of many investigators, a number of whom are cited in Ref. (2). The continuum approach provides a macroscopic interpretation of the nature of the interactions among the various species in the multicomponent fluid. The kinetic approach provides molecular interpretations for the macroscopic variables and is essential for relating the phenomenological transport coefficients to the molecular interaction potentials. The two viewpoints are therefore complementary and both approaches are of interest. However, neither of the developments are brief enough to be presented here. Therefore, the reader is referred to the literature for derivations of the governing equation (2) (3). We shall merely quote the equations of aerothermochemistry and then offer explanations of the terms that appear in them.

1.3. Integral Form of the Governing Equations

In an inertial reference system for a fluid in three-dimensional Euclidean space, consider a volume \mathcal{V} bounded by a surface σ , the points of which move with velocity

$\dot{\mathbf{x}}$ which may be a function of time. If ρ is the density of the fluid and \mathbf{v} is its (mass average) velocity, then conservation of mass for the fluid contained in \mathcal{V} may be written as:

$$\frac{d}{dt} \left(\int_{\mathcal{V}} \rho d\mathcal{V} \right) + \int_{\sigma} \rho (\mathbf{v} - \dot{\mathbf{x}}) \cdot \mathbf{n} d\sigma = 0, \quad (\text{Eq. 6-1})$$

where \mathbf{n} is the outward pointing normal to the surface σ . The first term in Eq. 6-1 is the time rate of increase of mass inside \mathcal{V} ; the second term equals the mass per second flowing outward across the boundary σ , due to the motion of the fluid and the motion of the boundary.

The integral form of the equation for conservation of momentum (Newton's law) for the fluid inside \mathcal{V} is :

$$\frac{d}{dt} \left(\int_{\mathcal{V}} \rho \mathbf{x} d\mathcal{V} \right) + \int_{\sigma} \rho \mathbf{x} [(\mathbf{v} - \dot{\mathbf{x}}) \cdot \mathbf{n}] d\sigma = - \int_{\sigma} \mathbf{p} \cdot \mathbf{n} d\sigma + \int_{\mathcal{V}} \rho \sum_{i=1}^N Y_i \mathbf{f}_i d\mathcal{V} \quad (\text{Eq. 6-2})$$

where \mathbf{p} is the total pressure tensor (including the shear stress tensor \mathbf{T} and the product of the hydrostatic pressure p with the unit tensor \mathbf{U} , i.e., $\mathbf{p} = p\mathbf{U} + \mathbf{T}$), Y_i is the mass fraction of species i in the fluid and \mathbf{f}_i is the body force on species i per unit mass of species i . The quantity $\sum_{i=1}^N Y_i \mathbf{f}_i$ is clearly the total body force per unit mass acting on the fluid. The total number of chemical species in the fluid is N . In Eq. 6-2, the sum of the time rate of change of momentum of the fluid contained in \mathcal{V} and the net rate at which momentum flows out of \mathcal{V} across σ (due to the motion of the fluid and of σ) has been equated to the sum of the surface forces and the body forces acting on the fluid contained in \mathcal{V} .

Conservation of energy (the first law of thermodynamics) may be expressed in the form :

$$\begin{aligned} & \frac{d}{dt} \left[\int_{\mathcal{V}} \rho \left(h - \frac{p}{\rho} + \frac{v^2}{2} \right) d\mathcal{V} \right] + \int_{\sigma} \rho \left(h - \frac{p}{\rho} + \frac{v^2}{2} \right) [(\mathbf{v} - \dot{\mathbf{x}}) \cdot \mathbf{n}] d\sigma \\ & = - \int_{\sigma} \mathbf{q} \cdot \mathbf{n} d\sigma - \int_{\sigma} \mathbf{V} \cdot \mathbf{p} \cdot \mathbf{n} d\sigma + \int_{\mathcal{V}} \rho \sum_{i=1}^N Y_i \mathbf{f}_i \cdot (\mathbf{v} + \mathbf{V}_i) d\mathcal{V} \end{aligned} \quad (\text{Eq. 6-3})$$

Here h is the enthalpy per unit mass of the fluid, so that $h - \frac{p}{\rho}$ is its internal energy per unit mass. The energy flux vector is denoted by \mathbf{q} and v^2 represents the square of the magnitude of \mathbf{v} . The symbol \mathbf{V}_i denotes the diffusion velocity of species i , thus implying that the (mass-average) velocity of species i is $\mathbf{v} + \mathbf{V}_i$. The five terms in Eq. 6-3 represent the time rate of increase of internal plus ordered kinetic energy of the fluid contained in \mathcal{V} , the rate at which internal plus kinetic energy flows out of \mathcal{V} across its surface σ , the rate at which energy flows across σ into \mathcal{V} due to heat conduction, diffusion and radiation, the work done on the fluid inside \mathcal{V} by surface forces and finally the work done on the fluid inside \mathcal{V} by body forces.

In integral form, the equation for the conservation of mass of a particular chemical species i may be written as :

$$\frac{d}{dt} \int_{\mathcal{V}} \rho Y_i d\mathcal{V} + \int_{\sigma} \rho Y_i (\mathbf{v} + \mathbf{V}_i - \dot{\mathbf{x}}) \cdot \mathbf{n} d\sigma = \int_{\mathcal{V}} w_i d\mathcal{V}, \quad i = 1, \dots, N, \quad (\text{Eq. 6-4})$$

where the mass rate of production of species i per unit volume by chemical reactions is denoted by w_i . Here the rate of increase of mass of species i inside the volume \mathcal{V} , plus the net rate at which mass of species i flows out of \mathcal{V} across its surface σ (due to mass-average fluid motion, diffusion of species i and motion

of the surface), is equated to the mass rate of production of species i inside \mathcal{V} .

Since $\sum_{i=1}^N Y_i = 1$ by definition of Y_i , $\sum_{i=1}^N Y_i \underline{Y}_i = 0$ by definition of \underline{v} and $\sum_{i=1}^N w_i = 0$

due to conservation of mass in chemical reactions, by summing Eq. 6-4 of all species i we obtain Eq. 6-1, thus implying (in view of the vector character of Eq. 6-2) that Eqs. 6-1 to 6-4 constitute $N + 4$ independent integral conservation equations.

Before writing down the appropriate expressions for the transport and chemical rate terms, we shall derive the differential forms of the governing equations from Eqs. 6-1 to 6-4.

1.4. Differential Form of the Governing Equations

Two mathematical identities are needed in deriving the differential forms of the conservation equations from their integral forms. The first is the observation that for any scalar, vector or tensor function of space and time $f(\underline{x}, t)$, the time rate of change of its integral over \mathcal{V} is :

$$\frac{d}{dt} \left(\int_{\mathcal{V}} f d\mathcal{V} \right) = \int_{\mathcal{V}} \frac{\partial f}{\partial t} d\mathcal{V} + \int_{\sigma} f (\underline{\dot{x}} \cdot \underline{n}) d\sigma. \quad (\text{Eq. 6-5})$$

The second is the divergence theorem for any vector (or tensor) function of space and time, $\underline{f}(\underline{x}, t)$, viz.,

$$\int_{\sigma} \underline{f} \cdot \underline{n} d\sigma = \int_{\mathcal{V}} \underline{\nabla} \cdot \underline{f} d\mathcal{V}, \quad (\text{Eq. 6-6})$$

where $\underline{\nabla}$ is the gradient operator. It is also necessary to realize that, since the volume \mathcal{V} is arbitrary, an equation of the form $\int_{\mathcal{V}} f d\mathcal{V} = 0$ can be satisfied if and only if $f = 0$.

In Eq. 6-1, we may employ Eq. 6-5 with $f = \rho$ and Eq. 6-6 with $\underline{f} = \rho \underline{v}$, thereby obtaining :

$$\partial \rho / \partial t + \underline{\nabla} \cdot (\rho \underline{v}) = 0 \quad (\text{Eq. 6-7})$$

as the differential form of the overall mass conservation ('continuity') equation. Through similar operations, Eqs. 6-2, 6-3 and 6-4 reduce to :

$$\partial \underline{v} / \partial t + \underline{x} \cdot \underline{\nabla} \underline{v} = - \underline{\nabla} p / \rho - (\underline{\nabla} \cdot \underline{\tau}) / \rho + \sum_{i=1}^N Y_i \underline{f}_i, \quad (\text{Eq. 6-8})$$

$$\begin{aligned} \frac{\partial}{\partial t} \left(h + \frac{v^2}{2} \right) + \underline{x} \cdot \underline{\nabla} \left(h + \frac{v^2}{2} \right) &= \frac{1}{\rho} \frac{\partial p}{\partial t} - \frac{1}{\rho} \underline{\nabla} \cdot \underline{q} - \frac{1}{\rho} \underline{\nabla} \cdot (\underline{\tau} \cdot \underline{v}) \\ &+ \sum_{i=1}^N Y_i \underline{f}_i \cdot (\underline{\dot{v}} + \underline{V}_i), \end{aligned} \quad (\text{Eq. 6-9})$$

and:

$$\partial Y_i / \partial t + \underline{v} \cdot \underline{\nabla} Y_i = w_i / \rho - [\underline{\nabla} \cdot (\rho Y_i \underline{V}_i)] / \rho, \quad i=1, \dots, N. \quad (\text{Eq. 6-10})$$

Equation 6-8 is obtained from Eq. 6-2 by employing Eq. 6-5 with $f = \rho \underline{v}$ and Eq. 6-6 with $\underline{f} = \rho + \rho \underline{v} \underline{v}$, then utilizing the fact that \mathcal{V} is arbitrary and finally simplifying the terms $\partial \rho \underline{v} / \partial t + \underline{\nabla} \cdot (\rho \underline{v} \underline{v})$ by using Eq. 6-7. In deriving Eq. 6-9, use is made of Eq. 6-5 with $f = \rho (h - p/\rho + v^2/2)$, of Eq. 6-6 with $\underline{f} = \rho \underline{v} (h - p/\rho + v^2/2) + \underline{q} + \underline{v} \cdot \underline{\tau}$, and of Eq. 6-7 for simplifying the terms $\partial / \partial t [\rho (h + v^2/2)] + \underline{\nabla} \cdot [\rho \underline{v} (h + v^2/2)]$. The definition $p = pU + \underline{\tau}$ and well-known properties of the unit tensor are used in deriv-

ing both results appearing in Eqs. 6-8 and 6-9. To obtain Eq. 6-10 from Eq. 6-4 involves employing Eq. 6-5 with $f = \rho Y_i$, Eq. 6-6 with $\tilde{f} = \rho Y_i (\tilde{v} + \tilde{V}_i)$ and Eq. 6-7.

1.5. Transport Phenomena; Reaction Rates

There are many more dependent variables appearing in Eqs. 6-7 through 6-10 than there are independent equations. Additional equations of two different types are required for interrelating these variables. One type consists of the thermodynamic relations among the properties of the fluid medium; these are given in the following section. The second type, which is considered here, involves transport and rate phenomena.

We might emphasize that Eqs. 6-1 through 6-10 are applicable to any fluid. However, thermodynamic properties and transport processes depend upon the molecular structure and the state of aggregation of the fluid. Thus, some aspects of the equations that we shall now begin to present will be different for gases, liquids, glasses, etc. Molecular structure is understood sufficiently well to enable us to give detailed indisputable results only for rigid solids and for 'dilute', perfect, multi-component gases. The appropriate equations for solids are relatively simple and can be obtained by simplifying and slightly modifying the equations for gases. Therefore we shall consider only multicomponent ideal gas mixtures in the following discussions. Of course, many of the results will be applicable at least approximately for liquids as well, when properly interpreted.

The results concerning transport properties that we shall quote, all follow directly from the kinetic theory of near-equilibrium dilute gases, as developed by Chapman and Enskog. The justifiable approximation that molecular collisions may be treated in terms of a classical intermolecular potential, is employed. Although the basic approach would be to calculate the intermolecular potential from quantum mechanics, this cannot be done except for the simplest molecules, and therefore approximate potentials are employed, with coefficients that are adjusted empirically to fit experimental data on transport properties. This procedure is very satisfactory, in that all transport coefficients are related rigorously to a small number of empirical constants. For chemical reaction rates, the empiricism is nearly as satisfactory because only a small number of experimental constants appear in the rate formula, but the basis is not so sound since essentially quantum mechanical phenomena influence the process in a variety of ways and seldom are the reactions near equilibrium.

In Eqs. 6-8 and 6-9, the shear stress tensor τ is given by :

$$\tau = \left(\frac{2}{3} \mu - \kappa \right) (\nabla \cdot \mathbf{v}) \mathbf{U} - \mu [(\nabla \mathbf{v}) + (\nabla \mathbf{v})^T] \quad (\text{Eq. 6-11})$$

for a gas. Here μ is the coefficient of (shear) viscosity, κ is the coefficient of bulk viscosity, $(\nabla \mathbf{v})$ denotes a dyadic product (a second-rank tensor) and the superscript T identifies the transpose of the tensor. The quantity μ is independent of pressure and is proportional to a power of the temperature that generally lies between 1/2 and 1; an approximate formula for its dependence upon chemical composition is given on p. 424 of Ref. (3). The quantity κ vanishes unless translational-internal relaxation processes are of importance, in which case it is positive; κ is zero for monatomic gases and also for polyatomic gases provided the relaxation times are either very small or very large. Tables of viscosity coefficients are available for a number of gases. Further discussion and some data may be found (2), (4).

In Eq. 6-9, the energy flux vector \underline{q} for a gas is:

$$\underline{q} = \underline{q}_R - \lambda \nabla T + \rho \sum_{i=1}^N h_i Y_i \underline{V}_i + R^* T \sum_{i=1}^N \sum_{j=1}^N \frac{X_j \mathcal{D}_{T,i}}{m_i \mathcal{D}_{ij}} (\underline{V}_i - \underline{V}_j), \quad (\text{Eq. 6-12})$$

where \underline{q}_R denotes the radiant heat flux vector, λ is the coefficient of thermal conductivity, T denotes temperature, h_i is the enthalpy per unit mass for chemical species i , R^* denotes the universal gas constant, X_i represents the mole fraction of chemical species j , m_i is the molecular weight of chemical species i , \mathcal{D}_{ij} is the binary diffusion coefficient for the pair of chemical species i and j , and $\mathcal{D}_{T,i}$ is the coefficient of thermal diffusion for species i in the multicomponent gas mixture. The four terms on the right-hand side of Eq. 6-12 represent the energy fluxes arising, respectively, from radiation transport, from heat conduction, from the energy transport incidental to the diffusion of the various chemical species across a surface moving with the mass-average velocity, and from the Dufour effect, the heat flux process that is the inverse (in the sense of irreversible thermodynamics) to the thermal diffusion process. The \underline{q}_R term can be of importance when the system absorbs or emits radiation. In the second term, which is often dominant particularly for solids, the coefficient λ is independent of pressure, is proportional to a power of temperature that generally lies between 1/2 and 1 for gases and depends upon chemical composition in a rather complex manner (2) (4). The third term is readily understood to arise whenever diffusion occurs. The last term, which in principle is present whenever thermal diffusion can occur, nevertheless is almost always negligibly small; the coefficients appearing therein are discussed in the next paragraph where diffusion is considered.

For a gas, the diffusion velocities \underline{V}_i appearing in Eq. 6-10 are determined by the equations:

$$\begin{aligned} \nabla X_i = & \sum_{j=1}^N \left(\frac{X_i X_j}{\mathcal{D}_{ij}} \right) (\underline{V}_j - \underline{V}_i) + (\underline{V}_i - X_i) \left(\frac{\nabla p}{p} \right) + \left(\frac{\rho}{p} \right) \sum_{j=1}^N Y_i Y_j (\underline{f}_i - \underline{f}_j) \\ & + \sum_{j=1}^N \left[\left(\frac{X_i X_j}{\rho \mathcal{D}_{ij}} \right) \left(\frac{\mathcal{D}_{T,j}}{Y_j} - \frac{\mathcal{D}_{T,i}}{Y_i} \right) \right] \left(\frac{\nabla T}{T} \right), \quad i = 1, \dots, N. \end{aligned} \quad (\text{Eq. 6-13})$$

Equation 6-13 shows that concentration gradients can be maintained by diffusion, by a pressure gradient (for a species whose mole fraction differs from its mass fraction), by body forces (provided that the force per unit mass is not the same for all species) and by a temperature gradient (the Soret effect). Derivations of Eq. 6-13 may be found (2), (3). When multiplied by the total hydrostatic pressure p , the binary diffusion coefficients \mathcal{D}_{ij} for gases become functions of temperature alone and are proportional to T raised to a power lying between roughly 3/2 and 2; thus, each \mathcal{D}_{ij} is inversely proportional to p and is independent of chemical composition, a fact which makes Eq. 6-13 more appealing for gases than other diffusion equations employing composition-dependent 'multicomponent' diffusion coefficients. The thermal diffusion coefficients $\mathcal{D}_{T,i}$ appearing in Eq. 6-13 may be either positive or negative and are dependent on pressure, temperature and composition in a manner that, in general, can be rather complicated; thermal diffusion is often negligible because, in most cases, $\mathcal{D}_{T,i} / p \mathcal{D}_{ij} \lesssim 0.1$ for all pairs i and j . Formulas and tables for binary and thermal diffusion coefficients may be found in Refs. (2) and (4).

According to the phenomenological laws of chemical kinetics, the chemical production term w_i appearing in Eq. 6-10 is given by:

$$w_i = \sum_{k=1}^M \left(\nu'_{i,k} - \nu_{i,k} \right) B_k T^{\alpha_k} e^{-E_k/R^\circ T} \prod_{j=1}^N \left(\frac{X_j P}{R^\circ T} \right)^{\nu_{j,k}}, \quad i=1, \dots, N, \quad (\text{Eq. 6-14})$$

where $\nu_{i,k}$ is the stoichiometric coefficient for species i appearing as a reactant in reaction k , $\nu'_{i,k}$ is the stoichiometric coefficient for species i appearing as a product in reaction k , E_k represents the activation energy for the k 'th reaction, B_k is the temperature-independent coefficient of the frequency factor for the k 'th reaction, and α_k denotes the exponent determining the temperature dependence of the frequency factor for the k 'th reaction. There are M different reactions occurring and N different species present in the system. By definition, $\nu_{i,k}$, $\nu'_{i,k}$, E_k , B_k and α_k are constants. The last three of these constants must be obtained by experimental measurements, although reaction rate theories may be employed to justify the empirical values *a posteriori* and also to provide limits beyond which the experimental values cannot lie. Reviews of chemical kinetics may be found on pp. 358-389 of Ref. (3) and in Refs. (4-6).

1.6. Thermodynamic Relations; Counting of Variables

For an ideal gas, the equation of state is :

$$p = \rho R^\circ T / m, \quad (\text{Eq. 6-15})$$

where :

$$m = \sum_{i=1}^N X_i m_i = \left(\sum_{i=1}^N Y_i / m_i \right)^{-1} \quad (\text{Eq. 6-16})$$

is the mean molecular weight. The mole fractions are, of course, related to the mass fractions by the equation :

$$X_i = m Y_i / m_i, \quad i = 1, \dots, N. \quad (\text{Eq. 6-17})$$

It is also true that for an ideal gas, the total enthalpy per unit mass for the mixture is related to the enthalpy per unit mass for the individual species, according to the formula :

$$h = \sum_{i=1}^N Y_i h_i. \quad (\text{Eq. 6-18})$$

The quantities h_i are functions of temperature alone in ideal gas mixtures; specification of these functions along with Eq. 6-18, is equivalent to specifying the caloric equation of state of the system.

Equations 6-15 through 6-18 constitute the additional relations that are needed to form a closed set of equations. This can be seen by surveying Eqs. 6-7 through 6-18. Thus, we may, for example, choose ρ , χ , T and Y_i to be the principal set of dependent variables. Equations 6-7 through 6-10 provide the correct number of independent conservation equations for determining these variables. However, the additional dependent variables p , τ , f_i , n , q , V_i and w_i appear in these equations. The equation of state relates p to ρ , T and X_i , and the caloric equation of state relates h to T and Y_i (see Eq. 6-15, 6-16 and 6-18). The reaction rate equation (Eq. 6-14) relates w_i to the principal dependent variables in terms of presumed known reaction rate constants; (note that Eq. 6-17 implies that X_i is related to Y_i). The transport equations (Eqs. 6-11, 6-12 and 6-13) relate the variables, τ , q and V_i to f_i , q_i and the principal dependent variables (or quantities simply related to

them through Eqs. 6-15 to 6-18), in terms of transport coefficients, which are also known functions of the principal dependent variables. Hence, we need only specify f_{\pm} and q_{\pm} in terms of the principal dependent variables in order to obtain a closed set of equations. These last two specifications depend on the nature of the body forces and the radiative processes. Therefore we shall not give the appropriate formulas; we merely note that in principle, Eqs. 6-7 through 6-18 constitute the closed set of governing equations for aerothermochemistry.

1.7. Conservation Conditions at an Interface

We conclude our discussion of the equations of aerothermochemistry by deriving the forms that the conservation equations assume at an interface. These interface equations provide necessary boundary conditions in studies of solid propellant combustion. They are by no means the only boundary conditions that are needed in analyzing propellant burning. However, they must always be satisfied at the boundaries, either actively or trivially. It is therefore rather important that the correct forms of the interface conservation equations be recognized.

The interface conservation equations can be derived most easily from the integral forms of the conservation equations (Eqs. 6-1 to 6-4). Let the volume \mathcal{V} be in the shape of a thin slab, whose thickness approaches zero. In the limit, the surface area σ consists of two parts of equal area, one located on each side of the interface of interest. The outward normal at a point on one part of the surface approaches the inward normal at the corresponding point on the other part. By identifying one side of the interface by the subscript + and the other side by the subscript -, we may therefore replace the integral over σ by a single integral over the interface area σ_I in the conservation equations. Since \mathcal{V} goes to zero in the limiting process described above, Eqs. 6-1 to 6-4 reduce to :

$$\int_{\sigma_I} \left[\rho \left(\dot{x}_+ - \dot{x} \right) - \rho_- \left(\dot{x}_- - \dot{x} \right) \right] \cdot \bar{n}_+ d\sigma = - \lim_{\mathcal{V} \rightarrow 0} \left[\frac{d}{dt} \int_{\mathcal{V}} \rho d\mathcal{V} \right], \quad (\text{Eq. 6-19})$$

$$\int_{\sigma_I} \left\{ \rho_+ \dot{x}_+ \left[\left(\dot{x}_+ - \dot{x} \right) \cdot \bar{n}_+ \right] - \rho_- \dot{x}_- \left[\left(\dot{x}_- - \dot{x} \right) \cdot \bar{n}_+ \right] + \left(\tau_+ - \tau_- \right) \cdot \bar{n}_+ \right. \\ \left. + \left(p_+ - p_- \right) \bar{n}_+ \right\} d\sigma = \lim_{\mathcal{V} \rightarrow 0} \left[\int_{\mathcal{V}} \rho \sum_{i=1}^N Y_i \dot{x}_i d\mathcal{V} - \frac{d}{dt} \int_{\mathcal{V}} \rho x d\mathcal{V} \right], \quad (\text{Eq. 6-20})$$

$$\int_{\sigma_I} \left[\rho_+ \left(h_+ + \frac{v_+^2}{2} \right) \left(\dot{x}_+ - \dot{x} \right) - \rho_- \left(h_- + \frac{v_-^2}{2} \right) \left(\dot{x}_- - \dot{x} \right) + \dot{q}_+ - \dot{q}_- + \dot{x}_+ \cdot \tau_+ \right. \\ \left. - \dot{x}_- \cdot \tau_- \right] \cdot \bar{n}_+ d\sigma = \lim_{\mathcal{V} \rightarrow 0} \left[\int_{\mathcal{V}} \rho \sum_{i=1}^N Y_i \dot{x}_i \cdot (\dot{x} + \dot{x}_i) d\mathcal{V} - \frac{d}{dt} \int_{\mathcal{V}} \rho \left(h + \frac{p}{\rho} + \frac{v^2}{2} \right) d\mathcal{V} \right] \\ (\text{Eq. 6-21})$$

and:

$$\int_{\sigma_I} \left[\rho_+ Y_{i+} \left(\dot{x}_+ + \dot{x}_{i+} - \dot{x} \right) - \rho_- Y_{i-} \left(\dot{x}_- + \dot{x}_{i-} - \dot{x} \right) \right] \cdot \bar{n}_+ d\sigma \\ = \lim_{\mathcal{V} \rightarrow 0} \left[\int_{\mathcal{V}} w_i d\mathcal{V} - \frac{d}{dt} \int_{\mathcal{V}} \rho Y_i d\mathcal{V} \right] \quad i = 1, \dots, N. \quad (\text{Eq. 6-22})$$

Limits of volume integrals, appearing in Eqs. 6-19 to 6-22, account for events happening at the interface. For example, if mass is being accumulated at the interface, then $\lim_{\mathcal{V} \rightarrow 0} [d/dt \int_{\mathcal{V}} \rho d\mathcal{V}] \neq 0$. One may convert these volume integrals to sur-

face integrals by defining properties per unit surface area and introducing delta functions in the coordinate normal to the interface. For example, the mass per unit surface area may be defined as ρ' , so that $\rho = \rho' \delta$ and the right-hand side of

Eq. 6-19 reduces to $-d/dt \int a_1 \rho' d\alpha$. Seldom does mass accumulate at an interface. However, some of the limits of volume integrals are of importance. For example, at a solid-gas interface, heterogeneous reactions often occur preferentially, so that $\lim_{r \rightarrow 0} \int_V w_1' dV = \int_{a_1} w_1' d\alpha \neq 0$, where w_1' is the surface mass rate

of production of species i per unit area. For the sake of generality, none of the limits of volume integrals have been omitted in Eqs. 6-19 to 6-22. The physical meaning of each term in the equations should be clear from the form shown.

In the applications, numerous terms in Eqs. 6-19 to 6-22 either are negligibly small or vanish identically. In fact, it is often much easier to write down the appropriate interface conditions from simple phenomenological reasoning instead of deriving them from the general equations. Nevertheless, the general equations are useful as checks on the validity of phenomenological interface equations and as means of discovering what assumptions are implicit in an interface equation obtained phenomenologically. Such a variety of simplified phenomenological interface conservation conditions exist that we shall introduce them only when they are used and shall not attempt to enumerate them all here.

2. Theories of Homogeneous Solid Propellant Combustion

2.1. Adiabatic Theories

2.1.1. History - It appears that two general theoretical approaches to the study of both homogeneous and heterogeneous solid propellant combustion can be identified. One is the approach of the propellant chemist; the other is the approach of the aerothermochemist.

In the first approach, the emphasis is placed upon the character of the basic chemical processes that occur at the molecular level. An attempt is made to discover the precise chemical composition of the reactants, products and reaction intermediaries, the kinetic mechanism is studied in detail by utilizing every available tool and attempts are made to obtain the rate of each elementary step in the complex reaction mechanism. Often this involves analyzing reactions among a few isolated components that occur in the process by placing these components in a controlled, usually low-temperature environment. It is hoped that the knowledge gained from this type of theoretical analysis will provide the propellant chemist with the key ideas that he needs for the synthesis of new propellants and for the chemical modification of existing propellants to improve their ability to perform various prescribed missions. Indeed, regardless of whether the theories of the propellant chemists are right or wrong (and, we might point out here that there is great uncertainty as to the correctness of every existing theory of this type, simply because the chemical structures and kinetic mechanisms are always so complex), nevertheless it is these theories that have been responsible for most of the improvements in the state of the art of solid propellants, particularly for homogeneous propellants.

In the second approach, the emphasis is on the fluid mechanical and heat and mass transfer processes that occur in propellant combustion. Although the governing equations employed can, in principle, account for all of the elementary chemical processes that may occur, in practice this is always too difficult to accomplish and therefore the chemical kinetics are idealized by hypothesizing a few overall rate-controlling processes. Various models of the fluid dynamical system are analyzed, subject to a variety of assumptions concerning the rate-controlling chemical processes, in an effort to obtain agreement between theory and experiment. The advantage of this approach is that non-chemical processes, e.g. heat conduction, diffusion, fluid flow, etc., which often escape detection in the classical chemist's approach are not only discovered, but also analyzed relatively accurately by this

method. Indeed, under the high-temperature conditions of actual motor combustion, these processes are often of paramount importance and modify the dominant chemical kinetic mechanisms considerably. Aerothermochemical considerations have pointed out a number of related experiments that can be performed to clarify the burning mechanism and also have produced a number of suggestions that have been found useful for improving propellant performance by modifying physical properties of the propellant. Thus, the two approaches are complementary and both have been found useful.

We shall concern ourselves principally with the aerothermochemical approach, touching only briefly on a few aspects of the approach of the propellant chemist. Aerothermochemical analyses of homogeneous solid propellant combustion had their inception in the primitive (by current aerothermochemical standards) works of Rice and Ginell (9) and of Parr and Crawford (10). These studies began in the early 1940's and matured in close collaboration with experimental homogeneous solid propellant development work during and after the Second World War. More recently, many such analyses have been completed. It is these later analyses with which we shall principally be concerned. However, we shall describe briefly the models of Refs. (9) and (10) before presenting the later studies.

2.1.2. Theories of Rice and Ginell and of Parr and Crawford - The Rice and Ginell model of the reaction zone for steady combustion of a homogeneous propellant postulates a gas-phase reaction zone, well removed from the propellant surface, a 'fizz' reaction zone in the gas adjacent to the propellant surface and a rate-controlled surface decomposition process. The model differs from that shown in Fig. 6-1 only in that the distributed 'foam' zone is not present. Separate analyses of each of the three spatially separated processes must be combined appropriately, in order to describe correctly the overall combustion process.

The Parr and Crawford model of the reaction zone for steady combustion of a homogeneous propellant is illustrated in Fig. 6-1. It differs from the model of Rice and Ginell only in that the surface decomposition process is replaced by a distributed 'foam' reaction zone, in which exothermic processes and partial gasification of the solid occur. The model is similar to the one that was described in Chapter 5, Section 2 and was obtained from experiments carried out more recently on Cordite.

It is apparent from Fig. 6-1 that even the earliest models for the combustion of a homogeneous propellant were complex. Furthermore, the picture of exactly what reactions occur in each of the illustrated reaction zones was not very clear. The complexity of the models and the primitive stage of development of aerothermochemistry at the time that the models were developed, necessitated rather inaccurate analyses of each of the reaction zones, so that the theoretical results might now be termed 'qualitative'.

Nevertheless, as exemplified by Fig. 6-2, close agreement between theory and experiment was often obtained from these models. This agreement was achieved by empirically adjusting the values of one or more parameters that govern the processes occurring in each of the reaction zones. The temperature rise across each zone, the overall activation energy for the reaction occurring in each zone and the overall frequency factor for each reaction were the principal parameters of the theories. Some of these parameters were susceptible to measurement but others had to be chosen to provide the best fit with experimental burning rate data. It is therefore understandable that the close agreement between theory and experiment shown in Fig. 6-2 was obtained even though the analyses of each of the reaction zones were not very accurate.

Curiously, later analyses of homogeneous solid propellant combustion exhibit trends toward simpler models than those of Rice and Ginell and of Parr and Crawford.

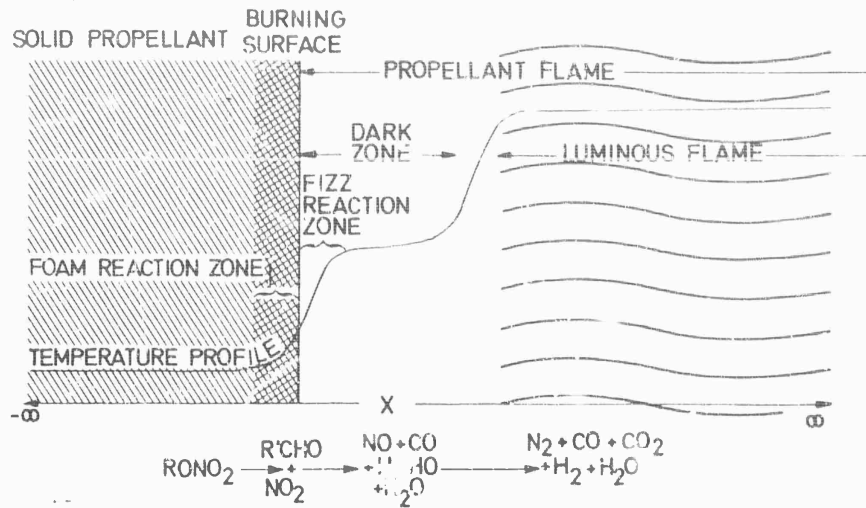


Fig. 6-1 Schematic representation of the model employed by Parr and Crawford for the combustion zone for a double-base propellant, (11).

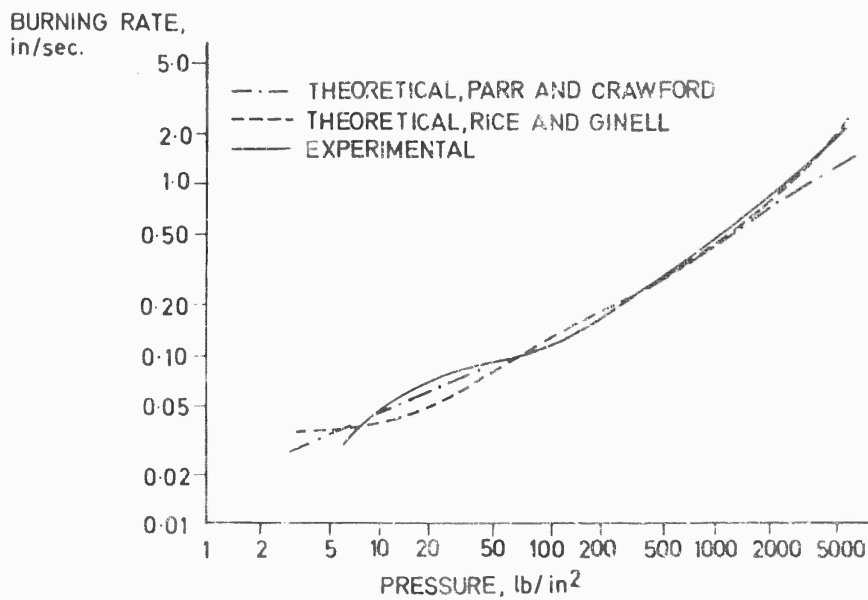


Fig. 6-2 Comparison of experimental and theoretical burning rate curves, propellant HES 4016, 25°C, (11).

ford. The simpler models do not necessarily suppose that the regions identified by the earlier workers are not present; instead, they suggest that the burning rate and other measurable properties of the burning propellant can be obtained from analyses, in which certain of the effects studied by the earlier workers are neglected. For example, it has been suggested that the distributed "foam" zone is not essential and that the two-stage gas-phase reaction region can be combined into a single gas-phase reaction zone. The advantage of simplifying the models is that modern, accurate aerothermochemical analyses of the simplified systems can readily be carried out, so that the theoretical predictions are tied much less questionably to the model employed. It then becomes possible to state with much greater certainty whether or not a given model is valid.

These improvements, contained in the models to be discussed in the following section, reduce the number of adjustable parameters whose values may be chosen in order to provide the best fit between theoretical and experimental burning rates. However, they do not eliminate adjustable parameters entirely. Empirical methods are still needed for obtaining burning rates and other steady-state combustion properties of homogeneous solid propellants.

Before proceeding to discussions of the later theories, we should emphasize that the more recent studies of homogeneous propellants are concerned primarily with exothermic solids that are employed as oxidizer components in composite propellants (e.g., ammonium perchlorate), while the investigations that we have been discussing in this section pertain to classical double-base propellants (nitrocellulose and nitroglycerin, plus stabilizers, other plasticizers, opacifiers, burning rate catalysts, etc.). This is an important practical distinction, because attempts to apply the later analyses to classical homogeneous double-base systems have not been made, although in principle such applications are quite feasible. Thus, practically everything we know about the theory of steady combustion of double-base propellants stems from the models of Rice and Ginell and of Parr and Crawford, or else from slight extensions of these models. A great deal of information is known about the low-temperature decomposition of nitrocellulose and nitroglycerin and many plausible suggestions based on this and other information have been made concerning the nature of the processes that occur in the various zones illustrated in Fig. 6-1. We shall not pursue this material here. The reader is referred to other reviews (11-14) for thorough discussions of these topics.

2.1.3 Theories of Johnson and Nachbar and of Spalding

2.1.3.1. Definition of the Johnson-Nachbar Model - Johnson and Nachbar (15) considered the steady, one-dimensional deflagration of pure ammonium perchlorate monopropellant and employed the model illustrated in Fig. 6-3. They accounted for a one-step overall exothermic chemical reaction in the gas and an unopposed heterogeneous pyrolysis process at the surface of the solid. A model of this type had previously been suggested and analyzed by Rosen (16); Johnson and Nachbar developed a more accurate method of calculation than that of Rosen, accounted for heat losses which were neglected by Rosen and made comparison between theory and experiment (see Section 2.2). Therefore we shall now discuss the adiabatic version of the theory of Johnson and Nachbar in some detail.

In the model illustrated in Fig. 6-3, the condensed material moves in the +x direction with the steady velocity :

$$r = \dot{m}/\rho_c \text{ cm/sec}$$

The principal objective of the theory is to obtain an expression for r , the 'linear

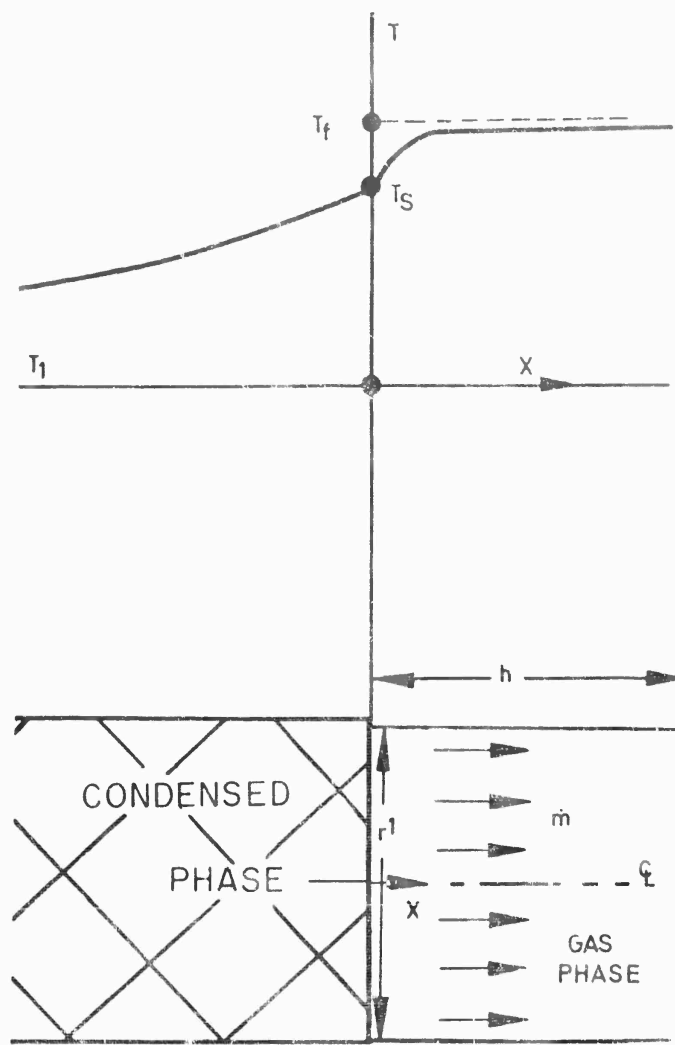


Fig. 6-3 Geometry of the linear deflagration of a monopropellant, (15).

regression rate' of the propellant, in terms of the underlying physicochemical and chemical kinetic properties of the system.

The next few pages will be concerned solely with the analysis of the processes that occur in the gas phase. After solving the gas-phase problem, we return to a consideration of the gasification process and of heat conduction in the solid phase, in order to obtain the complete solution for the regression rate.

2.1.3.2. Basic Equations Governing the Gas-Phase Problem - In the gas phase, a one-step reaction is postulated and the notation of Section 1 is employed, with $M = 1$ and with the reaction index k omitted for brevity. The notation:

$$Y_i^* = (\nu_i' - \nu_i) m_i / \sum_{j=1}^N \nu_j m_j, \quad i = 1, \dots, N. \quad (\text{Eq. 6-23})$$

is introduced. Constant and equal isobaric specific heats c_p are assumed for each species, so that the enthalpy per unit mass for each species is given by :

$$h_i = h_i^\circ + c_p(T - T^\circ), \quad i = 1, \dots, N, \quad (\text{Eq. 6-24})$$

where h_i° is the enthalpy of formation of species i at the reference temperature T° . The energy released per gram of product formed in the reaction is then given by :

$$q = - \sum_{i=1}^N Y_i^* h_i^\circ. \quad (\text{Eq. 6-25})$$

For this problem, the steady-state one-dimensional forms of the conservation equations, applicable in the region $x > 0$, (Eqs. 6-7, 6-8, 6-9 and 6-10) reduce to :

$$\rho v = \dot{m} = \text{constant}, \quad (\text{Eq. 6-26})$$

$$p = \text{constant}, \quad (\text{Eq. 6-27})$$

$$\dot{m} c_p \frac{dT}{dx} - \frac{d}{dx} \left(\lambda \frac{dT}{dx} \right) = q w \quad (\text{Eq. 6-28})$$

and:

$$\dot{m} \frac{dY_i}{dx} - \frac{d}{dx} \left(\rho \mathcal{D} \frac{dY_i}{dx} \right) = Y_i^* w, \quad i = 1, \dots, N, \quad (\text{Eq. 6-29})$$

respectively, where the mass rate of production of products per unit volume is defined as :

$$w \equiv w_i / Y_i^* \quad (\text{Eq. 6-30})$$

which is seen from Eq. 6-14 to be independent of i . In deriving Eq. 6-27, body forces are neglected, and it is assumed that the Mach number of the flow is small compared with unity ($v^2 \ll p/\rho$), as is generally true for solid deflagration. Derivation of Eq. 6-29 involves, in addition, neglecting thermal diffusion and pressure gradient diffusion and setting all binary diffusion coefficients equal to \mathcal{D} , so that Eq. 6-13 reduces to Fick's law,

$$Y_i \nabla_i = - \mathcal{D} \nabla Y_i \quad i = 1, \dots, N. \quad (\text{Eq. 6-31})$$

Since the derivation of Eq. 6-31 from Eq. 6-13 is not entirely trivial, the reader may wish to carry out the development himself.

Finally, in deriving Eq. 6-28, all of the previous assumptions and results are employed and furthermore, the radiative heat flux term is neglected in Eq. 6-12; although tedious, the manipulations are straightforward and therefore will not be reproduced here.

2.1.3.3. Boundary Conditions for the Gas-Phase Problem - Boundary conditions for Eqs. 6-28 and 6-29 at $x = \infty$ are that all gradients vanish ($d/dx \rightarrow 0$). The flux fractions at $x = 0+$ are determined from the composition of the propellant and the overall stoichiometry of the surface gasification process (via the appropriate form of Eq. 6-22); thus, the quantities :

$$\left(Y_i - \frac{\rho \mathcal{D}}{\dot{m}} \frac{dY_i}{dx} \right) \Big|_{x=0+} \equiv \epsilon_i, \quad i = 1 \dots N,$$

are presumed known for all species. For convenience, we shall let the subscript 1 identify a reactant that vanishes when the reaction goes to completion. Then, integration of Eq. 6-29 from $x = 0+$ to $x = \infty$ yields $\int_{0+}^{\infty} w dx = -(\epsilon_1/Y_1^*)\dot{m}$, thus implying that integration of Eq. 6-28 over the same range yields :

$$\left(\lambda \frac{dT}{dx} \right)_{x=0+} = \dot{m} \left[-\frac{\epsilon_1 q}{Y_1^*} - c_p (T_f - T_s) \right], \quad (\text{Eq. 6-32})$$

where the subscripts f and s identify conditions at $x = \infty$ and at $x = 0+$ respectively. If it is assumed that T_f and T_s are known, then Eq. 6-32 may be employed as a boundary condition for Eq. 6-28. In analyzing the gas-phase processes, we shall be able to employ Eq. 6-32 as a boundary condition, although determination of the correct value of T_s (and also of T_f when heat losses occur) requires considering the kinetics of the surface reaction.

2.1.3.4. Dimensionless Mathematical Formulation of the Gas-Phase Problem - Next, we define the dimensionless dependent temperature variable:

$$\tau \equiv 1 + Y_1^* c_p (T_f - T)/\epsilon_1 q \quad (\text{Eq. 6-33})$$

and the dimensionless independent variable :

$$\xi \equiv \int_0^x (\dot{m} c_p / \lambda) dx. \quad (\text{Eq. 6-34})$$

In terms of these variables, Eqs. 6-28 and 6-32 become :

$$\tau' - \tau'' = -\frac{\lambda Y_1^*}{\dot{m}^2 c_p \epsilon_1} w \quad (\text{Eq. 6-35})$$

and:

$$\tau'(0+) = \tau(0+), \quad \tau(\infty) = 1, \quad (\text{Eq. 6-36})$$

where a prime implies a derivative with respect to ξ and the last boundary condition is implied directly by Eq. 6-33. If (w, λ) is a known function of τ , then \dot{m} can be shown to be an eigenvalue of Eqs. 6-35 and 6-36.

However, the functions w and λ depend upon composition as well as temperature. If as a final restrictive assumption, we postulate that the Lewis number is unity,

$$c_p \rho D = \lambda, \quad (\text{Eq. 6-37})$$

then we can solve explicitly for the composition as a function of τ , thereby rendering (w, λ) a known function of τ . It can, in fact, be seen directly by substitution that the solutions :

$$Y_i = \epsilon_i - Y_i^* \epsilon_1 \tau / Y_1^*, \quad i = 1, \dots, N \quad (\text{Eq. 6-38})$$

satisfy Eq. 6-29 as well as previously stated conditions at $x = 0+$, provided that Eqs. 6-35 to 6-37 hold true. Therefore, by using Eqs. 6-33 and 6-38 to relate temperature and composition to τ , we can obtain an eigenvalue problem (Eqs. 6-35 and 6-36) for \dot{m} , involving a single ordinary differential equation.

We shall introduce the definition :

$$-\frac{\lambda Y_1^*}{\dot{m}^2 c_p \epsilon_1} w \equiv \Lambda \omega, \quad (\text{Eq. 6-39})$$

in which Λ is a dimensionless constant and ω is a dimensionless function of τ . Both Λ and ω are taken to be nonnegative (note that Y_1^* is negative). The unknown quantity \dot{m} is made to appear only in Λ , so that $\Lambda \sim 1/\dot{m}^2$ and ω is independent of \dot{m} . The quantity Λ then becomes the dimensionless eigenvalue. The order of magnitude of Λ is chosen in such a way that the maximum value of the function $\omega(\tau)$ is of the order of unity. It can be seen from Eqs. 6-14 and 6-33 that the function $\omega(\tau)$ will be approximately of the form :

$$\omega = \tau^m (1 - \tau)^n \exp[-\beta(1 - \tau)/(\alpha + \tau)] \quad (\text{Eq. 6-40})$$

where α , β , m and n are positive constants, all roughly of the order unity except β , which is something like $E_k/R^\circ T_f$ and is therefore usually large compared with unity (perhaps of the order of 20). We shall not give explicit expressions for α , β , m and n because such expressions depend upon exactly what approximations are made for the temperature and composition dependences of λ and w . It is sufficient to note that ω is very small at small values of τ , rises to a maximum of the order of unity at a value of τ somewhere between about 0.75 and 1 and then drops to zero at $\tau = 1$. An explicit expression for the constant Λ also depends upon what types of assumptions are made for λ and w , and therefore will not be given; it is always equal to a characteristic reaction rate (mass rate of production of product) multiplied by a characteristic value of ρD and divided by \dot{m}^2 . The substitution of Eq. 6-39 into Eq. 6-35 produces a neat form of the eigenvalue problem, governing the gas-phase processes.

The two-point boundary-value problem with eigenvalue Λ , defined by Eq. 6-35 (after the substitution given in Eq. 6-39) and by Eq. 6-36, has been studied at great lengths by laminar flame theorists because precisely the same differential equation and boundary conditions arise in the problem of calculating the flame speed of a purely gaseous combustible. As a consequence of these studies, a wide variety of approximate solutions are available (3). We state the simplest approximate analytical solution for Λ , originally obtained by Zeldovich and Frank-Kamenetski, viz.,

$$\Lambda = (\beta^2/2)[\alpha/(1 + \alpha)]^2.$$

This is an asymptotic formula which becomes increasingly accurate as the value of β increases. In view of the definition of Λ , this expression constitutes an explicit formula for the burning rate; it implies the proportionalities :

$$\dot{m} \sim \sqrt{w\lambda/c_p} \sim p^{n/2} e^{-E_k/2R^\circ T_f},$$

the last part of which gives the approximate dependence of \dot{m} on pressure and flame temperature. Here n is the overall order of the gas-phase reaction and E_k is the overall activation energy. Approximate formulas of this type were used in the earliest studies of propellant combustion (9), (10). A number of objections to their

use can be raised. For example, no dependence on the surface temperature T_s appears in them but the correct solution does depend on T_s . Furthermore, the correct solution produces a different pressure dependence from that shown by the preceding proportionality. Therefore, an incentive exists to develop more accurate methods for solving Eq. 6-35 in homogeneous propellant combustion problems. We shall now describe one of the more accurate procedures that is available. Corresponding procedures are applicable to purely gaseous systems (3).

2.1.3.5. Bounds for the Solution to the Gas-Phase Problem - Johnson and Nachbar developed an accurate method for solving the eigenvalue problem specified by Eqs. 6-35, 6-36 and 6-39 (15), (17). They treat :

$$g \equiv \tau' \quad (\text{Eq. 6-41})$$

as the dependent variable and τ as the independent variable. There is precedent in laminar flame theory for this and other transformations (3). Equations 6-35 and 6-36 then become :

$$g - g dg/d\tau = \Lambda \omega(\tau) \quad (\text{Eq. 6-42})$$

and :

$$g(\tau_s) = \tau_s, \quad g(1) = 0, \quad (\text{Eq. 6-43})$$

where τ_s is the value of τ at $\xi = 0+$. The procedure of Johnson and Nachbar involves deriving rigorous upper and lower bounds for Λ from Eqs. 6-42 and 6-43.

Integration of Eq. 6-42 from τ_s to 1 yields :

$$\Lambda \int_{\tau_s}^1 \omega d\tau = \tau_s^2/2 + \int_{\tau_s}^1 g d\tau, \quad (\text{Eq. 6-44})$$

where use has been made of Eq. 6-43. Dividing Eq. 6-42 by g and integrating from τ_s to τ gives :

$$g = \tau - \Lambda \int_{\tau_s}^{\tau} (\omega/g) d\tau. \quad (\text{Eq. 6-45})$$

By substituting Eq. 6-45 into the integral on the right-hand side of Eq. 6-44, it is found that :

$$\Lambda \int_{\tau_s}^1 \omega d\tau = \frac{1}{2} - \Lambda \int_{\tau_s}^1 \int_{\tau_s}^{\tau} [\omega(\tau')/g(\tau')] d\tau' d\tau,$$

which becomes :

$$2\Lambda \int_{\tau_s}^1 \omega \left[1 + \left(\frac{1-\tau}{g} \right) \right] d\tau = 1 \quad (\text{Eq. 6-46})$$

when the double integral is reduced to a single integral, through integration by parts. Equation 6-46 can be used to determine an upper bound for Λ .

Equation 6-42 may also be written in the form :

$$d(g^2)/d\tau = 2(g^2)/g - 2\Lambda\omega, \quad (\text{Eq. 6-47})$$

which resembles a linear equation for g^2 . If then equation 6-47 is multiplied by $\exp[-2 \int_{\tau_s}^{\tau} (1/g)d\tau]$; then it is found that

$$\frac{d}{d\tau} \left\{ g^2 \exp \left[- 2 \int_{\tau_s}^{\tau} \left(\frac{1}{g} \right) d\tau \right] \right\} = - 2\Lambda \omega \exp \left[- 2 \int_{\tau_s}^{\tau} \left(\frac{1}{g} \right) d\tau \right], \quad (\text{Eq. 6-48})$$

as can be seen by expanding the derivative on the left-hand side of Eq. 6-48 by parts. Integrating Eq. 6-48 from τ_s to 1 and employing the boundary conditions on g yields:

$$2\Lambda \left(\frac{1}{\tau_s^2} \right) \int_{\tau_s}^1 \omega \exp \left[- 2 \int_{\tau_s}^{\tau} \left(\frac{1}{g} \right) d\tau \right] d\tau = 1 \quad (\text{Eq. 6-49})$$

after dividing by τ_s^2 . Equation 6-49 can be used to determine a lower bound for Λ .

Since ω , $(1 - \tau)$ and g are all non-negative, it is clear that by substituting an upper bound for $g(\tau)$ into Eq. 6-46 a lower bound for the integral is obtained, and the resulting value of Λ given by Eq. 6-46 will be an upper bound. On the other hand, substituting this same upper bound for $g(\tau)$ into Eq. 6-49 will yield a lower bound for Λ , because the inner integral will be a lower bound, implying that the exponential and therefore the outer integral assume upper bounds. Equations 6-46 and 6-49 can therefore be used to provide limits between which the eigenvalue must lie.

Since $\Lambda \int_{\tau_s}^{\tau} (\omega/g) d\tau \geq 0$, it follows from Eq. 6-45 that :

$$g \leq \tau. \quad (\text{Eq. 6-50})$$

Hence τ may be used for the upper bound of g in Eqs. 6-46 and 6-49. Equation 6-46 then implies that :

$$\Lambda \leq \left[2 \int_{\tau_s}^1 (\omega/\tau) d\tau \right]^{-1}, \quad (\text{Eq. 6-51})$$

and Eq. 6-49 shows that :

$$\Lambda \geq \left[2 \int_{\tau_s}^1 (\omega/\tau^2) d\tau \right]^{-1} \quad (\text{Eq. 6-52})$$

after the inner integration over τ is performed. Equations 6-51 and 6-52 constitute explicit rigorous bounds for the burning rate eigenvalue Λ .

It is Eqs. 6-51 and 6-52 that Johnson and Nachbar employed in analyzing ammonium perchlorate deflagration. However, before proceeding further with this application, we shall briefly present the iterative method, developed later by Johnson and Nachbar (17), for obtaining the exact solution to the eigenvalue problem.

2.1.3.6. Iterative Solution of the Gas-Phase Problem - Integrating Eq. 6-45 from τ_s to τ yields :

$$\begin{aligned} \int_{\tau_s}^{\tau} g d\tau &= \frac{1}{2} (\tau^2 - \tau_s^2) - \Lambda \int_{\tau_s}^{\tau} \int_{\tau_s}^{\tau'} \frac{\omega(\tau'')}{g(\tau'')} d\tau'' d\tau' \\ &= \frac{1}{2} (\tau^2 - \tau_s^2) - \Lambda \int_{\tau_s}^{\tau} (\tau - \tau') \frac{\omega(\tau')}{g(\tau')} d\tau', \end{aligned} \quad (\text{Eq. 6-53})$$

where the last equality is obtained through integrating the last term by parts. Integrating Eq. 6-42 from τ_s to τ gives :

$$g^2/2 = \tau_s^2 / 2 - \Lambda \int_{\tau_s}^T \omega d\tau + \int_{\tau_s}^T g d\tau, \quad (\text{Eq. 6-54})$$

which becomes :

$$g^2 = \tau^2 - 2\Lambda \int_{\tau_s}^T \omega(\tau') \{ [(\tau - \tau') / g(\tau')] + 1 \} d\tau' \quad (\text{Eq. 6-55})$$

when Eq. 6-53 is substituted into the last term. Equations 6-49 and 6-55 provide the basis for the iterative procedure.

An upper bound for $g(\tau)$ is substituted into Eq. 6-49 in order to obtain a lower bound for Λ . If this value of Λ and the upper bound for $g(\tau)$ are substituted into the right-hand side of Eq. 6-55, then, since the integral in Eq. 6-55 will clearly assume a lower bound, the right-hand side of Eq. 6-55 will assume an upper bound, and hence a new upper bound for $g^2(\tau)$ will be given by Eq. 6-55. The fact that the resulting new upper bound for $g(\tau)$ is lower than the previous upper bound requires proof by mathematical induction.

It is obvious that if $g = \tau$ is used as the first approximation, then the second approximation obtained from Eq. 6-55 will be a lower upper bound. The induction proof is then completed by using the assumption that the n 'th approximation for g is a lower upper bound than is the $(n-1)$ 'th approximation, to prove that the $(n+1)$ 'th approximation is a lower upper bound than the n 'th approximation. This last proof is obtained quite simply from Eqs. 6-49 and 6-55, since the fact that the n 'th approximation for g is lower than the $(n-1)$ 'th approximation immediately shows (via Eqs. 6-49 and 6-55) that the right-hand side of Eq. 6-55 used in obtaining the $(n+1)$ 'th approximation, is smaller than the right-hand side of Eq. 6-55 used in obtaining the n 'th approximation. Equation 6-55 implies that the $(n+1)$ 'th approximation is smaller than the n 'th approximation. Throughout this reasoning, Eq. 6-55 could have been replaced by the simpler expression given in Eq. 6-45; however, convergence is usually slower when Eq. 6-45 is used instead of Eq. 6-55.

The n 'th approximation for g is then given by (see Eqs. 6-55 and 6-49) :

$$g_{[n]}^2 = \tau^2 - 2\Lambda_{[n-1]} \int_{\tau_s}^T \omega(\tau') \{ [(\tau - \tau') / g_{[n-1]}(\tau')] + 1 \} d\tau', \quad (\text{Eq. 6-56})$$

where :

$$\Lambda_{[n-1]} = \left\{ \frac{2}{\tau_s^2} \int_{\tau_s}^1 \omega(\tau) \exp \left[-2 \int_{\tau_s}^T \left(\frac{1}{g_{[n-1]}(\tau')} \right) d\tau' \right] d\tau \right\}^{-1} \quad (\text{Eq. 6-57})$$

In accordance with the preceding discussion, as $n \rightarrow \infty$, $g_{[n]}(\tau)$ approaches the correct solution from above and $\Lambda_{[n]}$ approaches the correct eigenvalue from below. It can also be seen that for each $g_{[n]}(\tau)$ a value of Λ may be computed from Eq. 6-46 and that the resulting sequence of values will approach the correct eigenvalue from above. Thus, successively narrower bounds for the burning rate and successively smaller upper bounds for $g = d\tau/d\xi$ are obtained.

The first estimates for the bounds of Λ given in Eqs. 6-51 and 6-52 are found to be quite close together and therefore it appears likely that few iterations would be required to obtain an exceedingly high degree of accuracy. However, for most applications, Eqs. 6-51 and 6-52 alone are sufficiently accurate and it is unnecessary to employ the iterative method just described.

2.1.3.7. The Surface Gasification Process - It is apparent from Eqs. 6-51 and 6-52, for example, that the solution which we have now obtained for \dot{m} (through Λ) involves the unknown surface temperature T_s (through τ_s) in addition to physico-chemical and chemical kinetic properties of the system. We now proceed to consider the surface gasification process, in order to obtain an additional independent relationship between \dot{m} and T_s , thereby determining the values of both of these parameters and the linear regression rate r , in terms of fundamental kinetic and physiochemical parameters

Johnson and Nachbar (15), like Rosen (16), follow the precedent set by Wilfong, Penner and Daniels (18) in employing the formula :

$$\dot{m} = B_s T_s^{\alpha_s} e^{-E_s/R \cdot T_s} \quad (\text{Eq. 6-58})$$

for the surface boundary condition. Here the constants B_s , α_s and E_s are interpreted as reaction rate constants for the gasification process. One justification for using Eq. 6-58 for the deflagration of ammonium perchlorate is provided by linear pyrolysis data obtained with this material, which has been used in Eq. 6-58 and yields numerical values for the rate constants. The pyrolysis experiments to which we refer are discussed in Refs. (19), (20) and (21) and also in Chapter 5 Section 3.1 and Chapter 6, Section 3. Before proceeding to the results obtained by combining Eq. 6-58 with the results of the gas-phase analysis, we shall discuss the theoretical basis of Eq. 6-58 and consider other possible surface boundary conditions.

2.1.3.8. Derivation of the Unopposed Surface Gasification Rate Law - Equation 6-58 is the phenomenological chemical rate law for an unopposed surface gasification process given by the generic process 'condensed material \rightarrow gaseous material', with E_s denoting the activation energy and $B_s T_s^{\alpha_s}$ representing the temperature-dependent frequency factor. It may be derived theoretically from the viewpoint of 'absolute reaction rate theory' (22), for example. For illustrative purposes, consider a one-component condensed material that sublimes in a one-step unimolecular process. One may assume that, in order to enter the gas phase, a surface molecule must first pass through a thermodynamically identifiable state located at the col of a potential energy barrier and termed an activated complex. One may further assume that the activated complex is in chemical equilibrium with the unactivated surface molecules and that the rate of gasification equals the rate at which the complex decays to gaseous molecules.

If c_s^\ddagger denotes the number of moles of activated complex per unit surface area and τ is the average time for a complex to decay to gas-phase products, then the gasification rate is :

$$\dot{m} = m c_s^\ddagger / \tau, \quad (\text{Eq. 6-59})$$

where m is the molecular weight of the gasifying species. According to the equilibrium hypothesis,

$$c_s^\ddagger = K_s^\ddagger c_s, \quad (\text{Eq. 6-60})$$

where K_s^\ddagger is an equilibrium constant for the activation process and c_s is the actual number of moles of condensed material per unit surface area. As with all surface equilibrium constants, K_s^\ddagger can be expressed in terms of a ratio of partition functions per unit surface area; specifically, it is the ratio of the partition function per unit surface area for the complex to that for the unexcited surface molecules. If we recall that the activated complex differs from an unexcited molecule principally in that one of the vibrational degrees of freedom is replaced by a translational de-

gree of freedom, e.g., in the coordinate normal to the surface of the condensed material, then we may explicitly remove the extra translational degree of freedom from the complex and at the same time remove the factor representing the ground-state energy of the complex, thereby obtaining :

$$K_s^{\ddagger} = (2\pi m kT_s/h^2)^{1/2} \delta (q_s^{\ddagger}/q_s) e^{-E_s/R^{\circ}T_s}, \quad (\text{Eq. 6-61})$$

where k is Boltzmann's constant, h is Planck's constant, E_s is the ground-state energy of the complex, q_s is the partition function of the unexcited surface molecules, q_s^{\ddagger} is the partition function for the complex (with translation in the reaction coordinate and ground-state energy factors removed) and δ is the distance in the reaction coordinate at the col over which the complex is assumed to exist. The quantity δ/τ may be interpreted as the average molecular velocity in the direction of gasification at the col and may be assumed to be given by the Maxwellian (thermodynamic equilibrium) translational velocity formula :

$$\delta/\tau = (kT_s/2\pi m)^{1/2}. \quad (\text{Eq. 6-62})$$

Combining Eqs. 6-59 through 6-62 yields :

$$\dot{m} = m c_s (kT_s/h)(q_s^{\ddagger}/q_s) e^{-E_s/R^{\circ}T_s} \quad (\text{Eq. 6-63})$$

as the formula for the gasification rate. Equations 6-63 and 6-58 become identical when the empirical approximation :

$$m c_s (kT_s/h)(q_s^{\ddagger}/q_s) = B_s T_s^{\alpha_s} \quad (\text{Eq. 6-64})$$

is made.

Geometrically, $c_s^{3/2}$ can be seen to be the number of moles per unit volume in the solid, whence,

$$c_s = (\rho_c/m)^{2/3} \quad (\text{Eq. 6-65})$$

In the simplest case, the complex differs from an unexcited surface molecule only in that one vibrational degree of freedom is converted to a translational mode. If q_v denotes the vibrational partition function that is converted, then :

$$q_s^{\ddagger}/q_s = 1/q_v \quad (\text{Eq. 6-66})$$

and Eq. 6-63 becomes :

$$\dot{m} = m^{1/3} \rho_c^{2/3} (kT_s/h)(1/q_v) e^{-E_s/R^{\circ}T_s} \quad (\text{Eq. 6-67})$$

Equation 6-67 provides a means for estimating the constants B_s and α_s , in terms of the molecular structure of the condensed material. However, the approximation given in Eq. 6-66, which leads to Eq. 6-67, is a gross oversimplification for many gasification processes. For example, rotational degrees of freedom of the complex may be vibrational modes (librations) of the normal surface molecule. Therefore, it is best to use the more general expression given in Eq. 6-64 for estimating B_s and α_s . In many applications, theoretical estimation of q_s^{\ddagger}/q_s is so difficult that it becomes expedient to measure \dot{m} as a function of T_s , thereby determining B_s and α_s experimentally, then use Eq. 6-64 to compute q_s^{\ddagger}/q_s , in an effort to ascertain how the structure of the activated complex differs from that of the normal surface molecule. It should be apparent from this abbreviated discussion that although it in-

volves a host of assumptions, absolute reaction rate theory is richly versatile in its ability to describe a wide variety of rate processes. We should emphasize that a formula similar to Eq. 6-63 can be developed for unopposed gasification processes of arbitrary order and complexity.

2.1.3.9. The Surface Equilibrium Boundary Condition - The assumption of unopposed gasification, which pervades the preceding discussion, need not necessarily be true. It is entirely conceivable that in the deflagration of a solid, surface equilibrium conditions would prevail at $x = 0$ in Fig. 6-3. If the overall surface process is :



where \mathcal{C}_i is the symbol for chemical species i and, if it is assumed that the gaseous material behaves as an ideal gas, then the surface equilibrium condition can be written in the form :

$$\prod_{i=1}^N c_i^{\nu_i''} = K_s, \quad (\text{Eq. 6-68})$$

where K_s is a function of T_s and represents the equilibrium constant (for concentrations) for the gasification process. Although K_s is usually an exponential function of $1/T_s$, Eq. 6-68 differs considerably from Eq. 6-58, notably in that \dot{m} does not appear in Eq. 6-68 and in that neither pressure nor gas-phase composition appears in Eq. 6-58. By using Eqs. 6-33 and 6-38 and the ideal gas relationship :

$$c_i = Y_{i,s} \bar{m} p / m_i R^\circ T_s, \quad i = 1, \dots, N \quad (\text{Eq. 6-69})$$

in Eq. 6-68, it becomes apparent that Eq. 6-68 constitutes a (pressure-dependent) formula for the surface temperature T_s , which may be used in Eq. 6-51 or 6-52 to determine the burning rate.

Spalding (23) has expressed the opinion that surface equilibrium conditions will prevail in combustion processes, only for the vaporization of liquid fuels such as hydrocarbons. He suggests that the surface process will be a rate process whenever a chemical reaction is involved and in particular for double-base propellants. However, there is no fundamental reason why surface chemical reactions cannot be reversible; for example, in the decomposition of organic nitrates, which are somewhat similar to nitrocellulose and nitroglycerin in structure, definite evidence has been cited for the reversibility of the initial dissociation step (11). Therefore, it appears that no sweeping criterion can be given for the use of either Eq. 6-58 or Eq. 6-68 for burning homogeneous propellants. The forward and reverse kinetics of the gasification process must be examined carefully for each system, in order to ascertain whether surface equilibrium or unopposed surface rate conditions prevail.

2.1.3.10. Intermediate Surface Boundary Conditions - It is also entirely possible that for a significant portion of the pressure range over which combustion occurs, the surface process may be intermediate between an unopposed rate process and an equilibrium process; finite rates in both the forward and reverse directions may be of importance. Methods of molecular gas kinetics may be employed in discussing finite recondensation rates. We shall briefly illustrate the reasoning by considering a one-component system experiencing a one-step, unimolecular gasification process.

If the subscript 1 identifies the reactant vapor, then the number of moles of this

vapor per unit area per second that strikes the surface is $c_1 \sqrt{kT_s/2\pi m_1}$, in which the second factor is the mean molecular velocity normal to the surface. Letting α represent the fraction of gas-phase molecules of species 1 striking the surface which adhere to the surface, we find through a simple mass balance that Eq. 6-58 must be replaced by :

$$\dot{m} = B_s T_s^{\alpha_s} e^{-E_s/R^\circ T_s} - m_1 c_1 \alpha \sqrt{kT_s/2\pi m_1}. \quad (\text{Eq. 6-70})$$

The quantity α is sometimes termed a surface accommodation coefficient for species 1; it may depend upon T_s but is usually independent of pressure and gas-phase composition and its value can, in principle, be predicted by molecular reaction rate theories such as the absolute reaction rate theory. An explicit pressure and composition dependence appears in Eq. 6-70, unlike Eq. 6-58, through the factor c_1 in the last term. When α is independent of pressure and gas-phase composition, it

is possible (3) to relate α to the forward gasification rate ($B_s T_s^{\alpha_s} e^{-E_s/R^\circ T_s}$) and to the equilibrium vapor pressure at temperature T_s , which is a thermodynamic property of the system and is therefore relatively easily obtainable. The result indicates that α generally exhibits the approximate form $AT_s^a e^{-b/T_s}$, where A , a and b are nonnegative constants. The resulting form of Eq. 6-70 is :

$$\dot{m} = B_s T_s^{\alpha_s} e^{-E_s/R^\circ T_s} [1 - pX_{1s}/p_1(T_s)], \quad (\text{Eq. 6-71})$$

where $p_1(T_s)$ is the equilibrium vapor pressure at temperature T_s . Equations 6-70 and 6-71 are modified somewhat when more general surface stoichiometry is considered.

Simultaneous surface rate processes in the forward and reverse directions have never been included in theoretical analyses of homogeneous propellant deflagration. It is possible that considerations of this type can remove an inconsistency that arises in theoretical attempts, to predict the experimentally observed value of the low pressure deflagration limit of pure ammonium perchlorate (14). This topic will be considered further in Section 2.2. We now return to a discussion of results for the adiabatic burning rate, obtained by using Eq. 6-58 in the results of the gas-phase analysis.

2.1.3.11. The Pressure Dependence of the Burning Rate for Unopposed Surface Gasification Process - According to Eq. 6-58, \dot{m} is a monotonically increasing function of T_s , with a shape somewhat as illustrated in Fig. 6-4 (solid line). This result may be used in the results of the gas-phase analysis in order to predict the pressure dependence of the burning rate. It is first necessary to note from Eqs. 6-14 and 6-39 that the eigenvalue Λ is proportional to p^n (where n is the overall order of the gas-phase reaction), is proportional to \dot{m}^{-2} , and exhibits no appreciable explicit dependence on T_s . It therefore follows from Eqs. 6-51 and 6-52 that p^n/\dot{m}^2 is bounded by two functions of T_s , each of which increases as T_s increases (recall Eq. 6-33 relating τ_s to T_s). Thus, we may write the solution to the gas-phase problem symbolically as :

$$p^n/\dot{m}^2 = f(T_s), \quad (\text{Eq. 6-72})$$

where $f(T_s)$ is an increasing function of T_s that begins at zero when $\tau_s = 0$ (i.e., when $T_s = T_f + \epsilon_1 q/Y_1^* c_p$; recall that Y_1^* is negative) and approaches ∞ when T_s approaches T_f (see Eqs. 6-33, 6-51 and 6-52). From these observations it is clear that Eq. 6-72 implies that curves of \dot{m} as a function of T_s behave qualitatively as

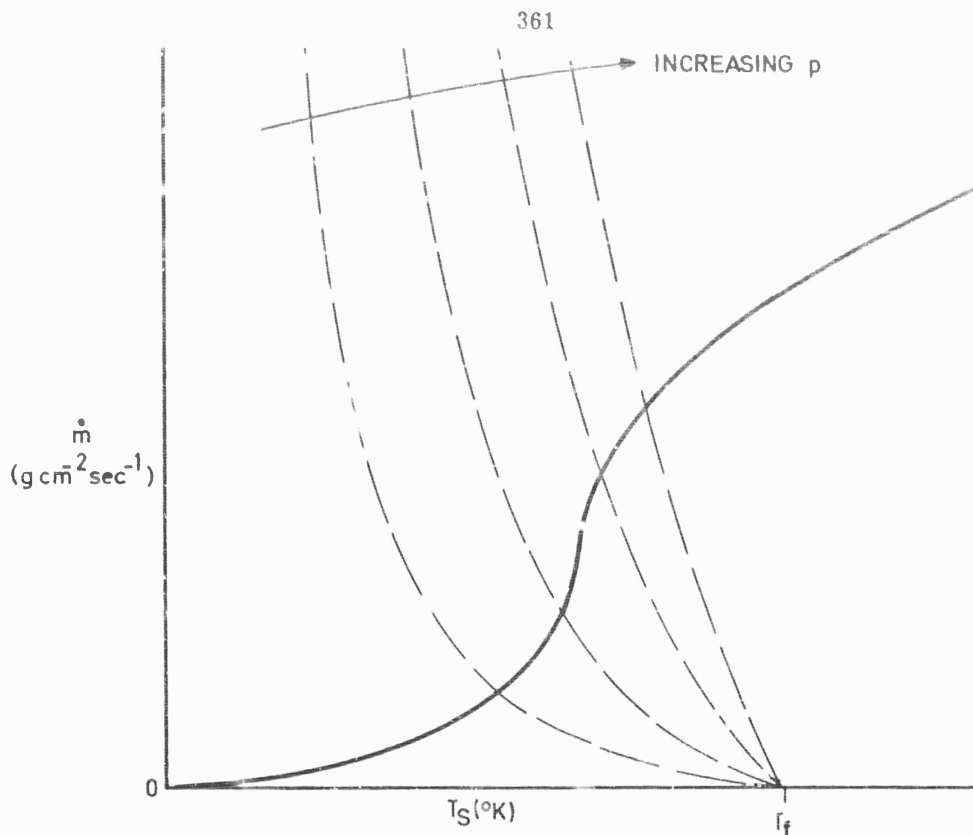


Fig. 6-4 The mass burning rate \dot{m} as a function of the surface temperature T_s , according to the unopposed surface rate law given in Eq. 6-58 (solid line) and the gas-phase reaction result bounded by Eqs. 6-51 and 6-52 (dashed lines).

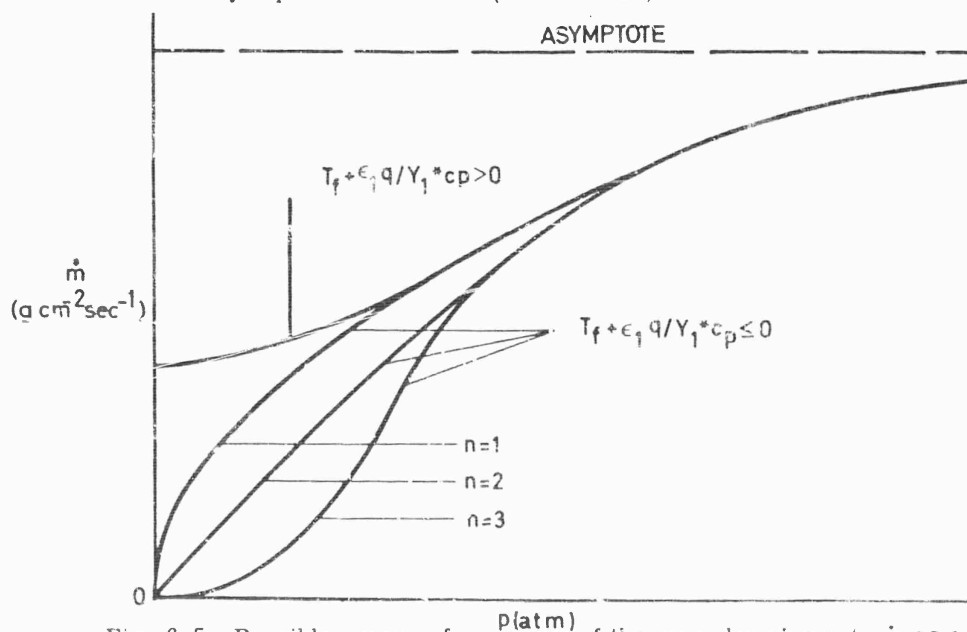


Fig. 6-5 Possible shapes of the curve of the mass burning rate \dot{m} as a function of pressure, according to the adiabatic theory of Johnson and Nachbar.

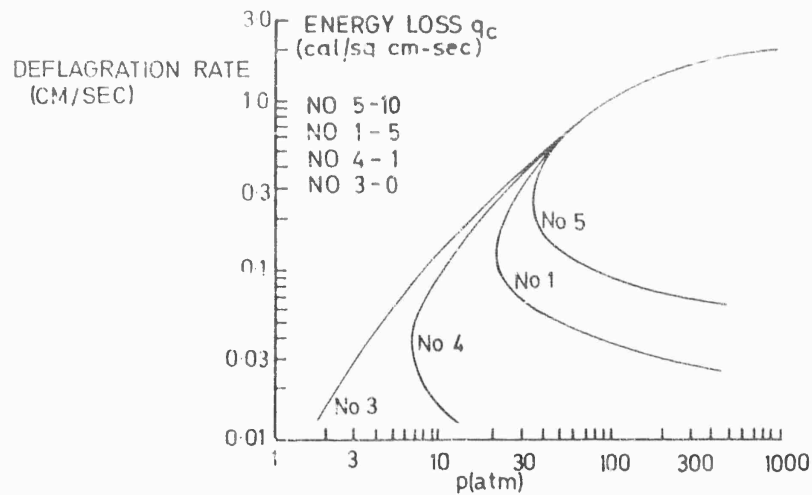


Fig. 6-6 Effect of variation of energy loss on theoretical deflagration rate vs. pressure curves for pure ammonium perchlorate, (15).

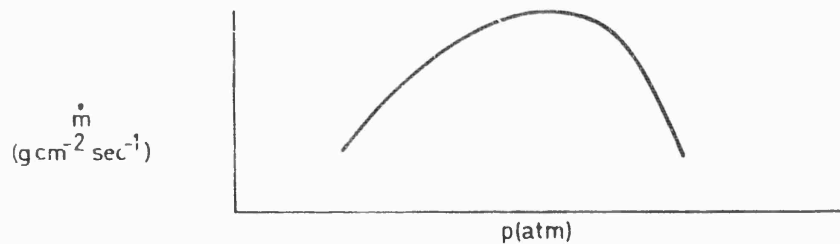


Fig. 6-7 Qualitative shape of the curve of the mass burning rate \dot{m} as a function of pressure, when surface equilibrium prevails (Eq. 6-68)

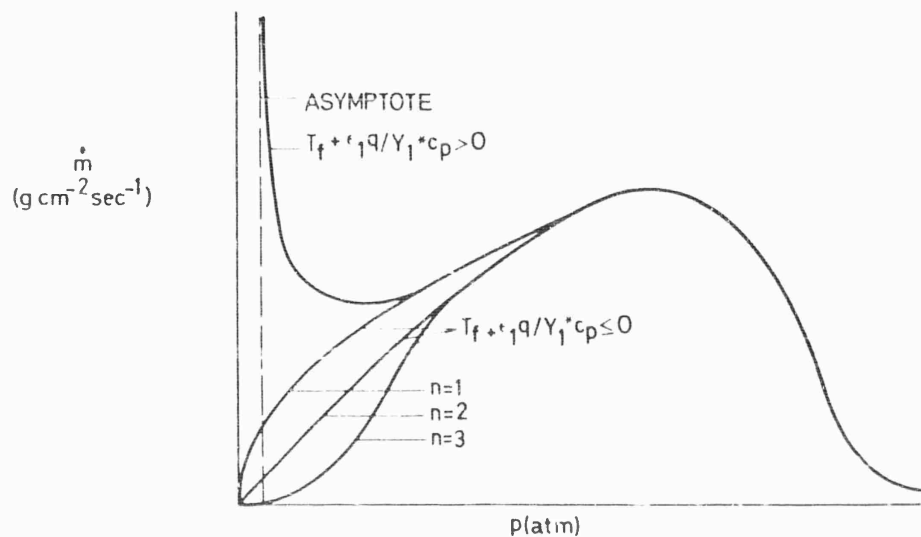


Fig. 6-8 Possible shapes of the curve of mass burning rate \dot{m} as a function of pressure when surface equilibrium prevails and the surface process is $A \rightleftharpoons B$, while the gas-phase reaction is $nB \rightarrow nC$, for adiabatic deflagration of a homogeneous propellant.

illustrated by the dashed lines in Fig. 6-4, for various constant values of p . The dashed curves in Fig. 6-4 are drawn for the case in which $T_i + \epsilon_1 q/Y_1^* c_p$ is positive. When the heat absorbed on gasification exceeds a critical value, the quantity $T_i + \epsilon_1 q/Y_1^* c_p$ becomes negative, so that the vertical asymptote of the dashed curves is located at a negative value of T_g . To see this, one must either consider the heat conduction process that occurs in the condensed phase (this is the only condensed-phase process that is permitted in the present models) or else, more simply, employ an overall energy balance for the system. This demonstration is left as an exercise for the reader. Except for bringing out this point, we do not have to consider condensed-phase processes or even to mention the interface energy conservation condition at all. The extent of progress that can be made without developing these topics is remarkable. It tends to underscore the insignificance of processes occurring solely within the condensed phase, as compared with gasification processes or gas-phase reactions, within the context of the present theory.

Since the intersection points of the solid and dashed curves in Fig. 6-4 represent the solution for the burning rate, it thus becomes clear that \dot{m} is an increasing function of p which varies from either zero (if $T_i + \epsilon_1 q/Y_1^* c_p < 0$) or a positive minimum value (if $T_i + \epsilon_1 q/Y_1^* c_p > 0$) at $p = 0$ to a finite maximum value as $p \rightarrow \infty$. Alternatively, this result follows by employing Eq. 6-58 to write Eq. 6-72 in the form :

$$p^n = g(\dot{m}),$$

where g is an increasing function of \dot{m} that varies from zero at $\dot{m} = \dot{m}[\max(0, T_i + \epsilon_1 q/Y_1^* c_p)]$ to infinity at $\dot{m} = \dot{m}(T_i)$. The possible shapes that result for the function $\dot{m}(p)$ are illustrated schematically in Fig. 6-5. It is clear that the high-pressure portions of these curves can all be approximated well, over a restricted pressure range, by the empirical formula $\dot{m} = ap^b$ or $\dot{m} = a + bp$. It is worthwhile to note that solutions exist for all values of p .

2.1.3.12. The Johnson-Nachbar Results for the Adiabatic Burning Rate of Ammonium Perchlorate - Johnson and Nachbar (15) have given results of numerical calculations of \dot{m} as a function of p , employing numbers believed at the time to be representative of ammonium perchlorate. The numerical values employed in the calculation are listed in Table 6-1. It will be recalled that ρ_c is the density of the solid and n is the order of the gas-phase reaction; T_i represents the initial temperature of the solid (at $x = -\infty$). The temperature dependence of the product of the thermal conductivity and the gas-phase reaction rate is assumed to be given by :

$$\lambda w \sim T^n e^{-E/R^* T},$$

so that the values listed for m and E represent a temperature exponent and a gas-phase activation energy. The quantity $(\Lambda r^2)^{1/n}/p$ (in which it should be remembered that r represents the linear regression rate or the deflagration rate, \dot{m}/ρ_c), is a constant (dependent upon the frequency factor for the gas-phase reaction and upon the transport properties) which appears in the definition of Λ through Eq. 6-39.

The results of the theoretical calculation appear as curve number 3 in Fig. 6-6. Equations 6-51 and 6-52 were each employed in the calculation, in order to obtain upper and lower bounds for \dot{m} . The difference between these two bounds is represented by the thickness of the line in Fig. 6-6; the upper bound for r is the upper edge of the black line and the lower bound is the lower edge. It is seen that the difference between the upper and lower bounds is negligible in this application.

2.1.3.13. The Pressure Dependence of the Burning Rate for Surface Equilibrium - Only Spalding (23) has considered systems in which Eq. 6-68 must be used in place of Eq. 6-58 as the surface boundary condition (3). He has not carried out detailed calculations for systems amenable to comparison with experiment. However, he

c_p	ρ_c	B_s	E_s	α_s	n
0.31	1.95	5.88	19.16		
cal/gm°K	gm/cm ³	cm/sec°K	kcal/mole	1	2
E	$(Ar^2)^{1/n}/p$	T_i	T_f	$-\epsilon_1 q/Y_1^* c_p$	m
60	3.46×10^5	298.16°K	1205°K	1415°K	2
kcal/mole	cm/sec atm				

Table 6-1. Input data used by Johnson and Nachbar in calculation of the adiabatic deflagration rate of NH_4ClO_4 .

c_p	ρ_c	B_s	E_s	α_s	n
0.31	1.95	5.88	19.16		
cal/gm°K	gm/cm ³	cm/sec°K	kcal/mole	1	2
E	$(Ar^2)^{1/n}/p$	T_i	T_{fa}	$-\epsilon_1 q/Y_1^* c_p$	m
60	4.19×10^5	298.16°K	1205°K	1415°K	2
kcal/mole	cm/sec atm				
q_c	q_R				
5	$1.36(T_s/1000)^4$				
cal/cm ² sec	cal/cm ² sec				

Table 6-2. Input data used by Johnson and Nachbar in calculation of the best-fit nonadiabatic deflagration rate curve for NH_4ClO_4 .

has deduced what the qualitative shape of the curves of \dot{m} vs. p must be for systems in which the gasification process is $A \rightarrow B$ and the gas-phase combustion process is $B \rightarrow C$ (i.e., only unimolecular reactions occur and the gas phase contains only two components). A rough illustration of his result is sketched in Fig. 6-7, where it can be seen that, under appropriate conditions, a maximum in the curve of burning rate vs. pressure may develop. Spalding also points out that in the high pressure regime, as p is increased, T_s is found to approach T_f , at which point \dot{m} drops to zero.

We may look more closely at the system studied by Spalding by specializing Eqs. 6-38 and 6-68 appropriately. Equation 6-68 reduces to the statement that the partial pressure of the gaseous reactant at the surface must equal the equilibrium vapor pressure at temperature T_s , which we denote by $p_e(T_s)$. Since the molecular weights of both gaseous species must be the same (for the unimolecular process $B \rightarrow C$), mole fractions are equal to mass fractions in the gas. Equation 6-38 therefore implies that, for the reactant, the mole fraction is $X_1 = (1 - \tau)$, where use has been made of the fact that $\epsilon_1 = 1$ in this simple case. The partial pressure of the gaseous reactant at the surface is therefore $p(1 - \tau_s)$ and Eq. 6-68 reduces to the expression :

$$p = p_e(T_s)/(1 - \tau_s) , \quad (\text{Eq. 6-73})$$

relating the total pressure to the surface temperature. The vapor pressure p_e is approximately proportional to e^{-L/R^*T_s} ($L \equiv$ molar heat of vaporization), whence it is seen from Eq. 6-73 that p is an increasing function of T_s , going from zero at $T_s = 0$ to infinity as $T_s \rightarrow T_f$ (i.e., $\tau_s \rightarrow 1$).

Equation 6-72 remains valid in the present problem. We must note, further, from Eqs. 6-40 and 6-51 or 6-52 that :

$$f(T_s) \sim 1/(1 - \tau_s)^{n+1}$$

near $\tau_s = 1$. Equations 6-72 and 6-73 therefore imply that, near $T_s = T_f$,

$$\dot{m}^2 \sim p_e(T_f)(1 - \tau_s) \approx [p_e(T_f)]^2/p$$

This relationship implies that \dot{m} approaches zero like $1/\sqrt{p}$ as p approaches infinity.

At small values of p , if $T_f + \epsilon_1 q/Y_1^* c_p < 0$ so that T_s reaches zero before τ_s can approach zero, we find from Eqs. 6-72 [since $f(T_s)$ is positive at $T_s = 0$ in this case] and 6-73 [recalling that p goes to zero at $T_s = 0$] that \dot{m} becomes proportional to $p^{n/2}$ as p goes to zero. This observation finally yields the \dot{m} vs. p curves labeled " $T_f + \epsilon_1 q/Y_1^* c_p \leq 0$ " in Fig. 6-8. On the other hand, if $T_f + \epsilon_1 q/Y_1^* c_p > 0$, then $f(T_s)$ reaches zero before T_s (or p) reach zero, thereby indicating via Eq. 6-72 a divergence in \dot{m} at $p = p_e(T_f + \epsilon_1 q/Y_1^* c_p)$. This divergence produces the curve labeled " $T_f + \epsilon_1 q/Y_1^* c_p > 0$ " in Fig. 6-8. It is seen by comparing Figs. 6-5 and 6-8 that a much richer variety of \dot{m} vs. p curves are obtainable, if surface equilibrium prevails than if the surface process is an unopposed rate process.

Of course, as \dot{m} begins to diverge, the assumption of surface equilibrium must eventually be violated and therefore Eq. 6-68 becomes inapplicable somewhere along the curve that approaches the asymptote in Fig. 6-8. Therefore, in particular, it does not appear that consideration of the possibility of surface equilibrium will produce ranges of p in which no solution for \dot{m} exists; pressure limits of flammability do not come out of the adiabatic theory. However, the possibility of the existence of a minimum in the \dot{m} vs. p curve at low pressures is not necessarily ruled out by these observations. It would be of interest to study adiabatic deflagration of homogeneous condensed materials subject to the more general boundary condition given

in Eq. 6-70, in an effort to categorize all of the possible shapes of the burning rate vs. pressure curves.

2.1.3.14. Structure of Gas-Phase Reaction Zone - The previous discussion centered around the burning rate and related only peripherally to the structure of the gas-phase reaction zone. It is known that reactant mass fractions and density decrease and that product mass fractions, temperature and velocity increase, all monotonically, as an element of the fluid flows downstream through the gas-phase flame. Pressure remains practically constant through the flame; it decreases slightly, by an amount that can be calculated from the momentum conservation equation, Eq. 6-8. The chemical heat release rate is usually small near the solid surface and small far downstream, exhibiting a rather sharp maximum at a point where the temperature is slightly below the adiabatic flame temperature. Radical composition profiles also often exhibit a peak in the flame zone. Summaries of theoretical results for purely gaseous systems may be found in Refs. (2-4). Profiles have not been calculated theoretically for cases in which the presence of the condensed phase is taken into account explicitly. Therefore, accurate theoretical predictions of the structure of the gas-phase reaction zone in homogeneous solid propellant combustion are not available yet. Of course, the iterative method described in Section 2.1.3.6 is capable of producing such predictions for one-step reactions. However, the results were not deemed to be of sufficient interest yet to warrant carrying out the computations.

Rough formulas for the height of the gaseous flame above the solid surface are available. These formulas were obtained for purely gaseous systems but due to their approximate character they can be transcribed to yield order-of-magnitude results for homogeneous propellants. One such formula for the flame height δ is (3):

$$\delta = \sqrt{\lambda / c_p w},$$

in which all quantities on the right-hand side are to be assigned appropriate average values for the flame zone. Convenient averages for the properties λ and c_p may be taken to be the values for an equilibrium mixture of reaction products at the adiabatic flame temperature. The average value of the reaction rate w can be estimated by evaluating the specific reaction rate constant at the adiabatic flame temperature and the reactant concentrations, at the values which they achieve in the gas phase at the solid surface; this yields an upper bound for w and a lower bound for δ , for one-step reactions. The approximate pressure dependence of the flame height implied by the formula is $\delta \sim p^{-n/2}$. The formula agrees with experiment in predicting very thin sub-millimeter gaseous flame heights at elevated pressures.

These results are of such an approximate nature that they are equally applicable to the nonadiabatic systems considered in the following section.

2.2. Nonadiabatic Theories

2.2.1. The Role of Heat Losses - Heat losses do not play a significant role in the conventional homogeneous propellant combustion concepts of the propellant chemist, which emphasize chemical kinetic aspects of the problem. Nor do they appear in the early aerothermochemically based theories of Rice and Ginell and of Parr and Crawford. Their importance was brought out vividly by the theory of Johnson and Nachbar (15), in which heat losses had to be introduced in order to obtain a low pressure deflagration limit for pure ammonium perchlorate. The fact that the nonadiabaticity produced by heat losses, can lead to deflagration limits in systems that exhibit no flammability limits under adiabatic conditions, was emphasized earlier by Spalding (24) and others, for purely gaseous systems. A detailed discussion of the history of the development of this subject and of the principles of how heat losses

produce flammability limits may be found in Chapter 8 of Ref. (3) for gaseous systems. Here we shall consider only the steady, one-dimensional combustion of homogeneous condensed propellants, showing how heat losses lead to flammability limits for these systems. Our development is based on the work of Johnson and Nachbar (15) and of Spalding (23).

2.2.2. Types of Heat Losses - Heat loss may occur from the gas phase, the condensed phase or the interface (illustrated in Fig. 6-3) through the processes of conduction, convection or radiation. The dominant loss mechanism and the location of the flow region from which the losses are most important, depend on various properties of the propellant and its environment. If losses occur primarily from the gas phase (e.g., via radiation from the hot combustion products or convective mixing with a cooler ambient atmosphere), then the effects of the losses will be qualitatively the same as for purely gaseous systems. Therefore, we need only consider here losses from the condensed phase and from the interface. This is fortunate, because the gas-phase analysis given in Sections 2.1.3.2 to 2.1.3.6 is then unchanged and we need only graft algebraic modifications onto the discussions appearing in Sections 2.1.3.11 to 2.1.3.13. Furthermore, it turns out that the results derived from this simpler analysis, exhibit the same qualitative behavior as the results of the analyses that include gas-phase losses.

2.2.3. Energy Conservation Equations, including Heat Losses - Equation 6-32 represents the overall energy conservation condition for the gas phase.

The interface energy conservation condition (applied at $x = 0$ in Fig. 6-3) may be derived formally from Eq. 6-21. If we neglect terms involving d/dt and \dot{x} (because of the steady-state assumption), $v^2/2$ and $\chi \cdot T$ (because of the assumption of low Mach number) and also f_A because of the assumed absence of body forces, then the one-dimensional form of Eq. 6-21 reduces to :

$$\rho_+ h_+ v_+ - \rho_- h_- v_- + q_+ - q_- = 0$$

where the subscripts + and - identify conditions at $x = 0+$ and at $x = 0-$, respectively. Neglecting thermal diffusion, noticing that $\chi_{A-} = 0$ due to the absence of diffusion within the solid, hypothesizing a transparent gas and an opaque solid with $q_{R-} = 0$, and assuming an ideal gas, we may employ Eq. 6-12 to express the preceding relationship in the form :

$$\rho_+ \sum_{i=1}^N h_{i+} Y_{i+} (v_+ + V_{i+}) - \rho_- h_- v_- + q_{R+} - (\lambda dT/dx)_+ + (\lambda dT/dx)_- = 0.$$

In view of the definition of ϵ_i and of the continuity equation :

$$\rho_+ v_+ = \rho_- v_- = \dot{m}$$

the first equality of which, incidentally, follows directly from Eq. 6-19, with the aid of Eq. 6-32 this expression may be written as :

$$(\lambda dT/dx)_- + \dot{m} \left[\sum_{i=1}^N h_{i+} \epsilon_i - h_- + \frac{\epsilon_1 q}{Y_1^*} + c_p (T_f - T_s) \right] + q_{R+} = 0. \quad (\text{Eq. 6-74})$$

The quantity :

$$L_s \equiv \sum_{i=1}^N h_{i+} \epsilon_i - h_-$$

is clearly the enthalpy per unit mass absorbed in the gasification process, while q_R obviously represents the heat loss (per unit area per second) by radiation from the surface.

The equation of energy conservation for the condensed phase may be employed to eliminate the first term in Eq. 6-74. The heat flux in the condensed phase is simply $\lambda dT/dx$, and therefore, under the prevailing assumptions, the integral of Eq. 6-9 is simply :

$$\dot{m}[h_c(T_s) - h_c(T_1)] - (\lambda dT/dx)_- = 0 ,$$

where $h_c(T_1)$ is the enthalpy of the solid at the initial temperature T_1 , $h_c(T_s)$ is the same quantity at the temperature T_s , and use has been made of the fact that $dT/dx \rightarrow 0$ as $x \rightarrow -\infty$. Now, this expression does not permit heat losses from the condensed phase. Such losses could be obtained formally by employing the correct non-one-dimensional form of Eq. 6-9 and defining appropriate average effective one-dimensional quantities. However, it is simpler to merely insert a phenomenological term into the equation, accounting for the total heat loss by both radiation and convection (conduction being considered a special case of convection). This has been done by Johnson and Nachbar (15). We shall let q_C denote the total energy per unit surface area per second lost from the condensed phase. Then the modified energy equation is :

$$\dot{m}[h_c(T_s) - h_c(T_1)] - (\lambda dT/dx)_- + q_C = 0. \quad (\text{Eq. 6-75})$$

The overall energy balance is obtained finally by combining Eqs. 6-74 and 6-75. The result is :

$$h_c(T_s) - h_c(T_1) + L_s + \frac{\epsilon_1 q}{Y_1^*} + c_p(T_f - T_s) + (q_R + q_C)/\dot{m} = 0. \quad (\text{Eq. 6-76})$$

Although Eq. 6-76 could, of course, have been written down immediately by phenomenological reasoning, the derivation given here may prove instructive.

2.2.4. The Origin of the Influence of Heat Loss on the Burning Rate - The essential difference between the adiabatic and nonadiabatic problems stems from the fact that T_f is a constant, independent of both \dot{m} and T_s , in the adiabatic case. The absence of a dependence on \dot{m} when $q_R + q_C = 0$, is evident from Eq. 6-76. The lack of a dependence on T_s is not obvious from the form quoted in Eq. 6-76, but it becomes clear when one realizes that the adiabatic form of Eq. 6-76 is simply the statement that the total (thermal plus chemical) enthalpy of the gaseous products at temperature T_f must equal the total enthalpy of the solid, at the fixed initial temperature T_1 . Since the composition of the solid is fixed and, in the present model, the composition of the reaction products is assumed to be constant, independent of p or T_s , the stated independence follows directly. It is seen from Eq. 6-76, that nonadiabaticity introduces an explicit dependence of T_f on \dot{m} and also on T_s , provided that $(q_R + q_C)$ depends on T_s .

2.2.5. Dependence of Heat Loss on Surface Temperature - Although $(q_R + q_C)$ does generally depend on T_s , the precise form of this dependence varies according to the nature of the heat loss. If the radiant surface energy loss occurs from a surface whose engineering emissivity is independent of T_s , and if no radiant energy from the environment is incident on the surface, then q_R is proportional to T_s^4 . If

the same approximations are valid for a condensed material losing energy by radiation, then q_c is proportional to a mean temperature to the fourth power, lying between T_1 and T_s . On the other hand, if convective losses from the condensed material are dominant, then q_c is more nearly linearly dependent on T_s . It is reasonable to approximate the dependence of $(q_m + q_c)$ on T_s over a sufficiently narrow range of values of T_s as a power dependence T_s^β , where β typically lies between 1 and 4.

2.2.6. The Modifications Produced in the Burning Rate Analysis by Nonadiabaticity - The dependence of T_f on \dot{m} and T_s associated with nonadiabaticity complicates the dependence of the eigenvalue Λ on \dot{m} and T_s , e.g., due to the fact that τ_s (appearing in Eqs. 6-51 and 6-52) becomes dependent on \dot{m} and also in a more complex way on T_s , as is seen from Eq. 6-33. Consequently, Eq. 6-72 becomes inapplicable. The appropriate modification to Eq. 6-72 may be inferred from Eqs. 6-33 and 6-76 to be :

$$p^n/\dot{m}^2 = f(T_s + (q_m + q_c)/\dot{m}c_p), \quad (\text{Eq. 6-77})$$

where the function f has the same properties, as previously prescribed in Section 2.1.3.11. Explicitly, $f(z)$ is an increasing function of z that begins at zero, when $z = T_{fa} + \epsilon_1 q/Y_1^* c_p \equiv z_0$ and approaches infinity when z approaches T_{fa} , where T_{fa} represents the (constant) adiabatic flame temperature.

2.2.7. Nonadiabatic Analysis with Unopposed Surface Rate Process - When the surface gasification process is an unopposed rate process, Eqs. 6-58 and 6-77 together determine the pressure dependence of the burning rate \dot{m} . However, to solve these two algebraic equations for $\dot{m}(p)$ is not trivial for nonadiabatic systems. From Eq. 6-58, it can be seen that the argument (denoted here by z) of the function f appearing in Eq. 6-77, when plotted vs. \dot{m} , behaves somewhat as illustrated in Fig. 6-9. It is seen from Fig. 6-9 that when heat losses occur, there is a minimum (which we denote by z_m) in the curve of z as a function of \dot{m} . From previously cited properties of the function f , it may then be seen that no solution for $p(\dot{m})$ exists unless $z_m < T_{fa}$; in other words combustion cannot be achieved at any pressure if the heat loss exceeds a critical value. When z_m is slightly less than T_{fa} , $p(\dot{m})$ exists and is single valued for $\dot{m}_1 < \dot{m} < \dot{m}_2$ (where \dot{m}_1 and \dot{m}_2 are finite positive limits): $p(\dot{m})$ approaches ∞ as $\dot{m} \rightarrow \dot{m}_1$ or $\dot{m} \rightarrow \dot{m}_2$. It follows that $\dot{m}(p)$ is multiple valued. The function $\dot{m}(p)$ exists for all values of p greater than a definite minimum value and it is generally double valued. When z_m is considerably below T_{fa} , the nature of the solutions $\dot{m}(p)$ depends on whether $z_0 \leq 0$ or $z_0 > 0$. The qualitative behaviors obtained in these two cases are illustrated in Figs. 6-10 and 6-11.

2.2.8. Interpretation of Double Eigenvalue Solution - The existence of two steady-state solutions for the burning rate when heat losses occur, was first discovered for gaseous systems. The preceding development shows that this same result holds for homogeneous propellants in which the losses occur from the condensed phase or the interface. When there are two steady-state burning rates, we must ask "Which one will be observed in an experiment?" It is the upper branch of the curve (the large value of \dot{m}) that is practically always observed experimentally. For gaseous systems, Spalding (24) argued theoretically that the lower burning velocity would usually be unstable. However, a thorough theoretical study of this question has not been reported in the literature. We shall assume in the rest of this discussion that when two steady-state burning velocities are predicted, the lower value is unstable.

2.2.9. Comparison of the Nonadiabatic Theory of Johnson and Nachbar with Experiment - The fact, illustrated in Figs. 6-10 and 6-11, that heat losses can produce a critical value of the pressure p below which no solution exists for the burning rate, constitutes a theoretical prediction that heat losses can produce low-pressure flammability limits for homogeneous solid propellants. As the pressure is de-

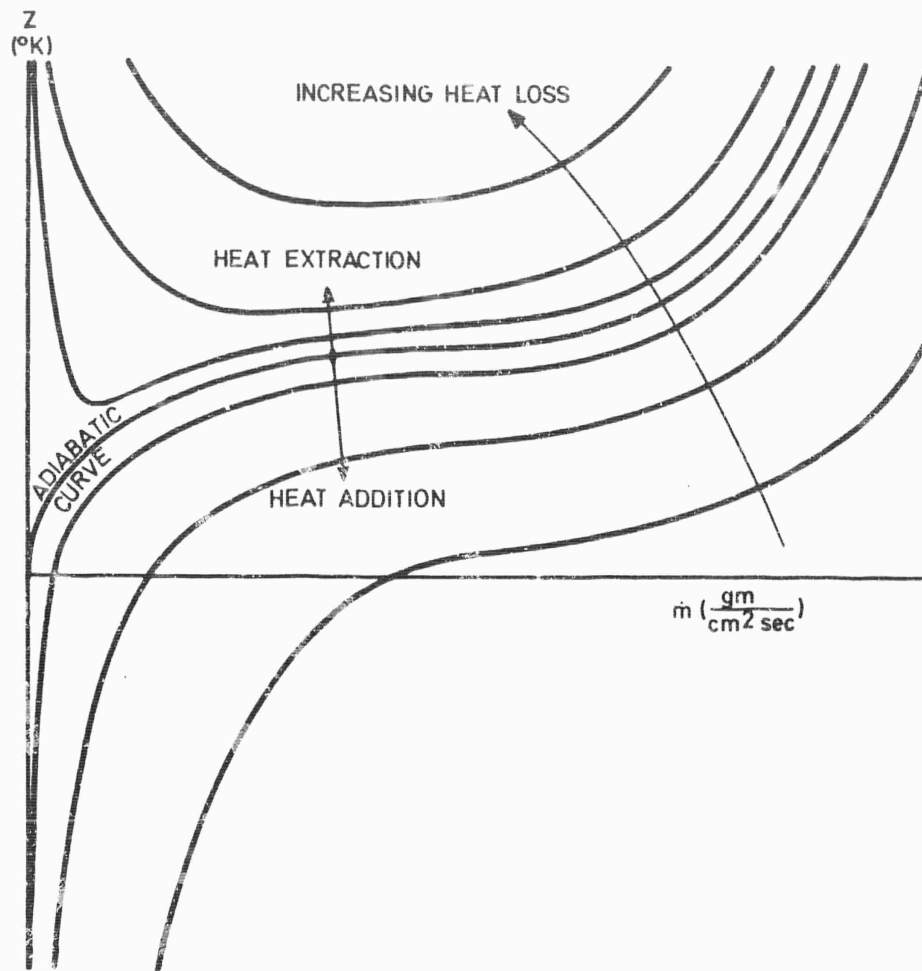


Fig. 6-9 Argument of the function f of Eq. 6-77, as a function of the burning rate \dot{m} , for nonadiabatic systems with an unopposed surface rate process.

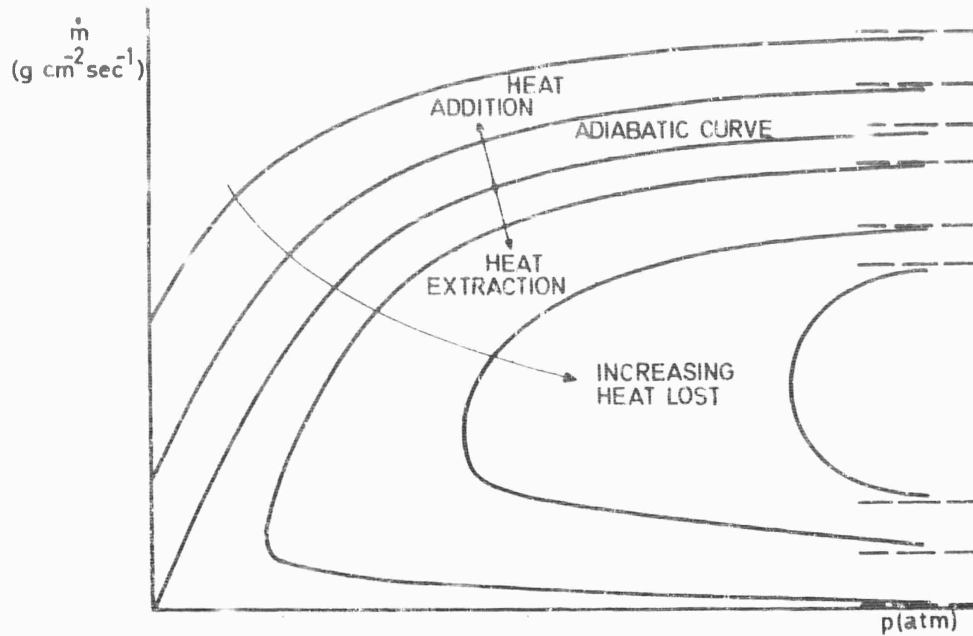


Fig. 6-10 Qualitative dependence of the mass burning rate \dot{m} on pressure for nonadiabatic systems with $z_0 \leq 0$ and with $n = 2$, when the surface process is an unopposed rate process (dashed lines are asymptotes).

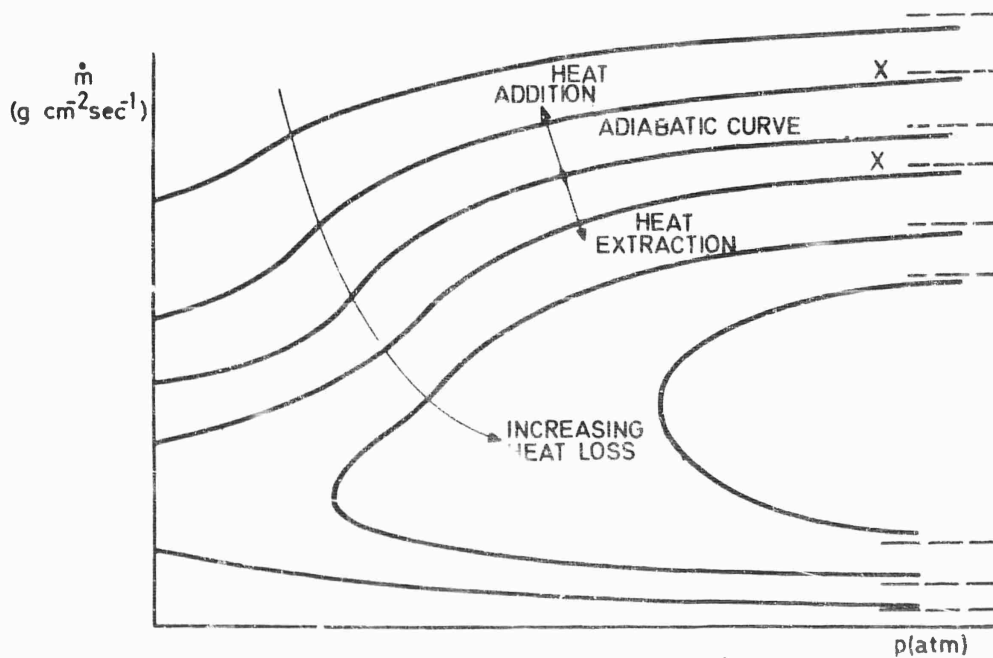


Fig. 6-11 Qualitative dependence of mass burning rate \dot{m} on pressure for nonadiabatic systems with $z_0 > 0$, when the surface process is an unopposed rate process (dashed lines are asymptotes; the two curves marked x correspond to the same values of the heat loss parameter).

creased, the burning rate moves along the upper branch of one of the curves in Fig. 6-10 or 6-11, until burning finally ceases at the point where the tangent to the curve is vertical. Such flammability limits have been observed experimentally in the deflagration of ammonium perchlorate (25). Johnson and Nachbar (15) attempted to apply their nonadiabatic theory (developed above) to correlate both the observed burning rate and flammability limit data for ammonium perchlorate, reported in (25). Their results for various trial calculations are shown in Fig. 6-6, while comparison with experiment for the theoretical trial calculation, that agreed most closely with the experimental results is shown in Fig. 6-12. As in the case of the adiabatic theory, Eqs. 6-51 and 6-52 were employed for A in obtaining these theoretical results and the width of the lines of the theoretical curves represent the difference between the two bounds on the solution so obtained. The data used for the theoretical curve shown in Fig. 6-12 are listed in Table 6-2 (see page no 364).

The close agreement between theory and experiment shown in Fig. 6-12 was obtained by making the following empirical adjustments. First, the values of E and $(Ar^2)^{1/n}/p$ were adjusted to fit the burning rate data. Next, q_c was adjusted to fit the deflagration limit. It was not deemed permissible to tamper with any of the other parameters listed in Table 6-2 because their values were presumed known independently; (e.g., the values of B_s and E_s were obtained from published results of linear pyrolysis experiments). Since there were no independent measurements bearing on the overall rate constants of the gas-phase reaction, checks on the empirical values of E and $(Ar^2)^{1/n}/p$ were not available. However, the magnitude of the heat loss q_c (that occurs in addition to the radiant heat loss from the surface) can be estimated from the known environmental conditions. Estimates of all possible heat loss mechanisms, e.g., gas-phase radiation, convective losses from the solid, etc., yield a much smaller total heat loss than the value of q_c , needed to fit the observed deflagration limit. Hence, the correlation of the deflagration limit is unsatisfactory.

Although it is, of course, conceivable that chemical effects could be responsible for the observed deflagration limit or that a dynamically unstable steady-state solution is encountered on the upper branch of the $\dot{m}(p)$ curve at pressures well above the critical limiting value, nevertheless a suitable modification of the surface boundary condition within the present theory, may conceivably produce satisfactory agreement. There is some question concerning the validity of the published pyrolysis results for B_s and E_s and of the hypothesis of an unopposed surface rate process for NH_4ClO_4 . It would therefore be of interest to employ in the Johnson-Nachbar theory a more general surface boundary condition, of the type given in Eq. 6-70, in order to see whether the observed deflagration limit can then be correlated by choosing a more reasonable value for the heat loss term q_c .

2.2.10. Nonadiabatic Analysis with Surface Equilibrium - Nonadiabatic systems with surface equilibrium have been discussed by Spalding (23). It appears that, in this case, heat losses again produce a double-valued burning rate $\dot{m}(p)$ and yield ranges of p for which no solution exists. At least for some values of the parameters, there appears to be no solution if p is sufficiently small and also if p is sufficiently large. Therefore, both low pressure and high pressure flammability limits seem to be produced by heat losses from systems that maintain surface equilibrium (3). No detailed analysis of nonadiabatic systems with surface equilibrium has been reported in the literature. It would be of interest to extend the study presented in Section 2.1.3.13 to include effects of nonadiabaticity. The problem is merely algebraic but the algebra is more complicated than that outlined in Section 2.2.7. The results might well be applicable to NH_4ClO_4 since recent unpublished work favors surface equilibrium for this material at elevated pressures.

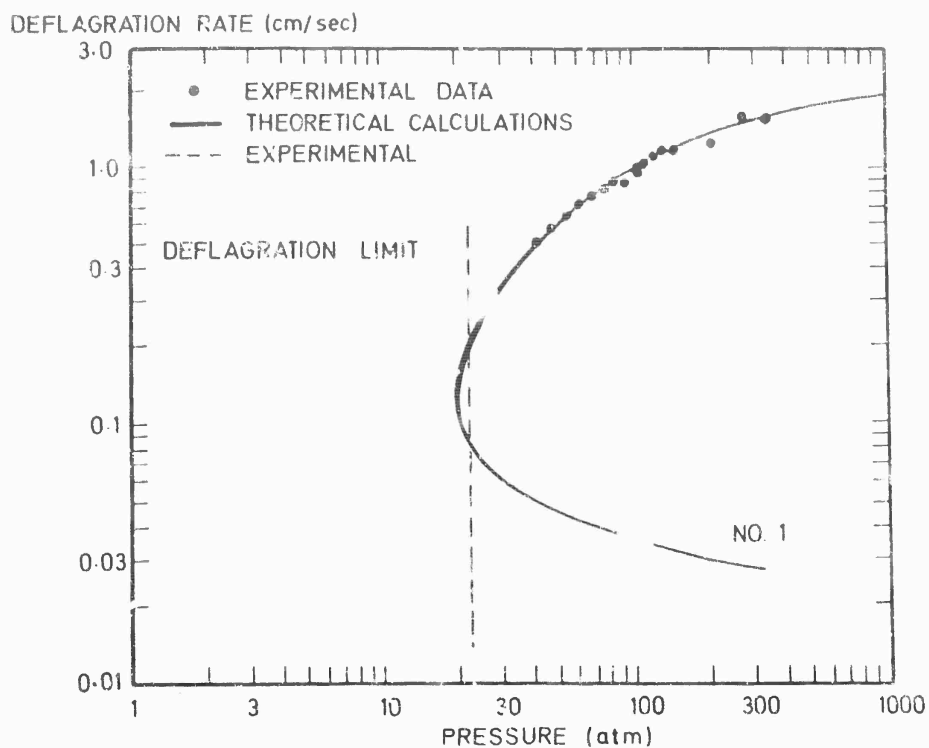


Fig. 6-12 Variation of deflagration rate of pure ammonium perchlorate with pressure, at 25°C initial temperature: comparison of theory with experiments, (15). The experimental data is taken from (25).

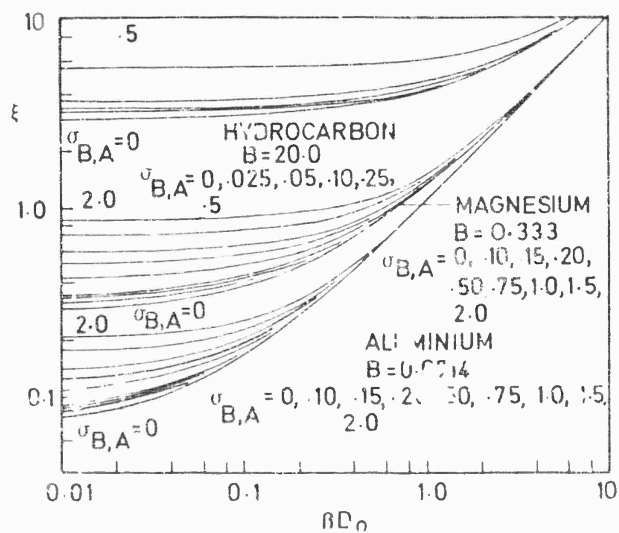


Fig. 6-13 Dimensionless burning rate ξ as a function of the dimensionless oxidizer flux βD_0 , the transfer number B and the radiation parameter $\sigma_{B,A}$, (63).

3. Theories of the Decomposition of Selected Constituents of Composite Propellants

3.1. Introduction

Researchers have always believed that a thorough theoretical understanding of the decomposition of individual constituents of a solid propellant, would aid them in discovering the burning mechanism of the propellant. This is one of the major motivations for experiments on propellant constituents, by methods such as thermogravimetric analysis (including both vacuum sublimation and decomposition in controlled atmospheres), differential thermal analysis and hot-plate pyrolysis. All of the methods have produced results that are interesting from the viewpoint of theoretical interpretation, (11-13), (19-21), (25-43). However, very few of the results have been shown to bear directly on propellant combustion. The source of the difficulty is the basic chemical fact that reaction mechanisms are strongly dependent upon conditions of pressure and especially temperature. Temperatures attained in propellant combustion are higher than those yet achievable in most of the experiments. Therefore, the mechanisms that dominate most of the experimental results are likely to be insignificant in propellant combustion. This makes results of experiments on constituents difficult to apply to propellant burning.

Constituents that can be made to decompose exothermically under appropriate conditions, can be studied at temperatures approaching propellant combustion temperatures. Examples of such constituents include nitrocellulose, ammonium perchlorate and hydrazine perchlorate. Experiments on the deflagration of these constituents provide information that aids in developing theories of propellant combustion. One theoretical analysis of constituent deflagration has been given in the preceding section. Chemical aspects, such as rate-controlling steps, activation energies, stoichiometry, etc., of theories of deflagration of other constituents must, of course, differ from chemical aspects of the preceding theory. Moreover, observations on deflagration of various exothermic constituents indicate that physical aspects of the theories may also have to differ. For example, some substances leave solid residues after deflagration; others may melt before gasifying, and some may produce bubbles in the liquid phase. Aerothermochemical theories accounting for such phenomena have not been developed and therefore cannot be presented here. This casts uncertainties on detailed interpretations of the results and makes it difficult to use the few available results with confidence, in investigating propellant combustion mechanisms.

A method for achieving high temperatures in experiments with nonexothermic (as well as exothermic) constituents, is to expose samples of the constituents to hot and/or reactive gases. This can be done by burning spheres of the constituent in a reactive gas or by making porous samples of the constituent and passing hot gases or reactive gases over or through the samples. Theories of sphere burning are well developed because the same geometry is encountered in hydrocarbon droplet combustion, which has received much study in the past. These theories have been discussed in textbooks (3) (4) and therefore will not be repeated here. The latest study of combustion of exothermic oxidizer spheres (44) accounts for the presence of the decomposition flame in addition to the diffusion flame. Aerothermochemical theories of the decomposition of porous constituent samples have not been developed yet and therefore cannot be discussed here. It would be of interest to develop such theories as aids in interpreting experimental results on porous-sample decomposition and in applying these results to problems of propellant combustion.

Of the various other experimental methods for studying constituents, the hot-plate pyrolysis technique produces temperatures closest to those encountered in propellant combustion and therefore is most likely to be pertinent under conditions of interest. A considerable amount of theoretical work on hot-plate pyrolysis has been reported. The objectives of this work are to uncover pyrolysis mechanisms that

agree with the experiments and to provide aerothermochemical bases for interpreting hot-plate pyrolysis results. Properly interpreted hot-plate results should be applicable in theories of propellant combustion. The rest of this section is devoted to theories of hot-plate pyrolysis.

Although we shall not discuss theories of the experiments carried out at lower temperatures, nevertheless it is appropriate to emphasize that much interesting work has been done with vacuum decomposition and with slow, homogeneous heating of constituents in various environments, (38-43).

3.2. Theories of Hot-Plate Pyrolysis

Before discussing chemical kinetic theories for the mechanism of pyrolysis of specific materials, we shall consider aerothermochemical theories of the hot-plate experiments, applicable in principle to all materials obeying a few rather general requirements. In discussing aerothermochemical theories, we must distinguish between flat-plate and porous-plate experiments. When the hot plate is impermeable, the flow is necessarily non-one-dimensional. On the other hand, with a porous hot-plate the flow can be made to be practically one-dimensional; the gaseous pyrolysis products pass through the porous plate. Theories of porous-plate pyrolysis are simpler to develop because of the one-dimensionality and rest on rather firm ground today. Two-dimensional theories for impermeable plates are more difficult and have been developed only for particular flow regimes. We begin by discussing porous-plate theory; impermeable plates will be considered later.

3.2.1. Porous Plate - A fairly general theory of porous-plate pyrolysis may be found (45). In order to illustrate the essence of the approach, we present here a simplified version of the analysis. We postulate steady-state, one dimensional flow in the x direction, assume that the sample of the solid constituent occupies the region $x < 0$ and that a one-component gaseous pyrolysis product occupies the region $0 < x < \ell$ and flows through the porous plate located in $\ell < x < \ell + t$. Homogeneous reactions in the solid or gas are neglected, as are any heterogeneous reactions of the pyrolysis product within the porous plate. Conditions at $x = -\infty, 0, \ell$ and $\ell + t$ are identified by the subscripts i, s, p and ∞ , respectively. Body forces and radiative energy transfer are neglected and the ordered kinetic energy is assumed everywhere to be negligible compared with the thermal enthalpy.

In the notation of Section 1, the conservation equations for mass Eq. 6-7, and energy, Eqs. 6-9 and 6-12, applicable for $x < 0$ and for $0 < x < \ell$, become :

$$\rho v = \dot{m} = \text{constant} \quad (\text{Eq. 6-78})$$

and :

$$\dot{m} dh/dx = d[(\lambda/c_p)(dh/dx)]/dx \quad (\text{Eq. 6-79})$$

In Eq. 6-79, the identity $\lambda dT/dx = (\lambda/c_p) dh/dx$, where c_p is the specific heat at constant pressure, has been employed and use has also been made of the demonstrable result that the term involving T in Eq. 6-9 is negligible compared with that involving q for reasonable values of the Prandtl number when kinetic energy is small compared with thermal enthalpy. Conservation of momentum (Eq. 6-8) implies that the pressure p is constant for $x < \ell$ under the present approximations. A phenomenological permeability P of the porous plate can be defined such that p and \dot{m} are related according to the formula :

$$\dot{m} = (p - p_\infty)(P/t), \quad (\text{Eq. 6-80})$$

where p_∞ is the pressure on the downstream side of the plate ($x = \ell + t$).

Equation 6-79 is the only differential equation that appears in the present simplified formulation. Its general solution is :

$$h = A + B e^{\xi}, \quad (\text{Eq. 6-81})$$

where :

$$\xi = \dot{m} \int_0^x (c_p / \lambda) dx \quad (\text{Eq. 6-82})$$

and A and B are constants. The rest of the problem is purely algebraic, involving application of appropriate boundary and interface conditions.

Boundary conditions at $x = -\infty$ imply that the first integration constant in Eq. 6-81 is $A_c = h_c(T_i)$, where the subscript c identifies conditions in the condensed phase and $h_c(T)$ is the enthalpy of the condensed material, which is a function of temperature. Equation 6-81 then shows that $B_c = h_c(T_s) - h_c(T_i)$. Interface energy conservation (Eq. 6-21) at $x = 0$ reduces to $\dot{m}L(T_s) \equiv \dot{m}[h_g(T_s) - h_c(T_s)] = [(\lambda/c_p) dh/dx]_g - [(\lambda/c_p) dh/dx]_c$, where the subscript g identifies conditions in the gas phase and L is the enthalpy of gasification per unit mass. This relationship implies that $B_g = L(T_s) + h_c(T_s) - h_c(T_i) = h_g(T_s) - h_c(T_i)$, see Eq. 6-81. Equation 6-81 evaluated in the gas phase at the interface, then yields $A_g = h_c(T_i)$. These observations serve to determine all constants in Eq. 6-81 in terms of the temperatures T_i and T_s .

The requirement that the temperature equal the plate temperature T_p at $x = \ell$ gives:

$$h_g(T_p) = A_g + B_g e^{\xi_p} = h_c(T_i) + [h_g(T_s) - h_c(T_i)] e^{\xi_p}, \quad (\text{Eq. 6-83})$$

where :

$$\xi_p = \dot{m} \int_0^{\ell} (c_p / \lambda) dx$$

Equation 6-83 provides a relationship between \dot{m} and T_s , in terms of T_p (and T_i). In hot-plate pyrolysis experiments, the experimenter fixes T_i , usually measures T_p with a thermocouple and also measures \dot{m} . Equation 6-83 should be used by experimenters to estimate the surface temperature T_s as closely as possible from the measurements of \dot{m} and T_p . In reducing data, the dependence of \dot{m} on this calculated surface temperature should be considered, because it is T_s , not T_p , that appears in the surface rate (or equilibrium) boundary conditions discussed below. All experimental results obtained so far have been presented in terms of T_p , not T_s . If we assume that heat capacities and thermal conductivities are constant, the equation for T_s given by Eq. 6-83 becomes :

$$T_s = \frac{c_{pg} T_p - (L + c_{pc} T_i) (e^{\dot{m} c_{pg} / \lambda_g} - 1)}{c_{pg} + c_{pc} (e^{\dot{m} c_{pg} / \lambda_g} - 1)} \quad (\text{Eq. 6-83a})$$

In using Eq. 6-83a, one must of course estimate the value of ℓ , which although quite small, must be larger than a molecular mean free path. An expansion of Eq. 6-83a, valid only for sufficiently small values of ξ_p , is :

$$T_s \approx T_p - [L + c_{pc} (T_p - T_i)] \ell \dot{m} / \lambda_g, \quad (\text{Eq. 6-83b})$$

which can be used in conjunction with an upper bound for ℓ , in order to obtain an upper bound for $(T_p - T_s)$.

The relatively general surface boundary condition given in Eq. 6-70 (where now $c_1 = p/R''T_s$ since a one-component gas has been postulated) can be used to provide the final relationship required in the present simplified model of porous-plate pyrolysis. If the thermodynamic properties, the thermal conductivity and all rate constants (B_s , α_s , E_s and α) for the system are known and if the permeability ratio P/t , the length l and the temperature T_p are specified, then Eqs. 6-70, 6-80 and 6-83 provide three independent equations that can be solved for the three unknowns \dot{m} , p and T_s . In the pyrolysis experiments, one of these three quantities \dot{m} , is measured and the objective is to obtain information concerning either thermodynamic properties or rate constants of materials for which this data is not available. Thus, in reducing porous-plate pyrolysis data, Eq. 6-80 would be used to obtain p , then Eq. 6-83 should be used to obtain T_s and finally Eq. 6-70 should be studied in an effort to extract the desired thermochemical or kinetic information. It might be remarked here that the last term in Eq. 6-70 has generally been neglected in interpretations of experimental results; this is difficult to justify because the sticking coefficient α is difficult to estimate. Nevertheless, in the interpretations discussed in the following sections, we shall follow this precedent, employing Eq. 6-58 instead of Eq. 6-70. The experimental results are thus interpreted as providing kinetic data for surface rate processes (not thermochemical data and not kinetic data for homogeneous processes). In this regard, it may be worth indicating that homogeneous solid-phase reactions can probably be approximated as surface reactions, if the temperature gradient in the solid is steep enough at the surface. It is also worth stating that if the surface process is near equilibrium, then from Eqs. 6-70, 6-80 and 6-83 the slope of a graph of $\ln \dot{m}$ as a function of $-1/R''T_s$ can be shown to equal the heat of gasification L (at least when $p_\infty \ll p$). This last observation shows that under appropriate conditions, porous-plate pyrolysis measurements may be used to measure unknown thermochemical properties.

3.2.2. Impermeable Plate - Aerothermochemical aspects of pyrolysis by means of a hot impermeable plate have been considered by Cantrell (46) (47) and by Chaiken et al. (48). Cantrell developed a thin-film lubrication theory (49). He adopted Eq. 6-58 so that it was possible to assume that there was no temperature variation over the surface of the sample. The theory then predicted a constant separation distance between the sample surface and the hot plate and a nearly linear temperature profile across the gas film, under the conditions of validity for lubrication theory. He was able to calculate theoretically both the separation distance and the surface temperature of the sample, in terms of the loading force applied to the sample, the radius of the sample strand and thermochemical, transport and chemical kinetic properties of the system. Steady-state, two-dimensional (axially symmetrical) forms of Eqs. 6-7 to 6-9 are employed in the analysis (46).

The assumptions made by Chaiken et al. (48) differ from those of Cantrell. For example, Chaiken assumes constant pressure within the gas film, while Cantrell's lubrication theory results in an appreciable radial variation of pressure across the surface of the sample, but none in the axial direction (48). Neither of the theories account for compressible fluid flow in the gas film but estimates show that sonic velocities may be approached in the gas film in some of the experiments (47). Thus, as yet there are no valid aerothermochemical theories for many of the impermeable-plate pyrolysis experiments that have been reported. This places in doubt some interpretations of experimental results obtained with impermeable hot plates. These doubts underlie the interpretations that we shall now discuss.

3.3. Pyrolysis of Propellant Constituents

3.3.1. Fuel Constituents - Chemical kinetic explanations of the mechanism of hot-plate pyrolysis have been published for a number of fuel and oxidizing constituents of solid propellants. Materials representative of fuel constituents that have been studied experimentally include rubber (GRS-32), polystyrene and polymethyl-

methacrylate. As an example of the associated theoretical work on fuel constituents, let us consider pyrolysis of polymethylmethacrylate (29), (35).

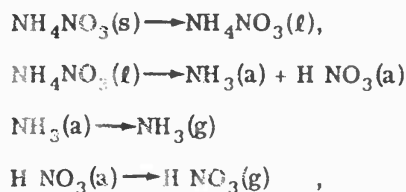
The earlier studies (29) supported the contention that the rate of surface pyrolysis is controlled by the same mechanism as the low-temperature, homogeneous, bulk thermal decomposition. Thus the rate-controlling process is the initial breaking of particular key bonds; unzipping to form monomers occurs rapidly after the key bonds are broken. This conclusion was supported by the observed activation energy, of the order of 30-40 kcal/mole.

Later work (35) at higher surface temperatures showed clearly that the apparent activation energy decreases as the surface temperature increases. These later results have been explained and correlated on the basis of the hypothesis that, at the higher temperatures, the rate-controlling step in the mechanism becomes desorption of the monomer from the surface (35). In the high-temperature limit, then, the pyrolysis rate is :

$$\dot{m} = A_s e^{-E_s/R^\circ T_s} \quad , \quad (\text{Eq. 6-84})$$

where $E_s \approx 11$ kcal/mole is assumed to be of the order of the heat of desorption and A_s was estimated (35) by considering reasonable molecular partition functions for the adsorbed monomer, according to the methods of transition state theory. Although this interpretation of the data may be correct, it should be pointed out that the possibility of an appreciable difference between the measured plate temperature and the sample surface temperature, developing at the higher temperatures, was not discussed in this study. It may well turn out that if gas-film effects are properly taken into account, then a graph of the pyrolysis rate vs. $1/T_s$ for the true T_s would be linear over the entire range of T_s values. This point of uncertainty, arising in addition to that mentioned at the end of the previous section, indicates need for closer scrutiny of the results. Lengelle (65) and others recently studied polymethylmethacrylate pyrolysis and concluded that hot-plate results are controlled by bulk degradation.

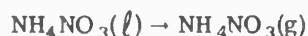
3.3.2. Ammonium Nitrate - A representative oxidizer constituent that has been studied in the same vein is ammonium nitrate. This too exhibits a very low apparent activation energy (about 7 kcal/mole) at the higher temperatures (19). The pyrolysis mechanism proposed to account for this observation is (19) :



with the last nitric acid desorption process as rate-controlling. Here, s denotes solid, l liquid, a adsorbed and g gas. The corresponding value of E_s in Eq. 6-84 is approximately the heat of desorption. The pre-exponential factor A_s was discussed (19) in terms of an argument leading to Eq. 6-63. In the partition function ratio q_s^\ddagger/q_s appearing in Eq. 6-63, it was assumed that the complex and the adsorbed molecule have the same vibrational and rotational partition functions. The partition functions for motion of the center of mass of the adsorbed molecule were taken to be vibrational functions of natural frequency $2.9 \times 10^{11} \text{sec}^{-1}$. It was then observed that if this same frequency was assigned to the two motions of the center of mass of the complex perpendicular to the reaction coordinate, then the theoretical pre-exponential factor exceeded the experimental one by two orders of magnitude, while if the partition functions for the two complex modes normal to the reaction coordinate were set equal to unity (corresponding to perpendicular escape of

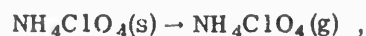
the complex), then the theoretical pre-exponential factor was about a tenth of the experimental result. It was concluded from this that theory and experiment would agree, if a significant fraction of the activated molecules was assumed to escape in a direction normal to the surface (corresponding to center-of-mass frequencies of the complex somewhat higher than $2.9 \times 10^{11} \text{sec}^{-1}$).

It has since been shown (45) that there is very little doubt that the measured temperature in the NH_4NO_3 experiments differs significantly from the surface temperature. It has been estimated from the existing experimental data that the true activation energy for NH_4NO_3 pyrolysis in the high-temperature regime lies between 25 and 30 kcal/mole (45). This activation energy is inconsistent with the assumption that a desorption process constitutes the rate-controlling step. The mechanism:



is consistent with the revised interpretation, provided that the vaporization step is rate-controlling and that the (unknown) heat of dissociation of associated gaseous ammonium nitrate is of the order of 10 or 15 kcal/mole. The need for more reliable determinations of surface temperatures in hot-plate pyrolysis is again underscored.

3.3.3. Ammonium Perchlorate - The experimental results on the oxidizing constituent NH_4ClO_4 , discussed in the previous chapter, also exhibit a break in the pyrolysis rate-temperature curve. The hypothesis that the rate-controlling process at the higher temperature is :



with $\Delta H \approx 25$ kcal/mole, is consistent with the hot-plate results, when a very rough estimate of the difference between the plate and surface temperatures is taken into account (45). However, other experimental results on NH_4ClO_4 have recently (66) been shown to suggest strongly that equilibrium for dissociative sublimation occurs in hot-plate pyrolysis. Space does not allow a thorough discussion of the wealth of information currently available on NH_4ClO_4 in acceptable manner.

4. Theories of Heterogeneous Solid Propellant Combustion

4.1. Introduction

Concerning the status of theories of heterogeneous solid propellant combustion, one point requires emphasis above all others. No truly acceptable theories of heterogeneous propellant combustion exist today. The reason for this is that processes of heat and mass transfer among the propellant constituents form an essential part of the combustion mechanism and these processes are too complex to be treated in a complete, accurate and realistic manner. We have available today only rudimentary concepts and models that may find application in acceptable theories, if and when such theories are developed.

The available concepts include heuristic and largely unjustified arguments based on diffusion flame-premixed flame relationships, more firmly based but as yet less versatile sandwich burner models and two-temperature concepts. These models are in such a primitive state of development that we shall not elaborate upon them in detail here. Instead, we shall consider each view very briefly, primarily with

the objective introducing the reader to a few of the basic aspects of each and directing him toward the original sources, few in number, where the concepts are presented. A recent theoretical discussion (64) of the relationship between composite propellant combustion and polymer degradation is not treated herein, nor is a recent accurate theory (65) for burning rates controlled by condensed-phase reactions of high activation energy.

4.2. Two-Temperature Concept

Obviously, in steady-state, one-dimensional combustion, the average linear regression rates of the fuel and oxidizer components of a composite propellant must be equal. Since we have seen that, in general, the linear pyrolysis rates of fuels and oxidizers differ whenever their surface temperatures are the same, it follows that the average surface temperatures of the fuel and oxidizer components must differ in steady-state combustion of composite propellants. This deduction forms the basis of the two-temperature postulate for composite propellant combustion.

In one form of the two-temperature hypothesis, it is proposed that the gaseous flame zone can be approximated as a plane slab with a uniform temperature gradient, in a direction normal to its faces and with zero temperature gradient in directions parallel to its faces. Fuel and oxidizer constituents are assumed to project into this slab of gas from its cold boundary. The two constituents project to different heights, so that their surface temperatures differ. The relationship between surface temperature and regression rate for each constituent is assumed to be the same as that measured in hot-plate pyrolysis experiments. The height to which each constituent projects into the flame slab can therefore be calculated from a measured burning rate of the composite propellant and an assumed value for the temperature gradient in the flame slab. If, as an additional requirement, we impose a surface energy balance at the surface of one of the constituents, stating that the amount of heat conducted from the gas into the condensed constituent at its surface, be just sufficient to gasify that material at the rate at which the propellant burns, then we can calculate the propellant burning rate (as well as the heights and surface temperatures of each constituent) from results of hot-plate pyrolysis experiments on constituents plus an assumed temperature gradient of the flame.

It is logical to suppose that application of a corresponding energy balance at the surface of the second constituent would fix the value of another unknown parameter. The only remaining parameter is the temperature gradient of the flame. It would be found, however, that the additional condition cannot determine the temperature gradient; instead, the condition would be inconsistent with the other relationships for all values of the temperature gradient and no acceptable solution would be obtained from the model. The basic physical reason for this paradox is that the gaseous flame structure is determined mostly by gas-phase chemical kinetic and transport processes, not by surface energy conservation conditions. A more accurate model would introduce additional assumptions regarding the gas-phase processes, in order to predict the gas flame structure. In such a model it might be possible to satisfy the second interface energy conservation condition by retaining a structure which is uniform in directions, parallel to the flame slab but which depends on the difference in height between the fuel and oxidizer surfaces. However, it would be more reasonable from a physical viewpoint to permit the structure of the gas flame zone above the fuel surfaces to differ from the structure of the gas flame zone above the oxidizer surfaces. Such a two-temperature model has not been developed.

The work that has been reported on a two-temperature model determines the (constant) temperature gradient in the gas flame zone from considerations of gas-phase kinetics and of oxidizer particle sizes. This work was concerned with propellants employing ammonium nitrate as an oxidizer and the nitrate decomposition flame was assumed to be the only gas-phase flame of any importance. No mention was made of any energy balance at the surface of the fuel constituent, and such an energy balance is not satisfied in the model. Nevertheless, if the diffusion flame neglected

in the model were considered, energy conservation might be restored while computed burning rates and surface temperatures might be modified very little. The present status of the work is clearly highly preliminary (19), (50), (51).

The basic idea that different constituents are likely to have different average surface temperatures, is an important one that should find application in many theories.

4.3. Ideas Concerning the Interplay of Diffusion Flames and Premixed Flames

Although the flame zones of homogeneous propellants are necessarily premixed, flames of heterogeneous propellants can be approximately premixed, if the appropriate ratio of diffusion time to chemical heat release time is sufficiently small; approximately unmixed diffusion flames, if the appropriate ratio of diffusion time to chemical reaction time is sufficiently large; or intermediate in character, for intermediate values of the ratio of the diffusion time to the reaction time. It is therefore reasonable to attempt to develop models of heterogeneous propellant combustion by postulating various arrangements of diffusion and premixed flames over the surface of the propellant. One might hope that by accounting for suitable distributions of diffusion and premixed flames and by considering appropriate interactions between these flames, it would be possible to avoid treating the difficult intermediate case in which the appropriate diffusion and reaction times are comparable.

A number of attempts to develop models along these lines have been reported (52), (53). Reviews and extensions of these studies may be found in Refs. (19), (37), (54) and (55).

The early results (52), (53), yielded the burning rate formula :

$$1/r = c_1/p + c_2/p^{1/3}$$

for the pressure (p) dependence of the burning rate (r), where c_1 and c_2 are independent of p . A later modification (54) produced the formula :

$$r = p^{1/2}/[c_3 p^{1/3} + c_4/p]^{1/2} ,$$

where c_3 and c_4 are independent of p . This formula fits the experimentally observed pressure dependence of the burning rate of ammonium perchlorate composite propellants about as accurately as the first formula does (54). The reader may consult Ref. (55) for derivations of new and more general burning rate formulas, that may be applicable in different combustion domains than those for which the preceding relationships correlate the available data.

We shall briefly reproduce here a recent argument (55) for deriving the first burning rate formula quoted above. An energy balance applied to the surface of the propellant yields :

$$\rho_c (\Delta H)r = \lambda (T_f - T_s)/h ,$$

where h is the flame height, ρ_c is the average density of the condensed phase, ΔH is the average heat absorbed (per gram) in gasification, λ is the thermal conductivity of the gas, T_f represents the adiabatic flame temperature and T_s denotes the surface temperature. The equation states that the heat needed for gasification is supplied by conduction and the right-hand side is an estimate of the temperature gradient in the gas adjacent to the surface. On highly questionable grounds, we assume that for a diffusion controlled process (52), (53) :

$$r_d \sim p^{1/3}/d ,$$

where d is the diameter of the oxidizer crystal and on much less questionable grounds we postulate that, for a process controlled by finite chemical reaction rates :

$$r_{ch} \sim p$$

From the fundamental equation describing the surface energy balance, applied first in the diffusion controlled limit and then in the chemically controlled limit, it follows that the heights of the diffusion and premixed flames are given, respectively, by :

$$h_d = c_5/p^{1/3}$$

and :

$$h_{ch} = c_6/p ,$$

where c_5 and c_6 are independent of p . We then postulate that a fraction α of the surface is covered by diffusion flames and a fraction $(1 - \alpha)$ of the surface is covered by premixed flames. The average flame height over the surface is therefore :

$$h = \alpha h_d + (1 - \alpha)h_{ch} = c_7/p^{1/3} + c_8/p .$$

When this formula for h is substituted into the surface energy balance equation, the original burning rate formula is obviously obtained with :

$$c_1 = c_8 \rho_c \Delta H / \lambda (T_f - T_s) ,$$

$$c_3 = c_7 \rho_c \Delta H / \lambda (T_f - T_s) .$$

The preceding argument is illustrative of the questionable foundations of existing models. For example, the relationship $r_d \sim p^{1/3}$ has not been shown to be consistent with the conservation equations. Indeed, there is reason to believe that this proportionality cannot be reconciled with the one-dimensionality implied in the rest of the arguments; it may be retrievable by introducing an effective pressure dependence of the thermal conductivity (which is absent in its original derivation), or by recourse to other physical or chemical phenomena or perhaps not at all. Phenomena associated with the processes of uncovering new oxidizer particles and burning out others as the grain regresses are also neglected in the preceding arguments. Many other questions can be raised.

However objectionable, these models nevertheless point up the important basic fact that it will probably be necessary to recognize the existence of both diffusion flames and premixed flames, in developing theories of heterogeneous propellant combustion.

4.4. Sandwich Burner Models

The final class of models that we shall consider are the so-called sandwich burner models, in which it is assumed that the heterogeneous propellant can be approximated as a series of parallel slabs of fuel and oxidizer, alternately placed side by side and pressed together. Burning is assumed to occur on a face that is perpendicular to the planes of the slabs. The burning zone is assumed to be composed of a series of parallel diffusion flames extending downstream from the intersections of the oxidizer and fuel slabs. The fuel and oxidizer surfaces exposed to the burning zone are assumed to remain plane but are permitted to extend to different heights into the flame zone. Although the model geometry constitutes an idealiza-

tion for real heterogeneous propellants, nevertheless sandwich geometries of composite propellants have been constructed and burned in the course of research programs. Price and Barrère observed that experimental surface geometries during burning differed from those postulated in the theoretical model, thus implying that the model requires further refinement, even within the context of the sandwich geometry.

In a sense, sandwich burner models are special cases of those emphasizing the interplay between diffusion and premixed flames. The sandwich burner studies emphasize in particular the diffusion-flame aspects of the combustion process. However, the theoretical developments of the sandwich burner models that have been reported in the literature are more firmly based on the conservation equations than are the published studies of the earlier models. Therefore the results of the existing sandwich burner studies are more believable, although of a much more restricted scope.

The solid propellant sandwich burner model of steady composite propellant combustion was first discussed in the literature in Ref. (19). Since then, the theory of this model has undergone extensive development (56), (57) and has been brought to the point of preliminary comparison between theory and experiment. In Ref. (56), the burning rate was derived for a sandwich experiencing unopposed surface gasification processes and diffusion flame combustion in the gas phase. The analysis provides an extension of the two-temperature hypothesis in predicting that the protruding propellant constituent with the higher gasification temperature controls the burning rate, while the other constituents with the lower gasification temperature, controls the difference in height between the surface of the two constituents; here "control" refers to the effect of a small change in pyrolysis rate on the composite propellant combustion behavior. Experimental evidence for the validity of this same conclusion, in pyrolysis experiments that do not involve diffusion flames, has been cited in Chapter 5, Section 3.1. In Ref. (57), the analysis of Ref. (56) is extended to include nonstoichiometric propellant composition. This extension enables comparison with experiment to be made concerning the effect of oxidizer particle size on the burning rate of composite propellants in the diffusion flame regime. The theory provided qualitative correlation of such experimental data for ammonium perchlorate propellants (57).

An important objection to the sandwich burner model in its present stage of development, is that it is incapable of yielding a pressure-dependent burning rate. To correlate experimental results over appreciable ranges of pressure, the model must be augmented by allowing for pressure-dependent gas-phase reactions. A prime candidate for the dominant pressure-dependent reaction in propellants employing NH_4NO_3 or NH_4ClO_4 as an oxidizer, is the decomposition flame of the oxidizer. Failure of the flame surface approximation in the gas-phase reaction between fuel and oxidizer, is another possibility; this approximation must break down at the planes of contact between solid fuel and oxidizer. It would be complicated but not prohibitively difficult to blend one or the other of these effects into the sandwich burner model.

5. Theories of Combustion of Metal Particles

5.1. Introduction

Metalized propellants exhibit combustion phenomena that differ from those of other heterogeneous propellants. Metals are characterized by relatively high ignition temperatures. On the basis of the two-temperature concept, one would therefore expect metal constituents to extend far into the gaseous reaction zone. This tendency is indeed observed experimentally. The typical metals are, in fact, so difficult to vaporize that in propellant combustion they have been observed to break off,

agglomerate, melt, coalesce and move about in the gaseous combustion zone before finally igniting and burning. Thus, the usual picture of a continuous, irregular surface separating the gaseous and condensed phases is not valid for metalized propellants. The metal constituents are more likely to burn as spherical particles in the hot gaseous products of the binder-oxidizer reaction. A key problem in understanding the combustion mechanism of metalized propellants is, therefore, to ascertain the burning mechanisms of spherical metal particles in various gaseous atmospheres.

One might expect that the complex behavior of metals in propellant combustion would greatly affect the burning rate of the propellant. However, at most metal concentrations of practical interest, this is not so. Generally speaking, a metalized propellant surface appears to regress at roughly the same rate as the surface of the nonmetalized system; as the metal is exposed, it moves and burns more or less independently in the gaseous flame. There are exceptions to this rule. For example, metals shaped as long wires can efficiently conduct heat to the interior of the propellant, thereby increasing the burning rate appreciably ("rate-controlled burning"). But the complexity of the combustion processes of metals seldom influences the burning rate or combustion mechanisms of the rest of the propellant. To a large extent, metal combustion can therefore be studied separately from propellant combustion.

The practical importance of understanding the metal combustion process stems from the fact that in an overall sense, the metal constituents burn more slowly than the rest of the propellant. Thus, metal particles have been observed to continue to burn well downstream from the gaseous reaction zone of the propellant. It is important to achieve a high combustion efficiency of the metal in order to realize the potential improvement in performance afforded by metalization. Particle burning times thus affect chamber dimensions required for acceptable performance. Furthermore, performance depends critically on the particle size of the condensed metal oxide reaction products (see Chapter 2) and final product particle sizes are controlled by the particle combustion mechanism. Therefore metal particle combustion mechanisms are of practical interest in themselves.

In the present section we consider theories of the combustion of small spherical metal particles in gaseous atmospheres. First, some peculiar characteristics of the combustion of metal spheres will be described. Next, the few theoretical studies that have been reported will be referenced and an incomplete set of assumptions will be outlined on which an improved theoretical treatment of aluminum sphere combustion might be based.

5.2. Description and Classification of Behavior of Various Burning Metals

The obvious starting point for a theory of metal sphere combustion is the well-developed theory of hydrocarbon fuel droplet combustion (3). However, there are essential differences between metal and hydrocarbon combustion. The principal new element that must be included in any metal combustion theory is the fact that condensed-phase products must be formed for combustion to occur at all. The reaction of condensed metal and gaseous oxidizer to form gaseous combustion products is almost always endothermic and therefore cannot support a flame. At least some condensed products must therefore be included in any realistic theory.

The nature of theories of metal combustion must also differ from one metal to another. These differences stem from differences in the properties of various metal-metal oxide systems. Here we describe some of the more important differences that should be considered. The differences affect ignition as well as combustion behavior. These ideas are due to Gordon (58) and to Brzustowski and Glassman (59) and have been reviewed in large part by Markstein (60).

The first characteristic of the system that must be ascertained, is the relative volatility of the metal and the metal oxide. Most metals are more volatile than their oxides. Boron is the principal example of a metal that is less volatile than its oxide. When the oxide is more volatile, it is possible for appreciable concentrations of gaseous oxide to exist in thermal equilibrium, in contact with condensed metal. In the burning of spheres of such metals, there may therefore exist a purely gaseous region in the vicinity of the surface of the metal in which the gaseous oxide is the principal constituent. The burning mechanism of such metals may be similar to that of carbon particles, in which oxygen diffuses through the gaseous product to the surface and reacts there in a surface reaction. Boron particles have been observed to burn slowly in oxygen without fragmentation (58), a result which is consistent with such a supposition. As the metal-oxide gases flow away from the burning sphere into cooler regions, nucleation and oxide condensation would begin to occur; in this respect the metal combustion differs from carbon combustion. The mechanism that we have just described cannot occur if the metal is more volatile than the oxide, because there can be no purely gaseous oxide layer around the surface of such metals.

Another characteristic of the metal-metal oxide system that can affect ignition and combustion behavior is the mutual solubility of the metal and its oxide. If the solid metal-metal oxide system is completely immiscible, then an oxide coating can develop on the surface of the metal particle, inhibiting combustion and preventing ignition under certain conditions. On the other hand, if the metal and metal oxide are completely miscible, oxide formed on the surface can be transported into the interior somewhat more rapidly, leaving more metal exposed for further attack by gaseous oxidizer. Thus, soluble systems are capable in principle, of supporting sustained surface combustion at an appreciable rate, while insoluble systems with nonvolatile oxides are not, at least at surface temperatures, below the melting temperature of the oxide. Above the melting temperature of both the oxide and the metal, motion of the liquids may expose additional metal to the gas. The melting point of the oxide has, in fact, been identified as the approximate value of the ignition temperature for certain insoluble systems with nonvolatile oxides (Al and Be). That such a relationship is only approximate has been borne out by the experiments of Friedman and Maček and others (60), (61). The true ignition temperature and ignition mechanism of metals is quite complex, is poorly understood and apparently depends on the particular metal and the method of ignition (60). Magnesium, aluminum and beryllium are typical metals for which the metal-metal oxide system is nonsoluble while titanium and zirconium are soluble in their oxides (59).

A third property of systems with nonvolatile oxides that affects ignition and combustion behavior, is the ease with which the metal can be vaporized. Magnesium has been termed a volatile metal, while aluminum, beryllium, titanium and zirconium were classified as nonvolatile (58), (59). Clearly, such a breakdown is somewhat subjective, involving for example, rather arbitrary identification of a critical equilibrium vapor pressure at some specified temperature. But magnesium and aluminum, for example, do exhibit different combustion behaviors, the former showing a greater tendency toward vapor-phase combustion. It is not yet clear however, whether the volatility categorization is an essential one that distinguishes what combustion domains can occur or one that is merely a convenient way of stating what relative temperature levels are required for achieving a given combustion domain.

The size of a metal particle has also been found to influence its combustion behavior. Two size categories, large and small, with a dividing diameter around 50 to 80 microns, have been proposed (59). The smaller particles tend to exhibit a greater degree of vapor-phase combustion. Again, it is not clear that particle size *per se* is an appropriate criterion for a particular combustion mechanism.

For metals with nonvolatile, insoluble oxides, (Mg, Al, Be) it is reasonable to assume that the combustion process involves vaporization of the metal, followed by reaction of the metal vapor with oxygen in a kind of diffusion flame in which solid metal-oxide combustion products are produced. The solid products would tend to be formed as particles that are much smaller than the burning metal particle; the existence of these very small oxide particles in metal-particle flame zones has been demonstrated clearly in experiments (60). The small oxide particles grow in size as they flow away from the metal sphere.

However, this model cannot constitute a complete picture of the combustion process under all sets of conditions. Fragmentation of burning metal particles has often been observed experimentally, especially for either large metal particles or non-volatile metals; it occurs for both insoluble (Mg, Al) and soluble (Ti, Zr) systems. The mechanism of fragmentation requires explanation. One possibility is that the oxide particles produced in the gas-phase reaction coalesce around the metal, eventually forming a cap that prevents gas flow until the pressure inside builds up sufficiently to puncture the cap, thereby causing the particle to be propelled (and perhaps fragmented) by the escaping gases. Another possibility is that such a cap is formed directly by means of a competing surface oxidation reaction. Oxide caps covering part or, in some cases all, of the metal particle have been observed experimentally (60). Other hypotheses concerning the mechanism of fragmentation have also been advanced (59).

A final important point that we have not mentioned yet, is the possibility that the composition of the gaseous oxidizing atmosphere exerts an appreciable influence on the combustion mechanism. Metal combustion in atmospheres containing water vapor sometimes is quite different from combustion in perfectly dry atmospheres (60). Chemical explanations for these effects can be proposed, on the basis of formation of different compounds. Experiments performed by different investigators are sometimes difficult to compare because different oxidizing atmospheres are used and also because in some cases the oxidizing atmosphere consists of lean, premixed, laboratory flames of changing or unknown chemical composition.

When metal alloys burn, they exhibit various special phenomena that differ from those of pure metals (59), (60).

5.3. Theories of the Combustion of Spheres of Metals with Nonvolatile, Insoluble Oxides

A few attempts to develop theories of metal particle combustion have been reported in the literature. These theories treat combustion of pure metals in gaseous atmospheres, in which oxygen is the only chemically active constituent. They pertain to the metal-metal oxide systems that are probably of greatest practical interest in solid propellant combustion, viz., insoluble condensed phases and relatively highly nonvolatile oxides. Most consider magnesium and aluminum explicitly.

5.3.1. Dilute Heterogeneous Diffusion Flame - Markstein (62) developed a theory of a dilute spherical diffusion flame for a magnesium-oxygen-argon system. He did not intend to construct a theory for the burning of metal particles. Thus, he purposely avoided considering processes occurring in the central part of the spherical flow region, by treating a dilute mixture of magnesium vapor in argon, injected in gaseous form at a point in the center of the spherical reaction zone. However, many of his results should have a direct bearing on the reaction kinetics in the burning of solid, spherical, magnesium particles. The combustion reaction between Mg and O_2 is assumed to be a heterogeneous one, occurring on the surfaces of small MgO particles. All nucleation processes are assumed to occur in a small region near the point of injection and analysis is attempted only outside this nucleation region. Thus, the process studied is the growth of the particles of MgO

(assumed spherical but permitted to have a size distribution) as they flow radially outward with the argon carrier gas. Additional assumptions include the approximations that the mole fraction of oxygen in the gas is practically constant, the mole fraction of argon is practically unity, temperature is constant, the radial convection velocity is negligible compared with the radial diffusion velocity of magnesium and the velocity of the condensed combustion products equals the radial velocity of the carrier gas. There is precedent for introducing assumptions of this type into dilute diffusion flame analyses.

Under these assumptions, mass conservation of magnesium implies that the sum of the diffusion flow rate of the reactant vapor and the volume flow rate of the condensed reaction product is a constant. This conservation equation is combined with a reaction rate law, in which it is assumed that the time rate of change of volume of a condensed product particle is proportional to the product of the concentration of magnesium in the gas and the surface area of the particle, in order to obtain two first-order, ordinary differential equations for the radial distributions of the mole fraction of gaseous magnesium and the volume of condensed products per unit gas volume. The final differential equations were solved numerically. Solutions for radial distributions of product particles were compared with microdensitometric analyses of photographs taken in earlier experiments of Markstein and it was inferred from the comparison, that most of the nucleation does indeed occur very near the center of the sphere, that a broad particle size distribution is produced during nucleation, that the sticking coefficient for gaseous Mg atoms on solid MgO particles is about 0.75×10^{-1} and that about 4×10^{12} solid product particles per cm^3 were present in the particular experiment analyzed. More recent experimental work has indicated that the value of the sticking coefficient may have to be revised.

Obviously, many of Markstein's assumptions require modification for application to burning of metal particles; for example, boundary conditions at the surface of the metal must be considered and practically all of the approximations peculiar to the dilute diffusion flame (e.g., constant temperature) must be abandoned. However, Markstein's kinetic scheme concerning oxide particle growth may remain applicable. The work constitutes a first step toward a theory of magnesium-sphere combustion.

5.3.2. Metal Sphere Combustion - Brzustowski and Glassman (63) treated theoretically the combustion of both aluminum and magnesium metal particles. Kuehl (61) applied essentially the same approach to aluminum and beryllium combustion; his formulation was slightly more general than that of Brzustowski and Glassman in that he allowed for oxidizers (other than oxygen) that may produce certain gaseous products and provided for somewhat more accurate computations of thermal conductivities and heat capacities. The two treatments are so similar that we need discuss only one of them here. We shall focus our attention on the Brzustowski-Glassman analysis of aluminum combustion.

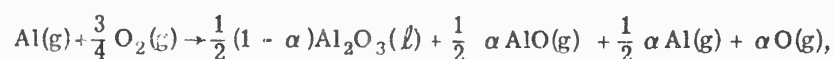
In some respects, the Brzustowski-Glassman development is modeled after the theory of hydrocarbon droplet combustion; it differs, of course, in allowing for the occurrence of condensed-phase products of reaction. The spherical metal particle is assumed to be surrounded by a concentric spherical flame surface of infinitesimal thickness which divides an interior region, in which metal vapor and reaction products interdiffuse from an exterior region in which oxygen and reaction products interdiffuse. Except for a finite rate of vaporization at the metal surface, all consideration of chemical rate processes is avoided by assuming infinite rates at the flame surface and zero rates elsewhere.

In developing diffusion equations, the interior and exterior regions are treated as kinds of stagnant films, a procedure which may be questionable and which induced the authors to erroneously set condensed particle velocities equal to mole-average rather than mass-average gas velocities. Although the formulations used in analyses of hydrocarbon droplet combustion enable one to avoid such film approx-

imations, the burning rate of aluminum may be small enough for results depending on the Brzustowski-Glassman diffusion equations to be valid.

Heat transfer by conduction and by radial convection from the flame surface to the metal surface and from the flame surface to the surroundings is properly included in the formulation, within the framework of the flame-surface model. Heat transfer by radiation is also included in the analysis. Radiant heat transfer may be of importance because condensed, hot products of combustion are formed. In the Brzustowski-Glassman treatment of radiation the infinitesimal flame surface is approximated as a solid surface and absorption or emission of radiation is permitted to occur only at the droplet surface, the flame surface and infinity. Brzustowski-Glassman results involving radiant energy transfer are thus qualitatively valid, at best. The radiant energy transfer problem is a difficult one that probably should be attacked only after one completes an analysis, neglecting radiation, that affords some insight into the radial distribution of condensed reaction products. The appropriate approximations for radiation transport will depend critically on the radial distribution of the condensed oxide.

Through various approximate integrations of the ordinary differential equations that they developed, Brzustowski and Glassman obtained graphs for the mass burning rate and for a variety of other properties of the system (e.g., flame radius, surface temperature, fraction of the products produced at the flame surface that are in the gaseous phase), as functions of composition of the oxidizing atmosphere, ambient temperature, radiation parameters, etc. The detailed approximations involved in the analysis are too numerous and too varied to be listed here. However, it may be worth indicating that in aluminum combustion the reaction that is assumed to take place at the flame surface is taken to be :



where α is defined as the fraction of reaction product vaporized and is calculated in the analysis from the assumption that the flame temperature equals the boiling point of the metal oxide. This chemical formula implies that the gaseous part of the reaction product is a mixture of AlO, Al and O. Evidence in support of this assumed composition is derived principally from vacuum sublimation experiments, which are carried out at very low (submillimeter) pressures and under reducing conditions. At the pressures (1 atm and above) and oxygen concentrations considered in the metal particle combustion analysis, such a high degree of dissociation of reaction products seems unlikely; it is possible that the most realistic approximation for the chemical composition of the gaseous part of the reaction product may well be simply $\text{Al}_2\text{O}_3(\text{g})$. The effect of the stoichiometry assumption on the results of the analysis cannot readily be estimated from the curves because they all refer to the same stoichiometry.

The following results of the analysis are not liable to be affected by any of the objections cited above: The dimensionless driving force for mass transfer from burning aluminum particles is of the order of 10^{-1} (less than 10^{-2} times the value for typical hydrocarbon droplets) if radiant energy transfer is neglected. The surface temperature of a burning aluminum particle is probably a few hundred degrees below its boiling temperature during burning at atmospheric pressure. The mole fraction of gaseous aluminum at the surface of a burning aluminum droplet is probably of the order of 10^{-1} or less. Results concerning other chemical compositions and results concerning the magnitude of the burning rate, such as that shown in Fig. 6-13, could depend appreciably on the approximations introduced.

Brzustowski and Glassman rightly conclude that their analysis provides a step toward an understanding of metal combustion.

5.3.3. Remarks Concerning Assumptions for an Improved Theoretical Treatment of Aluminum Sphere Combustion - The assumption that the entire reaction takes place at a flame surface is difficult to justify for systems that produce condensed-phase products because the overall heterogeneous reaction process, involving nucleation and particle growth, need not exhibit the simple kinetic and chemical equilibrium behavior known to be representative of many homogeneous reactions. Appreciable reaction times may be required for the production of condensed oxides. Hence it is desirable to refrain from invoking a flame-surface approximation at the outset of a theoretical treatment of aluminum combustion. It is known that most of the analysis of hydrocarbon droplet combustion can be completed without introducing a flame-surface approximation (3) and it would be of interest to investigate how much progress can be made along these same lines for aluminum particles.

It is reasonable to introduce a number of other simplifying assumptions for aluminum combustion. For example, it may be sufficient to permit only $Al(l)$, $Al(g)$, $O_2(g)$ and $Al_2O_3(l)$ to be present in the system. In any event, all chemical reactions except the condensation and evaporation steps can be treated as energetically neutral with reasonable accuracy. Small spherical particles of the liquid oxide can be assumed to be produced by the gaseous reactants. These particles should be permitted to grow at a rate that depends on the rate at which gaseous aluminum and oxygen molecules impinge on them. Product particle sizes are expected to be so small that the contribution of the particles to the hydrostatic pressure, due to their random Brownian motion, should be taken into account. A particle size distribution, continual homogeneous nucleation, which is perhaps the most difficult theoretical problem at this level, and particle agglomeration, should all be accounted for in the analysis as accurately as possible. Radiation should be neglected in the first approximation.

Recently Wilson (67) has reviewed from a common viewpoint all previous theories for aluminum combustion and has developed a variety of new models, some of which include certain of the preceding suggestions. He provides fundamental arguments for neglecting radiation in single-particle combustion. He has performed experiments which demonstrate by direct photography that the square of the particle diameter decreases linearly with time, thereby supporting hydrocarbon-droplet types of models. He has demonstrated that low accuracy of currently available experiments and absence of data on high-temperature transport properties prevent one from selecting a "best" model of the hydrocarbon-droplet type from the variety that are now available.

Much remains to be discovered about the burning mechanisms of metal particles.

References

- (1) Nachbar W., Williams F. and Penner S.S., Quart. Appl. Math. 17, 43, 1959.
- (2) Hirschfelder J.O., Curtiss C.F. and Bird R.B., Molecular Theory of Gases and Liquids. John Wiley and Sons, New York, 1954.
- (3) Williams F.A., Combustion Theory. Addison-Wesley, Reading, Mass., 1965.

- (4) Penner S.S., Chemistry Problems in Jet Propulsion. Pergamon Press, New York, 1957.
- (5) Glasstone S., Textbook of Physical Chemistry. Chapter 13, D. van Nostrand, New York, 1946.
- (6) Hinshelwood C.N., The Kinetics of Chemical Change. Clarendon Press, Oxford, 1940.
- (7) van Tiggelen A., Balacéaner J.C. and Sorlé B., Oxidations et Combustions. Revue de l'Institut Français du pétrole et annales de combustibles liquides, Paris, Vol. 17 (July-August 1962 and following).
- (8) Kondratiev V.N., Kinetics of Chemical Gas Reactions. Publication of Akad. Sic. U.S.S.R., Moscow, 1958.
- (9) Rice O.K. and Gineil R., J. Phys. Chem. 54, 885, 1950.
- (10) Parr R.G. and Crawford B.L., Jr., J. Phys. Chem. 54, 929, 1950.
- (11) Huggett C., "Combustion of Solid Propellants" in Combustion Processes, Vol. II of High Speed Aerodynamics and Jet Propulsion, pp.514-574, Princeton University Press, Princeton, 1956.
- (12) Geckler R.D., AGARD, Selected Combustion Problems, pp.289-339, Butterworths Scientific Publications, London, 1954.
- (13) Geckler R.D., Fifth Symposium (International) on Combustion, pp.29-40, Reinhold Publishing Corp., New York, 1955.
- (14) Penner S.S., Chemical Rocket Propulsion and Combustion Research, Chapter 4, Gordon and Breach, New York, 1962.
- (15) Johnson W.E. and Nachbar W., Eighth Symposium (International) on Combustion, pp.678-689, Williams and Wilkins Co., Baltimore, 1962.
- (16) Rosen G., J. Chem. Phys. 32, 89, 1960.
- (17) Johnson W.E. and Nachbar W., Arch. Rat. Mech. Anal. 12, 59-92, 1963.
- (18) Wilfong R.E., Penner S.S. and Daniels F., J. Phys. Chem. 54, 863, 1950.
- (19) Schultz R., Green L. Jr. and Penner S.S., Combustion and Propulsion Third AGARD Colloquium, pp.367-420, Pergamon Press, New York, 1958.
- (20) Andersen W.H. and Chaiken R.F., On the Detonality of Solid Composite Propellants, Part I, Aerojet-General Corp. TM 809, Azusa, Calif. Jan. 1959.
- (21) Schultz R.D. and Dekker A.O., Sixth Symposium (International) on Combustion, pp.618-626, Reinhold Publ. Corp., New York, 1957.
- (22) Glasstone S., Laidler K.J. and Eyring H., The Theory of Rate Processes. McGraw-Hill, New York, 1941.
- (23) Spalding D.B., Combustion and Flame 4, 59-76, 1960.
- (24) Spalding D.B., Proc. Roy. Soc. (London) A240, 83-100, 1957.

- (25) Friedman R., Levy J.B. and Rumble K.E., The Mechanism of Deflagration of Pure Ammonium Perchlorate, AFOSR TN 59-173, Atlantic Research Corp., Alexandria, Va., 1959.
- (26) Friedman R., Nugent R.G., Rumble K.E. and Scurlock A.C., Deflagration of Ammonium Perchlorate, Sixth Symposium (International) on Combustion, pp.612-618, Reinhold Publ. Corp., New York, 1956.
- (27) Levy J.B. and Friedman R., Eighth International Symposium on Combustion, pp.663-672, Williams and Wilkins Co., Baltimore, 1962.
- (28) Schultz R.D. and Dekker A.O., The Absolute Thermal Decomposition Rates of Solids: Part I, Aerojet-General Corp., TN No. 2, AFOSR Contract AF18 (600)-1026, Azusa, Calif. Nov. 1954.
- (29) Schultz R.D. and Dekker A.O., Fifth Symposium (International) on Combustion, pp.260-267, Reinhold, New York, 1955.
- (30) Bills K., et al., The Linear Vaporization Rate of Solid Ammonium Chloride, TN No. 10, AFOSR Contract No. AF 18(600)-1026, Azusa, Calif., July 1955.
- (31) Schultz R.D. and Dekker A.O., The Absolute Thermal Decomposition Rates of Solids: Part III, Aerojet-General Corporation, TN No. 7, AFOSR Contract No. AF 18(600)-1026, Azusa, Calif., July 1955.
- (32) Schultz R.D. and Dekker A.O., The Absolute Thermal Decomposition Rates of Solids: Part IV, Aerojet-General Corporation, TN No. 8, AFOSR Contract No. AF 18(600)-1026, Azusa, Calif., July 1955.
- (33) Barsh M.K. et al., Rev. Sci. Instr. 29, 392, 1958.
- (34) Chaiken R.F. and Van de Mark D.K., Rev. Sci. Instr. 30, 375-376 (1959).
- (35) Chaiken R.F., Andersen W.H., Barsh M.K., Mishuck E., Moe G. and Schultz R.D., J. Chem. Phys., 32, 1, 141-146, 1960.
- (36) Coates R.L., Linear Pyrolysis Rate Measurements of Propellant Constituents, AIAA Preprint No. 65-55, January, 1965.
- (37) Barrère M. and Williams F.A., Analytical and Experimental Studies of the Steady-State Combustion Mechanism of Solid Propellants. To appear in AGARD Colloquium Proceedings, 1966.
- (38) Grassie N., Chemistry of High Polymer Degradation Processes. Intersciences Publishers, Inc., New York, 1956.
- (39) Jellinek H.H.G., Degradation of Vinyl Polymers. pp.3-90, Academic Press, New York, 1955.
- (40) Feick G., J. Am. Chem. Soc. 76, 5858, 1954.
- (41) Luft N.W., Ind. Chemist, 31, 502, 1955.
- (42) Bircumshaw L.L. and Phillips T.R., J. Chem. Soc., 4741, 1957.
- (43) Galwey A.K. and Jacobs P.W.M., J. Chem. Soc., 837, 1959.

- (44) Barrère M. and Nadaud L., Combustion of Ammonium Perchlorate Spheres in a Flowing Gaseous Fuel. 10th Symposium (International) on Combustion, pp. 1381-1393, The Combustion Institute, Pittsburgh, 1965.
- (45) Nachbar W. and Williams F.A., On the Analysis of Linear Pyrolysis Experiments. Ninth Symposium (International) on Combustion, Academic Press, New York, pp. 345-357, 1963.
- (46) Cantrell R.H., Gas Film Effects in the Linear Pyrolysis of Solids. AIAA Journal, Vol. 1, pp. 1544-1555, 1963.
- (47) Cantrell R.H., AIAA Journal, Vol. 2, pp. 406-407, 1964.
- (48) Chaiken R.F., Sibbett D.H., Sutherland J.E., Vande Mark D.K. and Wheeler A., Rate of Sublimation of Ammonium Halides. J. Chem. Phys., Vol. 37, pp. 2311-2318, 1962.
- (49) Schlichting H., Boundary Layer Theory. pp. 87-90, Pergamon Press, New York, 1955.
- (50) Chaiken R.F., A Thermal Layer Mechanism of Combustion of Solid-Composite Propellants with Application to Ammonium Nitrate Propellants. Aerojet-General Corp. TM 290, Azusa, California, 1957.
- (51) Andersen W.H., Bills K.W., Mishuck E., Moe G. and Schultz R.D., An Investigation of the Combustion of Composite Propellants Containing Ammonium Nitrate. Aerojet-General Corporation, Azusa, California.
- (52) Sutherland G.S., The Mechanism of Combustion of an Ammonium Perchlorate-Polyester Resin Composite Solid Propellant. Ph.D. Thesis, pp. 34-44 and pp. 142-154; Princeton University, 1956.
- (53) Summerfield M., Sutherland G.S., Webb M.J., Tabak H.J. and Hall K.P., Burning Mechanism of Ammonium Perchlorate Propellants. In Solid Propellant Rocket Research, pp. 141-182, Vol. 1 of ARS series Progress in Astronautics and Rocketry, Academic Press, New York, 1960.
- (54) Penner S.S., Chemical Rocket Propulsion and Combustion Research. Chapter 4. Gordon and Breach, New York, 1962.
- (55) Barrère M. and Nadaud L., Les Domaines de Combustion des Poudres Composites. La Recherche Aérospatiale, No. 98, pp. 15-31, 1964.
- (56) Nachbar W., A Theoretical Study of the Burning of a Solid Propellant Sandwich. In Solid Propellant Rocket Research, pp. 207-226, Vol. 1 of ARS series Progress in Astronautics and Rocketry, Academic Press, New York, 1960.
- (57) Nachbar W. and Cline G.B., Jr., The Effects of Nonstoichiometric Composition and Particle Size on the Burning Rates of Composite Solid Propellants. Fifth AGARD Combustion and Propulsion Colloquium, Braunschweig, 1962.
- (58) Gordon D.A., Combustion Characteristics of Metal Particles. Solid Propellant Rocket Research, edited by M. Summerfield, pp. 271-278, Vol. 1 of Progress in Astronautics and Rocketry, Academic Press, New York, 1960.

- (59) Brzustowski T. A. and Glassman I., Spectroscopic Investigation of Metal Combustion, Heterogeneous Combustion, edited by H. S. Wolfhard, I. Glassman and L. Green, Jr., pp. 41-73, Vol. 15 of Progress in Astronautics and Aeronautics, Academic Press, New York, 1964.
- (60) Markstein G. H., AIAA Journal 1, 550-562, 1963.
- (61) Kuehl D. K., AIAA Journal 1, 550-562, 1963.
- (62) Markstein G. H., Analysis of a Dilute Diffusion Flame Maintained by Heterogeneous Reaction. Heterogeneous Combustion, edited by H. G. Wolfhard, I. Glassman and L. Green, Jr., pp. 177-202, Vol. 15 of Progress in Astronautics, Academic Press, New York, 1964.
- (63) Brzustowski T. A. and Glassman I., Vapor-Phase Diffusion Flames in the Combustion of Magnesium and Aluminum: I. Analytical Developments, Heterogeneous Combustion, edited by H. G. Wolfhard, I. Glassman and L. Green, Jr., pp. 75-115, Vol. 15 of Progress in Astronautics and Aeronautics, Academic Press, New York, 1964.
- (64) Rabinovitch B., Tenth Symposium (International) on Combustion, pp. 1395-1404, The Combustion Institute, Pittsburgh, 1965.
- (65) Lengelle G., PhD Thesis, University of California, San Diego, to be published.
- (66) Guirao C., PhD Thesis, University of California, San Diego, to be published.
- (67) Wilson R., PhD Thesis, University of California, San Diego, to be published.

Chapter 7

Erosive Burning

Nomenclature

α	burning rate constant defined in Eq. 7-12; average value of sound velocity in the central port
A_b	burning surface area
A_c	$P^2/4\pi$
A_p	port cross-sectional area at downstream end of tubular grain
A_t	nozzle throat area
a_0, a_1, \dots, a_5	erosion constants defined in Eq. 7-13
B	driving force for mass transfer; frequency factor of solid-phase gasification
b	burning rate parameter defined in Eq. 7-12
c^*	characteristic velocity
C_F	friction coefficient
C_{Fo}	friction coefficient in the absence of mass injection
C_H	Stanton number
C_{Ho}	Stanton number in the absence of mass injection
c_p	specific heat at constant pressure for gas
c_s	specific heat of propellant
D	diameter of port
d	crystal diameter
E	activation energy of solid-phase gasification
G	axial mass flux
g	optical magnification factor
h	heat transfer coefficient; enthalpy per unit mass; width of two-dimensional chamber
h_l	enthalpy in the bulk of the fluid
h_w	enthalpy at the wall
h_o	conventional Chilton-Colburn coefficient without mass injection
I_{sp}	specific impulse
k_u	K_4

K_I	A_b/A_t
K_{II}	A_p/A_t
K_1, K_2, \dots, K_{13}	erosion constants defined in Eqs. 7-3 - 7-17.
L	length of grain
M	Mach number
m	erosion exponent defined in Eq. 7-4
\dot{m}	mass flow rate
MR	mixture ratio
n	number of moles per unit mass; pressure exponent for regression rate
P	perimeter of a cross section of the central port
p	pressure
\bar{p}	average chamber pressure
Pr	Prandtl number
r	linear regression rate; radial coordinate
R°	universal gas constant
Re	Reynolds number
r_e	erosion contribution to r
S	fraction of the surface composed of binder material
T	temperature
t	time
T_f	adiabatic flame temperature
T_{fox}	temperature of oxidizer at the flame
T_i	initial temperature
T_s	surface temperature
$T_{s,ox}$	temperature of oxidizer at the surface
u	axial gas velocity
U_i, V_i	axial and radial components of diffusion velocity of chemical species i
v	radial component of velocity

w_b	burned web thickness
w_i	mass rate of production of species i by chemical reactions
x	axial distances from upstream end of motor
x_i	mole fraction of species i
Y	distance between two sample surfaces
Y_f	combustion zone thickness
Y_i	mass fraction of species i
y'_i	transition height
Y_{Ox}	oxidizer mass fraction for propellant
β	erosion factor defined in Eq. 7-5
γ	ratio of specific heats
ΔL	energy required to vaporize solid propellant
ΔL_b	heat of vaporization of binder
ΔL_{Ox}	heat of vaporization of oxidizer
ϵ	erosion function, r/r_o
λ	thermal conductivity
μ	coefficient of viscosity
ξ	$\rho_p r/G$
ρ	density
τ_w	shear stress at the wall
Φ_w	heat flux at the wall
χ	A_c/A_p
Script Letters	
\mathcal{D}_{ij}	binary diffusion coefficient for species pair i and j
m	molecular weight
γ	gas volume
Superscripts	
*	sonic conditions

Subscripts

c	chamber
e	erosive contribution
F	fuel
g	gas
h	head
i, j	chemical species
L	conditions at $X = L$
O, OX	oxidizer
o	upstream end of grain; nonerosive conditions
p	port; propellant
s	propellant; conditions at propellant surface
T	turbulent
t	throat; erosion threshold

Erosive Burning

1. Introduction

The phrase 'erosive burning of a propellant grain' refers to the sensitivity of the burning velocity to the gas-flow conditions parallel to the burning surface. Most modern grains have a central port through which the combustion gases flow. In this geometry the erosive effect is most pronounced in the early stages of motor combustion, when the ratio of the port cross-sectional area to the nozzle throat area is smallest. This erosive effect can lead to large variations in the performance of the rocket engine, since it prevents the grain from burning in parallel layers as is generally assumed for simplicity in performance calculations. The time evolution of the chamber pressure will thus exhibit discrepancies between theory and experiment. The differences, which consist chiefly of an increase of pressure for a short time after motor ignition, are due to a local increase of the burning velocity toward the downstream end of the grain. The flame front reaches the engine casing earlier than predicted and difficulties may appear with respect to the heat resistance of the material in the downstream part of the case. The duration of the pressure tail is then more or less increased, according to the nature of the propellant and the shape and dimensions of the grain and of the nozzle. The erosive effect could be diminished by increasing the initial port cross-sectional area, but the volumetric loading factor and the engine performance are thereby decreased. The ratio of the port cross-sectional area to the nozzle throat area lies between 2 and 5 in practical applications. Thus the erosive effect cannot be eliminated and must be taken into account, if one wishes to estimate accurately the performance and the structural resistance of the engine.

For this reason, many experimental studies have been carried out and several theories developed in order to determine the dependence of the burning velocity on the mass flow rate and on other flow characteristics in the central port. Although the theories sometimes agree very well with the various experimental results, they do not seem to be of an universal character. It has therefore been considered useful to devote a chapter to erosion phenomena. We do not claim to solve the problem but rather to summarize the state of knowledge on the question, for both the published experimental results and the theoretical models presently proposed.

2. Experimental Aspect (1) (2) (3) (4) (5) (6)

When the ratio A_p/A_t of the port cross-sectional area to the throat area of an engine is sufficiently small the pressure recordings resemble those of Fig. 7-1 for which $A_p/A_t \sim 2$; a pressure peak is observed at the beginning, due to an increase of burning velocity, and the flame front reaches the engine casing earlier than predicted at the nozzle end of the grain. The thrust tail duration is also longer than predicted by theory. The pressure diagrams at the upstream and downstream ends of the grain (p_0 and p_1) differ appreciably, at least at the beginning of the run, due to the flow velocity in the central port (dynamic pressure drop).

Under these conditions the burning velocity will depend upon many parameters such as the chamber pressure p_c , the gas velocity of the propellant surface, the temperature of the burnt gases, their composition, the nature of the propellant, its initial temperature, and the shape of the port cross-section. The experimental techniques must permit one to study the influence of each of these parameters on the burning velocity. Before summarizing the experimental results, we shall describe the methods presently in use, which may be divided into two broad categories, laboratory methods and engine measurement methods.

2.1. Laboratory Methods for Determining the Erosion Function

Three laboratory techniques have been developed, differing according to the gas generator used and the method for measuring the regression rate of the propellant surface exposed to the gas flow.

a) Method of Marklund and Lake. (7)

In the method of Marklund and Lake, a propellant sample is located in a hot gas stream generated by a main chamber. This main chamber is loaded with the same propellant as the one constituting the sample. The operating pressure and the gas flow rate in the test section can be varied by modifying the nozzle throat cross-section. The various specific arrangements employed are summarized in Figs. 7-2 and 7-3.

In the diagram at the bottom of Fig. 7-2 the sample is located in a tube connecting the chamber to the nozzle. It is assumed that the sample burning starts simultaneously with the main chamber burning and after a variable interval of time an X ray flash is triggered. The sample geometry is thus recorded on a film located very close to the sample. From this photograph and the initial dimensions of the grain one can compute the burnt web thickness and the burning velocity.

This method has been replaced by the one depicted on the top of Fig. 7-2. Small propellant pellets are attached to the end of a pressure transducer. As soon as the combustion is completed the transducer indicates the chamber pressure and the time interval between ignition of the chamber and indicated pressure rise gives the burning duration of a tablet of known thickness. By varying the tablet thickness one obtains different values of the burning velocity as a function of the gas flow rate in the channel and of the pressure.

In order to determine the erosion function under sonic stream conditions the above-mentioned apparatus and procedure have been slightly modified. The propellant sample is now located at the throat of the nozzle, where the stream reaches sonic velocity. These experiments and measurements are chiefly intended to study the possibility of using an engine with a constriction ratio $K_{II} = A_p/A_t$ close to unity, (A_p being the port cross-sectioned area at the downstream end of a tubular grain). This device is depicted schematically at the bottom of Fig. 7-3 and employs two pellets on opposite sides of the nozzle.

Larger samples have been used in which the pellets are replaced by propellant strips located in the stream, as indicated on the top of Fig. 7-3. For each strip two pressure transducers record the time when the flame front reaches the casing. From the strip thickness and the burning duration, as given by the pressure transducer recordings, one obtains the average burning velocity at two points of the sample. As in the preceding experiments one can double the number of measurements by placing two strips on opposite sides of the channel. The major disadvantage of these procedures is that many runs are necessary to determine the time development of the surface contour.

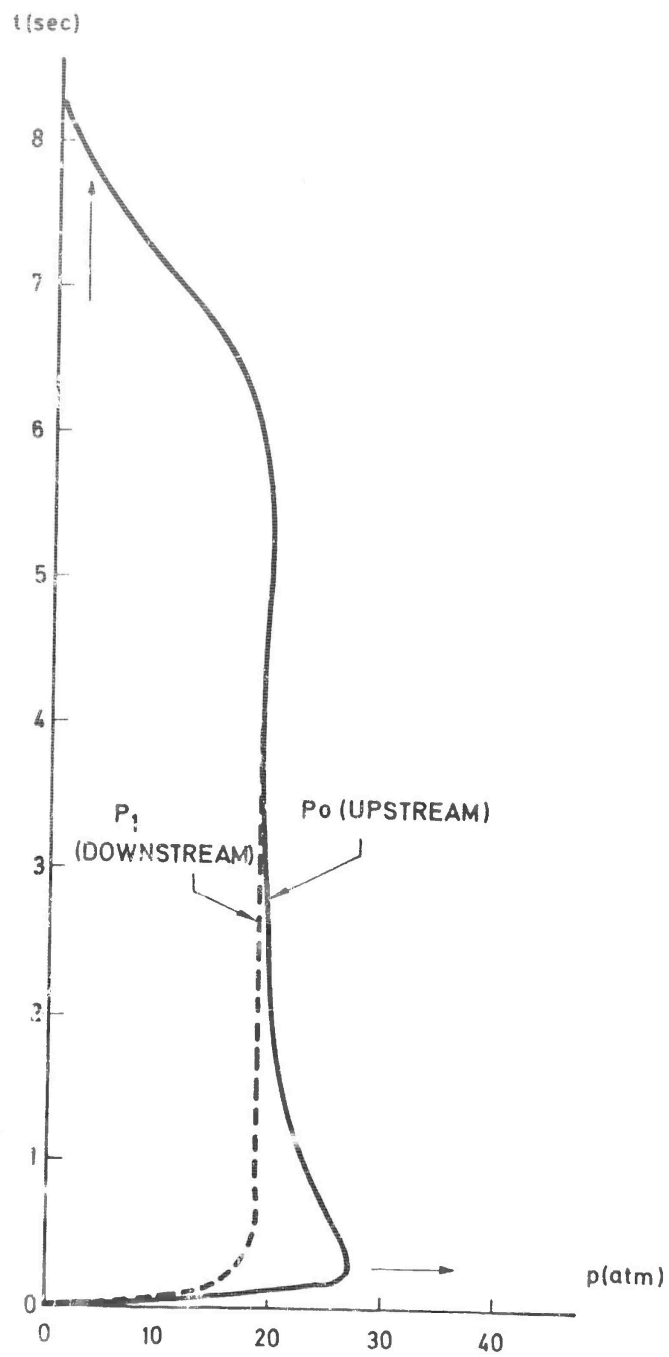
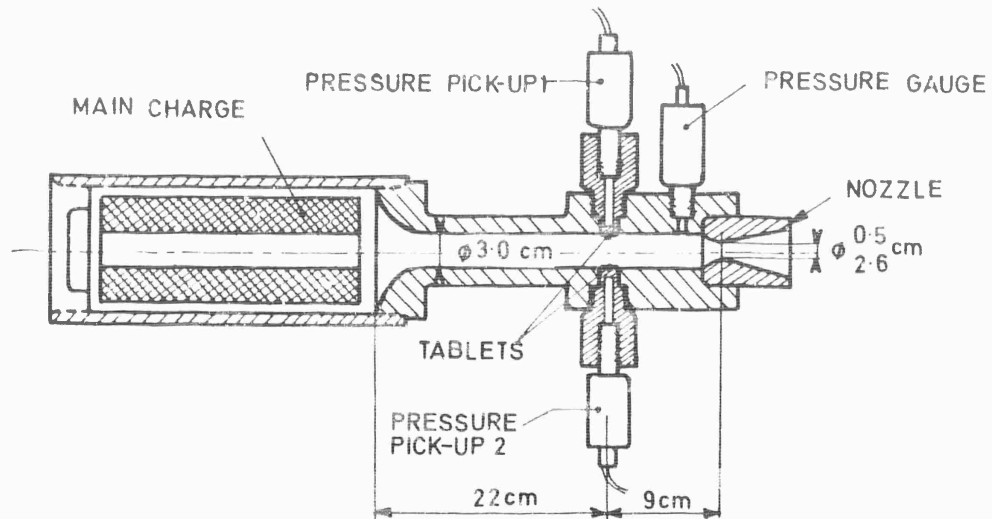
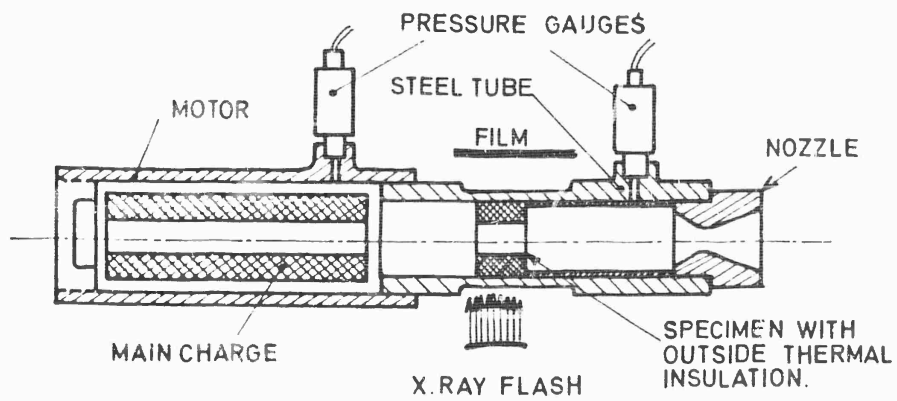


Fig. 7-1 Upstream and downstream pressure in the grain port.



Pellet method with pressure pick-up indication



The X ray flash method

Fig. 7-2 Marklund and Lake test equipment.

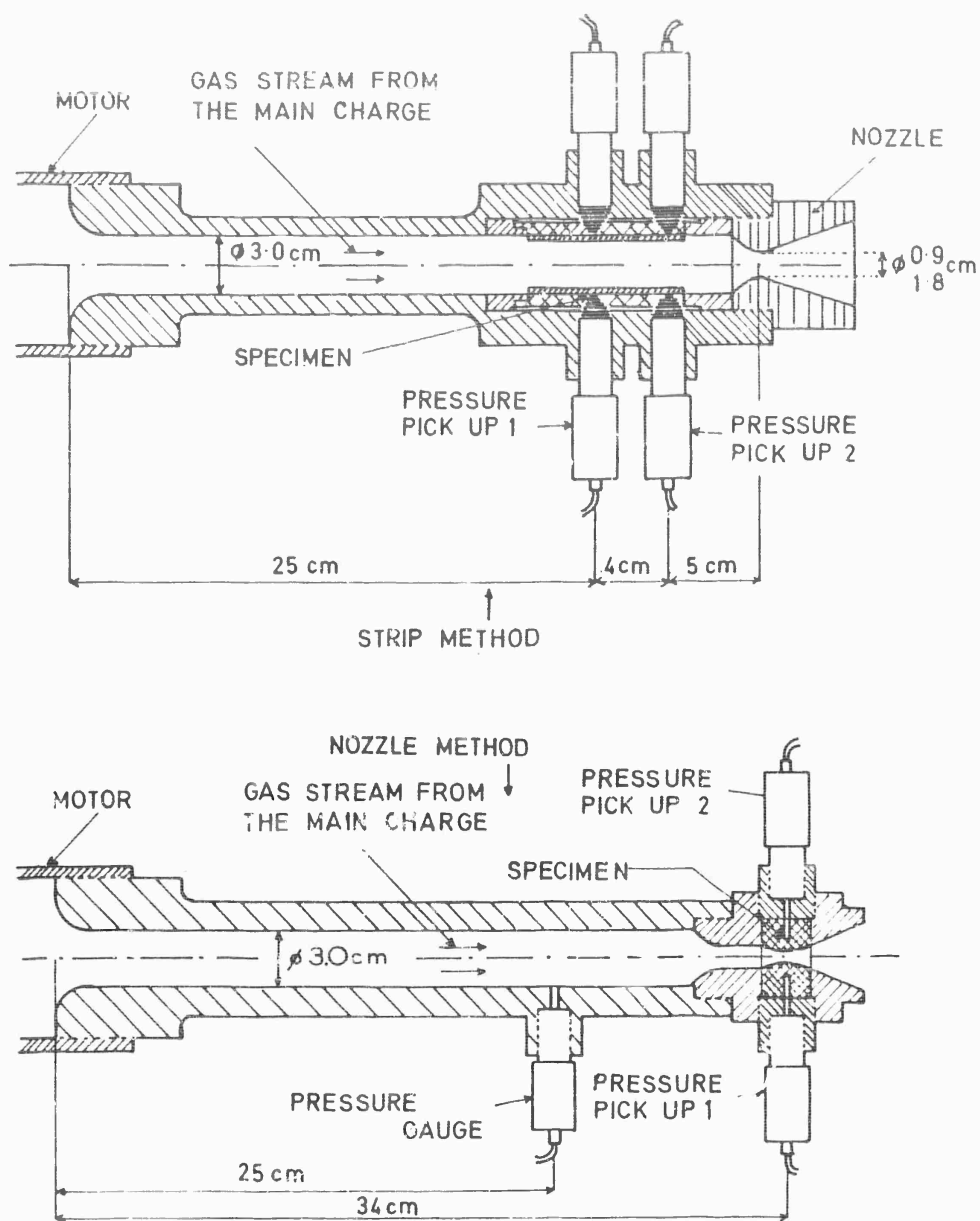


Fig. 7-3 Marklund and Lake test equipment.

b) Zucrow's Method (8)

The experimental apparatus used by Zucrow and his co-workers is similar in principle to Marklund's. A solid propellant rocket motor is used as a gas generator and the exhaust gases stream through a two dimensional test section (Fig. 7-4). Two opposite sides of this section are formed by transparent plexiglas windows. Propellant parallelepipeds are mounted on the metallic sides of the channel. A diverging section brings the flow to the test section and the gas velocity is approximately constant close to the samples. Surface contours are observed by means of motion picture photography.

The propellant constituting the sample is the same as the one in the gas generator and there are two samples, one on each side of the flow. However only one sample is photographed during the run (at 720 Fps). The film also records timing marks, which are synchronized with the other recordings made during the run (pressures, upstream and downstream of the sample).

The burning velocity is determined by measuring on the film the web thickness ΔY burnt during a time interval Δt (which is also read on the film). Let g be the enlargement factor due to the optical system. The burning velocity r is then given by :

$$r = g \cdot \frac{\Delta Y}{\Delta t} .$$

In order to determine the flow characteristics at the sample location, one can use the mass conservation equation relating the ratio between the port cross-sectional area A_p at the sample location and the nozzle throat area A_t , to the Mach number M at the sample location :

$$\frac{A_p}{A_t} = \frac{1}{M} \left[\frac{1 + \frac{\gamma-1}{2} M^2}{\frac{\gamma+1}{2}} \right]^{\frac{\gamma+1}{2(\gamma-1)}} ;$$

from the value of A_p/A_t one computes the Mach number M , and the gas velocity is then given by the definition of M :

$$u = M \sqrt{\gamma n R T_g} .$$

These experiments thus allow one to determine the burning velocity as a function of the pressure and the gas velocity u .

c) Nadaud's Method (9)

The apparatus used by Nadaud is shown in Figs. 7-5, 7-6 and 7-7. It is composed of a hybrid gas generator that uses a solid fuel contained in the combustion chamber and a liquid oxidizer, such as nitric acid. This device allows one to change the nature of the combustion gases by changing the nature of the fuel and of the oxidizer. The pressure and the velocity in the test section are adjusted for each run by choosing a suitable throat size. One can also vary the mixture ratio by modifying the length of the fuel grain. A preliminary study of the gas generator has defined the working conditions which enable one to cover, for a solid propellant, the useful operating regime of a rocket engine. The operating characteristics lead to determining the oxidizer mass flow rate \dot{m}_o , the average fuel consumption rate during the

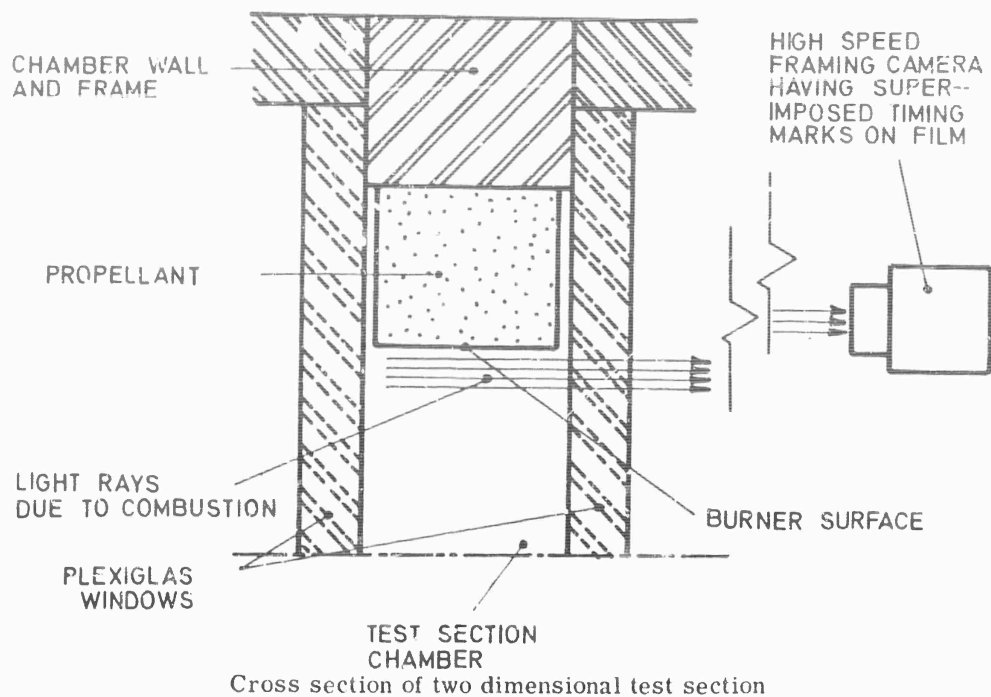


Fig. 7-4 Schematic diagram of photographic method for determining the burning rate of a solid propellant sample (Zucrow, Osborn and Murphy).

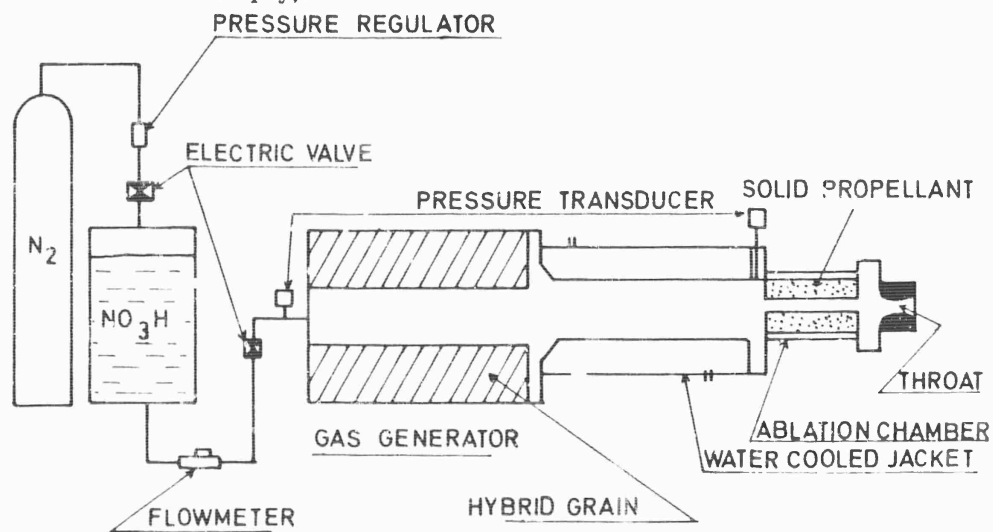


Fig. 7-5 ONERA - schematic set-up.

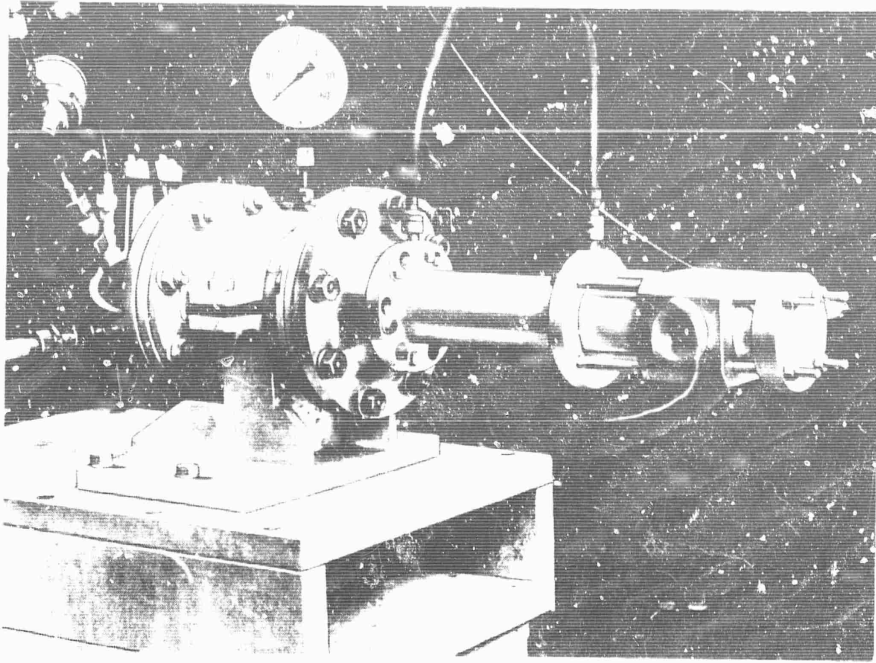


Fig. 7-6 General view of apparatus.

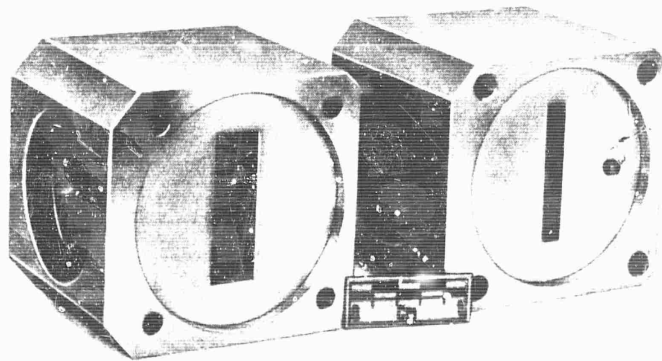


Fig. 7-7 Ablation chamber types.

run \dot{m}_p , the total flow rate $\dot{m}_g = \dot{m}_o + \dot{m}_p$ and the mixture ratio $MR = \dot{m}_p / \dot{m}_o$.

Two sample parallelepipeds are located in the test section, and two windows allow one to photograph the samples during the combustion. A diverging section, which is not shown in Fig. 7-5, channels the flow to the test section.

From the film recordings one can, at each instant of time, determine the burning velocity of each sample and the port area since the samples are glued to the viewing windows. These windows are made of quartz, and the surface in contact with the propellant has been roughened in order to increase the adherence of the propellant. This makes glueing easier and increases the accuracy of the data reduction, since the flame front thus appears more sharply on the film. The static pressure at the sample surface is also recorded.

At any time t , it is possible to compute, for a given position x on the sample, the regression rate $r(x, t)$:

$$r(x, t) = \frac{g}{2} \frac{\partial}{\partial t} [Y(x, t)].$$

in which $Y(x, t)$ is the distance between the two sample surfaces at the streamwise position x . The curve $Y(x, t)$ is plotted as a function of time for a given position x , then differentiated.

The specific mass flow rate ρu through the port area $A_p(x, t) = h Y(x, t)$, is given by the relation :

$$\dot{m}_p(t) + \dot{m}_o(t) + \rho_p \int_0^x h r(x, t) dx = (\rho u)_{x,t} h Y(x, t).$$

The area ratio $A_p(x, t)/A_t$ determines the Mach number $M(x, t)$, which in turn determines the average gas velocity $u(x, t)$, since the mean velocity of sound a is determined from the overall characteristic velocity.

In this apparatus the regression rate r can then be studied as a function of the static pressure in the test section, the specific mass flow rate, the nature of the combustion gases and the mixture ratio.

d) General Remarks on the Laboratory Methods

The method developed by Nadaud leads to reproducible results. By using two samples and special viewing windows, it allows one to determine the burning rate r with an accuracy of the order of 2 to 3%. It is possible to fit the $Y(x, t)$ vs t data to a simple mathematical formula and to differentiate this formula analytically in order to obtain a good approximation to the instantaneous sample regression rate. The hybrid gas generator can also easily be replaced by a solid propellant generator.

The chief disadvantage of the laboratory approaches, arises from the nature of the boundary layer, which differs in laboratory devices and in a real engine. In a real engine the boundary layer develops all along the grain (boundary layer with mass injection), whereas in a laboratory device it starts close to the sample, without any mass injection. The consequent difference in flow structure is likely to modify the energy and mass transfer processes between the surface and the gas. These processes control the erosive effect.

Another disadvantage arises from the method for measuring the burning velocity r_o in the absence of external flow parallel to the surface. It is impossible to determine the values of r and r_o simultaneously in the same laboratory experiment, and

it is necessary to obtain r_0 either from special engine runs or from bomb measurements. It is known that for certain propellants there is a difference between the burning velocity as measured in a strand burner and as measured in an engine. These and other uncertainties make it difficult to compare r and r_0 . Zucrow determines r_0 by using a small two-dimensional motor, with transparent windows, containing propellant which burns in a nonerosive environment. The value of r_0 is then obtained from a film recording of the run. Heron (17) burns two propellant samples simultaneously one under zero, the other under the chosen gas velocities. Sample burning was interrupted, giving a direct comparison between the burning rates, so that no independent no-flow condition regression rate measurement was required.

2.2. Direct Measurement of Erosive Burning Velocity on Rocket Motors

The three most important rocket motor techniques which have been developed for studying erosive burning are the burn interruption technique with subsequent measurement of the web thickness, the direct examination of the regression rate by an appropriate method (X rays, gamma rays) and the use of probes embedded in the grain.

a) Burn Interruption Technique (1)

In this method the combustion process is stopped abruptly after a certain duration of the run. The interruption is achieved by quickly opening of the upstream end of the rocket casing in order to produce a sudden expansion of the combustion gases. Explosive bolts unfasten the end-closure of a vertically mounted rocket, and in some experiments the propellant grain falls into a water quench tank. After each run the burnt web thickness is determined at different axial positions along the grain. Runs made with the same initial conditions, but interrupted after different durations, allow one to plot the burnt web thickness versus time, for each axial location. Differentiating this curve, one obtains the burning velocity $r(x, t)$, and the burning velocity without erosion is determined at the upstream end of the grain, $x = 0$ ($r_0 = r(0, t)$). In order to determine the erosion function r/r_0 , a large number of runs is necessary when using this method.

A static pressure measurement is also made upstream and downstream of the grain. The local characteristic flow parameters (static pressure, velocity, specific mass flow rate, temperature, Mach number ...) are often difficult to determine very accurately because of their coupling with r and also because of the heterogeneity of the flow. This determination is usually made by means of a one-dimensional, simplified theory. The burnt propellant mass flow rate at time t and axial position x is given by the relation :

$$\dot{m}_b(x, t) = \rho_p \int_0^x r(x, t) P(x, t) dx.$$

where $P(x, t)$ is the function of x representing at time t the perimeter of a cross section of the central port, whose area is $A_p(x, t)$. This relation can be checked by weighing the grain, and it can be used to determine the specific mass flow rate for a given time and position :

$$G(x, t) = \rho u = \frac{\dot{m}_b(x, t)}{A_p(x, t)}.$$

The approach is sometimes simplified by introducing the total mass flow rate :

$$\dot{m}_b(L, t) = \frac{p_c A_t}{c^*}$$

and then using the approximation:

$$G(x, t) = \frac{A_t p_c}{c^*} \frac{1}{A_p(x, t)} \frac{x}{L}$$

where L is the length of the grain.

Near the exit section of the grain the Mach number and the static pressure are obtained from the one-dimensional flow relations:

$$M(L, t) = f(A_p(L, t) / A_t^*),$$

and $p(L, t)$ is obtained from $M(L, t)$.

At a given position x one introduces a fictitious throat area A_t^* such that:

$$\frac{A_t^*}{A_t} = \frac{\dot{m}_b(x, t)}{\dot{m}_b(L, t)},$$

so that

$$M(x, t) = f(A_p(x, t) / A_t^*)$$

and $p(x, t)$ is obtained from $M(x, t)$.

The gas velocity $u(x, t)$ is obtained from $M(x, t)$ by using an average sound velocity, which is computed from the measurement of the characteristic velocity c^* .

The operating pressure can be varied by changing the ratio $K_I = A_b/A_t$ of the burning area to the throat area.

b) Radiographic and Cineradiographic Techniques (10) (11)

In this case a two-dimensional motor is used, with two rectangular propellant grains each covered with an inhibitor on three sides. The geometry simulates the cross section of a normal motor, but in a two dimensional chamber the port cross sectional area increases less rapidly than in the usual configuration with a central perforation. A concentrated beam of X rays is directed toward the motor and the image of the propellant grain is produced on a phosphorescent screen which is then photographed. The dimensions of the grain at each moment is obtained from these photographs. The advantage of this method is that it yields an instantaneous value of the burning velocity. The number of runs is reduced in comparison with the number required in method (a), and the propellant combustion is not influenced.

A two dimensional chamber with viewing windows can also be used to determine the erosion function, but in this case it is often difficult to achieve proper working conditions.

Another method consists in using radioactive element (such as cobalt 60) which emits gamma rays. The radiation intensity through the motor is determined with a scintillation counter. The intensity I is related to the absorbing medium thickness by a law of the form $I = I_0 \exp(-\mu x)$ where μ is the linear absorption coefficient. By measuring I one can determine the evolution of x with time and the burning velocity. A grain with a circular cross-section port gives the law:

$$r = \frac{\exp(\mu x)}{2 \mu I_0} \cdot \frac{dI}{dt}$$

The data reduction methods in paragraph (b) are identical to the ones in paragraph (a), at least in so far as the characteristic flow parameters are concerned.

c) Probe Techniques (12) (13) (14)

In this method probes are buried in the grain to detect the passing of the flame front. The most usual probes are of the ionization type with two electrical leads, connected to a measurement circuit which incorporates a DM 160 type gas triode. At rest the film recordings of a luminous spot show the normal operation of a gas triode. A polarisation voltage of 3 volts brings the spot to extinction. The small dimensions of these tubes (diameter 6 mm, length 20 mm) allow one to build very compact units. The recordings are made on a simple strip film camera. Fig. 7-8 shows two recordings used at ONERA; they yield a total of 100 measurement points. The film recording shows a series of straight lines which are interrupted when the flame front passes the corresponding probes. From the positions of the probes and the times recorded, one can determine the evolution with time of the burnt web thickness.

It is always difficult to assure good insulation between the electric leads.

The measurement of the distance between the probes or between one probe and the initial grain surface is made by means of a micro-comparator with an accuracy of 1 micron. In view of the accuracy of the time measurements for a distance between the probes of the order of 2 mm, the distance measurement leads to an accuracy on the burning velocity of about 2%.

Fig. 7-9 shows how the probes are set into a cross section of the grain. This side of the cross section is then glued to the other side of the grain.

In a grain with a star-shaped port the probes are placed along star points or star recesses in order to study the influence of the geometry, as indicated on Fig. 7-10. The number and locations of the test stations are chosen in such a way that a particular aspect of the phenomena can be studied. For example the study of negative erosion is achieved by placing probes in the upstream part of the grain.

Fig. 7-11 is a photograph of a grain equipped with probes. The various measurement sections are marked with tape which protects the electrical leads. Instrumented grains are mounted in the motor as shown in Fig. 7-12 for a short grain.

Other probe types have been used, such as thermocouples embedded in the grain or variable conductivity probes which melt when the flame front passes them. It seems however that the type described above, with two closely spaced conductors allowing the current to flow when the flame front passes, gives the best results.

2.3. Indirect Methods on Rocket Motors (15)

The pressure evolution curves inside a rocket motor give indications of erosive effects. In particular one observes a sharp pressure peak at the upstream end of the grain. It is reasonable to ask whether one can extract the erosion function from this pressure distribution curve, which is sensitive to erosion. To study this question, one must first specify the form of the erosion law which has to be introduced, then adjust the parameters appearing in it to bring the computed pressure distribution curves into agreement with the experiment curve. A law of the form :

$$r = r_0(p) \cdot \epsilon(G, p)$$

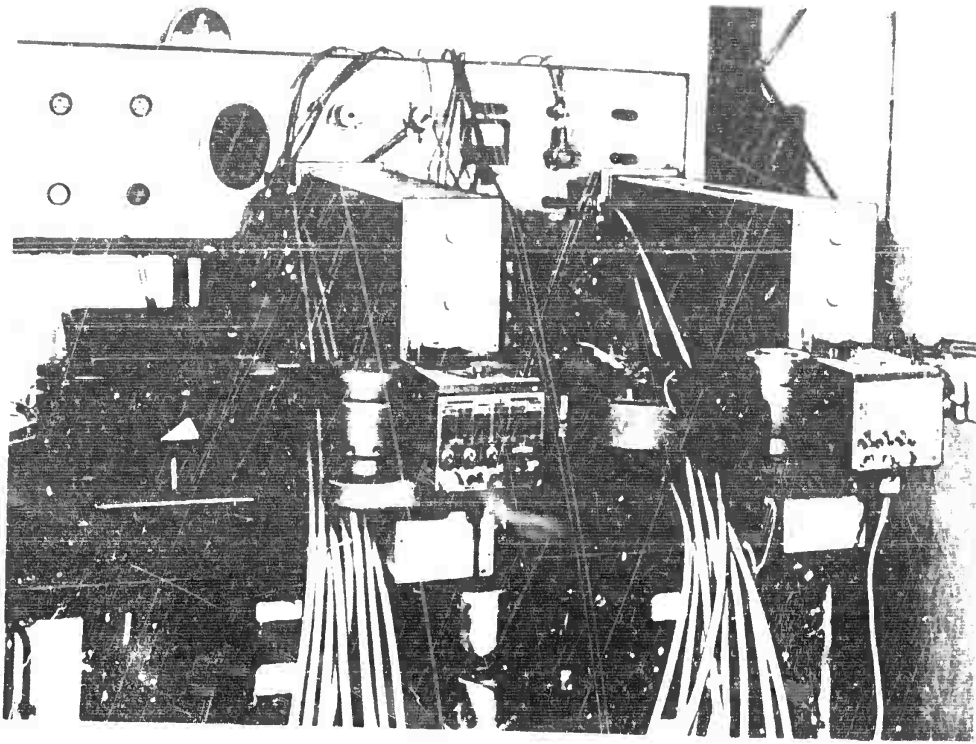


Fig. 7-8 Recorders.

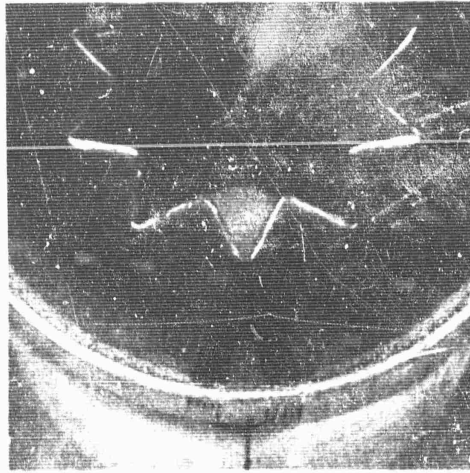
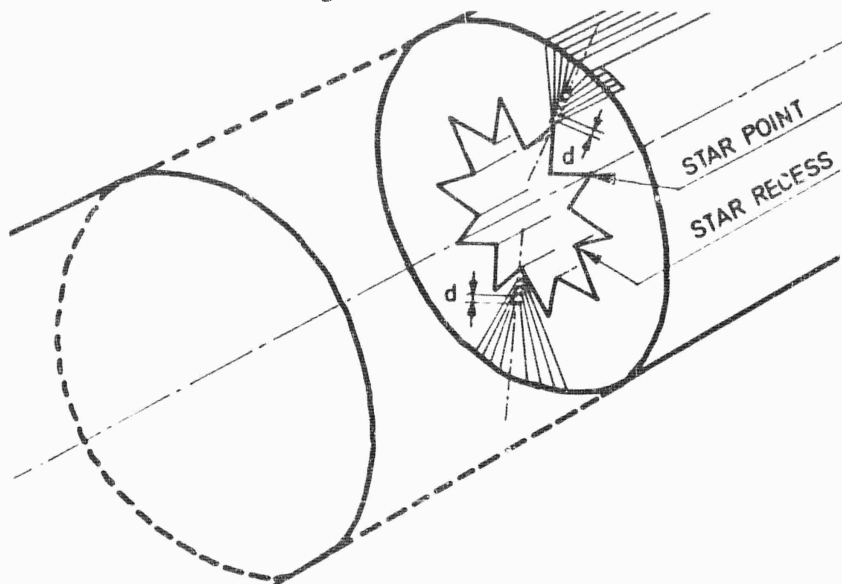
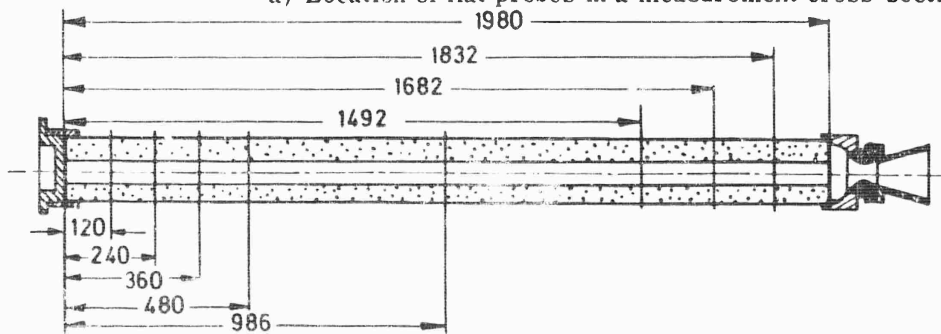


Fig. 7-9 Flat Probes.



a) Location of flat probes in a measurement cross-section.



b) Distribution of measurement cross-section.

Fig. 7-10 Grain with star shaped cross-section.

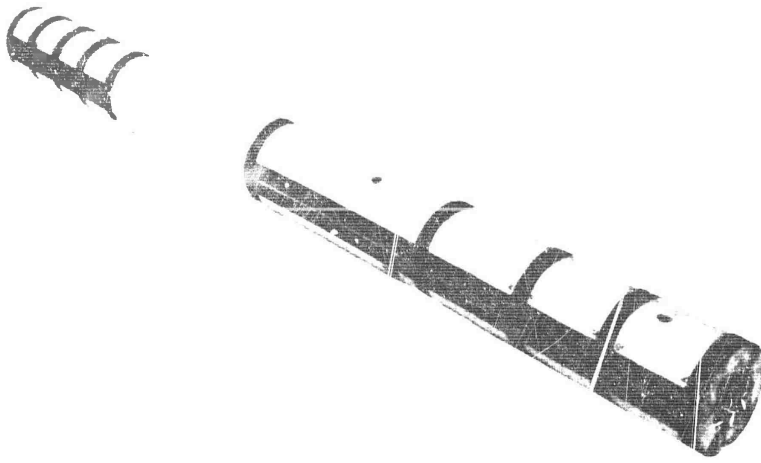


Fig. 7-11 Star shaped port grain with probes.

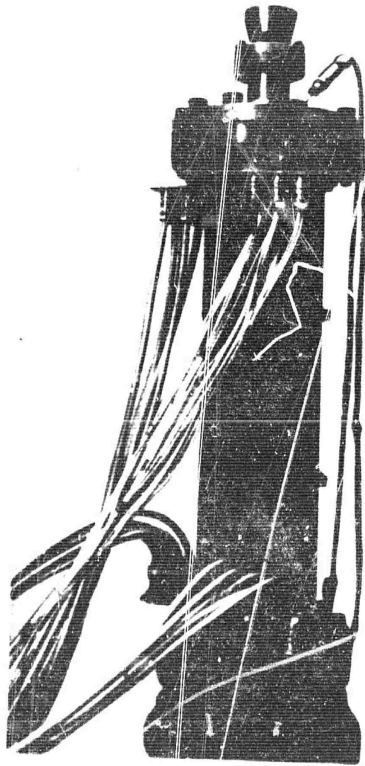


Fig. 7-12 Rocket engine with tubular port grain, before firing.

TECHNIQUES		OPERATING CONDITIONS	ACCURACY	REMARKS
SAMPLE METHODS				
X ray		semi-realistic	Poor	Average burning rates or instantaneous burning rates
Photographic		semi-realistic	Good	Instantaneous burning rates
Probes		semi-realistic	Poor	Average burning rates
Pressure Pickup		semi-realistic	Good	Average burning rates
DIRECT MOTOR FIRING METHODS				
Interrupted burning		Realistic	Fair	Average burning rates numerous firings
Collimated radioactive beam		Realistic	Unknown	Instantaneous burning rates
PROBES	Thermocouples Conductivity Ionisation	Realistic	Poor Fair Good	Average burning rates
INDIRECT MOTOR FIRING METHODS				
Analysis of the pressure time record		Realistic	Poor	Instantaneous

Table 7-1 Comparison of Experimental Techniques.

DISTANCE FROM
HEAD END(in)

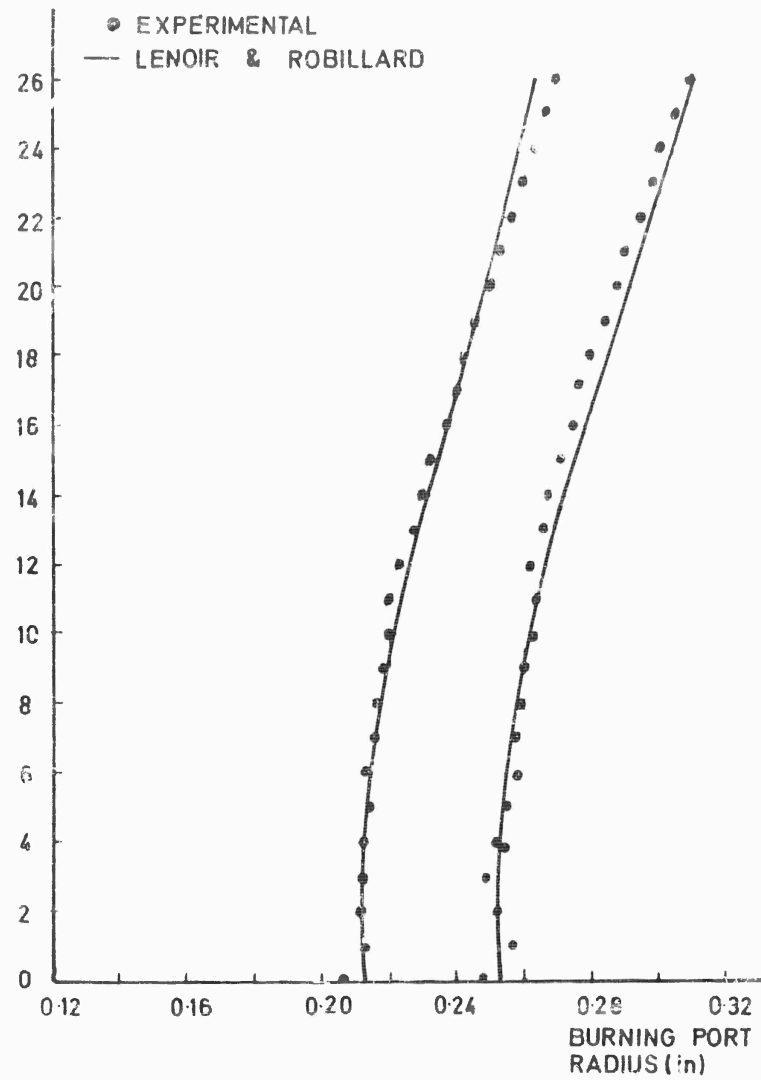


Fig. 7-13 Lenoir and Robillard's theory; comparison with experiment.

of the burning velocity with respect to the no-flow burning velocity; this "negative erosion" phenomenon has been observed with homogeneous and heterogeneous solid propellants. In the vicinity of the nozzle the gas velocity in the central channel and the cross-sectional area increase simultaneously, giving evidence for an increasing influence of erosion phenomena. In the downstream part of the motor the central port is approximately conical in shape. From the evolution of the grain geometry, one can thus distinguish two regions: the negative erosion region [which for certain propellants, can completely disappear or lead to cylindrical profiles ($r = r_0$)] and the normal erosion region in which the cross sectional area increases with the axial distance. These two regions are separated by an erosion threshold boundary, defined to be the position where the measured burning velocity is equal to the no-flow burning velocity. Due to the erosion phenomena, the grain profile becomes time dependent, but the time evolution is controlled by numerous parameters (in particular the grain geometry), the grain profile will not be the same in an axial plane passing through a star point or a star recess (see Fig. 7-14). The effect of erosion on a star recess in the presence of a gas flow, is much stronger than the effect on a star point.

The evolution of the burnt web thickness w_b is shown in Fig. 7-14 as a function of the downstream distance x for various burning times within the first second of the run. One can notice a pronounced erosive effect on a star recess. At the beginning of the run there is no negative erosion at a star recess; it appears and becomes marked only after 0.5 sec (Fig. 7-14a). On a star point the negative erosion appears as soon as the run starts (Fig. 7-14b). The smaller burnt web thickness at the star point than at the star recess after 0.25 sec may be due to an unsymmetrical ignition of the grain. The grain length over which there is negative erosion decreases as the burning time increases and is always longer at a star point than at a star recess. This figure shows how complex the phenomena with a star shaped grain are and this complexity makes it difficult to give a general erosion law. From known values of burnt web thicknesses at star points and star recesses, we have represented on Fig. 7-15 the evolution of a cross section of the central port during the first second of a run (which is when the erosion phenomena are most important).

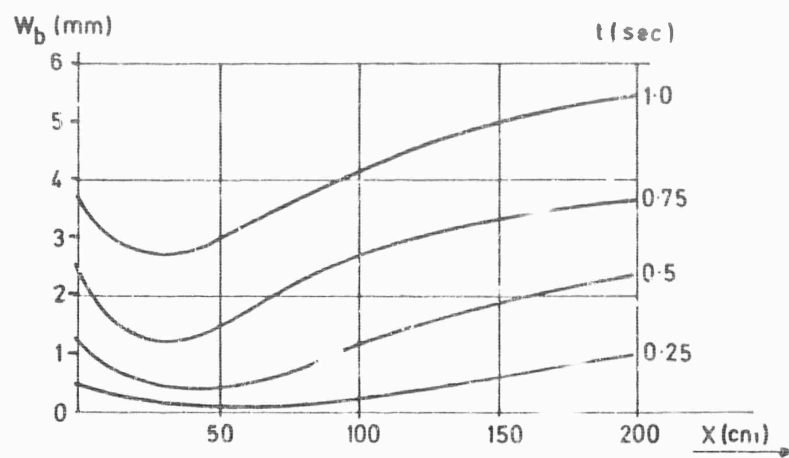
The burnt web thickness is plotted versus time on Fig. 7-16 for positions $x = 0$, $x = 50$, 100, 150 and 200 cm. The local instantaneous burning velocity $r(x, t)$ is computed from these curves, the burning velocity r_0 being determined at $x = 0$.

Before studying the various laws which have been proposed to represent the burning velocity, we shall discuss the importance of the various parameters.

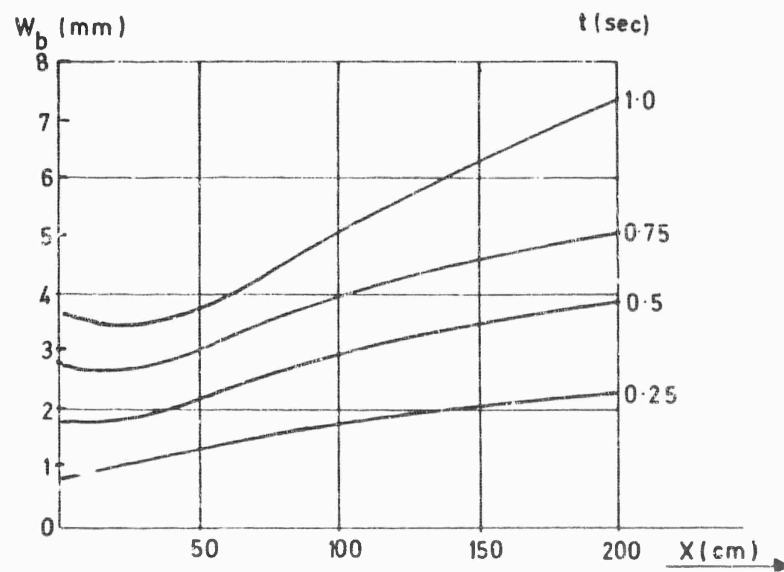
2.4.2. Influence of the Various Parameters - The burning velocity we are considering here is a local value. The geometry and the burning velocity depend, as seen above, upon the location on the burning surface and on time. The time variable can be eliminated and replaced by local properties of the fluid on the surface. Thus r will depend upon numerous parameters which we shall classify as follows:

Gas-flow - Gas flow is characterized by the pressure p , the gas velocity u , the gas temperature T_g , its composition (expressed by its molar mass) and its nature (one or two phases). In the boundary layer regime, one would like to know local values at the edge of the boundary layer but the measurements are difficult to perform in a hot gas stream and only average values are available.

Propellant - Erosion phenomena can be different for homogeneous or heterogeneous propellants since the boundary layer structure can change as well as the distribution of the flames on the surface. The initial propellant temperature T_1 can also modify the erosion function. The grain geometry and, in particular the shape of the central port cross-section, can also be of some importance.



a) Star recess



b) Star point

Fig. 7-14 Evolution of longitudinal port profile.

SYMMETRY AXIS ALONG
A STAR POINT.

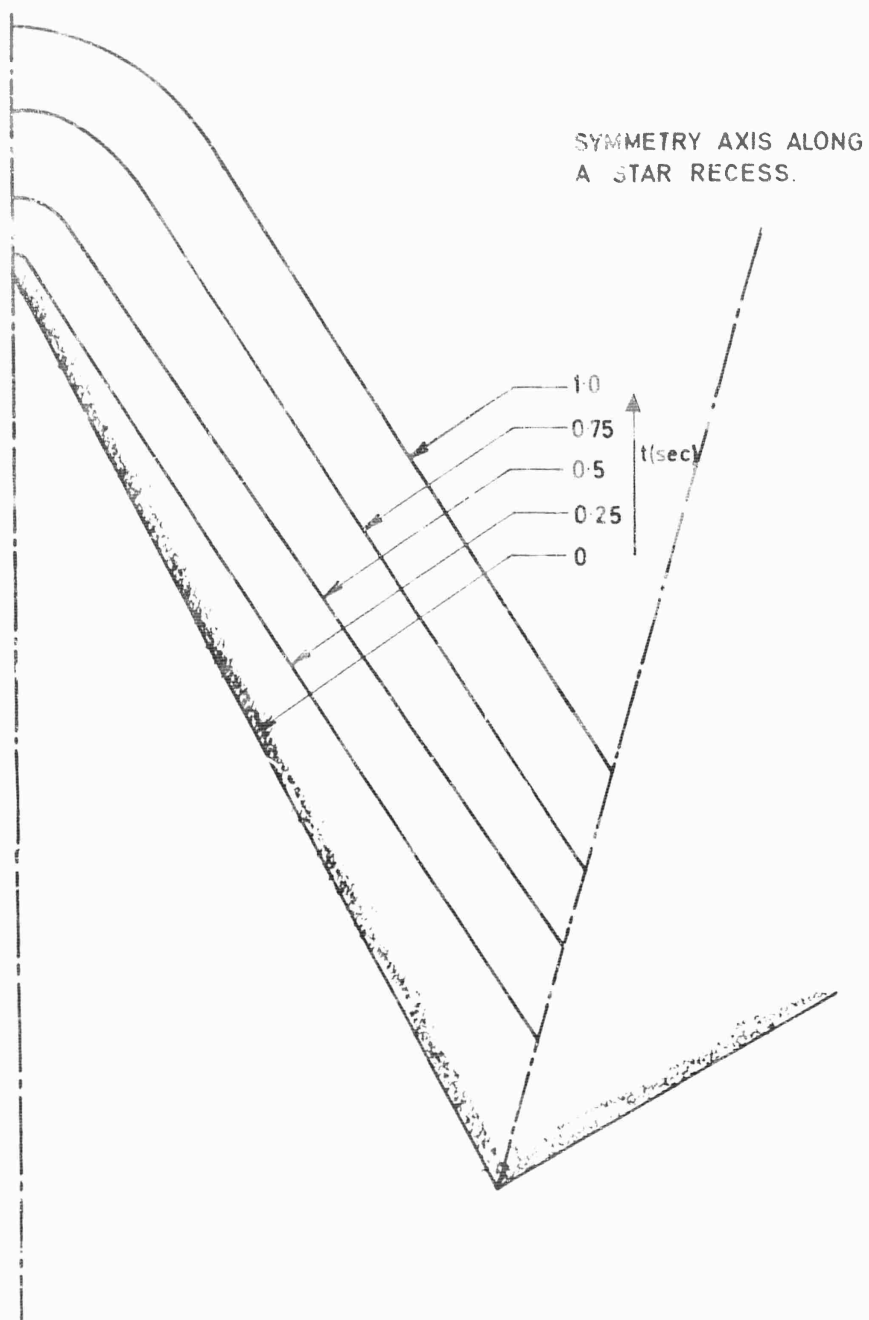


Fig. 7-15 Evolution with time of the burning surface at $x = 100$ cm.

aa*

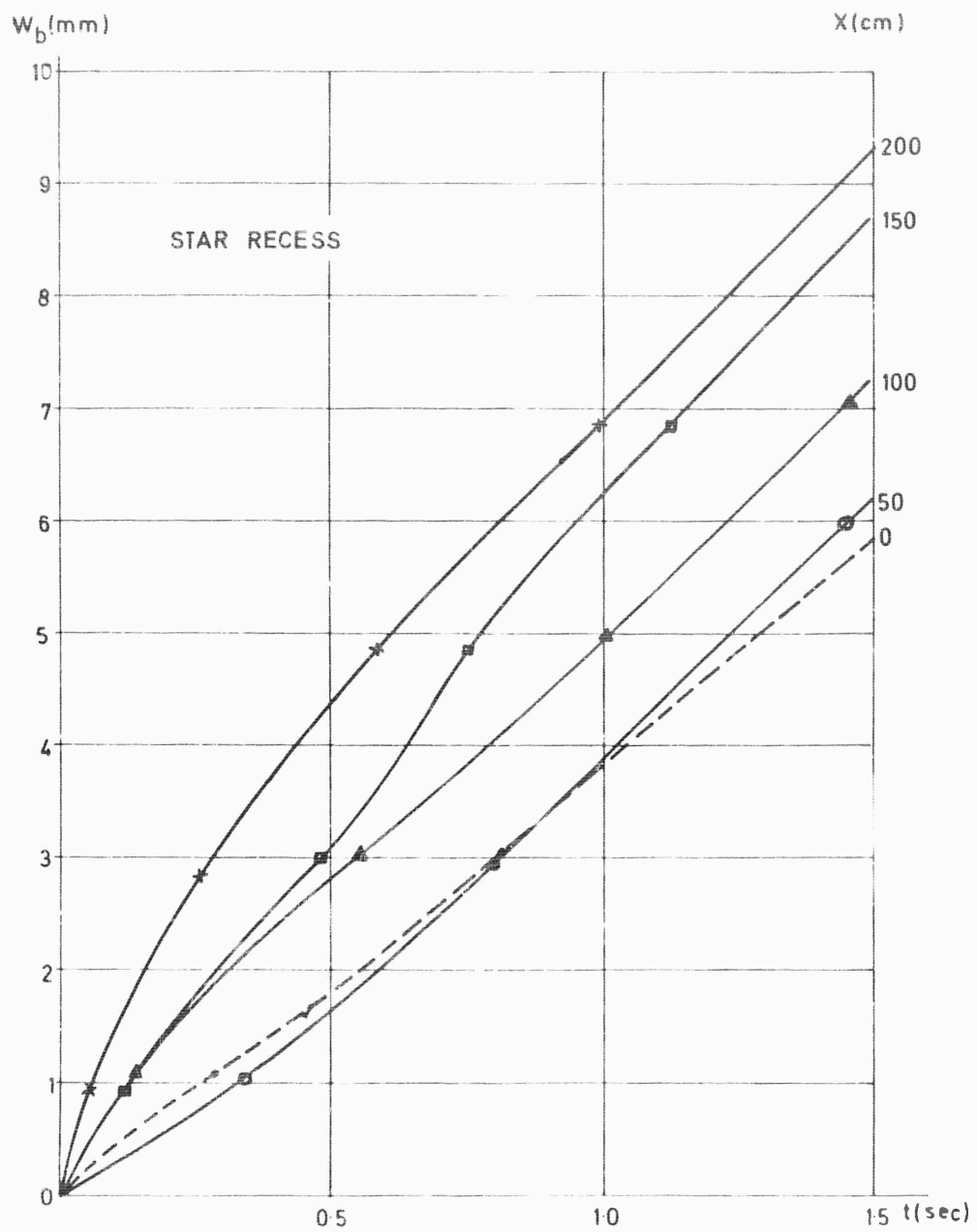


Fig. 7-16 W_b versus t , at different stations; tubular port grain.

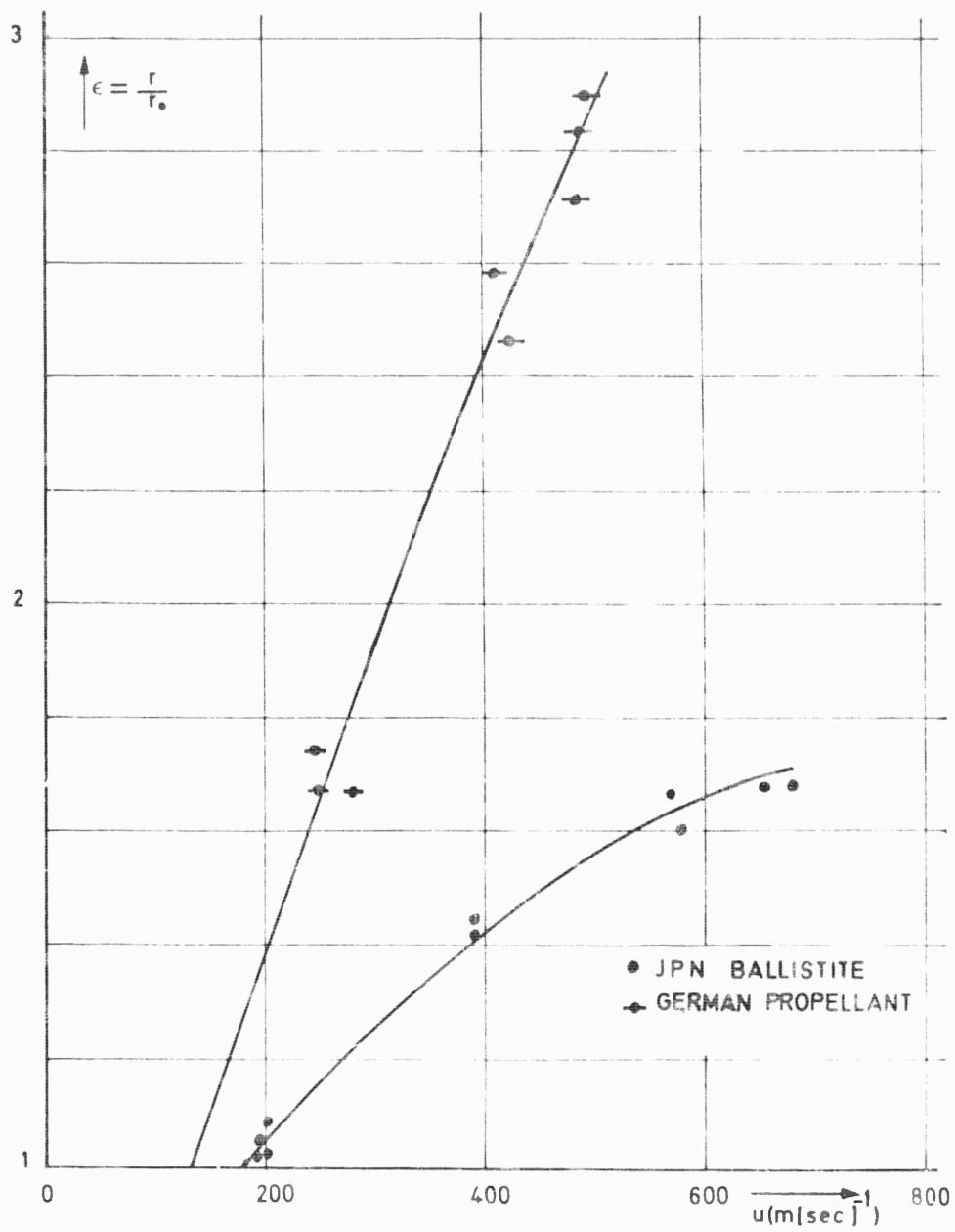


Fig. 7-17 Wimpress' experiments; erosion factor ϵ versus gas velocity u .

Operating Conditions - The operating conditions of the motor also influence the erosion function. Spinning the motor for instance modifies the force field close to the burning surface and can, for a sufficiently high rotation speed and when the combustion gases contain condensed phases, affect the erosion function. Transient regimes (ignition, combustion instabilities and extinction) can also exhibit erosion laws which differ from steady state laws.

a) **Influence of the Gas-flow** - The gas stream velocity parallel to the burning surface plays a predominant role. The larger u is, the larger the erosive effect will be, at least above a threshold velocity under which, for certain propellants, the erosion is either zero or negative.

The threshold velocity u_t has been observed by many experimenters and its existence is beyond doubt, although it was initially attributed more to errors caused by experimental difficulties in measuring small erosive effects than to negative erosive phenomena. This threshold velocity depends upon numerous parameters and from all available experimental results, one can say that the larger r_0 is, the larger the threshold velocity will be. Composite propellants of the A P-Polyurethane type show a threshold velocity which depends upon the pressure and the nature of the binder. The effect of pressure upon u_t is not well defined. Krciller (10), for instance finds, on a motor using a composite-modified double-base, aluminized propellant, that the threshold velocity decreases slightly when the pressure increases; Zucrow (8) reaches the same conclusion after studying a (polyurethane, aluminum, ammonium perchlorate) propellant sample and gives the following values :

u_t (ft/sec)	p_c (psia)
2060	400
1940	500
1700	600

On the other hand, Larue's experiments on rocket motors indicate a higher threshold velocity u_t at low pressures than at high pressure for a Plastisol type propellant (12).

Figure 7-17 stresses the influence of the gas velocity on the erosion function. It shows the variation of the erosion function $\epsilon = r/r_0$ with the gas velocity u for a homogeneous JPN propellant. It is seen that the normal burning velocity can be tripled when the gas velocity u reaches 500 m/s (1500 ft/sec.). This velocity effect is therefore far from negligible. Heron's experiments on colloidal propellants lead to the same conclusions (17). The effect is however, less pronounced than above; for the same velocity the burning rate is increased by about 60%. Propellants with a low burning velocity r_0 lead to higher erosive effects (17). These results are similar to the ones given in Fig. 7-18, showing the negative erosion zone, the erosion threshold and the positive erosion zone. For homogeneous propellants, the erosion function increases as the normal burning velocity decreases. When the results are represented on a diagram, the velocity u is sometimes replaced by the local Mach number M . This representation is equivalent to the first one, since an average sound velocity in the central port is assumed (see in particular Heron's experiments (17)).

The local static pressure in the gas affects the rate of heat transfer to the grain and modifies the erosion function. The results of various experimenters are in qualitative but not quantitative agreement. Figure 7-19 refers to a heterogeneous propellant using ammonium perchlorate as an oxidizer and polyvinyl chloride as a binder. It shows the influence of pressure, which is greatest when the gas velocity in the central port is high. Similar results have been obtained by Marklund and Lake with two propellants, propellant A (polyester-ammonium perchlorate,

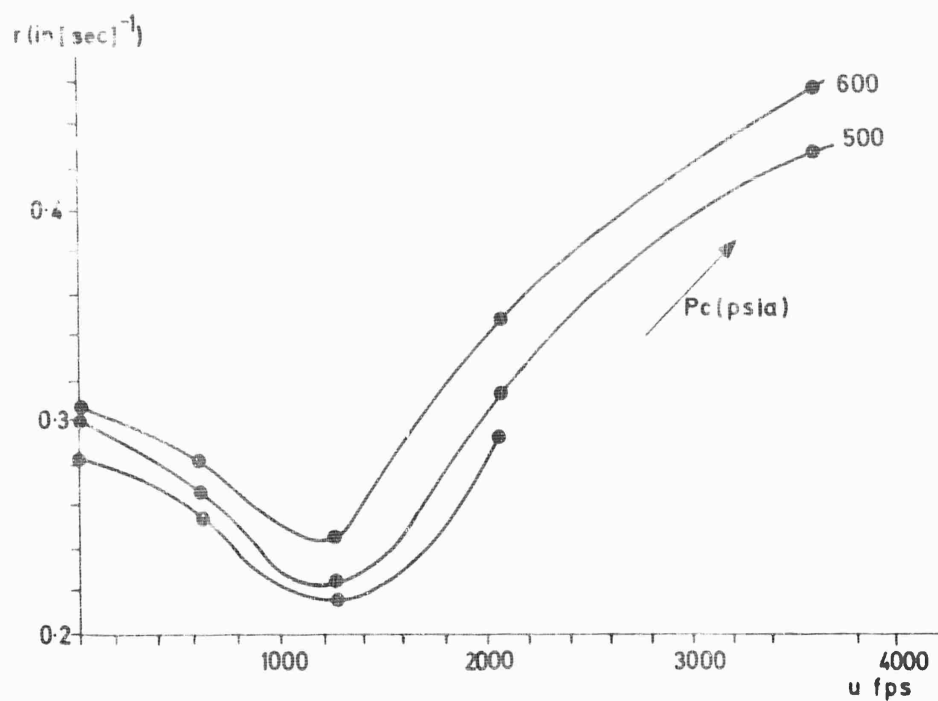


Fig. 7-18 Zucrow's experiments; effect of combustion gas velocity and combustion pressure on the total burning rate r .

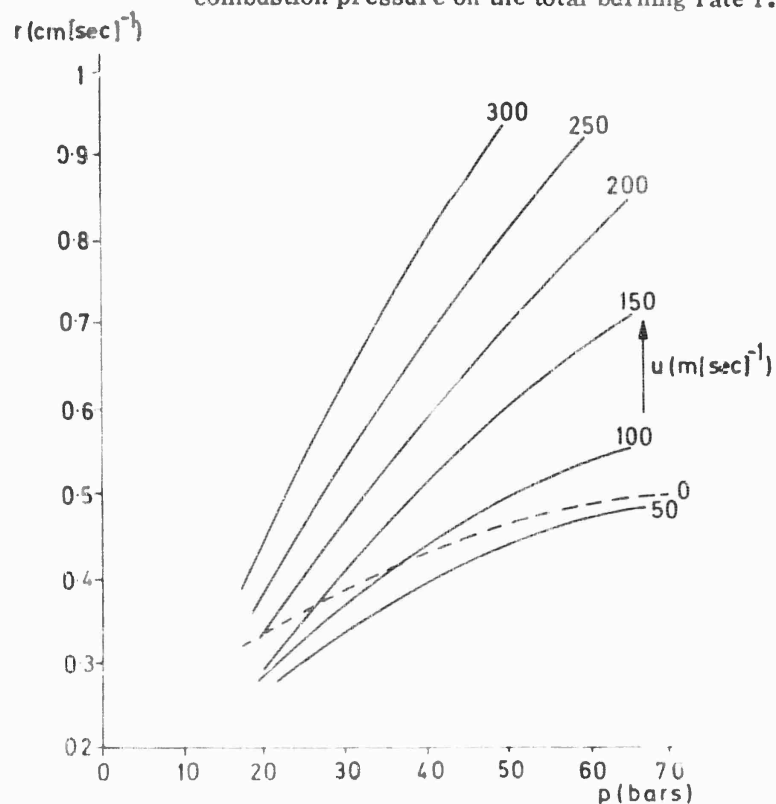


Fig. 7-19 ONERA experiments. Burning rate r versus pressure for several values of u .

35-65 weight percentages) and propellant B (polysulfide epoxy - ammonium perchlorate, 25-75 weight percentages). Figures 7-20a and 7-20b show the results, which indicated a greater sensitivity to pressure as the gas velocity in the central port increases. According to Zucrow, this sensitivity to pressure is not as pronounced, for polyurethane-ammonium perchlorate - aluminum type propellants (Fig. 7-21). It is also less marked for certain propellants in the plateau domain.

The combined effect of pressure and velocity can be introduced into the erosion function by using the mass flux $G = \dot{m}(x)/A_p$, where $\dot{m}(x)$ is the flow rate of the combustion gases at position x and A_p the port cross sectional area. A representative curve is shown in Fig. 7-22 for a (polyurethane - aluminum - ammonium perchlorate) composite propellant. In this diagram the erosion function ϵ is given as a function of the mass flux $\dot{m}/A_p = \rho u$ and shows a negative erosion domain, an erosion-threshold value of the mass flux, then at higher flow rates a linear variation of ϵ with $G = \rho u$. The G -representation is often used, and it includes effects of the pressure and of the velocity, since $G = \rho u = \gamma p u/a^2$, where a is an average value of the sound velocity in the central port. The product $M p$, where M is the Mach number, is sometimes substituted for G ; both expressions are equivalent when one employs an assumed value of the sound velocity.

Green (1) characterized the flow by introducing the parameter G/G^* , where G^* is the critical mass flux at the section considered. Since G^* is proportional to the pressure in the chamber, G/G^* is related to the velocity parameter rather than to the mass flux. The critical mass flux is defined as the mass flux attained at Mach number unity in a steady, frictionless, adiabatic, ideal gas flow in a constant-area channel with gas injection normal to the flow direction. In using non-dimensional parameters, u is sometimes divided by u^* , the sonic speed at the throat of a fictitious nozzle of throat area A_t^* , of throat total pressure $p + \rho u^2$, and of nozzle mass flow rate $\dot{m}(x)$. By definition $G = \dot{m}(x)/A_p$ and $G^* = \dot{m}(x)/A_t$, so that G/G^* can be replaced by:

$$\frac{G}{G^*} = \frac{A_t^*}{A_p} = \frac{A_t^*}{A_t} \frac{A_t}{A_p} \approx \frac{\dot{m}(x)}{\dot{m}(L)} \frac{A_t}{A_p} \approx \frac{x}{L} \frac{A_t}{A_p}.$$

This relation is approximately equivalent to the Blatz relation (30) which makes use of the mass flux at the exit section of the grain G_L , since :

$$\frac{G}{G_L} \cdot \frac{A_t}{A_p} \approx \frac{\dot{m}(x)}{\dot{m}(L)} \frac{A_t}{A_p} \approx \frac{x}{L} \frac{A_t}{A_p}.$$

Figure 7-23 shows the variation of the erosion function ϵ with Green's parameter G/G^* . The correlation is practically linear above threshold, except for four data points attributed to unstable burning. The parameter G/G^* can also be expressed as a function of the local Mach number M :

$$\frac{G}{G^*} = \frac{M}{1 + \gamma M^2} \left[2(\gamma + 1) \left(1 + \frac{\gamma - 1}{2} M^2 \right) \right]^{\frac{1}{2}}.$$

The composition of the combustion gases has little influence on the erosion function. Nadaud has shown on composite propellant samples that the mixture ratio of the gas generator does not appreciably change the value of the erosion function.

Although no systematic experiments have been carried out to study the influence of alumina in the flow, it is possible that this two-phase flow influences the burning

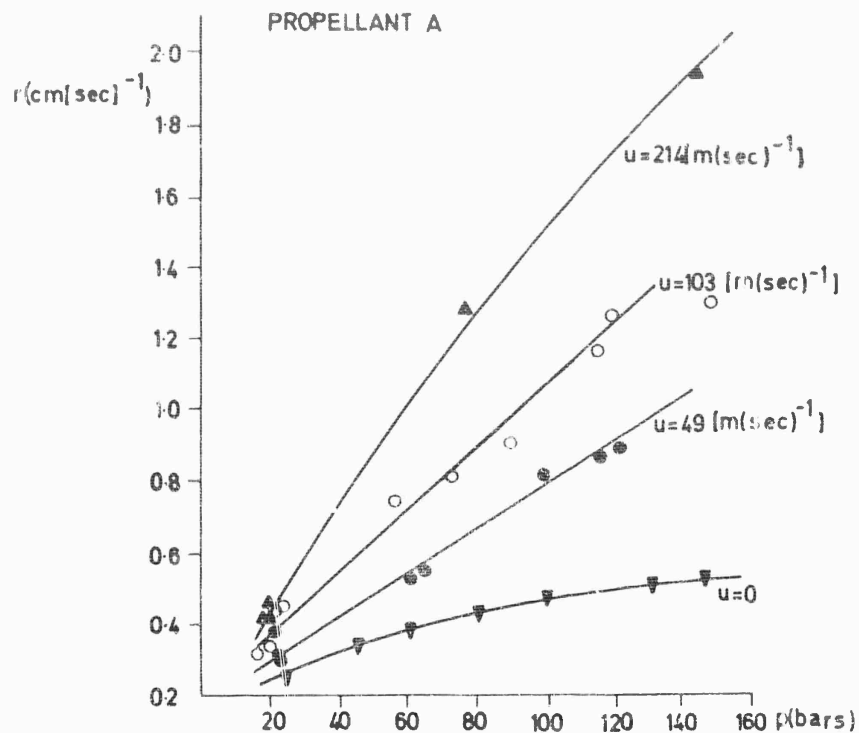


Fig. 7-20a Lake and Marklund's experiment; influence of pressure and gas flow velocity on combustion rate.

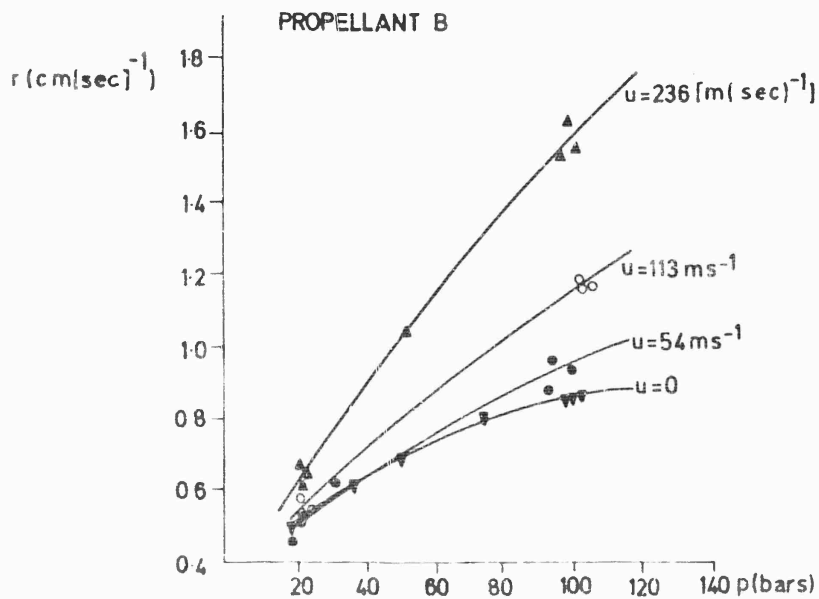


Fig. 7-20b Lake and Marklund's experiment; influence of pressure and gas flow velocity on combustion rate.

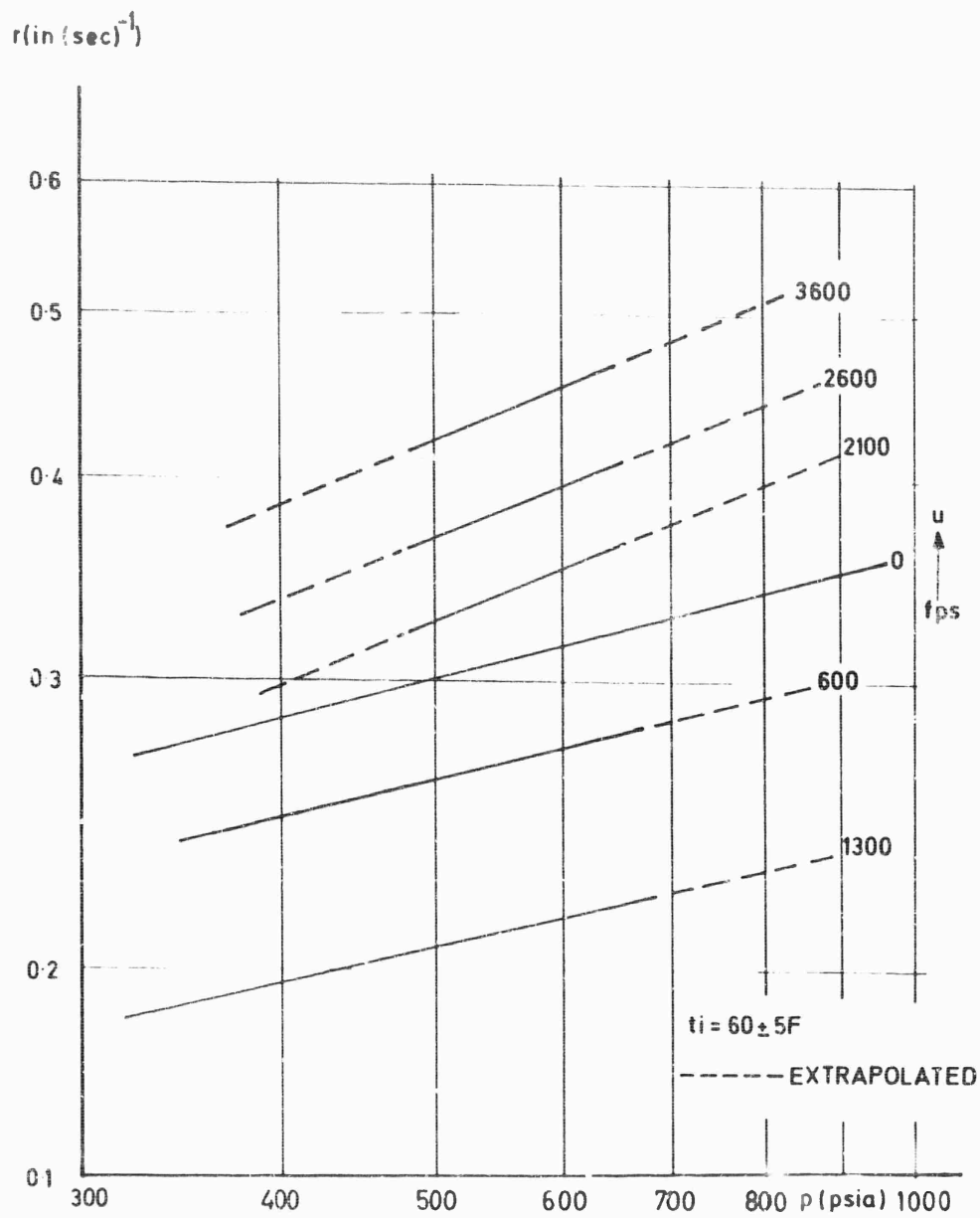


Fig. 7-21 Zucrow's experiments; burning rate as a function of chamber pressure with the gas velocity as a parameter.

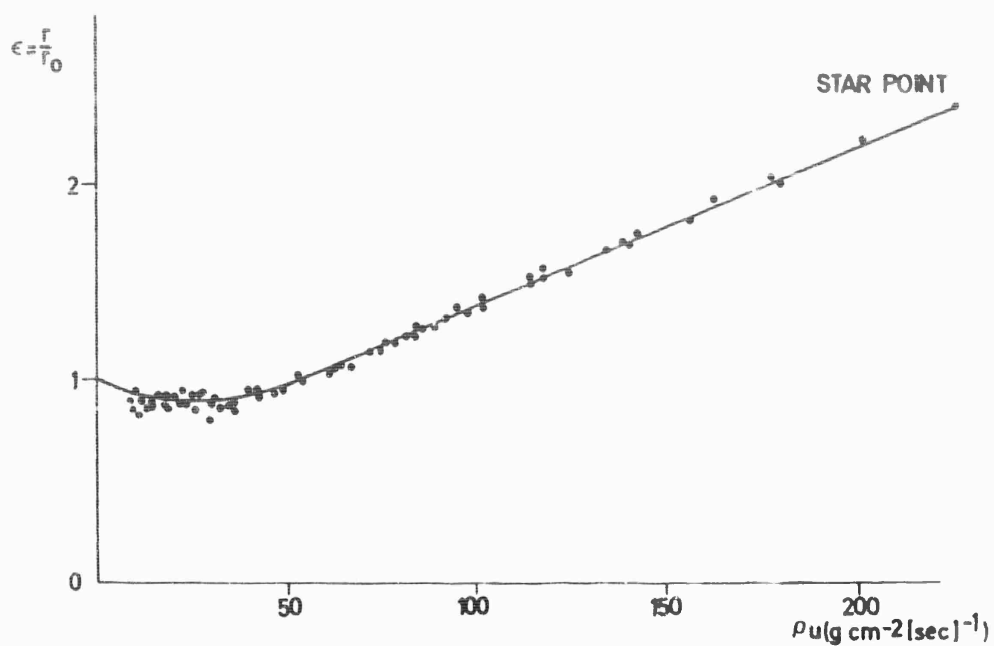


Fig. 7-22 ONERA experiments; erosion factor ϵ versus ρu for a plateau propellant.

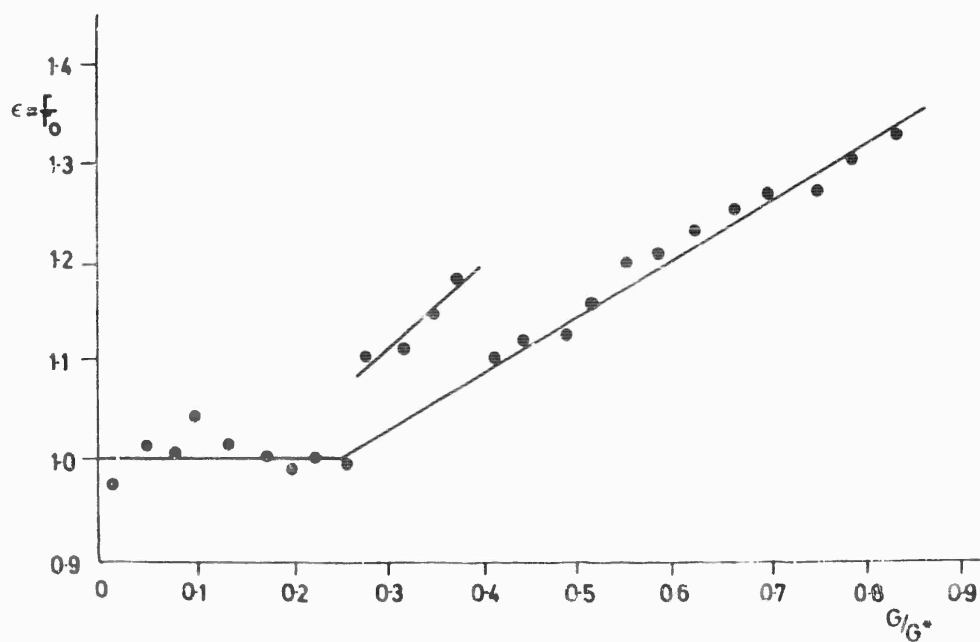


Fig. 7-23 Green's experiment; erosion factor ϵ versus G/G^* ratio.

rate as much by mechanical effects as by a modification of the energy transfer process to the surface.

The influence of the gas temperature has not been studied systematically. By changing the mixture ratio of the gas generator, the gas temperature is altered, but according to Nadaud's experiment this temperature effect is small, the important factor being the adiabatic flame temperature of the solid propellant sample.

It is not possible to classify the flows into laminar and turbulent since the Reynolds number varies along the grain from zero to roughly 10^7 .

b) Influence of the Nature of the Propellant and of Grain Geometry - The erosion function depends strongly upon the nature of the propellant. In order to illustrate this fact Figs. 7-24a and 7-24b show Dickinson and Jackson's results with propellants of the following weight compositions:

	A	B	C	D	E	F
Ammonium Perchlorate	75	70	70	65	70	56
Polyurethane	25	25	25	20	25	25
Aluminum		5	5	15	5	19
LiF(added parts)			1.8			
Copper chromite (added parts)					1.0	
T_c °K	2100	2340	2220	3170	2290	2810
m g/mole	21.54	22.16	22.14	25.94	22.38	24.92
p_o (1000 psi)	0.21	0.24	0.15	0.33	0.33	0.16
c^*	4650	4820	4560	5010	4760	4760
I_{sp} sec	216	221	210	235	218	226
ρ_p (lb/cm ³)	0.058	0.0584	0.0585	0.062	0.0586	0.0601

Aluminum does not seem to have an appreciable influence on the erosion function. At high pressures (1000 psia) the erosion effect is little influenced by the propellant composition and the oxidizer/fuel mixture ratio. The smallest erosion effect is observed with propellants having the largest burning velocity r_o . The smaller the erosion effect, the larger is the erosion threshold. The erosion function r/r_o is modified little by the initial grain temperature. Erosion effects on propellants used in the plateau domain are much more complex. The plateau effect can be obtained with double base propellants by adding catalysts which increase the burning velocity. The effect of these catalysts is greater at low pressures than at high pressures. Catalytic effects can be noticeably reduced or entirely suppressed by a flow parallel to the surface. The sensitivity to the flow thus depends upon the pressure. This explains why an appreciable influence of the gas flow parallel to the surface and of the pressure is observed in the plateau domain for double base solid propellant.

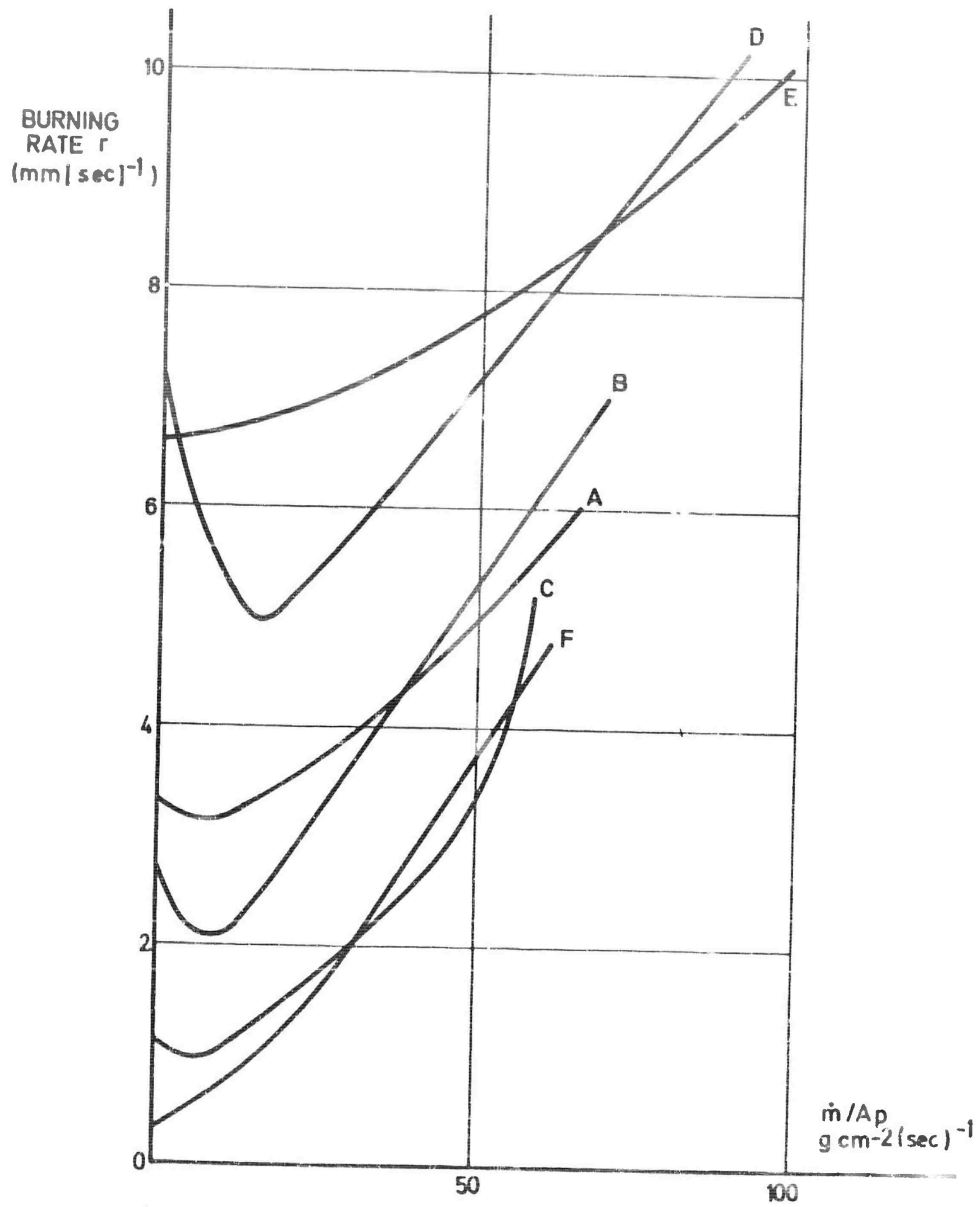


Fig. 7-24a Variation of burning rate with local mass flux (Dickinson and Jackson).

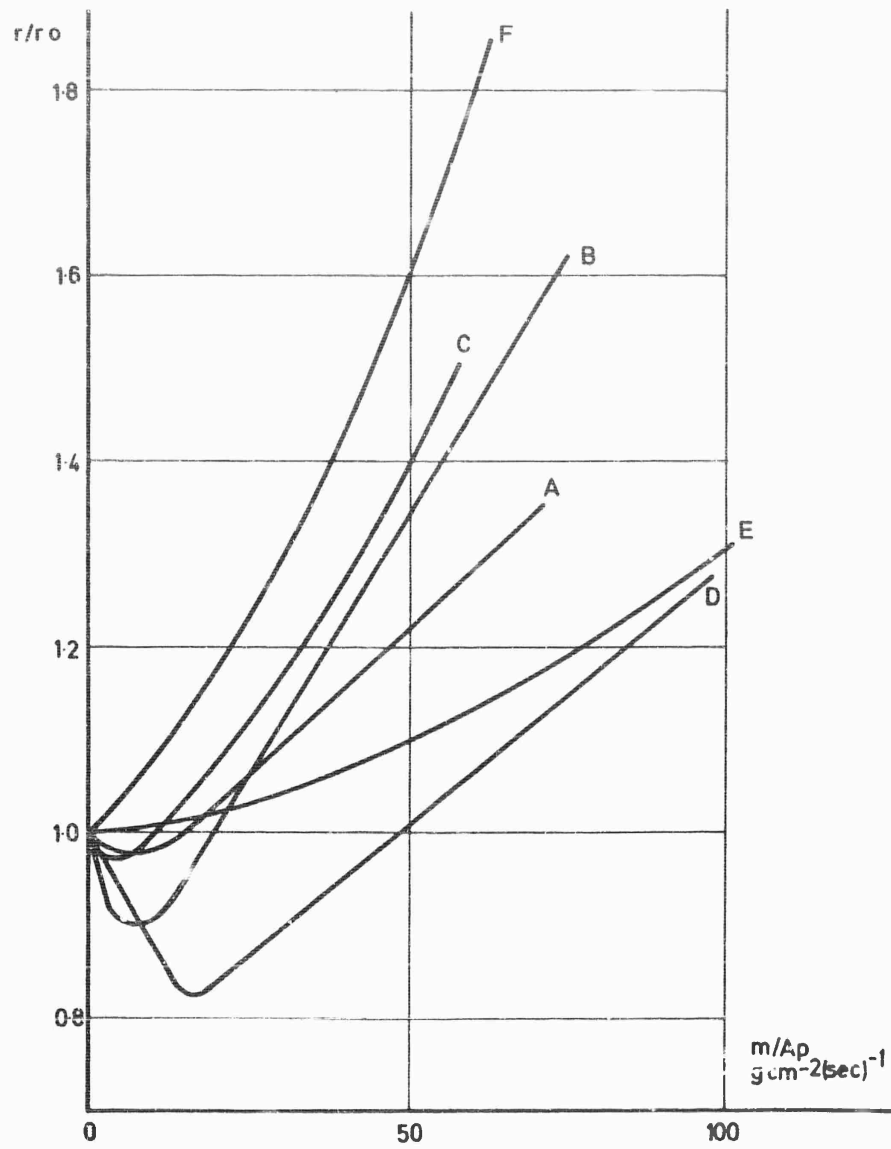


Fig. 7-24b Variation of erosion factor r/r_0 with local mass flux (Dickinson and Jackson).

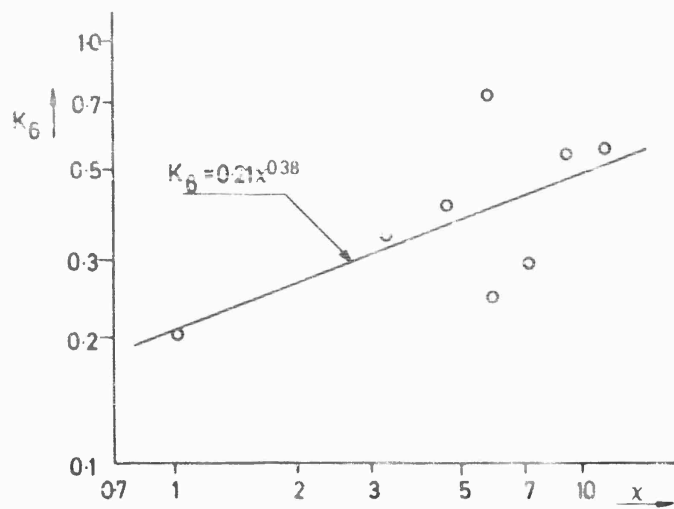


Fig. 7-25 Fenech and Billheimer's experiments; correlation of erosive burning constant with configuration factor.

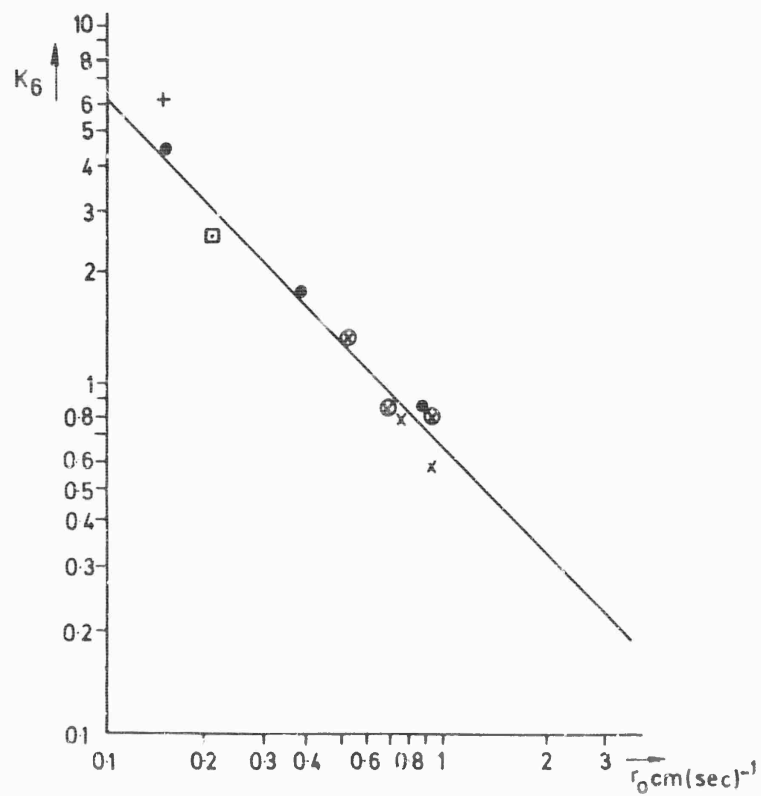


Fig. 7-26 Green's correlation of erosive burning constant as function of burning rate.

In composite propellants the plateau effect is due to a more rapid combustion of the AP crystals followed by a local momentary extinction on certain points of the surface. A flow parallel to the surface can modify the distribution of the extinction zones and in certain cases destroy the plateau effect.

According to Fenech and Billheimer (18) the grain geometry influences the erosion function. (We have already noted that the burning velocity is different at a star point and at a star recess.) Reference (18) introduced a parameter which depends on the grain geometry and which is related to the hydraulic diameter. Designating by A_p the area of the cross section of the central port of perimeter P , one can define the area A_c of a circle of perimeter P ($A_c = P^2/4\pi A_p$). The non-dimensional parameter which appears is then :

$$\chi = \frac{A_c}{A_p} = \frac{P^2}{4\pi A_p}$$

The erosion function measured for various geometries can be correlated roughly by replacing Green's parameter G/G^* by $\frac{G}{G^*} \chi^{0.38}$, as the experimental points of Fig. 7-25 indicate. The points for which the correlation is poorest, correspond to a five pointed star and a wagon wheel configuration.

c) Influence of the Operating Conditions - Few results have been published concerning the influence of the motor operating conditions on the erosion function.

Rotating a motor using metalized propellants leads to a modification of the burning velocity when the rotation speed exceeds 50 rps. It has also been noted that in certain cases a longitudinal acceleration of more than 100 g's can influence the burning rate. This influence can be due to a modification of the flow conditions at the surface, actually an erosion effect.

It has also been noted that the burning velocity laws in the steady state regime and in transient regimes are different (see Chapter 5). These differences can be explained by an erosion effect. In particular, it is possible to show that the increase of the burning velocity during extinction can be attributed to an increase of gas velocity in the central port during the expansion process.

d) Summary - In summary, the following trends appear to be well established:

- The erosion effect is more pronounced at low burning velocities r_b .
- The erosion threshold velocity increases as the erosion effect decreases. This threshold is pressure-sensitive.
- At high pressures (> 1000 psia) the propellant composition and the mixture ratio have little influence on the erosion function. At intermediate and low pressures this function is sensitive to the propellant composition, while the mixture ratio still has little influence.
- Loading the propellant with aluminum seems to have little influence on the erosive function.
- The grain geometry generally modifies the erosion function.
- The transverse velocity destroys the plateau effect.

2.4.3. Proposed Experimental Laws - From the experimental results described above, many laws have been proposed, but they are often essentially equivalent,

since the same parameters are assumed to be constant. It can be assumed in certain cases that the burning velocity is the sum of two terms :

$$r = r_o + r_e, \quad (\text{Eq. 7-1})$$

where r_o is the burning velocity in no-flow conditions and r_e the erosion contribution. One can also divide the burning velocity by r_o , thus defining the erosion function :

$$\frac{r}{r_o} = \epsilon \quad (\text{Eq. 7-2})$$

Tavernier and Boisson's laws are of the form of Eq. 7-1 :

$$r = r_o + K_1 u \quad (\text{Eq. 7-3})$$

or :

$$r = r_o + K_1' \frac{u}{u^*}$$

where u^* is the critical velocity, reached at the throat of the above-mentioned fictitious nozzle. These laws involve the flow velocity u .

Marklund's laws are also of the form of Eq. 7-1 :

$$r = r_o + K_2 G^m \quad (\text{Eq. 7-4})$$

The exponent m , of the order of 0.3, generally increases for high mass fluxes, according to the authors, because of a mechanical erosion effect.

Marklund and Lake's experiments are reasonably well correlated by more complex laws of the form proposed by Lenoir and Robillard (19), such as :

$$r = r_o + K_3 G^{0.8} \exp\left(-\beta \frac{\rho_p r}{G}\right) \quad (\text{Eq. 7-5})$$

where $\frac{\rho_p r}{G}$ is the ratio of the mass fluxes perpendicular and parallel to the surface, and K_3 and β are constants.

The erosion function ϵ is more widely used than the function r_e .

In early work simple laws have been proposed by Heron, such as :

$$\epsilon = \frac{r}{r_o} = 1 + K_4 (u - u_t) \quad (\text{Eq. 7-6})$$

where u_t is the erosion threshold velocity u_t appears.

Geckler replaced the velocity by the specific mass flow rate, so that :

$$\epsilon = \frac{r}{r_o} = (1 + K_5 G) \quad (\text{Eq. 7-7})$$

Green's relation :

$$\epsilon = \frac{r}{r_0} = 1 + K_6 \frac{G}{G^*} \quad (\text{Eq. 7-8})$$

has often been used.

Fenech and Billheimer introduce in coefficient K_6 the influence of the grain geometry :

$$K_6 = K_7 \chi^{0.38} \quad (\text{Eq. 7-9})$$

With the propellants used by Fenech the value of K_7 was 0.21.

K_6 depends upon the propellant used and upon the burning velocity r_0 . Generally K_6 decreases when r_0 increases, as Green's experiments show (Fig. 7-26). This definition of $K_6 \approx K'_6 / r_0$ justifies Marklund's additive formula with $m = 1$.

Geckler's formula has been modified by Dickinson in order to yield an expression of the form :

$$\epsilon = \frac{r}{r_0} = 1 + K'_5 (G - G_t) \quad (\text{Eq. 7-10})$$

which takes into account the threshold effect for a threshold mass flux G_t . Larue and Guinet, after studying composite propellants experimentally, have generalized this law (see Fig. 7-27). They introduced the formula :

$$\epsilon = 1 + K''_5 p_c^n (G^n - G_t^m) \quad (\text{Eq. 7-11})$$

where the constant K''_5 can take into account the geometry of the grain.

Using Summerfield's representation Barrère and Larue showed that, for composite propellants outside the plateau domain, the erosive burning velocities can be written in the form :

$$\frac{1}{r} = \frac{A}{p} + \frac{B (d, u)}{p^\alpha} \quad (\text{Eq. 7-12})$$

where A is a constant independent of the flow velocity, and B is a function of the

average oxidizer grain diameter and of the gas velocity u viz., $B = \frac{B' (d)}{a + u}$.

The exponent α is of the order of $1/3$ (20).

More complex empirical relations have been proposed by Saderholm (21), namely :

$$\ln r = a_0 + a_1 X + a_2 Y + a_3 (a_4 X + a_5 Y)^2 \quad (\text{Eq. 7-13})$$

STAR RECESS

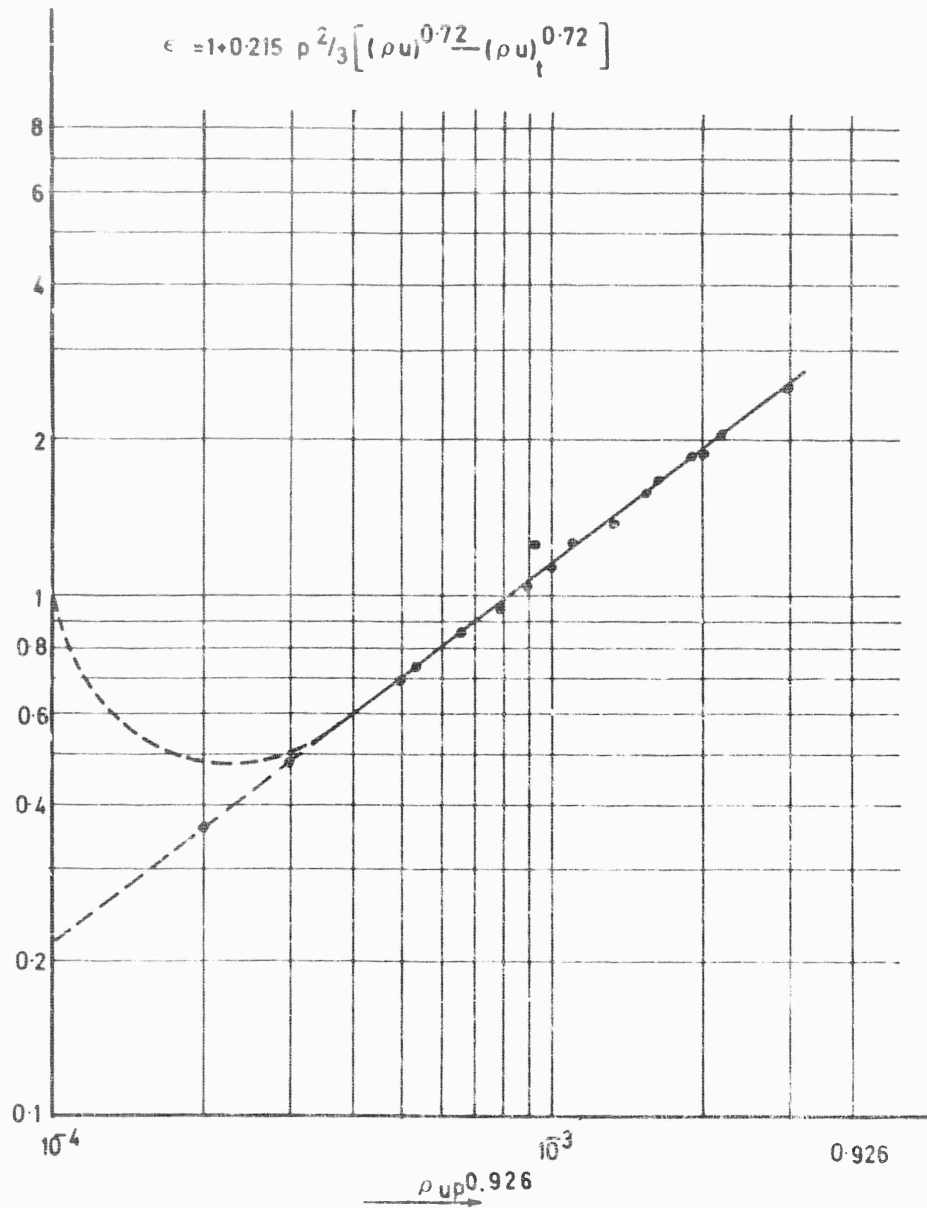


Fig. 7-27 ONERA experiments; erosion factor ϵ versus $\rho u p^{0.926}$.

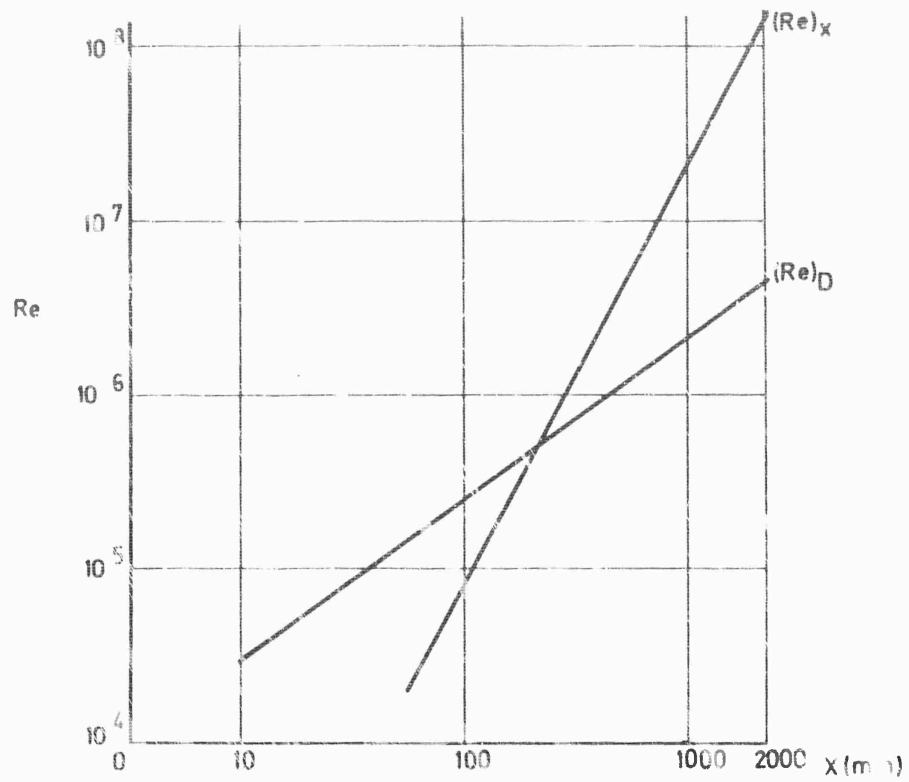


Fig. 7-28 Variation of Reynolds numbers Re_x and Re_D with axial distance X .

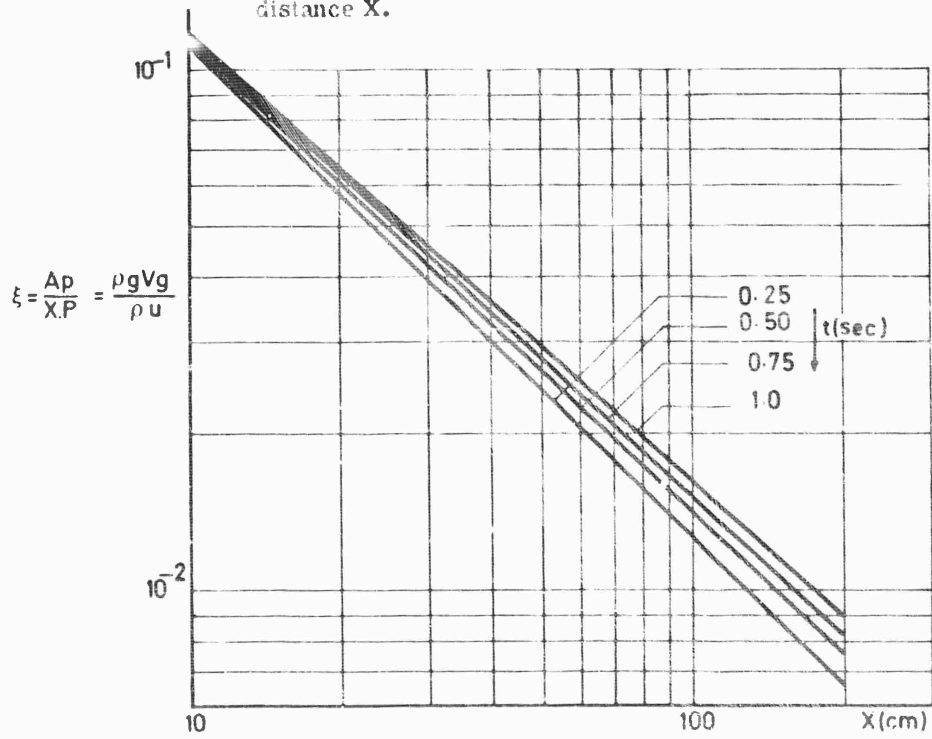


Fig. 7-29 Injection parameter ξ versus axial distance X .

where $X = \ln p_c$ and $Y = \ln (1 + u)$. a_0, a_1, a_2, a_3, a_4 and a_5 are constants. Along the same line one must note Kreidler's relation :

$$\epsilon = \frac{r}{r_0} = 1 + \frac{K_8 (G - K_9 - K_{10} p_c)}{p_c^{n'}} \quad (\text{Eq. 7-14})$$

with $n' = 0.485$, $K_8 = 3.272$, $K_9 = 0.26$, $K_{10} = .00151$ and p_c - chamber pressure (psi), G = mass flux (lb/in².sec), for a particular composite double base propellant.

Zucrow proposed the following relation :

$$r = p_c^{n''} (a_0 + K_{11} u) \quad (\text{Eq. 7-15})$$

where the constant a_0 is a function of the propellant composition its initial temperature and the velocity threshold u_t . K_{11} is a constant which differs according to whether u is smaller or larger than u_t ; the exponent n'' depends upon the composition and the velocity u of the gases.

Variations of Marklund's relation are sometimes used of the form :

$$r = K_{12} (M p_c)^{0.7} \quad (\text{Saderholm}) \quad (\text{Eq. 7-16})$$

or else :

$$\epsilon = \frac{r}{r_0} = 1 + K_{13} (p_c M)^{0.8} L^{-0.2} \quad (\text{Shuey}) \quad (\text{Eq. 7-17})$$

These variations can be related either to Green's formula (Eq. 7-8) or to Eq. 7-11, which are the empirical laws that are used most generally.

3. Theoretical Aspects

This paragraph will be divided into two parts, the first reviewing the proposed semi-empirical theories, the second establishing the fundamentals of a more complete theory, based upon the equations of aerothermochemistry.

3.1. Semi-Empirical Theories

The proposed semi-empirical theories all make use of a certain number of constants which have to be determined from experimental results. Therefore they are of no use if one wishes to predict the erosion function of new propellants and one has to rely on experiments.

Before studying this problem a few general remarks are of importance. The Reynolds numbers $Re_x = \frac{\rho u x}{\mu}$ and $Re_D = \frac{\rho u D}{\mu}$ vary in a wide range along the grain.

In particular at the upstream end one cannot speak of a boundary layer since most of the flow is perpendicular to the surface. Farther downstream the flow lines bend and become parallel to the surface, and a boundary layer develops while the Reynolds number varies along the central port. As an example Fig. 7-28 shows the variation of Re_x and Re_D versus x for a two meter long grain with a ratio $K_{11} = A_p/A_c$ close to unity. The Reynolds numbers vary from zero up to 10^8 for Re_x and 10^6 for Re_D .

They vary from values corresponding to a laminar regime up to values corresponding to a turbulent regime. This large variation could bear some relationship to the different regimes of negative, zero and positive erosion. Cinephotographs of two dimensional chambers with transparent windows show at the upstream end a very luminous zone and a low flow rate. Farther downstream the gas velocity increases, the flow becomes very turbulent, and vortices appear. A further remark concerns the parameter $\xi = \frac{\rho_p r}{G}$, the ratio of the mass injection flux to the mass flux in the central port G. In boundary layer problems with surface mass injection, the injection rate through the surface should be small compared with G ($\xi \approx 10^{-3}$ to 10^{-2}). In the erosion problem, ξ varies from 10^{-1} to 10^{-2} as x goes from 0.1 to 1 m (see Fig. 7-29).

The boundary layer problem is complicated by the variation of the free stream conditions with x .

The simplest boundary layer model which can be assumed is shown on Fig. 7-30. Close to the surface there is a combustion zone of thickness Y_f . At Y_f the gas velocity is u_f . The temperature at ordinate Y_f is the adiabatic flame temperature T_f . At ordinate δ is the edge of the boundary layer determined by the velocity profile. Several semi-empirical theories have been derived from this model.

a) Lenoir and Robillard's Theory (19) - The temperature profile is the one shown on Fig. 7-31 with a propellant at the initial temperature T_1 . T_s is the surface temperature and T_f the adiabatic flame temperature. The energy balance equation, without a surface reaction, is :

$$h (T_f - T_s) = \rho_p r_e [c_s (T_s - T_1)]$$

where h is the convection coefficient giving rise to the erosive burning velocity component r_c and c_s is the specific heat of the propellant.

In the presence of surface mass injection Rannie has shown that the convection coefficient is expressed as an exponential function of ξ :

$$h = h_0 e^{-\beta \xi} = 0.0288 \text{ Re}_L^{-0.2} P_r^{-2/3} G c_p e^{-\beta \xi},$$

where h_0 is the conventional Chilton-Colburn coefficient without mass injection and c_p the specific heat of the gas. The erosive burning velocity is thus given by the relation :

$$r = r_0 + r_c = r_0 + \frac{0.0288}{\rho_p} G \text{ Re}_L^{-0.2} P_r^{-2/3} \frac{c_p (T_f - T_s)}{c_s (T_s - T_1)} e^{-\beta \xi}$$

where Spalding's heat transfer parameter B appears :

$$B = c_p (T_f - T_s) / c_s (T_s - T_1),$$

β is a constant which must be experimentally determined.

Lenoir and Robillard's relation is reasonably well verified by experiment as shown in Fig. 7-32. It does not account for negative erosion but does produce the erosion threshold. When computing the value of the function :

$$\zeta(x) = G(x) \text{ Re}_x^{-0.2} \exp(-\beta \xi(x))$$

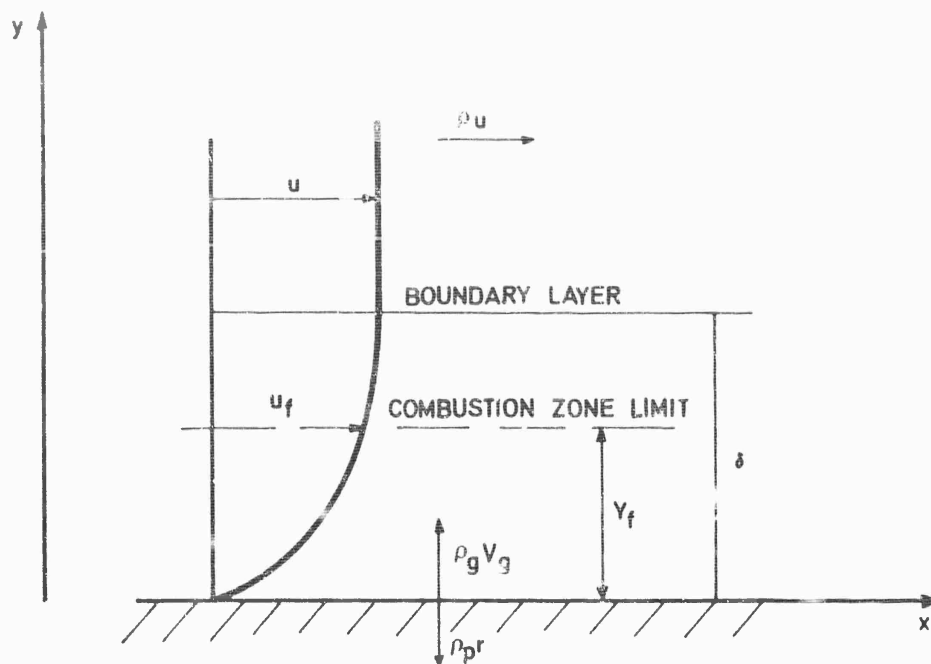


Fig. 7-30 Simplest model for solid propellant combustion.

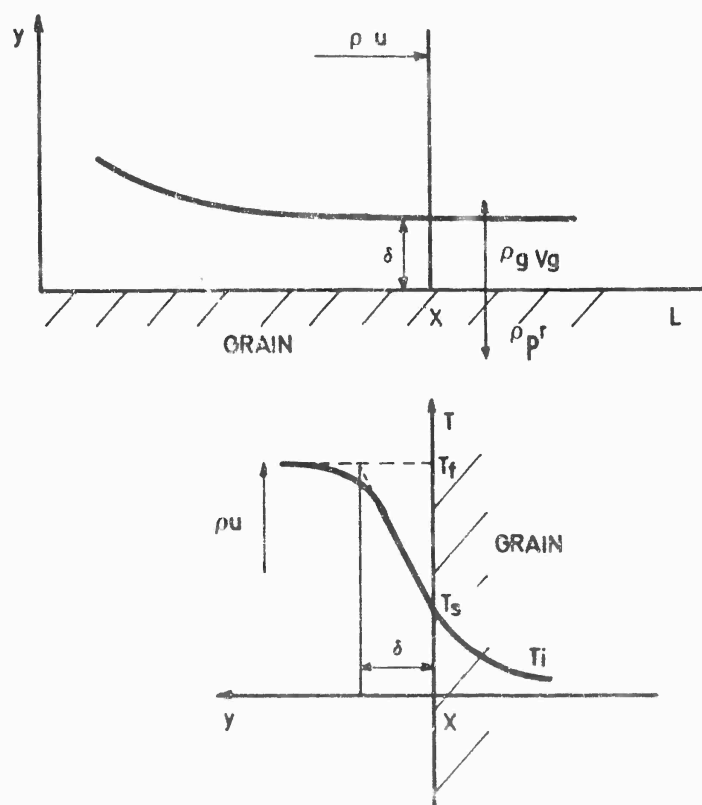


Fig. 7-31 Simplified model for solid propellant combustion; temperature profile at station

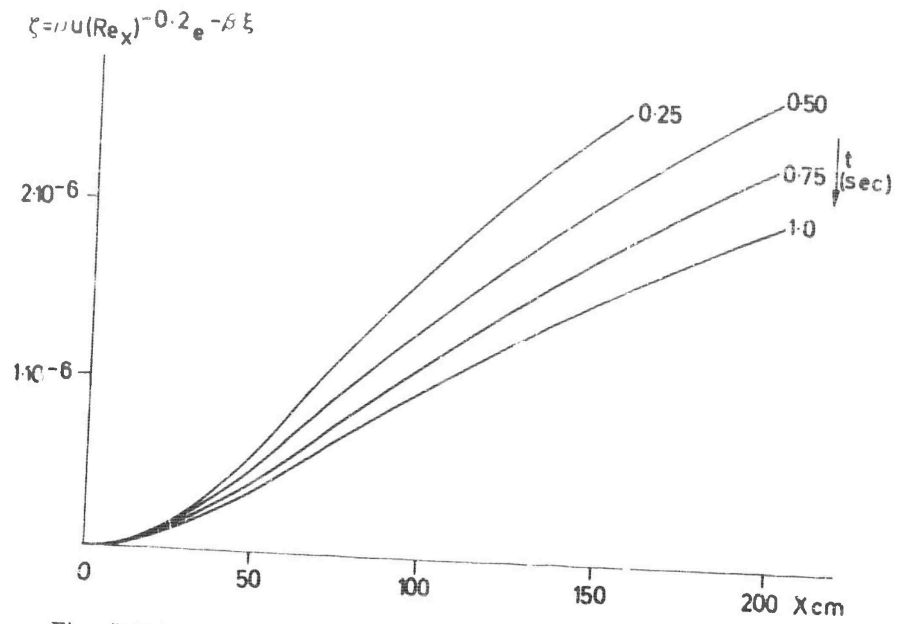


Fig. 7-32 Erosive velocity term ζ versus axial distance .

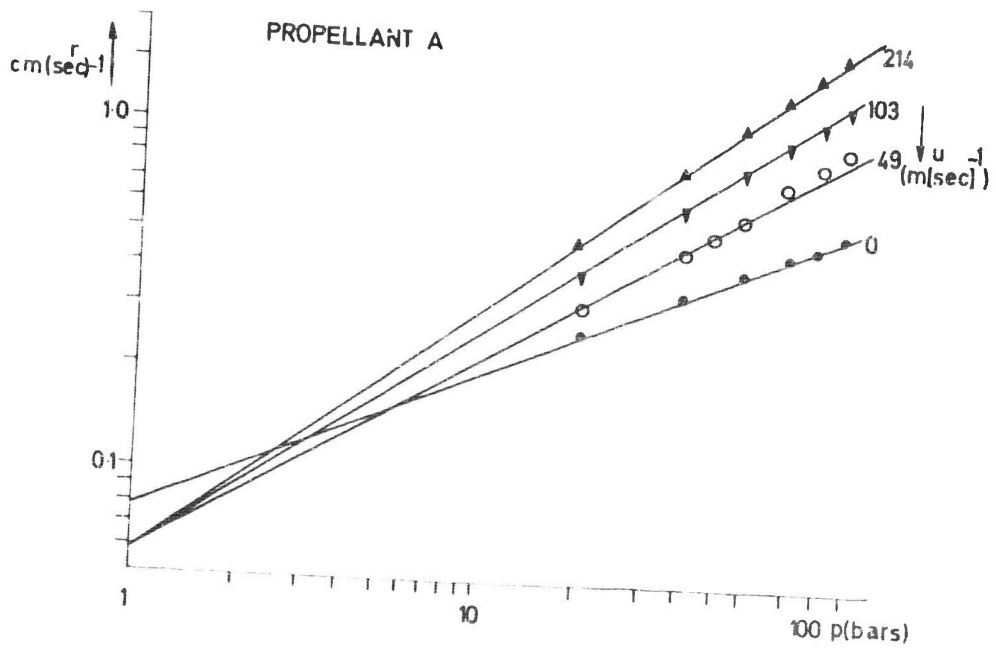


Fig. 7-33 Lake and Marklund's experiments; burning rate r versus pressure p for several values of u .

it can be seen that the erosion effect is very small for low values of x as shown in Fig. 7-32. This is due to the exponential term which approaches unity for high values of x .

In terms of the erosion function ϵ one can write :

$$\epsilon = \frac{r}{r_0} = 1 + 0.0288 \xi \text{ Re}_L^{-0.2} \text{Pr}^{-2/3} \text{Be}^{-\beta \xi}$$

A similar theory proposed by Marklund leads to approximately the same relation. The heat transfer coefficient is introduced into the Stanton number without mass injection. The value of ξ is taken with reference to r_0 ($\xi_0 = \frac{\rho_p r_0}{\rho u}$) and Spalding's transfer parameter includes in the denominator the heat of vaporization ΔL_{OX} of the oxidizer, its mass fraction being Y_{OX} . Thus :

$$r = r_0 + \frac{C_{HO} G}{\rho_p} \cdot \frac{c_p (T_f - T_s) e^{-\beta \xi_0}}{Y_{OX} [\Delta L_{OX} + \beta' c_p (T_{fOX} - T_{sOX})]}$$

where β' is a constant chosen so as to insure the best fit with experiments, T_{fOX} and T_{sOX} being respectively the temperature of the oxidizer at the flame and at the surface.

Another version of this theory has been proposed, by Zucrow who modified Spalding's parameter, writing it :

$$B = \{ S c_p (T_f - T_{sb}) + (1 - S) c_p (T_f - T_{sOX}) \} \{ Y_{OX} [\Delta L_{OX} + c_s (T_{sb} - T_i) + \beta_T c_p (T_f - T_{sOX})] + (1 - Y_{OX}) [\Delta L_b + c_s (T_{sOX} - T_i) + \beta_T c_p (T_f - T_{sb})] \}^{-1}$$

where the parameter S characterizes the fraction of the surface composed of binder material.

The expression for r is then :

$$r = r_0 + \frac{GB}{\rho_p} (C_{HO} - \beta_T \xi_0)$$

All these semi-empirical theories are derived from Reynolds' analogy as applied to a flow with mass injection. This analogy is also used in the solid fuel regression rate theories in hybrid systems such as the one formulated by Marxman (24).

The chief points of this theory are summarized briefly here.

Reynolds' analogy is based upon a correspondence between friction, characterized by the friction coefficient C_F , and heat transfer, characterized by the Stanton number C_H so that :

$$C_F / C_H = 2.$$

It is also assumed that the surface mass injection modifies C_F and C_H according to the law :

$$\frac{C_F}{C_{F_0}} = \frac{C_H}{C_{H_0}} \approx \frac{\ln(1+B)}{B}$$

C_{H_0} and C_{F_0} are the Stanton number and friction coefficient in the absence of mass injection and B is Spalding's transfer parameter defined here as the ratio of the enthalpy difference between the bulk of the fluid and the propellant surface, divided by the amount of energy required to vaporize the propellant :

$$B = (h_f - h_w) / \Delta L$$

The above law assumes that the effect of the mass injection is the same on the friction coefficient and on the Stanton number since B is a thermodynamic parameter and C_F depends upon an aerodynamic parameter $B_a = \frac{\rho_p r u}{\tau_w}$ where τ_w is the shear stress at the wall. In other words it assumes $B_a = B$. This law in $(\ln(1+B))/B$ has been given more elaborate forms later but the conclusions remain approximately unchanged.

The heat flux at the wall Φ_w is $\Phi_w = \rho u (C_f/2) [h_f - h_w]$ where h_f and h_w represent the enthalpies in the bulk of the fluid and at the wall. The law of conservation of energy yields $\rho_p r = \Phi_w / \Delta L$, where ΔL is the energy required to vaporize the solid propellant.

The burning velocity contribution due to the flow is found to be :

$$r_e = G C_{F_0} \ln(1+B)$$

It can be seen that this relation resembles Lenoir and Robillard's which used Cloubern's relation to express C_{H_0} .

b) Theory of Vandenkerckhove - This theory has first been applied to homogeneous propellants. It assumes that the burning velocity is a function of the surface temperature T_s according to a law of the form :

$$r = K B \exp(-E/R T_s) ,$$

where K is a numerical constant, B the frequency factor and E the activation energy of the process of gasification of the solid phase.

Let T_{s_0} and r_0 be the surface temperature and the burning rate without erosion. The elimination of the unknown factors yields :

$$r = r_0 \exp \left(\frac{E}{R} \left(\frac{1}{T_{s_0}} - \frac{1}{T_s} \right) \right) ,$$

the surface temperature with erosion T_s differing from the temperature without erosion.

The theory also assumes that the erosion effect is due to the turbulence in the fizz zone and the threshold velocity u_t corresponds to the moment when the turbulence reaches this zone. The turbulent boundary layer theory allows us to define a transition height y_1' which depends upon the average flow velocity u . This height y_1' and the energy conservation equation yield the surface temperature T_s and (by using the above relation) r/r_0 . The values of u and r/r_0 are thus obtained for each value of y_1' and a relation of the form :

$$r/r_0 = 1 + k_u (u - u_t) .$$

gives the value of k_u .

The following table gives a few values relative to the JPN Ballistic propellant ($u_t = 180$ m/s) :

y'_1 (cm)	T_{s_0} (°K)	r/r_0	u (m.sec ⁻¹)	k_u (sec.m ⁻¹)
0.001	845.3	1.962	205.3	0.00245
0.008	855.5	1.186	263.3	0.00225
0.006	870.8	1.390	362.0	0.00214

These values of k_u agree with the value of 0.00219 sec.m⁻¹ given by Green for the JPN propellant, close to the threshold velocity.

This theory has then been extended to composite propellants by considering the oxidizer decomposition zone instead of the fizz zone.

c) Theories Based upon the Flame Structure - In a wide pressure and velocity range, the burning velocity of a propellant in the no-flow conditions can be written in the classical form :

$$r_0 = a p^n .$$

In the presence of erosion the laws keep the same form, as Fig. 7-33 shows but a and n are then functions of the velocity u :

$$r = a(u) p^{n(u)} .$$

The exponent n increases when the transverse velocity increases; this might be due to the extension of the pre-mixed flame conditions at the surface. It will be necessary to introduce into a theory the modifications of the flame structure due to the gas flow parallel to the surface.

Assuming a velocity law of Summerfield's type :

$$\frac{P}{r} = a + b (d) p^\alpha ,$$

the term a represents the contribution of pre-mixed flames and should vary little when the gas velocity varies, whereas the term b , related to diffusion flames, should decrease when the gas velocity increases. The exponent α must also decrease due to the nature of the transverse flow close to the oxidizer crystals of diameter d , since the flow there can change from laminar to turbulent.

Using a model of the same form as the one given in Chapter 6 for heterogeneous propellants, one obtains the following law :

$$\frac{P}{r} = a + b (d, u) p^{1/3}$$

The parameter b alone is sensitive to the velocity. Without any flow the exponent is 2/3; it becomes equal to 1/3 in the presence of flow.

The above law is reasonably well verified outside the plateau domain and for prop-

ellants which follow Summerfield's law. Figures 7-34 and 7-35 show this for the two propellants A and B discussed earlier.

Negative erosion would in this case be due to the influence of pressure, the exponent α going from the value $2/3$ for $u = 0$ to $1/3$. This simplified theory predicts an increase in transfer processes in the diffusion flames due to the transverse velocity. The pre-mixed flames are insensitive to the transverse velocity u , because their heights are smaller than those of the diffusion flames.

3.2. Aerothermochemical Approach to the Problem of Erosive Burning

In order to facilitate discussion of possible basic improvements in theoretical approaches to the problem of steady state erosive burning, let us consider here one simplified motor geometry in which erosive burning effects are important, viz., an internally burning tubular grain in a chamber whose head plate has a flat, non-ablative interior surface mounted flush against the upstream end of the grain. We also assume that there are no downstream obstructions or flow disturbances which produce recirculation or other spurious flows and we prohibit the occurrence of vortices (nonvanishing time-average tangential velocities) in the chamber. Let us further postulate that no condensed phase reaction products are produced and assume that we can treat the propellant grain as if it were homogeneous.

Under these conditions, the steady state, two dimensional form of the conservation equations given in Chapter 6, Section 1 are expected to govern the gas flow in the motor chamber. These equations are :

$$\begin{aligned} \frac{\partial}{\partial x} (r \rho u) + \frac{\partial}{\partial r} (r \rho v) &= 0 \quad ; \\ \rho u \frac{\partial u}{\partial x} + \rho v \frac{\partial u}{\partial r} &= - \frac{\partial p}{\partial x} - \frac{\partial}{\partial x} \left\{ \frac{2}{3} \mu \left(\frac{\partial u}{\partial x} + \frac{1}{r} \frac{\partial (rv)}{\partial r} \right) \right\} \\ &+ \frac{\partial}{\partial x} \left(2 \mu \frac{\partial u}{\partial r} \right) + \frac{1}{r} \frac{\partial}{\partial r} \left\{ r \mu \left(\frac{\partial u}{\partial r} + \frac{\partial v}{\partial x} \right) \right\} \quad ; \\ \rho u \frac{\partial v}{\partial x} + \rho v \frac{\partial v}{\partial r} &= - \frac{\partial p}{\partial r} - \frac{\partial}{\partial r} \left\{ \frac{2}{3} \mu \left(\frac{\partial u}{\partial x} + \frac{1}{r} \frac{\partial (rv)}{\partial r} \right) \right\} \\ &+ \frac{1}{r} \frac{\partial}{\partial r} \left(2 r \mu \frac{\partial v}{\partial r} \right) + \frac{\partial}{\partial x} \left\{ \mu \left(\frac{\partial u}{\partial r} + \frac{\partial v}{\partial x} \right) \right\} \quad ; \\ \rho u \frac{\partial (h + \frac{u^2}{2} + \frac{v^2}{2})}{\partial x} + \rho v \frac{\partial (h + \frac{u^2}{2} + \frac{v^2}{2})}{\partial r} &= \\ \frac{\partial}{\partial x} \left(\lambda \frac{\partial T}{\partial x} - \rho \sum_{i=1}^N h_i Y_i U_i \right) + \frac{1}{r} \frac{\partial}{\partial r} \left(r \lambda \frac{\partial T}{\partial r} - r \rho \sum_{i=1}^N h_i Y_i V_i \right) \\ &+ \frac{\partial}{\partial x} \left\{ \mu \left[2u \frac{\partial u}{\partial r} + v \left(\frac{\partial u}{\partial r} + \frac{\partial v}{\partial x} \right) - \frac{2}{3} u \left(\frac{\partial u}{\partial x} + \frac{1}{r} \frac{\partial (rv)}{\partial r} \right) \right] \right\} \\ &+ \frac{1}{r} \frac{\partial}{\partial r} \left\{ r \mu \left[2v \frac{\partial v}{\partial r} + u \left(\frac{\partial u}{\partial r} + \frac{\partial v}{\partial x} \right) - \frac{2}{3} v \left(\frac{\partial u}{\partial x} + \frac{1}{r} \frac{\partial (rv)}{\partial r} \right) \right] \right\} \quad ; \end{aligned}$$

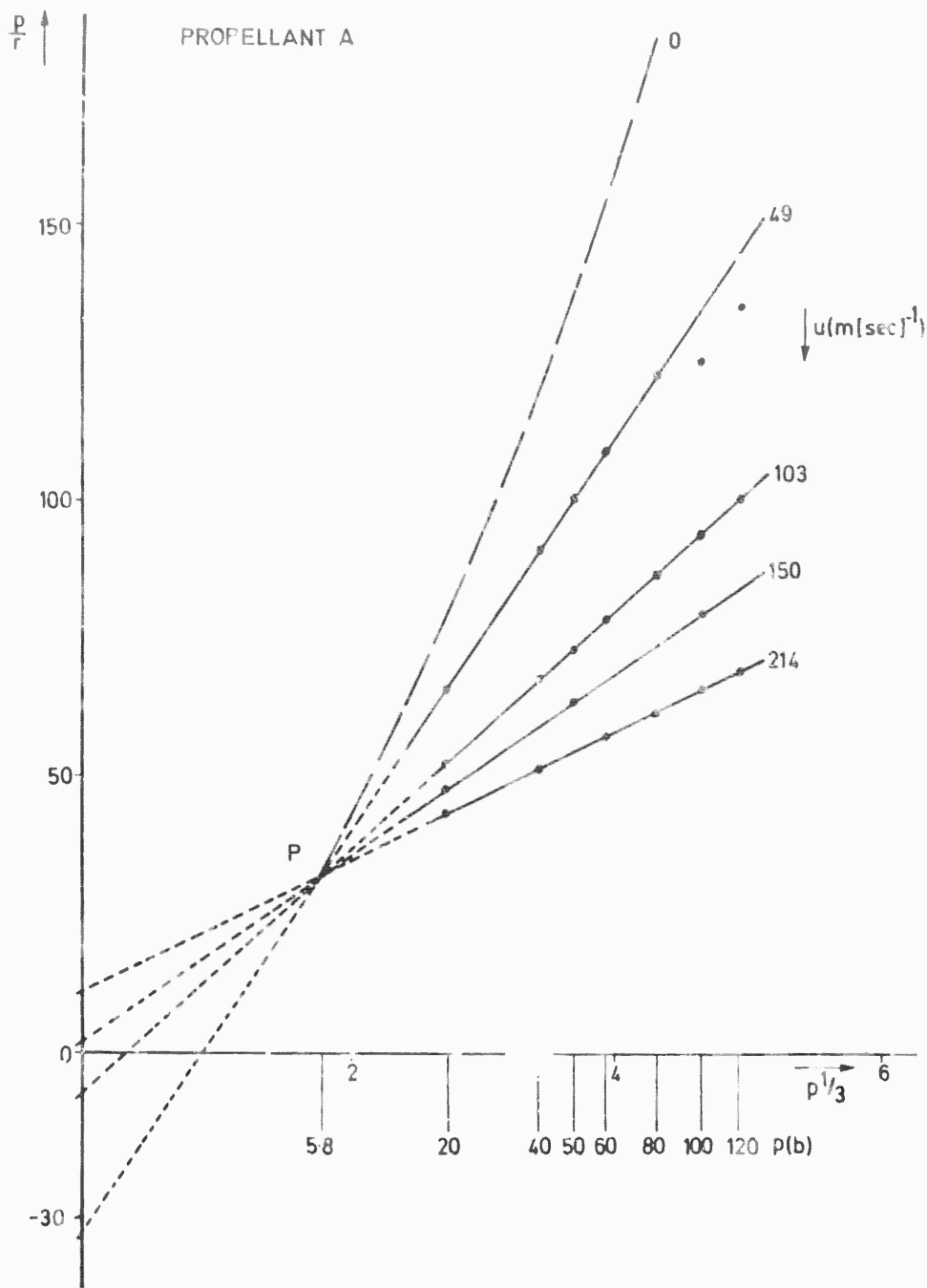


Fig. 7-34 Lake and Marklund's experiments; linear representation of p/r versus $p^{1/3}$ for $u \neq 0$.

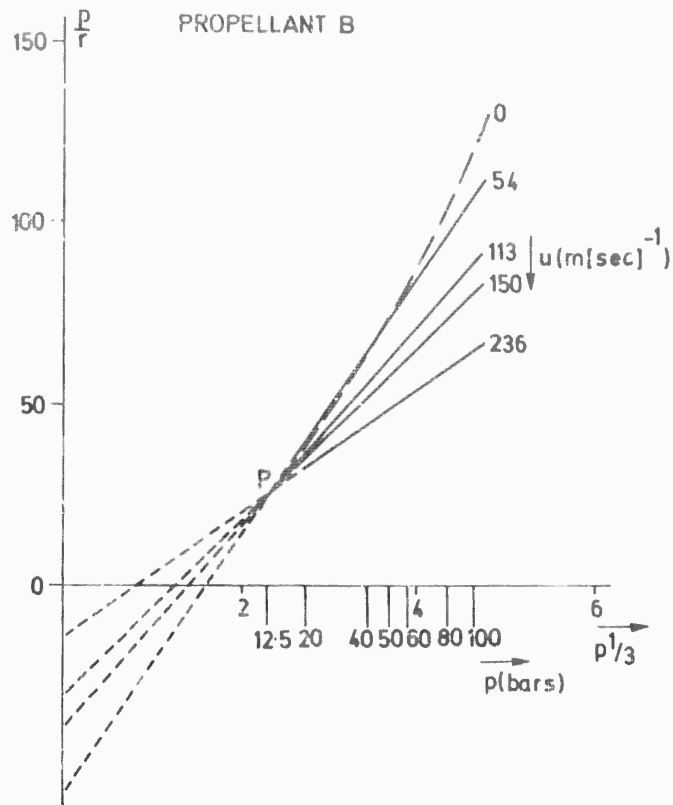


Fig. 7-35 Lake and Marklund's experiments; linear representation of p/r versus $p^{1/3}$ for $u \neq 0$.

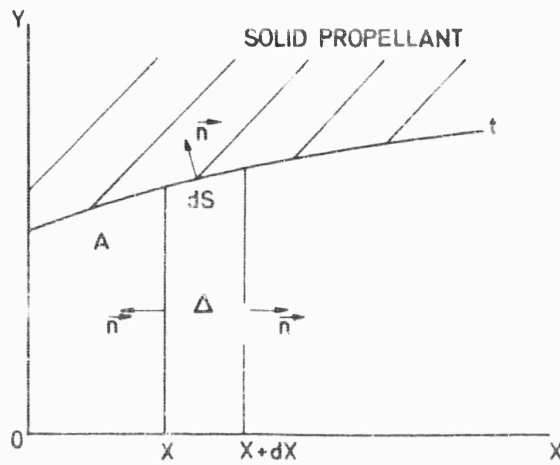


Fig. 7-36 Streamwise evolution of the port dimensions.

$$\rho u \frac{\partial Y_i}{\partial x} + \rho v \frac{\partial Y_i}{\partial r} = w_i - \frac{\partial}{\partial x} \left(\rho Y_i U_i \right) - \frac{1}{r} \frac{\partial}{\partial r} \left(r \rho Y_i V_i \right);$$

$$\frac{\partial X_i}{\partial x} = \sum_{j=1}^N \left(X_i X_j / \mathcal{D}_{ij} \right) (U_j - U_i);$$

$$\frac{\partial X_i}{\partial r} = \sum_{j=1}^N \left(X_i X_j / \mathcal{D}_{ij} \right) (V_j - V_i)$$

where x and r are the axial and radial coordinates, u and v are the corresponding (mass-average) velocity components, and U_i and V_i are the corresponding components of the diffusion velocity of chemical species i . All other symbols have been defined in Chapter 6, where algebraic relationships among them may also be found (equation of state, chemical reaction rate formula, etc.). Effects that are expected to be relatively minor, such as thermal diffusion, bulk viscosity, body forces and gas-phase radiative energy transport have been neglected here.

The equations hold in a region bounded by the head plate ($x = 0$), the propellant surface [$r = R(x)$] and a somewhat ill defined downstream boundary which may be taken to be the exit of the port ($x = L$). The boundary conditions differ at each of these three boundaries; for example, $u = v = U_i = V_i = 0$ at $x = 0$, $u = 0$ and $\rho v = \dot{m}(x)$ (propellant mass burning rate) at $r = R(x)$, and in general $u \neq 0$ and $v \neq 0$ at $x = L$. These and other boundary conditions that must be employed entail additional reasonable assumptions (e.g. $dR/dx \ll R/x$, no viscous flow of the grain at its burning surface, etc.). Boundary conditions expressing energy conservation couple the gas-phase conservation equations to equations of heat conduction in the solid grain and in the head plate, viz,

$$\dot{m} c_s \partial T / \partial r = \partial [\lambda_s (\partial T / \partial x)] / \partial r + \frac{1}{r} \partial [r \lambda_s (\partial T / \partial r)] / \partial r$$

and :

$$\partial [\lambda_h (\partial T / \partial x)] / \partial x + \frac{1}{r} \partial [r \lambda_h (\partial T / \partial r)] / \partial r = 0$$

where c_s is the heat capacity of the propellant and the subscripts s and h identify propellant and head, respectively. Boundary conditions deep in the propellant and on the outside of the head plate are needed along with these two equations. Finally, at $r = R(x)$, a chemical boundary condition such as a pyrolysis law (or conceivably an interphase equilibrium condition) is needed in order to provide a sufficient number of conditions to determine the burning rate $\dot{m}(x)$ as an eigen value of this complicated set of partial differential equations.

Although we have not defined here precisely a reasonable mathematical model for the problem of erosive burning, we have given all of the partial differential equations that are needed. We state further that the problem can be defined in the manner that we indicate and it is physically apparent that the solution to the problem will yield $\dot{m}(x)$ in an environment of erosive flow. Such a solution might be termed an aerothermochemical analysis of the erosive burning problem. Present-day computing machines are capable of solving coupled partial differential equations in two dimensions by finite-difference techniques. Therefore, if the gas-phase chemistry is simplified so that only a few chemical species need to be considered, it is quite

conceivable that this erosive burning problem can be solved.

Were such a solution to be carried out, objections would immediately be raised on the grounds that the flow is usually turbulent during erosive burning, while the analysis treats laminar flow. Such objections would be unfair for two reasons. First it is only necessary to replace the laminar transport coefficient μ , λ and ρ_{ij} by turbulent transport coefficients μ_T , λ_T and ρ_{ijT} in order to obtain turbulent flow solutions which are as good as any that can be derived from current engineering approximations. It is true that numerical estimates for μ_T , λ_T and ρ_{ijT} are likely to be inaccurate. It is also true that even for much simpler flow fields, the more accurate expressions for μ_T , λ_T and ρ_{ijT} introduce more complicated differential factors into the governing equations. But appropriate differential factors for this complex, reacting flow are unknown and therefore cannot be expected to be included in a theory. Second, no turbulent shear flow theory can be claimed to be any good unless many detailed experimental measurements support it for precisely those flow conditions that it intends to describe. Few turbulence measurements exist (of mean and/or fluctuating flow variables) in reacting flows of any kind and very few in flows with highly exothermic reactions. Few turbulence measurements exist for cold one-component gases in the erosive burning geometry, and very few for multi-component or nonisothermal systems. Thus, it is impossible at present (and for some time to come) to construct an acceptable theory of turbulent erosive burning and it is unfair to criticize a theory for not doing something that is impossible. Progress toward well-founded analysis of turbulent erosive-burning must be made through experiment and not theory.

Another objection that would be raised against such a theory is that the results are not likely to describe well the erosive burning of heterogeneous propellants. It seems that comprehensive analyses accounting for effects of heterogeneities in erosive environments are too difficult to formulate today. Some progress may be made in this area by looking at specific effects of erosion on various aspects of heterogeneous burning mechanisms (e.g., by studying how a flow velocity parallel to the surface would affect the burning rate in a sandwich burner model) but comprehensive results are far in the future.

We have already pointed out that the equations given here are quite complicated. Approximation techniques are available for simplifying the equations. Numerous different approximations can be made. For example, in the solids' heat may be assumed to flow one-dimensionally, perpendicular to the internal face of the solid; this converts the heat conduction equations into ordinary differential equations that can be integrated readily. The region which is most strongly in need of additional simplifying assumptions is the gas phase, for which the differential equations are most complex. The boundary layer approximation constitutes a classical technique for effecting substantial simplification in the gas-phase conservation equations.

In the boundary layer approximation it is first assumed that the gas flow can be divided into two parts, a central, inviscid core and a thin, viscous boundary layer adjacent to the grain surface. The core flow is treated quasi-one-dimensionally, with an axially directed velocity and with axial variations in flow variables determined by chamber radius variations $R(x)$ and by mass, energy, etc. inflow rates at the gas-side edge of the boundary layer, through overall conservation equations. [As a further approximation it might be assumed that the core flow can be specified *a priori* thus implying that an iterative approach would eventually be needed for satisfying the overall conservation equations of the core flow (27) (a specific linear velocity gradient in the axial direction is assigned to the core flow).] In the viscous boundary layer, the boundary layer approximation involves neglecting the terms which represent axial molecular transport processes in the governing equations, so that the elliptic set of equations becomes parabolic and yields more readily to analytic techniques of solutions.

The boundary layer approximation can be valid only if the characteristic distance δ over which flow properties in the vicinity of the grain surface change in the r direction is small compared with the characteristic distance ℓ over which these properties change in the x direction (28). In view of the continuity equation, this condition implies that changes in $(r\rho v)$ be small compared with changes in $(r\rho u)$ or upon integration, that v be of the same order of magnitude as $u\delta/\ell$ (since v has been assumed to vanish in the core flow). The results are that $v^2/2$ is negligible in comparison with $u^2/2$, that all viscous terms except $\frac{1}{r} \frac{\partial}{\partial r} (r\mu \frac{\partial u}{\partial r})$ in the x component of the momentum conservation equation are negligible, that changes in pressure across the boundary layer (in the r direction) are negligible, that the r component of the momentum equation can be disregarded, that only the term :

$$\frac{1}{r} \frac{\partial}{\partial r} \left(r \lambda \frac{\partial T}{\partial r} - r \rho \sum_{i=1}^N h_i Y_i V_i + r \mu u \frac{\partial u}{\partial r} \right)$$

need be retained on the right-hand side of the energy equation, that the terms $\partial(\rho Y_i U_i)/\partial x$ are negligible in the species conservation equations and that the x component of the diffusion equation is not needed. When $\mu/\rho D_{ij}$ and $\lambda/\mu c_p$ are both roughly of order of unity, one can then show that the molecular transport terms which remain in the conservation equations are of the same order of magnitude as the convective terms only if the Reynolds number, $Re \equiv \rho u \ell/\mu$ is of the order $(\ell/\delta)^2$ which is large compared with unity. It has been pointed out (29) that this necessary condition ($Re \gg 1$) for the validity of the boundary layer approximation is not satisfied in the upstream portion of the rocket motor. The basic requirement that $v/u \sim \delta/\ell \ll 1$, cannot possibly be satisfied for a distance of 5 or 10 port diameters from the head plate. In particular, the flow velocities for which observations of negative erosion have been reported are too low for the boundary layer approximation to apply, one would not expect to be able to obtain predictions of negative erosion from boundary layer theory. Thus the boundary layer approximation is highly questionable in analyses of erosive burning, throughout important parts of most motors (29).

Besides suffering doubts about applicability, the boundary layer approximation does not simplify the analysis of the erosive burning problem to the same extent that it simplifies analyses of other problems (such as the problem of the burning of a solid fuel in an oxidizing gas stream). Exact analytical solutions to the differential equations that arise from the boundary layer approximation can be obtained in many problems for chemically nonpremixed systems, so that algebraic formulas for such quantities as the burning rate can be written down. However, solid propellant combustion is chemically premixed in this sense and at least one of the differential equations resulting from the boundary layer approximation retains complexities that usually force numerical integration procedures to be used. Accurate "similarity" solutions can often be found for nonpremixed systems, but to impose similarity on a premixed system generally involves appreciable inaccuracies. Thus, even within the framework of boundary layer theory, erosive burning constitutes one of the more difficult reacting flow problems.

The most detailed analysis of erosive burning that has been reported within the framework of boundary layer theory is that of Tsuji (27). Tsuji considers a one-step, gas phase, exothermic chemical reaction in the boundary layer of an ablating flat plate which has a constant surface temperature and is subjected to a constant velocity gradient in the external stream. Through various approximations, he was able to develop similarity solutions that necessitated the numerical integration of only one ordinary differential equation (an energy conservation equation) which contained the burning rate as an eigenvalue. The numerical integration was carried out for a particular example of a first order reaction and for a particular example

of a second order reaction. The results appear as curves of dimensionless burning rate vs. dimensionless velocity gradient and show that the burning rate increases with increasing velocity gradient. Too narrow a range of parameters was considered for statements to be made about parametric dependence of the burning rate. Therefore, neither the analysis nor the results will be reproduced here.

From the theoretical viewpoint, the problem of erosive burning is a very difficult one. Theoretical progress in this area will continue to be very slow unless entirely new analytical techniques are discovered.

4. Effect of Erosion Phenomena on the Geometry of the Central Port

The pressure distribution along a grain and the evolution of its geometry have been studied in Chapter 4 with simplifying hypotheses. To be more accurate the general flow equations will be changed due to the evolution of the geometry of the central port and to the surface mass injection. These general equations must be extended to a medium with variable boundaries and variable mass (30).

The port cross-sectional area A at abscissa x varies as a function of time through the ordinate of its boundary $Y(t)$. Applying the conservation equations to a vector field \vec{b} in a volume Δ of thickness dx we get :

$$\int_{\Delta} \frac{D\vec{b}}{Dt} \rho d\tau = \frac{\partial}{\partial t} \int_{\Delta} \vec{b} \rho d\tau + \int_A \vec{b} d\mu$$

where $d\mu$ is the mass flow into an elementary surface of area dA . ($d\mu = \rho \vec{u} \cdot \vec{n} dA$) $d\tau$ is an elementary volume of Δ , and D represents the total derivative sign.

This general relation allows one to write first the mass flow conservation differential equation in a medium having variable boundaries and mass. When \vec{b} is constant and $\frac{D\vec{b}}{Dt} = 0$ the conservation equation becomes :

$$\frac{\partial}{\partial t} \int_{\Delta} \rho d\tau + \int_A d\mu = 0$$

The elementary volume being $d\tau = \pi Y^2 dx$ (see Fig. 7-36) the time derivative term is equal to $\pi \frac{\partial}{\partial t} (\rho Y^2) dx$. The second term is a surface integral which includes, for frontal area the expression $\pi \frac{\partial}{\partial x} (\rho Y^2 u) dx$ and for the lateral area the burning contribution $2\pi Y dS \rho_p r$.

Since $dS = \sqrt{1 + Y'^2} dx$ the elimination of dx leads for the mass conservation equation, to the partial differential equation :

$$(a) \quad \frac{\partial}{\partial t} (\rho Y^2) + \frac{\partial}{\partial x} (\rho Y^2 u) - 2Y \sqrt{1 + Y'^2} \rho_p r = 0$$

To this equation must be added the expression for the burning velocity :

(b)

$$\frac{\partial Y}{\partial t} = r \frac{dx}{dS} = \frac{r}{\sqrt{1 + Y'^2}}$$

where r is the burning velocity normal to the surface.

The momentum and energy conservation equations can be established in the same way.

The momentum conservation equation is formed by replacing \vec{b} by \vec{u} and $\rho \frac{D\vec{u}}{Dt}$ by $-\text{grad } p$:

$$\int_{\Delta} \text{grad } p \, d\tau + \frac{\partial}{\partial t} \int_{\Delta} \rho \vec{u} \, d\tau + \int_A \vec{u} \, d\mu = 0$$

or:

$$Y^2 \frac{dp}{dx} + \frac{\partial}{\partial x} (\rho Y^2 u) + \frac{\partial}{\partial x} (\rho Y^2 u^2) - 2Y\sqrt{1+Y'^2} u \rho_p r = 0$$

This last equation is identical to the classical equation of conservation of momentum with fixed boundaries :

$$(c) \quad \frac{\partial u}{\partial t} + u \frac{\partial u}{\partial x} + \frac{1}{\rho} \frac{\partial p}{\partial x} = 0$$

The energy conservation equation is obtained in the same way by replacing \vec{b} by the total enthalpy. This equation forms with the equation of state : $p = \rho n RT$ and equations (a), (b) and (c), the system which allows one to solve the following problems :

- a - evolution of the geometry of the central port with time,
- b - evolution of the burnt propellant mass flow rate
- c - evolution of the total and static pressures along the grain as a function of time.

The integration of such a system is very complex and a few simplifying assumptions will be made. Assuming first that $\frac{\partial Y}{\partial x} \approx 0$ which is practically the case since the surface forms a small angle with the direction of the flow, equations (a) and (b) become :

$$\begin{cases} \frac{\partial (\rho Y^2)}{\partial t} + \frac{\partial}{\partial x} (\rho Y^2 u) = \rho_p \frac{\partial Y^2}{\partial t} \\ \frac{\partial Y}{\partial t} = a \left[1 + \frac{u}{u_0} \right] \end{cases}$$

This assumes an erosion law linear with the velocity u .

One can also assume, since the gas composition and temperature vary little along the central port, that p is a constant. The above system becomes then :

$$\begin{cases} Y \frac{du}{dx} = 2 \frac{\rho_p}{\rho} \frac{\partial Y}{\partial t} \\ \frac{\partial Y}{\partial t} = a \left[1 + \frac{u}{u_0} \right] \end{cases}$$

Solving this system leads to a parametric profile curve, the parameter being the velocity u .

$$\begin{cases} Y = Y_0 + a \left[1 + \frac{u}{u_0} \right] t \\ X = \frac{\rho}{2\rho_p} \left[\frac{u_0 Y_0}{a} \ln \left(\frac{1 + \frac{u}{u_0}}{2} \right) + u_0 t \left(\frac{u}{u_0} - 1 \right) \right] \end{cases}$$

Eliminating u leads to :

$$X = \frac{\rho}{2\rho_p} \left[\frac{u_0 Y_0}{a} - \ln \frac{Y - Y_0}{2at} + u_0 t \left(\frac{Y - Y_0}{at} - 2 \right) \right]$$

These problems are generally treated by a step by step integration technique employing the erosive burning velocity laws :

$$r = r_0 (p, u, \rho, T_p) .$$

5. Conclusions

There are technological and fundamental aspects to the difficult problem of erosive burning. In the technological approach, one proposes simplified models and equations for estimating the erosive burning rate. These equations are very useful to the designer; they simplify data reduction and enable one to carry out performance computations for rocket motors. In the fundamental approach, one attempts to describe possible erosion mechanism and to establish a theory for local erosion phenomena.

Although technological studies have been progressing, the fundamental approach is much more difficult and will still require much more attention. Fundamental studies must consider a complex heterogeneous boundary layer problem for which no satisfactory solution has been given. We have stressed herein possible future directions of research and have emphasized the necessity of accounting for effects of burning-surface heterogeneity on one hand and of a flow heterogeneity near the surface on the other hand. The importance of these phenomena has been pointed out in previous work (20) and in a recent publication by Miller, (31).

Flow heterogeneity effects occur for all propellants (both heterogeneous and homogeneous). This has been seen clearly by examining the flow structure in a two-dimensional chamber with transparent walls; during the erosive phase there is a high level of turbulence close to the surface and eddies can be seen.

The phenomena are rendered even more complex by the surface heterogeneity of composite propellants. In particular, it is difficult to explain the erosion laws obtained in the plateau domain because the flame structure changes, when a gas flows parallel to the surface.

Erosive burning is essentially a local phenomenon and until one can describe schematically the processes that occur in the vicinity of the surface, it will be difficult to propose a valid theory for erosion.

References

- (1) Green L., Erosive Burning of Some Composite Propellants, A.R.S. Journal Vol. 24, p. 9, 1954.
- (2) Wimpers R.N., Internal Ballistics of Solid Fuel Rockets. McGraw-Hill New York, p. 129, 1950.

- (3) **Tavernier P., et Boisson J.,** La Combustion Erosive des Poudres Colloïdales, Chimie et Industrie vol. 78, no.5, Paris 1957.
- (4) **Tavernier P., Prache P., et Berger J.,** Contribution à l'Etude de l'Erosion des Poudres Colloïdales, Mémorial des Poudres, no.87, 1955.
- (5) **Tavernier P., et Boisson J.,** Contribution à l'Etude de la Combustion Centrale d'un Bloc de Poudre Perforé. Mémorial des Poudres tome 41, p.285, 1959.
- (6) **Geckler R.D.,** The Mechanism of Combustion of Solid Propellants, Selected Combustion Problems, Combustion Colloquium Cambridge University, England, Butterworths Scientific Publications, 1954.
- (7) **Marklund T., and Lake A.,** Experimental Investigations of Propellant Erosion, J.A.R.S. vol. 30, no.2, February 1960.
- (8) **Zucrow M.J., Osborn J.R., and Murphy J.M.,** An Experimental Investigation of the Erosive Burning Characteristics of a Non-Homogeneous Solid, A.I.A.A. Preprint 64, 107.
- (9) **Barrère M., et Moutet A.,** La Propulsion par Fusées Hybrides, Congrès International d'Astronautique, Paris, 25 Sept., 1963.
- (10) **Kreidler J.W.,** Erosive Burning - New Experimental Techniques and Methods of Analysis, A.I.A.A. Preprint 64, 155.
- (11) **Monks R.E.,** Burning Rate Measurements by Radiographic Examination of Operating Hybrid Motors. NOTS Publication 3252. NAVWEPS Report 8359, 1964.
- (12) **Larue P., et Guinet M.,** Dispositif Expérimental d'Etude de la Combustion Erosive d'un Propergol Solide. La Recherche Aérospatiale no.103, Nov. - Dec. 1964.
- (13) **Dickinson L.A., Jackson F., and Odgers A.L.,** Erosive Burning of Polyurethane Propellants in Rocket Engines. VIII Symposium (International) on Combustion. The Williams and Wilkins Company, p.754, 1962.
- (14) **Dickinson L.A., and Jackson F.,** Combustion in Solid Propellant Rockets Engines. Fifth AGARD Combustion and Propulsion Colloquium. Pergamon Press p.531-550, 1963.
- (15) **Boisson J., et Betin P.,** Etude de la Balistique Interne des Fusées à Poudre AGARD Colloquium Proceeding. La Jolla, 1966.
- (16) **Murphy J.M.,** A Summary of the Results of Experimental Investigations of Erosive Burning. Control No. 64-4555, Third Conference on the Performance of High Temperature Systems, Pasadena, California.
- (17) **Heron R.,** Internal Ballistic Problems of Solid Propellant Rocket Propulsion Technology vol.1, Plenum Press, New York, 1961.
- (18) **Fenech E.J., and Billheimer J.S.,** Use of Internal Configuration to Predict Erosive Burning Constant. The Combustion Institute, Western States Section Paper No.61-8, April 1961.

- (19) Lenoir J. M., et Robillard G., A Method to Predict the Effects of Erosive Burning in Solid Propellant Rockets. Sixth Symposium on Combustion, Reinhold, 1957.
- (20) Barrère M., et Larue P., Contribution à l'Etude de la Combustion Erosive des Poudres Composites. La Recherche Aérospatiale no. 95, Juillet-Août 1963.
- (21) Saderholm C. A., A Characterization of Erosive Burning for Composite H. Series Propellants. A.I.A.A. Solid Propellant Meeting, January 1964.
- (22) Zucrow M. J., Osborn J. R., and Murphy J. M., Erosive Burning of Solid Propellants Air Research and Development Command, United States Air Force Technical Note No. 2, Contract AF. 61 (052) 354, July 1961.
- (23) Murphy J. M., Analytical Approaches to Erosive Burning. Third Conference of Performance of High Temperature Systems, Dec., 1964.
- (24) Marxman G. A., and Wooldridge C. E., Research on the Combustion Mechanism of Hybrid Rockets. 25th meeting AGARD Combustion and Propulsion Panel, La Jolla, California, 22 - 24 April 1965.
- (25) Vandekerckhove J., Erosive Burning of a Colloidal Solid Propellant Jet Propulsion 28, no. 9, Sept. 1938.
- (26) Vandekerckhove J., and Jaumotte A., Remarks on the Burning Mechanism and Erosive Burning of Ammonium-Perchlorate Propellants. 8th Symposium (International) on Combustion, The Williams and Wilkins Company, 1962.
- (27) Tsuji H., Ninth Symposium (International) on Combustion. Academic Press New York, pp. 384-393, 1963.
- (28) Schlichting H., Boundary Layer Theory. McGraw Hill, New York, 1960.
- (29) Green L. Jr., Ninth Symposium (International) on Combustion. Academic Press, New York, p. 392, 1963. (Comment on H. Tsuji's paper).
- (30) Blatz P. J., A Simplified Approach to Erosive Burning. Eighth Symposium (International) on Combustion. The Williams and Wilkins Company, p. 745, 1962.
- (31) Miller E., Erosive Burning of Composite Solid Propellants. Combustion and Flame Vol. 10, No. 4, p. 330, 1966.

Chapter 8

Ignition and Extinction of Solid Propellants

Nomenclature

a	sound speed
A_b	instantaneous burning surface area
A_{bi}	burning area of igniter propellant
A_d	burst diaphragm area
a_f	thermal diffusivity, defined in Eq.8-2
A_t	motor nozzle throat area
A_{ti}	total orifice cross-sectional area for igniter
a_3	g_1
B	frequency factor
c	heat capacity per unit mass for propellant
c^*	characteristic velocity
c_∞	value of c_1 at $x = \infty$
c_p	specific heat at constant pressure
c_v	specific heat at constant volume
c_1	concentration of hyperbolic constituent in gas
D	tube diameter
D_p	diameter of central channel
e	specific internal energy of gas in the central channel
F	thrust
G	mass flow rate per unit area
g	gravitational acceleration
Gr	Grashof number ($Gr = L^3 \rho_1^2 g \beta_1 \Delta T / \mu_1^2$)
h	heat transfer coefficient; enthalpy per unit mass
$H(x)$	energy flux into the surface at position x (cal/cm ² sec)
J	A_t/A_p
K	A_b/A_t
κ	ratio of the central channel cross-sectional perimeter to the square root of the port area
L	length of flat plate; motor length

L^*	characteristic length of motor
M	mass of gases inside the chamber
\dot{M}	dM/dt
\dot{m}	mass flow rate
\dot{m}_b	burned propellant flow rate
\dot{m}_{bi}	burned propellant flow rate for igniter
M_i	mass of combustion products in igniter chamber
\dot{m}_v	liquid flow rate of hyperbolic constituent injected into the chamber
m_{pi}	total propellant mass contained within igniter
\dot{m}_t	flow rate through the main motor nozzle
\dot{m}_{ti}	flow rate through the injection orifices into the main chamber
m_w	mass of water injected
\dot{m}_w	water injection rate
n	order of surface reaction; pressure exponent; heat flux component
Nu	Nusselt number
Pr	Prandtl number
p	pressure
\dot{p}	dp/dt
p_a	ambient pressure
p_c	steady-state chamber pressure
p_i	stagnation pressure in igniter chamber
Q	heat released in the surface reaction per mole of gaseous species 1 consumed
q	heat flux
q_c	convective heat flux
q_R	incident radiant energy flux
r	linear regression rate; flame perimeter propagation velocity
r_{bi}	linear regression rate for igniter propellant
Re	Reynolds number ($Re = \rho_1 v_1 L / \mu_1$)

r_p	flame propagation velocity
r_0	regression rate under no-flow conditions
s	Laplace transform variable
T	temperature
t	time
\overline{T}	Laplace transform of $T - T_0$
T_A	activation temperature
t_a	sound propagation time
T_{bi}	combustion temperature for igniter
t_{bi}	igniter burning time
T_C	steady-state combustion temperature
t_d	diffusion time
t_{ex}	minimum exposure time for ignition
T_f	stagnation temperature of flow
T_g	gas stagnation temperature ($^{\circ}\text{K}$); temperature in the bulk of the gas
T_i	temperature in igniter chamber; ignition temperature for flamespread process
T_{ign}	ignition temperature; ignition delay
t_{inj}	injection time
t_m	molecular ignition time
T_o	initial sample temperature of unignited propellant or propellant grain temperature; constant temperature
t_p	characteristic time for flame propagation along the grain
t_R	ignition time under radiant heating conditions
t_r	residence time of gases in the chamber
T_s	surface temperature
t_{th}	thermal delay time for propagation of heat in solid phase
T_w	propellant surface temperature
t_w	water injection time
T_{∞}	temperature in bulk of gas

	nozzle velocity of the gases at the nozzle exit section
v_i^*	characteristic velocity for ignition, F/m
v_m	average molecular velocity
v_l, v_g	gas velocity parallel to surface
y	axial distance from igniter exit to measurement position
x	coordinate normal to propellant surface
Y_{O_2}	oxygen mass fraction
Y_p	mass fraction of condensed phase
Z	surface temperature difference, $T_l(0) - T_c$
α	thermal accommodation coefficient; dimensionless parameter defined in Eq. 8-52
β	dimensionless activation energy T_A/T_0 ; coefficient of proportionality relating propellant sensitivity to temperature
β_1	volume expansion coefficient of the gas
Γ	function of specific heat ratio defined in Chapter 2
γ	dimensionless radiant flux defined in Eq. 8-54; polytropic exponent
ΔT	difference in temperature between gas and surface
Δt_{50}	difference between time at which the pressure reaches half its initial value and the time at which the diaphragm ruptures
ϵ_1	ratio of the igniter exit section diameter to the main motor port diameter ($\epsilon_1 = D_t/D_p$)
η	combustion efficiency
θ	dimensionless temperature defined in Eq. 8-50; time characteristic of pressure evolution
λ	thermal conductivity (refers to propellant when not subscripted)
μ	viscosity coefficient
ξ	fractional energy losses in the main motor
ξ_1	fraction of the energy lost in the igniter chamber
ρ	density (refers to propellant when not subscripted)
τ	dimensionless ignition time defined in Eq. 8-51; or delay
τ_1	inflection value of τ

φ ratio of the volume of the converging portion of the nozzle to the central channel volume for a cylindrical motor

$\psi(\gamma)$ function of the specific heat ratio which relates the velocity of sound to the characteristic velocity

Script Letters

\mathcal{D}_1 diffusion coefficient for gas

\mathcal{L} Laplace transform operator

\mathcal{L}^{-1} inverse Laplace transform operator

ℓ_m molecular mean free path

m molecular weight

V chamber volume

Superscripts

— Laplace transform

Subscripts

b burning surface

e extinction; nozzle exit

g gas

i igniter

ℓ integer, takes on values 1, 2, 3

o identifies initial conditions

p propellant; port

ss steady-state

t throat

∞ identifies conditions at $x = \infty$ in the gas

1 gas phase

2 solid phase

3 gas-phase diffusion

Ignition and Extinction of Solid Propellants

1. Ignition

1.1. Introduction

This chapter is divided into two parts, ignition and extinction. In ignition studies, two types of activities can be distinguished, according to whether they concentrate on the fundamental aspects or the practical aspects of the subject. The first type of activity concerns the study of ignition conditions for propellant materials. In a representative experiment from this category, a propellant sample is subjected to an energy flux for a certain duration. During this time the behavior of the sample is studied and measurements are made of the ignition delay, defined as the time interval between the initiation of the energy flux and the appearance of the first flame. Related theoretical and experimental studies are performed in an effort to discover the mechanism of ignition and to determine the influences of various parameters on the ignition mechanism and on the ignition delay. Although such studies are of a fundamental nature, their results are useful in practical ignition problems.

The second, more practical, type of activity involves investigating motor ignition. Its aim is to enable one to design an ignition system that produces a pressure-increase curve which is known in advance. Instead of using lengthy and expensive empirical methods of igniter design that require trial-and-error tests in full-scale motors, it is desirable to develop techniques for predicting the pressure-increase curve that are based on some understanding of motor-ignition processes and that minimize the necessary amount of large-scale testing.

In Section 1, we shall firstly analyze experimental results pertaining to the ignition of a propellant sample. After a short review of the experimental techniques, we shall discuss the influence on the ignition delay of the major parameters, such as the nature of the propellant and of the ambient gas, the pressure and the sample temperature. A somewhat pedagogic summary of current theories of ignition will then be presented. Finally, ignition of a motor will be studied and various successive processes, that occur during the period of pressure increase, will be distinguished.

1.2. Experimental Methods in Ignition Studies

For purposes of presentation, it is convenient to identify two kinds of experimental techniques for studying the ignition of a sample of solid propellant. In static methods heat is applied instantaneously to the propellant surface, focusing on the surface the image of an arc-source so that the energy required for ignition is transferred by radiation. In dynamic methods the heat source moves with respect to the propellant surface; this occurs when the propellant is located in a stream of hot gases. These two kinds of techniques seem to be of equal interest, the first being closer to the theoretical models, the second closer to the actual ignition process in an engine.

Unfortunately, the two techniques produce different time histories of the heat flux, thereby making comparisons difficult.

a) Static Methods

The simplest method consists of introducing a propellant sample into a furnace heated to a known temperature. The furnace used by Baer and Ryan (1) is shown in Fig. 8-1. Temperatures of 1000°C can be attained over a pressure range of 0.2 to 20 atm and 1500°C can be produced at atmospheric pressure (inert atmosphere). The sample is introduced into the furnace suddenly; the introduction process lasts for 20 to 30 msec. An infrared sensitive photocell detects the ignition of the sample. To calculate accurately the heat flux received by the sample surface in this device, sometimes requires introducing corrections for heat losses from the surface caused by radiation reemission and by free convection.

A related method that has been used is to press the sample against a heated plate.

Another prevalent technique involves using an arc-image furnace. The apparatus illustrated in Fig. 8-2 was described by Rosser, Fishman and Wise (2). The arc image is focused on a sample, thereby permitting heat fluxes in excess of $120\text{ cal cm}^{-2}\text{ s}^{-1}$ to be obtained. The flux range usually quoted is 2 to $300\text{ cal cm}^{-2}\text{ sec}^{-1}$. The spectral energy distribution of the emitted light extends from about 0.2 to 2 microns with a maximum around 0.5 micron. A shutter allows one to adjust the irradiation time, which typically lies in the range of 100 to 200 msec. The sample is located in a cylinder fitted with a window. The nature of the ambient atmosphere and the gas pressure in the cylinder can both be changed. For certain experiments a gas flow around the sample can also be established. The heat flux received by the propellant surface is calibrated in a preliminary calorimetric experiment; calibrations should be standardized to facilitate accurate comparisons between results obtained in different research laboratories. Disadvantages of arc-image methods are variable absorption of incident heat flux by the sample and the low temperature of the ambient atmosphere.

The arc-image experimental procedure involves exposing the sample to a given incident flux, in a given ambient atmosphere at a given pressure, for varying lengths of time. The minimum exposure time for the occurrence of an ignition that leads to sustained combustion can generally be determined within $\pm 5\%$. Sometimes the exposure is not terminated and the ignition delay, which is the time interval between the start of exposure and the appearance of the first flame, is measured. The ignition delay differs somewhat from the minimum exposure time. Both times can be studied as functions of various parameters in arc-image devices.

b) Dynamic Methods

We shall describe here the two methods that are used most widely. The first technique involves placing a propellant sample in a gaseous flow and observing the ignition of the propellant and the propagation of the flame by cine-photography or with a photocell. An experiment of this type is shown in Fig. 8-3. The experimental results are strongly dependent on the sample geometry and its location in the flow, both of which must therefore be determined accurately. With this method, the ignition delay can be studied as a function of various parameters such as the nature of the gas, its velocity, its temperature, its pressure, the sample temperature, its geometry and the nature of the propellant (3).

The second technique consists of using a shock tube to generate a high-temperature gas flow around the sample. The high-pressure portion of the shock tube must be sufficiently long, to insure that the high-temperature flow duration exceeds the ignition delay. There are two ways to mount the sample in a test chamber. If one

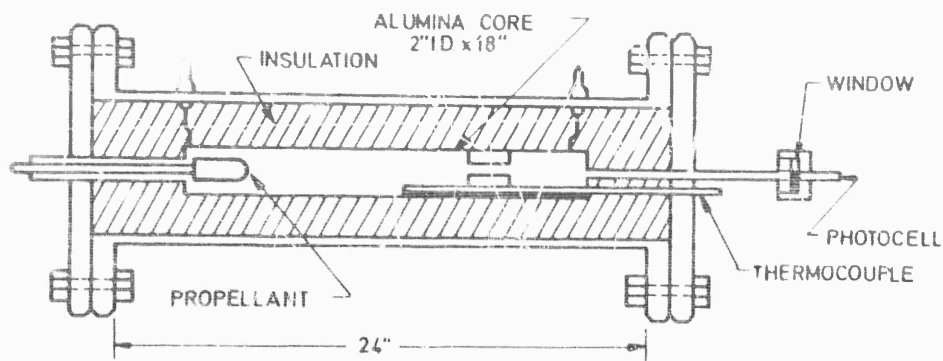


Fig 8-1 A sectional view of the sealed, low-temperature radiation furnace. Propellant samples are pushed rapidly into the furnace from the left end of the furnace and are stopped in the position shown.

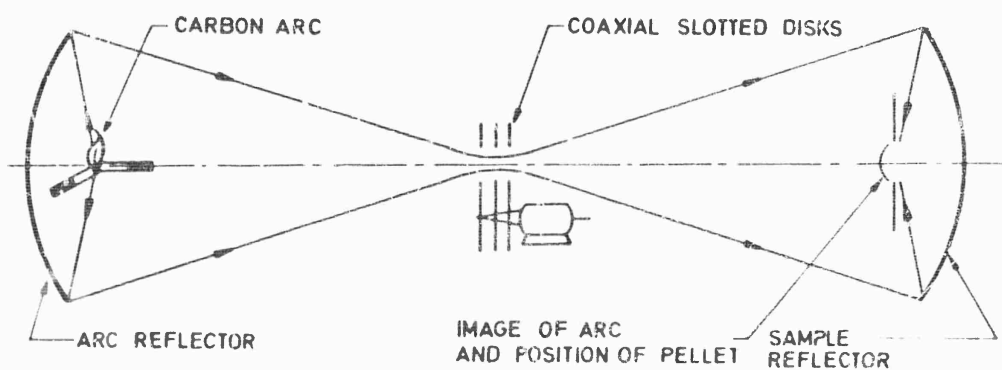


Fig. 8-2 Schematic drawing of double-ellipsoidal carbon arc image system(2).

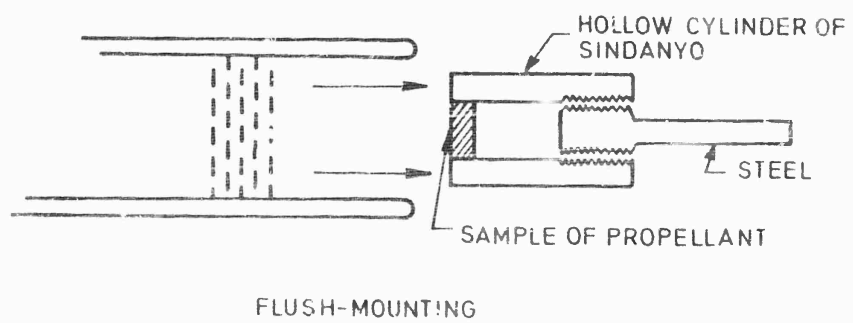
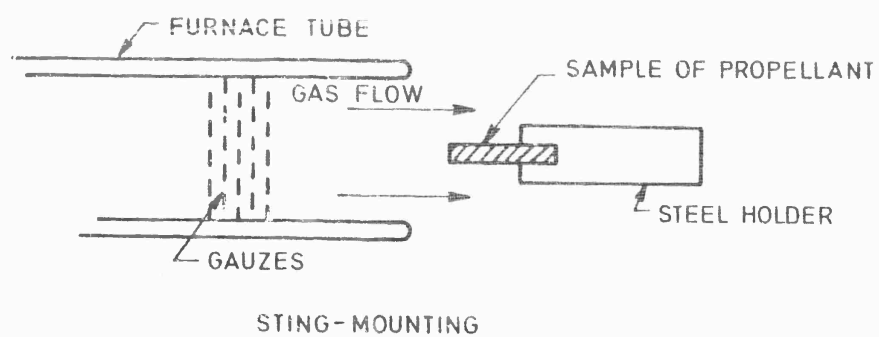
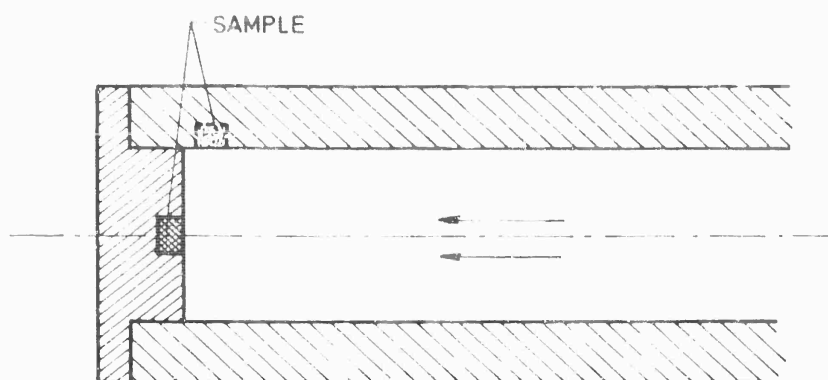
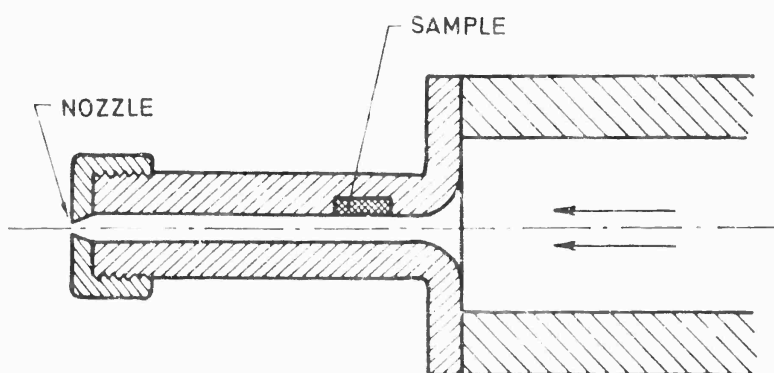


Fig. 8-3 Sting-mounted and flush-mounted samples (3).



A) CONDUCTIVE HEAT TRANSFER



B) CONVECTIVE HEAT TRANSFER

Fig. 8-4 Ignition of composite solid propellant samples in a shock tube.

desires to measure the delay under the influence of conductive heat transfer alone, then the sample should be attached to the end of the tube, as shown in Fig. 8-4a. If one is interested in a convective heat transfer environment then the mounting arrangement shown in Fig. 8-4b can be used. The propellant surface is mounted flush on the tube wall and a nozzle at the end of the tube maintains an approximately constant gas flow rate during the entire experiment. The nozzle throat dimensions and the pressure levels in the high pressure and in the low pressure chambers can be adjusted to achieve the desired flow conditions at the position of the sample. The ignition delay can be measured for various values of the pressure, the temperature, the velocity and the nature of the gas. The time history of the heat flux received by the sample can be determined by preliminary experiments in which the sample is replaced by a fluxmeter, but some heat-flux corrections are necessary in order to account for the fact that the surface conditions of the sample differ from those of the platinum film that supports the fluxmeter. Various measuring devices on a shock tube are shown in Fig. 8-5; these include photocells sensitive to light of different wavelengths, a high-speed motion picture camera, ionization gauges, an electronic chronometer for determining the shock wave velocity and a fast-response pressure transducer. The luminous energy generated during the ignition process varies with time as shown in Fig. 8-6. This shock-tube technique has produced interesting results. It was used by Summerfield and McAlevy (4) as well as by Ryan and Baer (5) and later by Kling, Maman and Brulard (6).

In addition to the conductive, convective and radiative mechanisms of heat transfer that we have been considering, energy can be generated at the propellant surface by exothermic chemical reactions between the propellant and hypergolic substances. For example, liquid or gaseous chlorine trifluoride (ClF_3), reacts strongly when brought into contact with the propellant surface. This reaction is sufficiently energetic to ignite the propellant. Techniques have been developed to study the hypergolic ignition delay as a function of pressure, active species concentration, solid temperature, etc.

In all of these fundamental experiments attempts have been made to simulate the actual motor ignition conditions. The essential characteristic of motor conditions is a high heat flux to the surface during very short times (a few milliseconds). The resulting ignition delay is extremely short, also of the order of a few milliseconds. Moreover, the pressure varies considerably during the ignition phase. Most experiments depart from these conditions. Therefore each of the techniques discussed above has certain disadvantages. In the oven technique, for example, natural convection and reradiation play an important role in determining the time evolution of the surface temperature; these conditions are noticeably different from those found in a motor. In arc-image experiments, although the incident energy flux and the ambient conditions are known accurately, a major inconvenience arises from the presence of cold gases close to the surface when ignition takes place, because in a motor the gas temperature close to the surface is usually very high. Dynamic methods seem to correspond more closely to actual motor ignition phenomena, but these techniques suffer from the defect that the heat flux to the surface varies with time, thereby causing conditions to be less well-defined than with static methods.

Many ignition delay results have been obtained with various types of propellants. Results obtained by different experimenters with the same propellant sometimes differ appreciably because of differing operating conditions. Comparisons are therefore often difficult to make. Comparison and application of experimental results could be greatly facilitated by standardizing some of the experimental techniques.

1.3. Experimental Results

The chief variables of interest in ignition are the energy required for ignition, the

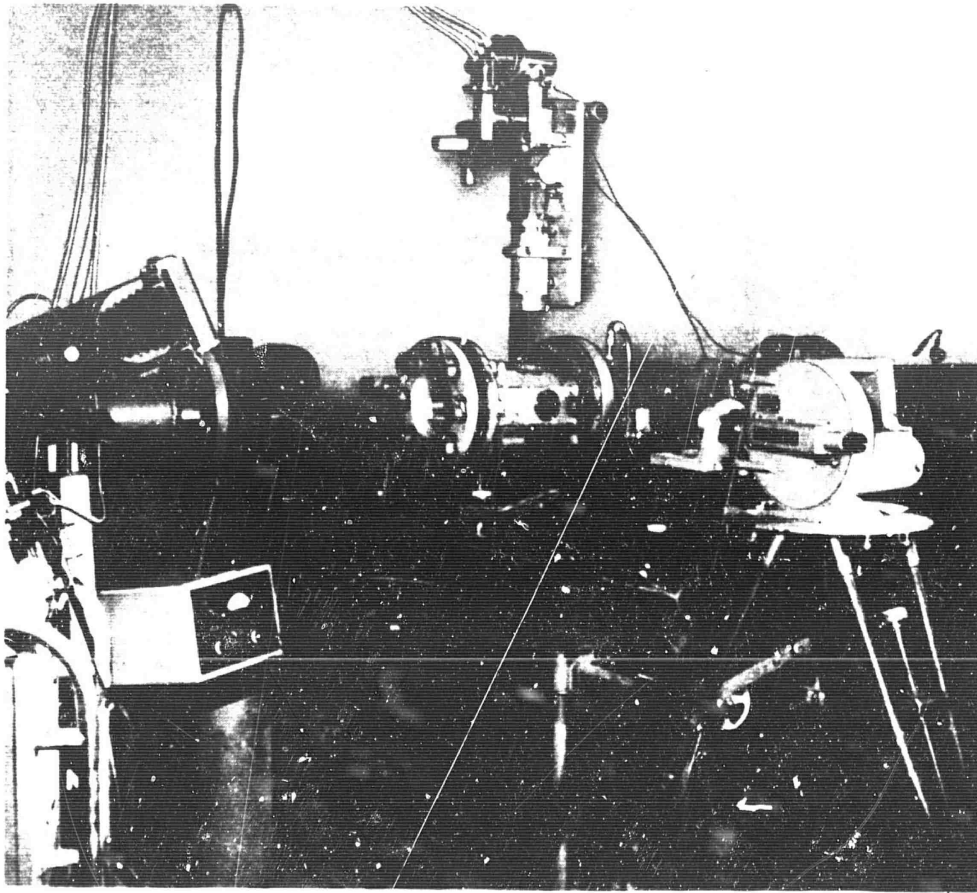


Fig. 8-5 General view of shock tube.

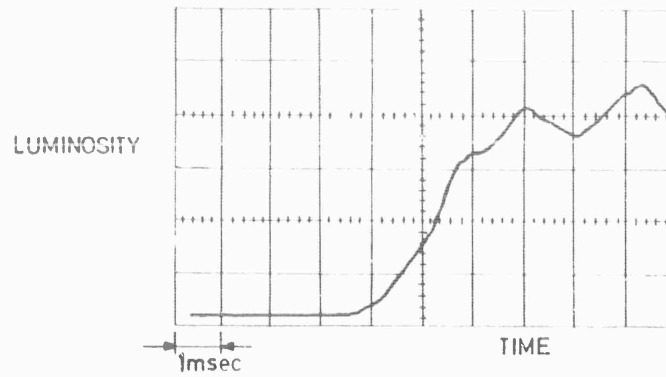


Fig. 8-6 Typical photocell oscillograph recording.

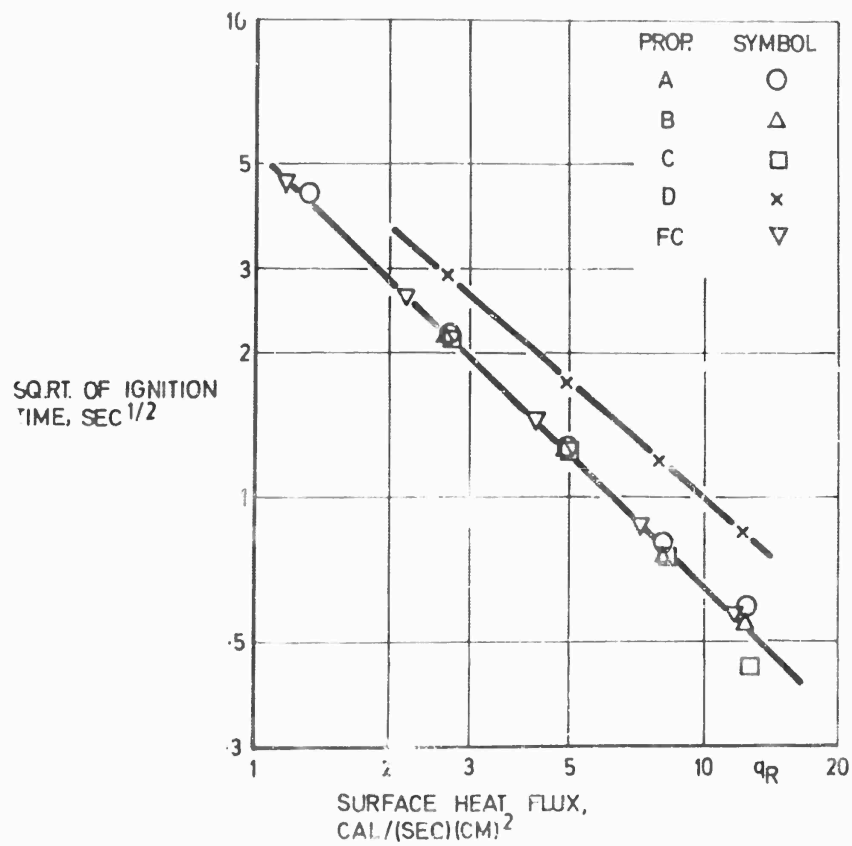


Fig. 8-7 The effect of surface heat flux on propellant ignition times - (1)

nature of the gases surrounding the sample, the pressure, the gas velocity near the surface, the propellant temperature, the nature of the propellant and the influence of certain catalysts.

a) Required Energy

In static methods the radiant energy flux q_R incident on the solid is kept constant during the ignition period. Most experiments (2), (7), (8) have shown that reasonable correlations for the ignition delay t_R are provided by formulas of the form :

$$t_R^{1/2} = a/q_R^n,$$

where a is a constant deduced from experiments and n is an exponent close to unity which, according to Baer and Ryan (1) can be expressed in the form :

$$n = 1 - 4.2 T_0/T_A,$$

In which T_0 is the initial sample temperature and T_A is the activation temperature related to the chemical ignition process. As Fig. 8-7 shows, this relation is reasonably well verified for five propellants, the properties of which are given in Table 8-1. The results can be correlated by plotting $\ln [(t_R/\lambda \rho c)^{1/2} (B/T_A)]$ as a function of $\ln (q_R/B)$, where B is the assumed frequency factor for the surface reaction, λ is the propellant thermal conductivity, ρ is the propellant density and c is the heat capacity per unit mass for the propellant.

We have indicated previously that with the arc-image technique, the ignition delay is often replaced by the minimum exposure time t_{ex} to achieve ignition. Rosser, Fishman and Wise (2) have proposed correlating the experimental results by a formula of the form :

$$q_R t_{ex} = (\alpha/q_R) + \beta,$$

where α and β are constants; this law is reasonably well verified by experiment (Fig. 8-8), but the results can also be correlated well by the previous formula :

$$t_{ex}^{1/2} = a/q_R^n$$

with $n = 0.8$, or else by the expression :

$$t_{ex}^{1/2} = a'/(q_R + K),$$

both of which are in good agreement with thermal theories that include exothermic surface reactions. Price's work (9) shows (Fig. 8-9) that when the total amount of heat q received by the propellant ($q = q_R \cdot t_{ex}$) is plotted as a function of q_R , one sometimes finds a minimum value of q at a particular value of q_R . The low- q_R portion of this figure is in agreement with the thermal theory, but the increase in q with increasing q_R at large values of q_R is an enigma that has not yet received a satisfactory explanation. It would be desirable to know both the ignition delay t_{ign} and the minimum exposure time for each experiment. From the few experiments for which such information is available, we find that for laws of the form :

$$t_{ex}^{1/2} = a_{ex}/q_R^{n_{ex}}$$

and :

$$t_{ign}^{1/2} = a_{ign}/q_R^{n_{ign}},$$

Propellant	A	B	C	D	F ²
Fuel Binder	Polysulfide	Polyurethane	BD/MVP Rubber	BD/MVP Rubber	PBAA
Oxidizer Crystal	AP	AP	AP	NH ₄ NO ₃	AP
Approximate Weight %					
Oxidizer crystal	76	82	86	84	80
Aluminum	2	2	0	0	0
Catalyst ³	1	in fuel	2	2	2 ³
Fuel binder	21	16	12	14	18
Density gr/cc	1.75	1.70	1.70	1.53	1.63
Thermal diffusivity cm ² /sec	0.00167	0.00139	0.00196	0.00196	0.00170
Thermal responsivity ($\Gamma = \sqrt{k\rho c}$) cal/(sec) ^{1/2} (cm ² (°C)	0.0229	0.0202	0.0233	0.0270	0.0212

¹ These values are at approximately 60°C. For calculation purposes, the surface absorptivity was assumed to be 0.9 for the propellants.

² The FC propellant was the same as F except a surface coating of carbon black was used during testing and an absorptivity of 1.0 was assumed.

³ The F propellant catalyst was Harshaw Chemical Co. Cu-0202-p copper chromite. The other catalysts were various compounds of iron.

Table 8-1. Summary of Propellant Chemical and Thermal¹ Properties (1).

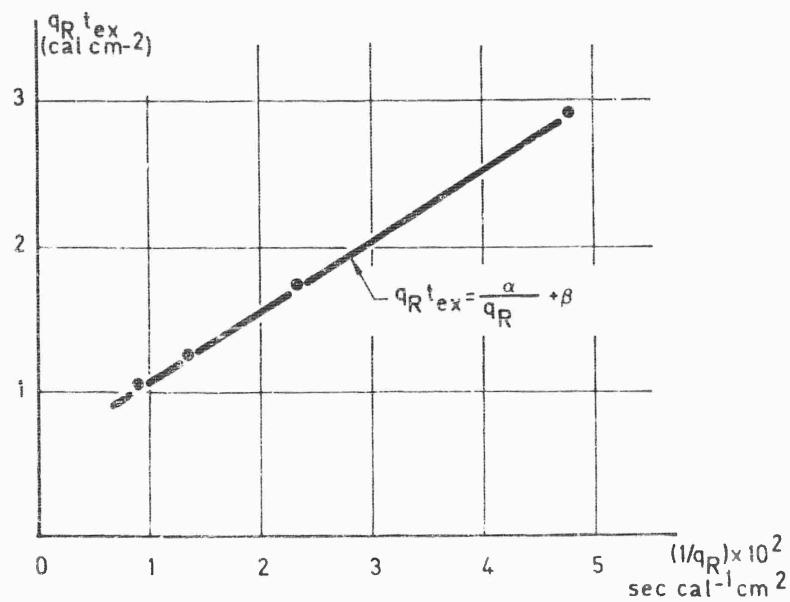
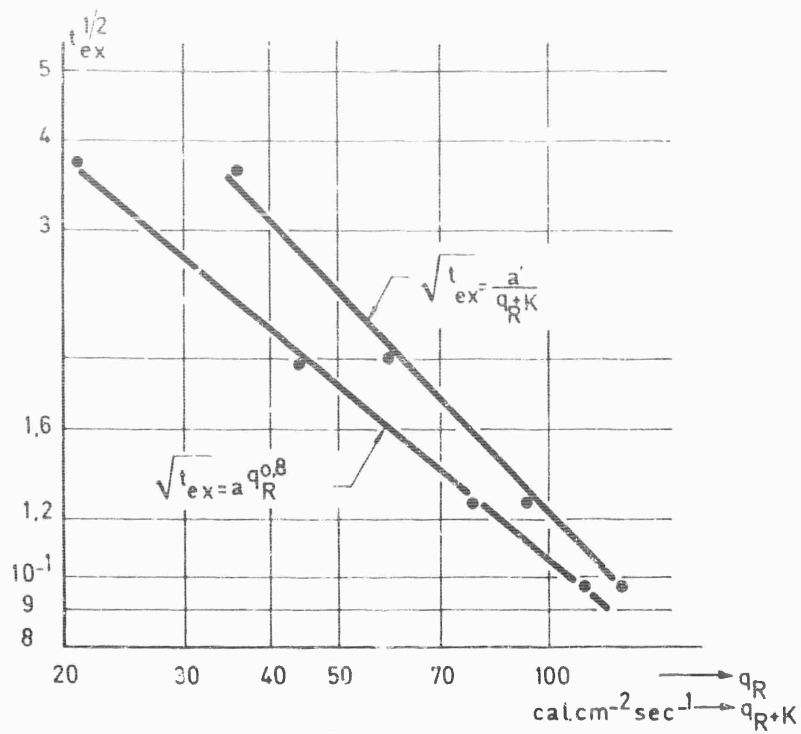


Fig. 8-8 A comparison of different expressions relating exposure time to radiant flux.

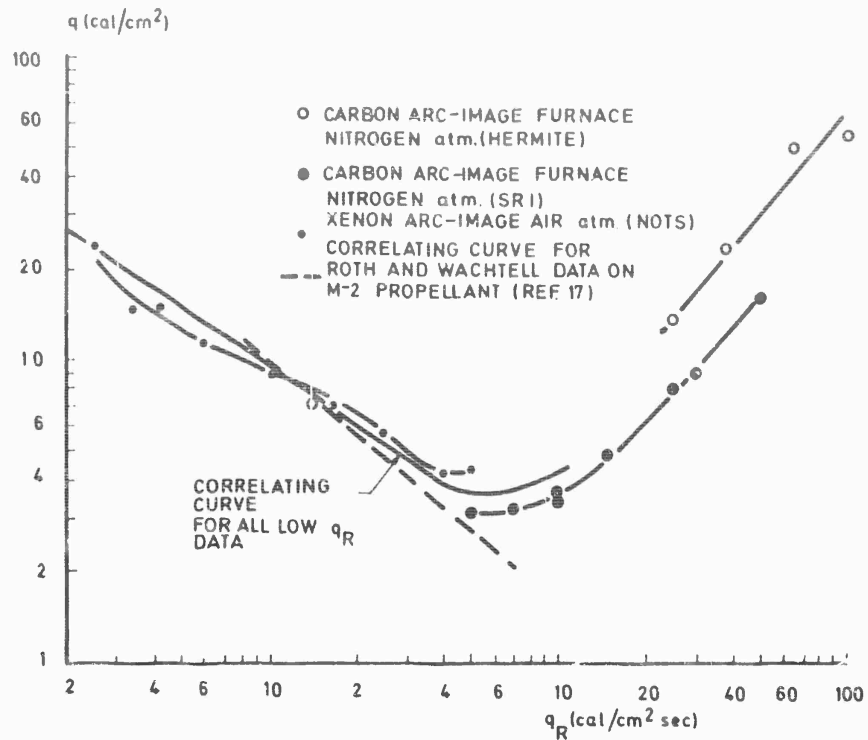


Fig. 8-9 Ignition energy of JPN double-base propellant at atmospheric pressure (70°F) (9).

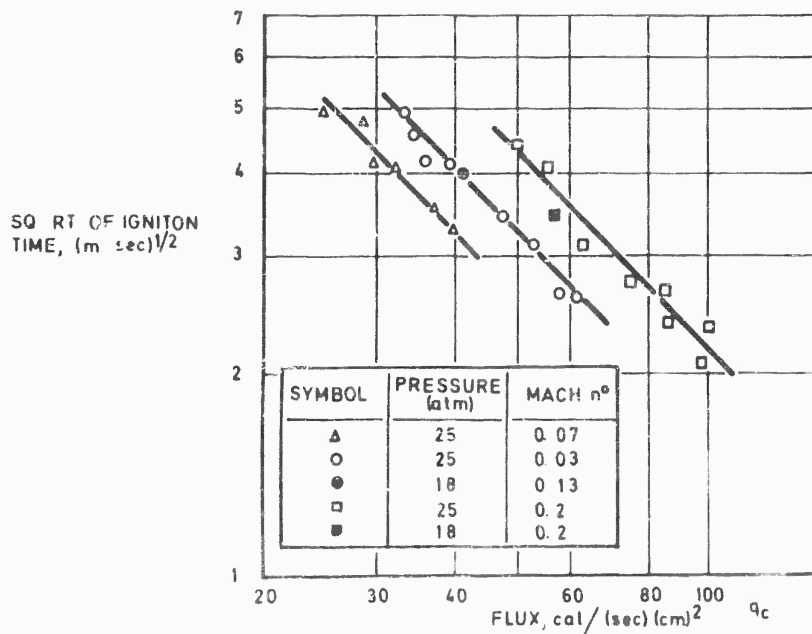
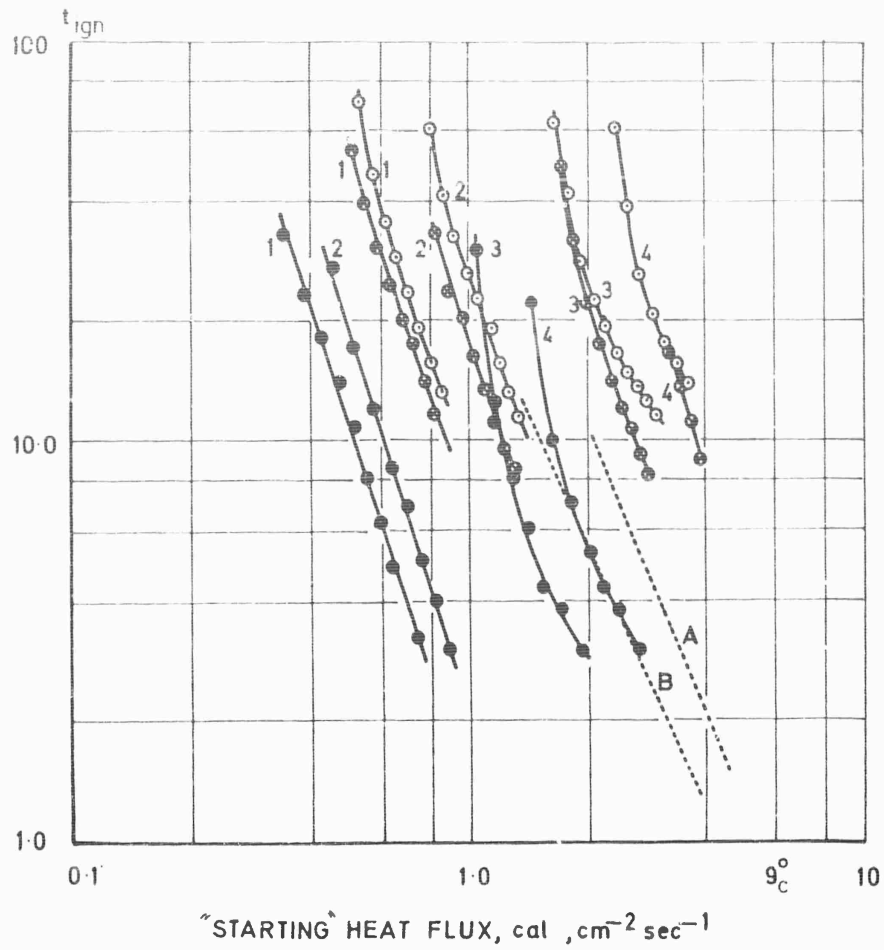


Fig. 8-10 Ignition of propellant J in nitrogen (12).



CURVE N°	EQUIVALENT FLOW RATE OF AIR, cc/sec AT N.T.P.	SYMBOL	PROPELLANT
1	125	●	RD 2406
2	250	○	E 3176
3	1250	●	SC CORDITE
4	2500		

CURVE No	DIAMETER OF SAMPLES
1	SC CORDITE 0-10 INCH
2	RD 2406 } 0-125 INCH
3	E 3176 }
4	FURNACE TUBE 0-90 INCH I.D.

Fig. 8-11 Variation of ignition delay time with "starting" heat flux for plastic propellants E 3176 and RD 2406 and SC cordite propellant sting-mounted (3).

SQ. RT. OF IGNITION TIME, (m sec) $^{1/2}$

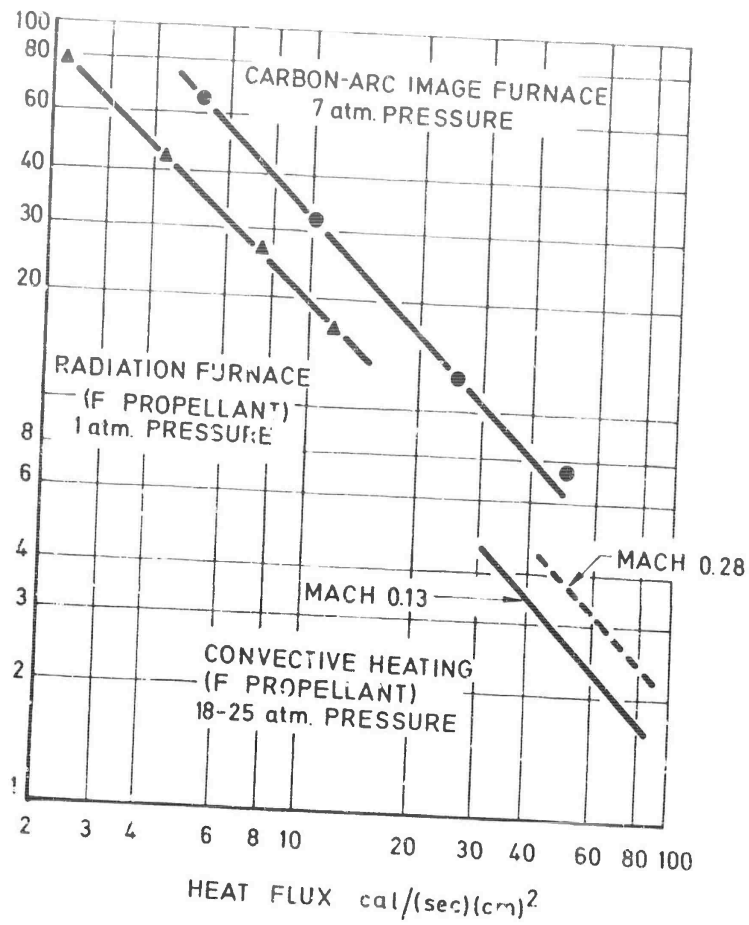


Fig. 8-12 Comparison between various methods (12).

ion, then atmospheric properties related to mass transport (diffusion) can be as important as those related to heat transport in affecting ignition times.

According to Sutton (3) the ignition delay of a sample in a hot gas stream decreases when nitrogen is replaced by helium in the 200° to 280°C temperature range (3). Other investigators who conducted studies in the 400° to 1000°C temperature range found that at low temperatures, the ignition delay is shorter in nitrogen than in helium, while the opposite is true at higher temperatures. These last results behave as if the activation temperature defined by the $|\ln t_{ign}|$ as a function of $1/T$ curve is higher for helium than for nitrogen and they can be interpreted theoretically by considering the effect of the diffusion rate of helium on the species concentration near the surface.

Reactive gases - If the ambient gas participates in surface or gas-phase reactions, then the ignition delay depends upon gas-phase concentrations. In order to separate pressure and composition effects, it is desirable to express gas-phase compositions in terms of mass or mole fractions, since the concentrations vary directly with pressure.

The influence of the presence of oxygen on the ignition delay has been studied principally with dynamic methods (4-6), (14-16). Two ignition regimes have appeared, corresponding to different ignition processes. For low or moderate oxygen mass fractions (Y_{O_2}) in the ignition delay remains approximately constant, while at higher oxygen mass fractions the ignition delay decreases rapidly with increasing oxygen mass fraction, approaching a minimum value in pure oxygen. The experimental data obey the equation :

$$t_{ign} Y_{O_2}^m = \text{constant} .$$

The value of m depends upon the ignition regime and the composition of the sample (Figs. 8-13a and 8-13b). Figure 8-14 shows the ignition delay versus oxygen concentration (from experiments performed by McAlevy and Summerfield (14)).

We have indicated that certain materials, principally fluorine and its compounds, produce hypergolic propellant ignition. The dependence of ignition delay times on the concentrations of hypergolic constituents resembles the dependence on the concentration of oxygen (13), (19).

c) Influence of the Pressure

The pressure dependence of the ignition delay is subject to debate. From all of the available experimental results, it is not possible to state generally valid trends (11).

Static methods yield differing results. Baer's work (1) shows that the ignition delay is independent of pressure (Fig. 8-15), but arc-image experiments reveal a pressure sensitivity (Fig. 8-16) for the minimum exposure time which is more marked at low pressures and at high incident fluxes. Pressure effects have been observed on both the minimum exposure time and the ignition delay. In an argon or helium atmosphere, the minimum exposure time is not very sensitive to the pressure, but the sensitivity is appreciable in a nitrogen atmosphere (2). This effect depends strongly upon the nature of the propellant.

With dynamic methods an inverse dependence of ignition delay on pressure has been observed (Fig. 8-17). However, it is difficult to separate the temperature and velocity effects from the pressure effect in shock-tube techniques.

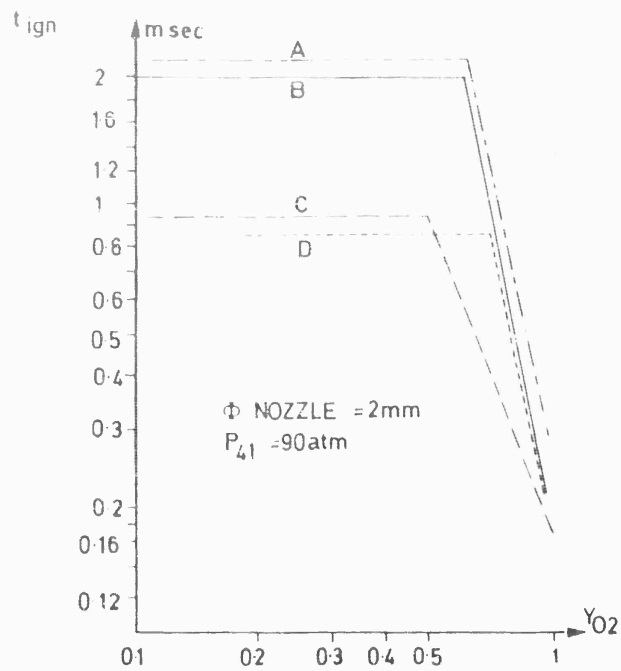


Fig. 8-13a Effect of oxygen mass fraction in the ambient gas on ignition delays of various composite propellants (15).

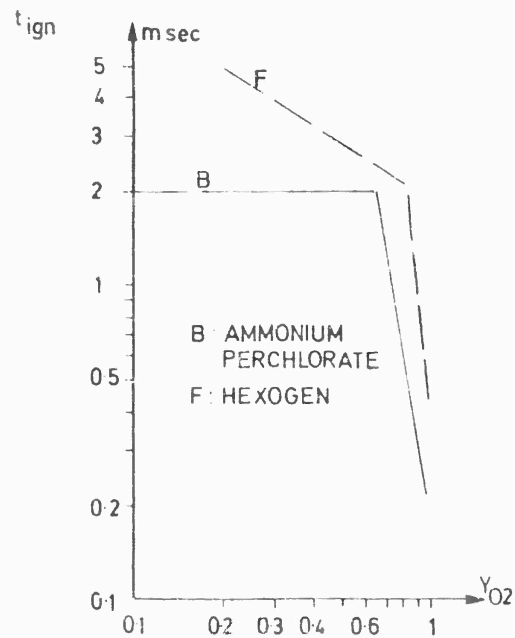


Fig. 8-13b Effect of oxygen mass fraction in the ambient gas on ignition delay with two different oxidizers (15).

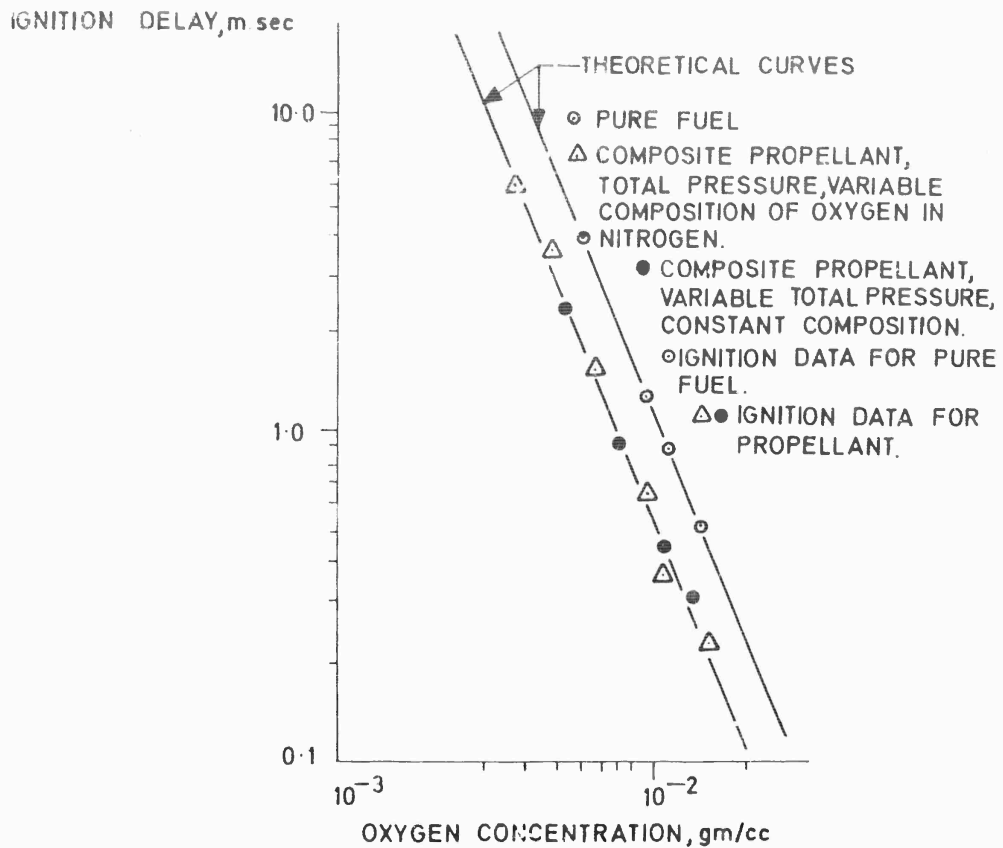


Fig. 8-14 Comparison of theory with experiment for the oxygen-polystyrene system (19).

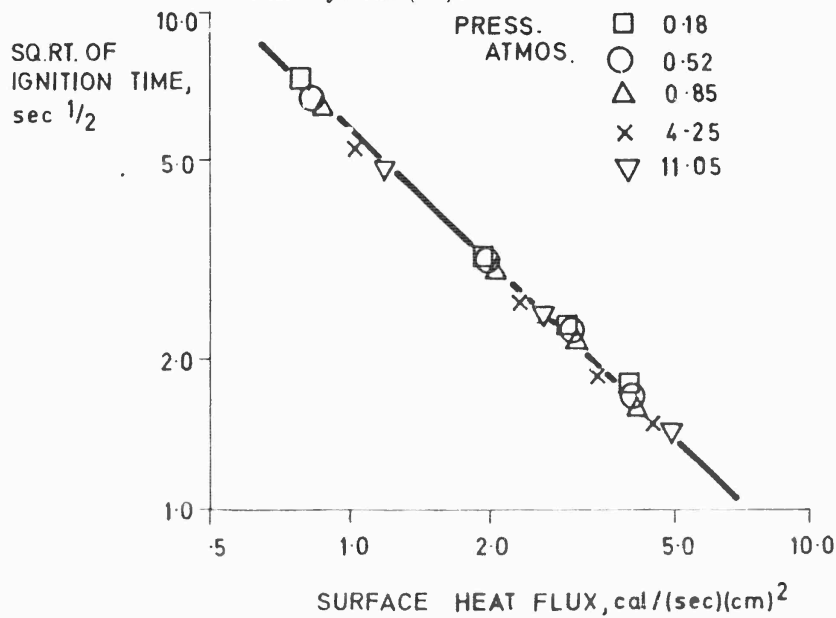


Fig. 8-15 The effect of pressure on the ignition times of the A propellant (1).

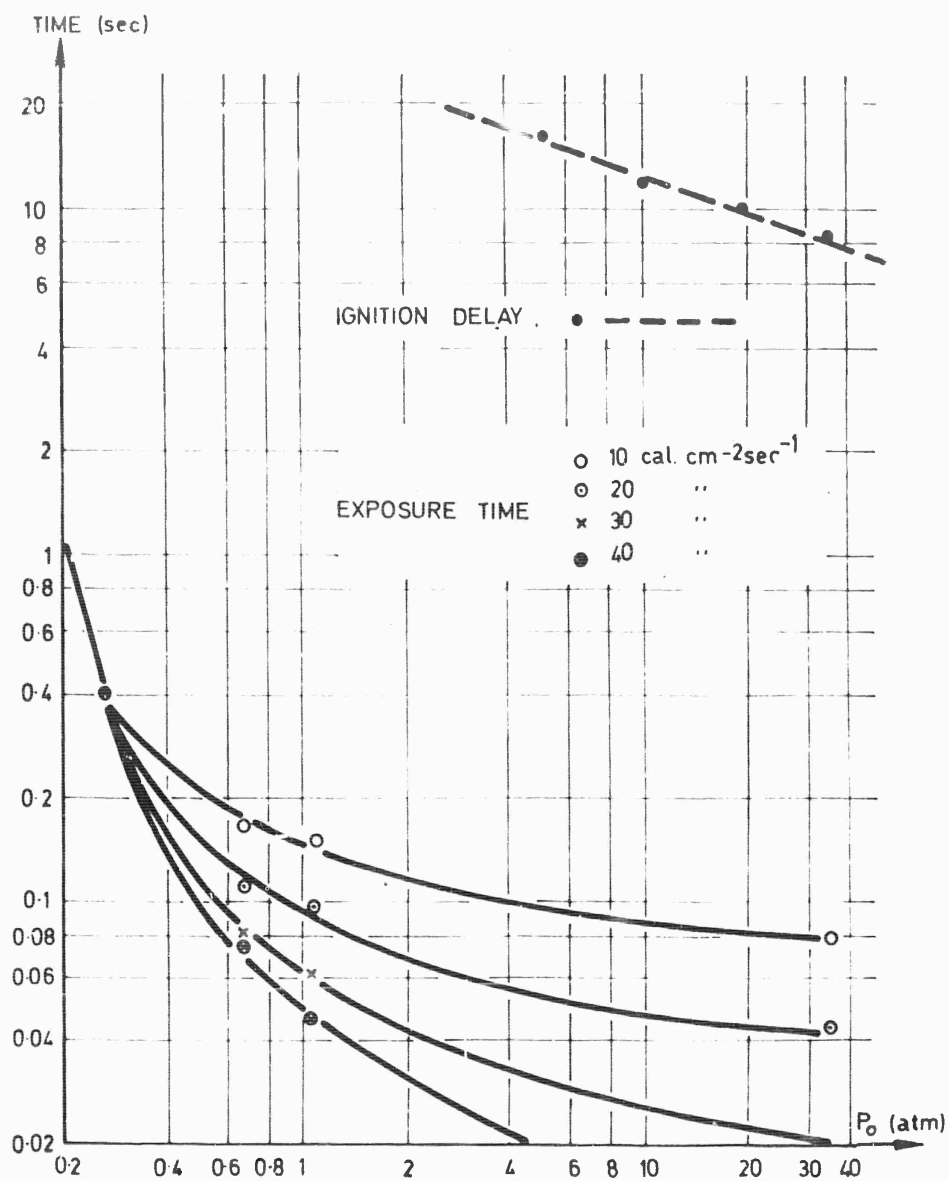


Fig. 8-16 Variation of ignition delay and exposure time with pressure (arc-image furnace).

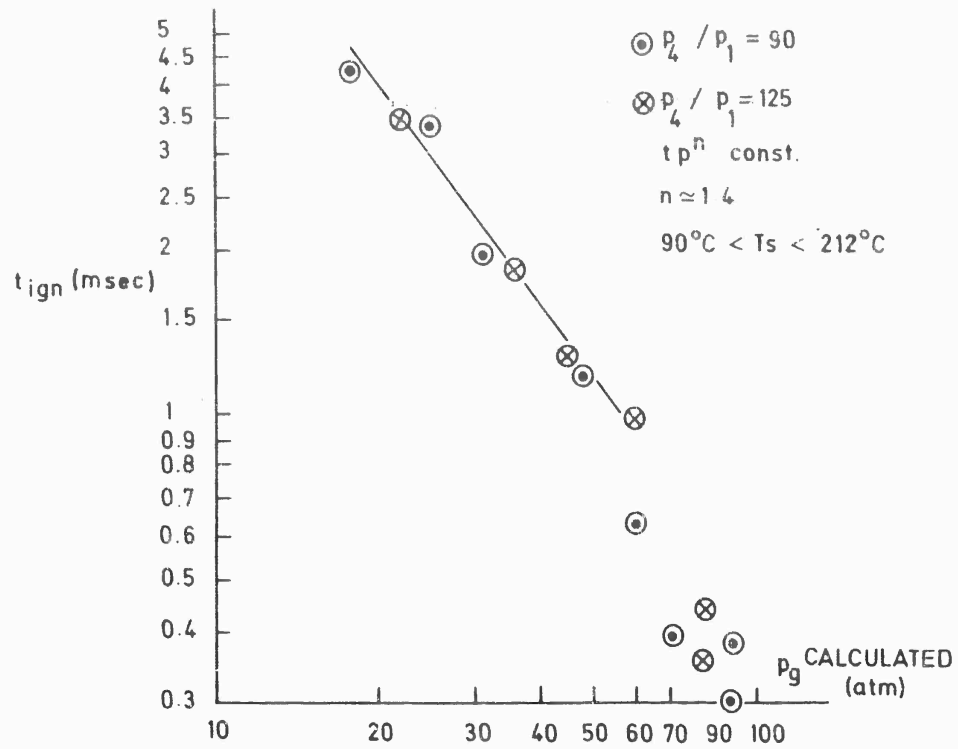
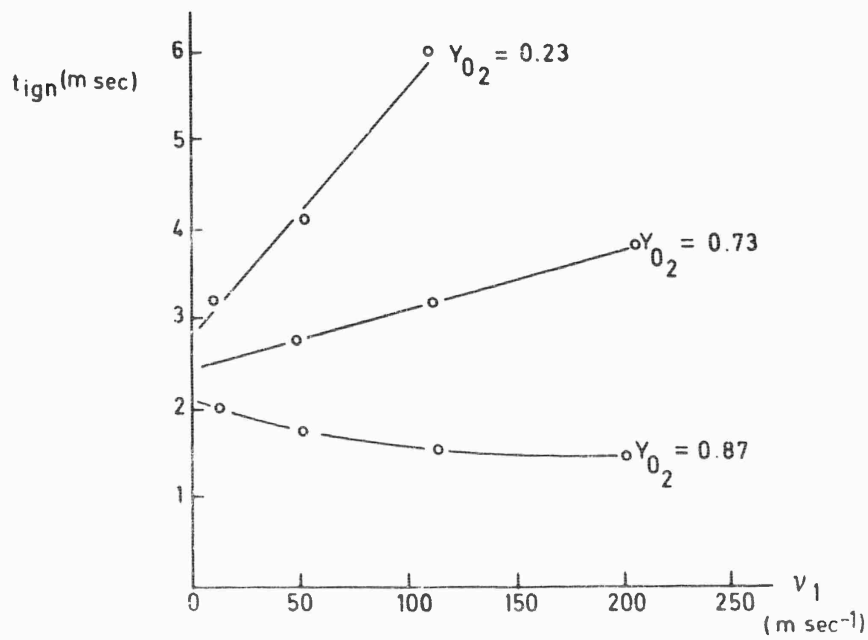


Fig. 8-17 Effect of pressure on ignition delay.

Fig. 8-18 Effect of oxidizer mass fraction and velocity on ignition delay; $p \approx 49$ atm.

d) Influence of Gas Velocity

The shock-tube technique shows that the ignition delay decreases when the Mach number increases, as shown in Fig. 8-10. This velocity effect is as difficult to discuss as is the pressure effect, since pressure, velocity and mass concentration effects operate simultaneously. Figure 8-18 illustrates this fact and shows that the ignition delay increases with increasing velocity at low oxygen concentrations but decreases slightly with increasing velocity at high oxygen concentrations. When a small sample of a propellant is placed in a hot, constant-temperature gas stream, the ignition delay generally decreases when the gas velocity increases. The velocity exponent is usually small (3) and depends much on the nature of the propellant and the sample geometry.

e) Influence of the Propellant and Gas Temperatures

The propellant grain temperature T_0 is often of importance. The magnitude of the effect depends on the nature of the propellant. Generally a decrease in ignition delay occurs when the temperature increases (see Fig. 8-19), but the experimental laws relating t_{ign} to T_0 are generally complex. Experiments at different propellant temperatures have been performed mostly with static methods; few results with dynamic methods have been recorded.

Dynamic methods enable one to study the variation of the ignition delay with the stagnation temperature of the gases flowing around the sample. Laws of the form :

$$t_{ign} = \eta \exp (T_A / T_g)$$

are generally obtained, as Fig. 8-20 shows. The activation temperatures are low and depend on the flow velocity, the nature of the surrounding gases and the nature of the propellant. Activation temperatures range from 3000° to 6000°K.

Attempts have been made to deduce the surface temperature at ignition from ignition delay experiments. In static methods this temperature T_s is computed from the delay measurements by using a simplified theory of ignition (1). The resulting surface temperature is independent of the initial grain temperature and is approximately proportional to the heat flux.

The surface temperature at ignition can be measured in the dynamic methods. An Arrhenius-type law relating the temperature to the ignition delay is then found.

f) Influence of the Nature of the Propellant

The physical properties of the propellant, as well as its chemical properties, have a definite influence on ignition delay which can be studied by varying the nature of the oxidizer, the nature of the fuel, the nature of the additives, the granule size or scale of heterogeneity of the ingredients and the surface composition.

The proportion of oxidizer and fuel at the surface of the propellant is obviously of importance in the propellant ignition. When the grain is manufactured by a casting process, the mass fraction of binder is larger at the surface than in the bulk of the propellant. This produces shorter ignition delays with a milled or freshly cut surface than with surfaces formed during the casting process. According to the experiments of Keller, Baer and Ryan (10) all of the results obtained with a certain number of propellants can be correlated in graphs of $(t_{ign}/\sqrt{\lambda \rho c})(B/T_A)$ as a function of q_R/B or q_c/B . The physical properties of the propellant play a role through λ , ρ and c and the chemical properties enter through the frequency factor B and the activation temperature T_A . In spite of the ever present difficulty of obtaining a

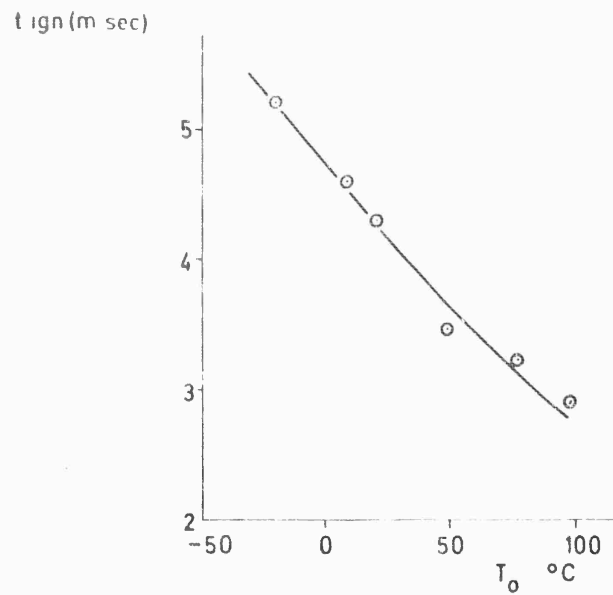


Fig. 8-19 Effect of initial propellant temperature on ignition delay.

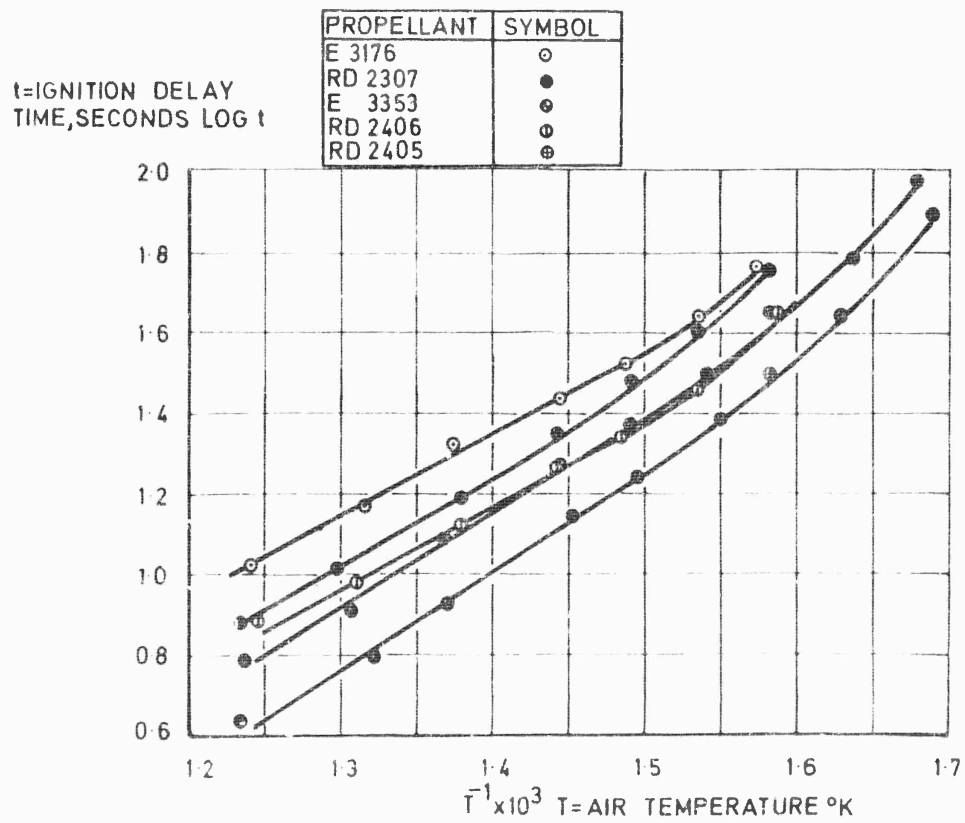


Fig. 8-20 Variation of ignition delay time with air temperature, shown as $\log t = f(T^{-1})$ for various plastic propellants, sting-mounted (3).

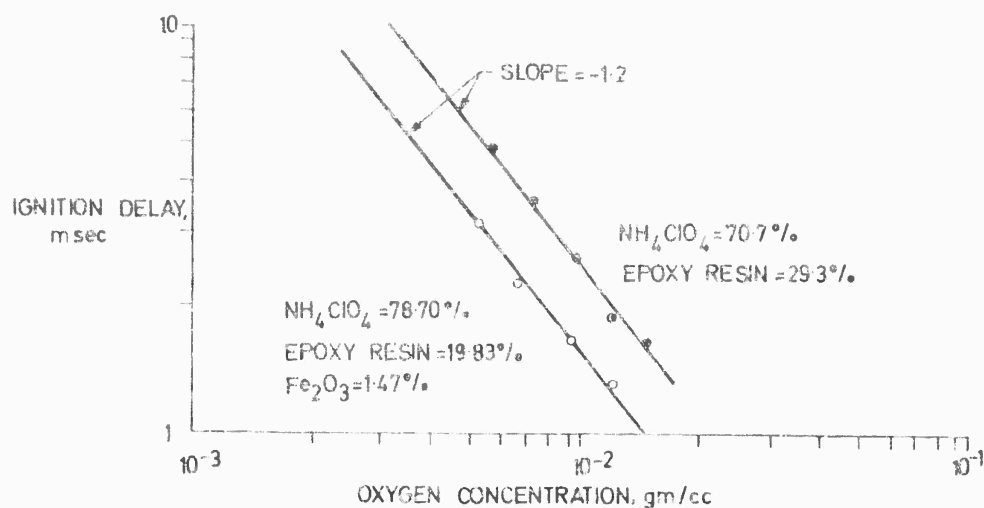


Fig. 8-21 Effect of catalyst on ignition delay time (19).

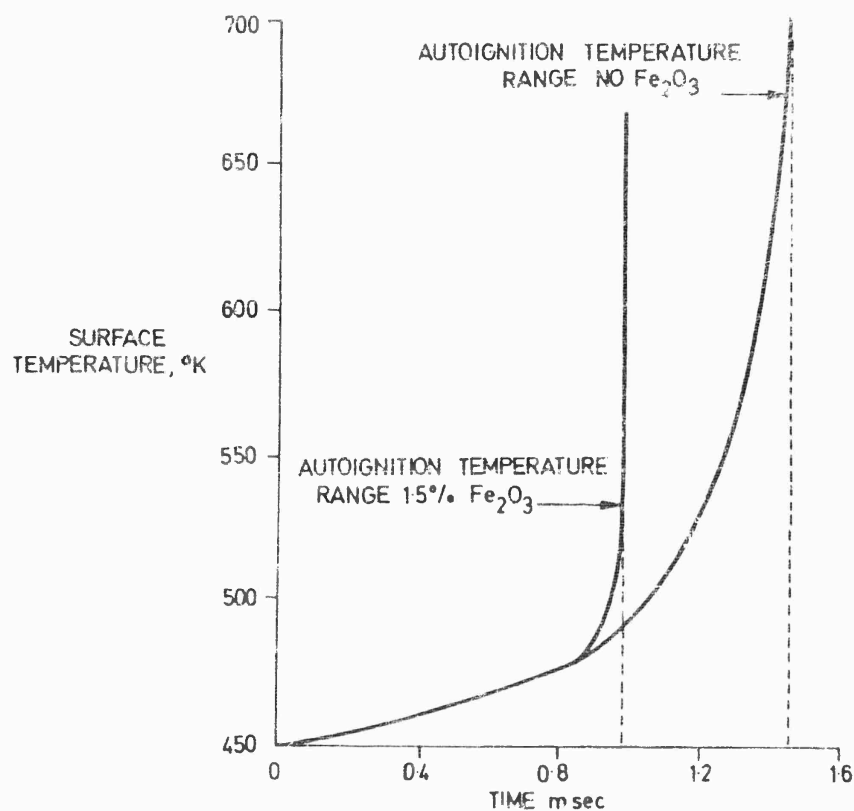


Fig. 8-22 Effect of catalyst on surface temperature history (19).

value for the frequency factor, good correlations are obtained for various propellants using ammonium perchlorate as an oxidizer and polysulfides, polyurethanes, methylvinylpyridenebutadiene or graphite as fuels (Fig. 8-7). However, the results are different if ammonium nitrate is the oxidizer.

The influence of the granule size upon the ignition delay is small; there is a slight increase in delay when the mean crystal diameter of ammonium perchlorate is decreased. This effect is noticeable principally when particle diameters are of the order of 20 microns and can be attributed to roughness of the surface. Roughness modifies the convective heat flux received by the sample. Much work has been devoted to the study of the ignition of each propellant component, in efforts to elucidate the important mechanisms controlling the ignition. We shall cite only the work of Hermance, Shinnar and Summerfield (20).

g) Influence of Catalysts

Many catalysts can influence the ignition delay. The most important ones are copper chromite and iron oxide (18). Figure 8-21 shows the influence of Fe_2O_3 . The ignition delay decreases when a small amount of iron oxide is added. This decrease can be attributed to a more rapid increase in surface temperature (see Fig. 8-22).

1.4. Theoretical Analyses of Ignition

1.4.1 Introduction

Because of the many different methods of ignition of solid propellants and because of the variety of different processes that may be of critical importance in the ignition mechanism, it is unreasonable to attempt to develop a general theory of solid propellant ignition. Indeed, even the most tedious numerical methods that have been employed, account for only a small fraction of the total number of phenomena that may be of importance. In view of this situation, we shall present highly simplified analyses of a few of the possible modes of ignition, with the aim of developing an understanding of various ignition mechanisms and as a basis for beginning a theoretical study of the qualitative influences of the variables on the ignition time lag (ignition delay) and on the conditions needed for ignition to occur. After obtaining some insight in this manner, we shall discuss other modes of ignition and shall review critically the published theoretical research on solid rocket ignition.

1.4.2 Ignition by Means of a Stagnant Hot Gas

Let us first consider ignition of a propellant, by means of a stagnant hot gas adjacent to the surface of the propellant. The gas may be heated by reflecting a shock wave from the propellant surface, for example. For times $t \leq 0$, the propellant and the gas are both at the constant temperature T_0 . At $t = 0$, the gas is instantaneously raised to the temperature T_∞ . One-dimensional, unsteady heat conduction ensues in both the gas and the solid. As a first approximation, all chemical reactions and phase changes prior to ignition will be neglected and ignition will be assumed to occur if and when the solid propellant attains a critical ignition temperature T_{ign} at some point.

The system is illustrated schematically in Fig. 8-23. One-dimensionality is postulated, and the origin of the spacial coordinate x is taken to be the solid-gas interface. Subscripts 1 and 2 will identify conditions in the gas and solid, respectively. The governing differential equations are :

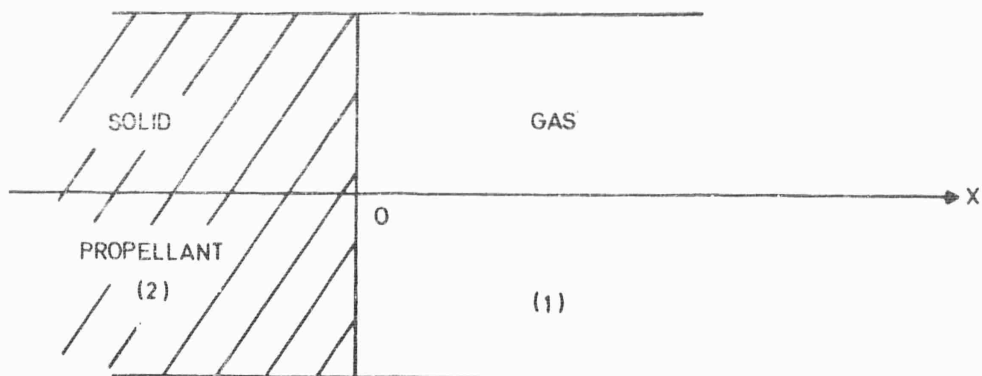


Fig. 8-23 Schematic illustration of propellant ignition model; stagnant hot gas.

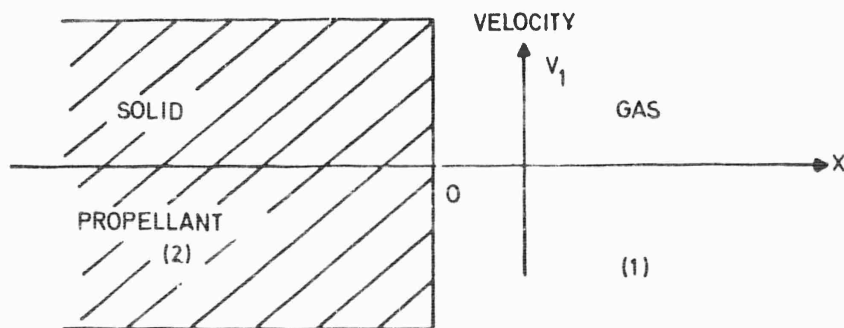


Fig. 8-24 Schematic illustration of propellant ignition model; flowing hot gas.

$$\frac{\partial T_\ell}{\partial t} = a_\ell \frac{\partial^2 T_\ell}{\partial x^2}, \quad \ell = 1, 2, \quad (\text{Eq. 8-1})$$

where the thermal diffusivity of medium ℓ is :

$$a_\ell = \lambda_\ell / \rho_\ell c_{p,\ell}, \quad \ell = 1, 2 \quad (\text{Eq. 8-2})$$

in which the space and time dependences of the thermal conductivity λ_ℓ , the density ρ_ℓ and the specific heat at constant pressure $c_{p,\ell}$ have been neglected for simplicity. Coordinate transformations may be introduced to remove these assumptions. The initial and boundary conditions to be employed for Eq. 8-1 are :

$$\left. \begin{aligned} T_1 &= T_\infty & \text{at } t &= 0(+) \quad (0 < x \leq \infty) \\ T_2 &= T_0 & \text{at } t &= 0(+) \quad (-\infty \leq x < 0) \\ T_1 &= T_\infty & \text{at } x &= \infty \quad (0 < t < \infty) \\ T_2 &= T_0 & \text{at } x &= -\infty \quad (0 < t < \infty) \end{aligned} \right\} \quad (\text{Eq. 8-3})$$

In addition, energy conservation at $x = 0$ implies that :

$$\lambda_1 \frac{\partial T_1}{\partial x} = \lambda_2 \frac{\partial T_2}{\partial x} \quad \text{at } x = 0 \quad (0 < t < \infty), \quad (\text{Eq. 8-4})$$

and continuity of temperature requires that :

$$T_1 = T_2 \quad \text{at } x = 0 \quad (0 < t < \infty). \quad (\text{Eq. 8-5})$$

Equations 8-1 through 8-5 define a classical heat conduction problem, the solutions to which depend only upon the single independent variable $x/2\sqrt{a_\ell t}$ in the appropriate region ℓ . Straightforward analysis yields :

$$T_1 = T_\infty - \frac{T_\infty - T_0}{1 + \frac{\lambda_1 \rho_1 c_{p1}}{\sqrt{\lambda_2 \rho_2 c_{p2}}}} \operatorname{erfc} \left(\frac{x}{2\sqrt{a_1 t}} \right), \quad 0 < x \leq \infty, \quad 0 < t < \infty \quad (\text{Eq. 8-6})$$

and :

$$T_2 = T_0 + \frac{T_\infty - T_0}{1 + \frac{\lambda_2 \rho_2 c_{p2}}{\sqrt{\lambda_1 \rho_1 c_{p1}}}} \operatorname{erfc} \left(\frac{-x}{2\sqrt{a_2 t}} \right), \quad -\infty \leq x < 0, \quad 0 < t < \infty, \quad (\text{Eq. 8-7})$$

where the complementary error function is defined as :

$$\operatorname{erfc}(z) \equiv \frac{2}{\sqrt{\pi}} \int_z^\infty e^{-y^2} dy. \quad (\text{Eq. 8-8})$$

The maximum temperature of the solid always occurs at the propellant surface and is given by :

$$T_2(0) = T_1(0) = T_0 + \frac{T_\infty - T_0}{1 + \sqrt{\frac{\lambda_2 \rho_2 c_{p2}}{\lambda_1 \rho_1 c_{p1}}}} \quad (\text{Eq. 8-9})$$

for all values of $t > 0$. According to Eq. 8-9, ignition will occur only if the initial gas temperature exceeds the critical value :

$$T_{\infty, cr} = T_{ign} + (T_{ign} - T_0) \sqrt{\frac{\lambda_2 \rho_2 c_{p2}}{\lambda_1 \rho_1 c_{p1}}} \quad (\text{Eq. 8-10})$$

which may be well in excess of the ignition temperature, if the propellant is dense and highly conductive or if the gas pressure is low. The pressure dependence of the critical initial gas temperature for ignition, given by Eq. 8-10, is :

$$(T_{\infty, cr} - T_{ign}) / (T_{ign} - T_0) \propto 1/\sqrt{p} \quad ,$$

in which the constant of proportionality is of the order of 10^2 when p is expressed in atmospheres. This result indicates that ignition by means of a stagnant hot gas will be difficult to achieve at very low pressures.

Since Eq. 8-9 implies that the propellant surface temperature is independent of time, the present model predicts that ignition will occur instantaneously if it occurs at all. Physically, the ignition time lag can, of course, never approach zero. Molecular considerations imply that the minimum time required for a hot gas to transfer its thermal energy to an adjacent solid is of the order of $\ell_m / v_m \alpha$, where v_m is an average molecular velocity, ℓ_m is a molecular mean free path and α is a thermal accommodation coefficient (21) for the surface with respect to the gas molecules. Unless α is extremely small ($\lesssim 10^{-6}$), this minimum molecular time is very short ($< 10^{-8}$ sec) and other phenomena, neglected in the present very simple model, will govern the ignition time lag.

1.4.3 Ignition by Means of a Flowing Hot Gas

Analysis - Let us next investigate the ignition of a solid propellant by means of a hot gas that is caused to flow over its surface. The flow may result from either forced or natural convection. At times $t \leq 0$, the propellant temperature T is constant and uniform ($T = T_0$). Convective heat transfer from the gas to the propellant begins at $t = 0$ due, for example, to the passage of a shock wave through the gas adjacent to the propellant surface, or to the arrival of a slug of hot gas at the surface. The gas-phase processes may be treated in terms of a phenomenological heat transfer coefficient h , defined in such a way that the energy per unit area per second transferred from the gas to the solid is $h [T_g - T(0)]$, where T_g is the temperature in the bulk of the gas and $T(0)$ is the surface temperature. We shall assume that one-dimensional, unsteady heat conduction occurs in the solid and shall neglect all chemical reactions and phase changes prior to ignition, employing an ignition temperature criterion, as in the preceding section.

The simplified model of ignition by a flowing gas is illustrated in Fig. 8-24. Equations 8-1 and 8-2 with $\ell = 2$ govern the heat flow in the solid; omitting the subscript 2 for brevity, we obtain :

$$\frac{\partial T}{\partial t} = a \frac{\partial^2 T}{\partial x^2} \quad (0 < t < \infty, -\infty \leq x < 0) \quad (\text{Eq. 8-11})$$

with

$$T = T_0 \quad \left\{ \begin{array}{l} \text{at } t = 0(+) \quad (-\infty < x < 0) \\ \text{at } x = -\infty \quad (0 < t < \infty) \end{array} \right.$$

as the governing differential equation and boundary conditions. The energy conservation condition at the interface is :

$$\lambda \frac{\partial T}{\partial x} = h (T_g - T) \text{ at } x = 0 \quad (0 < t < \infty). \quad (\text{Eq. 8-12})$$

It is again physically obvious that, with the present ignition model, the maximum temperature of the solid will occur at its surface, $x = 0$. Therefore, if we are interested only in ignition criteria, it is unnecessary for us to obtain the complete temperature distribution in the solid as a function of time. It will be sufficient for us to calculate the time development of the surface temperature. Since Laplace transform techniques (22) are rather well adapted to this type of calculation, they will be used here and also in subsequent paragraphs.

Let :

$$\bar{T}(x, s) = \mathcal{L}\{T - T_0\} \equiv \int_0^\infty (T - T_0) e^{-st} dt \quad (\text{Eq. 8-13})$$

denote the Laplace transform of $T - T_0$. Since $T = T_0$ at $t = 0(+)$, the governing heat equation becomes :

$$s \bar{T} = a \bar{T}'' , \quad (\text{Eq. 8-14})$$

where primes indicate derivatives with respect to x . The solution to this equation obeying the boundary condition $T = T_0$ at $x = -\infty$ is :

$$\bar{T} = A e^{\sqrt{\frac{s}{a}} x} \quad (\text{Eq. 8-15})$$

in which A is a function only of s . The only boundary condition now remaining to be satisfied is Eq. 8-12. Assuming that h is constant, we may write the transform of Eq. 8-12 as :

$$\lambda A \sqrt{\frac{s}{a}} = h (\bar{T}_g - A) , \quad (\text{Eq. 8-16})$$

where \bar{T}_g is the Laplace transform of $T_g - T_0$ and use has been made of Eq. 8-15. It will be recalled that λ and a have already been assumed constant. These restrictions can be lessened at the expense of reduced clarity. The solution of Eq. 8-16 for A is :

$$A = \bar{T}_g / (1 + \frac{\lambda}{h} \sqrt{\frac{s}{a}}) . \quad (\text{Eq. 8-17})$$

In view of Eqs. 8-13 and 8-15, the surface temperature is therefore given by :

$$T(0) = T_0 + \mathcal{L}^{-1} \left\{ \bar{T}_g / \left(1 + \frac{\lambda}{h} \sqrt{\frac{s}{a}} \right) \right\} , \quad (\text{Eq. 8-18})$$

where \mathcal{L}^{-1} denotes the inverse Laplace transform.

Once the gas temperature is specified as a function of time, the surface temperature may be computed as a function of time from Eq. 8-18, by first calculating the transform \bar{T}_g and then calculating the inverse transform appearing in Eq. 8-18. As an example, let us assume that T_g is constant for $t > 0$. Then :

$$\bar{T}_g = (T_g - T_0)/s ,$$

and Eq. 8-18 yields (23) :

$$T(0) = T_0 + (T_g - T_0) [1 - e^{h^2 at/\lambda^2} \operatorname{erfc}(h \sqrt{at}/\lambda)] , \quad (\text{Eq. 8-19})$$

which shows that $T(0)$ increases continuously and monotonically from T_0 to T_g as t increases from 0 to ∞ .

Equation 8-19 implies that, for ignition by means of a flowing hot gas, ignition eventually occurs [i.e., $T(0)$ eventually exceeds the ignition temperature T_{ign}] whenever the gas temperature T_g exceeds T_{ign} . The ignition time can be obtained from Eq. 8-19 by setting $T(0)$ equal to T_{ign} and solving for t . Explicit formulas for the ignition time t_{ign} can be written down in two limiting cases of interest by expanding the quantity in the square brackets in Eq. 8-19 for large and small values of t . The results are :

$$t_{ign} = \frac{\pi \lambda^2 \rho_2 c_{p2}}{4h^2} \left(\frac{T_{ign} - T_0}{T_g - T_0} \right)^2 \quad \text{if } t_{ign} \ll \frac{\lambda^2 \rho_2 c_{p2}}{h^2} \quad (\text{Eq. 8-20a})$$

(i.e., if $T_{ign} - T_0 \ll T_g - T_0$)

and :

$$t_{ign} = \frac{\lambda^2 \rho_2 c_{p2}}{\pi h^2} \left(\frac{T_g - T_0}{T_g - T_{ign}} \right)^2 \quad \text{if } t_{ign} \gg \frac{\lambda^2 \rho_2 c_{p2}}{h^2} \quad (\text{Eq. 8-20b})$$

(i.e., if $T_g - T_{ign} \ll T_g - T_0$),

where use has been made of Eq. 8-2 for a and the subscript 2 has been reinserted as a reminder that these properties refer to the solid. Equation 8-20a has been estimated to be valid for the experiments of Baer, Ryan and Salt (5), and their experimental results indicate that $t_{ign} \propto [h(T_g - T_0)]^{-2}$, in agreement with the theoretical equation. From Eq. 8-20 or, more generally, directly from Eq. 8-19, it may be inferred that the dependence of t_{ign} on properties other than temperatures is given by :

$$t_{ign} \propto \lambda_2 \rho_2 c_{p2} / h^2 . \quad (\text{Eq. 8-21})$$

This dependence will be precise only if the ignition temperature is independent of the parameters on the right-hand side, which according to more complex theories that consider reactions with Arrhenius rate functions and employ different ignition criteria, is not exactly true but is very nearly true unless the activation energy for the ignition reaction is very low. Measurable effects begin at activation energies around 30 kcal/mole.

Discussion of Results - According to Eq. 8-21, the ignition time increases in proportion to the thermal conductivity, density and specific heat of the solid propellant. The dependence of t_{ign} upon the properties of the gas is contained in the relationship $t_{ign} \propto h^{-2}$ and is therefore governed by the manner in which the heat transfer coefficient depends upon the properties of the gas. This, in turn, is influenced by the heat transfer mechanism. Formulas for the heat transfer coefficient are given in a number of textbooks (24), (25). We shall neglect Prandtl number effects in

the following discussion because the Prandtl number is close to unity for most gases.

For laminar flow past a flat plate of length L , the heat transfer coefficient h in forced convection is proportional to $\sqrt{\text{Re}} \lambda_1/L$, where the Reynolds number $\text{Re} = \rho_1 v_1 L / \mu_1$ depends upon the gas density ρ_1 , the coefficient of viscosity of the gas μ_1 and the gas velocity v_1 parallel to the surface. The dependence of t_{ign} upon gas properties then becomes :

$$t_{\text{ign}} \propto \mu_1 L / \lambda_1 \rho_1 v_1 \quad (\text{Eq. 8-22})$$

Since μ_1 and λ_1 are functions only of temperature and composition, the pressure dependence of t_{ign} at a given position L , for a given gas temperature and a given gas composition, and at a given gas velocity v_1 , is predicted by Eq. 8-22 to be $t_{\text{ign}} \propto p^{-1}$. On the other hand, for a given position, gas temperature and composition and at a given mass flux ($\rho_1 v_1$) or mass velocity, t_{ign} is independent of pressure. At a given temperature, pressure, composition and position, the ignition time as given by Eq. 8-22 is seen to be inversely proportional to the gas velocity or to the mass flux. The influence of geometry on t_{ign} , at a given gas mass flux, is expressed by $t_{\text{ign}} \propto L$. Effects of varying other parameters are readily apparent from Eq. 8-22.

For turbulent flow past a flat plate of length L , the heat transfer coefficient in forced convection is often quoted (24) to be proportional to $(\text{Re})^{0.8} \lambda_1/L$. When this relationship is employed, Eq. 8-22 is replaced by the expression :

$$t_{\text{ign}} \propto \mu_1^{1.6} L^{0.4} / \lambda_1^2 \rho_1^{1.6} v_1^{1.6}, \quad (\text{Eq. 8-23})$$

which indicates that t_{ign} is inversely proportional to the gas mass flux raised to the power 1.6 and directly proportional to the length L raised to the power 0.4.

For laminar flow in a tube of diameter D and length L , the heat transfer coefficient has empirically been found to be proportional to $(24) \text{Re}^{1/3} (D/L)^{1/3} \lambda_1/D$, where the Reynolds number is based on the tube diameter. The consequent implication regarding t_{ign} is :

$$t_{\text{ign}} \propto \mu_1^{2/3} D^{2/3} L^{2/3} / \lambda_1^2 (\rho_1 v_1)^{2/3}. \quad (\text{Eq. 8-24})$$

For forced convective heat transfer to the walls of a tube of diameter D in which the flow is turbulent, empirically (24) $h \propto \text{Re}^{3/4} \lambda_1/D$ with Re based on tube diameter, so that :

$$t_{\text{ign}} \propto \mu_1^{3/2} D^{1/2} / \lambda_1^2 (\rho_1 v_1)^{3/2}. \quad (\text{Eq. 8-25})$$

Heat transfer correlations for turbulent flows in more complex geometries appear rather generally to predict that t_{ign} will be inversely proportional to the mass flux raised to a power approximately equal to 1.5 and directly proportional to a characteristic dimension raised to a power lying between 0.4 and 0.5.

For heat transfer by natural convection, to either a horizontal or vertical plate, it has been found (24) empirically that, for laminar flow, $h \propto \text{Gr}^{1/4} \lambda_1/L$ and for turbulent flow, $h \propto \text{Gr}^{1/3} \lambda_1/L$. Hence for laminar free convective heat transfer:

$$t_{ign} \propto \mu_1^{1/2} L^2 / \lambda_1 \rho_1 g^{1/2} \quad (\text{Eq. 8-26})$$

and for turbulent free convective heat transfer :

$$t_{ign} \propto \mu_1^{4/3} L^2 / \lambda_1 \rho_1 g^{2/3} \quad (\text{Eq. 8-27})$$

where :

L = characteristic dimension of the plate

$$\text{Gr (Grashof number)} = L^3 \rho_1 g \beta_1 \Delta T / \mu_1^2$$

in which g = gravitation acceleration

β_1 = volume expansion coefficient of the gas

(= $1/T_g$ in an ideal gas)

$\Delta T \equiv T_g - T(0)$ = difference in temperature between gas and surface

Explicit temperature dependences have been omitted because temperatures influence t_{ign} through other parameters besides h . According to Eq. 8-26, for a given temperature and gas composition, $t_{ign} \propto p^{-1}$, $t_{ign} \propto g^{-1/2}$ and $t_{ign} \propto L^{1/2}$. On the other hand, Eq. 8-27 yields the corresponding dependences $t_{ign} \propto p^{-4/3}$, $t_{ign} \propto g^{-2/3}$ and t_{ign} independent of L .

Relationship to Stagnant Hot Gas Analysis - One might ask why a zero ignition time was obtained for ignition by a hot stagnant gas (in the absence of molecular considerations) but a finite ignition time was obtained for ignition by a hot flowing gas. The reason can be traced to the use in the present section of standard heat transfer theory with a heat flux proportional to the difference between the gas and surface temperatures, as compared with the assumption in the previous section of instantaneous contact between the hot gas and the cool propellant. Neither approach is entirely correct. That of Section 1.4.2 is objectionable as the manner in which the contact is produced is not considered. The present approach may be questioned on the grounds that the standard heat transfer theory applies to steady-state systems while the ignition process is obviously unsteady. The ignition time must be sufficiently long for the approach to be valid. Whenever the results in the present section are employed, it should be ascertained (at least *a posteriori*) that the ignition time is large compared with the appropriate characteristic heat transfer time; otherwise the approach is fundamentally unsound. For heat transfer across a laminar flat-plate boundary layer, the appropriate heat transfer time is the boundary-layer diffusion time, which can be shown to be approximately L/v_1 ; thus, Eq. 8-22 can be used only if $t_{ign} \gg L/v_1$. Similar estimates can be made for the other modes of convective heat transfer.

1.4.4 Ignition Processes Involving Heterogeneous Reactions and Radiant Energy Transfer

Introduction - As a first step toward accounting for the effects of chemical reactions, we shall consider now ignition by means of an initially cool, stagnant gas containing an active constituent, that is capable of reacting exothermically at the surface of the solid propellant. This type of reaction is mathematically simpler than a homogeneous reaction because linear diffusion equations still govern the gas-phase and solid-phase processes; nonlinear partial differential equations do not appear. The active gaseous constituent diffuses to the solid surface and reacts there at a

rate that is a function of the surface temperature and surface concentrations. When the heat liberated by the surface reaction raises the surface temperature to a critical ignition temperature T_{ign} , ignition is assumed to occur. It is again obvious that the temperature of the solid is a maximum at the solid surface. This model is quite realistic for ignition by injection of a hypergolic gas and has also been employed to correlate successfully certain experimental results for ignition by means of heated air, which is not normally hypergolic at low temperatures.

Ignition may also be achieved by applying a radiant heat flux to the propellant surface. We have seen that in laboratory experiments, the radiant energy source may be an arc image furnace, for example. It is often reasonable to neglect absorption of radiation by the gas and to assume that a known energy flux q_R (cal/cm²sec), equal to the product of the applied flux and the surface transmittance, is absorbed at the surface of the propellant. In such a model, the propellant is assumed to be sufficiently black for the width of the solid radiation absorption zone to be negligible. Since a radiant energy input of this type affects only the interface energy conservation condition, simple diffusion equations may still be employed in the gas and solid phases. In this respect, radiant ignition is similar to ignition by a hypergolic gas. This fact enables us to treat radiant energy input and surface reactions simultaneously in a theoretical analysis, thereby making it possible to study ignition in systems in which both effects are present and also providing an economy in presentation for analyses of each effect individually. Such an analysis will now be presented.

Derivation of Governing Integral Equation - Figure 8-23 provides a reasonable illustration of the system. One-dimensional time-dependent heat conduction and diffusion processes are considered, with homogeneous reactions and phase changes neglected prior to ignition. For times $t \leq 0$, the propellant and the gas are both at the constant temperature T_0 . At $t = 0$, the hypergolic gas is introduced with a constant molar concentration c_∞ throughout the gas phase ($x > 0$) and the radiant flux q_R is turned on, but the gas and propellant temperatures are not changed. For $t > 0$, the temperature at $x = \pm \infty$ is maintained at T_0 and the concentration of the hypergolic constituent at $x = \infty$ is maintained at c_∞ .

The heat flow is governed by Eq. 8-1, with a_i given by Eq. 8-2. In addition, the concentration c_1 of the hypergolic constituent in the gas is governed by the diffusion equation :

$$\frac{\partial c_1}{\partial t} = \mathcal{D}_1 \frac{\partial^2 c_1}{\partial x^2}, \quad (\text{Eq. 8-28})$$

in which, for simplicity, the diffusion coefficient \mathcal{D}_1 has been assumed to be constant. Boundary and initial conditions for Eqs. 8-1 and 8-28 are :

$$\left. \begin{aligned} T_1 &= T_0 \text{ at } t = 0(+) \quad (0 < x \leq \infty) \\ T_2 &= T_0 \text{ at } t = 0(+) \quad (-\infty \leq x < 0) \\ c_1 &= c_\infty \text{ at } t = 0(+) \quad (0 < x \leq \infty) \\ T_1 &= T_0 \text{ at } x = \infty \quad (0 < t < \infty) \\ T_2 &= T_0 \text{ at } x = -\infty \quad (0 < t < \infty) \\ c_1 &= c_\infty \text{ at } x = \infty \quad (0 < t < \infty) \end{aligned} \right\} \quad (\text{Eq. 8-29})$$

Boundary conditions at the interface are: temperature continuity,

$$T_1 = T_2 \text{ at } x = 0 \quad (0 < t < \infty), \quad (\text{Eq. 8-30})$$

energy conservation,

$$\lambda_2 \frac{\partial T_2}{\partial x} - \lambda_1 \frac{\partial T_1}{\partial x} = Q \mathcal{G}_1 \frac{\partial c_1}{\partial x} + q_R \text{ at } x = 0 \quad (0 < t < \infty), \quad (\text{Eq. 8-31})$$

and reaction rate,

$$\mathcal{G}_1 \frac{\partial c_1}{\partial x} = B f(c_1) e^{-T_A/T_2} = w \text{ at } x = 0 \quad (0 < t < \infty). \quad (\text{Eq. 8-32})$$

In Eq. 8-31, Q (cal/mole) is the heat released in the surface reaction per mole of gaseous species 1 consumed. In Eq. 8-32, T_A is the (constant) activation temperature (activation energy divided by universal gas constant) for the surface reaction, and B is the (constant) pre-exponential rate factor. The dimensions of B depend upon the form of the function $f(c_1)$ which expresses the dependence of the surface reaction rate upon the concentration of species 1, in the gas phase at the surface. A conventional approximation is :

$$f(c_1) = c_1^n,$$

where n is termed the order of the reaction and in which case the dimensions of B become $(\text{cm/sec})(\text{moles/cm}^3)^{1-n}$. If species 1 is weakly adsorbed on the surface, then the empirical value of n is the actual molecularity of the surface process with respect to species 1 and one would expect to find $n \geq 1$. If species 1 is strongly adsorbed on the surface, then $f(c_1) = [c_1/(1 + Kc_1)]^n$ (K = constant) may be more realistic than the conventional approximation and the empirical value of n in the conventional formula may be less than unity (26). This discussion assumes that the molecular adsorption process is rapid compared with the surface reaction rate; otherwise a formula more complicated than Eq. 8-32 may be required.

Introducing the Laplace transforms,

$$\bar{T}_i \equiv \mathcal{L} \{ T_i - T_0 \}, \quad i = 1, 2 \quad (\text{Eq. 8-33})$$

and :

$$\bar{T}_3 \equiv \mathcal{L} \{ c_1 - c_\infty \}, \quad (\text{Eq. 8-34})$$

we find, in view of the initial conditions, that Eqs. 8-1 and 8-28 yield:

$$s \bar{T}_i = a_i \bar{T}_i'', \quad i = 1, 2, 3, \quad (\text{Eq. 8-35})$$

where $a_3 \equiv \mathcal{G}_1$. In the general solution to Eq. 8-35,

$$\bar{T}_i = A_i e^{-\sqrt{\frac{s}{a_i}} x} + B_i e^{\sqrt{\frac{s}{a_i}} x}, \quad (\text{Eq. 8-36})$$

we must have $B_1 = A_2 = B_3 = 0$ in order to satisfy the boundary conditions given in Eq. 8-29. The remaining functions of s , viz., A_1 , B_2 and A_3 , are determined by Eqs. 8-30, 8-31 and 8-32.

Equation 8-30 implies that :

$$B_2 = A_1. \quad (\text{Eq. 8-37})$$

The Laplace transform of Eq. 8-31 yields :

$$\lambda_2 \sqrt{\frac{s}{a_2}} B_2 + \lambda_1 \sqrt{\frac{s}{a_1}} A_1 = -Q \sqrt{\frac{s}{a_3}} A_3 + \bar{q}_R, \quad (\text{Eq. 8-38})$$

where :

$$\bar{q}_R = \mathcal{L} \{ q_R \} \quad (\text{Eq. 8-39})$$

The transform of Eq. 8-32 is :

$$- \sqrt{\frac{s}{a_3}} A_3 = \mathcal{L} \{ w \}, \quad (\text{Eq. 8-40})$$

in which w is a nonlinear function of $c_1(0)$ and $T_2(0)$. We wish to solve for the surface temperature $T_1(0)$, which is given by :

$$T_1(0) = T_0 + \mathcal{L}^{-1} \{ A_1 \} \equiv T_0 + Z. \quad (\text{Eq. 8-41})$$

The functions B_2 and A_3 can be expressed in terms of A_1 , by using Eqs. 8-37 and 8-36. Substituting the resulting expression for A_3 into Eq. 8-40 yields :

$$\left(\frac{\lambda_2}{\sqrt{a_2}} + \frac{\lambda_1}{\sqrt{a_1}} \right) A_1 \sqrt{s} - \bar{q}_R = Q \mathcal{L} \{ w \}. \quad (\text{Eq. 8-42})$$

The convolution theorem,

$$\mathcal{L}^{-1} \{ \bar{F} \bar{G} \} = \int_0^t F(t-t') G(t') dt',$$

may be employed with $\bar{F} = 1/\sqrt{s}$ and $\bar{G} = s A_1$ to show that the inverse transform of Eq. 8-42 is :

$$\left(\frac{\lambda_2}{\sqrt{a_2}} + \frac{\lambda_1}{\sqrt{a_1}} \right) \int_0^t \frac{1}{\sqrt{\pi(t-t')}} \frac{d}{dt'} [Z(t')] dt' - q_R = Qw. \quad (\text{Eq. 8-43})$$

In Eq. 8-43, the identity $\mathcal{L} \{ 1/\sqrt{\pi t} \} = 1/\sqrt{s}$ and the result $\mathcal{L} \{ dZ/dt \} = s \mathcal{L} \{ Z \}$, which follows from Eq. 8-41 and from the initial condition for T_1 , have been employed. We may treat the surface temperature difference Z as the independent variable and the time t as the dependent variable in Eq. 8-43, obtaining, since $Z = 0$ at $t = 0$,

$$\int_0^Z \frac{dZ'}{\sqrt{t(Z) - t(Z')}} = g(Z, t) \quad (\text{Eq. 8-44})$$

where:

$$g(Z, t) \equiv \sqrt{\pi} \left(\frac{\lambda_2}{\sqrt{a_2}} + \frac{\lambda_1}{\sqrt{a_1}} \right)^{-1} \left[q_R(t) + QBf(c_\infty + \mathcal{L}^{-1}\{A_3\}) e^{-T_A/(Z+T_0)} \right] \quad (\text{Eq. 8-45})$$

The last term in the brackets in the definition of $g(Z, t)$ is simply Qw ; the explicit form given is obtained from Eqs. 8-30, 8-32 and 8-41 and from the observation that the argument of the function f is $c_1 = c_\infty + \mathcal{L}^{-1}\{A_3\}$ at $x = 0$, according to Eqs. 8-34 and 8-36 and the fact that $B_3 = 0$. The inverse transform appearing in Eq. 8-45 may be obtained by using Eqs. 8-37 and 8-38 to express A_3 in terms of A_1 and then employing Eq. 8-41 and the convolution theorem. The result is :

$$\mathcal{L}^{-1}\{A_3\} = - \left(\frac{\lambda_2}{\sqrt{a_2}} + \frac{\lambda_1}{\sqrt{a_1}} \right) \frac{\sqrt{a_3}}{Q\mathcal{D}_1} Z + \frac{\sqrt{a_3}}{Q\mathcal{D}_1} \int_0^t \frac{q_R(t-t')}{\sqrt{\pi t'}} dt' \quad (\text{Eq. 8-46})$$

Substituting Eq. 8-46 into the right-hand side of Eq. 8-45, yields a formula that can generally be expressed as an explicit function of Z and of $t(Z)$, because q_R is generally a specified function of t . Equation 8-44 therefore constitutes a nonlinear integral equation for $t(Z)$. By setting $Z = T_{ign} - T_0$, this becomes an equation for the ignition time t_{ign} as a function of the ignition temperature.

Solution for Small Values of t - In general, numerical procedures are required for solving Eq. 8-44. The numerical methods will, however, be much less tedious than those required for solving the coupled set of partial differential equations with which we began. An approximate solution to Eq. 8-44, valid for small values of Z or t , may be obtained by expanding the integral on the left-hand side of Eq. 8-44 about $Z = 0$, $t = 0$. The result is :

$$t = \pi^2 Z^2 / 4[g(0)]^2, \quad (\text{Eq. 8-47})$$

which yields :

$$t_{ign} = \frac{\pi}{4} (T_{ign} - T_0)^2 (\sqrt{\lambda_2 \rho_2 c_{p2}} + \sqrt{\lambda_1 \rho_1 c_{p1}})^{-2} \times [q_R(0+) + QBf(\infty) e^{-T_A/T_0}]^{-2} \quad (\text{Eq. 8-48})$$

where Eqs. 8-2, 8-41, 8-45 and 8-46 have been employed.

Numerical Solution for Hypergolic Ignition without Radiant Flux - If $q_R = \text{constant}$ and $f(c) = c^n$, then Eq. 8-44 can be written in the simplified nondimensional form :

$$\int_0^\theta \frac{d\theta}{\sqrt{\tau(\theta) - \tau(\theta')}} = \frac{1}{\gamma + 1} \left[\gamma + \left(1 - \alpha\theta + \frac{2\alpha}{\pi} \frac{\gamma}{\gamma + 1} \sqrt{\tau} \right)^n e^{\beta\theta/(1+\theta)} \right] = G(\theta, \tau), \quad (\text{Eq. 8-49})$$

where a dimensionless temperature is :

$$\theta \equiv Z/T_0, \quad (\text{Eq. 8-50})$$

a dimensionless ignition time is :

$$\tau \equiv [g(0, 0)/T_0]^2 t = (\sqrt{\lambda_2 \rho_2 c_{p2}} + \sqrt{\lambda_1 \rho_1 c_{p1}})^{-2} \pi [q_R/T_0 + (QBc_\infty^{-n}/T_0) e^{-\beta}]^2, \quad (\text{Eq. 8-51})$$

if the dimensionless parameter α has been defined as :

$$\alpha \equiv (\sqrt{\lambda_2 \rho_2 c_{p2}} + \sqrt{\lambda_1 \rho_1 c_{p1}}) T_0 / c_\infty Q \sqrt{\theta_1} , \quad (\text{Eq. 8-52})$$

the dimensionless activation energy is :

$$\beta \equiv T_A / T_0 , \quad (\text{Eq. 8-53})$$

and the dimensionless radiant flux is :

$$\gamma \equiv q_R / (QB c_\infty^n e^{-\beta}) . \quad (\text{Eq. 8-54})$$

The finite difference approximation to Eq. 8-49, viz.,

$$\Delta \theta \sum_{k=0}^{m-1} (\tau_m - \tau_k)^{-1/2} = G(\theta_m, \tau_m) , \quad m = 1, 2, \dots , \quad (\text{Eq. 8-55})$$

can be solved sequentially in m , by employing a systematic trial-and-error search procedure for finding τ_m at each step.

Equation 8-55 has been solved on an electronic digital computer for $\gamma = 0$ (no radiant flux) with $\Delta \theta = 10^{-3}/\alpha$. The results are shown in Figs. 8-25 to 8-28, which illustrate the effects of varying β (Figs. 8-25 and 8-26), n (Fig. 8-27) and α (Fig. 8-28) on the solution to Eq. 8-49 for τ as a function of θ . Clearly, the value of β has a strong influence on the solution; except in rather special and probably uninteresting regimes, reasonable variations in n or α will not change τ by an order of magnitude. We note that, consistent with Eq. 8-41, τ always becomes proportional to θ^2 as θ goes to zero and that when $n > 0$, τ approaches ∞ as θ approaches $1/\alpha$ (which is also obvious from Eq. 8-49 with $\gamma = 0$).

It is apparent from Figs. 8-25 through 8-28 (and can also be deduced from Eq. 8-49 directly) that if β is sufficiently large, then there will be a wide range of values of θ , over which τ changes very little. Typical solution curves for large β exhibit a quadratic increase of τ over a small range of θ near zero, a rapid leveling off to a "pseudostationary" value of τ , which lasts for most of the range of θ , then an abrupt increase (eventually approaching ∞) in $d\tau/d\theta$, when θ becomes very near $1/\alpha$. The existence of this pseudostationary value implies that when β is sufficiently large, the ignition time is practically independent of the ignition temperature, for all reasonable values of the ignition temperature. Numerical estimates indicate that if the activation energy of the heterogeneous reaction exceeds about 15 kcal/mole, the (usually ill-defined and poorly known) ignition temperature has no appreciable effect on the ignition time. In such cases the complete curves of Figs. 8-25 through 8-28 are of little interest; only the pseudostationary values of τ are important.

In order to be definite one may define the pseudostationary value of τ to be the value at the inflection point in Fig. 8-26 (the second inflection point in Fig. 8-27 or Fig. 8-28). This inflection value is plotted as a function of β for $n = 1$ in Fig. 8-29; its dependence on n and α is rather weak (Fig. 8-30). An empirical analytical expression for the dependence of the inflection value τ_1 on β is therefore of interest. The formula :

$$\log \tau_1 + 4.5 = 45/\beta ,$$

fits the $n = 1$, $\alpha = 1$ curve in Fig. 8-29, within about 20% for $\beta \gtrsim 30$ and within a

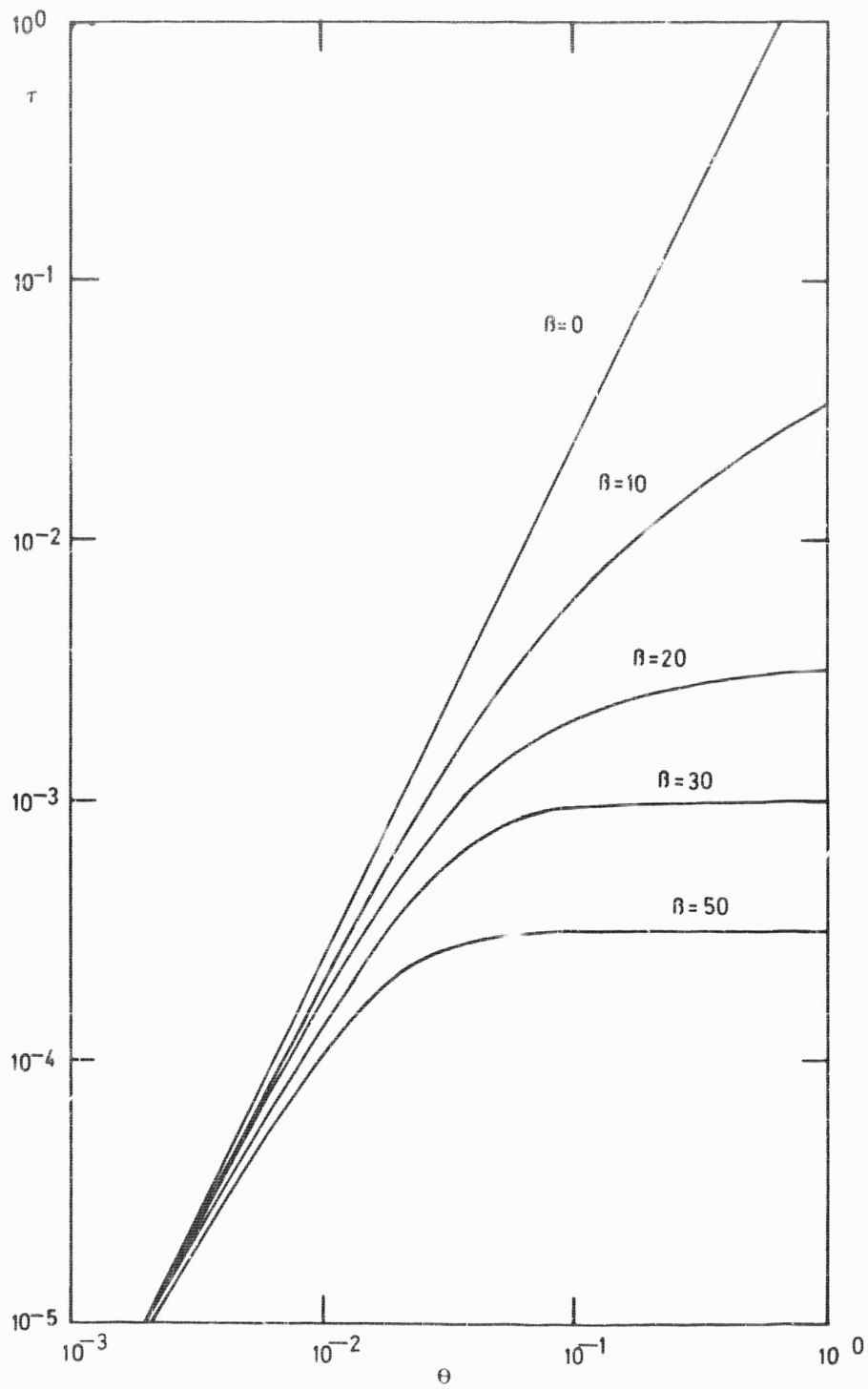


Fig. 8-25 Effect of β on ignition time for $n = 0$.

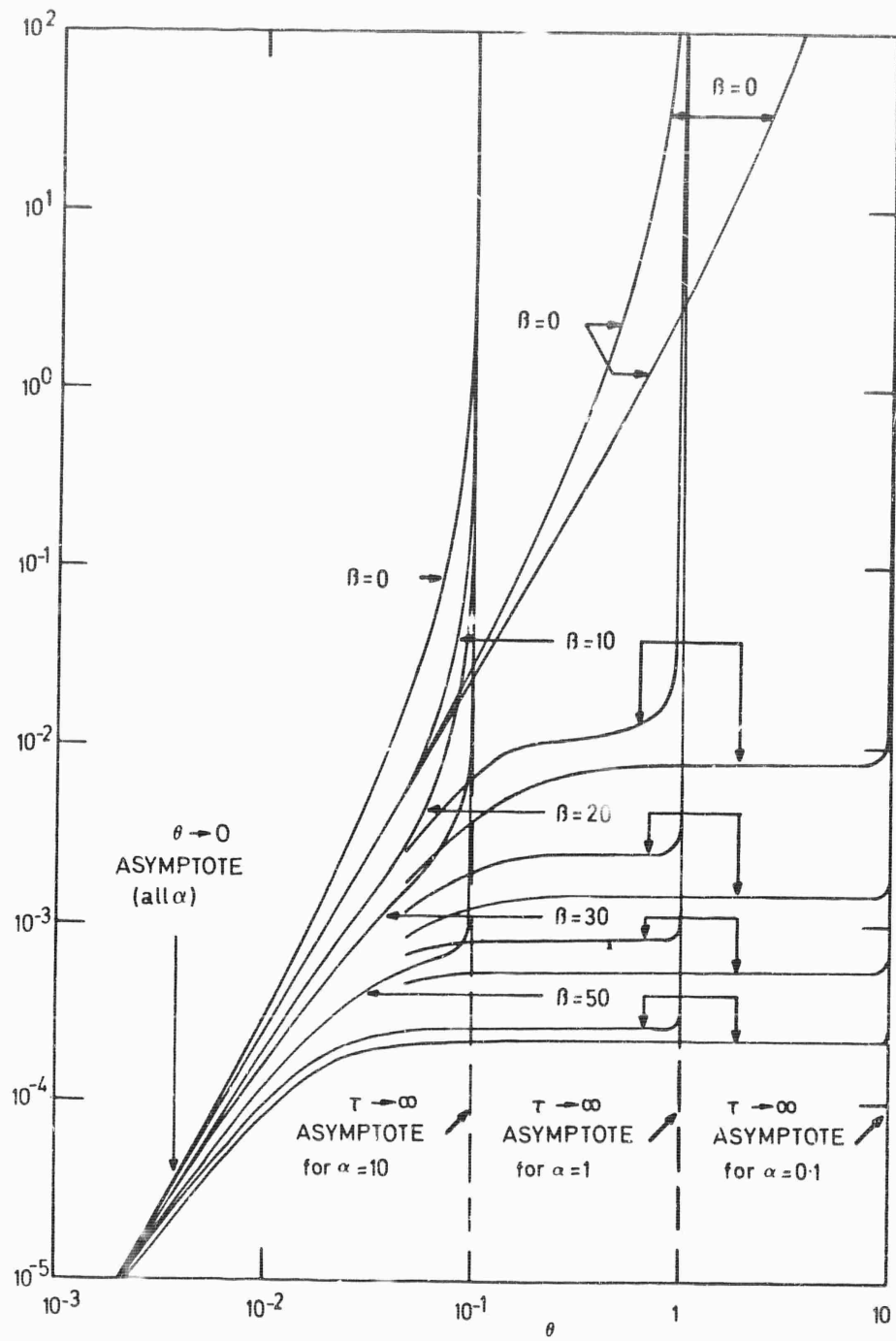


Fig. 8-26 Effect of β on ignition time for $n = 1$.

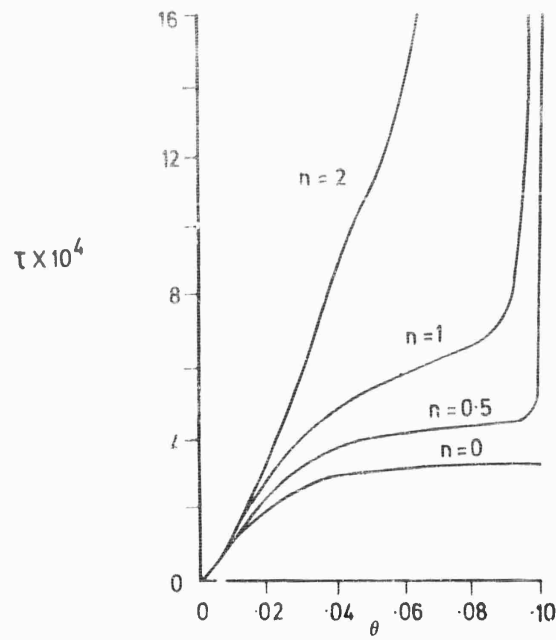


Fig. 8-27 Effect of n on ignition time for $\beta = 50$, $\alpha = 10$.

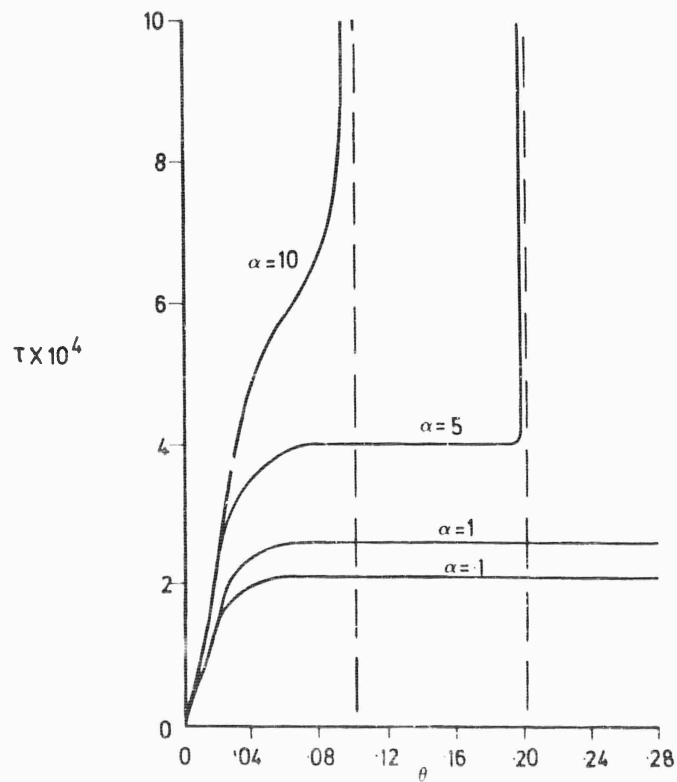


Fig. 8-28 Effect of α on ignition time for $\beta = 50$, $n = 1$.

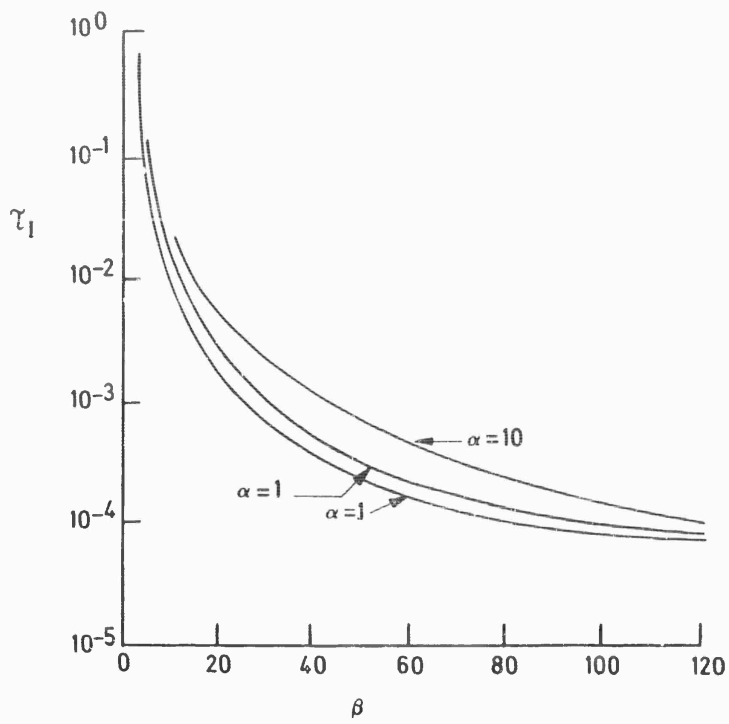


Fig. 8-29 Dependence of inflection point in ignition time on β for $n = 1$.

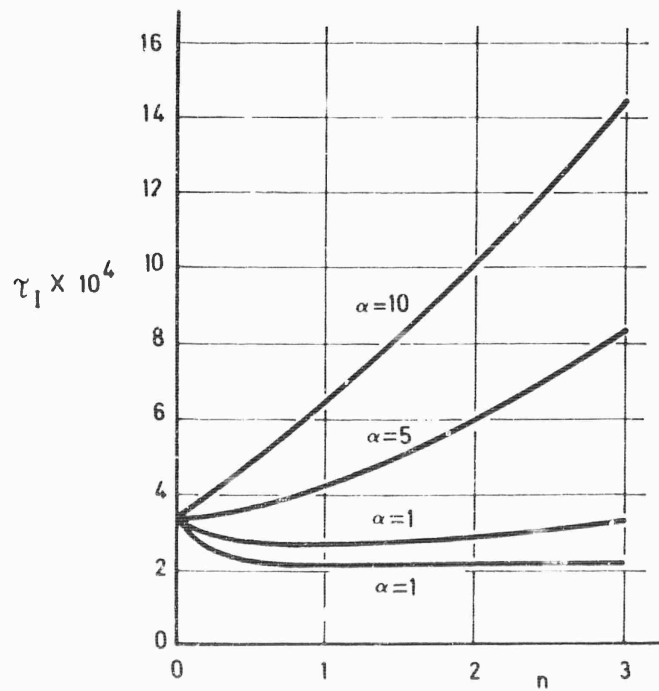


Fig. 8-30 Dependence of inflection point in ignition time on n and α for $\beta = 50$.

factor of 3 for $\beta \geq 20$. Agreement is always within an order of magnitude for $1 \lesssim \alpha \lesssim 10$, $0 \lesssim n \lesssim 2$ and $\beta \geq 20$. In terms of dimensional variables, the empirical formula yields for the ignition time :

$$t_i = (\sqrt{\lambda_2 \rho_2 c_{p2}} + \sqrt{\lambda_1 \rho_1 c_{p1}})^2 T_0^{-2} c_\infty^{-2n} (QB)^{-2} e^{2\beta - 11.5 + 100/\beta} \quad (\text{Eq. 8-56})$$

Discussion of Results for Hypergolic Ignition without Radiant Flux - Let us first consider the implications of Eqs. 8-48 and 8-56 for hypergolic ignition without an externally applied radiant heat flux. The following proportionalities can be inferred from Eqs. 8-48 or 8-56 if $q_R = 0$. Effect of heat of surface reaction:

$$t_{\text{ign}} \propto Q^{-2}; \quad (\text{Eq. 8-57a})$$

effect of rate of surface reaction:

$$t_{\text{ign}} \propto B^{-2}; \quad (\text{Eq. 8-57b})$$

effect of ignition temperature:

$$\begin{aligned} t_{\text{ign}} &\propto (T_{\text{ign}} - T_0)^2 && \text{if } T_A / T_0 \leq 5 \\ &\text{constant} && \text{if } T_A / T_0 \geq 20; \end{aligned} \quad (\text{Eq. 8-57c})$$

effects of thermodynamic and transport properties of solid and gas:

$$t_{\text{ign}} \propto (\sqrt{\lambda_2 \rho_2 c_{p2}} + \sqrt{\lambda_1 \rho_1 c_{p1}})^2; \quad (\text{Eq. 8-57d})$$

effect of concentration of hypergolic gaseous constituent:

$$t_{\text{ign}} \propto [f(c_\infty)]^{-2} = c_\infty^{-2n} \quad (\text{Eq. 8-57e})$$

with n = effective order of reaction (conventional approximation, the n of which may depend upon c_∞). Effect of pressure at constant gas temperature and relative composition:

$$t_{\text{ign}} \propto (1 + K_1 \sqrt{p})^2 p^{-2n} \quad (\text{Eq. 8-57f})$$

(conventional approximation). Here K_1 is a constant, the factor involving \sqrt{p} arises from the factor $(\sqrt{\lambda_2 \rho_2 c_{p2}} + \sqrt{\lambda_1 \rho_1 c_{p1}})^2$ and the value of K_1 is such that $K_1 \sqrt{p}$ is usually negligible compared with unity, at pressure below roughly 10 atmospheres. The value of n may depend upon p in the conventional approximation; if Langmuir adsorption occurs, then :

$$t_{\text{ign}} \propto (1 + K_1 \sqrt{p})^2 (1 + K_2 p)^{2n} p^{-2n}, \quad (\text{Eq. 8-57g})$$

where K_2 is a constant and now n is also constant. Effect of pressure at constant gas temperature and constant concentration of hypergolic constituent (pressurization by addition of inert):

$$t_{ign} \propto (1 + K_1 \sqrt{p})^2 \quad (\text{Eq. 8-57h})$$

This formula assumes that the inert is adsorbed to a negligible extent on surface reaction sites; if inerts can be adsorbed to inhibit the reaction, then we obtain, instead :

$$t_{ign} \propto (1 + K_1 \sqrt{p})^2 (1 + K_3 p)^{2n}, \quad (\text{Eq. 8-57i})$$

$K_3 = \text{constant}$.

Diffusion-Controlled and Rate-Controlled Limits - For surface reactions, a diffusion-controlled limit and a surface rate-controlled limit are often identified. These limiting cases are introduced in order to remove the nonlinear boundary condition given in Eq. 8-32, thereby facilitating solution of the partial differential equations. In the diffusion-controlled limit, the surface reaction is assumed to use up the reactants so rapidly that the boundary condition $c_1 = 0$ at $x = 0$ ($0 < t < \infty$) can be employed in place of Eq. 8-32. In the surface rate-controlled limit, the surface reaction is assumed to use up the reactants so slowly that the boundary condition $\partial c_1 / \partial x = 0$ at $x = 0$ ($0 < t < \infty$) can be employed in place of Eq. 8-32. In the latter case $c_1 = c_\infty = \text{constant}$ for all x and t in our present problem. Then $\mathcal{L}^{-1}\{A_3\} = 0$ and Eq. 8-57e, as well as all of the other proportionalities quoted in Eq. 8-57, except the one given in Eq. 8-57c are not subject to either the small t restriction employed in obtaining Eq. 8-48 or the pseudostationary approximation employed in obtaining Eq. 8-56. In the former case, a transient solution cannot be obtained from the present model. The condition $c_\infty \geq (\sqrt{\lambda_2 \rho_2 c_{p2}} + \sqrt{\lambda_1 \rho_1 c_{p1}}) (T_{ign} - T_0) / Q \sqrt{x_1}$ is obtained as an ignition criterion, but ignition is found to occur instantaneously if at all. This is a necessary condition for ignition whenever $q_R = 0$, as may be inferred from Eq. 8-49, for example. A molecular ignition time t_m can be inferred such that $c_1(0) = c_\infty e^{-t_m/\tau_m}$ and can be calculated to be $t_m / v_m \alpha_1$ (v_m = mean component of molecular velocity of species 1 normal to the surface, τ_m = mean free path of molecules of species 1, α_1 = "sticking" fraction or surface accommodation coefficient for molecules of species 1), but this involves introducing more physics than was contained in the original model. The exact solution to Eq. 8-44 with $q_R = 0$ is expected to approach that of the surface rate-controlled limit as B approaches zero and to yield a zero ignition time (the diffusion-controlled limit) when E approaches infinity.

Solution and Results for Radiant Ignition without Surface Reactions - Let us next consider ignition by radiant energy input, for systems that do not experience heterogeneous reactions prior to ignition. In this case, the second term inside the square brackets in Eq. 8-48 vanishes. This problem is, in fact, so simple that an exact analytical expression, not involving an integral equation, can be given for the surface temperature as a function of time. Since $w = 0$, dividing Eq. 8-42 by \sqrt{s} , taking the inverse transform and employing the convolution theorem, Eq. 8-2 and Eq. 8-41, we obtain :

$$Z = (\sqrt{\lambda_2 \rho_2 c_{p2}} + \sqrt{\lambda_1 \rho_1 c_{p1}})^{-1} \int_0^t \frac{q_R(t-t')}{\sqrt{\pi t'}} dt' \quad (\text{Eq. 8-58})$$

The special case in which q_R is constant is of practical interest; in this case Eq. 8-58 yields the exact solution :

$$t_{ign} = \frac{\pi}{4} (T_{ign} - T_0)^2 (\sqrt{\lambda_2 \rho_2 c_{p2}} + \sqrt{\lambda_1 \rho_1 c_{p1}})^2 q_R^{-2}, \quad (\text{Eq. 8-59})$$

which is seen to be identical with the corresponding limit of the approximate solution given in Eq. 8-48. The proportionalities 8-57c, 8-57d and 8-57h indicated above, are predicted by Eq. 8-59 for radiant ignition. In addition, Eq. 8-59 implies that the effect of the radiant energy flux is :

$$t_{ign} \propto q_R^{-2}. \quad (\text{Eq. 8-60})$$

This dependence has been verified in radiant ignition experiments, at flux levels, below roughly $10 \text{ cal/cm}^2\text{sec}$ in studies reported in Refs. (1), (7) and (9). These studies have been discussed in Sections 2 and 3.

Deviations from Eq. 8-60 occur at flux levels above $10 \text{ cal/cm}^2\text{sec}$. At present the most likely explanation for these deviations appears to be that gas-phase reaction times become important in the ignition process. The one-dimensional theory of ignition with combined radiant heat flux and heterogeneous reactions, developed in this section, does not appear to be capable of describing the observed deviations.

Discussion of Results with Combined Incident Radiation and Hypergolicity - With combined radiant flux and gas hypergolicity, Eq. 8-48 implies that the ignition time lag dependences given in Eqs. 8-57a, 8-57b, 8-57e and 8-60 will be weakened. For example, if exothermic surface reactions begin to become of importance in radiant ignition, then, in place of Eq. 8-60, t_{ign} will become proportional to $(q_R + K_4)^{-2}$, where K_4 is not explicitly dependent upon q_R when Eq. 8-48 is valid. Results of the integration of Eq. 8-49 with $\gamma \neq 0$ are not available yet and therefore only these qualitative statements, which are of limited validity, can be made at the present time.

Generalizations - We might add that the effect of heat loss from the propellant surface to a flowing cool gas can be included in Eqs. 8-48 and 8-56, in a rough manner. Forced convective gas flow increases the effective transport properties of the gas (viz., λ_1) by a factor of the form $(1 + a \text{Re}^m)$, where Re is the Reynolds number and a and m are constants. Values of m range from 0.3 to 0.8 and may be inferred from the discussion given in Section 1.4.3. This convective correction factor introduces into Eqs. 8-48 and 8-56 a dependence of t_{ign} on mass flow rate and on geometry; if a $\text{Re}^m \gg 1$, this dependence is contained in $t_{ign} \propto (1 + K_5 \text{Re}^m)^2$, where K_5 is independent of Re .

To include in the model given in this section the effects of conductive or convective heat transfer from a heated gas to the solid propellant requires a substantial extension of the analysis. Recently Waldman has included conductive heat transfer with shock-tube boundary conditions.

1.4.5 Ignition by Means of Condensed Materials

The preceding analyses considered only gaseous materials as ignition agents; any condensed materials contained in the igniter were assumed to vaporize before the beginning of the basic ignition process. This assumption is not always valid and some interesting new phenomena arise when the ignition agent contains a condensed phase.

First suppose that the igniter produces hot liquid or solid particles. A particular

example is ignition by means of hot Al_2O_3 . Then "contact" between the hot particles and the surface may lead to very high rates of heat transfer to the propellant, producing a correspondingly shortened ignition time. Exactly what constitutes "contact" is not yet clear. Do the solid particles rest on the surface of the propellant or is there a small gas film between the hot solid and the propellant, across which heat transfer takes place? Is a one-dimensional model sufficient, or must heat transfer along the surface, away from each solid particle, or flame spread along the surface, away from a hot ignition spot, be considered? The microscopic ignition mechanism is not known; many interesting problems concerned with the dynamics of heated spheres in a gas adjacent to a cool solid remain to be solved. Perhaps the analyses given in the Section 'Ignition by Means of a Stagnant Hot Gas' and 'Ignition by Means of a Flowing Hot Gas', will remain valid if only the gas density is replaced by the total mass per unit volume of the two-phase mixture and the gas heat capacity and gas thermal conductivity are replaced by mass-weighted average values, appropriate to the gas-solid (or gas-liquid) mixture. On the other hand, perhaps the particle dynamics must be studied to obtain a reasonable correlation of experimental ignition data. There appear to be no theoretical basic research results in this area.

Another ignition process falling under the present heading, is ignition by means of a cool hypergolic liquid. One might suppose that the analysis of hypergolic ignition given in Section 1.4.4, 'Ignition Processes', would apply to this process, if region 1 were assumed to be occupied by a liquid (so that Eqs. 8-57f, 8-57g, 8-57h and 8-57i would be invalid and t_{ign} would be independent of pressure); the model would then involve diffusion of liquid reactants to the surface and diffusion of the reaction products through the liquid, away from the surface. However, experiments with common hypergolic liquids have shown that the heterogeneous ignition reaction produces gaseous reaction products, that disturb the liquid and tend to disrupt the liquid-solid contact. When the heterogeneous reaction is very rapid, liquid droplets appear to shatter almost instantaneously upon reaching the surface; when the heterogeneous reaction is slow, a thick liquid layer appears to inhibit the heterogeneous reaction (perhaps by providing an additional heat sink, or possibly by preventing the escape of reaction products), and heterogeneous reactions appear to occur mainly where the liquid layer is thin, such as near the edge of a droplet resting on the propellant surface. Furthermore, the relative surface tension between the solid propellant and the hypergolic liquid appears to affect the overall ignition time; a liquid that wets the solid surface will produce ignition more rapidly. Processes of this type are clearly non-one-dimensional and also involve a number of physical phenomena that we have not considered above. The time required for flames produced at scattered hypergolic ignition sites to spread across the entire propellant surface may provide a substantial contribution to the total ignition time. The flame spread rate is treated on the basis of a very simple model in a later section concerned with pressure build-up in motors. The ignition time may also depend on the dynamical behavior of hypergolic liquid droplets resting on a propellant surface, which, as a theoretical problem, is very complex. Theoretical studies of realistic hypergolic liquid ignition processes apparently have not been attempted in the literature.

We may conclude that a theoretical understanding of ignition by means of condensed materials does not yet exist.

1.4.5 Critical Comparison of Existing Theoretical Studies

Hicks (27) has given a careful, detailed, theoretical analysis of an ignition model that is identical to the one considered in Section 1.4.3, 'Ignition by Means of a Flowing Hot Gas', except for the added complication that an exothermic reaction with an Arrhenius rate is included in the solid phase. This model is believed to be realistic for the ignition of certain homogeneous solid propellants which, at elevated tempera-

tures, experience exothermic solid-phase decomposition processes that proceed at non-negligible rates in the pre-ignition regime. Pre-ignition reactions in the solid may also occur for heterogeneous propellants. The essence of the analysis in Section 1.4.3 'Ignition by Means of a Flowing Hot Gas', is in fact, presented as a limiting case in the Appendix of Hicks' paper. Some numerical results for a model differing from that of Hicks only in that a constant specified radiant heat flux was employed in place of the convective heat flux, have been given in Ref. (9).

The distribution of temperature in the solid may be altered appreciably by solid-phase reactions. However, ignition always occurs at the surface in the Hicks model (except under very special conditions, when the external heat flux is turned on for a period of time too short to cause ignition, then shut off abruptly and the propellant is cooled from the surface), and the time required for the surface temperature to reach the ignition temperature is not influenced very much by the solid-phase reaction under representative ignition conditions. This is a consequence of the fact that, if the solid propellant has an acceptable degree of stability, then the solid-phase reaction rate is negligible for most of the heating time. After heat transfer causes the surface of the propellant to reach a temperature in the vicinity of the ignition temperature, the solid-phase reaction begins to release heat very rapidly at the surface, producing an extremely high time rate of change of surface temperature in a very short time. A consequence of this behavior is that, in the Hicks model, the ignition time is insensitive to the precise choice of ignition temperature; in place of a specified ignition temperature, a specified high time rate of change of surface temperature (e.g., 10^8 °K/sec) could be used in the Hicks theory as an ignition criterion and would produce no appreciable change in the calculated ignition time. This insensitivity does not appear in the theory of Section 1.4.3 'Ignition by Means of a Flowing Hot Gas', because the heat release mechanism that is responsible for it, is absent. Thus, analyses of the Hicks type can be useful for providing the appropriate ignition temperature for use in the above Section, if the rate constants for the exothermic solid-phase reaction are known. Since the high solid-phase reaction rate occurs only very near the surface, the exothermic process in the Hicks theory could probably be approximated very well as a heterogeneous surface reaction. Adding a temperature-dependent surface heat release rate to the analysis of Section 1.4.3 'Ignition by Means of a Flowing Hot Gas', should yield a theory that is much simpler than the Hicks theory (because the nonlinearity would affect only an ordinary differential equation instead of a partial differential equation) and that is capable of determining the appropriate ignition temperature from the Arrhenius rate constants. Numerical calculations based on a theory of this type for radiant ignition have been performed by Baer and Ryan (1).

Summerfield and coworkers (4), (11), (20) have made considerable progress in theoretical studies of solid propellant ignition processes involving exothermic gas-phase reactions. (A few consequences of a simplified gas-phase ignition theory have been discussed in Ref. (50)). They have been concerned with composite solid propellants containing NH_4ClO_4 as the oxidizer and also with pure binder-like fuels containing no oxidizer. It seems reasonable that gas-phase reactions and/or heterogeneous reactions will be of greater importance in the ignition of composite propellants than in the ignition of double-base propellants because the fuel and oxidizer constituents must be brought into molecular contact, before a significant amount of sustained heat release can occur in the composite system. Some of Summerfield's experimental results that apparently cannot be correlated by means of the simple theory given in Section 1.4.3 'Ignition by Means of a Flowing Hot Gas', have been interpreted qualitatively on the basis of gas-phase reactions (11). Unfortunately, the time-dependent gas-phase conservation equations become so complex when the necessary diffusion, flow and Arrhenius-type reaction rate terms are included that useful quantitative predictions of the results of specific ignition experiments, in which gas-phase reactions play an essential role, are very difficult to obtain. Thus far, lengthy finite-difference solutions to partial differential equations have been

necessary in order to study such basic problems as the pressure dependence of the ignition time.

The most complete analysis of gas-phase ignition that had been published before 1966 is contained in Ref. (20). Some of the assumptions in Ref. (20), may be listed as follows:

- a) A semi-infinite hot oxidizing gas is suddenly (at $t = 0$) brought into contact with a semi-infinite propellant.
- b) The propellant may be considered to consist of a single fuel which vaporizes and reacts with the gaseous oxidizer by a one-step Arrhenius rate process in the gas phase.
- c) One-dimensional, time-dependent conservation equations govern the process.
- d) The surface temperature remains constant during the entire ignition process.
- e) Either the gas-phase fuel concentration at the surface is constant or the mass flux of fuel at the surface is constant, during the entire process; in the gas phase the mass-average velocity is identically zero.
- f) In the gas phase the pressure and density are constant.

Assumptions (d) and (e) have been relaxed in the more recent work by these investigators.

Assumption (a) resembles an assumption of Hicks but it deserves closer scrutiny here, because the stated object is to obtain information concerning much shorter ignition times than those considered by Hicks. It is likely to be accurate for ignition of a material in the end of a shock tube by means of shock reflection. Assumptions (b) and (c) may be valid for liquid or solid hydrocarbons but are somewhat questionable for composite propellants. Experimental observations that during ignition binder pyrolysis usually begins before perchlorate decomposition, tend to support these two assumptions for NH_4ClO_4 composite propellants. Assumptions (d) and (e) appear to be unrealistic and have been replaced by physically acceptable interface conditions in newer works. The newer studies by Hermance and Summerfield employ the proper energy and species mass interfacial conservation equations, introduce an Arrhenius type of pyrolysis rate expression for the surface gasification rate and include a non-zero, time-dependent, mass-average velocity (which is spatially uniform in the gas phase); they predict values of ignition times that are near those of Ref. (20) for values of the initial grain temperature and fuel volatility that are of greatest interest in propellant ignition. Approximation (f) requires further study for rapid ignition processes; in parts of the gas, it causes the ratio of pressure to density to differ by about an order of magnitude, in representative cases from the ratio that is consistent with the equation of state and this difference may lead to appreciable pressure gradients and velocity gradients in the gas, for short ignition times.

Extensions of the study in Ref. (20) are beginning to produce results that have a direct bearing on propellant ignitions, involving gas-phase reactions. Detailed characteristics of gas-phase ignition mechanisms as well as parametric dependences of ignition times are beginning to emerge. One result which is already apparent, is that the specification of an ignition criterion is a somewhat sensitive and complex question for gas-phase ignitions. We would like to suggest here, on the basis of presently available results, that a reasonable definition of ignition time may be the time required for the first appearance of a temperature 'bulge' ($\partial T / \partial x \rightarrow 0$) at any point in the gas. Such a criterion cannot be used in other ignition models but it seems well-suited to gas-phase ignition and it appears to be relatively closely re-

lated to experimental definitions based on detection of luminosity. We feel that it is still a little too early to dwell at any greater length on theoretical models of gas-phase ignition.

It might be argued that representative gas-phase activation energies are so large that the gas-phase reactions proceed very rapidly once they begin and that therefore it should not be necessary to consider Arrhenius gas-phase heat release rates in propellant ignition. The gas-phase processes would merely help to determine the appropriate ignition temperature for use in simpler theories and this ignition temperature would not be very strongly dependent on the properties of the igniter gas. If this highly speculative view is correct, then heterogeneous processes are the only ones that can appreciably affect the dependence of ignition times on igniter properties. We have seen in Section 1.4.4, 'Ignition Processes . . .', that heterogeneous reaction theories are rather fertile in their ability to correlate experimental ignition-time data. Heterogeneous reactions have been studied by Anderson and co-workers (28-30).

Anderson (28) developed a theoretical model that is basically the same as that presented in Section 1.4.4, 'Ignition Processes . . .', except that the radiant energy transfer term was not included. The governing partial differential equations were solved by finite difference techniques on an electronic digital computer. Through appropriate adjustment of the activation energy for the surface process, the rate constant for the surface process and the effective order of the surface reaction, Anderson obtained excellent correlations of the experimental results (14) and of the results of a number of other experiments. This same agreement is, of course, also obtained from the analysis in Section 1.4.4, 'Ignition Processes . . .'. In some cases, Anderson's correlations also involved empirical adjustments, for the effects of varying the amount of oxidizer contained in the propellant and of adding a burning rate catalyst to the propellant. In each of these cases the qualitative nature of the effect was reasoned theoretically. The success serves to emphasize the versatility of a heterogeneous reaction hypothesis.

A few objections to the details of the theoretical formulation and qualitative arguments cited by Anderson can be mentioned. He states (28) that in the diffusion-controlled limit, $t_{ign} \propto c_{\infty}^{-2n}$ at constant total pressure and $t_{ign} \propto c_{\infty}^0$ at constant oxidizer mole fraction. These results are not consistent with our finding (Section 1.4.4 'Ignition Processes . . .') that $t_{ign} \equiv 0$ in the diffusion-controlled limit for Anderson's model. Many arguments can be given against the reasoning (29) that mechanical properties of the propellant constituents affect the ignition behavior; for example, the thermal skin depth is less than or equal to a typical oxidizer particle diameter and the temperature gradient will cause the perchlorate material closest to the surface to decompose most rapidly, thus causing the heterogeneous reactions to occur at the propellant surface instead of inside the solid. The heat balance equation (30) used by Anderson to account for convective heat (ignition in a flow environment) adds a convective heat input term to the surface boundary condition and at the same time retains a conductive heat loss from the surface to the gas. It also neglects convective effects on the transfer of oxidizer to the surface. The Anderson analysis is not likely to be valid when convection occurs. It would be straightforward and could prove interesting to apply the standard methods of mass and heat transfer theory to ignition by means of a flowing gas with the ignition process involving heterogeneous reactions. Such an analysis would constitute an extension of the theory of Section 1.4.3, 'Ignition by Means of a Flowing Hot Gas'.

The theory of ignition of solid propellants is a vast and often complex subject. We have insufficient space here to present a complete review of each aspect of all of the relevant theoretical studies. An excellent and much more thorough review, with which we agree on most, but not all points has been prepared recently by Price (8).

1.5. Motor Ignition

Introduction

During ignition, the pressure level in a solid propellant rocket motor increases from its initial value to the steady operating pressure. Depending upon the igniter, the propellant and the geometry, the pressure-time curve may be monotonic or a pressure peak may develop. The primary objective in this section is to obtain an understanding of the shape of the pressure-time curve during ignition.

Effects tending to increase the pressure are gas evolution by the igniter and gas evolution from the surface of the propellant. Gas flow through the nozzle tends to decrease the pressure. The time-dependent balance of these three mass flow processes, coupled with the appropriate energy balance for the gases in the chamber, should determine the pressure-time profile.

It has often been suggested that, under many sets of practical conditions, the following simplified view of the motor ignition process is applicable. First, the igniter burns completely and successfully ignites a small portion of the propellant surface. During this time, the pressure increases rapidly due to the evolution of igniter gas. Next, the flame spreads over the surface of the propellant. During this process, the pressure continues to increase but at a rate that depends on the burning rate of the propellant and on the rate of flame spread. Finally, the pressure in the motor builds up to a point at which the mass flow rate through the nozzle becomes appreciable and this tends to decrease the time derivative of the pressure, causing the pressure to approach asymptotically its equilibrium value, which is governed by a balance between the rate of production of gas at the propellant surface and the mass flow rate through the nozzle. Each of the steps involved in this simplified view of motor ignition is subject to experimental and theoretical investigation and will be considered below. In addition, we shall discuss ignition processes for which the simplified view requires modification.

Ignition Devices

The purpose of the ignition device is to bring to the propellant surface a sufficient amount of energy, to trigger a sustained combustion. In most applications, this energy is of chemical or electrical origin. In the first case the products of combustion of an auxiliary propellant can be used. Heat transfer then takes place by convection, conduction and radiation or by direct contact of a solid or liquid condensed phase with the propellant surface. Substances which are hypergolic with the propellant can also be used, such as chlorine trifluoride. Exothermic chemical reactions then start on the surface and increase the ambient temperature.

The earliest ignition device was made of black powder contained in a small bag. The combustion of this powder brings the pressure inside the motor up to a certain value and liberates enough energy at the propellant surface to initiate ignition of the grain and flame propagation. New igniter materials with better ballistic and energetic properties have now replaced black powder.

a) Solid Propellant Igniters

Most solid propellant igniters can be thought of as little rocket motors, which must present certain characteristic features to assure a good ignition. These igniters are characterized by their burned propellant flow rate $\dot{m}_{b,i}$ and their combustion duration $t_{b,i}$ or else by a time evolution curve of their mass flow rate $\dot{m}_{b,i}(t)$. The knowledge of the total propellant mass contained within the igniter :

$$m_{pi} = \int_0^{t_{bi}} \dot{m}_{bi}(t) dt ,$$

is not sufficient to characterize the igniter; one must also know the flow rate and the burning time. There is a minimum value of the propellant mass m_{pi} below which a correct ignition is not achievable. This minimum value is associated with a certain flow rate $(\dot{m}_{bi})_0$ and a certain burning time $(t_{bi})_0$. If t_{bi} is decreased below $(t_{bi})_0$ then the flow rate \dot{m}_{bi} must be increased to such an extent that the product $\dot{m}_{bi} t_{bi}$ becomes larger than $(\dot{m}_{bi})_0 (t_{bi})_0$. If t_{bi} is increased above $(t_{bi})_0$, the required flow rate will remain approximately constant and equal to $(\dot{m}_{bi})_0$, so that the propellant mass again increases. This simplified reasoning demonstrates the importance of two parameters; flow rate and combustion duration.

The commonly used igniter compositions contain a finely ground oxidizer such as ammonium perchlorate (NH_4ClO_4), potassium perchlorate ($KClO_4$), potassium nitrate (KNO_3) and a metallic fuel which is also a finely ground powder and can be aluminum, boron, magnesium or zirconium. These compositions are generally used in the form of powders or pellets. Their combustion products contain a large percentage of condensed materials: 65% with the propellant (KNO_3 -B) and 70% with ($KClO_4$ -Al).

The most important characteristics of igniter compositions are their high flame temperatures ($\approx 3000^\circ K$), their high burning rates (which follow pressure-dependence laws of the form $r = a p^n$) and their low ignition pressures. Figure 8-31 shows the characteristics of an (NH_4ClO_4 -Al) composition.

In place of igniter compositions shaped like pellets, one can use conventional metalized propellants cast into moulds or cast directly into the ignition motor. For a given propellant, experience shows that the flow rate \dot{m}_{bi} must be approximately proportional to the thrust F of the main motor. The coefficient of proportionality is defined as a characteristic velocity for ignition:

$$v_i^* = F / \dot{m}_{bi} ,$$

the value of which is of the order of $30,000 \text{ m s}^{-1}$ for current propellants and depends upon the nature of the propellant.

The choice of the igniter burning time t_{bi} is affected by the nature of the propellant and by the residence time of the gases in the chamber,

$$t_r = (1/\Gamma^2 c^*) (\gamma_0 / A_t) ,$$

where c^* is the characteristic velocity, γ_0 is the initial internal volume of the chamber and A_t is the nozzle throat area of the motor. As a first approximation one can set :

$$t_{bi} / t_r = A ,$$

where A is a constant, the value of which is determined by preliminary experiments.

Having obtained \dot{m}_{bi} and t_{bi} from the preceding considerations, one can proceed to develop a preliminary design of an igniter motor. Its operating pressure can be selected according to different criteria; two approaches are currently used in achieving short igniter burning times ($t_{bi} \approx 10$ to 100 msec) and high igniter flow

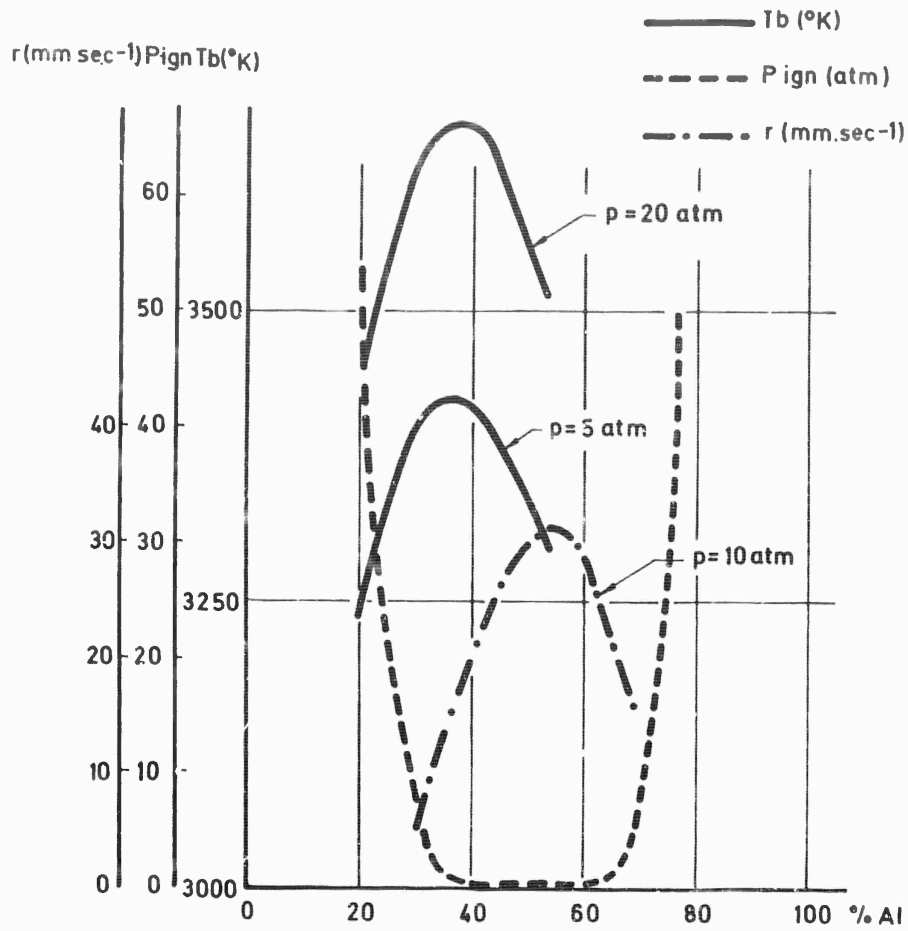


Fig. 8-31 Flame temperature, ignition pressure limit and burning rate vs. metal mass fraction for NH_4ClO_4 -Al mixtures.

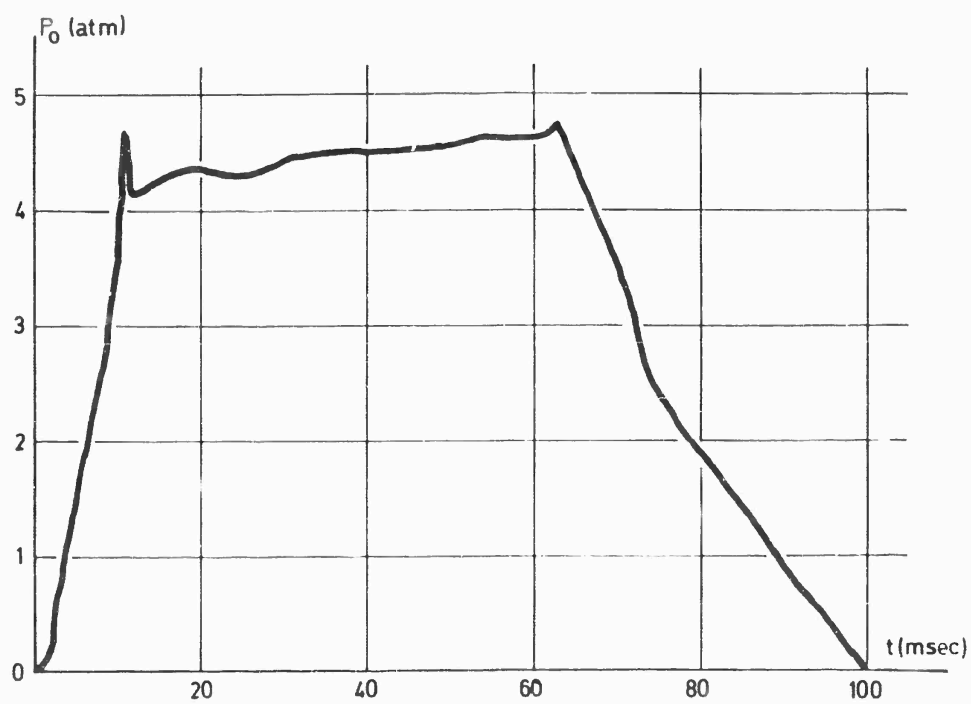
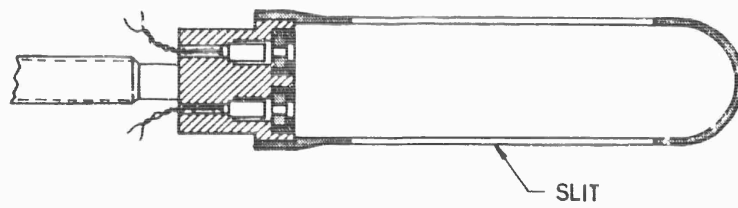


Fig. 8-32 Pressure variation in an ignition (pellet propellant).

rates:

1. High-pressure systems ($p_i \approx 100 \text{ atm}$) which have high burning velocities.
2. Low-pressure systems ($p_i \approx 10 \text{ atm}$) with large burning areas (pellets).

It is desirable to design igniters with reproducible operating conditions and with a constant mass rate of generation of hot gases, during the entire ignition period. Figure 8-32 illustrates characteristics of a slit igniter that uses propellant pellets.

In igniter tests, the mass flow rate can be determined from the pressure recordings:

$$\dot{m}_{bi} = f \left(p_i, \frac{dp_i}{dt}, t_{ri} \right).$$

Detailed igniter design is based on a certain number of fundamental equations which we list briefly (40). Conservation of mass:

$$\dot{M}_i = dM_i/dt = \dot{m}_{bi} - \dot{m}_{ti},$$

where \dot{M}_i is the mass of combustion products in the igniter chamber and \dot{m}_{ti} the flow rate through the injection orifices into the main chamber. The flow rate of products \dot{m}_{bi} depends upon the burning area A_{bi} and the burning rate r_{bi} ,

$$\dot{m}_{bi} = \rho_{pi} A_{bi} r_{bi};$$

since the flow through the injection orifices is choked, \dot{m}_{ti} depends upon the characteristic velocity, the stagnation pressure p_i and the total orifice cross-sectional area A_{ti}

$$\dot{m}_{ti} = p_i A_{ti} / c_i^*$$

Conservation of energy :

$$\frac{d}{dt} (c_v M_i T_i) = (1 - \xi_i) c_p T_{bi} \dot{m}_{bi} - c_p T_i \dot{m}_{ti}$$

where T_{bi} is the combustion temperature and ξ_i is the fraction of the energy lost in the igniter chamber. The specific heats at constant pressure and at constant volume must take into account the condensed phases;

$$c_p = Y_p c + (1 - Y_p) c_{lg},$$

$$c_v = Y_p c + (1 - Y_p) c_{vg},$$

where Y_p is the mass fraction of condensed phase.

Equation of state:

$$p_i - p_{0i} = (1 - Y_p) M_i \frac{RT_i}{m_g},$$

where m_g denotes the molecular weight of the gas phase.

Reasonable assumptions concerning the burning rate r_{bi} and the burning area A_{bi} enable one to calculate the time evolution of the igniter chamber pressure $p_i(t)$, the flow rate through the igniter orifices $\dot{m}_{ui}(t)$ and the combustion product temperature $T_i(t)$.

The preceding considerations enable one to establish a preliminary design for the igniter. Igniters must be designed to operate under severe ambient conditions (pressure, temperature, vibrations). Resistance to vibrations is particularly important for igniters used in successive stages of a multistage rocket. It is imperative to have a high reliability, which can be assured only by numerous test firings under conditions simulating actual operation.

b) Hypergolic Igniters

A typical hypergolic igniter consists of a chlorine trifluoride injection system, pressurized by an inert gas, such as helium. Relevant design variables are the liquid flow rate \dot{m}_l injected into the chamber, the duration t_{inj} , the degree of atomization of the liquid produced during injection and the orientation of the liquid jets with respect to the surface. Hypergolic ignition systems bear many resemblances to hybrid rockets.

A hypergolic fluid exhibits an ignition delay, which is defined as the lapse of time between liquid-solid contact and the appearance of the first flame. For a given igniter fluid, the value of the ignition delay τ depends principally on the nature of the propellant. With chlorine trifluoride, representative values of τ are of the order of one millisecond. Injection of large drops is sometimes preferred instead of fine atomization because liquid-solid contact is then assured, thereby making the value of τ insensitive to pressure. Propellant ignition with gaseous chlorine trifluoride is also possible but in this case the ignition delay depends strongly on both the pressure and the concentration of the gaseous oxidizer near the surface. Since motor ignition, with both solid propellant igniters and hypergolic igniters, involves direct ignition of a portion of the grain followed by flame propagation along the rest of the grain, there are many common aspects of motor ignition processes with hypergolic igniters and with hot-gas propellant igniters. We shall concentrate on motor ignition by hot-gas producers in the following discussion.

Analyses of the Various Processes

The motor ignition process described in Section 1.5., 'Introduction' involves establishment of preliminary flow patterns and pressure levels in the chamber by the hot igniter gases, heat transfer to the propellant surface, ignition of a part of the propellant surface, flame spreading and finally an intensification of combustion which may lead to the development of a pressure spike before the establishment of steady combustion. These five phenomena will be discussed separately in the present section.

Before beginning the discussion, it is helpful to define a number of characteristic delay times which play a role in the ignition process.

A thermal delay time t_{th} for propagation of heat in the solid phase is :

$$t_{th} = \lambda_2 / \rho_2 c_{p2} r^2 = a_2 / r^2 ,$$

where subscript 2 will always refer to the solid. This delay is independent of the length scale and is mainly a function of pressure :

$$t_{th} \propto p^{-2n}$$

if the regression rate varies as p^n . For pressures in the 10- to 100-atm range, t_{th} varies between 10^{-2} and 10^{-3} sec.

A characteristic residence time for gases in the chamber under steady-state conditions, has previously been shown to be :

$$t_r = 1/\Gamma^2 (V_0/A_t c^*) ,$$

in which the chamber volume V_0 and the throat area A_t of the main motor appear. If φ denotes the ratio of the volume of the converging portion of the nozzle to the central channel volume for a cylindrical motor, then the preceding formula can be written as :

$$t_r = \frac{1}{\Gamma^2} \frac{(1+\varphi)}{k} \frac{1}{\sqrt{KJ}} \frac{p F^{1/2}}{c^{*2} v_e^{1/2} (\rho_2 r)^{3/2}} ,$$

where k is the ratio of the central channel cross-sectional perimeter to the square root of the port area, $K = A/A_p$, $J = A_t/A_p$ and v_e is the exhaust velocity of the gases at the exit section of the nozzle. The residence time is thus proportional to the square root of the thrust $F^{1/2}$, and to $p^{1/2-n}$, provided that c^* and v_e are assumed to be independent of pressure. If the pressure exponent n is close to 0.5, then the residence time is independent of pressure and :

$$t_r (\text{sec}) \simeq 4 \times 10^{-5} \sqrt{F(\text{lbs})} .$$

Theories generally assume that the propagation time of an acoustic wave along the motor is small, compared with the residence time. Under this assumption, unsteady flow can be analyzed without using the method of characteristics. The propagation time is :

$$t_a = \frac{L}{a} = \frac{L}{\psi(\gamma) c^*} = \frac{\sqrt{KJ}}{k \psi c^*} \frac{F^{1/2}}{(\rho_2 r v_e)^{3/2}} ,$$

where L is the motor length, $\psi(\gamma)$ a function of the specific heat ratio which relates the velocity of sound to the characteristic velocity. As we did for t_r we find here :

$$t_a \propto p^{1/2-n} F^{1/2}$$

A numerical estimate shows that t_a is three to five times smaller than t_r . In other words, typical chamber Mach numbers appear to lie between 0.2 and 0.33.

When the Lewis number is close to unity, heat conduction and diffusion times in the gas phase are approximately equal and are given by :

$$t_1 = \frac{l^2}{v_1^2} = \frac{l^2 \rho_1^2}{\rho_2^2 r^2} \sim \frac{\lambda_1 \rho_1}{c_{pl} \rho_2 r^2} ,$$

so that :

$$t_d \propto p^{1-2n} .$$

The value of t_d is much smaller than that of t_{th} ; it is of the order of 10^{-5} to 10^{-6} sec and is independent of pressure for $n = 0.5$.

The longest characteristic times identified above, are the heat propagation time in the solid and to the residence time of the gases in the chamber. These two time delays are therefore likely to be primary factors affecting motor ignition.

A characteristic time for flame propagation along the grain can be defined as :

$$t_p = L/r_p ,$$

where r_p is the propagation velocity. Unfortunately, as we shall see later, r_p is not well-known.

a) Igniter-Produced Gas Flow in the Chamber

It is of importance to organize the gas flow from the igniter in the central channel, in order to transfer as much energy as possible to the propellant surface. Two configurations currently in use are forward injection with flow toward the nozzle and aft injection with counterflow. Figure 8-33 shows both principles.

In forward injection, the igniter can be fitted with lateral slits which have the same symmetry as the grain (number of slits equal to the number of star points, for example). This system intensifies the transfer processes near the surface and stratifies the flow. A single jet issuing from an auxiliary ignition motor can also be used. In this case the igniter nozzle has no diverging portion and its operating characteristics depend on the ratio of the igniter exit section diameter to the main motor port diameter $\epsilon_1 = D_{t1}/D_p$. If the ratio ϵ_1 is too small there is a jet effect and the igniter gases do not reach the propellant surface immediately.

In counterflow injection, the jet from the igniter motor must penetrate into the main motor nozzle without being diverted at the throat. Best penetration is achieved when the exit section of the igniter nozzle is located at the throat section of the main motor nozzle.

It is generally advantageous to study simulations of igniter flow patterns in a wind or water tunnel. Figure 8-34 is an example of such a study in a water tunnel.

Before ignition of the main propellant, the pressure increase in the chamber is due only to the igniter flow rate \dot{m}_{t1} . The equations of this process are: Mass conservation equation :

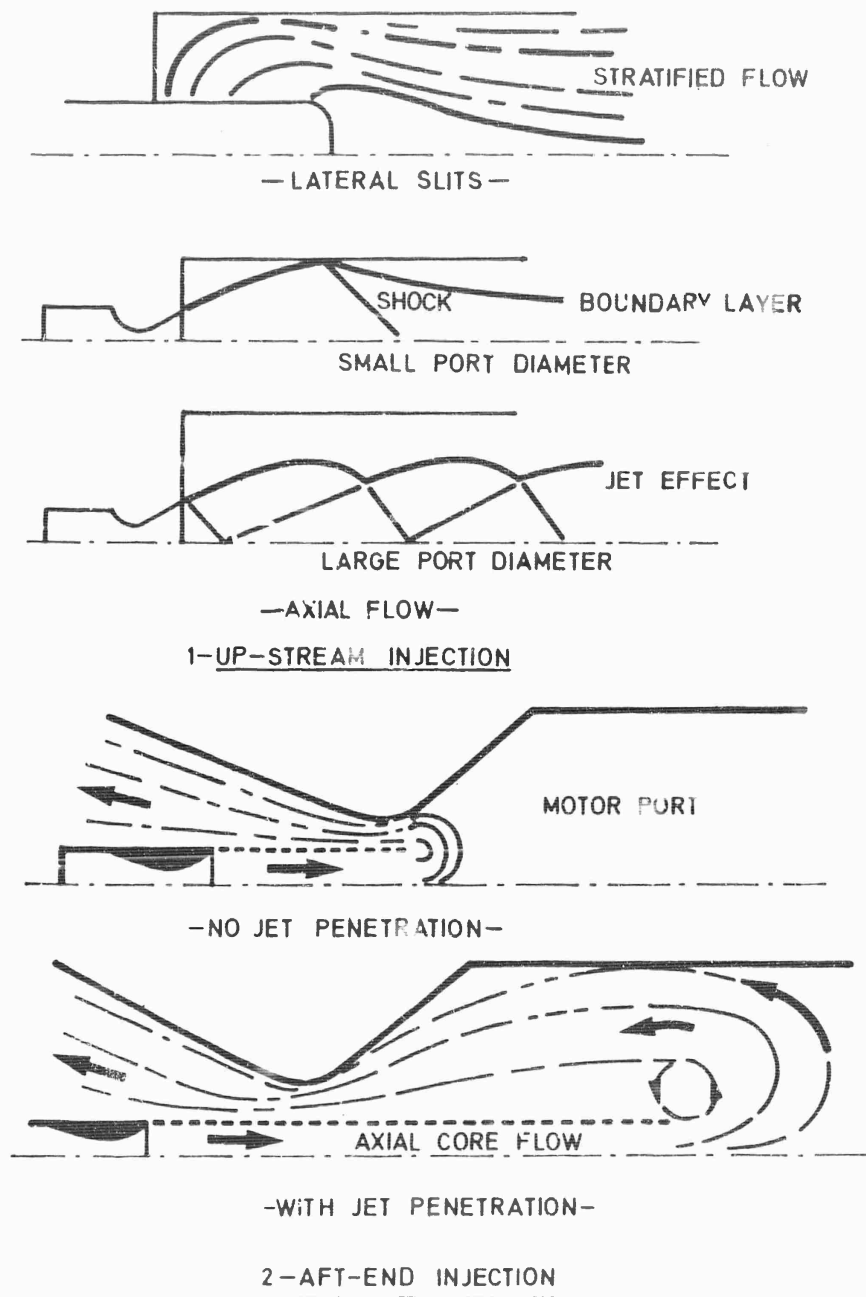


Fig. 8-33 Flow organization.

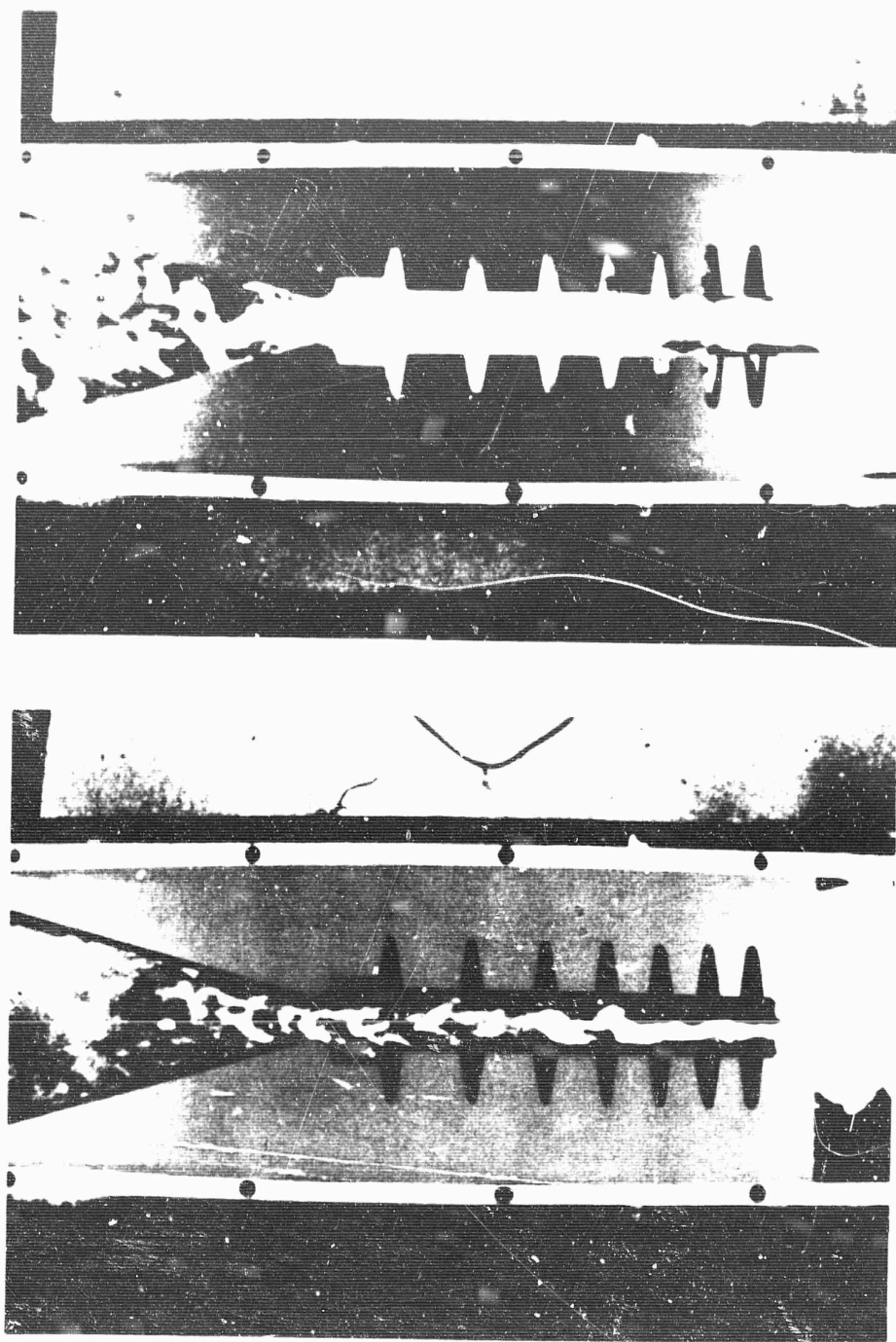


Fig. 8-34 Visualization of the flow pattern in a water tunnel during the ignition period.

$$dM/dt = \dot{M} = \dot{m}_{t1} - \dot{m}_t$$

where M is the mass of gases inside the chamber and \dot{m}_t the flow rate through the main motor nozzle. Energy conservation equation :

$$\frac{d(\dot{M}T)}{dt} = (1 - \xi) \gamma T_1 \dot{m}_{t1} - \gamma T \dot{m}_t$$

where ξ characterizes the losses in the main motor.

Introduction of known functions $\dot{m}_t(p, T)$, $\dot{m}_{t1}(t)$ and $M(p, T)$ into these expressions leads to two differential equations relating the pressure p and the temperature T to time t . Expressions for $\dot{m}_t(p, T)$ differ for choked and unchoked flow in the main nozzle.

b) Heat Transfer to the Propellant Surface

Heat transfer depends not only on the nature and thermodynamic properties of the gases produced during igniter combustion, but also upon the flow configuration in the central channel. The three most important types of heat transfer from igniter combustion products are transfer by convection, transfer by radiation and transfer by contact of hot condensed particles (e.g., alumina droplets) with the propellant surface. A theoretical study of such an unsteady energy transfer problem in a boundary layer is difficult, see Section 1.4.3 'Ignition by Means of a Flowing Hot Gas'. We shall therefore restrict ourselves to mentioning experimental results. A qualitative study of the transfer process can be made by examining the distribution of luminous flux in a laboratory apparatus (Fig. 8-35). One can construct a transparent model of the central port and the nozzle of the motor. The ignition system can be fired into this model, under conditions that closely approximate those of an actual motor. Motion pictures of the firing will show the distribution of luminous energy received by the surface. The heat flux distribution on the surface can thereby be obtained for both forward igniters and counterflow igniters. This apparatus is shown in Fig. 8-35. A quantitative determination of heat transfer to the surface during the transient ignition can be obtained by placing fluxmeters at various positions on the surface, in order to measure the time history of the heat flux received.

If the process is nonradiative, then heat is transferred to the surface by convection and the flux is expressed by :

$$q = h(T_1 - T_s)$$

where h is the heat transfer coefficient, T_1 is the stagnation temperature of the flow and T_s is the propellant surface temperature. The value of the coefficient h is determined from empirical laws relating the nondimensional Nusselt number to the Reynolds and Prandtl numbers.

Good correlations have been obtained by Carlson (41) by using dimensionless groups based on the diameter D_p of the central channel;

$$Nu = h D_p / \lambda$$

$$Re_D = 4 \dot{m}_{t1} / \pi D_p \mu$$

$$Pr = \mu c_p / \lambda$$

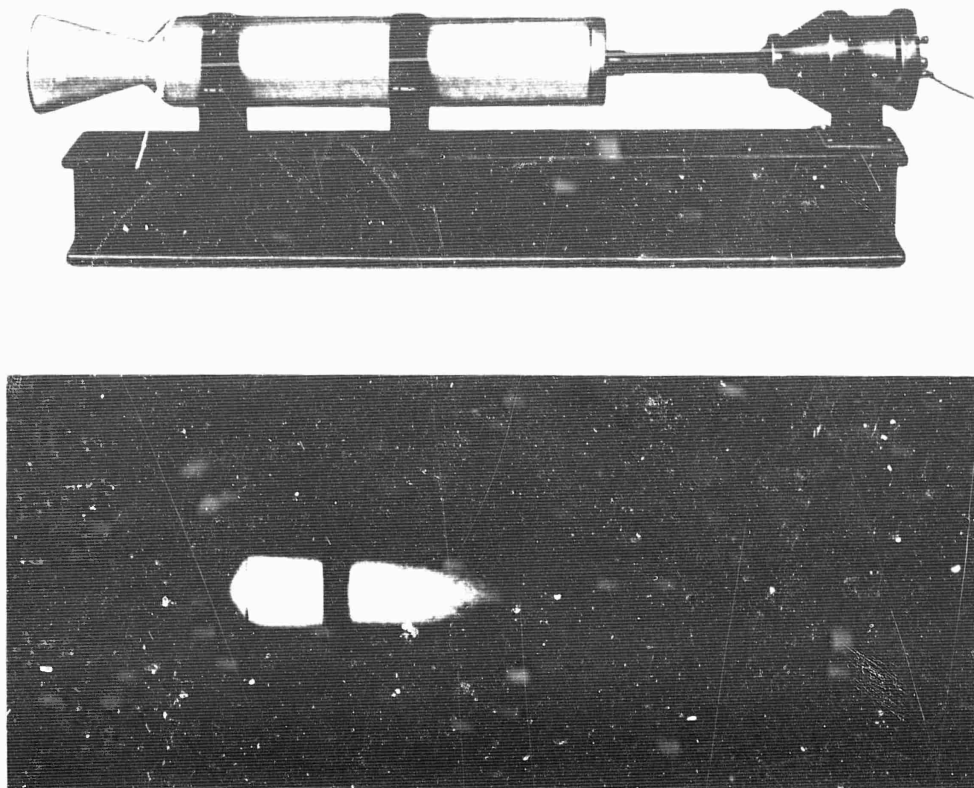


Fig. 8-35 Visualisation of the heat transfer during the ignition period

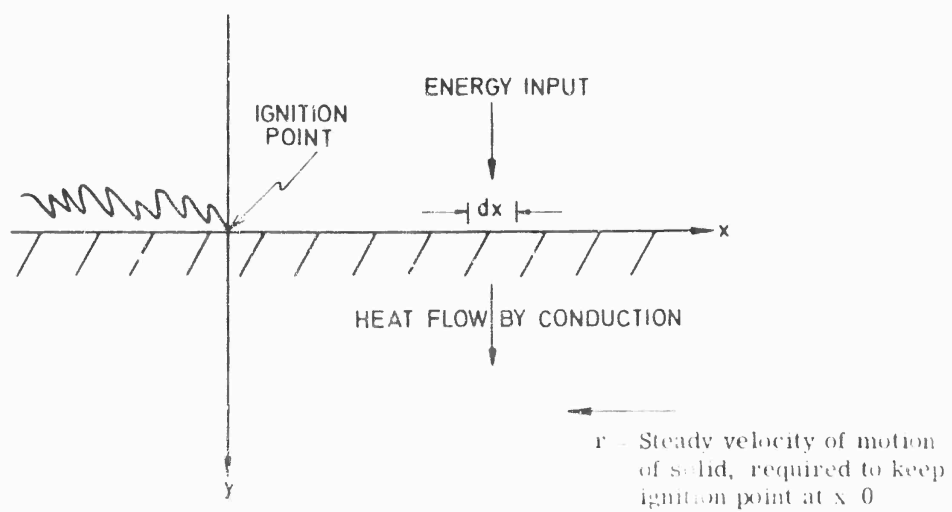


Fig. 8-36 Schematic model of flame spread process

In the case of head-end injection, laws of the form :

$$Nu = a Re_D^{0.8} Pr^{0.4}$$

were obtained. The important parameters were found to be the diameter D_p and the igniter flow rate \dot{m}_{ti} ; the grain length-to-diameter ratio L/D_p had little influence on the results. In the case of aft-end injection the Nusselt number was correlated by a relation of the form :

$$Nu = b Re_D^{0.5} Pr^{0.4}$$

Here D_p and \dot{m}_{ti} were found to have less influence but the heat flux to the surface was found to depend strongly on the value of the axial distance X , from the igniter exit to the measurement position. Data could be correlated in terms of the ratio X/L . A maximum rate of heat transfer is observed close to the injector, then q decreases as X/L increases. The location of the maximum flux point depends upon the ratio $\epsilon_i = D_{ti}/D_p$.

Allan and Bastress (42) based their dimensionless groups on the axial distance X instead of the diameter D_p and gave the correlation formula :

$$Nu = c Re_x^{0.8} Pr$$

with $Nu \equiv hX/\lambda$ and with $0.055 < c < 0.08$, depending on the igniter type. The heat fluxes were in the range 100 to 400 cal cm⁻² sec⁻¹.

It is difficult to evaluate the time history of the radiative flux to the surface but the contribution of radiation cannot be neglected, because the combustion products contain hot and highly emissive solid or liquid particles (at temperatures of the order of 3800°K).

Conductive heat transfer by contact between hot droplets and the fuel surface is also difficult to evaluate. Since the droplet diameters are of the order of a few microns, surface tension should prevent spreading of the droplets over the surface. Little data on heat transfer by contact are available.

c) Ignition of a Portion of the Grain Surface

We have seen that in all flow configurations there is a maximum heat flux at a certain distance from the igniter. This distance is typically of the order of two to three times the central channel diameter D_p . Ignition starts first in regions of maximum heat flux, since the ignition delay is approximately inversely proportional to the square of the heat flux. It is, however, difficult to define accurately an initial ignition zone because there is not a sufficient amount of data available to determine its boundaries. One can only make imprecise hypotheses relating the ignition delay to the significant parameters such as the heat flux, the oxidizer concentration, the gas velocity, the pressure, etc. Growth of the ignition zone occurs through continued ignition by hot igniter gases and also by flame spread along the grain.

d) Flame Spread

The process of flame spread from an ignited portion of the propellant to the remain-

der of the propellant surface can have a significant influence on a large portion of the pressure transient during ignition. This is especially true for large motors with small, lightweight igniters. The importance of the problem has prompted a number of analyses of the flame spreading process (30-35). These analyses will be discussed briefly after we indicate, by means of a highly simplified approach, the qualitative character of the process.

If it is assumed that, at $t = 0$, an area on the propellant surface is burning and an adjacent area is unignited, then heat transfer from the burning area to the unignited area will raise the temperature of the unignited area to a point at which exothermic self-sustaining reactions begin to occur. The time required for these reactions to begin, at any given point x in the unignited area, depends upon the geometry of the motor, the geometrical configuration of the initial burning area, the mechanism of ignition (discussed in Section 1.4), etc. Although complex geometrical configurations could produce a highly nonuniform dependence of the time required for ignition to occur upon the position x in the initially unignited area, it is reasonable to assume that in most simple geometries, the unignited points immediately adjoining the burning region will ignite sooner than points farther removed from the burning area. Thus, a flame perimeter that moves continuously with time should be identifiable.

Continuous flame spread of this type has been observed in the laboratory. In other experiments, laboratory photographs of the flame spreading process often seem to indicate that the flame appears to spread in discrete steps, with incipient ignition (small flamelets) occurring over a finite area, the flamelets developing into fully developed burning and then incipient ignition occurring over an adjacent finite area (31); however, on the average, even this process can be approximated as a continuous propagation of the flame perimeter with time. We are thus led to a model of an increasing flame area which eventually envelopes the entire surface of the propellant.

Within this model, the time rate of increase of flame area will depend in general on the size and shape of the ignited area. However, if the ignited area is not too small and the curvature of the flame perimeter is not too large, then a model in which the flame perimeter is a straight line propagating along the propellant surface should be applicable. This model, although perhaps often inaccurate in the early stages of flame spread, has been employed in the most accurate studies yet reported (30-33); to improve it requires a knowledge of the shape of the initially ignited area, which is seldom available.

Time-dependent analyses of the flame spread process, based on this model and assuming a stationary burning area at $t = 0$, show that the flame perimeter propagates at a speed that increases monotonically from zero at $t = 0$ and approaches a finite limiting value as $t \rightarrow \infty$ (31). To describe the time dependence of the flame perimeter propagation velocity requires the use of numerical methods at some stage in the analysis (30-33). However, as we shall show below, if one is interested only in the limiting ($t \rightarrow \infty$) steady-state perimeter propagation velocity, then a simplified model enables one to obtain an analytical expression for the propagation velocity. The highly simplified model discussed below is amenable to some refinement without loss of analyticity of the result. The steady-state velocity should prevail for most of the flame-spread period for large motors with small igniters. Even for small motors, uncertainties in the initial conditions raise a question as to whether the time-dependent results or the steady-state approximation better represent the actual flame-spread process.

The basis of the simplified model of the flame-spread process is illustrated in Fig. 8-36. Heat transfer from the flame and hot gases produces an energy input, $H(x) \ell dx$ (cal/sec) to an unignited surface strip of length ℓ and width dx ; i.e., $H(x)$ (cal/cm²sec) is defined as the energy flux into the surface at position x . This energy input gives rise to an increase in the surface temperature and to heat flow

into the bulk of the propellant by thermal conduction. For simplicity in the development, we adopt a coordinate system in which the ignition point remains at $x = 0$. An ignition temperature criterion will be employed; i.e., we shall assume that ignition occurs instantaneously when the surface temperature reaches a definite ignition temperature T_1 , so that $T = T_1$ at $x = 0$, $y = 0$. Our objective is to obtain an expression for the steady velocity r (cm/sec), with which the solid must move in the $-x$ direction in Fig. 8-36, in order to maintain the ignition point at $x = 0$. This velocity is the flame perimeter propagation velocity.

We shall assume that heat conduction in the solid occurs only in the y direction ($\partial T / \partial x \ll \partial T / \partial y$). Conduction in the x direction can be included in the present model but this is found merely to complicate the results somewhat without introducing any qualitatively new features into the problem. Indeed, machine calculations made with the most complete model that has been reported show that no observable effect in chamber pressure-time histories is produced by including heat conduction parallel to the propellant surface, in a representative case (33). The energy conservation equation in the solid becomes :

$$\lambda \frac{\partial^2 T}{\partial y^2} + r \rho c \frac{\partial T}{\partial x} = 0, \quad (\text{Eq. 8-61})$$

where λ , ρ and c (all assumed to be constant) are the thermal conductivity, density and specific heat of the solid. The second term in Eq. 8-61 accounts for the time rate of increase of energy of an element of the solid as it moves in the $-x$ direction. The boundary conditions for Eq. 8-61 are :

$$\left. \begin{array}{l} T = T_1 \quad \text{at } x = 0, y = 0 \\ T \rightarrow T_0 \quad \left\{ \begin{array}{l} \text{as } x \rightarrow \infty, (0 < y < \infty) \\ \text{as } y \rightarrow \infty, (0 < x < \infty) \end{array} \right. \end{array} \right\} \quad (\text{Eq. 8-62})$$

where T_0 is the initial temperature of the unignited propellant. In addition, conservation of energy at the surface yields :

$$-\lambda \partial T / \partial y = H(x) \quad \text{at } y = 0, (0 < x < \infty). \quad (\text{Eq. 8-63})$$

Equation 8-61 can be solved by separation of variables. Solutions exist of the form :

$$T = T_0 + A e^{-\alpha y} e^{-\frac{\alpha^2 \lambda}{r \rho c} x}, \quad (\text{Eq. 8-64})$$

where α and A are constants. Equation 8-64 satisfies the boundary conditions Eq. 8-62, if $\alpha > 0$ and if :

$$A = T_1 - T_0. \quad (\text{Eq. 8-65})$$

It also satisfies boundary condition in Eq. 8-63 if α can be chosen so that :

$$H(x) = \lambda \alpha (T_1 - T_0) e^{-\frac{\alpha^2 \lambda}{r \rho c} x} \quad (\text{Eq. 8-66})$$

This is possible only if $H(x)$ has the form :

$$H(x) = H_0 e^{-x/L}, \quad (\text{Eq. 8-67})$$

where H_0 and L are constants. Whether or not Eq. 8-67 is valid will depend upon the character of the heat transfer mechanism. In general, Eq. 8-67 will not be true and Eq. 8-64 will not represent the correct solution. However, any given $H(x)$ can be approximated by the functional form given in Eq. 8-67 by adjusting the parameters H_0 and L , which characterize the heat transfer process, for the best fit. Assuming that this has been done, we find, by comparing Eqs. 8-66 and 8-67, that :

$$\alpha = H_0 / \lambda (T_i - T_0) , \quad (\text{Eq. 8-68})$$

and that the flame perimeter propagation velocity is :

$$r = L H_0^2 / \lambda \rho c (T_i - T_0)^2 . \quad (\text{Eq. 8-69})$$

If Eq. 8-67 is not valid, then Eq. 8-64 is not exactly correct and the correct temperature distribution must involve an integral over the separation parameter α ; viz.,

$$T - T_0 = \int_0^\infty A(\alpha) e^{-\alpha y} e^{-\frac{\alpha^2 \lambda}{r \rho c} x} d\alpha , \quad (\text{Eq. 8-70})$$

with the function $A(\alpha)$ determined by the requirement that Eq. 8-63 be satisfied and with the value of r determined by the requirement that $T = T_i$ at $x = 0, y = 0$. Eq. 8-63 then yields :

$$\lambda \int_0^\infty \alpha A(\alpha) e^{-\frac{\alpha^2 \lambda}{r \rho c} x} d\alpha = H(x) , \quad (\text{Eq. 8-71})$$

which can be written as :

$$\int_0^\infty B(\beta) e^{-\beta x} d\beta = 2 H(x) / r \rho c , \quad (\text{Eq. 8-72})$$

where $\beta \equiv \alpha^2 \lambda / r \rho c$ and $B(\beta) \equiv A(\alpha)$. Equation 8-72 indicates that $2H(x)/r \rho c$ is the Laplace transform of $B(\beta)$; i.e.,

$$B = \mathcal{L}^{-1} \{ 2H / r \rho c \} . \quad (\text{Eq. 8-73})$$

In terms of β and B , Eq. 8-70 becomes :

$$T - T_0 = \frac{1}{2} \sqrt{\frac{r \rho c}{\lambda}} \int_0^\infty \frac{1}{\sqrt{\beta}} B(\beta) e^{-\sqrt{\frac{r \rho c \beta}{\lambda}} y} e^{-\beta^2 x} d\beta . \quad (\text{Eq. 8-74})$$

Evaluating Eq. 8-74 at $x = 0, y = 0$, employing Eq. 8-73 and solving for r , we find :

$$r = \left[\lambda \rho c (T_i - T_0)^2 \right]^{-1} \left[\int_0^\infty \frac{1}{\sqrt{\beta}} \mathcal{L}^{-1} \{ H \} d\beta \right]^2 , \quad (\text{Eq. 8-75})$$

which enables one to calculate r from a table of inverse Laplace transforms, by performing a single integration. The simple approximation given in Eq. 8-69 will be used instead of Eq. 8-75 in the following discussion; it can be seen from Eq. 8-75 that the qualitative dependence of r upon the controlling parameters ($\lambda, \rho c, T_i$, the magnitude of H , etc.) is given correctly by Eq. 8-69.

The effect of propellant density, heat capacity, thermal conductivity and ignition

temperature on the flame perimeter propagation rate is readily apparent from Eq. 8-69. The dependence of r on pressure, motor geometry and gas properties, on the other hand, appears through $H_0^2 L$ and therefore is governed by the heat transfer mechanism. If the dominant heat transfer occurs by radiation from the hot flame region, then it can be shown, in a rough approximation, that $H(x) \sim \left[1 + \left(\frac{a+x}{b} \right)^2 \right]^{-1}$, where a and b are constant lengths characteristic of the burning region and the constant of proportionality is approximately equal to the intensity of radiation emitted by the flame region. In most analyses, however, radiant energy transfer is assumed to be negligible in comparison with convective heat transfer from hot gaseous reaction products (30), (32-34). The precise expression used for $H(x)$ in convective heat transfer varies according to the assumptions employed regarding geometry, character of the flow, etc. That a variety of possible formulas exist may be inferred from the discussion in Section 1.4.3, 'Ignition by Means of A Flowing Hot Gas'. Since the convective heat transfer rate at $x = 0$ is $H_0 = h(T_g - T_0)$, where h is the heat transfer coefficient and T_g is the gas temperature at $x = 0$, Eq. 8-69 yields :

$$r = \frac{Lh^2}{\lambda \rho c} \left(\frac{T_g - T_0}{T_1 - T_0} \right)^2, \quad (\text{Eq. 8-76})$$

indicating that $r \propto Lh^2$. The variety of formulas enters chiefly through the variety of possible choices for h , which need not be enumerated here because they have been discussed in Section 1.4.3.

Reference (31) contains a theoretical analysis of flame spread that can be considered to represent the direct generalization of the preceding analysis, to the time-dependent problem in which the flame perimeter propagation rate is zero at $t = 0$. Experimental measurements of the flame perimeter propagation rate (for a double-base propellant) were performed with a variable externally imposed gas velocity, at a variety of different atmospheric pressures. Measurements in O_2 and N_2 atmospheres indicated a negligible influence of atmospheric composition. For $H(x)$ functions of the forms $H(x) \sim e^{-x/L}$ and $H(x) \sim (1 + x/L)^{-n}$, the function $H(x) \sim (1 + x/L)^{-1/2}$ was found to provide the best correlation with the theory, and experiment. Since the experimental results are reported in terms of a correlation with the theory, a comparison between the experiment and the simplified theoretical considerations given above cannot readily be made.

In Ref. (30), equations including two-dimensional time-dependent heat flow in the solid, one-dimensional, steady energy and oxidizer flow in the gas and an exothermic heterogeneous reaction, are proposed for performing a theoretical calculation of flame spread. The solution must be carried out by a numerical integration of a finite-difference approximation to the governing equations. Curves are given showing the qualitative dependence of the flame perimeter propagation rate upon gas temperature T_g and upon port diameter D . Except for a Prandtl number dependence, the approximation employed for h was $h = \text{const} (\lambda_g/D) \text{Re}^{0.8}$, where λ_g is the thermal conductivity of the gas and where the Reynolds number Re is defined as $\text{Re} = \rho_g v_g D / \mu_g$, in which ρ_g , v_g and μ_g are the density, velocity and viscosity of the gas. When this formula is substituted into Eq. 8-76, the primary dependence of r upon D and T_g is found to be :

$$r \propto D^{0.6} (T_g - T_0)^2,$$

where L has been assumed to be proportional to D . These D and T_g dependences are the same as those shown in Ref. (30), thus indicating that the heterogeneous re-

actions have no effect on these dependences. We might note that if the corresponding laminar expression for the heat transfer coefficient, $h = \text{const.} (\lambda_g/D) \text{Re}^{0.5}$, is employed, then r is found to be independent of D (and is proportional to the mass velocity $\rho_g v_g$).

Flame spread (32) was treated theoretically as part of a theoretical formulation of the problem of calculating ignition pressure transients in rocket motors. The flame-spread portion of the analysis is basically equivalent to the analysis of Ref. (31) (described previously), with the exception that the hypothesis of a laminar flat-plate boundary layer is employed, yielding $H(x) = \text{const.} \lambda_g \sqrt{\rho_g v_g / \mu_g} \text{Pr}^{1/3} [T_g - T(x, 0)] / \sqrt{x}$, where Pr is the Prandtl number of the gas. Both experimental and (numerically obtained) theoretical results are reported, in the form of pressure-time curves. Flame perimeter propagation velocities are obtained by an inverse calculation procedure that is dependent upon the other aspects of the model, for the pressure transient in the motor.

Reference (33) contains the most thorough theoretical formulation of the problem of flame spread in rocket motors that has yet been reported. Two-dimensional, time-dependent heat flow in the solid, one-dimensional, unsteady conservation equations in the gas and a variety of empirical heat transfer formulas are included; only the effect of heterogeneous reactions (30) is omitted. The equations must, of course, be solved numerically and they are programmed for solution as part of an ignition pressure transient calculation. Propagation velocities are not included in the results reported; only pressure-time curves are given.

Simplified approximations (34) that are analytical, to a large extent, were proposed for calculating flame spread times. The approximations differ from those of the other studies and, in some cases, are much cruder than the simplified model presented here. The objective of the study is to account for simultaneous upstream and downstream spread of the flame area in a motor of cylindrical bore ignited centrally.

Reference (35) primarily contains experimental results on the flame perimeter propagation velocity as a function of pressure and of oxygen concentration, for three double-base propellants burning in a quiescent atmosphere. The propagation velocity was observed to increase with increasing pressure and with increasing oxygen mole fraction.

e) Intensification of Combustion and Pressure Spike at Ignition

The instantaneous total mass flow rate of combustion products \dot{m}_b , during the later stages of ignition, can be determined from measurements of the pressure and its time derivative. A mass flow rate parameter which has the dimensions of a pressure, is $\dot{m}_b (c^*/A)$, a typical graph of which is plotted in Fig. 8-37. Although the evaluation of \dot{m}_b is not very accurate, the time evolution of $\dot{m}_b (c^*/A)$ shows the existence of a maximum \dot{m}_b in this particular example, due to the combined effects of p and dp/dt . There is, with respect to the steady regime, an increase in \dot{m}_b . This emphasizes that steady-state burning rate laws cannot be used accurately in transient regimes. In particular (39), the pressure exponent is usually higher in transient regimes. The increased propellant flow rate can cause pressure spikes at ignition (37), (38). We shall review explanations that have been offered for increased propellant flow rates.

Paul and Lovine (33) proposed that the burning rate depends not only on the instantaneous pressure p but also on the pressure-time derivative dp/dt . Energy considerations lead then to a transient burning rate formula:

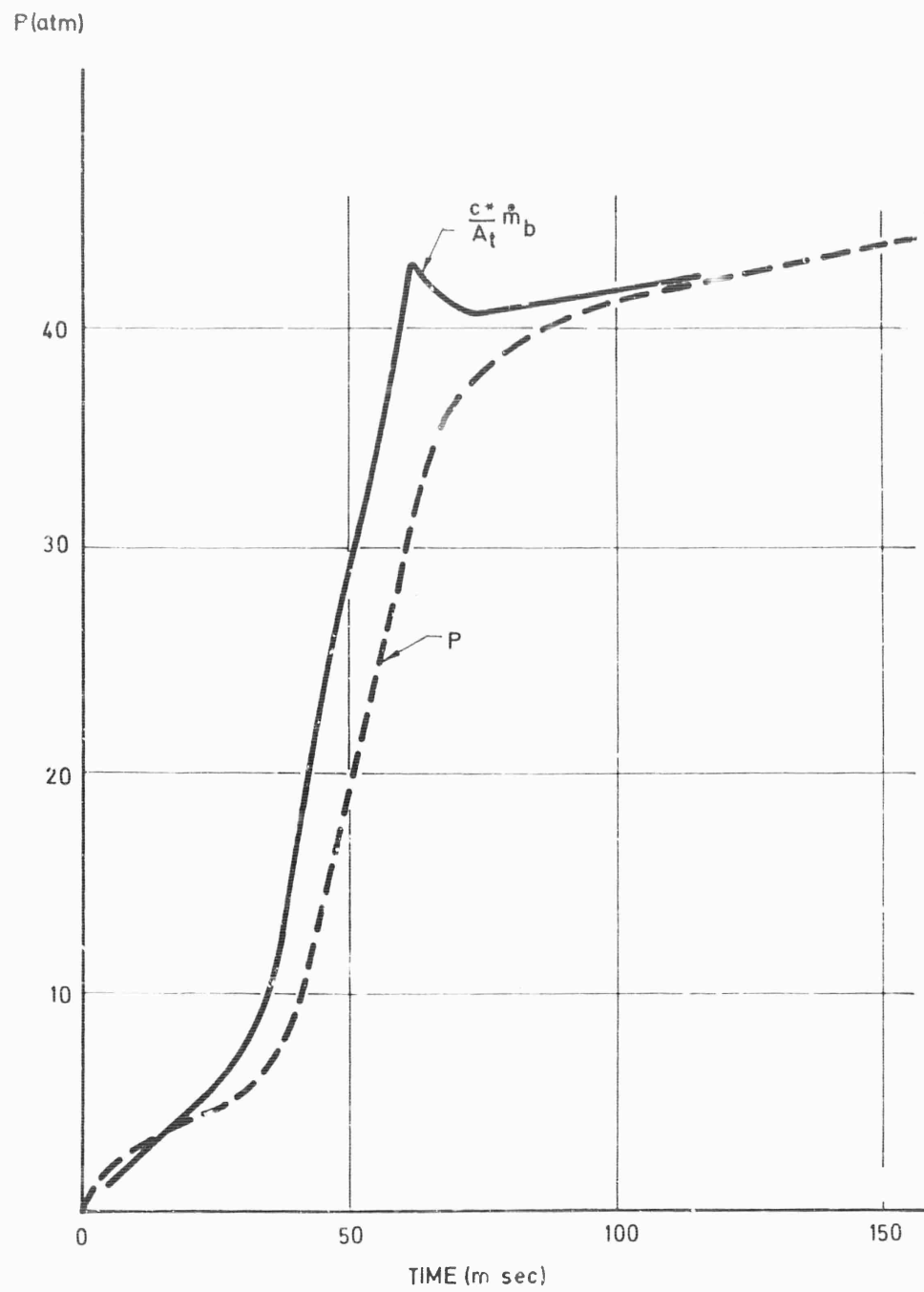


Fig. 8-37 Gas production rate during the transient phase.

$$r = r_{ss} \left[1 + \frac{n a_2}{r_{ss}} \left(\frac{\dot{p}}{p} \right) \right],$$

where r_{ss} is the steady-state burning rate ($r_{ss} = ap^n$) and $a_2 = \lambda/\rho c$ is the thermal diffusivity of the propellant. This increase in r with respect to r_{ss} is not negligible since for $n = 1/3$, $a_2 = 3 \times 10^{-4} \text{ in.}^2 \text{ sec}^{-1}$, $r_{ss} = 0.3 \text{ in. s}^{-1}$, $p = 200 \text{ psi}$ and $\dot{p} = 50,000 \text{ psi sec}^{-1}$, they found $r/r_{ss} = 1.28$. This expression for r shows the importance of two characteristic times, the thermal time defined previously and a time θ characteristic of the pressure evolution, $\theta \equiv dt/d \ln p$; one finds :

$$\frac{r}{r_{ss}} = 1 + n \frac{t_{th}}{\theta}.$$

Perhaps one should also take erosion effects into account in the expression for r .

We have already seen that the propagation time of an acoustic wave is smaller than the residence time. One might therefore approximate acoustic effects by assuming that the stagnation pressure at the nozzle throat at time t , is equal to the stagnation pressure in the central channel at time $t - \Delta t$. A delay Δt is thus introduced. It can be defined as the ratio of a reference length ℓ to the sound velocity 'a' in the chamber. The reference length can be taken to be the distance between the nozzle throat and the station at which the average pressure is defined. The effective chamber pressure for nozzle flow becomes :

$$p(t - \Delta t) = p(t) - \Delta t \dot{p}(t) = p(t) - (\ell/a) \dot{p}(t).$$

The mass flow rate through the nozzle is then :

$$\frac{p(t) A_t}{c^*} - \frac{\ell A_t}{F(\gamma) c^{*2}} \dot{p}(t),$$

where use has been made of the relationship between a and c^* .

A theoretical analysis based upon the mass and energy conservation equations leads to a relation between the pressure p or the temperature T in the central channel and time. Under the preceding hypotheses, it can be shown that a pressure spike can appear! such an analysis. This pressure spike is very sensitive to the temperature T and becomes more accentuated when temperature T departs from the adiabatic flame temperature. The spike disappears completely if an isothermal evolution of the gases is assumed during the transient ignition process.

Another point of view consists of assuming that during the transient phase the initial propellant temperature varies because of the energy transfer just prior to ignition. More generally, it can be assumed that the burning rate depends upon the surface temperature T_w and on the temperature gradient at the surface $(dT/dy)_w$. The burning rate can then be written as :

$$r = r_{ss} \left[1 + \beta T_w + \frac{\beta}{r} a_2 \left(\frac{dT}{dy} \right)_w \right].$$

The coefficient of proportionality β expresses the sensitivity of the propellant to temperature and a_2 is the thermal diffusivity. The heat conduction equation in the solid is of the form :

$$\frac{\partial T_2}{\partial t} = a_2 \frac{\partial^2 T_2}{\partial y^2} + r \frac{\partial T_2}{\partial y} .$$

Using this equation and the mass conservation equation, it can be shown theoretically that pressure spikes can be obtained which depend chiefly on the parameter $\mathcal{P}_1 = (t_r)_i / (t_{th})_i$ ratio of the residence time to the thermal time, both times being evaluated at ignition conditions. Pressure spikes are obtained when $\mathcal{P}_1 \ll 1$, i.e., when the initial thermal time $t_{th1} = a_2 / [r(p_i)^2]$ is large compared with the residence time.

The pressure spike is computed from the following equations :

- 1) Mass Conservation Equation :

$$\dot{M} = dM/dt = \dot{m}_b - \dot{m}_t .$$

- 2) Energy Conservation Equation in the Central Channel :

$$\frac{d Me(T)}{dt} = (1 - \xi) \dot{m}_b h(T_b) - \dot{m}_t h(T) ,$$

where e is the specific internal energy of the gas in the central channel.

- 3) Equation of State :

$$p = \rho RT/m$$

- 4) Surface Heat Transfer Equation :

$$\frac{\partial T_2}{\partial t} = a_2 \frac{\partial^2 T_2}{\partial y^2} + r \frac{\partial T_2}{\partial y} .$$

- 5) Boundary Conditions for this last equation, particularly conditions at the propellant surface.

- 6) Burning Rate r in Transient Regime.

This series of equations defines the time evolution of the pressure. More thorough studies of the burning rate r in transient regimes are required if additional progress is to be made on this problem, allowing then precise computation of the curve $p(t)$.

Scale Effects

As a first approximation, one may assume that the size of the motor is defined by the thrust F . We have indicated (Section 1.5., 'Analyses of the Various Processes') that the internal chamber volume varies as $V_0 \propto F^{3/2}$, the throat area varies as $A_t \propto F$ and the residence time varies as $t_r \propto F^{1/2}$. The igniter flow rate varies according to $\dot{m}_{i1} \propto F$, if it is assumed that v_i^* is constant in the formula (Section 1.5., 'Ignition Devices') $F = \dot{m}_{i1} v_i^*$. We shall also assume that igniter combustion time is proportional to the residence time, so that the propellant mass required for ignition is proportional to $F^{3/2}$. Again as a first approximation, we can assume the main motor burning time to be proportional to $F^{1/2}$ and the propellant flow rate to be proportional to F . The main propellant mass is then proportional to $F^{3/2}$, which means that igniter propellant mass and main propellant mass vary approximately proportionally.

These relationships are naturally exceedingly rough and do not define effects of motor size on igniter characteristics and on the time evolution of the pressure during ignition. Additional information that is needed for an improved discussion includes the influence of motor size on the distribution of heat flux over the propellant surface, on flame spread rates and on burning-rate laws in transient regimes.

2. Extinction

We have emphasized that the main disadvantage of solid propellant rocket motors, their lack of flexibility, can be remedied by developing methods for producing controlled extinctions. In Chapter 4 we saw that uncontrolled pressure tail-offs can be particularly detrimental at stage separations which require thrust termination over times of the order of 10 to 20 msec. Of the various techniques that have been proposed for achieving controlled motor extinction, we shall discuss only two, sudden depressurization and inhibitor injection.

2.1. Extinction by Depressurization

Extinction of a propellant grain subjected to sudden depressurization has been studied experimentally with small samples of a propellant and with full-scale motors.

Extinction of Samples by Depressurization

The apparatus used in laboratory depressurization experiments is shown in Fig. 8-38. A heated wire initiates combustion of the sample inside a bomb and combustion takes place in a controlled atmosphere at a prescribed pressure, ranging from one to some hundred atmospheres. This pressurized bomb is connected to a vacuum tank of large capacity, through a line with a burst diaphragm. At a specified time, a percussion device perforates the burst diaphragm thus lowering the pressure inside the bomb very rapidly. This rapid depressurization occurs over a time interval :

$$t_r = \frac{1}{\Gamma^2} \frac{V_0/A_d}{c^*},$$

where V_0 is the internal volume of the bomb, A_d the burst diaphragm area and c^* the characteristic velocity for the gases contained in the bomb. In most experiments the value of t_r is of the order of a millisecond; it can be varied by changing the value of A_d . For given pressures in the bomb and in the vacuum tank, the propellant sample is extinguished by a critical value of the burst diaphragm area $(A_d)_{lim}$; extinction occurs if and only if $A_d > (A_d)_{lim}$. Ciepluch (14-45) correlated extinction data on $(A_d)_{lim}$ in terms of the time interval Δt_{50} , which is defined as the difference between the time at which the pressure reaches half its initial value and the time at which the diaphragm ruptures. This time interval can be related to the previously introduced pressure evolution time :

$$\theta = \left| \frac{dt}{d \ln p} \right|,$$

according to the formula :

$$\theta = \frac{\Delta t_{50}}{p - \frac{p}{2}} = 2 \Delta t_{50}.$$

Experiments showed that extinction occurred at a limiting value $(\Delta t_{50})_{lim}$ (see Fig. 8-39). A typical propellant (composition 81% ammonium perchlorate, 19% poly-

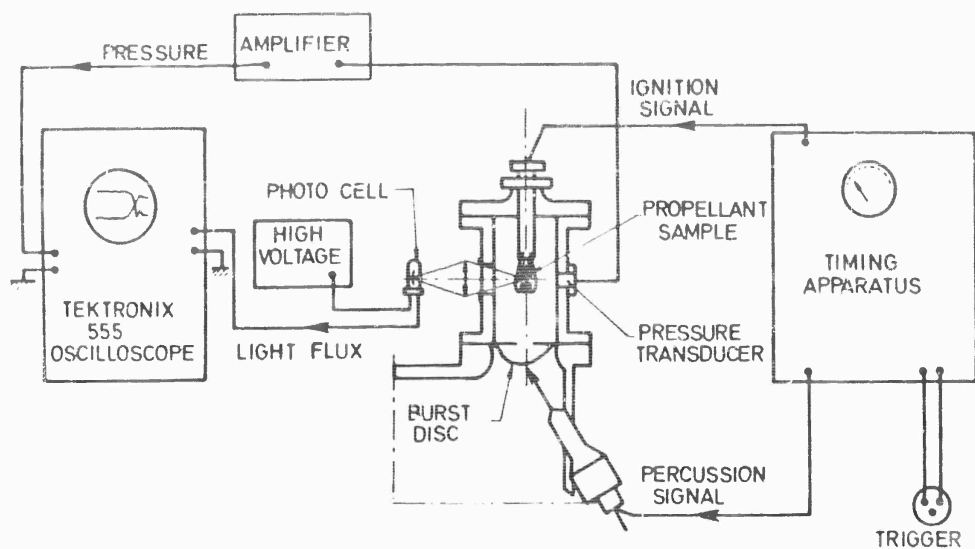


Fig. 8-38 Schematic diagram of apparatus for studying the extinction of a propellant sample by rapid depressurization.

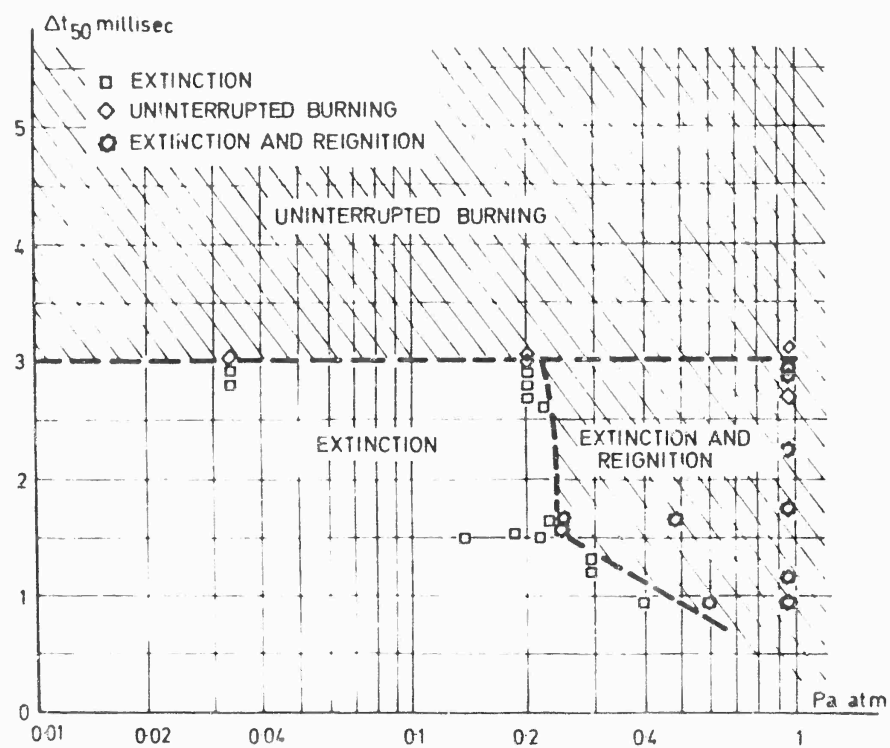


Fig. 8-39 Effect of ambient pressure on the critical expansion time Δt_{50} (44), (45).

butadiene-acrylic acid) has a value of $(\Delta t_{50})_{lim}$ of about 3.5 msec.

Some aspects of the extinction mechanism are evident. It is known that a pressure decrease produces an increase in the distance ϵ between the flame and the propellant surface, thereby reducing the temperature gradient $(T_f - T_w)/\epsilon$ and decreasing the heat flux received by the surface. Viewed differently, the decrease in the gas-phase reaction rates caused by the pressure decrease, introduces a thickening of the reaction zone and a tendency toward a more uniform temperature distribution with shallower temperature gradients. The eventual result of the decreased rate of heat transfer to the surface is a diminished pyrolysis rate and a reduced surface temperature. For heterogeneous propellants, these effects can be enhanced by a temporary change in gas-phase mixture ratio, resulting from unequal sensitivities of the pyrolysis rates of the two constituents to variations in surface heat flux. The gases temporarily become fuel rich and thereby suffer an appreciable reduction in flame temperature T_f , which in turn produces a further reduction in the heat flux to the surface.

The measured value of $(\Delta t_{50})_{lim}$ depends on the propellant but is insensitive to the value of the vacuum chamber pressure or the bomb pressure, except at the higher bomb pressures (> 0.2 atm), where reignition of the sample is observed to occur (see Fig. 8-39). Reignition is probably related to a residual heat bulge in the solid at its surface and may involve heterogeneous reactions.

Motor Extinction by Depressurization (43-47)

An experimental motor for studying extinction by depressurization is shown in Fig. 8-10. This conventional motor with a star-shaped grain normally operates with a nozzle throat area A_t . The nozzle can be jettisoned by explosive bolts in such a way that the throat area increases to A_{tc} . Nozzle removal requires about one millisecond. Provided that A_{tc}/A_t is sufficiently large and that dA_t/dt is also very large, depressurization is rapid enough to achieve extinction. Figure 8-41 shows depressurizations in which (a) the rate of pressure decrease $\dot{p}(t)$ is not sufficiently large to cause extinction (so that the motor continues to burn with the new nozzle throat area A_{tc}) and (b) extinction is achieved. Useful extinctions are not always complete at atmospheric pressure and above. Cool flames often appear at the nozzle exit because of combustion of volatile propellant components with air; complete extinction is assured only in a vacuum. Figure 8-42 shows photographs of the jet in normal operation and of the typical red residual flame that occurs after extinction. Figure 8-43 contains a representative pressure-time curve for the depressurization phase. It can be seen from Fig. 8-43 that in most experiments the depressurization curve is not smooth; acoustic-type combustion instabilities can be triggered during depressurization.

a) Extinction Conditions

Let us first consider cases in which $\theta = |dt/d \ln p|$ is close to the residence time t_r . If the ratio A_{tc}/A_t is sufficiently large, then complete extinction can be obtained if the ambient pressure p_a is lower than the flammability limit p_c ($p_a < p_c$); otherwise reignition can occur, followed by unstable combustion (Fig. 8-44). These low-frequency instabilities are easily recorded photographically (Fig. 8-45). The simultaneous conditions :

$$\theta \approx t_r,$$

$$A_{tc}/A_t > (A_{tc}/A_t)_{crit},$$

$$p_a < p_c$$

hh*

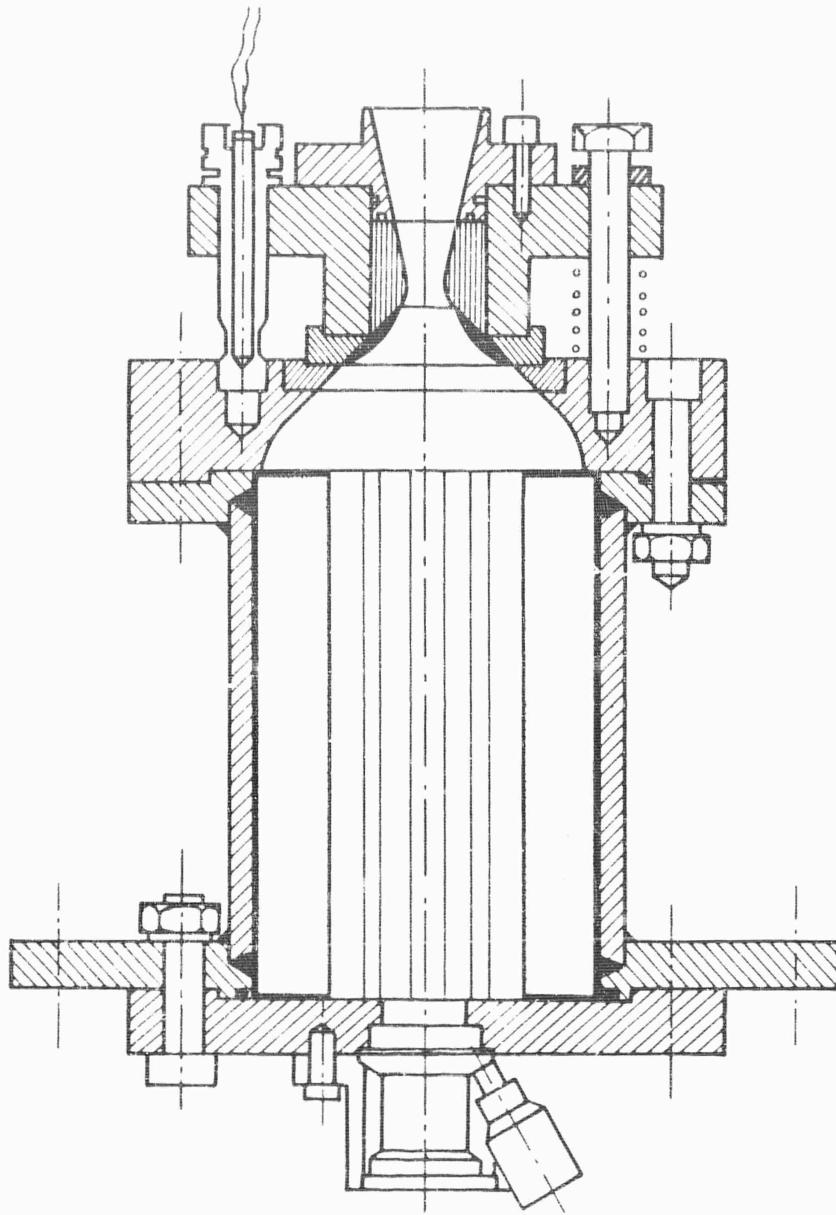
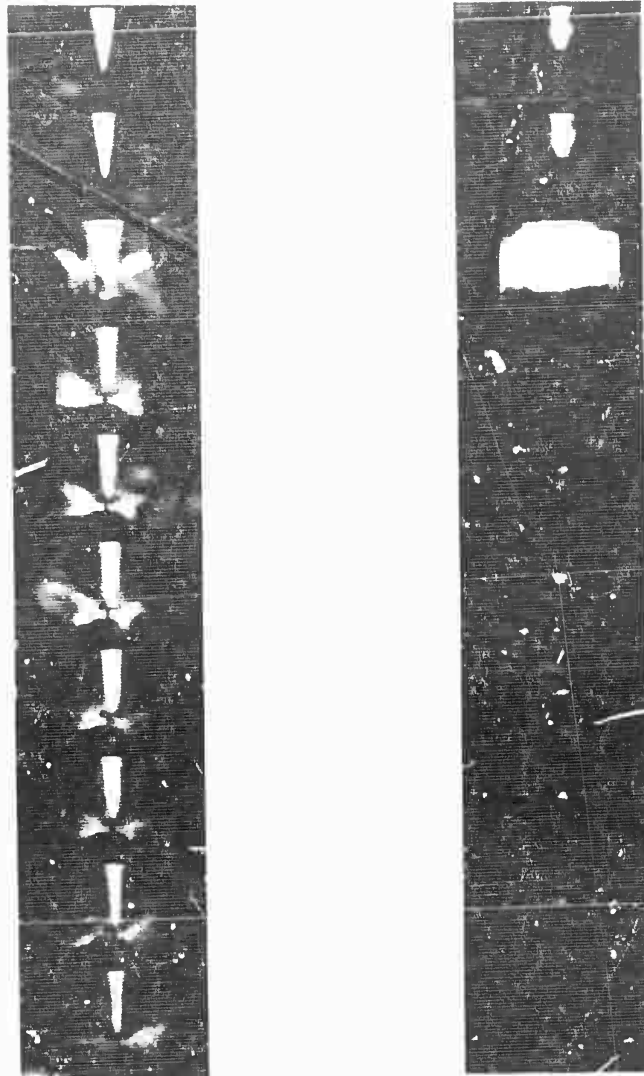


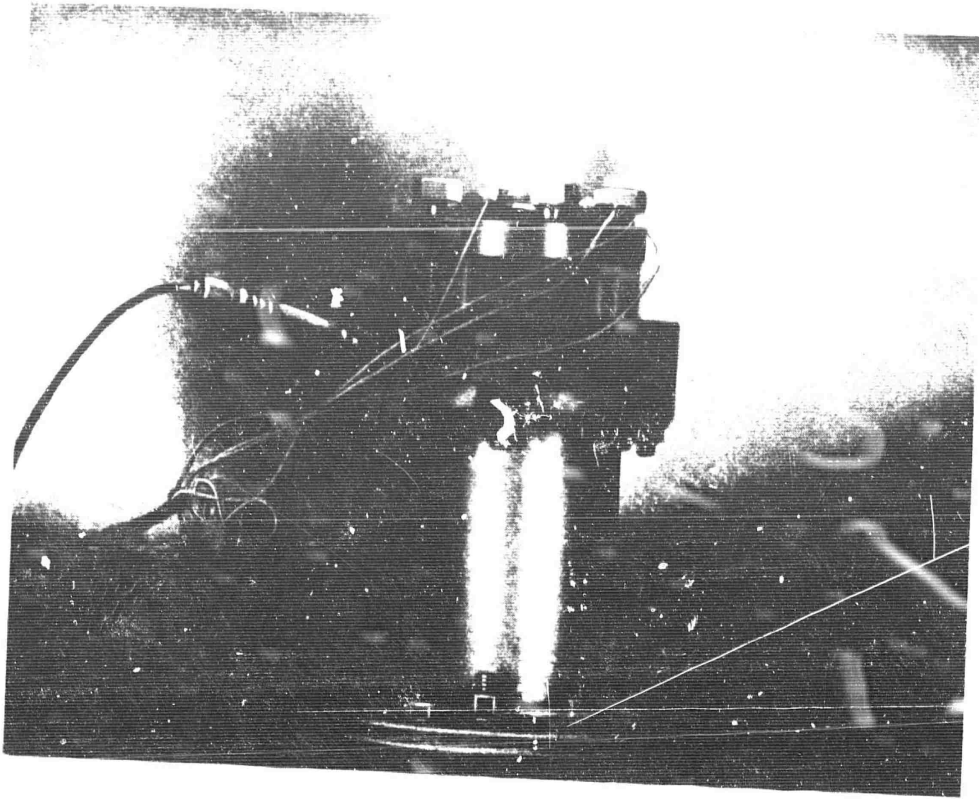
Fig. 8-40 Experimental apparatus for studying the extinction of solid rocket propellants by rapid depressurization.



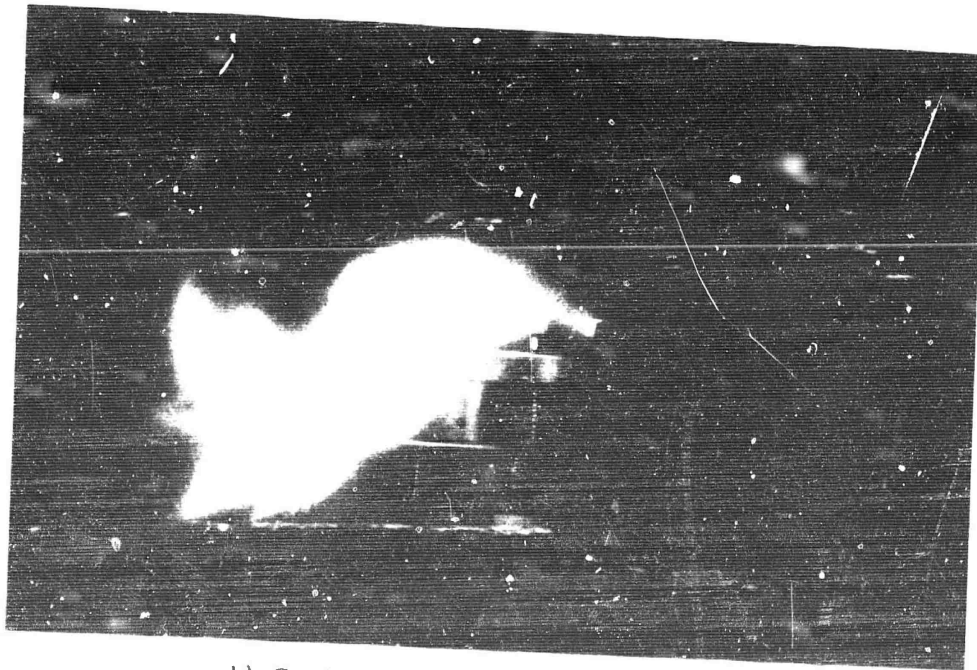
a) uninterrupted combustion

b) extinction

Fig. 8-41 Consecutive frames (40/sec) from films of rocket combustion during sudden depressurization



a) Steady-state combustion



b) Combustion during depressurization

Fig. 8-42 Extinction of solid rocket propellant by rapid depressurization

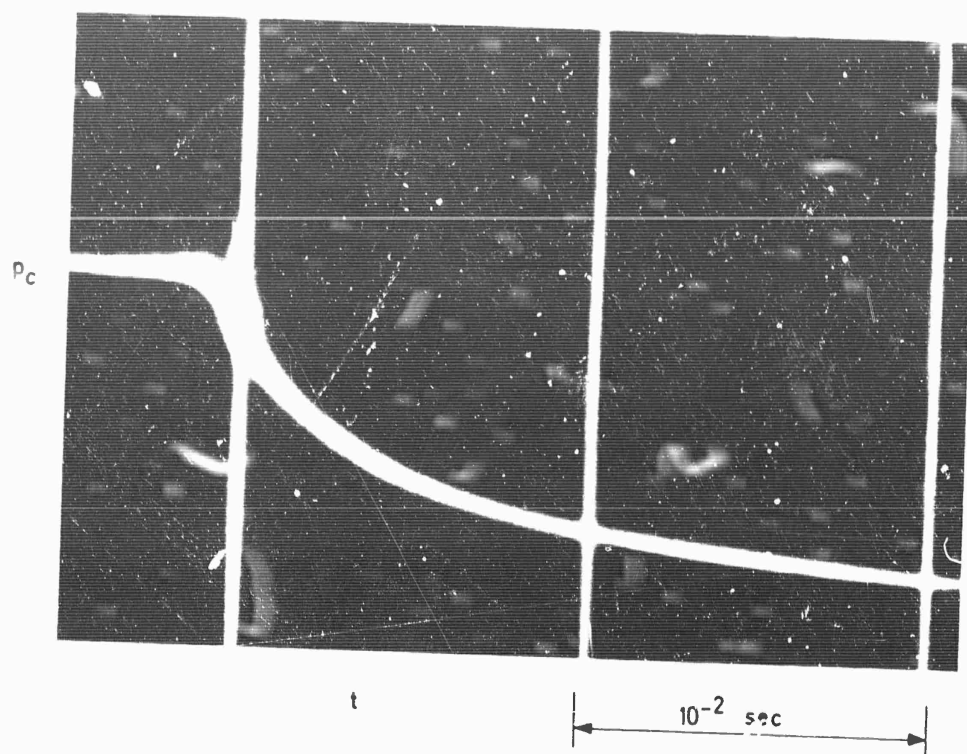


Fig. 8-43 Typical high-speed recording of pressure decay.

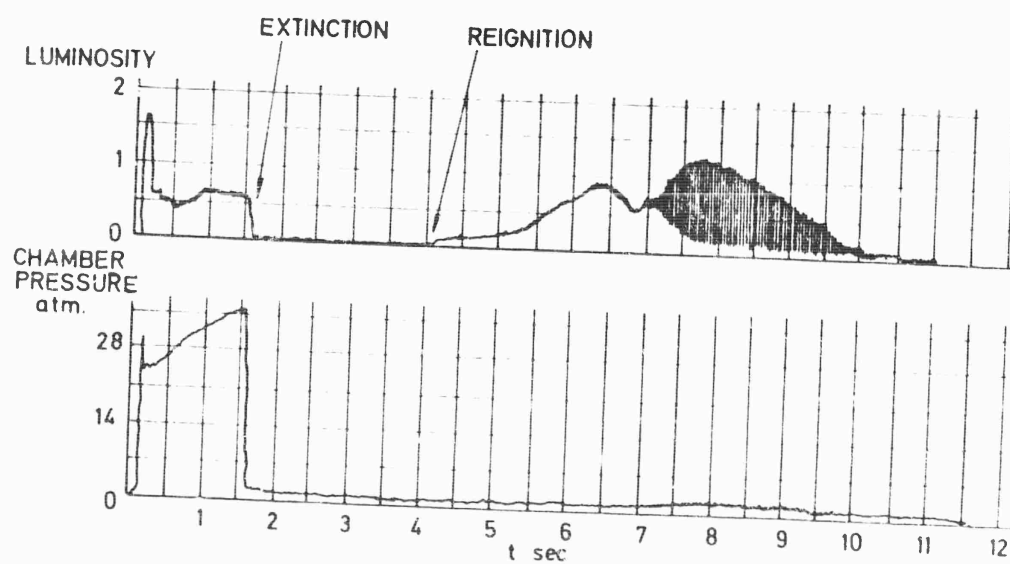


Fig. 8-44 Spontaneous reignition: variation of chamber pressure and luminosity with time (44), (45).



CAMERA SPEED: 40 Fps

Fig. 8-45 Combustion instability after spontaneous reignition.

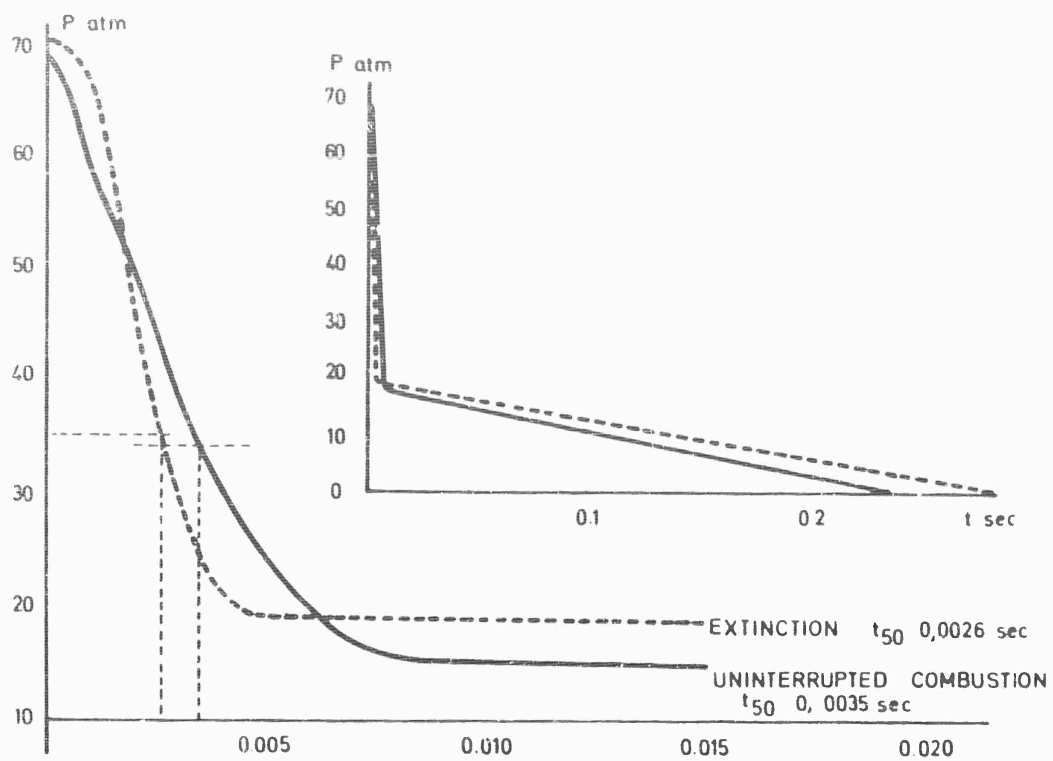


Fig. 8-46 Variation of chamber pressure with time during depressurization.

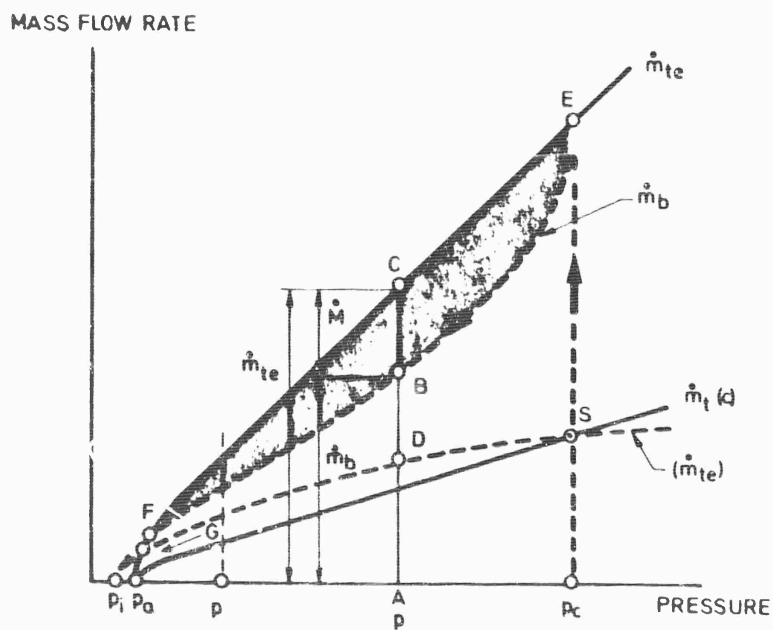


Fig. 8-47 Mass-flow-rate vs. pressure during the depressurization phase.

assure complete extinction.

If $\theta \approx t_r$ but $A_{te}/A_t < (A_{te}/A_t)_{crit}$, then two regimes occur, a rapid motor depressurization followed by a slow pressure decrease, as illustrated in Fig. 8-46. Extinction may still occur if θ or Δt_{50} is sufficiently small but it occurs slowly. The existence of two regimes can be explained by considering the pressure dependence of the propellant mass burning rate and of the mass flow rate through a nozzle of throat area A_{te} .

If θ is large compared with the residence time t_r (e.g., if the nozzle throat area increases), one can identify a critical extinction value for the ratio A_{te}/A_t . Under these conditions extinctions occur slowly with pressure curves that resemble those of Fig. 8-46, except in that the new initial rate of depressurization is slower. If the critical extinction area ratio is not achieved with the new throat A_{te} , then the motor approaches a new steady-state operating condition at a lower chamber pressure, corresponding to a balance between the burning rate and the nozzle mass flow rate through the larger throat. At these new low operating pressures, low-frequency instabilities often appear.

b) Determination of the Mass Flow

One can compute the mass flow rate of burned gases from experimental pressure-time curves. Use must be made of the mass and energy conservation equations :

$$\dot{m}_b = \dot{M} + \dot{m}_t$$

and :

$$M\dot{T} = \gamma [\eta T_c - T] \dot{m}_t + [\eta \gamma T_c - T] \dot{M} ,$$

where :

$$M = p \mathcal{V}^m / RT$$

and :

$$\dot{m}_t = \dot{m}_t(c) \left[\frac{p}{p_c} \cdot \frac{A_{te}}{A_t} \cdot \sqrt{\frac{T_c}{T}} \right] .$$

Here p_c is the steady-state chamber pressure, T_c is the steady-state combustion temperature, η is the combustion efficiency during depressurization, \mathcal{V} is the chamber volume at extinction, A_t is the initial nozzle throat area through which the mass flow rate is $\dot{m}_t(c)$ and A_{te} is the new throat area. The energy conservation equation may be replaced by an isothermal approximation $T = T_c$ or by a polytropic approximation $p/p_c = (T/T_c)^{\gamma/\gamma-1}$ in simplified, approximate calculation techniques. If we adopt the polytropic approximation, then the mass balance becomes :

$$\dot{m}_b = \frac{M(c)}{\gamma} \left(\frac{p}{p_c} \right)^{(1-\gamma)/\gamma} \frac{d(p/p_c)}{dt} + \dot{m}_{te}(t=0) \left(\frac{p}{p_c} \right)^{(\gamma+1)/2\gamma} ,$$

where the flow rate $\dot{m}_{te}(t=0)$ denotes the mass flow rate through the nozzle of throat area A_{te} at $t=0$ and $M(c)$ is the steady-state mass of gas contained in the chamber. Two important parameters that appear, are the initial characteristic length $L_t^* = \mathcal{V}/A_t$, which is related to a residence time t_r in steady operation $t_r = M(c)/\dot{m}_t(c)$, and the characteristic length after the throat area is increased $L_{te}^* = \mathcal{V}/A_{te}$, which is related to the residence time $t_{re} = M(c)/\dot{m}_{te}(t=0)$. Taking the

steady regime as a reference we can write the above equation in the form :

$$\frac{\dot{m}_b}{\dot{m}_t(c)} = \frac{t_r}{\gamma} \left(\frac{p}{p_c} \right)^{(1-\gamma)/\gamma} \frac{d(p/p_c)}{dt} + \frac{t_i}{t_{ie}} \left(\frac{p}{p_c} \right)^{(\gamma+1)/2\gamma} \quad (\text{Eq. 8-77})$$

Having measured $p(t)$, one can use Eq. 8-77 to plot \dot{m}_t , \dot{m}_b and \dot{M} as functions of pressure for the depressurization process. The result is shown in Fig. 8-47. The stable operation point is at pressure p_c where the steady nozzle flow rate $\dot{m}_t(c)$ equals the steady burned gases flow rate $(\dot{m}_b)_{ss}$. If the throat area is suddenly increased from A_t to A_{te} , the flow rate through the nozzle rises to \dot{m}_{te} at point E. It might be expected that the flow rate of products generated during depressurization follows the steady-state curve for $(\dot{m}_b)_{ss}$. This actually does not happen; a sizable increase in the burned gases flow rate is observed during the entire pressure history (curve \dot{m}_b). For example, at pressure p , the length of the line \overline{AB} represents \dot{m}_b , the length \overline{CB} (negative) represents \dot{M} and $\overline{AC} = \dot{m}_{te}$, flow rate through the nozzle. As can be seen from the diagram, the flow rate \dot{m}_b represented by the line \overline{AB} is much larger than the segment \overline{AD} which represents the steady-state flow rate of combustion products at the same pressure. This diagram also shows that for appropriate relative positions of curves \dot{m}_b and \dot{m}_{te} , there exist two special points, F and G. When the instantaneous operating point reaches F, new stable operating conditions can be established and the motor will eventually approach the operating point G. Point F exists only if the pressure at the flammability limit is below ambient (the case illustrated in Fig. 8-47); otherwise motor extinction occurs. If point G corresponds to an operating pressure below a critical value p^* which is a function of the characteristic length L_c^* , then combustion instabilities occur at the final operating conditions. Diagrams like Fig. 8-47 are very useful in discussing the operation conditions of a motor, in both steady and unsteady regimes. The maximum flow rate of the burned propellant during the transient process is usually smaller when extinction is achieved than when a new operation point, such as G, is reached (Fig. 8-48). The burned propellant flow rate \dot{m}_b is related to the burning rate by $r = \dot{m}_b / \rho_p A_b$ where A_b is the instantaneous burning surface area. For appropriate values of A_{te} , the calculated burning rates can exceed their steady-state values r_{ss} by more than an order of magnitude (Fig. 8-49).

There are many possible causes for this high burning rate during depressurization. The most obvious one is the erosion effect for the grain configuration shown in Fig. 8-40. The erosion function (see Chapter 7) is of the form :

$$\epsilon = r/r_0 = 1 + k(\rho_g u_g)^\beta,$$

where r_0 is the regression rate under no-flow conditions, $\rho_g u_g$ the mass flux in the central channel and β is an exponent of the order of 0.8. This formula neglects the threshold effect. Neglecting the mass of gases in the convergent portion of the nozzle, we can write, as a first approximation,

$$\rho_g u_g A_p \approx p A_{te} / c^*$$

and we find that the burning rate becomes :

$$r = r_0 \left[1 + k \left(\frac{p}{c^*} \frac{A_{te}}{A_r} \right)^\beta \right],$$

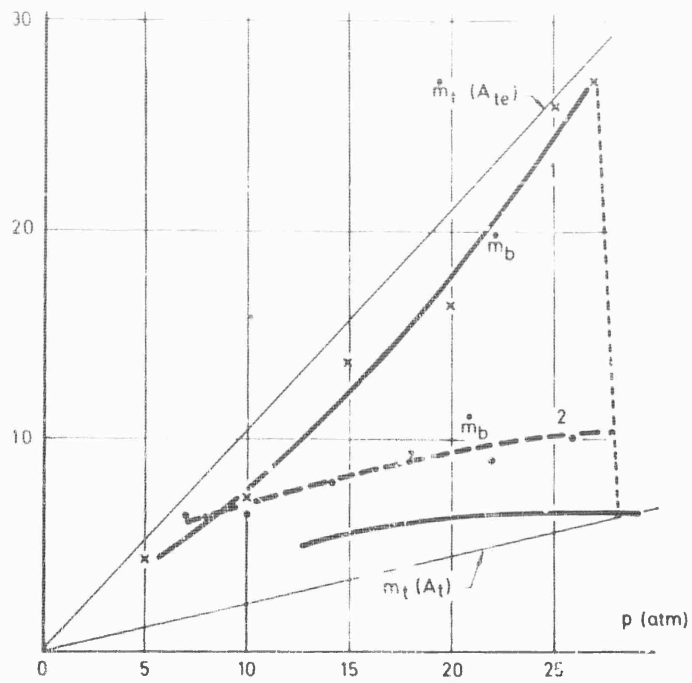


Fig. 8-48 Mass-flow-rate variation during the transient phase.

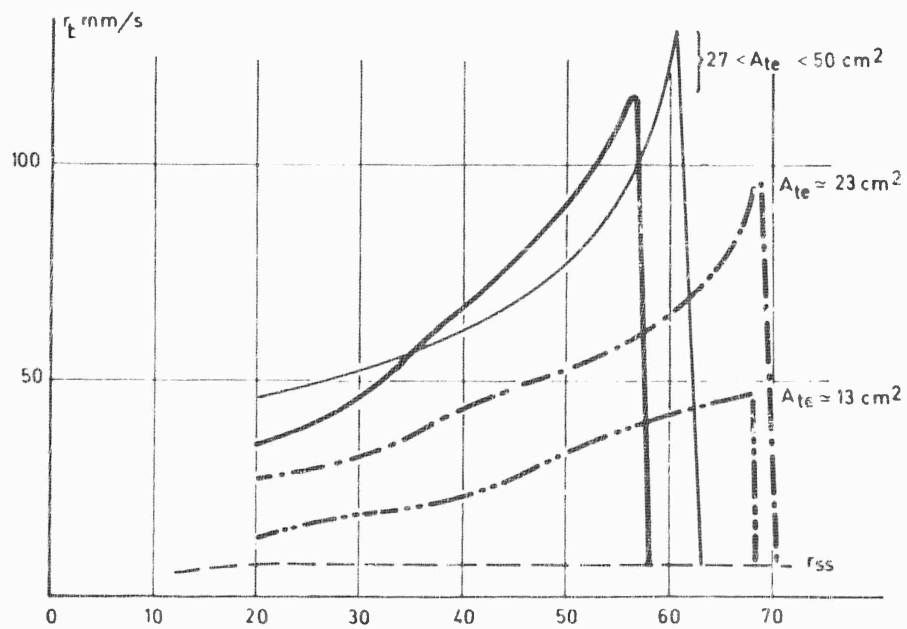
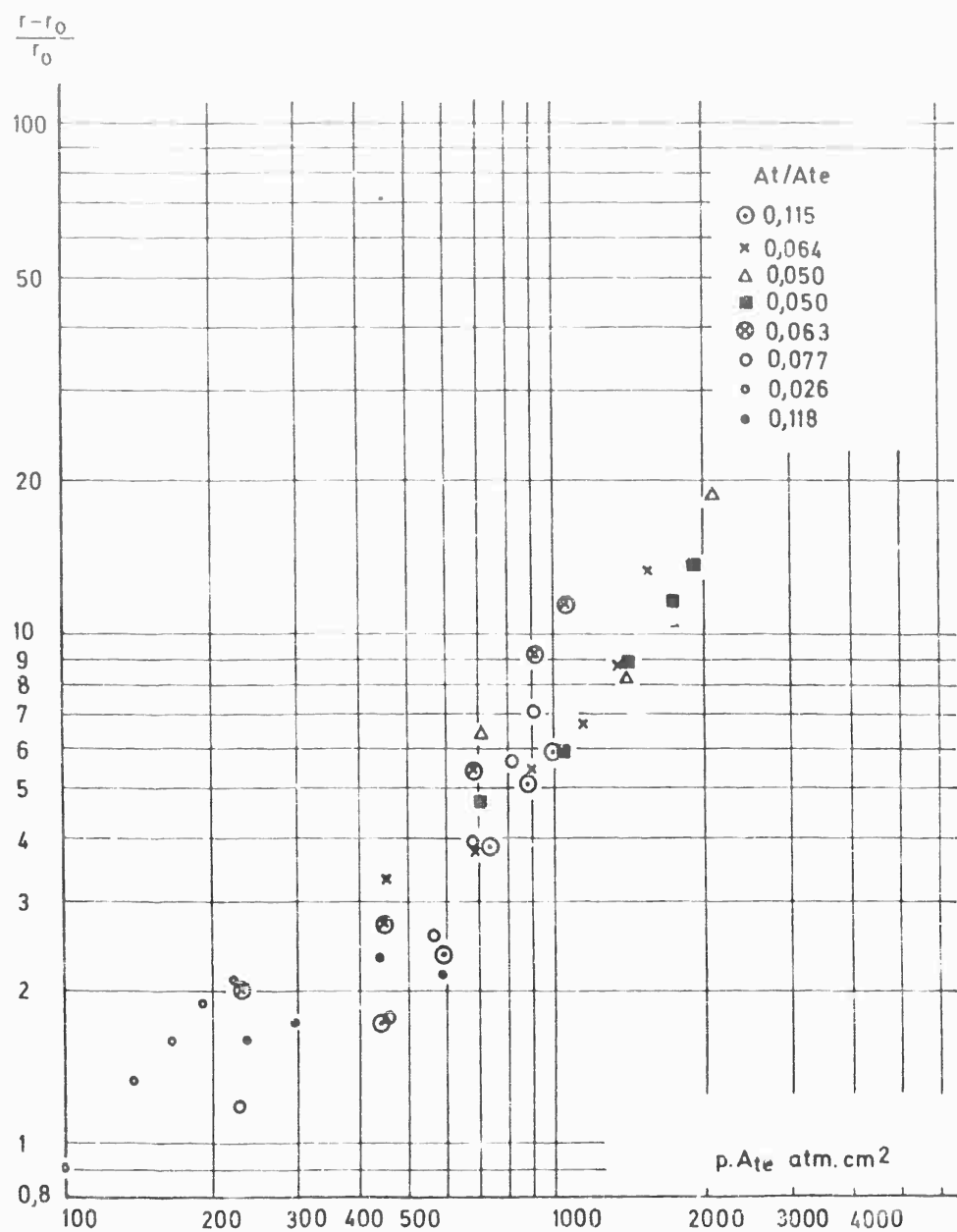


Fig. 8-49 Variation of burning rate with pressure during rapid depressurisation.



A_{te} = total discharge port area after opening of aft end closure
 A_p = grain port area at the extinction

Fig. 8-50 Experimental determination of the exponent m of the burning rate law: $f = ap^n + bp^m (A_{te}/A_p)$

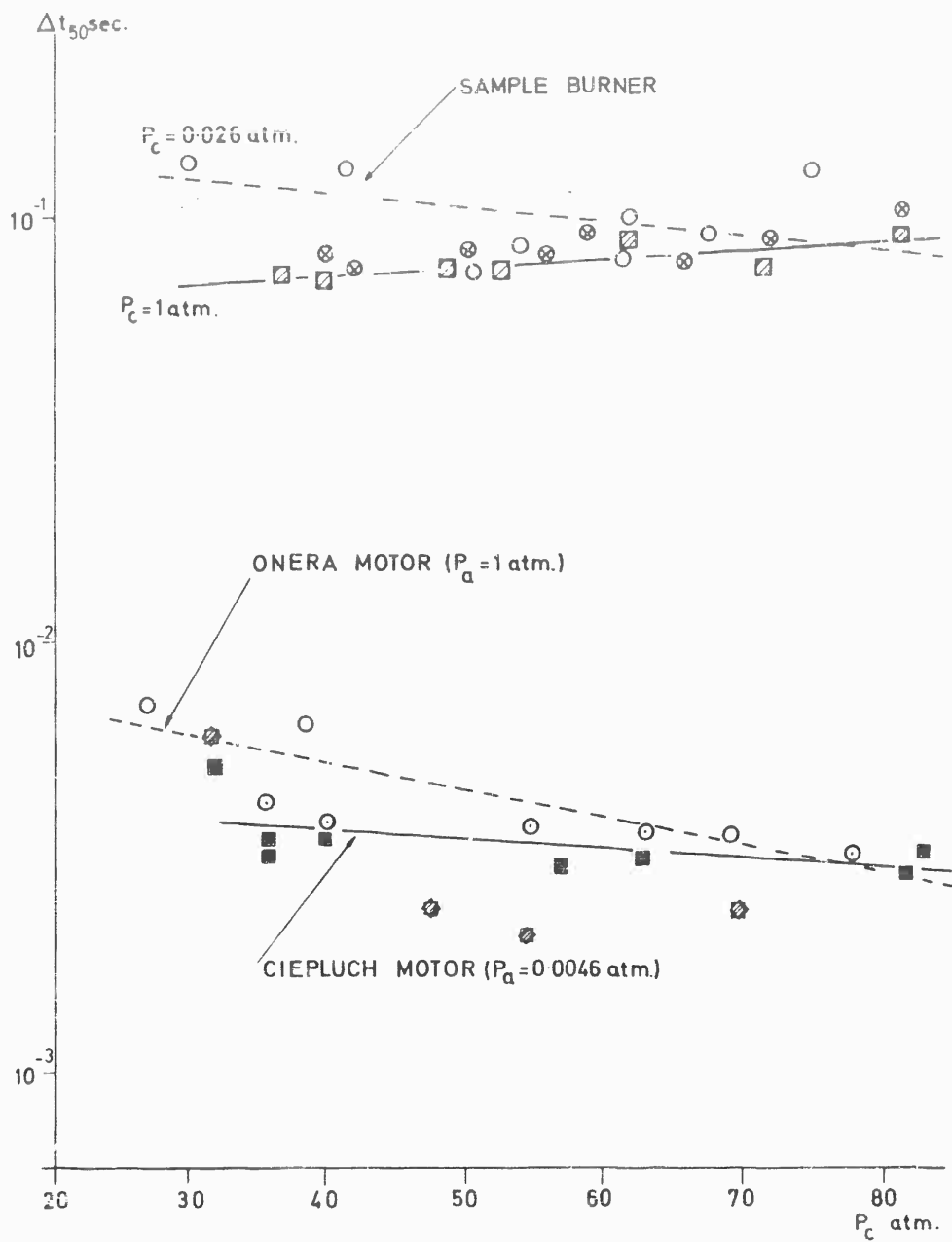


Fig. 8-51 Effect of chamber pressure on the critical expansion time with various experimental apparatus.

$$\text{or: } \frac{r - r_0}{r_0} = k' \left(\frac{p A_{te}}{A_p} \right)^{\beta}$$

A logarithmic plot of $(r - r_0)/r_0$ versus $p A_{te}$, yields a reasonable correlation of experimental points; A_p is approximately constant in this series of experiments. The empirical slope is unity which corresponds to $\beta = 1$ (Fig. 8-50).

In view of the amount of uncertainty in the values of various coefficients, the relation :

$$r = a p^n + k'' p^{n+1} \frac{A_{te}}{A_t} \frac{A_t}{A_p} \quad (\text{Eq. 8-78})$$

can be taken as a first approximation, for the pressure dependence of the burning rate during a rapid chamber depressurization.

Erosion effects certainly do not explain all of the experimental results since such a burning rate increase has been observed with end-burning grains, on which erosion effects are likely to be negligible. In order to isolate the erosion effect, comparative tests should be made with end-burning grains (zero erosion effect) and with radially burning grains with either forward or aft venting ports, for the same propellant.

c) Parameters controlling Motor Extinction

We have indicated in Section 2.1., 'Extinction of Samples by Depressurization', that Δt_{50} must be less than a critical value, for extinction of a given propellant to occur. The remaining problem is to relate Δt_{50} to motor operating conditions. We have stated that the critical value of Δt_{50} appears to be insensitive to chamber pressure. Evidence for the approximate validity of this same conclusion in motor extinction experiments is shown in Fig. 8-51; it appears that Δt_{50} decreases slightly when the pressure increases.

Assuming an isothermal chamber depressurization, one can show that the parameter Δt_{50} depends mainly upon the characteristic length L_c^* of the motor :

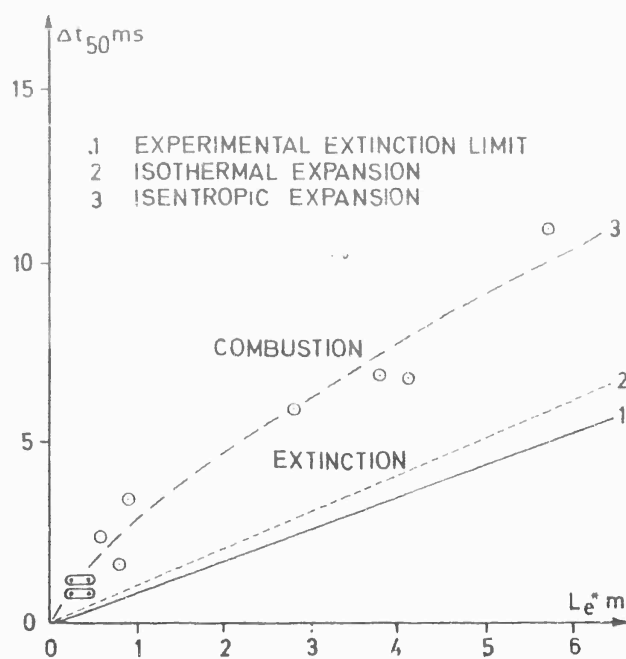
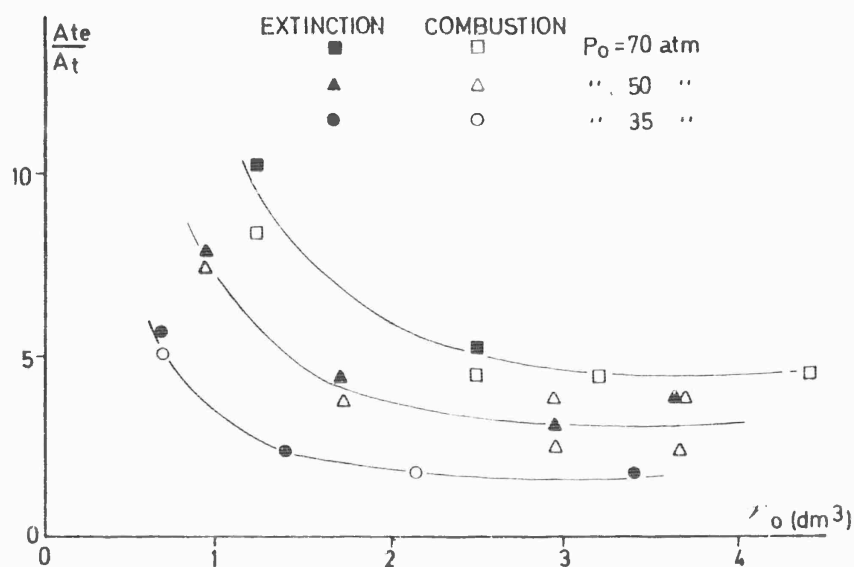
$$\Delta t_{50} = \frac{\ln 2}{\Gamma_c^2} L_c^* .$$

If an adiabatic depressurization is assumed, then the alternative expression :

$$\Delta t_{50} = \frac{2}{\gamma - 1} \frac{1}{\Gamma_c^2} (2^{\gamma-1/2\gamma} - 1) L_c^*$$

is obtained. These two values of Δt_{50} are shown as functions of L_c^* in Fig. 8-52. The formulas neglect propellant gas generation during depressurization.

A theory of extinction assuming an unsteady burning-rate law of the form $r = ap^n$ and an isothermal evolution of the gases leads to the relation :

Fig. 8-52 Extinction limit ($p_c = 70 \text{ atm}$).Fig. 8-53 Influence of the free port volume on the area ratio A_{te}/A_t required for extinction.

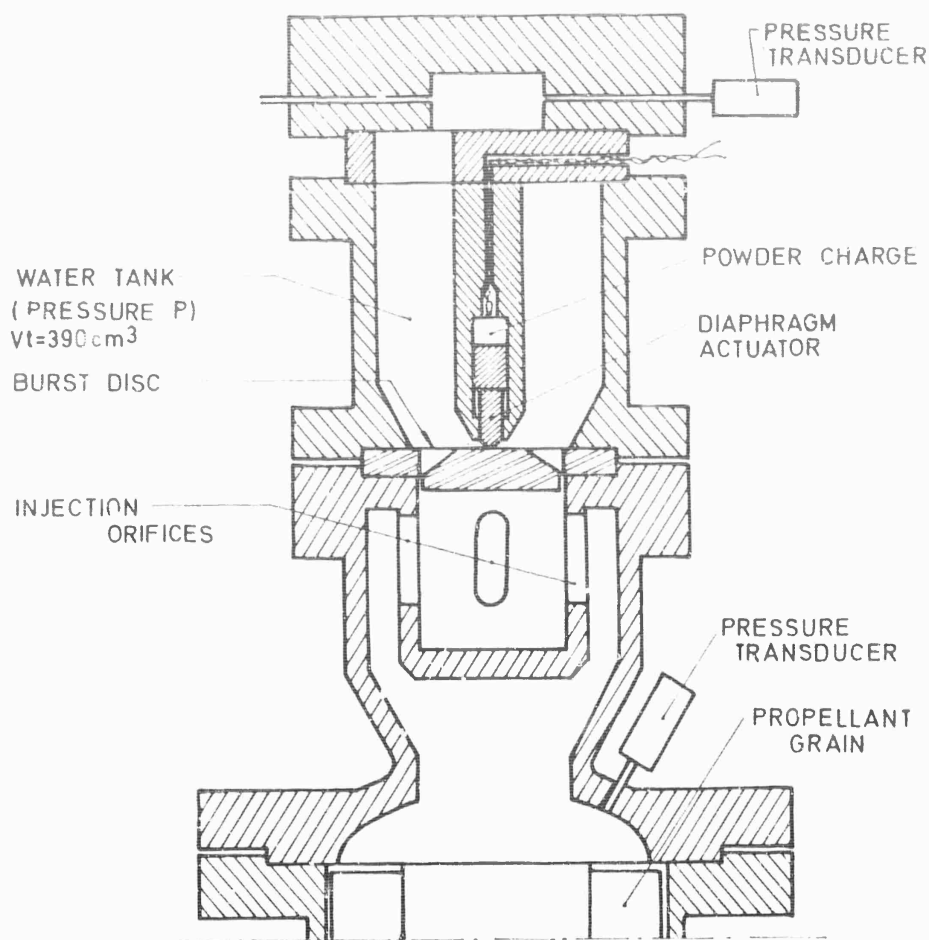


Fig. 8-54 Experimental apparatus for extinction by water injection.

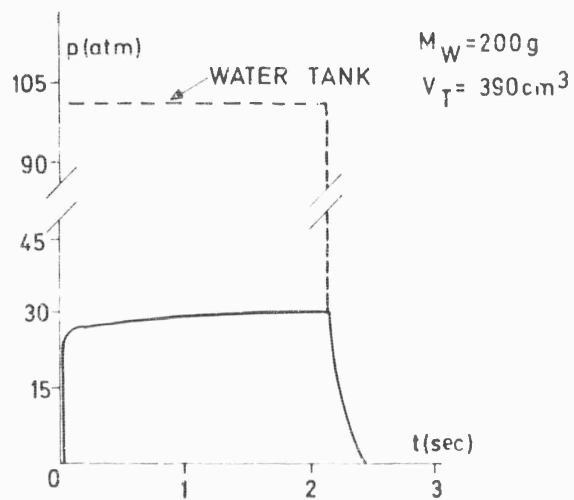


Fig. 8-55 Variation of pressure with time for extinction by water injection.

$$\Delta t_{50} = \frac{1 - \left(\frac{1}{2}\right)^{1-n}}{1-n} \cdot \frac{1}{\Gamma^2 c^*} \cdot \frac{A_{te}}{A_{te} - A_t} \cdot L_e^*$$

With a burning-rate law of the form $r = ap^n + kp$ (A_{te}/A_t [A_t/A_p is assumed to be constant], the expression :

$$\Delta t_{50} = \frac{1 - \left(\frac{1}{2}\right)^{1-n}}{1-n} \cdot \frac{1}{\Gamma^2 c^*} \cdot \frac{A_{te}}{A_{te} \left(1 - \frac{k}{a} p_c^{1+n}\right) - A_t} \cdot L_e^*$$

is obtained.

As can be seen from Fig. 8-52, the experimental values of Δt_{50} are larger than the isothermal and adiabatic values computed, without taking combustion into account. Moreover, the curve representing the variation of Δt_{50} as a function of L_e^* is not a straight line as the above theories predict. The linear relationship can be used only as a first approximation (43). The last two formulas also predict that for a given propellant, the critical ratio A_{te}/A_t for extinction increases as L_e^* or the chamber volume V increases. However, the experimental results shown in Fig. 8-53 exhibit the opposite trend. These contradictions may be explicable on the grounds that extinction conditions depend on dA_{te}/dt as well as on A_{te}/A_t ; the theoretical formulas are oversimplified.

We indicated earlier in this section that extinction will be complete only if the ambient pressure p_a is below the flammability limit and that if a new steady regime can occur, then the new operating conditions will be subject to low-frequency combustion instability whenever the new equilibrium operating pressure is below the critical pressure p^* (Fig. 8-47). This critical pressure varies with the characteristic length L_e^* according to the approximate formula :

$$p^{*2n} L_e^* = \text{constant} .$$

Extinction conditions are also affected by the configuration of the combustion zone (end or radial burning) and by the location of the venting ports (fore and aft of the grain). The function $A_{te}(t)$ must be adapted to the required pressure decay history.

2.2. Extinction by Injection of Inhibiting Substances

Studies of extinction by material injection have been directed toward discovering useful extinction materials and defining efficient injection conditions (48), (49). We shall discuss only two approaches, rapid injection of a small amount of water and explosive injection of an inhibiting powder.

Extinction by Water Injection

Results of experiments on motor extinction by water injection, reported by Jaroudi and McDonald (48), were interpreted as implying the existence of a minimum injection time of about 0.8 sec, below which extinction is not possible. Similar conclusions were drawn by Taback (49) who quoted a somewhat shorter minimum injection duration of the order of 0.1 sec. Values for extinction delay τ , $\theta \equiv \Delta t p/\Delta p$, obtained in these studies, are two to four times larger than the corresponding times

(~ 35 msec) required for extinction by depressurization. The required water mass was reported by these authors to depend on the gas mass M contained in the chamber and on the burning surface area A_b at the time of extinction. The formula quoted for the mass of water was :

$$m_w = 2 M + a A_b$$

where a is a constant.

On physical grounds, it seems that the required water mass and the extinction delay time for extinction by water injection, should depend on the injection rate \dot{m}_w or the injection time t_w . For very short injection times there may well exist a limiting minimum value of \dot{m}_w for extinction. For very long injection times, the required water mass for extinction should become proportional to t_w and the extinction requirements might then best be expressed in terms of a critical value of \dot{m}_w . The injection times (48), (49) appear to be rather long and therefore might fall in the second of these two limiting regimes.

Experiments conducted at ONERA have shown that complete extinction can be achieved with injection durations of the order of one millisecond when the flow rates are sufficiently large. The experimental apparatus is shown in Fig.8-54. The water is injected under a pressure of the order of 100 atm through slits which allow large flow rates for a short duration. Injection is initiated by puncturing a metal disc. Extinction has been achieved with a water mass of 200 g. Although the flow rate is very large there is no overpressure at injection (Fig.8-55).

Comparison of the three sets of experiments shows that the water flow rate per unit burning area is of the order of $1.7 \text{ g sec}^{-1} \text{ cm}^{-2}$ in Jaroudi's work, $4 \text{ g sec}^{-1} \text{ cm}^{-2}$ in Taback's experiments and $525 \text{ g sec}^{-1} \text{ cm}^{-2}$ in the ONERA study. At very short injection times, the high pressure level required for the high water flow rate may lead to a heavy injection system. In a practical design, a compromise between water mass and the injection system mass would have to be made and it seems likely that there would exist an optimum injection time, for which the total mass of the extinction system assumes a minimum value. In order to determine the optimum system, one would have to measure the water mass m_w required for extinction as a function of the injection time t_w . A coupling of this information with information on the weights of injection systems would provide the basis for a rational extinction-system design.

The extinction mechanism is complex. In many respects it resembles the motor extinction mechanism for depressurization. In order to obtain extinction, the rate of decrease of chamber pressure must be sufficiently high, i.e., $\theta = |dt/d \ln p|$ must be smaller than a critical value.

During the injection phase a portion of the burning surface is wetted by the water. Water vaporization then absorbs heat thereby lowering the surface temperature and the combustion temperature. This causes the propellant pyrolysis rate and the local and average pressures in the chamber to decrease. The consequent depressurization can then lead to extinction of the entire grain by the mechanisms that were described in Section 2.1., 'Extinction of Samples by Depressurization'. Water injection thus produces a decrease of temperature gradient and of surface temperature by liquid-solid contact, a decrease of bulk temperature by heat-sink effects due to water vaporization and ultimately a sharp pressure decrease in the entire chamber.

Extinction by Powder-Injection (Explosive Canister Technique)

- ii* Extinction can be achieved by quickly injecting a combustion-inhibiting powder which

is sprayed on the burning surface by an explosion. The best results were obtained with ammonium bicarbonate (CO_3KNH_4) which produced a delay of a few milliseconds before extinction. However, some difficulties in extinction-system design have been encountered with this technique.

3. Conclusions

Although the steady-state operation of a motor can be predicted with relatively good accuracy, the transient ignition and extinction regimes are poorly understood. In the present chapter, we have attempted to summarize the most important experimental results and the most recent theoretical developments on ignition and extinction, in an effort to indicate fruitful directions for future research. Such research, both in the laboratory and on the test stand, is of considerable practical importance for increasing the variety of applications of solid propellant rockets, by providing them with greater control and with restart capabilities.

Among specific topics that require additional study is the exact role of flame propagation in the pressure increase at ignition. The flame propagation process must be studied in greater detail.

Perhaps the most basic problem that arises in transient burning regimes, is the definition of the burning rate. Since transient burning-rate laws are known to differ appreciably from steady-state burning-rate laws, it is necessary to improve our understanding of the factors that affect the transient burning rate, in order to be able to compute ignition and extinction pressure-time histories with sufficient accuracy for use in motor design calculations.

From the fact that we devoted much more space to the discussion of ignition phenomena than to the discussion of extinction phenomena, it may be inferred that extinction processes are understood much less thoroughly than ignition processes. Extinction therefore requires a greater amount of research effort at present and the number of studies on extinction are currently increasing. These studies should aid in increasing the flexibility of solid propellant rockets.

References

- (1) Baer A. D., and Ryan N. W., Ignition of Composite Propellants by Low Radiant Heat Fluxes, Solid Propellant Rocket Conference, AIAA Preprint No. 64-119, 1964.
- (2) Rosser W. A., Fishman N., and Wise M., Ignition of Simulated Propellants based on Ammonium Perchlorate, AIAA J. 4, 1615-1622, 1966.
- (3) Sutton D., and Wellings P. C., The Ignition Delay Times of Solid Propellants Heated by Forced Convection, Rocket Propulsion Establishment, Westcott, Bucks, England, Report No. 45 (n/d).
- (4) McAlevy R. F., III, Cowan P. L., and Summerfield M., The Mechanism of Ignition of Composite Solid Propellants by Hot Gases, ARS Progress in Astronautics and Rocketry: Vol. I Solid Propellant Rocket Research (ed. M. Summerfield), pp. 623-652, Academic Press, New York, 1960.
- (5) Baer A. D., Ryan N. W., and Salt D. L., Propellant Ignition by High Convection Heat Fluxes, ARS Progress in Astronautics and Rocketry: Vol. I Solid Propellant Rocket Research (ed. M. Summerfield), pp. 653-672, Academic Press, New York, 1960.

- (6) Kling R., Maman A., and Brulard J., La cinétique de l'allumage des poudres composites sous l'influence de flux de chaleur élevés, La Recherche Aérospatiale No. 103, pp. 3-10, Nov.-Dec. 1964.
- (7) Beyer R.B., and Fishman N., Solid Propellant Ignition Studies with High Flux Radiant Energy as a Thermal Source, ARS Progress in Astronautics and Rocketry: Vol. I Solid Propellant Rocket Research (ed. M. Summerfield), pp. 673-692, Academic Press, New York, 1960.
- (8) Price E.W., Bradley H.H., Jr., Dehority G.L., and Ibricu M.M., Theory of Ignition of Solid Propellants, AIAA J. 4, 1153, 1966.
- (9) Price E.W., Bradley H.H., Jr., Hightower J.D., and Flemming R.O. Jr., Ignition of Solid Propellants, Solid Propellant Rocket Conference, Palo Alto, Calif., AIAA Preprint No. 64-120, 1964.
- (10) Keller J.A., Baer A.D., and Ryan N.W., Ignition of Ammonium Perchlorate Composite Propellants by Convective Heating, AIAA 3rd Aerospace Sciences Meeting, AIAA Preprint No. 66-65, 1966.
- (11) Summerfield M., Shinnar R., Hermance C.E., and Wenograd J., A Critical Review of Recent Research on the Mechanism of Ignition of Solid Rocket Propellants, 14th International Astronautical Conference, Paris, 1963; also Princeton University Aeronautical Engineering Report, No. 661, 1963.
- (12) Keller J.A., Baer A.D., and Ryan N.W., The Ignition of Composite Solid Propellant by Hot Gases, Pyrodynamics 3, 1-15, 1965.
- (13) Allen H., and Pinns M.L., Relative Ignitability of Typical Solid Propellants with Chlorine Trifluoride, NASA TN D-1533, 1963.
- (14) McAlevy R.F., III and Summerfield M., Ignition of Double Base Solid Rocket Propellants, ARS J. 32, 270, 1962.
- (15) McAlevy R.F., III, The Ignition Mechanism of Composite Solid Propellants, Ph.D. Thesis, Princeton University, June 1960; also Princeton University Aeronautical Engineering Laboratory Report No. 557, 1961.
- (16) Grant E.H., Jr., Lancaster R.W., Wenograd J., and Summerfield M., A Study of the Ignition of Solid Propellants in a Small Rocket Motor, AIAA Preprint No. 64-153, 1964.
- (17) Roth J.F., and Wachtell G.P., Heat Transfer and Chemical Kinetics in the Ignition of Solid Propellants, I & EC Fundamentals 1, 62, 1962.
- (18) Evans M.W., Beyer R.B., and McCulley L., Initiation of Deflagration Waves at Surfaces of Ammonium Perchlorate, J. Chem. Phys. 40, 2431-2438, 1964.
- (19) Anderson R., Brown R.S., and Shannon L.J., Critical Comparison of Solid Propellant Ignition Theories, United Technology Center Report No. TM 34-63 U2, Sunnyvale, Calif., 1963.

- (20) **Hernance C.E., Shinnar R., and Summerfield M.,** Ignition of an Evaporating Fuel in a Hot Oxidizing Gas including the Effect of Heat Feedback, AIAA J. 3, 1584, 1965.
- (21) **Kennard E.H.,** Kinetic Theory of Gases, pp. 311-327, McGraw-Hill, New York, 1938.
- (22) **Widder D.V.,** The Laplace Transform, Princeton University Press, Princeton, New Jersey, 1941.
- (23) **Handbook of Chemistry and Physics (36th Edition),** p.287, transform No. 42, Chemical Rubber Publishing Co., Cleveland, Ohio, 1954.
- (24) **Chapman A.J.,** Heat Transfer, Chapters 8 and 9, McMillan Co., New York, 1960.
- (25) **McAdams W.H.,** Heat Transmission (3rd Edition), McGraw-Hill, New York, 1954.
- (26) **Williams F.A.,** Combustion Theory, Appendix B, Addison-Wesley Publishing Co., Reading, Massachusetts, 1965.
- (27) **Hicks B.L.,** J. Chem. Phys. 22, 414, 1954.
- (28) **Anderson R., Brown R.S., Thompson G.T., and Ebeling R.W.,** Theory of Hypergolic Ignition of Solid Propellants, AIAA Preprint No. 63-514, 1963.
- (29) **Anderson R., Brown R.S., and Shannon L.J.,** Ignition Theory of Solid Propellants, AIAA Preprint No. 64-156, 1964.
- (30) **Brown R.S., Wirrick T.K., and Anderson R.,** Theory of Ignition and Ignition Propagation of Solid Propellants in a Flow Environment, AIAA Preprint No. 64-157, 1964.
- (31) **Mitchell R.C., and Ryan N.W.,** Flame Spread on Solid Propellant, AIAA Preprint No. 64-128, 1964.
- (32) **Parker K.H., Wenograd J., and Summerfield M.,** The Ignition Transient in Solid Propellant Rocket Motors, AIAA Preprint No. 64-126, 1964.
- (33) **DeSoto S., and Friedman H.A.,** Flame-Spreading and Ignition Transients in Solid Grain Propellants, AIAA Preprint No. 64-122, 1964.
- (34) **Paul B.E., Lovine R.L., and Fong L.Y.,** Propellant Surface Flame Propagation in Rocket Motors, AIAA Preprint No. 64-125, 1964.
- (35) **McAlevy R.F., III, Magee R.S., and Wrubel J.A.,** Flame Spreading over the Surface of Double Base Propellants, AIAA Preprint No. 64-109, 1964.
- (36) **Bradley H.H., Jr.,** Theory of a Homogeneous Model of Rocket Motor Ignition Transients, AIAA Preprint No. 64-127, 1964.

- (37) **Gibby H.**, The Control of Ignition Transients through Propellant Grain Inhibiting, AIAA Preprint No. 64-124, 1964.
- (38) **Paul B.E., Lovine R.L., and Fong L.Y.**, A Ballistic Explanation of the Ignition Pressure Peak, AIAA Preprint No. 64-121, 1964.
- (39) **Dubrow B., Guth E.D., and Wong M.W.**, Ballistics of Solid Propellants during Thrust Modulation, AIAA Preprint No. 64-130, 1964.
- (40) **Paul B.E., and Lovine R.L.**, Ignition Problems in Solid Propellant Rockets, presented at 25th AGARD Meeting, La Jolla, California, 22-24 April 1965 (to appear in Proceedings).
- (41) **Carlson L.W., and Seader J.D.**, A Study of Heat Transfer Characteristics of Hot Gas Ignition, AIAA 3rd Aerospace Sciences Meeting, New York, January 24-26, 1966.
- (42) **Allan D.S., Bastress E.K., and Smith K.A.**, Heat Transfer Processes during Ignition of Solid Propellant Rockets, AIAA 3rd Aerospace Sciences Meeting, New York, January 24-26, 1966.
- (43) **Coates R.L., Polzien R.E., and Price C.F.**, Design Procedures for Combustion Termination by Nozzle Area Variation, J. Spacecraft and Rockets 3, 419, 1966.
- (44) **Ciepluch C.**, Effect of Rapid Pressure Decay on Solid Propellant Combustion, ARS J. 31, 1584-1586, 1961.
- (45) **Ciepluch C.**, Effect of Composition on Combustion of Solid Propellant during a Rapid Pressure Decrease, NASA TN D-1559, Lewis Research Center, Cleveland, Ohio, December 1962.
- (46) **Rodeau H.C.**, Rocket Thrust Termination Transients, ARS J. 29, 406-409, 1959.
- (47) **Barry R.E., and Brothers J.E.**, Thrust Termination Transients in Solid Propellant Rockets, ARS J. 31, 848-849, 1961.
- (48) **Jaroudi R., and McDonald A.J.**, Injection Thrust Termination and Modulation in Solid Rockets, AIAA J. 2, 2036-2038, 1964.
- (49) **Taback H.J., Day E.E., and Brown T.P.**, J. Spacecraft and Rockets 2, 332-337, 1965.
- (50) **Lovine R.L., Fong L.Y., and Paul B.E.**, Diffusional Analyses of Composite Propellant Ignition, and its Application to Solid Rocket Ignition, AIAA Preprint No. 64-117, 1964.

Chapter 9

**Experimental Aspects of Combustion
Instability**

Nomenclature

A	burning surface area; propellant area; chamber cross-sectional area
a	sound speed
\bar{e}_0	average acoustic energy per unit volume in the chamber
h	outlet tube length
L^*	characteristic length of chamber
\bar{m}	propellant average mass burning rate (mass per unit area per second)
p	pressure
\bar{p}	mean chamber pressure
p_{b0}	pressure amplitude of the oscillation at the burning surface
p_0	local (complex) amplitude of the pressure oscillation
$\text{Re} \{ \}$	real part of
S	outlet tube cross-sectional area
t	time
V	chamber volume
\bar{v}_b	average velocity of the burned gases leaving the propellant surface
Y	acoustic admittance
y	dimensionless response function defined in Eq. 9-12
α	growth constant for the oscillations
α_A	growth constant with propellant in only one end of the chamber
α_d	dissipation rate constant defined in Eq. 9-3
α_i	growth constant for each mechanism i
α_1	growth constant caused by the processes occurring at the burning surface
α_{2A}	growth constant with propellant in both ends of the chamber
γ	ratio of specific heats for the gas in the chamber
ν	frequency (cps)
$\bar{\rho}$	mean density of gas in the chamber

ω oscillation frequency (radians/sec)

Script Letter

l cylindrical chamber length

Experimental Aspects of Combustion Instability

1. History; Suppression Techniques

Early in the Second World War irregular thrust-time curves were occasionally observed for solid propellant rockets. In extreme instances the chamber pressure would exceed the structural strength of the motor casing, causing the rocket to explode. These occurrences prompted closer investigations of the phenomenon, first in the United Kingdom (1), then in the United States (2). It was inferred that the irregular chamber pressure traces characteristic of the phenomenon (see Fig. 9-1) were often associated with oscillations in the flows (1). They could not be explained in terms of variations in burning area or ordinary erosive burning. The phenomenon, known as irregular burning, was therefore assumed to originate either in the combustion process itself or in the interaction of the combustion process, with acoustical wave motions in the chamber. This general view has now been substantiated even though the detailed mechanisms involved are not understood entirely.

Methods for suppressing irregular burning in particular motors were developed empirically before any understanding of the phenomenon was obtained (3), (4), (5). For example, the earliest instances of irregular burning occurred with internally burning tubular grains and it was found that inserting an axial metal rod of circular or flat cross section in the chamber, drilling radial perforations in the grain, or employing grains with noncircular axial perforations, all tended to eliminate the irregularities (3). Later, studies showed that with some propellants annular ports exhibited a greater tendency toward irregular burning than tubes did (6), while with others the tube was least regular (7); in some cases even internally burning stars behaved irregularly (6), thus the effect of motor geometry was found to be rather complex. For certain higher energy propellants, it was found that helical patterns of axial rods (5) and in some cases even more elaborate suppression devices (8), (9), were needed in order to eliminate irregular burning completely in tubular grains. Often, but not always, propellants with higher energy content or propellants with higher rate of energy release (10) exhibit greater tendencies toward irregular burning; hence irregularities can sometimes be suppressed by reducing the energy content of the propellant (9). A newer suppression technique that is generally more desirable, is to introduce additives such as carbon, aluminum, other metals or metal oxides into the propellant formulation (11). Appropriate metallic constituents usually tend to both increase the energy content and suppress irregular burning. Reviews of early experience with irregular burning and its suppression may be found (5), (9), (11), (12); a later review of suppression techniques is given in Ref. (13).

2. Classification of Instabilities

The general phenomenon of irregular burning, also termed 'secondary peaks', 'resonance burning' or 'combustion instability', may be divided into two main categories, acoustic instability and nonacoustic instability.

The early observations that irregular burning and blowup were often accompanied by pressure oscillations of acoustic frequencies, led investigators to assume that the phenomenon involved amplification of acoustic waves in the chamber by the combustion processes occurring therein. Further support for this view was provided by early experimental demonstrations, that wave patterns of the oscillations accompanying irregular burning usually exhibit characteristics expected for traveling or standing ('sloshing') tangential acoustic modes, standing longitudinal, 'organ-pipe' modes or occasionally radial modes in the chamber (8).

In Ref. (8), the first four or five harmonic modes were identified for longitudinal modes in long tubular motors and for traveling tangential modes in motors with annular ports. Furthermore, the effectiveness of most of the suppression devices discussed above, can be explained on the basis of an acoustic mechanism of instability; for example, rods and small radial perforations attenuate sound vibrations (thereby tending to offset any amplification effect of the combustion process), as do small solid or liquid metal oxide particles that condense in the combustion gases of propellants containing metals or metal oxides. Irregular burning produced by mechanisms involving sound vibrations in an essential way, is termed acoustic instability.

It has been demonstrated somewhat more recently, that unstable combustion and consequent irregular burning can occur without interaction between the combustion processes and sound waves in the chamber. For example, metalized propellants burning under isobaric conditions have recently been observed to burn irregularly, exhibiting burning rate oscillations of identifiable low frequencies that are presumably attributable to periodic shedding of agglomerated metal, from the surface of the propellant (14), (15). 'Chuffing' combustion oscillations at frequencies below any acoustic frequencies of the chamber, have long been known to occur in certain solid propellant formulations, at low pressures and inside small motors (7), (16), (17), (18). A variety of theoretical explanations of chuffing-like phenomena have been proposed (19), (20) and theories have also predicted the occurrence of non-acoustic instabilities at higher frequencies (21), (22). Any occurrence of irregular burning that does not involve interaction between the combustion process and a sound field in an essential way, can be termed nonacoustic instability.

We might mention that Green (9) has proposed a different terminology. He suggests that 'sonance' denotes the growth of high-amplitude waves from infinitesimal disturbances and 'resonance' denotes conditions under which a coupling between gas-phase oscillations and solid-phase decomposition occurs. Resonance would therefore be an acoustic instability while sonance could apparently be either acoustic or nonacoustic. Nonacoustic instabilities that do not involve oscillations, which are possible at least theoretically (22), do not appear to fit into either of Green's categories.

An additional breakdown of combustion instability into linear and nonlinear instabilities is useful. Linear instabilities are those which can be described in terms of small-amplitude perturbations about steady, normal burning. Nonlinear instabilities are those involving finite-amplitude perturbations. Both acoustic and non-acoustic instabilities, in principle, can be divided into linear and nonlinear sub-categories. Although small-amplitude, apparently linear oscillations have been observed in rocket motors, the occasionally destructive secondary pressure peaks characteristic of irregular burning are certainly finite-amplitude, nonlinear phenomena. Nevertheless, criteria for the occurrence of finite-amplitude disturbances in motors may often be the same as criteria for the occurrence of linear instabilities, i.e., the secondary peaks may result from amplification of small-amplitude disturbances. This is a premise of the first interpretations of acoustic instability. That this is not always so, has been borne out by recent experimental demonstrations of motors that are linearly stable but nonlinearly unstable (23 to 25). These

experiments imply that nonlinear instability is an important separate subcategory of acoustic instability. Nonacoustic mechanisms involving both linear (22) and nonlinear (16), (19) phenomena can also be envisaged and have been documented.

After the earliest era of experimental research on combustion instability, during which primary emphasis was placed on studying the severity of the nonlinear oscillations and their effect on the burning rate, in an effort to define the practical significance of the phenomenon (1 - 3), an era of intensive experimental research on linear acoustic instability developed because as we have said, most of the early theoretical attempts to explain irregular burning were based on linear acoustic mechanisms. As a consequence of this intensive research, the experimental techniques for studying linear, acoustic instability are most highly developed. Indeed, linear, acoustic mechanisms are capable of predicting a wide variety of conditions under which combustion instability will occur and the predicted trends agree with many experiments. However, not all experiments agree with the trends implied by linear, acoustic mechanisms (for example, the linearly stable, nonlinearly unstable motors mentioned above). It is therefore important to develop experimental methods for studying all types of combustion instability. Experimental techniques for studying nonlinear acoustic instabilities are not very well developed, partially because the importance of such mechanisms was reconfirmed only recently.

Another reason for the more primitive state of development of experimental methods for studying nonlinear, acoustic instabilities is that it is more difficult to design crucial, fundamental, experimental tests for them. One of the sources of difficulty is that a variety of different nonlinear, acoustic mechanisms can be envisaged and tests that are critical for one of these mechanisms may not be critical for another. Often, nonlinear mechanisms are too complex for critical experimental tests to be defined. Similar problems in designing relevant experiments also arise for non-acoustical instabilities, both linear and nonlinear; here too, a wide variety of mechanisms can occur, some (e.g., L^* instability (20) see Section 6.4.4) being relatively simple to define and others much more complex. An indication that the existence of these problems has been recognized is provided by the observation that in developing new motors, engineers sometimes undertake to demonstrate that when perturbed by shock pulses produced by explosive charges, the motor is stable (exhibiting both the absence of induced irregular burning and a sufficiently rapid recovery of normal burning).

In the following section, we shall discuss experimental methods that have been employed in the analysis of combustion instabilities. Fundamental, experimental results that have been obtained for linear, acoustic instability will be reviewed in Section 4. Experiments on acoustic instabilities in rocket motors will be considered in Section 5. The final section of this chapter is concerned with the relatively small amount of experimental information available on nonacoustic and nonlinear instabilities.

3. Experimental Methods for Analyzing Combustion Instabilities

In this section we shall concern ourselves with precisely what measurements are made and with the instrumentation employed. Chamber geometries and other aspects of overall experimental arrangements will be discussed later. Much of the material in the present section is drawn from the useful review given in Ref. (26).

3.1. Instantaneous Pressure Measurements

Instantaneous measurements of pressure, at various locations in the combustion chamber, has proved to be the most useful experimental technique in studying combustion instability. Depending on the type of instability, frequencies of the oscillations can range from 1 to 10^5 cps. Therefore time-response requirements for

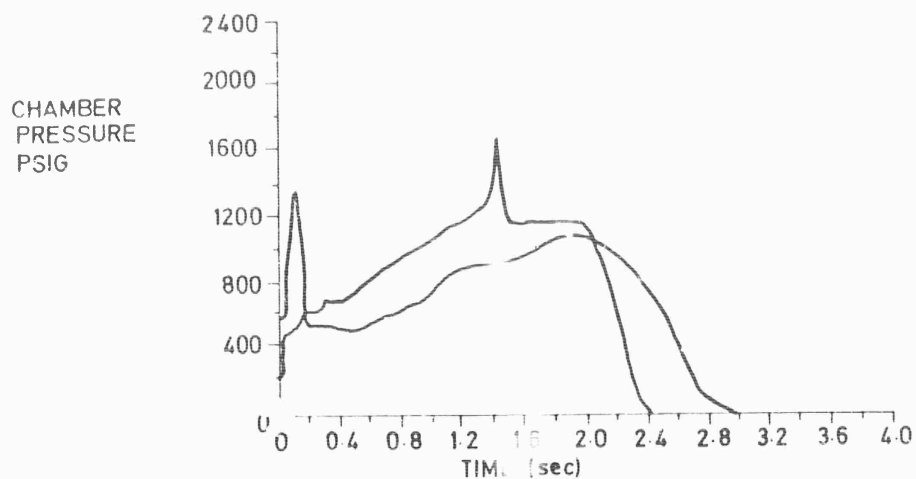


Fig. 9-1 Typical examples of irregular reaction of internal-burning cylindrical charges (5).

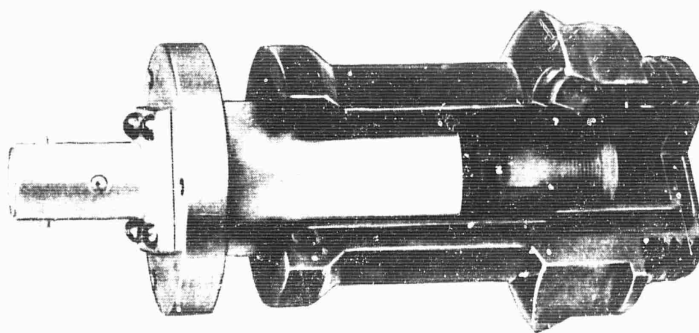
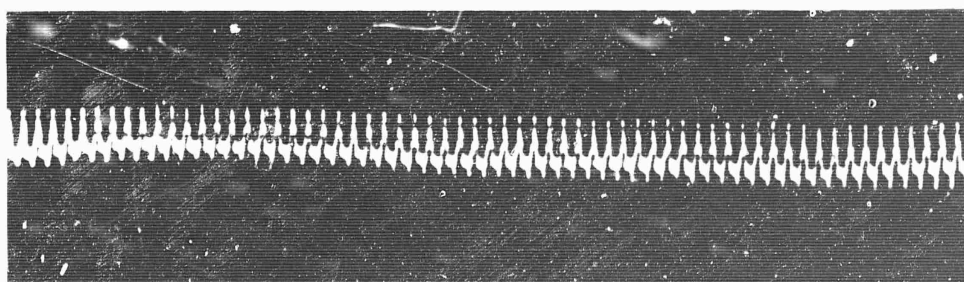


Fig. 9-2a Photograph of an ONERA pressure transducer.



FREQUENCY 3,600 cps
 AMPLITUDE 3.4 atm
 TANGENTIAL MODE

Fig. 9-2b Pressure recording from such a transducer.

pressure-measurement instrumentation vary considerably. Conventional pressure transducers are acceptable in the low-frequency portion of the frequency regime. Special pressure transducers are available that can be made to yield acceptable results, up to frequencies of about 2×10^4 cps. Accurate pressure measurement at the higher frequencies is quite difficult, although newly available equipment makes it possible, through some effort, to attain acceptable response over the entire frequency range of interest.

Sensing elements of pressure pickups can be made to operate on a variety of different principles. However, three main principles appear to be employed in present instruments suitable for measurements of combustion instability. These are (a) sensing the change in electrical capacitance of a chamber (capacitance-type or diaphragm-type gauges), (b) sensing the change in electrical resistance of a wire due to strain (conventional-type strain gauges) and (c) sensing the change in electrical polarization of a material due to stress (piezoelectric-type gauges) (27). Some evaluations have concluded that strain gauges are most promising (28), (29) while others imply that capacitance-type gauges are best for high-frequency response under combustion conditions (30). In this regard, it seems noteworthy that the Kistler transducers, currently adopted by many investigators as representing the most promising instruments for combustion instability work, operate on the piezoelectric principle. It is interesting to note that Ref. (29) states "... piezoelectric pickups are not suitable for high temperature operation ...". We may conclude that transducer performance is ultimately governed by design factors other than the principle of the sensing element.

There are too many manufacturers of pressure transducers for us to present a complete list here. We shall merely mention the names of three manufacturers whose transducers have been employed in combustion instability work: Norwood, Photocon and Kistler. Some laboratories have developed their own pressure transducer designs for use in combustion instability work. A cutaway view of one such transducer, developed at ONERA, is shown in Fig. 9-2a. This is a flush-mounted, water-cooled, capacitance-type gauge; the diaphragm is located at the bottom of the photograph, cooling water flows through the sleeve and the capacitance-sensing equipment is located in the central core. This transducer is capable of responding acceptably at frequencies up to about 3×10^4 cps. A pressure recording of combustion instability, obtained with such a transducer, is shown in Fig. 9-2b. Conditions of this recording correspond to a tangential mode in a star recess of a star-shaped, cylindrical grain; the frequency is 3600 cps, the amplitude is 2.4 atm and harmonics are evident.

Numerous problems besides transducer selection arise, in obtaining quantitative pressure measurements in combustion instability work (31). We shall discuss a few of them here.

The high-temperature gases, to which the sensor is exposed, pose a problem, since they are capable of burning out the sensing element in a fraction of a second. Recessing the transducer from the surface alleviates the problem somewhat but this can also degrade the frequency response seriously. The most satisfactory solution to the problem produced by the temperature environment appears to be to water-cool the sensor and flush-mount the gauge. The sensitivity of most pressure sensors appears to be influenced very little by water cooling. However, it is important that gauge calibration and testing be carried out at the same water flow rates because the coolant flow rate affects the calibration.

For high-frequency oscillations, care must be taken to insure that the size of the detection element is small compared with the wavelength of the chamber mode. This is necessary because the transducer output responds to the average pressure over the detection element. Effectively, this requirement eliminates certain

transducers from consideration for use at the higher frequencies.

Problems are sometimes posed by the requirements that the transducer output be compatible with reasonably long transmission lines to the recorder and be of sufficient magnitude to drive a high-speed recorder. Indeed, recording techniques constitute a major consideration in designing instrumentation. High-frequency instability measurements generally require a wide band width and necessitate instrumentation, not ordinarily found on rocket test stands. Oscillographs, oscilloscopes with cameras and magnetic tape recording systems can be used (26). The quality of tape recording techniques has recently been improving at a relatively rapid rate.

It is desirable for meaningful data analysis that the transducer exhibit a linear response and not manifest any tendency toward "ringing" at its own characteristic frequencies. Proper transducer mounting techniques usually insure acceptable response at the lower frequencies. Transducer design inevitably involves a trade-off between response time and overshoot; many of the transducers capable of responding to high frequencies exhibit one or more preferred ringing frequencies in the vicinity of 10^5 cps. Most investigators appear to believe that it is best to eliminate undesirable ringing and to assure linear response through the mechanics of transducer design (27). However, electronic compensation techniques can sometimes be used to correct the outputs of transducers with undesirable characteristics (26), (32). The use of electronic compensation involves, firstly, determining what undesirable characteristics the transducer output has and then designing an electronic system that operates on the transducer output, producing a new output in which the undesirable characteristics are removed. A variety of compensation techniques exist. One simple concept is to break the signal by a set of band pass filters and to apply a different amplifier gain to each band. A method for removing a linear oscillation at a characteristic ringing frequency is provided by the more sophisticated "Dynamic Analog Differential Equation Equalizer" (32). Here the response of the detection element is approximated by a linear differential equation with parameters adjusted to match the characteristics of the element and the compensator effectively uses the adjusted parameters and the transducer output to calculate the input to the detector. Somewhat sophisticated approaches to electronically compensating for nonlinearities in the pickup also exist (29). When attempted, electronic compensation should be based on characteristics exhibited by the transducer, in the particular mounting arrangement that is to be used in the experiment. It should also be performed as early as possible in the signal processing sequence.

A variety of practical problems arise in attempting to obtain high-frequency pressure measurements in motors designed for operational rather than research use (26).

It should be emphasized here that in order to characterize properly the acoustic properties of pressure vibrations in a rocket chamber, it is necessary to make pressure measurements at more than one point in the chamber. For example, standing waves cannot be distinguished from traveling waves by means of a single pressure measurement. Standing and traveling first tangential modes in a cylindrical chamber can be distinguished by measuring the relative phases of the pressure oscillations, seen by two sensors located 90° apart; in this case, if the phases differ by 0° or 180° , the oscillation is a standing mode while if the phases differ by 90° or 270° , the oscillation is a traveling mode (furthermore, the results will show either the direction in which the wave is traveling or from a relative amplitude measurement, the location of the nodal line). There may also be reasons for making measurements in both upstream and downstream parts of a cylindrical motor, in order to uncover the axial dependence of the wave shape, for example. In motors of complex internal geometry, it may be desirable to make pressure

measurements in various compartments that are expected to have different acoustic and/or mean flow properties.

3.2 Vibrations of the case

Pressure oscillations of the gases inside the combustion chamber necessarily produce vibrations of the solid propellant grain and the motor case. The influence of grain and case vibrations on the acoustic field in the gas is an important phenomenon that we shall discuss later. Here we merely wish to point out that the existence of these sympathetic vibrations provides an additional source potentially available for measurements of oscillatory combustion. Case or grain vibrations can be monitored by accelerometers, microphones or thrust gauges.

Instruments sensing case or grain motions and also motions of other key components of the rocket vehicle, are of practical utility, e.g., in failure analysis, since locations of local regions of high stress or fatigue can be inferred from the results. In principle, grain or case vibration measurements can also produce quantitative data concerning oscillation frequency, pressure amplitude, wave form and phase within the chamber. However, it is usually so difficult to relate local, instantaneous gas pressure or burning rates to local case movements, that such measurements yield quantitative data only for the frequency. Therefore, little quantitative information concerning the nature of the combustion instability itself can currently be provided by vibration measurements. There is one exception to this general conclusion: Imbedding vibration sensing instruments in the grain or on a surface of the grain can provide information concerning viscoelastic damping within the grain, provided that the grain geometry is not too complex. However, this sometimes poses formidable problems in instrument mounting. In practice, devices such as accelerometers are often attached externally to motor cases during development tests, merely as an inexpensive means of ascertaining whether or not combustion oscillations exist in the motor.

A wide choice of vibration-sensing equipment is available commercially. Instead of citing specific examples, we merely interject here the caution that in order to measure the oscillation frequency (or sometimes even to detect oscillations), one must select equipment which responds at sufficiently high frequencies and possesses no natural vibrational frequencies of its own, below roughly 10^5 cps.

3.3. Methods of Data Analysis

Data obtained by the measurement techniques that we have discussed represent pressures (Section 3.1) or in some cases, displacements or related quantities (Section 3.2) as functions of time. It is desirable for purposes of interpretation to extract from this data mean pressures (averaged over times long compared with oscillation periods but short compared with times required for internal geometry of the gas cavity to change appreciably), frequencies of the principal oscillation, wave shapes of the principal oscillations, amplitudes of oscillation for the major frequencies and relative phases of the major oscillations (particularly as seen by transducers mounted at different locations in the motor). Most of the information obtained so far has been in the form of curves of mean pressure vs. time, frequencies vs. time and pressure amplitude vs. time for various frequencies. This information has been obtained through data analysis methods that fall into two principal categories, real-time analysis and post-test analysis. The first category utilizes oscillograph and oscilloscope recording techniques while the second category utilizes tape recording.

Real-time analyses of mean pressure and of oscillatory pressure amplitude can be obtained quite easily, by passing the signal through a high-pass filter and recording on an oscilloscope the filter output and also the difference between the original signal and the filter output (26). An oscilloscope trace of this type is illustrated in Fig. 9-3. This type of separation is useful for weak oscillations because the

oscillatory amplitude can then be recorded with high amplification. A slightly more sophisticated technique is to rectify the a. c. filter output and record it with a relatively slow galvanometer, so that a single curve of the oscillatory amplitude is obtained (26). Further refinement can be made by employing a number of a. c. filters, each centered about the expected frequency of one of the important acoustic modes of the cavity, in order to obtain amplitude-time curves for each mode (26). Frequency-time measurements for various modes can be obtained by adding the signal to electrical oscillations of fixed frequencies near the expected acoustic modal frequencies and then measuring the resulting beat frequencies as functions of time (26). A variety of other real-time techniques can be proposed.

Most of the advanced methods for real-time data analysis that have been employed were developed in connection with laboratory research programs rather than motor test programs. One of the more sophisticated procedures is described in Ref. (33), which is concerned with measurement of the response of a burning solid propellant material to oscillations generated by a mechanical acoustic driver in a laboratory burner cavity. A rather elaborate servo system was employed to adjust the driver frequency to match the instantaneous, fundamental longitudinal frequency of the cavity and outputs from the servo system itself gave frequency, amplitude and band width of the cavity resonance (33). A representative oscillograph output is shown in Fig. 9-4; in this run the propellant did not excite cavity oscillations and the driver was shorted out for .0573 sec at 1 sec intervals marked by short vertical lines on the record, in order to observe the decay rate of the driver-produced oscillations.

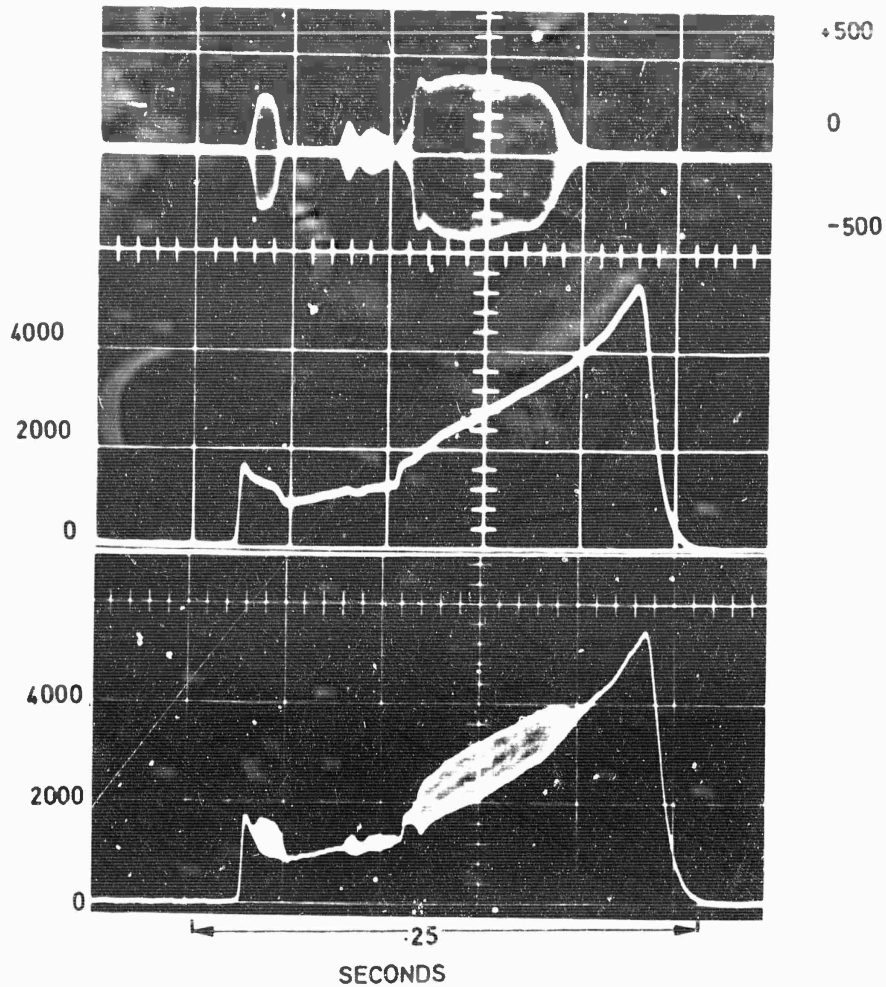
Post-test data analyses can be performed by the same types of techniques that are employed in real-time analyses (26). Tape recorded data also lends itself to a variety of operations that are not feasible on a real-time basis. For example, portions of tapes can be played back at low speed into an oscillograph, in order to obtain amplitudes and frequencies directly at critical points in the burning history (26). Tapes can be made in the form of a closed loop in order to facilitate analog-type frequency-amplitude analyses. Tape output can also be digitized and transferred to digital tape in order to facilitate more detailed analysis by means of programs on electronics digital computers.

A block diagram of two methods for analyzing tape recorded data to obtain amplitude-frequency-time information is shown in Fig. 9-5, where the particular recording system employed is also indicated (34). Results obtained from the two analytical techniques are shown in Figs. 9-6 and 9-7, respectively. The first method divides the frequency range from 40 cps to 30,000 cps into 30 $1/3$ -octave bands and then makes an amplitude-time analysis for each band. Results are then presented in the form of isoamplitude contours on frequency-time coordinates (Fig. 9-6). Objections to the method are that the frequency resolution is well below that of the original tape and the filtering process attenuates higher frequencies (34). The second method employs a magnetostrictive rod analyzer to identify frequencies of maximum amplitude, thereby providing finer frequency resolution of acoustic modes, at the expense of loss of some amplitude information (34). Modes identified in this manner may be seen in Fig. 9-7. Similar results, obtained by means of a related post-test technique of data analysis, are discussed, in Ref. (35). Data analysis facilities of this type are standard equipment in most research laboratories concerned with combustion instability problems.

3.4. Optical Methods for Combustion Instability Analysis

Optical techniques have been found to be of some use in experimental studies of combustion instability, especially for nonlinear acoustic instabilities and for non-acoustic instability, but with only limited success.

PRESSURE PSI



KEY

The bottom trace shows the direct signal.

The middle trace shows the signal with the oscillatory component filtered out.

The upper trace shows the oscillatory component with the "steady" component filtered out.

Fig. 9-3 Pressure-time history in a combustor with unstable combustion (26).

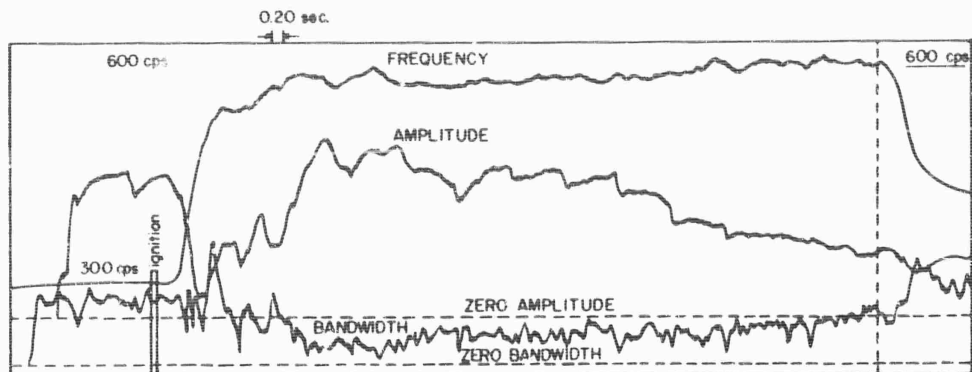
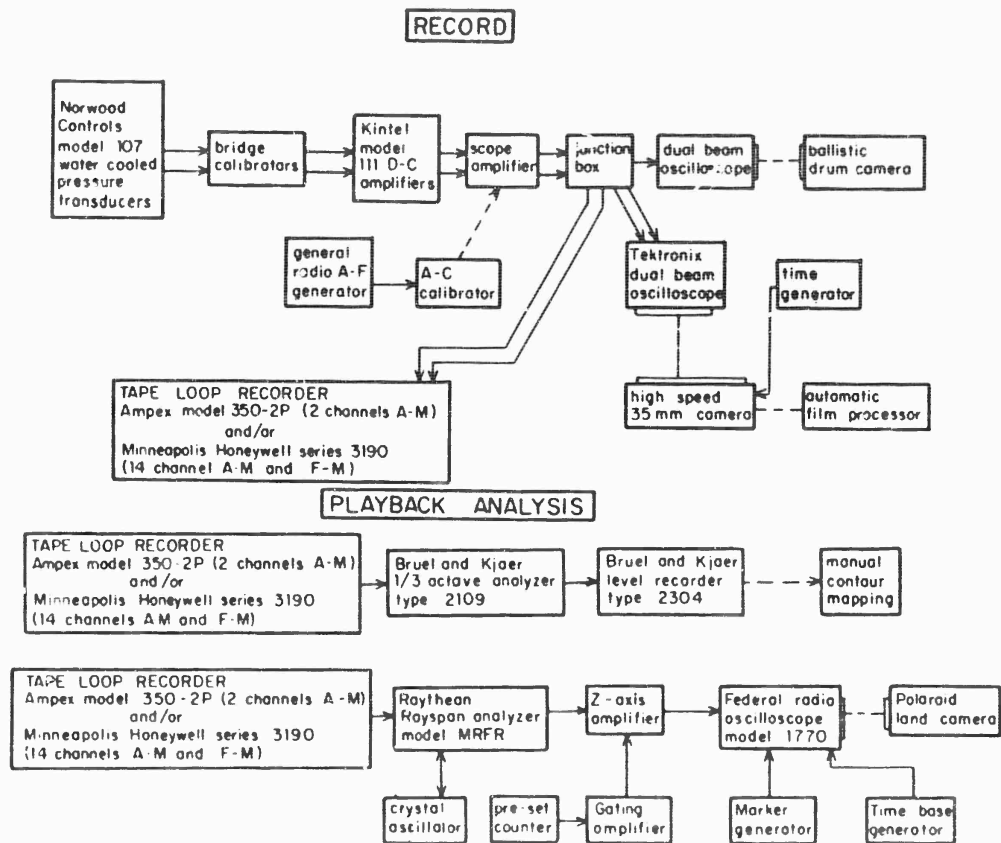


Fig. 9-4 Oscillograph recording of amplitude, bandwidth, and frequency. DQO propellant experiment (33).

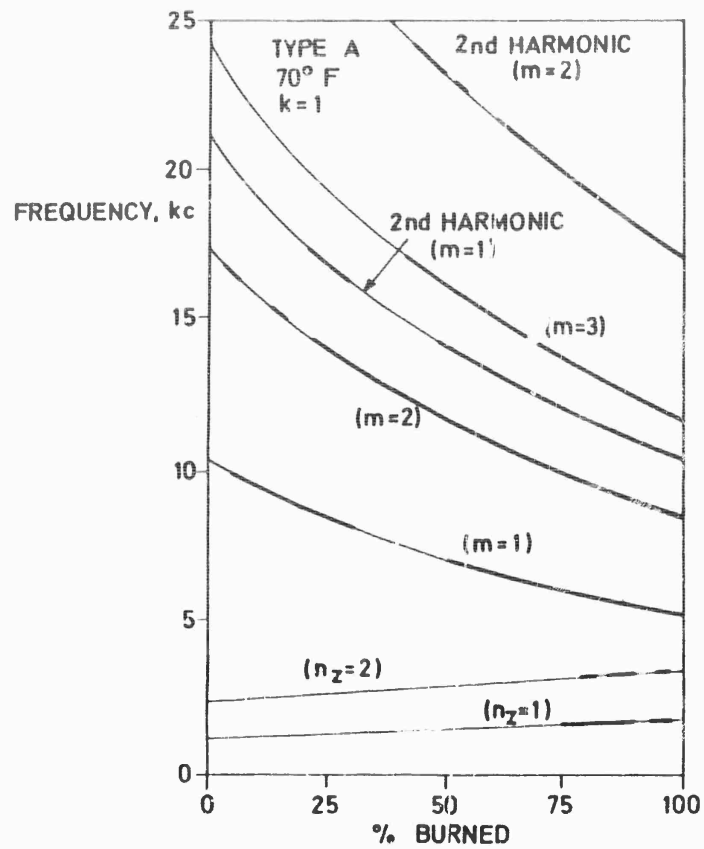


* This system designed and constructed at the Applied Physics Laboratory, Silver Spring, Md.

Fig. 9-5 Block diagram of instrumentation system at the Alleghany Ballistic Laboratory for unstable burning studies (34).

FREQUENCY
(c/s)





KEY

m tangential mode number

n_z longitudinal mode number for
internally burning tubular grain(heavy lines) amplification of
calculated acoustic
modes

Fig. 9-7 Frequency vs. percent of web burned analyses, depicting the various acoustic modes present (34).

In the studies of linear acoustic instability, attempts were made to measure the burning rate as a function of time, by high-speed cinematography of the burning surface of the propellant. An attempt to obtain the transient response of the burning rate to a shock wave was unsuccessful due to insufficient resolution (36). Mean burning rates were measured successfully to three significant figures, during oscillatory combustion in a tubular burner with transparent pyrex walls (37). The effect of a siren on mean burning rates of aluminized propellants has also been measured (38), (39). Through high-speed microcinematography, the structure of the reaction zone during oscillatory burning has been resolved (39). However, resolution sufficient for observing transient responses has not been achieved.

High-speed cinematography has also been employed to observe light emitted by gas-phase chemical reactions, inside a motor with a transparent fore-end and a tubular grain experiencing nonlinear, transverse, vortex-type modes of instability (40). Inferences concerning convective flow patterns were possible from these results.

Principally two optical approaches to the study of nonacoustic, oscillatory instabilities have been reported in the literature, high-speed cinematography that resolves the structure of the reaction zone and phototube intensity-time measurements of the total radiation emitted in the visible spectrum by the combustion process. An additional optical approach that has been employed is streak photography (44). Most of the information obtained from streak photographs could also be inferred by performing cinematographic measurements at sufficiently high speeds. The cinematographic method has already been mentioned in connection with studies of linear, acoustic instabilities; suggestions of the occurrence of low-frequency oscillations in aluminized propellants have been obtained by this method. The phototube method, which is intrinsically capable of attaining finer time resolution, has also demonstrated more conclusively the existence of low-frequency, nonacoustic oscillations (41), (42), (43), (74). The phototube method is amenable to radiation intensity-frequency-time analysis by methods analogous to those discussed in the preceding section. Representative intensity-frequency curves are shown in Fig. 9-8 (41). Measurements of relative phases of radiation intensity and pressure oscillations have also been obtained (42), (43). It is difficult to ascertain the fundamental significance of these measurements because the intensity fluctuations are related to the combustion mechanism in a complex manner.

3.5. Other Techniques

Ionization probe measurements in H_2 propellant gases (44) and gas sampling measurements (26) have also been made in experiments on combustion instability. The latter is of some use in suggesting instability mechanisms for nonacoustic instabilities. Ripples remaining after sudden extinction, on the surface of a propellant that was experiencing oscillatory combustion, provide some indication of the instability mechanism (44). A few additional techniques are described in Refs. (26) and (44).

4. Experimental Studies of Linear Acoustic Instabilities (Fundamental Viewpoint)

4.1. Basis for Fundamental Laboratory Studies

Linear acoustic combustion instability is known to involve an interplay between acoustic gains and losses; if the total rate of energy generation in a particular acoustic mode exceed the total rate at which energy is lost from that mode, then amplification of the mode will occur. Quantitative laboratory measurements of the magnitude of each contribution to the rate of acoustic energy amplification or attenuation therefore permit one to calculate whether linear acoustic instability will occur in a given chamber. Such measurements can be made in fundamental laboratory experiments that do not require motor firings. We now consider these experiments.

Numerous amplification and attenuation mechanisms occur in rocket motors and each of these mechanisms is amenable to laboratory study. Generally speaking, the list of attenuation mechanisms is longer than the list of possible amplification mechanisms; thus, viscoelasticity of the grain, viscosity, thermal conduction, diffusion and molecular and chemical relaxation processes in the gas phase, velocity and temperature responses of inert solid or liquid particles in the gas, convection and radiation of acoustic energy through the nozzle and radiation of acoustic energy through the motor case, all tend to attenuate sound vibrations. Fluid dynamical conversion of mean flow energy to acoustical energy, gas-phase chemical heat release processes and the burning zone at the surface of the solid propellant, comprise mechanisms that may amplify acoustic waves. Detailed experiments on each of these gain and loss mechanisms would require a highly ambitious laboratory program. Consequently, experiments have been performed only on mechanisms which (a) appear from *a priori* estimates to be among the more important processes in motor instabilities, (b) are not amenable to definitive theoretical calculation and (c) can be investigated in the laboratory in a meaningful way without undue difficulties.

A loss mechanism which meets these criteria [especially (a) and (c)] and has received experimental attention (45), (46), is the damping produced by small solid particles suspended in the gas. The experimental results support theoretical predictions fairly well (46), (58), (73).

The only gain mechanism that meets the criteria [especially (a) and (b)] is the response of the burning propellant surface to acoustic oscillations in the gas. The rest of Section 4 is concerned with experiments designed for studying this response. The burning zone is generally thin enough, compared with the wave lengths of the acoustic modes of interest, for the response to be expressed in terms of an acoustic admittance of the surface. The acoustic admittance is defined in Chapter 10. The objective of the more sophisticated fundamental laboratory experiments has been to measure the acoustic admittance.

4.2. Qualitative Experiments Employing Acoustic Generators

Principles and properties of acoustic generators are discussed in Ref. (47). Propellants burning in the open or in chambers whose dimensions are chosen without regard for acoustic phenomena, have been subjected to acoustic oscillations produced by sirens or other types of acoustic generators. Summerfield was one of the earliest investigators to discuss such studies. In the more refined versions of these experiments, outputs of pressure transducers located near the burning surface were used to characterize the acoustic field seen by the burning surface. The primary objectives of these studies have been to ascertain the effect of the acoustic field on the mean burning rate (a nonlinear phenomenon) (38), to observe visually the effect on the combustion process (also probably nonlinear) (39) and to measure the phase relationships between radiant energy output and pressure oscillations (43). Most of these studies were made on metalized propellants and details of metal burning mechanisms were investigated (39). A number of qualitative results have been obtained but quantitative measurements of response parameters, such as admittances, cannot be obtained from such studies.

4.3. Shock Tube Techniques

In principle, from observations of the response of a burning propellant surface to a weak shock wave, the acoustic admittance can be determined for all frequencies. Propellants have been ignited in shock tubes and then subjected to shock waves in efforts to obtain information about their response (26), (36). Unfortunately, the accuracy of measurement required to obtain useful information is so great that very few important results have been obtained by this technique.

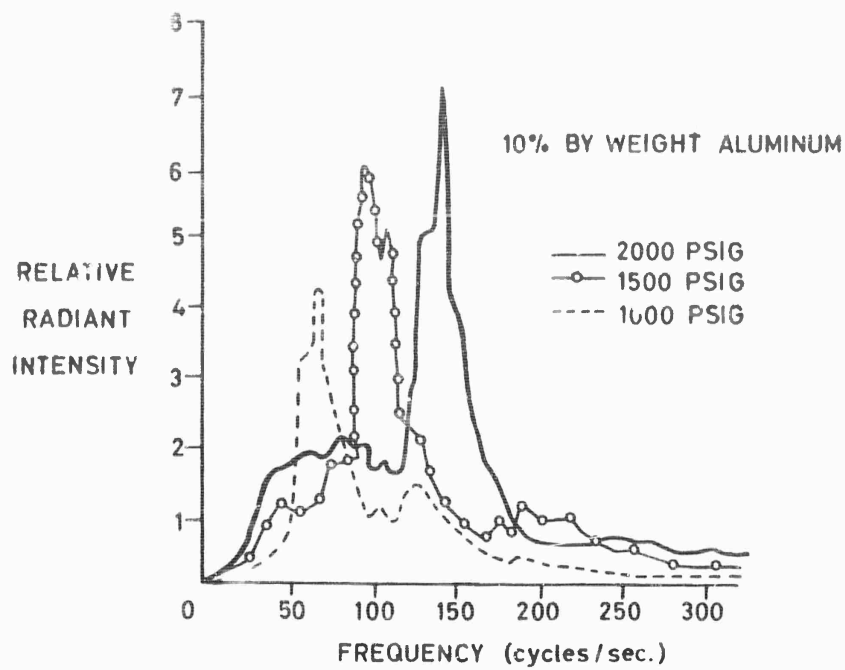


Fig. 9-8 Radiation pulsation frequencies of burning ammonium perchlorate as a function of aluminum content (6- μ particles) and pressure (41).

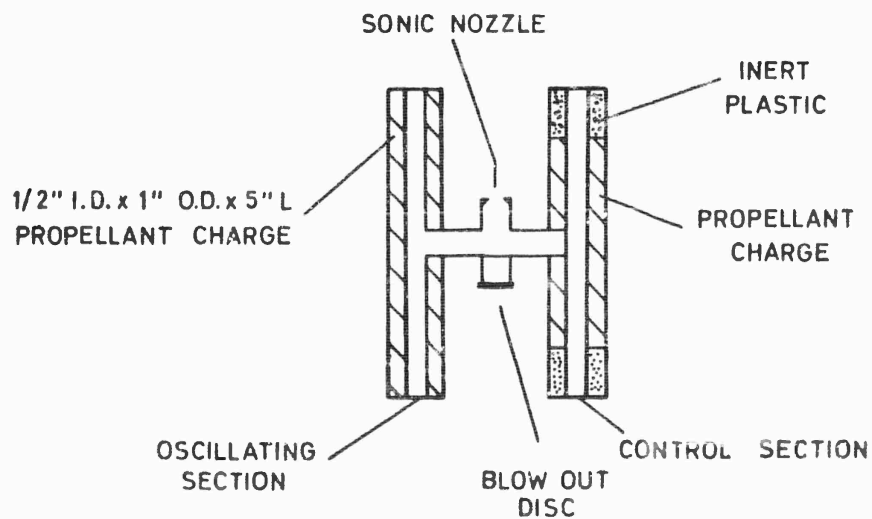


Fig. 9-9 Basic double motor arrangement (50)

4.4. Experiments with Small End-Burning Motors

Longitudinal oscillation modes in end-burning motors present the propellant surface with spatially uniform conditions across the entire surface. This uniformity facilitates interpretation of any experimental results. End-burning motors therefore afford useful instability research tools, for those propellants with which they can support oscillations. Little, if any, recent laboratory research with end-burning motors has been reported. One reason for this may be that the motors discussed below produce a more uniform acoustic environment that can be characterized more easily. Another is that few propellants can support oscillations in end-burning motors.

4.5. Experiments with Double Motors

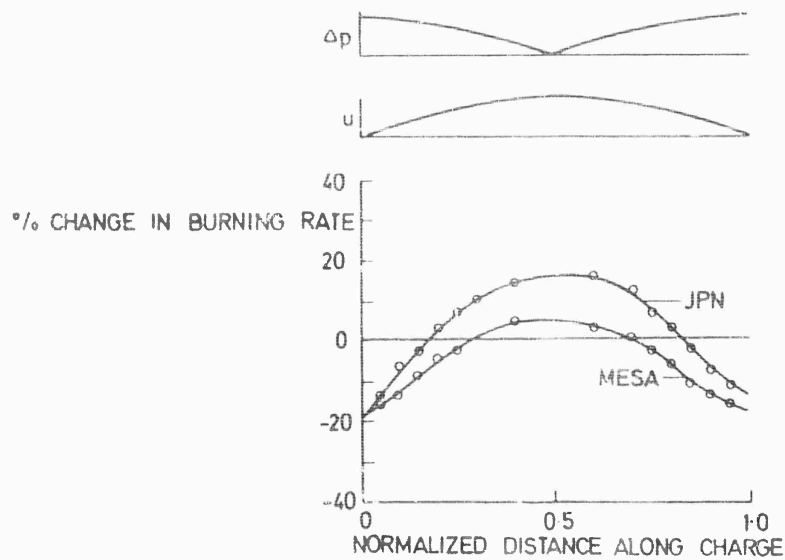
The rest of the experiments that we shall discuss in Section 4 deal with center-vented chambers, i.e., double-ended, cylindrical-type chambers with one or more exhaust ports located in the wall at or near the midpoint between the two ends. We shall call these devices motors, if the velocity reaches sonic conditions in the exhaust ports (choked flow) and burners if it does not.

We first consider the double motor designed by Price (48), (49), (50), (51); here two such center-vented chambers, each containing tubular grains, are arranged so that they discharge through a common nozzle (see Fig. 9-9), to insure that each chamber will operate at the same mean pressure band. The chambers are acoustically isolated from each other and can be ignited and extinguished simultaneously. By employing inert plastic for parts of the grain in one of the chambers, a propellant in this "control" chamber can be made to burn stably while the same propellant in the other chamber experiences oscillatory combustion. The double motor therefore provides a quick and easy means of comparing the results of oscillatory burning of a propellant, with results of stable burning of the same propellant.

The double motor is not of value in measuring linear, acoustic response of a burning propellant surface; the control motor would be unnecessary in such an endeavor. It has been used instead to measure the nonlinear change in mean burning rate, produced by oscillatory burning. This is accomplished by extinguishing both grains after a preset running time and comparing the grain shapes after extinguishment. Transducers monitor the pressure in each of the chambers to make sure that the control chamber burns stably and to determine the acoustic mode and amplitude of the waves in the oscillatory chamber. Results for the effect of oscillations in the first longitudinal mode on the burning rates of two double-base propellants, are shown in Fig. 9-10.

The percent change in burning rate, plotted in Fig. 9-10, is the ratio of the difference between mean burning rates under oscillatory and steady conditions to the steady burning rate. Figure 9-10 therefore implies that oscillations cause the mean burning rates of both propellants to increase in the central part of the grain (near velocity antinodes) and to decrease in the end parts of the grain (near velocity nodes). The increased burning rate at velocity antinodes is comprehensible in view of the fact that sufficiently high steady erosive velocities always increase the burning rate; the comparison must, however, be made with caution, because the frequencies involved are too high for the erosive response to be quasisteady (see Chapter 10, Section 6.2). The decreased burning rate at velocity nodes is more difficult to understand (see Chapter 10). The double motor provided the first clear demonstration of these two qualitative effects, although they had been inferred earlier from single-motor experiments.

Averaging over the normalized distance along the center line in Fig. 9-10 shows that the average burning rate of the entire grain is increased by the presence of oscillations for the JPN propellant and decreased by the presence of oscillations for the MESA propellant. This result is consistent with earlier single-motor observations



The upper curve is for JPN double-base propellant.
 The lower curve is for double-base MESA propellant.
 Δp and u curves show shape of acoustic mode.

Fig. 9-10 Graph showing change in burning rate as function of acoustic environment for combustion oscillations at 4200 cps (50).

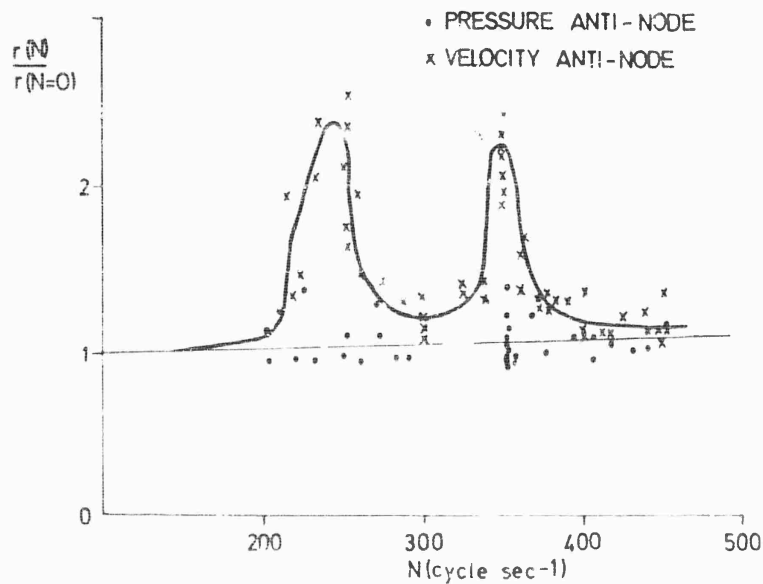


Fig. 9-11 ONERA measurements of frequency dependence of mean burning rate for a nonmetalized propellant

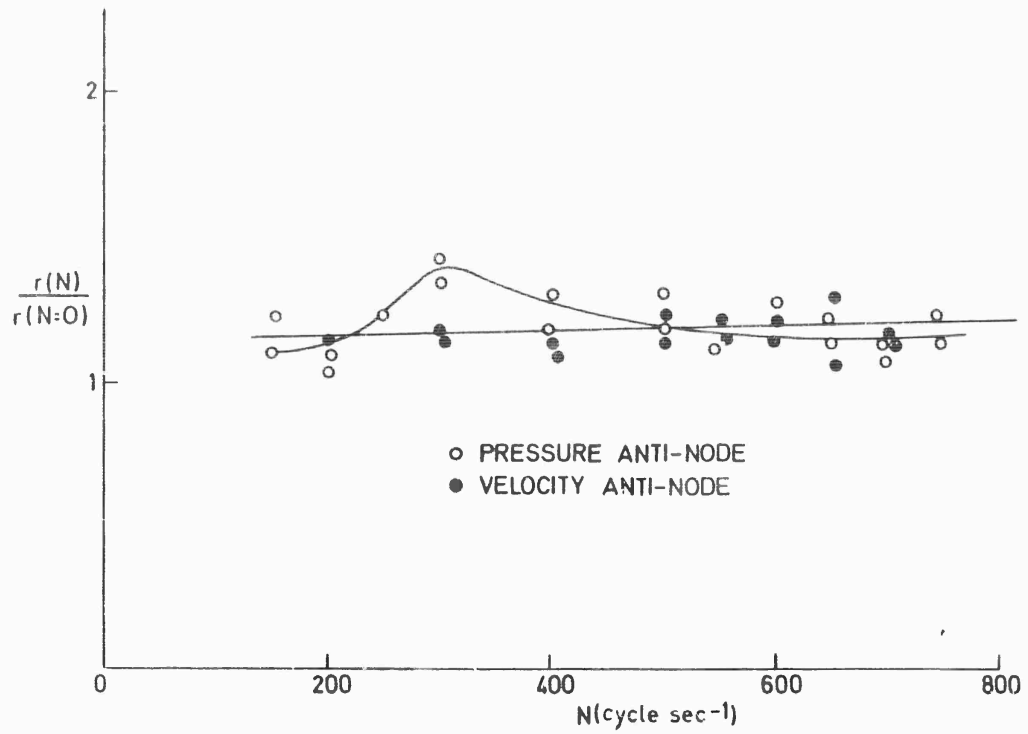


Fig. 9-12 ONERA measurements of frequency dependence of mean burning rate for a metalized propellant.

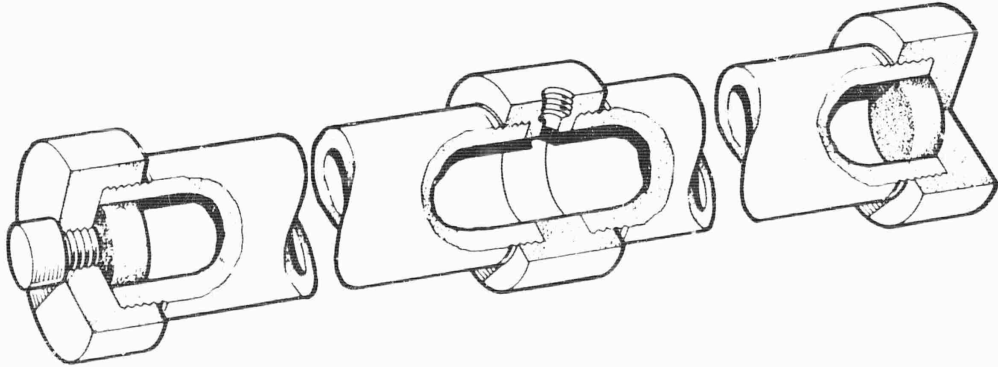


Fig. 9-13 Laboratory combustor for pressure coupled acoustic instability, used in measurements of acoustic admittance of the combustion zone (26).

of an increase in mean chamber pressure when oscillations begin to occur for JPN propellants and a corresponding decrease for MESA propellants.

In order to demonstrate that not all propellants experience a noticeable decrease in mean burning rate at velocity nodes under oscillatory conditions, we show curves of the ratio of the burning rate at frequency N to the burning rate at $N = 0$ (nonoscillatory conditions) for two composite propellants, one nonmetalized (Fig. 9-11) and the other metalized (Fig. 9-12). These results, obtained at ONERA by a technique different from the double motor, indicate that the change in burning rate at the velocity node is appreciably less for this metalized propellant than for the nonmetalized propellant.

An important point that should be noted regarding the double-motor geometry, is that different parts of the grain see different acoustic environments, ranging from velocity-node, pressure-antinode conditions to velocity-antinode, pressure-node conditions. This can be useful if qualitative observations of the effects of isobaric velocity oscillations and stagnant pressure oscillations are desired in the same experiment, but it does not enable one to obtain quantitative measurements of the response parameters for either limiting type of oscillation because the acoustic oscillations are produced by the response averaged over the entire surface. The same comment would apply to a single center-vented cylindrical motor containing a tubular grain that extends along its entire length. This objection is overcome in the T-motors and T-burners discussed below.

4.6. Experiments with T-Motors and T-Burners

4.6.1. Definition - Many researchers have worked with various forms of devices commonly called T-motors or T-burners (52-63). These are center-vented, cylindrical chambers in which the location of the propellant is adjusted in such a way that all of its burning surfaces experience the same acoustic environment. The name "T-motor" stems from the characteristic T-like shape of the assembled equipment for some early motors of this type. In this sense, Price's early single, center-vented, cylindrical motor with an internally burning tubular grain is also often called a T-motor but we prefer to restrict the definition to geometries in which acoustic conditions are uniform over the burning surface. Only in these cases have quantitative measurements of acoustic admittance been obtained.

4.6.2. Principles for Measurement of Acoustic Admittance - As explained in Section 4.1, the rates of growth of the amplitudes of linear acoustic oscillations that occur in motors, are governed by the relative magnitudes of the gain produced by the burning propellant surface and the sum of all losses present in the system. A method for measuring the surface gain is therefore to measure the growth rate of the oscillatory pressure amplitude. Generally, two different growth-rate measurements must be made in order to separate the surface gain from the sum of the losses because some of the contributing loss mechanisms are usually too complex for accurate theoretical calculations of total loss to be made. Once the contribution of the burning surface to the growth rate of the acoustic waves has been extracted, it is an easy matter to express this surface gain in terms of the surface acoustic admittance provided that acoustic conditions are uniform over the entire burning surface. Thus, the acoustic admittance of the surface is calculated directly from the growth rate measurements.

If a single, linear, acoustic mode is excited in a chamber that experiences gains and losses (homogeneously distributed throughout its volume and/or concentrated at its boundaries), then the pressure p at any point in the chamber is given by the real part of :

$$p = \bar{p} + p_0 e^{\alpha t} e^{i\omega t} \quad , \quad (\text{Eq. 9-1})$$

where \bar{p} is the mean chamber pressure, p_0 is the local complex amplitude of the pressure oscillation at $t = 0$, t is time measured from an arbitrary initial instant, ω is the (constant, real) frequency of oscillation, and α is the (real) growth constant for the wave. If $\alpha > 0$, the amplitude of the wave increases exponentially with time; it decreases if $\alpha < 0$. Neglecting nonhomogeneities such as those produced by mean flow, one can show that the quantity p_0 will be a function of position in the chamber but \bar{p} , ω and α will not. Thus, quantities α and ω characteristic of every point in the chamber can be obtained from the test record of a pressure transducer located at any one point in the chamber. From the growth constant α so obtained, the acoustic admittance is calculated.

We now introduce the assumption that $|\alpha| \ll |\omega|$. Under this condition, it can be shown from the linear, acoustic equation and its boundary conditions that the value of ω lies very near one of the normal oscillation frequencies of the chamber, as calculated for perfectly lossless conditions ($\alpha = 0$) and for perfectly rigid walls. It is also found under this condition that α is an additive property in the sense that if a number of loss and gain mechanisms contribute to α , then a growth constant α_1 exists for each mechanism i (in the absence of any other loss or gain mechanism)

$$\alpha = \sum_i \alpha_i \quad (\text{Eq. 9-2})$$

The additive property of α can be explained from the viewpoint that the fractional time rate of increase of the total acoustical energy contained in the chamber is 2α (43). It is perhaps physically understandable that the separate mechanisms will contribute additively to the fractional rate of production of acoustical energy, and the growth constant when all mechanisms are present simultaneously is the sum of all α_i :

The growth constant which one is interested in measuring, is that associated with the boundary condition at the burning surface and is denoted here by α_1 . The quantity α_1 may be positive or negative but it must generally be positive for oscillations to occur because α_1 is usually negative for $i \neq 1$. We define a dissipation rate constant as :

$$\alpha_d = - \sum_{i \neq 1} \alpha_i \quad (\text{Eq. 9-3})$$

thereby obtaining :

$$\alpha_1 = \alpha + \alpha_d \quad (\text{Eq. 9-4})$$

Measurements are made of the quantities α and α_d in Eq. 9-4, so that the quantity α_1 , which is expressible in terms of the acoustic admittance, can be calculated.

We cite here the formula for α_1 in terms of the acoustic admittance Y . The time rate of energy input to the acoustic field per unit surface area at $t = 0$ is shown in Chapter 10 to be $-\text{Re}\{Y\} |p_{b,0}|^2/2$, where $\text{Re}\{\}$ means 'real part of' and $p_{b,0}$ is the pressure amplitude of the oscillation at the burning surface, at $t = 0$. If the average acoustic energy per unit volume in the chamber at $t = 0$ is \bar{e}_0 , then the time rate of increase of acoustic energy in the chamber at $t = 0$ is $2\alpha\bar{e}_0V$, where V is the volume of the chamber. Letting A denote the area of the burning surface, we therefore find from an acoustic energy balance, that:

$$\text{Re}\{Y\} = -4\alpha_1 (\bar{e}_0 / |p_{b,0}|^2) (V/A). \quad (\text{Eq. 9-5})$$

Equation 9-5 is a general formula for the relationship between a surface-average

(see Chapter 10) value of $\text{Re}\{Y\}$ and α_1 [subject only to the condition $|\alpha| \ll |\omega|$ and the assumptions implicit in Eq. 9-1]. Equation 9-5 neglects acoustical energy convected into the chamber at the burning surface, due to the finite value of the mean mass flow rate of gas leaving the propellant. If this convective contribution to acoustical energy flow is balanced by an equal rate of convection of acoustical energy out of the exit port of the chamber, then it need not be mentioned (provided that one remembers not to include an exit-port, convective α_1 in α_d). In general, the two convective contributions do not cancel; the amplifying convective effect at the propellant surface may be larger. In such cases, the net convective effect must be accounted for in measurement procedures. It is largely a matter of semantics as to whether the phenomenon discussed here should be treated as part of a total convective contribution or part of the propellant response. A theoretical T-burner analysis, which attributes the phenomenon to propellant response and presents formulas for its computation, may be found in Ref. (64). The net result of this particular theory is that in drawing conclusions concerning the results of experimental measurement, $\text{Re}\{Y\}$ should sometimes be replaced by $\text{Re}\{Y\} - \bar{v}_b/\gamma\bar{p}$, where \bar{v}_b is the average velocity of the burned gases leaving the propellant surface. In Equation 9-5, in order to evaluate the ratio $(\bar{e}_0/|\bar{p}_{b0}|^2)$ one must specify the shape of the chamber, the size and location of the burning surface and the acoustic mode. For the special case of a longitudinal mode in a cylindrical chamber with the propellant located at velocity nodes, it can easily be shown that :

$$\bar{e}_0/|\bar{p}_{b0}|^2 = 1/(4\gamma\bar{p}) \quad , \quad (\text{Eq. 9-6})$$

where \bar{p} is the mean chamber pressure and γ is the ratio of specific heats for the gas in the chamber. Equations 9-5 and 9-6 yield :

$$\text{Re}\{Y\} = -\alpha_1 V/A\gamma\bar{p} \quad , \quad (\text{Eq. 9-7})$$

for this case. Since it is the real part of the admittance that is of primary interest (see Chapter 10), the desired information about Y is given explicitly in terms of measured quantities by substituting Eq. 9-4 into Eq. 9-7, viz.,

$$\text{Re}\{Y\} = -(\alpha + \alpha_d) V/A\gamma\bar{p} \quad (\text{Eq. 9-8})$$

It should be apparent from this discussion that measurements must be made during exponential growth or decay periods of oscillations (see Eq. 9-1). Figure 3-3, for example, shows that oscillations often exhibit exponential growth as they begin to build up, but later they may reach a more or less constant amplitude. The value of the maximum amplitude reached, depends on nonlinear phenomena and cannot be characterized in terms of linear parameters (such as acoustic admittance) alone. It can be argued that acoustic admittance is not a very important practical parameter because the final oscillation amplitude is likely to be the important quantity that determines the extent of performance degradation or motor damage. Counter arguments are that (a) the nonlinear phenomena are not understood well enough for estimates of peak amplitude in one motor to be obtained, from measurements of peak amplitude in another and that (b), if $\text{Re}\{Y\}$ is known, then a motor can be designed to be linearly stable ($\alpha < 0$) and it will then be somewhat unlikely that nonlinear oscillations will develop. The important point to be remembered by investigators concerned with measuring Y is that measurements must be made while the oscillation amplitudes are small enough to be linear and during periods of exponential growth or decay of pressure amplitude.

4.6.3. Specific Configurations - One particular T-motor configuration is illustrated schematically in Fig. 9-13; propellant charges are placed at each end of a cylindrical chamber which experiences longitudinal acoustic modes. All burning surfaces thus sit at velocity nodes, see the same acoustic conditions and respond acoustically to the pressure oscillations only. In all of the devices described in Section

4.6, the propellant surface experiences only pressure oscillations, no velocity oscillations. Acoustic admittance data thus all refer to responses to pressure oscillations. The problem of designing motors for quantitative measurement of response to acoustic velocity oscillations has not been solved yet, although some novel techniques have been proposed recently (see papers by E. E. Stepp and by J. L. Eisel in Proceedings of the Second Interagency Chemical Rocket Propulsion Group Combustion Conference, Pub. No. 105 of the Chemical Propulsion Information Agency, Washington, 1966). Indeed, there are theoretical questions associated with wave rectification and cancellation effects that have not been resolved entirely for velocity coupling. Thus, it is not clear exactly what quantities should be measured for characterizing the velocity effect. Nevertheless the velocity effects are believed to be important. The status of the theory is considered in Chapter 10.

A photograph showing two external views of a T-motor constructed at ONERA appears in Fig. 9-14; the horizontal pipe is the T-motor, the large tank regulates the pressure and the flexible leads are for instrumentation. In modifications of the motor illustrated in Fig. 9-13, a propellant charge may be placed in only one end of the cylinder (61), (37), the propellant may be moved forward at the average burning rate by means of a piston, so that larger charges and longer burning times can be obtained without any appreciable change in cavity volume during the experiment (63), or a mechanical acoustic generator may be placed at one end of the chamber in order to provide an external means of exciting and controlling the acoustic field (32). The first of these modifications simplifies instrumentation problems but introduces questions as to whether conditions are identical in the two ends and occasionally results in stable burning, thereby making it impossible to obtain data on oscillatory response. The second modification enables one to obtain information concerning the participation of interior parts of the grain in the oscillations. The third modification, which will be discussed later in greater detail, enables one to obtain oscillatory response data for propellants that cannot support oscillations in T-burners.

One advantage of a T geometry for oscillations in odd longitudinal modes, is that the chamber exit is located at a pressure node, a condition under which acoustic losses by radiation through the exit port are minimized. Thus, propellants that would burn stably in some other geometries can often excite odd longitudinal modes in these chambers. Nevertheless, for some propellants there are conditions under which $\alpha_d > \alpha_1 > 0$ in T geometries, i.e., a propellant with a negative value of $\text{Re}\{\gamma\}$ (a tendency to cause amplification) does not produce oscillations in the chamber. Since it is clear from Eq. 9-5, for example, that the growth constant α_1 increases in proportion to A , one possible means of achieving oscillations for such a propellant is to increase the total propellant area by increasing the diameter of the chamber (59), provided that the losses are of such a nature that they increase more slowly than the square of the diameter.

It is desirable to measure acoustic admittances as functions of the oscillation frequency ω . The frequency is related to the sound speed 'a' and to chamber dimensions; for example, for the n 'th longitudinal mode in a cylindrical chamber of length l , it is well known that :

$$2\pi\nu = \omega = n\pi a/l \quad n = 1, 2, \dots \quad (\text{Eq. 9-9})$$

(where ν is the frequency in cps). The lowest frequency corresponds to $n = 1$, the "fundamental", which is usually the dominant longitudinal mode. The value of ω is varied experimentally by changing the length l of the chamber. In this manner, frequencies up to 10^4 cps are easily achieved and there is little incentive for studying higher frequencies. In order to achieve very low frequencies, rather long chambers are needed. Chambers up to 60 ft. long have been tested (42), yielding acoustic frequencies below 10 cps. The long chambers often have relatively high damping coefficients α_d .

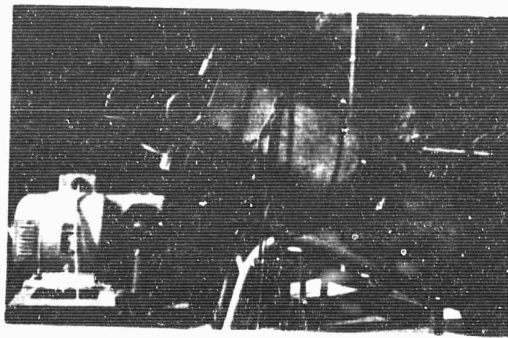
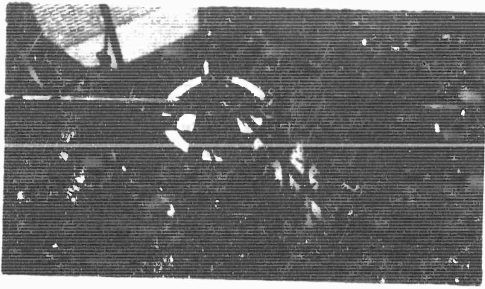


Fig. 9-14 Photograph of ONERA T-motor.

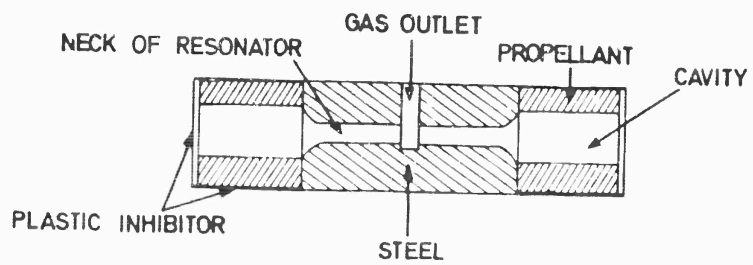


Fig. 9-15 Laboratory combustor for demonstration of instability in a Helmholtz mode (26).

An alternative means for achieving low natural frequencies is to employ a Helmholtz resonator (e.g., Fig. 9-15), which consists of a chamber vented without choking through a narrow tube to a pressure reservoir. Such a resonator exhibits a natural, nonacoustic vibrational frequency of :

$$\omega = a \sqrt{S/hV} \quad (\text{Eq. 9-10})$$

where V is the chamber volume, S is the cross-sectional area of the outlet tube and h is the length of the outlet tube. In the Helmholtz mode, the pressure is practically constant and the velocity is practically zero throughout the volume V , so that the location of the propellant surface inside the chamber is irrelevant, and pressure (not velocity) responses are measured. For a given frequency, the resonator is smaller and less expensive than an acoustic chamber and it sometimes has less loss (lower α_d). But it may lead to undesirable, complex flow patterns in the vicinity of the propellant surface and it is subject to problems associated with throat plugging.

4.6.4. Experimental Strategies - Since both α and α_d must be found in order to obtain the admittance (see Eq. 9-8), the experimenter must decide how to measure these quantities separately. The earliest and probably still the most prevalent strategy, is to use relatively thin propellant grains to obtain α from the initial growth rate of the oscillations and to obtain α_d from the decay rate that is observed after the propellant burns out. Pressure recordings that are suitable for the application of this method are shown in Fig. 9-16. The method is illustrated in Fig. 9-17 where the logarithm of the maximum amplitude of the pressure oscillation seen by a transducer, is plotted as a function of time. It is found from Fig. 9-17 that a very well-defined growth constant α is obtained from the graph but the decay curve is not quite linear. Two different straight lines have been fitted to different portions of the decay curve, giving two slightly different values for α_d . It can be argued that if burnout is complete at time t_3 , then the earlier value for α_d is the best because the mean flow rates during this period are closer to those during growth than the mean flow rates long after burnout. However, questions have been raised as to whether either of the decay constants obtained after burnout accurately represents the 'required' decay constant operative during growth. This objection has been supported by theoretical arguments to the effect that the losses should differ substantially and also by experimental observations of appreciable and somewhat irregular fluctuations of loss with time (33). It should be emphasized, however, that seldom will such discrepancies affect the admittance by an order of magnitude; we are speaking here of differences that are usually less than a factor of 2 and often only about 10 percent.

A brute-force solution to this measurement problem is to make the propellant area so large that $\alpha \gg \alpha_d$. Then errors in α_d do not affect Y appreciably. Unfortunately, this approach is not feasible for propellants that have relatively weak tendencies to oscillate.

A study of the measurement problem is reported (62). In addition to considering the standard measurement technique, these authors propose making growth rate measurements for various values of the propellant area A in the same burner. If it is assumed that the decay constant is independent of A , (e.g. independent of total mass flow rate), then α_1 can be extracted from a plot of α vs. A ; decay rate measurements then become unnecessary. The simplest version of this technique is to make only two growth rate measurements at each frequency, one with propellant charges in both ends of the chamber and the other with a propellant charge in only one end of the chamber. For this simplified experimental method, Eq. 9-8 implies :

$$\text{Re} \{ Y \} = - (\alpha_{2A} - \alpha_A) V / A \gamma \bar{p} \quad , \quad (\text{Eq. 9-11})$$

where A is the cross-sectional area of the chamber, α_A denotes the growth constant

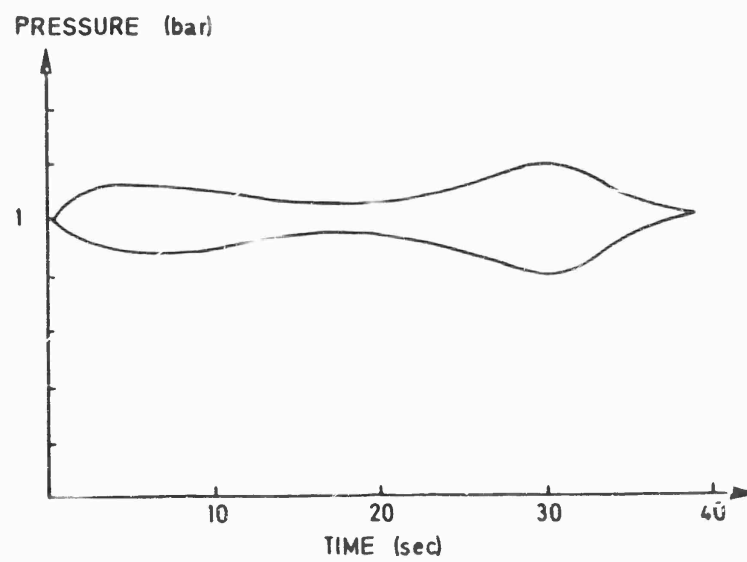
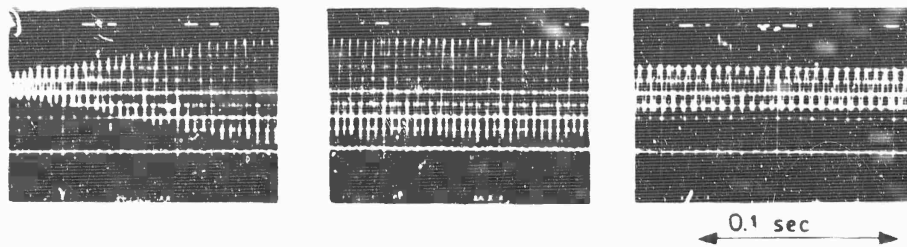


Fig. 9-16 Pressure recordings in a T-motor, obtained at ONERA.

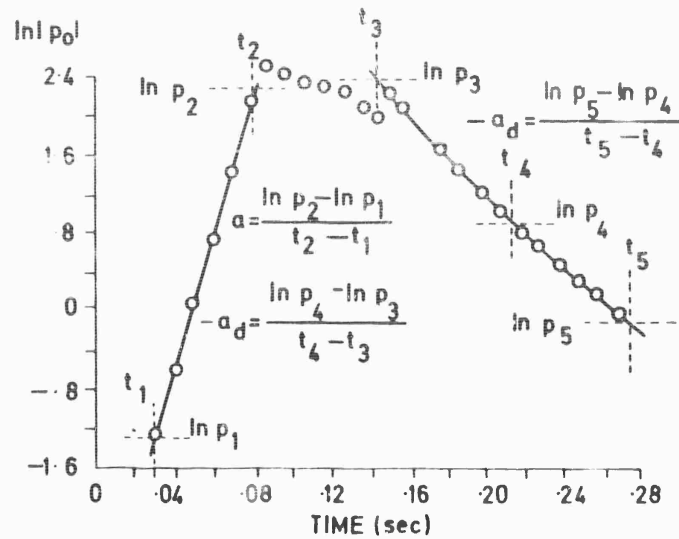


Fig. 9-17 Typical growth and decay of pressure oscillations in the combustor in Fig. 9-13, showing range of applicability of linear theory (26).

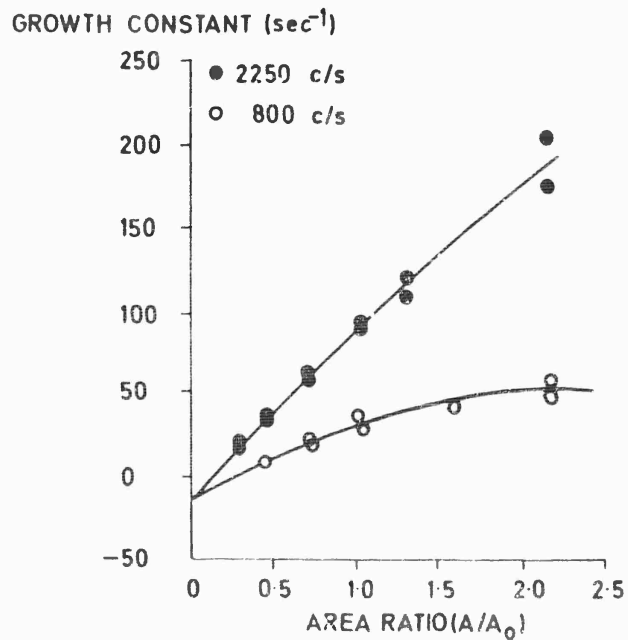


Fig. 9-18 Data showing the effect of changes in the burning surface area on the measured growth constant (62). (Data is for a polybutadieneacrylic acid/ammonium perchlorate/copper chromite composite propellant with relative weight ratios 18/80/2, burning at 200 psia mean pressure with $\bar{p}/\bar{m}a \approx 106$; \bar{m} = mean mass burning rate of propellant).

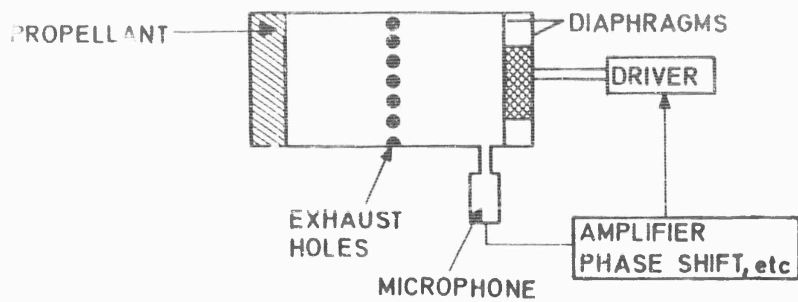


Fig. 9-19 Simplified schematic diagram of an acoustic oscillator for measuring response of a solid propellant (33).

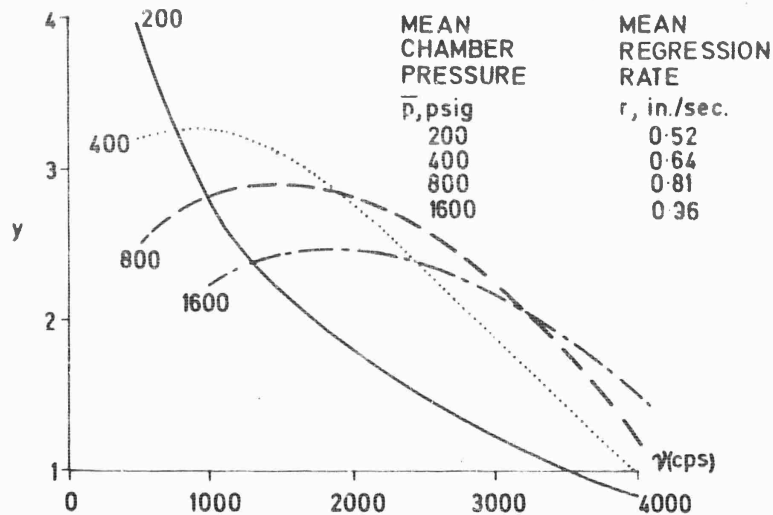


Fig. 9-20 Dimensionless response function for MESA (extruded, double-base) propellant, at various values of the mean chamber pressure (43).

Mean linear regression rate.

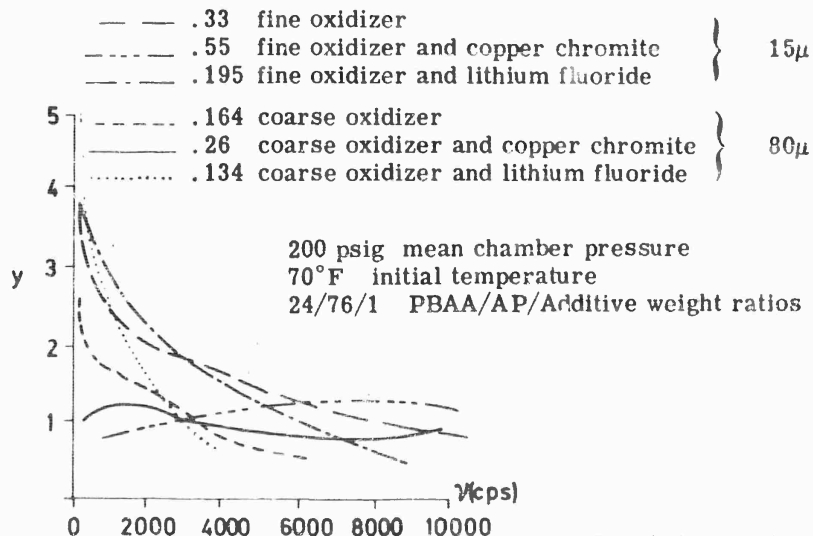


Fig. 9-21 Dimensionless response function for a PBAA/AP, demonstrating the effects of oxidizer particle size and burning rate modifiers (62)

with propellant in only one end and α_{2A} denotes growth constant with propellant in both ends. Curves of measured growth constant as a function of A , are found to be nearly straight lines (Fig. 9-18), thus lending credence to the hypothesis that α_d is independent of A . However, the conclusion of Ref. (32) shows that the safest approach is to use a variety of strategies (e.g., Eq. 9-11 and also Eq. 9-8) and to select the final value of $\text{Re } \{Y\}$ on the basis of a comparison of the results.

By far the most difficult problem of admittance measurement occurs for propellants that either are inherently stable or are not unstable enough to naturally excite acoustic modes of the cavity ($\alpha_d > \alpha_1$). A relatively simple approach to this problem discussed recently by N.W. Ryan, is to employ a sufficiently energetic and long burning igniter which will produce oscillations during the ignition process. Identical igniters are fired in a chamber without propellant and in the same chamber with propellant, the acoustic admittance is obtained from the difference between decay constants of the igniter-induced oscillations with and without propellant. The difficulty with this technique arises from differences in chamber losses with and without combustion, see also (33). The authors used the T-burner (see Fig. 9-19), which was placed in a large constant-pressure tank. In Fig. 9-19, the box marked "amplifier, phase shifter, etc." is actually a rather complex servo system which enables the experimenter to program the driver to oscillate at various power levels, either in phase or 180° out of phase with the cavity oscillations. Thus, for various periods during a run, the driver can be made to add acoustical energy to the cavity, extract acoustical energy from the cavity or it can also be shorted out so that it does not affect the acoustical energy in the cavity. The response of the oscillatory pressure amplitude to changes in the state of the driver is used to provide information needed for calculating the natural decay rate of the cavity containing the (stable) burning propellant. One such response curve is shown in Fig. 9-4; the driver establishes an equilibrium pressure amplitude then, when it is interrupted at one second intervals the decay rate constant is obtained from the rate of decrease of pressure amplitude. Two other types of data contained in Fig. 9-4 (viz., the bandwidth and the equilibrium pressure amplitude itself) provide independent measurements of the decay rate constant. The equipment can also be used to measure growth rates in systems for which $\alpha_1 > \alpha_d$ and α is very small. One of the techniques discussed earlier must be adopted for obtaining α_d , so that α_1 can be estimated from the α measurement. The standard technique of measuring the decay constant after burnout is not very satisfactory here because α is observed to vary appreciably during the run, so that post-burnout measurements will yield α_1 values only just before burnout. The technique corresponding to Eq. 9-11 is more promising under these conditions but it was not considered in Ref. (33). High precision measurements are needed when α is negative because α_1 and the admittance are then obtained from the difference between two numbers that may be quite close together (see Eq. 9-4 or Eq. 9-8). One is tempted to question whether, in these cases, admittance values are of sufficient practical importance to warrant expending the effort required to obtain them.

4.6.5. Experimental Results - Useful compilations of experimental results concerning admittance measurements may be found (43), (55), (61). In Figs. 9-20 and 9-21, a dimensionless response function y , which is related to the acoustic admittance, is plotted as a function of frequency. The quantity y is given by :

$$y \equiv (\alpha + \alpha_d) V \bar{\rho} / A \gamma \bar{m} = - (\bar{p}/\bar{v}_b) \text{Re } \{Y\} + 1/\gamma, \quad (\text{Eq. 9-12})$$

where $\bar{\rho}$ is the mean density of the gas in the chamber, \bar{m} is the average mass burning rate of the propellant (mass per unit area per second) and all other quantities have been defined previously. The first equality in Eq. 9-12 is the experimental definition of y , the second equality is its relationship to Y , based on the theory of Ref. (64). The curves in Fig. 9-20 show how the mean pressure level influences the y curves of a double-base propellant. Fig. 9-21 illustrates the dependence of the y

curves on oxidizer particle size and on burning rate catalysts, for a composite propellant.

Some general properties of these curves are worth noting. First and most important, they exhibit a very broad-band, smooth response, in agreement with the predictions of most of the theories discussed in the following chapter. Second, the quantity y appears to be somewhat less dependent on pressure and burning rate than the quantity $\sqrt{p_b/\bar{p}}$; this is also in agreement with most theories. A third trend is that y itself appears usually to increase as frequency or pressure decrease; some theories are also roughly in agreement with these two results. No major difference between the responses of composite and double-base propellants is discernible.

Properties of a more specific character may also be noted from Fig. 9-21. There is a tendency for y to decrease as the perchlorate particle size increases under otherwise fixed conditions. Burning rate catalysts and other additives affect the value of y appreciably. Other results show that the nature of the binder and the binder-oxidizer ratio also influence y . Generally speaking, the value of y depends somewhat on all aspects of the propellant formulation.

5. Experimental Studies of Acoustic Instabilities in Motors

A systematic summary of experimental results, on acoustic combustion instability in real solid rocket motors, is difficult to present because many of the results tend to be applicable only to the particular motor studied and seem to defy an appreciable amount of logical generalization. A large number of experimental studies of acoustic instabilities in motors have been carried out (1-13), (16), (17), (19), (23-26), (34), (35), (40), (65-69). It is not reasonable for us to attempt to discuss fully each of the studies here. Instead, we shall select a small variety of topics for further emphasis. A number of the investigations were touched on earlier in this chapter, particularly in Section 2.

First, we make a few remarks about which modes have been observed in motors. Most of the observations have been made on cylindrical motors with internally burning grains, usually tubular. Acoustic modes in such motors naturally divide themselves into longitudinal, standing tangential, traveling tangential, radial and mixed modes. It is difficult to identify mixed modes experimentally and also to distinguish between standing and traveling tangentials. Longitudinal and tangential modes have been clearly identified in experiments; a variety of other modes have been observed under appropriate geometrical and operating conditions. Within any mode category, the first, lowest frequency mode is usually dominant with higher modes becoming relatively less intense. This observation is consistent with the result (Section 4.6.5) that the dimensionless propellant response function generally decreases with increasing frequency and also with the fact that homogeneous (viscous and heat-conduction) gas-phase losses are known to increase as the frequency increases. However, it should be pointed out that the fundamental is not always dominant; occasionally second, third or fourth natural modes appear strongly while vibrations of lower frequency are not discernible. There are a number of possible explanations of these anomalies, one being viscoelastic grain damping.

The fact that radial modes are seldom observed is explicable, on the grounds that their frequencies are relatively quite high in experimental motors of typical dimensions and so they should have low surface amplification and high homogeneous damping in the gas and solid phases. Generally speaking, the modes with the lowest frequencies tend to occur most often, except that sometimes there may be a preference for tangential modes over longitudinal modes.

Experimental identification of acoustic modes is usually achieved from a frequency analysis of the oscillations. Sometimes it is helpful to note how the frequency chan-

ges with time during burning; for example, in internally burning tubular grains the frequencies of longitudinal modes will be practically independent of time, while the frequencies of transverse modes will decrease appreciably during burning. Inspection of quenched grains provides information about the mode structure but this technique is used more often to obtain information concerning the effect of the instability of the mean burning rate of the propellant, as a function of position on the surface of the grain.

Motors usually burn stably at sufficiently high chamber pressures (35). The critical chamber pressure needed for stability, depends strongly on the propellant and the motor, sometimes it is too high to be attained experimentally. However, most studies have shown that instability intensity tends to decrease with increasing pressure. These observations are consistent with the experimental measurements (Section 4.6.5), showing that the magnitude of the dimensionless acoustic admittance of burning propellant surfaces generally tends to decrease as the pressure increases.

Another motor operating parameter which affects combustion instability, is the grain temperature. There is usually an optimum grain temperature for stability (35), (66); if the temperature is too high or too low, irregular burning is more pronounced. The explanation of this effect doubtlessly lies in the temperature dependence of the mechanical (e.g., viscoelastic) and combustion properties of the propellant but it has not received much theoretical exploration.

The thickness of the grain and its means of support within the case, are design parameters that have an appreciable effect on motor instabilities. The influence of the grain thickness is rather complex (57), (63), (66). For example, in three motor tests in which the principal quantity that was varied was the grain thickness, it was found that combustion instability occurred for the thickest and thinnest grains but not for the grain of intermediate web size (66). That the means of support is important and the thickness influence is complex are both comprehensible, from the viewpoint that the grain participates in the acoustic oscillations and that viscoelastic damping within the grain is an important damping mechanism. The wave patterns within the grain and the total rate of dissipation occurring therein, depend on grain thickness in a complicated way; dissipation peaks occur for grain dimension and grain-case boundary conditions that produce the proper reflection and reinforcement conditions, when the system is driven by the cavity oscillations. Although some theoretical progress on this problem has been made recently, quantitative calculations cannot be carried out for real motors.

Practically all other geometrical parameters of the system exert an appreciable influence on acoustic combustion instability. It is obvious that chamber dimensions determine mode frequency. We have also mentioned that various geometric modifications (e.g., 'resonance rods') to grain and chamber shape, affect instability by introducing acoustic losses (Section 1). Specific empirical geometric changes not previously mentioned, that have been found to be beneficial in certain instances, include curvature of the forward end of the propellant, shaping of a star perforation, providing a forward cavity in the case, eliminating a cavity just downstream of the grain and lengthening the converging section of the nozzle (69). Making a long, thin motor shorter and fatter sometimes decreases the severity of instability (66). Such changes do not always work, they are purely 'cut-and-try'.

It should be clear from these observations that simple scaling laws do not exist for acoustic combustion instability. The only rational approach to scaling acoustic instability is broadly and roughly as follows. First, obtain admittance data such as that in Figs. 9-20 and 9-21 for the propellant to be used. From assumed dimensions of the smaller and larger motors, calculate burning surface area, volume, acoustic frequencies, mean chamber pressure, etc., all as functions of time. Also,

estimate magnitudes for losses associated with all known mechanisms (viscoelasticity, solid particle damping, etc.) in each motor, as functions of time. Very wide limits of uncertainty appear in many of these estimates. Using these results, estimate instability growth constants as functions of time, for each motor. Then, if the estimated growth constants for the larger motor do not exceed those for the smaller motor and if the smaller motor operates sufficiently stably in tests, one has some basis for believing that the larger motor will also operate in an acceptable manner. This 'scaling' procedure obviously consists of making the best possible theoretical calculation of linear acoustic instability in the motors of interest; it does not result directly in simple scaling laws. Ten years ago it would have been foolish to suggest that such a calculation should be attempted. With information that is now available, it is at least conceivable that an attempt can be made to obtain the required estimates.

6. Experimental Studies of Nonacoustic and Nonlinear Combustion Instabilities

6.1. Introduction

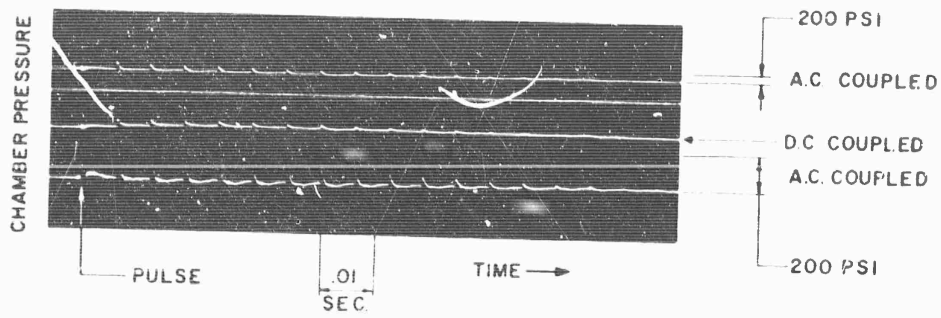
We have already covered a few aspects of nonlinear acoustic instabilities e.g., equilibrium pressure-amplitude of oscillations, change in mean burning rate, change in mean chamber pressure. Brief discussions of two specific nonlinear acoustic phenomena (shock-induced oscillations and vortex flow) are given in this section. Nonacoustic phenomena will also be considered here.

6.2. Shock-Induced Oscillations

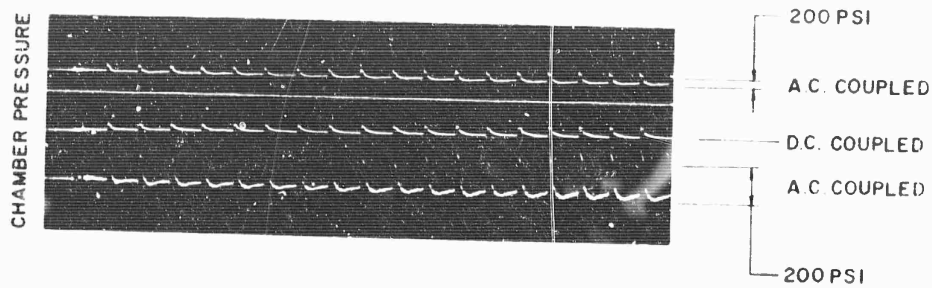
Experiments have been performed on certain cylindrical motors with internally burning tubular grains (23), (24), (67). It has been shown that there are operating conditions under which these motors experience unstable burning when subjected to a shock pulse, even though they burn stably in the absence of perturbations. These nonlinear instabilities, which occur in the axial mode and exhibit a sharp-fronted wave form, which is more reminiscent of shock waves than sound waves, are triggered by setting off small explosive charges in the head end of the chamber. Motor tests are carried out with four separate explosive charges, each being fired at a different time in the burning history of the motor. Each explosion produces a shock wave which propagates back and forth axially in the chamber. Oscilloscope traces of the response of a pressure transducer located in the chamber show whether the shock strength increases or decreases on subsequent transits. Figure 9-22 shows two such traces, one in which the pulse decays and the other in which the pulse grows. When amplification occurs, appreciable increase in the mean chamber pressure is observed. Conditions for nonlinearly unstable, but linearly stable, burning are identified as conditions under which shock-wave amplification occurs.

Contrary to the usual behavior of acoustic instabilities, it was found that these nonlinear instabilities are most severe for propellants with low rates of heat release and for motors operating at high chamber pressures. For a given motor geometry, a critical chamber pressure can be identified above which the system is nonlinearly unstable. The axial pulse technique provides one useful method for rating instability behavior of engines in development programs (23).

It has also been found that nonlinear acoustic instabilities in the first traveling tangential mode can be triggered in tubular solid rocket chambers, by means of brief tangential pulses of high-pressure nitrogen, released by means of a solenoid valve (25). Tangential pulsing can also be achieved by imbedding a small charge in the propellant grain, as shown in Fig. 9-23. Although tangential pulse techniques have often been employed in studies of combustion instability in liquid propellant rocket motors, very little data are yet available on the effects of tangential pulses in solid propellant motors. One might expect that nonlinear instabilities in linearly stable



(A). Pulse decays under stable conditions



(B). Pulse grows to axial mode oscillations under unstable conditions

Fig. 9-22 Oscilloscope traces of shock-induced, nonlinear, longitudinal, acoustic instability (23).

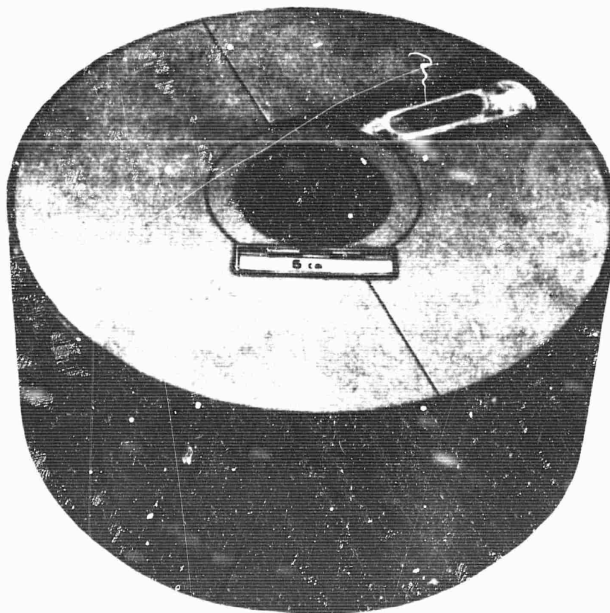


Fig. 9-23 ONERA photograph of impulse charge for tangential mode studies.

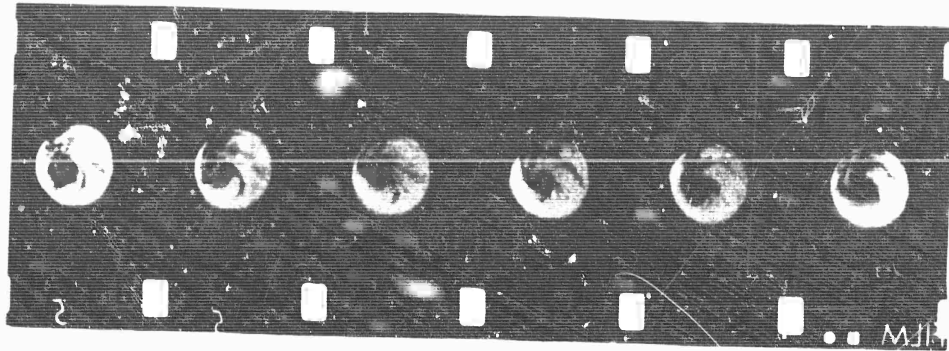


Fig. 9-24 ONERA photographs of vortex flow in the central port of a cylindrical motor.

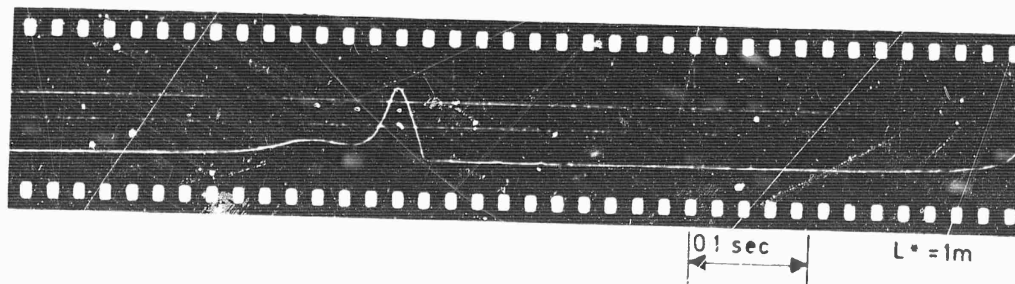
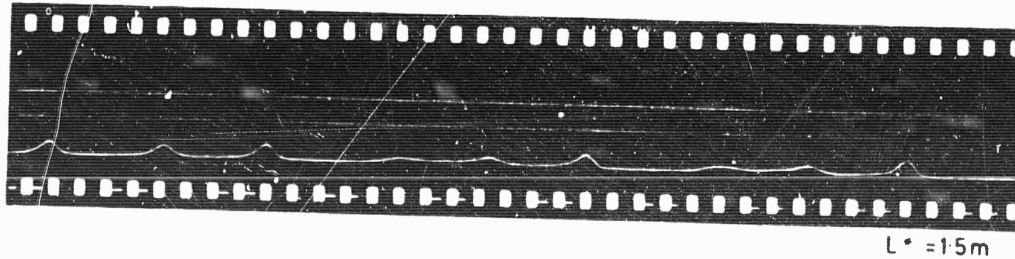
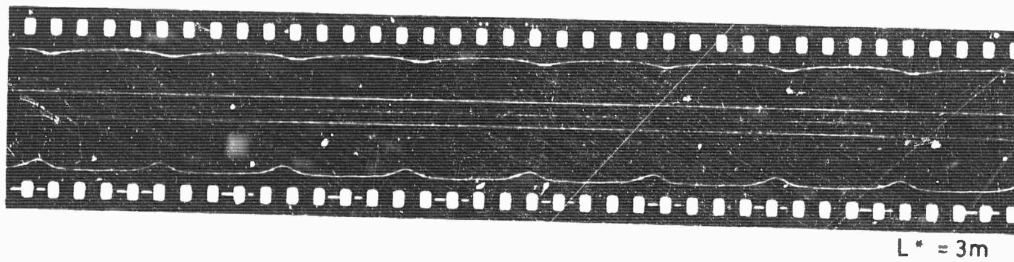


Fig. 9-25 Typical recordings of low frequency instabilities, from ONERA.

motors would be as likely to occur in tangential modes as in axial modes. Therefore further study of tangential pulse techniques in solid propellant motors appears to be warranted.

6.3. Vortex Development

The occurrence of finite-amplitude, vortex-like rotations in the flow of cylindrical motors during combustion instability was suggested as early as 1956, (6), (70). These rotations were presumed to occur inside the star-point cavities of some internally burning, cylindrical star grains. If an even number of counter-rotating vortices of equal strengths occur inside the motor then no net torque will be produced, but if an odd number of equal-strength, vortex-like rotations occur (e.g., if a single vortex occurs inside the cavity of an internally burning tubular grain), then the motor will experience a net torque which will tend to impart spin to a vehicle. Such unexpected spins have been observed in missile firings. The most recent experimental roll torque measurements in static firings have provided data from which the net value of the vortex strength can be inferred (68).

The most detailed studies yet reported on vortex-like rotations in cylindrical motors, are those described in Refs. (25) and (40). The experiments were performed with internally burning tubular grains. The principal observational technique was high-speed (1000 to 3200 frames/sec) photography of the interior of the combustion chamber, as seen through a transparent plexiglas window fitted into the chamber head. Photographs of this type have also been taken at ONERA; six frames of an ONERA film are shown in Fig. 9-24. In Refs. (25) and (40) dark areas which occurred in the center of the chamber were interpreted as representing carbon smoke accumulated in vortex centers. From the observed motion of smoke blobs, peripheral velocities up to 400 ft/sec at the head end of the motor were estimated for the vortices. The shapes of the dark areas provided evidence for the existence of one, four and eight vortices at different times in the burning history; particular vortex patterns typically lasted for 0.1 sec. The vortex-like patterns were presumed to be generated by nonlinear acoustic streaming phenomena resulting from linear tangential acoustic instabilities.

The mean burning rate and mean chamber pressure increased during vortex occurrence, presumably due to erosive phenomena and to vortical throat blockage phenomena. Further evidence for the occurrence of the eight vortex patterns was provided by observations of eroded shapes of propellant grains. Pressure transducer measurements lent support to the hypotheses that single vortices arise from the first and second tangential traveling acoustic modes, that four vortices arise from the first tangential standing mode and the eight vortices arise from the second tangential standing mode. A preliminary theoretical investigation provides qualitative support for these interpretations of experimental results (25).

The likelihood of the occurrence of nonlinear vortical phenomena is not understood well. Necessary and sufficient conditions for vortex development have not been defined.

6.4. Nonacoustic Oscillatory Instabilities at Low Pressure

6.4.1. Introduction - Of the wide variety of conceivable types of nonacoustic instabilities mentioned in Section 2, one particular broad class has been the subject of virtually all of the investigations that have been reported on nonacoustic instabilities. We close the present chapter with a discussion of this class of instabilities. Oscillatory phenomena are involved here; we have nothing to say about nonoscillatory instabilities. Certain aspects of the instabilities to be considered here are obviously nonlinear but the question of whether most of the essential attributes of the instabilities are explicable on the basis of linear concepts has not been resolved. Some

investigators appear to believe that it is unreasonable to include all of the phenomena discussed here in a single category; they contend that different subregimes are controlled by entirely different underlying processes. This view may or may not be correct, but there are certain obvious relationships among the studies that we shall review here and the instabilities do all occur under the same operating and design conditions (low pressures, usually metal-containing propellants, etc.). Therefore we find it convenient to include all of the phenomena in a single class. We begin with a discussion of manifestations of nonacoustic instabilities in motor firings and then proceed to consider research on the subject.

6.4.2. Motor Observations; Practical Consequences - One of the earliest forms of instability observed in solid-propellant rocket motors was the phenomenon of 'chuffing' (7), (16), (17), (19), (72), in which the motor experiences brief spurts of combustion followed by periods at near ambient pressures. The periods involved here can be very long, greater than one second; they certainly do not correspond to acoustic or Helmholtz modes of the system. The same statement is true for the so-called 'low-frequency instability', which was discovered more recently. In this phenomenon, the chamber pressure varies somewhat more regularly and at a somewhat higher frequency than in chuffing and the minimum pressure achieved during a cycle exceeds ambient. The frequencies involved in both chuffing and low frequency instability are below about 500 cps. Both phenomena have been observed in systems in which high-frequency pressure transducers showed no evidence of acoustic vibrations. Representative chamber pressure-time recordings are shown in Fig. 9-25; schematic curves illustrating the overall pressure history of the phenomena are shown in Fig. 9-26. Both phenomena occur mainly at low chamber pressures; neither has been observed above 850 psi.

A somewhat more detailed list of general conclusions drawn from motor observations is presented in (17) and is reproduced below:

- a) Chuffing and low frequency instability phenomena (not unique to a given class of solid propellant) have been observed in conventional double-base, double-base containing lead salts and metal additives, cast-modified double base and polyurethane-ammonium perchlorate composite propellants.
- b) Both chuffing and low frequency instability are experienced at pressures well below 500 psi, although low frequency instability has been noted at pressures up to 850 psi.
- c) The frequency of low frequency instability increases almost linearly with increasing base pressure, which is the lowest pressure between successive pressure peaks. The frequency range experienced with low frequency instability has ranged from a few cps to 250 cps. Chuffing frequency generally ranges from a fraction of cycle per second to a few cycles per second. The amplitude of low frequency instability generally decreases with increasing base pressure; hence, the amplitude generally decreases with increasing frequency (see Fig. 9-27).
- d) The frequency of chuffing decreases as the peak pressure of the chuff increases.
- e) There is indication that the frequency and amplitude of low frequency instability increase with increasing propellant conditioning temperature.
- f) The amplitude of low frequency instability increases as the concentration of metal additive increases. No significant effect of concentration on frequency has been noted (17), although such an effect has been observed in stand tests (41).
- g) There is good indication that frequency, not amplitude, is influenced by the

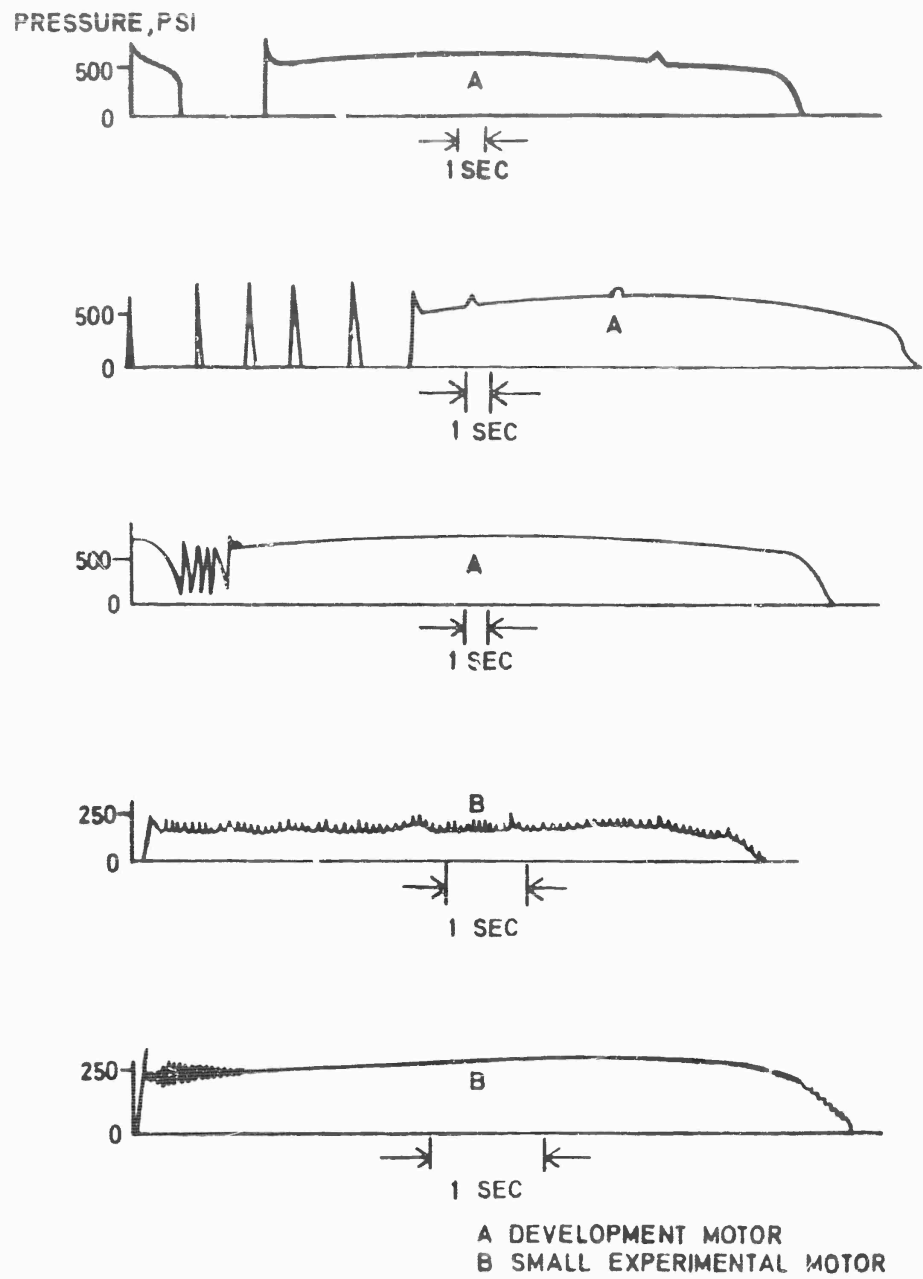
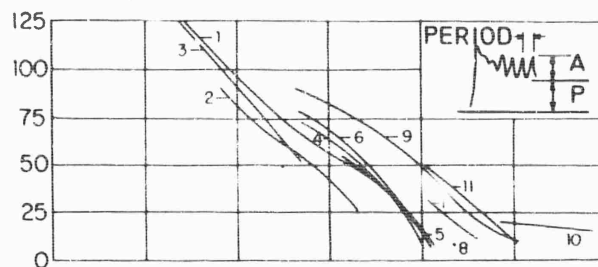


Fig. 9-26 Examples of chuffing and low frequency instability (17).

No.	Additive	Cond. Temp.
1	2.90% Al	70° F.
2	3.25% Mg/Al (30/70) Alloy	-40° F.
3	3.25% Mg/Al (50/50) Alloy	-40° F.
4	3.25% Mg/Al (50/50) Alloy	70° F.
5	3.25% Mg/Al (30/70) Alloy	70° F.
6	3.25% Mg/Al (70/30) Alloy	70° F.
7	4.30% Mg/Al (30/70) Alloy	-40° F.
8	4.30% Mg/Al (30/70) Alloy	77° F.
9	6.00% Mg/Al (50/50) Alloy	-40° F.
10	6.00% Mg/Al (50/50) Alloy	77° F.
11	3.25% Mg	15° F.

AMPLITUDE, PSI



FREQUENCY, c/s

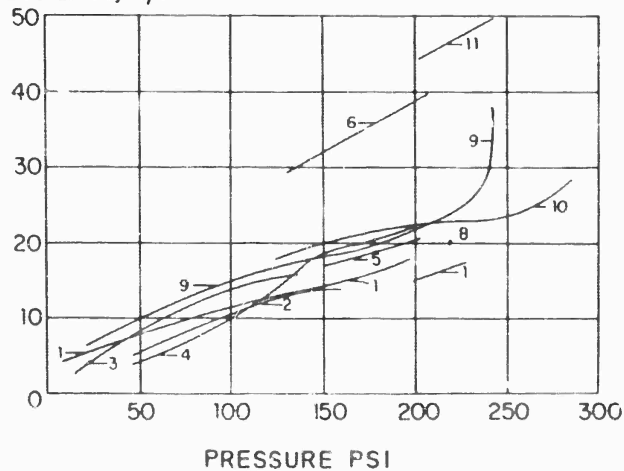


Fig. 9-27 Relationship of amplitude and frequency to operating pressure for double-base composition with various metal additives (72).

reactivity or reaction rate of the metal additive used.

h) Neither amplitude nor frequency of low frequency instability has been affected by changing the charge size.

Chuffing and low frequency instability are seldom sufficiently severe to destroy the motor. However, they do give rise to highly variable thrust and can thereby prevent many types of rocket vehicle missions from being completed successfully. Also, the frequencies involved correspond to natural frequencies of many vehicle systems and therefore they may excite damaging mechanical oscillations of the vehicle or its components. The problem is likely to become increasingly important in space applications because of the advantages of employing low chamber pressures in space. There is also concern that, with the future development of very large motors in which acoustic frequencies coincide with these instability frequencies, disastrous reinforcement of oscillations may occur.

6.4.3. Explanations in Terms of Intrinsic Combustion Characteristics; Strand Observations - The size and shape of the combustion chamber played no part in the earliest explanations of chuffing. The phenomenon was presumed to arise solely from the combustion properties of the propellant. Periodic thermal explosions were presumed to occur in the heated surface layer of the propellant because of an exothermic solid-phase reaction (7), (19). Thermal explosion theory was then applied to the process and the period of the oscillation was identified with an explosion induction time. Reasonable agreement with experimental frequencies was obtained, although other investigators found that a theory postulating a thermal explosion, due to an exothermic gas-phase reaction, provided best agreement with some experiments (16). These early results prompted more recent measurements of ignition times for propellant surfaces, which had been brought rapidly into contact with a heated plate (17). The early theories have also been extended to provide correlations for newly measured chuffing frequencies (17).

Support for this early view is provided by the observation that the occurrence and character of chuffing and low frequency instability depend on the propellant formulation and on the initial temperature. Recently, further experimental support for the existence of mechanisms, with characteristics somewhat akin to those of thermal explosions, has been provided by observations of intrinsic periodicities in the isobaric combustion of propellant strands. High-speed photography of the combustion of strands of an aluminized double-base propellant in the 200 to 900 psia pressure range revealed a periodicity (frequency 300-700 cps) in the mass flux of aluminum leaving the surface (39). Periodic ejection of burning aluminum globules, from the surface of a somewhat similar propellant, was also observed at pressures of 20 to 100 psig (17). In this last case, flame intensity fluctuations with a frequency of about 10 cps were also observed (17). A more accurate frequency analysis of the radiant intensity emitted by a burning strand of pure ammonium perchlorate and aluminum also revealed a characteristic oscillation frequency (see Fig. 9-8) when aluminum particles of the proper size ($\leq 10\mu$) were employed (41). No periodicities were discernable either with 40μ aluminum particles or with fine molybdenum particles (41). The periodicity with the fine aluminum particles, which exhibited a frequency that increased linearly with the aluminum concentration, can apparently be explained on the basis of aggregation of critical amounts of aluminum on the propellant surface followed by ignition of the agglomerate (41).

It is thus clear that a variety of processes inherent in propellant combustion can give rise to oscillations in the frequency ranges of chuffing and low frequency instability. However, it has not been demonstrated beyond doubt, that these processes alone account for all instances of oscillatory, nonacoustic instabilities at low pressures in motors. Indeed, there is experimental evidence that motor parameters often affect the instabilities (20), (71) and therefore some type of interaction

between motor processes and the combustion must be of importance. Possible effects of motor parameters are considered below.

6.4.4. Explanations in Terms of Combustion Response - Residence Time Interactions; L^* Instability - All of the processes that we have just discussed are highly nonlinear phenomena. Good correlation of the pressure limits, below which nonacoustic instabilities are observed, have been obtained on the basis of a linear theory (20). Recently, the linear theory has been extended to obtain correlations for observed oscillation frequencies below the pressure limit (71). Thus, the mechanisms controlling oscillatory nonacoustic instabilities remain unclear.

It has been proposed that the interaction between the time lag in the propellant burning rate response to an applied chamber pressure and the time lag in exhausting burnt gases from the chamber through the nozzle, gives rise to a nonacoustic instability (20). This type of instability is mathematically very similar to low-frequency instabilities of liquid propellant motors. The time lag of the propellant response is attributed to and calculated from the heat conduction processes in the solid propellant. Stability conditions are obtained from the type of analysis employed in studying feedback servomechanisms. Results of the analysis may be expressed in a graph of L^* of the motor (free chamber volume divided by throat area) versus chamber pressure, for marginally stable burning with a given propellant. Such a graph is shown in Fig. 9-28. The theory predicts two stability limits for the propellant of Fig. 9-28 and the upper limit agrees well with experimental data. Instabilities conforming to the assumptions of Ref. (20) are sometimes called L^* instabilities.

In a later analysis, the same general type of physical concept was used in studying the dependence of oscillation frequency on L^* and chamber pressure (71). The objective was to correlate experimental pressure frequencies (see Fig. 9-29) obtained with an aluminized composite propellant in a small end-burning motor. Suitable choices of kinetic constants provided reasonably good correlation of the results.

Additional pressure frequency data in small motors may be found in Refs. (42), (43).

6.4.5. Interaction of Acoustic and Nonacoustic Phenomena - Experiments have been performed in very long T burners in an effort to find whether abnormal oscillatory phenomena can develop, when the natural acoustical frequency of the chamber coincides with the nonacoustic oscillation frequency of a propellant (26), (42), (43). Definite evidence that such an interaction occurs for metalized propellants has been obtained (42), (43). As the pressure in the burner gradually increases, transducers recording transient pressures show that oscillations begin to develop, grow to a maximum amplitude at a critical mean pressure and then begin to die out, finally disappearing when the chamber pressure becomes sufficiently high. These oscillations are quite regular and their frequency increases roughly linearly with pressure, exhibiting approximately the same pressure dependence as the frequencies observed with the same propellants in small motors. The amplitudes of the oscillations are maximum at frequencies in the vicinity of the natural acoustic frequency of the chamber. The phenomenon has been termed 'preferred frequency oscillatory combustion' (42), (43).

In an effort to obtain additional information about the phenomenon, the radiation intensity from the combustion zone was monitored and its frequency and phase were compared with those of the pressure oscillations (42), (43). It was found that at the higher frequencies the radiation output lagged behind the pressure in phase and at the lower frequencies the radiant intensity led the pressure oscillations in phase (see Fig. 9-30 for strand-burner results that are almost identical to T-motor results); both oscillations maintained the same frequency at pressures in the vicinity of the peak amplitude, but there was a tendency for the radiation to skip a cycle now and then at the higher frequencies and occasionally to pick up an extra cycle at the lower

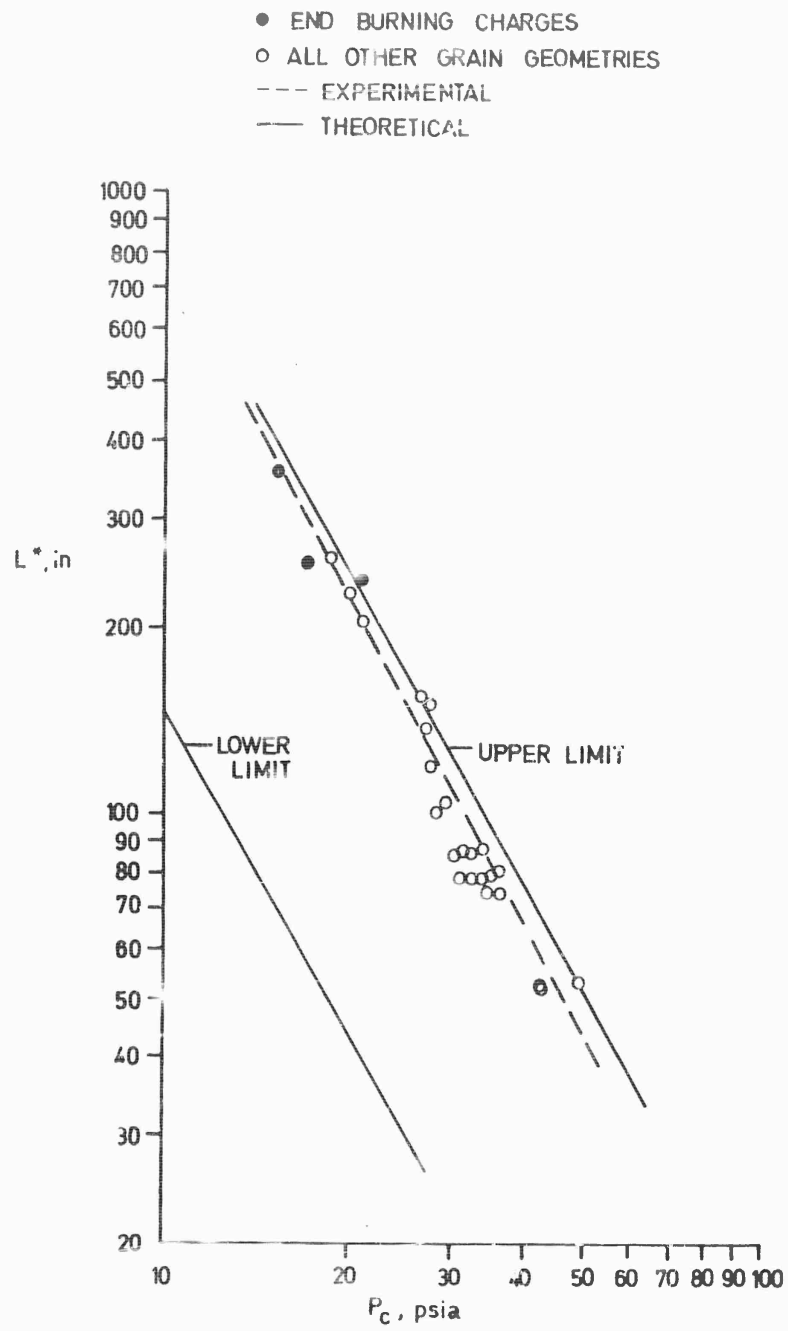


Fig. 9-28 L^* vs. pressure for conditional stability; JPL-534 propellant; 80°F, (20).

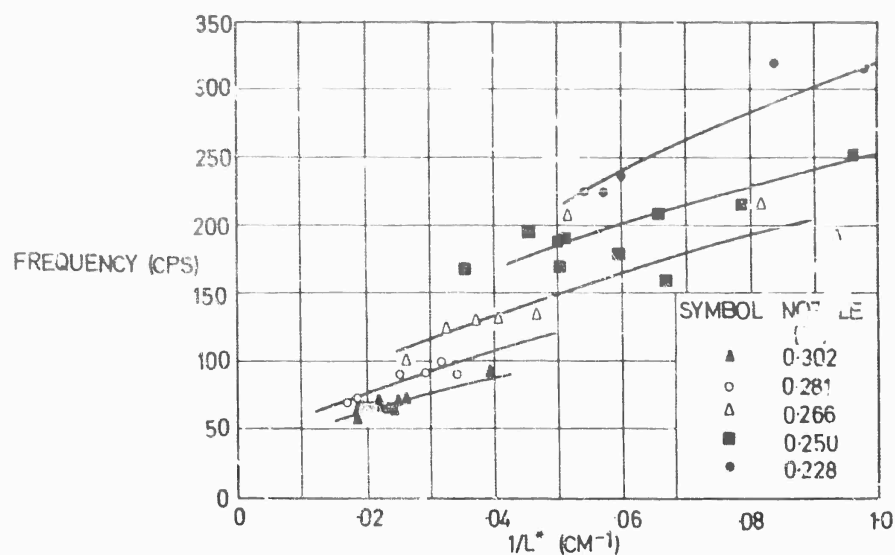


Fig. 9-29 Frequency versus $1/L^*$, solid lines have been drawn through approximately constant pressure data. Bottom line ~ 40 psia, top line ~ 200 psia. (7).

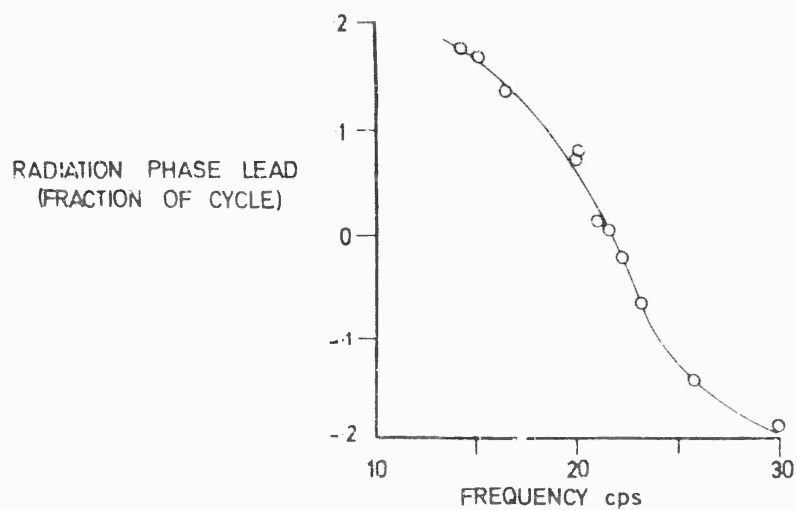


Fig. 9-30 Combustion radiation phase lead relative to pressure, determined from a burning propellant strand in a pressure vessel with forced pressure oscillations (43). Mean pressure, 55 psia; cast double-base propellant with magnesium-aluminum alloy powder.

frequencies. The fundamental significance of these orderly results is unclear, partially because the relationship between radiation intensity and other combustion phenomena, such as heat release, is not understood well under oscillatory conditions. An intuitive discussion of these results is available (43), also empirical observations of the influences of propellant composition and other parameters (42), (43).

The peak pressure amplitudes of these oscillations are not very large in the T motor. However, large T-motors are 'lossy' and so amplitudes may be quite high in very large motors of conventional design. The phenomenon therefore warrants further study.

References

- (1) Boys S. F., and Schofield A., Investigations on Secondary Peaks, British Advisory Council on Scientific Research and Technical Development Report AC 5649/Rep./20/43, March, 1943.
- (2) Sage B. H., Burning Characteristics in the Axial Perforations of Extruded Ballistite Grains, C.I.T. NDRC Report No. A-83, CIT-JDC, OSRD No. 815, August, 1943.
- (3) Wimpress R. N., Internal Ballistics of Solid-Fuel Rockets, pp. 122-132, McGraw-Hill, New York, 1950.
- (4) Green L., Jr., Jet Propulsion, 24, 252, 1954.
- (5) Green L., Jr., Jet Propulsion, 26, 655, 1956.
- (6) Green L., Jr., Jet Propulsion, 28, 483, 1958.
- (7) Huffington J. D., Trans. Faraday Soc., 50, 942, 1954.
- (8) Smith R. P., and Sprenger D. F., Fourth Symposium (International) on Combustion, pp. 893-906, Williams and Wilkins, Baltimore, 1953.
- (9) Schultz R., Green L., Jr. and Penner S. S., Studies of the Decomposition Mechanism, Erosive Burning, Sonance and Resonance for Solid Composite Propellants, Combustion and Propulsion, 3rd AGARD Colloquium, Pergamon, London, 1958.
- (10) Green L., Jr., Jet Propulsion, 28, 159, 1958.
- (11) Price E. W., Combustion Instability in Solid-Propellant Rocket Motors, IXth Annual Congress of the International Astronautical Federation, Astronautica Acta (Springer-Verlag), 1959.
- (12) Geckler R. D., Fifth Symposium (International) on Combustion, p. 29, Reinhold, New York, 1955.
- (13) Trubridge G. F. P., and Badham H., High Temperature Phenomena, Fifth AGARD Combustion and Propulsion Colloquium, The MacMillan Co., New York, 1963, Summerfield Research Station Technical Report B. D. 36, Dec. 1961.
- (14) Arden E. A., Powling J., and Smith W. A. W., Combustion and Flame, 6, 21, 1962.

- (15) Inami Y.H. and Shanfield H., AIAA Preprint No. 64-147, January, 1964.
- (16) Crawford B.L., Huggett C.M., McBrady J.J. and Rusoff I.I., Univ. of Minnesota, Contract OE MSTV-716, Rept. UM 32, July 11, 1945, also part of Rept. OSRD-6374.
- (17) Yount R.A. and Angelus T.A., AIAA J. 2, 1307, 1964.
- (18) Eisel J.L., Horton M.D., Price E.W. and Rice D.W., AIAA Preprint No. 64-149, Jan. 1964.
- (19) Clemmow D.M. and Huffington J.D., Trans. Faraday Soc., 52, 385, 1956.
- (20) Sehgal R. and Strand L., AIAA J. 2, 696, 1964.
- (21) Shinnar R. and Dishon M., Heat Transfer Stability Analysis of Solid Propellant Rocket Motors, Solid Propellant Rocket Research, Vol. I of ARS Series Progress in Astronautics and Rocketry, edited by M. Summerfield, Academic Press, New York pp. 359-374, 1960.
- (22) Denison M.R. and Baum E., ARS J. 31, 1112, 1961.
- (23) Dickinson L.A., ARS J. 32, 643, 1962.
- (24) Brownlee W.G., AIAA J. 2, 275, 1964.
- (25) Swithenbank J. and Sotter G., AIAA J. 2, 1297, 1964.
- (26) Price E., Experimental Measurements in Solid Propellant Rocket Combustion Instability, pp. 53-74 of Section 3.4, Experimental Methods in Combustion Research edited by J. Surugue, Pergamon Press, New York, 1961.
- (27) Posel K., ARS J. 31, 1242, 1961.
- (28) Draper C.S., and Li Y.T., J. Aero. Sci. 16, 1949.
- (29) Liu F.F. and Berwin T.W., Jet Propulsion 28, 83, 1958.
- (30) Barden R.G., Rev. Sci. Inst. 32, 936, 1961.
- (31) Mathes H.B., Eighth Symposium (International) on Combustion, p. 894, Williams and Wilkins, 1962.
- (32) Liu F.F. and Berwin T.W., Rev. Sci. Inst. 29, 14, 1958.
- (33) Foner S.N., Hudson R.L. and Nall B.H., AIAA J. 2, 1123, 1964.
- (34) Angelus T.A., Unstable Burning Phenomena in Double-Base Propellants, in Solid Propellant Rocket Research, Vol 1, ARS Series Progress in Astronautics and Rocketry, pp. 527-559, edited by M. Summerfield, Academic Press, New York, 1960.
- (35) Brownlee W.G. and Marble F.E., An Experimental Investigation of Unstable Combustion in Solid Propellant Rocket Motors, *ibid.*, pp. 455-494.
- (36) Landsbaum E.M., The Effect of a Shock Wave on a Burning Solid Propellant, Vols. 3-4, Advances in Aeronautical Sciences, pp. 497-511, Pergamon Press, New York, 1961.

- (37) Engler J. F. and Nachbar W., AIAA J. 2, 1279, 1964.
- (38) Watermeier L. A., ARS J. 31, 564, 1961.
- (39) Watermeier L. A., Aungst W. P. and Pfaff S. P., Ninth Symposium (International) on Combustion, pp. 316-27, Academic Press, New York, 1963.
- (40) Swithenbank J. and Sotter G., AIAA J. 1, 1682, 1963.
- (41) Inami J. H. and Shanfield H., AIAA J. 2, 1314, 1964.
- (42) Eisel J. L., Horton M. D., Price E. W. and Rice D. W., AIAA J. 2, 1319, 1964.
- (43) Price E. W., Review of the Combustion Instability Characteristics of Solid Propellants, 25'th Meeting of AGARD Combustion and Propulsion Panel, San Diego, April 1965 (proceedings to be published).
- (44) Price E. W., et al., Combustion and Flame 5, 149, 1961.
- (45) Zink J. W. and Delsasso L. P., J. Acoust. Soc. Am. 30, 765, 1958.
- (46) Dobbins R. A. and Temkin S., AIAA J. 2, 1106, 1964.
- (47) Heute T. F. and Bolt R. H., Sonics, John Wiley & Sons, New York, 1955.
- (48) Price E. W. and Sofferis J. W., Jet Propulsion 28, 190, 1958.
- (49) Price E. W., Eighth Symposium (International) on Combustion, pp. 925-929, Williams and Wilkins Co., Baltimore, 1962.
- (50) Crump J. E. and Price E. W., ARS J. 31, 1026, 1961.
- (51) Crump J. E. and Price E. W., AIAA J. 2, 1274, 1964.
- (52) Ryan N. W., Eighth Symposium (International) on Combustion, pp. 924-925, Williams and Wilkins Co., Baltimore, 1962.
- (53) Horton M. D., ARS J. 31, 1596, 1961.
- (54) Horton M. D., ARS J. 32, 644, 1962.
- (55) Horton M. D. and Price E. W., Ninth Symposium (International) on Combustion, pp. 303-310, Academic Press, New York, 1963.
- (56) Strittmater R., Watermeier L. and Pfaff S., Ninth Symposium (International) on Combustion, pp. 311-315, Academic Press, New York, 1963.
- (57) Ryan N. W., Coates R. L. and Baer A. D., Ninth Symposium (International) on Combustion, pp. 328-332, Academic Press, Inc., New York, 1963.
- (58) Horton M. D. and McGie M. R., AIAA J. 1, 1319, 1963.
- (59) Horton M. D. and Rice D. W., Combustion and Flame, 8, 21, 1964.
- (60) Rice D. W., AIAA J. 2, 1654, 1964.

- (61) Horton M.D., AIAA J. 2, 1112, 1964.
- (62) Coates R.L., Horton M.D. and Ryan N.W., AIAA J. 2, 1119, 1964.
- (63) Ryan N.W. and Coates R.L., AIAA J. 2, 1130, 1964.
- (64) McClure F.T., Hart R.W. and Cantrell R.H., AIAA J. 1, 588, 1963.
- (65) Hart R.W., Panel discussion on Unstable Combustion in Solid-Fuel Rocket Engines, Eighth Symposium (International) on Combustion, pp. 904-918, Williams and Wilkins Co., Baltimore, 1962.
- (66) Landsbaum E.M., Kuby W.C. and Spaid F.W., Experimental Investigation of Unstable Burning in Solid Propellant Rocket Motors, Solid Propellant Rocket Research, Vol. 1 ARS Series Progress in Astronautics and Rocketry, pp. 495-525, edited by M. Summerfield, Academic Press, New York, 1960.
- (67) Dickinson L.A. and Jackson F., Combustion in Solid Propellant Rocket Engines, Fifth AGARD Colloquium: High-Temperature Phenomena, pp. 531-550, The MacMillan Co., New York, 1963.
- (68) Flandro G.A., AIAA J. 2, 1303, 1964.
- (69) Wall R.H., Resonant Burning of Solid Propellants: Review of Causes, Cures and Effects, Solid Propellant Rocket Research, Vol. 1, of ARS Series Progress in Astronautics and Rocketry, pp. 603-619, Academic Press, New York, 1960.
- (70) Green L., Jr., Studies on the Reaction Stability of Solid Propellant Charges, Rept. No. 1077, Aerojet-General Corp., Azusa, California, pp. 23-26, 1956.
- (71) Beckstead M.W., Ryan N.W. and Baer A.D., Nonacoustic Instability of Composite Propellant Combustion, AIAA Paper No. 66-111, 1966.
- (72) Angelus T.A., Panel discussion on Unstable Combustion in Solid-Fuel Rocket Engines, Eighth Symposium (International) on Combustion, pp. 921-924, Williams and Wilkins Co., Baltimore, 1962.
- (73) Oberg C.L. and Huebner A.L., Effects of Aluminum on Solid-Propellant Combustion Instability, Rept. No. AFOSR-66-1847, R-6654, Air Force Office of Scientific Research Contract No. AF 49(638)-1575, Rocketdyne, North American Aviation, Inc., Canoga Park, Calif., July, 1966.
- (74) Diedrichsen J., Further Development of Stability Grading of Solid Propellants by the Oscillatory Strand Burner Technique, Proc. of 4th Meeting of the Technical Panel on Solid Propellant Combustion Instability held at Stanford Research Institute, Feb. 1, 1964: Applied Physics Laboratory - The Johns Hopkins University document No. T9371-7, April 1964.

Chapter 10

**Theoretical Analyses of Combustion
Instability**

Nomenclature

A	cross-sectional area of a boundary
a	speed of sound; also constant defined in Eq. 10-72
B	pre-exponential rate factor
b	square of ratio of frozen to equilibrium sound speeds; length of a one-dimensional system; constant defined in Eq. 10-72
c	specific heat
c_p	specific heat at constant pressure for the gas
c_s	heat capacity per unit mass, for the condensed material
E	activation energy for gas-phase reaction
e	acoustic energy density defined in Eq. 10-23
E_s	activation energy for gasification process
h	enthalpy per unit mass
j	steady state temperature sensitivity coefficient
k	dimensionless frequency defined in Eq. 10-70; erosion constant
L_s	heat of gasification per unit mass of reactant mixture consumed
M	Mach number
\dot{m}	mass burning rate per unit area or mass flow rate per unit area
n	reaction order for gas-phase reaction
n_s	number of condensed particles per unit volume
\underline{n}	unit normal vector
P	complex pressure-amplitude coefficients
p	pressure
R	cylinder radius
r	radial distance; particle radius; linear regression rate
R°	universal gas constant
s	entropy per unit mass; dimensionless frequency defined in Eq. 10-64
T	temperature
t	time
u	erosive velocity parallel to propellant surface

V	chamber volume
v	velocity
\vec{v}	velocity vector
x	axial spatial coordinate; spatial coordinate normal to burning surface
\vec{x}	spatial coordinate vector
Y	acoustic admittance; mass fraction of principal reactant
y	coordinate normal to the wall; dimensionless acoustic admittance defined in Eq. 10-60
Z	ratio of the total mass of condensed material to the total mass of gas contained within the cavity
α	growth constant for acoustic pressure
β	dimensionless frequency, $\omega (x_t - x_\ell) / (a_t - \bar{v}_\ell)$ in Section 4.2 and $2\rho_s r^2 \omega / 9\mu$ in Section 4.5.
γ	ratio of specific heat
δ	acoustic phase angle; also $\bar{\rho}_g / \rho_s$
θ	azimuthal angle
λ	wavelength; thermal conductivity
μ	viscosity coefficient; also pressure sensitivity coefficient defined in Eq. 10-61.
ν	dimensionless velocity variable; parameter accounting for sensitive time lag; oxidizer-fuel mass ratio in the bulk of the propellant
ξ	dimensionless distance variable defined in Eq. 10-64
ρ	density
ρ_c	solid propellant density
ρ_s	specific gravity of the condensed material
σ	dimensionless density variable
τ	characteristic relaxation time; time lag; characteristic burning time of an oxidizer sphere
τ_1	explosion induction time
φ	velocity potential
ω	(angular) acoustic frequency

Script Letter

l one-dimensional cavity length; cylinder length

Superscripts

o identifies complex amplitude of an oscillatory quantity

$'$ a perturbation quantity (difference between instantaneous value and time-average value); also derivative with respect to an argument; occasionally a modified dimensionless parameter

$-$ time-average value

$*$ complex conjugate

$\langle \rangle$ denotes space average

Subscripts

B binder

b condition at the burning propellant surface but on the hot side of the gas-phase combustion zone

c implies that the quantity is to be evaluated in the chamber; also conditions in the condensed phase at the extreme solid side of the interfacial combustion and heat conduction zone

d dilatation

e equilibrium

f flame; frozen

g properties of the gas

i conditions in the bulk of the propellant (at $\xi = -\infty$)

k identifies a normal mode of the cavity

m identifies a normal mode of the cavity

n identifies a normal mode of the cavity

O oxidizer

s properties of the condensed phase; conditions at solid-gas interface; shear

t conditions at the throat of the nozzle

w implies that the quantity is to be evaluated at the wall

l condition at the nozzle entrance plane

Theoretical Analyses of Combustion Instability

1. Introduction

In view of the variety of different kinds of combustion instability described in Chapter 9 Section 2, it is not surprising that no general theoretical approach exists for the problem of predicting when oscillatory and irregular burning will occur. A rather well-defined theoretical framework does exist for linear acoustic instabilities. But for nonlinear instabilities and for nonacoustic instabilities, there are only isolated theoretical analyses of a few specific mechanisms. In this chapter we shall therefore discuss primarily linear acoustic combustion instability. Acoustic vibrational modes are described in Section 2, the basis for describing acoustic amplification is presented in Section 3 and the available analyses of acoustic damping mechanisms are reviewed in Section 4. Theoretical studies of the heart of the problem of linear acoustic instability, analyses of the acoustic amplification mechanism, are considered in Section 5. Existing theories of non-linear and nonacoustic instabilities are discussed in Section 6. Finally, a few remarks concerning comparison of theory with experiment are made in Section 7.

Regarding linear acoustic gain and loss mechanisms, the various processes that are thought to be of importance were listed in Chapter 9 Section 4.1. The discussions in the following three sections will make clear which of these mechanisms are amenable to theoretical analysis.

2. Acoustic Vibrational Modes

2.1. Derivation of Wave Equation

First we develop the equations describing sound propagation in a gas, by considering small-amplitude departures from a uniform, quiescent state. Body forces and all transport fluxes are neglected, so that Eqs. 6-7, 6-8 and 6-9 of Chapter 6 become :

$$\partial \rho / \partial t + \nabla \cdot (\rho \mathbf{x}) = 0, \quad (\text{Eq. 10-1})$$

$$\partial \mathbf{x} / \partial t + (\nabla p) / \rho = 0, \quad (\text{Eq. 10-2})$$

and :

$$\partial h / \partial t - (\partial p / \partial t) / \rho = 0. \quad (\text{Eq. 10-3})$$

The terms $\mathbf{x} \cdot \nabla \mathbf{x}$, $v^2/2$ and $\mathbf{x} \cdot \nabla h$ have been omitted here because the amplitudes of the oscillations are assumed to be small; all three of the neglected terms are quadratic (second-order) in small quantities, since $\mathbf{x} = 0$ in the quiescent state and $\nabla h = 0$ in the uniform state. The symbols are those defined in Chapter 6.

If we assume that either chemical equilibrium or chemical frozen conditions prevail in the sound oscillations, then :

$$Tds = dh - dp/\rho \quad (\text{Eq. 10-4})$$

according to Eq. 2-50 of Chapter 2 and therefore Eq. 10-3 implies that :

$$\partial s / \partial t = 0; \quad (\text{Eq. 10-5})$$

the entropy is independent of time. Assuming further that the entropy is uniform at some time, we find that the solution to Eq. 10-5 is :

$$s = \text{constant}. \quad (\text{Eq. 10-6})$$

We consider isentropic sound waves and employ Eq. 10-6 in place of Eq. 10-3.

For Eqs. 10-1 and 10-2 to be valid, the quantity v must be small compared with the sound speed a and the thermodynamic properties ρ and p must be expressible as :

$$\rho = \bar{\rho} + \rho', \quad p = \bar{p} + p' \quad (\text{Eq. 10-7})$$

where $|\rho'| \ll \bar{\rho}$, $|p'| \ll \bar{p}$, and both $\bar{\rho}$ and \bar{p} are independent of x and t . In view of Eq. 10-6, the quantities ρ' and p' in Eq. 10-7 must be related by :

$$p' = (\partial p / \partial \rho)_s \rho' \equiv a^2 \rho', \quad (\text{Eq. 10-8})$$

where a is either the equilibrium or frozen sound speed, in the undisturbed gas, depending on the reason for the validity of Eq. 10-4. If one substitutes Eqs. 10-7 and 10-8 into Eqs. 10-1 and 10-2 eliminating ρ' , retains first-order terms only and finally eliminates $\nabla \cdot \underline{v}$ from the equations obtained from the time derivative of Eq. 10-1 and the divergence of Eq. 10-2, then one finds that :

$$\partial^2 p' / \partial t^2 - a^2 \nabla^2 p' = 0, \quad (\text{Eq. 10-9})$$

which is the usual scalar wave equation for the sound field.

After Eq. 10-9 is solved for p' , the velocity field may be computed from the time integral of the equation :

$$\partial \underline{v} / \partial t = - \nabla p' / \bar{\rho}, \quad (\text{Eq. 10-10})$$

which follows from Eq. 10-2. An alternative approach is to introduce a velocity potential ϕ such that :

$$\underline{v} = \nabla \phi, \quad p' = - \bar{\rho} \partial \phi / \partial t, \quad (\text{Eq. 10-11})$$

where the last equality is implied by Eq. 10-10. The potential ϕ clearly satisfies the same wave equation as p' , Eq. 10-9. The sound field in a gas thus is described completely by a single scalar function.

2.2. Modes in Cavities

The solution to Eq. 10-9 will depend on what the boundary conditions are and where they are applied. The boundary condition at a rigid wall with normal vector \underline{n} is $\underline{v} \cdot \underline{n} = 0$, which implies that $\partial \phi / \partial n = 0$ and $\partial p' / \partial n = 0$. The boundary condition at an open isobaric boundary is $p' = 0$ or $\partial \phi / \partial t = 0$. More complex boundary conditions will be introduced later.

The waves of particular concern in rocket chambers are monochromatic waves or superpositions of a relatively small number of monochromatic waves. They are characterized by a harmonic time dependence and for convenience are usually writ-

en as the real part $\text{Re} \{ \}$ of a complex quantity, viz.,

$$p' = \text{Re} \{ p_0(\underline{x}) e^{i\omega t} \} \quad , \quad (\text{Eq. 10-12})$$

where p_0 is the (complex) pressure amplitude and ω is the (angular) frequency. Similar definitions are employed for the other variables, e.g.,

$$\underline{v} = \text{Re} \{ \underline{v}_0(\underline{x}) e^{i\omega t} \} = \text{Re} \left\{ - \frac{\nabla p_0}{i\omega \rho} e^{i\omega t} \right\} \quad (\text{Eq. 10-12a})$$

$$\varphi = \text{Re} \{ \varphi_0(\underline{x}) e^{i\omega t} \} = \text{Re} \left\{ - \frac{p_0}{i\omega \rho} e^{i\omega t} \right\} \quad , \quad (\text{Eq. 10-12b})$$

in which the last equalities are consequences of Eq. 10-11. Equation 10-9 shows that p_0 satisfies the equation :

$$\nabla^2 p_0 + (\omega^2/a^2) p_0 = 0 \quad . \quad (\text{Eq. 10-13})$$

When proper boundary conditions are applied at all boundaries of a cavity, the quantity ω becomes an eigenvalue of Eq. 10-13 which then possesses solutions only for an (infinite) sequence of definite frequencies ω , each corresponding to a different acoustical mode of the system.

As the simplest example, let us consider a one-dimensional cavity of length ℓ with perfectly rigid end walls. Equation 10-13 and its boundary conditions become :

$$d^2 p_0 / dx^2 + (\omega^2/a^2) p_0 = 0 ; \quad dp_0 / dx = 0 \text{ at } x = 0, \ell . \quad (\text{Eq. 10-14})$$

The general solution to Eq. 10-14 is :

$$p_0 = \sum_{n=1}^{\infty} P_n \cos(\omega_n x/a) \quad , \quad \omega_n = n\pi a/\ell, \quad n = 1, 2, \dots, \quad (\text{Eq. 10-15})$$

where P_n are arbitrary complex constants and ω_n are the frequency eigenvalues. Each term in the sum in Eq. 10-15 represents a normal acoustical mode of the cavity and each value ω_n is the corresponding normal frequency of the mode. From Eqs. 10-12 and 10-10, it is then seen that for any normal mode n , the pressure perturbation and velocity are given by

$$\left. \begin{aligned} p' &= \left| P_n \right| \cos(\omega_n x/a) \cos(\omega_n t + \delta_n) \\ v &= \left(\left| P_n \right| / a\rho \right) \sin(\omega_n x/a) \sin(\omega_n t + \delta_n) \quad , \end{aligned} \right\} \quad (\text{Eq. 10-16})$$

where δ_n is the argument of the complex number P_n . Equation 10-16 shows that at any given time t all points x in the cavity are oscillating in the same phase ($\omega_n t + \delta_n$) and that the phases of pressure and velocity oscillations differ by 90° . These properties identify standing waves. The standing waves described by Eq. 10-16 have nodal points for velocity (points where the velocity is always zero) at $\omega_n x/a = 0, \pi, 2\pi, \dots$ and nodal points for pressure at $\omega_n x/a = \pi/2, 3\pi/2, \dots$; pressure antinodes which are points where the pressure amplitude is maximum, are located at $\omega_n x/a = 0, \pi, 2\pi, \dots$, while velocity antinodes occur at $\omega_n x/a = \pi/2, 3\pi/2, \dots$. Acoustic modes in cavities are often standing waves analogous to these just described and pressure nodes and velocity antinodes often coincide, as do velocity

nodes and pressure antinodes (note preceding numbers).

In two or three dimensional cavities of sufficiently symmetrical shapes, traveling waves can also occur. Consider a rigid, two-dimensional, circular cavity of radius R . In polar coordinates, Eq. 10-13 and its boundary conditions become :

$$\frac{1}{r} \frac{\partial}{\partial r} \left(r \frac{\partial p_0}{\partial r} \right) + \frac{1}{r^2} \frac{\partial^2 p_0}{\partial \theta^2} + \frac{\omega^2}{a^2} p_0 = 0 ; \quad \frac{\partial p_0}{\partial r} = 0 \text{ at } r = R, \text{ all } \theta \quad (\text{Eq. 10-17})$$

By separating variables it is seen that Eq. 10-17 possesses solutions of the form :

$$p_0 = P_m^{(+)} J_m(\omega r/a) e^{i m \theta} \quad (\text{Eq. 10-18})$$

where the $P_m^{(+)}$ are complex constants and the J_m are the m 'th order Bessel functions of the first kind. The frequency ω must satisfy the equation :

$$J_m'(\omega R/a) = 0 \quad (\text{Eq. 10-19})$$

where the prime denotes derivative with respect to the argument. There are an infinite number of roots (labeled here $k = 0, 1, 2, \dots$) to this equation, for each value of m . The corresponding values of ω will be denoted by ω_{km} . A traveling wave can be illustrated by the $(+)$ solution for $k = 0, m = 1$; according to Eqs. 10-12 and 10-10 it has :

$$\left. \begin{aligned} p' &= |P_{01}^{(+)}| J_1(\omega_{01} r/a) \cos(\omega_{01} t + \theta + \delta_{01}^{(+)}) \\ v_r &= (- |P_{01}^{(+)}| / a \bar{\rho}) J_1'(\omega_{01} r/a) \sin(\omega_{01} t + \theta + \delta_{01}^{(+)}) \\ v_\theta &= (- |P_{01}^{(+)}| / a \bar{\rho}) [J_1(\omega_{01} r/a) / (\omega_{01} r/a)] \\ &\quad \cos(\omega_{01} t + \theta + \delta_{01}^{(+)}) \end{aligned} \right\} (\text{Eq. 10-20})$$

where $\delta_{01}^{(+)}$ is the argument of $P_{01}^{(+)}$ and the subscripts on v identify vector components. According to Eq. 10-20, at any given radial distance r the quantities p' and v are functions of $(\omega_{01} t + \theta)$ and are constant for angles θ at time t , such that $\theta = \text{constant} - \omega_{01} t$. This property describes waves that propagate in the $-\theta$ direction with angular velocity ω_{01} . Furthermore, the velocity component $-v_\theta$ in the direction of propagation is seen from Eq. 10-20 to be exactly in phase with p' . No stationary nodes or antinodes are identifiable from Eq. 10-20. These characteristics are representative of traveling waves. Standing waves can, of course, also be formed from Eqs. 10-18 and 10-19, e.g. by taking $P_{01}^{(+)} = P_{01}^{(-)}$.

It would take too much space for us to derive equations giving pressure and velocity fields and vibrational frequencies for cavities of all shapes and boundary conditions, that are of interest in rocket combustion instability. Therefore, we cite here only a general formula for the pressure field in what is perhaps the most important geometry for rocket instability, a cylinder of length ℓ and radius R with rigid walls. The result is :

$$\begin{aligned} p' = \sum_{k,m,n} J_m(\beta_{mk} r/R) \cos(n\pi x/\ell) & \left[|P_{kmn}^{(+)}| \cos(\omega_{kmn} t + m\theta + \delta_{kmn}^{(+)}) \right. \\ & \left. + |P_{kmn}^{(-)}| \cos(\omega_{kmn} t - m\theta + \delta_{kmn}^{(-)}) \right], \end{aligned} \quad (\text{Eq. 10-21})$$

where k , m and n are integers, β_{mk} is the k 'th root of the equation $J_m'(\beta) = 0$, $|P_{kmn}|^{(+)}$ are arbitrary positive constants, $\delta_{kmn}^{(+)}$ are arbitrary constants lying between $-\pi$ and π and the frequencies ω_{kmn} are given by :

$$\omega_{kmn} = a[(\beta_{mk}/R)^2 + (n\pi/\ell)^2]^{1/2} \quad (\text{Eq. 10-22})$$

Terms with $m = k = 0$, $n \neq 0$ represent standing longitudinal modes; terms with $m = n = 0$, $k \neq 0$ represent standing radial modes; terms with $k = n = 0$, $m \neq 0$ describe both standing and traveling tangential modes; all terms with $n = 0$ are transverse modes; other terms correspond to mixed modes.

Modes in other configurations will be discussed later as needed.

2.3. Acoustic Energy in a Sound Field

The total energy, internal plus kinetic, per unit mass at any position and time in a gas is $h - p/\rho + v^2/2$, since the internal energy is known to equal $h - p/\rho$. Multiplying this quantity by the density, we obtain for the energy per unit volume the expression :

$$\bar{\rho}\bar{h} + p' \frac{d(\rho h)}{dp} + \frac{1}{2} p'^2 \frac{d^2(\rho h)}{dp^2} = \bar{p} - p' + \frac{1}{2} \bar{\rho} v^2,$$

where terms through second order in small quantities, have been retained. The derivatives here are all taken at constant entropy (see Eq. 10-6) and are evaluated at the mean state; Eq. 10-4 with $ds = 0$ can be used to show that $d(\rho h)/dp = 1 + h/a^2$ and $d^2(\rho h)/dp^2 = 1/\rho a^2 + h d^2\rho/dp^2$. The terms $\bar{\rho}\bar{h} - \bar{p}$ obviously represent the energy of the uniform, quiescent, mean state and therefore should not be associated with the acoustic field. The total energy per unit volume contained in the acoustic field may therefore be written as :

$$p'\bar{h}/a^2 + \frac{1}{2} p'^2 \bar{h} \frac{d^2\rho}{dp^2} + \frac{1}{2} p'^2/\bar{\rho} a^2 + \frac{1}{2} \bar{\rho} v^2.$$

Since, to second order in small quantities :

$$\rho' = p' \frac{d\rho}{dp} + \frac{1}{2} p'^2 \frac{d^2\rho}{dp^2} = p' \frac{1}{a^2} + \frac{1}{2} p'^2 \frac{d^2\rho}{dp^2},$$

it is clear that the energy expression can be rewritten as :

$$\rho'\bar{h} + p'^2/2\bar{\rho}a^2 + \bar{\rho}v^2/2.$$

If this energy per unit volume is integrated over the volume of a cavity which contains a fixed mass, then the mass conservation condition $\int(\bar{\rho} + \rho') dV = \int\bar{\rho} dV$ implies that $\int\rho' dV = 0$ and so the integral of the first term in the energy expression vanishes. This first term, which merely accounts for the change in energy per unit volume due to the change in mass per unit volume, conventionally is not included in the energy density of the sound field. The local instantaneous energy per unit volume contained in an acoustic field is therefore defined as :

$$e \equiv p'^2/2\bar{\rho}a^2 + \bar{\rho}v^2/2. \quad (\text{Eq. 10-23})$$

It will be noted from Eq. 10-23 that e is a quantity of the second order. Expressions for p' and \underline{v} valid to first order may be substituted into Eq. 10-23 in order to calculate e .

A conservation equation for acoustic energy may be derived from Eqs. 10-1, 10-8, 10-10 and 10-23. According to Eq. 10-23, the time derivative of e can be written as :

$$\partial e / \partial t = p' (\partial p' / \partial t) / \bar{\rho} a^2 + \bar{\rho} \underline{v} \cdot \partial \underline{v} / \partial t ,$$

to second order in small quantities. Since Eq. 10-3 implies that $\partial p' / \partial t = a^2 (\partial \rho' / \partial t)$ in this expression, Eq. 10-1 may be substituted into the first term and Eq. 10-10 into the last term, yielding :

$$\partial e / \partial t = - p' \underline{\nabla} \cdot (\rho \underline{v}) / \bar{\rho} - \underline{v} \cdot \underline{\nabla} p' .$$

To second order in small quantities, this equation reduces to :

$$\partial e / \partial t + \underline{\nabla} \cdot (p' \underline{v}) = 0 . \quad (\text{Eq. 10-24})$$

It is seen from this expression that the vector $p' \underline{v}$ represents the local, instantaneous, acoustical energy flux.

Often, local time-average values of the acoustical energy and energy flux are of interest. In this respect, it is worth noting that for a sound field composed of a superposition of a number of monochromatic waves, the time-average energy and flux may each be expressed as a sum over all of the monochromatic waves. This conclusion follows from Eqs. 10-10 and 10-12 and the observation that the time average of $e^{i(\omega_1 - \omega_2)t}$ is essentially zero for $\omega_1 \neq \omega_2$. It might be remarked here that if a cavity can support more than one mode of the same frequency, then interference can occur between these degenerate modes and their modal contributions to the energy and flux may not be additive.

The average over the cavity volume of the energy per unit volume was denoted by \bar{e} in Chapter 9. Thus,

$$\bar{e} V = \int_V e dV , \quad (\text{Eq. 10-25})$$

which is the total acoustic energy contained in the cavity. Equation 10-24 implies that :

$$\frac{d}{dt} \int_V e dV = - \oint_A p' \underline{v} \cdot \underline{n} dA \quad (\text{Eq. 10-26})$$

where \underline{n} is an outward pointing normal to the surface of the cavity and the second integral is carried over the entire cavity boundary. The last term in Eq. 10-26 is the rate at which the boundaries of the cavity do work on the acoustic field. In the next section these results will be used to express the rate of change of acoustic energy of a cavity, in terms of the acoustic admittance of its boundaries.

3. Acoustic Amplification

3.1. The Acoustic Admittance

The ratio of the complex velocity amplitude to the complex pressure amplitude for a

monochromatic wave is a complex vector function of \underline{x} which we denote by \underline{Y} . Thus:

$$\underline{Y} = \underline{v}_0 / p_0,$$

where p_0 and \underline{v}_0 are defined in Eqs. 10-12 and 10-12a. The outward normal component of \underline{Y} at a boundary will be termed the acoustic admittance of the boundary and is given by:

$$Y = [(\underline{v}_0 \cdot \underline{n}) / p_0]_b, \quad (\text{Eq. 10-27})$$

where the subscript b identifies conditions at the boundary. (The reciprocal of this quantity is called the 'normal specific acoustic impedance' by acousticians; we do not employ the adjectives 'specific' or 'normal', nor do we exploit the well-known electrical and mechanical analogies). The quantity Y is useful for calculating monochromatic wave fields in acoustic cavities and transmission lines, whose homogeneous losses or gains are negligible compared with corresponding boundary effects. Its value depends on properties of the boundary and of the medium outside the boundary.

We note here that the acoustic energy, radiated through a boundary by a monochromatic wave in a cavity, can be expressed in terms of the pressure amplitude at the boundary and the admittance Y . Thus, Eqs. 10-12, 10-12a and 10-27 imply that :

$$\begin{aligned} \int_A \underline{p}' \cdot \underline{v} \cdot \underline{n} \, d\mathcal{A} &= \int_A \text{Re} \{ p_0 e^{i\omega t} \} \text{Re} \{ \underline{v}_0 \cdot \underline{n} e^{i\omega t} \} \, d\mathcal{A} \\ &= \int_A \text{Re} \{ p_0 e^{i\omega t} \} \text{Re} \{ Y p_0 e^{i\omega t} \} \, d\mathcal{A} \\ &= \int_A |p_0|^2 [\text{Re} \{ Y \} \cos^2(\omega t + \delta) - \text{Im} \{ Y \} \frac{1}{2} \sin(2\omega t + 2\delta)] \, d\mathcal{A}, \end{aligned}$$

where the complex quantity p_0 has been written as $p_0 = |p_0| e^{i\delta}$. If this energy flow rate is averaged over one oscillation period, then it is found that :

$$\int_A \langle \underline{p}' \cdot \underline{v} \rangle \cdot \underline{n} \, d\mathcal{A} = \frac{1}{2} \int_A |p_0|^2 \text{Re} \{ Y \} \, d\mathcal{A}, \quad (\text{Eq. 10-28})$$

where the angular brackets represent a time average over an oscillation period.

3.2. Relationship Between Admittance and Energy Growth Rate for Monochromatic Waves in Cavities

Let us consider a monochromatic wave field, in a cavity with negligibly small homogeneous and boundary losses or gains. The acoustic energy in such a cavity will be seen to be independent of time. First, we shall relate the energy to the pressure amplitude for such a wave field. Then we shall consider a small boundary loss as a perturbation to this field and compute the consequent time rate of change of acoustic energy. Homogeneous losses or gains are not permitted here.

Since the product of Eq. 10-13 with p_0 can be written as :

$$\underline{\nabla} \cdot (p_0 \underline{\nabla} p_0) - \underline{\nabla} p_0 \cdot \underline{\nabla} p_0 + p_0^2 \omega^2 / a^2 = 0,$$

it follows that :

$$\int_V (\nabla p_0 \cdot \nabla p_0) dV = \int_V p_0^2 dV \omega^2 / a^2, \quad (\text{Eq. 10-29})$$

provided that either $p_0 = 0$ or $\nabla p_0 \cdot \mathbf{n} = 0$ on the boundary of the volume V . The second of these boundary conditions is equivalent to $\mathcal{L}_0 \cdot \mathbf{n} = 0$ because $\mathcal{L}_0 = \nabla p_0$ (see Eq. 10-12a). It is seen from the definition of acoustic energy flux that this flux vanishes at the boundaries of V , only if one or the other of these two boundary conditions is satisfied; i. e., these are the boundary conditions for zero surface work and they correspond to either $Y = \infty$ or $Y = 0$ (see Eq. 10-27). The lossless cavities that concern us have rigid-wall boundaries and therefore obey Eq. 10-29 because $\nabla p_0 = 0$ ($Y = 0$) at the boundary of V . It is easy to show from Eqs. 10-12, 10-12a, 10-23, 10-25 and 10-29 that for a monochromatic wave field in such cavities :

$$\bar{e} = \int_V |p_0|^2 dV / 2\bar{\rho} a^2 V. \quad (\text{Eq. 10-30})$$

The demonstration of Eq. 10-30 entails a little manipulation with complex numbers. In view of our rigid-wall boundary conditions, Eq. 10-26 implies that $d\bar{e}/dt = 0$ here, as is in fact implied by Eq. 10-30 and the early assumption that p_0 is independent of t .

Next, we permit the value of Y at the boundary to differ from zero but still require that its magnitude be small compared with the characteristic admittance (reciprocal of characteristic impedance) of the internal gaseous medium, $a/\bar{\rho}$. In general, for monochromatic waves in cavities, Eqs. 10-25, 10-26 and 10-28 show that the value of \bar{e} , averaged over one oscillation cycle, changes with time according to :

$$\langle d\bar{e}/dt \rangle = - \oint_A |p_0|^2 \operatorname{Re} \{ Y \} d\mathcal{A} / 2V. \quad (\text{Eq. 10-31})$$

Under the present assumption of small losses and gains, Eq. 10-30 may be used as an approximation to \bar{e} in Eq. 10-31 and the resulting equation implies that the pressure amplitude $|p_0|$ will change with time. Since the geometry of the cavity remains fixed, the solution to Eq. 10-13 can change with time through a time-dependent multiplicative constant that is independent of position in the chamber. Hence, we may replace p_0 approximately by $p_0 f(t)$ with $f(0) = 1$ in Eqs. 10-12, 10-12a, 10-30 and 10-31. We then deduce from Eqs. 10-30 and 10-31 that $d|f|^2/dt = 2\alpha|f|^2$, where :

$$\alpha \equiv - \oint_A [|p_0|^2 / \bar{e}_0] \operatorname{Re} \{ Y \} d\mathcal{A} / 4V. \quad (\text{Eq. 10-32})$$

in which \bar{e}_0 is the value of \bar{e} at $t = 0$. The solution to the equation for $|f|^2$ is $|f|^2 = e^{2\alpha t}$, which implies that :

$$\bar{e} = \bar{e}_0 e^{2\alpha t} \quad (\text{Eq. 10-33})$$

and leads to replacement of $|p_0|$ by $|p_0|e^{\alpha t}$. The quantity \bar{e} appearing in Eq. 10-33 must be considered to be averaged over an oscillation period because when $\alpha \neq 0$ there exist periodic variations in \bar{e} during an oscillation cycle that are washed out by the average in Eq. 10-31.

Clearly, this heuristic derivation can be meaningful, only if $|\alpha| \ll |\omega|$ because the time derivative in Eq. 10-31 is an average over one cycle; the changes brought

about by gains and losses at the boundaries must represent small fractional changes in energy or amplitude during one oscillation cycle. That this condition is approximately equivalent to the originally stated condition that $|Y| \ll a/\bar{p}$, is apparent from Eqs. 10-30 and 10-32 and the order-of-magnitude relationship $\omega \approx aA/V$, since Eqs. 10-30 and 10-32 imply $\alpha \approx \bar{p} a^2 \operatorname{Re} \{Y\} A/V \approx [|Y|/(a/\bar{p})] aA/V$. If $|Y|$ were as large as a/\bar{p} , then the boundary would be properly matched with the cavity and all of the acoustic energy could be transmitted through the boundary in a time of the order of an oscillation period.

3.3. Alternatives and Generalizations

The results obtained in Section 3.2 were quoted previously in Chapter 9. The arguments can be made much more precise by treating specific geometries. When the geometry and the boundary values of Y are specified, exact formulas can be derived for the growth constant α and also for the frequency ω (which differs slightly from the usual formulas such as Eq. 10-22, if $\alpha \neq 0$ but $|\alpha| \ll |\omega|$). We shall not quote any of these exact results because they differ for cavities of different shapes.

Since energy densities, averaged over a cycle, are additive for monochromatic waves of different frequencies, the reasoning of Section 3.2 may be carried out independently for the oscillations in each natural frequency of a cavity.

The results of all theoretical studies of amplification of linear acoustic waves in solid propellant rockets that have been reported are expressible basically in terms of acoustic admittances of burning surfaces; homogeneous amplification mechanisms have not been investigated. Therefore, the theories of amplification that we shall review in this chapter are theories of the surface acoustic admittance. Before continuing with our discussion of amplification, we shall review existing theories of acoustic damping. Both homogeneous and boundary damping mechanisms have been considered.

4. Acoustic Damping Mechanisms

4.1. Introduction

We plunge immediately into details of analyses of specific damping mechanisms, considering boundary damping first and then homogeneous damping. A summary of the relative importance of the various mechanisms and of the depth of our theoretical understanding of the mechanisms is given at the end of Section 4.

4.2. Nozzle Damping

4.2.1. End-Vented Chambers - Literature - The first analysis of the acoustic admittance of a choked nozzle was given by Tsien (1), who considered quasi-one-dimensional nozzle flow subjected to isothermal longitudinal oscillations in the flow variables at the entrance plane. He obtained results for oscillations of very low frequencies and very high frequencies. His analysis was extended by Crocco (2), (3) to include arbitrary longitudinal oscillations at the entrance plane and for the most important case of isentropic entrance-plane conditions, to include also arbitrary frequencies. Crocco's results are applicable directly to longitudinal modes in a cylindrical chamber, with a choked nozzle at one end. Some results for transverse and mixed modes in this same geometry have been obtained more recently (4). The currently available results are summarized in Ref. (3). We review here the essentials of the work in Ref. (5).

Formulation - The objective of the analysis is to obtain a relationship between p_0 and v_0 at the entrance plane of the nozzle for monochromatic waves. In order to accomplish this, the quasi-one-dimensional, time-dependent conservation equations are written for a nonreacting, calorically perfect, ideal gas that is presumed to

flow through the nozzle with negligible transport fluxes and negligible body forces. Each dependent flow variable is written as the sum of a mean quantity, that is a function only of the axial coordinate x and a fluctuating quantity that is a function of both x and t . Thus, the formulas given in Eq. 10-7 are employed for ρ and p and the x component of the velocity v_x is expressed in a similar manner :

$$v = \bar{v} + v'$$

All fluctuating quantities including v' , are assumed to be small compared with the corresponding mean quantities, so that the governing conservation equations, Eqs. 6-7, 6-8 and 6-9 of Chapter 6, can be expanded to first order in these small quantities. Reasoning analogous to that leading to Eq. 10-6 shows that if the oscillations are isentropic at the entrance to the nozzle, then they remain isentropic throughout the nozzle and p' and ρ' are related according to Eq. 10-8, where 'a' is now the local speed of sound, which depends on x . Although entropy oscillations are permitted (3), we consider here only the isentropic case. The resulting conservation equations (generalizations of Eqs. 10-1 and 10-2) can then be expressed in the form :

$$\partial (\rho'/\bar{\rho})/\partial t + \bar{v} \partial (\rho'/\bar{\rho} + v'/\bar{v})/\partial x = 0 \quad (\text{Eq. 10-34})$$

and :

$$\partial (v'/\bar{v})/\partial t + \bar{v} \partial (v'/\bar{v})/\partial x = [-2v'/\bar{v} + (\gamma - 1)\rho'/\bar{\rho}]d\bar{v}/dx - (a^2/\bar{v})\partial (\rho'/\bar{\rho})/\partial x, \quad (\text{Eq. 10-35})$$

where γ is the constant ratio of specific heats. Monochromatic waves are considered next, i.e., Eqs. 10-12 and 10-12a are introduced, so that the set of ordinary differential equations :

$$\left. \begin{aligned} \bar{v} d\nu/dx + \bar{v} d\sigma/dx + i\omega \sigma &= 0 \\ \bar{v} d\nu/dx + (a^2/\bar{v}) d\sigma/dx + (2d\bar{v}/dx + i\omega) \nu - (\gamma - 1)(d\bar{v}/dx) \sigma &= 0 \end{aligned} \right\} \quad (\text{Eq. 10-36})$$

is obtained. Here :

$$\nu \equiv v_0/\bar{v}, \quad \sigma \equiv \rho_0/\bar{\rho} \quad \rho_0/\gamma \bar{p},$$

and the admittance that we wish to obtain is :

$$Y = (\bar{v}/\gamma \bar{p})_{\ell} (\nu/\sigma)_{\ell}, \quad (\text{Eq. 10-37})$$

in which the subscript ℓ identifies conditions at the entrance plane of the nozzle. In Eq. 10-36, \bar{v} and a^2 are functions of x , that are presumed known from the steady-state solution for quasi-one-dimensional flow through the nozzle, ω and γ are presumed known constants and ν and σ are the unknown dependent variables.

Equation 10-36 is a second-order system and therefore would be expected to require two boundary conditions for determining a solution. The quantity σ_{ℓ} may be thought of as being specified. The second boundary condition is the restriction that no waves can be transmitted upstream from the supersonic divergent section of the nozzle. It is easy to see that the throat ($\bar{v} = a$) is a singularity of Eq. 10-36 and it turns out that an alternative form of the second boundary condition is the restriction that the solution to Eq. 10-36 remain regular at the throat. Thus, one need only find the solution to Eq. 10-36 that is regular at the throat, adjust the arbitrary multiplicative constant appearing therein so that σ_{ℓ} takes on a prescribed value, then calculate the resulting ν_{ℓ} and finally compute Y from Eq. 10-37. This procedure can be carried out for any nozzle shape; the solution to Eq. 10-36 would be found by first expanding Eq. 10-36 about the nozzle throat in order to obtain the first few terms in the series expansion of the regular solution and then continuing the solution

upstream by numerical integration. If one is interested only in frequencies ω that are either very small or very large, then one can alternatively expand Eq. 10-36 in powers of either $i\omega$ or $1/i\omega$ and thereby extract analytical solutions for nozzles of arbitrary shape. For nozzle shapes that cause \bar{v} to increase linearly with x , Crocco succeeded in obtaining accurate solutions for all values of ω , without resorting to numerical integration.

Solution for Linear Velocity Profiles - If \bar{v} is a linear function of x , one can write:

$$d\bar{v}/dx = \bar{v}/x = a_t/x_t = (a_t - \bar{v}_\ell)/(x_t - x_\ell) \quad , \quad (\text{Eq. 10-38})$$

where the subscript t identifies conditions at the throat and the origin of the x coordinate has been selected for convenience in simplifying the representation of the solution. In terms of the dimensionless dependent variable :

$$z \equiv (x/x_t)^2 = (\bar{v}/a_t)^2 \quad ,$$

which can be shown to be related to the local Mach number M according to :

$$z = (\gamma + 1) M^2 / [2 + (\gamma - 1)M^2] \quad ,$$

it can then be shown that Eq. 10-36 implies that ν is given in terms of σ by means of the formula :

$$\nu = [(\gamma - 1 + i\beta) \sigma - (\gamma + 1)(1 - z) d\sigma/dz] / (2 + i\beta) \quad (\text{Eq. 10-39})$$

and that σ is the solution to the equation :

$$z(1-z)d^2\sigma/dz^2 - [2 + 2i\beta/(\gamma + 1)] z d\sigma/dz - [i\beta(2 + i\beta)/2(\gamma + 1)] \sigma = 0, \quad (\text{Eq. 10-40})$$

where a dimensionless frequency has been defined as :

$$\beta \equiv \omega x_t/a_t = \omega(x_t - x_\ell)/(a_t - \bar{v}_\ell) \quad ,$$

which is seen to involve, as the characteristic frequency, the ratio of the sound speed at the throat (provided that the Mach number at the entrance to the nozzle is sufficiently small) to the length of the subsonic portion of the nozzle. Equation 10-40 is the well-known hypergeometric equation. The solution that remains regular at the throat ($z = 1$) is :

$$\sigma = CF(a, b, c; 1-z) \quad , \quad (\text{Eq. 10-41})$$

where C is an arbitrary (complex) constant, F is the hypergeometric function and the parameters a , b and c are related to γ and β according to :

$$c = 1 + a + b = 2 + 2i\beta/(\gamma + 1); \quad ab = i\beta(2 + i\beta)/2(\gamma + 1) \quad .$$

Equations 10-37, 10-39 and 10-41 yield Y directly.

The asymptotic expansion of F as z approaches zero, is useful in obtaining numerical values of Y for the chamber Mach numbers M_ℓ of greatest practical interest (3). Explicit expansion formulas for large and small values of β are also given in Ref. (3). The results of the calculations are conveniently shown as graphs of the real and imaginary parts of $Y(\gamma\bar{p}/\bar{v})_\ell = (\nu/\sigma)_\ell$ as functions of the dimensionless frequency β , for various values of γ and of the mean Mach number M_ℓ at the entrance to the nozzle. Such curves for $\gamma = 1.2$ are shown in Figs. 10-1 and 10-2. It will be noted that the real and imaginary parts of Y are both always non-negative and are typically of the order of magnitude of $(\bar{v}/\bar{p})_\ell$. We might also remark that $\text{Re}\{(\nu/\sigma)_\ell\}$

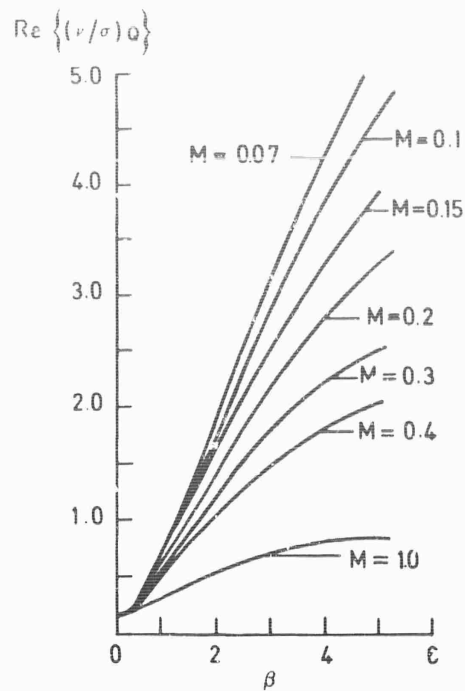


Fig. 10-1 Real part of the dimensionless nozzle admittance $(\gamma \bar{p}/\bar{v})_0 Y$ as a function of the dimensionless frequency $\omega(x_t - x_\ell)/(a_t - v_\ell)$, for various values of the nozzle entrance Mach number M_ℓ , with isentropic oscillations and with $\gamma = 1.2, (3)$.

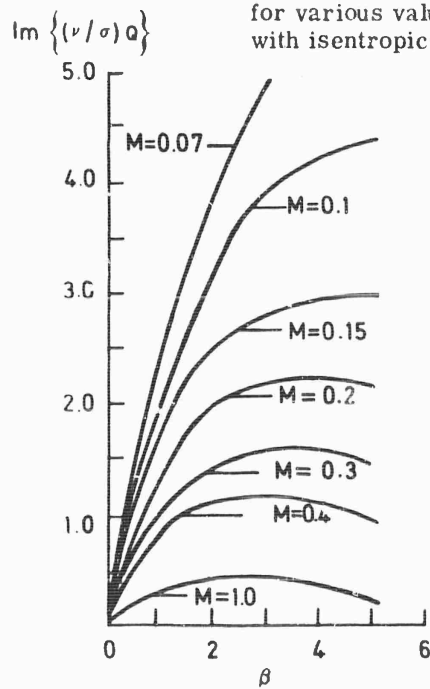


Fig. 10-2 Imaginary part of the dimensionless nozzle admittance $(\gamma \bar{p}/\bar{v})_0 Y$ as a function of the dimensionless frequency $\omega(x_t - x_\ell)/(a_t - v_\ell)$, for various values of the nozzle entrance Mach number M_ℓ , with isentropic oscillations and with $\gamma = 1.2, (3)$.

approaches $(\gamma-1)/2$ and $\text{Im} \{(\nu/\sigma)\ell\}$ approaches zero linearly as β approaches zero, while $\text{Re} \{(\nu/\sigma)\ell\}$ approaches $1/M\ell$ and $\text{Im} \{(\nu/\sigma)\ell\}$ approaches zero like $1/\beta$ as β approaches infinity.

Discussion of Results - Since these quasi-one-dimensional results imply that sonic end nozzles produce contributions to Y that are roughly of the order of $(\bar{v}/\bar{p})\ell$, it follows that the effect of the nozzle on longitudinal chamber oscillations can be accounted for by means of the perturbation approach of Section 3 as long as the gas Mach number, at the entrance to the nozzle, is small compared with unity. If this condition is not satisfied, then the nozzle produces a sizeable effect on the waveform. When this condition is satisfied, then the nozzle losses turn out to be roughly of the same order of magnitude as the amplification due to the combustion zone and therefore nozzle losses are always important. What the admittance term gives is the radiative contribution to the nozzle loss; there is also a convective loss which is of the same order of magnitude but can be calculated much more simply (5). It should be apparent from Eq. 10-26, for example, that if a mean outward normal component \bar{v} of velocity exists at a boundary b , then the acoustic energy $(e\bar{v})$ is convected out of the system at the boundary, per unit area per second.

Non-One-Dimensional Oscillations - The results of Ref. (3) were extended (4) to include non-one-dimensional oscillations in quasi-one-dimensional nozzle flow. The basis of the extended analysis closely resembles that of Ref. (3); for example, the assumption of a linear mean velocity profile is retained. The new aspects arising here are that partial differential equations are obtained in place of Eq. 10-36 and that separation-of-variables techniques must be employed in a suitable coordinate system, in order to obtain solutions. The results are expressed in curves similar to Figs. 10-1 and 10-2, but an additional parameter arises which characterizes the departure of the mode from one-dimensionality and is essentially equivalent to the quantity β_{mk} of Eq. 10-21. The intriguing aspect of the new results is that for certain combinations of values of β and the new parameter β_{mk} , the value of $\text{Re}\{Y\}$ is found to be negative, corresponding to amplification of oscillations by the sonic nozzle, i.e. conversion of mean-flow energy into acoustic energy. Closer scrutiny of the results reveal that at any given value of β_{mk} , significant amplification is predicted only for dimensionless frequencies β which correspond to values of ω below that given by Eq. 10-22; i.e., appreciable negative radiative damping by the nozzle is not realized for any of the natural modes of the cylindrical chamber cavity. For purely transverse modes, the radiative nozzle damping is found to be very small, while for mixed longitudinal-transverse modes, the damping is of the same order of magnitude as for longitudinal modes [$|Y| \sim (\bar{v}/\bar{p})\ell$]. However, the convective term is of the same order of magnitude for transverse, longitudinal and mixed modes.

Comparison of Theory and Experiment - Experimental tests of the admittance results described here for longitudinal modes have been reported (6), (7). The admittance at the entrance plane to a choked nozzle was measured as a function of the dimensionless frequency β by means of a pressure transducer and a hot wire anemometer (6). Agreement between theory and experiment was good, within experimental error, for $\text{Im}\{Y\}$ (6). Good agreement for the frequency dependence of $\text{Re}\{Y\}$ was also obtained after empirical corrections for the existence of nonisentropic conditions were introduced; without these corrections, which served the purpose of bringing experiment into agreement with theory, measured values of $\text{Re}\{Y\}$ were larger than theoretical values by as much as a factor of 2 at low frequencies and low mean pressures (3). Recent measurements of the "Q" of a chamber and also of the decay rate of oscillations in the chamber, were interpreted as providing values of $\text{Re}\{Y\}$ in the limit $\beta \rightarrow 0$ (very short nozzles) on the grounds that all other losses were believed to be negligible (7). The initial results (7) implied values of $\text{Re}\{Y\}$ that were as much as an order of magnitude above the theoretical value but more recent unpublished results appear to exceed the theoretical value by

no more than a factor of 2. It is not yet clear how accurate the experiments (7) are; furthermore, other loss mechanisms such as viscous wall losses may be of some importance or the abrupt nozzle geometry may induce mean flow separation well upstream from the actual nozzle entrance, so that the effective value of β is appreciably greater than zero and the proper theoretical value of $\text{Re}\{Y\}$ is larger than presumed (see Fig. 10-1). At any rate, close experimental verification of the theoretical value of $\text{Re}\{Y\}$ for sonic end nozzles subjected to longitudinal modes is lacking today. This maybe an example in which the theory is more accurate than the existing experiments.

4.2.2. Side-Vented Chambers - Sonic Nozzles - For side-vented chambers with sonic nozzles, the convective energy flux can be evaluated relatively simply but the only theory available for the acoustic admittance is the one discussed in Section 4.2.1 'Non-One-Dimensional Oscillations', which is based on a quasi-one-dimensional mean flow approximation. The quasi-one-dimensional approximation is poor for typical side nozzles and therefore an acceptable procedure for calculating Y in these cases does not exist yet. The losses are expected to be very small for small sonic side nozzles located at pressure nodes (5). The theoretical problem posed here is difficult but probably not insurmountable.

Literature on Subsonic Orifices - Many theoretical papers are available on the acoustic losses of subsonic orifices located in the sides of cylindrical chambers. The earliest studies and some of the later ones neglected mean flow effects entirely (8), (9), most later theories (5), (10-12) accounted for low-Mach-number flowthrough the orifice. Consideration of mean flow appears to provide only a relatively easily estimable convective loss; the admittance characterizing the radiative loss is not affected appreciably by mean flow of sufficiently low Mach number. Small centrally located vents experiencing pressure antinode conditions, e.g., even longitudinal chamber modes, and pressure node conditions, e.g. odd longitudinal chamber modes, have been analyzed (10), (11). Small vents located at arbitrary axial positions along a cylindrical chamber have also been studied (9). This last study permitted arbitrary orifice length and orifice cross-sectional geometry, subject only to the condition that the orifice shape be symmetrical about a plane transverse to the axis of the cylinder. The principal conclusion of the study was that the piston-like radiation mode, encountered when the orifice is located at a pressure antinode, will be the dominant term in the orifice admittance under practically all conditions. For example, if the center of a short circular vent of radius r is located at an axial distance x from the midpoint of a cylindrical chamber, which experiences an odd longitudinal mode of wave length λ , then the piston-like contribution to the admittance exceeds the antisymmetric contribution, which is the only contribution that is present for $x = 0$, whenever $x/r \geq 1.2r/\lambda$. Values of r and λ commonly encountered in T-burners are such that according to this criterion, errors considerably less than a millimeter in centering the orifice at the midpoint, can cause the piston-like contribution to become dominant. Since the piston-like contribution depends appreciably on x (increasing linearly with $|x|$), a corollary of this observation is that variations which generally occur in internal chamber dimensions during burning, will cause the orifice loss of a T-burner operating in the usual first longitudinal mode to vary appreciably during an experimental run. Experimental evidence for the occurrence of such variations was cited in Chapter 9 Section 4.6.4.

The rate of dissipation of acoustic energy by a short subsonic side vent of cross-sectional area A , is roughly of the order of :

$$(\bar{p}a) \left| \frac{p_0}{\bar{p}} \right|^2 A(A/\lambda)^2, \quad \text{etc.}$$

where $n = 1$ for the piston-like contribution to dissipation and $n = 3$ for the antisymmetric contribution. In this formula, the pressure amplitude p_0 is to be evaluated at the center of the orifice for $n = 1$; it is the peak pressure amplitude in

the chamber for the antisymmetric case. The dissipation rate due to the piston-like effect is often significant; the other is not.

4.3. Other Boundary Damping Processes

4.3.1. Wall Friction - Introduction

As an elementary example of a classical boundary damping mechanism, we calculate here the energy dissipation caused by the no-slip boundary condition that must be imposed at the solid wall of a cavity. Our analysis will be highly simplified and designed only to convey physical ideas. More accurate results will be summarized later in Section 4.3.1, 'Accurate Formulas for Dissipation due to Wall Friction'. Effects of related boundary damping processes (e.g., wall heat transfer) will also be discussed later in Section 4.3.2.

Associated with acoustical waves are nonvanishing velocity components parallel to the walls at surfaces of the cavity. These acoustical velocities produce oscillatory viscous boundary layers adjacent to the walls. The study of oscillatory boundary layers dates back more than a century and a half (13), (14); a relatively recent review may be found (15). It is well known that energy dissipation occurs within these boundary layers.

Formulation - Let us examine a flat element of the surface of the cavity, at which the complex amplitude of the component of velocity parallel to the surface is v_{0b} . For the sake of simplicity, we shall assume that the mean gas velocity relative to the wall is zero and that the local acoustical density oscillations are negligibly small. We also neglect the dependence of the acoustical amplitudes on the spacial coordinates parallel to the wall. The system under study is therefore a plane wall subjected to incompressible harmonic velocity oscillations of the fluid adjacent to it, the oscillations being spacially uniform in planes parallel to the wall. We wish to solve for the dependence of the velocity on the coordinate normal to the wall and to calculate the rate of viscous dissipation per unit surface area.

The governing conservation equations of fluid dynamics are easily written down for this problem. It is simplest to write these equations in the noninertial coordinate system in which the acoustical velocity is zero and the wall oscillates with a complex velocity amplitude v_{0b} . In this coordinate system, a noninertial term in the momentum conservation equation cancels the pressure gradient term and the momentum equation (a combination of Eqs. 6-8 and 6-11 of Chapter 6) reduces to :

$$\rho \partial v / \partial t = \partial (\mu \partial v / \partial y) / \partial y, \quad (\text{Eq. 10-42})$$

where ρ and μ are the constant, mean, fluid density and coefficient of viscosity, v is the component of fluid velocity in the direction of oscillation of the wall and y is the coordinate normal to the surface. The other conservation equations are satisfied automatically by the character assumed for the flow field. Letting the wall be located at $y = 0$, we find that the boundary conditions for Eq. 10-42 become :

$$v = v_{0b} e^{i\omega t} \text{ at } y = 0 \quad \text{and} \quad v \rightarrow 0 \text{ as } y \rightarrow \infty.$$

Solution and Result - The solution to Eq. 10-42 subject to the imposed boundary conditions is straightforward. With $v_0(y)$ defined by :

$$v = v_0 e^{i\omega t},$$

Eq. 10-42 implies that :

$$d^2 v_0 / dy^2 = (i \omega \rho / \mu) v_0 \quad ; \quad v_0 = v_{0b} \text{ at } y = 0, \quad v_0 = 0 \text{ at } y = \infty,$$

and therefore :

$$v_0 = v_{0b} e^{-(1+i)y \sqrt{\omega \rho / 2\mu}}.$$

This formula shows that the oscillatory viscous boundary layer extends a distance of the order of $\sqrt{2\mu/\rho\omega}$ from the wall into the gas; for typical chamber conditions this distance, which depends on oscillation frequency but not on amplitude, is of the order of 10^{-2} cm.

The time-average rate of dissipation, energy per unit volume per second, is easily shown to be (8);

$$\frac{1}{2} \mu (dv_0/dy) (dv_0/dy)^*$$

where the star identifies the complex conjugate and therefore the rate of energy dissipation per unit surface area per second is :

$$\int_0^\infty \frac{1}{2} \mu (dv_0/dy) (dv_0/dy)^* dy = \frac{1}{2} |v_{0b}|^2 \sqrt{\mu \omega \rho / 2}. \quad (\text{Eq. 10-43})$$

This dissipative energy flux is roughly of the order of :

$$a^2 \sqrt{\mu \omega \rho} |p_0/\bar{p}|^2,$$

increases in proportion to the square root of the mean chamber pressure at constant mean temperature and constant velocity amplitude and turns out to have a numerical value that is perhaps $\sim 10\%$ of the acoustical energy flux, that is generated by representative surface combustion processes. Thus, wall friction may well constitute an important dissipation mechanism. Its relative importance, of course, depends strongly on chamber geometry and on what modes are excited; there are geometries in which it is negligible and others in which it is dominant.

Accurate Formulas for Dissipation Due to Wall Friction - In view of the approximations involved in its derivation, Eq. 10-43 is surprisingly close to an accurate formula for the viscous dissipation rate at a solid wall. A variational technique has been employed to account for effects of mean flow at low Mach number and of mean temperature gradients on damping, by wall friction (16). The result is that the dissipation rate given in Eq. 10-43 is replaced by the quantity :

$$\frac{1}{2} |v_{0b}|^2 (T_w/T_c)^2 \sqrt{\mu_w \omega \rho_w / 2},$$

where T is the time-average temperature, the subscript w implies that the quantity is to be evaluated at the wall and the subscript c implies that the quantity is to be evaluated in the chamber, outside the boundary layer. Since the walls are usually cooler than the gases in rocket combustion chambers, this formula implies that use of Eq. 10-43 will lead to an overestimate of the wall friction losses. In T-motor operation, T_w usually increases during an experimental run; wall friction can therefore provide an additional cause of time-dependent losses in these research devices.

Two different physical phenomena influence the modified dissipation formula quoted here. First, if a mean temperature boundary layer exists, then the wall temperature differs from the temperature in the bulk of the gas and therefore the mean properties μ and ρ which are functions of temperature, vary through the mean temperature boundary layer. In Eq. 10-43, one has the problem of deciding at what temperature to evaluate μ and ρ . In view of the derivation of Eq. 10-43, these quantities should obviously be evaluated in the oscillatory boundary layer. At virtually all frequencies and geometries of interest for gas-filled chambers, the oscillatory boundary layer is much thinner than any mean temperature boundary layer and is buried deep within it, next to the surface. Therefore, the properties μ and ρ that are 'seen' by the oscillatory boundary layer are the wall properties, μ_w and ρ_w . This explains the physical reason for the subscripts w on the quantities under the radical sign in the formula.

Secondly, if there is a mean temperature boundary layer then the amplitude of the velocity oscillation varies through this boundary layer. The reason for this is that the pressure, both mean and oscillatory amplitude, remains constant across any boundary layer (15), and therefore, if the temperature varies then the density varies inversely with T. Such a density variation produces a variation in the velocity amplitude that is inversely proportional to ρ and therefore directly proportional to T (see Eq. 10-12a, for example). Since the oscillatory boundary layer is so thin, the velocity amplitude 'at infinity' for this boundary layer is the velocity amplitude at the wall surface of the mean temperature boundary layer. Since the amplitude v corresponds to mean temperature T_c and is calculated without regard for the presence of a mean temperature boundary layer, it then follows that v_{ob} must be corrected by the factor (T_w/T_c) , in order to obtain the effective external velocity amplitude for the dissipation-producing oscillatory boundary layer. The factor $(T_w/T_c)^2$ in the formula quoted arises in this manner.

In addition to allowing for a mean temperature boundary layer, the analysis (16) also permits a mean velocity boundary layer. It is interesting to note that such a boundary layer was found to produce a negligible direct effect on the dissipation formula obtained here. The first correction term is of the order of the square of the mean external Mach number. For many modes in typical chambers, the square root of the mean external Mach number is roughly of the same order as the ratio of the oscillatory to mean velocity boundary layer thicknesses.

The results obtained (16) have been used in Ref. (5) to calculate the contribution to the pressure decay exponent - α (Eq. 9-1 of Chapter 9) produced by friction on the side walls of a rigid-walled cylindrical chamber, experiencing an arbitrary standing-wave acoustic oscillation mode. In the notation of Eq. 10-21, the result given (5) is :

$$-\alpha = \frac{T_w}{T_c} \left(\frac{n\pi\mu_w a}{2\rho_w \ell R^2} \right)^{\frac{1}{2}} \frac{[1 + (m\ell/n\pi R)^2]}{[1 - (m/\beta_{mk})^2][1 + \beta_{mk} \ell/n\pi R]^2}^{3/4}. \quad (\text{Eq. 10-44})$$

As expected from Eq. 10-43, α is seen to be inversely proportional to the square root of chamber pressure at constant chamber temperature. We might remark here that formulas analogous to Eq. 10-44, for practically all contributions to gains and losses that have been subjected to theoretical analyses, are given (5) for standing modes in cylindrical chambers with rigid walls.

4.3.2. Wall Heat Transfer - The phenomenon analyzed in Section 4.3.1 arose from acoustic velocity oscillations in the vicinity of a wall and the corresponding dissipation vanishes when $v_{ob} = 0$. Temperature oscillations in the vicinity of a wall also dissipate the acoustical energy in the cavity; such heat transfer effects

vanish only when $p_{0b} = 0$.

The approach to a theoretical analysis of the heat transfer effect closely resembles the approach of Section 4.3.1. So long as the temperature of the solid wall does not exactly follow the acoustical temperature oscillations of the gas in the cavity at the wall, an oscillatory temperature boundary layer is established adjacent to the wall. As in the previous section, this temperature boundary layer is generally thin compared with any mean temperature boundary layer which may be present, due to a difference between the mean gas and wall temperatures. Under the assumption of an isothermal wall, a simple analysis analogous to Section 4.3.1, 'Solution and Results', yields as the rate of acoustical energy dissipation per unit surface area per second :

$$\left[(\gamma - 1)/2\gamma \right] \bar{p} \left| p_{0b}/\bar{p} \right|^2 (\omega \lambda / 2\bar{\rho} c_p)^{\frac{1}{2}},$$

where γ is the ratio of specific heats, c_p is the time-average specific heat at constant pressure for the gas, λ is the time-average thermal conductivity of the gas and p_{0b} is the pressure amplitude evaluated at the surface in question. Consideration of the presence of any mean temperature or velocity boundary layers merely directs one to evaluate λ , ρ and c_p in this formula, at the wall temperature attained in the mean boundary layers. The first correction term to this formula is roughly of the order of the square root of the external mean flow Mach number, as opposed to the square in the previous section and arises as a result of the gradient of the mean temperature in the gas at the surface of the wall (16).

The formula for thermal losses that corresponds to Eq. 10-44 is (5) :

$$-\alpha = (\gamma - 1)(n\pi \lambda_w a / 2\rho_w c_{pw} \ell R^2)^{\frac{1}{2}} \left[1 + (\beta_{mk} \ell / n\pi R)^2 \right]^{\frac{1}{4}} / \left[1 - (m/\beta_{mk})^2 \right] \quad (\text{Eq. 10-45})$$

The contribution to α given by Eq. 10-45 is usually small compared with that given by Eq. 10-44.

4.3.3. Complex Wall Loss Phenomena - Many other wall loss mechanisms might be discussed. For example, solid walls are never perfectly rigid and mechanical elastic responses may be of importance, particularly at sharp orifices or in regions of high acoustic amplitudes. For high acoustic velocities, acoustic streaming may begin and transition to a turbulent kind of acoustic boundary layer may occur. At high mean flow velocities, conversion of mean flow kinetic energy to acoustical energy may occur in boundary layers of proper geometries, with a resulting tendency toward amplification of the acoustic wave field. Appreciable modification of wall damping may occur, usually leading to increased dissipation, if solid or liquid materials condense on the wall; such effects would be very difficult to calculate. None of these additional phenomena have received accurate theoretical study.

4.4. Homogeneous Damping

4.4.1. Viscous and Heat Conduction Losses - Since the acoustic amplitudes are functions of position in the cavity, gradients in velocity and temperature are produced by the acoustic oscillations and in turn, cause viscous stress and molecular heat conduction processes to occur. These processes, which occur throughout the volume of the gas not preferentially at boundaries, dissipate acoustical energy. Subject to reasonable approximations, the equations describing sound propagation with viscous and heat conduction effects included, are linear and are therefore amenable to rather accurate analytical treatment. Many such theoretical analyses appear in the literature. However, for our purposes these results are unimportant. For conditions of interest in rocket combustion instability, these homogeneous losses are so small that they can always be calculated as small perturbations on the

inviscid acoustic field and indeed they are usually entirely negligible (4), (5). We now substantiate this claim by comparing the order of magnitude of these losses with the order of magnitude of the wall friction losses.

The acoustical energy per unit volume per second dissipated homogeneously by viscous phenomena, is of the order of :

$$\mu \sum_{i,j} (\partial v_i / \partial x_j)^2 \sim \mu |v_0|^2 / \lambda^2,$$

where $\lambda = a/\omega$ is the wave length of the acoustic wave. The total acoustical energy per second dissipated in the chamber is therefore approximately :

$$\mu |v_0|^2 (\omega^2 / a^2) V,$$

where V is the volume of the chamber. We have seen in Section 4.3.1, 'Solutions and Results', (Eq. 10-43), that the acoustical energy dissipated at the wall, per unit surface area per second, is of the order of $|v_0|^2 \sqrt{\mu \omega \rho}$. Therefore, the total acoustical energy per second dissipated at walls of the cavity is roughly :

$$|v_0|^2 \sqrt{\mu \omega \rho} A,$$

where A is the wall area. The ratio of the homogeneous dissipation to the boundary dissipation is therefore :

$$[\sqrt{\omega \mu / \rho} \quad \omega / a^2] (V/A).$$

For the representative numbers $\mu/\rho = 10^{-1} \text{ cm}^2/\text{sec}$, $\omega = 10^3 \text{ sec}^{-1}$, $a = 10^5 \text{ cm/sec}$ and $(V/A) = 10^2 \text{ cm}$, this ratio is 10^{-4} . Thus, homogeneous viscous dissipation is usually negligible. An analogous argument for heat conduction shows that homogeneous dissipation by molecular heat conduction is negligible in comparison to wall heat conduction losses, by approximately this same factor. These homogeneous dissipation mechanisms will be of importance only for very large chambers (V/A large) and for the high-frequency modes, note the $\omega^{3/2}$ dependence of the ratio. These homogeneous losses become very large for wave lengths approaching a molecular mean free path.

4.4.2. Chemical and Molecular Relaxation Losses - Homogeneous dissipation might also be produced by intermolecule and intramolecule relaxation responses of the gas to the acoustic field. Under appropriate conditions, these effects are much more pronounced than the homogeneous dissipation mechanisms discussed above. In order to illustrate concepts, here we shall talk in terms of intermolecule relaxation of chemical reaction. Intramolecule relaxation of vibrational and other degrees of freedom, can be discussed in exactly the same way but chemical relaxation is likely to be more important under most of the conditions that prevail in rocket chambers.

First, it is necessary to realize that when relaxation processes can occur, two different sound speeds must be considered, an equilibrium sound speed and a frozen sound speed. The definitions of these two quantities and the differences between them are discussed in Chapter 2 Section 2. This observation poses the question of which sound speed should be used in calculating the acoustical frequencies of the cavity. The obvious answer is, that if nearly frozen conditions prevail in the acoustic oscillations then the frozen sound speed should be used while the equilibrium sound speed is the appropriate one, if the oscillations are nearly in equilibrium. Before calculating the chamber frequencies, one should decide whether each of the relaxation processes that can occur will be frozen or in equilibrium. Fort-

unately, frozen and equilibrium sound speeds usually differ so little that it is not very important to make the distinction; the calculated frequencies can seldom be in error by as much as a few percent. The usual approach is to use the frozen sound speed in analyzing the nondissipative acoustic field.

Associated with every relaxation process is a characteristic relaxation time τ , which is proportional to the reciprocal of the rate of the process. For any given acoustic frequency ω , the process will be nearly frozen during the sound vibrations if $\omega\tau \gg 1$ and it will be nearly in equilibrium if $\omega\tau \ll 1$. We now show that the effect of a relaxation process on the decay of an acoustic mode can be characterized in terms of ω , τ and the frozen and equilibrium sound speeds.

It can be shown (17) that when a chemical relaxation process occurs in the gas, the acoustic wave equation assumes the modified form :

$$\frac{\partial}{\partial t} \left(\frac{1}{a_f^2} \frac{\partial \tilde{y}}{\partial t} - \nabla^2 \tilde{y} \right) + \frac{1}{\tau} \left(\frac{1}{a_e^2} \frac{\partial \tilde{y}}{\partial t} - \nabla^2 \tilde{y} \right) = 0 \quad (\text{Eq. 10-46})$$

where a_f and a_e are the frozen and equilibrium sound speeds, respectively. If we seek solutions of the form :

$$\tilde{y} = \tilde{V} e^{i\mathbf{k} \cdot \mathbf{x} + st}$$

where \tilde{V} , \mathbf{k} and s are constants, then we obtain :

$$\tau s^3 + bs^2 + \tau \omega^2 s + \omega^2 = 0 \quad ,$$

where $b \equiv a_f^2/a_e^2$ and $\omega^2 \equiv a_f^2 k^2$. We demand that the ω defined here be real in order to investigate standing modes and since b is near unity, we set $s = i\omega + \alpha$ and assume that $|\alpha| \ll |\omega|$ so that s^2 and s^3 can be evaluated by expanding to the first power in α . Solving the resulting approximate characteristic equation for α , we obtain :

$$\alpha = -\omega \left(\frac{b-1}{2} \right) \frac{\omega\tau + ib}{b^2 + (\omega\tau)^2} \quad .$$

Since b is near unity, the real part of $-\alpha$ is approximately :

$$-\alpha = \omega \left[(a_f^2/a_e^2 - 1)/2 \right] \left\{ \omega\tau / [1 + (\omega\tau)^2] \right\} \quad , \quad (\text{Eq. 10-47})$$

and ω is approximately a natural vibrational frequency. The quantity $-\alpha$ in Eq. 10-47 represents the decay constant appearing in Eq. 9-1 of Chapter 9, which is seen to be proportional to the difference between the squares of the frozen and equilibrium sound speeds, $a_f^2 - a_e^2$. The general thermodynamic result that $a_f > a_e$ ensures that $-\alpha > 0$. More detailed derivations of formulas equivalent to Eq. 10-47 may be found (18) for chemical relaxation and (19) for vibrational relaxation.

Equation 10-47 shows that the dimensionless ratio α/ω depends on the product $\omega\tau$ as well as a_f and a_e . The quantity in the curly brackets in Eq. 10-47 approaches zero, when $\omega\tau \rightarrow 0$ and when $\omega\tau \rightarrow \infty$; it achieves its maximum value of $\frac{1}{2}$ when $\omega\tau = 1$. Thus, the peak value of the decay constant is $\omega(a_f^2/a_e^2 - 1)/4$, which is attained when the relaxation time is of the same order as the oscillation period. The decay constant is negligibly small when the oscillations are either nearly frozen or nearly in equilibrium.

Most vibrational relaxation times are very small compared with typical oscillation periods, and the corresponding contributions to dissipation are therefore small, although they generally exceed the homogeneous viscous and heat conduction losses. Relaxation times for other internal molecular degrees of freedom are even shorter. However, chemical relaxation times span a wide spectrum of values and some of the chemical times in the product gases may well be comparable with the oscillation period. The value of $(a_1^2/a_0^2 - 1)$, obtained by considering only these critical chemical processes, will usually determine the extent of dissipation by homogeneous relaxation. It follows that the result will depend strongly on the propellant combination and on chamber pressure and temperature. In this regard, it is worth noting that relaxation times usually decrease rather rapidly as the mean temperature increases and, whenever the relaxation processes involve only two-body collisions, vary inversely with pressure. Since the effective value of $(a_1^2/a_0^2 - 1)$ practically never exceeds a few percent, the value of $-\alpha$ produced by relaxation effects practically never exceeds $10^{-2}\omega$. Calculated nozzle and wall damping usually exceeds relaxation damping.

4.4.3. Other Homogeneous Damping Processes - A number of other homogeneous damping processes might be discussed. For example, if chemical equilibrium is nearly maintained in the acoustic oscillations, then concentration gradients are produced by the sound waves and molecular diffusion processes can occur, contributing additionally to the dissipation. Acoustic losses due to thermal diffusion phenomena may be present in any case and pressure-gradient diffusion losses might be produced by the pressure oscillations provided that mean species mole fractions differ from mass fractions. None of these processes have been investigated in any detail. However, there is reason to believe that these and other homogeneous damping processes are small compared with relaxation damping.

4.5. Particle Damping

4.5.1. Overview and Literature - When solid or liquid particles are present in the product gases, they can produce a considerable amount of acoustical dissipation provided that they are of the appropriate size. Like the homogeneous damping discussed in Section 4.4, this damping is distributed throughout the volume of the gas in the cavity.

In view of the results that we were able to obtain in Chapter 2 Section 3 for gas-particle nozzle flow, one might expect at first glance that a similar formulation could be employed to analyze particle damping relatively easily. A closer look reveals that many new problems may arise. There are at least three characteristic distances that can occur in the particle damping problem, the particle radius r , the acoustic wave length λ and the thickness of the acoustic boundary layer $\sqrt{\mu/\rho\omega}$, which was identified in Section 4.3.1. The nature of the problem will depend upon the relative magnitudes of these three length scales.

The length $\sqrt{\mu/\rho\omega}$ is greater than or comparable with λ , only for wave lengths less than or comparable with a molecular mean free path and we have seen in Section 4.4.1 that such waves are rapidly damped by homogeneous viscous dissipation. Thus we care only about the cases where $\sqrt{\mu/\rho\omega} \ll \lambda$; indeed, for typical conditions we saw that $\lambda \sim 10^3$ cm and $\sqrt{\mu/\rho\omega} \sim 10^{-2}$ cm. Cases in which $r \gtrsim \lambda$ are also uninteresting to us, since realistic systems will always have $r \ll \lambda$. This leaves two size regimes that concern us, (a) $\sqrt{\mu/\rho\omega} < r \ll \lambda$ and (b) $r \ll \sqrt{\mu/\rho\omega} \ll \lambda$. In typical motors, $r \sim 10^{-4}$ cm (see Chapter 2 Section 3) and therefore the system will be in regime (b), but $\sqrt{\mu/\rho\omega}$ is small enough for regime (a) also to be potentially of interest.

From our prior knowledge we can infer qualitatively what the flow will be like in regimes (a) and (b). In regime (a), since the particle is large compared with the thickness of the oscillatory boundary layer, an acoustic boundary layer much like that analyzed in Section 4.4.1 will develop on the surface of the particle. We could, in fact, obtain a reasonable estimate of the acoustic attenuation produced by a particle in this regime, by taking the results of Section 4.4.1 and setting the wall area A equal to the surface area of the particle. However, we shall not proceed with an analysis of regime (a) because regime (b) is of greatest interest. In regime (b) where the unsteady boundary layer is thick compared with the size of the particle, there is time for essentially quasisteady viscous flow to develop around the particle during each oscillation cycle and the instantaneous flow field about a spherical particle will correspond very closely to Stokes flow about a sphere. In regime (b) it will therefore be possible for us to employ the Stokes drag law and to adopt a formulation which is similar to that of Chapter 2 Section 3. From this discussion, it will be seen to be somewhat fortuitous that the ideas of Chapter 2 Section 3 are applicable for the particle damping conditions of greatest interest.

Before proceeding to present a simplified analysis of particle damping in regime (b), we should mention that treatments, which are much more comprehensive than ours, are available in the literature. The source which is generally quoted for the theory of particle damping is Ref. (20), in which regimes (a) and (b) are treated simultaneously by the same technique and the effects of both heat conduction and viscosity are included. Actually, the physical content of the theory (20) is only slightly more general than that of Ref. (21), which was published in 1910 and is reviewed in Lamb's textbook (22). In fact, analyses of many of the other damping processes that we have considered (Section 4.3.1, 4.3.2, 4.4.1) are given by Lamb (22), who also discusses and analyzes some damping mechanisms that we have not mentioned. The main point that is not treated entirely adequately in the early literature (21), (22) is the question of motion of the sphere due to its finite inertia. Although the analysis (20) improves on this aspect of the problem, nevertheless, objections can still be raised on the grounds that (20) the amplitude of the displacement of the sphere is assumed to be small compared with the radius of the sphere. More recent work (23) has removed this restriction. The analysis given below does not contain this restriction either.

4.5.2. Analysis for Very Small Particles - In studying the acoustic response of small, rigid spheres of a condensed material, we shall neglect the effects of heat conduction and shall assume that Stokes drag law holds for the sphere. We employ the notation of Chapter 2 Section 3, letting the subscripts g and s identify properties of the gas and condensed phases, respectively. A sinusoidal gas velocity will be assumed to be prescribed :

$$\tilde{v}_g = \text{Re} \left\{ \tilde{v}_{g0} e^{i\omega t} \right\} ,$$

and we shall solve for the amplitude and phase of the response of the velocity of the particle :

$$\tilde{v}_s = \text{Re} \left\{ \tilde{v}_{s0} e^{i\omega t} \right\} .$$

Having obtained v_s in terms of v_g , we shall use the result to compute the acoustic dissipation of the sound field in the gas. It will be shown that the phenomenon is very similar to that of chemical or molecular relaxation treated in Section 4.4.2.

From Eq. 2-72 of Chapter 2, it is apparent that the equation of motion of the spherical particle is :

$$\frac{4}{3} \pi r^3 \rho_s \frac{d\tilde{y}_s}{dt} = 6\pi r\mu (\tilde{y}_g - \tilde{y}_s) ,$$

where ρ_s is the specific gravity of the condensed material. Substituting for v_g and solving for v_{so} , we find :

$$\tilde{y}_{so} = \tilde{y}_{go} (1 - i\beta)/(1 + \beta^2) , \quad (\text{Eq. 10-48})$$

where now the dimensionless frequency or dimensionless particle radius is defined as :

$$\beta \equiv 2\rho_s r^2 \omega / 9\mu .$$

The next task is to compute the rate of dissipation of acoustic energy. From the ideas involved in the derivation of Eqs. 2-69 and 2-70 of Chapter 2, it can be seen rather easily that Eq. 6-7 of Chapter 6 is unchanged, while the appropriate generalizations of Eqs. 6-8 and 6-9 of Chapter 6 that are required, in order to account for the force exerted on the gas by condensed particles are :

$$\rho_g \frac{\partial \tilde{y}_g}{\partial t} = - \nabla p + n_s 6\pi r\mu (\tilde{y}_s - \tilde{y}_g)$$

and:

(Eq. 10-49)

$$\rho_g \frac{\partial h}{\partial t} = \partial p / \partial t + n_s 6\pi r\mu (\tilde{y}_s - \tilde{y}_g) \cdot \tilde{y}_g ,$$

where n_s is the number of particles per unit volume and the nonlinear and molecular transport terms have both been omitted. Using the equation of state for an ideal gas with constant heat capacities and constant mean molecular weight, we find that :

$$dh_g = \left(\frac{\gamma}{\gamma-1}\right) dp/\rho_g - \left(\frac{a^2}{\gamma-1}\right) d\rho_g/\rho_g$$

where a is the frozen sound speed. Therefore, by substitution of the linearized form of Eq. 6-7 of Chapter 6 into the last of these two equations, we obtain :

$$\partial p / \partial t = - \rho_g a^2 \nabla \cdot \tilde{y}_g + (\gamma-1) n_s 6\pi r\mu (\tilde{y}_s - \tilde{y}_g) \cdot \tilde{y}_g . \quad (\text{Eq. 10-50})$$

In this case the acoustical energy is (Eq. 10-23) :

$$e = p^2 / 2\bar{\rho}_g a^2 + \bar{p} v_g^2 / 2 ;$$

hence, dotting Eq. 10-49 into \tilde{y}_g multiplying Eq. 10-50 by $p'/\bar{\rho}_g a^2$ and adding the two results, we obtain :

$$\partial e / \partial t + \nabla \cdot (p' \tilde{y}_g) = n_s 6\pi r\mu (\tilde{y}_s - \tilde{y}_g) \cdot \tilde{y}_g , \quad (\text{Eq. 10-51})$$

where a term containing the additional factor $(p'/\bar{p})(\gamma-1)/\gamma$ has been omitted on the right-hand side since it is small compared with unity. Equation 10-51 is the appropriate generalization of Eq. 10-24 when viscous particle damping is taken into account; if heat transfer to the particles were also taken into account here, then an additional term, proportional to $(\gamma-1)/\gamma$ and arising from the analog of the last term in Eq. 2-70 of Chapter 2, would appear on the right-hand side of Eq. 10-51.

If Eq. 10-51 is integrated over the total volume of a cavity for which the acoustic flux term $p'\tilde{y}_g$ vanishes at the walls, then it is found that :

$$d\bar{c}/dt = \int_V n_s 6\pi r \mu (\underline{v}_s - \underline{v}_g) \cdot \underline{v}_g dV/V.$$

Using Eq. 10-33, we then see that the growth constant α is given by :

$$\alpha = \frac{1}{2} \int_V n_s 6\pi r \mu \langle (\underline{v}_s - \underline{v}_g) \cdot \underline{v}_g \rangle dV / \bar{c}_0 V, \quad (\text{Eq. 10-52})$$

where the angular brackets denote an average over a cycle of oscillation. The result expressed in Eq. 10-48, along with the definitions of \underline{v}_{s0} and \underline{v}_{g0} show that :

$$\langle (\underline{v}_s - \underline{v}_g) \cdot \underline{v}_g \rangle = - (|\underline{v}_{g0}|^2 / 2) \beta^2 / (1 + \beta^2),$$

then Eq. 10-52 reduces to :

$$-\alpha = \frac{1}{2} n_s 6\pi r \mu [\beta^2 / (1 + \beta^2)] (|\underline{v}_{g0}|^2 / 2) / \bar{c}_0$$

for conditions under which $(n_s r \mu)$ and β are independent of position within the cavity.

Generally $\bar{c}_0 = \bar{\rho}_g (|\underline{v}_{g0}|^2 / 2)$ and therefore this result can be written in the final form:

$$-\alpha = \omega (Z/2) \beta / (1 + \beta^2), \quad (\text{Eq. 10-53})$$

where :

$$Z \equiv \frac{4}{3} \pi r^3 \rho_s n_s / \bar{\rho}_g$$

is the ratio of the total mass of condensed material to the total mass of gas contained within the cavity.

4.5.3. Interpretation of Results - It will be noted that at constant mass ratio Z , Eq. 10-53 predicts that for any given frequency ω , the value of $-\alpha$ increases linearly with β for small values of β , reaches a maximum value :

$$(-\alpha)_{\max} = \omega Z/4$$

at $\beta = 1$ and decreases inversely with β for large values of β . Considering β to be a dimensionless particle size, we see that there is an optimum particle radius r_{opt} given by :

$$r_{\text{opt}} = \sqrt{9\mu/2\rho_s \omega},$$

such that damping is maximum. Representative numerical values of r_{opt} lie in the 1 to 10 micron range.

This type of behavior is reminiscent of the dependence of α on the relaxation time τ , obtained in Section 4.4.2 (see Eq. 10-47). As a matter of fact, although the present development appears superficially to be quite different from that of Section 4.4.2, it is not too difficult to show that if the sound speed a^2 is identified with the frozen sound speed a_f^2 , then Eq. 10-46 can be derived (24) for the quantity v_g by using the equations of Section 4.5.2 and by defining the relaxation time as :

$$\tau = 2\rho_s r^2 / 9\mu = \beta / \omega$$

and the equilibrium sound speed as :

$$a_e \equiv a / (1 + \frac{4}{3} \pi r^3 \rho_s n_s / \bar{\rho}_g)^{\frac{1}{2}} = a / \sqrt{1 + Z} .$$

With these identifications, it is apparent that Eq. 10-47 is identical to Eq. 10-53. Thus, the gas-particle mixture behaves in exactly the same way as a relaxing gas. The relaxation time is the e-folding time for the velocity of a particle to approach the velocity of the gas. For frozen vibrations the particles remain nearly stationary, while for equilibrium vibrations the particles follow the gas motion very closely. The value of Z can be as high as 0.3 for highly metalized systems and therefore the equilibrium sound speed can be appreciably (15%) below the ordinary sound speed. Since chemical and molecular relaxation processes have much smaller differences between frozen and equilibrium sound speeds, it is clear from Eq. 10-47 that at reasonable mass ratios Z , the maximum particle damping exceeds the maximum damping due to chemical and molecular relaxation.

4.5.4. Accurate Formulas - In actual rocket motors there is a distribution of particle sizes. Since α is additive, if we let $Z_\beta d_\beta$ denote the mass ratio of particles with dimensionless radius in the range $d\beta$ about β , then the appropriate generalization of Eq. 10-53 for the total particle damping coefficient $-\alpha$ is clearly :

$$-\alpha = \omega \int_0^\infty [(Z_\beta/2) \beta / (1 + \beta^2)] d\beta .$$

This formula is likely to be sufficiently accurate for practical motors because particle heat conduction losses are usually small and because in order to avoid performance losses due to particle lags in the nozzle, the relaxation time τ and hence r , will generally have to be small enough for the Stokes drag law to hold. However, the radius r_{opt} for peak attenuation can sometimes be close to the limiting size $\sqrt{\mu/\rho\omega}$, above which the Stokes law is invalid. For laboratory experiments designed to verify the existence of a peak attenuation, it is therefore useful to have the results of the complete theory (20).

In our present notation, the theory (20) yields :

$$-\alpha = \frac{\omega (Z/2) \beta (1 + 3\sqrt{\beta\delta}/2)}{1 + \beta^2 + 9\beta\delta/2 + 3\sqrt{\beta\delta}(1 + \beta)} \quad (\text{Eq. 10-54})$$

as the generalization of Eq. 10-53 for viscous damping. Here :

$$\delta \equiv \bar{\rho}_g / \rho_s$$

is the ratio of the specific gravity of the gas to that of the condensed material. The corresponding contribution of heat conduction to $-\alpha$ is :

$$-\alpha = \left(\frac{\gamma-1}{2}\right) \frac{\omega Z' \beta' (1 + \sqrt{\beta'\delta'})}{1 + \beta'^2 + 2\beta' \sqrt{\beta'\delta'}} , \quad (\text{Eq. 10-55})$$

where :

$$Z' \equiv (c_s/c_p) Z = \frac{4}{3} \pi r^3 \rho_s c_{ns} / \bar{\rho}_g c_p ,$$

$$\beta' \equiv (3\mu_s/2\lambda) \beta = \rho_s c_p r^2 \omega / 3\lambda ,$$

and :

$$\delta' \equiv (3c_p/2c_s) \delta = 3\bar{\rho}_g c_p / 2\rho_s c_s ,$$

in which c_s is the specific heat capacity of the condensed material, c_p is the specific heat at constant pressure for the gas and λ is the thermal conductivity of the gas.

4.5.5. Experimental Verification - Experimental results (23), (25), verify the existence of a maximum in the curve of attenuation as a function of particle radius. The experimental points are shown in Fig. 10-3, along with curves representing the total damping predicted by the accurate theory (the sum of Eqs. 10-54 and 10-55). The experiments employed different materials for the particles (23), (25) and should fall on different curves in the figure; the solid curve should agree with the circles and the dashed curve with the dots. Agreement between theory and experiment is seen to be reasonably good. More recent experimental work by Dobbins and Temkin has greatly improved the accuracy of the experimental results and has shown very close agreement (better than about 5%) between theory and experiment for $0.1 \leq \beta \leq 10$. The accuracy of the theory may therefore be considered to have been proved experimentally, beyond any doubt.

4.6. Viscoelastic Damping in the Solid

4.6.1. General Aspects of Solid-Phase Losses - It is well known that when a sinusoidal, plane, traveling, acoustic wave in a gas with mean density $\bar{\rho}_g$ and mean sound speed a_g , is normally incident on the surface of another medium with mean density $\bar{\rho}_s$ and mean sound speed a_s , then a fraction :

$$R \equiv \left[\left(\frac{1}{\bar{\rho}_g a_g} - \frac{1}{\bar{\rho}_s a_s} \right) / \left(\frac{1}{\bar{\rho}_g a_g} + \frac{1}{\bar{\rho}_s a_s} \right) \right]^2$$

of the energy in the wave is reflected back into the gas, while a fraction $1-R$ of the energy in the wave is transmitted into the adjacent medium. The quantities $(\bar{\rho}_g a_g)^{-1}$ and $(\bar{\rho}_s a_s)^{-1}$ are the characteristic admittances of the two media. Therefore acoustic energy contained in standing modes of a motor cavity will be transferred at a certain rate to the solid grain or motor case which bounds the cavity. This energy transfer will modify the cavity oscillations and can lead to losses by acoustic radiation to the surroundings or by damping within the solid materials. The maximum rate of energy transfer can be estimated from the observation that the effective value of the factor $(\bar{\rho}_s a_s / \bar{\rho}_g a_g)$ generally exceeds 10^3 for the propellant grain and 10^4 for the motor case. Thus the factor $1-R$ is less than about 4×10^{-3} for the grain and 4×10^{-4} for the case, so that less than 1% of the energy flux at the cavity surface can be transmitted into the solid. One is therefore tempted to treat as perturbations the influence of these phenomena on the cavity oscillations. We shall see that this can be done sometimes but not always.

The relative magnitudes of the grain and case transmission factors further imply that transmission of energy to the propellant will probably be more important than transmission to the case; this conclusion is further supported by the observation that viscous damping within the grain is expected to occur at a greater rate than in the case because the grain viscosity coefficients are generally higher. For these reasons, we shall focus our attention on the influence of the grain and neglect the case. We shall also neglect the rate of radiation of energy out of the system on the grounds that the case-environment transmission coefficient is also of the order of 10^{-3} , giving an overall coefficient of the order of 10^{-6} for radiation losses. However, it should be emphasized before proceeding further that the types of estimates employed here are extremely rough and there may exist special conditions, under which the general conclusions are invalid. We shall not discuss possible violations of our conclusions concerning the relative unimportance of case vibrations and radiation losses, but some of these possibilities should be discernable from our discussion of grain losses.

One can envisage two extreme limiting conditions of the behavior of a propellant grain that is subjected to gas cavity oscillations at its surface (26). The grain may

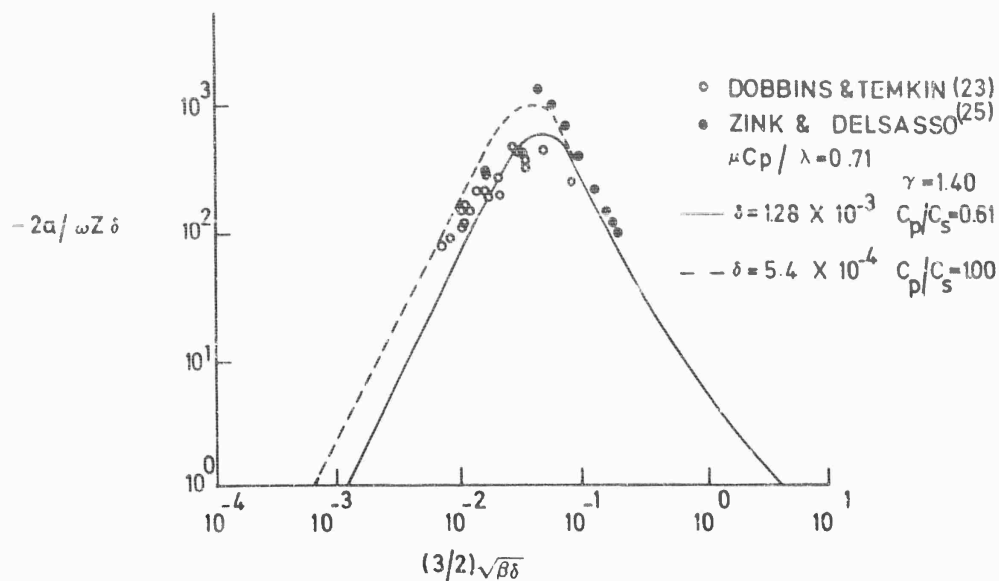


Fig. 10-3 Comparison of theory and experiment concerning dimensionless particle attenuation as a function of dimensionless particle radius (23). Vertical scale is $\alpha / (\frac{4}{3}\pi r_s^3 n_s \omega)$, where $\frac{4}{3}\pi r_s^3 n_s$ is the volume fraction of condensed material; horizontal scale is $(\rho_g r^2 \omega / 2\mu)^{1/2}$, ratio of particle radius to oscillatory boundary layer thickness.

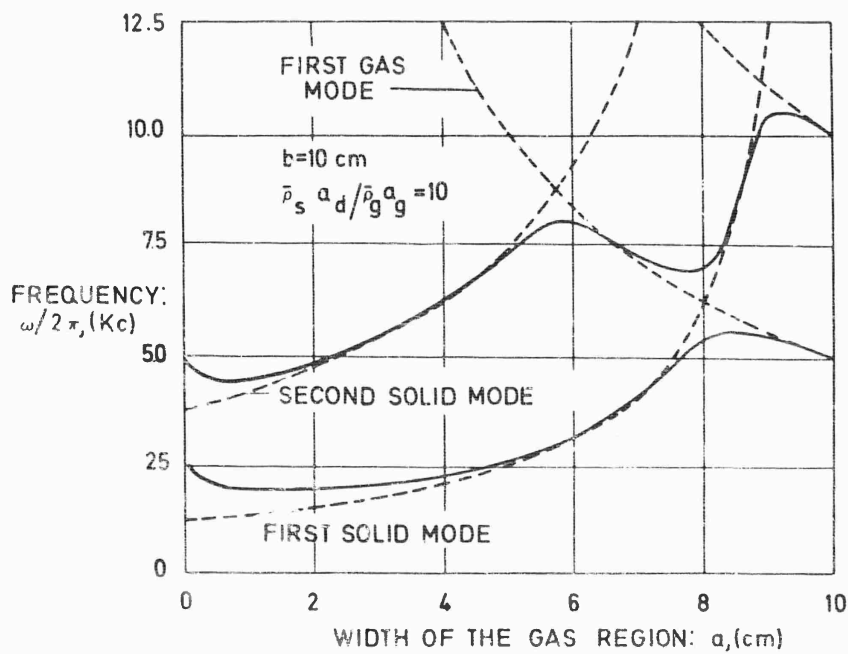


Fig. 10-4 The first and second acoustic modes of a one-dimensional, two-medium cavity as the width of the gas region varies, (27).

dissipate viscoelastically all of the energy transmitted into it, in a distance which is small compared with the web thickness or else the grain may dissipate a very small fraction of the acoustical energy contained within it, so that the entire grain essentially reaches an oscillation amplitude that is consistent with standing modes in the composite gas cavity-solid grain system. In the former case, grain losses can be estimated rather simply; they do not depend on values of the viscosity coefficients of the grain, they are proportional to the interior surface area of the grain and they are found to be usually less than but of the same order of magnitude as the combustion amplification considered in Section 5, (26). In the latter case, to calculate grain losses one must first calculate the lossless acoustic modes of the gas-solid system, the results show that the grain losses are likely to vary abruptly during the burning history of a motor. It is this latter case that we shall consider in the rest of Section 4.6. Available data on viscosities of solid propellants are too sparse for us to decide which of the two limiting cases will generally be encountered in practice, but the data that is available implies that the low-loss limit will sometimes occur.

4.6.2. Vibrations of Gas-Solid Systems (27) - Waves propagating in elastic solids are not described by an equation quite so simple as Eq. 10-9, primarily because the relationship for the stress tensor $\mathbf{p} = p \mathbf{U} + \mathbf{T}$, with \mathbf{T} given by Eq. 6-11 of Chapter 6, is not valid for elastic or viscoelastic materials. If we assume that the material is isotropic (as many solid propellant matrices will be), then for sinusoidal oscillations it can be shown that the velocity amplitudes \mathbf{v}_{0s} of Eq. 10-12a for the solid obey the vector wave equation :

$$a_d^2 \nabla(\nabla \cdot \mathbf{v}_{0s}) - a_s^2 \nabla \times (\nabla \times \mathbf{v}_{0s}) + \omega^2 \mathbf{v}_{0s} = 0, \quad (\text{Eq. 10-56})$$

where \times denotes the vector (cross) product, a_d is the dilatational sound speed of the material and a_s is the shear sound speed of the material. Both a_d and a_s are complex numbers which are known functions of ω , assumed real. The imaginary parts of a_d and a_s account for viscoelastic damping and are assumed to be small compared with the corresponding real parts. The companion gas-phase equation is Eq. 10-13 with a replaced by a_g and ω replaced by $\omega - i\alpha$. If the combustion zone is neglected, then gas-solid interface conditions are, of course, continuity of normal velocity and normal stress and vanishing of the tangential stress in the solid. The conditions to be applied at other boundaries depend on the method of propellant support; a variety of possibilities exist (see Section 4.6.4.). The complete set of boundary and interface conditions permit solutions to the differential equations governing \mathbf{v}_{0s} and p_{0g} to be found only for a discrete set of frequencies ω .

An excellent pedagogical discussion of vibrational modes in gas-solid systems is given (27). A few of the essentials will be covered here. Clearly, the effective characteristic admittance of the solid is so low that the part of the system containing gas should oscillate in a gas mode with practically a fixed boundary condition at the interface, while the characteristic admittance of the gas is so high that the part of the system containing the solid should oscillate in a solid mode, with practically a free boundary condition at the interface. The overall system should therefore support two distinct types of modes, one (gas modes) in which the acoustical energy in the solid is very low and the other (solid modes) in which the acoustical energy in the gas is very low. This view is tenable except when the frequencies of two modes of opposite types coincide. For systems in which the gas and solid sound speeds and dimensions are roughly comparable, such situations are likely to develop at certain times during propellant burning because as the propellant is consumed, the characteristic dimension of the gas part of the cavity increases and that of the solid part decreases, causing the frequencies of the gas modes to decrease and those of the solid modes to increase with time. At a time of frequency coincidence, the interface condition is both free and fixed by the above

arguments, which is impossible. What actually happens at such times is that roughly speaking, the thickness of the solid becomes equal to an integral number of solid wave lengths for the frequency of the imposed gas mode and vice versa, so that proper reflection conditions occur in the solid and gas parts to cause wave interference that results in intermediate interface conditions, neither free nor fixed. These interference phenomena eliminate the nonpermissible mode crossing and result in transitions from solid modes to gas modes, etc., as time increases. This situation is illustrated in Fig. 10-4.

Figure 10-4 was calculated for the idealized case of a one-dimensional system of a specified length b , with fixed, zero-displacement boundary conditions at each end and with gas occupying the region $0 < x < a$ and solid the region $a < x < b$. The case shown has $a_g = 10^5$ cm/sec and $a_d = 5 \times 10^4$ cm/sec. The ratio $\bar{\rho}_s a_d / \bar{\rho}_g a_g = 10$ was purposely chosen to be two orders of magnitude, too low in order to make the gas-solid mode transitions easily visible on the figure; in real cases the transitions would be much sharper. The departure from the solid mode as $a \rightarrow 0$ is caused by the fixed boundary condition at $x = 0$, which differs from the normal free boundary condition at the interface for the solid mode. Calculated curves for transverse modes in cylindrical solid propellant motors with tubular grains are qualitatively very similar to Fig. 10-4.

Further study of amplitude details in the two types of modes reveals, as would be expected, that for the solid modes the velocities in each medium are comparable but the normal stresses are much larger in the solid, while for the gas modes the normal stresses in each medium are comparable but the velocities are much larger in the gas (27). These results imply that the acoustic energy density is much larger in the gas for the gas modes and in the solid for the solid modes. This means that if a fixed amount of acoustic energy remains in the system as the propellant burns (a increases), then the energy is transferred alternately from the solid to the gas and from the gas to the solid, each time the mode type changes.

4.6.3. Implications Concerning Attenuation - It will be evident in Section 5 that amplification in the combustion zone at the solid-gas interface, results from the response of the burning rate to applied gas pressure oscillations. If pressure oscillations at the interface vanish, then the source of amplification also disappears. Since the solid modes correspond to free interface conditions of constant pressure, it is clear that the interfacial combustion process cannot amplify these modes. This explains why observed instabilities in Chapter 9 often correspond to gas modes but never solid modes. The fact that the frequencies of the gas modes of the system do not vary continuously with time but instead are occasionally 'interrupted' by incipient crossing of solid modes, may underlie certain observations of intermittency of instabilities in some gas modes of Chapter 9. The mere fact that the solid may participate in the oscillations thus modifies the amplification process and the occurrence of instabilities.

We have not yet discussed possible effects of viscoelastic damping under the present conditions. Clearly, this damping will be greatest when the fraction of the acoustical energy contained in the solid is greatest. This provides an additional effect that tends to damp the solid modes. It also implies that for highly viscous solids, small departures from gas modes may increase the solid-phase dissipation sufficiently to damp the oscillations, by increasing the fraction of the total oscillatory energy contained in the solid. This phenomenon thus tends to increase the duration of periods of interruption of vibrations in gas modes. The opposite effect would be observed if the homogeneous gas dissipation coefficients were to exceed the homogeneous solid dissipation coefficients.

4.6.4. Results of Calculations - Gas-solid vibrational modes for internally burning tubular grains in cylindrical motors have been analyzed, see (28-31). Except

for purely radial or purely axial modes, computation of the solid-mode frequencies in these thick-walled cylinders presents a problem which in general requires the use of electronic computers in its solution. For this reason, no results have been obtained until fairly recently (32).

The results that have been reported for solid propellant grains are restricted to three different sets of boundary conditions at the outer surface of the cylinder: (a) vanishing radial and tangential stresses, representing a free surface and believed to be applicable for some unbonded propellants or for propellants bonded to nonrigid cases, (b) vanishing radial displacement and vanishing tangential stresses, representing a supported surface and believed to be applicable for unbonded propellants free to rotate in rigid cases and (c) vanishing radial and tangential displacements, representing a clamped outer surface and believed to be applicable for propellants bonded to rigid cases. Radiation of acoustical energy from the outer surface vanishes for all of these boundary conditions. Either the vibrations are assumed to exhibit no axial dependence (28-30), or else the fore and aft boundary conditions are taken to be vanishing, normal, axial, displacements in both the solid and the gas and vanishing tangential stresses (28), (31); these conditions also eliminate radiation losses.

The intermittency effect discussed in Section 4.6.3, is demonstrated (28) through the results of calculations for values of parameters that are believed to be representative of real rocket motors. The calculations for infinitely long cylinders (29), show that 'ring modes', which are modes in which there is no displacement node extending across the entire web thickness, have low frequencies but are highly damped by shear viscosity for supported or clamped outer boundary conditions. These modes can also couple only weakly to the gas vibrations. 'Thickness modes' which have at least one displacement node or antinode extending across the web thickness, have higher frequencies and result in low damping for the gas modes except near incipient mode crossing points. The thickness modes naturally divide themselves into two groups, shear modes and dilatational or compressional modes, which correspond respectively, to the first or second term in Eq. 10-56 being negligible. It is found that, except for the lowest thickness-mode frequencies, the coupling between the shear waves and the compressional waves in the solid is very weak. This observation provided the basis for an approximate analytical calculation of the frequencies of the higher thickness modes (30). A further study (31) shows that coupling of the solid to low-frequency, longitudinal gas modes does not result in the intermittency effect because incipient mode crossing does not occur, but instead leads to smoothly-varying viscoelastic solid damping which might tend to cause oscillations to occur during either the first part or the last part of a motor firing.

4.7. Summary

It is difficult to summarize the material in Section 4, which in itself is little more than an introduction to and a summary of acoustic damping mechanisms in solid propellant rockets. Clearly, a great deal of information is known about damping mechanisms and a great deal remains to be discovered. As gross generalizations of the relative importance of the various loss mechanisms in real motors, the following remarks may be made. Losses through choked end nozzles are probably the dominant losses, provided that longitudinal components of the acoustic field occur. For metalized propellants, the next most important loss is likely to be particle damping in the gas. The participation of the solid in the oscillations should have an appreciable effect on what modes occur and on their time of occurrence, for oscillations with transverse components. Wall damping is likely to exceed homogeneous gas-phase damping, particularly for long T-motors which may well be dominated by wall damping.

5. Theories of Acoustic Amplification Mechanisms

5.1. Introduction

Having discussed mechanisms by which acoustic oscillations in rocket motors are attenuated, we now return to the problem of describing how the vibrations are generated. It has been indicated earlier that a variety of amplification mechanisms may occur; combustion at burning surfaces, finite rates of homogeneous chemical heat release, conversion of mean flow energy into acoustical energy through aerodynamic noise generation in regions of nonvanishing mean velocity within the motor, etc. At least rudimentary knowledge exists concerning all of the mechanisms that have been mentioned. Thus, there is an appreciable body of background literature on the generation of noise by jets (33). Furthermore, the influence of homogeneous chemical rate processes on acoustic amplification in liquid propellant rocket motors has been studied at some length (3). In one paper (70) the time-lag approach of Ref. (3) was modified slightly in order to provide a basis for discussing amplification caused by heat release from the combustion of solid propellant additives such as aluminum, whose burning processes are distributed more or less homogeneously throughout the chamber. Except for this isolated example, insofar as specific application to solid propellant motors is concerned, the only acoustic amplification mechanism that has received more than passing mention in the literature is the combustion process which occurs at the burning surface.

There are good reasons for this state of affairs. All solid propellants that have been observed to support acoustic oscillations, experience a combustion process in the vicinity of the solid surface. None of the other possible generation mechanisms are so universal. Thus, acoustic oscillations have been observed for conditions under which distributed homogeneous heat release and aerodynamic noise generation are unlikely. There may well exist special conditions under which these other processes are of importance. For example, acoustic amplification by means of burning metal particles homogeneously distributed throughout the chamber may warrant further investigation for metalized propellants and jet noise generation may be significant when narrow annular ports empty into a wider, prenozzle chamber. However, the omnipresence of the interfacial combustion zone justifies the extensive consideration that it has received.

In view of the absence of a significant amount of theoretical work on acoustic amplification mechanisms other than surface combustion, we consider here only the contribution of the surface combustion process. It has been shown in Section 3 that the amplification produced by surface combustion can be expressed in terms of the acoustic admittance of the surface. The condition for the validity of this formulation is that the overall thickness of the combustion zone, extending from a position in the solid at which the temperature practically equals the temperature of the bulk of the solid, to a position in the gas at which the chemical reactions are practically completed, must be small compared with all characteristic wavelengths of the acoustic field in the chamber. This condition is satisfied in almost all of the motors for which acoustic instability is of any concern. Hence, all of the theories discussed in this section are, at least in principle, theories of the acoustic admittances of burning surfaces. Certain nonlinear or nonacoustic aspects of some of the theories considered here do not pertain to acoustic admittance, but these aspects will not be discussed until Section 6.

We shall begin by giving some general characteristics of acoustic admittances of burning interfaces. We then discuss theories that employ the concept of a time lag. Mechanistic models for homogeneous propellants that avoid the use of time-lag concepts are considered next. Application of the full equations of aerothermochemistry to models of homogeneous propellants is discussed in Section 5.5. Next, approaches directed specifically toward heterogeneous propellants will be considered. Fin-

ally, in Section 5.7, linear, erosive effects will be discussed for homogeneous propellants.

5.2. General Properties of Interfacial Acoustic Admittance

5.2.1. Relationship Between Admittance and Perturbation of Mass Flow Rate - The admittance has been defined in Eq. 10-27; the value of its real part determines whether acoustic amplification can occur (see Eqs. 10-28, 10-31 or 10-32). In any theoretical approach to the analysis of the surface combustion process, it is usually convenient to investigate the pressure response of the mass burning rate \dot{m} instead of the velocity. Since by definition, with \mathbf{n} pointing into the solid and with \dot{m} being considered positive for flow from the solid into the gas :

$$\dot{m} = -\rho \chi \cdot \mathbf{n} \quad , \quad (\text{Eq. 10-57})$$

we find by setting :

$$\dot{m} = \bar{\dot{m}} + \text{Re} \{ \dot{m}_0 e^{i\omega t} \} \quad (\text{Eq. 10-58})$$

and by using similar formulas for ρ and χ , that :

$$\dot{m}_0 = -\bar{\rho} \chi_0 \cdot \mathbf{n} - \bar{\chi} \cdot \mathbf{n} \rho_0 \quad ,$$

where the quadratic term $\rho_0 \chi_0 \cdot \mathbf{n}$ has been discarded as being of higher order. Utilizing Eq. 10-8 with the ideal gas result $a = \sqrt{\gamma p/\rho}$ for the relationship between ρ_0 and p_0 , we may write this formula in the form :

$$\dot{m}_0 = -\bar{\rho} \chi_0 \cdot \mathbf{n} + \bar{\dot{m}} p_0 / \gamma \bar{p}$$

where the relationship $\bar{\dot{m}} = -\bar{\rho} \bar{\chi} \cdot \mathbf{n}$, which follows from Eq. 10-57, has again been employed. In view of Eq. 10-27, this result implies that :

$$Y = -(\bar{\dot{m}}/\bar{\rho} \bar{p})_b [(\dot{m}_0/\bar{\dot{m}}) / (p_0/\bar{p}) - 1/\gamma]_b \quad . \quad (\text{Eq. 10-59})$$

Equation 10-59 is the formula that is required for expressing Y in terms of steady-state quantities and the ratio of the mass flow rate perturbation to the pressure perturbation.

Since Eq. 10-27 applies to conditions at the boundary of the gas cavity, the subscript b in Eq. 10-59 identifies conditions on the gas-cavity side of the interfacial combustion zone. In calculating the ratio $[(\dot{m}_0/\bar{\dot{m}})/(p_0/\bar{p})]_b$ in Eq. 10-59 from an analysis of the combustion zone, one must therefore evaluate this quantity at the extreme gas-side boundary of the combustion region. Thus, if the model of the combustion zone postulates a layer of finite thickness, then the subscript b identifies properties at the 'outer' or gas edge of the layer. On the other hand, if the model of the combustion zone is mathematically infinite in extent as one-dimensional models often are, then the subscript b will denote conditions at the gas-side infinity which we denote by a value of the normal coordinate x of $+\infty$ in our later analyses. It is not inconsistent with the definition in Eq. 10-27 to treat subscript b conditions as being applied at $x = +\infty$ in analyzing the combustion zone, because all properties vary so little outside of the thin combustion region that from the viewpoint of the combustion zone, $x = +\infty$ corresponds to the boundary of the cavity.

It will be noted that here we have assumed that the velocity amplitude $\chi_0 \cdot \mathbf{n}$ is small compared with the mean velocity $\bar{\chi} \cdot \mathbf{n}$. This restriction did not appear in Eq. 10-27, where in fact $\bar{\chi}$ was zero. The only restriction present in the earlier discussion was that $|\chi_0|$ be small compared with 'a', a much less stringent condition. In this regard, it is worth emphasizing that the velocity amplitude χ_0 of

interest in the present discussion is always evaluated in the vicinity of the combustion zone at the boundary of the cavity; the velocity amplitude may be small compared with \bar{v} in this region even if it is large compared with \bar{v} throughout most of the cavity. Thus, the present linearization does not provide additional restrictions on the amplitude of the oscillations within the cavity, away from its combustion boundaries. The fact that $\chi \neq 0$ here does introduce a convective acoustic energy flux into the cavity at the boundary, which was neglected in the development of Eq. 10-27, but this additional flux is easily calculated from the value of χ_b and from the acoustical energy distribution within the cavity; its evaluation does not require analysis of the combustion zone. The convective term, which has already been discussed in Chapter 9 Section 4.6.2, does not affect the calculation of the admittance.

When vibrations of the solid propellant are taken into account, the useful interface admittance is $Y = [\chi_0 \cdot p_0 / p_0]_b - [\chi_0 \cdot p_0 / p_0]_c$, where the subscript c identifies conditions in the condensed phase at the extreme solid side of the interfacial combustion and heat conduction zone. For the interface admittance to be an appropriate concept, the interfacial zone must be small enough for the approximation $p_{0b} = p_{0c}$ to be valid. Provided that the density of the solid is high compared with that of the gas, it is easy to show that Eq. 10-59 is an excellent approximation to this generalized admittance (28).

It has been suggested that the term $1/\gamma$ in Eq. 10-59 is only approximately correct and that when suitable account is taken of 'entropy waves', then this term assumes a value lying between $1/\gamma$ and 1 (5), (34). This idea has been carried so far as to suggest that there exists a 'temperature response function' of the combustion zone, which determines the departure of the term from the value $1/\gamma$ and which can be calculated from an analysis of the combustion zone analogous to that used in obtaining the 'mass response function', $[(\dot{m}_0/\bar{m})/(p_0/\bar{p})]_b$ (5). We agree that the $1/\gamma$ term actually lies between $1/\gamma$ and 1. However, we believe that the value of this term is governed by processes occurring in the bulk of the cavity and not by processes occurring in the combustion zone. A number of bulk processes, e.g., heat conduction, produce slightly nonisentropic cavity oscillations which move the $1/\gamma$ term toward its isothermal value of unity. But, it has not been demonstrated clearly that processes occurring within the thin interfacial zone can affect the value of this term at all. By this statement, we imply that we do not understand the analysis given in Ref. (34). Our views on this matter are discussed further in Section 5.4. Pending further investigation, we recommend retaining the value $1/\gamma$ in Eq. 10-59; superficially, this value appears to be very close to the correct one.

5.2.2. Qualitative Properties of Admittance - A few properties of the admittance Y are already apparent from Eq. 10-59. It is reasonable to suppose that the ratio $[(\dot{m}_0/\bar{m})/(p_0/\bar{p})]_b$ will be roughly of the order of magnitude of unity. Hence, Y should be of the order of magnitude of $(\dot{m}/\bar{p})_b$, where it will be recalled that \bar{p}_b and \bar{p}_b are the mean density and pressure of the gas in the cavity. The ratio $(\dot{m}/\bar{p})_b$ is obviously the mean normal velocity of the gaseous combustion products with respect to the propellant surface, so that Y is roughly of the order of the ratio of the burned gas velocity to the chamber pressure. This quantity is small compared with the characteristic admittance $(a/\bar{p})_b$ of the chamber gases and therefore the approach of treating the amplification process as a perturbation is justified. However, numerical estimates typically show that the contribution of the combustion zone admittance to the amplification or decay factor α is of the same order as the largest contribution of any of the damping mechanisms discussed in Section 4. Thus, the validity of the assumption that the surface combustion process is generally the dominant acoustic amplification mechanism, is found to be supported by numerical estimates.

We note that in the solid phase :

$$\dot{m} = \rho_c r$$

where ρ_c is the density of the solid propellant and r is the instantaneous linear regression rate, see Chapter 6 Section 2.1.3.1. Since ρ_c is essentially constant, mass flow rate oscillations in the solid phase are essentially the same as linear regression rate oscillations. It follows that \bar{m} is ρ_c times the mean regression rate, but \dot{m}_{0b} is not related to the amplitude of the regression rate oscillation r_0 in this same simply way, because in unsteady flow the instantaneous mass flow rate in the gas away from the solid surface is not equal to that at the solid surface.

Theories of oscillations in the combustion zone are most comprehensible physically when expressed in terms of the response of the mass burning rate or the linear regression rate to pressure oscillations. The theories therefore yield most directly the dimensionless admittance or response function (5) :

$$y \equiv [(\dot{m}_0/\bar{m})/(\bar{p}_0/\bar{p})]_b \quad . \quad (\text{Eq. 10-60})$$

The rest of the discussion in Section 5 will be given almost entirely in terms of this dimensionless admittance y , without reference to the admittance Y of Eq. 10-59. It is seen from Eqs. 10-59 and 10-60 that the condition $\text{Re } \{Y\} < 0$ translates to $\text{Re } \{y\} > 1/\gamma$; this is a necessary condition for amplification, if acoustical convection effects cancel. In any event, $\text{Re } \{y\} > 0$ is a necessary condition for amplification. The definition of y in Eq. 10-60 agrees with that in Eq. 9-12 of Chapter 9.

5.3. Time Lag Theories

5.3.1. Simplified Time Lag Concept - An impelling physical idea is that if a pressure pulse is applied to a steadily burning propellant, then the regression rate will take a certain amount of time to reach its new steady level. As an obvious extreme version of this idea, one may assume that if a pressure change is applied at time t , then the propellant's burning rate experiences no change at all until $t + \tau$, at which time the mass burning rate instantaneously assumes its steady-state value at all positions x in the combustion zone appropriate to the new pressure. This time lag τ can be assumed to be a constant, independent of pressure, pressure history, etc. Such an hypothesis results in what is probably the simplest conceivable time lag theory.

The steady-state pressure dependence of the mass burning rate can be linearized about the mean pressure according to :

$$\dot{m}_b = \bar{m}_b + (\bar{m}/\bar{p})_b \mu (p - \bar{p})_b \quad ,$$

where the sensitivity coefficient is defined as :

$$\mu \equiv (d \ln \bar{m} / d \ln \bar{p}) \quad , \quad (\text{Eq. 10-61})$$

in which the steady-state function $\bar{m}(p)$ is to be employed. According to the time lag hypothesis, the linearized burning rate equation implies that :

$$\dot{m}_b(t) = \bar{m}_b + (\bar{m}/\bar{p})_b \mu [p(t - \tau) - \bar{p}]_b \quad .$$

Substitution of Eqs. 10-7, 10-12 and 10-58 into this formula yields :

$$\dot{m}_{0b} e^{i\omega t} = (\bar{m}/\bar{p})_b \mu p_{0b} e^{i\omega(t-\tau)} \quad ,$$

whence in view of Eq. 10-60 ,

$$y = \mu e^{-\omega\tau} \quad (\text{Eq. 10-62})$$

Equation 10-62 provides a simple expression for the dimensionless admittance Y in terms of the sensitivity coefficient μ and the time lag τ .

Equation 10-62 predicts that amplification can occur only if μ is sufficiently large and if also $\omega\tau$ is in the right range ($\cos \omega\tau > 0$). The maximum tendency toward amplification occurs if $\cos \omega\tau = 1$, one solution to which is zero time lag, $\tau = 0$; this maximum value of $\text{Re}\{y\}$ is μ , the steady-state sensitivity coefficient, which is always less than unity and is typically about 0.2. If the time lag is short enough so that $\cos \omega\tau \approx 1$, we need not know its precise value in order to calculate the admittance. If it isn't short enough, then we must find τ somehow and this, of course, will present problems. But we can still rest assured that abnormally large values of $\text{Re}\{y\}$ will not occur. These are the predictions of the simplified time-lag viewpoint.

5.3.2. Improved Time Lag Theories - The simple time lag idea is amenable to a great deal of embellishment. There are at least two incentives for this. First, the τ introduced above is difficult to estimate theoretically or to measure experimentally and improved theories could conceivably lead to physically more well defined time lags. Second and probably more important, the preceding theory is not very versatile; a single measurement for which $\text{Re}\{y\} > \mu$ and such measurements in fact exist today, see Fig. 9-20 or 9-21 of Chapter 9, disproves the theory. All time lag theories that have been proposed are more complex than the one we have just given and most of them may be interpreted in such a way that they contain a sufficient number of parameters to prevent them from being disproven by existing measurements. We review here very briefly the time-lag theories that have been published.

The first theoretical analysis of acoustic instability apparently is due to Grad (35). Although he focused much of his attention on the acoustic field, he did develop a time lag analysis of combustion zone amplification. His analysis permitted the mass burning rate \dot{m} to depend on chamber temperature as well as chamber pressure, thus affording a generalization of the results of Section 5.3.1. However, he assumed as we did above, that the time lag was constant and he obtained a result rather similar to Eq. 10-62. He appeared to consider that the time lag represented a response time of a solid-phase chemical reaction and that gas-phase combustion was unimportant.

Moore and Maslen (36) also offered an early analysis of acoustic instability. In order to compute the rate at which acoustic energy was fed into the gas in the combustion chamber, they postulated a constant time lag between application of a temperature change and the ensuing change in heat release rate in the combustion zone. They seemed to associate the time lag with a gas-phase chemical reaction.

Cheng (37), (38) has developed rather elaborate time lag models for the response of the interfacial combustion processes. Following Crocco (39), he suggested that the time lag should not be constant but instead should vary during oscillations because of a pressure dependence. In this manner, he obtained an expression differing appreciably from Eq. 10-62 and yielding essentially :

$$\text{Re}\{y\} = (\nu + \mu/2) - (\nu - \mu/2) \cos \omega\tau \quad ,$$

where ν is an additional response parameter which accounts for the variability of the time lag and which is difficult to estimate from first principles. Cheng originally viewed his time lag as describing gas-phase chemical heat release processes; specifically, it was said to represent the time interval between gasification of a fuel

element and the instant at which it releases its chemical energy (37). However, later interpretations appear to imply that it can be considered to include most any processes (38).

The first step away from describing the interfacial combustion processes solely in terms of time lags may be attributed to Green (40), (41), (42). Green employed a time lag to represent the response of the surface gasification rate to the temperature of the interface, viz., $\dot{m}(t) = B_s e^{-E_s/R^0 T_s(t-\tau)}$ at the surface (compare Eq. 5-58 of Chapter 6). However, the rest of his model for the response of the combustion zone included a number of other physical processes. The time-dependent heat conduction equation was used for the temperature within the solid; the later mechanistic theories have generally found this process to be the dominant one at low frequencies and its first use in an acoustic instability theory appears to be that of Green (40). A pyrolysis law with the forementioned time lag, was employed for the solid-gas interface condition. The gas was treated as a boundary-layer, apparently thought of as a two-dimensional one, much like an ordinary fluid dynamical boundary layer, across which heat is transferred from a gas flame (which was not analyzed) to the surface. The heat transfer coefficient for the boundary layer is ascribed a pressure dependence and it is through this dependence that pressure oscillations produce a combustion response.

There is one further important aspect in which the analysis (40), (42) differ from the other theories considered in Section 5. The acoustic admittance was not computed (40), (42). No consideration was given to the acoustic amplification produced by the combustion response. The reason for this omission was that the stated objective of these studies was to investigate a particular nonlinear acoustic mechanism by means of which the time-average burning rate can be modified as a result of acoustic oscillations. We shall return to a discussion of this nonlinear effect in Section 6. More recently, this same nonlinear effect has been studied by Barrère and Bernard (43), who extended the analysis of Refs. (40) and (42) by introducing a distribution of time lags over the surface of the propellant, in order to account for the variable surface structure of composite propellants. We shall also defer discussion of the results of Ref. (43) until Section 5.6.

5.3.3. Results and Critique of Time Lag Theories - Most of the time lag theories that predict acoustic admittances agree in showing that short time lags and high steady-state pressure and temperature sensitivities of the burning rate promote acoustic instability. There are some qualitative differences among the theoretical results; for example, one of Cheng's theories (37) appears to imply that the tendency toward instability decreases when the steady-state pressure sensitivity is increased. However, in most respects the theoretical predictions are qualitatively mutually compatible and differ only quantitatively. Many examples of qualitative agreement of these theoretical results with experimental measurements have been cited (41); typically, the experiments will show that one motor is more stable than another and the theories will predict this same relative stability. However, such qualitative agreement does not provide very strong evidence for the validity of the theories. Other types of theories may well predict the same qualitative relationships and experiments can be found that disagree with the qualitative theoretical predictions. It is difficult or impossible to define what specific propellant burning mechanisms are properly described by a given time lag theory. Perhaps few of the experimental results quoted in support for a particular theory actually fall within the domain of validity of the theory. Significant quantitative comparisons of theory with experiment have never been possible because none of the time lags have been amenable to experimental measurement.

Another general objection to time lag theories which is often raised is that they always tend to predict the existence of a number of frequency bands of amplification. This prediction arises through the $\cos \omega \tau$ dependence in Eq. 10-61, for example.

Experimental measurements of acoustic admittances of propellants have always shown just one very broad band of frequencies over which an amplification tendency exists, thus tending to discredit time lag hypotheses. In defense of the time lag theories on this charge, it may be remarked that if the time lag τ is sufficiently small, then $\omega\tau$ will be less than $\pi/2$ at all frequencies for which admittance measurements have been made and in view of large damping at high frequencies, at all frequencies that can reasonably be expected to occur in motors. Thus, time lag theories with short time lags ($\lesssim 10^{-4}$ to 10^{-5} sec) are not vulnerable to this common objection.

It should be recognized that introduction of a time lag is equivalent to a statement of ignorance. This observation has formed the basis of some of the most derogatory criticism of time lag theories. For example, Ref. (5) points out that the interfacial combustion processes 'are governed by the familiar fluid-dynamic equations and attempting to represent them in terms of distribution of time lags would apparently tend to conceal rather than reveal the nature of the phenomena'. We agree, but we feel that one should also keep in mind that time lag concepts provide relatively rapid and simple means for analyzing many complex phenomena, when they are first encountered. The value of the time lag approach lies in the wide range of problems to which it can be applied with relative ease and not in the physical insight that it produces concerning underlying mechanisms.

5.4. Mechanistic Models

5.4.1. Basic Model - Hart and McClure (44) presented the first analysis of the acoustic response of the combustion zone that entirely avoided the use of a time lag. The combustion-zone model employed in Ref. (44) is rather elaborate, containing a solid-phase heat conduction region, a narrow region approximated as an interface at the surface of the solid where a gasification reaction occurs, a heat conduction region in the gas adjacent to the surface of the solid and finally a flame surface where the heat release occurs, located in the gas and separating the gas-phase heat conduction region from the inert gaseous reaction products (see Fig. 10-5). We choose to call this model and its various generalizations (34), (45), (46) 'mechanistic' because of the spatial structure ascribed to the gas-phase reaction zone. The purpose of this structure is to retain the essence of gas-phase combustion while avoiding the necessity of considering species conservation equations and chemical heat release terms. It is not entirely clear that this aim is achieved, although there are indications of qualitative success. We prefer to push the level of approximation one step deeper, out of the conservation equations and into the chemical kinetics; theories that attempt to do this are discussed in Section 5.5 under the heading 'Aerothermochemical Approaches'.

The model, see Ref. (44), refers to one-dimensional burning of a homogeneous propellant. It employs one-dimensional, time-dependent forms of the continuity and energy (heat-conduction) equations in the solid phase and in the gas-phase heat-conduction zone. Total mass and energy conservation conditions at the surface of the solid and at the flame surface provide boundary conditions needed to connect solutions in the various regions. The temperature deep within the solid is taken to be a known constant. Heat release rate conditions applied at the solid and flame surfaces contain two terms with phenomenological coefficients, one proportional to temperature and the other proportional to temperature gradient. The phenomenological rate coefficients at the solid interface are related to gasification rate parameters; those at the flame are related to the steady-state pressure and temperature sensitivities of the propellant's burning rate. A sinusoidal pressure perturbation (proportional to $e^{i\omega t}$) is imposed on the system and solutions with sinusoidal time dependences of the same frequency are sought. Solution of the resulting linear ordinary differential equations in x , subject to the imposed boundary conditions, finally yields the time-dependent mass flow rate into the flame surface from which the admittance is computed.

The final algebraic admittance formula obtained (44) is very long and complicated. It contains eleven dimensionless parameters and therefore a complete investigation of the predictions of the theory would be laborious. The approach that has been adopted in investigating the results of the theory is to select values that appear to be reasonable for most of the parameters and then observe how the admittance changes when one or another of the remaining parameters is varied. One such curve, see Ref. (44), is given in Fig. 10-6, which shows the effect of steady-state temperature sensitivity $j \equiv (\partial \ln \bar{m} / \partial \ln \bar{T}_c)_p$ ($\bar{T}_c \equiv$ initial propellant temperature) on the frequency dependence of the real part of the dimensionless admittance y , when the pressure sensitivity μ defined in Eq. 10-61 is 0.5 and when other parameters are assigned values (44). The single broad band of frequencies favoring amplification in the vicinity of 10^3 to 10^4 cps is typical of the predictions of Ref. (44) and also of many experimental results in Chapter 9. Quantitative comparison of this theory or of its extensions with experiment, has not been attempted and generally has not been possible because of lack of sufficient propellant property data to evaluate the parameters of the theory.

Critics of the theory of Ref. (44) often claim that it is not useful because of the large number of parameters that it contains. This is not a very tenable objection since the parameters can all be evaluated experimentally, more easily than can the parameters of time lag theories. The primary drawback of the theory appears to be that the mechanistic model of Fig. 10-5 may not represent the combustion processes very well. An appealing ground for objection to the model is the observation that diffusion phenomena are left out of it entirely. However, we feel that accounting for diffusion would not affect the results very much because of the similarity between diffusion and heat conduction. Instead, we believe that the artificial separation of the gas-phase combustion zone into a heat conduction zone and a flame surface may well be the primary source of inaccuracies. Indeed, it is possible that more realistic treatments of the gas-phase combustion zones of homogeneous propellants may produce fewer parameters that influence y and may make it somewhat less likely to find conditions of strong acoustic amplification (see Section 5.5).

5.4.2. Extensions - The model of Hart and McClure was extended in Ref. (45) to include the effects of compressibility and thermal expansion of the propellant; Ref. (44) treats the solid density as a constant. Aside from these two generalizations, the approach is essentially the same as in Ref. (44). The results show that compressibility and thermal-expansion effects both tend to decrease the real part of y and that the former effect is the larger of the two. The decreased tendency toward amplification is not very great, since $\text{Re } y$ is seldom changed by more than 10%.

A further extension reported in Ref. (34) is aimed at including in the analysis effects of isobaric temperature variations ('entropy waves') produced in oscillatory combustion zones and transported downstream at the convective velocity of the gases. This study has been mentioned earlier, at the end of Section 5.2.1, where it is indicated that the results affect the $1/\gamma$ term and not the y appearing in Eq. 10-60. The model of Ref. (34) differs from that of Fig. 10-5 in that a distributed 'product gas near zone' is added just downstream from the flame surface. It is stated that there are two admittances, one for this nonisentropic near zone and the other for the isentropic 'far zone' located downstream from the near zone; the results appear to predict that both admittances have modified values of the $1/\gamma$ term. The existence of two spatial admittances is probably a peculiar property of the model. Conditions vary continuously through a real flame zone, thereby producing a continuous x variation of admittance, with the limiting value as $x \rightarrow \infty$ governing acoustic amplification. It is suggested (34) that both admittances are amenable to experimental measurement, but to us it seems questionable that the inner one would be defined in a real flame and unlikely that the flame zone would be sufficiently stratified and ex-

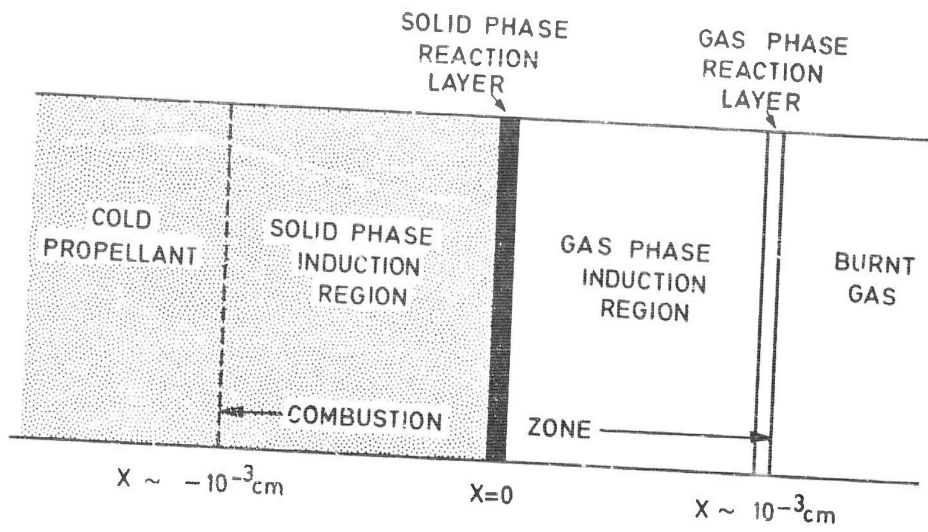


Fig. 10-5 Mechanistic model of one-dimensional combustion zone, (45).

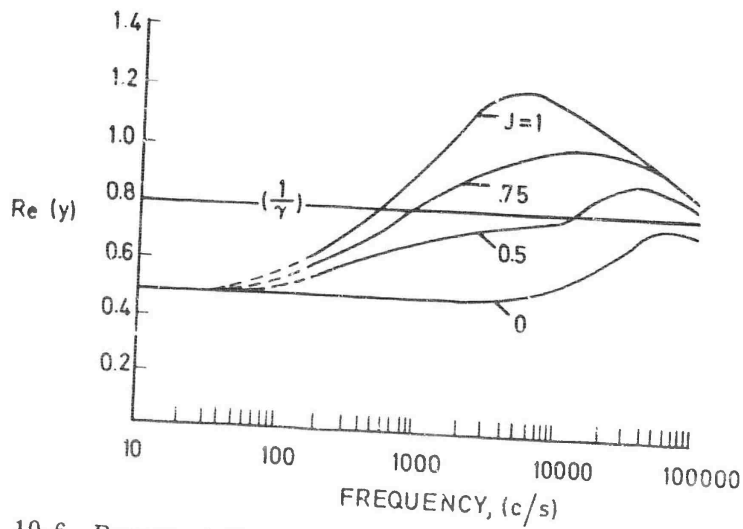


Fig. 10-6 Representative influence of steady-state sensitivity to conditioning temperature on frequency dependence of real part of dimensionless acoustic admittance, (44).

tended to permit it to be measured. However, we have a deeper reason for objecting to the approach of Ref. (34). Counting equations and boundary conditions in the distributed-zone models of Section 5.5 reveals that only y , not the $1/\gamma$ term in the 'far zone' can be determined from the full formulation. In other words, it does not appear to be possible even in principle for the combustion zone response to affect the $1/\gamma$ term without violating the basic premise that the process is one of boundary amplification rather than homogeneous amplification i.e., combustion zone thin compared with wave length. Our present view is therefore that this finding of Ref. (34) is traceable to a hidden overdeterminancy of the model employed. These conclusions are only tentative, however, because we have not studied Ref. (34) thoroughly enough to be certain of our interpretation.

The final extension of the mechanistic model of Ref. (44) that we wish to mention here is the inclusion of radiative energy transfer from the hot propellant gases to the surface of the solid (46). Radiant emission is treated in a gray-gas approximation by means of a perturbation technique, in which the small expansion parameter is the ratio of the radiative to convective heat flux to the surface of the solid; absorption is assumed to occur in a surface layer of negligible thickness. These physical assumptions appear to us to be the most reasonable ones to employ in order to make the complex radiative transfer problem tractable. Therefore, we tend to believe the qualitative trends predicted by the analysis. The principal result is that the effects of radiation on both the magnitude and the real part of the dimensionless admittance y are greatest at low burning rates and for low oscillation frequencies. Resulting response curves (47), indicate that consideration of radiation usually tends to increase the tendency toward acoustic amplification.

5.5. Aerothermochemical Approaches

5.5.1. Low-Frequency Response - In the absence of radiant heat transfer to the solid, the low-frequency response of the interfacial combustion zone is usually controlled by the heat conduction process inside the solid. Order-of-magnitude estimates indicate that a characteristic heat-conduction response time is $(\bar{\rho} \bar{\lambda} / c \bar{m}^2)$, where $\bar{\rho}$, $\bar{\lambda}$ and \bar{c} are the mean density, thermal conductivity and heat capacity of the medium. Typically, $(\bar{\rho} \bar{\lambda} / c)$ for the solid exceeds the same quantity for the gas by one or two orders of magnitude and therefore, provided that gas diffusion times are not large compared with gas heat conduction times and that chemical times are sufficiently rapid, the heat conduction time in the solid is the largest of all characteristic times. It is therefore reasonable that at low frequencies, say below 10^3 cps which is of the order of the reciprocal of typical solid heat conduction times (10^{-3} to perhaps 10^{-4} sec), all processes can be treated as quasisteady except the heat-conduction process in the solid. This observation enables one to use more realistic combustion zone models in relatively simple theories of acoustic response. The first acoustic response analysis emphasizing the solid-phase heat conduction process alone appears to be due to Smith (48), who did not consider proper interface or gas-phase conservation equations. A greatly improved theory was given by Denison and Baum (49). Various extensions of the work of Denison and Baum have recently begun to appear.

The differential equation employed in Ref. (49) is the one-dimensional transient heat conduction equation for the temperature of the solid,

$$\rho_c c_c \frac{\partial T}{\partial t} + c_c \dot{m} \frac{\partial T}{\partial x} - \lambda_c \frac{\partial^2 T}{\partial x^2} \quad (\text{Eq. 10-63})$$

(see Eqs. 6-9 and 6-12 of Chapter 6), in which ρ_c , c_c and λ_c , the density, specific heat and thermal conductivity of the solid, are assumed to be constant. The coordinate system is chosen so that the surface of the solid remains at $x = 0$. We may investigate small-amplitude, sinusoidal oscillations about a steady-state by first introducing Eq. 10-58 and a similar equation for T , then linearizing; since the

solid is incompressible, \dot{m} will be independent of x , making \dot{m}_0 constant but \bar{T} and T_0 will be functions of x . If :

$$\xi \equiv x \bar{m} c_c / \lambda_c \quad \text{and} \quad s \equiv i \omega \rho \lambda_c / \bar{m}^2 c_c, \quad (\text{Eq. 10-64})$$

we easily obtain :

$$s T_0 + d T_0 / d \xi + (\dot{m}_0 / \bar{m}) d \bar{T} / d \xi = d^2 T_0 / d \xi^2, \quad (\text{Eq. 10-65})$$

in which the solution to the steady-state equation :

$$\bar{T} = T_i + (\bar{T}_s - T_i) e^{\xi} \quad (\text{Eq. 10-66})$$

where T_i is the constant initial temperature at $\xi = -\infty$ and \bar{T}_s is the time-average surface temperature at $\xi = 0$, implies that $d \bar{T} / d \xi = (\bar{T}_s - T_i) e^{\xi}$.

Boundary conditions for Eq. 10-65 are $T_0 = 0$ at $\xi = -\infty$, plus an interface condition at $\xi = 0$. We may derive the useful form of the interface condition as follows. First, \dot{m} is related to T_s by the surface pyrolysis hypothesis :

$$\dot{m} = B_s \exp(-E_s / R T_s)$$

with B_s and E_s presumed to be known constants (see Chapter 6 Sections 2.1.3.7 and 2.1.3.8). This formula may be used to express \bar{T}_s in terms of \bar{m} , but here we need only the linearized result for \dot{m}_0 as a function of T_{cs} , viz.,

$$\dot{m}_0 / \bar{m} = (E_s / R \bar{T}_s)(T_{os} / \bar{T}_s) \quad (\text{Eq. 10-67})$$

Next, we use the interface energy conservation equation (Eq. 6-21 of Chapter 6), and introduce the assumption that all gas-phase processes are quasisteady, so that Eq. 6-32 of Chapter 6 is applicable. This leads directly to Eq. 6-74 of Chapter 6, which we may rewrite as :

$$\bar{m} c_c (dT / d \xi)_s + \dot{m} [L_s - Q + c_p (T_f - T_s)] = 0$$

where $L_s = \bar{L}_s + (c_p - c_c)(T_s - \bar{T}_s)$, according to thermodynamics, is the heat of gasification per unit mass of reactant mixture consumed (assumed constant), c_p is the specific heat at constant pressure for the gas (assumed constant), T_f is the flame temperature and radiative energy fluxes have been neglected. The time average of this result taken with Eq. 10-66 merely defines \bar{T}_f ; the linear perturbation of the equation can be expressed in the form :

$$(dT_0 / d \xi)_s - (\bar{T}_s - T_i)(\dot{m}_0 / \bar{m}) - (c_p / c_c) T_{o1} - T_{os} = 0, \quad (\text{Eq. 10-68})$$

where T_{o1} is the complex amplitude of the flame temperature perturbation. Finally, in order to avoid the more complicated aspects of Chapter 6 Section 2.1.3, the simple approximate formula for the quasisteady gas-phase mass burning rate \dot{m} given at the end of Chapter 6 Section 2.1.3.4 may be employed :

$$\dot{m} = C p^{n/2} \exp(-E / 2R T_f),$$

where C is a constant, n is the reaction order and E is the activation energy for the gas-phase reaction. This formula, which yields :

$$\dot{m}_0/\bar{m} = (n/2)(p_0/\bar{p}) + (E/2R^\circ \bar{T}_f)(T_{of}/\bar{T}_f) \quad (\text{Eq. 10-69})$$

upon linearization, is seen from the results of Chapter 6 Section 2.1 to be only a very rough approximation to the quasisteady solution of the aerothermochemical gas-phase problem. When Eqs. 10-67 and 10-69 are used to eliminate \dot{m}_0 and T_{of} from Eq. 10-68 a surface boundary condition is obtained which involves only T_{os} , $(dT_o/d\xi)_s$, the pressure perturbation p_0 which is assumed to be given and known constants.

In order to solve Eq. 10-65 subject to the prescribed boundary conditions, one may note that a particular solution to the nonhomogeneous equation is (see Eqs. 10-66 and 10-67) :

$$-T_{os} (E/R^\circ \bar{T}_s) (1 - T_1/\bar{T}_s) e^{\xi/s}$$

and that solutions to the homogeneous equation are of the form :

$$A e^{k\xi}$$

where :

$$k^2 - k - s = 0$$

The boundary condition $T_o = 0$ at $\xi = -\infty$ implies that $\text{Re}\{k\} > 0$ and therefore the acceptable solution to the characteristic equation is :

$$k = (1 + \sqrt{1 + 4s})/2 \quad (\text{Eq. 10-70})$$

With this value of k , the constant A can easily be adjusted to make the sum of the particular solution and the homogeneous solution satisfy the surface boundary condition. Evaluation of the resulting formula for T_o at the solid-gas interface, utilization of Eq. 10-67 to express this result as a relationship between \dot{m}_0 and p_0 and finally the introduction of Eq. 10-60, yields after a little algebra :

$$y = (n/2) b k / [k^2 - (1 + a - b)k + a] \quad (\text{Eq. 10-71})$$

where :

$$a \equiv (E_s/R^\circ \bar{T}_s)(1 - T_1/\bar{T}_s) \quad , \quad b \equiv 2 E_s c_p \bar{T}_f^2 / E c_c \bar{T}_s^2 \quad (\text{Eq. 10-72})$$

Equation 10-71 is a two-parameter formula for the dimensionless acoustic admittance $2y/n$ as a function of the dimensionless frequency k .

Curves of $\text{Re}\{2y/n\}$ as a function of (s/i) for various values of a and b , which could easily be computed from Eq. 10-71 were not given in Ref. (49) because the main concern of the work was to investigate inherent, nonacoustic instability of the combustion process instead of the acoustic response. The study shows that there is a region in the ab plane in which the system is inherently unstable; for propellants with values of a and b that fall within this region, it is not very meaningful to discuss acoustic responses. We shall return to this nonacoustic aspect of the study in Section 6. Recently, extensive admittance results have been given for a model which basically is very similar to that of Ref. (49) (see J. C. Friedly and E. E. Petersen, AIAA J. 4, 1604, 1966). These results agree qualitatively with those developed below for $a \sim 1 + b$. The analysis of Ref. (49) has been generalized by in-

roducing a linear temperature dependence of the thermal conductivity of the solid (M. Imber, AIAA J. 4, 1610, 1966).

At present, we may note that it is possible to infer how $\text{Re}\{y\}$ behaves by expanding Eq. 10-71 for small and large values of $|s|$. While there is no question about the validity of the expansion for small $|s|$, it should be remembered that the basis of this low-frequency theory becomes questionable at high $|s|$. Nevertheless, the result of the large $|s|$ expansion may provide qualitative information about the nature of the solution at intermediate values of $|s|$, where the theory is more likely to be reasonably good. The expansions are given below :

$$y = \frac{n}{2} \left[1 + \left(\frac{a-1}{b} \right) s + \frac{a^2 - (b+1)(2a-1)}{b^2} s^2 + \dots \right], \quad |s| \ll 1;$$

$$y = (n/2) b (1-i) / \sqrt{8|s|} + \dots, \quad |s| \gg 1.$$

The first of these expressions shows that as the frequency approaches zero, y approaches the quasisteady pressure exponent of the burning rate, $n/2$, thereby giving an amplification effect for $n > 0$. As ω increases from zero, $\text{Im}\{y\}$ becomes positive if $a > 1$ and negative if $a < 1$. Since $\text{Im}\{y\}$ is always negative at sufficiently large ω according to the second expression, it may be inferred that the two expansions can approximately have overlapping regions of validity only if $a < 1$, which physically is perhaps somewhat less likely to occur than $a > 1$. The second expression exhibits an amplification tendency in the high-frequency limit, the magnitude of which approaches zero as $\omega \rightarrow \infty$. The last term of the first expression implies that $\text{Re}\{y\}$ decreases as ω increases at small ω , if a is either small or large; there is a region in the neighborhood of $a = 1 + b$ where $\text{Re}\{y\}$ increases with increasing ω at small ω . For $a \ll 1$, it seems likely from these results that $\text{Re}\{y\}$ is a monotonically decreasing function of ω with its maximum value at the quasisteady limit $\omega = 0$. For $a \approx 1+b$, there must be at least one peak value of $\text{Re}\{y\}$ which exceeds the quasisteady value. For $a \gg 1$, the situation is not clear from the expansions, in that there may or may not exist an intermediate range of frequencies over which $\text{Re}\{y\}$ exceeds its quasisteady value. The qualitative character of the curve of $\text{Re}\{y\}$ as a function of ω appears to depend more strongly on the value of a than on the value of b . All values of a considered in Ref. (44) were greater than unity (~ 10 or 20), and this may account for the fact that Ref. (44) generally found peak values of $\text{Re}\{y\}$ that were appreciably above the quasisteady values.

5.5.2. Response at Arbitrary Frequencies - Two pertinent objections that can be raised against the preceding low-frequency theory are first that it is restricted to low frequencies and second that the quasisteady solution employed for the gas-phase problem (Eq. 10-69) is somewhat primitive according to the standards set in Chapter 6 Section 2. To remedy either of these objections adequately will almost certainly require going to numerical computations at an earlier stage in an analysis. Although the second objection can certainly be corrected more easily than the first, it seems reasonable to attempt to remedy both simultaneously if extensive numerical computations are to be employed. In this section we give the pertinent governing equations, first derived in Ref. (50), which will have to be solved numerically in such an approach. No effort has been made to obtain numerical solutions yet.

The physical system studied in Ref. (50) is the time-dependent generalization of the Johnson-Nachbar model which was described in Chapter 6 Section 2.1.3.1. It will be recalled that the same essentials, a surface pyrolysis and a one-step gas-phase reaction, appeared in the model of the previous section. Besides tractability, a good reason for treating this model is some success with steady-state burning of pure ammonium perchlorate; thus, the response theory might be tested experimentally by experiments on ammonium perchlorate.

Equation 10-63 is the only nontrivial conservation equation for the solid phase, under the assumption that mechanical vibrations of the solid are negligible. The one-dimensional, unsteady forms of the gas-phase conservation equations are easily written down from Eqs. 6-7 to 6-10 of Chapter 6 and the momentum equation is easily shown by order of magnitude estimates, to reduce to the statement that the pressure p is independent of x ; differential forms of all of the other gas-phase conservation equations remain. Equations 6-11 to 6-18 of Chapter 6 provide necessary subsidiary relationships and all of the assumptions, e.g., binary diffusion of Chapter 6 Section 2.1.3.2, excluding the steady-state assumption, are introduced. We might note that to assure their validity, all equations are written in an inertial frame in which the velocity of the constant-density solid is constant. This causes the location of the solid-gas interface to vary sinusoidally about its mean position $x = 0$ and the motion must be accounted for in the simplified forms of Eqs. 6-19 to 6-22 of Chapter 6, the solid-gas interface conditions, used in the analysis. A term involving motion of the surface also enters into the surface pyrolysis law and the motion makes it necessary to give some thought to assuming that temperature and pressure is continuous at the interface. In addition to these interface conditions, the boundary condition $T \rightarrow T_i = \text{const.}$ at $x = -\infty$ is specified and isentropic, frozen-composition sound-wave boundary conditions are imposed on p , T , ρ and Y_i at $x = +\infty$, with $p(t)$ at $+\infty$ presumed to be prescribed. With the steady-state solution known from Chapter 6 Section 2.1.3, it is then possible to derive a set of linear, ordinary differential equations with variable coefficients for the complex perturbation amplitudes associated with sinusoidal oscillations of any given frequency ω . Solution to these equations, subject to the specified boundary and interface conditions, will yield in particular \tilde{m}_{0f} , the value of the complex mass flux perturbation at $x = \infty$. The ratio of \tilde{m}_{0f} to the prescribed p_0 gives directly the desired admittance.

The derivation and even the initially resulting complete set of linear equations are too lengthy to be reproduced here. Nevertheless, a partial solution to the set may be obtained analytically. Thus, since the coefficients in the heat conduction equation for the solid are constant, an analytical solution for T in the condensed phase can be obtained and the result is essentially the same as that of the previous section. Furthermore, since no external forcing function is applied directly to the species mass fractions and since equal diffusivities is postulated, one would expect that even in the time-dependent case, all mass fraction perturbations would be simply expressible in terms of the perturbation of mass fraction of a principal reactant. This expectation is borne out. After these eliminations are made, only three linear, nonhomogeneous, ordinary differential equations with variable coefficients remain. These are the perturbation form of the first-order overall continuity equation for the gas, the perturbation form of the second-order equation for conservation of the principal reactant in the gas and the perturbation form of the second-order energy conservation equation in the gas. This fifth-order system has five independent boundary conditions, two at $x = \infty$ (subscript f) and three at $x = 0$ (subscript s). The equations and boundary conditions are given below :

$$\begin{aligned} \tilde{p}s(\tilde{p}_0 - \tilde{p}T_0) + d\tilde{m}_j/d\xi &= 0, \\ \tilde{p}sY_j + dY_0/d\xi - d^2Y_0/d\xi^2 + \tilde{m}_0 d\bar{Y}/d\xi &= -w_Y Y_0 - w_T \tilde{T}_0 - w_p \tilde{p}_0, \\ \tilde{p}s(\tilde{T}_0 + qY_0) + d(\tilde{T}_0 + qY_0)/d\xi - d^2(\tilde{T}_0 + qY_0)/d\xi^2 &= s\tilde{p}_0(\gamma - 1)/\gamma, \end{aligned} \quad \left. \begin{array}{l} \\ \\ \end{array} \right\} \text{(Eq. 10-73)}$$

with :

$$\begin{aligned} Y_{0f} &= 0, & \tilde{T}_{0f} &= \tilde{p}_0(\gamma - 1)/\gamma, \\ sE'\tilde{T}_{0s} &= \tilde{m}_{0s}(s + hE'/\rho'), \end{aligned} \quad \left. \begin{array}{l} \\ \\ \end{array} \right\} \begin{array}{l} \text{(Eq. 10-74)} \\ \text{cont'd on} \\ \text{p. 653)} \end{array}$$

$$\begin{aligned}
 (dY_0/d\xi)_s &= Y_{0s} - \tilde{m}_{0s} h_i/q, \\
 (d\tilde{T}_0/d\xi)_s &= [1 - (c'/2)(1 - \sqrt{1 + 4\beta\rho's})] \tilde{T}_{0s} \\
 &\quad + 2\tilde{m}_{0s} (1 + \sqrt{1 + 4\beta\rho's})^{-1} [h(1 - \beta c') - (\ell/2)(1 - \sqrt{1 + 4\beta\rho's})] .
 \end{aligned}
 \tag{Eq. 10-74}$$

In these equations, s and ξ are defined as in Eq. 10-64, except that the steady-state gas properties at $x = \infty$ replace the solid properties ρ_c , λ_c and c_c . The tilde indicates that a quantity has been made dimensionless by dividing it by its steady-state value at $x = \infty$. The quantity Y is the mass fraction of the principal reactant. The notation w_Y , w_T and w_p stands for the steady-state partial derivatives $(\partial \bar{w}/\partial Y)_{p,T}$, $\bar{T}_f(\partial \bar{w}/\partial T)_{p,Y}$ and $\bar{p}(\partial \bar{w}/\partial p)_{T,Y}$, where $\bar{w}(p, T, Y) c_p \bar{m}^2/\lambda_g$ is the local mass per unit volume per second of the principal reactant consumed in the steady state. Other notation is: $c_p \bar{T}_f q \equiv$ gas phase heat release per unit mass of principal reactant consumed.

$c' \equiv c_c/c_p$, $\rho' \equiv \rho_c/\bar{\rho}_f$, $\beta \equiv \lambda_c c_p/\lambda_g c_c$, $\gamma \equiv$ specific heat ratio for gas, $E' \equiv E_s \bar{T}_f/R^\circ \bar{T}_s^2$ the dimensionless activation energy for pyrolysis, $c_p \bar{T}_f h \equiv$ steady-state enthalpy change in going from solid at initial temperature T_i to gas at temperature \bar{T}_s , $c_p \bar{T}_f \ell \equiv$ heat of gasification per unit mass. In writing Eq. 10-74, it is assumed that the solid density is large compared with the gas density at the interface and that the steady-state gas-phase chemical reaction rate is negligibly small at the interface.

Since Eqs. 10-73 and 10-74 are complex, they are actually equivalent to a tenth-order system in real variables. The variable coefficients in the differential equation enter through ρ , $d\bar{Y}/d\xi$ and the w derivatives; they are known from the steady-state solution but in general are available only numerically. To obtain a numerical solution to Eqs. 10-73 and 10-74 is a challenging problem. Simplifications can, of course, be made through suitable choices of values for the various parameters but it appears that in any case accurate numerical calculations would be quite lengthy.

In Ref. (50) an approximate analytical solution to Eqs. 10-73 and 10-74 is extracted for the limiting case of low-frequency response of a system, with a high activation energy for the gas-phase heat release process. The restriction to high activation energies causes the steady-state pressure exponent of the burning rate to vanish, so that the results can be applicable only for 'mesa' type propellants; they may also be approximately correct for pure ammonium perchlorate at sufficiently high pressures. In the low-frequency regime, in order to approximate mesa propellants the theory of the preceding section must take $n = 0$ and then predicts that $y \equiv 0$. What we are investigating here is the extent to which an approximation for the gas-phase region which differs from that of Section 5.5.1 can alter the null result. It is found (50) that the result is not altered very much at all. The value of $|\text{Re}\{y\}|$ is found to remain below roughly 10^{-2} in the region where the low-frequency approximation is valid, for systems with reasonably assigned parameter values. As ω increases from zero, $\text{Re}\{y\}$ is found to first drop to very small negative values then return to zero and begin to become positive and somewhat larger in magnitude as the low-frequency approximation begins to fail. These results are said to involve a 'totally unrealistic and misleading overapproximation' (5). The results certainly are unrealistic for propellants other than mesa-type and the approximation will be misleading, if this restriction is not borne in mind.

It is clear that much work remains to be done in obtaining unobjectionable theoretical predictions of the acoustic response of homogeneous propellants.

5.6. Models for Heterogeneous Propellants

It appears that only three investigators have addressed themselves specifically to

the problem of acoustic amplification by heterogeneous propellants. Cheng studied a two-constituent system in which one of the constituents burns throughout the chamber volume, producing homogeneous rather than surface amplification; this work has been referred to in Section 5.1 and will not be discussed here. It was indicated in Section 5.3.2 that Barrère extended the analysis of Green and Nachbar to account for propellant heterogeneities in an approximate way; the elements of this extension are discussed briefly in the following paragraph. Finally, Wood (51) proposed and analyzed a model which accounts for variations in stoichiometry, during oscillatory combustion of composite propellants. Most of this section will be concerned with Wood's work.

Barrère and Bernard (43) suggest that one way to account for propellant heterogeneities in the model of Refs. (40) and (42) is to allow the time lag τ for the gasification rate response to vary in a random way over the surface of the propellant. This is accomplished by introducing a probability ξ , which lies between 0 and 1 and which is defined with respect to the random variable τ . The function $\xi(\tau)$ is the probability that the value of the time lag lies between 0 and τ . The gasification rate which should appear in the analyses of Refs. (40) and (42) then becomes :

$$\dot{m}(t) = \int_0^1 \dot{m}(t, \xi) d\xi = \int_0^1 B_s e^{-E_s/R} [t - \tau(\xi)] d\xi ,$$

where the inverse function $\tau(\xi)$ is assumed to exist. In Ref. (43), this equation is linearized and used in an analysis which otherwise is the same as that of Refs. (40) and (42). Results are obtained for a number of physically reasonable probability functions $\xi(\tau)$. The conclusion drawn in Ref. (43) is that, in general, the introduction of a distribution of time lags decreases any tendency toward 'resonance' deduced in Refs. (40) and (42) and discussed later in Section 6.2.

Wood (51) obtained expressions for the acoustic admittance of composite propellants containing two constituents (oxidizer O and binder B) which gasify independently. He points out that there is a characteristic time for the burning propellant surface to regress a distance equal to the diameter of the average oxidizer particle, which may lie between 2×10^{-4} sec (for 2 micron particles in a propellant whose mean burning rate is 1 cm/sec) and 2×10^{-1} sec (for 200 micron particles in a propellant whose mean burning rate is 10^{-1} cm/sec), and which perhaps is typically of the order of 2×10^{-3} sec. When the oscillation period is long compared with this time, many new oxidizer particles are exposed during a cycle, thereby causing the overall stoichiometry to be approximated reasonably well during a cycle by its constant average value for steady-state combustion at the instantaneous chamber pressure. Thus, at low frequencies :

$$A_O \dot{m}_O / A_B \dot{m}_B = \nu ,$$

where \dot{m}_i is the mass flux of species i gasifying from the propellant surfaces on which species i is exposed, A_i denotes the propellant surface area that is covered by species i and ν is the oxidizer-fuel mass ratio in the bulk of the propellant. On the other hand, when the oscillation period is short compared with this time, then there is a negligible change in the exposed surface area of each constituent during a cycle and periodic oscillations in overall stoichiometry may develop, if the oscillatory pressure responses of the gasification rates of both species are not related in such a way that the ratio \dot{m}_O / \dot{m}_B remains constant during the cycle. The condition for maintaining constant stoichiometry at high frequencies may therefore be expressed as $\overline{\dot{m}_{O0}} / \overline{\dot{m}_{B0}} = \overline{\dot{m}_{BO}} / \overline{\dot{m}_{BB}}$, where the bar denotes the time-average value and the subscript o again identifies the complex amplitude; only for special propellant combinations will this condition be satisfied. Reference (51) addresses the question of

what the effects on the surface-average propellant admittance will be when this condition is not satisfied.

The model of Ref. (51) postulates independent gasification of species O and B, followed by gas-phase mixing and combustion of O and B. The gas-phase processes are all assumed to be rapid enough for a quasisteady treatment of them to hold; thus, the analysis is inapplicable at very high frequencies. Instantaneous surface gasification rates of each species are assumed to be given by :

$$\dot{m}_f / \dot{m}_i = (p/\bar{p})^{\mu_i} ,$$

where both μ_i are constants. The total binder surface area A_B is assumed to be constant and the binder regression rate is taken as that of the propellant. The oxidizer particles are taken to be spheres which are released by the propellant at a rate (number per unit propellant area per second) determined by the binder regression rate. The sphere radius at the time of release is taken to be constant and the sphere radius is assumed to decrease with time at the regression rate of the oxidizer. Certain generalizations of these assumptions are also considered in Ref. (51) e.g. variable binder surface area and binder regression rate differing from propellant regression rate, but the corresponding results will not be discussed here.

Space limitations prevent us from giving the analysis of Ref. (51) here. The result is :

$$y = \mu_B + \nu (\mu_O - \mu_B) [(1 + \nu)^{-1} + (\alpha - \beta)] \psi , \quad (\text{Eq. 10-75})$$

where α and β are the isobaric, quasisteady composition sensitivities :

$$\alpha \equiv \partial \ln T_f / \partial \nu , \quad \beta \equiv \partial \ln m_f / \partial \nu$$

where $T_f \equiv$ flame temperature and $m_f \equiv$ mean molecular weight of final reaction products and where :

$$\psi = 1 + (3/i) \left(\frac{1}{\omega \tau} - \frac{2i}{\omega^2 \tau^2} - \frac{2}{\omega^3 \tau^3} + \frac{2 \exp(i\omega \tau)}{\omega^3 \tau^3} \right) ,$$

in which ω is the frequency and τ is a characteristic burning time of an oxidizer sphere, defined as the ratio of the initial sphere radius r_0 to the mean oxidizer regression rate \dot{m}_0 / ρ_0 . The value of $\text{Re} \{\psi\}$ goes monotonically from 0 at $\omega \tau = 0$ to 1 as $\omega \tau \rightarrow \infty$. Furthermore, for most current propellants the quantity in the square brackets in Eq. 10-75 is positive (51). It follows that the sign of the difference between $\text{Re} \{y\}$ and its quasisteady value μ_B is the same as the sign of $\mu_O - \mu_B$; i.e., at frequencies comparable with or greater than $1/\tau$, stoichiometry fluctuations produce increased amplification if $\mu_O > \mu_B$ and decreased amplification if $\mu_O < \mu_B$. Assuming that μ_O is the pressure exponent for the linear deflagration rate of the pure oxidizer, one may estimate the magnitude of the effect of stoichiometry fluctuations. Reference (51) gives numbers for a propellant combination with $\mu_O = 1.2$ and $\mu_B = 0.6$ which indicate that the effect can be quite large at frequencies above 10^3 cps for ammonium perchlorate oxidizer particles larger than about 20 microns in diameter.

In view of the primitive state of our present understanding of steady-state combustion mechanisms of heterogeneous propellants (Chapter 6 Section 4), it is not surprising that there are many theoretical uncertainties concerning their acoustic response. The different complexions of the models adopted in Refs. (43) and (51) underscore these uncertainties. Thus, propellant constituents are distinguished only by assigning them different gasification time lags in Ref. (43), while the pyrolysis law of Ref. (43) is not even considered in Ref. (51) where gasification instead is assumed to be

expressible in the usual empirical form $\dot{m} \sim p^n$ for each constituent independently. There is very little basis for either of these assumptions. The use of a time lag in the conventional pyrolysis formula has not been justified from first principles and in any event it would seem to be desirable to permit different constituents to have different activation energies and frequency factors in the analysis of Ref. (43). Similarly, the p^n dependences, if at all applicable for individual constituents, certainly must conceal many fluid mechanical and chemical kinetic mechanisms. These statements are not meant to detract from the work in Refs. (43) and (51); in our current state of ignorance nothing better could be offered. The comments are intended merely to emphasize that there is doubt about the physical meaning of the results.

5.7. Small-Amplitude Erosive Effects

5.7.1. Introduction - At the outset of any discussion of erosive phenomena, one must distinguish between steady-state erosive velocities and acoustic oscillatory erosive velocities. Depending on the motor geometry and the excited acoustic mode, either type of erosion may occur in the absence of the other, or both may occur together. First we consider steady-state erosion in the absence of acoustic erosion, next acoustic erosion alone and finally combined effects. Our principal conclusion will be seen to be that at present there exist no theories of acoustic response for any type of erosive conditions.

5.7.2. Acoustic Response with Steady-State Erosion - Radial modes in cylindrical motors with tubular grains constitute one example for which erosively burning charges respond to acoustic pressure oscillations, in the absence of any oscillations in the component of velocity parallel to the surface. A few theoretical analyses exist for steady-state erosive burning; these are based on the boundary-layer approximation for the velocity field and have been reviewed in an earlier chapter. A reasonable approach to the problem at hand would be to introduce a small-amplitude, sinusoidal pressure oscillation into the models employed in these theories and to calculate the resulting time-dependent velocity normal to the surface at the outer edge of the boundary layer. Such calculations would be difficult, but not prohibitively so. Calculations of this type have been completed recently for fuel surfaces burning in oxidizer streams, but the premixed character of the combustion in the boundary layer of a solid propellant would make the calculations more difficult. Nevertheless, the time is near when these acoustic response calculations for specific models of erosive burning can reasonably be attempted. The theory of Ref. (40) and its generalizations may be thought of as accounting for erosion in a sense, because the gas layer across which heat is transferred for this model apparently is thought of as a fluid dynamical boundary layer. However, the treatment of this layer in the theory is too crude for useful predictions to be made, concerning the effect of erosion on acoustic response.

Unfortunately, the boundary-layer approximation, on which existing steady-state erosive burning theories are based, is not valid everywhere on the surface of the grain. At the upstream end of a tubular charge, steady erosive velocities usually go to zero and there can be an appreciable part of the motor over which the erosive velocities are too small for the use of boundary-layer theory. The controversial phenomenon of 'negative erosion' pertains to these regions. No acceptable models of steady erosive burning exist for these regions and therefore response calculations cannot yet be attempted for them.

5.7.3. Acoustic Erosion Without Steady-State Erosion - Transverse modes in an end-burning, cylindrical motor give rise to acoustic erosive velocities even though the steady-state erosive velocity vanishes. The intuitively expected influence of such purely acoustic erosion on propellant response is peculiar. It is reasonable to assume by symmetry that the burning rate depends only on the local magnitude

but not the direction of the erosive velocity vector and its time derivatives. If this assumption is true under oscillatory conditions, then sinusoidal erosive velocity oscillations of frequency ω produce a burning rate response at frequency 2ω and also higher harmonics at frequencies $2n\omega$ ($n = 2, 3, \dots$), but no response at the original frequency ω . These conclusions follow directly from the Fourier cosine expansion of $|\cos \omega t| = [(1 + \cos 2\omega t)/2]^{1/2}$. Although harmonic generation is characteristic of nonlinear phenomena, in the present problem it can arise from a linear dependence of \dot{m} on $|u|$, the absolute value of the erosive velocity. Such a linear dependence has usually been assumed to exist for sufficiently small values of $|u|$ (52), thus giving rise to a linear proportionality between the erosive component of the burning rate response and the magnitude of the amplitude of the erosive velocity oscillation $|u_0|$ under the present conditions. This linearity tempts one to term the phenomenon 'linear' in spite of its nonlinear attributes, but upon noting that the proportionality to $|u_0|$ has little or no physical basis (e.g., response proportional to $|u_0|^m$ with $m \neq 1$ at low amplitudes is equally acceptable), one realizes that the phenomenon is essentially nonlinear in all ways. Thus, small-amplitude, acoustic erosion in the absence of steady-state erosion is a non-linear effect which intuitively cannot contribute to acoustic admittance because of the absence of a Fourier component at frequency ω .

This nonlinear phenomenon might be important because it can conceivably come into play at lower amplitudes than other nonlinear phenomena. Some of its possible effects on motor stability are discussed (53), to which some corrections and extensions are made (54). The conclusions of Ref. (53) are that there are conditions under which a linearly stable motor can become nonlinearly unstable by this mechanism and there are also conditions under which the mechanism can cause a linearly unstable motor to achieve a time-independent limiting amplitude of oscillation. It should be remembered that the detailed reasoning involved in these deductions is highly speculative. Since no theories of steady erosive burning exist for small erosive velocities, it is not surprising that no theories exist for the burning-rate response to acoustic erosion in the absence of steady-state erosion.

5.7.4. Combined Steady-State and Acoustic Erosion - There are numerous instances e.g., axial or tangential modes in cylindrical motors with tubular grains, in which steady-state erosion and acoustic erosion are superimposed. In view of the complicated nonlinearities associated with purely acoustic erosion, one might expect that combined effects would be complex and nonlinear. In general they are. For example, if the acoustic erosive velocity vector is normal to the steady erosive velocity vector, then the attractive hypothesis that the burning rate is independent of the direction of the local erosive velocity vector again leads to the conclusion that acoustic erosion generates harmonics but produces no burning-rate response at the applied acoustic frequency. One expects to find Fourier components of the burning rate response at the applied frequency only when there is a component of the acoustic erosive velocity parallel to the steady erosive velocity, e.g., longitudinal modes inside tubular grains.

There is one limiting case of combined steady-state and acoustic erosion which is relatively simple in that the time-dependent effects are truly linear. This is the case in which the magnitude of the velocity amplitude vector for acoustic erosion is small compared with the magnitude of the steady-state erosive velocity. Provided that the steady erosive velocity is high enough for the boundary-layer approximation to be applicable, the burning-rate response in this limiting case can be analyzed by the same methods and with the same degree of complexity discussed in the first paragraph of Section 5.7.2. The result of the calculation would be an admittance formula containing two types of terms, one corresponding to Section 5.7.2, giving the pressure response and the other proportional to the ratio of acoustic erosive velocity to pressure amplitudes, giving the acoustic erosive response. By treating acoustic erosive velocities that are perpendicular to the steady erosive velocity in

such an analysis, one could either verify or disprove the hypothesis of directional independence of the burning-rate response for the adopted model of the combustion zone. By treating acoustic erosive velocities that are parallel to the steady erosive velocity in such an analysis, one could obtain acoustic-erosion admittance formulas for the only conditions under which everyone agrees that there should exist a purely linear effect of acoustic erosion on response. Even in this case, one might ask how acoustic energy at the given frequency fed into the cavity, in such a way that its acoustic velocity vector is normal to the burning surface (as always occurs in boundary-layer response) can be redistributed into the original chamber mode, in which a component of the acoustic velocity is parallel to the burning surface and whether there are appreciable losses associated with the redistribution.

Although no analyses of linear acoustic erosive response have been presented, a discussion of possible linear erosive effects on motor stability is given (52). The discussion is based on assumptions which are equivalent to the statement that for sinusoidal waves the burning rate can be expressed as the real part of :

$$\dot{m} = \bar{m} + (\partial \dot{m} / \partial p) p' + (\partial \dot{m} / \partial |\bar{u}|) |\bar{u}| + (\partial \dot{m} / \partial u') u' , \quad (\text{Eq. 10-76})$$

where $|\bar{u}|$ is the magnitude of the steady-state erosive velocity, u' is the complex component of acoustic erosive velocity which is parallel to the steady erosive velocity ($|u'| < |\bar{u}|$ by assumption), p' is the complex pressure perturbation, \bar{m} and $(\partial \dot{m} / \partial |\bar{u}|)$ are evaluated for zero steady erosive velocity and for zero oscillation amplitude. The other two partial derivatives may be complex and depend on frequency as well as on steady, nonerosive conditions. Thus steady erosion, in addition to acoustic erosion, is assumed to be expressible in a linearized manner; it is not clear to what extent this questionable assumption is essential to the development or to the results. A conclusion (52) is that for internally burning tubular grains, the linear erosive effects are appreciably different for end-vented chambers than for side-vented chambers oscillating in odd longitudinal modes; in the former case steady erosion is found to be more important than acoustic erosion, while the opposite is found in latter case. An indication is also obtained that acoustic erosive velocities may dominate stability when the frequencies of two different natural modes of the chamber coincide, provided that the combined effects of the two modes correspond to neutral stability in the absence of acoustic erosion ('degeneracy'). Thus, it is possible to draw a few tentative conclusions without knowing what the linear, acoustic, erosive response of the propellant is.

When local sinusoidal acoustic erosive velocities are parallel to the local steady-state erosive velocity but are not always small compared with it, an interesting sequence of events may occur. If linear amplification occurs, the acoustic erosion may gradually build up until its amplitude reaches and eventually becomes much larger than the steady erosive velocity. In the course of this buildup, more and more energy may be transferred from the original frequency ω to higher harmonics by the acoustic erosive effect. This rate of energy removal may eventually balance the linear amplification rate, so that a steady amplitude is reached for oscillations at the original frequency under conditions such that the acoustic oscillations in the bulk of the chamber are still well within the linear range. Similar balances may develop for all of the harmonics, so that a steady linear condition is reached in which the amplitudes of all harmonics are constant, independent of time. A mechanism of this type was described (55) for Rijke tube oscillations. By itself, it would not appear to produce peak amplitudes of oscillation that would be of practical concern in real motors. See Ref. (53) for discussions of this and other mechanisms.

6. Theories of Nonlinear and Nonacoustic Instabilities

6.1. Introduction

We now abandon the ideas of acoustic admittance and of linear acoustic amplification

and damping and we proceed to consider specific nonlinear and/or nonacoustic mechanism for combustion instability. The possibilities are manifold but the theories are few and disconnected. We shall review existing theories under four separate headings, changes in mean burning rate (Section 6.2), inherent instabilities (Section 6.3) low-frequency instabilities (Section 6.4) and nonsinusoidal wave forms (Section 6.5). The first category is an example of a nonlinear acoustic effect, as are some of the items in the last category. Most items in the second and third categories are nonacoustic, linear phenomena. Certain theoretical aspects of nonlinear or nonacoustic phenomena have already been discussed (e.g., Section 5.7.4). The background for nomenclature, physical aspects and experimental basis is given in Chapter 9 Sections 2 and 6.

6.2. Changes in Mean Burning Rate

It has been remarked in Chapter 9 that experimentally, changes in mean chamber pressure resulting from changes in mean burning rate are perhaps more noticeable consequences of acoustic instability than are the oscillations themselves. Some theoretical effort has therefore been expended on the problem of predicting the cause and extent of changes in mean burning rate which accompany finite-amplitude, acoustic oscillations.

The most obvious candidate for producing mean burning rate changes is acoustic erosion. If steady-state erosion effects are known and the mode shape and amplitude are also known, then the magnitude of this effect can easily be estimated provided that one postulates sinusoidal and quasisteady erosive conditions. Crudely, by approximating the steady-state erosion in terms of an erosion constant k such that :

$$\bar{m}(\bar{u}) = \bar{m}(0) (1 + k |\bar{u}|) ,$$

one easily can show that the quasisteady change in mean burning rate, produced by an acoustic erosive velocity which is parallel to the steady erosive velocity, is :

$$\Delta \bar{m} = \bar{m}(0)(2k/\pi) [-|\bar{u}| \cos^{-1}(|\bar{u}|/|u_o|) + (|u_o|^2 - |\bar{u}|^2)^{1/2}] \quad (\text{Eq. 10-77})$$

for $|u_o| \geq |\bar{u}|$ and zero for $|u_o| < |\bar{u}|$. Here u_o is the complex amplitude of the acoustic erosive velocity and the angle represented by \cos^{-1} is defined to lie between 0 and $\pi/2$. This formula predicts an increase in the mean burning rate due to acoustic erosion whenever $|u_o| > |\bar{u}|$ and $k > 0$; for a given value of $|u_o|$, the largest increase occurs when $\bar{u} = 0$ and is given by $\Delta \bar{m} = \bar{m}(0)(2k/\pi) |u_o|$. The case $k < 0$ corresponds to negative steady-state erosion and leads to a quasisteady decrease in mean burning rate, due to acoustic erosion. The sign and the order of magnitude of $\Delta \bar{m}$ predicted by Eq. 10-77 often agrees with experimental measurements made at pressure nodes (see Chapter 9 Section 4.5). However, the predicted numerical value seldom agrees well with experiment and it is not expected because estimates generally indicate that acoustic erosion is not quasisteady. Unfortunately, we do not yet have any good way to estimate values of nonquasisteady effects of acoustic erosion on mean burning rates.

The only other finite-amplitude phenomenon that has received appreciable study as a possible mechanism for producing changes in the mean burning rate, is the nonlinearity of the usual surface pyrolysis law (Eq. 6-58 of Chapter 6) (40), (42). The effect is embedded in a particular model of the oscillatory combustion zone. The elements of the model were stated near the end of Section 5.3.2. A perturbation attack was adopted; the theoretical approach was to complete the linearized analysis and then to calculate the amplitude of the surface temperature oscillations for a prescribed pressure amplitude or heat-transfer coefficient amplitude.

The nonlinear mean burning rate was then computed from the formula :

$$\bar{m} = [B_s \exp(-E_s/R^\circ \bar{T}_s)] ,$$

which differs from the formula for the linear mean burning rate, $B_s \exp(-E_s/R^\circ \bar{T}_s)$ because of the nonlinearity of the exponential function. A straightforward expansion in powers of $(T_s - \bar{T}_s)/\bar{T}_s$ yields for the change in the mean gasification rate

$$\Delta \bar{m} = (B_s E_s / R^\circ \bar{T}_s) \exp(-E_s / R^\circ \bar{T}_s) (E_s / 2R^\circ \bar{T}_s - 1) [(T_s - \bar{T}_s) / \bar{T}_s]^2 + \dots ,$$

(Eq. 10-78)

where $+\dots$ signifies terms involving time-averages of higher powers of $(T_s - \bar{T}_s)/\bar{T}_s$. Equation 10-78 clearly shows that as the oscillation amplitude begins to become finite, the mean burning rate begins to increase if $E_s/2R^\circ \bar{T}_s > 1$ or decrease if $E_s/2R^\circ \bar{T}_s < 1$. Typical values of E_s and \bar{T}_s imply that an increase should usually be observed. The magnitude of $\Delta \bar{m}$ for the present model can be calculated from Eq. 10-78 provided that \bar{T}_s , the pyrolysis parameters and the oscillation amplitude of T_s are known. Since Eq. 10-78 implies that $\Delta \bar{m}$ is proportional to the square of the amplitude of T_s , effort was expended (40), (42) to find conditions called 'resonance', under which the T_s amplitude was large for moderate or small pressure amplitudes. These are the conditions for which the model predicts large changes in mean burning rate and mean chamber pressure at moderate pressure amplitudes.

The resulting formula for $(T_s - \bar{T}_s)/\bar{T}_s$ (42) reveals the qualitative and quantitative influence of various propellant and operating parameters on 'resonance'. For example, increasing B_s always promotes resonance; decreasing E_s promotes resonance substantially in the range of representative values of E_s . Furthermore, resonance never occurs in the model, if the time lag τ for gasification is either too small or too large.

The precise definition of 'resonance' that was used (42) is the condition under which linear harmonic theory predicts that the amplitude of surface temperature oscillations is infinite for nonzero amplitude of oscillation of the gas-phase heat-transfer coefficient. This condition requires that for given propellant and operating parameters, the time lag τ of the theory (Section 5.2.2) as well as the oscillation frequency ω , must both assume specific values. Since τ is supposed to be a propellant property, it is extremely unlikely that such 'resonance' would ever occur in a real propellant. The practical objective of the study was to find near-'resonant' propellant and operating conditions, for which a range of frequencies would exist over which an appreciable change in mean burning rate would occur. The qualitative dependences cited in the preceding paragraphs are approximately applicable to near-'resonances'.

The occurrence of 'resonance' according to the precise definition of Ref. (42) is generally symptomatic of more deep-rooted interpretive difficulties in linear harmonic theories. If the assumption of an harmonic time dependence is relaxed and the inherent stability of the system is investigated, it is generally found that systems with physical properties falling on one side of the resonance are inherently stable while those with properties on the other side are inherently unstable (see Section 6.3). The implication is that some of the near-'resonance' conditions found (40), (42), may correspond to systems that are inherently unstable; this inherent instability would not be revealed by the harmonic analysis employed. It is difficult to see how linear models of inherently unstable systems can properly represent real propellants because if the model were correct the propellant would not burn stably under isolation conditions and probably would never have been developed.

Thus, it is possible that some of the near-resonances (40), (42), cannot be physically meaningful. The way to test this question is to investigate the inherent stability of the system. In defense of the work of Refs. (40) and (42), it should be emphasized that the complexity of the model is such that an investigation of inherent stability would be somewhat difficult. Furthermore, inherent instabilities might occur in all of the models discussed in Section 5 but they have not been considered for any of these models except the one discussed in Section 5.5.1.

Although some gross, qualitative indications of agreement between theory and experiment are cited in Refs. (40) and (42), there are some experimental results that are difficult to reconcile with the model. For example, although it is not quite clear what physical features are intended to be ascribed to the gas-phase boundary layer, it appears that the model was intended to be constructed in such a way that it would be applicable under both steady-erosive and nonerosive conditions. If the model is assumed to be valid under nonerosive conditions, then it should agree with the observation (Chapter 9 Section 4.4) of a decrease in the mean burning rate at velocity nodes during instability. This effect can be extracted from the theory only by taking $E_s/2R^0T_s < 1$, which is possible but appears on *a priori* grounds to be rather unlikely. Another point of possible qualitative disagreement is that changes in mean burning rate are observed experimentally to accompany large-amplitude acoustic instability over broad frequency ranges, for the same propellant in chambers of different size. This behavior is inconsistent with the 'resonance'-like result of the theory. There may well exist particular propellants for which finite-amplitude changes in mean burning rate are properly described by the mechanism studied in Refs. (40) and (42). But the model certainly is not universally valid.

A variety of other finite-amplitude mechanisms can be proposed for changes in mean burning rate. One of the most naive approaches is to assume that the conventional formula $\dot{m} = a p^n$ holds under finite-amplitude, nonerosive, time-dependent conditions. An expansion of this formula about mean conditions readily yields :

$$\Delta \bar{m} = a \bar{p}^n \left[n(n-1)/2 \right] \left[(\bar{p} - \bar{p})/\bar{p} \right]^2 + \dots, \quad (\text{Eq. 10-79})$$

which predicts a decrease in the mean burning rate at finite amplitudes for the usual case of $0 < n < 1$. Although other general proposals can be made, the correct mechanism is likely to be highly specific and to depend on properties of the motor as well as of the propellant.

6.3. Inherent Instability

The steady-state solution to the conservation equations describing a model of any physical system, may be linearly unstable to small-amplitude perturbations. By this we mean that if the time-dependent conservation equations are linearized about the steady solution and are solved subject to initial conditions that differ slightly from the steady-state conditions, then as time goes on the solution diverges away from the steady solution instead of converging to it. We term any such steady-state solution as inherently unstable. Clearly, for any given model there may exist ranges of the physical parameters for which the solution is inherently unstable and other ranges for which it is inherently stable. It would seem that any model of a combustion zone can be physically realistic only for ranges of its physical parameters that correspond to inherent stability; under inherently unstable conditions, in the absence of external interactions the flame will either go out, blow up or make a transition to a regime in which some other model is required. This behavior is a property of the model itself and has nothing to do with externally applied acoustic waves. In principle, the inherent stability of the steady solution for any model of a combustion zone should be demonstrated before the model is accepted and before it is used for investigations of oscillatory instabilities. In practice, this is seldom

ever done because the inherent stability analysis is too difficult. Of all the models that we have considered so far, inherent stability has been investigated only for the model described in Section 5.5.1 (49).

We shall not present the details of the inherent stability analysis of Ref. (49). The approach is similar to that taken in Section 5.5.1; instead of seeking harmonic solutions at the outset, the Laplace transform of the governing equations with respect to time is taken. An equation which is identical in form to Eq. 10-71, is obtained for the ratio of the Laplace transform of the surface gasification rate to the Laplace transform of the pressure, with s being the Laplace transform variable. Inverting the transforms for the case of a step function in pressure at $t = 0$ yields the inherent stability; this is one of a number of possible procedures. The results are shown in Fig. 10-7, where the notation is that of Section 5.5.1. The dashed curves labeled s/i give the frequencies of inherent instabilities that grow in an oscillatory fashion. It is seen from Fig. 10-7 that the model of Section 5.5.1 and the admittances reported therein, are not physically meaningful for real propellants if the value of 'a' is too large or the value of 'b' is too small. In view of Eq. 10-72, this roughly requires that the activation energies for the surface and gas-phase processes not be too high; inherent instability sets in if either of them becomes very large.

Incidentally, Ref. (49) obtains the condition which was called 'resonance' in the preceding section (42) at the boundary of the stable region, viz., when $a + b = (a - b)^2$. Appreciable changes in mean burning rate at small oscillatory pressure amplitudes may occur for systems with physical parameters lying near this line, provided that the oscillatory frequency is in the favorable range.

In Ref. (56), a combustion zone model is considered which is more complex than that of Ref. (49) in that time-dependent heat transfer, in a gas-phase region located between the propellant surface and a flame surface, is taken into account. An analysis of the inherent stability of the system was not actually carried out in Ref. (56), but a step in this direction was taken by obtaining 'dispersion' equations. The character of the approach is appropriate for investigating inherent stability but not acoustic response.

6.4. Low-Frequency Instability and Chuffing

The background for discussing low-frequency instabilities and chuffing is given in Chapter 9 Section 6.4. Here we consider first a few theoretical aspects of linear phenomena and then nonlinear phenomena.

The recent linear theories for the onset of low-frequency instability are reviewed briefly in Chapter 9 Section 6.4.4; the analyses are developed in Refs. (57-59). The specific models employed in Refs. (57-59) for the combustion process are quite similar to that presented in Ref. (49) and developed in Section 5.5.1; the only differences lie in the way in which the quasisteady gas-phase flame is treated (and, for Ref. (59), in brief consideration of an equilibrium interface condition in place of Eq. 10-67). In Ref. (58), for example, use of the overall energy balance (Eq. 10-68) and of the flame speed formula (Eq. 10-69) is avoided by essentially assuming that the rate of heat transfer from the gas to the surface of the solid is proportional to p^{2n}/\dot{m} , where 'n' is the empirical pressure exponent of the burning rate. This assumption leads to a linear relationship for \dot{m}_0 in terms of p_0 and $(dT_0/d\xi)_s$ which is said to define quasisteady gas-phase behavior. Rather than treating the inherent stability of this combustion zone model, the authors of Ref. (58) couple the combustion behavior to the chamber response by means of the overall mass balance :

$$A_b \dot{m} = A_t \dot{m}_t + d(\rho_g V)/dt \quad ,$$

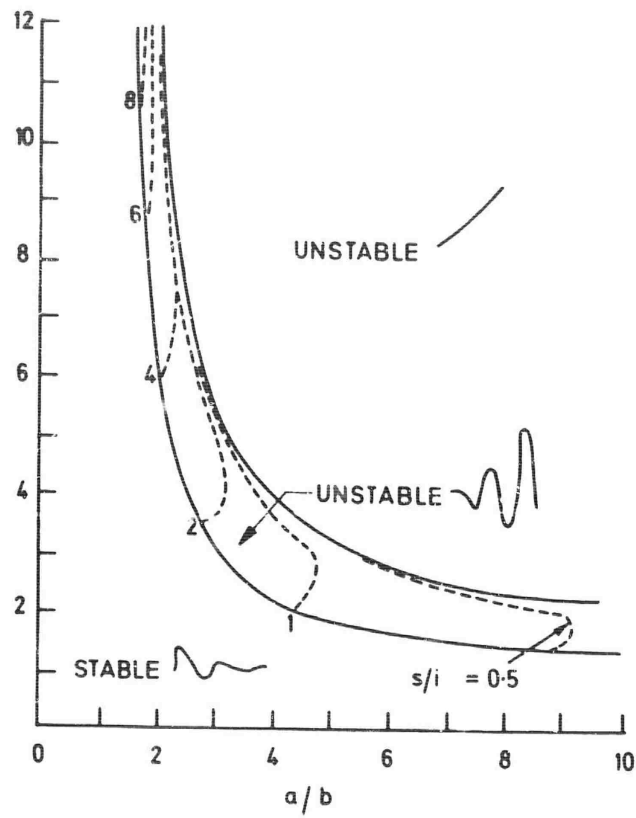


Fig. 10-7 Inherent instability: stable and unstable regions; s/i = frequency of oscillatory instability, (49).

where A_b is the surface area of the burning propellant, A_t is the throat area of the nozzle, \dot{m}_t is the mass flux through the nozzle, ρ_g is the density of the chamber gases and V is the chamber volume. Under the assumptions that pressures everywhere in the chamber are the same and that $\dot{m}_t \sim p$ and $d\rho_g/dt \sim dp/dt$, the linearized form of the mass balance is :

$$\dot{m}/\bar{m} = (p_0/\bar{p})(1 + K s) \quad , \quad (\text{Eq. 10-80})$$

where s is given in Eq. 10-64 and K is a dimensionless parameter which is proportional to the value of the characteristic length $L^* \equiv V/A_t$ of the motor, multiplied by the square of the mean burning rate. The use of Eq. 10-80 along with the modified version of Eq. 10-71 which results from the combustion model, yields a relationship for ' s ' which can be studied in order to determine the stability of the coupled system. The method of Nyquist was used (58) to investigate the stability of the coupled system. The results were discussed in Chapter 9 Section 6.4.4 and were shown in Fig. 9-20 of Chapter 9. The two stability limit lines shown in Fig. 9-20 correspond to two critical values of the dimensionless parameter K appearing in Eq. 10-80. These critical values for the coupled system are analogous for the problem of combustion-zone response to the resonances of Ref. (42) and to the inherent stability limits (49). For each critical value of K there is a nondimensional natural oscillation frequency of the coupled system, which is neither damped nor amplified. In Ref. (59), consideration of the troublesome gas-phase part of the combustion model is avoided by introducing an empirically inferred phase relationship between pressure oscillations and oscillations of the rate of heat transfer to the surface of the propellant, thereby permitting self-excited frequencies to be extracted.

The essential difference between these linear, nonacoustic, low-frequency instability theories and the linear theories of acoustic instability lies in the introduction of the mass balance for the chamber, Eq. 10-80, in place of the analysis of an acoustic field. Thus, the frequency is assumed to be lower than any natural acoustic frequency of the chamber and the chamber responds to the combustion in a modified Helmholtz-type mode (see end of Chapter 9 Section 4.6.3). Explanations for the lower frequency, nonsinusoidal phenomenon of chuffing, rely on nonlinear mechanisms and consider the behavior of the propellant alone, without coupling the propellant dynamics to chamber dynamics in any way. Theories of chuffing are thus basically theories of particular nonlinear inherent instabilities. The periodic thermal explosion model is the most prevalent picture of the process (60-63). We discuss certain details of this model briefly below. A broader view is given in Chapter 9 Section 6.4.3.

The thermal explosion models explain only qualitatively why the periodic pressure spikes are observed in chuffing. Presumably, during the long periods of low pressure, slow reactions are taking place which heat up a sub-surface layer of appreciable thickness and bring the surface to a point of incipient explosion. Rapid burning of the preheated layer, after initiation of the explosion, is supposed to cause the pressure spike. After the preheated layer burns off, the reaction rates return to their low interspike values and the pressure decays. The slow explosion-induction reactions then set in again. Since low-pressure, slow-reaction conditions prevail during most of the cycle, the chuffing period should be approximately equal to the total induction time for the thermal explosion. Detailed estimates of explosion induction times depend on precisely what reactions are assumed to be important. In general, chemical reaction times are given by $[B \exp(-E/R^{\circ}T)]^{-1}$, where B is a pre-exponential rate factor, E is an activation energy and T is the temperature prevailing during the reaction. If it is assumed that the explosion occurs at the surface (63), the temperature T may be identified with the surface temperature and may be related to the interspike chamber pressure p_i by assuming that during the induction period the regression rate is given by a pyrolysis law $\dot{m} = B_s \exp(-E_s/R^{\circ}T_s)$ and also by an empirical pressure sensitivity $\dot{m} = a p_1^n$. Eliminating \dot{m} between

these two formulas relates T_s to p_i ; then substituting the result into the formula for the chemical reaction time yields for the explosion induction time :

$$\tau_i = B^{-1} (B_s/a) \left(\frac{p_i}{E_s} \right)^{1-n} = \frac{n E}{E_s} \quad (\text{Eq. 10-81})$$

In a particular test of Eq. 10-81, when B and E were obtained from independent experimental measurements of explosion induction times of a propellant outside a motor and when 'a' and 'n' were determined from low-pressure regression rate measurements, then physically reasonable values of B_s and E_s could be found which would make Eq. 10-81 provide a good correlation of the observed pressure dependence of the chuffing period (63). These results typify the extent of experimental support for the thermal explosion models of chuffing.

Effort is needed in reconciling the theories of low-frequency instability and chuffing discussed here. Although our discussion makes them appear to be very different phenomena, they have many features in common, both experimentally and also deeply buried in their theories. For example, study of the quantity K in Eq. 10-80 and of the τ_i of Eq. 10-81 reveals that both theories yield frequencies that increase as a power of the burning rate. Both phenomena should be explained as limiting cases in an appropriate theory of low-pressure behavior of solid rocket motors.

6.5. Nonsinusoidal Wave Forms

In addition to the peculiar wave shapes which occur in chuffing, the occurrence of nonsinusoidal wave shapes at much higher pressures has also been observed. These observations, which have been reviewed in Chapter 9 Section 6.2 (where it is pointed out that the distortions are observed most often for axial modes in cylindrical motors with internally burning tubular grains), may conceivably be explicable on the basis of rectification effects of acoustic erosion (54), provided that the amplitudes are sufficiently low. Another possible explanation might be derived from studies of shock wave dynamics (64). Theoretical methods for treating such problems have undergone a considerable amount of development recently (65-69) and have been applied to a model of combustion instability for axial modes in an end-burning, cylindrical motor (64). Although the connection between theory and experiment is not very close yet, possible future successes warrant a discussion of the novel approach.

Qualitatively, the model of Ref. (64) pictures a disturbance in which shock waves propagate back and forth, axially, in a cylindrical chamber. 'Shock wave' appears to be the only suitable term to use at this stage in the discussion. Certain qualifications will be stressed later, that may modify the image that this term brings to the minds of many readers. Flow and the shock propagation occur one-dimensionally in an ideal, nonreacting gas. The shock waves interact only with a short, choked nozzle at the downstream end of the chamber and with a thin combustion zone at the upstream face. So far as the analysis was carried in Ref. (64), the model permits only one shock to exist in the chamber at any time. Thus, the shock alternately bounces off the combustion zone and the choked nozzle, being reflected with modified properties at each encounter. The analysis therefore divides itself naturally into three parts, the periodic shock propagation in the chamber, the interaction of the shock with the nozzle and the interaction of the shock with the combustion zone. The main concern (64) was the first of these parts, which is a difficult problem in itself and the one in which the developments in Refs. (65-69) are helpful. Thus, the simplest assumption of quasisteady, quasi-one-dimensional nozzle flow was employed yielding a constant Mach number at the nozzle entrance as the applicable downstream boundary condition, see Section 4.2.1, and rough approximations were tolerated in the analysis of the response of the combustion zone.

A recent review (5) singles out for emphasis the approximations made in Ref. (64) in analyzing the combustion zone, pointing out that changes in surface heat transfer and in pyrolysis rate due to the wave are neglected and that only changes in the gas-phase reaction rate are taken into account. In defense of these assumptions, it should be noted that the analysis was originally designed to deal with instability of an experimental rocket in which premixed gaseous combustibles were injected through an upstream porous plate; the possible application to end-burning solids was only secondary and relatively unimportant, since instabilities of this type do not seem to have been observed experimentally for end-burning solid rockets. Nevertheless, it seems physically plausible that neglecting solid-phase response may not be too bad an approximation for this type of instability, because the response during the short shock-reflection time may be the dominant part of the response and the slower solid-phase processes are not likely to have time to respond appreciably during the reflection. Additional questions may be raised concerning the details of the treatment of the gas-phase response processes e.g., the isentropic relationship between the pressure and temperature perturbations is employed throughout the reaction region. However, any such criticism is largely irrelevant; the analysis of the response of the combustion zone can be improved at a later date. Also, pertinent response parameters can be deduced experimentally by measuring wave shapes (64). The contribution of Ref. (64) lies in the analysis of the wave dynamics.

The exact nature of the dynamics of cyclic shock propagation (64), (68), (69), is difficult to explain. The analyses unfold through a perturbation method in which the small parameter is the departure of a representative flow variable from time-independent, spatially uniform conditions. Solutions are obtained only to first order in this parameter, although it is necessary to introduce some second-order effects in order to obtain the complete first-order solution. Since third-order effects are not treated at all, the wave processes are all entirely isentropic. Nevertheless, shock discontinuities occur in the flow. But these discontinuities are weak enough to be isentropic. A propagating shock, across which the pressure changes by an appreciable fraction of its initial value, is inconsistent with these small-amplitude analyses.

Although the final results are valid only to first order in the amplitude parameter, they do not resemble the usual first-order acoustic results developed in Section 2. Second-order effects have crept in and back out again in order to change the acoustic waves into shock discontinuities separating regions of continuously varying inviscid flow. The admittance concepts of Section 3 are inapplicable since they refer to harmonic waves. However, boundary admittances can still be defined since the boundary processes must still determine the relationship between velocity and pressure at the boundary. Actually, it is necessary in the final result to retain terms of second order at the boundary and only at the boundary, when homogeneously distributed combustion in the chamber is neglected, in order to obtain a first-order solution for the wave field; thus, one employs:

$$(v - \bar{v})_b = Y_1 (p - \bar{p})_b + Y_2 (p - \bar{p})_b^2 + \dots \quad (\text{Eq. 10-82})$$

as the boundary condition, where Y_1 and Y_2 are negatives of first-order and second-order admittances. Needless to say, the analyses of Section 5 do not give Y_1 directly and are totally inappropriate for determining Y_2 . It appears that, in general, the Y_i should be functionals of the pressure history over a cycle at the boundary.

The core of the technique is to treat the characteristic lines as the independent var-

ables in place of the physical coordinates. For an ideal gas with constant heat capacities, it is well known that the one-dimensional, time-dependent, isentropic characteristic equations are (17) :

$$\left. \begin{aligned} da + [(\gamma - 1)/2] dv &= 0 & \text{for } dx/dt &= v + a \\ da - [(\gamma - 1)/2] dv &= 0 & \text{for } dx/dt &= v - a \end{aligned} \right\} \quad (\text{Eq. 10-83})$$

where 'a' is the sound speed and 'v' is the velocity in the +x direction, γ = ratio of specific heats. In terms of the characteristic lines α and β defined by the equations for dx/dt , as independent coordinates, these equations imply that :

$$\left. \begin{aligned} \partial a / \partial \alpha + [(\gamma - 1)/2] \partial v / \partial \alpha &= 0 \\ \partial a / \partial \beta - [(\gamma - 1)/2] \partial v / \partial \beta &= 0 \\ \partial x / \partial \alpha - (u + a) \partial t / \partial \alpha &= 0 \\ \partial x / \partial \beta - (u - a) \partial t / \partial \beta &= 0 \end{aligned} \right\} \quad (\text{Eq. 10-84})$$

is the governing set of partial differential equations. Amplitude expansions of the physical coordinates x and t as well as the dependent variables a and v are then introduced, viz.,

$$\left. \begin{aligned} v &= \bar{v} + \epsilon v_1(\alpha, \beta) + \epsilon^2 v_2(\alpha, \beta) + \dots \\ a &= \bar{a} + \epsilon a_1(\alpha, \beta) + \epsilon^2 a_2(\alpha, \beta) + \dots \\ x &= \bar{x}(\alpha, \beta) + \epsilon x_1(\alpha, \beta) + \epsilon^2 x_2(\alpha, \beta) + \dots \\ t &= \bar{t}(\alpha, \beta) + \epsilon t_1(\alpha, \beta) + \epsilon^2 t_2(\alpha, \beta) + \dots, \end{aligned} \right\} \quad (\text{Eq. 10-85})$$

where one may define the small parameter to be :

$$\epsilon \equiv (\bar{p}/\bar{v})(Y_{1b} - Y_{1a}) \quad , \quad (\text{Eq. 10-86})$$

in which Y_{1a} is the first-order nozzle admittance. By substituting Eq. 10-85 into Eq. 10-84 and collecting terms of like powers of ϵ , a sequence of linear, partially nonhomogeneous, partial differential equations with constant coefficients is obtained for $(\bar{x}, \bar{t}, v_1, a_1), (x_1, t_1, v_2, a_2)$, etc. The complete solution to these equations through terms of order ϵ yields the first-order wave dynamics.

The physical ideas behind the definition of ϵ given in Eq. 10-86 provide some insight into the character of this instability. If $\epsilon > 0$, then more mechanical energy is fed into the wave pattern at the upstream face than is extracted at the nozzle. In an ordinary acoustic theory, this would imply that the wave amplitudes grow exponentially with time. Such is not the case in the present theory, which imposes the condition that the flow pattern be cyclic. One might therefore view the present theory as describing one possible long-time flow pattern that may develop in systems that experience a small net linear, acoustic amplification. An attribute of the analytical technique employed, is its ability to describe long-time behavior of systems that cannot conveniently be treated by any other technique. In this cyclic pattern, the net mechanical energy that is fed into the wave field is somehow dissipated at the same rate by the shock wave, although the mechanism by which this occurs in first order is not entirely transparent from the analysis. It is easy to prove (64) that if the dimensionless admittance difference defined in Eq. 10-86 is larger than order ϵ , with ϵ being the expansion parameter in Eq. 10-85, then cyclic

solutions cannot be obtained to first order; the shock cannot dissipate enough energy. Equation 10-86 causes the shock strength to be of order ϵ .

The method of solution of the sequence of partial differential equations is lengthy and cannot be given here. At the outset, it is necessary to define the origins of the α and β coordinates carefully and it is especially necessary to observe what changes occur where the characteristics meet the shock. The x - t space may be separated into regions bounded by the shock wave and for some purposes properties in these different regions must be handled separately. Reference (64) develops a method for extending solutions from each region a distance ϵ across the shock wave, in order to facilitate the application of shock conditions. Application of the cyclicity assumption results in equations that can eventually be solved analytically for shock strengths, for flow variables in intershock regions, for shock propagation velocities and for the cycle period, all to order ϵ . The final formulas are a little too long for us to write down all of them, but we illustrate the resulting wave shapes schematically in Fig. 10-8 and give the formula for the pressure jump across the shock wave:

$$\Delta p_{\pm} = \frac{\epsilon \bar{p} \left(1 \pm \frac{\gamma-1}{2} \bar{M} \right)}{Y_{2b} \bar{p}^2 / \bar{v} + (\gamma^2 - 1) / 8\gamma^2} \left(\frac{1 - e^{-\lambda}}{1 + e^{-\lambda}} \right), \quad (\text{Eq. 10-87})$$

where the upper sign is for a shock propagating downstream, the lower sign is for a shock propagating upstream, \bar{M} is the Mach number of the mean flow, ϵ is given by Eq. 10-86, Y_{2b} is defined in Eq. 10-82, and:

$$\lambda = \frac{(\gamma - 1) \bar{M} (1 - \bar{M}^2) [1 + (Y_{2b} \bar{p}^2 / \bar{v}) 8\gamma^2 / (\gamma^2 - 1)]}{\{ 1 - [(\gamma - 1)/2]^2 \bar{M}^2 \} [1 + (2 - \gamma) \bar{M}^2]} \quad (\text{Eq. 10-88})$$

The sawtooth shape of the predicted pressure-time curves is apparent in Fig. 10-8.

Whether these waves are important experimentally remains to be discovered. If they are, much more theoretical work should be done in analyzing other modes of propagation e.g., axial propagation with multiple shocks in the chamber simultaneously, tangential propagation, etc. and also in analyzing nozzle and combustion zone 'admittances'. The 'admittance' problems that would arise would open a rich and practically unexplored field of research.

7. Comparison of Theory with Experiment

Theories concerning specific amplification and damping phenomena have occasionally been compared favorably with experiment. Examples of this have already been cited, see Fig. 10-3. However, in general the parameters that appear in the theories are not sufficiently well known to permit comparisons of instability theories with experiment to be made, according to the usual scientific meaning of such comparisons. All that can be done today is to compare qualitative theoretical trends with experimental trends. Many comparisons of this type have been made and have been discussed earlier in the text. The qualitative agreement is encouraging, in suggesting that many aspects of the various theories may have counterparts in reality. The next logical step in comparison is to attempt to determine the values of the parameters that appear in the theories for specific propellant-motor combinations, through quantitative comparisons with experiment. This step has seldom ever been taken, perhaps because the theoreticians do not have enough faith in the detailed elements of their models, to believe that the step is warranted.

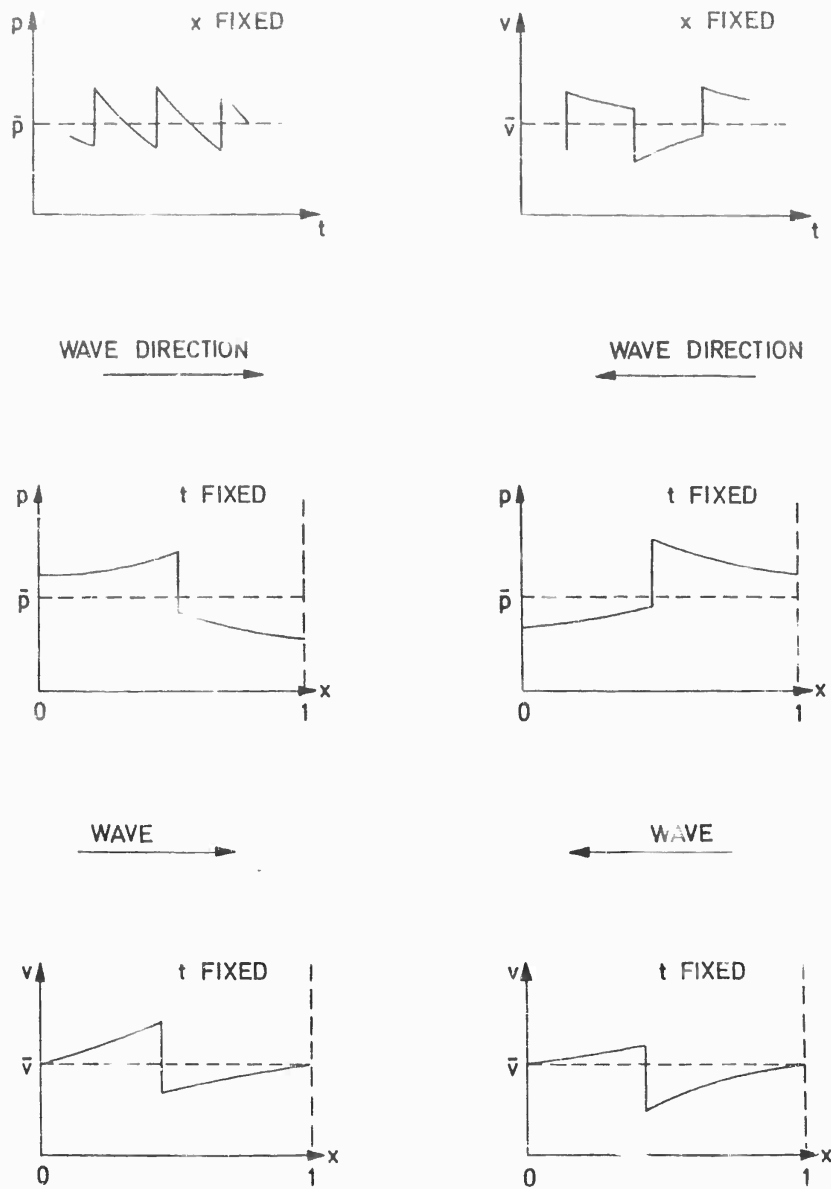


Fig. 10-8 Theoretically calculated nonsinusoidal wave shapes, (64).

References

- (1) Tsien H.S., J. Amer. Rocket Soc., 22, 139, 162, 1952.
- (2) Crocco L., Aerotecnica, Roma, 33, 46, 1953.
- (3) Crocco L. and Cheng S.I., Theory of Combustion Instability in Liquid Propellant Rocket Motors, AGARDograph, No.8, Butterworths Scientific Publications, London, Appendix B, 1956.
- (4) Culick F.E.C., AIAA J. 1, 1097, 1963.
- (5) Hart R.W. and McClure F.T., Tenth Symposium (International) on Combustion, The Combustion Institute, Pittsburgh, 1047-1064, 1965.
- (6) Crocco L., Monti R. and Grey J., ARS J. 31, 771, 1961.
- (7) Buffum F.G., Jr., Dehority G.L., Slates R.O. and Price E.W., Acoustic Attenuation Experiments on Subscale, Cold-Flow Rocket Motors, AIAA Paper No. 66-110, 1966.
- (8) Lambert R.F., J. Acoust. Soc. Am., 25, 1068, 1953.
- (9) Smith P.W. Jr., The Acoustics of T-Burners, Tech. Rept. No.1, Contract No. DA-19-020-AMC-5755-R, Bolt, Beranek and Newman, Inc. Rept. No. 1077, Cambridge, Mass., November 1963.
- (10) McClure, F.T., Hart R.W. and Cantrell R.H., AIAA J. 1, 586, 1963.
- (11) Hart R.W. and Cantrell R.H., J. Acoust. Soc. Am. 35, 18, 1963.
- (12) Cantrell R.H. and Hart R.W., J. Acoust. Soc. Am. 36, 697, 1964.
- (13) Stokes G.G., Trans. Camb. Phil. Soc. 9, 8, 1851.
- (14) Lord Rayleigh, Phil. Mag. 21, (6), 697, 1911.
- (15) Stewartson K., The Theory of Unsteady Laminar Boundary Layers, pp. 1-37, Advances in Applied Mechanics, Vol. VI, Academic Press, New York, 1960.
- (16) Cantrell R.H., McClure F.T. and Hart R.W., J. Acoustic Soc. Am. 35, 500, 1963.
- (17) Williams F.A., Combustion Theory, pp. 84-89, Addison-Wesley Publishing Co., Reading, Mass. 1965.
- (18) Clarke J.F., J. Fluid Mech. 7, 577, 1960.
- (19) Blackman V., J. Fluid Mech. 1, 61, 1956.
- (20) Epstein P.S. and Carhart R.R., J. Acoust. Soc. Am. 25, 553, 1953.
- (21) Sewell C.J.T., Phil. Trans. Roy. Soc. London A. 210, 239, 1910.
- (22) Lamb H., Hydrodynamics, Sixth Edition, Dover, New York, pp. 645-663, 1945.

- (23) Dobbins R.A. and Temkin S., AIAA J. 2, 1106, 1964.
- (24) Carrier G.F., J. Fluid Mech. 4, 376, 1958.
- (25) Zink J.W. and Delsasso L.P., J. Acoust. Soc. Am. 30, 765, 1958.
- (26) Bird J.F., McClure F.T. and Hart R.W., Acoustic Instability in the Transverse Modes of Solid Propellant Rockets, Proc. 12th International Astronautical Congress, pp. 459-473, Academic Press, New York, 1963.
- (27) McClure F.T., Hart R.W. and Bird J.F., Solid Propellant Rocket Motors as Acoustic Oscillators, Solid Propellant Rocket Research, Vol. I of Progress in Astronautics and Rocketry, pp. 295-358, edited by M. Summerfield, Academic Press, New York 1960.
- (28) McClure F.T., Hart R.W. and Bird J.F., J. Appl. Phys. 31, 884, 1960.
- (29) Bird J.F., Hart R.W. and McClure F.T., J. Acoust. Soc. Am. 32, 1404, 1960.
- (30) Bird J.F., J. Acoust. Soc. Am. 32, 1413, 1960.
- (31) Deters O.J., ARS J. 32, 378, 1962.
- (32) Gazis D.C., J. Acoust. Soc. Am. 30, 786, 1958; 31, 568, 573, 1959.
- (33) Lighthill M.J., AIAA J. 1, 1507, 1963.
- (34) Hart R.W., and Cantrell R.H., AIAA J. 1, 398, 1963.
- (35) Grad H., Commun. Pure Appl. Math., 2, 1, 1949.
- (36) Moore F.K. and Maslen S.H., Transverse Oscillations in a Cylindrical Combustion Chamber, NACA, TN. 3152, Oct. 1954.
- (37) Cheng S.I., Jet Prop. 24, 27, 1954.
- (38) Cheng S.I., Eighth Symposium (International) on Combustion, p. 81, Williams and Wilkins, Baltimore, 1962.
- (39) Crocco L., J. Am. Rocket Soc. 21, 163, 1951, 22, 7, 1952.
- (40) Green L., Jr., Jet Propulsion, 28, 386, 1958.
- (41) Schultz R., Green L., Jr. and Penner S.S., Studies of the Decompositions Mechanism, Erosive Burning, Sonance and Resonance for Solid Composite Propellants, Combustion and Propulsion, 3rd AGARD Colloquium, Pergamon, London, 1958.
- (42) Nachbar W. and Green L., Jr., J. Aero. Sci. 26, 518, 1959.
- (43) Barrère M. and Bernard J.J., Eighth Symposium (International) on Combustion, pp. 886-894, Williams and Wilkins Co., Baltimore 1962.
- (44) Hart R.W. and McClure F.T., J. Chem. Phys. 30, 1501, 1959.
- (45) Bird, J.F., Haar L., Hart R.W. and McClure F.T., J. Chem. Phys. 32, 1423, 1960.

- (46) Cantrell R.H., McClure F.T. and Hart R.W., AIAA J. 3, 418, 1965.
- (47) Cantrell R.H., Hart R.W. and McClure F.T., AIAA J. 2, 1100, 1964.
- (48) Smith A.G., A Theory of Oscillatory Burning of Solid Propellants Assuming a Constant Surface Temperature, in Solid Propellant Rocket Research, Vol. 1 of ARS Series Progress in Astronautics and Rocketry, pp. 375-392, edited by M. Summerfield, Academic Press, New York, 1960.
- (49) Denison, M.R. and Baum, E., ARS J. 31, 1112, 1961.
- (50) Williams F.A., J. Appl. Phys. 33, 3153, 1962.
- (51) Wood W.A., Oscillatory Burning of Solid Composite Propellants, Ninth Symposium (International) on Combustion, pp. 335-344, Academic Press, New York, 1963.
- (52) Hart R.W., Bird J.F. and McClure F.T., Progress in Astronautics and Rocketry, Vol. 1, Solid Propellant Rocket Research, pp. 423-451, edited by M. Summerfield, Academic Press, New York 1960.
- (53) McClure F.T., Bird J.F. and Hart R.W., ARS J. 32, 374, 1962.
- (54) Hart R.W., Bird J.F., Cantrell R.H. and McClure F.T., AIAA J. 2, 1270, 1964.
- (55) Carrier G.F., Quart. Appl. Math. 12, 383, 1955.
- (56) Shinnar R. and Dishon M., Heat Transfer Stability Analysis of Solid Propellant Rocket Motors, Solid Propellant Rocket Research, Vol. 1 of ARS Series Progress in Astronautics and Rocketry, pp. 359-374, edited by M. Summerfield, Academic Press, New York, 1960.
- (57) Akiba R. and Tanno M., Low Frequency Instability in Solid Rocket Motors, pp. 74-82, Proceedings of the First Symposium (International) on Rockets and Astronautics, Tokyo, 1959.
- (58) Sehgal R. and Strand L., AIAA J. 2, 696, 1964.
- (59) Beckstead M.W., Ryan N.W. and Baer A.D., Nonacoustic Instability of Composite Propellant Combustion, AIAA Paper No. 66-111, 1966.
- (60) Crawford F.L., Huggett C.M., McBrady J.J. and Rusoff I.I., Univ. of Minnesota, Contract OE MSTV-716, Rept. UM 32, July 11, 1945, also part of Rept. OSRD-6374.
- (61) Huffington J.D., Trans. Faraday Soc., 50, 942, 1954.
- (62) Clemmow D.M. and Huffington, J.D., Trans. Faraday Soc., 52, 385, 1956.
- (63) Yount R.A. and Angelus T.A., AIAA J. 2, 1307, 1964.
- (64) Sirignano W.A. and Crocco L., AIAA J. 2, 1285, 1964.
- (65) Lighthill, M.J., A Technique for Rendering Approximate Solutions to Physical Problems Uniformly Valid, Phil. Mag. 40, 1179-1201, 1949.

- (66) Lin C.C., On a Perturbation Theory Based on the Method of Characteristics, J. Math. Phys. 33, 117-134, July 1954.
- (67) Fox P.A., On the Use of Coordinate Perturbations in the Solution of Physical Problems, Massachusetts Institute of Technology Project DIC-6915, 1, pp. 1-52, November 1953.
- (68) Chu B.T. and Ying S.J., Thermally Driven Nonlinear Oscillations in a Pipe with Traveling Shock Waves, Air Force Office of Scientific Research TN 686, April 1961.
- (69) Chu B.T., Analysis of a Self-Sustained Nonlinear Vibration in a Pipe Containing a Heater, Air Force Office of Scientific Research TN 1755, September 1961.
- (70) Cheng S.I., Combustion Instability in Solid Rockets using Propellants with Reactive Additives, Solid Propellant Rocket Research, Vol. 1 of ARS Series Progress in Astronautics and Rocketry, pp. 393-422, edited by M. Summerfield, Academic Press, New York, 1960.

Chapter 11

**Mechanical Properties and Stress Analysis
of Solid Propellant Grains**

Nomenclature

A	constant, Eq. 11-152; surface area of the cut ($A = 2bh$)
a	constant
a_{ij}	coefficients in Eq. 11-90
\bar{a}_{ij}	coefficients in Eq. 11-93
$A^{(m)}$	cross-sectional area of wire
a_0	initial port radius
$a(t)$	inner radius of hollow cylinder at time t
B	constant, Eq. 11-152; elastic casing constant, Eq. 11-170
b	outer radius of hollow cylinder; length of cut
B^*	complex bulk compliance
b_{ij}	coefficients in Eq. 11-84
\bar{b}_{ij}	coefficients in Eq. 11-93
$\begin{matrix} C_{ij} \\ C_{ijkl} \end{matrix} \right)$	coefficients
$\begin{matrix} c_{ij} \\ c'_{ij} \\ c_{ij}(\alpha) \end{matrix} \right)$	coefficients
c_1, c_2	constants
D	dissipation function
D	3 x 3 deformation gradient matrix
D_{ij}	defined in Eq. 11-99
$\begin{matrix} D_{ijkl} \\ D'_{ijkl} \\ D_{ijkl}^{(\alpha)} \\ D_{ijkl}^e \end{matrix} \right)$	coefficients
$x - b$	
E	Lagrangian strain matrix
E, E_1	spring constant, elastic modulus
E_e	rubbery modulus or delayed elastic modulus
e_{ij}	strain deviator tensor
$E^{(m)}$	elastic modulus of wire
$E^*(\omega)$	complex tensile modulus

$E(t)$	tensile relaxation modulus
E_v	modulus of spring in parallel with the dashpot
$E_1(\omega)$	real part of $E^*(\omega)$
$E_2(\omega)$	imaginary part of $E^*(\omega)$
F	elastic compliance; Helmholtz free energy
\mathcal{F}	tensor functional
F_g	glassy compliance or instantaneous compliance
f_i	body force
F_0	constant
$F(t)$	tensile creep compliance
$F^*(\omega)$	complex tensile compliance
$F_1(\omega)$	real part of $F^*(\omega)$
$F_2(\omega)$	negative imaginary part of $F^*(\omega)$
G	shear modulus
g	gravitational acceleration
$G(t)$	shear relaxation modulus
$G^*(\omega)$	complex shear modulus
G_1	real part of G^*
G_2	imaginary part of G^*
h	thickness of casing; sheet thickness
H_1	heat in system I
$H(t)$	Heaviside step function
i	integer
\mathbf{I}	unit matrix
j	integer
J^*	complex shear compliance
$J(s)$	defined in Eq. 11-218
$J(\tau)$	$\tau E(\tau)$
K	bulk modulus

k	Boltzmann constant; constant
K_i	kernel functions
K_{ijk}	defined in Eq. 11-97
$K(t)$	bulk relaxation modulus
$K^*(\omega)$	complex bulk modulus
$L_{ijk}(t)$	defined in Eq. 11-95
$\ell_i^{(m)}$	direction cosine of m-th set of wires
$L(\tau)$	$\tau/E(\tau)$
M	number of different stress levels to which sample is subjected; number of different strain rates
m	integer; molecular weight
n	constant, Eq. 11-154; element index for analysis of crack propagation
N_{Fi}	number of cycles at the i-th stress level required for failure
N_i	number of cycles that the sample experiences at the i-th stress level
n_i	failure exponent at i-th stress level or strain rate
$n^{(m)}$	number of wires per unit cross-sectional area
n_o	constant
P	linear differential operator
p	Laplace transform variable
P'	linear differential operator
p_v	material constants, Eq. 11-2
Q	linear differential operator
Q'	linear differential operator
Q_i	generalized external force
q_i	generalized coordinates
q_v	material constants, Eq. 11-2
R	rotation matrix
r	radial coordinate; normal regression rate or burning velocity of propellant

R°	ideal gas constant
R_{ij}	stress deviator tensor
S	stress functional
S^*	defined in Eq. 11-110
S_n	defined in Eq. 11-106
$S(t)$	defined in Eq. 11-241
$S_{1,2}$	entropy in system I or II
T	absolute temperature; surface free energy or surface tension
\bar{T}	reference temperature
t	time
t^*	failure time
t_a	retardation time
t_b	relaxation time
t_f	total burning time
t_{F1}	time to failure at the strain rate $\dot{\epsilon}_1$
T_G	grain temperature
T_i	time over which a sample is held at the strain rate $\dot{\epsilon}_1$
T_i°	prescribed surface traction
t_o	time interval, Fig. 11-1
t_n	time at which element n breaks
T_1	temperature on the ablating surface
u_1	displacement vector
u_1°	prescribed surface displacement vector
U_1	internal energy in system I
V	total energy; elastic energy stored in the sheet
v	speed of ablation
v_m	crack propagation velocity when crack has progressed to m -th element
V_1	stored energy
V_2	energy loss

W_{d10}	critical strain energy
x	coordinate parallel to the cut
X_i	Cartesian coordinates of material particle in undeformed body; generalized force conjugate to q_i in the expression of entropy production
x_i	Cartesian coordinates of material particle in deformed body
y	coordinate normal to the cut
z	axial coordinate
α	coefficient of thermal expansion; Eq.11-150; angle of helical wire
α_c	coefficient of thermal expansion of casing
α_T	thermorheological shift factor
β	defined in Eq. 11-148
$\beta(r)$	defined in Eq. 11-234
β_1	value of $\beta(r)$ for $r < 0.75b$
β_2	value of $\beta(r)$ for $r > 0.75b$
δ	distance along the axial direction between two neighboring wires; phase lag; length of material element
δ_{ij}	Kronecker delta
$\delta(t)$	Dirac delta function
ϵ^*	constant ultimate strain
ϵ_b	rupture strain
ϵ_C	$2\epsilon_m/3$
ϵ_e	long-time, equilibrium strain
ϵ_F	maximum permissible strain in pure shear
$\dot{\epsilon}_i$	i-th strain rate
ϵ_{ij}	strain tensor
ϵ_L	strain for extrapolation of the linear part of the stress-strain curve to maximum stress
ϵ_M	$\epsilon_b/2$
$\epsilon^{(m)}$	normal strain along the direction of m-th set of wire
ϵ_m	strain at maximum stress

$\epsilon_n^{(m)}$	strain in n-th element just before m-th element cracks
ϵ_o	constant strain, Fig. 11-1; complex strain
ϵ_R	strain at which grain in rocket motor ruptures
ϵ_r	radial normal strain
$\epsilon(t)$	uniaxial strain at time t
ϵ_z	axial normal strain
ϵ_θ	circumferential normal strain
$\epsilon_1, \epsilon_2, \epsilon_3$	principal strains
ζ_o	monomeric friction coefficient
η	dashpot of viscosity
η_i	viscosity of dashpot
θ	polar angle
κ	thermal conductivity
λ	port size factor; Lamè's constant
λ_α	nonnegative constant
μ	Lamè's constant
ν	Poisson's ratio
ν_c	Poisson's ratio of casing
ν_j	direction cosine of outward normal
ξ	reduced time; continuous distance variable for large values of m
ξ^*	defined in Eq. 11-223
π_o	constant
$\pi(t)$	internal pressure in hollow cylinder
ρ	density
σ_b	stress at rupture
σ_{cr}	critical stress for crack formation
σ_i	i-th stress level
σ_{ij}	stress tensor
$\sigma^{(m)}$	total stress in wires

σ_m	stress in m-th set of wires
σ_m	maximum stress
$\sigma_n^{(m)}$	stress in n-th element just before m-th element cracks
σ_c	tensile stress; mean value of the principal stress difference; constant stress, Fig. 11-1; complex stress
σ_r	radial normal stress
$\sigma(t)$	uniaxial stress at time t
σ_x	x component of the normal stress
σ_y	y component of the normal stress
σ_z	axial normal stress
σ_θ	circumferential normal stress
$\sigma_1, \sigma_2, \sigma_3$	principal stresses
τ	time parameter; retardation time ($\tau = \eta / E_v$)
τ_b	defined in Eq. 11-61
ω	frequency; angular velocity of spin
ω_o	constant
Ω	reduced frequency

Mechanical Properties and Stress Analysis of Solid Propellant Grains

1. Introduction

1.1. Overview

Structural aspects of solid propellant rocketry comprise a vast subject about which many volumes can be written. In the present chapter, we must therefore make a selection of the relevant material. We shall concern ourselves primarily with structural problems of solid propellant grains, since these problems are of paramount importance for improving motor performance. Furthermore, we shall discuss only particular aspects of these problems, but we shall attempt to call the reader's attention to other aspects by pointing out suitable references.

Solid propellant grains are viscoelastic materials. Many structural problems for propellant grains can be (and have been) solved with sufficient accuracy by using methods lying within the domain of infinitesimal, linear elasticity, nevertheless there are problems, associated for example with grain slump, reinforced grains, grain flow (creep) and with finite deformations, in which viscoelastic concepts are essential. An increasing number of the numerical techniques for the stress analysis of grains of complex geometries, are beginning to employ viscoelastic equations and when accurate stress analyses are required, viscoelasticity must always be taken into account. For these reasons, we believe that the time has come for solid propellant rocket engineers and grain analysts to become thoroughly familiar with the analytical basis of viscoelasticity. Therefore, in Section 2, we delve at length into methods for describing the stress-strain relations of viscoelastic materials. We present three different, complementary but equivalent formulations for linear viscoelasticity, discuss thermodynamic aspects of viscoelasticity and present the basis of a rigorous although complex approach to the difficult problem of describing nonlinear, viscoelastic, stress-strain relations. We only touch (Section 2.4) on the basis of viscoelastic behavior in molecular physics and in polymer chemistry because this is a controversial and complicated subject, in which many uncertainties remain.

The basic material on stress-strain relations in viscoelasticity presented in Section 2, does not tell the rocket engineer why he must concern himself with structural mechanics or what aspects of structural analysis are most relevant to motor performance. Answers to such questions can be approached only from a practical orientation, which emphasizes the structural problems that have arisen and that may be expected to arise in the future. Insofar as propellant grains are concerned, there are two types of practical structural problems, viz., those associated only with grain deformations and those associated with grain failure. The latter type of problem, grain failure, is by far the most important of the two, in a practical sense. It is therefore extremely important for us to discuss grain failure at some length and such a discussion is given in Section 4. This discussion provides a natural opportunity for us to emphasize practical and empirical aspects of structural problems

(indeed, rigorous approaches to failure analysis are not available) from which the engineer can obtain motivation and orientation. Thus, although the viewpoint adopted in Section 4 is in most respects the antithesis of that adopted in Section 2, we feel that at present both viewpoints are needed in studies of solid propellant rockets.

In discussing failure analysis in Section 4, after emphasizing the many difficulties that arise in failure studies, we attempt to develop a phenomenological understanding of grain failure by describing crack formation and propagation. Most of the background for this discussion draws on elasticity, viscoelasticity apparently does not enter at all, although it can be considered to be present in a deeply submerged fashion. Although this unfortunately further obscures the relationships between the material in Sections 2 and 4, it is nevertheless essential because current concepts of crack propagation in viscoelastic materials have been taken virtually without modification from earlier ideas on crack propagation, in elastic-plastic materials. The viscoelastic nature of the propellant grain is also subdued in current empirical approaches to the development of failure criteria (Section 4.3), although viscoelasticity is beginning to be recognized in some of the more recent approaches to the evaluation and interpretation of cumulative damage. The general idea of Section 4 is that failure analysis is a very difficult but very important subject.

Section 4 helps to answer the question of why structural analyses are needed; i.e., one wishes to know what the deformations and stresses will be, not merely because of their intrinsic interest but more important to determine whether they will remain within the bounds of grain failure. From the viewpoint of Section 4, it is therefore quite clear why the topic of stress analysis, considered in Section 3, is of importance. When grain designs are carried out, stress analyses should be made for a variety of the more severe conditions that the motor is expected to experience, such as sudden application of internal pressures and high surface temperatures during motor ignition, high axial accelerations during rocket flight and long-time oscillations during transportation or storage of the grain, leading to thermal stresses through thermomechanical coupling.

Because of space limitations, it is impossible for us to present a complete discussion of stress analysis for solid propellant grains in Section 3. Even restricting ourselves only to viscoelastic analyses, we find it necessary to be highly selective in choosing the topics that we shall discuss. Except in the general discussion of methods of viscoelastic stress analyses given in Section 3.1, the primary restriction on the stress analysis problems discussed in Section 3 is that only infinitely long, hollow, tubular grains with circular ports are considered. This forces the reader to consult other references to find analyses of grains of most practical geometries (see next paragraph). But it also offers a number of advantages, primarily in relationship to the kinds of operational and grain-support conditions that can be treated and in relationship to the accuracy and simplicity of the analysis. Thus, effects of the external motor case, motor spin, ablation (or burning) of the internal surface of the grain, nonisothermal temperature distributions, axial acceleration and wire reinforcement of the grain, are all discussed. The objective of the discussion is to provide the reader with an understanding of the stress and strain effects of these conditions of motor operation and grain support, through simple analytical solutions to the corresponding dynamical problems in viscoelasticity.

The methods of stress analysis for viscoelastic materials described in Section 3.1 (and used in the rest of Section 3) are in a basic sense the most appealing, since they enable us to use actual measured relaxation or creep data in the analysis, thereby providing improved accuracy by avoiding errors associated with the introduction of spring-dashpot models. Nevertheless, many other techniques are used in structural analyses of real grains with complex geometries. These other techniques, while inherently less accurate, are of value because they currently comprise essentially the only practical methods for analyzing grains of complicated

shapes. These techniques include a number of well-justified numerical finite-difference methods, a few well-founded finite-element methods, in which the grain is broken into either triangular or tetrahedral elements, and a host of *ad hoc* methods that rest on less firm grounds, such as a 'redundant force method' (77), in which the grain is assumed to be represented by a collection of bars, panels and joints. Experimental techniques, such as three-dimensional photoelasticity, can also provide approximate information concerning stress and strain distributions. These approaches have been used in structural analyses of grains for both cylindrical and spherical motors. Because of space limitations, we shall not discuss these techniques here. The reader may consult Refs. (63), (64), (66), (67), (76) and (77) for entry to the literature on these subjects.

1.2. Viscoelasticity

As implied in the preceding section, it is found that both double-base and composite propellant grains exhibit significant time-dependent mechanical properties and therefore may be considered as viscoelastic materials. This time dependency is most clearly illustrated in such phenomena as creep and stress relaxation of a cylindrical bar under uniaxial stress. Figure 11-1a shows the longitudinal strain response, due to a suddenly applied stress which is maintained at a constant value σ_0 for a period t_0 and is then removed. The line OA represents the instantaneous elastic response of strain. The curve AB shows the time dependence of strain due to viscoelastic flow. When the stress is removed suddenly at $t = t_0$, the strain in turn is reduced immediately by an amount BC equal to the instantaneous elastic response. The remaining strain recovers gradually along the curve CD. In Fig. 11-1b, the behavior of stress relaxation due to a suddenly applied longitudinal strain ϵ_0 at zero time is shown. The instantaneous elastic stress response in this case is represented by OA'. When the strain is maintained at a constant value ϵ_0 for a period t_0 , the stress decreases along the curve A'B'. At $t = t_0$, the strain is suddenly removed and as expected, is accompanied by an instantaneous stress drop B'C'. The remaining stress then relaxes gradually along the curve C'D'.

Experimental evidence indicates that when the stress level is below a certain limit, dependent on the material considered, viscoelastic behavior is approximately linear. Stress analysis procedures are considerably simplified by this assumption in the theory. For linear viscoelastic solids, the strain at a given time due to a step function stress is proportional to the magnitude of the stress. This linearity in viscoelastic response was observed experimentally by Blatz (3) in creep tests on solid propellant. Blatz's results are shown in Fig. 11-2.

2. Mechanical Properties of Viscoelastic Solids

The first subjects that we shall present in this section are a variety of different representations of linear viscoelastic properties. Within the linear range of stress-strain relations, there are three distinct but equivalent representations. These are developed in Sections 2.1 to 2.3. For demonstrative purposes, we shall begin the discussion with an example of simple tension and later generalize the results to the three-dimensional stress-strain relations. More extensive coverages of the material in these sections may be found in Refs. (1) to (28).

Since viscoelastic characteristics are strongly influenced by temperature, the critical stress in design problems may be reduced considerably by the appropriate choice of temperature history. A discussion of the effect of temperature on the stress-strain relations is included in Section 2.4.

Molecular and thermodynamic aspects of viscoelastic properties are discussed in Sections 2.4 and 2.5. Nonlinear stress-strain relations are considered in Section 2.6.

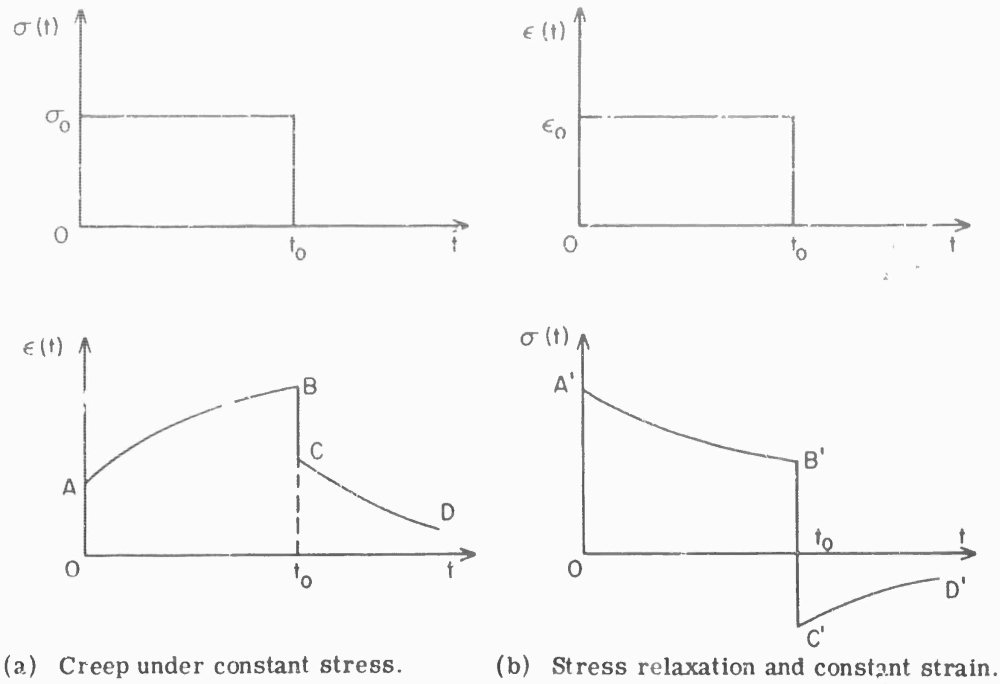


Fig. 11-1 Creep and stress relaxation

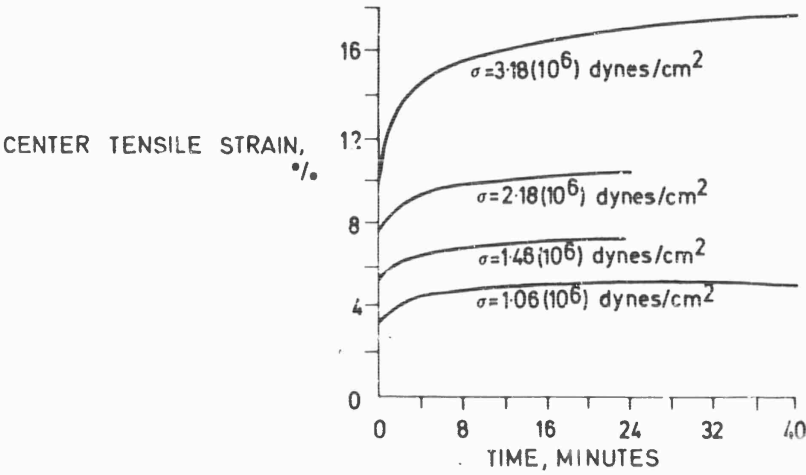


Fig 11-2 Effect of load on creep of propellant, due to Blatz (3).

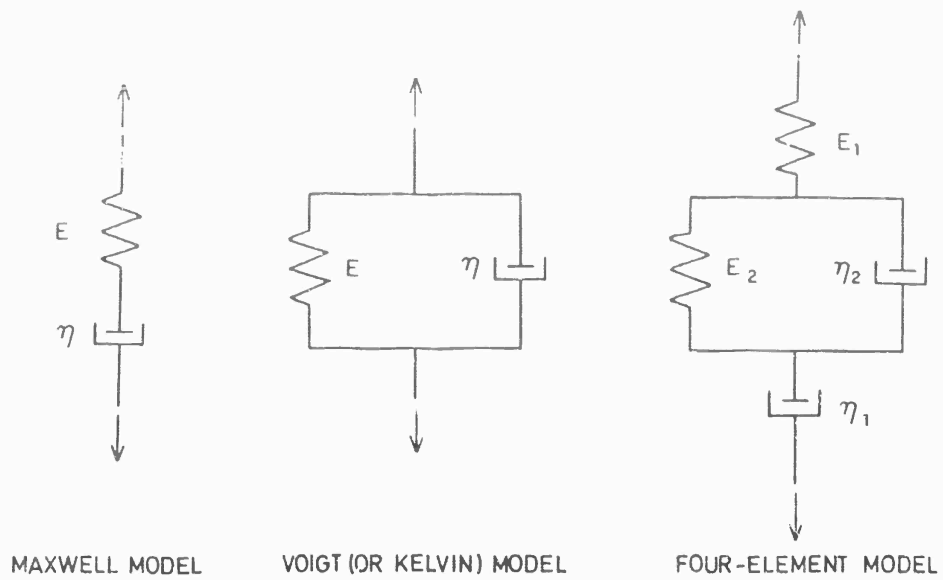


Fig. 11-3 Model representations.

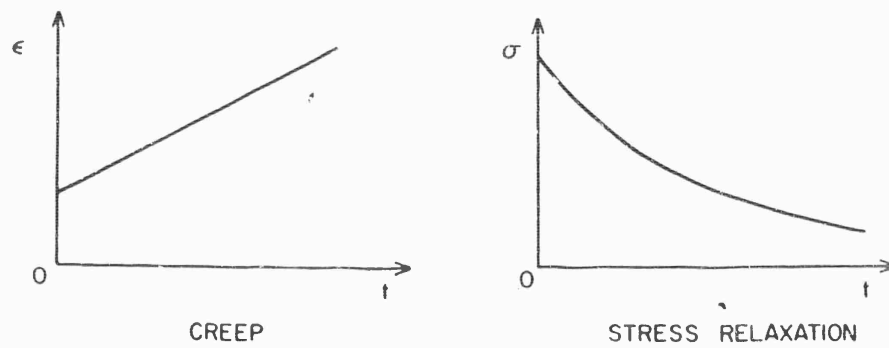


Fig. 11-4 Creep and stress relaxation curves for Maxwell model.

2.1. Differential Operator Representation

The linear one-dimensional stress-strain relation in viscoelasticity can be represented by the following differential equation :

$$P[\sigma(t)] = Q[\epsilon(t)] \quad (\text{Eq. 11-1})$$

where $\sigma(t)$ and $\epsilon(t)$ are the time-dependent stress and strain, P and Q are linear differential operators with respect to the time t . We can express these operators as :

$$P = \sum_{r=0}^p p_r \frac{\partial^r}{\partial t^r} \quad \text{and} \quad Q = \sum_{r=0}^q q_r \frac{\partial^r}{\partial t^r} \quad (\text{Eq. 11-2})$$

where p_r and q_r are material constants. In order to present the viscoelastic properties accurately over several decades of time, high-order differential operators are required. But it is clear that attempts at such applications are usually accompanied by mathematical complications.

In some instances, it is possible to describe the viscoelastic properties of materials by spring-dashpot models. For a spring the stress is proportional to the strain, but for a dashpot the stress is proportional to the time rate of change of the strain. Some simple models are shown in Fig. 11-3, where the strain is identified with the relative displacement of the upper and lower extremities of the system. The stress-strain relation of the Maxwell model is :

$$\frac{1}{\eta} \sigma(t) + \frac{1}{E} \frac{\partial}{\partial t} \sigma(t) = \frac{\partial}{\partial t} \epsilon(t) \quad (\text{Eq. 11-3})$$

This equation can also be obtained from Eq. 11-2 by setting $p = q = 1$, $p_0 = \frac{1}{\eta}$, $p_1 = \frac{1}{E}$, $q_0 = 0$ and $q_1 = 1$. Due to a suddenly applied constant stress on the Maxwell model, the strain consists of an instantaneous elastic response followed by viscous creep flow (Fig. 11-4). Similarly, if the strain is applied suddenly and maintained, the stress first experiences an instantaneous elastic response and then relaxes, due to a continuous flow of the dashpot. These creep and relaxation behaviors can be visualized directly from the mechanism of the model.

The differential equation of the Voigt or Kelvin model is :

$$\sigma(t) = E \epsilon(t) + \eta \frac{\partial}{\partial t} \epsilon(t) \quad (\text{Eq. 11-4})$$

which is equivalent to Eq. 11-1 with $p = 0$, $q = 1$, $p_0 = 1$, $q_0 = E$ and $q_1 = \eta$. Note that the spring and the dashpot are parallel in the Voigt model. Thus, when we compare the creep strain of this model with that of a Maxwell model, we find that the instantaneous elastic response here is eliminated through the action of the dashpot. Also the indefinite flow of the material is prevented by the action of the spring.

The differential equation of the four-element model of Fig. 11-3 is :

$$\begin{aligned} \frac{\partial^2}{\partial t^2} \sigma(t) + \left(\frac{E_1}{\eta_1} + \frac{E_1}{\eta_2} + \frac{E_2}{\eta_2} \right) \frac{\partial}{\partial t} \sigma(t) + \frac{E_1 E_2}{\eta_1 \eta_2} \sigma(t) &= E_1 \frac{\partial^2}{\partial t^2} \epsilon(t) \\ &+ \frac{E_1 E_2}{\eta_2} \frac{\partial}{\partial t} \epsilon(t) \end{aligned} \quad (\text{Eq. 11-5})$$

which is related to Eq. 11-2 through the following constants: $p = q = 2$,

$$p_0 = \frac{E_1 E_2}{\eta_1 \eta_2}, \quad = \frac{E_1}{\eta_1} + \frac{E_1}{\eta_2} + \frac{E_2}{\eta_2}, \quad p_2 = 1, \quad q_0 = 0, \quad q_1 = \frac{E_1 E_2}{\eta_2} \text{ and } q_2 = E_1.$$

In this case, both the instantaneous response and the asymptotic behavior of viscous flow appear on the creep curve, due to a suddenly applied constant stress. Note that two initial conditions are needed in order to solve Eq. 11-4 for $\sigma(t)$ when $\epsilon(t)$ is given or vice versa.

The one-dimensional stress strain relation described by Eq. 11-1 can be generalized to three-dimensions. In elasticity, we know that the linear stress strain relation for isotropic elastic solids can be described by two elastic constants. The shear modulus G and the bulk modulus K are the constants commonly used to characterize the elastic properties of materials. Any other elastic constants, e.g., the elastic modulus E , can be expressed in terms of these two constants. The same situation holds in viscoelasticity. Here, we can describe the viscoelastic material properties by two differential operator relations :

$$P [s_{ij}(t)] = Q [e_{ij}(t)] \quad (\text{Eq. 11-6})$$

and :

$$P' [\sigma_{ii}(t)] = Q' [\epsilon_{ii}(t)] \quad (\text{Eq. 11-7})$$

where $s_{ij}(t)$ and $e_{ij}(t)$ are the stress deviator tensor and the strain deviator tensor respectively. Tensor indices and the summation convention are employed in this chapter. Equation 11-6 can be written alternatively as :

$$\left. \begin{aligned} P (\sigma_{11} - \sigma_{22}) &= Q (\epsilon_{11} - \epsilon_{22}) \\ P (\sigma_{22} - \sigma_{33}) &= Q (\epsilon_{22} - \epsilon_{33}) \\ P (\sigma_{12}) &= Q (\epsilon_{12}) \\ P (\sigma_{23}) &= Q (\epsilon_{23}) \\ P (\sigma_{31}) &= Q (\epsilon_{31}) \end{aligned} \right\} \quad (\text{Eq. 11-8})$$

Equations 11-6 and 11-7 are analogous to the following relations in elasticity :

$$s_{ij} = 2 G e_{ij} \quad (\text{Eq. 11-9})$$

and :

$$\sigma_{ii} = 3 K \epsilon_{ii} \quad (\text{Eq. 11-10})$$

Hence the viscoelastic relations can be obtained directly from the elastic relations by replacing $2 G$ by the operator $\frac{Q}{P}$ and $3 K$ by the operator $\frac{Q'}{P'}$.

In elasticity, we have :

$$E \epsilon_{ij} = \sigma_{ij} + \nu (\sigma_{ij} - \delta_{ij} \sigma_{kk}) \quad (\text{Eq. 11-11})$$

rr The elastic modulus E and Poisson's ratio ν can be expressed in terms of G and K by the equations :

$$E = \frac{9KG}{3K+G} \quad (\text{Eq. 11-12})$$

and :

$$\nu = \frac{3K - 2G}{6K + 2G} \quad (\text{Eq. 11-13})$$

The equivalent relation in viscoelasticity is :

$$E[\epsilon_{ij}(t)] = \sigma_{ij}(t) + \nu [\sigma_{ij}(t) - \delta_{ij} \sigma_{kk}(t)], \quad (\text{Eq. 11-14})$$

where E and ν are operators which can be obtained from Eqs. 11-12 and 11-13 ;

$$E = \frac{3 Q Q'}{2 P Q' + P' Q} \quad (\text{Eq. 11-15})$$

and :

$$\nu = \frac{P Q' - P' Q}{2 P Q' + P' Q} \quad (\text{Eq. 11-16})$$

Substituting Eqs. 11-15 and 11-16 into 11-14, we obtain the following equation for the three-dimensional stress strain relation :

$$3 Q Q' [\epsilon_{ij}(t)] = (2 P Q' + P' Q) [\sigma_{ij}(t)] + (P Q' - P' Q) [\sigma_{ij}(t) - \delta_{ij} \sigma_{kk}(t)] .$$

2.2. Integral Operator Representation

As mentioned in the previous section, the use of the low-order differential operator representations may hinder the accurate description of viscoelastic properties, over several decades of time range. To remedy this situation, the integral operator representation may be used. The chief advantage here is that the kernel function in the integrals can be obtained directly from experiments and thus can represent the actual material properties accurately.

The creep curve due to a unit step function of stress at time τ , $\sigma(t) = H(t - \tau)$, is denoted by $F(t - \tau)$ and is known as the creep compliance. The value of $F(t - \tau)$ can be viewed as the influence of a step function of stress applied at time τ on the strain at time t . We shall assume that the material has no ageing effect so that the form of the creep compliance does not change with time. If we apply a step function in stress $\sigma(t) = \sigma_1 H(t - \tau_1)$ at $t = \tau_1$, the strain at time t is $\sigma_1 F(t - \tau_1)$. Similarly, due to $\sigma(t) = \sigma_2 H(t - \tau_2)$, the strain at time t is $\sigma_2 F(t - \tau_2)$. When both of these step-function stresses are applied, the strain at time t is $\epsilon(t) = \sigma_1 F(t - \tau_1) + \sigma_2 F(t - \tau_2)$. This result is known as the Boltzmann superposition principle for linear viscoelastic behavior. Therefore when the stress history $\sigma(\tau)$ for $\tau \leq t$ is given, we can consider the strain at time t as the summation of infinitesimal strains $d\epsilon(t)$ introduced by the infinitesimal stress increments $d\sigma(\tau)$ from $\tau = -\infty$ to $\tau = t$. That is:

$$\epsilon(t) = \int_{-\infty}^t F(t - \tau) \frac{d\sigma(\tau)}{d\tau} d\tau . \quad (\text{Eq. 11-17})$$

Eq. 11-17 is known as the convolution integral. If $\sigma(\tau)$ is a step function of τ , then from Eq. 11-17, $\epsilon(t) = F(t)$. Thus $F(t)$ can be considered as the solution of $P[H(t)] = Q[F(t)]$ in the equivalent differential operator expression. If the stress is applied suddenly at $t = 0$, $[\sigma(t) = 0 \text{ for } t < 0]$, then Eq. 11-17 can be written as either :

$$\epsilon(t) = F(0) \sigma(t) + \int_0^t \sigma(\tau) \frac{dF(t-\tau)}{d\tau} d\tau \quad (\text{Eq. 11-18})$$

or

$$\epsilon(t) = \int_{-\infty}^t \sigma(t-\tau) \frac{dF(\tau)}{d\tau} d\tau \quad (\text{Eq. 11-19})$$

In Eq. 11-16, the first term represents the instantaneous elastic response of strain to the current stress $\sigma(t)$ and the integral term stands for the response to the past history of stress.

As an example, we note that the creep compliance of the Voigt model can be obtained from the solution of Eq. 11-4 by setting $\sigma(t) = H(t)$, viz.

$$F(t) = \frac{1}{E} \left(1 - e^{-t/t_b} \right), \quad (\text{Eq. 11-20})$$

where $t_b = \eta/E$ is called the retardation time. Since $F(t_b)/F(\infty) = 1 - e^{-1}$, the retardation time can be used to measure the rate of growth of $F(t)$ curve. Consider a group of Voigt elements in series. Denote the spring constant and retardation time for each element by E_i and $(t_b)_i$. The creep compliance of this group of Voigt elements is :

$$F(t) = \sum_{i=1}^n \frac{1}{E_i} \left[1 - e^{-t/(t_b)_i} \right]. \quad (\text{Eq. 11-21})$$

If an infinite number of Voigt elements are in series with a spring of spring constant $1/F_g$ and with a dashpot of viscosity η , then the discrete system represented by Eq. 11-21 is replaced by a continuous system and the summation in Eq. 11-21 is replaced by integration :

$$F(t) = F_g + \frac{t}{\eta} + \int_0^\infty \frac{1}{E(\tau)} (1 - e^{-t/\tau}) d\tau \quad (\text{Eq. 11-22})$$

$$= F_g + \frac{t}{\eta} + \int_{-\infty}^\infty L(\tau) (1 - e^{-t/\tau}) d \ln \tau$$

where $L(\tau) = \tau/E(\tau)$ is referred to as the retardation spectrum and F_g is called the instantaneous (glassy) compliance.

In the complementary formulation, the curve of stress relaxation at time t due to a unit step function strain applied at time τ is denoted by $E(t-\tau)$ and is called the relaxation modulus. A typical curve of relaxation modulus is shown in Fig. 11-5. For most viscoelastic materials, the value of $E(t)$ changes rapidly at early times, immediately after the application of strain. The logarithmic time scale is adopted for this reason. Since it is difficult to measure the relaxation modulus at early times from direct relaxation tests, a high-frequency, sinusoidal stress pattern is used. We shall discuss this approach further in the next section. The relaxation modulus immediately following the application of strain is called the glassy modulus or instantaneous modulus. At large t , the relaxation modulus approaches a constant value, known as the rubbery modulus or delayed elastic modulus. For a given history of strain, the stress at any time t can be expressed by the following

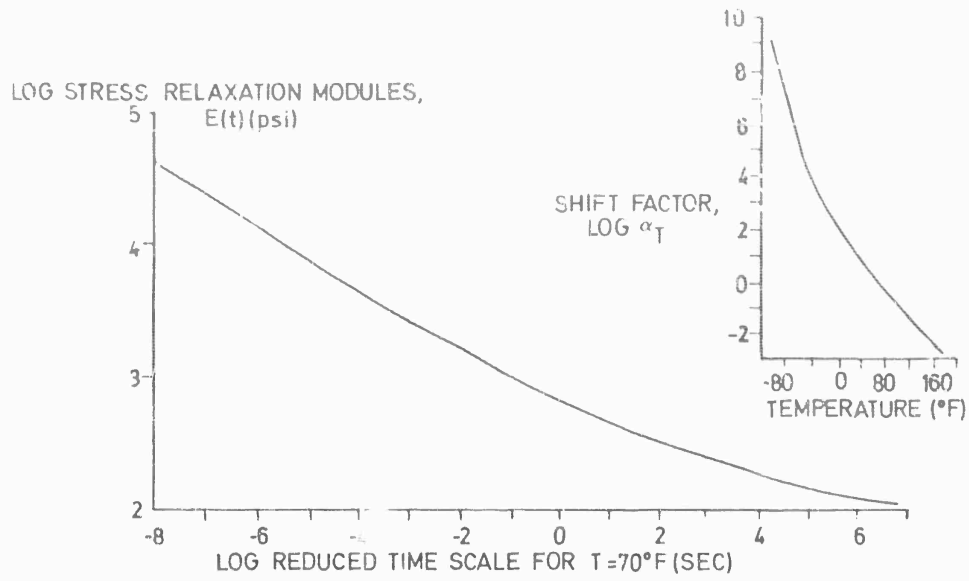


Fig. 11-5 Master stress relaxation modulus at $T = 70^{\circ}\text{F}$ and shift factor, PBAA propellant (7).

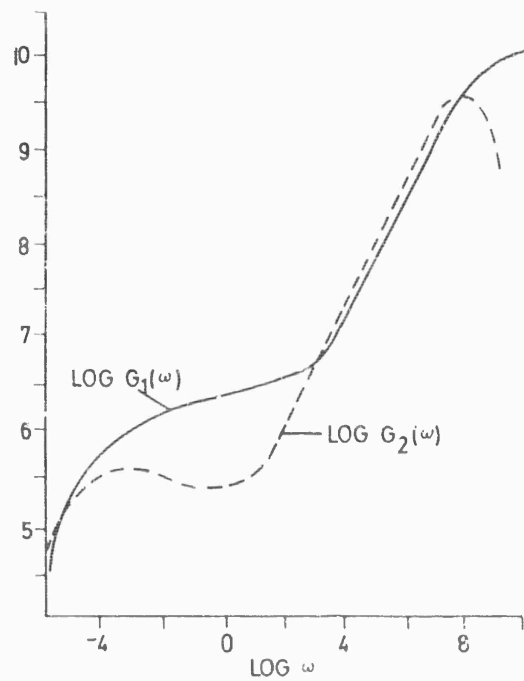


Fig. 11-6 Dynamic shear moduli of polyisobutylene (16).

integral :

$$\sigma(t) = \int_{-\infty}^t E(t-\tau) \frac{d\epsilon(\tau)}{d\tau} d\tau \quad (\text{Eq. 11-23})$$

In a manner similar to that of the creep compliance, the relaxation modulus $E(t)$ can be considered to be the solution of $P[E(t)] = Q[H(t)]$ in the equivalent differential operator expression. When the strain is applied suddenly at $t = 0$, i.e., $\epsilon(t) = 0$ for $t < 0$, Eq. 11-23 can also be written as either :

$$\sigma(t) = E(0)\epsilon(t) - \int_0^t \sigma(\tau) \frac{dE(t-\tau)}{d\tau} d\tau \quad (\text{Eq. 11-24})$$

or

$$\sigma(t) = \int_{-\infty}^t \epsilon(t-\tau) \frac{dE(\tau)}{d\tau} d\tau \quad (\text{Eq. 11-25})$$

In Eq. 11-24, the first term is the stress due to the instantaneous elastic response of the current strain $\epsilon(t)$ and the integral term is the stress due to the past history of strain.

By way of illustration, the relaxation modulus of the Maxwell model can be obtained from Eq. 11-3 by setting $\epsilon(t) = H(t)$. We obtain :

$$E(t) = Ee^{-t/t_a} \quad (\text{Eq. 11-26})$$

where $t_a = \eta/E$ is called the relaxation time. Since $E(t_a)/E(0) = e^{-1}$, the relaxation time is a measure of the decay rate of the relaxation curve. For a group of parallel Maxwell elements, we have :

$$E(t) = \sum_{i=1}^n E_i e^{-t/(t_a)_i} \quad (\text{Eq. 11-27})$$

where E_i and $(t_a)_i$ are the spring constant and the relaxation time of each element, respectively. If an infinite number of Maxwell elements and a spring constant E are in parallel, then we can define a continuous relaxation spectrum $J(\tau) = \tau E(\tau)$ such that :

$$E(t) = E_e + \int_{-\infty}^{\infty} J(\tau) e^{-t/\tau} d \ln \tau = E_e + \int_{-\infty}^{\infty} J(\tau) e^{-t/\tau} d \ln \tau \quad (\text{Eq. 11-28})$$

where E_e is the rubbery modulus or delayed elastic modulus.

By using the Laplace transform technique, we can prove that the creep compliance $F(t)$ and the relaxation modulus $E(t)$ are related by the equations :

$$\int_{-\infty}^t E(t-\tau) \frac{dF(\tau)}{d\tau} d\tau = \int_{-\infty}^t F(t-\tau) \frac{dE(\tau)}{d\tau} d\tau = 1 \quad (\text{Eq. 11-29})$$

rr* and :

$$\int_0^t E(t-\tau) F(\tau) d\tau = \int_0^t F(t-\tau) E(\tau) d\tau = t \quad (\text{Eq. 11-30})$$

From Eq. 11-29, we have :

$$E(t) F(t) = 1 + \int_0^t [E(t) - E(t-\tau)] \frac{dF(\tau)}{d\tau} d\tau \quad (\text{Eq. 11-31})$$

Since the integrand of the integral in Eq. 11-31 is always negative, we have :

$$E(t) F(t) \leq 1 \quad (\text{Eq. 11-32})$$

The foregoing one-dimensional stress strain relations can also be extended to three-dimensions. From the generalized Hooke's law in elasticity, we can obtain the following relation for viscoelastic materials :

$$\sigma_{ij}(t) = 2 \int_{-\infty}^t \mu(t-\tau) \frac{d\epsilon_{ij}(\tau)}{d\tau} d\tau + \delta_{ij} \int_{-\infty}^t \lambda(t-\tau) \frac{d\epsilon_{kk}(\tau)}{d\tau} d\tau \quad (\text{Eq. 11-33})$$

where $\mu(t)$ and $\lambda(t)$ are the relaxation moduli equivalent to Lamé's constants in elasticity. Alternatively, the viscoelastic stress strain relation can be expressed by the following equations :

$$s_{ij}(t) = 2 \int_{-\infty}^t G(t-\tau) \frac{de_{ij}(\tau)}{d\tau} d\tau \quad (\text{Eq. 11-34})$$

and

$$\sigma_{ii}(t) = 3 \int_{-\infty}^t K(t-\tau) \frac{de_{ii}(\tau)}{d\tau} d\tau \quad (\text{Eq. 11-35})$$

where $s_{ij}(t)$ is the stress deviator, $e_{ij}(t)$ is the strain deviator, $G(t)$ is the shear relaxation modulus and $K(t)$ is the bulk relaxation modulus.

In analogy with the elastic case, when two basic stress strain relations (Eqs. 11-34 and 11-35) are given, the other stress strain relations can also be determined from them. For example, $E(t)$ can be derived from $G(t)$ and $K(t)$. In elasticity, we have

$E = \frac{9KG}{3K+G}$ (see Eq. 11-12). The corresponding integral expression in viscoelasticity is :

$$9 \int_{-\infty}^t K(t-\tau) \frac{dG(\tau)}{d\tau} d\tau = \int_{-\infty}^t [3K(t-\tau) + G(t-\tau)] \frac{dE(\tau)}{d\tau} d\tau ,$$

or :

$$\begin{aligned} [3K(0) + G(0)] E(t) - \int_0^t E(\tau) [3K'(t-\tau) + G'(t-\tau)] d\tau &= 9K(0) G(t) \\ - 9 \int_0^t G(\tau) K'(t-\tau) d\tau , \end{aligned} \quad (\text{Eq. 11-36})$$

where $G'(t) = \frac{dG(t)}{dt}$ and $K'(t) = \frac{dK(t)}{dt}$. Equation 11-36 is a nonhomogeneous Volterra integral equation of the second kind for $E(t)$. When $G(t)$ and $K(t)$ are given,

Eq. 11-36 can be solved for $E(t)$ numerically. Similarly, in elasticity we can express the Poisson's ratio in terms of the shear modulus and the bulk modulus according to Eq. 11-13. In viscoelasticity, we have the following integral equation for $\nu(t)$:

$$[6K(0) + 2C(0)] \nu(t) - \int_0^t \nu(\tau) [6K'(t-\tau) + 2G'(t-\tau)] d\tau = 3K(t) - 2G(t) \quad (\text{Eq. 11-37})$$

The viscoelastic expression corresponding to the generalized Hooke's law (Eq. 11-11) is :

$$\begin{aligned} \int_{-\infty}^t E(t-\tau) \frac{d\epsilon_{ij}(\tau)}{d\tau} d\tau &= \sigma_{ij}(t) + \int_{-\infty}^t \nu(t-\tau) \frac{d\sigma_{ij}(\tau)}{d\tau} d\tau \\ &- \delta_{ij} \int_{-\infty}^t \nu(t-\tau) \frac{d\sigma_{kk}(\tau)}{d\tau} d\tau \end{aligned} \quad (\text{Eq. 11-38})$$

2.3 Complex Modulus and Complex Compliance Representations

The ideal instantaneous application of stress or strain as described in the previous section, is usually impossible to achieve in practice. It is extremely difficult to obtain data for creep compliance or relaxation modulus at very short times from creep or relaxation tests. In order to provide short-time information on viscoelastic properties, sinusoidal stress patterns are useful.

Consider the steady state strain response of a viscoelastic material due to an applied sinusoidal stress of frequency ω . If the viscoelastic behavior is linear, then the strain response is also sinusoidal with the same frequency, but it is not in phase with the stress because of the influences of delayed elasticity and viscous flow. It is convenient to express the stress and the strain as the real parts of :

$$\sigma^* = \sigma_0 e^{i\omega t} \quad (\text{Eq. 11-39})$$

and :

$$\epsilon^* = \epsilon_0 e^{i\omega t} \quad (\text{Eq. 11-40})$$

where σ_0 and ϵ_0 are both complex. The complex modulus and the complex compliance are defined respectively as :

$$E^*(\omega) = \frac{\sigma^*}{\epsilon^*} = \frac{\sigma_0}{\epsilon_0} = E_1(\omega) + i E_2(\omega) \quad (\text{Eq. 11-41})$$

and :

$$F^*(\omega) = \frac{\epsilon^*}{\sigma^*} = \frac{\epsilon_0}{\sigma_0} = \frac{1}{E^*(\omega)} = F_1(\omega) - i F_2(\omega) \quad (\text{Eq. 11-42})$$

where E^* and F^* are independent of the amplitude of oscillation on account of linearity. If we decompose the stress vector into two components, one in phase with the strain and the other 90° out of phase, then the real part of the complex modulus E_1 is the ratio of the in-phase component of the stress to the magnitude of the strain, and the imaginary part E_2 is the ratio of the out-of-phase component to the magnitude of the strain. The ratio of the peak stress to the peak strain is the magnitude of the complex modulus :

$$|E^*| = \left(E_1^2 + E_2^2 \right)^{1/2} \quad (\text{Eq. 11-43})$$

and the phase lag can be expressed as the angle :

$$\delta = \tan^{-1} (E_2/E_1) \quad . \quad (\text{Eq. 11-44})$$

The total energy input from zero time to time t is :

$$V = \int_0^t \sigma \frac{d\epsilon}{dt} dt \quad . \quad (\text{Eq. 11-45})$$

If $\bar{\epsilon}(t) = \bar{\epsilon} \cos \omega t$, where $\bar{\epsilon}$ is a real number, we have :

$$\sigma(t) = \bar{\epsilon} (E_1 \cos \omega t - E_2 \sin \omega t) \quad (\text{Eq. 11-46})$$

and from Eq. 11-45 :

$$V = V_1 + V_2 \quad , \quad (\text{Eq. 11-47})$$

where :

$$V_1 \equiv \frac{1}{4} E_1 \bar{\epsilon}^2 (\cos 2\omega t - 1) \quad (\text{Eq. 11-48})$$

and :

$$V_2 \equiv \frac{1}{4} E_2 \bar{\epsilon}^2 (2\omega t - \sin 2\omega t) \quad . \quad (\text{Eq. 11-49})$$

The quantity V_1 varies between zero and $-\frac{1}{2} E_1 \bar{\epsilon}^2$. It can be considered to represent the stored energy. The quantity V_2 oscillates about a continuously growing quantity $\frac{1}{2} E_2 \bar{\epsilon}^2 \omega t$ and can be interpreted as the energy loss. Therefore, E_1 is called the storage modulus and E_2 is termed the loss modulus. At $t = \frac{\pi}{2\omega}$, the magnitude of V_1 reaches a maximum and the absolute value of the ratio V_2/V_1 at this moment is equal to $\frac{\pi}{2} \tan \delta$. By similar reasoning, F_1 and F_2 are named storage compliance and loss compliance, respectively.

One can also define the complex shear modulus G^* , complex shear compliance $J^* = 1/G^*$, complex bulk modulus K^* and complex bulk compliance $B^* = 1/K^*$. The complex compliances F^* , J^* and B^* are related by the equation :

$$F^* = \frac{1}{3} J^* + \frac{1}{9} B^* \quad , \quad (\text{Eq. 11-50})$$

(compare Eq. 11-12).

The curves of the dynamic shear modulus of polyisobutylene, which are typical of many viscoelastic materials, are shown in Fig. 11-6, where G_1 and G_2 are in dyne/cm².

The relationship between the complex modulus and the differential operator expression can be obtained by substituting Eqs. 11-39 and 11-40 into Eq. 11-1. The result is :

$$E^*(\omega) = Q(i\omega) / P(i\omega) \quad . \quad (\text{Eq. 11-51})$$

The complex modulus can be expressed in terms of the relaxation modulus by the following equations of Fourier transforms :

$$E_1(\omega) = E(\infty) + \omega \int_0^{\infty} [E(t) - E(\infty)] \sin \omega t dt, \quad (\text{Eq. 11-52})$$

$$E_2(\omega) = \omega \int_0^{\infty} [E(t) - E(\infty)] \cos \omega t dt. \quad (\text{Eq. 11-53})$$

However, these equations are not very useful in practice. There are other approximate methods suggested by a number of authors (20), (21), (22) for evaluating the complex moduli from the relaxation modulus.

On the other hand, if $E_1(\omega)$ and $E_2(\omega)$ are given, the following approximate formula from Ninomiya and Ferry (23) can be used to evaluate the relaxation modulus:

$$E(t) = E_1(\omega) + 0.40 E_2(0.40\omega) - 0.014 E_2(10\omega) \quad \left| \omega = 1/t \right. \quad (\text{Eq. 11-54})$$

In particular, when $E(t)$ changes very slowly, we have :

$$E(t) = E_1(1/t). \quad (\text{Eq. 11-55})$$

From Eq. 11-54 or 11-55, the value of $E(t)$ for small times can be obtained indirectly, if the values of E_1 and E_2 for high frequencies are available. The difficulty of measuring $E(t)$ for early times is thus resolved. Equations similar to Eqs. 11-54 and 11-55 hold also for the shear modulus and the bulk modulus.

By a procedure similar to that presented in the previous section, we can express the complex moduli and the complex compliances as integrals of the relaxation spectrum and retardation spectrum :

$$E_1(\omega) = E_e + \int_{-\infty}^{\infty} J(\tau) \frac{\omega^2 \tau^2}{1 + \omega^2 \tau^2} d \ln \tau, \quad (\text{Eq. 11-56})$$

$$E_2(\omega) = \eta \omega + \int_{-\infty}^{\infty} J(\tau) \frac{\omega \tau}{1 + \omega^2 \tau^2} d \ln \tau \quad (\text{Eq. 11-57})$$

$$F_1(\omega) = F_g + \int_{-\infty}^{\infty} L(\tau) \frac{1}{1 + \omega^2 \tau^2} d \ln \tau, \quad (\text{Eq. 11-58})$$

$$F_2(\omega) = \frac{1}{\omega \eta} + \int_{-\infty}^{\infty} L(\tau) \frac{\omega \tau}{1 + \omega^2 \tau^2} d \ln \tau. \quad (\text{Eq. 11-59})$$

We can show that the integrals in Eqs. 11-56 and 11-57 are functionally dependent. Of course, the integrals in Eqs. 11-58 and 11-59 have the same property.

2.4. Temperature Effects

The discussion of the phenomenological theory of linear viscoelasticity so far has dealt with the representations of viscoelastic properties, based on the Boltzmann's superposition principle. It provides no physical insight into the molecular origin

of viscoelastic phenomena. In order to examine the physical behavior of viscoelastic materials in greater detail, we shall discuss one particular molecular model for the origin of viscoelasticity.

As we have said earlier, a polymer is a long chain of chemically linked primary molecular units termed monomers. The number of monomer units z , which is called the degree of polymerization, is of the order of hundreds or thousands. Thermal energy causes the polymer chain to writhe and squirm, but this Brownian-like motion is constrained by the presence of neighboring molecules. In the Rouse's model of the viscoelasticity (24) of dilute solutions of polymers, the polymer is viewed as a chain of z identical segments with completely flexible junctions. The spatial orientation of each segment is assumed to be such that the cartesian components of its length each have a Gaussian probability distribution function. The chain is said to be 'free-draining,' in the sense that it is assumed that the interaction of the polymer with its environment can be described by assigning a resistance, characterized by a friction coefficient, to each of its moving junctions. From arguments of the type that are used in describing Brownian motion, Rouse derived the following formula for the shear relaxation spectrum :

$$\bar{J}_s(t) = \frac{\rho R^\circ T}{m} \sum_{p=1}^N \tau_p \delta(\tau - \tau_p) , \quad (\text{Eq. 11-60})$$

with :

$$\tau_p \equiv \frac{a^2 z^2 \zeta_0}{6 \pi^2 p^2 k T} , \quad (\text{Eq. 11-61})$$

where ρ is the density, R° is the ideal gas constant, T is the absolute temperature, m is the molecular weight, a is a constant depending on local geometric parameters, ζ_0 is the monomeric friction coefficient and k is the Boltzmann constant.

From Eq. 11-60 we obtain :

$$G(t, T) = \frac{\rho R^\circ T}{m} \sum_{p=1}^N e^{-t/\tau_p} , \quad (\text{Eq. 11-62})$$

and :

$$G_1(\omega, T) = \frac{\rho R^\circ T}{m} \sum_{p=1}^N \frac{\omega^2 \tau_p^2}{1 + \omega^2 \tau_p^2} . \quad (\text{Eq. 11-63})$$

The constants a and ζ_0 in these formulas are temperature dependent. Let $a = \bar{a}$, $\rho = \bar{\rho}$, $\zeta_0 = \bar{\zeta}_0$ and $\tau_p = \bar{\tau}_p$ when $T = \bar{T}$. From Eq. 11-61 we have :

$$\tau_p = \alpha_T \bar{\tau}_p , \quad (\text{Eq. 11-64})$$

where :

$$\alpha_T = \frac{\bar{a}^2 \bar{\zeta}_0 \bar{T}}{\bar{a}^2 \bar{\zeta}_0 T} . \quad (\text{Eq. 11-65})$$

Define a reduced time variable ξ by the relation :

$$\xi = \frac{t}{\alpha_T}, \quad (\text{Eq. 11-66})$$

so that :

$$\log \xi = \log t - \log \alpha_T \quad (\text{Eq. 11-67})$$

From Eqs. 11-62 and 11-64 we then have :

$$G(t, T) = \frac{\rho T}{\rho \bar{T}} G(\xi, \bar{T}) \quad (\text{Eq. 11-68})$$

If we plot $\log G$ against $\log t$, the curve for temperature $T > \bar{T}$ can be obtained from the curve for temperature \bar{T} , by shifting the curve upward by an amount $\log \frac{\rho T}{\rho \bar{T}}$ and to the left by an amount $\log \alpha_T$ while the shape of the curve remains unaltered. These operations may, of course, produce a universal curve even if the Rouse model is not valid. The quantity α_T , as defined in this operational sense, is called the shift factor. Equation 11-65 gives the shift factor for the Rouse model.

The relation between α_T and T can be determined experimentally. The choice of \bar{T} is arbitrary. The shift factor curve for poly-n-octyl methacrylate with $\bar{T} = 100^\circ\text{C}$ is shown in Fig. 11-7. The following empirical formula from Williams, Landel and Ferry (46) has proven to be widely applicable :

$$\log \alpha_T = -c_1 (T - \bar{T}) / (c_2 + T - \bar{T}) \quad (\text{Eq. 11-69})$$

where c_1 and c_2 are determined experimentally. For most unfilled elastomeric systems, it is found that $c_1 = 8.86$ and $c_2 = 101.6$.

If we define a reduce frequency variable :

$$\Omega = \alpha_T \omega \quad (\text{Eq. 11-70})$$

then we have from Eq. 11-63 :

$$G_1(\omega, T) = \frac{\rho T}{\rho \bar{T}} G_1(\Omega, \bar{T}) \quad (\text{Eq. 11-71})$$

When $\log G_1$ is plotted against $\log \omega$, the curve for temperature $T > \bar{T}$ can be obtained from the curve for temperature \bar{T} by shifting the curve upward by an amount $\log \frac{\rho T}{\rho \bar{T}}$

and to the right by an amount $\log \alpha_T$, while the shape of the curve remains unaltered. Using this method, we can plot the relaxation modulus or complex modulus referred to a certain constant temperature from experiments which are performed at various temperatures. The curve obtained in this manner is known as the master curve or composite curve. The master curve of relaxation modulus at $T = 70^\circ\text{F}$ for PBAA propellant, is shown in Fig. 11-5.

To use the reduced time or reduced frequency variables outlined above is to invoke the principle of 'thermorheological simplicity'. Materials with this property are called thermorheologically simple materials. Since the vertical shift of the modulus curves is often quite small, for the purpose of applicational convenience, we are often permitted to ignore the vertical shift by making a slight modification in

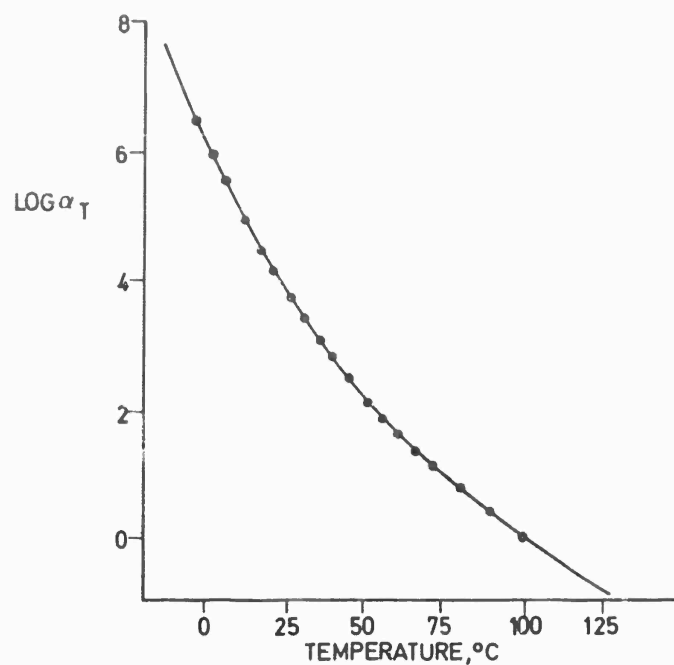


Fig. 11-7 Temperature dependence on the shift factor α_T for poly-n-octyl methacrylate with $T = 100^\circ\text{C}$.

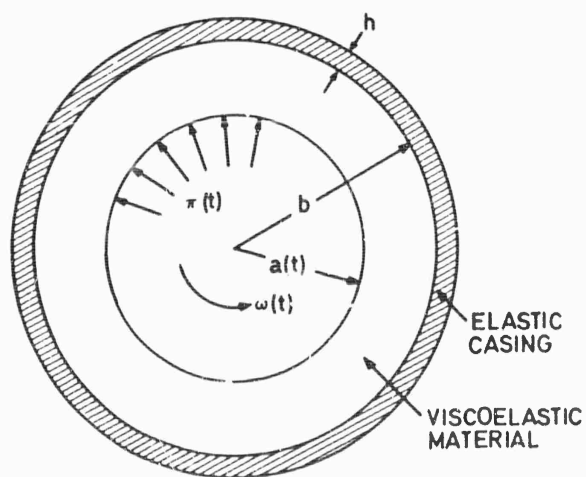


Fig. 11-8 Cross section of the encased viscoelastic cylinder.

α_T . Thus, Eqs. 11-68 and 11-71 are often approximated by :

$$G(t, T) = G(\xi, \bar{T}) \quad (\text{Eq. 11-72})$$

or :

$$G_1(\omega, T) = G_1(\Omega, \bar{T}) \quad (\text{Eq. 11-73})$$

In the region of rapid change of the modulus, it is possible to obtain a good matching of the adjacent curves from experimental data by using Eq. 11-72 or 11-73. However, in the region where the modulus is flat, the vertical shift is found to be necessary for satisfactory matching.

If the experiments are performed under continuously changing temperatures, the reduced time variable defined by Eq. 11-66 must be replaced by the variable :

$$\xi = \int_0^t \frac{d\tau}{\alpha_T [T(\tau)]} \quad (\text{Eq. 11-74})$$

This equation was proposed by Morland and Lee (22). At constant temperature, it reduces to Eq. 11-66.

2.5. Representation Based on Irreversible Thermodynamics

Deformation of solids is associated with a change of entropy. In particular, for viscoelastic materials, a large amount of heat is generated continuously during viscoelastic flow. These aspects of viscoelasticity can be approached from the theory of irreversible thermodynamics. Here we shall discuss the theory formulated by Biot (29).

Consider a system I defined by n state variables q_i . These state variables are presumed to be general enough to include unobservable variables, such as molecular configurations in a polymer. The generalized external forces Q_i are defined in such a manner that the external work done on the system is $Q_i dq_i$, when q_i is changed by an amount dq_i . In viscoelasticity the non-vanishing external forces are six stress components σ_{ij} with conjugate state variables of six strain components ϵ_{ij} . The remaining $n - 6$ state variables represent the internal degree of freedom, known as the hidden state variables. The characteristic function in the stress strain relation is influenced by the hidden variables.

Consider also a system II which is a large heat reservoir at absolute temperature T . When these two systems are connected thermally and insulated from their surroundings, the heat obtained by system I can be expressed in accordance with the first law of thermodynamics as :

$$dH_1 = dU_1 - Q_1 dq_1, \quad (\text{Eq. 11-75})$$

where U_1 is the internal energy of the system I. The change of entropy of the system II is :

$$dS_2 = - \frac{dH_1}{T} = - \frac{dU_1}{T} + \frac{1}{T} Q_1 dq_1. \quad (\text{Eq. 11-76})$$

The total change of entropy of the system I + II is :

$$dS = dS_1 + dS_2 = dS_1 - \frac{dU_1}{T} + \frac{1}{T} Q_1 dq_1 \quad (\text{Eq. 11-77})$$

The system is assumed to be close enough to the equilibrium state for the entropy S_1 and the internal energy U_1 of the system I to be expressible as functions of state variables; i.e.,

$$dS_1 = \frac{\partial S_1}{\partial q_i} dq_i \quad (\text{Eq. 11-78})$$

and :

$$dU_1 = \frac{\partial U_1}{\partial q_i} dq_i \quad (\text{Eq. 11-79})$$

Substituting Eqs. 11-78 and 11-79 into Eq. 11-77, we have:

$$T dS = \left(Q_1 - \frac{\partial F}{\partial q_i} \right) dq_i \quad (\text{Eq. 11-80})$$

where $F = U_1 - TS_1$ is the Helmholtz free energy. Note that this differs from the Gibbs free energy, for which the same symbol was used in Chapter 3. The second law of thermodynamics requires that :

$$dS \geq 0, \quad (\text{Eq. 11-81})$$

where the equality sign holds for reversible processes.

If X_i is defined as the generalized force conjugate to q_i in the expression of entropy production, viz.,

$$dS = X_i dq_i. \quad (\text{Eq. 11-82})$$

then Eq. 11-80 implies that :

$$X_i = \frac{1}{T} \left(Q_1 - \frac{\partial F}{\partial q_i} \right) \quad (\text{Eq. 11-83})$$

When the system is close to the equilibrium state, we may relate X_i to the time rate of change of q_j , viz., \dot{q}_j , by a linear equation,

$$X_i = \frac{1}{T} b_{ij} \dot{q}_j. \quad (\text{Eq. 11-84})$$

According to Onsager's principle, the coefficients b_{ij} are symmetric;

$$b_{ij} = b_{ji} \quad (\text{Eq. 11-85})$$

From Eqs. 11-83 and 11-84,

$$Q_i = \frac{\partial F}{\partial q_i} + b_{ij} \dot{q}_j. \quad (\text{Eq. 11-86})$$

Equations 11-82 and 11-84 imply that the quadratic form :

$$D = \frac{1}{2} b_{ij} \dot{q}_i \dot{q}_j \quad (\text{Eq. 11-87})$$

obeys the relationships :

$$TdS = 2D \geq 0 \quad (\text{Eq. 11-88})$$

Thus, the matrix b_{ij} is positive semidefinite. From Eqs. 11-86 and 11-87, we have :

$$\dot{F} + 2D = Q_i \dot{q}_i \quad (\text{Eq. 11-89})$$

The right-hand side of Eq. 11-89 represents the power input and the first term of the left-hand side is the rate of change of free energy. Hence the term $2D$ has a physical meaning as the rate of energy dissipation and D is called the dissipation function of the system.

At the thermodynamic equilibrium state, $\dot{q}_i = 0$ and $Q_i = 0$; hence, from Eq. 11-86, the linear term of q_i in the Taylor expansion of $F(q_i)$ must vanish. If we expand F through terms of second degree and adopt the convention that F and q_i are zero in the equilibrium state, then we obtain :

$$F = \frac{1}{2} a_{ij} q_i q_j \quad (\text{Eq. 11-90})$$

Without loss of generality, we may assume a_{ij} to be symmetric. Since F is assumed to be nonnegative, the matrix a_{ij} is positive definite. After substitution of Eq. 11-90 into Eq. 11-86, we obtain the equation of evolution :

$$a_{ij} q_j + b_{ij} \dot{q}_j = Q_i \quad (\text{Eq. 11-91})$$

This equation can be written in the Lagrangian form :

$$\frac{\partial F}{\partial q_i} + \frac{\partial D}{\partial \dot{q}_i} = Q_i \quad (\text{Eq. 11-92})$$

Whenever the temperature change is sufficiently small, the coefficients a_{ij} and b_{ij} are assumed to be temperature independent.

Note that the subscript i in Eq. 11-91 runs from 1 to n . If the variables q_i ($i = 1, 2, \dots, m$) really participate in the irreversible entropy production and q_i ($i = m+1, m+2, \dots, n$) are reversible variables which do not participate in the entropy production, then we have $b_{ij} = 0$ for either $i > m$ or $j > m$. The reversible variables can be expressed in terms of the irreversible variables by solving $n - m$ simultaneous algebraic equations. Substituting these solutions into the first m equations, we get :

$$\bar{a}_{ij} q_j + \bar{b}_{ij} \dot{q}_j = Q_i \quad (i, j = 1, 2, \dots, m) \quad (\text{Eq. 11-93})$$

It can be shown that $\bar{a}_{ij} = \bar{a}_{ji}$, $\bar{b}_{ij} = \bar{b}_{ji}$ and the matrix \bar{b}_{ij} is positive definite if the equilibrium state is stable.

Using the Laplace transform techniques for $q_i(0) = 0$, we can eliminate the hidden variables and obtain a relation between the observed variables and their conjugate forces,

$$Q_{ij}(t) = \sum_{j=1}^6 \left[c_{ij} q_j(t) + c'_{ij} \dot{q}_j(t) + \sum_{\alpha=1}^{m-6} c_{ij}(\alpha) \int_0^t e^{-\lambda_\alpha(t-\tau)} q_j(\tau) d\tau \right],$$

where $\lambda_\alpha \geq 0$, c_{ij} , c'_{ij} and $c_{ij}(\alpha)$ are characteristic constants. Expressed in terms of stress and strain tensors, it becomes :

$$\sigma_{ij}(t) = \sum_{\alpha=1}^{m-6} \int_0^t e^{-\lambda_\alpha(t-\tau)} D_{ijk\ell}(\alpha) \epsilon_{k\ell}(\tau) d\tau + D_{ijk\ell} \epsilon_{k\ell}(t) + D'_{ijk\ell} \dot{\epsilon}_{k\ell}(t).$$

If the number of hidden variables is infinite, a continuous spectrum of λ must be used, and the above equation is replaced by :

$$\sigma_{ij}(t) = \int_0^t L_{ijk\ell}(t-\tau) \epsilon_{k\ell}(\tau) d\tau + D_{ijk\ell} \epsilon_{k\ell}(t) + D'_{ijk\ell} \dot{\epsilon}_{k\ell}(t), \quad (\text{Eq. 11-94})$$

where :

$$L_{ijk\ell}(t) = \int_0^\infty D_{ijk\ell}(\lambda) e^{-\lambda t} d\lambda. \quad (\text{Eq. 11-95})$$

The quantities q_i can be solved from Eq. 11-93 and we can obtain the expression of strains in terms of stresses :

$$\epsilon_{ij}(t) = \int_0^t K_{ijk\ell}(t-\tau) \sigma_{k\ell}(\tau) d\tau + C_{ij} \sigma_{k\ell}(t) \quad (\text{Eq. 11-96})$$

where :

$$K_{ijk\ell}(t) = \int_0^\infty C_{ijk\ell}(\lambda) e^{-\lambda t} d\lambda. \quad (\text{Eq. 11-97})$$

Equation 11-94 can be interpreted as the stress strain relation for a model consisting of infinite Maxwell elements connected in parallel, where one element has a dashpot with infinite viscosity (infinite relaxation time) and another element has a rigid spring (zero relaxation time). Equation 11-96 shows the material is represented by a model of Voigt elements in series where one element has a dashpot with zero viscosity and another element has a spring with zero spring constant. These models are the same as the models we have considered in the investigation of the relaxation and retardation spectra. Therefore, the relaxation and retardation spectra defined by Eqs. 11-28 and 11-22 are consistent with the stress strain relation from an irreversible thermodynamic standpoint.

2.6. Nonlinear Stress-Strain Relations

Some solid propellants under high stresses or at high temperatures exhibit nonlinearity in the stress-strain relation even when the strain level is low. There are two types of nonlinearities: geometric nonlinearity and physical nonlinearity. As pointed out by Fitzgerald (7), (15) strains in solid propellant grains are quite limited, e.g., long term strains are not permitted to exceed 10 or 20 percent. The geometric nonlinearity of solid propellant materials is not so important as compared with their physical nonlinearity. Experimental studies performed by Lockheed Propulsion Company (62) shows that marked physical nonlinearities can be observed

for strain range from 1 to 5 percent in relaxation tests. The general theory of nonlinear stress strain relations was developed by Green and Rivlin (33) and also by Noll (34).

The deformation of any three-dimensional body can be described by the following equations :

$$x_i = x_i(X_1, X_2, X_3, t) \quad i = 1, 2, 3, \quad (\text{Eq. 11-98})$$

where x_i is the Cartesian coordinates of any material particle at time t and X_j is the coordinates of the same particle in the undeformed body. The deformation gradient at any time t is represented by a 3×3 matrix :

$$D = \| D_{ij} \| = \left\| \frac{\partial x_i}{\partial X_j} \right\| \quad (\text{Eq. 11-99})$$

The Lagrangian strain $E = \| \epsilon_{ij} \|$ is related to D by :

$$2E = D^T D - I, \quad (\text{Eq. 11-100})$$

where I is the unit matrix.

We call materials Green-Rivlin hereditary materials if the stresses at any particle at any time depend only on the history of the deformation gradient of that particle and the form of this dependence is independent of time, i.e.,

$$T(t) = \| \sigma_{ij}(t) \| = F \left[D \begin{matrix} \infty \\ (t - \tau) \\ \tau = 0 \end{matrix} \right] \quad (\text{Eq. 11-101})$$

where F is a tensor functional. Stresses in the body should be independent of the position of the observer. If we superpose a time dependent rigid body rotation to the body, stress fields also change by the same rotation. This is known as the principle of material indifference or principle of objectivity. Denoting this arbitrary rigid body rotation by a matrix $R(t)$, we have :

$$R(t) T(t) R^T(t) = F \left[R \begin{matrix} \infty \\ (t - \tau) \\ \tau = 0 \end{matrix} D \begin{matrix} \infty \\ (t - \tau) \\ \tau = 0 \end{matrix} \right]. \quad (\text{Eq. 11-102})$$

From this equation, by using polar decomposition of the matrix D , we can show that:

$$T(t) = D(t) S \left[E \begin{matrix} \infty \\ (t - \tau) \\ \tau = 0 \end{matrix} \right] D^T(t), \quad (\text{Eq. 11-103})$$

where S is a tensor functional called the stress functional and :

$$\dot{E} = \frac{\partial}{\partial t} E, \quad (\text{Eq. 11-104})$$

differentiated at constant X_j .

If a small change in the strain history causes only a small change of present stress, we may assume the stress functional to be continuous and express S by its Frechét expansion (35) which is a finite sum of multiple integrals :

$$\mathbf{S} = \sum_{n=1}^N \mathbf{S}_n \quad . \quad (\text{Eq. 11-105})$$

Here we have assumed that the undeformed state is stress free. The component of \mathbf{S}_n is :

$$\begin{aligned} S_n^{pq} = & \int_{-\infty}^t \int_{-\infty}^t \dots \int_{-\infty}^t K_{r_1 s_1 \dots r_n s_n}^{pq}(t - \tau_1, \dots, t - \tau_n) \\ & \dot{\epsilon}_{r_1 s_1}(\tau_1) \dots \dot{\epsilon}_{r_n s_n}(\tau_n) d\tau_1 \dots d\tau_n \quad . \end{aligned} \quad (\text{Eq. 11-106})$$

For initially isotropic materials, the integrand of \mathbf{S}_n must be a symmetric matrix polynomial in the matrices $\mathbf{E}(\tau_k)$ ($k = 1, 2, \dots, n$) and linear in each one. Here, the kernel functions in general depend on the total number of terms of expansion N . If the deformation is finite but sufficiently small, we may treat the Fréchet expansion Eq. 11-105 as the n th partial sum of a series expansion analogous to Taylor's series expansion of an analytic function. Hence in this case, the kernel functions are independent of the total number of terms of expansion. For a large strain history, we need only to add more terms. Taking this into consideration Pipkin (37) expressed the stress functional up to the third order term as :

$$\begin{aligned} S = & \int_{-\infty}^t [K_1(t - \tau) \mathbf{I} \text{tr} \dot{\mathbf{E}}(\tau) + K_2(t - \tau) \dot{\mathbf{E}}(\tau)] d\tau \\ & + \int_{-\infty}^t \int_{-\infty}^t \left\{ K_3(t - \tau_1, t - \tau_2) \mathbf{I} \text{tr} \dot{\mathbf{E}}(\tau_1) \text{tr} \dot{\mathbf{E}}(\tau_2) \right. \\ & \quad + K_4(t - \tau_1, t - \tau_2) \mathbf{I} \text{tr} [\dot{\mathbf{E}}(\tau_1) \dot{\mathbf{E}}(\tau_2)] \\ & \quad + K_5(t - \tau_1, t - \tau_2) \dot{\mathbf{E}}(\tau_1) \text{tr} \dot{\mathbf{E}}(\tau_2) \\ & \quad \left. + K_6(t - \tau_1, t - \tau_2) [\dot{\mathbf{E}}(\tau_1) \dot{\mathbf{E}}(\tau_2) + \dot{\mathbf{E}}(\tau_2) \dot{\mathbf{E}}(\tau_1)] \right\} d\tau_1 d\tau_2 \\ & + \int_{-\infty}^t \int_{-\infty}^t \int_{-\infty}^t \left\{ K_7(t - \tau_1, t - \tau_2, t - \tau_3) \mathbf{I} \text{tr} \dot{\mathbf{E}}_1(\tau_1) \text{tr} [\dot{\mathbf{E}}_2(\tau_2) \dot{\mathbf{E}}_3(\tau_3)] \right. \\ & \quad + K_8(t - \tau_1, t - \tau_2, t - \tau_3) \mathbf{I} \text{tr} \dot{\mathbf{E}}_1(\tau_1) \text{tr} \dot{\mathbf{E}}_2(\tau_2) \text{tr} \dot{\mathbf{E}}_3(\tau_3) \\ & \quad + K_9(t - \tau_1, t - \tau_2, t - \tau_3) \dot{\mathbf{E}}_1(\tau_1) \text{tr} \dot{\mathbf{E}}_2(\tau_2) \text{tr} \dot{\mathbf{E}}_3(\tau_3) \\ & \quad + K_{10}(t - \tau_1, t - \tau_2, t - \tau_3) \dot{\mathbf{E}}_1(\tau_1) \text{tr} [\dot{\mathbf{E}}_2(\tau_2) \dot{\mathbf{E}}_3(\tau_3)] \\ & \quad + K_{11}(t - \tau_1, t - \tau_2, t - \tau_3) [\dot{\mathbf{E}}_1(\tau_1) \dot{\mathbf{E}}_2(\tau_2) + \dot{\mathbf{E}}_2(\tau_2) \dot{\mathbf{E}}_1(\tau_1)] \text{tr} \dot{\mathbf{E}}_3(\tau_3) \\ & \quad \left. + K_{12}(t - \tau_1, t - \tau_2, t - \tau_3) [\dot{\mathbf{E}}_1(\tau_1) \dot{\mathbf{E}}_2(\tau_2) \dot{\mathbf{E}}_3(\tau_3) \right. \\ & \quad \left. + \dot{\mathbf{E}}_3(\tau_3) \dot{\mathbf{E}}_2(\tau_2) \dot{\mathbf{E}}_1(\tau_1)] \right\} d\tau_1 d\tau_2 d\tau_3 \end{aligned} \quad (\text{Eq. 11-107})$$

The material properties are characterized by the twelve kernel functions shown in Eq. 11-107.

Equations 11-103, 11-105 and 11-106 are too general to be applied to practical engineering problems. Coleman and Noll (38) and Pipkin (37) formulated finite linear viscoelasticity for materials with a fading memory. Their theory is restricted to the case that the deformations in the recent past relative to the present configuration are small. Pipkin and Lee (39) considered problems of infinitesimal time-dependent deformation superposed on a small, finite, suddenly applied, constant deformation for incompressible materials. The multiple integrals are reduced to single integrals. Huang and Lee (40) established an approximate stress strain relation for short time ranges, in which only single integrals are involved. Their equations can be used to evaluate the early time solution, e.g., the critical stress in solid propellant which usually occurs immediately after ignition. When the deformation is either infinitesimal ($D \approx I$) or irrotational, Eq. 11-103 can be written as :

$$T(t) = S \left[\begin{array}{c} \dot{E}(t - \tau) \\ \tau = 0 \end{array} \right] \quad (\text{Eq. 11-108})$$

which is the general stress strain relation for geometrically linear but physically nonlinear materials. Dong (41) has used this equation to solve several stress analysis problems. If the material property is linear, then $K_3 = K_4 = \dots = K_{12} = 0$ in Eq. 11-107. Thus the stress strain relation for linear viscoelastic solids becomes :

$$T(t) = \int_{-\infty}^t [K_1(t - \tau) I \text{tr} \dot{E}(\tau) + K_2(t - \tau) \dot{E}(\tau)] d\tau \quad (\text{Eq. 11-109})$$

which is the same as Eq. 11-33. The inverse relation of Eq. 11-108 is :

$$E(t) = S^* \left[\begin{array}{c} \dot{T}(t - \tau) \\ \tau = 0 \end{array} \right] \quad (\text{Eq. 11-110})$$

Equation 11-110 can be used to compare theory with experiments. For example, if the stress field is uniaxial, the uniaxial stress strain relation can be expressed by the following expansion :

$$\epsilon(t) = \sum_{n=1}^N S_n^* \quad (\text{Eq. 11-111})$$

where :

$$S_n^* = \int_{-\infty}^t \dots \int_{-\infty}^t F_n(t - \tau_1, \dots, t - \tau_n) \dot{\sigma}(\tau_1) \dots \dot{\sigma}(\tau_n) d\tau_1 \dots d\tau_n \quad (\text{Eq. 11-112})$$

When $N = 1$, it reduces to Eq. 11-17. Uniaxial creep test based on this equation has been performed by Ward and Onat (42), Lifshitz (43) and Onaran and Findley (44).

3. Stress Analysis of a Solid Propellant Rocket

In problems of stress analysis of solid propellant rocket motors, the configuration of the propellant grain is usually idealized for purposes of simplification. First of all, the grain is assumed to be monolithic and encased in a cylindrical casing. The star grain, furthermore, is approximated as a hollow circular cylinder composed of homogeneous isotropic viscoelastic material. Analyses based on this idealized model could furnish sufficient information for rocket design. Especially in prob-

lems involving transient thermal stresses, ablating conduit surface, longitudinal acceleration, reinforced grains, etc., the idealization could provide remarkable computational conveniences. However, the actual stress distribution in the star grain is different from those calculated in the model. The discrepancy is particularly serious in the region close to the star point where the stress is critical. Analyses of the star grain can be approached by finite-element methods, (63), (64) photoelastic experiments (17), (54), (55) or the conformal mapping technique (45), (56). Nevertheless, the idealized model is sufficiently important for us to spend the rest of this section on it, after an introductory discussion (Section 3.1) concerning the general nature of stress analysis in linear viscoelasticity. In addition to the simplest stress analysis problems, we treat spinning motors, ablating grains, non-isothermal grains, grain slump and reinforced grains.

3.1. Stress Analysis in Linear Viscoelasticity

Problems of stress analysis in viscoelasticity can be classified by nature into three groups: (a) the quasi-static problems, (b) the sinusoidal oscillation problems, and (c) the dynamic problems. The choice for representations of the stress strain relations is based on the type of problem to be analyzed.

Consider a three-dimensional body with volume V and surface S subjected to the prescribed surface traction T_i° over the portion S_σ of the surface and to the prescribed surface displacement u_i° over the remaining portion S_u of the surface. Denote the body force by f_i and density by ρ . The equation of motion is :

$$\frac{\partial \sigma_{ij}(t)}{\partial x_j} + f_i(t) = \rho \frac{\partial^2 u_i(t)}{\partial t^2} \quad (\text{Eq. 11-113})$$

For infinitesimal strains, the strain displacement relation can be written as :

$$\epsilon_{ij}(t) = \frac{1}{2} \left(\frac{\partial u_i(t)}{\partial x_j} + \frac{\partial u_j(t)}{\partial x_i} \right) \quad (\text{Eq. 11-114})$$

On the surface S_σ , the stress components must satisfy the equation :

$$\sigma_{ij}(t) \nu_j = T_i^\circ(t) \quad \text{on } S_\sigma, \quad (\text{Eq. 11-115})$$

where ν_j is the direction cosine of the outward normal. On the surface S_u , the displacement is :

$$u_i = u_i^\circ \quad \text{on } S_u \quad (\text{Eq. 11-116})$$

Equation 11-113 is a vector form of three equations and Eq. 11-114 is a tensor form of six equations. The three-dimensional stress strain relations furnish six other equations. The fifteen unknown quantities, three displacement components, six stress components and six strain components, are determined by these fifteen field equations. When the right-hand side of Eq. 11-113 is negligibly small, the problem is considered quasi-static. For these problems, the conditions imposed on the relaxation moduli for unique solutions have been discussed by Bruer and Onat (47) and also by Gurtin and Sternberg (12).

Since the material properties are time-dependent, viscoelastic problems are usually found to be more difficult than the equivalent elastic problems. Further complexities are caused by temperature effects, moving boundaries and the interchange of stress-prescribed boundaries and displacement-prescribed boundaries during deformation.

Consider a viscoelastic body under stress in an isothermal condition with no interchange of S_σ and S_u during deformation. The time variable here can be removed by taking the Laplace transform with respect to time in the field equations. If we denote the Laplace transform by :

$$\bar{g}(p) = \int_0^{\infty} g(t) e^{-pt} dt$$

and assume zero initial conditions, Eqs. 11-113 to 11-116 become :

$$\frac{\partial \bar{\sigma}_{ij}}{\partial x_j} + \bar{f}_i = \rho p^2 \bar{u}_i \quad (\text{Eq. 11-117})$$

$$\bar{\epsilon}_{ij} = \frac{1}{2} \left(\frac{\partial \bar{u}_i}{\partial x_j} + \frac{\partial \bar{u}_j}{\partial x_i} \right) \quad (\text{Eq. 11-118})$$

$$\sigma_{ij} n_j = \bar{T}_i^\circ \quad \text{on } S_\sigma \quad (\text{Eq. 11-119})$$

and :

$$\bar{u}_i = \bar{u}_i^\circ \quad \text{on } S_u. \quad (\text{Eq. 11-120})$$

If the stress strain relations are represented in the differential operator form, from Eqs. 11-6 and 11-7 we have :

$$P(p) \bar{s}_{ij} = Q(p) \bar{\epsilon}_{ij} \quad (\text{Eq. 11-121})$$

and :

$$P'(p) \bar{\sigma}_{ii} = Q'(p) \bar{\epsilon}_{ii} \quad (\text{Eq. 11-122})$$

On the other hand, if the integral operators are used, from Eqs. 11-34 and 11-35 and applying the convolution theorem, we have :

$$\bar{\epsilon}_{ij} = 2\bar{G}(p) p \bar{e}_{ij} \quad (\text{Eq. 11-123})$$

and :

$$\bar{\sigma}_{ii} = 3\bar{K}(p) p \bar{\epsilon}_{ii} \quad (\text{Eq. 11-124})$$

Consider an equivalent problem but with elastic materials. If we take the Laplace transform, we would have the same field equations (Eqs. 11-117 to 11-120). But the stress strain relations in transformed variables (Eqs. 11-121 to 11-124) would be replaced by :

$$\bar{s}_{ij} = 2G\bar{e}_{ij} \quad (\text{Eq. 11-125})$$

and :

$$\bar{\sigma}_{ii} = 3K\bar{\epsilon}_{ii} \quad (\text{Eq. 11-126})$$

Thus, if the solution for the transformed variables in the elastic case can be written explicitly in terms of the elastic constants G and K , the viscoelastic solution of the

transformed variables can then be obtained by replacing G by $\frac{Q(p)}{2P(p)}$ or $\bar{G}(p)$ and replacing K by $\frac{Q'(p)}{3P'(p)}$ or $\bar{K}(p)$. The solution of the original viscoelastic problem is then found by the inverse transform. This technique is known as the correspondence principle. Note that the functional forms of $G(t)$ and $K(t)$ are needed in applying this principle. Difficulty usually arises in the process of inverse transformation, particularly when the empirical equations of relaxation functions are complicated.

When the empirical formulas for the complex moduli G^* and K^* are available, it is convenient to apply the one-sided Fourier transform :

$$\tilde{g}(\omega) = \int_0^{\infty} e^{-i\omega t} g(t) dt .$$

The inverse transform is ($\text{Rl} [\]$ denotes 'real part of') :

$$g(t) = \frac{1}{\pi} \text{Rl} \left[\int_0^{\infty} e^{i\omega t} \tilde{g}(\omega) d\omega \right] .$$

Again, when zero initial conditions are imposed, after transformation, Eqs. 11-113 to 11-116 become :

$$\frac{\partial \tilde{\sigma}_{ij}}{\partial x_j} + \tilde{f}_i + \rho \omega^2 \tilde{u}_i = 0 , \quad (\text{Eq. 11-127})$$

$$\tilde{\epsilon}_{ij} = \frac{1}{2} \left(\frac{\partial \tilde{u}_i}{\partial x_j} + \frac{\partial \tilde{u}_j}{\partial x_i} \right) , \quad (\text{Eq. 11-128})$$

$$\tilde{\sigma}_{ij} \nu_j = \tilde{T}_i^{\circ} \quad \text{on } S_{\sigma} \quad (\text{Eq. 11-129})$$

and :

$$\tilde{u}_i = \tilde{u}_i^{\circ} \quad \text{on } S_u . \quad (\text{Eq. 11-130})$$

From Eqs. 11-6, 11-7 and 11-51 we have :

$$\tilde{s}_{ij} = \frac{Q(i\omega)}{P(i\omega)} \tilde{e}_{ij} = 2 G^*(\omega) \tilde{e}_{ij} \quad (\text{Eq. 11-131})$$

and :

$$\tilde{\sigma}_{ii} = \frac{Q'(i\omega)}{P'(i\omega)} \tilde{\epsilon}_{ii} = 3 K^*(\omega) \tilde{\epsilon}_{ii} . \quad (\text{Eq. 11-132})$$

For the equivalent elastic problem, Eqs. 11-127 to 11-130 remain the same but Eqs. 11-131 and 11-132 are replaced by :

$$\tilde{s}_{ij} = 2G \tilde{e}_{ij} \quad (\text{Eq. 11-133})$$

and :

$$\tilde{\sigma}_{ii} = 3K \tilde{\epsilon}_{ii} .$$

Hence we can establish the following correspondence principle : The one-sided Fourier transform solution of a viscoelastic problem can be obtained from the transform solution of an equivalent elastic problem by replacing G by $G^*(\omega)$ and K by $K^*(\omega)$.

The transform techniques mentioned above can be applied to both the dynamic and the quasi-static problems. In the quasi-static case, we can set $\rho = 0$ in the equation of motion. The viscoelastic solution for the transformed quantities can then be obtained directly from the known elastic solution. Radok proposed another correspondence principle for quasi-static problems (14): If the solution of the equivalent elastic problem can be expressed explicitly in terms of the elastic constants, the viscoelastic solution can then be obtained by a similar expression in which the elastic constants are replaced by corresponding differential or integral operators. In other words, if the equivalent elastic solution for stresses is $f(x_i, t, G, K)$, then the viscoelastic solution for stresses is either $f(x_i, t, \frac{Q}{2P}, \frac{Q'}{3P'})$ or $f(x_i, t, G, K)$ with G and K as the hereditary integral operators. Radok's correspondence principle usually leads to an integro-differential equation for the required quantities which can then be solved by either integral transform methods or finite difference technique. Note that even if the corresponding elastic problem has no explicit form of solution, Radok's correspondence principle can still be applied to any of the equations found in the intermediate steps of derivation of the elastic solution.

From elasticity, one finds that the only elastic constant in the Betrami-Michell compatibility equation is Poisson's ratio ν . If only the stress boundary conditions are prescribed, the elastic solutions of stresses would then contain no elastic constants except ν . Hence, in this case, when the material is incompressible ($\nu = 1/2$), the integral operators in the viscoelastic solution of stresses would degenerate to a constant multiplier. Thus the viscoelastic solution and the elastic solution would be identical. This theorem is due to Alfrey (20). Another applicational example of Radok's correspondence principle is found in the generalized plane stress problems with absent body forces and stress boundary conditions. Here, the elastic solution does not contain any elastic constants and hence is identical with the viscoelastic solution. Radok's correspondence principle can be applied successfully in most problems. However, there are cases in which the application of this principle must be considered with extreme care. For example, the term Ga^2 in the corresponding elastic solution may come from the multiplication aGa . When we change G to an integral operator in obtaining the viscoelastic term, these two expressions would lead to different results. It is necessary to check the derivation of the corresponding elastic solution step by step and see whether the equation in each step can be converted into a similar viscoelastic equation, by Radok's correspondence principle.

In sinusoidal oscillation problems, it is convenient to express the stress and strain components as real parts of the expressions :

$$\sigma_{ij} = \sigma_{ij}^* e^{i\omega t} \quad (\text{Eq. 11-135})$$

and :

$$\epsilon_{ij} = \epsilon_{ij}^* e^{i\omega t}, \quad (\text{Eq. 11-136})$$

where ω is the frequency of oscillation. The quantities σ_{ij}^* and ϵ_{ij}^* are, in general, complex and therefore are known as the complex stress and strain tensors. From Section 2.3, the viscoelastic properties can be represented by the complex moduli G^* and K^* such that :

$$s_{ij}^* = 2G^* e_{ij}^* \quad (\text{Eq. 11-137})$$

and :

$$\sigma_{ii}^* = 3K^* \epsilon_{ii}^* \quad (\text{Eq. 11-138})$$

where s_{ij}^* and e_{ij}^* are the complex stress deviator and strain deviator tensors. If the displacement, the body force and the prescribed surface traction vectors are also expressed as the real parts of :

$$u_i = u_i^* e^{i\omega t} \quad (\text{Eq. 11-139})$$

$$f_i = f_i^* e^{i\omega t} \quad (\text{Eq. 11-140})$$

and :

$$T_i^\circ = T_i^{\circ*} e^{i\omega t} \quad (\text{Eq. 11-141})$$

then from Eqs. 11-113 to 11-116, we have :

$$\frac{\partial \sigma_{ij}^*}{\partial x_j} + f_i^* + \rho \omega^2 u_i^* = 0 \quad (\text{Eq. 11-142})$$

$$\epsilon_{ij}^* = \frac{1}{2} \left(\frac{\partial u_i^*}{\partial x_j} + \frac{\partial u_j^*}{\partial x_i} \right) \quad (\text{Eq. 11-143})$$

$$\sigma_{ij}^* \nu_j = T_i^{\circ*} \quad \text{on } S_\sigma \quad (\text{Eq. 11-144})$$

and :

$$u_i^* = u_i^{\circ*} \quad \text{on } S_u \quad (\text{Eq. 11-145})$$

Equations 11-137, 11-138 and 11-142 to 11-145 constitute a boundary value problem. After the solutions for σ_{ij}^* and ϵ_{ij}^* are found, σ_{ij} and ϵ_{ij} can be obtained by taking the real parts of Eqs. 11-135 and 11-136.

When the complex moduli G^* and K^* in Eqs. 11-137 and 11-138 are replaced by the shear modulus G and the bulk modulus K , the above boundary value problem would become an elastic problem. Thus, the viscoelastic solution can be obtained from the corresponding elastic problem by the following correspondence principle: If the solution of the corresponding elastic sinusoidal oscillation problem can be found explicitly as $\sigma_{ij} = R [f(G, K, x, t) e^{i\omega t}]$, then the viscoelastic solution is $\sigma_{ij} = R [f(G^*, K^*, x, t) e^{i\omega t}]$.

In applying the transform technique, explicit forms of relaxation moduli or complex moduli are required. When differential operators are used, the degree of the operators must be high such that the mechanical properties of viscoelastic materials can be accurately represented over several decades of time or frequency. For real materials, the analysis based on the technique of integral transform is usually complicated. Approximate methods for taking inverse transforms have been proposed by Schapery (57) and Papoulis (58). For practical reasons, it is convenient to use the integral operators for stress strain relations so that the measured relaxation functions can be applied directly in the stress analysis. This technique has the advantage of avoiding not only the difficulty of the inverse transform in the integral transform method but also the error introduced by using differential operators to

express the real material characteristics. It can be effectively applied to problems with moving boundaries or transient temperatures. The resulting integro-differential equations can be solved numerically by finite difference techniques.

3.2. Stresses in an Encased Viscoelastic Cylinder

As we have suggested earlier, the stress distribution in a solid propellant motor can best be analyzed by considering the problem of an encased infinitely long viscoelastic hollow cylinder, subjected to internal pressure as shown in Fig. 11-8. Here we shall consider a quasi-static case, without spinning and ablation, i.e., $\omega(t) = 0$ and $a(t) = a$. The dynamic version of the same problem was studied by Baltrukonis (59) and Achenbach (60), (61). Furthermore, the casing is assumed to be elastic with elastic modulus E_c and Poisson's ratio ν_c . Since the cylinder is infinitely long, we can treat the analysis as an axially symmetrical plane strain problem. Here the boundary conditions do not change with time and therefore the Laplace transform method and the correspondence principle can be applied.

The solution for the corresponding elastic problem can be derived easily. The radial and circumferential stress components of the elastic problem are, respectively,

$$\sigma_r = -\pi \frac{\beta \left(\frac{b^2}{r^2} + 1 \right) - \left(\frac{b^2}{r^2} - 1 \right)}{\beta \left(\frac{b^2}{a^2} + 1 \right) - \left(\frac{b^2}{a^2} - 1 \right)} \quad (\text{Eq. 11-146})$$

and :

$$\sigma_\theta = \pi \frac{\beta \left(\frac{b^2}{r^2} - 1 \right) - \left(\frac{b^2}{r^2} + 1 \right)}{\beta \left(\frac{b^2}{a^2} + 1 \right) - \left(\frac{b^2}{a^2} - 1 \right)} \quad (\text{Eq. 11-147})$$

where :

$$\beta = \frac{1 - \nu^2}{\nu(1 + \nu) - \frac{(1 - \nu_c^2) b E}{h E_c}} \quad (\text{Eq. 11-148})$$

and E and ν are the elastic modulus and Poisson's ratio of the cylinder. Expressed in terms of the shear modulus G and bulk modulus K , the quantity β can be written as :

$$\beta = \frac{3K + 4G}{3K - 2G - \frac{4}{\alpha} G(3K + G)} \quad (\text{Eq. 11-149})$$

where :

$$\alpha = \frac{h E_c}{(1 - \nu_c^2) b} \quad (\text{Eq. 11-150})$$

We shall assume that the viscoelastic material is incompressible with Voigt shear behavior, i.e.,

$$\bar{K}(p) = \infty$$

(Eq. 11-151)

and :

$$\bar{G}(p) = \frac{1}{2} (Ap + B)$$

(Eq. 11-152)

From Eqs. 11-149, 11-151 and 11-152,

$$\bar{\beta}(p) = \left[1 - \frac{2}{\alpha} (Ap + B) \right]^{-1}$$

(Eq. 11-153)

If the internal pressure is prescribed to be :

$$\pi(t) = \pi_0 (1 - e^{-nt}) H(t) \quad n > 0,$$

(Eq. 11-154)

then the Laplace transform is :

$$\bar{\pi}(t) = \pi_0 \frac{n}{p(p+n)}$$

(Eq. 11-155)

Using the correspondence principle, we have from Eqs. 11-146, 11-147, 11-153 and 11-155 :

$$\bar{\sigma}_r = - \frac{n\pi_0}{p(p+n)} \frac{(Ap + B) \left(\frac{b^2}{r^2} - 1 \right) + \alpha}{(Ap + B) \left(\frac{b^2}{a^2} - 1 \right) + \alpha}$$

(Eq. 11-156)

and :

$$\bar{\sigma}_0 = \frac{n\pi_0}{p(p+n)} \frac{(Ap + B) \left(\frac{b^2}{r^2} + 1 \right) - \alpha}{(Ap + B) \left(\frac{b^2}{a^2} - 1 \right) + \alpha}$$

(Eq. 11-157)

The inverse transform gives :

$$\sigma_r = - \pi_0 \left\{ \frac{B \left(\frac{b^2}{r^2} - 1 \right) + \alpha}{B \left(\frac{b^2}{a^2} - 1 \right) + \alpha} - \frac{(B - nA) \left(\frac{b^2}{r^2} - 1 \right) + \alpha}{(B - nA) \left(\frac{b^2}{a^2} - 1 \right) + \alpha} e^{-nt} \right. \\ \left. - \frac{nA \alpha \left(\frac{b^2}{a^2} - \frac{b^2}{r^2} \right)}{\left[B \left(\frac{b^2}{a^2} - 1 \right) + \alpha \right] \left[(nA - B) \left(\frac{b^2}{a^2} - 1 \right) - \alpha \right]} e^{-nt} \right\}$$

(Eq. 11-158)

and :

$$\sigma_{\theta} = \pi_0 \left\{ \frac{B \left(\frac{b^2}{r^2} + 1 \right) - \alpha}{B \left(\frac{b^2}{a^2} - 1 \right) + \alpha} - \frac{(B - nA) \left(\frac{b^2}{r^2} + 1 \right) - \alpha}{(B - nA) \left(\frac{b^2}{a^2} - 1 \right) + \alpha} e^{-nt} - \frac{B \left(\frac{b^2}{a^2} - 1 \right) + \alpha}{A \left(\frac{b^2}{a^2} - 1 \right)} t \right\} + \frac{nA \alpha \left(\frac{b^2}{a^2} + \frac{b^2}{r^2} \right)}{\left[B \left(\frac{b^2}{a^2} - 1 \right) + \alpha \right] \left[(nA - B) \left(\frac{b^2}{a^2} - 1 \right) - \alpha \right]} e^{-nt} \quad (\text{Eq. 11-159})$$

If the internal pressure is applied instantaneously at $t = 0$, the solution of σ_r and σ_{θ} can then be obtained by setting $n = \infty$ in Eqs. 11-158 and 11-159. The distributions of σ_r and σ_{θ} are shown in Fig. 11-9 for the following data: $b/a = 2$, $A/B = 10^{-2}$ sec, $B = \frac{2}{3} \times 10^5$ psi and $\alpha = 10^6$ psi, (8). It is found that the critical tensile circumferential stress occurs on the cavity surface immediately after the application of pressure and the response is elastic at that instant. Fracture may occur if this circumferential stress is beyond the tensile strength of the propellant grain. The circumferential stress decreases algebraically as time goes on. At large time, the state of stress approaches a delayed elastic state with $G = B/2$ and $K = \infty$. The radial stress is always compressive and has less importance from a practical point of view. If the internal pressure were applied gradually, the circumferential stress on the cavity surface would increase algebraically with time and then decrease to its final negative value. The shorter the application time, the higher would be the critical circumferential stress. Thus, in order to prevent the grain from internal failure, the internal pressure must be applied as gradually as possible.

3.3. Stresses in an Encased Viscoelastic Spinning Cylinder with Ablating Cavity Surface

In the previous section, we considered the case of a viscoelastic cylinder with fixed inner radius. For a solid propellant rocket under launching conditions, the rocket grain is gradually burned and removed as gas. The inner radius is therefore a function of time (Fig. 11-8);

$$a = a(t) \text{ and } da/dt > 0. \quad (\text{Eq. 11-160})$$

We shall also consider the cylinder to be spinning about its axis with angular velocity $\omega = \omega(t)$. The Laplace transform method cannot be used in this case on account of the moving boundary. We shall follow a procedure suggested by Rogers and Lee (49).

Again, we shall consider an axially symmetric plane strain problem. Let u be the radial displacement. The radial, circumferential and axial strains are:

$$\epsilon_r = \frac{\partial u}{\partial r}, \quad (\text{Eq. 11-161})$$

$$\epsilon_{\theta} = \frac{u}{r} \quad (\text{Eq. 11-162})$$

and:

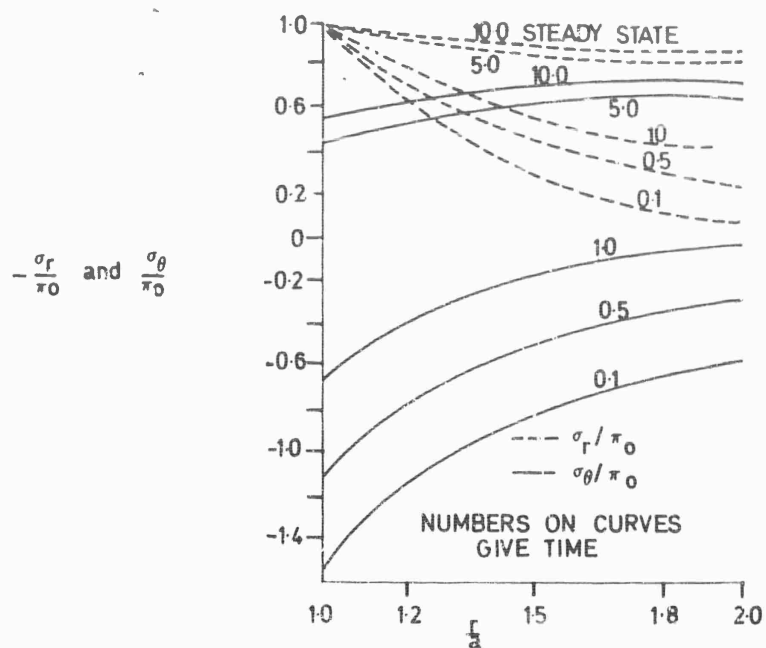


Fig. 11-9 Stresses in a reinforced incompressible Voigt cylinder $\pi(t) = \pi_0 H(t)$.

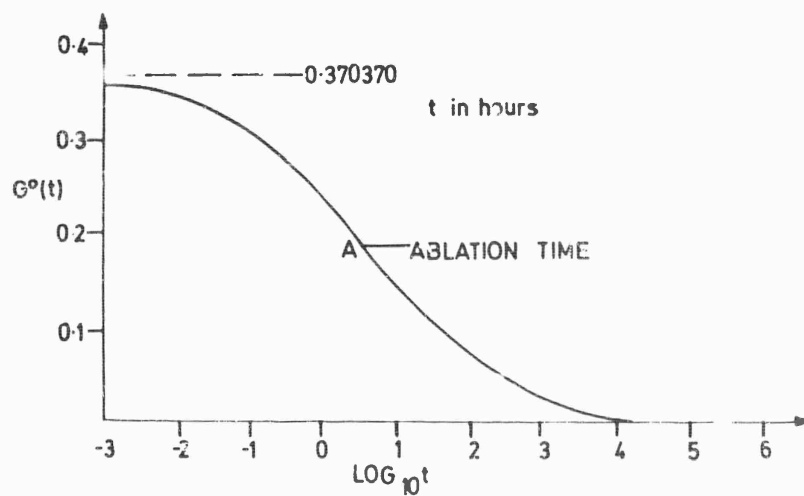


Fig. 11-10 Relaxation modulus in shear for polymethylmethacrylate at 80°C (52).

$$\epsilon_z = 0 \quad . \quad (\text{Eq. 11-163})$$

The equation of equilibrium can be written as :

$$\sigma_\theta = \frac{\partial}{\partial r} (r \sigma_r) + \rho \omega^2 r^2 \quad , \quad (\text{Eq. 11-164})$$

where ρ is the mass density of the viscoelastic material.

For purposes of mathematical convenience and due to the lack of contrary experimental evidence for most viscoelastic materials, the material here is assumed to be elastic in dilatation with bulk modulus K . The influence of viscoelastic compressibility is discussed in (50). From Eqs. 11-8, 11-161, 11-162 and 11-163, we have :

$$\sigma_r + \sigma_\theta + \sigma_z = 3K(\epsilon_r + \epsilon_\theta + \epsilon_z) = 3K\left(\frac{\partial u}{\partial r} + \frac{u}{r}\right) \quad , \quad (\text{Eq. 11-165})$$

$$\sigma_\theta - \sigma_r = 2 \int_{-\infty}^t G(t-\tau) \frac{\partial}{\partial \tau} (\epsilon_\theta - \epsilon_r) d\tau = 2 \int_{-\infty}^t G(t-\tau) \frac{\partial}{\partial \tau} \left(\frac{u}{r} - \frac{\partial u}{\partial r}\right) d\tau, \quad (\text{Eq. 11-166})$$

$$\sigma_\theta - \sigma_z = 2 \int_{-\infty}^t G(t-\tau) \frac{\partial}{\partial \tau} (\epsilon_\theta - \epsilon_z) d\tau = 2 \int_{-\infty}^t G(t-\tau) \frac{\partial}{\partial \tau} \left(\frac{u}{r}\right) d\tau \quad . \quad (\text{Eq. 11-67})$$

The internal pressure is prescribed as $\pi(t)$ at $r = a(t)$, i.e.,

$$\sigma_r [a(t), t] = -\pi(t) \quad . \quad (\text{Eq. 11-168})$$

On the surface of the elastic casing, the boundary condition is :

$$\sigma_r (b, t) = -B\epsilon_\theta (b, t) \quad , \quad (\text{Eq. 11-169})$$

where :

$$\frac{1}{B} = \frac{b}{h} \frac{1 - \nu_c^2}{E_c} \quad . \quad (\text{Eq. 11-170})$$

From Eqs. 11-161, 11-162, 11-164 and 11-166, we have :

$$r \frac{\partial \sigma_r}{\partial r} + \rho r^2 \omega^2 = -2r \int_{-\infty}^t G(t-\tau) \frac{\partial^2 \epsilon_\theta}{\partial \tau^2} d\tau \quad . \quad (\text{Eq. 11-171})$$

By integrating once with respect to r , we get :

$$\sigma_r = -\frac{1}{2} \rho r^2 \omega^2 - 2 \int_{-\infty}^t G(t-\tau) \frac{\partial \epsilon_\theta}{\partial \tau} d\tau + f(t) \quad . \quad (\text{Eq. 11-172})$$

We will assume that the internal pressure and angular velocity are applied at $t = 0$. Eq. 11-172 can be written as :

$$\sigma_r = f(t) - \frac{1}{2} \rho r^2 \omega^2 - 2G(0)\epsilon_\theta + 2 \int_0^t \epsilon_\theta \frac{\partial}{\partial \tau} G(t-\tau) d\tau \quad . \quad (\text{Eq. 11-173})$$

Setting $r = b$ in Eq. 11-173 and using the boundary condition given in Eq. 11-169, we get :

$$\sigma_r(b, t) - \frac{2\mu}{E} \int_0^t \sigma_r(b, \tau) \frac{\partial}{\partial \tau} G(t - \tau) d\tau = \frac{\mu B}{E} \left[\frac{1}{2} \rho b^2 \omega^2(t) - f(t) \right], \quad (\text{Eq. 11-174})$$

where :

$$\mu = \frac{E}{2 G(0) - B}. \quad (\text{Eq. 11-175})$$

Equation 11-174 is an integral equation for $\sigma_r(b, t)$. In order to determine the function $f(t)$, an additional equation is required.

Eliminating σ_θ , σ_z and u from Eqs. 11-162, 11-165, 11-166 and 11-167, we have :

$$3\sigma_r = \frac{3K}{r} \frac{\partial}{\partial \tau} (r^2 \epsilon_\theta) + 2 \int_{-\infty}^t G(t - \tau) \frac{\partial}{\partial \tau} \left(\epsilon_\theta + 2r \frac{\partial \epsilon_\theta}{\partial r} \right) d\tau. \quad (\text{Eq. 11-176})$$

The integral term in Eq. 11-176 can be eliminated from Eqs. 11-172 and 11-176; the result is :

$$\Omega(r, t) = \frac{1}{2} f(t) - \frac{5}{4} \rho r^2 \omega^2 + \frac{3K}{2r} \frac{\partial}{\partial r} (r^2 \epsilon_\theta), \quad (\text{Eq. 11-177})$$

where :

$$\Omega(r, t) = \frac{1}{r} \frac{\partial}{\partial r} (r^2 \sigma_r). \quad (\text{Eq. 11-178})$$

Also, from Eqs. 11-171 and 11-172, we have :

$$\Omega(r, t) = 2f(t) - 2\rho r^2 \omega^2 - \frac{2}{r} \int_{-\infty}^t G(t - \tau) \frac{\partial^2}{\partial \tau \partial r} (r^2 \epsilon_\theta) d\tau. \quad (\text{Eq. 11-179})$$

From Eqs. 11-177 and 11-179, the term $\frac{\partial}{\partial r} (r^2 \epsilon_\theta)$ can be eliminated. We obtain :

$$\begin{aligned} \Omega + \frac{4}{3K} \int_{-\infty}^t G(t - \tau) \frac{\partial \Omega}{\partial \tau} d\tau &= 2f(t) - 2\rho r^2 \omega^2 + \frac{1}{3K} \int_{-\infty}^t G(t - \tau) \\ &\times \frac{\partial}{\partial \tau} (2f - 5\rho r^2 \omega^2) d\tau. \end{aligned} \quad (\text{Eq. 11-180})$$

If we define an R-function by the integral equation :

$$R(t) + \frac{4}{3K} \int_{-\infty}^t G(t - \tau) \frac{\partial R(\tau)}{\partial \tau} d\tau = 2G(t), \quad (\text{Eq. 11-181})$$

Then Eq. 11-180 can be reduced to :

$$\Omega(r, t) = 2f(t) - 2\rho r^2 \omega^2(t) + \frac{1}{K} \int_{-\infty}^t R(t - \tau) \frac{\partial}{\partial \tau} \left[\frac{1}{2} \rho r^2 \omega^2(\tau) - f(\tau) \right] d\tau, \quad (\text{Eq. 11-182})$$

or :

$$\Omega(r, t) = \left[2 - \frac{R(0)}{K} \right] f(t) - \rho r^2 \omega^2(t) \left[2 - \frac{R(0)}{2K} \right] + \frac{1}{K} \int_0^t f(\tau) \frac{\partial}{\partial \tau} R(t - \tau) d\tau - \frac{\rho r^2}{2K} \int_0^t \omega^2(\tau) \frac{\partial}{\partial \tau} R(t - \tau) d\tau. \quad (\text{Eq. 11-183})$$

Integrating Eq. 11-183 with respect to r from $r = a(t)$ to r and using Eq. 11-68, we have :

$$r^2 \sigma_r(r, t) = \frac{1}{2} [r^2 - a^2(t)] \left[\left(2 - \frac{R(0)}{K} \right) f(t) + \frac{1}{K} \int_0^t f(\tau) \frac{\partial}{\partial \tau} R(t - \tau) d\tau \right] - \frac{\rho}{4} [r^4 - a^4(t)] \left[\left(2 - \frac{R(0)}{2K} \right) \omega^2(t) + \frac{1}{2K} \int_0^t \omega^2(\tau) \frac{\partial}{\partial \tau} R(t - \tau) d\tau \right] - a^2(t) \pi(t). \quad (\text{Eq. 11-184})$$

At $r = b$,

$$b^2 \sigma_r(b, t) = \frac{1}{2} [b^2 - a^2(t)] \left[\left(2 - \frac{R(0)}{K} \right) f(t) + \frac{1}{K} \int_0^t f(\tau) \frac{\partial}{\partial \tau} R(t - \tau) d\tau \right] - \frac{\rho}{4} [b^4 - a^4(t)] \left[\left(2 - \frac{R(0)}{2K} \right) \omega^2(t) + \frac{1}{2K} \int_0^t \omega^2(\tau) \frac{\partial}{\partial \tau} R(t - \tau) d\tau \right] - a^2(t) \pi(t). \quad (\text{Eq. 11-185})$$

Equations 11-174 and 11-185 constitute a pair of integral equations for $\sigma_r(b, t)$ and $f(t)$. If the solution of $f(t)$ is obtained, $\sigma_r(r, t)$ and $\Omega(r, t)$ can then be determined from Eqs. 11-184 and 11-183 respectively and $\sigma_\theta(r, t)$ can be calculated from the equation :

$$\sigma_\theta(r, t) = \Omega(r, t) - \sigma_r(r, t) + \rho r^2 \omega^2(t). \quad (\text{Eq. 11-186})$$

Let us introduce the following dimensionless quantities :

$$t^\circ = t/t_0, \quad \sigma^\circ(t^\circ) = \frac{\sigma_r(b, t)}{E}, \quad f^\circ(t^\circ) = \frac{f(t)}{E}, \quad B^\circ = B/E, \quad G^\circ(t^\circ) = \frac{G(t)}{E}, \\ R^\circ(t^\circ) = \frac{R(t)}{E}, \quad \omega^\circ(t^\circ) = \frac{\rho b^2 \omega^2(t)}{4E}, \quad a^\circ(t^\circ) = \frac{a^2(t)}{b^2} \quad \text{and} \quad \pi^\circ(t^\circ) = \frac{\pi(t)}{E},$$

where t_0 is the total time of ablation and E is the initial value of the elastic modulus of the viscoelastic material. Equation 11-176 and 11-185 can be rewritten as :

$$\sigma^\circ(t^\circ) = 2\mu \int_0^{t^\circ} \sigma^\circ(\tau) \frac{\partial}{\partial \tau} G^\circ(t^\circ - \tau) d\tau + \mu B^\circ [2\omega^\circ(t^\circ) - f^\circ(t^\circ)] \quad (\text{Eq. 11-187})$$

and :

$$\sigma^\circ(t^\circ) = 2L(t^\circ) \int_0^{t^\circ} f^\circ(\tau) \frac{\partial}{\partial \tau} R^\circ(t^\circ - \tau) d\tau + H(t^\circ) + I(t^\circ) f^\circ(t^\circ), \quad (\text{Eq. 11-188})$$

where :

$$L(t^\circ) = \frac{3}{4} (1 - 2\nu_0) [1 - a^\circ(t^\circ)] ,$$

$$H(t^\circ) = - \left\{ 1 - [a^\circ(t^\circ)]^2 \right\} \left[\frac{3 - 2\nu_0}{2(1 - \nu_0)} \omega^\circ(t^\circ) + \frac{3(1 - 2\nu_0)}{2} \int_0^{t^\circ} \omega^\circ(\tau) \frac{\partial}{\partial \tau} R^\circ(t^\circ - \tau) d\tau \right] - a^\circ(t^\circ) \pi^\circ(t^\circ),$$

$$I(t^\circ) = \frac{1}{2(1 - \nu_0)} [1 - a^\circ(t^\circ)] ,$$

and $\nu_0 = \frac{1}{2} (1 - \frac{E}{3K})$ is the initial Poisson's ratio of the viscoelastic material.

Equations 11-187 and 11-188 can be solved by the finite difference method (48).

In the numerical calculation we shall use the shear modulus for polymethyl methacrylate at 80°C. which is calculated from the measured tensile modulus in the functional form (52) (see appendix page 744).

$$\log_{10} E(t) = 8.85 - 1.5 \operatorname{erf} [0.31 (\log_{10} t - 3.6)] , \quad (\text{Eq. 11-189})$$

where $E(t)$ is in dyn/cm², t is in hours and the value of $\nu(0)$ is assumed to be 0.35. The shear relaxation curve is shown in Fig. 11-10. The inner surface ablates according to the equation :

$$a(t) = \frac{a_0}{1 - (1 - a_0) t} ,$$

where $a_0 = a(0) = \frac{4}{9}$. The total ablation time is taken as $t_0 = 3.64$ hours. The internal pressure is prescribed as :

$$\pi(t) = \pi_0 (1 - e^{-5t}) .$$

The spinning velocity is prescribed as :

$$\omega(t) = \omega_0 (1 - e^{-5t}) ,$$

which is equivalent to 86 rps for the following data :

$$\pi_0 = 2000 \text{ psi}, E = 3.246 \times 10^5 \text{ psi}, \rho = 1 \text{ gm/cc. and } b = 30 \text{ cm.}$$

The radial and circumferential stress distributions at various times are shown in Fig. 11-11 and 11-12, where $M = 13590$ psi. The three elastic casing constants considered here, $B^\circ = 1/3, 1, 2.4$ are chosen so as to indicate the effect of the different elastic materials and the different thickness ratios. The three values may be considered to correspond to aluminum with $b/h = 100$, steel with $b/h = 100$, and steel with $b/h = 40$, respectively. For $B^\circ = 1/3$, the circumferential stress reaches the maximum value of approximately 3800 psi at $t = 2.2$ hours. This critical tensile surface stress can be reduced by the use of stiffer casings. However, it should be noted from Fig. 11-11 that the use of stiffer casing may bring about a larger radial stress at the interface and thus produce higher hoop stress in the casing.

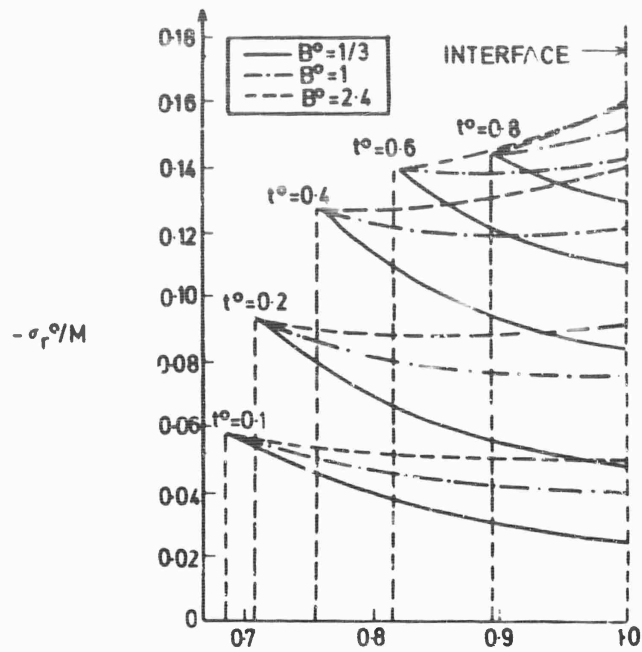


Fig. 11-11 Histories of radial stress distribution for different elastic casings.

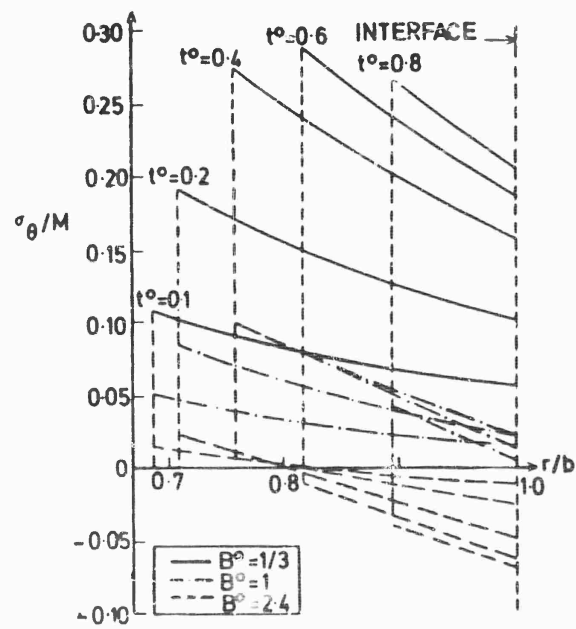


Fig. 11-12 Histories of circumferential stress distribution for different elastic casings.

3.4. Stress Analysis for Non-Isothermal Viscoelastic Cylinders

In the previous section, we have assumed that the temperature distribution in the viscoelastic cylinder is uniform and hence stress analysis can be carried out under isothermal conditions. In reality, during burning, the temperature distribution is non-isothermal and the port temperature is found to be much higher than the casing temperature. Since the viscoelastic properties are affected by temperature, the correspondence principle cannot be applied directly here. We shall assume the viscoelastic material to be thermorheologically simple and analyze the stress distribution by using the reduced time variable.

The stress displacement relations and the equation of equilibrium are the same as those stated in Section 3.3. Equations 11-161 to 11-164 also hold in the present case. However, the stress strain relations must be modified as follows :

$$\sigma_r + \sigma_\theta + \sigma_z = 3K \{ \epsilon_r + \epsilon_\theta + \epsilon_z - 3\alpha [T(r, t) - T_0] \} , \quad (\text{Eq. 11-190})$$

$$\sigma_r - \sigma_\theta = 2 \int_{-\infty}^t G [\xi(r, t) - \xi(r, t_1)] \frac{\partial}{\partial t_1} (\epsilon_r - \epsilon_\theta) dt_1 , \quad (\text{Eq. 11-191})$$

$$\sigma_\theta - \sigma_z = 2 \int_{-\infty}^t G [\xi(r, t) - \xi(r, t_1)] \frac{\partial}{\partial t_1} (\epsilon_\theta - \epsilon_z) dt_1 . \quad (\text{Eq. 11-192})$$

In the above equations, α is the coefficient of thermal expansion of the viscoelastic material, $T(r, t)$ is the temperature distribution at time t , $T_0 = T(r, 0)$ is the initial temperature which is considered to be uniform and $\xi(r, t)$ is the reduced time variable as defined by Eq. 11-74. We shall assume that the temperature change is sufficiently small so that α can be considered to be time independent.

From Eqs. 11-161 to 11-164 and 11-190 to 11-192 we can derive the following two equations after eliminating σ_θ , σ_z , ϵ_r , ϵ_θ and ϵ_z :

$$\sigma_r - K \left\{ \frac{\partial u}{\partial r} + \frac{u}{r} - 3\alpha [T(r, t) - T_0] \right\} - \frac{2}{3} \int_{-\infty}^t G [\xi(r, t) - \xi(r, t_1)] \frac{\partial}{\partial t_1} \left(2 \frac{\partial u}{\partial r} - \frac{u}{r} \right) dt_1 = 0 , \quad (\text{Eq. 11-193})$$

$$\frac{\partial \sigma_r}{\partial r} + \rho \omega^2 r + 2 \int_{-\infty}^t G [\xi(r, t) - \xi(r, t_1)] \frac{\partial}{\partial t_1} \frac{\partial}{\partial r} \left(\frac{u}{r} \right) dt_1 = 0 . \quad (\text{Eq. 11-194})$$

The boundary condition at the inner surface of the cylinder is the same as Eq. 11-168 and the boundary condition at the interface of the casing can be written as :

$$u(b, t) = -c\sigma_r(b, t) + d(t) \quad (\text{Eq. 11-195})$$

where $c = \frac{b^2}{h} \frac{1 - \nu_c^2}{E_c}$ $d(t) = \alpha_c b [T(b, t) - T_0]$ and α_c is the coefficient of thermal expansion of the casing.

The temperature along the ablating boundary is assumed to be constant and is denoted by T_1 . The temperature field of the cylinder must satisfy the heat conduction equation :

$$\frac{\partial^2 T}{\partial r^2} + \frac{1}{r} \frac{\partial T}{\partial r} = \frac{1}{\kappa} \frac{\partial T}{\partial t} \quad (\text{Eq. 11-196})$$

where κ is the thermal conductivity of the cylinder. The boundary condition at the ablating surface is :

$$T[a(t), t] = T_1, \quad (\text{Eq. 11-197})$$

and a radiation boundary condition must be prescribed at the interface of the casing.

Let us introduce the following dimensionless quantities :

$$\eta = K/E, \quad x = r/b, \quad \kappa b^2 = \gamma, \quad \tau = t/\gamma, \quad \lambda(t) = \frac{\rho b^2 [\omega(t)]^2}{3 \alpha E (T_1 - T_0)},$$

$$\bar{c} = \frac{b}{h} \frac{E}{E_c} (1 - \nu_c^2), \quad \bar{a}(\tau) = a(t)/b, \quad \bar{d}(\tau) = \frac{1}{3} \frac{\alpha_c}{\alpha} \Theta(1, \tau),$$

$$\bar{\pi}(\tau) = \frac{\pi(t)}{3 \alpha E (T_1 - T_0)}, \quad \bar{G} = 2G/E, \quad \Theta(x, \tau) = \frac{T(r, t) - T_0}{T_1 - T_0},$$

$$v(x, \tau) = \frac{u(r, t)}{3 \alpha b (T_1 - T_0)}, \quad \sigma(x, \tau) = \frac{\alpha_r(r, t)}{3 \alpha E (T_1 - T_0)}, \quad s(x, \tau) = \frac{\sigma_\theta(r, t)}{3 \alpha E (T_1 - T_0)}$$

$$\bar{T}(x, \tau) = T(r, t), \quad \zeta(x, \tau) = \int_0^\tau \frac{d\tau_1}{\alpha_T[\bar{T}(x, \tau_1)]}, \quad (') \equiv \frac{\partial}{\partial x} ().$$

Expressed in terms of these dimensionless quantities, Eqs. 11-164, 11-193, 11-194, 11-168, 11-195, 11-196 and 11-197 can be rewritten as :

$$s = (x\sigma)' + \lambda x^2 \quad (\text{Eq. 11-198})$$

$$\sigma = \eta \left(v' + \frac{v}{x} - \Theta \right) - \frac{1}{3} \int_{-\infty}^\tau \bar{G} \{ \gamma [\zeta(x, \tau) - \zeta(x, \tau_1)] \} \frac{\partial}{\partial \tau_1} \left(2v' - \frac{v}{x} \right) d\tau_1 = 0 \quad (\text{Eq. 11-199})$$

$$v' + \lambda x + \int_{-\infty}^\tau \bar{G} \{ \gamma [\zeta(x, \tau) - \zeta(x, \tau_1)] \} \frac{\partial}{\partial \tau_1} \left(\frac{v}{x} \right)' d\tau_1 = 0 \quad (\text{Eq. 11-200})$$

$$\sigma[\bar{a}(\tau), \tau] = -\bar{\pi}(\tau) \quad (\text{Eq. 11-201})$$

$$v(1, \tau) = -\bar{c} \sigma(1, \tau) + \bar{d}(\tau) \quad (\text{Eq. 11-202})$$

$$\Theta' + \frac{1}{x} \Theta' = \dot{\Theta} \quad (\text{Eq. 11-203})$$

and :

$$\Theta[\bar{a}(\tau), \tau] = 1. \quad (\text{Eq. 11-204})$$

The discontinuity at $\tau = 0$ can be removed by integration by parts. Equations 11-199 and 11-200 can be written as :

$$\sigma = \eta \left(v' + \frac{v}{x} - \Theta \right) - \frac{1}{3} \bar{G}(0) \left(2v' - \frac{v}{x} \right) + \frac{1}{3} \int_0^\tau \left(2v' - \frac{v}{x} \right) \frac{\partial}{\partial \tau_1} \bar{G} \{ \gamma [\zeta(x, \tau) - \zeta(x, \tau_1)] \} d\tau_1 = 0, \quad (\text{Eq. 11-205})$$

$$\sigma' + \lambda x + \bar{G}(0) \left(\frac{v}{x} \right)' - \int_0^\tau \left(\frac{v}{x} \right)' \frac{\partial}{\partial \tau_1} \bar{G} \{ \gamma [\zeta(x, \tau) - \zeta(x, \tau_1)] \} d\tau_1 = 0 \quad (\text{Eq. 11-206})$$

These two linear first order integro-differential equations for $\sigma(x, \tau)$ and $v(x, \tau)$ associated with boundary conditions given in Eqs. 11-201 and 11-202 can be solved numerically by the finite difference method (48).

For the given ablation conditions, it is too difficult to determine the temperature field analytically. Here we shall use the approach as indicated in Ref. (51), to obtain the position of ablating boundary and temperature distribution approximately.

Consider an infinite solid with a cylindrical hole of dimensionless radius $\bar{a}(0)$. Let temperature on the cylindrical surface be prescribed as :

$$\Theta [\bar{a}(0), \tau] = \sum_{n=0}^{\infty} \alpha_n \tau^{\frac{n}{2}}. \quad (\text{Eq. 11-207})$$

At infinity, the boundary condition is :

$$\Theta'(\infty, \tau) = 0. \quad (\text{Eq. 11-208})$$

By the Laplace transform method the solution Eqs. 11-203, 11-207 and 11-208 is :

$$\begin{aligned} \Theta(x, \tau) = & \sqrt{\frac{\bar{a}(0)}{x}} \sum_{n=0}^{\infty} \left[\alpha_n \Gamma \left(1 + \frac{n}{2} \right) (4\tau)^{\frac{n}{2}} i^n \operatorname{erfc} \frac{x - \bar{a}(0)}{2\sqrt{\tau}} \right] \\ & + \frac{8 - \bar{a}(0)}{8 \bar{a}(0) x} \sum_{n=0}^{\infty} \left[\alpha_n \Gamma \left(1 + \frac{n}{2} \right) (4\tau)^{\frac{n}{2}} i^{n+1} \operatorname{erfc} \frac{x - \bar{a}(0)}{2\sqrt{\tau}} \right] \\ & + \frac{9 [\bar{a}(0)]^2 - 2 \bar{a}(0) x - x^2}{128 [\bar{a}(0)]^2 x^2} \sum_{n=0}^{\infty} \left[\alpha_n \Gamma \left(1 + \frac{n}{2} \right) (4\tau)^{\frac{n+2}{2}} \times \right. \\ & \quad \left. i^{n+2} \operatorname{erfc} \frac{x - \bar{a}(0)}{2\sqrt{\tau}} \right] \\ & + \dots \end{aligned} \quad (\text{Eq. 11-209})$$

where $i^n \operatorname{erfc} x = \int_x^\infty i^{n-1} \operatorname{erfc} \xi d\xi$ and $i^0 \operatorname{erfc} x = \operatorname{erfc} x$. For given values of α_n ,

$\Theta(x, \tau)$ is calculated, and the location of the ablating boundary $\bar{a}(\tau)$ is found from Eq. 11-204 numerically. The values of α_n are chosen in such a way that the curve of $\bar{a}(\tau)$ coincides with the experimental result. The ablation curve with $\alpha_2 = 303$ and $\alpha_n = 0$ for $n \neq 2$ is shown in Fig. 11-13, where $\bar{a}(0)$ is taken as $2/3$. Ablation starts at $\tau = 0.004$, which is equivalent to 65 seconds for $\kappa = 8 \text{ cm}^2/\text{hr}$ and $b = 6 \text{ cm}$. The total ablation time is $\tau_u = 0.04$ (648 seconds). The temperature distributions at various times are shown in Fig. 11-14.

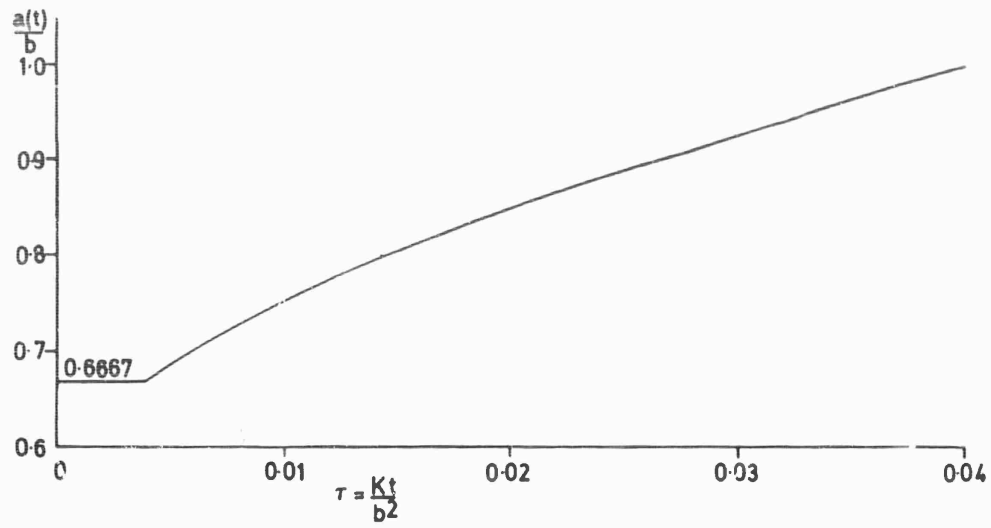


Fig. 11-13 Motion of ablating boundary.

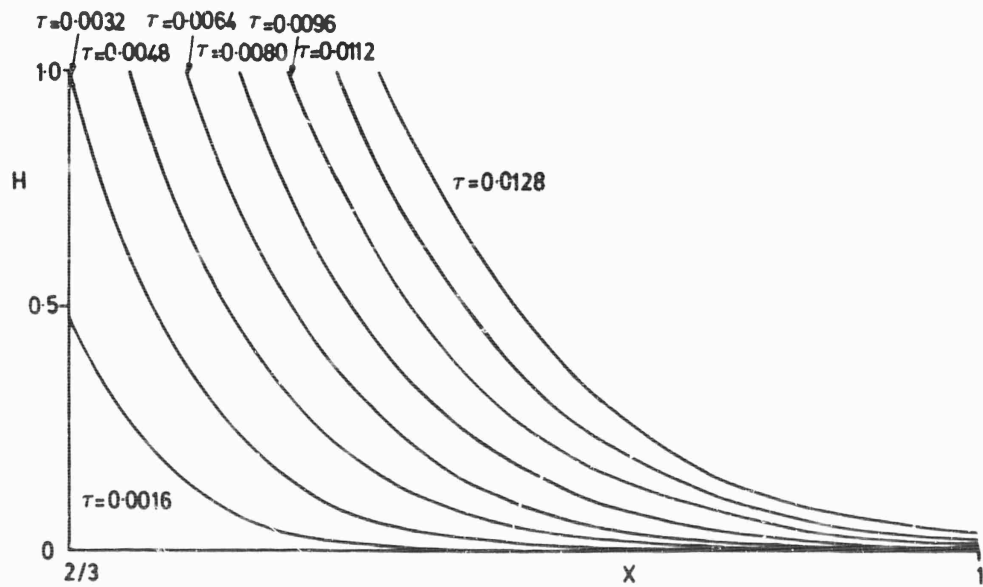


Fig. 11-14 Temperature distribution at various times.

The numerical calculation can be carried out based on the experimental data of polymethyl methacrylate (52). The relaxation shear modulus at 80°C is shown in Fig. 11-10. The variation of the shift function $\alpha_T(T)$ is obtained from Ref. (52) and is shown in Fig. 11-15. For $\eta = 0.111$ [equivalent to $\nu(0) = 0.35$], $\bar{c} = 3.0$, $\alpha_c/\alpha = 0.01$, $T_0 = 80^\circ\text{C}$, $T_1 = 105^\circ\text{C}$, $\bar{\eta}(\tau) = -\frac{1}{3} \frac{\tau}{\tau_a} e^{-2.5\tau/\tau_a}$ and $\lambda(\tau) = 0.0933 (1 - e^{-5\tau/\tau_a})$, the stress distributions at $\tau = 0.0064$ and $\tau = 0.0128$ are shown in Figs. 11-16 and 11-17 for both viscoelastic and elastic cases. The temperature rise is localized in the region near the ablating boundary. The thermal expansion in this region is resisted by the constraint of the outer portion of the cylinder. Thus the circumferential stress due to thermal expansion is compressive near the port surface but tensile near the interface of the casing. Viscoelasticity has a marked influence on the circumference stress in the heated region, in conformity with the marked influence of temperature on viscoelasticity through the scale of $\alpha_T(T)$. When the heated region spreads out at later time, localization of the viscoelastic influence will disappear. Since the effect of viscoelasticity can decrease the magnitude of the critical stress, the design based on the elastic solution would be on the safe side. The thermal stress is essentially caused by the temperature gradient. In order to reduce the thermal stress, the thermal conductivity of the propellant grain and the surface conductance on the interface of the casing must be as high as possible.

3.5. Grain Slump due to Axial Acceleration

One of the important considerations in the design of solid propellant rockets is the effect of axial acceleration. For rockets under storage conditions, the grain is under 1 g gravitational body force and the critical strain occurs at long time. But for rocket under launching conditions, we need to consider the short time solution due to the high body force imposed by acceleration.

Here, let us consider a simple example of an axial inertia force. The rocket is idealized as an encased, infinitely long, hollow cylinder. We assume the ends of the cylinder to be unsupported, thus free from constraints of axial motion. Due to the axial inertia loading $\rho g n(t)$, the cylinder is under shear deformation with maximum shear strain on the interface of the casing. If the acceleration is too high, the grain will separate from the casing. This problem was considered by Lindsey and Williams (53).

Using the axially symmetrical condition, we can write the equation of equilibrium in the axial direction (z direction) as :

$$\frac{1}{r} \frac{\partial}{\partial r} (r \sigma_{rz}) + \rho g n(t) = 0, \quad (\text{Eq. 11-210})$$

the solution to which is σ_{rz} is :

$$\sigma_{rz}(r, t) = -\frac{1}{2} \rho g n(t) \left[\frac{c(t)}{r} + r \right], \quad (\text{Eq. 11-211})$$

where $c(t)$ is an unknown function which can be determined by the boundary condition at the ablating boundary,

$$\sigma_{rz}[a(t), t] = 0. \quad (\text{Eq. 11-212})$$

By Eq. 11-212, Eq. 11-211 can be rewritten as :

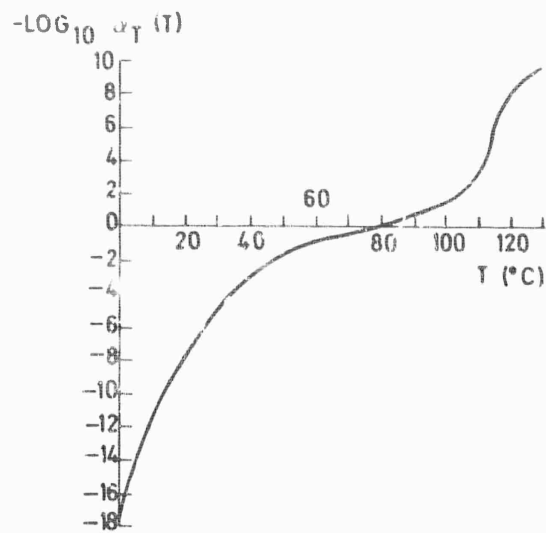


Fig. 11-15 Temperature dependence of the shift factor for polymethylmethacrylate (32).

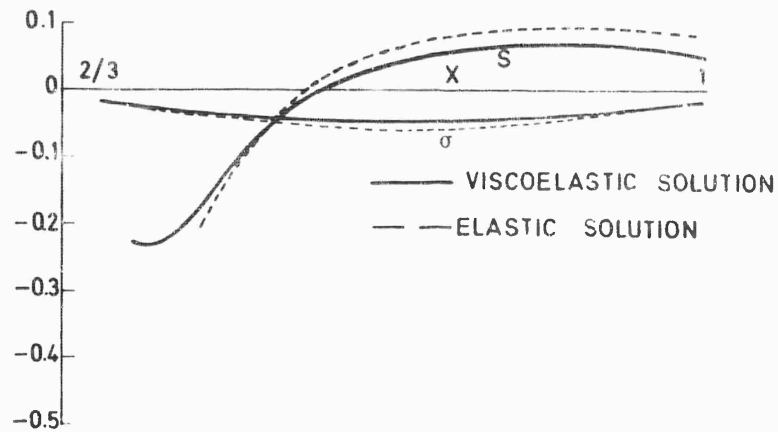


Fig. 11-16 Stress distribution in ablating cylinder at $\tau = 0.0064$.

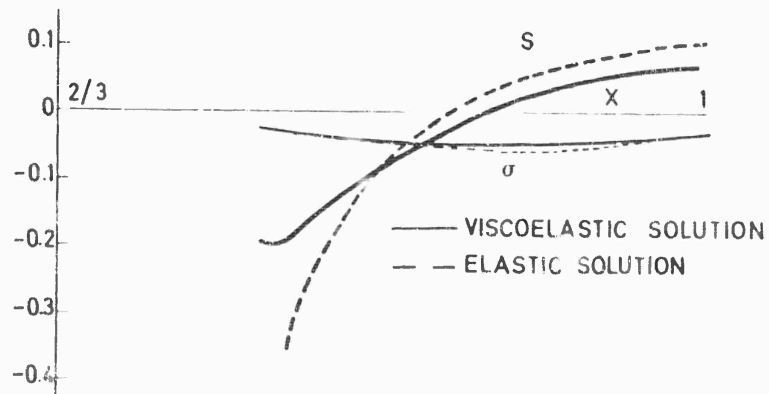


Fig. 11-17 Stress distribution in ablating cylinder at $\tau = 0.0128$.

$$\sigma_{rz}(r, t) = \frac{1}{2} \rho g n(t) \left[\frac{a^2(t)}{r} - r \right] \quad (\text{Eq. 11-213})$$

The shear strain can be found from the following convolution integral :

$$\epsilon_{rz}(r, t) = \int_{-\infty}^t J(t - \tau) \frac{\partial}{\partial \tau} \sigma_{rz}(\tau) d\tau, \quad (\text{Eq. 11-214})$$

where $J(t)$ is the shear modulus.

The acceleration is here applied as a step function of time, i.e.,

$$n(t) = n_0 H(t) \quad (\text{Eq. 11-215})$$

Let a_0 be the initial radius of the inner boundary, b the outside radius and t_f the total burning time. If the ablating rate is constant, we have :

$$a(t) = a_0 + (b - a_0) \frac{t}{t_f} = a_0 + m t, \quad (\text{Eq. 11-216})$$

where $m = (b - a_0)/t_f$. Substituting Eqs. 11-213, 11-215 and 11-216 into Eq. 11-214, we have :

$$\begin{aligned} \epsilon_{rz}(r, t) = & - \frac{\rho g n_0 r}{2} \left\{ \left[1 - \frac{1}{(r/a_0)^2} \right] J^{(0)}(t) - 2 \frac{m/a_0}{(r/a_0)^2} J^{(1)}(t) \right. \\ & \left. - 2 \frac{(m/a_0)^2}{(r/a_0)^2} J^{(2)}(t) \right\}, \end{aligned} \quad (\text{Eq. 11-217})$$

where :

$$J^{(n+1)}(t) = \int_0^t J^{(n)}(\eta) d\eta \quad \text{and} \quad J^{(0)}(t) = J(t). \quad (\text{Eq. 11-218})$$

The critical strain occurs on the interface $r = b$,

$$\begin{aligned} \epsilon_{rz}(b, t) = & - \frac{\rho g n_0 b}{2} \frac{\lambda^2 - 1}{\lambda^2} \left\{ J(t) - \frac{2}{\lambda + 1} \left(\frac{t}{t_f} \right) \frac{J^{(1)}(t)}{t} \right. \\ & \left. - \frac{2(\lambda - 1)}{\lambda + 1} \left(\frac{t}{t_f} \right)^2 \frac{J^{(2)}(t)}{t^2} \right\}, \end{aligned} \quad (\text{Eq. 11-219})$$

where $\lambda = b/a_0$ is the port size factor.

For incompressible materials, the shear compliance and tensile compliance are related by :

$$J(t) = 3 F(t) \quad (\text{Eq. 11-220})$$

Within a certain range of time, the tensile compliance of most propellants can be satisfactorily approximated by the following equation :

$$F(t) = F_0 \left(\frac{t}{\alpha_T} \right)^k, \quad (\text{Eq. 11-221})$$

where t/α_T is the reduced time and k is a constant. Therefore the critical shear strain can be written as :

$$\epsilon_{rz}(b, t) = -\frac{3}{2} \rho g n_0 b \frac{\lambda^2 - 1}{\lambda^2} F_0 \left(\frac{t}{\alpha_T} \right)^k \left\{ 1 - \frac{1}{k+1} \frac{2}{\lambda+1} \left(\frac{t}{t_f} \right) - \frac{2}{(k+1)(k+2)} \frac{\lambda-1}{\lambda+1} \left(\frac{t}{t_f} \right)^2 \right\}. \quad (\text{Eq. 11-222})$$

In the non-ablation case, the wall strain, which is proportional to the total weight of the viscoelastic cylinder, increases with time as a result of the flow of material. When the viscoelastic material is burned out, the total weight then decreases with time. The wall strain reaches its maximum value at a critical time $t = t^*$ such that :

$$\xi^* = t^*/t_f = \frac{1}{2(\lambda-1)} \left\{ \left[(k+1)^2 + 2k(k+1)(\lambda^2-1) \right]^{1/2} - (k+1) \right\}. \quad (\text{Eq. 11-223})$$

The maximum strain is :

$$\epsilon_{rz}(b, t^*) = -\frac{3}{2} \rho g n_0 b \frac{\lambda^2 - 1}{\lambda^2} F_0 \xi^{*k} \left(\frac{t_f}{\alpha_T} \right) \left[1 - \frac{1}{k+1} \frac{2}{\lambda+1} \xi^* - \frac{2}{(k+1)(k+2)} \frac{\lambda-1}{\lambda+1} \xi^{*2} \right] \quad (\text{Eq. 11-224})$$

The interface shear strain history curves for a typical design configuration are shown in Fig. 11-18. Maximum wall shear strain of approximately $(\epsilon_{rz})_{\max} \approx 0.9$ occurs at $t = 0.302t_f$. This critical strain is important in the failure analysis of rocket design.

3.5. Viscoelastic Cylinder Reinforced by Elastic Wires (65)

The strength of a solid propellant rocket could be increased by reinforcing the rocket grain with metallic wires. This is done by winding sets of wires around a cylindrical surface with identical angles to the axis of the cylinder, thereby forming a cylindrical net. The grain is thus composed of the viscoelastic material and several layers of such cylindrical nets.

Consider a viscoelastic body consisting of sets of parallel wires running in different directions. The direction cosine of the m th set of wires is denoted by $\ell_1^{(m)}$. These wires are set so closely together that we may assume the composite medium to be continuous and homogeneous. The normal strain along the direction of the m th set of wires is:

$$\epsilon^{(m)} = \ell_p^{(m)} \ell_q^{(m)} \epsilon_{pq}. \quad (\text{Eq. 11-225})$$

We shall assume the wire to be completely flexible and elastic. The stress in each wire is :

$$\sigma_R^{(m)} = E^{(m)} \epsilon^{(m)} = E^{(m)} \ell_p^{(m)} \ell_q^{(m)} \epsilon_{pq}, \quad (\text{Eq. 11-226})$$

where $E^{(m)}$ is the elastic modulus of the wire. The total force in the wire in a unit area of the medium is :

$$\sigma^{(m)} = n^{(m)} A^{(m)} \sigma_R^{(m)} = n^{(m)} A^{(m)} E^{(m)} \epsilon^{(m)}, \quad (\text{Eq. 11-227})$$

where $n^{(m)}$ is the number of wires per unit cross-sectional area and $A^{(m)}$ is the cross-sectional area of each wire. The stresses in the viscoelastic material are given by Eq. 11-33. The total stress is the sum of the stress in the viscoelastic material and the stress due to the force in the wire, i.e.,

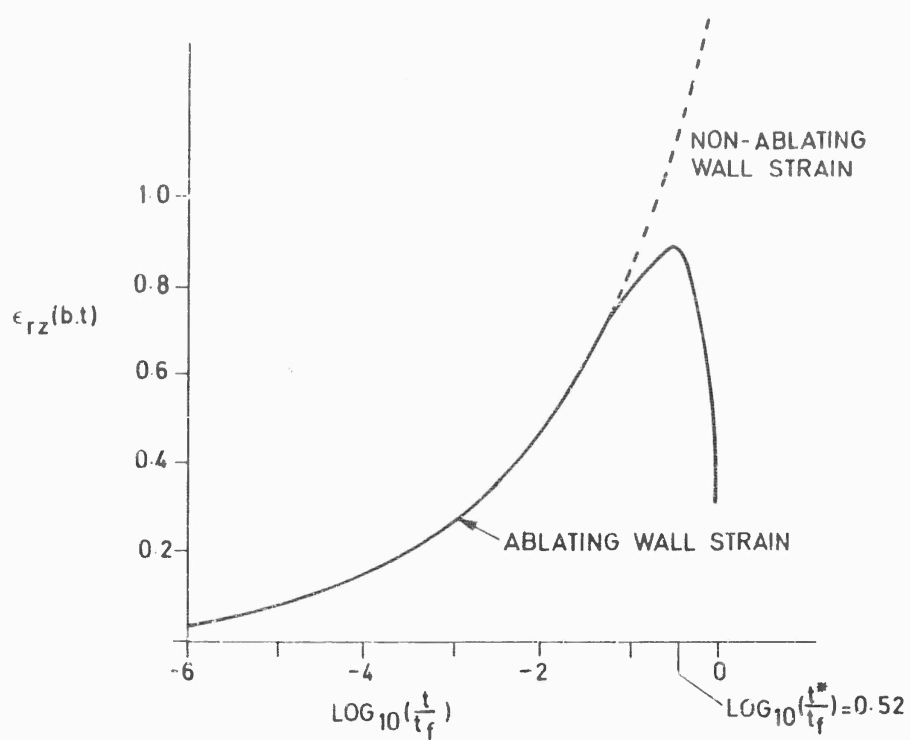


Fig. 11-18 Shear strain for a typical design configuration, $\lambda=2$,
 $t_f/\alpha_T = 1$, $\rho g n_0 b F_0 = 1$.

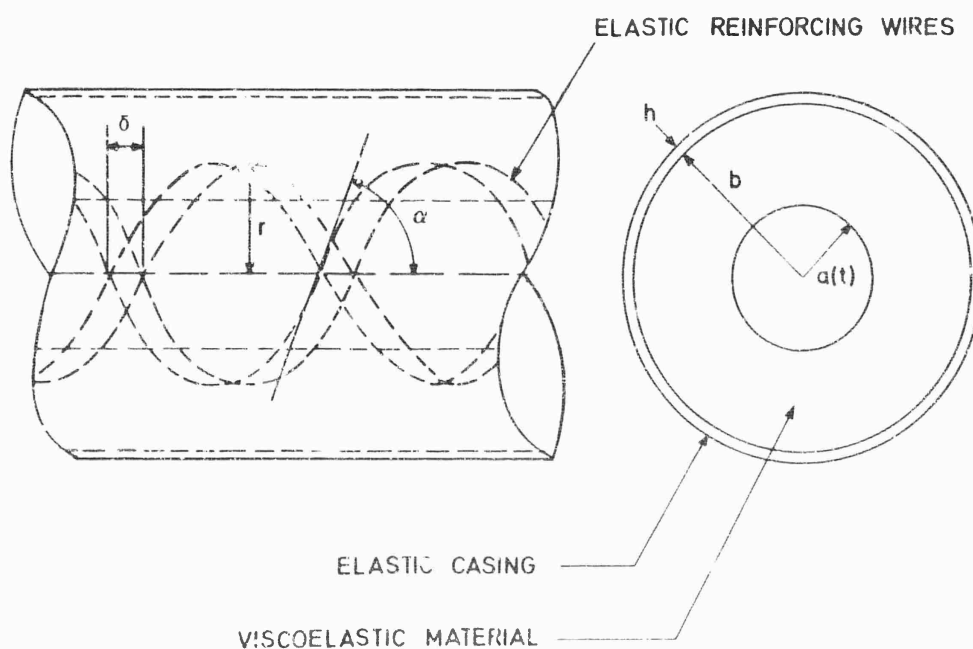


Fig. 11-19 Geometry of reinforced cylinder.

$$\sigma_{ij}(t) = 2 \int_{-\infty}^t \mu(t-\tau) \frac{\partial \epsilon_{ij}(\tau)}{\partial \tau} d\tau + \delta_{ij} \int_{-\infty}^t \lambda(t-\tau) \frac{d\epsilon_{kk}(\tau)}{d\tau} d\tau + \sum_m n^{(m)} A^{(m)} E^{(m)} \ell_1^{(m)} \ell_j^{(m)} \ell_p^{(m)} \ell_q^{(m)} c_{pq}(t). \quad (\text{Eq. 11-228})$$

This equation shows that if the composite material is considered as a whole, it is no longer isotropic but is orthotropic, i.e., the coefficient of $\epsilon_{pq}(\tau)$ for $-\infty < \tau \leq t$ in the expression of $\sigma_{ij}(t)$ is the same as the coefficient of $\epsilon_{ij}(\tau)$ in the expression of $\sigma_{pq}(t)$.

The geometry of the reinforced cylinder is shown in Fig. 11-19. Each layer of the reinforcing net is formed by two sets of parallel helical wires. The equation of each wire in the layer with radius r is :

$$z = j\delta \pm r\theta \cot \alpha, \quad (\text{Eq. 11-229})$$

where j is any integer, δ is the distance along the axial direction between two parallel neighboring wires and α is the angle of the helix (Fig. 11-19).

If we take an infinitesimal element from the cylindrical layer, the reinforcements in it can be considered as two parallel sets of wires. For this element, we set the x_1 axis along the radial direction, the x_2 axis along the circumferential direction and the x_3 axis along the axial direction. Then, $\ell_1^{(m)} = 0$, $\ell_2^{(m)} = \sin \alpha$ and $\ell_3^{(m)} = \cos \alpha$ ($m = 1, 2$). Put $n^{(m)} = n(r)$ and $A^{(m)} = A(r)$. The stress in the wire can be found from Eq. 11-226 as :

$$\sigma_R = E \epsilon_\theta \sin^2 \alpha \quad (\text{Eq. 11-230})$$

The stress strain relations are found from Eq. 11-228 :

$$\sigma_r = \int_{-\infty}^t [\lambda(t-\tau) + 2\mu(t-\tau)] \frac{\partial \epsilon_r(\tau)}{\partial \tau} d\tau + \int_{-\infty}^t \lambda(t-\tau) \frac{\partial \epsilon_\theta(\tau)}{\partial \tau} d\tau, \quad (\text{Eq. 11-231})$$

$$\sigma_\theta = \int_{-\infty}^t [\lambda(t-\tau) + 2\mu(t-\tau)] \frac{\partial \epsilon_\theta(\tau)}{\partial \tau} d\tau + \int_{-\infty}^t \lambda(t-\tau) \frac{\partial \epsilon_r(\tau)}{\partial \tau} d\tau + \beta(r) \epsilon_\theta, \quad (\text{Eq. 11-232})$$

$$\sigma_z = \int_{-\infty}^t \lambda(t-\tau) \frac{\partial}{\partial \tau} [\epsilon_r(\tau) + \epsilon_\theta(\tau)] d\tau + \beta(r) \epsilon_\theta \cot^2 \alpha, \quad (\text{Eq. 11-233})$$

where we have assumed that $\epsilon_r = 0$ and that $\beta(r)$ in Eqs. 11-232 and 11-233 is :

$$\beta(r) = 2 n(r) A(r) E \sin^4 \alpha. \quad (\text{Eq. 11-234})$$

Here the radial normal stress σ_r is resisted entirely by viscoelastic material. The part of the circumferential normal stress resisted by the viscoelastic material is given by the integral terms in Eq. 11-232, i.e.,

$$\tau_\theta = \int_{-\infty}^t [\lambda(t-\tau) + 2\mu(t-\tau)] \frac{\partial \epsilon_\theta(\tau)}{\partial \tau} d\tau + \int_{-\infty}^t \lambda(t-\tau) \frac{\partial \epsilon_r(\tau)}{\partial \tau} d\tau. \quad (\text{Eq. 11-235})$$

The strain displacement relations are given by Eqs. 11-161 and 11-162. From these

equations a compatibility equation can be obtained :

$$\epsilon_r = \frac{d}{dr} (r \epsilon_\theta) . \quad (\text{Eq. 11-236})$$

The equation of equilibrium remains identical with Eq. 11-164.

Substituting Eq. 11-236 into Eqs. 11-231 and 11-232 and expressing these in terms of relaxation moduli G and K , we obtain :

$$3\sigma_r = 2 \int_{-\infty}^t [3K(t-\tau) + G(t-\tau)] \frac{\partial \epsilon_\theta(\tau)}{\partial \tau} d\tau + r \int_{-\infty}^t [3K(t-\tau) + 4G(t-\tau)] \frac{\partial^2 \epsilon_\theta(\tau)}{\partial r \partial \tau} d\tau , \quad (\text{Eq. 11-237})$$

$$3\sigma_\theta = 2 \int_{-\infty}^t [3K(t-\tau) + G(t-\tau)] \frac{\partial \epsilon_\theta(\tau)}{\partial \tau} d\tau + r \int_{-\infty}^t [3K(t-\tau) - 2G(t-\tau)] \frac{\partial^2 \epsilon_\theta(\tau)}{\partial r \partial \tau} d\tau + 3\beta(r) \epsilon_\theta . \quad (\text{Eq. 11-238})$$

From Eqs. 11-164 and 11-238, we can eliminate σ_θ and have :

$$\frac{\partial \sigma_r}{\partial r} + 2 \int_{-\infty}^t G(t-\tau) \frac{\partial^2 \epsilon_\theta(\tau)}{\partial r \partial \tau} d\tau - \beta(r) \frac{\epsilon_\theta}{r} + \rho \omega^2 r = 0 . \quad (\text{Eq. 11-239})$$

From Eqs. 11-235, 11-237 and 11-238, it can be shown that :

$$\int_{-\infty}^t [3K(t-\tau) + 4G(t-\tau)] \frac{\partial \epsilon_\theta(\tau)}{\partial \tau} d\tau = \int_{-\infty}^t [3K(t-\tau) - 2G(t-\tau)] \frac{\partial \epsilon_\theta(\tau)}{\partial \tau} d\tau + 4 \int_{-\infty}^t S(t-\tau) \frac{\partial \epsilon_\theta(\tau)}{\partial \tau} d\tau , \quad (\text{Eq. 11-240})$$

where :

$$S(t) = \int_{-\infty}^t G(t-\tau) \frac{\partial}{\partial \tau} [3K(\tau) + G(\tau)] d\tau \quad (\text{Eq. 11-241})$$

When there is a discontinuity in $\beta(r)$, the quantities σ_r and ϵ_θ nevertheless remain continuous and τ_θ would also be continuous from Eq. 11-24. However, a discontinuity may occur in σ_θ .

The boundary conditions of this problem are the same as Eqs. 11-168 and 11-169. Equations 11-237, 11-239, 11-168 and 11-169 constitute a boundary value problem which can be solved numerically by the finite difference method. In the numerical calculation, the bulk modulus $K(t)$ is assumed to be elastic and equal to K and the tensile relaxation modulus is given by Eq. 11-189. The shear relaxation modulus $G(t)$ is calculated by assuming that $\nu(0) = 1/3$ and solving a Volterra integral equation numerically. The computations were carried out for $\omega = 0$, $B = K$, $\pi(t) = p_0 H(t)$, $a(t) = b(0.5 + vt)$ and $\beta(r) = \beta_1[1 - H(r - 0.75b)] + \beta_2 H(r - 0.75b)$. Stresses are directly proportional to the magnitude of the internal pressure. The port stresses in the non-ablating cylinder ($v = 0$) are plotted against time in Fig. 11-20. As time goes on, the tension in the wires increases gradually while the

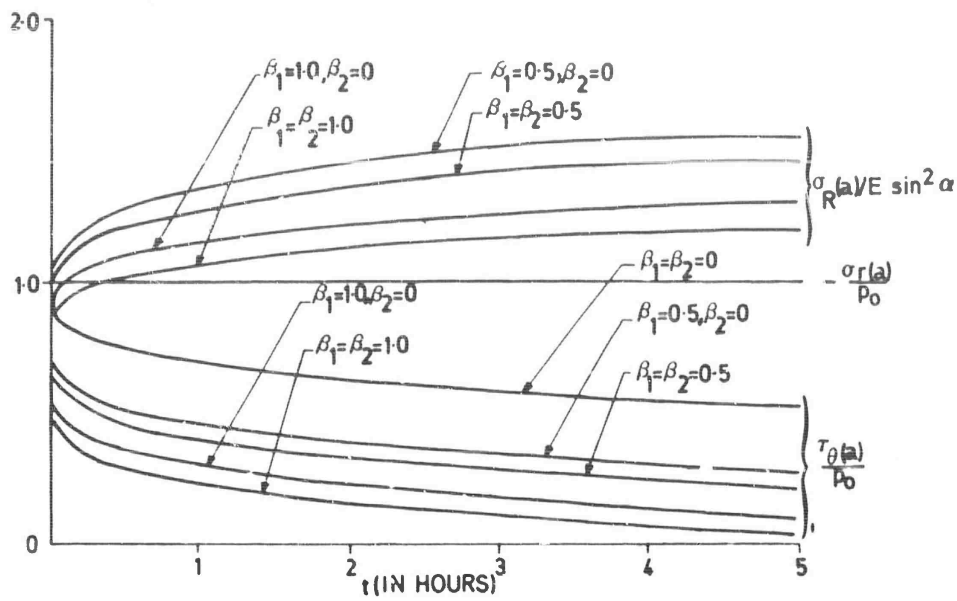


Fig. 11-20 Dimensionless radial stress (σ_r/p_0), dimensionless circumferential stress (τ_θ/p_0) and dimensionless stress in reinforcement ($\sigma_R/E \sin^2 \alpha$) at cavity surface for several reinforcement densities (β), for nonabating case $B = K$.

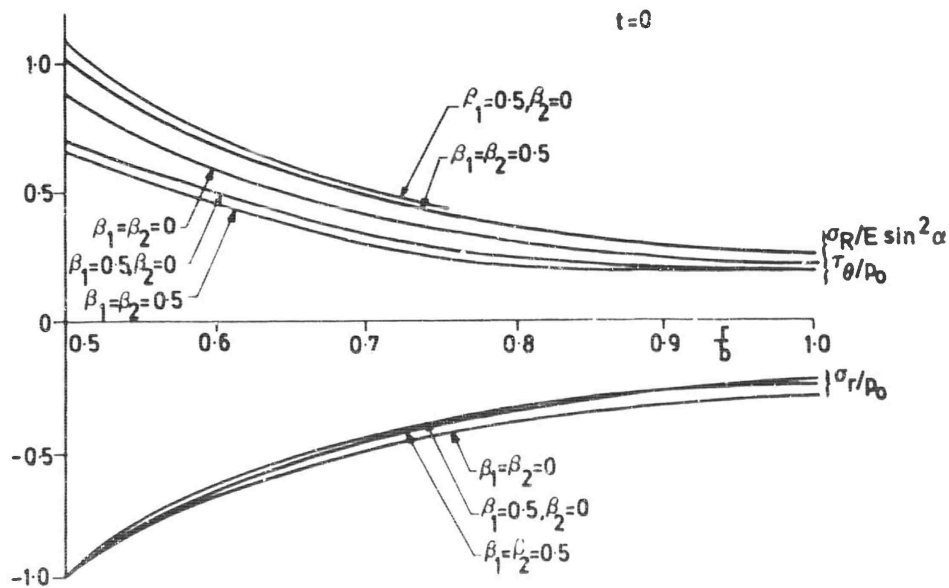


Fig. 11-21 Distribution of radial (σ_r/p_0), circumferential (τ_θ/p_0) and reinforcement ($\sigma_R/E \sin^2 \alpha$) stress for ablating case at $t=0$, $B = K$.

circumferential stress resisted by the viscoelastic material decreases. The critical circumferential stress in the viscoelastic material occurs immediately after the application of internal pressure. The circumferential stress in the unreinforced cylinder is shown by the line $\beta_1 = \beta_2 = 0$. A reduction of approximately 50% of the critical tensile stress is found as the result of utilizing reinforcements $\beta_1 = \beta_2 = 1.0$. Stress distributions in the ablating cylinder at $t = 0$ and $t = 2$ hrs. are shown in Figs. 11-21 and 11-22. The critical tension in the wire occurs on the port surface and has a maximum at $t = 0$. Its value changes slightly during ablation. Since the radial stress σ_r and circumferential stress τ_θ in the viscoelastic material have the same characteristics as those discussed in Section 3.3, we shall omit further discussions here.

4. Failure and Failure Criteria for Solid Propellant Rockets

4.1. Preliminary Remarks

The problem of determining whether specified forces or deformations will produce deterioration of a solid propellant grain is complex and has not yet received a satisfactory solution. Grain deterioration can result in motor failure through the formation of fissures in the propellant which by rapidly increasing the exposed surface area, produce an increase in the rate of production of burned gases and hence in the chamber pressure. It is therefore important from a practical viewpoint to make certain that grain failure does not occur, so that the anticipated motor performance will be realized.

The first difficulty that one encounters in attempting to evaluate the quality of a grain arises from using test results, obtained with a propellant sample for ascertaining conditions under which the grain will rupture in a motor. Samples are generally subjected to uniaxial forces at constant strain rates, while the grain in a motor is subjected to multiaxial forces and to time-dependent deformations. Application of test results to real motors therefore involves a number of uncertainties.

The second difficulty in failure analysis stems from the large number of parameters that affect failure. One must take into consideration the entire history of the grain from fabrication to combustion. Stresses and strains can develop slowly or rapidly, at the time of manufacture, during storage of the grain or during combustion. The environmental temperature and composition during manufacture are of particular importance. The storage time and storage conditions are relevant because slow chemical transformations can modify mechanical properties during storage; one should remember that the mechanism of formation of fissures originates at the molecular scale. Finally, during firing and particularly during ignition, the grain is subjected to large forces that vary rapidly with time. Criteria for grain selection cannot properly utilize all of these parameters and must therefore be imperfect. A collection of relevant parameters has been given by Majerus (68).

A third difficulty concerns conditions under which the grain is used and methods by which the grain is supported. It is not sufficient to consider the grain by itself, since conditions for grain failure vary with the nature of the motor case and with the technological methods used in motor construction. For example, metallic cases and fiberglass cases produce different failure conditions for a given grain; for given applied forces, grain deformations will be appreciably larger inside fiberglass cases than inside metal cases. Failure analyses must consider the complete motor and must take into account the degree of adherence of the grain to the liner and of the liner to the case. Related to the fact that one must treat the entire motor is the observation that the size of the system can play an important role in grain failure; failure problems are quite different for motors with thrusts of a few tons than for motors with thrusts of a few thousand tons. The acceleration of the motor also affects rupture conditions for the grain.

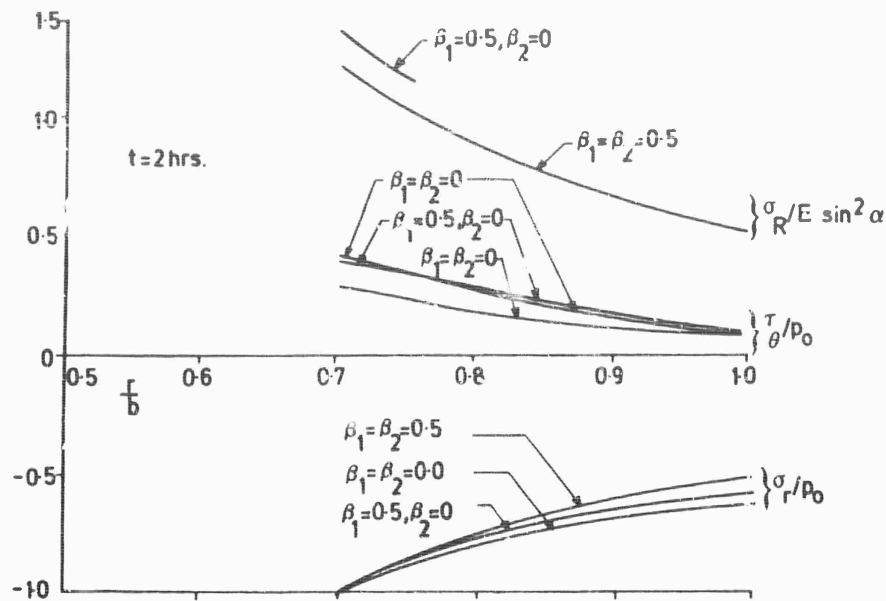


Fig. 11-22 Distribution of radial (σ_r/p_0), circumferential (τ_θ/p_0) and reinforcement ($\sigma_R/E \sin^2 \alpha$) stress for ablating case at $t = 2$ hrs. $B = K$.

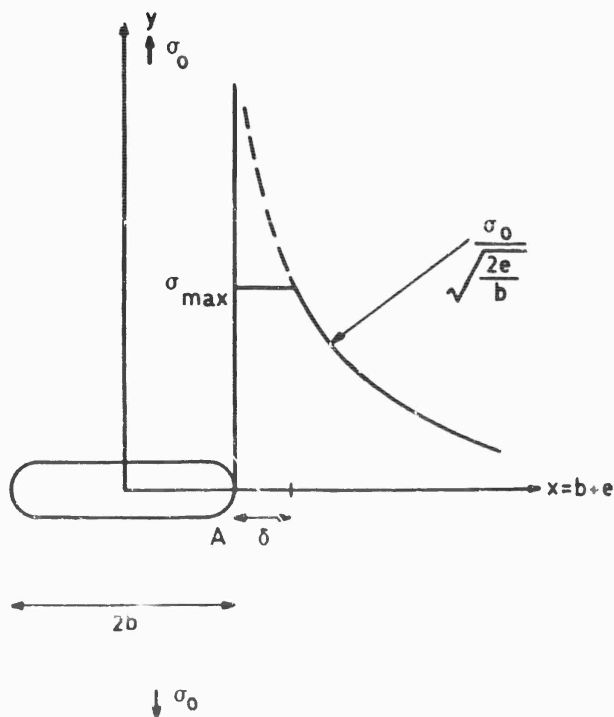


Fig. 11-23 Crack formation

A final difficulty pertains to the mathematical analysis of the failure phenomenon. Rigorous mathematical analyses cannot be carried out because the multiplicity of possible choices of rupture criteria precludes precise determination of failure. It is necessary to use empirical techniques in practice.

Before proceeding with a discussion of these basic difficulties that arise in the problem of formulating specific fracture criteria, we shall present a simplified description of the mechanism of crack formation and crack propagation, in an effort to provide the reader with a rudimentary physical understanding of grain fracture. This problem has been discussed in greater detail by Williams (69).

4.2. Formation and Propagation of Cracks

The simplest model that one can examine for investigating crack formation and propagation is a sheet of thickness h containing a cut of length $2b$, as illustrated in Fig. 11-23. The sheet is subjected, at an infinite distance from the crack, to a tensile stress σ_0 perpendicular to the cut. Under the influence of this stress, a crack forms at point A provided that $\sigma_0 \geq \sigma_{cr}$, where the critical stress σ_{cr} , defined by Griffith (70), is given by the formula :

$$\sigma_{cr} = (4ET/\pi 2b)^{1/2} \quad (\text{Eq. 11-242})$$

Here E is Young's modulus and T is the surface free energy or surface tension defined as :

$$T = - \partial V / \partial A , \quad (\text{Eq. 11-243})$$

where V is the elastic energy stored in the sheet and the surface area of the cut is $A = 2bh$. The values of E and T depend only on the material of which the sheet is composed; the material property T varies from 1.8×10^{-4} kg/cm for glass to 18 kg/cm for rubber materials.

The value of σ_{cr} can be investigated in a simplified manner by assuming that the potential energy V is composed of two parts, the strain energy and the work of surface stresses, viz.,

$$V = \pi (2b)^2 \sigma_0 h / 4E - 2AT . \quad (\text{Eq. 11-244})$$

The limiting condition for a crack to begin to form can then be defined by the neutral stability requirement :

$$[\partial V / \partial (2b)]_{cr} = 0 , \quad (\text{Eq. 11-245})$$

which leads immediately to $\sigma_0 = \sigma_{cr}$, where σ_{cr} is given by Eq. 11-242.

Under the assumption of small deformations, the elastic solution for the distribution of stresses along a line containing the crack, is given by (69) :

$$\sigma_x(x, 0) = \sigma_y(x, 0) - \sigma_0 = \sigma_0 b^2 / \{ \sqrt{x^2 - b^2} [x + \sqrt{x^2 - b^2}] \} , \quad (\text{Eq. 11-246})$$

where x is the coordinate parallel to the cut, y is the coordinate normal to the cut, the origin of coordinates is located at the center of the cut, σ_x is the x component of the stress and σ_y is the y component of the stress. Near the edge of the cut, where $e \equiv x - b$ is small compared with b , one finds from an expansion of Eq. 11-246 that :

$$\sigma_x = \sigma_0 / \sqrt{2e/b} + \dots, \quad (\text{Eq. 11-247})$$

which is plotted in Fig. 11-23. It is evident that near $e = 0$ the elastic solution is invalid and a plastic flow regime occurs, in which the value of σ is approximately constant over a distance δ . This terminology is highly qualitative because solid propellants do not conform to the assumptions of perfect plasticity.

In order to determine the velocity of propagation of the crack in a first rough approximation, one can estimate the constant value of σ in the region $e < \delta$, by equating the areas A_1 and A_2 shown in Fig. 11-24. Although this approximation produces a discontinuity in σ at $e = \delta$, it nevertheless possesses the desirable feature of preserving over-all force balance, since the total force is $n \int \sigma dx$. We then divide the material into elements of equal lengths δ , identified by the index n . We assume that the crack jumps from the first to the second element when the one-dimensional strain in the first element exceeds a critical value ϵ^* .

From Eq. 11-246, the stress components in each element n are related by the equation :

$$\sigma_{ny}^{(m)} = \sigma_{nx}^{(m)} + \sigma_0, \quad (\text{Eq. 11-248})$$

where the superscript (m) is intended to denote that the time is such that the element $m - 1$ has parted but the element m has not. In view of Eq. 11-246, the equality of the areas A_1 and A_2 leads to the approximate expression :

$$\sigma_{ny}^{(m)} = 2 \sigma_0 / \sqrt{2\delta / (b + m\delta)} \quad (\text{Eq. 11-249})$$

To relate the strain ϵ to the stresses given above, we may adopt a Voigt model, in which the modulus E is modified according to the relationship :

$$E \rightarrow E_V \left(\tau \frac{d}{dt} + 1 \right), \quad (\text{Eq. 11-250})$$

where E_V is the modulus of the spring in parallel with the dashpot of viscosity η and where $\tau = \eta/E_V$ is the retardation time. Inserting Eq. 11-250 into the elastic formula :

$$\epsilon_y = (1/E) \left(\sigma_y - \frac{1}{2} \sigma_x \right) \quad (\text{Eq. 11-251})$$

(which is applicable for an incompressible medium with Poisson's ratio equal to $1/2$), we obtain (after eliminating σ_x by use of Eq. 11-248) the differential equation :

$$\tau d \epsilon_{ny}^{(m)} / dt + \epsilon_{ny}^{(m)} = (\sigma_0 / 2E_V) [\sigma_{ny}^{(m)} / \sigma_0 + 1], \quad (\text{Eq. 11-252})$$

where the indices on ϵ have the same meaning as those on σ .

Let the stress be applied at time $t = 0$ and let the first element break at time $t = t_0$. Then, solving Eq. 11-252 for the first element during this first time interval, we obtain :

$$\epsilon^* = \epsilon_{0e}^{(0)} \left(1 - e^{-t_0/\tau} \right) \quad (\text{Eq. 11-253})$$

where $\epsilon_{0e}^{(0)}$ is the long-time equilibrium strain that would develop in element 0, if the element did not break. It can be seen from Eq. 11-252 that :

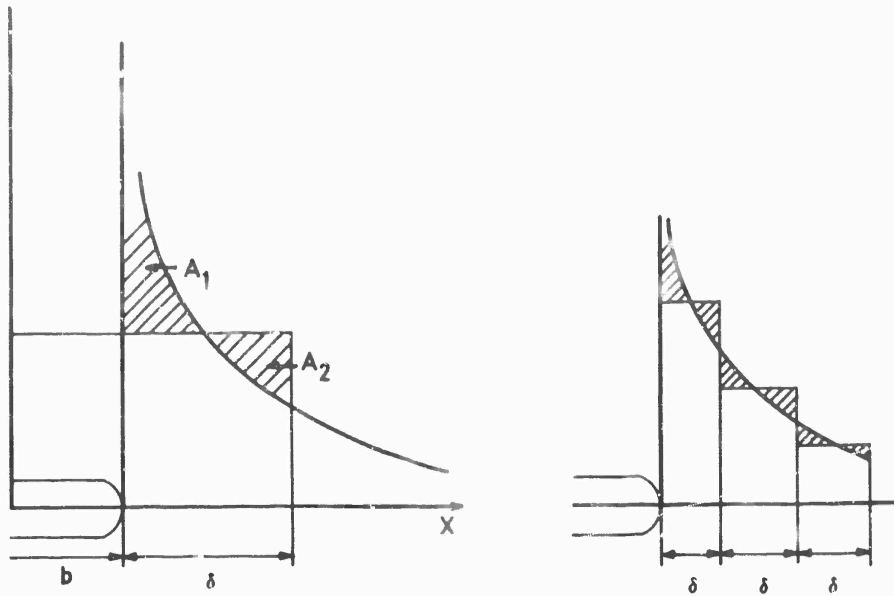


Fig. 11-24 Model for crack propagation

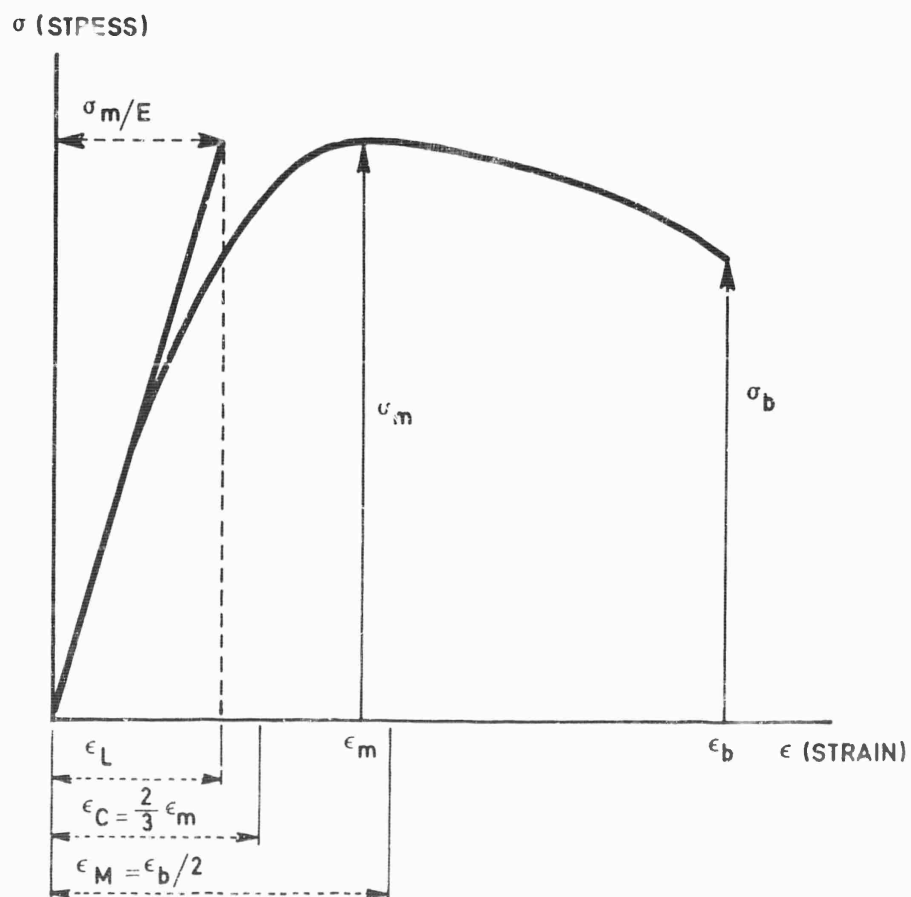


Fig. 11-25 Empirical design failure criteria

$$\left. \begin{aligned} \epsilon_{0e}^{(0)} &= (\sigma_0 / 2E_V) [\sigma_{0y}^{(0)} / \sigma_0 + 1] \\ &= (\alpha_0 / E_V) [1/\sqrt{2\delta/b} + 1/2 + (1/8)\sqrt{2\delta/b} + \dots] \end{aligned} \right\} \quad (\text{Eq. 11-254})$$

in which the second equality follows from Eq. 11-249. When $\delta/b \ll 1$, we then have from Eqs. 11-253 and 11-254,

$$t_0/\tau = -\ln [1 - (\epsilon^* \sqrt{2\delta/b}) / (\sigma_0/E_V)] . \quad (\text{Eq. 11-255})$$

By similar manipulations for element 1, applied to the time interval $[0, t_0]$ and also to the time interval $[t_0, t_1]$, where t_1 is the time at which element 1 breaks, one obtains :

$$\epsilon^* = \epsilon_{1e}^{(0)} \left[1 - e^{-t_0/\tau} \right] e^{-(t_1-t_0)/\tau} + \epsilon_{1e}^{(1)} \left[1 - e^{-(t_1-t_0)/\tau} \right] , \quad (\text{Eq. 11-256})$$

whence :

$$(t_1 - t_0)/\tau = \ln \left\{ 1 + \epsilon^* \left[1 - \epsilon_{1e}^{(0)} / \epsilon_{0e}^{(0)} \right] / \left[\epsilon_{1e}^{(1)} - \epsilon^* \right] \right\} \quad (\text{Eq. 11-257})$$

If $\tau \gg t_1 - t_0$, this formula yields :

$$\frac{t_1 - t_0}{\tau} = \frac{\epsilon^*}{\epsilon_{1e}^{(1)}} \left[1 - \frac{\epsilon_{1e}^{(0)}}{\epsilon_{0e}^{(0)}} \right] = \frac{\epsilon^* \sqrt{\frac{2\delta}{b}} (2 - \sqrt{2})}{\sigma_0/E_V} , \quad (\text{Eq. 11-258})$$

in which relationships for $\epsilon_{0e}^{(1)}$ and $\epsilon_{1e}^{(1)}$ have been employed. The velocity of propagation of the crack, in the time interval $[t_0, t_1]$, is therefore given by :

$$v_1 = \delta / (t_1 - t_0) \approx (\sigma_0/E_V) \sqrt{b\delta} / [\tau \epsilon^* 2(\sqrt{2} - 1)] . \quad (\text{Eq. 11-259})$$

Equation 11-259 enables us to see what parameters affect the initial velocity of propagation of the crack. From a practical viewpoint, cracks that are formed during motor ignition will be of importance, only if their propagation velocity exceeds the normal regression rate r of the propellant. In a representative example ($\delta \sim 10^{-3}$ cm, $b \sim 0.5$ cm, $\sigma_0 \sim 14$ kg/cm²), the propagation velocity v_1 is of the order of 5×10^{-2} cm/sec, which is in fact less than representative values of r . Thus, cracks formed during ignition might not be as important as cracks formed during manufacture or storage.

Generalizations of the equations derived here have been given by Williams (69), who shows that the propagation velocity at later times (viz., when the crack has progressed to the m -th element), is given by the relationship :

$$v_m \approx \frac{\pi}{2\sqrt{2}} \frac{\sigma_0/E_V}{\epsilon^*} \frac{b}{\tau} \sqrt{\frac{m\delta}{b}} \left(1 + \frac{m\delta}{b} \right) , \quad (\text{Eq. 11-260})$$

which is valid for $m \geq 4$. Letting $\xi = m\delta$ become a continuous distance variable for large values of m , one finds that Eq. 11-260 becomes :

$$v = d\xi/dt \approx \frac{\pi}{2\sqrt{2}} \frac{\sigma_0/E_V}{\epsilon^*} \frac{b}{\tau} \sqrt{\frac{\xi}{b}} \left(1 + \frac{\xi}{b} \right) \quad (\text{Eq. 11-261})$$

for $\xi \gg 4\delta$. Thus, v is proportional to $\sqrt{\xi/b}$ for $4\delta/b \leq \xi/b \ll 1$ and v is proportional to ξ/b for $\xi/b \gg 1$. Many further details on crack formation and propagation may be found in Ref. (69).

Although highly simplified, the analysis presented here serves to reveal the principal parameters on which crack formation and propagation depend.

4.3. Definition of Failure Criteria

In order to establish rules for grain acceptability, it is necessary to specify load conditions that grains must be able to meet. Such conditions might be stated in terms of the maximum stress or strain, the maximum principal stress or strain difference, the maximum total strain energy, the maximum distortional strain energy or the maximum conserved distortional strain energy, which the grain must be able to withstand without experiencing fracture. In practice one generally specifies a critical strain of some sort, as defined below. Such a specification constitutes an approximate, empirical criterion for grain failure.

a) Empirical Criteria - Since a failure criterion that is known in advance to be applicable to both propellant samples and complete grains cannot be given, it is necessary to investigate ways for applying sample-test results to motor configurations. Consider the typical stress-strain curve for a propellant sample under uniaxial forces, shown in Fig. 11-25. Three different characteristic strains can be identified from this curve. The rupture strain is ϵ_b , the strain at maximum stress is ϵ_m and the strain for extrapolation of the linear part of the curve to maximum stress is $\epsilon_L = \sigma_m / E$. Milloway and Weigand (71) suggested that for application of sample tests to failure criteria of grains in motors, it should be assumed that failure occurs when the strain of the grain in the motor is $\epsilon_M = \epsilon_b / 2$. Landel (72) suggested that motor-grain strains of either ϵ_L or $\epsilon_C \equiv 2/3 \epsilon_m$ should be assumed to correspond to failure. Of these three criteria, ϵ_L is usually the most conservative. A schematic comparison of the three criteria is shown in Fig. 11-25, and sample data for various propellants are plotted in Fig. 11-26, from which it may be noted that usually $\epsilon_M \geq \epsilon_L$ and $\epsilon_C \geq \epsilon_L$. Scatter in data obtained with samples is typically greater for ϵ_M than for ϵ_C , as can be seen from Fig. 11-26. However, the degree of scatter depends greatly on the nature of the propellant. There exists no unambiguous statistical justification for selecting one criterion over another.

Having obtained values of ϵ_L , ϵ_C and ϵ_M from sample tests, one should compare the results with experimental observation on motor failure. Experimental results reported by Majerus, et al. (73), in which strains ϵ_R were measured in small rocket motors at the instant of grain failure, show that the value of the ratio ϵ_R / ϵ_L depends appreciably on the temperature T_G of the grain. The quantity ϵ_R was found to decrease linearly with T_G as T_G increased, while ϵ_L tends to increase as the sample temperature increases. The ratio ϵ_R / ϵ_L is less than unity only for grain temperatures above 0°C . This observation might help to explain instances of motor failure that have occurred at grain temperatures below -30°C . A statistical analysis of motor firing results has been made (73) and motor failure was found to begin to occur only for $\epsilon_R / \epsilon_L \geq 0.8$. One of the more obvious effects that might cause this result is the fact that the samples are tested under uniaxial forces while the grain in the motor is subjected to a biaxial stress field. Statistical approaches are always needed in evaluating motor failures (73).

b) Cumulative Damage - It has been observed that failure conditions for a propellant depend on its stress history, in addition to its instantaneous strain; results of failure tests are affected by the rates at which forces are applied. This phenomenon, first found in metals, is a form of fatigue. It is related to long-term, microscopic changes in the structure of the material. A method of accounting for these cumulative damage effects in failure analysis of metals was proposed by Miner (74),

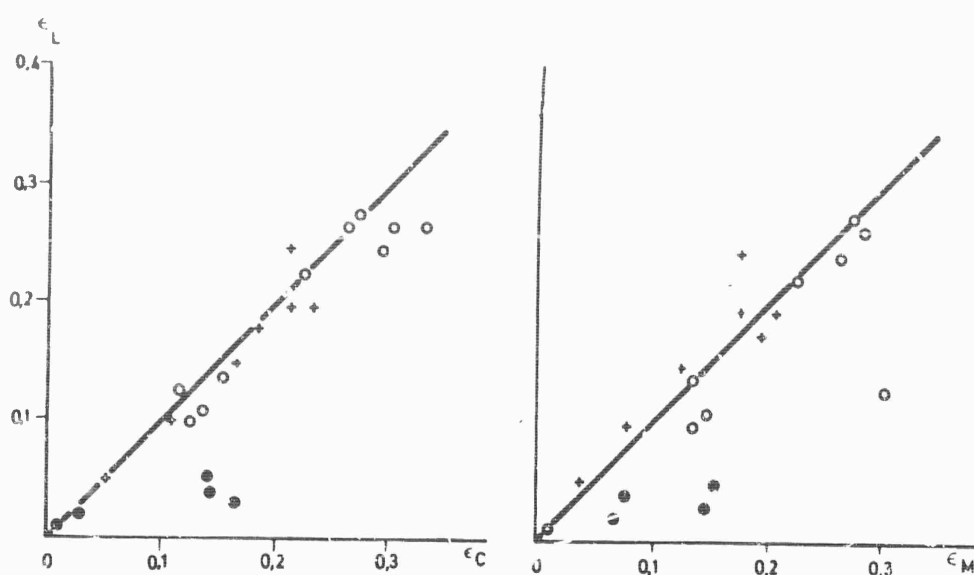
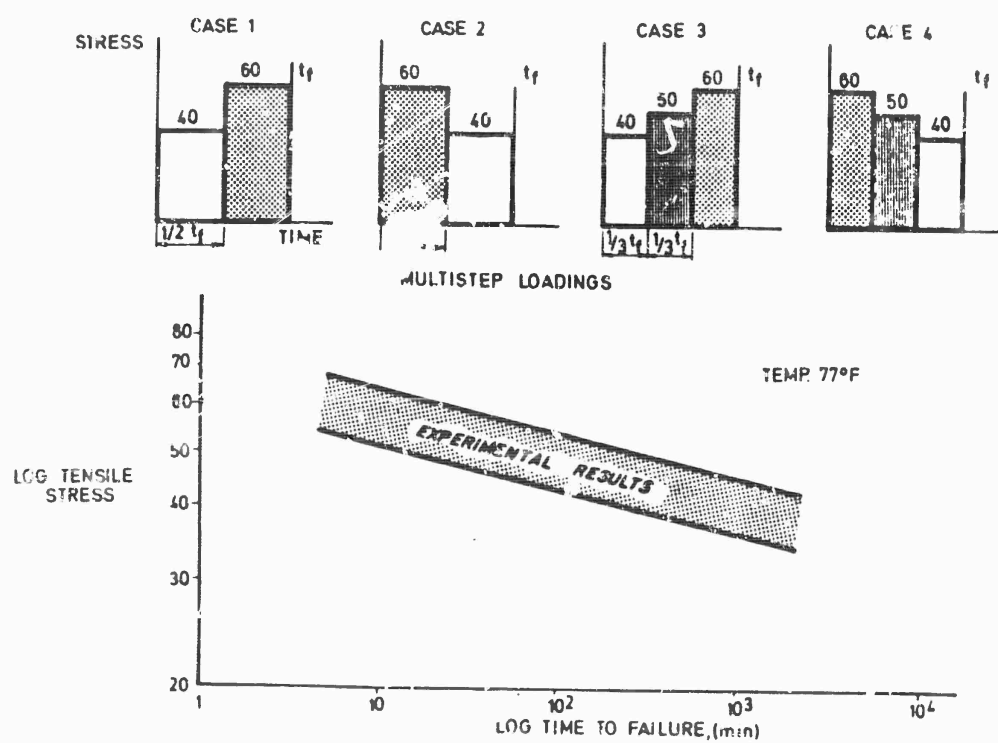
Fig. 11-26 ϵ_L , ϵ_C , ϵ_M relationship

Fig. 11-27 Log-log plot of constant potential stress vs. time to failure

who made a detailed study of cumulative damage in aluminum. With some modifications, Miner's technique can be applied to propellants and to liners.

Miner proposed that damage accumulates linearly, in the sense that failure occurs when :

$$\sum_{i=1}^M N_i/N_{Fi} = 1 \quad , \quad (\text{Eq. 11-262})$$

where N_i is the number of cycles that the sample experiences at the i -th stress level, N_{Fi} is the number of cycles at the i -th stress level required for failure and M is the number of different stress levels to which the sample is subjected. The experimental observation that large and small stresses require different weightings in calculations of failure caused by cumulative damage, has been introduced formally by replacing Eq. 11-262 by the failure condition :

$$\sum_{i=1}^M (N_i/N_{Fi})^{n_i} = 1 \quad , \quad (\text{Eq. 11-263})$$

in which the exponent n_i depends on the magnitude of the i -th stress level σ_i . In Eq. 11-263, n_i is empirically greater than unity for weak stresses and less than unity for strong stresses. This result has been further modified by Williams (2), through the introduction of times in place of numbers of cycles. If t_i denotes the time over which the sample is held at the strain rate $\dot{\epsilon}_i$ and t_{Fi} denotes the time to failure at the strain rate $\dot{\epsilon}_i$, then the failure criterion of Williams (2) is :

$$\sum_{i=1}^M (t_i/t_{Fi})^{n_i} = 1 \quad , \quad (\text{Eq. 11-264})$$

where the exponent n_i is permitted to depend on the value of $\dot{\epsilon}_i$ and M is now the number of different strain rates. The total time to failure, in this formulation, is:

$$t^* = \sum_{i=1}^M t_i \quad (\text{Eq. 11-265})$$

If $n_i = 1$, the Williams formulation can readily be extended to continuously varying strain rates through replacement of Eq. 11-264 by :

$$\int_0^{t^*} \frac{dt(\dot{\epsilon})}{t_F(\dot{\epsilon})} = 1 \quad , \quad (\text{Eq. 11-266})$$

in which the meanings of the symbols should be obvious.

To illustrate the application of Eq. 11-266 to viscoelastic materials, we may introduce a Voigt model such that :

$$\epsilon = \epsilon_0 (1 - e^{-t/\tau}) \quad . \quad (\text{Eq. 11-267})$$

Then :

$$\dot{\epsilon} = \dot{\epsilon}_0 e^{-t/\tau}, \quad (\text{Eq. 11-268})$$

where $\dot{\epsilon}_0 \equiv \epsilon_0/\tau$ and if we assume that :

$$t_F \approx \epsilon^* / \dot{\epsilon} \quad (\text{Eq. 11-269})$$

with a constant ultimate strain ϵ^* , then we find by substitution into Eq. 11-266 that :

$$1 = \int_{\epsilon_0}^{\dot{\epsilon}(t^*)} \frac{1}{t_F(\dot{\epsilon})} \left(\frac{dt}{d\dot{\epsilon}} \right) d\dot{\epsilon} = - \frac{\tau}{\epsilon^*} \left[\dot{\epsilon}(t^*) - \dot{\epsilon}_0 \right], \quad (\text{Eq. 11-270})$$

which in view of Eq. 11-268 yields :

$$t^* = -\tau \ln (1 - \epsilon^* / \tau \dot{\epsilon}_0). \quad (\text{Eq. 11-271})$$

Equation 11-271 gives the failure time in terms of the initial strain rate, the fracture strain and the relaxation time.

Measurements have been made on failure behavior of composite propellants that were subjected to various loading histories (75). In particular, multistep loadings such as those illustrated at the top of Fig. 11-27, were employed. For each of the steps illustrated in Fig. 11-27, the exposure time was a specified fraction of the failure time at constant loading for the applied stress. The fractions are given at the top of Fig. 11-27 and the failure time at constant loading is shown as a function of stress at the bottom of Fig. 11-27. The failure time of course increases as the loading decreases.

Equation 11-262 for cumulative damage, implies that the failure time does not depend on the order in which the different stresses are applied. Hence, for example, failure in Case 1 of Fig. 11-27 should occur in the same time as failure in Case 2 of Fig. 11-27. The experiments with propellants do not support this result (73), (75); the experimental failure times depend on the order in which the stress magnitudes are applied. This shows that it is necessary to use formulas such as Eq. 11-263 or Eq. 11-264 for correlating experimental results on cumulative damage of composite solid propellants. The failure mechanism involves the formation of flaws through detachment of the binder from the perchlorate crystals. This in turn, leads to the formation and propagation of cracks through the coalescence and growth of these flaws. At stress levels of 40 psi, for example, very few flaws are formed and when the stress is increased to 60 psi the material has very little memory of the fact that it had been subjected earlier to 40 psi. On the other hand, at 60 psi many flaws are produced and when the stress is then reduced to 40 psi the material is much more prone to failure; the earlier exposure to the higher stress has appreciably changed the mechanical properties of the propellant. These interpretations are supported by microcinematography. It is clear from the interpretations that mechanical properties of the grain are affected not only by the strength of the binder but also by the degree to which the binder can adhere to the oxidizer or metallic additives. Corresponding adherence properties of liner materials are obviously relevant to cumulative damage of assembled motors.

c) Other Criteria - The maximum stress or strain at any given point in the grain is the largest of the three principal stresses or strains ($\sigma_1, \sigma_2, \sigma_3, \epsilon_1, \epsilon_2, \epsilon_3$). Failure criteria could be specified in terms of maximum allowable stress or strain. Von Mises proposed an alternative failure criterion, based on a maximum allowable mean value of the principal stress difference (or the mean deviatoric stress) defined

as :

$$\sigma_0 = \left[(\sigma_1 - \sigma_2)^2 + (\sigma_2 - \sigma_3)^2 + (\sigma_3 - \sigma_1)^2 \right]^{1/2} / \sqrt{2} . \quad (\text{Eq. 11-272})$$

An analogous quantity may be defined for strain, such as :

$$\epsilon_0 = \left[(\epsilon_r - \epsilon_\theta)^2 + (\epsilon_\theta - \epsilon_z)^2 + (\epsilon_z - \epsilon_r)^2 \right]^{1/2} / \sqrt{2} (1 + \nu) \quad (\text{Eq. 11-273})$$

for a tubular grain or a cylinder subjected to uniaxial tension. A maximum value of ϵ_0 might be assumed to correspond to failure. If $\epsilon_z = 0$ and $\epsilon_r = \epsilon_\theta$, then Eq. 11-273 reduces simply to :

$$\epsilon_0 = \epsilon_\theta / (1 + \nu) = (2 \sqrt{3}/3) \epsilon_F = 1.15 \epsilon_F \quad (\text{Eq. 11-274})$$

when $\nu = 1/2$, where ϵ_F is the maximum permissible strain in pure shear (e.g., at a star point in a grain with a star-shaped port) which is seen to be 85% of the yield strain measured in uniaxial tension.

One can also discuss failure in terms of a critical strain energy criterion, such as :

$$W_{d11} = \frac{1}{2} \sigma \epsilon \quad , \quad (\text{Eq. 11-275})$$

where :

$$\sigma \equiv (\sigma_1 + \sigma_2 + \sigma_3)/3 \quad , \quad \epsilon \equiv (\epsilon_1 + \epsilon_2 + \epsilon_3) . \quad (\text{Eq. 11-276})$$

There is fragmentary experimental evidence supporting the contention that critical strain energies are useful in formulating failure criteria for viscoelastic materials.

There are many other criteria of the type mentioned here which, although ignoring cumulative damage and time-dependent behavior, are nevertheless potentially capable in principle of providing appreciable improvements over the empirical failure criteria currently in use.

4.4. Conclusion

Although much progress has been made in applying the results of failure tests on propellant samples to the formulation of practical failure criteria for motors, many uncertainties still remain. Failure criteria currently in use do not account either for effects of motor geometry and propellant support or for changes in propellant properties brought about by the stress, strain, temperature and environmental history, to which the propellant may be subjected. Experimental attempts to improve this state of affairs must necessarily involve lengthy and costly studies for the accumulation of statistically significant data. We may recommend that the reader who is interested in following the future developments in this field should consult continuing publications of Solid Rocket Structural Integrity Abstracts (76).

Appendix

Our choice of polymethylmethacrylate as a representative viscoelastic material requires comment, particularly since it is used not only in section 3.3 but also in Sections 3.4 and 3.6, e.g., for all of the representative results shown in Figs. 11-10 through 11-22. This material was selected because, in comparison to representative propellants, its viscoelastic properties are known extremely well. Thus,

the relaxation curve shown in Fig. 11-10 extends over nine orders of magnitude in time, while corresponding results for solid propellants are available only over three or four orders of magnitude. All of the significant structural features of the curve in Fig. 11-10 are clearly evident. On the other hand, essential structures of solid-propellant relaxation curves for short times are not currently available because of experimental difficulties in making measurements at the very small time scales (roughly 10^{-3} times those of polymethylmethacrylate) that are of importance in solid-propellant viscoelastic behavior. For example, although the reduced time in Fig. 11-5 extends over 15 orders of magnitude, nevertheless Fig. 11-5 was constructed from sets of data for different temperatures, each of which extended only over three orders of magnitude in time (1 sec to 10^3 sec). It would be quite questionable to use Fig. 11-5 for real times less than 1 sec. The absence of essential data on solid propellants therefore motivates the selection of polymethylmethacrylate.

Some consequences of the choice of polymethylmethacrylate should be explained here, in order to prevent confusion in some of the discussions. Since the 'relaxation time' for polymethylmethacrylate to the extent that such a quantity can be defined, is roughly two or three orders of magnitude greater than that of a typical propellant, the time scales over which calculations should be made to obtain comparable viscoelastic behavior, are roughly 10^2 to 10^3 times greater for polymethylmethacrylate than for representative propellants. Therefore, in the figures and discussions, burning or ablation times of the order of hours appear. These long times do not imply irrelevance of the analysis to realistic combustion conditions of solid propellant rockets; on the contrary, they are necessary because of the choice of polymethylmethacrylate, for producing viscoelastic behavior that is representative of what a real solid propellant would experience over a realistic burning time. Of course, the dimensional numerical results cannot be applied directly to solid propellants. Our aim here is to develop an understanding of the phenomena and techniques, not to make calculations for specific solid propellants. Indeed, accurate calculations for specific propellants are not possible at present because of the lack of important data on the relaxation modulus.

References

- (1) Lee E.H., Viscoelastic Stress Analysis, Structural Mechanics, Proceedings of the First Symposium on Naval Structural Mechanics, edited by J.N. Goodier and N.J. Hoff, Pergamon Press, New York, 1960.
- (2) Williams M.L., Structural Analysis of Viscoelastic Materials, AIAA Journal, Vol. 2, p. 785, 1964.
- (3) Blatz P.J., Rheology of Composite Solid Propellants, Industrial and Engineering Chemistry, Vol. 48, Part I, p. 727, 1956.
- (4) Biot M.A., Linear Thermodynamics and the Mechanics of Solids, Proceedings of the Third U.S. National Congress on Applied Mechanics American Society of Mechanical Engineers, p. 1, 1958.
- (5) Ferry J.D., Viscoelastic Properties of Polymers, John Wiley and Sons, Inc., New York, 1961.
- (6) Summerfield M., Solid Propellant Rocket Research, Progress in Astronautics and Rocketry, Vol. 1, New York, 1960.
- (7) Fitzgerald J.E., Propellant Grain Structural Integrity Problems: Engineering Status, Solid Rocket Structural Integrity Abstracts. Graduate Aeronautical Laboratories, California Inst. of Technology, Pasadena, 1965.

- (8) Bland D.R., The Theory of Linear Viscoelasticity, Pergamon Press, New York, 1960.
- (9) Corneliussen A.H., and Lee E.H., Stress Distribution Analysis for Linear Viscoelastic Materials, Creep in Structures, edited by N.J. Hoff, Academic Press Inc., New York, p.1, 1962.
- (10) Gross B., Mathematical Structure of the Theories of Viscoelasticity, Hermann, Paris, 1953.
- (11) Stuart H.A., Die Physik der Hochpolymeren, Vol. 4, Springer-Verlag, Berlin, 1956.
- (12) Gurtin M.E., and Sternberg E., On the Linear Theory of Viscoelasticity, Archive for Rational Mechanics and Analysis, Vol.11, p.291, 1962.
- (13) Zeuer C., Elasticity and Anelasticity of Metals, The University of Chicago Press, 1948.
- (14) Radok J.R.M., Viscoelastic Stress Analysis, Quarterly of Applied Mathematics, Vol.15, p.198, 1957.
- (15) Fitzgerald J.E., Engineering Methods for Grain Structural Integrity Analysis, Lockheed Propulsion Company Report 578/556-F-3, Contract No. AF 04(611)-9013 and DA-04-495-ORD-3260, May, 1963.
- (16) Marvin R.S., Aldrich R., and Sack H.S., The Dynamic Bulk Viscosity of Polyisobutylene, Journal of Applied Physics, Vol.25, p.1213, 1954.
- (17) Williams M.L., Blatz P.J., and Schapery R.A., Fundamental Studies Relating to Systems Analysis of Solid Propellants, Graduate Aeronautical Laboratories, California Institute of Technology, S.M. 61-5, February 1961.
- (18) Schwarzl F., Näherungsmethoden in der Theorie des viscoelastischen Verhaltens I, Physica, Vol.17, p.830, 1951.
- (19) Leaderman H., Approximations in Linear Viscoelasticity Theory: Delta Function Approximations, Journal of Applied Physics, Vol.25, p.294, 1954.
- (20) Alfrey T., Mechanical Behavior of High Polymers, Interscience Publishers, New York, 1948.
- (21) Hopkins I.L., and Hamming R.W., On Creep and Relaxation, Journal of Applied Physics, Vol.28, p.906, 1957.
- (22) Bland D.R., and Lee E.H., On the Determination of a Viscoelastic Model for Stress Analysis of Plastics, Journal of Applied Mechanics, Vol.23, p. 416, 1956.
- (23) Ninomiya K., and Ferry J.D., Some Approximate Equations Useful in the Phenomenological Treatment of Linear Viscoelastic Data, Journal of Colloid Science, Vol.14, p.36, 1959.
- (24) Rouse P.E. Jr., A Theory of the Linear Viscoelastic Properties of Dilute Solutions of Coiling Polymers, Journal of Chemical Physics, Vol.21, p.1272, 1953.
- (25) Zimm B.H., Dynamics of Polymer Molecules in Dilute Solution: Visco-

- elasticity, Flow Birefringence and Dielectric Loss, *Journal of Chemical Physics*, Vol. 24, p. 269, 1956.
- (26) Bueche F., *Physical Properties of Polymers*, Interscience Publishers, 1962.
 - (27) Leaderman H., *Elastic and Creep Properties of Filamentous Materials and Other High Polymers*, The Textile Foundation, 1943.
 - (28) Morland L.W., and Lee E.H., *Stress Analysis for Linear Viscoelastic Materials with Temperature Variation*, *Transactions of the Society of Rheology*, Vol. 4, p. 233, 1960.
 - (29) Biot M.A., *Theory of Stress-Strain Relation in Anisotropic Viscoelasticity and Relaxation Phenomena*, *Journal of Applied Physics*, Vol. 25, p. 1385, 1954.
 - (30) Schapery R.A., *Application of Thermodynamics to Thermomechanical Fracture, and Birefringent Phenomena in Viscoelastic Media*, *Journal of Applied Physics*, Vol. 35, p. 1451, 1964.
 - (31) Fung Y.C., *Foundation of Solid Mechanics*, Chapter 13, Prentice-Hall, Inc, 1965.
 - (32) Ziegler H., *Some Extremum Principle in Irreversible Thermodynamics with Application to Continuum Mechanics*, *Progress in Solid Mechanics*, Vol. 4, edited by I.N. Sneddon and R. Hill, North-Holland Publishing Company, Amsterdam, p. 91, 1963.
 - (33) Green A.E., and Rivlin R.S., *The Mechanics of Nonlinear Materials with Memory, Part I*, *Archive for Rational Mechanics and Analysis*, Vol. 1, p. 1, 1957.
 - (34) Noll W., *A Mathematical Theory of the Mechanical Behavior of Continuous Media*, *Archive for Rational Mechanics and Analysis*, Vol. 2, p. 197, 1958.
 - (35) Fréchet M.M., *Sur les fonctionnelles continues*, *Annales scientifiques de l'école normale supérieure, Series 3*, Vol. 27, p. 193, 1910.
 - (36) Volterra V., *Theory of Functionals and of Integral and Integro-differential equations*, Dover Publications, 1959.
 - (37) Pipkin A.C., *Small Finite Deformations of Viscoelastic Solids*, *Reviews of Modern Physics*, Vol. 36, p. 1034, 1964.
 - (38) Coleman B.D., and Noll W., *Foundation of Linear Viscoelasticity*, *Reviews of Modern Physics*, Vol. 33, p. 239, 1961.
 - (39) Appleby E.J., and Lee E.H., *Superposed Deformations in Nonlinear Viscoelasticity*, Technical Report No. 149, Division of Engineering Mechanics, Stanford University, Stanford, California, 1964.
 - (40) Huang N.C., and Lee E.H., *Nonlinear Viscoelasticity for Short Time Ranges*, *Journal of Applied Mechanics*, Vol. 33, p. 313, 1966.
 - (41) Dong R., *Studies in Mechanics of Nonlinear Solids*, Ph.D. Thesis, University of California, UCRL-12039, June 1964.

- (42) **Ward I. M., and Onat E. T.**, Nonlinear Mechanical Behavior of Oriented Polypropylene, *Journal of the Mechanics and Physics of Solids*, Vol. 11, p. 217, 1963.
- (43) **Lifshitz J. M.**, Multiple Integral Representation of Mechanical Behavior of Polyethylene, Brown University Report No. 10, Contract No. 562(30), December, 1964.
- (44) **Onaran K., and Findley W. N.**, Combined Stress-Creep Experiments on a Nonlinear Viscoelastic Material to Determine the Kernel Functions for a Multiple Integral Representation of Creep, *Transactions of the Society of Rheology*, Vol. 9, Part 2, p. 299, 1965.
- (45) **Parr C. H.**, The Application of Numerical Methods to the Solution of Structural Integrity Problems of Solid Propellant Rockets, Solid Rocket Structural Integrity Abstract, Graduate Aeronautical Laboratories, California Institute of Technology, Pasadena, 1964.
- (46) **Williams M. L., Landel R. F., and Ferry J. D.**, The Temperature Dependence of Relaxation Mechanisms in Amorphous Polymers and Other Glass-Forming Liquids, *Journal of American Chemical Society*, Vol. 77, p. 3701, 1955.
- (47) **Bruer S., and Onat E. T.**, On Uniqueness in Linear Viscoelasticity, *Quarterly of Applied Mathematics*, Vol. 19, p. 355, 1962.
- (48) **Lee E. H., and Rogers T. G.**, Solution of Viscoelastic Stress Analysis Problems Using Measured Creep or Relaxation Functions, *Journal of Applied Mechanics*, Vol. 30, p. 127, 1963.
- (49) **Rogers T. G., and Lee E. H.**, The Cylinder Problem in Viscoelastic Stress Analysis, *Quarterly of Applied Mathematics*, Vol. 22, p. 117, 1964.
- (50) **Huang N. C., Lee E. H., and Rogers T. G.**, On the Influence of Viscoelastic Compressibility in Stress Analysis, *Proceedings of the Fourth International Congress on Rheology*, John Wiley and Sons, Inc., New York, Part 1, p. 213, 1965.
- (51) **Rogers T. G., and Lee E. H.**, Thermo-Viscoelastic Stresses in a Sphere with an Ablating Cavity, *Progress in Applied Mechanics (The Prager Anniversary Volume)*. The Macmillan Company, New York, p. 355, 1963.
- (52) **Bischoff J., Catsiff E., and Tobolsky A. V.**, Elastoviscous Properties of Amorphous Polymers in the Transition Region - I, *Journal of the American Chemical Society*, Vol. 74, p. 3378, 1952.
- (53) **Lindsey G. H., and Williams M. L.**, Structural Integrity of an Ablating Rocket Subjected to Axial Acceleration, *AIAA Journal*, Vol. 3, p. 258, 1965.
- (54) **Fourney M. E., and Parmerter R. R.**, Stress-Concentrations for Internally Perforated Star Grains, Bureau of Naval Weapons, NAVWEPS Report 7758, December, 1961.
- (55) **Fourney M. E., and Parmerter R. R.**, Photoelastic Design Data for Pressure Stresses in Slotted Rocket Grains, *AIAA Journal*, Vol. 1, p. 697, 1963.
- (56) **Wilson H. B., Jr.**, Stresses Owing to Internal Pressure in Solid Propellant Rocket Grains, *ARS Journal*, Vol. 31, p. 309, 1961.

- (57) **Schapery R.A.**, Approximate Methods of Transform Inversion for Viscoelastic Stress Analysis, Proceedings of the Fourth U.S. National Congress of Applied Mechanics, p. 1075, 1962.
- (58) **Papoulis A.**, The Fourier Integral and Its Applications, McGraw-Hill Co., Inc., New York, p. 53, 1962.
- (59) **Baltrukonis J.H.**, The Dynamics of Solid Propellant Rocket Motors, Technical Report No. 9, National Aeronautics and Space Administration, Research Grant No. NaG-125-61 (Suppl. 3), June 1965, The Catholic University of America, Washington, D.C., 20017.
- (60) **Achenbach J.D.**, Dynamic Response of a Long Case-bonded Viscoelastic Cylinder, AIAA Journal, Vol. 3, p. 673, 1965.
- (61) **Achenbach J.D.**, Dynamic Response of a Viscoelastic Cylinder with Ablating Inner Surface, Journal of Applied Mechanics, Vol. 33, p. 275, 1966.
- (62) **Lockheed Propulsion Company**, Solid Propellant Structural Integrity Investigations: Dynamic Response and Failure Mechanisms. Contract No. AF04(611)-9953, January 1965.
- (63) **Argyris J.H.**, Recent Advances in Matrix Methods of Structural Analysis, The Macmillan Co., New York, 1964.
- (64) **Argyris J.H.**, and **Kelsey S.**, Modern Fuselage Analysis and the Elastic Aircraft, Butterworths Inc., Washington, D.C., 1963.
- (65) **Huang N.C.**, and **Lee E.H.**, On Elastic Filament Reinforcement of a Viscoelastic Cylinder, Technical Report No. 168, Div. of Engineering Mechanics, Stanford University, February 1967.
- (66) **Frocht M.M.**, Photoelasticity, Vols. 1 and 2, Wiley, New York, 1961.
- (67) **Hildebrand F.B.**, Introduction to Numerical Analysis, McGraw-Hill, New York, 1956.
- (68) **Majerus J.N.**, A Unified Approach to Failure and Its Application to Highly Filled Polymers, J. Polymer Science A3, 3361-3383, 1965.
- (69) **Williams M.L.**, The Fracture of Viscoelastic Material, Fracture of Solids, Interscience Publishers, New York, pp. 157-188, 1963.
- (70) **Griffith A.A.**, Phil. Trans. Roy. Soc. London A221, 163, 1921.
- (71) **Milloway W.T.**, and **Wiegand J.H.**, J. Appl. Polymer Sci. 7, 1325, 1963.
- (72) **Landel R.F.**, Tensile Testing of Composite Propellants, Summary No. 66, Jet Propulsion Laboratory, California Institute of Technology, Pasadena, August 1958.
- (73) **Majerus J.N.**, **Briar H.D.**, and **Wiegand J.M.**, Behavior and Variability of Solid Propellants and Criteria for Failure and for Rejection, J. Spacecraft and Rockets 2, 833-846, 1965.
- (74) **Miner I.A.**, J. Eng. Power 76, 627, 1954.
- (75) **Majerus J.N.**, and **Tamekuni M.**, The Effect of Material Nonlinearity and

Failure Criteria upon Predicted Grain Reliability, Aerojet-General Corp.
Technical Paper TP-3, October 1964.

- (76) Williams M.L., Solid Rocket Structural Integrity Abstracts, Contract No. AF 04(611)-9572; University of Utah, Salt Lake City, July 1964 - present.
- (77) Meillette R.V., et al., A Grain Structural Analysis on a Spherical Motor, Report No. SM-52244, Douglas Missile and Space Systems Division, Santa Monica, California, February 1966.

Chapter 12

The Future of Solid Propellant Rocketry

The Future of Solid Propellant Rocketry

1. Introduction

The current value of solid propellant rockets is uncontested. There are numerous mission categories ranging from a host of tactical military missiles, to small upper stage and space vehicle propulsion systems, to large boosters, in which solid propellant motors are clearly superior to any of their current rivals. Our aim in this chapter is to attempt to predict whether these advantages will be maintained and whether solid propellants will emerge as the optimum power sources in new areas of application. This task is obviously very difficult, as there are always uncertainties associated with attempts to predict the future. Realizing that in many instances history may prove us to be wrong, we nevertheless offer here our views on the future of solid propellant rocketry.

The future standing of solid propellant rockets in the field of propulsion will depend in large measure on improvements in solid propellant rocketry. There are many prospects for enhancing the utility of solid propellant systems. Realization of enhancement is subject to progress in many areas of research and development. To provide the basis for discussing future uses of solid propellant rockets, it is necessary for us to summarize the possibilities for new research and technological advances. Summaries are presented in the next four sections, where we discuss various details of: newly emerging propellants, potential advances in fundamental research on the combustion of new propellants, new ideas on unsteady processes such as ignition and combustion instability and technological developments of improved flexibility and control capabilities of solid propellant systems. Future uses of solid propellant rockets which may result from this work, are considered in the final section of the chapter.

2. Future of Propellants

The orientation of research into new solid propellant formulations is governed by three different kinds of measures of the propellant quality, viz., (a) energetic qualities, such as the specific impulse and the volumetric specific impulse, which are related to the heat released by combustion and to the transformation of this thermal energy into kinetic energy within the nozzle, (b) kinetic qualities, such as the burning rate, the ignition delay and the burning time, which depend on combustion phenomena and influence both steady-state and transient motor behavior and (c) utilization qualities, such as ease of manufacture, storability, safety, mechanical grain properties, manufacturing costs, etc., which depend on conditions of propellant use and not on combustion phenomena. As we have indicated in Chapter 3, the various quality requirements are often incompatible and therefore a compromise is necessary in order to obtain the most suitable propellant. The numerous criteria for propellant choice depend strongly on the particular mission. Consequently it is necessary to put a wide variety of propellant formulations at the disposal of the

users, in order to cover the entire domain of applications. In the following paragraphs we shall try to explain the present trends and problems in propellant development.

(a) Energetic qualities

As indicated in Chapter 1, the performance of a rocket depends chiefly on the specific impulse and the density of the propellant. We have seen that a high specific impulse generally corresponds to a low density. To select a propellant for a given application, it is necessary to know which of these two parameters is more important. Propellant research is directed toward increasing both density and specific impulse.

The basic properties that influence the specific impulse are the flame temperature and the molecular weight of the combustion products; high flame temperatures and low molecular weights are needed for high specific impulse. Although propellant combinations can be selected which produce flame temperatures as high as 4500°K , serious technological difficulties occur in connection with heat transfer, when the flame temperature exceeds 3500°K . From an engineering viewpoint, it is therefore more desirable to lower the molecular weight than to increase the flame temperature. When the propellant type is not specified, product molecular weights in the range 25 g/mole to 16.5 g/mole are achievable by selecting fuels that contain a large percentage of hydrogen. However, for solid propellants the minimum obtainable molecular weight is higher due to the restriction that the propellant be a solid. Solid compounds containing hydrogen, beryllium, lithium or boron as a fuel and oxygen or fluorine as an oxidizer are attractive, provided that the propellant compounds are not bonded too strongly. Low propellant bond energies must be maintained to insure that a small fraction of the heat of combustion is lost in breaking propellant bonds. The use of light elements and low bond energies is difficult to reconcile. Therefore the specific impulse of solid propellants appears to be limited theoretically to a value of about 300 sec, the current practical values being in the range of 250 sec.

Let us examine a few of the possible ways to increase the performance of solid propellants. One may replace aluminum in the propellant by a lighter and more energetic element such as beryllium. Propellants using polybutadiene as a binder, ammonium perchlorate and beryllium are under development, the chief difficulty being to achieve complete combustion of the beryllium. In order to ignite beryllium, it is necessary to achieve a high flame temperature ($> 2300^{\circ}\text{K}$) with the binder and the oxidizer and also to obtain binder-oxidizer product gases that are sufficiently oxidizer rich. One approach to this problem is to use auxiliary metals such as magnesium and aluminum, which ignite more readily than beryllium, as agents for initiating the combustion of beryllium. The utility of these metals as combustion 'relays' is still poorly defined.

Another possibility is to use metallic hydrides, which lead to better performance than the metal itself and which sometimes have a lower ignition temperature than the metal. The cost of these hydrides is sometimes high and they are often incompatible with commonly used binders. The introduction of metallic hydrides into propellants, the study of their compatibility with certain binders and investigations of hydride burning processes are important steps in the development of new solid propellants.

In addition to using energetic additives, one may increase the specific impulse of solid propellants by developing new, highly energetic, plastic binders. Energetic binders can be either fuels containing a maximum amount of hydrogen and using nitrogen in place of carbon as a binding element, wherever possible, or oxidizers containing fluorine or oxygen atoms with nitrogen as a binding agent. It is also

possible to include simultaneously both fuel and oxidizer elements in the binder molecules, but to achieve stability of such combinations often necessitates tolerating lower values of the specific impulse. To be useful as binders, energetic materials containing (N, H) or (N, F) elements must retain acceptable mechanical properties when loaded with high percentages (>85%) of finely ground substances, which constitute the other fraction of the propellant.

Parallel to the development of high energy binders, new oxidizers are also being studied. The initial aim of these studies is to improve ammonium perchlorate by replacing the relatively useless NH_4 group by groups derived from hydrazine (e.g., hydrazine dperchlorate) or by oxidizer-containing groups such as NO_2 , NO (nitronium perchlorate) or even fluorine derivatives. In our opinion, the chemistry of new oxidizers has evolved little and significant advances may be achieved in the synthesis of new solid oxidizers based upon fluorine and oxygen.

The best available substances for a high energy propellant generally are not mutually compatible because they may, for example, enter into a more or less rapid chemical reaction when certain components are brought into contact at a stage of manufacture or casting. In order to develop such a propellant, it is necessary to separate the reactive constituents. This leads to the basic concept of heterogeneous propellants with a controlled heterogeneity. One example is afforded by the use of nitronium perchlorate, which is hypergolic with many fuel binders; if the nitronium perchlorate grains were coated with a thin layer of inert plastic which is compatible with the oxidizer, with the plastic binder fuel and with any metallic additive, then the propellant might be rendered stable. Certain metallic hydrides might also be protected by this type of encapsulation.

Along the same line, it is possible to imagine a solid propellant in which the fuel and oxidizer constituents are completely separated; for example, blocks of oxidizer with a well-defined geometry might be glued to fuel elements of a suitable geometry. One can envisage a grain containing the right proportions of fuel and oxidizer, made for instance from assemblies of small pressed oxidizer parallelepipeds bound by a plastic fuel which produces the desired mechanical properties. Such arrangements might facilitate the use of highly energetic fuels and oxidizers. Since the ratio of the contact surface area to the volume is small compared with that of conventional propellants using oxidizer crystals embedded in a binder, the chances of a chemical reaction developing spontaneously on the surface are smaller. Degradation during storage and explosion hazards thus would be lessened; these advantages may be quite important for large, high-energy grains. The dimensions of parallelepipeds of pressed propellant are typically a few millimeters, thus small compared with the over-all dimensions of the grain. Problems associated with combustion efficiency and with design of grain shapes therefore need not arise. Fabrication techniques would be more complex than the technique of casting the propellant into a mold or into the rocket casing. But improved safety in manufacture and stability of propellants using powerful oxidizers such as nitronium perchlorate, may more than offset this disadvantage.

A further speculative point worth mentioning is the concept of cryogenic solid propellants. Storage conditions differ on earth and in space and certain propellants which are liquids on the earth are stored most conveniently as solids in space. One can thus imagine frozen solid propellants which, due to their low temperature, are chemically more stable than under familiar storage conditions. In this way many more highly energetic propellants might be used.

These various lines of research into the development of high-energy propellants present complex problems. Progress requires a great deal of study in propellant chemistry and in the organization of components of heterogeneous propellants.

It should be remarked that densities of high-energy liquid propellants are usually less than those of the solid propellants commonly used today. Because of their high volumetric specific impulse, exceeding 400 sec, current solid propellants are likely to retain their advantages in a number of applications for some time to come.

(b) Kinetic qualities

The main parameter characterizing the kinetic quality of a propellant is its burning rate. For different applications, it is necessary to have propellants with a wide range of burning velocities from which to choose. High burning velocities are generally desirable for booster-type missions or for systems requiring a high starting acceleration, while much lower burning velocities are required for upper stages and for sustainers.

At the present time, catalysts are available to control the burning velocity, but the mechanism of their action is still poorly understood and the range of the regression rates that can be achieved is too narrow in certain cases. One can also use physical means in order to vary the burning velocity, such as modifying the local thermal conductivity by introducing into the grain metal wires or inserts of other shapes. At present, burning velocities from a few millimeters per second to a few centimeters per second are achievable. Studies are currently under way to obtain the highest possible burning velocities for high-acceleration, boost missions. A wide field of research is available concerning new catalysts and other techniques, for extending the current range of burning velocities.

Motor operation is related to the pressure dependence of the burning rate. Depending on the application, propellants with differing pressure exponents of the burning rate are desirable. A few means are available at present, to modify the pressure exponent but these means are more empirical than scientific and they require more thorough study.

There are also practical reasons for attempting to reduce the influence on the burning velocity of quantities, such as the propellant temperature and the gas velocity parallel to the burning surface.

The influence of the various parameters on the burning velocity is imposed *a priori* during the development of the propellant. It would be desirable to be able to influence the burning velocity during the combustion process, to control the exhaust gas mass flow rate. Few methods have been proposed and none have been demonstrated to be of very great practical utility. Weinberg suggested applying electrostatic fields to the propellant or to the flame zone. He showed experimentally that in certain configurations, the fields had an appreciable effect on the burning rate but positioning of the electrodes poses technological problems in practical applications. Summerfield suggested using acoustic fields generated by sirens. However, the weight of a siren required to produce an appreciable effect is quite large.

Among the kinetic qualities of a propellant are parameters related to ignition, extinction and unstable combustion regimes. The use of new energetic oxidizers, such as nitronium perchlorate or hydrazine diperchlorate, is likely to aggravate problems of extinction and combustion instability, as we shall discuss further in Section 4.

(c) Utilization Qualities

It is not possible to find a propellant which will fulfill completely all utilization requirements, namely: good mechanical properties, ease and safety of manufacture, good storability, low sensitivity to ambient temperature variations, low shock sensitivity, nontoxic reactants and combustion products, ease of handling, low cost

The development of high energy propellants has shown that it is difficult to obtain mechanical properties that are good in comparison with those of conventional propellants; a special effort must be made to improve the physical properties in the operational temperature range from -75°F to 160°F (-59°C to 71°C). Degradation of physical characteristics and performance in various ambient storage conditions is also a potential problem in the development of new propellants.

3. Fundamental Research on the Combustion of New Propellants

Contributions of combustion research to improved rocket performance are necessarily indirect. More direct is the influence of propellant performance considerations on changes in combustion research. The trend toward the development of higher energy propellants focuses increasingly greater attention on heterogeneous propellants. Consequently, we may expect an increased percentage of the combustion research effort to be devoted to heterogeneous propellants.

From one particular aspect of the viewpoint of basic research, this is an unfortunate occurrence. Homogeneous propellants were developed at a time when the experimental and theoretical techniques for analysis in aerothermochemistry were in their infancy. Although much is known about the burning mechanisms of homogeneous propellants, a great deal remains to be discovered. Many tools that are needed to make these advances are now at hand. However, it is unlikely that these tools will ever be applied to homogeneous propellants because of their decreasing practical importance.

On the other hand, in areas related to heterogeneous propellant combustion, the future for combustion research is brighter. Let us first discuss research on the decomposition of oxidizing constituents of composite propellants. We have indicated that new oxidizers are continually emerging and that they are generally capable of deflagrating by themselves at sufficiently high pressures. We may certainly expect that pyrolysis rates and deflagration rates will be studied at least experimentally and perhaps by means of aerothermochemical theories for each new oxidizer as it begins to be used. Studies of homogeneous oxidizers may indeed partially compensate the basic researcher for the de-emphasis of homogeneous propellant studies; quite similar analytical techniques are applicable to both systems.

The decomposition and deflagration mechanisms of the early oxidizer ammonium nitrate are not understood as well today as are decomposition and deflagration mechanisms of today's oxidizer, ammonium perchlorate. The difference is due primarily to advancements in scientific techniques of study for example, the use of pressed samples and monocrystal samples. If the same effort that was devoted to ammonium perchlorate is applied to each new oxidizer that is developed, then we may expect our understanding of decomposition and deflagration mechanisms of future oxidizers to exceed that of ammonium perchlorate. An indication that at least some combustion research effort will be spent on new oxidizers, is provided by the observation that experimental studies have already been reported on the deflagration of hydrazine perchlorate and other new oxidizers and on porous plate pyrolysis of new oxidizers. These studies show that new oxidizers often tend to exhibit unique regimes of deflagration and decomposition e.g., gas-producing decomposition at a solid-liquid interface beneath a melted layer. Thus, new oxidizers present scientists with many new and interesting research problems.

However, we should perhaps express some reservations about whether the new oxidizers will be studied as thoroughly as ammonium perchlorate. For more than five years, ammonium perchlorate has been used almost universally as the chief oxidizer in composite propellants. Usually a new oxidizer will not be studied as thoroughly unless it develops comparable predominance and longevity. An additional reservation to the prediction of great progress arises from the observation that research on

pure ammonium perchlorate appears now to be decreasing, even though many unanswered questions and contradictions remain concerning its decomposition and deflagration processes and even though it continues to be the dominant practical oxidizer. In spite of these reservations, one may confidently predict research advances in studies of the decomposition and deflagration of new oxidizers.

One may also predict new experimental and theoretical studies of the combustion of new oxidizers in simplified, idealized geometries, designed to elucidate the fuel-oxidizer burning mechanism. These studies are likely to assume greater practical importance in the future for a number of reasons.

First of all, energetic oxidizers that have to be protected from the main fuel binder by means of encapsulation or related techniques are likely to burn in a very complex way in a propellant. To aid the understanding of this burning mechanism, it would be helpful to know how a pure oxidizer crystal decomposes in an inert atmosphere, how a protected oxidizer crystal decomposes in an inert atmosphere, how a pure oxidizer crystal decomposes in an atmosphere consisting of vapors of the protective material, how a pure oxidizer crystal burns in atmospheres of various fuel vapors, how a protected oxidizer crystal burns in fuel atmospheres and how a pure oxidizer crystal burns in atmospheres consisting of mixtures of fuels with gasification products of the protection material. Numerous other model studies pertinent to protected oxidizers can be suggested. These studies all bear on such practical questions as flammability limits of propellants employing protected oxidizers, regularity of the combustion of these propellants, pressure dependence of the burning rate, combustion efficiencies, etc.

A second reason for the pertinence of model studies of oxidizer combustion is that with the development of large boosters, it becomes conceivable to increase appreciably the sizes of oxidizer particles in the propellant without paying any penalty in combustion efficiency. One can imagine composite propellant grains, with relatively small numbers of large oxidizer particles with dimensions perhaps of the order of a millimeter or a centimeter, which exhibit improved mechanical properties at over-all mixture ratios that yield optimum specific impulse. Burning mechanisms, erosive effects etc. for such grains would differ appreciably from those for the grains with which we are most familiar. Model experiments and theories for large oxidizer particles, which are relatively easy to carry out, should provide information that is related directly to the combustion and flammability of such grains.

Many other reasons can be cited for the possible increased future importance of model studies of oxidizer combustion. These examples underscore the importance of continued research on the combustion mechanisms of heterogeneous propellants themselves. There are many problems in this area even for ammonium perchlorate based propellants, particularly questions about flame distributions over the surface and burning mechanisms in the plateau domain of combustion and about the influences of some catalysts on the burning behavior. In the process of achieving safety in the formulation of new high-energy composite propellants, problems of unsustained flammability, residue formation, irregular combustion and erratic burning rates, may well arise. Fundamental research on the combustion mechanisms of heterogeneous propellants is needed in order to help to indicate where such difficulties might occur, what their causes would be and how to correct them.

The final area of combustion research that we wish to mention here is the topic of metal combustion. Metalized grains receive increasing use and the metals employed become more exotic as one attempts to improve specific impulse. Combustion efficiency which is basically related to metal flammability and to burning rates and agglomeration behavior of metal particles, is an important practical problem for metals in solid propellant grains, particularly for the smaller combustion chambers and at the lower chamber pressures. Techniques for achieving efficient metal

combustion may well arise from basic research on metal combustion mechanisms. Results of metal combustion research can bear on answers to such questions as whether lithium-beryllium mixtures can substantially improve the combustion efficiency of beryllium in propellants. It seems safe to predict that fundamental research on the combustion of metals will continue.

A prediction about the overall level of effort in fundamental research on solid propellant combustion may be worth making. There have been no large increases in the research effort in recent years and there are no clear signs of future increases. We estimate that the total expenditure on research will continue at its present level or perhaps decrease slightly. In view of the increased number of pertinent research topics that we foresee, it appears that the works of various researchers must tend to drift farther apart if they are to cover the entire field.

4. New Ideas on Unsteady Combustion

The research discussed in the preceding section referred primarily to steady-state combustion. Here we wish to consider briefly unsteady combustion, still remaining for the most part in the domain of fundamental research. Our remarks will first concern ignition - extinction phenomena and then combustion instability.

The current level of theoretical understanding of solid-propellant ignition processes is not high. One does not expect or desire to obtain accurate time histories of the detailed chemical and dynamical processes that accompany ignition in motors using real igniters but one does hope to be able to make estimates of ignition times of plane propellant surfaces exposed uniformly to different ignition stimuli, of quasi-steady rates of flame spread along a plane propellant surface and of rates of buildup of pressure inside motors during ignition. A great deal of basic information that is required for making such estimates is lacking. There are appreciable gaps in our current understanding of convective heat transfer from hot gases to a solid surface, heat transfer in two-phase boundary-layer flows, heat-transfer effects produced by impingement of hot condensed particles on surfaces and mechanisms of heat production, when hypergolically reactive liquids contact propellant surfaces. Research in these areas is needed for purposes of improving igniter design, so that rapid motor ignitions, without pressure overshoot and with predictable pressure-time histories, can be obtained by using relatively simple and lightweight igniters.

Today we do not understand the dynamics of motor extinction as well as we understand motor ignition processes. Very little fundamental research has been performed on problems related to motor extinction. Since efforts to obtain greater flexibility and control of solid propellant rockets are increasing, we may expect to see the inception of research programs on extinction phenomena *per se*. The ultimate objective is, of course, to obtain lighter and more versatile extinction devices.

A great deal of progress has been made on fundamental research into combustion instabilities of solid propellant rocket motors. Present-day empirical 'fixes' of combustion instability problems in solid propellant motors, can often be based on a partial understanding of the phenomenon. No such rational basis was available ten years ago. There seems to be a tendency to relax the level of research effort on solid rocket combustion instability, due to the conviction that practical methods for eliminating instabilities are now at hand. Although there are specific types of instabilities for which this conviction is not warranted, it appears to be rather well justified for acoustic instabilities in motors using conventional propellants, even though a thorough theoretical understanding of the mechanisms of acoustic amplification does not exist. However, we wish to offer a word of caution about the possible emergence of new acoustic instability problems as new high-energy propellants begin to be used. The acoustic admittances of grain surfaces formed from high-energy propellants, may exhibit enhanced tendencies toward acoustic amplification.

In the rest of this section, we wish to summarize particular types of nonacoustic combustion instabilities that may possibly become increasingly troublesome in the future.

In many applications of solid propellant rockets to space propulsion there are advantages in using small motors with low chamber pressures. Particularly for metalized propellants, this places the motor near its limit of efficient combustion. Oscillations of the gases in the chamber-nozzle system have been observed to occur under such conditions (L^* instability). These low-frequency instabilities detract appreciably from motor performance. The extent to which solid propellant rockets will be used in space, will depend partially on the degree of success that is achieved in solving this low-frequency, nonacoustic instability problem.

As solid propellant boosters have increased in size, instability problems have been encountered less often. There are some reasons to question whether this trend will continue. Current propellants, especially metalized propellants, are known to exhibit small-amplitude oscillations in definite low frequency ranges that are inherent in their combustion processes. These nonacoustic oscillations are of little consequence in current motors because their amplitudes are too low. However, as motors increase in size, the acoustic frequencies of their chambers are approaching these natural, nonacoustic frequencies of the propellant combustion processes. There is laboratory evidence that appreciable coupling between the acoustic and nonacoustic oscillations may occur in the vicinity of frequency coincidence. This complex phenomenon, for which no adequate theoretical understanding yet exists, may establish a barrier to the development of very large solid propellant boosters. If it does, then intensive research on combustion instability will have to be renewed.

There are many other specific problem areas of solid-propellant combustion instability. For example, acoustic instabilities may be troublesome in application where metalized propellants cannot be used for communications reasons or other reasons. Problems may also develop in connection with attempts to provide greater motor flexibility e.g. Helmholtz modes might occur in multiple-chamber motors. Because of these and other potential areas of difficulty, research on combustion instability in solid propellant motors will continue. However, we speculate that solid propellant systems will experience fewer instability problems than liquids.

5. Technological Development - Improvement of Flexibility and Thrust Control Capabilities

We have emphasized that one of the major inconveniences of solid propellant systems is its lack of flexibility. It can be predicted that methods of increasing flexibility will progress in the future. We now wish to describe in detail some potential avenues for advancement.

Let us first consider techniques for controlling the magnitude of the thrust vector. For a mission with a pre-established thrust program, the necessary control of the thrust-time history can be achieved through grain design; it is much more difficult to control the thrust during the flight. Several techniques are under development. One consists of pulsing the thrust by using a propellant made of parallel layers separated by a restrictor. Each layer has its own ignition system. The working principle of the engine is the following: The first layer is ignited and the combustion stops when the flame front reaches the restrictor. The igniter of the second layer destroys the thin restrictor film and reinitiates combustion of the propellant; the impulse is thus partitioned and impulse segments can be triggered at will. (Designs of this type are called wafer motors or pulse rockets). The geometry is easy to envisage for cylindrical cigarette-burning grains. The burning time of each a grain is long so that many pulses can be obtained. The amount of restrictor required for a given mission must be determined according to the mission; its

mass is proportional to the number of pulses. Pulse techniques are also applicable to radially burning grains which offer a larger burning area. Manufacturing such wafer-type grains is complex however, and the cost is certainly high.

Division of a grain into several elements which burn sequentially can be achieved in several ways. In addition to wafer propellants, one might consider assembling individual blocks into the complete grain, each block leaving a small cavity (honeycomb) in shape for example) after burning. The best element shape is the one which leads to a minimal restrictor mass.

Another technique for achieving thrust control consists in extinguishing and reigniting the motor several times by injecting a liquid into the chamber. This topic has been discussed in Chapter 8. It appears to be possible to extinguish a motor by injecting water and to reignite it by injecting ClF_3 . Two separate liquid feed systems are required, thereby introducing many technological complications and making the complexity of the system comparable to that of liquid propellant engines. The technique is currently attractive only when few extinctions and reignitions are required because the additional complexity of the system is then minimized. Research on the technique is in progress and technologically acceptable solutions may soon evolve. However, it remains to be demonstrated that the over-all weight of the liquid injection system is lower than that of the restrictors and igniters needed in a wafer-type propellant.

Liquid-injection thrust-control devices can be made both simpler and more flexible by using a single liquid, for instance an oxidizer such as ClF_3 , which is hypergolic with the solid propellant. The thrust can be modulated by modifying the liquid injection rate, as is done in hybrid motors. On-off capabilities can be achieved by using a solid propellant that is fuel rich and burns only when oxidizer is injected. By suddenly interrupting liquid injection, even propellants capable of self-sustained combustions can be extinguished, because of the resulting abrupt pressure drop in the chamber. Reignition can always be achieved by a new injection of a hypergolic liquid. Techniques of this type are expected to produce an increase in performance and an improvement in flexibility of solid propellant motors without requiring highly complex devices. The methods entail the development of special propellants which have a suitable pressure sensitivity for their burning rate, since large variations in the over-all mixture ratio of the propellants during thrust modulation must be avoided, in order to maintain sufficiently high performance. The fuel-rich grains which are best suited to liquid-injection thrust control also exhibit improved mechanical properties as a subsidiary consequence of their modified mixture ratio.

Another way to modulate thrust is to use two solid propellant motors connected by a valve. The upstream motor operates with a fuel-rich propellant, while the downstream motor uses a fuel-lean propellant. A secondary combustion process then takes place in the downstream motor between the fuel-rich exhaust gases from the upstream motor and the excess oxidizer from the downstream propellant. The exhaust nozzle is located at the aft end of the downstream motor and the igniter is placed in the head end of the upstream motor. Thrust modulation is achieved by controlling the valve, which modifies the rate of gas flow into the downstream motor. Opening the valve decreases the pressure in the upstream chamber. The mass flow rate through the valve is proportional to the pressure to the n -th power, where n is the exponent of the burning velocity law. Thus, to achieve a wide range of flow-rate variation, one must use propellants having a highly pressure-sensitive burning velocity in the upstream motor. On the other hand, the burning velocity of the propellant in the downstream chamber must be made sensitive primarily to the gas velocity in the central port as in a hybrid system, in order to maintain a constant over-all mixture ratio in the upstream and downstream chambers, during thrust modulation. The grain geometries will differ in these chambers. There are development problems associated with this system, particularly in rela-

tion to constructing a valve that is resistant to high temperature gases.

A thrust modulation technique which has undergone a few tests consists of employing a nozzle with a variable throat area. In a first approximation, the motor thrust is proportional to the nozzle throat area to the power $1/(n-1)$, where n is the pressure exponent of the burning velocity law. The thrust can be varied over a wide range, provided that a propellant with a pressure exponent close to unity is used. In practice, one might consider a neutral propellant grain with an annular port, containing a central plug which allows one to change the throat geometry by moving the plug axially. With a pressure exponent of 0.75, for example, if the nozzle throat area is reduced by a factor of 2, then the thrust increases by a factor of 8, but the chamber pressure increases by a factor of 16. This large pressure variation is an inconvenience of the technique, since it necessitates using propellants and structures that are adapted to a wide range of pressures. The structural weight penalty is appreciable. Heat protection of the central plug also presents design difficulties. Heat resistance problems can be alleviated by developing new grain and motor geometries, such as toroidal motors. Variable-area nozzles can also be used to produce motor extinction, since a rapid pressure rarefaction propagates through the motor, if the nozzle throat area is suddenly increased by quickly displacing the central plug.

It is thus apparent that several means are available for in-flight control of the magnitude of the motor thrust vector. Useful techniques must produce minimum amounts of additional complexity and weight in the system.

Let us now turn to techniques for controlling the orientation of the thrust vector. In liquid propellant systems, this 'thrust vector control' is achieved by gimbaling the entire combustion chamber. As it is not possible to apply this technique to solid propellant motors, multiple nozzles which can be moved so that the thrust axis is changed have been employed. Fluid-injection approaches to thrust vector control have also been used. These techniques have been described in Chapter 2. Injection of hot chamber gases through a high-temperature valve is perhaps the most interesting long-term approach. We might remark that for plug nozzles and expansion-deflection nozzles, the flow pattern at the chamber exit and in the nozzle should facilitate control of the thrust vector orientation.

These and many other examples that can be cited, demonstrate that it should be possible to increase the flexibility of solid propellant motors without approaching the complexity of liquid propellant systems. A number of variable-thrust missions previously reserved for liquids, will therefore be able to be performed by solids, as development of the thrust-control techniques progresses.

Technological advances that can lead to the improvement of solid propellant motors depend on the development of lightweight structures, e.g. rocket cases, restrictor layers, heat shields and nozzles. Rocket case technology has recently experienced great advances, due to the development of new materials and new fabrication techniques such as glass-filament winding. Further advances can be made by improving the bonding between case, restrictors, heat shields and the propellant grain. These improvements are essential in developing a variable-thrust motor or a motor with stop-start capabilities since the danger of cracks increases under variable operating conditions, especially for motors that use glass-reinforced plastic cases with large dilatations on pressurization. Although the problem of thermal protection has been solved for large motors in which the thickness of the thermal insulation is not critical, it remains an important area of investigation for smaller motors, for which thermal protector weights are not negligible fractions of the total structural weight.

With highly energetic propellants, new technological problems will arise because of high flame temperatures. Ablative materials will be used in nozzles. Although

there has been some progress recently in ablator development, there remain many scientific and technological problems. New nozzle geometrics such as plug nozzles may be used in large motors. Annular-shaped grains are well adapted to plug nozzles. These nozzles offer the possibility of achieving better performance and smaller mass. However, they present difficult technological problems with respect to heat transfer at the nozzle throat and the use of ablative materials, since the ablation effect is more pronounced with plug nozzles than with conventional ones.

Air-Augmented Solid Propellant Rockets

For applications in the earth's atmosphere, it is possible to increase the performance of solid propellant rockets by burning the excess fuel contained in the exhaust gases with ambient air. Some 15 years ago experiments showed that it was possible to increase the thrust by using ambient air as an auxiliary oxidizer. This technique seems to have regained some interest and experimental work is under way to determine the performance gain, produced by such a rocket-ramjet combination. Solid propellant systems are particularly well adapted to air augmentation, since they generally operate under fuel-rich conditions and may contain metallic additives. The propellant composition should however be chosen to yield maximum performance under augmentation conditions: Boron derivative fuels or even boron itself used instead of aluminum in the propellant, appear to constitute high-performance additives. Fluorine containing binders also produce good performance under augmentation conditions.

The few ideas proposed in Section 5 show that there are still many technological areas for advancement of solid propellant rockets, always directed toward simpler methods for achieving flexibility, a high reliability and a low cost.

6. New Uses for Solid Propellant Rockets

The solid propellant rocket motor's basic attribute of simplicity remains unchallenged by other modes of propulsion. The consequent inherent advantages of reliability, storability and readiness, coupled with the basic property of high volumetric specific impulse, would seem to insure the continued dominance of solid propellant rockets in many of the fields in which they now excel. Particular examples of such fields are various tactical military applications, such as air-to-air, air-to-ground and short-range, ground-to-ground missiles. Although liquid or hybrid systems may contest certain surface-to-air missions, it will be difficult to increase liquid or hybrid burning rates to a point where they can challenge solids in anti-missile applications. The recent solid propellant booster successes point also to their continued importance in long-range military missiles.

Large solid propellant boosters possess certain long-term advantages for satellite launching and for other space-launch missions. In Chapter 1, we have emphasized the low development costs of large solid propellant boosters. Future improvements in techniques for grain manufacturing and casting may lessen the propellant costs to a point at which high specific-impulse liquid propellant boosters will find it very difficult to compete with solids economically. Provided that combustion instability problems do not arise in very large solid propellant motors, one can envisage establishing a series of solid propellant boosters of different sizes as standard first-stage booster motors. The required boost energy would be calculated for each space-launch mission and a booster of an appropriate size would be selected. On-site fabrication of the larger boosters, using standard mobile equipment and standard motor segments, would constitute part of this program. The logistics problems would be considerably simpler than for re-usable boosters and cost reductions, associated with the use of increased numbers of boosters, could well make this the most economical approach to large-scale space exploration.

In upper stage and space propulsion applications, liquid propellant systems with improved reliability and storability may take over some tasks that are currently assigned to solids, particularly those tasks which do not specifically require impulsive manoeuvres with high thrust for short duration. Solid rocket manufacturers must therefore attempt to win missions that would traditionally be thought to lie in the domain of liquid propulsion. Research on high-energy solid propellants and on improved flexibility (thrust vector control, start-stop capabilities and thrust modulation) of solid propellant rocket motors is ultimately directed toward this type of objective. The progress of solid propellants in these new areas of application will depend largely on the degree of success that the research efforts achieve.

Evaluations of over-all costs of development work and of mission accomplishment show that any increase in performance produces a decrease in over-all weight at the expense of an increase in development cost. It is usual to say that an increase of 5% in the performance increases the development cost by 50%. For this reason, systems with higher initial masses are often preferred, at a slight increase in the cost of mission accomplishment, to better performance systems. Although their specific impulse is lower than that of other systems and therefore their initial masses are higher, nevertheless solid propellant rockets appear to be highly competitive with other systems when the total cost of development and mission accomplishment is considered. Such cost considerations permit prognostication of new applications for solid propellant motors and planning new missions, especially in space, thereby widening the scope of solid propellant rocketry.

Addendum

Unit Conversion Tables

Table 1 Conversion Factors for Units of Length

Multiply by appropriate entry to → obtain ↓	cm	m	in.	ft.	yd.
1 cm	1	0.01	0.3937	0.032 808 333	0.010 936 111
1 m	100	1	39.37	3.280 833 3	1.093 611 1
1 in.	2.540 005 1	0.025 400 051	1	0.083 333 333	0.027 777 778
1 ft.	30.480 061	0.304 800 61	12	1	0.333 333 333
1 yd.	91.440 183	0.914 401 83	36	3	1

Table 2 Conversion Factors for Units of Area

Multiply by appropriate entry to → obtain ↓	cm ²	m ²	sq. in.	sq. ft.	sq. yd.
1 cm ²	1	10 ⁻⁴	0.154 999 69	1.076 386 7 × 10 ⁻³	1.195 985 3 × 10 ⁻³
1 m ²	10 ⁴	1	1,549.9969	10.763 867	1.195 985 3
1 sq. in.	6.451 625 8	6.451 625 8 × 10 ⁻⁴	1	6.944 444 4 × 10 ⁻³	7.716 049 4 × 10 ⁻⁴
1 sq. ft.	929.034 12	0.092 903 412	144	1	0.111 111 11
1 sq. yd.	8,361.3070	0.836 130 70	1296	9	1

Table 3 Conversion Factors for Units of Volume

Multiply by appropriate entry to → obtain ↓	ml	liter	gal.
1 ml	1	0.001	$2.641\,779 \times 10^{-4}$
1 liter	1,000	1	0.264 177 9
1 gal.	3,785 329	3.785 329	1
1 cm ³	0.999 972 0	$0.999\,972\,0 \times 10^{-3}$	$2.641\,704\,7 \times 10^{-4}$
1 cu. in.	16,386 70	$1.638\,670 \times 10^{-2}$	$4.329\,004\,3 \times 10^{-3}$
1 cu. ft.	28,316 22	28.316 22	7.480 519 5
	cm ³	cu. in.	cu. ft.
1 ml	1.000 028	0.061 025 09	$3.531\,544 \times 10^{-5}$
1 liter	1,000.028	61.025 09	0.035 315 44
1 gal.	3,785 434 5	231	0.133 680 56
1 cm ³	1	0.061 023 378	$3.531\,445\,5 \times 10^{-5}$
1 cu. in.	16.387 162	1	$5.787\,037\,0 \times 10^{-4}$
1 cu. ft.	28,317.017	1,728	1

Table 4 Conversion Factors for Units of Pressure

Multiply by appropriate entry to → obtain ↓	dyne/cm ²	bar.	atm	kg(wt.)/cm ²
1 dyne/cm ²	1	10 ⁻⁶	0.986 923 3 $\times 10^{-6}$	1.019 716 2 $\times 10^{-6}$
1 bar.	10 ⁶	1	0.986 923 3	1.019 716 2
1 atm	1,013,250	1.013 250	1	1.033 227 5
1 kg(wt.)/cm ²	980,665	0.980 665	0.967 841 1	1
1 mm Hg	1,333.223 7	1.333 223 7 $\times 10^{-3}$	1.315 789 5 $\times 10^{-3}$	1.359 509 8 $\times 10^{-3}$
1 in. Hg	33,863.95	0.033 863 95	0.033 421 12	0.034 531 62
1 lb. (wt.)/sq. in.	68,947.31	0.068 947 31	0.068 045 70	0.070 306 69
	mm Hg	in. Hg	lb. (wt.)/sq. in.	
1 dyne/cm ²	7.500 617 $\times 10^{-4}$	2.952 993 $\times 10^{-5}$	1.450 383 0 $\times 10^{-5}$	
1 bar.	750.061 7	29.529 93	14.503 830	
1 atm	760	29.921 20	14.696 006	
1 kg(wt.)/cm ²	735.559 2	28.958 97	14.223 398	
1 mm Hg	1	0.039 37	0.019 336 850	
1 in. Hg	25.400 05	1	0.491 157 0	
1 lb. (wt.)/sq. in.	51.714 73	2.036 009	1	

Table 5 Conversion Factors for Units of Mass and Weight

Multiply by appropriate entry to obtain ↓	g	kg	lb.	metric ton	ton
1 g	1	10^{-3}	$2.204\,622\,3 \times 10^{-3}$	10^{-6}	$1.102\,311\,2 \times 10^{-6}$
1 kg	10^3	1	2.204 622 3	10^{-3}	$1.102\,311\,2 \times 10^{-3}$
1 lb.	453.592 43	0.453 592 43	1	$4.535\,924\,3 \times 10^{-4}$	0.0005
1 metric ton	10^6	10^3	2,204.622 3	1	1.102 311 2
1 ton	907,184.86	907,184 86	2000	0.907 184 86	1

Table 6 Conversion Factors for Units of Density

Multiply by appropriate entry to obtain ↓	g/cm ³	g/ml	lb./cu. in.	lb./cu. ft.	lb./gal.
1 g/cm ³	1	1.000 028	0.036 127 504	62.428 327	8.345 453 5
1 g/ml	0.999 972 0	1	0.036 126 49	62.426 58	8.345 220
1 lb./cu. in.	27.679 742	27.680 52	1	1,728	231
1 lb./cu. ft.	0.016 018 369	0.016 018 82	$5.787\,037\,0 \times 10^{-4}$	1	0.133 680 56
1 lb./gal.	0.119 825 72	0.119 829 1	$4.329\,004\,3 \times 10^{-3}$	7.480 519 5	1

Table 7 Conversion Factors for Units of Specific Energy

Multiply by appropriate entry to obtain ↓	abs. joule/g	int. joule/g	cal/g	I. T. cal/g	BTU/lb.
1 abs. joule/g	1	0.999 835	0.239 006	0.238 849	0.429 929
1 int. joule/g	1.000 165	1	0.239 045	0.238 889	0.430 000
1 cal/g	4.184 0	4.183 3	1	0.999 346	1.798 823
1 I. T. cal/g	4.186 74	4.186 05	1.000 654	1	1.8
1 BTU/lb.	2.325 97	2.325 58	0.555 919	0.555 556	1

Table 8 Conversion Factors for Units of Energy

Multiply by appropriate entry to obtain ↓	→ g mass (energy equiv.)	abs. joule	int. joule	cal	I. T. cal
1 g mass (energy equiv.)	1	8.986 56 $\times 10^{13}$	8.985 08 $\times 10^{13}$	2.147 84 $\times 10^{13}$	2.146 44 $\times 10^{13}$
1 abs. joule	1.112 772 $\times 10^{-14}$	1	0.999 835	0.239 006	0.238 849
1 int. joule	1.112 956 $\times 10^{-14}$	1.000 165	1	0.239 045	0.238 889
1 cal	4.655 84 $\times 10^{-14}$	4.184 0	4.183 3	1	0.999 346
1 I. T. cal	4.658 88 $\times 10^{-14}$	4.186 74	4.186 05	1.000 654	1
1 BTU	1.174 019 $\times 10^{-11}$	1,055,040	1,054.866	252.161	251.996
1 int. kWh	4.006 64 $\times 10^{-8}$	3,600,594	3,600,000	860,563	860,000
1 ft.-lb. (wt.)	1.508 720 $\times 10^{-14}$	1.355 821	1.355 597	0.324 049	0.323 837
1 cu. ft.-lb. (wt.) /sq. in.	2.172 56 $\times 10^{-12}$	195.238 2	195.206 0	46.663 0	46.632 5
1 liter-atm	1.127 548 $\times 10^{-12}$	101.327 8	101.311 1	24.217 9	24.202 1
1 horsepower-h	2.987 27 $\times 10^{-8}$	2,684,525	2,684,082	641,617	641,197

Table 8 Conversion Factors for Units of Energy

BTU	int. kWh	ft.-lb. (wt.)	cu. ft.- lb. (wt.)/sq. in.	liter-atm	horsepower -h
8,517.75 $\times 10^{10}$	2,495.86 $\times 10^7$	6,629.14 $\times 10^{13}$	4,602.37 $\times 10^{11}$	6,666.60 $\times 10^{11}$	3,347.54 $\times 10^7$
0.947 831 $\times 10^{-3}$	2.777 32 $\times 10^{-7}$	0.737 561	5.121 995 $\times 10^{-3}$	9.868 96 $\times 10^{-3}$	3.725 05 $\times 10^{-7}$
0.947 988 $\times 10^{-3}$	2.777 778 $\times 10^{-7}$	0.737 682	5.122 79 $\times 10^{-3}$	9.870 58 $\times 10^{-3}$	3.725 67 $\times 10^{-7}$
3.965 73 $\times 10^{-3}$	1.162 030 $\times 10^{-6}$	3.085 95	2.143 02 $\times 10^{-2}$	4.129 17 $\times 10^{-2}$	1.558 562 $\times 10^{-6}$
3.968 32 $\times 10^{-3}$	1.162 791 $\times 10^{-6}$	3.087 97	2.144 43 $\times 10^{-2}$	4.131 87 $\times 10^{-2}$	1.559 582 $\times 10^{-6}$
1	2.930 18 $\times 10^{-4}$	778.156	5.403 86	10.412 15	3.930 08 $\times 10^{-4}$
3,412.76	1	2,655,656	18,442.06	35,534.1	1.341 241
1.285 089 $\times 10^{-3}$	3.766 55 $\times 10^{-7}$	1	6.944 44 $\times 10^{-3}$	1.338 054 $\times 10^{-2}$	5.050 51 $\times 10^{-7}$
0.185 052 9	5.422 39 $\times 10^{-5}$	144	1	1.926 797	7.272 73 $\times 10^{-5}$
0.096 041 7	2.814 20 $\times 10^{-5}$	74.735 4	5.189 96	1	3.774 52 $\times 10^{-5}$
2,544.48	0.745 578	198,000	13,750	26,493.5	1

Names Index

- Abbett, M. 101
 Achenbach, J.D. 713, 749
 Adams, G.K. 280, 300, 329, 330
 Adamson, T.C. Jr. 104
 Adclberg, M. 105
 Akiba, R. 672
 Aldrich, R. 746
 Alexander, R.V. 36
 Alfrey, T. 711, 746
 Allan, D.S. 553
 Allen, H. 551
 Altman, D. 101, 102, 183
 Amick, J.L. 104
 Andersen, W.H. 269, 276, 279, 328, 390, 391, 392
 Anderson, R. 509, 551, 552
 Angelus, T.A. 601, 603, 672
 Appleby, E.J. 707, 747
 Arden, E.A. 330, 600
 Argyris, J.H. 748
 Aroeste, H. 101
 Arribat, J.G. 251
 Attali, C. 35
 Aungust, W.P. 331, 602

 Badham, H. 600
 Baer, A.D. 464, 468, 471, 478, 491, 507, 550, 551, 602, 603, 672
 Bahn, G.S. 183
 Bailey, W.S. 102
 Balaceaner, J.C. 390
 Baltrukonis, J.H. 713, 749
 Bankston, L.T. 104
 Barden, R.G. 601
 Barnes, G.G. 104
 Barrère, M. 35, 100, 183, 250, 251, 329, 331, 391, 392, 436, 455, 456, 644, 654, 671
 Barrère, S. 183, 184
 Barry, R.E. 553
 Barsh, M.K. 391
 Bartley, C.E. 250
 Bartz, D.R. 103
 Bastress, E.K. 319, 330, 553
 Bauer, A.B. 103
 Baum, E. 601, 648, 672
 Beckstead, M.W. 603, 672
 Berger, J. 455

 Bernard, J.J. 643, 654, 671
 Berwin, T.W. 601
 Betin, P. 36, 250, 455
 Beyer, R.B. 551
 Bierlein, J.A. 104
 Billheimer, J.S. 434, 436, 455
 Bills, K. 391, 392
 Biot, M.A. 701, 745, 747
 Bircumshaw, L.L. 391
 Bird, J.F. 671, 672
 Bird, R.B. 389
 Bischoff, J. 748
 Blackman, A.W. 184
 Blackman, V. 670
 Bland, D.R. 746
 Blatz, P.J. 328, 426, 456, 745, 746
 Blodgett, K.B. 102
 Boisson, J. 36, 183, 250, 435, 455
 Bolt, R.H. 602
 Boys, S.F. 600
 Bradley, H.H. 250, 551, 552
 Brainerd, J.J. 101
 Brandon, R.L. 251
 Braun, J.V. 236, 251
 Bray, K.N.C. 100, 101
 Briar, H.D. 749
 Briar, H.P. 251
 Brinkley, S.R. 128, 144, 146, 147, 183
 Broadwell, J.E. 104
 Brothers, J.E. 553
 Brown, B. 103
 Brown, R.S. 551, 552
 Brown, T.P. 553
 Brownlee, W.G. 601
 Bruer, S. 708, 748
 Brulard, J. 330, 468, 551
 Bryce Wilhite, V.H. 250
 Brzustowski, T.A. 330, 384, 387, 393
 Buchanan, J. 28, 36
 Bueche, F. 747
 Burger, J. 293, 296, 318, 329

 Caldin, E.F. 103
 Campbell, G.T. 184
 Cantrell, R.H. 269, 279, 328, 377, 392, 603, 670, 671, 672
 Carhart, R.R. 670

- Carlson, D.J. 81, 103, 104, 105
 Carlson, L.W. 520, 553
 Carrier, G.F. 671, 672
 Carter, J.M. 101, 102, 183
 Carton, D.S. 35
 Catsiff, E. 748
 Caveny, L.M. 251
 Chaiken, R.F. 276, 328, 377, 390, 391, 392
 Chapkis, R.L. 104
 Chapman, A.J. 552
 Cheng, S.I. 643, 644, 670, 671, 673
 Cheung, H. 103
 Chidlovsky, A.A. 329
 Chu, B.T. 673
 Ciepluch, C. 531, 553
 Clarke, J.F. 670
 Clemmow, D.M. 601, 672
 Cline, G.B. Jr. 392
 Coates, R.L. 269, 328, 391, 553, 602, 603
 Cohen, N.S. 103
 Cole, E.H. 100
 Cole, R.B. 330
 Coleman, B.D. 707, 747
 Colucci, S.E. 103
 Congreve, W. 8
 Corneliussen, A.H. 746
 Courtney, W.G. 102
 Cowan, P.L. 550
 Crampel, B. 183
 Crawford, B.L. Jr. 250, 347, 349, 366, 390, 601, 672
 Crocco, L. 617, 643, 670, 671, 672
 Crump, J.E. 602
 Culick, F.E.C. 103, 670
 Cummings, G.A. McD. 296, 329, 330
 Curtiss, C.F. 100, 389

 Daniels, F. 250, 280, 390
 Dantzig, G.B. 183
 D'Atorre, L. 104
 Davis, A. 331
 Davis, D. 102
 Day, E.E. 553
 DeGroat, J. 101
 Dehority, G.L. 250, 551, 670
 Dekker, A.O. 268, 390, 391
 Delsasso, L.P. 602, 671
 Denison, M.R. 601, 648, 672
 DeSoto, S. 552
 Deters, O.J. 671
 Dickenson, W. 102
 Dickinson, L.A. 430, 436, 455, 601, 603
 Diedrichsen, J. 603
 Dishon, M. 601, 672
 Dobbins, R.A. 602, 671
 Doljanski, J.M. 35
 Dong, R. 707, 747
 Dorléac, B. 250
 Dowdy, M.W. 105
 Draper, C.S. 601
 Dubrow, B. 331, 553
 Ducarme, J. 184

 Eastman, D.W. 104
 Ebeling, R.W. 552
 Eisel, J.L. 601, 602
 Emanuel, G. 101
 Engler, J.F. 602
 Epstein, P.S. 670
 Evans, M.W. 551
 Eyring, H. 390

 Favin, S. 101
 Feick, G. 391
 Fenech, E.J. 434, 436, 455
 Ferry, J.D. 745, 746, 748
 Findley, W.N. 748
 Fishman, N. 464, 471, 550, 551
 Fitzgerald, J.E. 704, 745, 746
 Flandro, G.A. 603
 Flemming, R.O. Jr. 551
 Foley, W.M. 251
 Foner, S.N. 601
 Fong, L.Y. 552
 Foster, C.R. 104
 Fournay, M.E. 748
 Fournier, C.A. 36
 Fox, P.A. 673
 Fraeijs de Veubeke, B. 35, 100, 183, 250
 Frechét, M.M. 747
 Friedman, H.A. 552
 Friedman, R. 282, 329, 330, 391
 Frocht, M.M. 749
 Fuchs, N.A. 103
 Fulmer, R.D. 81, 105
 Fung, Y.C. 747

 Galwey, A.K. 391
 Gazis, D.C. 671
 Geckler, R.D. 35, 250, 390, 435, 436, 455, 600
 Gibby, H. 553
 Gilbert, M. 102
 Ginell, R. 347, 349, 366, 390
 Glassman, I. 330, 384, 387, 393
 Glasstone, S. 390
 Glauz, R.D. 102
 Goddard, 8
 Golub, G. 250
 Gordon, D.A. 384, 392
 Gordon, L.J. 102, 184
 Gordon, S. 183
 Gorny, L.S. 251

- Grad, H. 671
 Grant, E.H. Jr. 551
 Grassie, N. 391
 Gravalos, F.G. 101
 Green, A.E. 747
 Green, C.J. 104
 Green, L. 104, 328, 390, 426, 436, 454, 456, 560, 600, 603, 644, 654, 671
 Greene, S.A. 102
 Grey, J. 670
 Griffin, D.N. 184
 Griffith, A.A. 736, 749
 Grigsby, C.E. 104
 Gross, B. 746
 Guinet, M. 269, 276, 279, 328, 436, 455
 Gurtin, M.E. 708, 746
 Guth, E.D. 331, 553

 Haar, L. 671
 Hall, A.R. 296, 330
 Hall, K.P. 250, 330, 392
 Hall, N.A. 100
 Hale, W. 8
 Hamming, R.W. 746
 Hansel, J.M. 276, 328
 Hardt, A.P. 244, 251
 Harshbarger, F. 104
 Hart, R.W. 603, 645, 646, 670, 671, 672
 Hausmann, G.F. 104
 Hays, P.B. 104
 Heath, G.A. 267, 328
 Heims, S.P. 100
 Hermance, C.E. 486, 551, 552
 Heron, R. 410, 455
 Heute, T.F. 602
 Hicks, B.L. 506, 552
 Hightower, J.D. 551
 Hildebrand, F.B. 749
 Hinshelwood, C.N. 390
 Hinze, J.O. 103
 Hirschfelder, J.O. 100, 389
 Hirst, R. 328
 Hoffman, J.D. 105
 Hogland, R.F. 102
 Hopkins, I.L. 746
 Horton, M.D. 601, 602, 603
 Hsia, H. T-S. 105
 Huang, N.C. 707, 747, 748, 749
 Hudson, R.L. 601
 Huebner, A.L. 603
 Huff, V.N. 138, 139, 183
 Huffington, J.D. 600, 601, 672
 Huggett, C. 35, 250, 390, 601, 672
 Hurden, D. 55

 Inami, J.H. 601, 602
 Irvin, O.R. 280, 329

 Jackson, F. 430, 455, 603
 Jacob, M. 103
 Jacobs, P.W.M. 279, 331, 391
 Jaroudi, R. 548, 553
 Jaubert, J. 183
 Jaumotte, A. 35, 100, 183, 250, 456
 Jellinek, H.H.G. 391
 Johnson, S.M. 183
 Johnson, W.E. 349, 354, 363, 366, 372, 390
 Jonath, A.D. 251
 Jube, G. 35

 Kallis, J.M. 105
 Kandratiev, V.N. 390
 Karamcheti, K. 105
 Kaye, J. 100
 Keenan, J.H. 100
 Keller, J.A. 551
 Kelsey, S. 749
 Kennard, E.H. 552
 Kiczek, C.R. 293, 329
 Klager, K. 250
 Kliegel, J.R. 102
 Kling, R. 330, 468, 551
 Koelle, H.H. 36, 184
 Kreidler, J.W. 425, 455
 Krieger, F.J. 100
 Kubby, W.C. 603
 Kurov, V.D. 35
 Kuehl, D.K. 184, 393

 Laidler, K.J. 390
 Lake, A. 402, 435, 455
 Lam, S.H. 100
 Lamb, H. 630, 670
 Lambert, R.F. 670
 Lampens, G. 183
 Lancaster, R.W. 551
 Landel, R.F. 740, 748, 749
 Landsbaum, E.M. 601, 603
 Langumuir, I. 102
 Larue, P. 184, 250, 251, 436, 455, 456
 Laurona, J. 250
 Lawrence, W.R. 183
 Leaderman, H. 746, 747
 Lee, E.H. 701, 707, 745, 746, 747, 748, 749
 Lee, J.F. 100, 184
 Lee, L.P. 104
 Lee, S.Y. 328, 329
 Le Grives, E. 184
 Lemaitre, P. 183
 Lenard, M. 101
 Lenoir, J.M. 435, 440, 444, 456
 Levinsky, E.S. 101
 Levy, J.B. 119, 329, 391
 Lewis, C.H. Jr. 104

- Li, W.H. 100
 Li, Y.T. 601
 Lieberherr, 269, 279
 Lifshitz, J.M. 748
 Lighthill, M.J. 671, 672
 Lindblad, N.R. 103
 Lindsey, G.H. 748
 Linn, C.C. 673
 Liu, F.F. 601
 Lorenc, S.A. 105
 Love, E.S. 104
 Lovine, R.L. 552, 553
 Luft, N.W. 391
 Lype, E.F. 102

 McAdams, W.H. 103, 552
 McAlevy, R.F. 276, 293, 328, 329, 468, 478, 550, 551, 552
 McArty, K.P. 103
 McBrady, J.J. 601, 672
 McCarty, K.P. 330
 McClure, F.T. 603, 645, 646, 670, 671, 672
 McCulley, L. 551
 McCullough, F.Jr. 104
 McDonald, A.J. 548, 553
 Macek, A. 330
 McGie, M.R. 602
 McKenney, J.D. 104
 Magee, R.S. 552
 Mager, A. 104
 Majerus, J.N. 251, 734, 749
 Maman, A. 468, 551
 Marble, F.E. 102, 103, 601
 Marklund, T. 402, 435, 436, 443, 455
 Marks, L.S. 100
 Markstein, G.H. 384, 386, 393
 Marvin, R.S. 746
 Marxman, G.A. 443, 456
 Maslen, S.H. 643, 671
 Mathes, H.B. 601
 Maxwell, W.R. 35, 102
 Mayer, J.E. 184
 Mayer, M.G. 184
 Mellette, R.V. 750
 Merrington, L.E. 331
 Miller, E. 456
 Miloway, W.T. 740, 749
 Mills, M.M. 250
 Miner, M.A. 740, 743
 Mishuck, E. 391, 392
 Mitchell, R.C. 552
 Moe, G. 391, 392
 Monks, R.E. 455
 Monti, R. 670
 Moore, F.K. 643, 671
 Morell, V.E. 183
 Moretti, G. 101

 Morgenthaler, J.H. 102
 Morland, L.W. 701, 747
 Moutet, A. 322, 455
 Murphy, J.M. 455, 456

 Nachbar, W. 269, 328, 349, 354, 363, 366, 372, 389, 390, 392, 602, 654, 671
 Nadaud, L. 184, 328, 329, 331, 392, 406
 Nall, B.H. 601
 Napoly, C. 183
 Newman, B.M. 330
 Newton, J.F.Jr. 104, 105
 Nicholls, J.A. 104
 Nickerson, G.R. 102
 Nilson, E.N. 102
 Ninomiya, K. 746
 Noll, W. 707, 747
 Nugent, R.G. 391

 Oberg, C.L. 603
 Oberth, 8
 Odgers, A.L. 455
 Ohlemiller, T.J. 330
 Olson, W.T. 100
 Onaran, K. 748
 Onat, E.T. 708, 748
 Osborn, J.R. 455, 456

 Papoulis, A. 712, 749
 Parker, K.H. 552
 Parmerter, R.R. 748
 Parr, C.H. 748
 Parr, R.G. 347, 349, 366, 390
 Paul, B.E. 552, 553
 Pearson, G.S. 329
 Pelterie, E. 8
 Penner, S.S. 100, 101, 183, 184, 280, 328, 389, 390, 392, 600, 671
 Peskin, R.L. 103
 Peters, C.F. 105
 Petersen, E.E. 329
 Pfaff, S.P. 331, 602
 Phillips, B.R. 251
 Phillips, T.R. 391
 Pinns, M.L. 551
 Pipkin, A.C. 706, 707, 747
 Poggi, J.C. 250
 Polzien, R.F. 553
 Pontvianne, 251
 Posel, K. 601
 Povinelli, L.A. 103, 330
 Powling, J. 300, 302, 316, 318, 327, 330, 600
 Prache, P. 455
 Price, C.F. 553

- Price, E.W. 250, 471, 475, 551, 574,
600, 601, 602, 670
- Quentin, D. 183
- Rabinovitch, B. 393
- Radok, J.R.M. 711, 746
- Radtke, L.P. 104
- Rannie, W.D. 102
- Ranz, W. 102
- Rao, G.V.R. 88, 103, 104
- Rayleigh, (Lord), 670
- Rice, D.W. 601, 602
- Rice, O.K. 374, 349, 366, 390
- Rivin, M.A. 35
- Rivlin, R.S. 747
- Robillard, G. 435, 440, 444, 456
- Robins, A.B. 330
- Rodean, H.C. 553
- Rogers, K.H. 251
- Rogers, T.G. 748
- Rosen, J. 349, 390
- Rosenstein, R.A. 103
- Rosser, W.A. 464, 471, 475, 550
- Roth, J.F. 551
- Ronse, P.E. Jr. 746
- Rudin, M. 101
- Rumble, K.F. 391
- Rusoff, I.I. 601, 672
- Russell-Jones, A. 279, 331
- Ryan, N.W. 464, 468, 471, 491, 507,
550, 551, 552, 602, 603,
672
- Sabadell, A.J. 328
- Sack, H.S. 746
- Saderholm, C.A. 436, 456
- Sage, B.H. 600
- Salt, D.L. 491, 550
- Schapery, R.A. 712, 746, 747, 749
- Scheller, J.A. 104
- Schieler, L. 119, 183
- Schlichting, H. 104, 392, 456
- Schluter, P.M. 236, 251
- Schofield, A. 600
- Schultz, R.B. 268, 269, 328, 600, 671
- Schultz, R.D. 390, 391, 392
- Schwarzl, F. 746
- Scurlock, A.C. 282, 391
- Seader, J.D. 105, 553
- Sears, F.W. 100
- Segal, H.M. 230, 251
- Sehgal, R. 103, 601, 672
- Seifert, H.S. 105
- Selzer, H. 331
- Semonin, R.G. 103
- Serra, R.A. 102
- Sewell, C.J.T. 670
- Shafer, J.I. 35
- Shardor, M. 104, 105
- Shanfield, H. 601, 602
- Shannon, L.J. 282, 329, 551, 552
- Shapiro, A.H. 100
- Shinnar, R. 486, 551, 552, 601, 672
- Sibbett, D.H. 392
- Siegel, B. 119, 163
- Silla, M. 331
- Sirignano, W.A. 672
- Slates, R.O. 370
- Smith, A.G. 648, 672
- Smith, J.E. 101
- Smith, K.A. 553
- Smith, P.W. Jr. 670
- Smith, R.P. 600
- Smith, W.A. 316, 330, 600
- Sofferis, J.W. 602
- Soo, S.L. 103
- Sorlé, B. 390
- Sotter, G. 602
- Spaid, F.W. 104, 105, 603
- Spalding, D.B. 100, 359, 363, 366,
366, 369, 390
- Sprenger, D.F. 600
- Sternberg, E. 708, 746
- Stewartson, K. 670
- Stokes, G.G. 670
- Stollery, J.L. 101
- Stone, A.R. 104
- Stone, M.W. 250
- Strand, L. 601, 672
- Strittmater, R. 602
- Stuart, H.A. 746
- Summerfield, M. 35, 104, 250, 312, 328,
330, 392, 436, 446, 468,
478, 468, 507, 550, 551,
552, 745
- Sutherland, G.S. 250, 392
- Sutherland, J.E. 392
- Sutton, D. 478, 550
- Sutton, G.P. 35, 100, 105
- Swain, R.L. 250
- Swan, W.C. 104
- Swithenbank, J. 601, 602
- Taback, H.J. 546, 553
- Tabak, M.J. 250, 392
- Tanger, G.E. 251
- Tanno, M. 672
- Tavernier, P. 435, 455
- Temkin, S. 602, 671
- Ternier, 251
- Thackwell, H.L. 251
- Thibodaux, J.G. 230, 250
- Thompson, G.T. 552
- Tobolsky, A.V. 748
- Trubridge, G.F.P. 600

- Tsien, H.S. 617, 670
 Tsuji, H. 451, 456
 Turner, C.F. 184

 Vacelet, 251
 Van de Mark, D.K. 391, 392
 Vandenkerckhove, J. 35, 100, 101, 133, 250, 444, 456
 Van Tiggelen, 293, 318, 329, 390
 Veillacott, R.J. 251
 Vincenti, W.G. 101
 Volterra, V. 747
 Von Elbe, G. 119, 329

 Wachtell, G.P. 551
 Wagner, W.R. 105
 Walker, R.E. 104, 105
 Wall, R.H. 603
 Wang, J. 102
 Ward, I.M. 748
 Watermeier, L.A. 331, 602
 Webb, M.J. 250, 392
 Weigand, J.H. 740, 749
 Weinberg, 756
 Wellings, P.C. 550
 Wenograd, J. 328, 330, 551, 552
 Westenberg, A.A. 101
 Wheeler, A. 392
 White, W.B. 138, 141, 183
 Widder, D.V. 552
 Wiegand, J.H. 251
 Wilde, K.A. 102

 Wilfong, R.E. 250, 250, 390
 Williams, F.A. 100, 101, 183, 269, 328, 389, 391, 392, 552, 670, 672
 Williams, M.L. 739, 742, 745, 746, 748, 749, 750
 Wilson, H.B. Jr. 748
 Wimpres, R.N. 35, 454, 600
 Wirrick, T.K. 552
 Wirtz, D.P. 81, 105
 Wise, M. 464, 471, 550
 Wong, M.W. 331, 553
 Wood, W.A. 672
 Woodling, M.J.
 Wooldridge, C.E. 456
 Wright, G. 250
 Wrubel, J.A. 552
 Wu, J.M. 104

 Ying, S.J. 673
 Yount, R.A. 601, 672

 Zeldovich, Y.B. 35
 Zeuer, C. 746
 Ziegler, H. 747
 Zimm, B.H. 746
 Zimmerman, C.A. 250, 251
 Zink, J.W. 602, 671
 Ziolkowsky, 8
 Zucrow, M.J. 406, 426, 443, 455, 456
 Zukoski, E.E. 105, 183
 Zupnik, T.F. 102

Subject Index

AEROTHERMOCHEMISTRY

activation energy, 344
 approach to erosive burning, 446
 Arrhenius equation, 344
 chemical kinetics, 343
 chemical reaction rate, 334
 differential form, 341
 diffusion coefficient, 343
 diffusion velocities, 343
 energy flux vector, 343
 equations of, 339
 frequency factor, 344
 integral form, 339
 interface equations, 345
 reaction rates, 342
 shear stress tensor, 342
 thermal conductivity, 343
 thermodynamic relations, 344
 transport phenomena, 342
 viscosity, 342

BOOSTERS, 11

JATO, 15
 large, applications for, 763
 large, chamber pressure, 29
 large, segmentation, 27
 motor, 260 inch, 11
 motor, TITAN IIIc, 11
 space exploration, 763
 zero stage, 11

CASE, 4

development, 762
 glassy, 6
 liner, 6
 metallic, 6
 thermal insulation, 762
 wound, 6

CHILTON - COLBURN

coefficient, 440

COMBUSTION

absolute reaction rate theory, 357
 acceleration effect, 434
 accommodation coefficient, 360
 activated complex, 357
 activation energy, 279, 353
 adiabatic burning rate, 363
 adiabatic deflagration, 365
 adiabatic flame temperature, 369
 agglomeration, 384

air-augmentation, 763
 aluminium, 387
 AP burning rate, 363
 AP combustion, 306
 AP deflagration, 280
 AP flammability limit, 372
 AP particle size, 280
 AP pyrolysis, 273, 276, 279
 AP strands, 300
 atom conservation, 127, 69
 basis, 122
 burning rate, 353, 360, 363, 368, 756
 burning rate bounds, 354
 burning rate calculation, 355
 burning rate laws, 192, 300, 316, 381, 545
 burning rate control, acoustic field, 756
 burning rate control, electrostatic field, 756
 burning rate curves, 365
 burning rate measurements, 196
 burning surface evolution, 211, 212
 burning velocity, 191, 267, 406, 412
 burning velocity laws, 191, 267
 burn interruption technique, 410
 cap formation, 306, 386
 catalysts, 196, 282, 285, 290
 chamber, 3
 chamber mass, 243
 chamber pressure, 61, 62, 178
 chamber temperature, 62, 159
 chemical equilibrium, 127, 130, 66, 68
 chemical potential, 130
 Chilton-Colburn coefficient, 440
 condensed products, 384
 decomposition, 374
 deflagration, 192, 349
 deflagration limit, 366
 detonation, 192
 diffusion flame, 290, 306, 327, 379, 381
 dilute heterogeneous diffusion flame, 386
 droplet combustion (metals) 306
 dual-chamber motor, 761
 emissivity, 316
 end burning grain, 201
 energy conservation, 367
 erosive burning, semi-empirical theories, 439
 erosion function, 402, 410, 416, 425, 426, 435, 541

- erosion law, 412
- erosion threshold, 430, 434
- erosion threshold velocity, 435
- erosive burning, formulation of problem, 449
- erosive burning velocity
 - measurement, 410
- erosive combustion, 193, 401, 450
- erosive velocity, 401
- equilibrium compositions, 122, 147
- equilibrium compositions, calculations Brinkley method, 144
- equilibrium compositions, calculations, Huff method, 138
- equilibrium compositions, calculations, White method, 141
- equilibrium vapor pressure, 360
- equivalence ratio, 114
- evaporation coefficient, 360
- extinction, 323
- fizz zone, 258, 347
- flame height, 366
- flame structure (double base propellant) 258
- flame temperature, 302
- flammability limit, 319, 367, 548
- flashback, 302
- foam zone, 258, 265, 347
- fragmentation, 386
- friction coefficient, 444
- fuel, 113
- fuel pyrolysis, 276
- gas generator, 409
- gas-phase kinetics, 296
- gas-phase reaction zone, 366
- gas velocity, 425
- Gibbs free energy, 141
- heat losses, 366, 367, 368
- heat of vaporization, 365
- heterogeneous propellants, 757
- high pressure domain, 327, 328
- high pressure flammability limit, 372
- hot jet experiment, 276
- hot plate experiment, 269
- hot-plate pyrolysis, 375
- hybrid burner, 293
- hydrocarbon fuel droplet, 384
- ignition temperatures, 382, 385
- impermeable plate experiment, 268
- impermeable plate pyrolysis, 377
- instabilities, 30, 533, 759
- instability, theoretical analysis, 609
- linear pyrolysis rates, 268, 374
- liquid augmentation, 165
- liquid injection, 165
- low pressure domain, 318
- low-pressure flammability limit, 369
- mass flow rate, 191
- mass flow rate history, 453
- magnesium, 386
- mechanisms, 304
- metals, 304, 306, 382, 758
- metal agglomeration, 306
- metal alloys, 386
- metal melting temperature, 385
- metal solubility, 385
- metal sphere, 387
- metal volatility, 385
- metalized propellant, 306
- mixture ratio, 414, 409
- motor enthalpy, 130
- motor entropy, 130
- motor free energy, 130
- moderate pressure domain, 319
- motor extinction, 531
- motor ignition, 510
- motor tests, 197
- Muraour's law, 202
- negative erosion, 419, 426
- non-adiabatic burning, 366
- operating pressure, 192, 202
- optical techniques, 197
- oscillatory, erosive effects, 656
- oxidizer, 113
- oxidizer pyrolysis, 276
- partition function, 358
- plateau domain, 196, 323, 430
- plateau effect, 302
- polymethacrylate, 293
- polystyrene pyrolysis, 276
- port geometry history, 453
- preferred frequency oscillatory, 597
- premixed flames, 306, 327, 379, 381
- pressed strands, 296
- pressure history, 401, 412, 453
- pressure measurements, 173, 197
- porous burner, 296
- porous core burner, 290
- porous plate experiment, 269
- porous plate pyrolysis, 375
- quenched samples, 312
- radiative augmentation, 316
- reactants, 113
- reaction kinetics, 296
- reaction zone, 347
- regression rate, 380, 409
- research, 757
- residence time, 597
- restriction ratio, 201
- Reynolds analogy, 443

- Reynolds number, 290, 430, 46, 439
 sandwich burner, 382
 Saint-Robert's law, 192, 202
 "similarity" solutions, 451
 sphere combustion, 282
 spectrographic techniques, 316
 spin effect, 434
 stability condition, 201, 202, 203
 Stanton number, 443, 444
 standard heat of reaction, 122
 strand burner, 196
 Summerfield's law, 193, 202
 surface equilibrium, 359, 363
 surface gasification, 357
 surface rate processes, 359
 surface temperature, 302, 368, 379, 265, 316
 temperature profiles, 312
 temperature sensitivity, 193,
 thermal explosion, 596
 thermocouple measurement, 265
 threshold velocity (gas flow), 425
 time lag, 597
 transition state theory, 357
 turbulent flow, 450
 two-temperature concept, 380
 unopposed surface gasification, 360
 unopposed surface gasification rate, 357
 unsteady, 759
 vapor pressure, 365
 water gas reaction, 132
 Zeldovich, Frank-Kamenetski equation, 353
 zone structure, 260
- CONTROL** (see also **EXTINCTION**)
- BERENICE, 15
 control surfaces, 92
 dual-chamber motor, 761
 extinction, 531
 fluid injection, 92, 95, 548, 761
 gimbals, 92
 hot gas injection, 99
 hot gas valves, 99
 inhibitor injection, 548
 motors, 764
 powder injection, 549
 pulse rockets, 760
 side force, 92, 95, 96
 solid sublimation motors, 244
 thrust, 760
 thrust vector, 92, 762
 vane deflectors, 92
 wafer motors, 760
- COST**, 27
 economist's criterion, 240
 of development, 29, 764
- EXHAUST**
- external jet, 91
 heat transfer, 91
 plumes, 91
- EXTINCTION** (see also **CONTROL**), 531, 759
- burning rate law, 545
 combustion instabilities, 533, 548
 conditions, 533, 545, 548
 depressurization, 531, 533
 flammability limit, 548
 inhibitor injection, 548
 motor characteristic length, 545
 powder injection, 549
 pressure history, 541
 water injection, 548
- FANNO**
- line, 54
- FICK**
- law, 351
- FLEXIBILITY**, 760
- HISTORY**, 7
- HUYGEN**
- principle (optics), 211
- IGNITION/IGNITERS**, 3, 4, 463
- activation energy, 495
 aft injection, 517
 ammonium perchlorate, 4
 arc image, 469
 black powder, 510
 burning rate laws, 527
 catalysts, 486
 characteristic velocity, 511
 chlorine trifluoride, 515
 compositions, 511
 condensed materials, 505
 conductive, 464, 486
 conservation of energy, 514, 520, 524, 530
 conservation of mass, 514, 530
 convective, 463, 489
 criterion, 504, 508
 delay, 464, 471, 489, 492, 497
 delay, effect of atmosphere, 478

- delay, hypergolic, 503, 504, 515
- delay, pressure dependence, 478
- delay, pseudostationary, 498
- delay, radiant, 504, 505
- delay, time, thermal, 515
- design, 515
- diffusion, controlled limits, 504
- energy, 471
- equation of state, 514
- experiments, 483
- flame spread, 517, 522
- flame spread rate, 523, 525, 526
- forward injection, 517
- furnace, 464
- gas phase theory, 507
- gas residence time, 516
- 'Grashof' number, 493
- heat transfer, 520
- heat transfer, coefficient, 475, 489, 492, 520
- heterogeneous, 493
- heterogeneous theory, 509
- hot flow, 464
- hypergolic, 468, 515
- hypergolic liquid, 506
- laminar correction, 492
- Laplace transform, 525
- mass conservation, 517
- minimum exposure time, 464, 471, 491
- motor, 510
- Nusselt number, 520
- potassium nitrate, 511
- potassium perchlorate, 511
- potassium perchlorate/metal, 7
- pressure history, 510, 529
- pressure spike, 527
- processes, 759
- pyrogenic, 511
- pyrotechnic, 7, 511
- radiative, 463, 493
- rate controlled limits, 504
- reaction order, 495
- Reynolds number, 492
- shock tube, 464, 469
- solid phase theory, 507
- solid propellant, 510
- surface temperature, 483
- temperature, 383, 385, 489, 491
- theory, 486
- turbulent convection, 492
- acoustic amplitude, 578
- acoustic boundary layer, 623
- acoustic convection, 579, 641
- acoustic damping, 617
- acoustic energy, 613
- acoustic erosion, 656, 657, 659
- acoustic frequency, 578, 588
- acoustic generators, 572
- acoustic growth constant, 616
- acoustic modes, 560, 597, 609
- acoustic reflection coefficient, 634
- acoustic response, 572
- acoustic response, steady state erosion, 656
- acoustic scaling, 588
- acoustic transmission coefficient, 634
- acoustical energy flux, 614
- admittance theories, 645
- amplification mechanisms, 572
- amplitude, 593, 611
- antinodes, 611
- attenuation mechanisms, 572
- boundary damping, 623
- burning rate response, 640
- burning surface amplification, 639
- chemical relaxation, 628
- chuffing, 560, 593, 662
- data analysis, 565
- decay constant, 628
- Denison-Baum model, 648
- dilational modes, 638
- dilational sound speed, 636
- dissipation constant, 578
- double motors, 574
- end burning motors, 574
- energy conservation, acoustic, 614
- entropy waves, 641, 646
- equilibrium sound speed, 627
- erosive effects in oscillatory combustion, 656
- frequency, 593, 611
- frozen sound speed, 627
- gas modes, 636
- gas-solid oscillations, 636, 638
- growth constant (wave) 578, 632
- harmonic generation, 657
- Hart-McClure model, 645
- heat conduction damping, 626
- Helmholtz resonator, 582
- homogeneous amplification, 639
- homogeneous damping, 626, 638
- inherent, 661
- instrumentation, 566
- intermittent instabilities, 637
- intrinsic oscillations, 596
- intrinsic periodicities, 596

INSTABILITY

- acoustic, 560, 587
- acoustic admittance, 577, 614, 640
- acoustic amplification, 614, 639

- irregular burning, 559
 - isentropic sound waves, 610
 - jet noise generation, 639
 - L^* , 561, 760, 597, 664
 - Laplace transform, 662
 - limiting amplitude, 658
 - linear, 560
 - linear acoustic, 571
 - longitudinal modes, 613
 - low frequency, 593, 611
 - mean burning rate during oscillation, 659
 - mixed modes, 613
 - mixture ratio oscillations, 654
 - momentum conservation, 623
 - monochromatic waves, 610
 - nodal points, 611
 - nonacoustic, 560, 589, 592
 - nonlinear, 560, 589
 - nonsinusoidal wave forms, 665
 - nozzle admittance, 619, 620
 - nozzle damping, 617, 638
 - optical analysis, 566
 - oscillation frequency, 597
 - oscillatory combustion zone models, 645, 648
 - oscillatory combustion zone models, heterogeneous propellants, 653
 - particle damping, 572, 629, 638
 - particle radius, optimum, 632
 - peak amplitude, 579
 - periodic thermal explosion, 664
 - preferred frequency oscillatory combustion, 597
 - radial modes, 613
 - radiative energy transfer, 648
 - relaxation damping, 627
 - relaxation time, 628
 - residence time, 597
 - resonance, 560, 660, 662
 - resonance burning, 559
 - resonance rods, 559
 - response arbitrary frequencies, 651
 - response function, 586, 642, 650, 655
 - ring modes, 638
 - secondary peaks, 559
 - second order admittances, 666
 - sensitivity coefficient, 643
 - shear modes, 638
 - shear sound speed, 636
 - shock induced, 589, 665
 - shock tube techniques, 572
 - shock waves, 665
 - solid modes, 636
 - solid phase acoustic losses, 634
 - sonance, 560
 - sound speed, 610
 - standing waves, 611
 - Stokes drag law, 630
 - strand observations, 596
 - subsonic orifices, 622
 - suppression techniques, 559, 588
 - surface pyrolysis, 659
 - T-burners, 577
 - T-motors, 577
 - tangential modes, 613
 - temperature, response function, 641
 - theoretical analyses, 609
 - thermal conductivity (gas), 626
 - thermal explosion, 596, 664
 - thickness modes, 638
 - time lag, 642, 643
 - time lag, pressure-dependent, 643
 - time lag, surface distribution of, 654
 - time lag, theories, 642
 - transverse modes, 613
 - travelling waves, 612
 - velocity potential, 610
 - vibrational relaxation, 628
 - vibrations of gas-solid systems, 636
 - viscoelastic damping, 654
 - viscous damping, 626
 - vortex, 592
 - wall heat transfer damping, 625
 - wall friction damping, 623, 638
 - wave equation, 609
 - wave interference, 637
- IONIZATION**
- exhaust, 92
- KNUDSEN**
- relation, 244
- LEWIS**
- number, 352
- MISSILES**
- ENTAC, 18
 - FALCON, 18
 - HAWK, 18
 - HONEST JOHN, 18
 - MINUTEMAN, 15
 - NIKE HERCULES, 18
 - NIKE ZEUS, 18
 - PERSHING, 18
 - POLARIS, 18

SERGEANT, 18
 SPRINT A, 18
 SUBROC, 19
 TITAN II, 11
 TITAN IIc, 11

MISSION

performance evaluation, 19

MURAOUR,

law, 192, 202
 stability condition, 203

NOZZLE

ablation, 85
 ablative material, 85
 adiabatic wall temperature, 83
 admittance, 613
 agglomeration, 78
 aluminium oxide, 80
 annular, 99
 area ratio, 60, 156
 bell-shaped, 80
 boundary layer, 82
 boundary layer growth, 89
 ceramic throat inserts, 85
 characteristic lengths, 75
 characteristic velocity, 62, 156, 159
 choking, 51, 53
 condensation, 72, 78
 conical, 80
 contoured, 88
 convective heat transfer, 83
 convergent section, 7
 damping, 617
 de Laval, 51, 53
 deposition, 80, 81, 86
 design, 80, 81, 99
 displacement thickness, 89
 divergence losses, 80
 divergent section, 7
 double cone, 99
 drag, 73
 equilibrium flow, 156
 erosion, 78, 80, 81
 exhaust velocity, 58
 exit velocity, 68
 expansion-deflection, 99
 expansion ratio, 88
 flow, 51, 58
 free-stream conditions, 83
 heat flux, 82, 85
 heat transfer, 80, 81, 82
 heat transfer coefficient, 83, 84
 jet detachment, 90

laminar boundary layer, 89
 large lag limit, 76
 Mach number, 619
 mass, 243
 mass flow rate, 58
 method of characteristics, 86
 non-one-dimensional flow, 86
 normal shock, 53
 nucleation, 78
 oblique shock waves, 55, 57
 optimum contours, 80
 overall heat transfer coefficient, 85
 particle lag, 71, 73
 plug, 99, 762
 Prandtl-Meyer expansion, 55
 radiative heat transfer, 78, 86
 rarefaction fan, 58
 recovery factor, 83
 residence time, 75
 restriction ratio, 201
 shock waves (in nozzle), 53
 skin friction, 82
 small lag limit, 77
 sudden freezing, 71
 temperature lag, 72, 81
 thermal conductivity, 82
 throat, 7
 throat area, 61
 thrust coefficient, 90
 turbulent boundary layer, 82
 turbulent heat transfer, 83
 two-dimensional flow, 78
 two phase flow, 71, 73
 unsteady heat conduction, 82
 variable thrust, 762
 velocity lag, 72, 81

PARAMETERS

aerothermochemistry, 339
 atom conservation, 69, 127
 Brownian motion, 72
 caloric equation of state, 40, 344
 characteristic, 43
 chemical equilibrium, 66, 68, 129
 chemical potential, 66, 130
 chemical reaction rate, 344
 conservation of energy, 340, 367
 conservation of mass, 340, 341
 conservation of momentum, 340
 control volume, 44
 Daltons law, 131
 density, 44
 displacement work, 47, 48
 drag, 46
 drag coefficient, 48
 energy conservation, 47, 74, 75, 367

enthalpy, 44, 73
 enthalpy of formation, 66
 entropy, 48, 66
 entropy of mixing, 66
 equation of state, 49, 67, 72, 74, 152, 344
 equilibrium constant, 68
 equilibrium flow, 66, 68
 equilibrium sound speed, 152, 627
 equilibrium specific heat, 153
 equivalence ratio, 114
 evaporation coefficient, 244
 external work, 47
 friction coefficient, 444
 friction factor, 46
 frozen flow, 66, 67
 frozen sound speed, 152, 627
 frozen specific heat, 152
 heat, 47
 heat capacity, 49
 heat conduction, 74
 hydraulic diameter, 46
 ideal gas, 49
 influence coefficients, 157
 internal energy, 44, 47, 48
 irreversible thermodynamics, 701
 isentropic flow, 48
 kinetic energy, 47
 Knudsen's relation, 244
 lag, 75
 Laplace transform, 490, 495, 693, 709
 Mach number, 49
 mass conservation, 44, 73
 mass flow factor, 62
 mass flow fraction, 72
 mass flow rate, 44
 mass flux fraction, 73
 mass fraction, 114, 343
 molar enthalpy, 130
 molar entropy, 130
 molar free energy, 130
 mole fraction, 66, 344
 molecular weight, 64, 113, 344
 momentum conservation, 44
 Nusselt number, 84
 partial pressures, 131
 partition function, 358
 Prandtl number, 83
 pressure, 44, 46
 radiant energy transfer, 388
 Radok's correspondence principle, 711
 ratio specific heats, 49, 152
 reaction kinetics, 296
 Reynolds analogy, 443
 Reynolds number, 46, 290, 430, 439

Schmidt number, 84
 sound speed, 610
 species conservation, 340
 specific heat, 49, 72
 specific heat ratio, 73
 stagnation density, 50
 stagnation enthalpy, 48
 stagnation pressure, 50
 stagnation temperature, 50
 Stanton number, 443
 Stokes drag law, 630
 temperature, 48, 75
 thrust decay loss, 321
 total temperature, 50
 vapour pressure, 244, 365
 velocity (see VELOCITY) 44, 75
 velocity of sound, 49
 viscosity, 46

PERFORMANCE, 156, 159, 113, 154

adiabatic flame temperature, 154
 ballistic equations, 240
 calculations, 154
 characteristic velocity, 156, 159, 178, 179
 criteria, 21
 effective exhaust velocity, 22, 65
 engineers criterion, 240
 equilibrium composition, 122
 equilibrium nozzle flow, 156
 experimental determination, 165
 flexibility, 30
 frozen nozzle flow, 156
 impulse, 64
 influence coefficients, 157
 L^* (chamber vol/throat area), 65
 mass flow rate, 179, 191
 mass fractions, 65
 mass ratio, 21, 241
 mission evaluation, 19
 propellant, 147
 quality indices, 179, 182
 sample analysis, 135
 specific fuel consumption, 65
 specific impulse, 22, 29, 30, 62, 81, 116, 156, 159, 178, 179
 structural index, 241
 total impulse, 64
 volumetric specific impulse, 23, 29, 65

PROPELLANT

air-augmentation, 763
 aluminium, 304
 ammonium nitrate, 119
 ammonium perchlorate, 118, 316, 754

- AP, 115
 - atom conservation, 127, 69
 - base, 114
 - beryllium powder, 304, 754
 - binder modification, 165
 - burning rate, 756
 - burning rate control, acoustic field, 756
 - burning rate control, electrostatic field, 756
 - catalysts, 116
 - chemical equilibrium, 127, 130, 66, 68
 - chemical potential, 130
 - composite, 306, 316
 - cryogenic, solid, 755
 - dual composition, 230
 - encapsulation, 755
 - energetic binders, 121
 - energetic qualities, 753, 754
 - evaporation coefficient, 244, 248
 - fuels, 118
 - grain geometry, 211
 - heat of formation, 118
 - heater, 248
 - heterogeneous propellant combustion, 379
 - heterogeneous solid, 114, 116, 118, 257, 757
 - homogeneous solid, 114, 257, 258, 757
 - hydrazine perchlorate, 118, 280
 - JPN, 445
 - kinetic qualities, 753, 756
 - Knudsen number, 248
 - lithium perchlorate, 119
 - mass, 243
 - mass fraction, 115
 - metallic hydrides, 754
 - mixture ratio, 115, 116
 - molar enthalpy, 130
 - molar entropy, 130
 - molar free energy, 130
 - monopropellants, 280, 349
 - nitric ester-based, 316
 - nitronium perchlorate, 118, 280
 - opacifier, 116
 - overall mixture ratio, 115
 - oxidizers, 118
 - oxidizers, new, 755
 - polybutadiene, 754
 - polybutadiene-acrylic-acid (PBAA) 121
 - polyethylene binder, 121
 - polysulfide binders, 118
 - polyurethane binders, 118
 - potassium perchlorate, 119
 - PU, 115
 - pyrolysis, 377
 - regression rate, 316, 351
 - single base, 114
 - solid, future of, 753
 - solid, military applications, 763
 - solid, new uses, 763
 - solid sublimation, 244
 - stoichiometric mixture ratio, 115
 - stabilizers, 116
 - studies, experimental, 264
 - surface temperature, 316
 - temperature profiles, 312
 - thermodynamic properties, 147
 - utilization qualities, 753, 756
 - vapor pressure, 244
 - volume fractions, 121
- PROPELLANT, Composite, 115, 257**
- aluminium oxide, 80
 - ammonium perchlorate/aluminium, 4
 - black powder, 8
 - GALCIT, 8
 - HC-NP-AL-26
 - molecular weight, 113
 - overall equivalence ratio, 115
 - PBAA, 18
 - PU-AP-AL, 26
 - UDMH-N₂O₄, 26
- PROPELLANT, Double-base, 114, 134, 257, 349**
- aluminized double-base, 138
 - flame structure, 258
 - heterogeneous, 257
 - homogeneous, 258
 - nitrocellulose/nitroglycerin, 4, 114
 - smokeless powder, 8
- PROPELLANT, Fuel, 4, 113**
- additives, 164
 - ammonia, 302
 - ammonium perchlorate, 4
 - benzoic acid, 302
 - carbon, 302
 - formaldehyde, 302
 - hydrazine, 165
 - hydrocarbon droplet combustion, 384
 - hydrogen, 165
 - polyformaldehyde, 303
 - polymethylmethacrylate, 378, 716
 - polystyrene, 302
 - propane, 302
 - pyrolysis, 276
 - stearic acid, 302

PROPELLANT, Grain, 3, 4

- average curvatures, 211
- axially non-uniform, 222
- Boltzmann superposition principle, 690
- bulk modulus, 689
- bulk relaxation modulus, 694
- burning surface evolution, 211, 212
- complex bulk compliance, 696
- complex bulk modulus, 696
- complex compliance, 695
- complex compliance representations, 695
- complex modulus, 695
- complex modulus representations, 695
- complex shear compliance, 696
- complex shear modulus, 696
- crack formation, 736
- crack propagation, 736
- crack propagation velocity, 739
- creep, 685
- creep compliance, 690
- critical strain, 740
- critical strain energy, 744
- cumulative damage, 740
- cylinder with ablating cavity surface, 715
- cylindrical, 6
- deformations, 683
- delayed elastic modulus, 693
- differential operator representation, 688
- dual burning rate configuration, 228, 229
- dual composition, 236
- elastic modulus, 689
- empirical failure criteria, 740
- end closures, geometry, 221
- failure, 683, 734
- failure analysis, 684
- failure criteria, 734, 740
- failure time, 743
- fatigue, 740
- finite-difference analysis, 685
- finite-element analysis, 685
- geometry, 211
- Gibbs free energy, 702
- glassy compliance, 691
- helical configuration, 226
- Helmholtz free energy, 702
- Hooke's law, 694
- integral operator representation, 690
- irreversible thermodynamics, 701
- Kelvin model, 688
- Lamé's constants, 694
- Laplace transform, 693, 709
- linear regression rate, 3
- linear viscoelasticity, 685
- loading fraction, 221
- loss compliance, 696
- loss modulus, 696
- mass flow rate history, 453
- maximum permissible strain, 744
- mechanical properties, 683
- mechanical properties, 30
- neutral, 4
- neutral star geometry, 236
- nonlinear stress-strain relations, 704
- Onsager's principle, 702
- photoelasticity, 685
- Poisson's ratio, 689, 695
- polybutadiene binder, 754
- polymer, 698
- polymethylmethacrylate, 716, 727, 744
- port, 401
- port geometry, 452
- port geometry history, 453
- pressure history, 453
- progressive, 4
- propellant mass, 243
- quenched, 588
- Radock's correspondence principle, 711
- recess-type singularity, 214
- redundant force analysis, 685
- regressive, 4
- relaxation modulus, 691
- relaxation time, 693
- retardation spectrum, 691
- Rouse's model, 698
- rubbery modulus, 693
- segmented grains, 221
- shear modulus, 689
- shear relaxation modulus, 694
- shift factor, 699
- slenderness ratio, 243
- sliver loss, 221
- slotted grains, 222
- slump due to axial acceleration, 726
- spherical, 6
- spherical configurations, 225, 226, 227
- spike-type singularity, 214
- star configuration, 217
- storage, 734
- storage compliance, 696
- storage modulus, 696
- strain, 688

- strain response, 685
 - stress analysis, 683, 684
 - stress analysis for non-isothermal viscoelastic cylinders, 722
 - stress analysis in linear viscoelasticity, 708
 - stress functional, 705
 - stresses in encased viscoelastic cylinder, 713
 - stress in encased viscoelastic spinners, 715
 - stress relaxation, 685
 - stress-strain relations, 683
 - temperature dependence of viscoelastic properties, 697
 - thermorheological simplicity, 699
 - thrust decay loss, 221
 - thrust tail-off, 230
 - total curvatures, 211
 - tubular, 684
 - viscoelasticity, 685
 - viscoelastic cylinder reinforced by elastic wires, 729
 - viscoelastic materials, 683
 - Voigt model, 688
 - wagon-wheel configuration, 217
- PROPELLANT, Manufacture, 30**
- casting, 30
- PROPELLANT, Oxidizer, 4, 113**
- ammonium nitrate, 287, 378, 757
 - ammonium perchlorate, 4, 287, 293, 349, 757, 379
 - AP combustion, 287
 - AP deflagration, 280
 - AP particle size, 280
 - AP spheres, 287
 - AP strands, 300
 - constant, 287
 - decomposition flame, 383
 - deflagration, 280
 - deflagration rates, 280
 - encapsulation, 755, 758
 - hydrazine dperchlorate, 755
 - hydrazine perchlorate, 757
 - nitronium perchlorate, 755
 - nitronium perchlorate, 165
 - oxidizer spheres, 282
 - perchloric acid, 296
 - potassium nitrate, 287
 - potassium perchlorate, 287
 - pyrolysis, 278
 - studies, 165
- RAYLEIGH**
- Line, 54
- RECOMBINATION, 69**
- RELIABILITY, 29**
- SAINT-ROBERTS**
- law, 192
- SATELLITES**
- launchers, 14
 - SYNCOM, 12
- STORABILITY, 29, 734**
- SUMMERFIELD**
- law, 193, 202, 319
- TESTING, TEST EQUIPMENT**
- accelerometers, 565
 - acoustic generators, 572
 - diaphragm gauges, 563
 - double motors, 574
 - electronic compensation, 564
 - end burning motors, 574
 - experimental techniques, 264
 - hybrid burner, 293
 - instability analysis, optical, 566
 - instability instrumentation, 566
 - ionization gauge, 412
 - laboratory measurement of erosion function, 402
 - line reversal, 264
 - measurement of erosive burning velocity, 410
 - micro-cinematography, 304, 571
 - microphones, 565
 - motor operating characteristics, 201
 - operating pressure, 202
 - optical techniques, 197
 - oscilloscope recording, 565
 - phototube measurements, 571
 - piezoelectric gauges, 563
 - porous burner, 296
 - post-test analysis, 565, 566
 - pressed strands, 296
 - pressure measurements, 561
 - pressure transducers, 563
 - pyrolysis, 276, 273, 262, 269, 279, 377
 - radiographic techniques, 411
 - real time analysis, 565, 566
 - recording techniques, 564
 - regression rate, gas generator, 409

rocket motor, 178, 197
 shock tube techniques, 572
 spectrographic techniques, 316
 stands, 178
 static firing, 178
 strain gauges, 563
 surface temperature (pyrolysis)
 379
 tape recording, 565
 thrust gauges, 565
 T - burners, 577
 T - motors, 577
 vibration gauges, 555

WEIGHT

at launch, 19
 engineer's criterion, 240
 mass ratio, 241
 structural index, 241

THEORY

absolute reaction rate, 357,
 equilibrium sublimation hypothesis,
 302
 hydrocarbon fuel droplet com-
 bustion, 384
 quasi-one dimensional fluid flow
 43
 semi-empirical, of erosive
 burning, 439
 transition state, 357
 two-temperature hypothesis, 280

THRUST, 60, 61, 530

axial, 60
 coefficient, 61, 90, 156, 178
 control, 760
 increase, air augmentation, 763
 termination, 7
 testing, 178
 vector control, 92, 762

VEHICLES, 11

ARCAS, 14
 BERENICE, 15
 GEMINI, 12
 NIKE - CAJON, 14
 SCOUT, 14
 SEREB Diamant launcher, 12
 sounding rockets, 14
 space, 12
 SURVEYOR, 12

VELOCITY

change in (mission), (see
 PARAMETERS), 19
 characteristic, 62
 measurement, 173